DTIC FILE COPY

(2)

DNA EM-1
PART I

DEFENSE NUCLEAR AGENCY EFFECTS MANUAL NUMBER 1

CAPABILITIES OF NUCLEAR WEAPONS

Document released under the Freedom of Information Act, DNA Case No. 86-1273

AD-A955 403

1 JULY 1972

HEADQUARTERS
Defense Nuclear Agency
Washington, D.C. 20305

DTIC ELECTE S D 1989 E

This document has been approved for public release and sale; its distribution is unlimited.

89 3 02 029

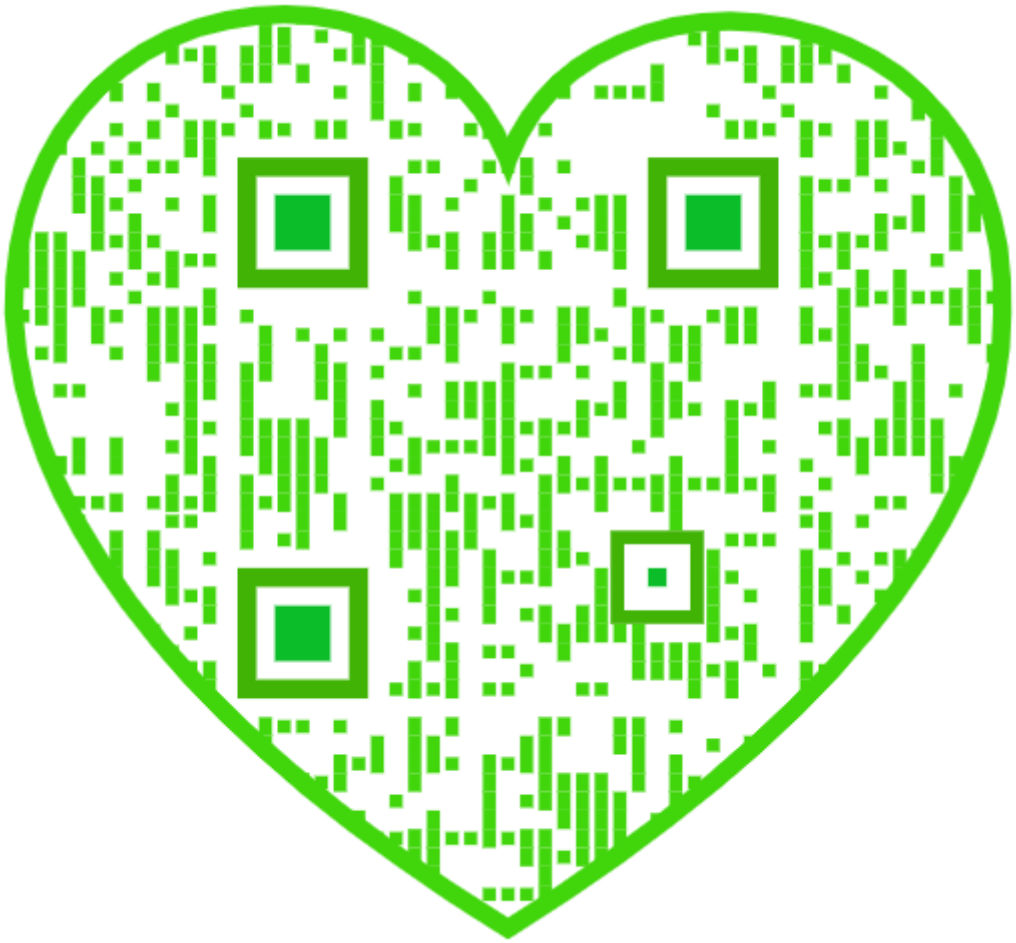

DNA EM-1
PART I
CHANGE 1
1 JULY 1978

DEFENSE NUCLEAR AGENCY EFFECTS MANUAL NUMBER 1

CAPABILITIES OF NUCLEAR WEAPONS

PART I PHENOMENOLOGY

HEADQUARTERS
Defense Nuclear Agency
Washington, D.C. 20305

EDITOR
PHILIP J. DOLAN
SRI INTERNATIONAL

LIST OF EFFECTIVE PAGES

The following is a list of current pages for Part 1, *Phenomenology*, of DNA Effects Manual Number 1 (DNA EM-1), *Capabilities of Nuclear Weapons*. When applicable, insert latest change pages, dispose of superceded pages in accordance with applicable regulations.

Total number of pages in this part of the Handbook is , consisting of the following:

i through ii ..... change 1
iii through xlii ..... original
xliii through xliv ..... change 1
xlv through xlviii ..... original
1-1 through 1-30 ..... original
2-1 through 2-276 ..... original
3-1 through 3-114 ..... original
4-1 through 4-50 ..... original
5-1 through 5-144 ..... original
5-145 through 5-152 ..... change 1
6-1 through 6-4 ..... original
6-5 through 6-8 ..... change 1
6-9 through 6-16 ..... original
7-1 through 7-40 ..... change 1
8-1 through 8-94 ..... original

DNA EM-1
PART I
CHANGE 2
1 AUGUST 1981

DEFENSE NUCLEAR AGENCY EFFECTS MANUAL NUMBER 1

CAPABILITIES OF NUCLEAR WEAPONS

PART I PHENOMENOLOGY

HEADQUARTERS
Defense Nuclear Agency
Washington, D.C. 20305

EDITOR
PHILIP J. DOLAN
SRI INTERNATIONAL

LIST OF EFFECTIVE PAGES

The following is a list of current pages for Part I, *Phenomenology*, of DNA Effects Manual Number 1 (DNA EM-1), *Capabilities of Nuclear Weapons*. When applicable, insert latest change pages; dispose of superceded pages in accordance with applicable regulations.

Total number of pages in this part of the Handbook is consisting of the following:

i through ii	change 2
iii through vi	original
vii through viii	change 2
ix through xxii	original
xxiii through xxv	change 2
xxv-a through xxv-b	change 2
xxvi	change 2
xxvii through xl	original
xli through xlii	change 2
xliii through xliv	change 1
xlv through xlvi	change 2
xlvii through xlviii	original
1-1 through 1-30	original
2-1 through 2-146	original
2-147 through 2-204	change 2
2-205 through 2-304 (Renumbered from 2-177 through 2-276)	original
3-1 through 3-114	original
4-1 through 4-50	original
5-1 through 5-144	original
5-145 through 5-152	change 1
6-1 through 6-4	original
6-5 through 6-8	change 1
6-9 through 6-16	original
7-1 through 7-40	change 1
8-1 through 8-94	original

[redacted]

DNA EM-1

HEADQUARTERS
DEFENSE NUCLEAR AGENCY
WASHINGTON, D.C. 20305

1 July 1972

EFFECTS MANUAL NUMBER 1

CAPABILITIES OF NUCLEAR WEAPONS [redacted]

The Revised Edition January 1968, *Capabilities of Nuclear Weapons* [redacted], DASA EM-1 is hereby superseded and cancelled.

With the concurrence of the Military Services, this document was redesignated DASA Effects Manual Number 1 (DASA EM-1) by action of the Joint Chiefs of Staff on 8 July 1966. With the change of the Defense Atomic Support Agency to the Defense Nuclear Agency on 1 July 1971, this document was redesignated the DNA Effects Manual Number 1 (DNA EM-1). Publication and initial distribution of future changes and revisions of this document will be effected by the Defense Nuclear Agency.

FOR THE DIRECTOR:

John A. Northrop

JOHN A. NORTHROP
Deputy Director (Science & Technology)

[redacted]

[redacted]

FOREWORD

This edition of the *Capabilities of Nuclear Weapons* represents the continuing efforts by the Defense Nuclear Agency to correlate and make available nuclear weapons effects information obtained from nuclear weapons testing, small-scale experiments, laboratory effort and theoretical analysis. This document presents the phenomena and effects of a nuclear detonation and relates weapons effects manifestations in terms of damage to targets of military interest. It provides the source material and references needed for the preparation of operational and employment manuals by the Military Services.

The *Capabilities of Nuclear Weapons* is not intended to be used as an employment or design manual by itself, since more complete descriptions of phenomenological details should be obtained from the noted references. Every effort has been made to include the most current reliable data available on 31 December 1971 in order to assist the Armed Forces in meeting their particular requirements for operational and target analysis purposes.

Comments concerning this manual are invited and should be addressed:

Director
Defense Nuclear Agency
ATTN: STAP
Washington, D. C. 20305

C. H. DUNN
Lt General, USA
Director

[redacted]

[redacted]

TABLE OF CONTENTS

PART I PHENOMENOLOGY

CHAPTER 1 INTRODUCTION [redacted]

	Page
PURPOSE	1-1
CHARACTERISTICS OF NUCLEAR EXPLOSIONS	1-1
1-1 Fission Energy and the Chain Reaction	1-2
1-2 Fusion (Thermonuclear) Reactions	1-4
1-3 Weapon Yield Ratings	1-5
1-4 Effects of Environment and Time	1-6
1-5 Early Time History	1-6
AIR BURST	1-7
1-6 Development	1-7
1-7 Thermal Radiation	1-9
1-8 The Blast Wave	1-9
1-9 Nuclear Radiation	1-11
1-10 Electromagnetic Pulse	1-11
1-11 Electromagnetic Wave Propagation	1-11
1-12 The Cloud	1-12
THE SURFACE BURST	1-12
1-13 Ground Shock	1-12
1-14 The Crater	1-12
1-15 Thermal Radiation	1-12
1-16 Initial Nuclear Radiation	1-12
1-17 Residual Nuclear Radiation	1-14
1-18 Electromagnetic Pulse (EMP) Radiation	1-14
1-19 Electromagnetic Wave Propagation	1-14
1-20 The Cloud	1-14
1-21 Water Surface Bursts	1-14
THE TRANSITION ZONE BETWEEN AN AIR BURST AND A SURFACE BURST	1-14
THE HIGH-ALTITUDE BURST	1-15
1-22 Description	1-15
1-23 Development	1-15
1-24 The Blast Wave	1-17
1-25 Thermal Radiation	1-19
1-26 Nuclear Radiation	1-19
1-27 Electromagnetic Pulse	1-19
1-28 Electromagnetic-Wave Propagation	1-19

ERRATA entered. [redacted] 5/23/88

[redacted]

TABLE OF CONTENTS (Continued)

CHAPTER 1 INTRODUCTION [redacted] (Continued)

	Page
THE UNDERGROUND BURST	1-20
1-29 Development	1-20
1-30 Air Blast	1-20
1-31 Column, Cloud, and Base Surge	1-20
1-32 Ground Shock	1-20
1-33 Crater	1-20
1-34 Thermal and Nuclear Radiation	1-23
1-35 Electromagnetic Pulse	1-23
THE UNDERWATER BURST	1-23
1-36 Development	1-23
1-37 Water Shock Waves and Other Pressure Pulses	1-27
1-38 Air Blast	1-27
1-39 Surface Effects	1-27
1-40 Thermal and Nuclear Radiation	1-29
1-41 Electromagnetic Pulse	1-29
BIBLIOGRAPHY	1-30

CHAPTER 2 BLAST AND SHOCK PHENOMENA [redacted]

INTRODUCTION	2-1
SECTION I AIR BLAST PHENOMENA	2-1
RELIABILITY	2-2
2-1 Interpretation of Reliability Statements	2-3
2-2 Errors Due to Yield Scaling	2-3
2-3 Errors Due to Altitude Scaling	2-3
2-4 Errors at Long Ranges	2-3
2-5 Effects of the Earth's Surface	2-3
2-6 Effect of Weapon Characteristics	2-3
BLAST WAVE CALCULATIONS IN FREE AIR	2-4
2-7 Peak Overpressure	2-4
2-8 Peak Dynamic Pressure	2-4
2-9 Time of Arrival	2-5
2-10 Duration of the Positive Phases of Overpressure and Dynamic Pressure	2-5
2-11 Impulse	2-5
2-12 Waveforms	2-17

[redacted]

DNA EM-1
PART I
1 JULY 1972

DEFENSE NUCLEAR AGENCY EFFECTS MANUAL NUMBER 1

CAPABILITIES OF NUCLEAR WEAPONS

PART I PHENOMENOLOGY

HEADQUARTERS
Defense Nuclear Agency
Washington, D.C. 20305

EDITOR
PHILIP J. DOLAN
STANFORD RESEARCH INSTITUTE

Accession For
NTIS GRA&I
DDC TAB
Unannounced
Justification
By
Distribution/
Availability Codes
Dist | Avail and/or Special
A-1

UNANNOUNCED

SPECIAL

TABLE OF CONTENTS (Continued)

CHAPTER 2 BLAST AND SHOCK PHENOMENA [redacted] (Continued)

	Page
2-69 Bottom Reflection	2-~~198~~ 226
2-70 Secondary Shocks and Pressure Waves	2-~~198~~ 226
2-71 Refraction of Shock Waves	2-~~200~~ 228
2-72 Air Blast	2-~~203~~ 231
SURFACE EFFECTS OTHER THAN WAVES	2-~~203~~ 231
2-73 Spray Dome	2-~~214~~ 242
2-74 Plumes, Column, Cauliflower Cloud	2-~~214~~ 242
2-75 Base Surge	2-~~214~~ 242
2-76 Foam Patch and Ring	2-~~215~~ 243
WATER SURFACE WAVES	2-~~216~~ 244
2-77 Generation and Propagation of Water Surface Waves	2-~~216~~ 244
2-78 Refraction and Shoaling	2-~~223~~ 251
UNDERWATER CRATERING	2-~~223~~ 251
BIBLIOGRAPHY	2-~~270~~ 298

CHAPTER 3 THERMAL RADIATION PHENOMENA [redacted]

RADIANT EXPOSURE	3-1
3-1 Thermal Partition	3-2
3-2 Range Effects	3-5
TRANSMITTANCE	3-5
3-3 Specification of Transmittance	3-5
3-4 Model Atmospheres	3-6
3-5 Effects of Clouds and Reflecting Surfaces	3-27
3-6 Transmittance to Targets Above the Surface	3-30
3-7 Visual Range	3-33
3-8 Nighttime Visual Range	3-36
APPROXIMATE CALCULATIONS OF RADIANT EXPOSURE	3-37
SURFACE AND SUBSURFACE BURSTS	3-42
3-9 Surface Bursts	3-42
3-10 Subsurface Bursts	3-42
THE THERMAL PULSE	3-46
3-11 Thermal Power-Time Curve	3-46
3-12 Energy-Time Curve	3-46

[redacted]

TABLE OF CONTENTS (Continued)

CHAPTER 5 NUCLEAR RADIATION PHENOMENA [redacted] (Continued)

	Page
FALLOUT	5-65
5-15 Early Fallout	5-65
5-16 Air Bursts	5-66
5-17 Land Surface Bursts	5-66
5-18 Deposition Patterns	5-67
5-19 Idealized Contours	5-67
5-20 Dose Rate Contour Dimensions	5-70
5-21 Decay of Early Fallout	5-72
5-22 Bursts in the Transition Zone	5-75
5-23 Underground Bursts	5-76
5-24 Beta Radiation	5-76
RESIDUAL RADIATION FROM WATER SURFACE AND UNDERWATER BURSTS	5-104
5-25 Water Surface Bursts	5-104
5-26 Underwater Bursts	5-106
DOSE RECEIVED WHILE FLYING THROUGH A NUCLEAR CLOUD	5-139
PRECIPITATION EFFECTS	5-145
5-27 Precipitation Scavenging	5-145
5-28 Prediction of Ground Contamination from Precipitation Effects	5-146
5-29 Some Specific Examples of Possible Contamination Resulting from Precipitation	5-148
BIBLIOGRAPHY	5-154

CHAPTER 6 TRANSIENT-RADIATION EFFECTS ON ELECTRONICS (TREE) PHENOMENA [redacted]

INTRODUCTION	6-1
ENVIRONMENT	6-3
6-1 Weapon Output	6-3
6-2 Time Considerations	6-4
6-3 Description of Radiation Fields	6-4
INTERACTIONS BASIC TO TREE	6-6
6-4 Ionization	6-6
6-5 Displacement	6-8
6-6 Heating	6-10

[redacted]

TABLE OF CONTENTS (Continued)

CHAPTER 4 X-RAY RADIATION PHENOMENA [redacted] (Continued)

		Page
SECTION II	X-RAY ENVIRONMENTS PRODUCED BY NUCLEAR WEAPONS	4-25
4-9	Exoatmospheric (Vacuum) Detonations	4-25
4-10	Endoatmospheric Detonations	4-25
4-11	The Standard Atmosphere	4-25
4-12	Direct X-Ray Fluence in the Atmosphere	4-27
4-13	Scattered X-Ray Fluence	4-30
4-14	Low Altitude Endoatmospheric Detonations	4-30
4-15	High Altitude Endoatmospheric Detonations	4-39
BIBLIOGRAPHY		4-48

CHAPTER 5 NUCLEAR RADIATION PHENOMENA [redacted]

INTRODUCTION		5-1
SECTION I	INITIAL NUCLEAR RADIATION	5-1
NEUTRONS		5-2
5-1	Neutron Source	5-2
5-2	Exoatmospheric (Vacuum) Transport	5-5
5-3	Neutron Transport Through Materials	5-5
GAMMA RAYS		5-17
5-4	Gamma Ray Sources	5-17
5-5	Prompt Gamma Rays	5-18
5-6	Air-Ground Secondary Gamma Rays	5-22
5-7	Fission Product Gamma Rays	5-23
INITIAL RADIATION DOSE TO PERSONNEL		5-24
5-8	Initial Neutron Dose	5-24
5-9	Air-Ground Secondary Gamma Ray Dose	5-25
5-10	Fission Product Gamma Ray Dose	5-25
5-11	Total Dose	5-25
SECTION II	NEUTRON-INDUCED ACTIVITY IN SOILS	5-52
5-12	Height of Burst	5-52
5-13	Soil Types	5-52
5-14	Dose Rate and Dose Predictions	5-55
SECTION III	RESIDUAL RADIATION	5-65

TABLE OF CONTENTS (Continued)

CHAPTER 3 THERMAL RADIATION PHENOMENA [redacted] (Continued)

Page

3-13 The Standard Thermal Pulse 3-46
3-14 Effect of Thermal Pulse Duration 3-52
3-15 Effect of Altitude on Pulse Shape 3-52
3-16 The Effects of Thermal Pulse Specifications on Thermal Partition 3-52

FIREBALL BRIGHTNESS 3-55

THE THERMAL PULSE FROM SPECIAL WEAPONS 3-56
3-17 Effective Thermal Yield of Special Weapons 3-57
3-18 Thermal Pulse Shape from Special Weapons 3-59

HIGH ALTITUDE THERMAL PHENOMENA 3-63
3-19 Thermal Partition 3-63
3-20 High Altitude Thermal Pulse Duration 3-64
3-21 Bursts Above 250 Kilofeet 3-70

RELIABILITY OF THERMAL SOURCE DATA 3-72

RELATION OF RADIANT EXPOSURE TO PEAK OVERPRESSURE 3-74

PHYSICS OF FIREBALL DEVELOPMENT 3-104
3-22 Black Body Radiation 3-104
3-23 Opacity 3-104
3-24 The Fireball Before Final Maximum 3-105
3-25 History of Fireball Evolution 3-107
3-26 Comparison with Recent Analysis of Experiments 3-109

BIBLIOGRAPHY 3-113

CHAPTER 4 X-RAY RADIATION PHENOMENA [redacted]

INTRODUCTION 4-1
4-1 Production of X-Rays 4-1
4-2 Black Body Radiation 4-3
4-3 Interactions of X-Rays with Matter 4-8

SECTION I NUCLEAR WEAPONS AS X-RAY SOURCES 4-9
4-4 X-Ray Production in Nuclear Weapons 4-9
4-5 X-Ray Energy Emitted 4-11
4-6 Rate of X-Ray Emission 4-11
4-7 Spectral Distribution of X-Rays 4-12
4-8 Real Nuclear Weapons as X-Ray Sources 4-12

[redacted]

TABLE OF CONTENTS (Continued)

CHAPTER 6 TRANSIENT RADIATION EFFECTS ON ELECTRONICS (TREE) PHENOMENA [redacted] (Continued)

Page

MANIFESTATIONS OF TREE IN MATERIALS 6-10
6-7 Ionization Effects 6-10
6-8 Displacement Effects 6-13
6-9 Heating Effects 6-14
BIBLIOGRAPHY 6-16

CHAPTER 7 ELECTROMAGNETIC PULSE (EMP) PHENOMENA [redacted]

ENVIRONMENT – GENERAL DESCRIPTION 7-1
7-1 Weapon Gamma Radiation 7-1
7-2 Compton Current 7-2
7-3 Air Conductivity 7-2
7-4 Radial Electric Field 7-2
ELECTROMAGNETIC FIELD GENERATION 7-5
7-5 Medium Altitude Air Burst 7-5
7-6 Surface Burst 7-9
7-7 High Altitude Burst 7-11
INTERNAL EMP 7-15
7-8 General Description 7-15
7-9 IEMP Generation 7-15
7-10 Problem Definition 7-17
COMPUTER CODE DESCRIPTIONS 7-17
7-11 Code Utility 7-17
7-12 Code Classes 7-18
SYSTEMS EFFECTS 7-18
7-13 System Definitions 7-18
7-14 Threat Definition 7-19
7-15 Effects Comparisons 7-20
BIBLIOGRAPHY 7-32

CHAPTER 8 PHENOMENA AFFECTING ELECTROMAGNETIC WAVE PROPAGATION [redacted]

INTRODUCTION 8-1

[redacted]

TABLE OF CONTENTS (Continued)

CHAPTER 8 PHENOMENA AFFECTING ELECTROMAGNETIC WAVE PROPAGATION [redacted] (Continued)

Page

SECTION I PHENOMENA AFFECTING RADIO FREQUENCIES 8-2

IONIZATION AND DEIONIZATION 8-2

8-1 Electron Density Within the Fireball 8-4
8-2 Electron Density Caused by Prompt Radiation Outside the Fireball 8-9
8-3 Electron Density Caused by Delayed Gamma Radiation Outside the Fireball 8-11
8-4 Electron Density Caused by Beta Particles Outside the Fireball 8-13
8-5 Electromagnetic Propagation in Ionized Regions 8-14

TRAVELING DISTURBANCES IN E AND F REGIONS OF IONOSPHERE 8-15

ELECTROMAGNETIC RADIATIONS 8-16

ABSORPTION 8-16

8-6 Absorption Within the Fireball 8-19
8-7 Absorption Caused by Prompt Radiation Outside the Fireball 8-20
8-8 Absorption Caused by Delayed Radiation Outside the Fireball 8-20

PHASE CHANGES 8-20

8-9 Velocity of Propagation 8-20
8-10 Frequency of Propagation 8-21
8-11 Direction of Propagation 8-21
8-12 Scatter and Scintillation 8-21

SECTION II METHODS FOR CALCULATING ABSORPTION OF RADIO FREQUENCIES 8-23

8-13 Size and Location of Fireball and Debris Regions for Detonations Below 85 kilometers 8-25
8-14 Size and Location of Fireball and Debris Regions for Detonations Between 85 and 120 kilometers 8-25
8-15 Size and Location of Fireball and Debris Regions for Detonations Above 120 kilometers 8-25

BIBLIOGRAPHY 8-93

PART II DAMAGE CRITERIA

CHAPTER 9 INTRODUCTION TO DAMAGE CRITERIA [redacted]

SECTION I CONTENT AND LIMITATIONS OF PART II 9-1

[redacted]

TABLE OF CONTENTS (Continued)

CHAPTER 9 INTRODUCTION TO DAMAGE CRITERIA (Continued)

	Page
SECTION II BLAST AND SHOCK DAMAGE	9-2
LOADING	9-3
RESPONSE AND DAMAGE	9-11
SECTION III THERMAL RADIATION DAMAGE	9-13
INTRODUCTION	9-13
THERMAL RESPONSE OF MATERIALS	9-15
SURVIVAL IN FIRE AREAS	9-28
SECTION IV THERMAL RADIATION DEGRADATION OF STRUCTURAL RESISTANCE TO AIR BLAST	9-31
THERMAL ENERGY ABSORBED	9-32
CHANGES IN MATERIAL STATE AND MATERIALS PROPERTIES	9-38
RESISTANCE TO LOAD	9-63
SECTION V X-RAY DAMAGE EFFECTS	9-67
INTRODUCTION	9-67
X-RAY ENERGY DEPOSITION CALCULATIONS	9-68
INITIAL PRESSURIZATION OF MATERIALS DUE TO X-RAY DEPOSITION	9-93
SHOCK WAVE PROPAGATION AND DAMAGE PREDICTIONS	9-103
IMPULSE AND STRUCTURAL RESPONSE ANALYSIS	9-107
REENTRY VEHICLE HARDENING	9-115
SECTION VI NUCLEAR RADIATION SHIELDING	9-118
SECTION VII TREE – COMPONENT PART AND CIRCUIT RESPONSE	9-121
SEMICONDUCTOR COMPONENT PARTS	9-122
OTHER ELECTRONIC COMPONENT PARTS	9-147
ELECTRONIC CIRCUITS	9-155
SECTION VIII ELECTROMAGNETIC PULSE (EMP) DAMAGE MECHANISMS	9-170
ENERGY COUPLING	9-170
COMPONENT DAMAGE	9-172
EMP HARDENING	9-175
TESTING	9-178

TABLE OF CONTENTS (Continued)

CHAPTER 10 PERSONNEL CASUALTIES

	Page
INTRODUCTION	10-1
SECTION I AIR BLAST	10-1
MECHANISMS AND CRITERIA FOR INJURY	10-1
CASUALTY PREDICTION	10-4
SECTION II THERMAL RADIATION	10-10
SKIN BURNS	10-10
CLASSIFICATION OF BURNS	10-10
BURN INJURY ENERGIES AND RANGES	10-11
EFFECTS OF THERMAL RADIATION ON THE EYES	10-15
SECTION III NUCLEAR RADIATION	10-23
INITIAL RADIATION	10-23
RESIDUAL RADIATION	10-25
SECTION IV COMBINED INJURY	10-31
CASUALTY CRITERIA	10-33
PERSONNEL IN THE OPEN	10-33
PERSONNEL IN STRUCTURES	10-35
TREATMENT	10-35

CHAPTER 11 DAMAGE TO STRUCTURES

INTRODUCTION	11-1
SECTION I DAMAGE TO ABOVEGROUND STRUCTURES	11-1
AIR BLAST EFFECTS	11-2
SECTION II DAMAGE TO BELOWGROUND STRUCTURES	11-40
STRUCTURES BURIED IN SOIL	11-40
LINED AND UNLINED OPENINGS IN ROCK	11-49
SECTION III SHOCK VULNERABILITY OF EQUIPMENT AND PERSONNEL	11-97
SECTION IV DAMS AND HARBOR INSTALLATIONS	11-109
AIR BLAST	11-109

TABLE OF CONTENTS (Continued)

CHAPTER 11 DAMAGE TO STRUCTURES [redacted] (Continued)

Page

WATER SHOCK 11-109
CRATERING 11-109
WATER WAVES 11-110
THERMAL-RADIATION DAMAGE 11-110
SECTION V PETROLEUM, OIL, AND LUBRICANT (POL) STORAGE TANKS ... 11-110
SECTION VI FIELD FORTIFICATIONS 11-118
SECTION VII FIRE IN URBAN AREAS 11-127
INTRODUCTION 11-127
EVOLUTION OF MASS FIRES 11-127
ESTIMATION AND CONTROL OF THERMAL DAMAGE 11-130

CHAPTER 12 MECHANICAL DAMAGE DISTANCES FOR SURFACE SHIPS AND SUBMARINES SUBJECTED TO NUCLEAR EXPLOSIONS [redacted]

INTRODUCTION 12-1
SECTION I DAMAGE TO SURFACE SHIPS FROM AIR BURSTS 12-2
BLAST DAMAGE 12-2
DAMAGE FROM OTHER AIR BURST PHENOMENA 12-6
SECTION II SURFACE SHIP DAMAGE FROM UNDERWATER BURSTS 12-8
DAMAGE FROM THE SHOCK WAVE IN THE WATER 12-8
DAMAGE FROM OTHER UNDERWATER BURST PHENOMENA 12-17
SECTION III SUBMARINE DAMAGE FROM UNDERWATER BURSTS 12-17
DAMAGE FROM THE SHOCK WAVE IN THE WATER 12-17
DAMAGE FROM OTHER UNDERWATER BURST PHENOMENA 12-19

CHAPTER 13 DAMAGE TO AIRCRAFT [redacted]

INTRODUCTION 13-1
SECTION I BLAST AND THERMAL EFFECTS ON AIRCRAFT 13-1
NUCLEAR WEAPON EFFECTS ANALYSIS 13-4

[redacted]

TABLE OF CONTENTS (Continued)

CHAPTER 13 DAMAGE TO AIRCRAFT [redacted] (Continued)

Page

SECTION II AIRCRAFT RESPONSE TO BLAST AND THERMAL EFFECTS 13-10
AIRCRAFT RESPONSE TO GUST EFFECTS 13-10
AIRCRAFT RESPONSE TO OVERPRESSURE EFFECTS 13-50
AIRCRAFT RESPONSE TO THERMAL RADIATION EFFECTS 13-59
BURST-TIME ENVELOPES 13-67

CHAPTER 14 DAMAGE TO MILITARY FIELD EQUIPMENT [redacted]

INTRODUCTION 14-1
SECTION I AIR BLAST DAMAGE 14-1
SECTION II DAMAGE PREDICTIONS 14-17
SECTION III DAMAGE FROM CAUSES OTHER THAN BLAST AND NUCLEAR RADIATION 14-57
SECTION IV TREE DAMAGE CRITERIA 14-59
SYSTEMS ANALYSIS 14-60
REVIEW OF ELECTRONIC SUSCEPTIBILITY TO NUCLEAR RADIATION 14-62
TREE-DAMAGE ESTIMATES 14-64

CHAPTER 15 DAMAGE TO FOREST STANDS [redacted]

INTRODUCTION 15-1
SECTION I AIR BLAST 15-1
SECTION II TROOP AND VEHICLE MOVEMENT 15-41
SECTION III THERMAL RADIATION 15-52

CHAPTER 16 DAMAGE TO MISSILES [redacted]

SECTION I BLAST DAMAGE TO TACTICAL MISSILE SYSTEMS 16-1
SERGEANT WEAPON SYSTEM 16-3
LANCE WEAPON SYSTEM 16-12

TABLE OF CONTENTS (Continued)

CHAPTER 16 DAMAGE TO MISSILES [redacted] (Continued)

Page

HAWK WEAPON SYSTEM 16-19

SAMPLE PROBLEM: AIR BLAST DAMAGE TO A TACTICAL MISSILE SYSTEM 16-26

SECTION II BLAST AND THERMAL VULNERABILITY OF IN-FLIGHT STRATEGIC SYSTEMS 16-34

INTRODUCTION 16-34

BLAST LOADING ON REENTRY (RV) SYSTEMS 16-39

RESULTS OF SOME RV BLAST AND THERMAL LOAD AND VULNERABILITY CALCULATIONS 16-66

ANTIMISSILE (ABM) SYSTEMS 16-81

BLAST AND THERMAL LETHALITY 16-96

CHAPTER 17 RADIO FREQUENCY SIGNAL DEGRADATION RELEVANT TO COMMUNICATIONS AND RADAR SYSTEMS [redacted]

INTRODUCTION 17-1

SECTION I DEGRADATION MECHANISMS 17-2

ATTENUATION 17-2

INTERFERENCE 17-6

SIGNAL DISTORTION 17-6

SECTION II SYSTEM CHARACTERISTICS AND EFFECTS 17-7

VLF AND LF SYSTEMS 17-7

HF SYSTEMS 17-13

SATELLITE COMMUNICATION SYSTEMS 17-19

TROPOSCATTER COMMUNICATION SYSTEMS 17-22

IONOSCATTER COMMUNICATION SYSTEMS 17-26

RADAR SYSTEMS 17-30

APPENDIX A SUPPLEMENTARY BLAST DATA [redacted]

SECTION I MATHEMATICAL DESCRIPTION OF THE SHOCK FRONT A-1

SECTION II PHYSICAL DESCRIPTION OF SHOCK WAVE BEHAVIOR A-8

[redacted]

TABLE OF CONTENTS (Continued)

Page

APPENDIX B USEFUL RELATIONSHIPS [redacted] B-1

APPENDIX C PROBABILITY CONSIDERATIONS [redacted]

SECTION I DAMAGE PROBABILITIES C-2
DAMAGE CAUSED BY MOTION INPUT C-2
DAMAGE CAUSED BY PRESSURE C-7
SECTION II DERIVATION OF EQUATIONS USED IN SECTION I C-14

APPENDIX D ABSTRACTS OF DNA HANDBOOKS [redacted] D-1

APPENDIX E GLOSSARY [redacted] E-1

APPENDIX F LIST OF SYMBOLS [redacted] F-1

[redacted]

LIST OF ILLUSTRATIONS

PART I

Figure	*Title*	*Page*
1-1	Development of an Air Burst	1-10
1-2	Development of a Surface Burst	1-13
1-3	Altitude-Yield Map Showing Differing Regions of Phenomenology	1-17
1-4	Photographs of High Altitude Bursts, t = 100 sec	1-18
1-5	Development of a Shallow Underground Burst	1-21
1-6	Development of a Deep Underground Burst	1-22
1-7	Development of a Shallow Underwater Burst	1-24
1-8	Development of a Deep Underwater Burst	1-25
2-1	Ideal Pressure-Time Relationships for a Blast Wave in the Low Pressure Region (below 5 psi)	2-1
2-2	Peak Overpressure from a 1 kt Free Air Burst in a Standard Sea Level Atmosphere	2-7
2-3	Peak Overpressure in Free Air as a Function of Yield and Slant Range	2-8
2-4	Peak Dynamic Pressure from a 1 kt Free Air Burst in a Standard Sea Level Atmosphere	2-10
2-5	Time of Arrival of the Shock Front from a 1 kt Free Air Burst in a Standard Sea Level Atmosphere	2-12
2-6	Duration of Positive Overpressure and Dynamic Pressure Phases for a 1 kt Free Air Burst in a Standard Sea Level Atmosphere	2-14
2-7	Overpressure and Dynamic Pressure Impulse from 1 kt Free Air Burst in a Standard Sea Level Atmosphere	2-16
2-8	Positive Overpressure Waveforms for an Ideal Shock Wave in a Standard Sea Level Atmosphere	2-18
2-9	Positive Dynamic Pressure Waveforms for an Ideal Shock Wave in a Standard Sea Level Atmosphere	2-19
2-10	Effective Triangular Duration Correction Factors ($t\Delta = C_t t_p^+$ or $t\Delta = C_t t_q^+$)	2-20
2-11	Altitude Scaling Factors for Blast Wave Calculations	2-27
2-12	Shock Front Velocity, Peak Particle Velocity and Peak Density for a Shock Wave in Air	2-34
2-13	Peak Reflected Overpressure at Normal Incidence and Peak Dynamic Pressure as Functions of Peak Overpressure in a Standard Sea Level Atmosphere	2-36

[redacted]

LIST OF ILLUSTRATIONS (Continued)

Figure	*Title*	*Page*
2-14	[redacted] Distortion of Blast Wave by a Stratum of Warm Air [redacted]	2-37
2-15	[redacted] Growth of the Mach Stem (Idealized) [redacted]	2-40
2-16	[redacted] Precursor Characteristics [redacted]	2-42
2-17	[redacted] Peak Overpressures at the Surface for a 1 kt Burst Over a Near-Ideal Surface, Very High Overpressure Region [redacted]	2-53
2-18	[redacted] Peak Overpressures at the Surface for a 1 kt Burst Over a Near-Ideal Surface, High Overpressure Region [redacted]	2-54
2-19	[redacted] Peak Overpressures at the Surface for a 1 kt Burst Over a Near-Ideal Surface, Low Overpressure Region [redacted]	2-55
2-20	[redacted] Peak Overpressures at the Surface for a 1 kt Burst Over a Near-Ideal or Thermally Nonideal Surface, Very Low Overpressure Region [redacted]	2-56
2-21	[redacted] Peak Overpressures at the Surface for a 1 kt Burst Over a Thermally Nonideal Surface, High Overpressure Region [redacted]	2-57
2-22	[redacted] Peak Overpressures at the Surface for a 1 kt Burst Over a Thermally Nonideal Surface, Low Overpressure Region [redacted]	2-58
2-23	[redacted] Peak Overpressure from a Contact Surface Burst [redacted]	2-59
2-24	[redacted] Peak Dynamic Pressure at the Surface from a 1 kt Explosion Over an Ideal Surface [redacted]	2-61
2-25	[redacted] Peak Dynamic Pressure at the Surface from a 1 kt Explosion Over a Surface with Light Dust Conditions [redacted]	2-62
2-26	[redacted] Peak Dynamic Pressure at the Surface from a 1 kt Explosion Over a Surface with Heavy Dust Conditions [redacted]	2-63
2-27	[redacted] Comparison of Predicted Ideal, Light-Dust, and Heavy-Dust Dynamic Pressures for a 1 kt Explosion at a Height of Burst of 200 feet in a Sea Level Atmosphere [redacted]	2-64
2-28	[redacted] Time of Arrival of the Blast Wave Along the Surface from a 1 kt Explosion Over a Near-Ideal Surface, High Overpressure Region [redacted]	2-66
2-29	[redacted] Time of Arrival of the Blast Wave Along the Surface from a 1 kt Explosion Over a Near-Ideal Surface, Low Overpressure Region [redacted]	2-67
2-30	[redacted] Time of Arrival of the Blast Wave Along the Surface from a 1 kt Explosion Over a Thermally Nonideal Surface, Very High Overpressure Region [redacted]	2-68
2-31	[redacted] Time of Arrival of the Blast Wave Along the Surface from a 1 kt Explosion Over a Thermally Nonideal Surface, High Overpressure Region [redacted]	2-69

[redacted]

[redacted]

LIST OF ILLUSTRATIONS (Continued)

Figure	*Title*	*Page*
2-121	[redacted] Peak Air Blast Overpressure Along the Water Surface from Underwater Nuclear Explosions [redacted]	2-~~248~~ 276
2-122	[redacted] Velocity of Shock Wave in Free Water vs Peak Shock Pressure [redacted]	2-~~254~~ 279
2-123	[redacted] Plume Dimensions for Deep and Very Deep Underwater Bursts [redacted]	2-~~258~~ 281
2-124	[redacted] Column and Cloud Dimensions for Shallow and Very Shallow Bursts [redacted]	2-~~254~~ 282
2-125	[redacted] Height of Visible Base Surge Cloud as a Function of Time After Burst [redacted]	2-~~252~~ 285
2-126	[redacted] Reduced Base Surge Radius vs Reduced Time for Shallow and Very Shallow Bursts [redacted]	2-~~258~~ 286
2-127	[redacted] Reduced Base Surge Radius vs Reduced Time for Deep and Very Deep Bursts [redacted]	2-~~259~~ 287
2-128	[redacted] Peak Wave Height H as a Function of Yield W Range R and Water Depth d_w [redacted]	2-~~262~~ 290
2-129	[redacted] Apparent Crater Radius as a Function of Yield for Various Water Depths Over a Clayey Sand Bottom, where d_w = Water Depth in Feet. Shaded Areas Denote Possible Transition Regions from a Washed to an Unwashed Crater for d_w = 20, 40, and 60 [redacted]	2-~~266~~ 294
2-130	[redacted] Apparent Crater Depth as a Function of Yield for Various Water Depths Over a Clayey Sand Bottom, where d_w = Water Depth in Feet. Shaded Areas Denote Possible Transition Regions from a Washed to an Unwashed Crater for d_w = 20, 40, and 60 [redacted]	2-~~267~~ 295
2-131	[redacted] Average Height of Crater Lip as a Function of Yield for Various Water Depths with the Charge Near a Clayey Sand Bottom, where d_w = Water Depth in Feet. Shaded Areas Denote Possible Transition Regions from Crater for d_w = 20, 40, and 60 [redacted]	2-~~268~~ 296
2-132	[redacted] Estimated Critical Water Depth as a Function of Yield for a Clayey Sand Bottom [redacted]	2-~~269~~ 297
3-1	[redacted] Thermal Partition as a Function of Yield and Altitude [redacted]	3-4
3-2	[redacted] Effective Height of Model Atmosphere (Visual Range = 16 Miles) [redacted]	3-10
3-3	[redacted] Transmittance Between a Burst Within 1/4 Mile of the Surface and a Target on the Ground [redacted]	3-11
3-4	[redacted] Transmittance to a Target on the Ground on a Clear Day (Visual Range = 1 Mile) [redacted]	3-15

[redacted]

LIST OF ILLUSTRATIONS (Continued)

Title	Page
Transmittance to a Target on the Ground on a Clear Day Visual Range = 1 Mile)	3-16
Transmittance to a Target on the Ground on a Clear Day Visual Range = 2 Miles)	3-17
Transmittance to a Target on the Ground on a Clear Day Visual Range = 2 Miles)	3-18
Transmittance to a Target on the Ground on a Clear Day Visual Range = 4 Miles)	3-19
Transmittance to a Target on the Ground on a Clear Day Visual Range = 4 Miles)	3-20
Transmittance to a Target on the Ground on a Clear Day Visual Range = 8 Miles)	3-21
Transmittance to a Target on the Ground on a Clear Day Visual Range = 8 Miles)	3-22
Transmittance to a Target on the Ground on a Clear Day Visual Range = 16 Miles)	3-23
Transmittance to a Target on the Ground on a Clear Day Visual Range = 16 Miles)	3-24
Transmittance to a Target on the Ground on a Clear Day Visual Range = 16 Miles)	3-25
Transmittance to a Target on the Ground on a Clear Day Visual Range = 32 Miles)	3-26
Atmospheric Transmittance for Thermal Radiation from High titude Nuclear Bursts (Height of Burst ⩾ 100 kft)	3-28
Equivalent Daytime Visual Range as a Function Nighttime Visual Range	3-38
Approximate Values of Radiant Exposure ough a Clear Atmosphere	3-40
Approximate Values of Radiant Exposure ough a Clear Atmosphere	3-41
Thermal Partition for Surface Bursts	3-45
Calculated Power-Time Curve for a 200 kiloton Burst at 5,000 Feet	3-47
Power-Time and Energy-Time Curves for a 200 kiloton rst at 5,000 Feet	3-48
Time of Final Maximum as a Function of Yield and Altitude	3-51
Power-Time Curve for a 200 kiloton Burst at 100,000 Feet	3-53
Power-Time Curve for a 200 kiloton Burst at 40 kilometers	3-54

[redacted]

LIST OF ILLUSTRATIONS (Continued)

Figure	*Title*	*Page*
3-24	[redacted] Distribution of Deposited X-ray Energy in a Sea Level Atmosphere as a Function of Source Spectrum [redacted]	3-62
3-25a	[redacted] Density of Deposited Energy from Various Energy Sources [redacted]	3-67
3-25b	[redacted] Density of Deposited Energy from Various Energy Sources [redacted]	3-68
3-26	[redacted] A Comparison of Calculated Effective Times of Final Maximum with Predictions from the Simplified Equation [redacted]	3-69
3-27	[redacted] Equivalent Point Source at Median Radius When Height of Burst Exceeds Distance of Target, X, from Ground Zero [redacted]	3-71
3-28	[redacted] Fraction of Absorbed X-ray Energy Reradiated [redacted]	3-73
3-29	[redacted] Free Field Radiant Exposure and Air Blast Overpressure at the Surface, as a Function of Height of Burst and Ground Distance, for 0.01 kilotons, No Atmospheric Attenuation, High Overpressure Region [redacted]	3-76
3-30	[redacted] Free Field Radiant Exposure and Air Blast Overpressure at the Surface, as a Function of Height of Burst and Ground Distance, for 0.01 kilotons, No Atmospheric Attenuation, Low Overpressure Region [redacted]	3-77
3-31	[redacted] Free Field Radiant Exposure and Air Blast Overpressure at the Surface, as a Function of Height of Burst and Ground Distance, for 0.01 kilotons, 16 Mile Visual Range, Hig[redacted] Overpressure Regio[redacted]	3-78
3-32	[redacted] Free Field Radiant Exposure and Air Blast Overpressure at the Surface, as a Function of Height of Burst and Ground Distance, for 0.01 kilotons, 16 Mile Visual Range, Low Overpressure Region [redacted]	3-79
3-33	[redacted] Free Field Radiant Exposure and Air Blast Overpressure at the Surface, as a Function of Height of Burst and Ground Distance, for 0.1 kilotons, No Atmospheric Attenuation, High Overpressure Region [redacted]	3-80
3-34	[redacted] Free Field Radiant Exposure and Air Blast Overpressure at the Surface, as a Function of Height of Burst and Ground Distance, for 0.1 kilotons, No Atmospheric Attenuation, Low Overpressure Region [redacted]	3-81
3-35	[redacted] Free Field Radiant Exposure and Air Blast Overpressure at the Surface, as a Function of Height of Burst and Ground Distance, for 0.1 kilotons, 16 Mile Visual Range, High Overpressure Region [redacted]	3-82
3-36	[redacted] Free Field Radiant Exposure and Air Blast Overpressure at the Surface, as a Function of Height of Burst and Ground Distance, for 0 [redacted]otons, 16 Mile Visual Range, Low Overpressure Region [redacted]	3-83
3-37	[redacted]e Field Radiant Exposure and Air Blast Overpressure at the S[redacted], as a Function of Height of Burst and Ground Distance, for 1 kiloton, No Atmospheric Attenuation, High Overpressure Region [redacted]	3-84

[redacted]

LIST OF ILLUSTRATIONS (Continued)

Figure	*Title*	*Page*
3-38	[redacted] Free Field Radiant Exposure and Air Blast Overpressure at the Surface, as a Function of Height of Burst and Ground Distance, for 1 kiloton, No Atmospheric Attenuation, Low Overpressure Region [redacted]	3-85
3-39	[redacted] Free Field Radiant Exposure and Air Blast Overpressure at the Surface, as a Function of Height of Burst and Ground Distance, for 1 kiloton, 16 Mile Visual Range, High Overpressure Region [redacted]	3-86
3-40	[redacted] Free Field Radiant Exposure and Air Blast Overpressure at the Surface, as a Function of Height of Burst and Ground Distance, for 1 kiloton, 16 Mile Visual Range, Low Overpressure Region [redacted]	3-87
3-41	[redacted] Free Field Radiant Exposure and Air Blast Overpressure at the Surface, as a Function of Height of Burst and Ground Distance, for 10 kilotons, No Atmospheric Attenuation, High Overpressure Region [redacted]	3-88
3-42	[redacted] Free Field Radiant Exposure and Air Blast Overpressure at the Surface, as a Function of Height of Burst and Ground Distance, for 10 kilotons, No Atmospheric Attenuation, Low Overpressure Region [redacted]	3-89
3-43	[redacted] Free Field Radiant Exposure and Air Blast Overpressure at the Surface, as a Function of Height of Burst and Ground Distance, for 10 kilotons, 16 Mile Visual Range, High Overpressure Region [redacted]	3-90
3-44	[redacted] Free Field Radiant Exposure and Air Blast Overpressure at the Surface, as a Function of Height of Burst and Ground Distance, for 10 kilotons, 16 Mile Visual Range, Low Overpressure Region [redacted]	3-91
3-45	[redacted] Free Field Radiant Exposure and Air Blast Overpressure at the Surface, as a Function of Height of Burst and Ground Distance, for 100 kilotons, No Atmospheric Attenuation, High Overpressure Region [redacted]	3-92
3-46	[redacted] Free Field Radiant Exposure and Air Blast Overpressure at the Surface, as a Function of Height of Burst and Ground Distance, for 100 kilotons, No Atmospheric Attenuation, Low Overpressure Region [redacted]	3-93
3-47	[redacted] Free Field Radiant Exposure and Air Blast Overpressure at the Surface, as a Function of Height of Burst and Ground Distance, for 100 kilotons, 16 Mile Visual Range, High Overpressure Region [redacted]	3-94
3-48	[redacted] Free Field Radiant Exposure and Air Blast Overpressure at the Surface, as a Function of Height of Burst and Ground Distance, for 100 kilotons, 16 Mile Visual Range, Low Overpressure Region [redacted]	3-95
3-49	[redacted] Free Field Radiant Exposure and Air Blast Overpressure at the Surface, as a Function of Height of Burst and Ground Distance, for 1 megaton, No Atmospheric Attenuation, High Overpressure Region [redacted]	3-96

[redacted]

LIST OF ILLUSTRATIONS (Continued)

Figure	Title	Page
3-50	[redacted] Free Field Radiant Exposure and Air Blast Overpressure at the Surface, as a Function of Height of Burst and Ground Distance, for 1 megaton, No Atmospheric Attenuation, Low Overpressure Region [redacted]	3-97
3-51	[redacted] Free Field Radiant Exposure and Air Blast Overpressure at the Surface, a Function of Height of Burst and Ground Distance, for 1 megaton, 16 Mile Visual Range, High Overpressure Region [redacted]	3-98
3-52	[redacted] Free Field Radiant Exposure and Air Blast Overpressure at the Surface, as a Function of Height of Burst and Ground Distance, for 1 megaton, 16 Mile Visual Range, Low Overpressure Region [redacted]	3-99
3-53	[redacted] Free Field Radiant Exposure and Air Blast Overpressure at the Surface, as a Function of Height of Burst and Ground Distance, for 10 megatons, No Atmospheric Attenuation, High Overpressure Region [redacted]	3-100
3-54	[redacted] Free Field Radiant Exposure and Air Blast Overpressure at the Surface, as a Function of Height of Burst and Ground Distance, for 10 megatons, No Atmospheric Attenuation, Low Overpressure Region [redacted]	3-101
3-55	[redacted] Free Field Radiant Exposure and Air Blast Overpressure at the Surface, as a Function of Height of Burst and Ground Distance, for 10 megatons, 16 Mile Visual Range, High Overpressure Region [redacted]	3-102
3-56	[redacted] Free Field Radiant Exposure and Air Blast Overpressure at the Surface, as a Function of Height of Burst and Ground Distance, for 10 megatons, 16 Mile Visual Range, Low Overpressure Region [redacted]	3-103
3-57	[redacted] Fireball Properties after Breakaway [redacted]	3-106
3-58	[redacted] Calculated Power-Time Curves for a 200 kiloton Burst at 5,000 Feet [redacted]	3-107
3-59	[redacted] Altitude Variation of Phenomena for a 200 kiloton Burst [redacted]	3-110
3-60	[redacted] Comparison of Equations for t_{min} and t_{max}, $HOB = 180W^{0.4}$ Feet [redacted]	3-112
4-1	[redacted] Properties of Electromagnetic Radiation [redacted]	4-2
4-2	[redacted] Wavelength, Frequency, and Temperature as a Function of Electromagnetic Photon Energy [redacted]	4-3
4-3	[redacted] Spectral Distribution of a Black Body Source [redacted]	4-7
4-4	[redacted] Mass Attenuation Coefficients for Air [redacted]	4-10
4-5	[redacted]	4-13
4-6	[redacted]	4-16
4-7	[redacted]	4-17
4-8	[redacted]	4-18

DNA (1.1|3)

[redacted]

LIST OF ILLUSTRATIONS (Continued)

Figure	Title	Page
4-9	[redacted]	4-19
4-10	[redacted]	4-21
4-11	[redacted]	4-22
4-12	X-Ray Fluence in a Vacuum	4-26
4-13	The Standard Atmosphere	4-29
4-14	Energy Fluence and Build-up Factor for a 50 keV Monoenergetic Source in Homogeneous Air	4-31
4-15	[redacted]	4-32
4-16	[redacted]	4-33
4-17	Mass Integral for Specified Coaltitude Separation Distances as a Function of Altitude	4-36
4-18	Transmission of Direct X-Ray Fluence Through Air for Various Black Body Sources	4-37
4-19	X-Ray Fluence Through Air for Various Black Body Sources	4-38
4-20	[redacted]	4-40
4-21	[redacted]	4-41
5-1	Spectrum for a Fission Weapon (Normalized to 1 kt)	5-3
5-2	Spectrum for a Thermonuclear Weapon (Normalized to 1 kt)	5-4
5-3	Spectra from the Fission Source of Figure 5-1 with the Receiver On or Near the Surface of the Earth at Various Slant Ranges	5-8
5-4	Spectra from the Thermonuclear Source of Figure 5-2 with the Receiver On or Near the Surface of the Earth at Various Slant Ranges	5-9
5-5	Neutron Fluence Incident on a Receiver Located On or Near the Surface of the Earth from the Fission Spectrum Shown in Table 5-1 and Figure 5-1	5-10
5-6	Neutron Fluence Incident on a Receiver Located On or Near the Surface of the Earth from the Thermonuclear Spectrum Shown in Table 5-1 and Figure 5-2	5-11
5-7	Neutron Energy Build-Up Factors for Various Monoenergetic Sources in Homogeneous Air	5-15
5-8	Calculated Time Dependence of the Gamma Ray Output from a Large Yield Explosion, Normalized to 1 kt	5-19

LIST OF ILLUSTRATIONS (Continued)

Figure	*Title*	*Page*
5-9a	Neutron Dose as a Function of Slant Range from a 1 kt Surface Burst, Weapon Types I through IV, Short Ranges	5-33
5-9b	Neutron Dose as a Function of Slant Range from a 1 kt Surface Burst, Weapon Types I through IV, Long Ranges	5-34
5-10a	Neutron Dose as a Function of Slant Range from a 1 kt Surface Burst, Weapon Types V through VIII, Short Ranges	5-35
5-10b	Neutron Dose as a Function of Slant Range from a 1 kt Surface Burst, Weapon Types V through VIII, Long Ranges	5-36
5-11	Burst Height Adjustment Factors for Neutrons and Secondary Gamma Rays	5-37
5-12a	Secondary Gamma Ray Dose as a Function of Slant Range from a kt Surface Burst, Weapon Types I through IV, Short Ranges	5-38
5-12b	Secondary Gamma Ray Dose as a Function of Slant Range from a kt Surface Burst, Weapon Types I through IV, Long Ranges	5-39
5-13a	Secondary Gamma Ray Dose as a Function of Slant Range from a 1 kt Surface Burst, Weapon Types V through VIII, Short Ranges	5-40
5-13b	Secondary Gamma Ray Dose as a Function of Slant Range from a kt Surface Burst, Weapon Types V through VIII, Long Ranges	5-41
5-14a	Fission Product Gamma Ray Dose as a Function of Slant Range from a 1 kt (Fission Yield) Surface Burst, Short Ranges	5-42
5-14b	Fission Product Gamma Ray Dose as a Function of Slant Range from a 1 kt (Fission Yield) Surface Burst, Intermediate Ranges	5-43
5-14c	Fission Product Gamma Ray Dose as a Function of Slant Range from a 1 kt (Fission Yield) Surface Burst, Long Ranges	5-44
5-15	Range Dependent Burst Height Adjustment Factors for Fission Product Gamma Rays	5-45
5-16	Yield Dependent Burst Height Adjustment Factors for Fission Product Gamma Rays	5-46
5-17a	Fission Product Gamma Ray Hydrodynamic Enhancement Factors as a Function of Slant Range for Relative Air Density of 1.1	5-47
5-17b	Fission Product Gamma Ray Hydrodynamic Enhancement Factors Function of Slant Range for Relative Air Density of 1.0	5-48
5-17c	Fission Product Gamma Ray Hydrodynamic Enhancement Factors Function of Slant Ranges for Relative Air Density of 0.9	5-49
5-17d	Fission Product Gamma Ray Hydrodynamic Enhancement Factors as a Function of Slant Range for Relative Air Density of 0.8	5-50

LIST OF ILLUSTRATIONS (Continued)

Figure	*Title*	*Page*
5-17e	Fission Product Gamma Ray Hydrodynamic Enhancement Factors as a Function of Slant Range for Relative Air Density of 0.7	5-51
5-18	Neutron-Induced Gamma Dose Rate as a Function of Slant Range at a Reference Time of 1 Hour After Burst	5-57
5-19	Decay Factors for Neutron-Induced Gamma Activity	5-59
5-20	Total Radiation Dose Received in an Area Contaminated by Neutron-Induced Gamma Activity, Soil Type I	5-61
5-21	Total Radiation Dose Received in an Area Contaminated by Neutron-Induced Gamma Activity, Soil Type II	5-62
5-22	Total Radiation Dose Received in an Area Contaminated by Neutron-Induced Gamma Activity, Soil Type III	5-63
5-23	Total Radiation Dose Received in an Area Contaminated by Neutron-Induced Gamma Activity, Soil Type IV	5-64
5-24	Idealized Early Fallout Dose Rate Contour	5-68
5-25	Comparison of Idealized Dose Rate Contours with Observed Contours from a Low Yield Explosion	5-69
5-26	Hodograph of a Typical Summer Wind Structure Over Fort Worth, Texas	5-70
5-27	Comparison of Idealized Dose Rate Contours with Those Calculated by a Complex Computer Code for a 2 Mt Explosion and the Winds of Figure 5-25	5-71
5-28	Downwind Distance as a Function of Yield, 10 Knot Effective Wind	5-79
5-29	Downwind Distance as a Function of Yield, 20 Knot Effective Wind	5-80
5-30	Downwind Distance as a Function of Yield, 40 Knot Effective Wind	5-81
5-31	Maximum Width as a Function of Yield, 10 Knot Effective Wind	5-82
5-32	Maximum Width as a Function of Yield, 20 Knot Effective Wind	5-83
5-33	Maximum Width as a Function of Yield, 40 Knot Effective Wind	5-84
5-34	Distance to Maximum Width as a Function of Yield, 10 Knot Effective Wind	5-85
5-35	Distance to Maximum Width as a Function of Yield, 20 Knot Effective Wind	5-86
5-36	Distance to Maximum Width as a Function of Yield, 40 Knot Effective Wind	5-87
5-37	Ground Zero Width as a Function of Yield	5-88

LIST OF ILLUSTRATIONS (Continued)

Figure	Title	Page
5-38	Height of the Stabilized Cloud Bottom as a Function of Yield	5-89
5-39	Height of the Stabilized Cloud Top as a Function of Yield	5-90
5-40	Fission Product Decay Factors Normalized to Unity at 1 Hour After Detonation	5-92
5-41	Normalized Dose Accumulated in a Fallout Contaminated Area from H + 1 Hour to H + 1,000 Days	5-94
5-42	Total Radiation Dose from Early Fallout as a Function of Entry Time and Stay Time, Normalized to Unit Time Reference Dose Rate	5-96
5-43	Minimum Height of Burst for No Fallout as a Function of Yield	5-99
5-44	Height of Burst Adjustment Factors for Various Yields	5-100
5-45	Depth Multiplication Factor for Linear Dimensions of the Fallout Pattern from a 1 kt Explosion as a Function of Depth of Burst	5-103
5-46	Base Surge Radiation Exposure Rate 15 Feet Above the Water Surface from a 10 kt Explosion at a Depth of 65 Feet in 5,000 Feet of Water, No-Wind Environment	5-109
5-47	Base Surge Radiation Exposure Rate 15 Feet Above the Water Surface from a 10 kt Explosion on the Bottom in 65 Feet of Water, No-Wind Environment	5-110
5-48	Base Surge Radiation Exposure Rate 15 Feet Above the Water Surface from a 10 kt Explosion at a Depth of 150 Feet in 5,000 Feet of Water, No-Wind Environment	5-111
5-49	Base Surge Radiation Exposure Rate 15 Feet Above the Water Surface from a 10 kt Explosion at a Depth of 500 Feet in 5,000 Feet of Water, No-Wind Environment	5-112
5-50	Base Surge Radiation Exposure Rate 15 Feet Above the Water Surface from a 10 kt Explosion at a Depth of 1,000 Feet in 5,000 Feet of Water, No-Wind Environment	5-113
5-51	Base Surge Radiation Exposure Rate 15 Feet Above the Water Surface from a 10 kt Explosion at a Depth of 1,500 Feet in 5,000 Feet of Water, No-Wind Environment	5-114
5-52	Pool Radiation Exposure Rate 15 Feet Above the Water Surface from a 10 kt Explosion at a Depth of 65 Feet in 5,000 Feet of Water, No-Current Environment	5-115
5-53	Pool Radiation Exposure Rate 15 Feet Above the Water Surface from a 10 kt Explosion on the Bottom in 65 Feet of Water, No-Current Environment	5-116

[redacted]

LIST OF ILLUSTRATIONS (Continued)

Figure	*Title*	*Page*
5-54	[redacted] Pool Radiation Exposure Rate 15 Feet Above the Water Surface from a 10 kt Explosion at a Depth of 150 Feet in 5,000 Feet of Water, No-Current Environment [redacted]	5-117
5-55	[redacted] Pool Radiation Exposure Rate 15 Feet Above the Water Surface from a 10 kt Explosion at a Depth of 500 Feet in 5,000 Feet of Water, No-Current Environment [redacted]	5-118
5-56	[redacted] Pool Radiation Exposure Rate 15 Feet Above the Water Surface from a 10 kt Explosion at a Depth of 1,000 Feet in 5,000 Feet of Water, No-Current Environment [redacted]	5-119
5-57	[redacted] Pool Radiation Exposure Rate 15 Feet Above the Water Surface from a 10 kt Explosion at a Depth of 1,500 Feet in 5,000 Feet of Water, No-Current Environment [redacted]	5-120
5-58	[redacted] Two-Minute Total Exposure 15 Feet Above the Water Surface from a 1 kt Explosion at a Depth of 30 Feet in 5,000 Feet of Water, 15 Knot Wind, No-Current Environment [redacted]	5-121
5-59	[redacted] Ten-Minute Total Exposure 15 Feet Above the Water Surface from a 1 kt Explosion at a Depth of 30 Feet in 5,000 Feet of Water, 15 Knot Wind, No-Current Environment [redacted]	5-122
5-60	[redacted] Thirty-Minute Total Exposure 15 Feet Above the Water Surface from a 1 kt Explosion at a Depth of 30 Feet in 5,000 Feet of Water, 15 Knot Wind, No-Current Environment [redacted]	5-123
5-61	[redacted] Two-Minute Total Exposure 15 Feet Above the Water Surface from a 10 kt Explosion at a Depth of 65 Feet in 5,000 Feet of Water, 15 Knot Wind, No-Current Environment [redacted]	5-124
5-62	[redacted] Ten-Minute Total Exposure 15 Feet Above the Water Surface from a 10 kt Explosion at a Depth of 65 Feet in 5,000 Feet of Water, 15 Knot Wind, No-Current Environment [redacted]	5-125
5-63	[redacted] Thirty-Minute Total Exposure 15 Feet Above the Water Surface from a 10 kt Explosion at a Depth of 65 Feet in 5,000 Feet of Water, 15 Knot Wind, No-Current Environment [redacted]	5-126
5-64	[redacted] Two-Minute Total Exposure 15 Feet Above the Water Surface from a 100 kt Explosion at a Depth of 140 Feet in 5,000 Feet of Water, 15 Knot Wind, No-Current Environment [redacted]	5-127
5-65	[redacted] Ten-Minute Total Exposure 15 Feet Above the Water Surface from a 100 kt Explosion at a Depth of 140 Feet in 5,000 Feet of Water, 15 Knot Wind, No-Current Environment [redacted]	5-128

[redacted]

LIST OF ILLUSTRATIONS (Continued)

Figure	Title	Page
5-66	[redacted] Thirty-Minute Total Exposure 15 Feet Above the Water Surface from a 100 kt Explosion at a Depth of 140 Feet in 5,000 Feet of Water, 15 Knot Wind, No-Current Environment [redacted]	5-129
5-67	[redacted] Two-Minute Total Exposure 15 Feet Above the Water Surface from a 1 kt Explosion at a Depth of 280 Feet in 5,000 Feet of Water, 15 Knot Wind, No-Current Environment [redacted]	5-130
5-68	[redacted] Ten-Minute Total Exposure 15 Feet Above the Water Surface from a 1 kt Explosion at a Depth of 280 Feet in 5,000 Feet of Water, 15 Knot Wind, No-Current Environment [redacted]	5-131
5-69	[redacted] Thirty-Minute Total Exposure 15 Feet Above the Water Surface from a 1 kt Explosion at a Depth of 280 Feet in 5,000 Feet of Water, 15 Knot Wind, No-Current Environment [redacted]	5-132
5-70	[redacted] Two-Minute Total Exposure 15 Feet Above the Water Surface from a 10 kt Explosion at a Depth of 500 Feet in 5,000 Feet of Water, 15 Knot Wind, No-Current Environment [redacted]	5-133
5-71	[redacted] Ten-Minute Total Exposure 15 Feet Above the Water Surface from a 10 kt Explosion at a Depth of 500 Feet in 5,000 Feet of Water, 15 Knot Wind, No-Current Environment [redacted]	5-134
5-72	[redacted] Thirty-Minute Total Exposure 15 Feet Above the Water Surface from a 10 kt Explosion at a Depth of 500 Feet in 5,000 Feet of Water, 15 Knot Wind, No-Current Environment [redacted]	5-135
5-73	[redacted] Two-Minute Total Exposure 15 Feet Above the Water Surface from a 100 kt Explosion at a Depth of 890 Feet in 5,000 Feet of Water, 15 Knot Wind, No-Current Environment [redacted]	5-136
5-74	[redacted] Ten-Minute Total Exposure 15 Feet Above the Water Surface from a 100 kt Explosion at a Depth of 890 Feet in 5,000 Feet of Water, 15 Knot Wind, No-Current Environment [redacted]	5-137
5-75	[redacted] Thirty-Minute Total Exposure 15 Feet Above the Water Surface from a 100 kt Explosion at a Depth of 890 Feet in 5,000 Feet of Water, 15 Knot Wind, No-Current Environment [redacted]	5-138
5-76	[redacted] Cloud Diameter as a Function of Time After Burst [redacted] Various Weapon Yields [redacted]	5-141
5-77	[redacted] Height of Cloud Bottom as a Function of Time for [redacted] Weapon Yields [redacted]	5-142
5-78	[redacted] Height of Cloud Top as a Function of Time for Various Weapon Yields [redacted]	5-143

[redacted]

LIST OF ILLUSTRATIONS (Continued)

Figure	*Title*	*Page*
5-79	[redacted] Dose Received While Flying Through a Nuclear Cloud as a Function of Transit Time Through the Cloud [redacted]	5-144
6-1	[redacted] Gamma Ray Interaction with Matter [redacted]	6-7
6-2	[redacted] Displacement Damage in a Crystalline Solid [redacted]	6-9
6-3	[redacted] Annealing Due to Vacancy-Interstitial Recombination and Escape of Defects from Semiconductor [redacted]	6-10
6-4	[redacted] Heating [redacted]	6-10
6-5	[redacted] Thermomechanical Shock Effects [redacted]	6-15
7-1	[redacted] The Compton Effect [redacted]	7-2
7-2	[redacted] Compton Current at 500 Meters from a 1-Mt Ground Burst [redacted]	7-3
7-3	[redacted] Conductivity at 500 Meters from a 1-Mt Low Altitude Burst [redacted]	7-4
7-4	[redacted] Charge Separation Model [redacted]	7-5
7-5	[redacted] Limits on Electric Field Time Waveforms [redacted]	7-6
7-6	[redacted] Simple Illustration of Air-Burst EMP [redacted]	7-7
7-7	[redacted] Comparison of General Waveforms for the Dipole Moment, the Current, and the E-Field [redacted]	7-8
7-8	[redacted] Simple Illustration of Surface Burst EMP [redacted]	7-9
7-9	[redacted] Shape of Magnetic Field for Toroid Model [redacted]	7-10
7-10	[redacted] Illustration of the Basic Geometry of the High-Altitude Burst [redacted]	7-11
7-11	[redacted] Ground Coverage for Bursts of 100, 300, and 500 km (about 62, 186, and 310 miles) [redacted]	7-12
7-12	[redacted] Maximum Peak Electric Field as a Function of Gamma Ray Yield for Selected Burst Heights [redacted]	7-13
7-13	[redacted] Time Waveform of High-Altitude Radiated Signal [redacted]	7-14
7-14	[redacted] Amplitude of High-Altitude Radiated Signal [redacted]	7-15
7-15	[redacted] Geometry of Propagation Effects on Exoatmospheric Systems [redacted]	7-15
7-16	[redacted] IEMP Generation [redacted]	7-16
7-17	[redacted] Categories of System Operation Regions [redacted]	7-18
7-18	[redacted] Mission/Environment Matrix [redacted]	7-19
7-19	[redacted] Field Directions of Ground-Burst EMP [redacted]	7-20
7-20	[redacted] Peak Magnetic Field B_φ Versus Overpressure for Varying Ground Conductivities and Yields [redacted]	7-21
7-21	[redacted] Peak Radial Electric Field E_r Versus Overpressure for Varying Ground Conductivities and Yields [redacted]	7-22
7-22	[redacted] Peak Transverse Electric Field E_θ Versus Overpressure for Varying Ground Conductivities and Yields [redacted]	7-23

[redacted]

LIST OF ILLUSTRATIONS (Continued)

Figure	Title	Page
7-23	[redacted] Peak Air Conductivity Versus Overpressure for Yields of 100 kt and 1 Mt [redacted]	7-24
7-24	[redacted] B_φ Time Waveform at the Air-Ground Interface for Several psi Levels [redacted]	7-25
7-25	[redacted] Fourier Amplitude of B_φ Waveform of Figure 7-24 [redacted]	7-26
7-26	[redacted] E_r Time Waveform at the Air-Ground Interface for Several psi Levels, $\sigma_g = 10^{-2}$ mho/m [redacted]	7-27
7-27	[redacted] Fourier Amplitude of E_r Waveform of Figure 7-26 [redacted]	7-28
7-28	[redacted] E_θ Time Waveform of the Air-Ground Interface for Several psi Levels, $\sigma_g = 10^{-2}$ mho/m [redacted]	7-29
7-29	[redacted] Fourier Amplitude of E_θ Waveform of Figure 7-28 [redacted]	7-30
7-30	[redacted] Air Conductivity Time Waveforms at the Air-Ground Interface for Several psi Levels, $\sigma_g = 10^{-2}$ mho/m [redacted]	7-31
8-1	[redacted] Optical and Radio Frequency Bands [redacted]	8-2
8-2	[redacted] Fireball Electron Density and Temperature, 1-Mt at 25 km [redacted]	8-5
8-3	[redacted] Fireball Electron Density and Temperature, 1-Mt at 50 km [redacted]	8-6
8-4	[redacted] Fireball Electron Density and Temperature, 1-Mt at 75 km [redacted]	8-7
8-5	[redacted] Fireball Electron Density and Temperature, 1-Mt at 150 km [redacted]	8-8
8-6	[redacted] Fireball Electron Density and Temperature, 1-Mt at 400 km [redacted]	8-10
8-7	[redacted] Ion-Pair Density Due to Prompt Radiation from a 1-Mt Burst Detonated at 120 km, $t = 0$ [redacted]	8-11
8-8	[redacted] D-Region Electron Density Caused by Prompt Radiation (Saturation) [redacted]	8-12
8-9	[redacted] Quasi-Equilibrium Electron Density Due to Gamma Rays [redacted]	8-13
8-10	[redacted] Location of Delayed Ionization Regions [redacted]	8-14
8-11	[redacted] Quasi-Equilibrium Electron Density Due to Beta Particles, Debris Altitude Greater Than 60 km [redacted]	8-15
8-12	[redacted] Incremental Absorption Due to Electron-Neutral Collisions [redacted]	8-17
8-13	[redacted] Incremental Absorption Due to Electron-Ion Collisions, Electron Temperature = 1000°K [redacted]	8-18
8-14	[redacted] Radiation Sources Causing Absorption Outside the Fireball [redacted]	8-19
8-15	[redacted] Apparent Fireball Surface Scattering Coefficient at 400 MHz [redacted]	8-22
8-16	[redacted] Examples of Fireball Geometry [redacted]	8-24
8-17	[redacted] Debris Behavior for Detonation Altitudes Greater Than 85 km [redacted]	8-26
8-18	[redacted] Illustration of Debris and Beta-Particle Absorption Regions for Times Later Than 10 Minutes After Burst, H_0 Above 120 km [redacted]	8-27
8-19	[redacted] Maximum Fireball Rise [redacted]	8-31
8-20	[redacted] Time for Fireball to Reach Its Maximum Altitude [redacted]	8-32

LIST OF ILLUSTRATIONS (Continued)

Figure	Title	Page
8-21	Altitude Normalizing Factor h_N	8-33
8-22	Fireball Height Factor	8-34
8-23	Initial Fireball Radius	8-35
8-24	Fireball Radius	8-36
8-25	Change in Fireball/Debris-Region Radius after Seven Minutes	8-37
8-26	Magnetic Equilibrium Radius	8-41
8-27	Debris Height Factor	8-41
8-28	Maximum Debris Offset	8-42
8-29	Debris Offset Correction Factor	8-42
8-30	Fraction of Total Debris Transported to Conjugate Region (Region 3)	8-52
8-31	Altitude of Debris Region 1, 10-kt Burst	8-53
8-32	Altitude of Debris Region 1, 100-kt Burst	8-53
8-33	Altitude of Debris Region 1, 1-Mt Burst	8-54
8-34	Altitude of Debris Region 1, 10-Mt Burst	8-54
8-35	Radius of Debris Region 1, 10-kt Burst	8-55
8-36	Radius of Debris Region 1, 100-kt Burst	8-55
8-37	Radius of Debris Region 1, 1-Mt Burst	8-56
8-38	Radius of Debris Region 1, 10-Mt Burst	8-56
8-39	One-Way Absorption Through Debris Region Due to Beta-Particle Ionization	8-64
8-40	Reference Weapon Yield W_r	8-67
8-41	One-Way Vertical Absorption Due to Prompt Radiation	8-68
8-42	Geometry for Gamma Ray Absorption	8-73
8-43	One-Way Absorption Due to Gamma Rays, f = 1000 MHz, θ_d = +60 Degrees	8-74
8-44	One-Way Absorption Due to Gamma Rays, f = 1000 MHz, θ_d = 0 Degrees	8-75
8-45	One-Way Absorption Due to Gamma Rays, f = 1000 MHz, θ_d = -60 Degrees	8-76
8-46	Gamma Radiation Intensity Nomogram	8-77
8-47	Correction Factor for Gamma Ray Flux	8-78
8-48	One-Way Vertical Absorption Due to Gamma Rays	8-79
8-49	Offset of Beta-Absorption Region	8-83
8-50	Beta Radiation Intensity Nomogram	8-84
8-51	One-Way Vertical Absorption Due to Beta Particles, Debris Altitude Above 60 km	8-85

LIST OF ILLUSTRATIONS (Continued)

Figure	*Title*	*Page*
8-52	Sketch of Absorption-Region Geometry for Example 2	8-86
8-53	Magnetic Conjugate Map	8-88
8-54	World Map of Magnetic Dip	8-90
8-55	Secant θ Chart	8-92

[redacted]

(This page intentionally left blank)

[redacted]

LIST OF TABLES (Continued)

Table	Title	Page
5-1	Weapon Neutron Output Spectra	5-2
5-2	The Standard Atmosphere	5-12
5-3	Representative Types of Nuclear Weapons	5-25
5-4	Chemical Composition of Illustrative Soils	5-54
5-5	Relative Theoretical Dose Rates from Early Fallout at Various Times After a Nuclear Explosion	5-73
5-6	Percentage of the Infinite Residence Dose Received from 1 Hour to Various Times After Explosion	5-75
5-7	Examples Selected for Base Surge and Pool Exposure Rates	5-108
5-8	Examples Selected for Total Exposure	5-108
7-1	Variation of Range, R_o, at Which the Radiation Region Begins, with Yield	7-10
8-1	Approximate Stopping Altitudes for Principal Weapon Outputs Causing Ionization	8-3
8-2	Fireball Location and Dimensions for Detonations Above 80 km	8-47
8-3	Absorption (dB) Through Fireball for Detonations Below 80 km, W = 10 kt	8-59
8-4	Absorption (dB) Through Fireball for Detonations Below 80 km, W = 100 kt	8-60
8-5	Absorption (dB) Through Fireball for Detonations Below 80 km, W = 1 Mt	8-61
8-6	Absorption (dB) Through Fireball for Detonations Below 80 km, W = 10 Mt	8-62
8-7	Absorption (dB) Through Fireball at 1000 MHz for Detonations Above 80 km	8-63

[redacted]

(This page intentionally left blank)

[redacted]

[redacted]

Security Classification

14. KEY WORDS	LINK A		LINK B		LINK C	
	ROLE	WT	ROLE	WT	ROLE	WT
Nuclear Weapon Effects						
Blast and Shock Phenomena						
Air Blast Phenomena						
Cratering Phenomena						
Ground Shock Phenomena						
Water Shock Phenomena						
Underwater Cratering Phenomena						
Water Surface Phenomena						
Thermal Radiation Phenomena						
X-Ray Radiation Phenomena						
Nuclear Radiation Phenomena						
Initial Nuclear Radiation						
Neutron Induced Activity						
Residual Radiation						
Transient Radiation Effects on Electronics Phenomena						
TREE Phenomena						
Electromagnetic Pulse Phenomena						
EMP Phenomena						
Phenomena Affecting Electromagnetic Wave Propagation						
Blast and Shock Damage						
Thermal Radiation Damage						
X-Ray Damage						
Nuclear Radiation Shielding						
TREE Damage Mechanisms						
EMP Damage						
Personnel Casualties						
Blast Injury						
Thermal Injury						
Nuclear Radiation Injury						
Combined Injury						
Damage to Structures						
Shock Vulnerability of Equipment and Personnel						
Damage to Field Fortifications						
Damage to Dam and Harbor Installations						
Damage to POL Tanks						
Fire in Urban Areas						
Damage to Naval Equipment						
Damage to Surface Ships						
Damage to Subsurface Ships						
Damage to Aircraft						
Damage to Military Field Equipment						
Air Blast Damage to Military Field Equipment						
Thermal Damage to Military Field Equipment						
TREE Damage to Military Field Equipment						
Forest Stand Damage						
Air Blast in Forest Stands						
Blowdown						
Thermal Damage in Forests						
Forest Blowdown Effects on Mobility						
Damage to Missiles						
Radio Frequency Signal Degradation Relevant to Communications Systems						
Radio Frequency Signal Degradation Relevant to Radar Systems						

[redacted]

Security Classification

LIST OF PROBLEMS (Continued)

Problem	*Title*	*Page*
5-12	Calculation of Fallout Gamma Radiation Dose Rate Contours for Bursts in the Transition Zone	5-97
5-13	Calculation of Fallout Gamma Ray Dose Rate Contours for Underground Bursts	5-101
5-14	Calculation of Dose Received While Flying Through a Nuclear Cloud	5-140
8-1	Calculation of Fireball Size, Shape, and Location for a Burst Below 85 kilometers	8-29
8-2	Calculation of Fireball Size, Shape, and Location for a Burst Between 85 and 120 kilometers	8-38
8-3	Calculation of Size, Shape, and Location of Fireball and Debris Regions for a Burst Above 120 kilometers	8-43
8-4	Absorption through the Fireball	8-57
8-5	Absorption Due to Prompt Radiation Outside the Fireball	8-65
8-6	Absorption Outside the Fireball Due to Delayed Gamma Rays	8-69
8-7	Calculation of Absorption Outside the Fireball Due to Beta Particles	8-80
8-8	Magnetic Conjugate Map	8-87
8-9	Geomagnetic Dip Angle Map	8-89
8-10	Secant θ Chart	8-91

[redacted] Classification

DOCUMENT CONTROL DATA - R & D

(Security classification of title, body of abstract and indexing annotation must be entered when the overall report is classified)

1. ORIGINATING ACTIVITY (Corporate author)
Director
Defense Nuclear Agency
Washington, D.C. 20305

2a. REPORT SECURITY CLASSIFICATION
[redacted]

2b. GROUP

3. REPORT TITLE
Capabilities of Nuclear Weapons Effects Manual Number 1

4. DESCRIPTIVE NOTES (Type of report and inclusive dates)
Handbook

5. AUTHOR(S) (First name, middle initial, last name)
N. A.

6. REPORT DATE	7a. TOTAL NO. OF PAGES	7b. NO. OF REFS
1 July 1972	~~822~~ 858	

8a. CONTRACT OR GRANT NO.	9a. ORIGINATOR'S REPORT NUMBER(S)
DASA 01-69-C-0022 b. PROJECT NO. NWER XXAXD c. Task and Subtask A002 d. Work Unit 01 and 02	DNA EM-1, Part I 9b. OTHER REPORT NO(S) (Any other numbers that may be assigned this report)

10. DISTRIBUTION STATEMENT
None

11. SUPPLEMENTARY NOTES	12. SPONSORING MILITARY ACTIVITY
Supersedes and cancels "Capabilities of Nuclear Weapons," DASA EM-1 dated January 1968.	Director Defense Nuclear Agency Washington, D.C. 20305

13. ABSTRACT

[redacted] This edition of the "Capabilities of Nuclear Weapons" represents the continuing efforts by the Defense Nuclear Agency to correlate and make available nuclear weapons effects information obtained from nuclear weapons testing, small-scale experiments, laboratory effort and theoretical analysis. This document presents the phenomena and effects of a nuclear detonation and relates weapons effects manifestations in terms of damage to targets of military interest. It provides the source material and references needed for the preparation of operational and employment manuals by the Military Services.

[redacted] The "Capabilities of Nuclear Weapons" is not intended to be used as an employment or [redacted] manual by itself, since more complete descriptions of phenomenological [redacted] should be obtained from the noted references. Every effort has been made [redacted] the most current reliable data available on 31 December 1971 in order [redacted] the Armed Forces in meeting their particular requirements for operati[redacted] target analysis purposes.

[redacted] Due to the physical size of the document, it is published in two (2) parts, [redacted]

DD FORM 1 NOV 65 1473

[redacted]
Security Classification

Best Available Copy

DTIC FILE COPY

Accession For
NTIS GRA&I ☒
DTIC TAB ☐
Unannounced ☐
Justification
By
Distribution/
Availability Codes
Dist | Avail and/or Special
A-1

QUALITY INSPECTED 4

UNANNOUNCED

DTIC ELECTE 2 MAR 1989 S D E

AD-A955 404

[redacted]

PART I
PHENOMENOLOGY

Chapter 1
INTRODUCTION

[redacted] PURPOSE [redacted]

[redacted] This manual presents a summary of the capabilities of nuclear weapons. Quantitative treatments are presented graphically in most cases. The manual is divided into two parts. Part I. Phenomenology, treats the basic phenomena of blast and shock. thermal radiation, X-ray radiation. nuclear radiation, transient radiation effects on electronics, electromagnetic pulse phenomena. and phenomena affecting electromagnetic propagation. Part II, Damage Criteria, discusses the mechanisms of casualty production and damage to military targets. and describes the response of these targets by correlating the basic physical phenomena with various defined degrees of damage.*

[redacted] The data presented here are interpretations of complex results of the nuclear weapons effects research and test programs of the Department of Defense. A constant effort is made to deduce theoretical models and scaling laws for the various weapons effects that permit a quantitative prediction of the extent of a given effect from a weapon of one yield related to weapons of other yields. Since the initiation of the limited nuclear test ban treaty, a large amount of effort has been devoted to the development of complex computer codes to predict the environments created by the various phenomena resulting from nuclear explosions and the interactions of these environments with personnel and military systems. A large number of the scaling laws presented herein were derived from the results of calculations performed with these codes.

[redacted] An estimate of the degree of reliability accompanies most of the data presented herein. Statements of the reliability of damage data only pertain to the basic effects data, which, for the target analyst represent the "radius of effect." They should not be confused with the terms variability and probability of damage, which pertain to target response; nor do these estimates include operational considerations such as linear, circular, or spherical aiming and fuzing errors, yield variations, and target intelligence.

[redacted] CHARACTERISTICS OF NUCLEAR EXPLOSIONS [redacted]

[redacted] An explosion, in general, results from the very rapid release of a large amount of energy within a limited space. This is true for a conventional "high explosive," such as TNT, as well as for a nuclear explosion. The sudden liberation of energy causes a considerable increase of temperature and pressure, so that all the materials present are converted into hot compressed gases. Detonation of high explosives results from chemical reactions, and the energy manifests primarily as blast energy, regardless of environmental conditions. For a given amount

*[redacted] The unclassified publication "The Effects of Nuclear Weapons," which contains a more detailed qualitative discussion of these basic phenomena, supplements this manual.

[redacted]

This document has been approved for public release and sale; its distribution is unlimited.

89 3 02 028

of energy, the mass of a nuclear explosive would be much less than that of a conventional high explosive. Consequently, there is a much smaller amount of material in the weapon itself to be converted into the hot, compressed gases mentioned above in the former than in the latter case. Also, the temperatures reached in a nuclear explosion are much higher than in a conventional explosion. In a nuclear explosion the energy manifests itself in the form of blast, thermal radiation, nuclear radiation, and other electromagnetic phenomena that will be discussed in succeeding paragraphs. The energy released from a nuclear explosion is released essentially from a point source, whereas a comparable amount of energy released from a detonation of high explosives would require an enormous volume of explosive. Additionally, the energy released in a nuclear explosion results from a fission process, a fusion process, or a combination of the two, each of which involve the formation of different atomic nuclei and the release of large quantities of energy for each reaction. As mentioned previously, the energy derived from the detonation of high explosives arises from chemical reactions; these involve the rearrangement among the atoms, e.g., of hydrogen, carbon, oxygen, and nitrogen present in the high explosive material. The forces between the protons and neutrons within atomic nuclei are tremendously greater than those between atoms; consequently, nuclear energy is of a much higher order of magnitude than conventional (or chemical) energy when equal masses are considered.

1-1 Fission Energy and the Chain Reaction

The materials used to produce nuclear explosions by fission are certain isotopes of uranium and plutonium. Natural uranium consists mainly of two isotopes, uranium-235 (about 0.7 percent), and uranium-238 (about 99.3 percent). Uranium-235 is the much less abundant of these isotopes, but is the readily fissionable species that is commonly used in nuclear weapons. Another isotope, uranium-233, does not occur naturally, but it is readily fissionable and it can be made artificially starting with thorium-232. Since the element plutonium has no natural isotopes, the fissionable isotope used in nuclear weapons, plutonium-239, is made artificially from uranium-238.

When a free (or unattached) neutron enters the nucleus of a fissionable atom, it can cause the nucleus to split into two smaller parts. This is the fission process, which is accompanied by the release of a large amount of energy. The smaller (or lighter) nuclei which result are called the "fission products." The complete fission of 1 pound of uranium or of plutonium releases as much explosive energy as does the explosion of about 8,000 (short) tons of TNT.

The significant point about the fission of a uranium (or plutonium) nucleus by means of a neutron, in addition to the release of a large quantity of energy, is that the process is accompanied by the instantaneous emission of two or more neutrons; thus,

$$\text{Neutron} + \left\{\begin{array}{l}\text{uranium-235}\\ \text{(or uranium-233)}\\ \text{(or plutonium-239)}\end{array}\right\} \rightarrow \begin{array}{l}\text{fission fragments} +\\ \text{2 or 3 neutrons} +\\ \text{energy.}\end{array}$$

The neutrons liberated in this manner are able to induce fission of additional uranium (or plutonium) nuclei, each such process resulting in the emission of more neutrons which can produce further fission, and so on. Thus, in principle, a single neutron could start off a chain of nuclear fissions, the number of nuclei involved, and the energy liberated, increasing at a tremendous rate.

There are many different ways in which the nuclei of a given fissionable species can split up into two fission fragments, but the total amount of energy liberated per fission does not vary greatly. A satisfactory average value of this energy is 200 million electron volts. The million

[redacted]

electron volt (or 1 MeV) unit has been found convenient for expressing the energy released in nuclear reactions; it is equivalent to 1.6×10^{-6} erg or 1.6×10^{-13} joule. The manner in which this energy is distributed among the fission fragments and the various radiations associated with fission is shown in Table 1-1.

Table 1-1. [redacted] Distribution of Fission Energy [redacted]

	MeV
Kinetic energy of fission fragments	165 ± 5
Instantaneous gamma-ray energy	7 ± 1
Kinetic energy of fission neutrons	5 ± 0.5
Beta particles from fission products	7 ± 1
Gamma rays from fission products	6 ± 1
Neutrinos from fission products	10
Total energy per fission	200 ± 8.5

[redacted] The results in the table may be taken as being applicable to either uranium-233, uranium-235, or plutonium-239. These are the only three known substances, which are reasonably stable so that they can be stored without appreciable decay, that are capable of undergoing fission by neutrons of all energies. Hence, they are the only materials that can be used to sustain a fission chain. Uranium-238, the most abundant isotope in natural uranium, and thorium-232 will suffer fission by neutrons of high energy only, but not by those of lower energy. For this reason these substances cannot sustain a chain reaction. However, when fission does occur in these elements, the energy distribution is quite similar to that shown in the table.

[redacted] Only part of the fission energy is immediately available in a nuclear explosion; this includes the kinetic energy of the fission fragments, most of the energy of the instantaneous gamma rays, which is converted into other forms of energy within the exploding weapon, and also most of the neutron kinetic energy, but only a small fraction of the decay energy of the fission products. There is some compensation from energy released in reactions in which neutrons are captured by the weapon debris, and so it is usually accepted that about 180 MeV of energy are available per fission. There are 6.02×10^{23} nuclei in 235 grams of uranium-235 (or 239 grams of plutonium-239), and by making use of familiar conversion factors (Appendix B) the results quoted in Table 1-2 may be obtained for the energy (and other) equivalents of 1 kiloton of TNT. The calculations are based on an accepted, although somewhat arbitrary, figure of 10^{12} calories as the energy released in the explosion of this amount of TNT.*

Table 1-2. [redacted] Equivalents of 1 Kiloton of TNT [redacted]

Complete fission of 0.057 kg (57 grams or 2 ounces) fissionable material
Fission of 1.45×10^{23} nuclei
10^{12} calories
2.6×10^{25} million electron volts
4.18×10^{19} ergs
1.16×10^{6} kilowatt-hours
3.97×10^{9} British thermal units

[redacted] The majority of the experimental and theoretical values of the explosive energy released by TNT range from 900 to 1,100 calories per gram. At one time, there was some uncertainty as to whether the term "kiloton" of TNT referred to a short kiloton (2×10^{6} pounds), a metric kiloton (2.205×10^{6} pounds), or a long kiloton (2.24×10^{6} pounds). In order to avoid ambiguity, it was agreed that the term "kiloton" would refer to the release of 10^{12} calories of explosive energy. This is equivalent to 1 short kiloton of TNT if the energy release is 1,102 calories per gram.

[redacted]

1-2 Fusion (Thermonuclear) Reactions

In nuclear fusion, a pair of light nuclei unite (or fuse) together, to form a nucleus of a heavier atom. An example is the fusion of the hydrogen isotope known as deuterium or "heavy hydrogen." Under suitable conditions, two deuterium nuclei may combine to form the nucleus of a heavier element, helium, with the release of energy.

Nuclear fusion reactions can be brought about by means of very high temperatures, and they are then referred to as "thermonuclear processes." The actual quantity of energy liberated, for a given mass of material, depends on the particular isotope (or isotopes) involved in the nuclear fusion reaction. As an example, the fusion of all the nuclei present in 1 pound of the hydrogen isotope deuterium would release roughly the same amount of energy as the explosion of 26,000 tons of TNT.

Energy production in the sun and stars is undoubtedly due to fusion reactions involving the nuclei of various light (low atomic weight) atoms. From experiments made in laboratories with charged-particle accelerators, it was concluded that the fusion of isotopes of hydrogen was possible. This element is known to exist in three isotopic forms, in which the nuclei have mass numbers of 1, 2, and 3, respectively. These are generally referred to as hydrogen (^{1}H), deuterium (^{2}H or ^{2}D), and tritium (^{3}H or ^{3}T). All the nuclei carry a single positive charge, i.e., they all contain one proton, but they differ in the number of neutrons. The lightest (^{1}H) nuclei (or protons) contain no neutrons; the deuterium (^{2}H) nuclei contain one neutron, and tritium (^{3}H) nuclei contain two neutrons.

Several different fusion reactions have been observed between the nuclei of the three hydrogen isotopes, involving either two similar or two different nuclei. In order to make these reactions occur to an appreciable extent, the nuclei must have high energies. One way in which this energy can be supplied is by means of an accelerator, such as a cyclotron. Another possibility is to raise the temperature to very high levels. In this last circumstance the fusion processes are referred to as "thermonuclear reactions," as mentioned previously.

Five thermonuclear fusion reactions appear to be of interest for the production of energy because they are expected to occur sufficiently rapidly at realizable temperatures; these are

$$^2D + {}^2D = {}^3He + n + 3.3 \text{ MeV}$$

$$^2D + {}^2D = {}^3T + {}^1H + 4.0 \text{ MeV}$$

$$^3T + {}^2D = {}^4He + n + 17.6 \text{ MeV}$$

$$^3T + {}^3T = {}^4He + 2n + 11.3 \text{ MeV}$$

$$^2D + {}^3He = {}^4He + {}^1H + 18.3 \text{ MeV},$$

where He is the symbol for helium and n (mass = 1) represents a neutron. The energy liberated in each case is given in million electron volt (MeV) units. The first two of these reactions occur with almost equal probability at the temperatures associated with nuclear explosions (several tens of million degrees Kelvin), whereas the third reaction has a much higher probability and the fourth and fifth a much lower probability. Thus, a valid comparison of the energy released in fusion reactions with that produced in fission can be made by noting that, as a result of the first three reactions given above, five deuterium nuclei, with a total mass of 10 units, will liberate 24.8 MeV upon fusion. On the other hand, in the fission process, e.g., of uranium-235, a mass of 235 units will produce a total of about 200 MeV of energy (paragraph 1-1). Weight for weight, therefore, the fusion of deuterium nuclei would produce nearly three times as much energy as the fission of uranium or plutonium.

In order to make the nuclear fusion reactions take place at an appreciable rate, tempera-

[redacted]

[redacted]

tures of the order of several tens of million degrees are necessary. The only practical way at present in which such temperatures can be obtained on earth is by means of a fission explosion. Consequently, by combining a quantity of deuterium (or a mixture of deuterium and tritium) with a fission device, it should be possible to initiate one or more of the thermonuclear fusion reactions given above. If these reactions accompanied by energy evolution, can be propagated rapidly through a volume of the hydrogen isotope (or isotopes) a thermonuclear explosion may be realized.

[redacted] Another reaction of interest in thermonuclear weapons is

$$^{6}Li + n \rightarrow {}^{4}He + {}^{3}T + 4.8 \text{ MeV},$$

where ^{6}Li is the symbol for the lithium-6 isotope, which makes up about 7.4 percent of natural lithium. Other reactions can occur between both lithium-6 and the more abundant isotope lithium-7 and various particles that are present within the weapon. However, the reaction shown above is of most interest for two reasons: (1) it has a high probability of occurrence; (2) if the lithium is placed in the weapon in the form of lithium-deuteride, the tritium that results from the reaction has a high probability of reacting with the deuterium to produce large amounts of energy as well as additional neutrons (see the third of the previously listed fusion reactions).

[redacted] As discussed above, several of the fusion processes between nuclei of hydrogen isotopes produce high energy neutrons. These can cause fission in uranium-238, the most abundant isotope in natural uranium, as well as in uranium-235 and plutonium-239. Consequently, association of the appropriate fusion reactions with fissile materials can result in an extensive utilization of the latter for the release of energy.

[redacted] Fission weapon yield also may be enhanced by a process known as boosting. In this process thermonuclear reactions are used to produce fast neutrons. While some energy gain is realized as a result of the thermonuclear reactions that occur, the primary increase in the yield is due to the additional fissions produced by the interaction of the fast neutrons with the fissionable materials.

1-3 Weapon Yield Ratings [redacted]

[redacted] The "yield" of a nuclear weapon is a measure of the amount of explosive energy it can produce. It is the usual practice to state the yield in terms of the quantity of TNT that would generate the same amount of energy when it explodes. Thus, a 1-kiloton nuclear weapon is one which produces the same amount of energy in an explosion as does 1 kiloton (or 1,000 tons) of TNT. As discussed in paragraph 1-1, this quantity of energy has been somewhat arbitrarily established at 10^{12} calories (see footnote on page 1-3). Similarly, a 1-megaton weapon would have the energy equivalent of 1 million tons (1,000 kilotons) of TNT, or 10^{15} calories. Since about 10 percent of the total fission energy is released in the form of residual nuclear radiation some time after the detonation (Table 1-1), this is not included when the energy yield of a nuclear explosion is stated, e.g., in terms of a TNT equivalent. Hence, in a pure fission weapon the explosion energy is about 90 percent of the total fission energy. In a thermonuclear device, the explosion energy is less than the total energy by about 10 percent of the fission contribution, e.g., if the total energy is equally divided between the fission and fusion processes, the explosion energy would be about 95 percent of the total energy of the fission and fusion reactions. This common convention will be adhered to in subsequent chapters. For example, when the yield of a nuclear weapon is quoted or used in equations, figures, etc., it will represent that por-

[redacted]

[redacted]

[redacted]

tion of the energy delivered within a minute or so, and will exclude the contribution of the residual nuclear radiation.

[redacted] Another method used in comparing nuclear explosion yields with conventional explosives, and one that is often confused with the rating of energy in terms of TNT energy equivalents, is the rating of effects in terms of TNT effects equivalence, i.e., the effect of a particular phenomenon of a nuclear detonation expressed in terms of the amount of TNT that would produce the same effect. An example of TNT effect equivalence is the expression of the crater radius of a nuclear surface burst in terms of the amount of TNT that would be required to produce the same radius.

[redacted] A "nominal" weapon is one whose yield is 20 kt. The use of this term arose from the approximately 20-kt yields at Hiroshima, Nagasaki, and the Bikini (Crossroads) tests. In some reports nuclear weapons effects data are based on the nominal weapon.

[redacted] For simplicity and convenience, most physical phenomena data and much of the damage data are presented as a function of the range from a 1-kt explosion, from which the phenomena or damage for other yields may be obtained readily, by the appropriate scaling procedures given wherever their use is required.

1-4 Effects of Environment and Time [redacted]

[redacted] The effects of nuclear weapons of a particular design and yield are determined by the environment in which the weapon is burst, and the time frame under consideration. The initial physical phenomena from nuclear detonations are grossly the same during the first microsecond after initiation. Several minutes after detonation, the remaining effects will be only those of residual radiation, e.g., fallout, atmospheric ionization and associated phenomena. Since the density, composition, physical state, and pressure of the medium surrounding the detonation primarily determine the resulting effects after the first microsecond, an early time history of a nuclear detonation is given in the following paragraph. This description is carried to the point when the energy released in the explosion begins to interact with its environment. Succeeding paragraphs provide brief descriptions of the phenomena that occur in different burst regimes. More complete descriptions of each phenomenon are provided in Chapters 2 through 8.

1-5 Early Time History [redacted]

[redacted] When a nuclear weapon is detonated, the actual duration of the process varies considerably, depending on the design of the weapon. It is sufficient, however, to assume that the energy is released during the first microsecond. In this period all prompt nuclear radiation (neutrons, gammas, and X-rays) has been emitted and has departed from the immediate environment of the weapon disintegration, leaving behind the energetic reaction and weapon products. These products are at high temperatures and behave as an efficient thermal radiator (see Sections I and II, Chapter 4). Although reaction products from fission will continue to decay radioactively and will emit additional gamma radiation and beta particles, they are considered as secondary effects in this time frame.

[redacted] The high temperature results in tremendous internal pressures. Under the influence of these pressures, the hot debris expands at a very high velocity. Because it is radiating energy rapidly and is being cooled by expansion, the residual weapon debris cools rapidly. Within about the first microsecond for most weapons, 70 to 80 percent of the explosion energy is emitted as thermal energy, most of which consists of X-rays. At the end of this period, most of the remaining weapon energy is kinetic energy. At this time, when all important detonation processes have taken place, the weapon debris has begun to react with its environment.

[redacted]

[redacted]

[redacted] AIR BURST [redacted]

[redacted] An air burst is defined as the explosion of a nuclear weapon at such a height that the weapon phenomenon of interest is not significantly modified by the earth's surface. (Also see description of high altitude burst in paragraph 1-26 to 1-29.) For example, when considering blast this height is such that the reflected wave passing through the fireball does not overtake the incident wave above the fireball (heights greater than about 160 $W^{0.35}$ ft ± 15 percent, where W is the weapon yield in kilotons). For thermal radiation, an air burst occurs at such heights above the surface that the apparent thermal yield viewed from the ground is not affected by surface phenomena, such as heat transfer to the surface, distortion of the fireball by the reflected shock wave, thermal reflection from the surface (heights above the surface greater than about 180 $W^{0.4}$ ft ± 20 percent for yields of 10 kt to 100 kt, and ± 30 percent for other yields). When considering fallout, an air burst occurs at such heights that militarily significant local fallout does not result (a minimum height of burst has generally been set at 100 $W^{0.35}$ feet, but for yields above 100 kt, 180 $W^{0.35}$ feet is recommended for a conservative estimate). For certain other phenomena of interest, e.g., neutron-induced activity, the height of burst at which the earth's surface fails to produce an effect is difficult or impossible to distinguish.

1-6 Development [redacted]

[redacted] The first interaction between weapon output and the surrounding atmosphere comes from the initial gamma rays emitted during the weapon detonation. These initial gammas arise both from the fission gammas and from gammas produced by inelastic neutron scattering in the weapon mass. These gamma rays interact mainly by Compton collisions with the electrons of the air molecules, resulting in ionization of the air and degradation of the gamma ray energy. The results of such interactions are described in Chapters 5 through 8.

[redacted] Another important interaction between the weapon output and the atmosphere comes from the neutrons produced during the fission and fusion reactions. Inelastic scattering of high-energy neutrons by nuclei of the air and the ground, and capture of slow neutrons by nitrogen in the air and by various elements in the ground provide sources of secondary gamma rays. The relative importance of the inelastic and capture gamma rays depends strongly upon the neutron spectrum of the source.

[redacted] As a result of X-ray and debris interactions, a very hot plasma remains in the vicinity of the explosion. This plasma consists of electrons and stripped nuclei of the fission and fusion products, of the elements of the weapon case and components, and of any other elements in the immediate vicinity, such as nitrogen and oxygen in the air. The radiating temperature depends on the weapon design and the total yield, but it may range from a few million to many tens of millions of degrees Kelvi[redacted] see Introduction and Section 1, Chapter 4). Although the spectrum of the emissions from this plasma is not exactly that of a black body, particularly because the temperature is by no means uniform, it often does approximate a black body spectrum[redacted] see Section 1, Chapter 4). Plasmas at these temperatures emit electromagnetic radiation that is primarily in the X-ray region of the spectrum (see Introduction, Chapter 4). If the burst occurs in the lower part of the atmosphere, the radiated energy is absorbed by the air in a sphere that initially may be only a few yards larger than the weapon. Since this sphere itself is at a high temperature, it again radiates X-rays (although at a lower temperature). The process of absorption and re-radiation continues until the energy radiated by the weapon may occupy a sphere of air

[redacted]

of several tens of yards in diameter. The emission of this additional electromagnetic radiation covers a wide range of frequencies from about 1 cycle per second through radio, infrared, and visible to the soft X-rays.

The photon mean free paths in the hot fireball are of the order of (or longer than) the fireball diameter, and as a result the energy distribution and temperature are fairly uniform throughout the volume of hot gas. During this phase of growth, the fireball is consequently referred to as the "isothermal sphere." This name is something of a misnomer, since temperature gradients do exist, particularly near the advancing radiation front. As the fireball cools, the growth by re-radiation of energy continues at a progressively slower rate because the mean free path of the photons becomes smaller than the fireball dimensions. The decreasing velocity of the fireball front causes the pressure of the heated air behind the front to increase, and a shock wave begins to form. This is referred to as the "outer" shock wave.

During the isothermal sphere phase, the initially hot, high-pressure mass of weapon residues begins to expand outward as a pressure relief mechanism. Within a few microseconds, the material forms a thin, high-density shell, the hydrodynamic front, moving at high velocity. When this shell reaches the hot air outside the weapon, it begins to "snowplow" air ahead of it, and thereby transfers hydrodynamic energy into the air. The air is consequently heated further, and the additional radiation from the heated air contributes to fireball growth by radiation. Within a very short time, the hydrodynamic front becomes a strong shock wave, called the "inner" shock wave, propagating away from the burst point, but still within the fireball. All the phenomena described so far occur in the first few hundred microseconds after the explosion. During this period, fireball growth is dominated by radiation transport, with hydrodynamic energy dissipation playing a relatively minor role in the interior.

Since the transfer of energy by radiation becomes less rapid as the fireball cools, the inner shock front begins to advance faster than the radiation front and soon the two coincide. The inner shock front continues to advance more rapidly than the radiation front and moves ahead of it at the time when the temperature of the isothermal sphere has fallen to about 300,000°C (540,000°F). This phenomenon is called "hydrodynamic separation." For a 20-kiloton explosion it occurs at about 0.1 milliseconds (10^{-4} second) after the burst time when the fireball radius is roughly 40 feet. The partition of energy between blast and thermal at the time of hydrodynamic separation is determined by the relationship between photon mean free paths, fireball radius, and time after burst. The detonation conditions determine these quantities. The final character of the environment at some distance from the burst is not determined, however, until the time at which the inner shock wave overtakes the outer one that was formed at the radiation front. At low and moderate altitudes, the inner shock front appears to catch up with the outer at hydrodynamic separation. (At higher altitudes, the inner and outer fronts do not coincide at hydrodynamic separation, and the inner shock wave does not catch up until some later time, determined by the burst conditions.)

As the (combined) shock front from a normal air burst moves ahead of the isothermal sphere it causes a tremendous compression of the ambient air and the temperature is thereby increased to an extent sufficient to render the air incandescent. The luminous shell thus formed constitutes the advancing visible fireball during this "hydrodynamic phase" of fireball growth. The fireball now consists of two concentric regions. The inner (hotter) region is the isothermal sphere of uniform temperature, and

it is surrounded by a layer of luminous, shock-heated air at a somewhat lower, but still high, temperature. The surface of separation between the very hot core and the somewhat cooler outer layer is the radiation front. The development of an air burst described in these and subsequent paragraphs is shown in Figure 1-1.

1-7 Thermal Radiation

The relatively large amount of thermal radiation emitted by a nuclear explosion is one of its most striking characteristics. This radiant energy may amount to from one-third to one-half of the total energy released by an air burst weapon (see Chapter 3).

During the early stages of expansion of the incandescent shock front, the emitted radiant power increases as the luminous sphere increases in size, even though expansion causes a temperature decrease, until a maximum (the first maximum) is reached. At this point, the effect of the rapid rate of decrease in temperature overrides the enhancement of radiant power resulting from the increasing area of the luminous sphere.

Subsequently, further expansion causes a reduction in the radiant power. Eventually the shock front temperature is reduced to a point where the shock front is no longer incandescent, at which time the rate of emission of radiation from the shock front will be negligible. In effect, the shock front has become transparent, and the hotter incandescent inner core would be expected to be observable. Initially, however, the radiation emitted from the inner core is absorbed by compounds formed in the shock-heated air, and the radiant power reaches a minimum. As these compounds break down, the radiant power emitted from the inner core begins to pass through, and the inner core becomes the visible source of radiation. Thus, the radiant power increases again. This change in boundary of the observable luminous sphere from the shock front to the incandescent inner core gives rise to the term "breakaway."

As the opacity of the shock-heated air decreases, the apparent temperature as measured from a distance approaches that of the hot gases of the inner core, and the emitted radiant power approaches a second maximum. Further expansion and radiative cooling of the hot gases, however, give rise to a slow decrease in the radiant power. This decrease is so slow, relative to the previous rise and decline, that a large percentage of the total radiant energy emitted is delivered during this period. Finally, the rate of delivery of radiant energy drops to a low value.

The subsequent characteristics of the shock, or blast, wave are discussed in paragraph 1-8 below and Chapter 2. The effects of the thermal pulse are discussed in Chapter 3.

1-8 The Blast Wave

A blast wave is characterized by a sharp rise in pressure, temperature, and density at its shock front. Thus, upon the arrival of a blast wave at a given location from the burst point, the sequence of events is a sudden increase in pressure, temperature, and density, followed by a subsequent decrease in pressure, temperature, and density to values below ambient, and a more gradual return to ambient conditions with the temperatures going slightly above ambient. The overall characteristics of the blast wave are preserved over long distances from the burst point, but vary in magnitude with distance. With increase in distance, for example, the maximum pressure in the shock wave decreases, and the length of time over which the blast pressure is above ambient, the "positive phase," increases. Also, under conditions of high relative humidity (50 percent or higher), the drop in air pressure below ambient lowers the temperature sufficiently to cause condensation of atmospheric moisture to form a large cloud called the Wilson Cloud. When the air pressure again becomes nor-

[redacted]

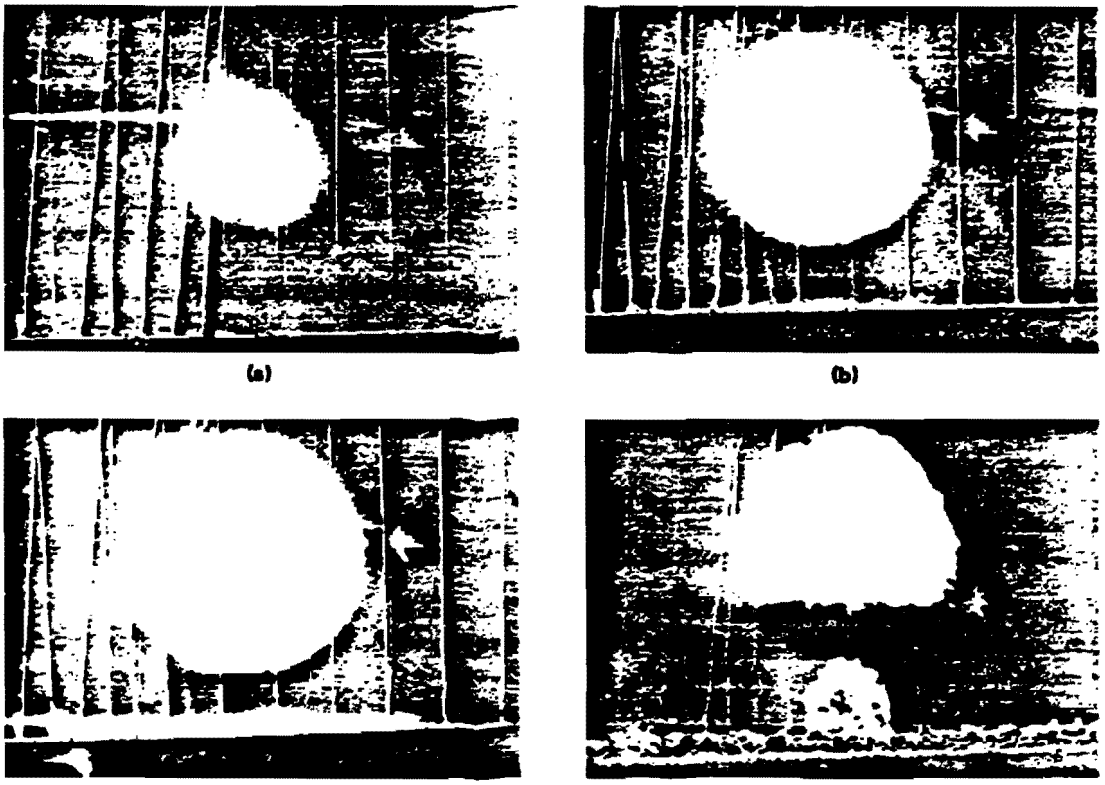

(a) (b)

(c) (d)

Figure 1-1. [redacted] Development of an Air Burst [redacted]

[redacted]

mal, in a matter of seconds, the cloud disappears. Although the Wilson Cloud is spectacular, because it always occurs too far behind the shock front to modify the blast effects, and too late to reduce the thermal effects appreciably, it has no military significance.

The motion of the air away from the burst point during the positive phase and toward the burst point during the negative phase, is also characteristic of a blast wave. The pattern of the air motion or air velocity is the same as for the other characteristics, with maximum velocity occurring just behind the shock front and decreasing with distance from the burst point. At 300 yards from the burst point of a 1-kt weapon, the peak wind velocity is about 240 miles per hour.

1-9 Nuclear Radiation

A unique feature of a nuclear explosion is the nuclear radiation released. This consists of, but is not limited to, gamma rays, neutrons, alpha particles, and beta particles. About a third of this energy is emitted within the first second after detonation, the remainder being released from radioactive fission products and unfissioned bomb materials over long periods of time after the burst. The effects of radiation can be increased during the first few seconds as a result of the disturbance of the atmosphere by the blast wave. Such enhancement of the effects compared to the effects in an undisturbed atmosphere is called hydrodynamic enhancement. The primary direct effect of nuclear radiation is an anti-personnel effect, with the penetrating radiations (gamma rays and neutrons) being the most dangerous. Residual nuclear radiation, due either to fallout or to neutron-induced gamma activity, can under certain conditions deny entry in a bombed area for some period of time after a detonation. Direct nuclear radiation effects on materials and equipment are of less significance, except for sensitive detector materials and certain electronic components. However, nuclear radiation produces indirect effects, such as EMP and blackout, which are discussed in Chapter 7 and 8, respectively. The nuclear radiation environment and the effects on personnel are discussed in Chapter 5. The effects of nuclear radiation on electronic components are discussed in Chapter 6.

1-10 Electromagnetic Pulse

The electrons that are separated from the atoms of the air by the gamma rays (paragraph 1-6) lose energy to surrounding air molecules. The energy lost in these collisions is used to free additional electrons, i.e., further ionization. The net result is a flow of negatively charged electrons radially outward from the explosion, while the heavier ions remain behind. If the explosion occurs in a homogeneous (constant density) atmosphere, two shells of charge are created: an inner positive ion shell, and an outer negative electron shell. A large local electric field is created in the radial direction; however, under such conditions, no electromagnetic field is radiated away. In practice, various asymmetries will occur that will result in electromagnetic fields being radiated from the source region. The potential importance of these fields will depend strongly on the circumstances of each individual burst. These effects are discussed in more detail in Chapter 7.

1-11 Electromagnetic Wave Propagation

Air burst effects on electromagnetic wave propagation are essentially associated with the fireball region. While relatively small, this region can be highly ionized for a few tens of seconds, and may have seriously degrading effects on the propagation of radio and radar signals. The effects of nuclear explosions on the propagation of electromagnetic signals are discussed in Chapter 8.

[redacted]

1-12 The Cloud [redacted]

[redacted] Because of its relatively low density compared to ambient conditions, the mass of hot gases making up the fireball rises. The rate of rise may reach several hundred feet per second, after which it decreases rapidly. As the gases rise, they expand, cool, and condense forming a radioactive cloud that consists largely of water vapor and metallic oxides from the weapon. As the fireball cools, the color changes gradually from red to a reddish brown, and ultimately water vapor from the air condenses sufficiently to produce a white color. As the heated mass of air in the fireball rises, cool air is pulled in from the sides and below, which may cause a doughnut-shaped ring to form around the column of hot air. This part of the cloud rolls violently as it rises. The cloud from a 1-kt detonation may reach a height of 5,000 to 10,000 ft above the burst point, after which is moves and diffuses according to the prevailing meteorological conditions.

[redacted] THE SURFACE BURST [redacted]

[redacted] A surface burst is defined as the explosion of a nuclear weapon at the earth's surface. (Figure 1-2 shows the development of a surface burst.) When a nuclear weapon is burst at the surface of the earth the sequence of events in the development of the fireball and the formation of the blast wave is the same as that for an air burst, except that the fireball boundary and the shock front are roughly hemispherical. Since the earth's surface is an almost perfect reflector for the blast wave, the resulting blast effects are almost the same as for a burst of twice the yield in free air.

1-13 Ground Shock [redacted]

[redacted] When a burst takes place on the ground surface, part of the energy is directly transmitted to the earth in the form of ground shock. Also, the air blast wave induces a ground shock wave that, at shallow depths, has essentially the same magnitude as the air blast wave at the same distance from the burst. The directly transmitted ground shock, although of higher magnitude initially, attenuates radially faster than the air blast induced shock. These effects are discussed in greater detail in Chapter 2.

1-14 The Crater [redacted]

[redacted] A land surface explosion of a nuclear weapon exerts initial shock pressures of hundreds of thousands pounds per square inch on the surface of the earth. The pressures result in displacement of material as well as downward compression of the soil to form a crater. In addition to the material that is thrown out, some earth will be vaporized by the intense heat. As will be discussed in Section II, Chapter 2, the size of the crater will depend upon the type of soil on which the explosion occurs. A crater of approximately 120 feet in diameter and 28 feet in depth is formed by a 1 kt weapon burst on a dry soil surface.

1-15 Thermal Radiation [redacted]

[redacted] As a result of the heat transfer to the surface, the hemispherical shape of the fireball, and the partial obscuration of the fireball by earth or water, the radiant exposure received by surface targets from a nuclear weapon burst on the surface is somewhat less than would be delivered by an air burst nuclear weapon of the same yield.

1-16 Initial Nuclear Radiation [redacted]

[redacted] In view of the absorption by the earth, initial nuclear radiation generally is less at the same distance from a surface burst than from an air burst; however, the hydrodynamic enhancement for high yield weapons may result in an increase in the initial gamma radiation. Each case should be examined separately by the methods described in Chapter 5 to determine the total initial nuclear radiation dose for a given situation.

[redacted]

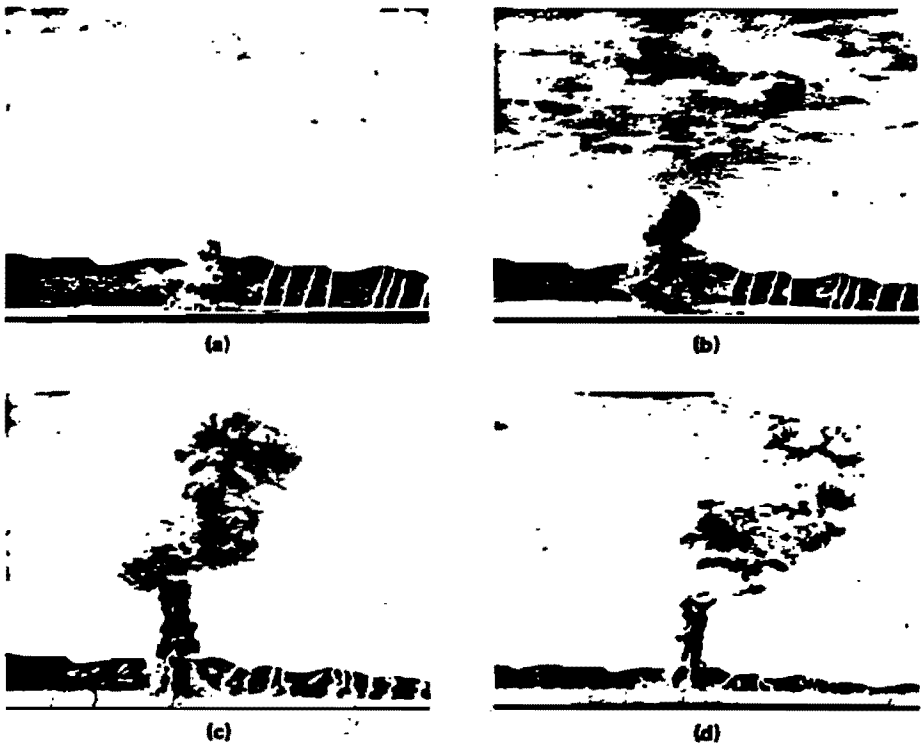

Figure 1-2. [redacted] Development of a Surface Burst [redacted]

[redacted]

1-17 Residual Nuclear Radiation [redacted]

[redacted] The contamination effects of residual nuclear radiation from a surface burst are greater than for an air burst, and hazardous radiological effects are produced over greater areas than those seriously affected by blast or by thermal radiation. Roughly half the available radioactivity resulting from a nuclear explosion on land, for example, can be expected to fall out in the general vicinity of the burst point. Dose rate contours near the burst point as great as 10,000 r/hr at H + 1 hr have been observed at tests, regardless of yield.

1-18 Electromagnetic Pulse (EMP) Radiation [redacted]

[redacted] If the detonation occurs at or near the surface of the earth, the EMP phenomenon mentioned in paragraph 1-11 produces intense electric and magnetic fields that may extend to distances of several thousand yards, depending on the weapon yield. The affected region is highly ionized and large electric currents flow in the air and the ground. Beyond this ionized region, the pulse strength drops fairly sharply, eventually as the inverse of the distance from the explosion. The strong fields may damage electrical and electronic equipment at distances exceeding those at [redacted] air blast damage may occur (see Chapter 7).

1-19 Electromagnetic Wave Propagation [redacted]

[redacted] Surface burst effects on electromagnetic wave propagation are essentially associated with the fireball region (see paragraph 1-11). Surface material drawn up with the fireball can cause attenuation by scattering of incident radar signals and obscuration or scintillation of optical radiation.

1-20 The Cloud [redacted]

[redacted] A great quantity of material is thrown out from the point of explosion of a nuclear weapon that bursts on the surface. As the fireball rises, some material is drawn up under the fireball, forming a stem and sometimes forming a second cloud below the one that develops from the fireball. The stem and cloud(s) continue to rise and follow the course described for air burst.

1-21 Water Surface Bursts [redacted]

[redacted] In general, the phenomena as outlined in paragraph 1-13 through 1-20 will occur for a surface burst on water. Also, the expanding sphere of hot gases depresses the water, causing the formation of a surface wave train and the transmission of a directly coupled shock wave into the water. The expanding air blast wave induces a shock wave in the water, which at shallow depths has essentially the same magnitude as the air blast wave at the same distance from the burst. Although the directly coupled water shock is of higher magnitude initially, it attenuates faster than the air blast induced water shock. As the height of burst increases from zero, depression, surface waves, and directly coupled water shock become smaller in magnitude. The formation of a crater on the bottom as the result of a surface burst in shallow water will depend on the depth of the water, yield of the weapon, and other factors. A 1 kt weapon, for example, burst on the surface of water 40 feet deep with a soft rock bottom, will form a crater 60 feet in diameter and 2 feet deep.

[redacted] THE TRANSITION ZONE BETWEEN AN AIR BURST AND A SURFACE BURST [redacted]

[redacted] There is a sizable zone above the earth's surface where, for weapons burst in the zone, the presence of the earth's surface modifies one or more of the basic weapon phenomena significantly. As the height of burst is successively lowered in this transition zone, the earth's surface plays an increasingly important role in modify-

[redacted]

[redacted]

ing weapon phenomena; there is a gradual transition from the characteristics of an air burst to those of a surface burst. The upper boundary of the transition zone varies depending upon the phenomenon being considered, because the effect of the earth's surface ceases to be of importance at different scaled heights of burst for different phenomena. These variations are described in detail for each phenomena in Chapters 2 through 8.

[redacted] THE HIGH-ALTITUDE BURST [redacted]

1-22 Description [redacted]

[redacted] As the detonation altitude increases, the interaction of weapon energy with the atmosphere changes markedly and is affected by weapon design and atmospheric conditions (pressure, density, and composition). There are several rather broadly defined altitude regions in which the formation and subsequent motion of the fireball differ. The term high-altitude bursts as used in this document refers to these regions collectively and includes air bursts in the lowest region.

1-23 Development [redacted]

[redacted] For detonations below about 350,000 feet, a large fraction of the X-ray energy is deposited near the burst point, heating the air to incandescence. As the detonation altitude increases above sea level, the air density decreases and the X-ray mean-free path increases. The principal mechanism for the initial fireball growth gradually changes from hydrodynamic motion (shock heating) to radiation heating. After the fireball reaches the initial size where growth by the heating of surrounding air ceases, it expands and rises in a manner related to the atmospheric scale height. The atmospheric scale height is the altitude separation where the density (or pressure) differs by a factor of e (2.7); the scale height varies from 15,000 to 25,000 feet below an altitude of 350,000 feet.

[redacted] If the initial fireball radius is smaller than the atmospheric scale height, the fireball expands to pressure equilibrium with the atmosphere. The subsequent fireball motion is similar to that described for air bursts; that is, the fireball rises principally due to buoyant forces. For yield-altitude combinations where the initial fireball radius is comparable to or exceeds an atmospheric scale height, large vertical pressure gradients are produced that cause an upward force on the fireball, giving it a boost or ballistic impulse upward. The fireball can be carried to altitudes far above the detonation point before expanding to pressure equilibrium with the surrounding atmosphere. As a result of the rapid decrease in atmospheric density with increasing altitude, the fireball density may become greater than the surrounding atmosphere. After reaching maximum altitude, the fireball then falls ballistically until encountering air of comparable density. This late-time fireball behavior will be modified if the fireball density at the maximum altitude is low enough that the ionized component of the fireball gas is trapped by the geomagnetic field.

[redacted] For detonations below about 200,000 feet, the fireball region forms a toroid. The time required appears to depend on weapon yield and detonation altitude.

[redacted] For low-altitude bursts, large temperature and pressure gradients at the boundary of the radiation fireball produce a strong shock wave (see paragraph 1-6). As the detonation altitude increases and the radiation (X-ray) fireball becomes large, the gradients at the boundary become weaker; the principal shock wave is then produced by the initial radial expansion of the debris within the X-ray fireball.

[redacted] The fireball starts as a highly ionized plasma. As it expands, it pushes the geomagnetic field out ahead of it. For detonations above about 250,000 feet, the magnetic pressure caused by the deformation of the field eventual-

[redacted]

[redacted]

[redacted]ly slows the expansion across the field while the expansion along the field continues. The fireball gradually becomes cylindrical in shape. After the expansion across the magnetic field has slowed, the magnetic field reenters the fireball turbulently, causing the local ionized fireball gas to become striated along the direction of the field.

[redacted] For detonations above about 350,000 feet, X-rays have a large mean-free path, deposit their energy over a large distance, and do not produce a localized fireball. However, below about 900,000 feet a fireball can be formed by deposition of the debris kinetic energy. Hydromagnetic coupling between the debris and the ionized air around the burst point results in the deposition of most of the debris kinetic energy (roughly one-fourth of the total weapon energy) near the burst point, producing a local fireball.

[redacted] The geomagnetic field plays an increasingly important role in fireball formation as the detonation altitude increases. The hydromagnetic coupling is actually quite complex. Instabilities in the interface between the expanding debris and the magnetic field can cause jetting of debris across field lines. Debris initially directed downward is stopped by the denser air below the burst point, while upward-directed debris travels to large distances. If in being stopped by the atmosphere, the downward-directed debris heats and ionizes the air, the heated region will subsequently rise and expand. Some upward-directed ionized debris will follow geomagnetic field lines across the geomagnetic equator before being deposited in the atmosphere.

[redacted] For large-yield bursts detonated above about 350,000 feet, X-ray energy, while not producing a localized fireball, will heat the atmosphere below the burst sufficiently to cause upward motion, changing the atmospheric density and composition at higher altitudes. This phenomenon is primarily important in the analysis of sequential bursts, where changes in atmospheric properties caused by one burst affect the deposition of energy (and thus the phenomenology) of succeeding bursts.

[redacted] As the fireball rises, most of the weapon debris is carried with it. After altitude stabilization takes place, the debris continues to be dispersed by diffusion and atmospheric winds. Both expansion and horizontal displacement of the debris center occur; the specific rates depend on prevailing wind motion and eddy diffusion at the debris stabilization altitudes, but they generally increase with increasing stabilization altitude. For detonations above about 200,000 feet, where the geomagnetic field acts to confine the debris, much of the debris may be trapped above several hundred thousand feet where the air density is low and wind motion negligible. However, after a period of minutes to perhaps several hours, most of the debris will have diffused or settled down the field lines to altitudes where wind motion can spread the debris over large areas. The detailed debris distribution during the early fireball growth and rise, and within the toroid at later times, is poorly known at present; however, many electromagnetic propagation effects are dependent only on the gross debris distribution.

[redacted] The differing regions of phenomenology are illustrated in the altitude-yield map shown in Figure 1-3. Figure 1-4 shows photographs taken after BLUE GILL [redacted], TEAK [redacted] 250 kilofeet), and CHECK MATE [redacted]. The formation of a toroid, characteristic of detonations in the buoyant rise region, is illustrated in Figure 1-4a. [redacted]

DNA (L-Y3)

[redacted] The photograph of TEAK at 100 seconds illustrates the difficulty in defining simple geometrical boundaries for fireball and debris regions. The innermost region is mostly weapon debris and heated air; the horizontal and vertical dimensions are about 450 kilofeet and 800 kilo-

[redacted]

[redacted]

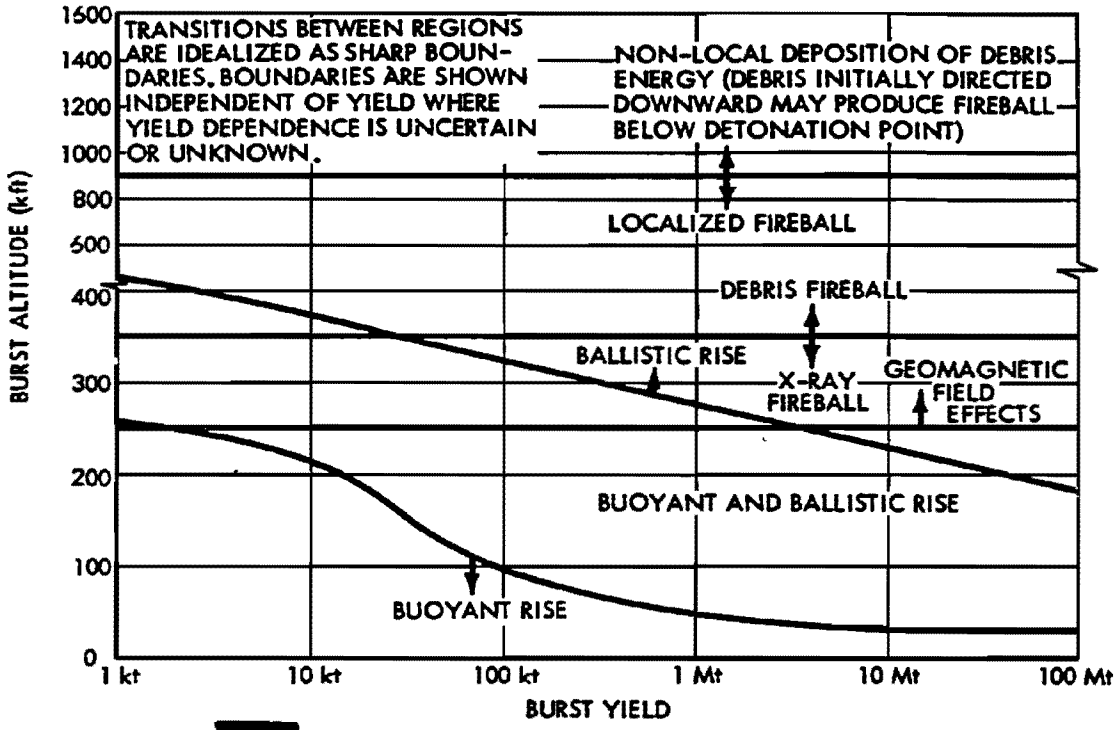

Figure 1-3. [redacted] Altitude-Yield Map Showing Differing Regions of Phenomenology [redacted]

[redacted]

feet, respectively. Most of the weapon debris appears to be concentrated near the bottom of the region. Some of the material near the top of the region is beginning to be affected by the geomagnetic field. The outer edge of the luminous region is a shock wave moving about 10,000 feet per second. While not defined as a fireball, there is still significant modification of the natural air chemistry within the region.

[redacted] The influence of the geomagnetic field on fireball formation and growth is clearly evident in Figure 1-4c. The overall fireball diameter is about 300 kilofeet, and the length along the geomagnetic field is about 1,000 kilofeet. The heated air within the fireball is highly ionized, with many striations oriented along the geometric field. (The dark spots within the fireball are rocket trails.)

1-24 The Blast Wave [redacted]

[redacted] As the burst height is raised, the X-rays are absorbed at longer distances from the burst as a result of their greater penetrating ability in the less dense air. The blast wave develops more slowly at higher altitudes, and at about 100,000 feet burst altitude the effective blast yield begins to decrease, until at a burst altitude of about 150,000 feet the effective blast yield is only 20 to 40 percent of what it would be at sea level for the same total energy yield.

[redacted]

[redacted]

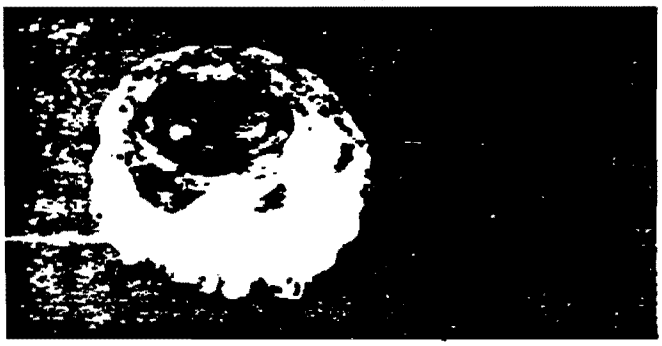

(a) Blue Gill Taken From Burst Locale

(b) Teak Taken From Maui (1300 km Away)

(c) Check Mate Taken From Burst Locale

Figure 1-4. [redacted] Photographs of High Altitude Bursts, t = 100 sec [redacted]

[redacted]

[redacted]

1-25 Thermal Radiation [redacted]

[redacted] Two factors affect the thermal partition of energy at high altitudes. First, as mentioned in paragraph 1-24, shock waves form much less readily in the thinner air; consequently the fireball is able to radiate thermal energy that would, at lower altitude, have been transformed to hydrodynamic energy of the blast wave. Second, the thinner air allows energy from the nuclear source to travel much farther than is possible at sea level. Some of this energy travels so far from the source that it makes no contribution to the energy contained in the fireball. In general, the first of these factors becomes effective between about 100,000 and 140,000 feet, and the thermal efficiency rises. Above about 140,000 feet the second factor becomes more important, and the thermal efficiency drops. For burst altitudes between about 290,000 feet and 350,000 feet, a layer of incandescent air may be formed below the local fireball that was described in paragraph 1-23. This layer will be on the order of 45,000 feet thick and may be centered between about 250,000 feet and 270,000 feet, depending on the effective X-ray temperature of the weapon. This heated air will reradiate at longer wavelengths that will reach the ground and will be the primary source of thermal damage at the surface of the earth; however, the thermal radiation from the local fireball (radiation of the weapon debris and nearby air) is a potential source of eye damage, i.e., retinal burns and/or flashblindness (see Chapter 10).

1-26 Nuclear Radiation [redacted]

[redacted] Nuclear radiation also extends over large regions from high altitude bursts as a result of the thinner air. This radiation may be damaging to electronic equipment in missiles in flight (see Chapter 6 and Section VII, Chapter 9). The radiation will also produce ionization over regions large in comparison to the size of the fireball region. The extent of the ionization depends on the mean-free path of the radiation, which differs for the several nuclear radiations, and on the detonation altitude. Since the fission debris is one source for gamma rays and beta-particles, the location of the fission debris as a function of time after burst is required to determine the extent of the ionization. Energy deposition in the atmosphere from nuclear radiation also results in radiation in the optical band of the electromagnetic spectrum.

1-27 Electromagnetic Pulse [redacted]

[redacted] Detonations above about 130,000 feet produce EMP effects on the ground over areas that may encompass thousands of square miles. Although the strengths of these fields are less than half those in the highly ionized region surrounding a surface burst, they are of sufficient magnitude to damage electrical and electronic equipment. The mechanisms of formation of EMP are treated in Chapter 7.

1-28 Electromagnetic-Wave Propagation [redacted]

[redacted] A phenomenological effect of considerable interest for high detonation altitudes is persistent ionization of the atmosphere. Electromagnetic waves propagating through the ionized atmosphere can incur amplitude and phase changes, and radar and communication systems dependent on electromagnetic propagation through the atmosphere can be affected. Electromagnetic radiation emitted by the burst or by disturbed regions in the atmosphere can reduce the signal-to-noise ratio by increasing the noise background.

[redacted] For detonations below about 50,000 feet, the principal region affecting electromagnetic propagation is the fireball. While relatively small, it can be intensely ionized for a few tens of seconds. For detonations above 50,000 feet, the fireball can remain intensely ionized for tens to hundreds of seconds. A significant fraction of the primary products of the weapon can escape

[redacted]

[redacted]

to great distances, and the attendant ionization (in the atmosphere) can persist for minutes to hours.

[redacted] THE UNDERGROUND BURST [redacted]

1-29 Development [redacted]

[redacted] An underground burst is defined as the explosion of a nuclear weapon in which the center of the detonation lies at any point beneath the surface of the ground. Figure 1-5 shows the development of a shallow underground burst. When a nuclear weapon is detonated at a sufficient depth underground, the ball of fire formed is composed primarily of vaporized materials from the bomb and vaporized earth. At shallow depths, light from the fireball generally may be seen from the time it breaks through the surface until it is obscured by dust and vapor clouds, a matter of a few milliseconds. The characteristics of the explosion and their related effects depend upon the depth, yield, and soil type. As the depth below the surface is increased, the characteristics depart gradually from those of a surface burst and finally, at depths of the order of 20 feet for a 1 kt detonation, the explosion exhibits the phenomena commonly associated with underground explosions. It is emphasized that the transition from the observed characteristics of a surface burst to those of an underground burst is not sudden, but that the characteristics change gradually.

1-30 Air Blast [redacted]

[redacted] Bursts at depths shallow enough to permit significant venting will produce air blast waves similar to those of air or surface bursts. As the depth of burst increases, the magnitude of the air blast will decrease.

1-31 Column, Cloud, and Base Surge [redacted]

[redacted] The first physical manifestation of an underground explosion at shallow depths is an incandescence at the ground surface directly above the point of detonation. This is almost immediately followed by large quantities of material being thrown vertically as a consequence of the direct ground shock reflection along the ground surface. Concurrently, large quantities of gas are released. These gases entrain additional quantities of material and carry them high into the air in the form of a cylindrical column. As the column rises it fans out and forms a dense cloud. Some of the particles thrown vertically, together with the entrained particles behave like an aerosol with a density considerably greater than the surrounding air. This aerosol subsequently falls in the immediate vicinity of ground zero, and the finer soil particles spread out radially along the ground to form a low dust cloud called the base surge. For a 1 kt weapon burst at a depth of 20 ft, it is estimated that the column will reach a height of approximately 420 ft and a diameter of 660 ft, the base surge will be 4,400 ft in diameter and the upper cloud will be 5,000 ft in height. Dimensions of the base surge are discussed in Section II, Chapter 2. For shallower depths of burst, the column tends to assume the shape of an inverted cone rather than a cylindrical column and has a more pronounced radial throwout. Shallower depths of burst also become less favorable for the formation of a base surge, approaching the conditions of a surface burst where no base surge is expected.

1-32 Ground Shock [redacted]

[redacted] As a burst is moved deeper and deeper into the ground, the directly transmitted ground shock increases in importance and the air induced ground shock becomes less important.

1-33 Crater [redacted]

[redacted] Formation of the crater from an underground burst is essentially the same as for a surface burst, except that at shallow depths more material is thrown vertically. Subsequently,

[redacted]

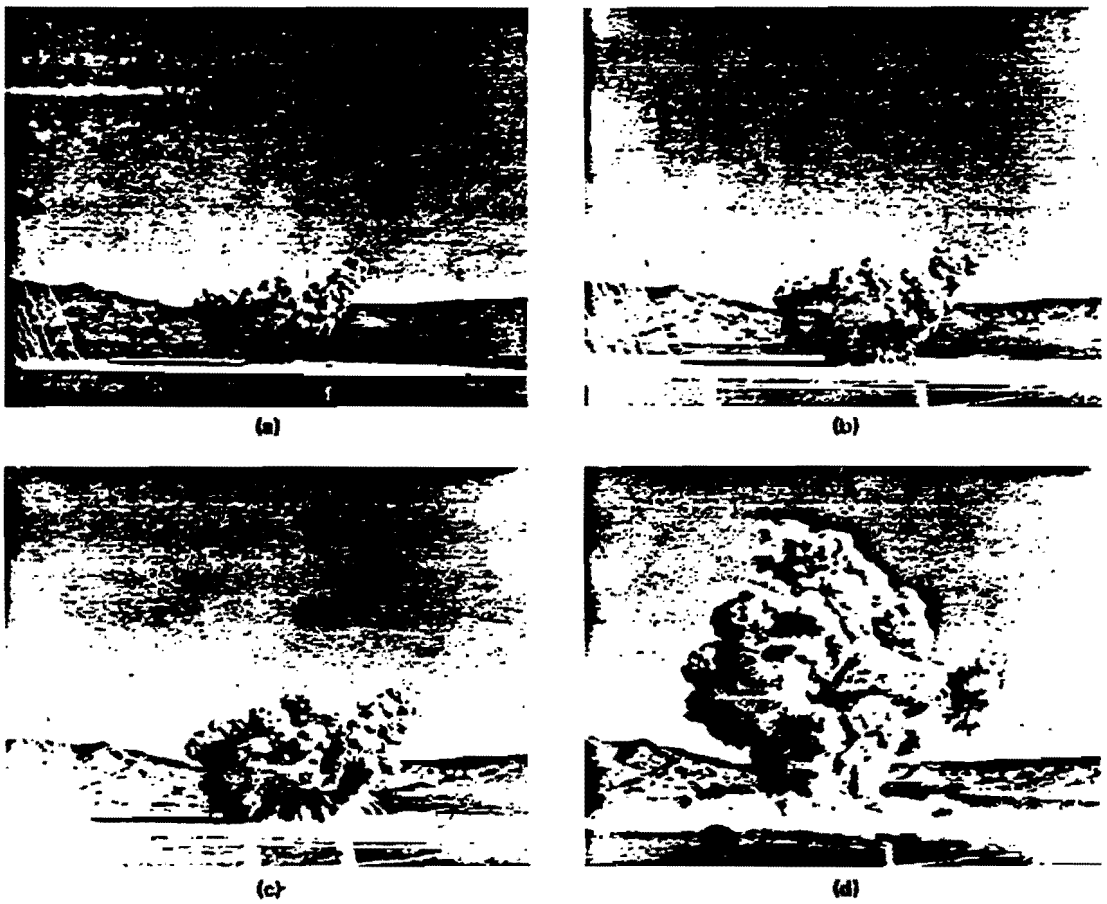

Figure 1-5. [redacted] Development of a Shallow Underground Burst [redacted]

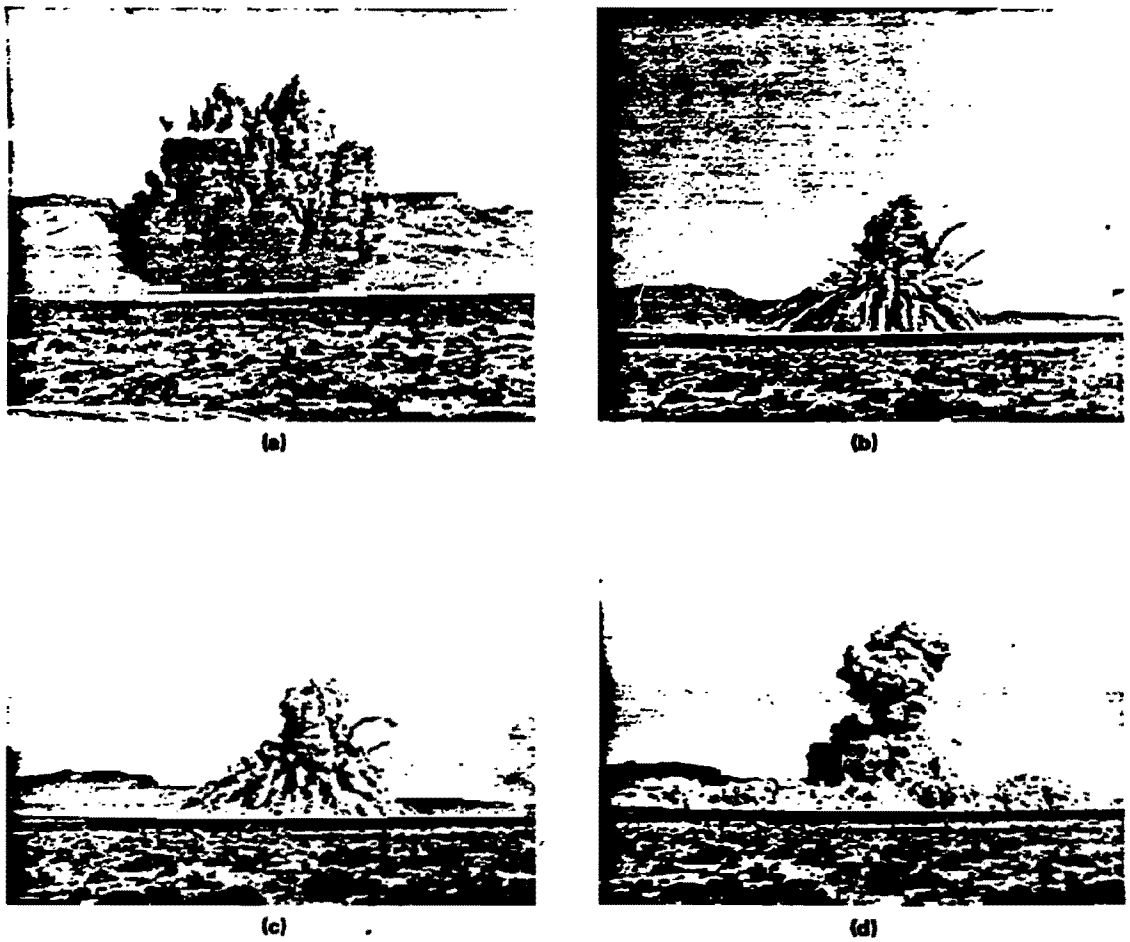

Figure 1-6. [redacted] Development of a Deep Underground Burst [redacted]

[redacted]

[redacted]

much of the ejected material collapses and falls back, partly into the newly formed crater and partly onto the surrounding "lip." The general term "fallback" is used to describe the material that immediately falls back into the crater. The term "ejecta" describes material which has fallen onto the crater lip. The size of the remaining (or "apparent") crater depends on the energy yield of the detonation and on the nature of the excavated medium. In general, for equivalent conditions, the volume of the crater is roughly proportional to the yield of the explosion.

[redacted] The size of the apparent crater increases with increasing depth until a certain optimum depth is reached. The scaled optimum depth is different for the crater radius than for the crater depth and also varies markedly for different media. At depths below the optimum for the particular medium surrounding the burst, the crater dimensions decrease with increasing depth. At sufficiently deep depths the explosion will not vent to the surface and a cavity (camouflet) will be formed. There may or may not be disturbances at the surface, depending on the depth of the detonation and the material comprising the ground.

1-34 Thermal and Nuclear Radiation [redacted]

[redacted] As a general rule, the thermal radiation will be almost completely absorbed by the ground material, so that it does not represent a significant hazard. Most of the neutrons and early gamma rays will also be removed, although the capture of the neutrons may cause a considerable amount of induced radioactivity in various materials present in the soil. This will constitute a small part of the residual nuclear radiation, of importance only in the close vicinity of the point of burst. The remainder of the residual radiation will be due to the contaminated base surge and fallout. For shallow depths of burst, the fallout effects are similar to those of a surface burst. As the depth of burst increases however, more and more of the contaminant is deposited in the immediate vicinity of the detonation, until for the case of no surface venting, all of the contaminant is contained in the volume of the ruptured earth surrounding the point of detonation.

1-35 Electromagnetic Pulse [redacted]

[redacted] For shallow depth of burst, the electromagnetic pulse should be similar to, but of lesser magnitude than, that for a surface burst of the same size. As depth of burst increases, the extent and magnitude of the pulse will diminish. In general, the electromagnetic pulse from such bursts should be a much less significant damage mechanism than ground shock. Adequate test data for prediction are, however, lacking.

[redacted] THE UNDERWATER BURST [redacted]

1-36 Development [redacted]

[redacted] An underwater burst is defined as the explosion of a nuclear weapon in which the center of the detonation lies at any point beneath the surface of the water. (Figure 1-7 shows development of a shallow underwater burst; Figure 1-8 shows development of a deep underwater burst.) An underwater nuclear explosion releases large amounts of thermal and nuclear radiation, essentially all of which is absorbed by the surrounding water within several feet of the explosion. (Some radiation within the visible spectrum can be radiated to greater distances depending on the transparency of the water.)

[redacted] During the early stages of the explosion, the bomb materials attain a very high temperature (on the order of millions of degrees) and a very high pressure (on the order of millions of atmospheres). Energy acquired by these materials is transferred to the layer of water closest to the bomb, which is heated and compressed and which, then, heats and compresses the next

[redacted]

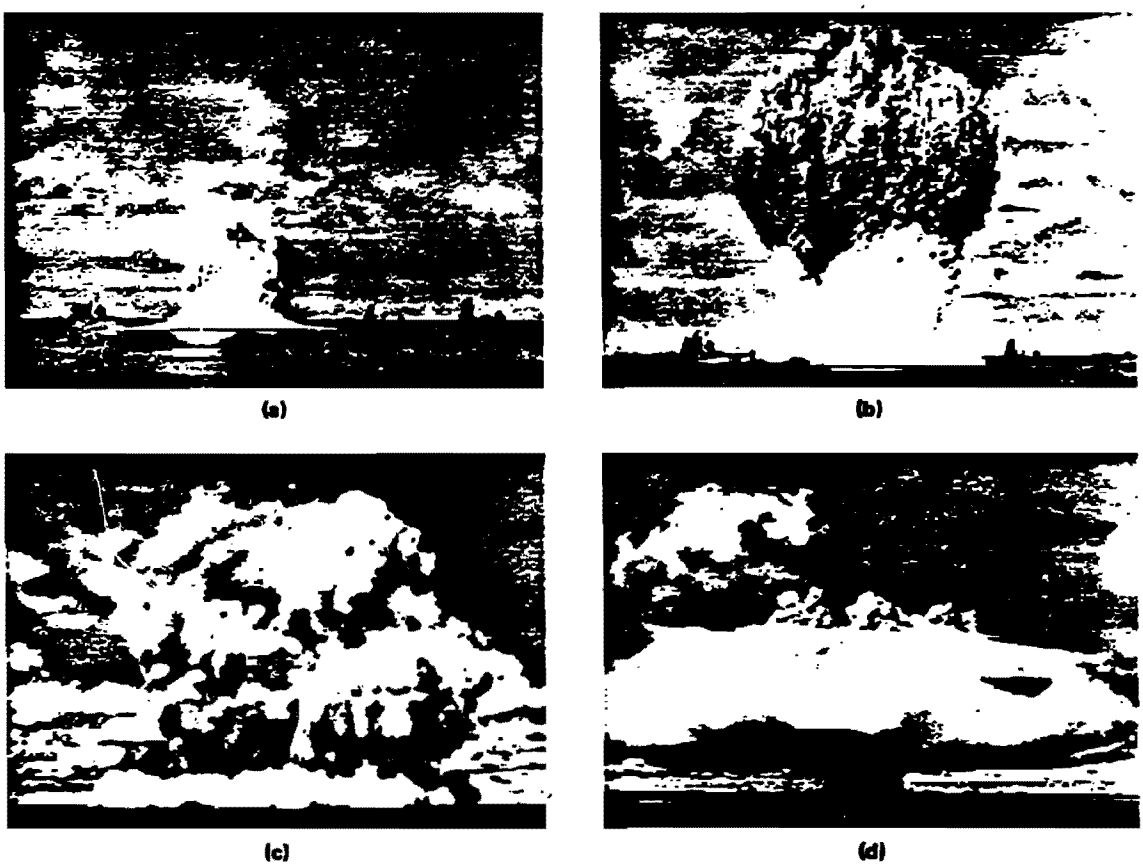

(a) (b)

(c) (d)

Figure 1-7. [redacted] Development of a Shallow Underwater Burst [redacted]

[redacted]

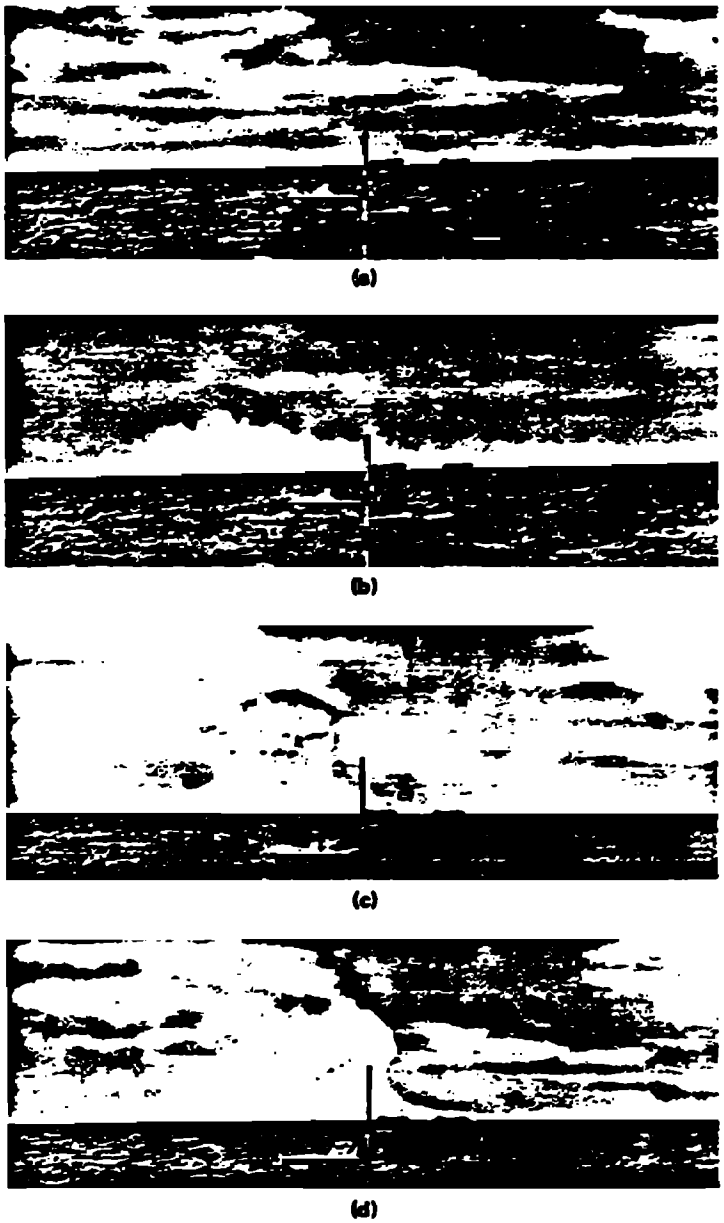

(a)

(b)

(c)

(d)

Figure 1-8. [redacted] Development of a Deep Underwater Burst [redacted]

[redacted]

[redacted]

outward layer. By this mechanism, a wave of compression (the hydrodynamic or shock front) is formed and moves outward from the bomb. This front moves faster than the material it engulfs, which also moves outward but at a slower rate.

[redacted] As the shock front moves away from the point of explosion, energy is dissipated in the form of heat, which raises the temperature of the water passed over by the front. The largest temperature increase occurs near the center of the explosion, where it is great enough that the water is not only vaporized, but dissociated as well. At somewhat greater distances, the water is vaporized and turned to steam; at still greater distances, the water is heated, but not to its boiling point.

[redacted] Thus, shortly after an underwater burst, an expanding bubble is formed. This bubble is composed largely of vaporized water with radioactive debris at its center, surrounded by heated water. Continued expansion of this bubble results in a pressure reduction within it. As the bubble pressure falls below the vapor pressure of the heated water, vaporization of additional water occurs at the interface of the bubble and the water.

[redacted] In a deep underwater explosion, the bubble continues to expand at a decreasing rate until a maximum size is reached. If not too near the surface or the bottom, the bubble remains roughly spherical to this point. As a result of the inertia of the water set in motion by the early expansion of the bubble it actually overexpands, i.e., when it does attain its maximum size, its contents are at a pressure well below the ambient water pressure.

[redacted] The higher pressure around the bubble causes it to contract, with a resultant increase in internal bubble pressure, and condensation of some of the bubble contents. Because the hydrostatic pressure at the bubble bottom is larger than at the top, the bubble does not remain spherical during the contracting phase. Its bottom moves inward faster than its top (which may remain stationary or even rise slightly), contacts the top (forming a doughnut-shaped bubble viewed from above), and causes turbulence and mixing of the bubble contents with the surrounding water.

[redacted] The inertia of the water set in motion by contraction of the bubble causes it to overcontract, and its internal pressure once more becomes higher than the ambient water pressure. A second compression (shock) wave in the water commences after the bubble reaches its minimum volume. This compression wave has a lower peak overpressure but a longer duration than the initial shock wave in the water. A second cycle of bubble expansion and contraction then begins.

[redacted] During the initial expansion cycle, the bubble is relatively stationary, but upon contracting begins to migrate upward under the action of buoyant forces. The rate of upward migration is greatest at times of bubble minimum size, and is almost zero at times of maximum size, when the bubble is again almost spherical.

[redacted] If the explosion occurs far enough from the surface, the bubble continues to pulsate and rise, though after three complete cycles enough condensation of steam has taken place to make it unlikely that additional pulsations will occur. During pulsation and upward migration, however, the water in the vicinity of the bubble acquires considerable upward momentum, and eventually breaks through the surface with some violence.

[redacted] For shallow bursts, the bubble may break through the surface during one of the early pulsations or even before completion of a single pulsation cycle. If such a breakthrough occurs during the portion of the cycle at which bubble pressure is higher than ambient pressure (as with a very shallow explosion), a phenomenon known as a blowout occurs. If breakthrough

[redacted]

occurs when bubble pressure is below ambient pressure, the reverse phenomenon, blow-in, occurs. The character of the surface effects differs for the two phenomena. (See paragraph 1-39.)

If a burst occurs near the sea (or harbor) bottom, the general bubble behavior is as described above. A pulsating bubble, however, is drawn toward the bottom and, therefore, bubble migration toward the surface is slowed.

1-37 Water Shock Waves and Other Pressure Pulses

The primary shock wave that moves out from the explosion center is characterized by an extremely rapid increase in pressure (virtually instantaneous) to a very high initial or peak pressure, and then an almost exponential decrease to a value less than the hydrostatic pressure at the explosion point. Though a water shock wave resembles an air blast wave superficially, its peak pressures are generally much higher, and durations much shorter. In the absence of nearby boundaries, the shock wave proceeds outward radially at a very high initial velocity, which soon decreases to nearly the velocity of sound in water (about 5,000 ft/sec). Shock wave velocity depends on water temperature, density, and salinity; and therefore, a shock wave may be bent (refracted) as it moves through regions of differing characteristics.

Shock wave reflections from the surface and bottom affect the shock and pressure field at a point distant from the explosion. Since reflection from the surface is in the form of a negative, or tension wave, it can cause a shortening of the pressure pulse (cutoff), and, when the shock wave encounters the surface at a small enough angle, reflection can even reduce the magnitude of the primary pressure pulse. Reflection from the bottom generates a second compression wave in the water that can be effective in damaging ships.

Additional shock and pressure waves, generally of lesser importance than the primary shock wave or the bottom reflected shock waves, can be generated by shock wave energy that has been transmitted to bottom material or to the air and retransmitted to the water, by the collapse of a cavitation region near the surface, and by re-reflections of any of these.

Shock or compression waves from subsequent bubble pulses generally behave in the same manner as the initial shock wave and undergo reflection and refraction of the same character.

1-38 Air Blast

As in the case of an underground burst, air blast waves are formed by an underwater burst. Their propagation depends upon the depth of burst. The first air blast wave from an underwater burst is that formed by the transfer of the shock front across the water-air interface. This front appears as a flat dome. The second air blast wave is transmitted by the venting bubble. This front will propagate essentially hemispherically. For shallow burst depths, the air blast wave resulting from venting is more intense than the shock wave transmitted across the water-air interface. For deep bursts, on the other hand, the shock wave transmitted across the water-air interface yields the higher pressures.

1-39 Surface Effects

The first surface effect of an underwater burst is caused by the intersection of the primary shock wave and the surface. Viewed from above, the effect appears to be a rapidly expanding ring of darkened water (often called the "slick"). Following closely behind the darkened region is a white circular patch (the "crack") probably caused by underwater cavitation produced by the reflected rarefraction wave. Shortly after appearance of the crack, the water above the explosion rises vertically and forms a white mound of spray (the "spray dome"). This dome

[redacted]

[redacted]

is caused by the velocity imparted to the water near the surface by the reflection of the shock wave and to the subsequent breakup of the surface layer into drops of spray. The initial upward velocity of the water is proportional to the pressure of the direct shock wave, and so it is greatest directly above the detonation point. Consequently, the water in the center rises more rapidly (and for a longer time) than water farther away. As a result, the sides of the spray dome become steeper as the water rises. The upward motion is terminated by the downward pull of gravity and the resistance of the air. The total time of rise and the maximum height depend upon the energy of the explosion, and upon its depth below the water surface. Additional slick, crack, and spray-dome phenomena may result if the shock wave reflected from the water bottom and compression waves produced by the gas bubble reach the surface with sufficient intensity.

[redacted] For shallow bursts, the spray dome appears to be rapidly converted to a column formed by the upward and outward acceleration of the water surrounding the explosion. If blowout occurs, the upper part of the column is likely to be marked by a crown of explosion products. If blow-in occurs, the crown is likely to be absent. In its later stages, the column may break up into plumes (relatively broad jets or spouts of water that disintegrate into spray as they travel through the air).

[redacted] For bursts deep enough that blowout does not occur, but not so deep that bubble pulsation has ceased, plumes will be formed.

[redacted] If an explosion takes place deep enough for bubble pulsations to have ceased before the bubble reaches the surface, plumes caused by the upwelling of the water (and any uncondensed vapor or gas) may occur.

[redacted] Upon subsidence of the column and plumes from an underwater explosion, a misty, generally highly radioactive, "doughnut-shaped ring" or series of rings, the "base surge" may be formed. In the few instances in which base surge formation has been observed over water, the visible configuration has been quite irregular. Nevertheless, to a good approximation, the base surge can be represented as a hollow cylinder with the inner diameter about two-thirds of the outer diameter. The heights of the visible base surge clouds have generally ranged between 1,000 and 2,000 feet.

[redacted] The necessary conditions for the formation of a base surge have not been definitely established, although it is reasonably certain that no base surge would accompany bursts at great depths. The underwater test shots upon which the present analysis is based have all created both a visible and an invisible (see below) base surge. The only marked difference between the phenomena at the various tests is that at Bikini BAKER there was an airborne cloud, evidently composed of fission debris and steam. The other shots, which were at somewhat greater depths, produced no such cloud. The whole of the plume fell back into the surface of the water where the low-lying base surge cloud was formed.

[redacted] From the weapons effects standpoint, the importance of the base surge lies in the fact that it is likely to be highly radioactive because of the fission (and other) residues present either at its inception, or dropped into it from the radioactive cloud. Because of its radioactivity, it may represent a serious hazard for a distance of several miles, especially in the downwind direction. The fission debris is suspended in the form of very small particles that occupy the same volume as the visible base surge at early times, that is, within the first 3 or 4 minutes. However, when the small water droplets which make the base surge visible evaporate and disappear, the radioactive particles and gases remain in the air and continue to move outwards as an invisible radioactive base surge. There may well be some fallout or rainout on the surface of the water (or

[redacted]

[redacted]

[redacted]

ship or shore station) from the radioactive base surge, but in many cases it is expected to pass over without depositing any debris. Thus, according to circumstances, there may or may not be radioactive contamination on the surfaces of objects in the vicinity of an underwater nuclear burst.

[redacted] The radioactive base surge continues to expand in the same manner as would have been expected had it remained visible. It drifts downwind either as an invisible, doughnut-shaped cloud, or as several such possibly concentric clouds that approximate a low-lying disc with no hole in the center. The latter shape is more probable for deeper bursts. The length of time this base surge remains radioactive will depend on the energy yield of the explosion, the burst depth, and the nearness of the sea bottom to the point of burst. In addition, weather conditions will control depletion of debris due to rainout and diffusion by atmospheric winds. As a general rule, it is expected that there will be a considerable hazard from the radioactive base surge within the first 5 to 10 minutes after an underwater explosion and a decreasing hazard for half an hour or more.

[redacted] After dissipation of the visible base surge, the water surface around the explosion is seen to be white. This area (the "foam patch") results from the upward motion of the water and uncondensed explosion products in the vicinity of the bubble, their spreading over the surface of the patch, and their downward motion at the edge of the patch. In its later stages, this area is marked mainly by a ring of foam and debris that shows where downward circulation has taken place.

1-40 Thermal and Nuclear Radiation [redacted]

[redacted] Thermal radiation and initial nuclear radiation effects are considered to be insignificant for underwater bursts, except for the radioactivity accompanying the base surge (paragraph 1-39). Residual nuclear radiation effects (fallout) will approximate those of a ground surface burst if the explosion occurs in shallow water.

1-41 Electromagnetic Pulse [redacted]

[redacted] The degree to which an electromagnetic pulse is generated by an underwater burst is not known, but it is expected to be insignificant except for very shallow bursts. In such cases, it is believed that a diminishing effect above the surface, approximating that described for a shallow underground burst, will result.

[redacted]

[redacted]

BIBLIOGRAPHY*

Bethe, H. A., et al., *Blast Wave*, LA 2000, Los Alamos Scientific Laboratory, Los Alamos, New Mexico, March 27, 1958[redacted]

Brode, H. L., *Review of Nuclear Weapons Effects*, Annual Review of Nuclear Science, *18*, 153, 1968[redacted]

Engineering with Nuclear Explosives: Proceedings of the Third Plowshare Symposium, TID 7695, U.S. Atomic Energy Commission, April 1964[redacted]

Glasstone, S., *Public Safety and Underground Nuclear Detonations*, TID 25708, U.S. Atomic Energy Commission, June 1971[redacted]

Johnson, G. W., and C. E. Violet, *Phenomenology of Contained Nuclear Explosions*, UCRL 5124 Rev. 1, University of California, Lawrence Radiation Laboratory, Livermore, California, December 1958[redacted]

Johnson, G. W., et al., *Underground Nuclear Detonations*, UCRL 5626, University of California, Lawrence Radiation Laboratory, Livermore, California, July 8, 1959[redacted]

Symposium on Engineering with Nuclear Explosives, January 14-16, 1970, Las Vegas, Nevada, Proceedings, CONF-700101, Vols. 1 and 2, May 1970[redacted]

Proceedings for the Symposium on Public Health Aspects of Peaceful Uses of Nuclear Explosives, Las Vegas, Nevada, April 1969, U.S. Department of Health, Education and Welfare, Public Health Service, SWRHL-82[redacted]

Proceedings of the Special Session on Nuclear Excavation, Nuclear Applications and Technology, *7*, 188-327, 1969[redacted]

Snay H. G., and R. C. Tipton, *Charts for the Parameters of Migrating Explosion Bubbles*, NOLTR 62-184, U.S. Naval Ordnance Laboratory, 15 October, 1962[redacted]

Steiger, W. R., and S. Matsushita, *Photographs of the High Altitude Nuclear Explosion TEAK*, Journal of Geophysical Research, *65*, 545, 1960[redacted]

Strange, J. N., and L. Miller, *Blast Phenomena from Explosions and an Air-Water Interface*, Report 1, Misc. Paper No. 1-814, U.S. Army Engineer Waterways Experiment Station, Vicksburg, Miss., June 1966[redacted]

Taylor, G. I., *The Instability of Liquid Surfaces When Accelerated in a Direction Perpendicular to Their Planes, Part I*, Proceedings of the Royal Society, London, A 201, 192, 1950[redacted]

Teller, E., et al., *The Constructive Uses of Nuclear Explosives*, McGraw-Hill Book Company, 1968[redacted]

*Additional reference material concerning the subject matter of this chapter may be found in the handbooks described in Appendix D and in the more specific bibliographies of Chapters 2 through 8.

[redacted]

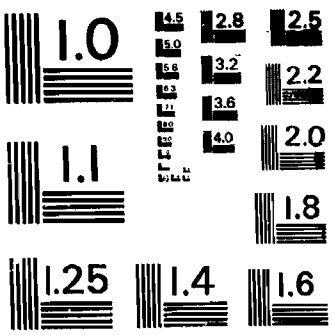
1.0
1.1
1.25
1.4
1.6
1.8
2.0
2.2
2.5
2.8
3.2
3.6
4.0
4.5
5.0
5.6
6.3

AD-A955 405

Chapter 2

BLAST AND SHOCK PHENOMENA

INTRODUCTION

Most of the physical damage to material that is caused by nuclear explosions near the earth's surface results from the blast and shock phenomena or from the thermal radiation phenomena associated with such explosions. This chapter describes the blast and shock phenomena, while the thermal radiation phenomena are described in Chapter 3.

Damage to structures or materiel from blast and shock depends upon the location of the explosion (air burst, surface burst, subsurface burst), and the location of the structure or materiel (in the air, on or under the surface of the earth, or on or under a water surface). Accordingly, this chapter is divided into four sections. Section I describes the air blast phenomena from air and surface bursts. Section II deals with cratering phenomena and the associated problems of ejecta. Section III describes ground shock phenomena from near surface and subsurface (ground) explosions. Section IV describes the phenomena associated with underwater explosions.

SECTION I

AIR BLAST PHENOMENA

The shock wave that propagates through air as a consequence of a nuclear explosion is commonly referred to as a blast wave. The destructive effects of a blast wave are produced by its overpressure and its dynamic pressure, both expressed in pounds per square inch (psi). Overpressure, Δp, is the amount by which the static pressure in the blast wave exceeds the ambient pressure. Dynamic pressure, q, is associated with the mass motion of air in the blast wave. It is approximately equal to the pressure that this strong wind develops when it hits a stationary object. Dynamic pressure is defined more completely in paragraph 2-8.

When an ideal blast wave passes a given point, the first disturbance that is felt coincides with the arrival of the shock front, a discontinuity at which both overpressure and dynamic pressure rise abruptly to their peak values, as illustrated at point B in Figure 2-1. The overpressure then follows an approximately exponential decline to a negative value, i.e., to a pressure below ambient, and gradually returns to zero. The phase that is above ambient pressure (between points B and C) is termed the positive phase; the phase that is below ambient pressure

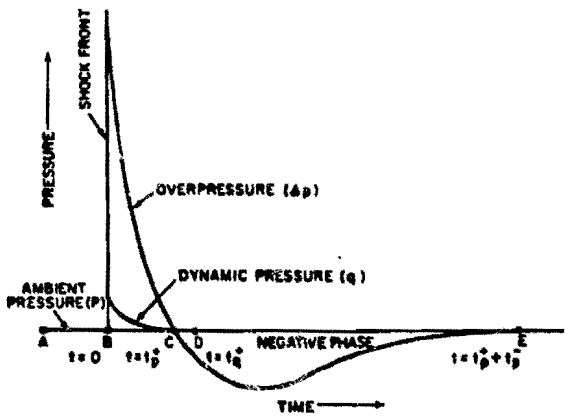

Figure 2-1. Ideal Pressure-Time Relationships for a Blast Wave in the Low Pressure Region (below 5 psi)

must be assumed for possible military encounters.

2-1 Interpretation of Reliability Statements

The reliability statement that accompanies each set of blast-wave data in this chapter is, when possible, based on the width of the band that contains 90 percent of all data points. In the example given above (free air overpressure), there are many data points, and the width of this band may be established readily. In other cases, the reliability statements must be based on judgment. This is necessary when the data are too few to indicate the amount of scatter clearly, when large systematic errors are suspected, and when curves are obtained from theory and lack the support of experimental data.

2-2 Errors Due to Yield Scaling

Yield scaling is sufficiently accurate that the errors introduced are, in most air blast problems, masked by uncertainties in the experimental data. The exact amount of error attributable to yield scaling is unknown, but it is estimated to be a few percent. There are some exceptions to this rule.

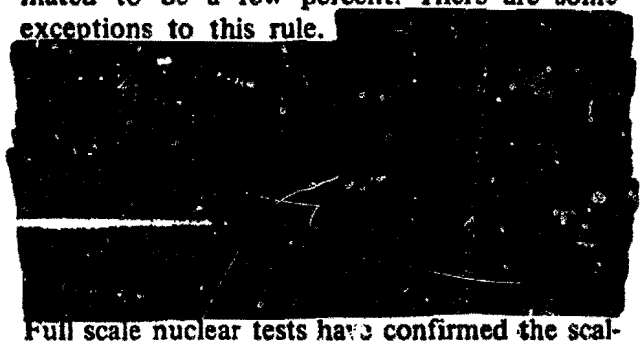

Full scale nuclear tests have confirmed the scaling laws for yields to about 10 megatons (Mt), and scaling to 20 Mt is considered a reasonable extrapolation of available data. However, there is reason to question whether the scaling laws maintain their accuracy for still larger yields. Since the fireball of a 20 Mt burst is over a mile in diameter, nonuniformity of the atmosphere is a sufficiently large factor to modify development of both the fireball and the blast wave, as will be described in subsequent paragraphs. This modification may cause significant deviations from the scaling laws. The scaling laws may be applied to yields less than 1 kt or more than 20 Mt, but the additional uncertainties involved should be recognized.

2-3 Errors Due to Altitude Scaling

Altitude scaling is less accurate than yield scaling, and the problem becomes significant at altitudes above about 40,000 feet. Below 40,000 feet, available data are not adequate to establish the magnitude of errors introduced by altitude scaling, but they indicate that these errors are probably small. Above 40,000 feet, where scaling errors become fairly large, the overpressure and dynamic pressure waveforms depart from the predicted values more than other conditions at the shock front.

2-4 Errors at Long Ranges

As mentioned previously, a nonuniform atmosphere can distort the blast wave. Variations of wind velocity or of temperature with altitude can produce focusing effects by channeling more energy in one direction at the expense of energy propagating in another direction. This effect is most pronounced at long ranges. It is the principal reason for assigning a wider tolerance to overpressure data below 1/2 psi (paragraph 2-24).

2-5 Effects of the Earth's Surface

Since the earth is not a perfect reflector, blast waves interacting with its surface cannot be predicted as dependably as blast waves in free space. The reliability of blast-wave data at the surface is discussed in paragraph 2-23.

2-6 Effect of Weapon Characteristics

Warheads with unusual radiating properties develop a blast wave of

different intensity than the scaling laws predict (see paragraph 2-44).

BLAST WAVE CALCULATIONS IN FREE AIR

The physical characteristics of the blast wave change as a function of time and distance as the blast wave moves out from the explosion. In a homogeneous atmosphere, where no boundaries or surfaces are present, these changes take place in a definite manner as a result of spherical divergence and irreversible energy losses to the air. The shock front peak overpressure and other shock wave parameters, such as velocity, that depend on the overpressure decrease with increasing distance, and the shock strength is attenuated with distance.

2-7 Peak Overpressure

The curve for free-air peak overpressure in a standard sea-level atmosphere is shown in Figure 2-2 as a function of distance from a 1 kt explosion. This curve can be used directly to predict incident overpressures from air bursts up to about 5,000 feet height of burst. The curve also may be used to predict incident overpressures for heights of burst up to 40,000 feet by using the altitude scaling procedure described in the following subsection. The curve may also be used to predict incident overpressures for heights of burst above 40,000 feet by using a reduced effective blast yield obtained from Figure 2-64.

Figure 2-3 shows a family of free air overpressure curves as a function of slant range for selected yields between 0.001 kt and 1,000 Mt. This figure eliminates the requirement for yield scaling, so it is more convenient to use for selected yields at heights of burst below 5,000 feet. For other yields and for higher burst heights, the curve in Figure 2-2 provides more accurate data for scaling.

2-8 Peak Dynamic Pressure

Dynamic pressures cause stationary targets to experience drag forces associated with the high-velocity winds that follow the shock front. In an ideal blast wave, dynamic pressure rises abruptly at the shock front to its peak value and then diminishes as overpressure decreases. Because of this decay behind the shock front, these strong gusts of wind cannot be compared directly with steady winds of the same velocity. During the negative overpressure phase, the transient winds reverse and blow at reduced velocities; the resulting values of dynamic pressure are small and act in the opposite direction. As a result of the momentum of air in motion, the positive dynamic pressure phase lasts slightly longer than the positive overpressure phase.

The dynamic pressure is proportional to the square of the wind velocity and to the density of the air behind the shock front as follows

$$q = \frac{1}{2}\rho_s u^2,$$

where q is the dynamic pressure, ρ_s is the density of the air behind the shock front, and u is the particle (wind) velocity behind the shock front. These latter two quantities may be related to the overpressure under ideal conditions by equations that will be given in the succeeding subsection (paragraphs 2-15 and 2-17).

Peak dynamic pressure is shown as a function of distance from a 1 kt free air explosion in a standard sea level atmosphere in Figure 2-4.

Dynamic pressure and overpressure are considered separately not only because they have different origins, but also because they react differently with the target. For example, a telephone pole is not particularly sensitive to overpressure; but a dynamic pressure of the order of 1 psi is sufficient to break it.

2-9 Time of Arrival

At breakaway (i.e., the instant that the shock front moves beyond the fireball) the shock front from a sea-level burst has a velocity of approximately seven times the velocity of sound. Shock front velocity decreases as peak overpressure decreases; it approaches the velocity of sound as peak overpressure approaches zero. The time of arrival of the shock front is shown as a function of distance from a 1 kt free air explosion in a homogeneous sea level atmosphere in Figure 2-5.

2-10 Duration of the Positive Phases of Overpressure and Dynamic Pressure

As illustrated in Figure 2-1, both the overpressure and the dynamic pressure rise rapidly to peak values, decay to negative values, and finally return to zero. It is during the positive phase of the overpressure and/or the dynamic pressure that most of the physical damage is caused to structures, materiel, or personnel. The positive phase durations of the overpressure pulse (t_p^+) and the dynamic pressure (t_q^+) are shown in Figure 2-6 as a function of distance from a 1 kt free air explosion in a homogeneous sea level atmosphere.

2-11 Impulse

The ideal parameter for specifying the intensity of a blast wave would be one that has a simple definition and that relates directly to damage potential. Peak overpressure serves this function approximately for many applications. Impulse, which combines the effects of pressure and duration, is another of the parameters that approaches this ideal for some types of targets.

Impulse may be defined as the product of the average pressure and the time during which the pressure acts. Mathematically, the positive-phase overpressure impulse I_p is defined as

$$I_p = \int_{t=0}^{t=t_p^+} \Delta p(t)dt.$$

Negative-phase impulse is similarly defined in terms of the underpressure; it is usually less significant than the positive-phase impulse. For this reason, the term overpressure impulse is conventionally interpreted to mean positive phase overpressure impulse.

Dynamic pressure impulse is similarly defined as the time integral

$$I_q = \int_{t=0}^{t=t_q^+} q(t)dt.$$

Figure 2-7 shows positive overpressure impulse as a function of range from a 1 kt free air burst in a standard sea level atmosphere. Comparison of Figures 2-2 and 2-7 shows that overpressure impulse falls off much less rapidly with distance than does peak overpressure. This is because the pressure pulse broadens (becomes more extended in time) as the peak overpressure declines.

Figure 2-7 also shows a curve representing dynamic pressure impulse. Near the burst, dynamic pressure impulse is limited by the relatively small volume of air enclosed by the shock front. This small amount of air can only sustain a strong wind for a short time interval; consequently, the dynamic pressure pulse is very narrow (short duration) at short ranges. At scaled distances between 200 and 400 feet, the duration of the dynamic pressure pulse decreases almost as rapidly as peak dynamic pressure increases with decreasing distance; as a result, dynamic pressure impulse remains nearly constant over this range of distances.

Problem 2-1. Calculation of Free Air Peak Overpressure

Figure 2-2 shows the peak overpressure as a function of slant range from a 1 kt explosion in a homogeneous sea level atmosphere at heights of burst up to about 5,000 feet. For higher burst heights, this figure may be used together with the altitude scaling procedures described in paragraph 2-14 and illustrated in problem 2-6. Figure 2-2 only applies to *free air* overpressure. Overpressures at the surface should be obtained from the subsection "BLAST WAVE PHENOMENA AT THE SURFACE."

Scaling. For yields other than 1 kt, the distance for any specified overpressure is

$$\frac{d}{d_1} = W^{1/3},$$

where d_1 is the distance from the explosion obtained from Figure 2-2 for 1 kt, and d is the corresponding distance for a yield of W kt.

Example

Given: A 5 kt explosion at 4,000 feet.

Find: The coaltitude distance to which 7 psi overpressure will extend.

Solution: From Figure 2-2, an overpressure of 7 psi will extend to 1,000 feet for explosions below about 5,000 feet.

Answer: The corresponding distance for a 5 kt weapon is

$$d = d_1 \times W^{1/3} = 1{,}000 \times (5)^{1/3} = 1{,}710 \text{ feet.}$$

Reliability

The curve shown in Figure 2-2 is a theoretical curve that agrees well with experimental data. For scaled ranges up to 1,000 feet (overpressures greater than 7 psi at sea level) the values of peak overpressure obtained from the curve are estimated to be within ±15 percent of the overpressure that a given nuclear burst will produce. This portion of the overpressure-distance curve has been verified by analyses of data obtained by high-speed photography.

For scaled distances greater than 1,000 feet (overpressures below 7 psi) the values of peak overpressure obtained from the curve are estimated to be within ±30 percent the overpressures that a given burst will produce. This portion of the curve is based on theoretical calculations that agree closely with the empirical curve in the high overpressure region. The experimental data for this portion of the curve consist of both airborne pressure gages (either in parachuted canisters or aircraft in flight) and pressure gages mounted on towers above the ground. Since atmospheric effects (see paragraph 2-16) influence overpressures strongly, greater scatter is found in the data on both sides of the curve in this region.

Related Material: See paragraph 2-7. See also paragraph 2-14 through 2-15 and Problem 2-6 for scaling to altitudes up to 40,000 feet. See paragraphs 2-42 through 2-44 for scaling above 40,000 feet.

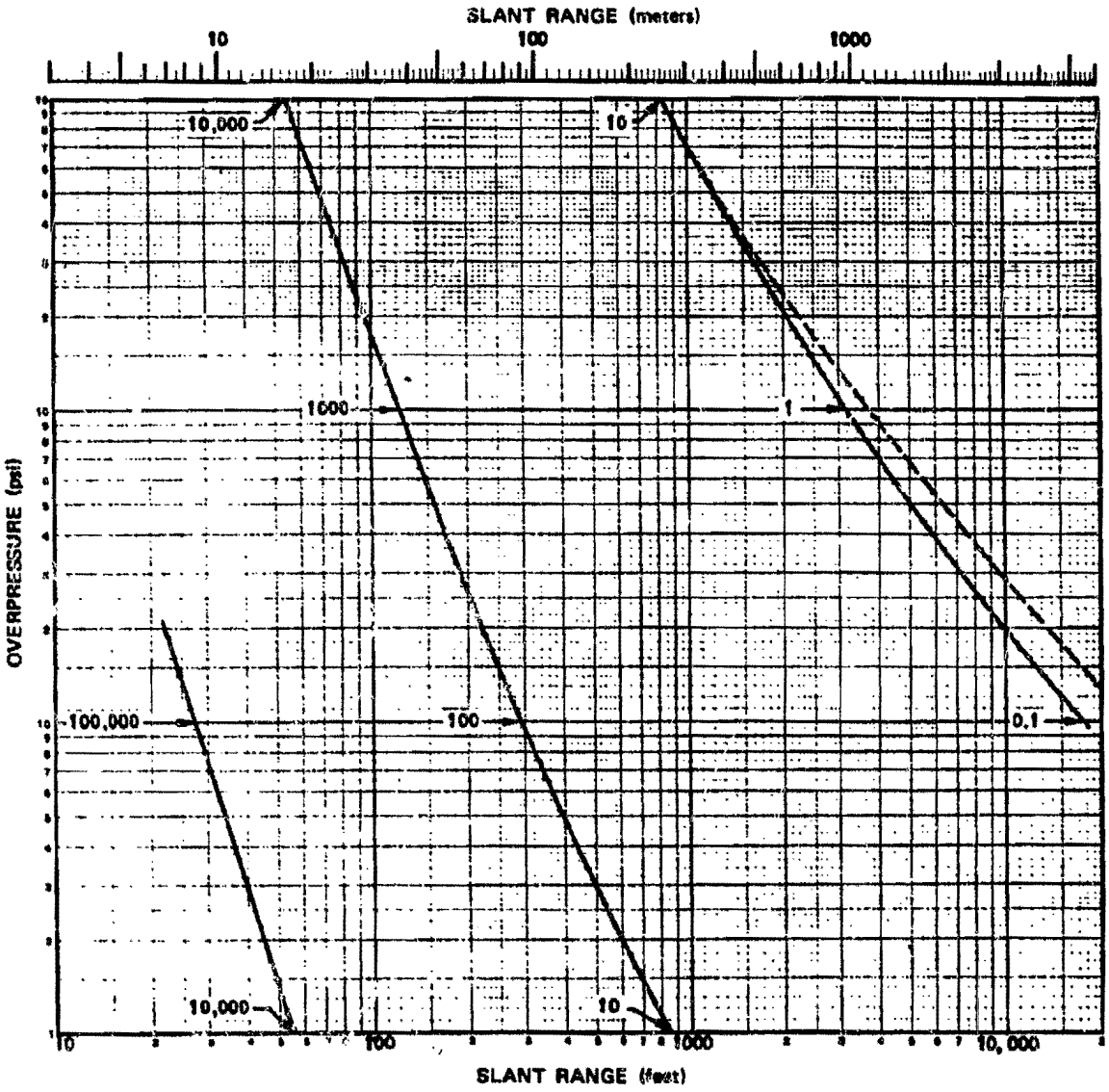

Figure 2-2. [redacted] Peak Overpressure from a 1 kt Free Air Burst in a Standard Sea Level Atmosphere [redacted]

[redacted]

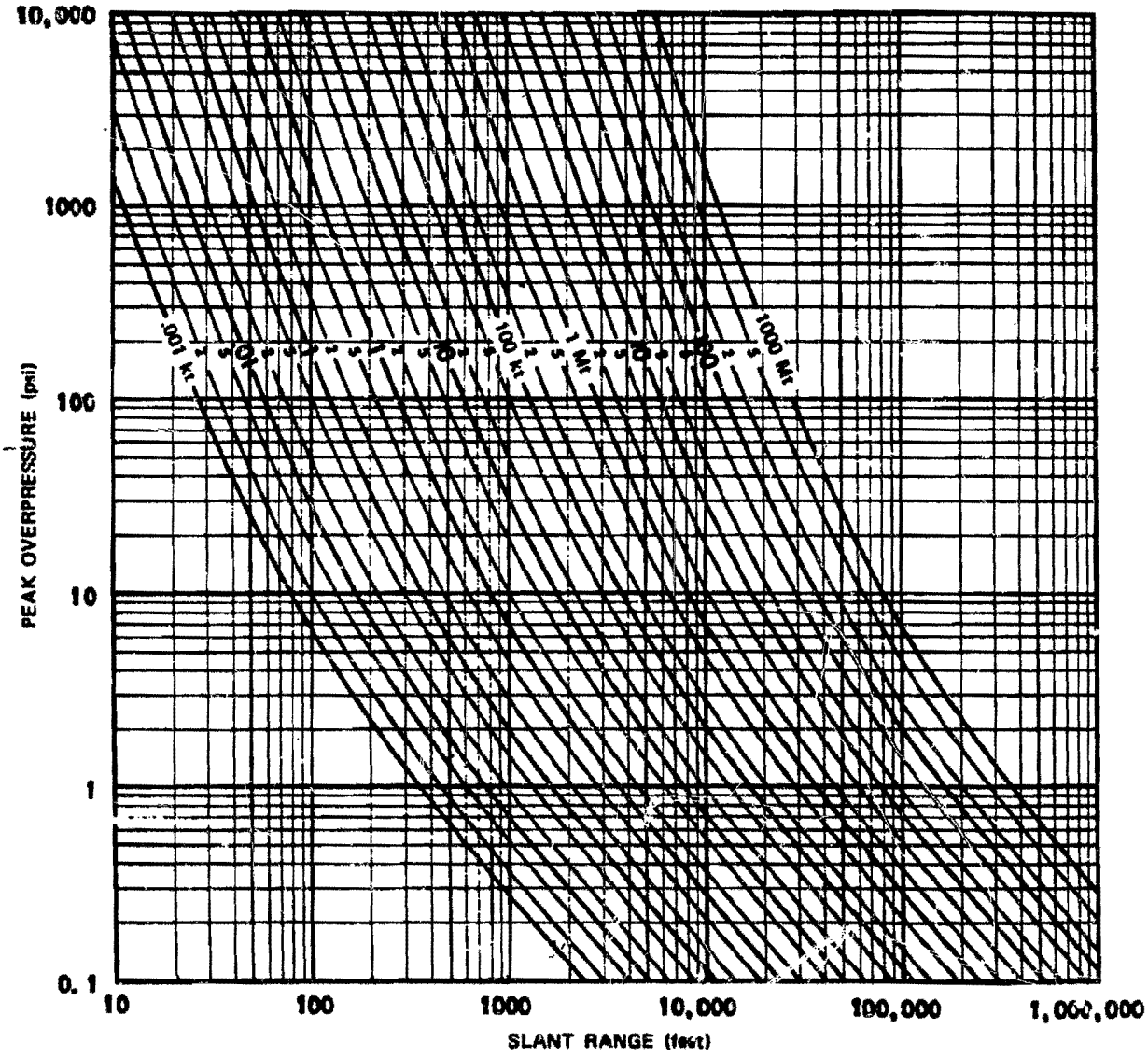

Figure 2-3. [redacted] Peak Overpressure in Free Air as a Function of Yield and Slant Range [redacted]

Problem 2-2. Calculation of Free Air Peak Dynamic Pressure

Figure 2-4 shows the peak dynamic pressure as a function of slant range from a 1 kt explosion in a homogeneous sea level atmosphere at heights of burst up to about 5,000 feet. For higher burst heights, this figure may be used together with the altitude scaling procedures described in paragraph 2-14 and illustrated in problem 2-6. Figure 2-4 only applies to *free air* peak dynamic pressure. The horizontal component of the peak dynamic pressure at the surface should be obtained from the subsection "BLAST WAVE PHENOMENA AT THE SURFACE."

Figure 2-4 shows peak dynamic pressure with respect to a stationary target. If the target velocity is appreciable compared to the peak particle velocity (wind) at the shock front, the procedures suggested in paragraph 2-15 should be used.

Scaling. For yields other than 1 kt, the distance for any specific peak dynamic pressure is

$$\frac{d}{d_1} = W^{1/3},$$

where d_1 is the distance from the explosion obtained from Figure 2-4 for 1 kt, and d is the corresponding distance for a yield of W kt.

Example

Given: A target is located at an altitude of 3,000 feet and is 2,600 feet from a 100 kt explosion at the same altitude.

Find: The peak dynamic pressure to which the target is expected to be exposed.

Solution: The corresponding distance from a 1 kt free air explosion is

$$d_1 = \frac{d}{W^{1/3}} = \frac{2{,}600}{(100)^{1/3}} = 560 \text{ feet.}$$

Answer: From Figure 2-4, a peak dynamic pressure of 12 psi is expected to occur 560 feet from a 1 kt free air explosion. This same peak dynamic pressure would be expected 2,600 feet from a 100 kt explosion.

Reliability: Peak dynamic pressures obtained from this curve are estimated to be reliable to ±15 percent for pressures greater than 2 psi and to ±20 percent for smaller pressures. These estimates of reliability apply to yields between 1 kt and 20 Mt. Outside this range of yields, the curve may be used with somewhat less confidence.

Related Material: See paragraph 2-8. See also paragraphs 2-13 through 2-15 and Problem 2-6 for scaling to altitudes up to 40,000 feet. See paragraphs 2-42 through 2-44 for scaling above 40,000 feet. See paragraph 2-25 for a discussion of dynamic pressure along the surface of the earth.

[redacted]

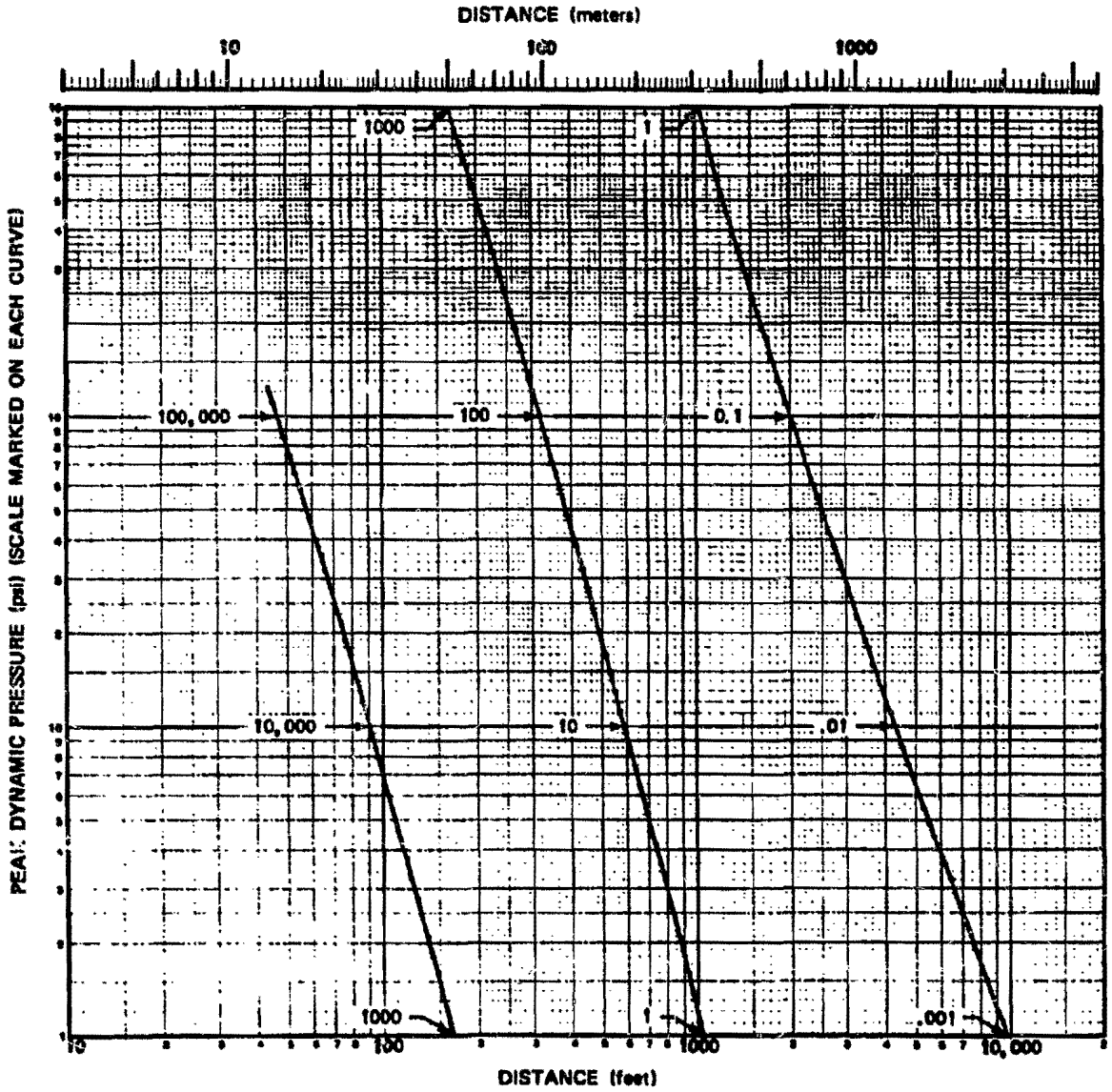

Figure 2-4. [redacted] Peak Dynamic Pressure from a 1 kt Free Air Burst in a Standard Sea Level Atmosphere [redacted]

[redacted]

Problem 2-3. Calculation of Time of Arrival of the Shock Front from a Free Air Burst

Figure 2-5 shows the time of arrival of the shock front from a 1 kt free air burst in a standard sea level atmosphere as a function of distance from the burst. Figure 2-5 applies to bursts at altitudes up to 5,000 feet.

Scaling. For yields other than 1 kt, scale as follows:

$$\frac{t}{t_1} = W^{1/3} = \frac{d}{d_1}$$

where t_1 is the time of arrival of the shock front at a distance d_1 from a 1 kt explosion, and t is the corresponding time at a distance d from a yield of W kt. At scaled distances greater than 1,500 feet ($d_1 > 1{,}500$ feet), the blast wave travels only slightly faster than the speed of sound, and the time of arrival may be approximated by

$$t = \frac{d - 600\ W^{1/3}}{1{,}116}\ \text{sec},$$

where d is the distance of interest, in feet, from an explosion of yield W kt, and t is the time of arrival of the shock front at that distance. The constant 1,116 is the speed of sound in air at a temperature of 59°F (15°C). The term 600 $W^{1/3}$ is a measure of the scaled distance from the burst beyond which the shock wave travels at approximately the speed of sound. The approximation may be extended by noting that the speed of sound increases by about 1 percent for each 10°F rise from the standard 59°F (1.8 percent for each 10°C rise from 15°C) and decreases by the same percentage for corresponding temperature decreases below standard.

Example

Given: A 100 kt explosion in free air in a sea level atmosphere.

Find: The time of arrival of the shock front at a point 40,000 feet from the explosion.

Solution: The corresponding distance from a 1 kt explosion is

$$d_1 = \frac{d}{W^{1/3}} = \frac{40{,}000}{(100)^{1/3}} = 8{,}600 \text{ feet.}$$

From Figure 2-5, the time of arrival of the shock front at a point 8,600 feet from a 1 kt explosion is 7.2 seconds.

Answer: The corresponding time of arrival at a distance of 40,000 feet from a 100 kt explosion is

$$t = t_1 W^{1/3} = 7.2 \times (100)^{1/3} = 33.4 \text{ sec.}$$

Since d_1 is greater than 1,500 feet, an alternate method for obtaining the time of arrival would be to use the equation presented above:

$$t = \frac{d - 600\ W^{1/3}}{1{,}116} = \frac{40{,}000 - (600)(100)^{1/3}}{1{,}116}$$

$$= 33.3 \text{ sec.}$$

Reliability: The times of arrival obtained from Figure 2-5 are estimated to be within ±15 percent of the true value for yields between 1 kt and 20 Mt. The curve may be used with less confidence outside this range of yields.

Related Material: See paragraph 2-9. See also paragraph 2-14 for scaling of times of arrival for burst altitudes above 5,000 feet. See paragraph 2-26 for time of arrival of the shock front at points on the surface.

[redacted]

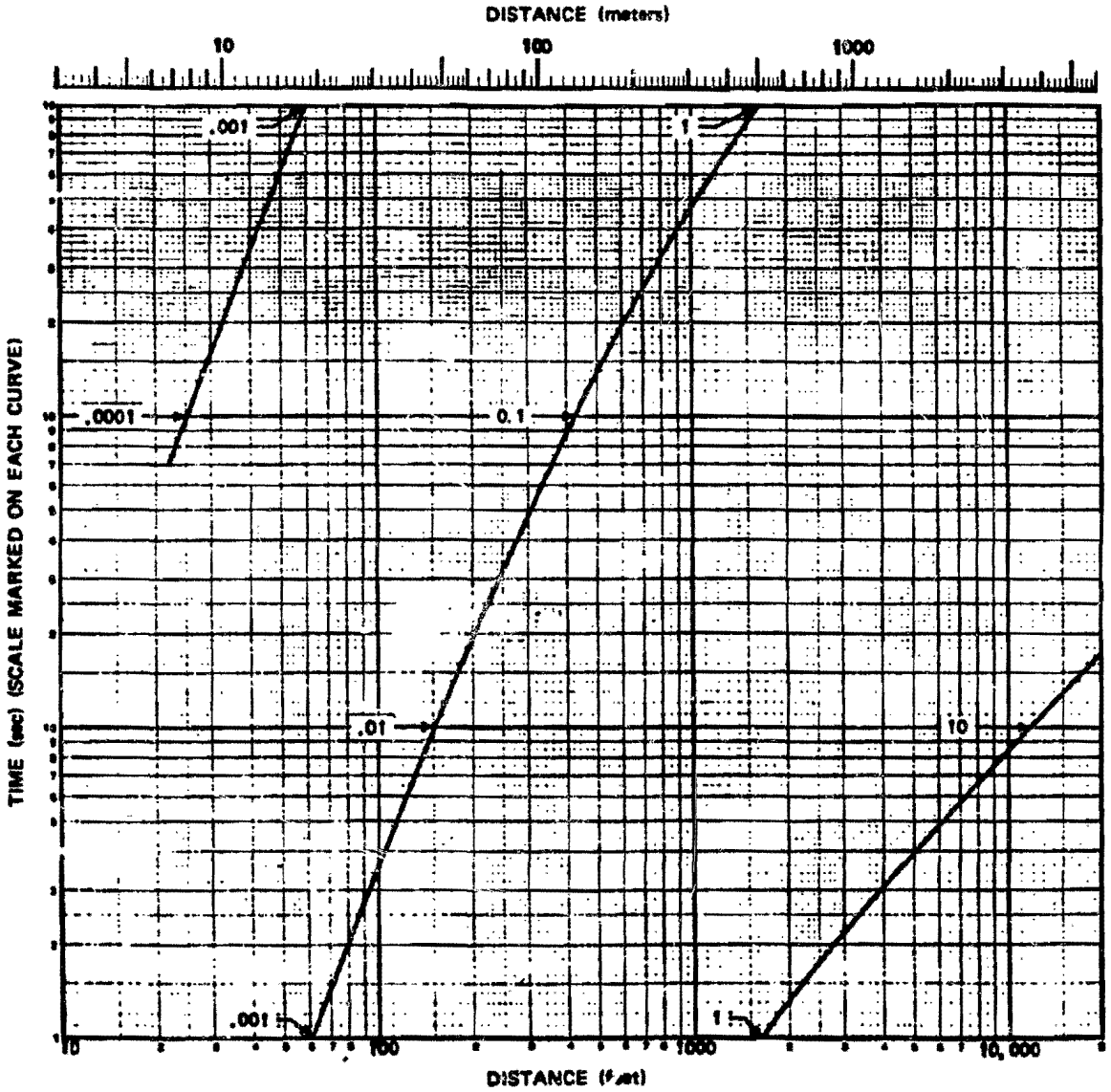

Figure 2-5. [redacted] Time of Arrival of the Shock Front from a 1 kt Free Air Burst in a Standard Sea Level Atmosphere [redacted]

[redacted]

Problem 2-4. Calculation of the Duration of the Positive Phase of the Overpressure and Dynamic Pressure

Figure 2-6 shows the durations of the positive phase of the overpressure and the dynamic pressure as a function of distance from a 1 kt free air explosion in a standard sea level atmosphere for heights of burst below 5,000 feet. For higher burst heights, this figure may be used together with the altitude scaling procedures described in paragraph 2-14. Figure 2-4 only applies to *free air* bursts. Positive phase durations at the surface should be obtained from the subsection "BLAST WAVE PHENOMENA AT THE SURFACE."

Scaling. For yields other than 1 kt, the positive phase durations scale as follows:

$$\frac{t_p^+}{t_{p1}^+} = \frac{t_q^+}{t_{q1}^+} = W^{1/3} = \frac{d}{d_1}$$

where t_{p1}^+ and t_{q1}^+ are the positive phase durations of the overpressure and the dynamic pressure, respectively, at a distance d_1 from a 1 kt explosion, and t_p^+ and t_q^+ are the corresponding positive phase durations at a distance d from a yield of W kt.

Example

Given: A 500 kt explosion in free air in a standard sea level atmosphere.

Find: The positive phase durations of the overpressure and the dynamic pressure at a point 8,000 feet from the explosion.

Solution: The corresponding distance from a 1 kt explosion is

$$d_1 = \frac{d}{W^{1/3}} = \frac{8{,}000}{(500)^{1/3}} = 1{,}000 \text{ feet.}$$

From Figure 2-6, the positive phase durations of the overpressure and the dynamic pressure at a distance of 1,000 feet from a 1 kt explosion are

$$t_{p1}^+ = 0.22 \text{ sec,}$$

$$t_{q1}^+ = 0.30 \text{ sec.}$$

Answer: The corresponding durations at a distance of 8,000 feet from a 500 kt explosion are

$$t_p^+ = t_{p1}^+ \times W^{1/3} = (0.22)(500)^{1/3} = 1.7 \text{ sec,}$$

$$t_q^+ = t_{q1}^+ \times W^{1/3} = (0.30)(500)^{1/3} = 2.4 \text{ sec.}$$

Reliability

Data for t_p^+ are derived from theoretical calculations that are supported by experimental data from bursts with yields between 1 and 50 kt. Over this range of yields, reliability is estimated to be ±15 percent. Since the accuracy of scaling to larger yields has not been confirmed experimentally, reliability is estimated to be ±30 percent for yields between 50 kt and 20 Mt. The curve may be used, with somewhat less confidence, for yields below 1 kt and above 20 Mt.

Data for t_q^+ are derived from theoretical calculations, and a few data points give limited experimental confirmation. The curve is estimated to be reliable within ±20 percent for yields between 1 and 50 kt and within ±40 percent for yields between 50 kt and 20 Mt. Outside these ranges of yields, the curve may be used with somewhat less confidence.

Related Material: See paragraph 2-10. See also paragraph 2-12 for a discussion of waveforms. See paragraph 2-27 for data concerning positive phase durations at the ground surface.

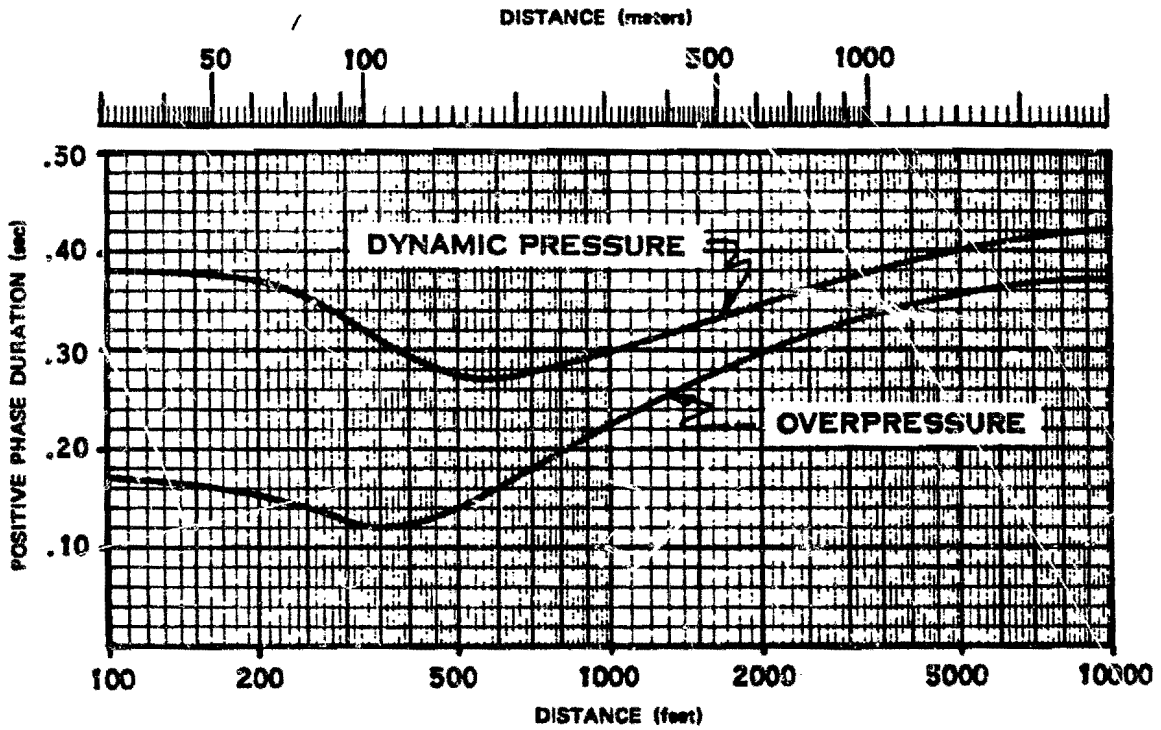

Figure 2-6. Duration of Positive Overpressure and Dynamic Pressure Phases for a 1 kt Free Air Burst in a Standard Sea Level Atmosphere

Problem 2-5. Calculation of Impulse

Figure 2-7 shows the overpressure and dynamic pressure impulse as a function of distance from a 1 kt free air explosion in a standard sea level atmosphere for heights of burst below about 5,000 feet. For higher burst heights, this figure may be used together with the altitude scaling procedures described in paragraph 2-14. Figure 2-5 applies only to *free air* bursts. Positive phase overpressure impulse should be obtained from the subsection "BLAST WAVE PHENOMENA AT THE SURFACE."

Scaling. For yields other than 1 kt, the overpressure impulse and dynamic pressure impulse scale as follows:

$$\frac{I}{I_1} = W^{1/3} = \frac{d}{d_1}$$

where I_1 is either the overpressure impulse or the dynamic pressure impulse at a distance d_1 from a 1 kt explosion, and I and d are the corresponding values of impulse and distance from a yield of W kt.

Example

Given: A 400 kt explosion in free air in a standard sea level atmosphere.

Find: The positive phase overpressure and dynamic pressure impulses at a distance of 4,400 feet.

Solution: The corresponding distance from a 1 kt explosion is

$$d_1 = \frac{d}{W^{1/3}} = \frac{4{,}400}{(400)^{1/3}} = 600 \text{ feet.}$$

From Figure 2-7, the overpressure and dynamic pressures at a distance of 600 feet from a 1 kt explosion are

$$I_{p1} = 8.5 \text{ psi-sec,}$$

$$I_{q1} = 4.4 \text{ psi-sec.}$$

Answer: The corresponding impulses at a distance of 4,400 feet from a 400 kt explosion are

$$I_p = I_{p1} \times W^{1/3} = (8.5)(400)^{1/3} = 62 \text{ psi-sec,}$$

$$I_q = I_{q1} \times W^{1/3} = (4.4)(400)^{1/3} = 32 \text{ psi-sec.}$$

Reliability: Conventional practice and availability of data have favored the use of peak overpressure rather than overpressure impulse for blast wave calculations. Consequently, there have been few impulse measurements, and reliable experimental data have not been obtained. The impulse curves were obtained theoretically. The overpressure impulse data were obtained from computer code calculations (Problem M, DASA 1200, see bibliography). Values for dynamic pressure impulse were calculated from the relations of effective triangular duration described in paragraph 2-12. Overpressure impulse as shown in Figure 2-7 is estimated to be reliable within ±20 percent. No reliability estimate can be assigned to the dynamic pressure impulse curve. A portion of the latter curve is broken to indicate that measurement of waveform area is less accurate at short ranges.

Related Material: See paragraph 2-11. See also paragraphs 2-13 through 2-15 for scaling to altitudes up to 40,000 feet. See paragraph 2-28 for a discussion of positive phase overpressure impulse along the surface of the earth.

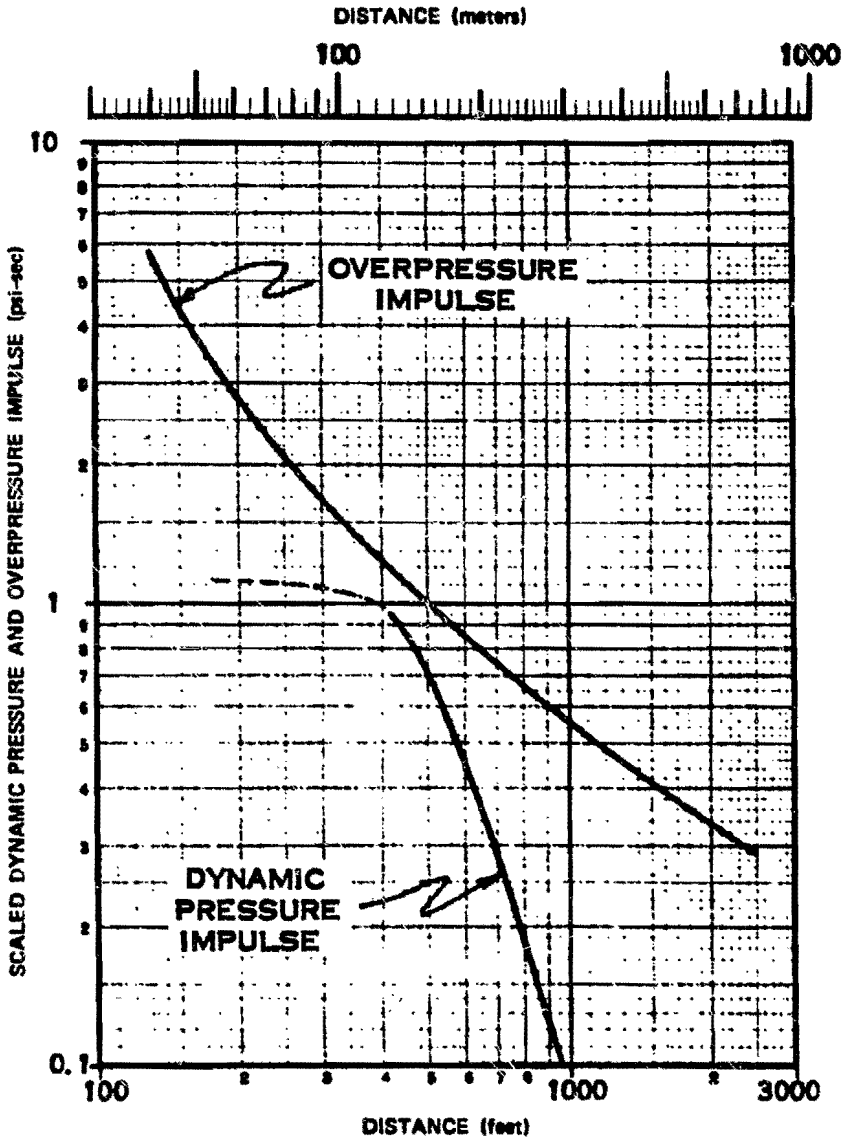

Figure 2-7. [redacted] Overpressure and Dynamic Pressure Impulse from 1 kt Free Air Burst in a Standard Sea Level Atmosphere [redacted]

2-12 Waveforms

Damage inflicted to a target by a blast wave generally is a complex function of peak overpressure, peak dynamic pressure, pulse durations, and structural response characteristics of the target. Usually, all details of the method by which a target interacts with a blast wave are not identified. The strength of the blast wave that will damage the target generally is specified in terms of a pair of parameters. For example, weapon yield and peak overpressure, distance and peak overpressure, or peak overpressure and positive-phase duration are, for an ideal blast wave, adequate to specify uniquely all properties of the blast wave. If a blast wave, so defined, is found by experiment to damage a certain target, further analysis of the interaction usually is not necessary.

This discussion of waveforms and the preceding discussion of impulse are not included so much to provide a basis for calculations as to provide an understanding of blast wave phenomena.

At a given point in space, the rate of decay of overpressure after the shock front passes depends on the peak overpressure. Overpressure waveforms are shown in Figure 2-8 in terms of normalized coordinates. The overpressure at a given time is expressed as a fraction of peak overpressure, and time is expressed as a function of positive phase duration. These normalized variables are $\Delta p(t)/\Delta p$ and t/t_p^+, where $\Delta p(t)$ and t are instantaneous values of overpressure and time, Δp is peak overpressure, and t_p^+ is the positive phase duration of the overpressure. Similarly, dynamic pressure waveforms are shown in Figure 2-9 in terms of the normalized variables for dynamic pressure, $q(t)/q$, where $q(t)$ is the instantaneous value of dynamic pressure and q is the peak value, and normalized time t/t_q^+. Note that, since dynamic pressure duration is longer than overpressure duration, Figures 2-8 and 2-9 do not have a common time base.

Both sets of waveforms show that close to the burst, where peak pressures are high, the pressure drops rapidly from its peak value. At greater distances and lower peak pressures, the drop in pressure is slower, and the waveform is much broader. This broadening of the pressure pulse with distance has more influence on effective pulse duration than changes in t_p^+ and t_q^+ have. At any specified distance, dynamic pressure decays more rapidly than overpressure for a given yield.

For low values of peak overpressure and peak dynamic pressure, the variation of pressure with time behind the shock front may be approximated by the equations

$$\Delta p(t) = \Delta p(1 - t/t_p^+)e^{-t/t_p^+}$$

$$q(t) = q(1 - t/t_q^+)^2 e^{-2t/t_q^+}.$$

These equations correspond most nearly to the 7.5 psi overpressure curve and the 7.5 psi dynamic pressure curve. They may be used with reasonable accuracy for peak pressures of 0 to 25 psi.

In damage estimates, it is frequently useful to approximate the actual shock waveform by the equivalent triangular waveform, which is defined as one that has the same peak amplitude and the same area as the actual waveform, but has a triangular shape and a shorter time duration than the actual waveform. Since the equivalent triangular waveform has the same area as the actual waveform, it represents the same impulse. The time duration of this equivalent waveform is obtained by multiplying actual time duration by the triangular duration correction factor C_t, which is shown in Figure 2-10 separately for overpressure and dynamic pressure.

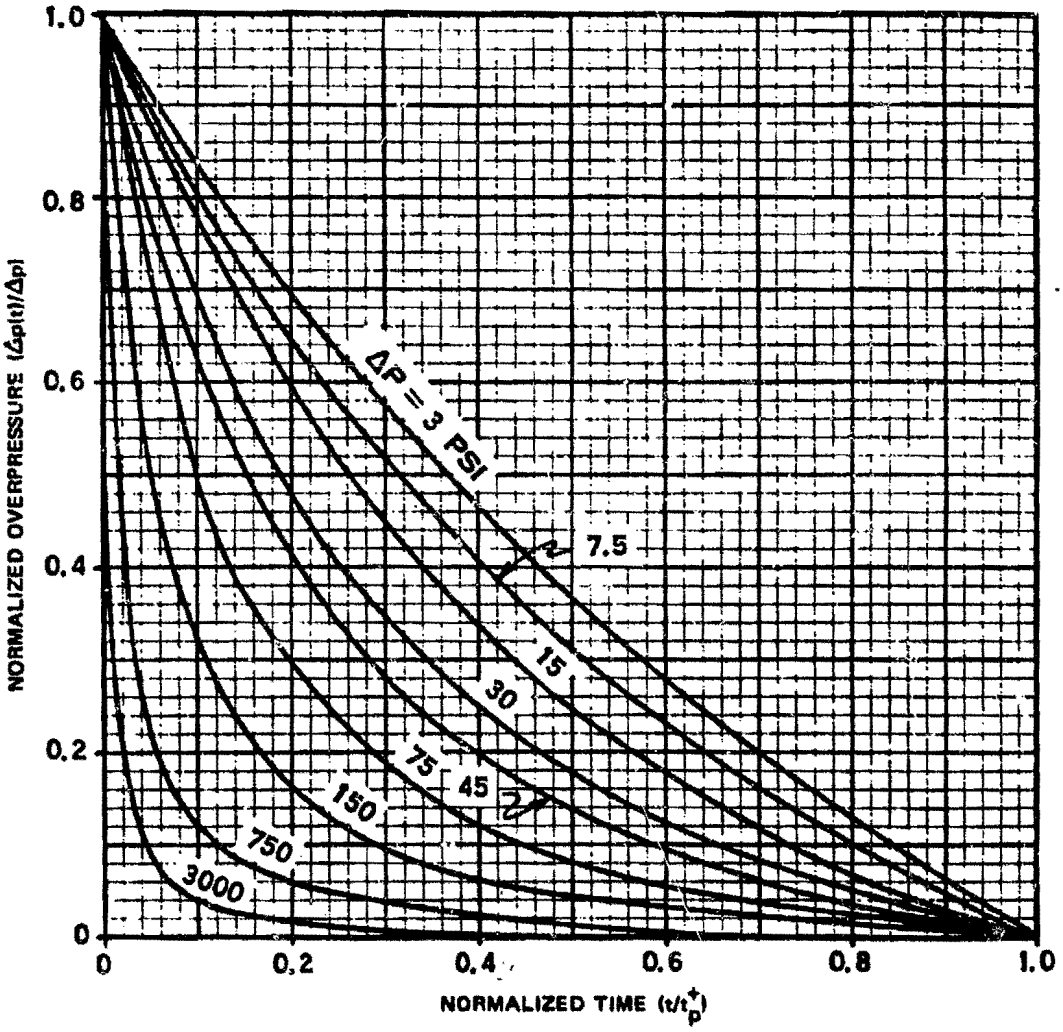

Figure 2-8. [redacted] Positive Overpressure Waveforms for an Ideal Shock Wave in a Standard Sea Level Atmosphere [redacted]

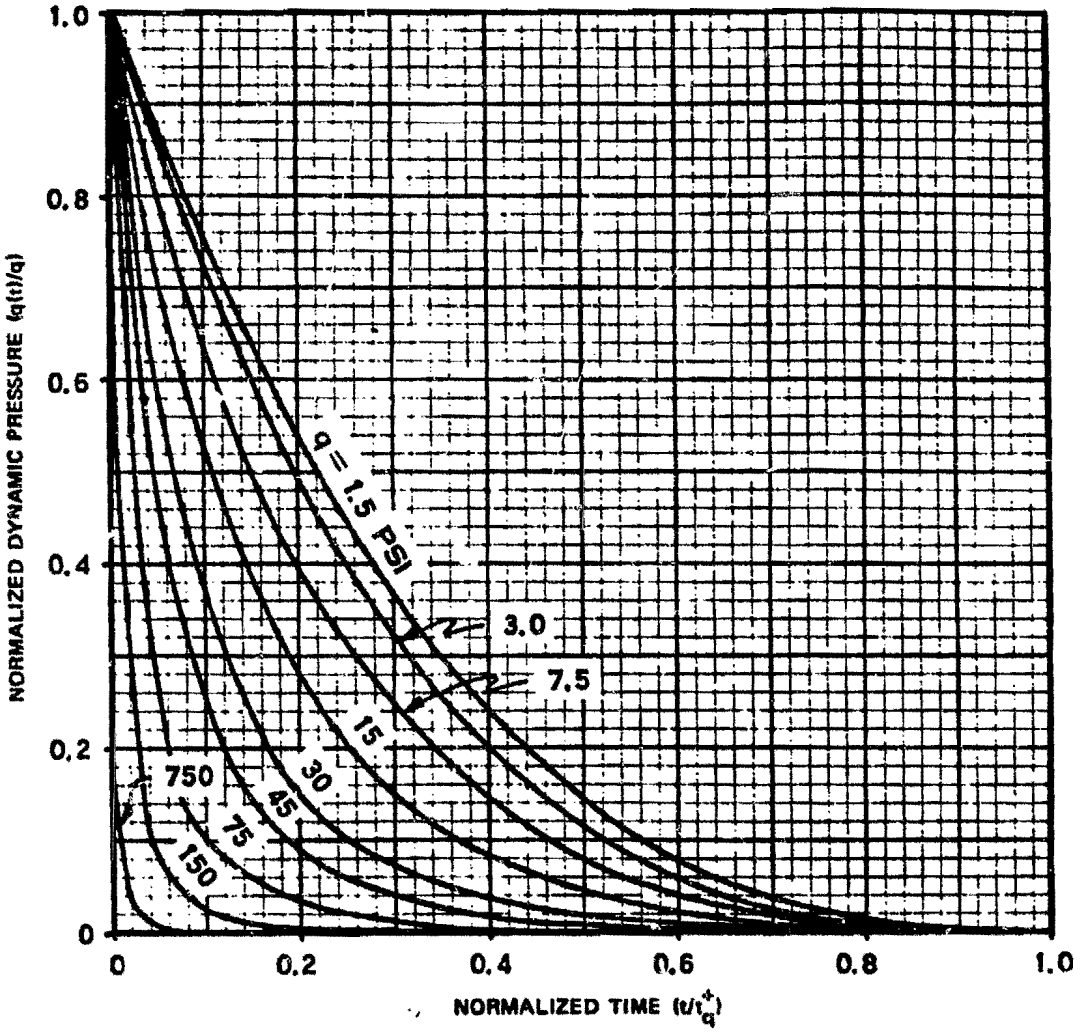

Figure 2-9. Positive Dynamic Pressure Waveforms for an Ideal Shock Wave in a Standard Sea Level Atmosphere

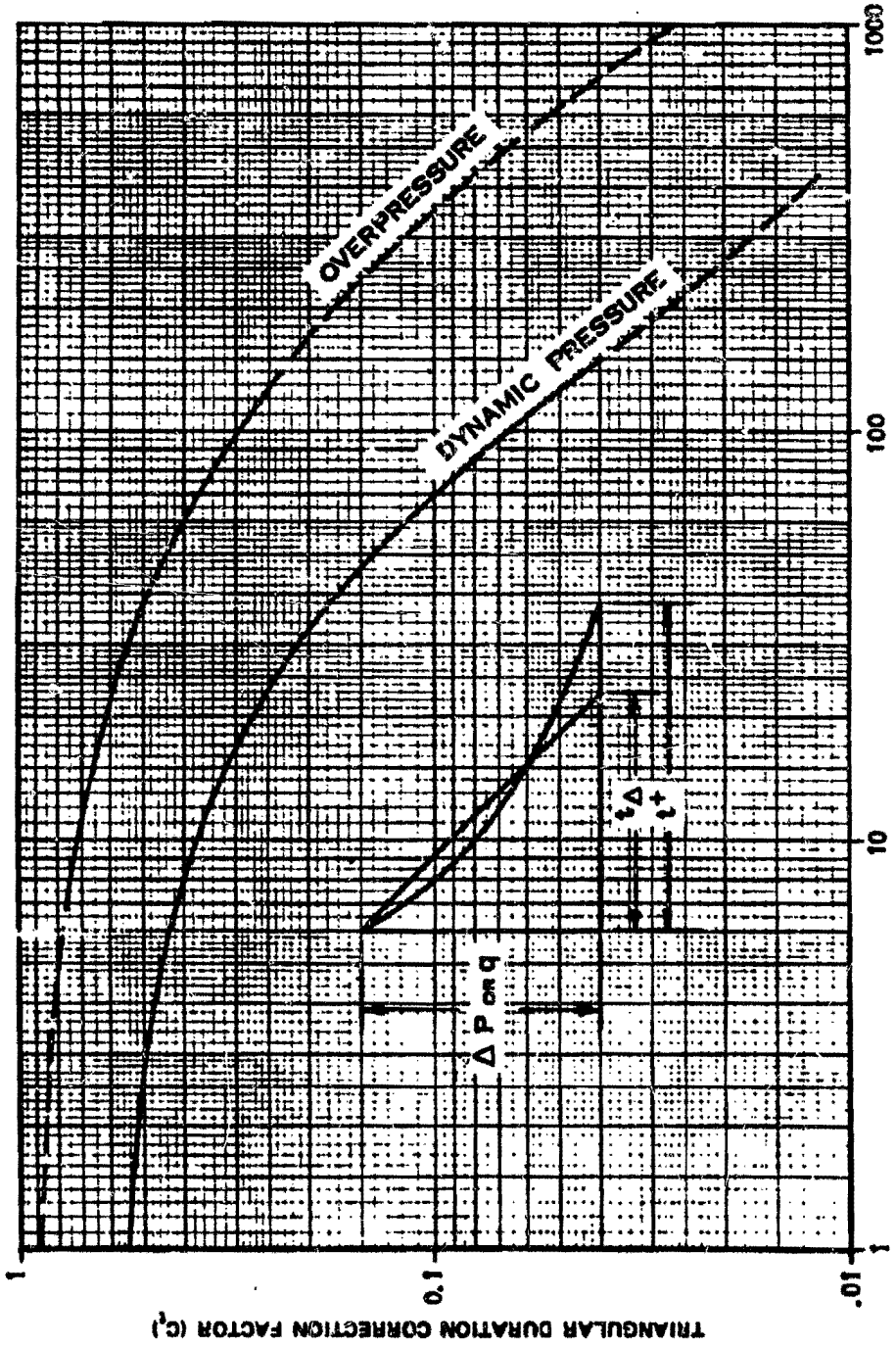

Figure 2-10. [redacted] Effective Triangular Duration Correction Factors ($t_\Delta = C_t t_p^+$ or $t_\Delta = C_t t_q^+$)

The time duration of the equivalent waveform is called the effective triangular duration of the pressure pulse, t_Δ, where

$$t_\Delta = C_{tp} t_p^+ \quad \text{or} \quad t_\Delta = C_{tq} t_q^+$$

for overpressure and dynamic pressure, respectively.

The curves shown in Figures 2-8 and 2-9 are based on theory, and specific estimates of the amount by which actual blast waveforms can be expected to deviate from these curves cannot be made. The effective triangular waveform obtained by use of the triangular duration correction factors shown in Figure 2-10 are simplified representations of the actual waveforms. These triangular waveforms do not represent structural loading functions. The latter are described in Section II, Chapter 9, and specific loading functions used in some of the structural damage analyses for this manual are shown in Figure 11-1.

RELATIONS BETWEEN SHOCK FRONT PARAMETERS

2-13 Generalized Scaling

The concept of scaling various blast wave parameters was introduced in the preceding subsection with reference to the corresponding parameter from a 1 kt explosion in a standard sea level atmosphere. The various curves were presented in terms of absolute values of distance, time, or impulse from a 1 kt explosion in free air in a standard sea level atmosphere. This convention of presenting the data in terms of a 1 kt explosion with scaling laws to relate the parameters to other yields will be adhered to in subsequent sections of this chapter as well as in succeeding chapters; however, the scaling laws are not necessarily limited to scaling from 1 kt. The "Sachs" scaling laws, which pertain to scaling of blast parameters, depend only on the relative yields of two weapons being considered. Thus, the distance scaling law given in Problems 2-1 and 2-2 could be written

$$\frac{d_2}{d_1} = \left(\frac{W_2}{W_1}\right)^{1/3},$$

where d_2 is the slant range (distance from the point of burst) from an explosion of W_2 kilotons and d_1 is the corresponding distance from an explosion of W_1 kilotons. Likewise, the time and impulse scaling laws given in Problems 2-3 through 2-5 could be written

$$\frac{t_2}{t_1} = \left(\frac{W_2}{W_1}\right)^{1/3}$$

$$\frac{t_{p2}^+}{t_{p1}^+} = \frac{t_{q2}^+}{t_{q1}^+} = \left(\frac{W_2}{W_1}\right)^{1/3},$$

and

$$\frac{I_2}{I_1} = \left(\frac{W_2}{W_1}\right)^{1/3},$$

where, in each case the subscript 2 refers to the value of the parameter for yield W_2 kt, and the subscript 1 refers to the value of the same parameter for a yield of W_1 kt. As mentioned above, W_1 will generally be taken to equal 1 kt as a matter of convenience in this manual.

The scaling laws are derived from the assumption that, at corresponding stages of development, the fireballs from two different nuclear explosions have the same energy per unit mass of air at points that are the same scaled distance from the point of burst. It is also assumed that, as the blast waves propagate outward from the fireballs, they maintain this property of equal energy densities at equal scaled

radii. The blast waves produced by two different nuclear explosions are thus assumed to be similar in all respects except for those relating to differences in size. Since, at a particular stage of development, the average energy densities throughout the two fireballs are equal, fireball volume is directly proportional to the amount of energy required to produce it; therefore, fireball radius is proportional to the cube root of the nuclear yield. Other pertinent distances, such as shock front radius, also follow this cube root scaling law.

2-14 Altitude Scaling

At higher altitudes, where air density is less than at sea level, the reasoning described above still applies. At equal scaled distances and corresponding times, equal masses of air contain equal amounts of energy. Therefore, the volume of a sphere needed to contain a given amount of energy in this manner is larger at higher altitudes where the air is thinner. Specifically, this volume is inversely proportional to air density; and corresponding radii are inversely proportional to the cube root of air density. However, better results are obtained by scaling distance with the cube root of the ambient pressure (up to altitudes of 40,000 feet).* The altitude scaling for distance is

$$\frac{d_2}{d_1} = \left(\frac{W'_2}{W'_1}\right)^{1/3} \left(\frac{P_o}{P}\right)^{1/3},$$

where P_o is the sea level ambient pressure, P is the ambient pressure at the altitude of interest, and the other quantities are as previously defined.

No pressure scaling factor is required for explosions in a standard sea level atmosphere since the effect of yield is taken into account by distance scaling, and, under similar ambient conditions, the pressures generated by explosions of different yields are equal at scaled distances. When altitude must be considered, equal "shock strengths" occur at equal scaled distances. The term shock strength means the ratio of the absolute pressure behind the front to the ambient pressure, i.e., the shock strength, ξ is,

$$\xi = \frac{\Delta p + P}{P} = \frac{\Delta p}{P} + 1,$$

which is a dimensionless quantity. At equal scaled distances,

$$\xi = \xi_o,$$

where ξ is the shock strength at the altitude of interest and ξ_o is the shock strength at the same scaled distance at sea level. This may be written

$$\frac{\Delta p}{P} + 1 = \frac{\Delta p_o}{P_o} + 1,$$

which leads to

$$\frac{\Delta p}{P} = \frac{\Delta p_o}{P_o},$$

*The reasons for dismissing density in favor of pressure as a basis for calculating the altitude scaling factor for distance may be described as follows. In the early fireball region, where energy absorbed from the weapon completely overshadows any effect of initial air temperature, it would be expected that the only important question is the number of air atoms present. In this region, density scaling is appropriate. Examples of equations that are based on density scaling are given in paragraph 2-44; however, the situation is different over most of the range through which the blast wave propagates. Shock-front parameters correspond more directly to the pressure ratio across the shock front than to the density ratio. After the shock front reaches air not directly heated by the nuclear source, pressure ratio provides the better basis for scaling. The corresponding energy model for Sachs' scaling laws is that two free air blast waves are equivalent when the ratio:

$$\frac{\text{energy enclosed by the shock front}}{\text{ambient internal energy of the air enclosed by the front}}$$

is the same for both blast waves. This model may be derived by noting that the pressure of an ideal gas is proportional to internal energy per unit volume.

and the altitude scaling for pressure is

$$\frac{\Delta p}{\Delta p_o} = \frac{P}{P_o},$$

where Δp is the overpressure at the altitude of interest, Δp_o is the overpressure at the same scaled distance at sea level, and P and P_o are the corresponding ambient pressures. This same relation holds for other characteristic pressures, such as the total pressure behind the shock front and the dynamic pressure.

Two factors influence time of arrival: the speed of the blast wave and the distance that it must travel. Under standard sea level conditions, the speed of the blast wave depends on overpressure, which, in turn, depends only on scaled distance from the burst. When the scaling problem is not limited to the case of a sea level atmosphere, the assumed relation between shock speed and overpressure must be stated in more general terms: for a given shock strength (and hence for a given scaled distance), the Mach number of the shock front is always the same. As altitude is increased, the time required for the shock to reach a given scaled distance increases because (1) the actual distance is farther and (2) at the lower temperatures generally associated with higher altitudes, sound speed is slower (therefore, a given Mach number corresponds to a slower shock front speed). The altitude scaling for time is

$$\frac{t_2}{t_1} = \left(\frac{W_2}{W_1}\right)^{1/3} \left(\frac{P_o}{P}\right)^{1/3} \left(\frac{T_o}{T}\right)^{1/2},$$

where T_o is the absolute temperature at sea level and T is the absolute temperature at the altitude of interest. The factor $T_o^{1/2}/T^{1/2}$ appears in this expression because sound speed is proportional to the square root of absolute temperature. The factors involving yield and pressure are those in scaling distance. The same scaling relationships may be used for scaling the positive duration of the overpressure.

The altitude scaling for impulse may be obtained by multiplying the scaling equation for time by the scaling equation for pressure, i.e.,

$$\frac{I_2}{I_1} = \left(\frac{W_2}{W_1}\right)^{1/3} \left(\frac{P}{P_o}\right)^{2/3} \left(\frac{T_o}{T}\right)^{1/2}.$$

In the foregoing scaling relations, the subscript o was defined to represent ambient conditions (pressure or absolute temperature) at sea level. Strictly speaking this is not necessary, since the ratios of the values are the important quantities. However, since these equations are for use with the curves presented in the previous subsection, which are all shown for standard sea level conditions, it is convenient to scale from those conditions. In order to facilitate calculations based on the preceding equations, the following factors have been defined and are tabulated in Tables 2-1 and 2-2:

$$S_d = \left(\frac{P_o}{P}\right)^{1/3}$$

$$S_p = \frac{P}{P_o}$$

$$S_t = \left(\frac{P_o}{P}\right)^{1/3} \left(\frac{T_o}{T}\right)^{1/2},$$

so that if, as usual, W_1 is taken to be 1 kt, the equations may be shown in an abbreviated form as follows:

$$d = d_1 W^{1/3} S_d$$

$$\Delta p = \Delta p_o S_p$$

$$q = q_o S_p$$

$$t = t_1 W^{1/3} S_t$$

$$I = I_1 W^{1/3} S_p S_t.$$

Table 2-1. [redacted] Data Based on U.S. Standard Atmosphere, 1962 English Units [redacted]

Altitude feet	Temperature °F	Pressure psi	Altitude Scaling Factors			Density Ratio*	Temperature Ratio	Sound Speed
			S_d	S_p	S_t	ρ/ρ_o	T/T_o	ft/sec
0	59.0	14.696	1.000	1.0000	1.000	1.0000	1.000	1116
1 000	55.4	14.17	1.012	.9644	1.016	.9711	.993	1113
2 000	51.9	13.66	1.025	.9298	1.032	.9428	.986	1109
3 000	48.3	13.17	1.037	.8963	1.048	.9151	.979	1105
4 000	44.7	12.69	1.050	.8637	1.065	.8881	.973	1101
5 000	41.2	12.23	1.063	.8321	1.082	.8617	.966	1097
10 000	23.4	10.11	1.133	.6878	1.174	.7386	.931	1077
15 000	5.5	8.297	1.210	.5646	1.278	.6295	.897	1057
20 000	-12.3	6.759	1.295	.4599	1.395	.5332	.863	1037
25 000	-30.0	5.461	1.391	.3716	1.528	.4486	.828	1016
30 000	-47.8	4.373	1.498	.2975	1.681	.3747	.794	995
35 000	-65.6	3.468	1.618	.2360	1.857	.3106	.760	973
40 000	-69.7	2.730	1.753	.1858	2.021	.2471	.752	968
45 000	-69.7	2.149	1.898	.1462	2.189	.1945	.752	968
50 000	-69.7	1.692	2.056	.1151	2.371	.1531	.752	968
55 000	-69.7	1.332	2.226	.09063	2.567	.1206	.752	968
60 000	-69.7	1.049	2.411	.07137	2.780	.09492	.752	968
65 000	-69.7	.826	2.611	.05620	3.011	.07475	.752	968
70 000	-67.4	.651	2.826	.04429	3.250	.05857	.756	971
75 000	-64.7	.514	3.058	.03496	3.504	.04591	.762	974
80 000	-62.0	.406	3.307	.02765	3.777	.03606	.767	978
85 000	-59.3	.322	3.574	.02190	4.068	.02837	.772	981
90 000	-56.5	.255	3.861	.01738	4.379	.02236	.777	984
95 000	-53.8	.203	4.168	.01381	4.711	.01765	.782	988
100 000	-51.1	.162	4.497	.01100	5.067	.01396	.788	991
110 000	-41.3	.103	5.225	7.011-3	5.817	8.692-3	.807	1003
120 000	-26.1	.0667	6.040	4.537	6.607	5.428	.836	1021
130 000	-10.9	.0438	6.948	2.982	7.470	3.446	.865	1038
140 000	4.3	.0292	7.953	1.988	8.410	2.222	.894	1056
150 000	19.4	.0197	9.064	1.343	9.431	1.454	.924	1073
160 000	27.5	.0135	10.29	9.176-4	10.62	9.770-4	.939	1082
170 000	27.5	9.23-3	11.68	6.283	12.05	6.690	.939	1082
180 000	18.9	6.31	13.26	4.292	13.80	4.652	.923	1072
190 000	8.1	4.27	15.09	2.908	15.89	3.225	.902	1060
200 000	-2.7	2.87	17.23	1.954	18.36	2.217	.881	1048

NOTE: 7.011-3 means 7.011×10^{-3}

*$\rho_o = 2.38 \times 10^{-3}$ slugs/ft^3
$= 7.65 \times 10^{-2}$ lbs/ft^3

[redacted]

Table 2-2. [redacted] Data Based on U.S. Standard Atmosphere, 1962 Metric Units [redacted]

Altitude km	Temperature °C	Pressure millibars	Pressure psi	Altitude Scaling Factors S_d	S_p	S_t	Density Ratio* ρ/ρ_o	Temperature Ratio T/T_o	Sound Speed m/sec
0	15.0	1013.25	14.696	1.000	1.0000	1.000	1.000	1.000	340.3
.5	11.8	954.61	13.845	1.020	.9421	1.026	.953	.989	338.4
1.0	8.5	898.76	13.035	1.041	.8870	1.053	.907	.977	336.4
1.5	5.3	845.60	12.264	1.062	.8345	1.081	.864	.966	334.5
2.0	2.0	795.01	11.531	1.084	.7846	1.110	.822	.955	332.5
3.0	-4.5	701.21	10.170	1.131	.6920	1.171	.742	.932	328.6
4.0	-11.0	616.60	8.943	1.180	.6085	1.237	.669	.910	324.6
5.0	-17.5	540.48	7.839	1.233	.5334	1.309	.601	.887	320.5
6.0	-24.0	472.18	6.848	1.290	.4660	1.387	.539	.865	316.5
7.0	-30.4	411.05	5.962	1.351	.4057	1.472	.482	.842	312.3
8.0	-36.9	356.52	5.171	1.416	.3519	1.564	.429	.820	308.1
9.0	-43.4	308.01	4.467	1.487	.3040	1.666	.381	.797	303.8
10	-49.9	265.00	3.843	1.564	.2615	1.777	.338	.775	299.5
12	-56.5	193.99	2.814	1.735	.1915	2.001	.255	.752	295.1
14	-56.5	141.70	2.055	1.927	.1399	2.222	.186	.752	295.1
16	-56.5	103.53	1.502	2.139	.1022	2.467	.136	.752	295.1
18	-56.5	75.65	1.097	2.375	.07466	2.739	.0993	.752	295.1
20	-56.5	55.29	.802	2.636	.05457	3.040	.0726	.752	295.1
22	-54.6	40.47	.587	2.925	.03995	3.359	.0527	.759	296.4
24	-52.6	29.72	.431	3.243	.02933	3.706	.0383	.765	297.7
26	-50.6	21.88	.317	3.591	.02160	4.086	.0280	.772	299.1
28	-48.6	16.16	.234	3.973	.01595	4.500	.0205	.779	300.4
30	-46.6	11.97	.174	4.391	.01181	4.952	.0150	.786	301.7
32	-44.7	8.89	.129	4.848	8.774-3	5.445	.0111	.793	303.0
34	-39.4	6.63	.0962	5.345	6.547	5.935	8.07-3	.811	306.5
36	-33.9	4.99	.0723	5.880	4.920	6.452	5.92	.830	310.1
38	-28.3	3.77	.0547	6.453	3.722	7.000	4.38	.850	313.7
40	-22.8	2.87	.0416	7.067	2.834-3	7.581	3.26-3	.869	317.2
42	-17.3	2.20	.0319	7.723	2.171	8.196	2.44	.888	320.7
44	-11.7	1.69	.0246	8.424	1.673	8.844	1.84	.907	324.1
46	-6.2	1.31	.0190	9.171	1.296	9.529	1.40	.926	327.5
48	-2.5	1.02	.0148	9.968	1.010	10.29	1.07	.939	329.8
50	-2.5	.798	.0116	10.83	7.874-4	11.17	8.38-4	.939	329.8
52	-2.5	.622	.00903	11.76	6.141	12.14	6.54	.939	329.8
54	-5.6	.485	.00703	12.78	4.786	13.27	5.15	.929	327.9
56	-9.5	.377	.00546	13.91	3.716	14.54	4.06	.915	325.5
58	-13.5	.291	.00423	15.15	2.876	15.96	3.19	.901	323.1
60	-17.4	.225	.00326	16.52	2.217-4	17.54	2.50-4	.888	320.6

NOTE: 8.774-3 means 8.774×10^{-3}

*$\rho_o = 1.225 \times 10^{-3}$ gm/cm^3 = 1.225 kg/m^3.

[redacted]

The use of other factors shown in Tables 2-1 and 2-2 will be explained in succeeding paragraphs. Figure 2-11 shows a curve for each of the scaling factors as a function of altitude, and thus presents the continuous variation of the scaling factors rather than the variation with incremental steps in altitude as provided in Tables 2-1 and 2-2.

Although S_d, S_p, and S_t are called altitude scaling factors, their use is not limited to correcting for differences in altitude. Even if a burst occurs at sea level, S_d and S_p are affected by barometric pressure variations (typically these variations are ±5 percent), and S_t is affected by temperature variations. When experimental data are analyzed, the actual pressure and temperature at the time of burst ordinarily are known and may be used in calculating the scaling factors. On the other hand, predictions of nuclear effects often must be made without any knowledge of what the weather will be when the burst occurs. In this case, S_d, S_p, and S_t are usually based on handbook values of temperature and pressure, which are functions of altitude only as shown in Tables 2-1 and 2-2 and in Figure 2-11.

To this point, nothing has been said about differences between burst altitude and target altitude. The explanation has been presented as though the blast wave were propagating from burst to target through a uniform atmosphere. For many problems this assumption is essentially correct, but for long ranges the source and the target may be at entirely different altitudes and the scaling factors may vary appreciably over the path traveled by the blast wave. When this complication arises the altitude scaling factors are calculated on the basis of target altitude (i.e., for the altitude at the point in space where overpressure etc. are to be determined) rather than on the basis of burst altitude. Basic physical concepts fail to explain in a simple manner why this choice is made. This method, called "modified Sachs scaling," is used because it comes closer to giving answers that agree with experimental data.

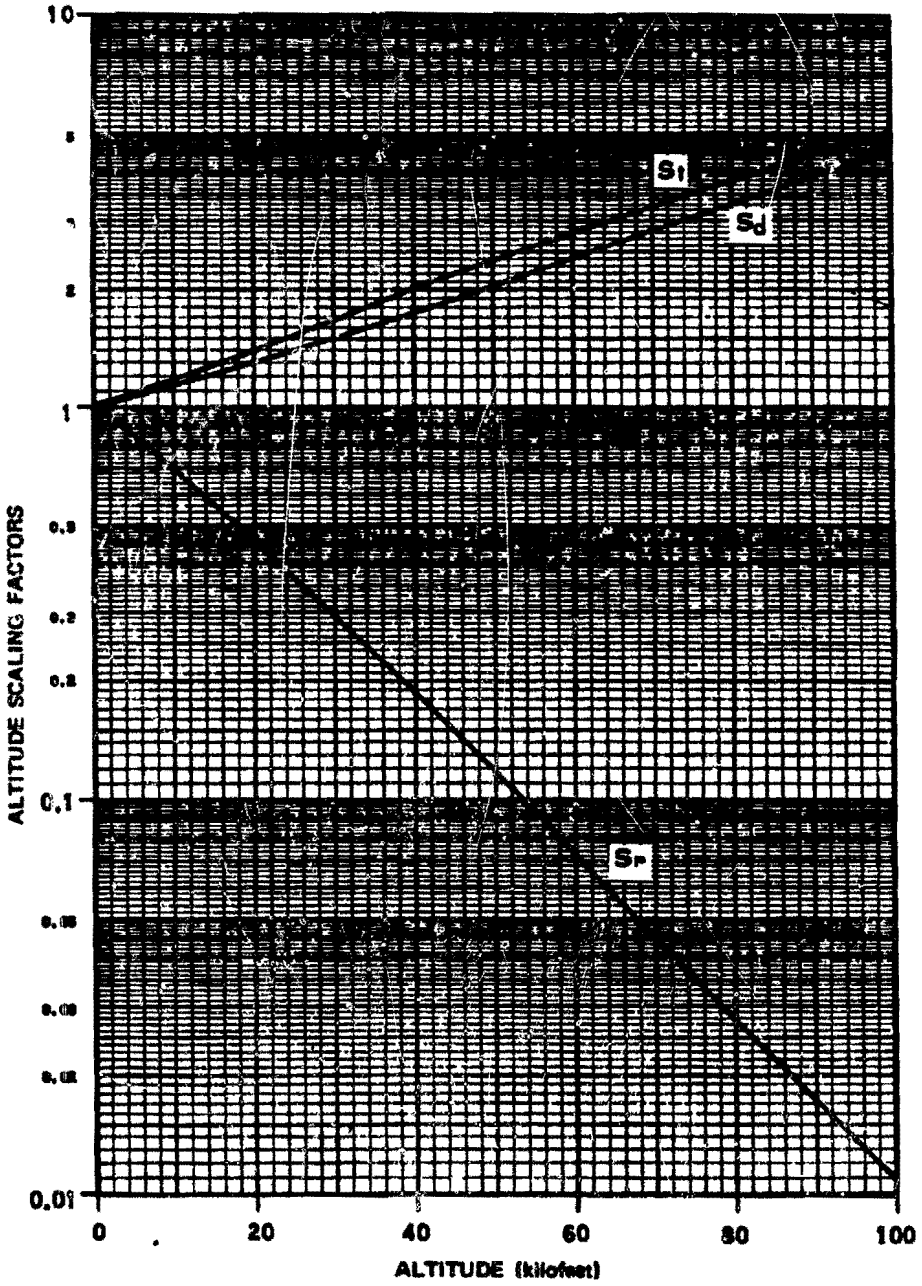

Figure 2-11. [redacted] Altitude Scaling Factors for Blast Wave Calculations [redacted]

[redacted]

Problem 2-6. Calculation of Free Air Blast Parameters at Altitudes up to 40,000 Feet

[redacted] The scaling factors presented in paragraph 2-14 may be used to scale the data from the curves for free air explosions in a sea level atmosphere presented in Figures 2-2 through 2-7 to higher altitudes. As mentioned in the last paragraph of 2-14, the scaling factors for the point of interest (target) are the factors to be used in making altitude corrections rather than the scaling factors for the burst altitude. These scaling factors apply to explosions or targets at altitudes up to 40,000 feet. The effective blast yield is reduced for explosions above about 40,000 feet, and, while the altitude scaling factors still may be applied, the reduced yield must be used in the scaling, as described in paragraph 2-42.

[redacted] *Example* [redacted]

Given: A 100 kt explosion at an altitude of 20,000 feet.

Find: The maximum altitude of a target directly below the explosion such that the target will not experience a peak overpressure exceeding 7 psi, and the peak dynamic pressure that the target might be expected to receive.

Solution: Since the target altitude is unknown, and since the altitude scaling factors should be applied for the target altitude, an approximate solution is obtained first by using the low altitude distance scaling law. From Figure 2-2, an overpressure of 7 psi will extend to 1,000 feet for low altitude explosions. From the scaling provided in Problem 2-1, the corresponding distance from a 100 kt explosion is

$$d = d_1 W^{1/3} = (1{,}000)(100)^{1/3} = 4{,}640 \text{ feet.}$$

The approximate target altitude is

$$20{,}000 - 4{,}460 \approx 15{,}400 \text{ feet.}$$

This target altitude will be used to determine the altitude scaling factors. It may prove to be an adequate basis for determining altitude scaling factors; if not, successive approximations must be used. From Table 2-1,

$$S_d = 1.22$$

$$S_p = 0.56.$$

From the pressure scaling equation in paragraph 2-14,

$$\Delta p_o = \frac{\Delta p}{S_p} = \frac{7}{0.56} = 12.5 \text{ psi.}$$

To account for the uncertainty of blast predictions (see Reliability, Problem 2-1), this overpressure is assigned of 12.5 ± 15 percent; i.e., it lies between 10.6 and 14.4 psi. Figure 2-2 shows that the corresponding scaled (1 kt) distance are between 840 and 725 feet. The corresponding distances from a 100 kt explosion are

$$d = d_1 W^{1/3} S_d = (840)(100)^{1/3}(1.22)$$
$$= 4{,}800 \text{ feet,}$$

and

$$d = d_1 W^{1/3} S_d = (725)(100)^{1/3}(1.22)$$
$$= 4{,}100 \text{ feet.}$$

The approximate target altitude is thus between

$$20{,}000 - 4{,}760 = 15{,}200 \text{ feet, and}$$

$$20{,}000 - 4{,}100 = 15{,}900 \text{ feet.}$$

Neither of these altitudes is sufficiently different from 15,400 feet to warrant repeating the calculation with new altitude scaling factors. In order

[redacted]

to insure that the peak overpressure will not exceed 7 psi, the lower altitude (greater distance from the explosion) is taken as the accepted altitude. For an actual distance of 4,800 feet, and a scaled distance of 725 feet (as determined above), the peak dynamic pressure obtained from Figure 2-4 is 4.6 psi. From the pressure scaling equation of paragraph 2-14,

$$q = q_o S_p = (4.6)(0.56) = 2.6 \text{ psi.}$$

The uncertainty in peak dynamic pressure is ±15 percent, therefore, the peak dynamic pressure is expected to fall between 2.2 and 3.0 psi.

Answer: The maximum altitude of a target directly below a 100 kt explosion at 20,000 feet such that the target will not experience an overpressure exceeding 7 psi is 15,200 feet. The peak dynamic pressure incident on the target will be between 2.2 and 3.0 psi, with an expected value of 2.6 psi.

Note: If the altitude at which the target would be assured of receiving at least 7 psi overpressure had been desired, an altitude of 15,900 feet would have been selected as the answer.

2-15 Velocity and Density

For most blast-wave calculations, peak overpressure and peak dynamic pressure provide a satisfactory description of the shock front; but in a few situations a more detailed description is required. An example is the problem of dynamic pressure acting on a moving target. For this problem, the dynamic pressure data presented in paragraph 2-8 and Problem 2-2 cannot be used; instead, the dynamic pressure must be calculated from its defined value,

$$q = \frac{1}{2}\rho_s u^2,$$

where u is peak wind velocity with respect to the target. To calculate this velocity, the peak wind velocity with respect to the ambient air must be evaluated first. This velocity may be calculated from the equation

$$u = \frac{c\Delta p}{\gamma P}\left(1 + \frac{\gamma + 1}{2\gamma} \cdot \frac{\Delta p}{P}\right)^{-1/2},$$

where c is the ambient speed of sound in air, γ is the ratio of the specific heat of air at constant pressure to the specific heat of air at constant volume, and the other quantities have been defined. The value of γ for air at moderate temperatures and pressures is 1.4. Using this value, the peak wind velocity becomes

$$u = \frac{5\Delta p}{7P} \cdot \frac{c}{\sqrt{1 + 6\Delta p/7P}}.$$

The value of the density, ρ_s, of the air behind the shock front is related to the ambient density, ρ, by

$$\frac{\rho_s}{\rho} = \frac{2\gamma P + (\gamma + 1)\Delta p}{2\gamma P + (\gamma - 1)\Delta p},$$

which becomes

$$\frac{\rho_s}{\rho} = \frac{7 + 6\Delta p/P}{7 + \Delta p/P}$$

for $\gamma = 1.4$. A third equation of interest is that for the shock velocity, U, which is

$$U = c\left(1 + \frac{\gamma + 1}{2\gamma} \cdot \frac{\Delta p}{P}\right)^{1/2},$$

which becomes

$$U = c\left(1 + \frac{6\Delta p}{7P}\right)^{1/2}$$

for $\gamma = 1.4$. These are three of the Rankine-Hugoniot equations, which are described in more detail in Appendix A.

A consistent set of units must be used in the equations presented above; however, since the pressures always appear as a ratio, if consistent units are used for the specific heats to obtain γ, as was done in obtaining a value of 1.4 for moderate temperatures and pressures, the only precaution necessary is to express Δp and P in the same units. Then u and U will be in the same units as c, and ρ_s will be in the same units as ρ. Appendix B provides conversion factors for the various units. As mentioned previously, these equations and others are discussed in more detail in Appendix A. For convenience, a normalized set of values of these shock front parameters is shown in Figure 2-12. Since all quantities are normalized with respect to local (ambient) atmospheric conditions in Figure 2-12, neither yield nor altitude scaling is necessary. The constants to which the values of the various parameters are normalized may be obtained from Tables 2-1 or 2-2.

It is frequently convenient to relate the peak dynamic pressure and the reflected overpressure to the incident overpressure. Figure 2-13 shows such a relationship. The data in Figure 2-13 may be obtained from other figures and

[redacted]

[redacted]

scaling relations in this chapter; however, this figure presents one convenient relation between peak overpressure and both peak dynamic pressure and reflected overpressure. The reflected overpressure curve in Figure 2-13 is for a normally incident blast wave, i.e., the reflecting surface is facing the direction of propagation of the incident blast wave. The curve is convenient for obtaining estimates of the peak reflected overpressures for systems subjected to a normally incident free air blast wave. Reflected pressures are discussed in more detail in paragraph 2-17. The reflected and dynamic pressures may be read directly from Figure 2-10 for any specific overpressure at sea level. For intermediate altitudes (up to 40,000 feet), the pressures must be scaled as described in paragraph 2-14 and illustrated in Problem 2-8.

[redacted]

[redacted]

Problem 2-7. Calculation of the Peak Density Behind the Shock Front for an Intermediate Altitude Free Air Explosion

[redacted] Figure 2-12 shows normalized values of the shock front velocity, peak particle (wind) velocity, and peak density for a shock wave in free air as a function of the shock strength. The shock and particle velocities are normalized to the local (ambient) speed of sound, which may be obtained directly from Tables 2-1 or 2-2 as a function of altitude. The peak density behind the shock front is normalized to the local air density, which also may be obtained from Tables 2-1 or 2-2 as a function of altitude by methods illustrated in the example below.

[redacted] *Scaling.* Since all quantities in Figure 2-12 are normalized, no scaling is required; however, for intermediate altitude bursts, the shock strength at a specified distance must be determined by the blast scaling factor described in paragraph 2-14, as illustrated in the example.

[redacted] *Example*

Given: A 10 kt explosion at 30,000 feet.

Find: The air density just behind the shock front 1,000 feet away and at the same altitude.

Solution: In order to find the shock strength, the peak overpressure must be determined. From Table 2-1, the altitude scaling factor for distance at 30,000 feet is

$$S_d = 1.5 .$$

The scaled (1 kt) distance at sea level corresponding to 1,000 feet from a 10 kt explosion at 30,000 feet is

$$d_1 = \frac{d}{S_d W^{1/3}} = \frac{1{,}000}{(1.5)(10)^{1/3}} = 310 \text{ feet.}$$

From Figure 2-2, the corresponding peak overpressure is

$$\Delta p = 84 \text{ psi.}$$

The reliability statement of Problem 2-1 suggests a ±15 percent tolerance for this overpressure. Therefore the shock strength is

$$\frac{\Delta p}{P} + 1 = \frac{84 + 14.7 \pm 12.6}{14.7} = 6.7 \pm 0.9 .$$

Since shock strengths are equal at equal scaled distance, this is the shock strength of interest. Figure 2-12 shows that the density ratios corresponding to shock strengths of 5.8 and 7.6 are

$$\rho_s/\rho = 3.1, \text{ and}$$

$$\rho_s/\rho = 3.5, \text{ respectively.}$$

From Table 2-1, the air density relative to sea level is

$$\rho/\rho_0 = 0.375.$$

Since $\rho_0 = 2.38 \times 10^{-3}$ slugs per cubic foot for the standard atmosphere (footnote, Table 2-1),

$$\rho = 0.375\ \rho_0 = 8.92 \times 10^{-4} \text{ slugs/ft}^3 .$$

Answer: The air density just behind the shock front is expected to lie between

$$\rho_s = 3.1 \times 8.92 \times 10^{-4}$$
$$\approx 2.8 \times 10^{-3} \text{ slugs/ft}^3$$

and

$$\rho_s = 3.5 \times 8.92 \times 10^{-4}$$
$$= 3.1 \times 10^{-3} \text{ slugs/ft}^3 .$$

[redacted] *Reliability*

[redacted] The curves in Figure 2-12 were calculated from the equations and the equation-of-

[redacted]

state data in Appendix A. At sea level, these curves are believed to be accurate within a few percent. The high degree of accuracy of these data results from the use of pressure rather than range as the independent variable; uncertainty in the pressure-distance curve does not affect the accuracy of these curves directly.

Altitude scaling of shock front and particle velocities is, for the range of shock strengths shown in Figure 2-12, accurate within a few percent even at altitudes as high as 300,000 feet. Density scaling is accurate within 1 or 2 percent for shock strengths below about 60; at higher shock strengths, the accuracy depends on both shock strength and altitude. At 100,000 feet, the scaling error is about 2 percent of the calculated value for shock strengths below 100, below 10 percent for shock strengths below 500, and below 20 percent for shock strengths below 900. At 200,000 feet, the error is about 2 percent for shock strengths below 60, below 10 percent for shock strengths below 80, below 20 percent for shock strengths below 130, and rises to almost 50 percent for a shock strength of 900. Whenever these errors are large, they are in such a direction that actual density is higher than calculated density.

Related Material: See paragraphs 2-14 and 2-15. See also Problems 2-1 through 2-6, and Appendix A.

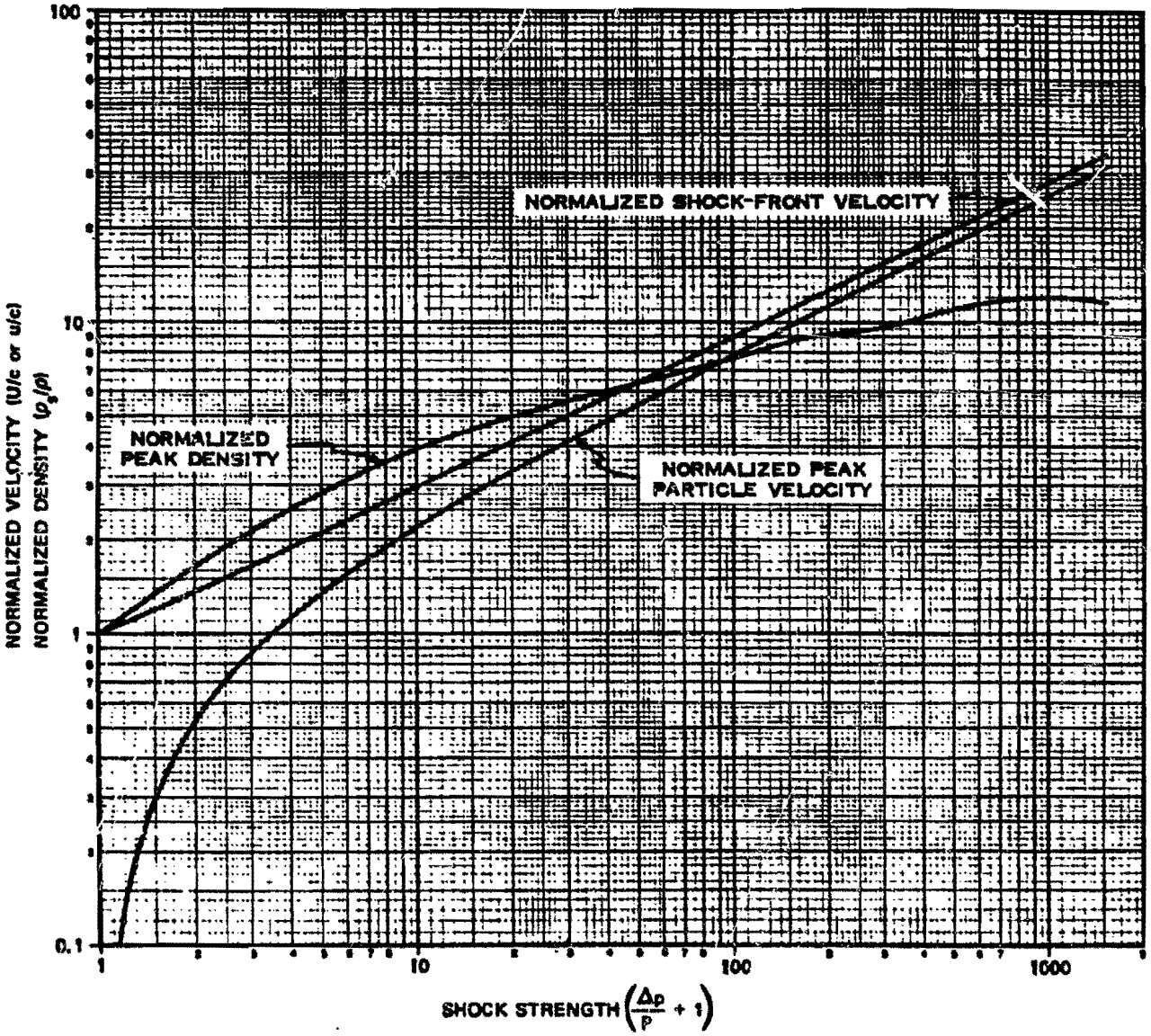

Figure 2-12. [redacted] Shock Front Velocity, Peak Particle Velocity and Peak Density for a Shock Wave in Air [redacted]

[redacted]

Problem 2-8. Calculation of Peak Dynamic Pressure for a Specified Overpressure

[redacted] Figure 2-13 shows the peak reflected overpressure at normal incidence and the peak dynamic pressure as a function of peak overpressure for explosions in a standard sea level atmosphere.

[redacted] *Scaling.* For intermediate altitude bursts (up to 40,000 feet), overpressure and dynamic pressure are scaled by the factors given in paragraph 2-14, i.e.

$$\Delta p = \Delta p_o S_p,$$

$$q = q_o S_p.$$

[redacted] *Example* [redacted]

Given: An explosion at 50,000 feet altitude.

Find: The peak dynamic pressure at a point coaltitude with the burst where the peak overpressure is 50 psi.

Solution: From Table 2-1, the pressure scaling factor is

$$S_p = 0.115.$$

The corresponding sea level overpressure is

$$\Delta p_o = \frac{\Delta p}{S_p} = \frac{50}{0.115} = 435 \text{ psi}.$$

From Figure 2-13, the peak dynamic pressure corresponding to a peak overpressure of 435 psi is 1,000 psi.

Answer: The corresponding peak dynamic pressure at 50,000 feet is

$$q = q_o S_p = (1{,}000)(0.115) = 115 \text{ psi}.$$

[redacted] *Reliability* [redacted]

The error in scaled values of dynamic pressure obtained from Figure 2-13 varies in almost exactly the same manner as the error in scaled density described in Problem 2-7.

[redacted] The curve in Figure 2-13 for peak reflected overpressure may be scaled accurately over the approximate range of altitudes and over about half the range of shock strengths for which dynamic pressure scaling is accurate.

[redacted] *Related Material:* See paragraphs 2-14 and 2-15. See also Problems 2-1 and 2-2 and Appendix A.

[redacted]

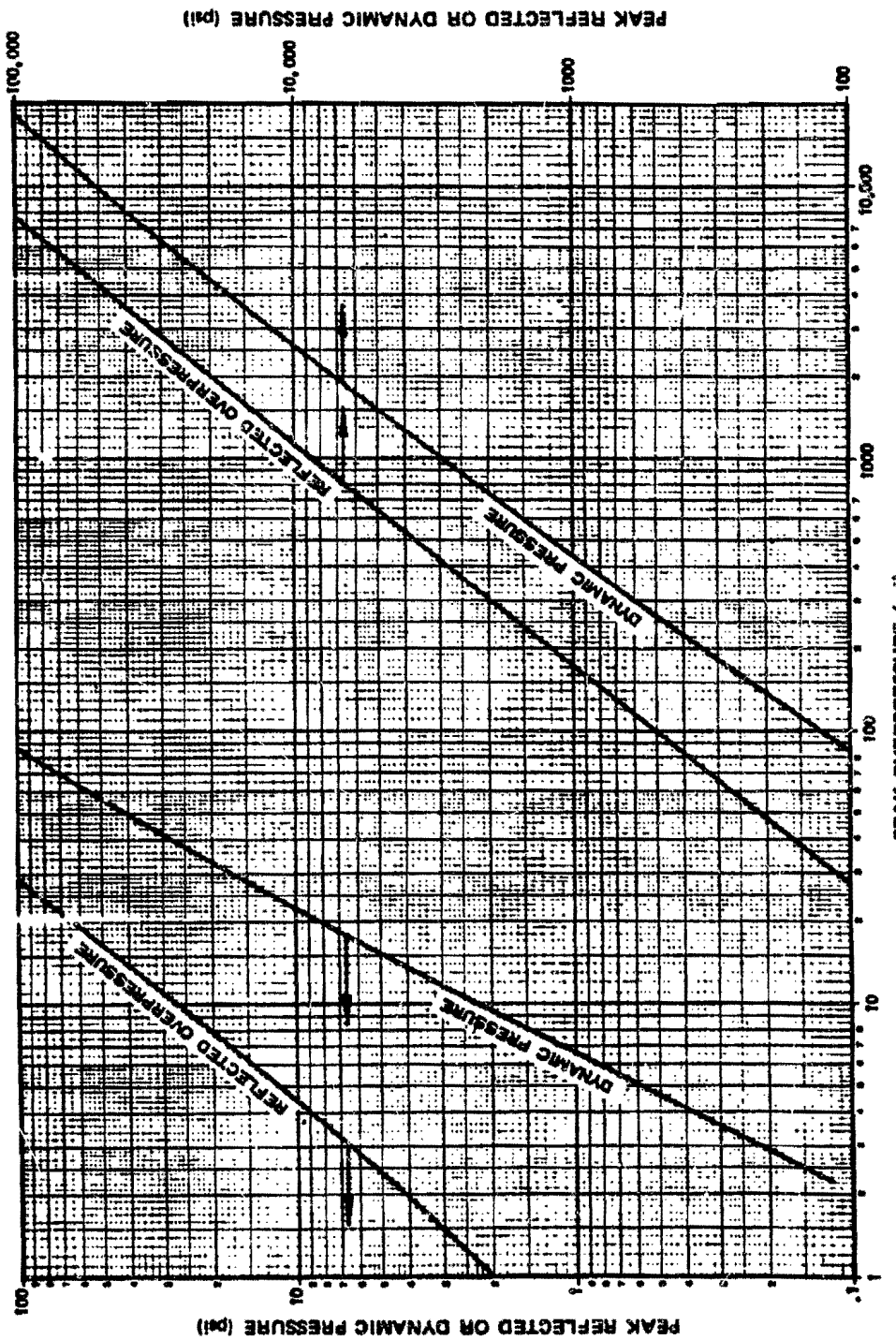

Figure 2-13. [redacted] Peak Reflected Overpressure at Normal Incidence and Peak Dynamic Pressure as Functions of Peak Overpressure in a Standard Sea Level Atmosphere

2-16 Meteorological Phenomena

Nonuniformities in the atmosphere can produce mild focusing and dispersing effects that strengthen some portions of the blast wave and weaken others. Although these effects frequently occur near the surface, they are possible at any altitude and they may affect the blast wave in free air.

The manner in which these meteorological phenomena modify the blast wave may be illustrated by considering a layer of warm air, centered at burst altitude, as shown in Figure 2-14. Since the shock front velocity is greater in the warmer air, the shock front deviates from a perfect sphere. The modified shape causes the portion of the shock front that propagates through the warmer air to diverge and become weaker than the shock front as a whole.

At high shock strengths, the velocity of the shock front is much greater than sonic velocity, and it is a strong function of shock strength. This property tends to maintain a spherical shock front in spite of perturbations such as shown in Figure 2-14. Weakening the shock front reduces its speed, and the advance of the bulge becomes slower relative to the remainder of the shock front. This limits the distortion of the sphere and the divergence and weakening of the shock wave within the heated layer.

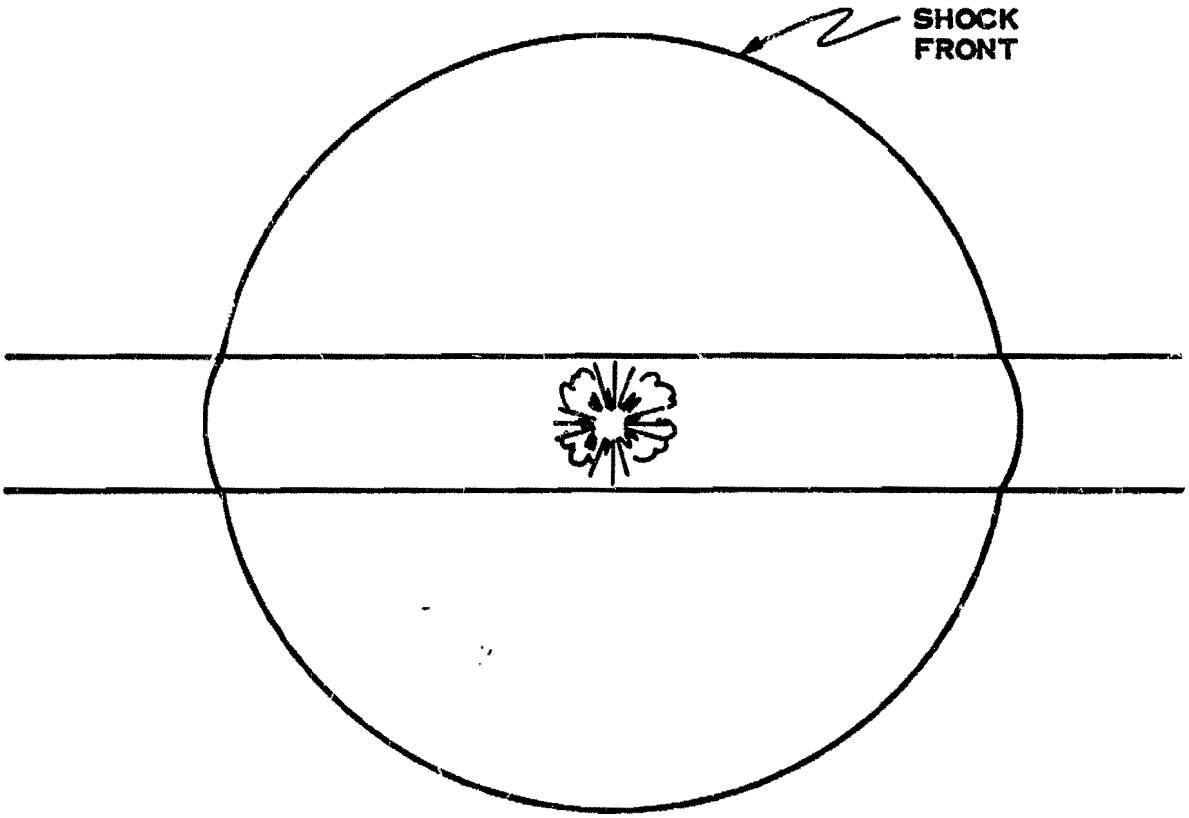

Figure 2-14. Distortion of Blast Wave by a Stratum of Warm Air

At low shock strengths, the reaction is different. The shock front velocity is only slightly greater than sound velocity and it is relatively insensitive to changes in shock strength. Development of a bulge and local weakening of the shock front can proceed much farther before changes in shock strength produce velocity changes that oppose further distortion.

For these reasons, a high overpressure blast wave is relatively insensitive to atmospheric disturbances, but a low pressure blast wave may be strongly affected. The factors that cause the disturbance can be any atmospheric nonuniformities that tend to distort the spherical shape of the shock front. Examples include shear winds and temperature gradients.

Shear winds are winds that change in velocity with changes in altitude. The velocity change may be in direction, in magnitude, or in both. Below 60,000 feet, the normal temperature gradient of the atmosphere produces lower temperatures at higher altitudes. This pattern tends to deflect blast energy upward. A temperature inversion is an increase in temperature with increasing altitude. This occurs normally at high altitudes. Above about 60,000 feet, temperature normally rises gradually with increasing altitude. The relatively sharp inversions that occur when a mass of warm air covers a mass of cold air are of more concern in blast calculations. Such an inversion can act as a mild reflecting surface, and downward deflection of the blast wave is intensified when the burst point is below the inversion.

These atmospheric effects normally produce only small deviations from predicted overpressure except for overpressures that are a small fraction of a psi. Larger deviations normally occur only when the blast wave is exposed to inhomogeneities in the atmosphere over an extended path. For example, when the burst and the target are at low altitudes and over 10 miles apart, observed overpressures have exceeded ten times the predicted values. Such strong focusing effects are possible only when sound travels faster aloft than it does on the ground. Incidents of this type have often been associated with the high winds in the jet stream; in these instances, abnormally high overpressures are observed only in the general direction of the wind motion. Prediction of the magnitude of the deviations that inhomogeneities in the atmosphere introduce into the values of the blast wave parameters is complex, and presentation of numerical methods to estimate the magnitude of these effects is beyond the scope of this manual.

BLAST-WAVE PHENOMENA AT THE SURFACE

When an air blast wave strikes a denser medium such as the earth's surface, it is reflected. If the surface is hard and flat, and if the incident blast wave has a very low peak overpressure, reflection follows simple laws, much like the reflection of light. If overpressures are moderate or high, or if the surface acts as a nonideal reflector, interactions between the blast wave and the surface can be complex. Study of the blast wave at the surface is largely concerned with these complex aspects of surface interactions.

2-17 Reflection at Normal Incidence

The peak reflected overpressure, Δp_r, produced by a normally incident* blast wave

*Although the various ways of describing the angle at which a blast wave strikes a surface are quite specific, they are not all consistent. A blast wave that strikes a surface head-on is said to be *normally incident*, because the direction of propagation makes an angle of 90° with the surface plane. However, the *angle of incidence* is defined as the angle between the shock front and the reflecting surface; its value is 0° for a head-on interaction. Reflection of a blast wave propagating along the surface as it strikes a rising slope is described in terms of slope angle, and slope angle is large for a steep slope. The head-on interaction that could occur at the face of a cliff occurs at a *slope angle* of 90°.

depends on the peak overpressure, Δp, and the peak dynamic pressure, q, of the incident blast wave. An approximate equation for peak reflected overpressure (valid for shock strengths up to 6 or 7, i.e., or overpressures of about 75 to 90 at sea level) is

$$\Delta p_r = 2\Delta p + (\gamma + 1)\, q,$$

where Δp_r is the peak reflected overpressure, and the other quantities have been defined. If γ is taken to be 1.4 (see paragraph 2-15),

$$\Delta p_r = 2\Delta p + 2.4\ q.$$

Using the defined value of q,

$$q = \frac{1}{2}\rho_s u^2,$$

and the Rankine-Hugoniot equations introduced in paragraph 2-15 leads to the relation

$$q = \frac{\Delta p^2}{2\gamma P + (\gamma + 1)\,\Delta p},$$

and, if $\gamma = 1.4$, this becomes

$$q = \frac{5}{2} \cdot \frac{\Delta p^2}{7P + \Delta p}.$$

Inserting this value of q into the equation for the reflected overpressure gives

$$\Delta p_r = 2\Delta p \left(\frac{1 + 4\Delta p/P}{1 + \Delta p/P}\right)$$

This equation shows that, in the limiting case of low overpressures (at overpressures sufficiently low that dynamic pressure is negligible), the peak reflected overpressure is simply twice the peak overpressure of the reflected wave. This relation is a general one that is valid for any angle of incidence. It is valid because at low overpressures the reflected shock wave has the same strength as the incident shock wave, and the peak reflected overpressure is the sum of the overpressures of the incident and reflected waves.

As Δp becomes very large the equation given above indicates that the peak reflected overpressure rises to eight times the incident

* No derivation of this expression for q will be provided, but one numerical example will be shown below to establish its validity. The values for ρ_s and u shown in paragraph 2-15 for $\gamma = 1.4$ are

$$\rho_s = \rho\left(\frac{7P + 6\Delta p}{7P + \Delta p}\right)$$

$$u = \frac{5\Delta p}{7P} \cdot \frac{c}{\sqrt{\frac{7P + 6\Delta p}{7P}}}$$

$$u^2 = \frac{25\Delta p^2}{7P} \cdot \frac{c^2}{7P + 6\Delta p}$$

$$q = \frac{1}{2}\left[\rho\left(\frac{7P + 6\Delta p}{7P + \Delta p}\right)\right]\left[\frac{25\Delta p^2}{7P} \cdot \frac{c^2}{7P + 6\Delta p}\right]$$

Rearranging terms in this expression leads to

$$q = \left[\frac{5}{2} \cdot \frac{\Delta p^2}{7P + \Delta p}\right]\left[\frac{5}{7} \cdot \frac{\rho c^2}{P}\right].$$

It will be noted that the first term in brackets corresponds to the expression previously given for q. It should also be noted that the second term in brackets is dimensionless since both the numerator and denominator are in units of force per unit area. The sea level values of the parameters in the second term are

$$\rho = 2.38 \times 10^{-3}\ \text{slugs/ft}^3$$

$$c = 1{,}116\ \text{ft/sec}$$

$$P = 2{,}117\ \text{pounds/ft}^2$$

Inserting these values into the second term gives

$$\left(\frac{5}{7}\right)\frac{(2.38 \times 10^{-3})(1{,}116)^2}{2{,}117} = 1.$$

overpressure. However, this equation fails at these high overpressures. It is based on the assumption that γ has a constant value, but γ drops to values below 1.4 in strongly shocked air. More accurate calculations for the high shock strengths show higher reflected overpressures than this equation predicts.

Users of this manual will not use the equation for reflected overpressure very frequently; they will use it principally as an aid in understanding the reflection process. The numerical results that ordinarily are needed already have been calculated and have been incorporated in the various figures in this chapter.

2-18 Regular and Mach Reflection

The interaction between a blast wave and the surface of the earth is shown schematically in Figure 2-15. The reflected wave near the surface travels through a region that is heated and made denser than the ambient atmosphere by the incident shock front as it passes. Since shock front velocity is greater in heated air, a portion of the reflected shock can, under appropriate conditions, overtake and merge with the incident shock. This forms a single shock front, called the Mach stem, which produces higher peak overpressures and peak dynamic pressures at or near the surface than would be produced at the same distance in free air. The characteristics of the blast wave at or near the surface depend on yield, height of burst, and properties of the reflecting surface. The region where the incident and reflected shocks have not merged to form a Mach stem is referred to as the region of regular reflection; the region where they have merged is referred to as the region of Mach reflection. As the Mach stem travels along the surface, the triple point (the point of intersection of the incident wave, the reflected wave, and the Mach stem) rises.

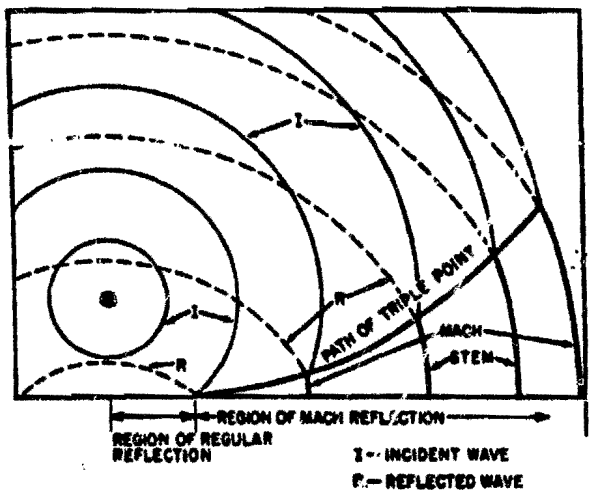

Figure 2-15. Growth of the Mach Stem (Idealized)

2-19 Blast Phenomena for Bursts in the Transition Zone

When the height of a burst is less than about $160W^{1/3}$ feet, additional phenomena affect the blast wave. If the burst is very close to the surface, within about $5W^{0.3}$ feet, fusion of the incident and reflected waves is complete, and the blast wave has a single, approximately hemispherical shock front. A burst this close to the surface is called a contact surface burst. The single shock front of a contact surface burst may be considered a special case of Mach stem formation in which the stem extends over the entire shock front.

If a warhead is detonated above $5W^{0.3}$ feet but below about $160W^{1/3}$ feet, the portion of the reflected shock front that passes through the central region of the fireball moves fast enough to overtake the incident wave and fuse with it. The blast wave thus forms a single shock front above the fireball, a double shock front between this area of fusion and the triple point (or the ground if the Mach stem is absent), and a single shock front below the triple point. The strength of the fused wave above the fireball

varies with burst height. Unless the burst is considerably closer to the surface than $160W^{1/3}$, the reflected wave only makes a weak contribution to this portion of the blast wave. One reason for this weak contribution is that the reflected shock front is strongly attenuated by spherical divergence (produced by the lens-like action of the fireball). Another factor may be the attenuation resulting from the dissipation of energy when the shock front passes through heated air. The region between about $5W^{0.3}$ feet and $160W^{1/3}$ feet is called the transition zone, and a burst within this region is a surface burst for purposes of air blast phenomena.

If a burst is above the transition zone, fusion of the incident and reflected shock fronts is confined to the Mach stem region, and the burst is called an air burst. An air burst that only produces weak reflection effects at the surface is called a free air burst. The properties of such explosions were discussed in paragraphs 2-7 through 2-12. A low air burst is sometimes called a near surface burst. As described in Chapter 1, the limits of the scaled heights of burst as well as the scaling laws for defining the various zones are different for the various phenomena. The definitions given above for the heights of a contact surface burst, a surface burst, the transition zone, and a free air burst only apply to air blast phenomena.

2-20 Near-Ideal and Nonideal Surface Conditions

An ideal surface is defined as a perfectly flat surface that reflects all of the energy, both thermal and blast, that strikes it. No part of the surface of the earth is ideal in this sense, but a few surfaces act essentially as ideal. These surfaces are classified as near-ideal. A near-ideal surface is one that provides blast wave phenomena that are essentially free of the mechanical and thermal effects that are described in succeeding paragraphs. Some of the surfaces considered most nearly ideal are reasonably flat and consist of ice, hard-packed snow, frozen tundra, and water.

The phenomena that are characteristic of a mechanically nonideal surface are illustrated best by examples. When a blast wave that is traveling along a flat plain suddenly encounters a rising slope, a stronger overpressure impulse is produced than if the surface had remained flat. Buildings can decrease overpressure in certain areas by providing shielding from the blast; they also can increase overpressure in other areas by reflecting the blast wave. A very thick layer of snow will absorb a large amount of the blast energy that strikes it, which will produce a lower reflected overpressure than a near-ideal reflecting surface.

In most cases, blast wave calculations over mechanically nonideal surfaces are performed by first finding the desired blast parameters over a near-ideal surface. The results thus obtained then are corrected to account for the changes in blast wave properties produced by the mechanically nonideal features of the surface.

The phenomena produced by a thermally nonideal surface can distort overpressure and dynamic pressure waveforms of the blast wave at the surface. Whether or not the distortions are significant depends on height of burst and yield as well as the properties of the surface. Severe thermal effects are accompanied by the formation of a precursor, which alters several blast parameters severely. Precursors are described in the following paragraph.

Thermally nonideal surfaces may be defined loosely as those that absorb heat; thermally near-ideal surfaces reflect thermal energy incident upon them. Radiation from the fireball incident on thermally nonideal surfaces produces a layer of heated air that interacts with the blast wave, and which may form a precursor. This type of surface is sufficiently common that nearly all blast wave data at the surface are pre-

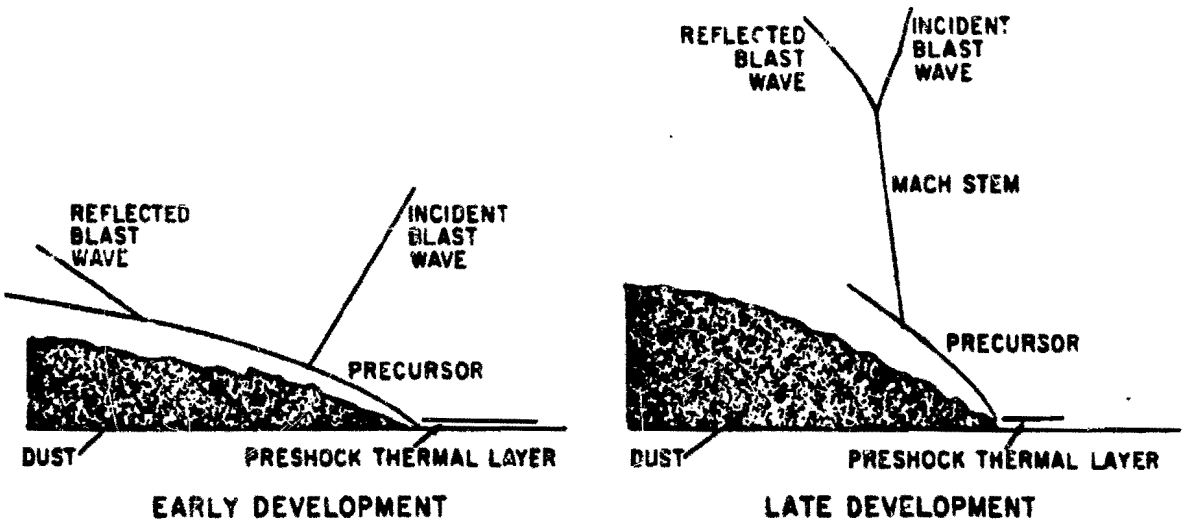

Figure 2-16. Precursor Characteristics

sented as two sets of charts: one set for near-ideal surfaces, and one set for thermally non-ideal surfaces. Methods of classifying surfaces with respect to thermal properties are discussed in paragraph 2-22.

2-21 Precursor Formation

Thermal radiation from the fireball of a surface or near-surface burst can cause the surface of the earth in the vicinity of ground zero to reach a temperature of several thousand degrees in a short time. "Popcorning" may then occur, wherein volatile substances vaporize explosively, throwing hot particles into the air. This (or similar heat transfer processes) produces a layer of heated air just above the surface almost instantly. When the height of burst is less than $650W^{1/3}$ feet, and when the earth is dusty and dark in color, the thermal layer usually is intense enough to disturb the blast wave near the ground surface seriously.

Under ideal conditions, none of the energy in a blast wave can propagate faster than the shock front itself; thus, the shock front forms an envelope within which the blast energy is confined. The thermal layer, however, provides a way for this energy to penetrate the confining surface. The energy in a blast wave propagates faster through hotter air, and the thermal layer allows energy to move ahead of the main shock front, which produces shock wave patterns such as those shown in Figure 2-16. The auxiliary blast wave that moves ahead of the main shock wave is called a precursor.

Although the details of precursor formation are not well understood, its general patterns of pressure and flow have been observed and can be described. After the precursor forms, the main shock front no longer extends to the ground; if it does, the lower portion is so weakened and distorted that it is not easily recognized. Between the ground and the bottom edge of the main shock wave is a gap, probably not sharply defined, through which the energy that feeds the precursor may flow. Wind speed in this gap is higher than the wind speed behind the

main shock front.* Overpressure in the gap is lower than that behind the main shock front, and it is this overpressure difference which produces the higher than ideal wind velocities in the gap.

Ahead of the main shock front, the blast energy in the precursor is free not only to follow the rapidly moving shock front in the thermal layer, but also to propagate upward into the undisturbed air ahead of the main shock front. A near-equilibrium condition exists, because the energy continually fed into the precursor from the main blast wave tends to strengthen the precursor shock front, and the diverging flow pattern within the precursor itself tends to weaken it.

This description of what happens within a precursor explains some of the precursor characteristics shown in Figure 2-16. Only that portion of the precursor shock front remaining in the thermal layer travels faster than the main shock front; the energy diverging upward, out of this layer loses some of its forward speed, and the intersection of the precursor and main shock fronts indicates that the main shock is continually overtaking this upward-traveling energy. Dust, typically billowing to heights of more than 100 feet, shows the upward flow of air in the precursor. At later times, the lower edge of the main shock front is distorted by the action of the precursor.

Overpressure and dynamic pressure waveforms add information to that supplied by blast wave photographs. Typically, the waveform of a fully developed precursor shows a rounded leading edge and a slow rise to its peak amplitude. In severely disturbed waveforms, the pressure jump at the leading edge may be completely absent. These characteristics indicate that the precursor shock front is strongly attenuated and that, at least close to the ground, the precursor does not always have a true shock front of significant amplitude. These results are consistent with the diverging flow pattern described above. Dynamic pressure waveforms often have high frequency oscillations that indicate severe turbulence. The long time durations seen in both overpressure and dynamic pressure waveforms indicate two effects: the early arrival of the initial pressure disturbance, and the sustaining effects of the strong winds developed within the precursor.

Peak amplitudes of the precursor waveforms show that overpressure has a lower peak value and dynamic pressure has a higher peak value than would appear over a surface that did not permit a precursor to form.† The drop in peak overpressure indicates the energy expended in producing the higher than ideal wind velocities. The higher dynamic pressure is partly due to the higher wind speeds, but dust loading, the increase in effective air density resulting from particulate matter carried by the wind, is believed to be a more important factor.

Additional information on precursors, particularly a description of typical precursor overpressure and dynamic pressure waveforms, is given in paragraphs 2-31 and 2-32.

---

* It is tempting to think of the wind in the gap as moving faster than the main shock front. However, two velocities characterize a shock wave: wind velocity and shock front velocity. The velocity of the main shock front is the velocity of propagation of the energy in the main shock. It should be compared not to the wind speed in the gap but to the velocity with which hydrodynamic energy propagates through the gap.

† In an ideal blast wave, this relative variation of peak values would be impossible. Peak overpressure and peak dynamic pressure have a fixed relation to one another, specified by the Rankine-Hugoniot equations (paragraph 2-17 and Appendix A). However, these equations only hold at the shock front. In an ideal blast wave, shock-front amplitudes are also peak amplitudes, but in a precursor the peak values do not occur at the shock front. Thus the relation between them is not limited by these equations.

2-22 Identification of Thermally Near-Ideal and Nonideal Surfaces

To predict blast-wave parameters accurately, the reaction of the surface to thermal radiation from the fireball should be known. Nuclear tests have shown that a few specific types of surface act essentially as thermally ideal surfaces and a few others tend to produce a significant thermal layer. Unfortunately, a theoretical model that quantitatively explains the phenomena of surface reaction and precursor formation has not yet been developed. Without such a model, the response of untested surfaces cannot be predicted with assurance.

Despite this uncertainty, predictions have been made. Surfaces are classified as either thermally near-ideal (unlikely to produce significant precursor effects) or thermally nonideal (expected to produce a precursor for suitable combinations of burst height and ground distance). No other categories are used, i.e., no attempt is made to subdivide surface classifications according to the strength of the precursor that can form.

Examples of surfaces that are considered thermally near-ideal and thermally nonideal are shown in Table 2-3. Items in the table that are confirmed by experiment are marked with an asterisk.

Dark surfaces tend to be thermally nonideal, because they absorb thermal radiation from the fireball. Light (reflecting) surfaces tend to be near-ideal. Asphalt is the strongest precursor-forming surface for which test results are known.

The effect of moisture has not been established definitely. Since any specified amount of absorbed energy can raise the temperature of a dry surface more than the same absorbed energy would raise the temperature of a wet surface, moisture is expected to inhibit the formation of a thermal layer. This should be particularly true when the moisture is in the form of ice. Nuclear tests show that the dry, sandy

Table 2-3. Examples of Thermally Near-Ideal and Thermally Nonideal Surfaces

Thermally Near-Ideal (precursor unlikely)	Thermally Nonideal (precursor may occur for low air bursts)
*Water	*Desert sand
*Ground covered by white smoke layer	*Coral
Heat reflecting concrete	*Asphalt
Frozen tundra	*Surfaces with low, thick vegetation
Ice	*Surfaces covered by a dark smoke layer
Packed snow	Dark colored rock
Moist soil with sparse vegetation	Most agricultural areas; Residential areas in cities
Commercial and industrial areas	Dry soil with sparse vegetation

soil of the Nevada Test Site is thermally nonideal, and that water is a near-ideal surface (however, a blast wave over rough seas may fill the air with spray and produce a dynamic pressure effect similar to the dust loading encountered over desert surfaces). Untested surfaces classed as thermally near-ideal are listed in Table 2-3 in the order of increasing uncertainty.

Sparse vegetation probably should be ignored. Leaves or thick vegetation shield the ground, prevent popcorning, and minimize dust loading, but they also generate a heat-absorbing cloud of dark smoke when they absorb radiation from the fireball. The gases driven from the leaves have high sonic velocities. As a result, they create a thicker, and probably cooler, thermal layer than that formed over desert sand or asphalt. Taller vegetation is expected to produce a thicker thermal layer and a stronger precursor. The REDWING-Inca shot, over a surface covered by low grass and vines dominated by broadleafed shrubs about 10 feet high, produced a precursor, but the characteristic precursor waveforms were apparently suppressed to some extent because higher-than-ideal blast-wave velocities near the surface were eliminated by the vegetation.

Tests at the Nevada Test Site show weakened precursor action over areas covered by dark smoke (the surface was desert sand which forms a strong precursor). Presumably the smoke absorbs enough heat to form a thermal layer, but it shields the ground to prevent popcorning and dust loading of the air.

Variable conditions occur in cities. Commercial and crowded industrial areas are expected to act as thermally near-ideal surfaces. Although these areas contain many surfaces that are favorable to precursor formation (e.g., asphalt-coated roofs), a continuous thermal layer would not be expected. The tendency to form a precursor would be offset by its difficulty in propagating through a heavily built up area. In typical residential areas, where the buildings are neither as close nor as tall as those in commercial areas, the surface is considered thermally nonideal.

The preceding descriptive information does not always provide clear guidelines for classifying surfaces. For example, the rules that might be applied to black, moist soil are conflicting. In such cases, blast-wave properties should be calculated for both near-ideal and thermally nonideal surface conditions in order to bracket the blast effects that can actually be expected.

BLAST-WAVE CALCULATIONS AT THE SURFACE

Height of burst (HOB) curves provide most of the data required to calculate blast-wave properties at the surface. The HOB charts in this subsection each show the distance from ground zero as a function of height of burst for several values of the various air blast parameters that would be expected to occur *along the surface* as a result of a 1 kt explosion.* For instance, any point on a curve for specified overpressure (see for instance Figure 2-17) shows a combination of burst height and ground distance at which a 1 kt explosion will produce that overpressure at the surface of the earth. Alternately, if a 1 kt burst occurs at a location corresponding to some point on a given overpressure curve, a target at the origin will receive that overpressure.

Separate families of curves are provided for near-ideal and thermally nonideal surface

*As described in paragraph 2-13, the heights of burst and distances from ground zero could be expressed in terms of scaled distances, e.g., $kt/W^{1/3}$, with W being the yield in kt. However, since other scaling laws apply to other phenomena, the convention of expressing absolute distances from a 1 kt explosion will be maintained throughout the remainder of this chapter and throughout the manual. When "scaled distances" are employed, e.g., Section I, Chapter 11, the exceptions will be indicated clearly.

conditions. Guidelines for classifying surfaces with respect to thermal properties are provided in paragraph 2-22. The effects of mechanically nonideal surfaces (paragraph 2-20) are discussed in paragraphs 2-37 through 2-41.

Many of the HOB curves show whether a given point on the surface is in the region of regular reflection or the Mach stem region (paragraph 2-18). This information is helpful if the target is some distance above the surface, because it indicates how closely blast-wave data at the surface correspond to blast-wave data at the target. The effect of target height on blast-wave parameters is discussed in paragraph 2-29.

The data for overpressure and dynamic pressure are peak values, regardless of where these peaks occur in the blast waveform. In an undisturbed blast waveform, these peak values occur at the shock front. If a precursor is present, they usually occur later in the waveform. Precursor overpressure and dynamic pressure waveforms are described in paragraphs 2-31 and 2-32.

Whenever ambient atmospheric conditions are different from standard sea level conditions (14.7 psi, 59°F), calculations of blast-wave parameters at the surface are more accurate if the altitude scaling factors described in paragraph 2-14 are applied. These factors may be used even if the departure from standard conditions is not caused by an altitude change.

2-23 Reliability

Blast-wave data at the surface are subject to the uncertainties described in paragraphs 2-1 through 2-6. As mentioned in paragraph 2-5, additional uncertainties arise because the earth is not a perfect reflector. Consequently, the blast wave at the surface is inherently less predictable than the blast wave in free air. Added to this problem is the difficulty of obtaining sufficient experimental data to cover all combinations of conditions. A blast parameter in free air may be represented by a single curve; at the surface, the available data must be scattered to cover a family of curves. Moreover, variable surface conditions require that more than one family be plotted. Consequently, a limited number of nuclear tests cannot document blast-wave data at the surface as completely as in free air. The usual reliability statements are supplemented in this section by showing portions of the curves as dashed lines. The solid lines are based upon experimental data from full-scale nuclear tests; the dashed portions are based upon theory and high-explosive experiments. In some cases, data for the dashed portions of curves are based on the assumption that for certain combinations of ground range and burst height the data for thermally nonideal surfaces should agree with data taken over near-ideal surfaces. In general, the reliability statements apply to the dotted as well as the solid portion of the HOB curves; however, the reliability of the dotted portions is purely an estimate, while the reliability stated for the solid portions is based on experimental data.

Uncertainties in the data presented in the HOB charts usually are expressed in terms of ground distance rather than in terms of blast parameters. This is an important distinction. For example, a ±10 percent uncertainty in ground distance corresponds to an uncertainty in peak overpressure that may be as high as ±30 percent. The curves become nearly horizontal close to ground zero, and a variation in ground distance produces very little change in blast parameters. For these portions of the HOB charts, the uncertainty should be applied to burst height rather than to ground distance. When a precursor forms, the air blast waveforms are distorted severely, and prediction of blast parameters becomes highly uncertain. As mentioned in paragraph 2-2, the scaling of most blast-wave parameters is reasonably dependable in the yield range of 1 kt to 20 Mt; however, scaling becomes questionable for yields over 50 kt at thermally non-

ideal surfaces as a result of the difficulty in predicting the criteria for precursor formation.

The scaling of subkiloton explosions at scaled heights of burst between 150 and 1,000 feet have shown large errors that correspond to discrepancies as high as factors of 2 or 3 in effective yield.

Additional uncertainties appear in the measured data for contact surface bursts as a result of less dependable experimental determination of yield. This is caused in part by the difficulties added to radiochemical yield determination as a result of the large amount of crater material in the cloud and to the uncertainty introduced into yield determination by fireball size that result from uncertainties in the amount of energy absorbed by the earth.

2-24 Peak Overpressure

Figures 2-17 through 2-22 show the peak overpressure at the surface of the earth as a function of height of burst and distance from ground zero from a 1 kt explosion. Figure 2-23 shows peak overpressure as a function of distance from ground zero from a 1 kt contact surface burst. The same data could be obtained in less convenient form along the abscissas of Figures 2-17 through 2-20.

These figures show that the same ground range for a given peak overpressure is produced by a burst either at the surface or some short distance above the surface. At low overpressures, the greatest distance from ground zero occurs for an explosion at some higher distance above the surface. This effect is prominent at overpressures of 15 psi and less, and contours for these overpressures show a pronounced "knee" (the knee is defined as the extreme right projection of a contour line).

Figures 2-17 through 2-20 apply to near-ideal surface conditions; Figures 2-21 and 2-22 apply to thermally nonideal surfaces (suggestions for classifying various types of surfaces are given in paragraph 2-22). Figure 2-23 applies to near-ideal surfaces, but since the 1 kt reference burst detonated in contact with the surface is not expected to form a precursor, the curve also applies approximately to thermally nonideal surfaces.

The shaded areas in Figure 2-20 reflect the uncertainty in the prediction of very low overpressures. The shaded areas in Figures 2-21 and 2-22 correspond to the ground distances at which precursor cleanup occurs. In this phenomenon, the hydrodynamic energy of the blast wave collects behind a single, well-defined shock front, forming a nearly ideal blast wave. As this occurs, the peak overpressure usually rises instead of undergoing the normal amount of attenuation with increasing ground range. Uncertainty in the ground range at which cleanup occurs is reflected in the HOB curves as additional uncertainty in peak overpressure data at this range. This is indicated by shading of the 10 psi contour and a portion of the 15 psi contour.

2-25 Peak Dynamic Pressure

Figures 2-24 through 2-26 show peak dynamic pressure at the surface as a function of scaled height of burst and ground distance from a 1 kt explosion. These curves show conditions after the blast wave has been reflected from the surface; therefore, these charts do not represent the dynamic pressure of the incident wave. At ground zero the wind in the incident blast wave is completely stopped by the ground surface, and all of the incident dynamic pressure is transformed to static overpressure. Therefore, the height of burst curves show that the peak dynamic pressure is zero at ground zero. At other locations, reflection of the incident blast wave produces winds that, at the surface, must

blow parallel to the surface.* The dynamic pressures associated with these winds tend to produce horizontal forces; however, the direction of wind forces on a target surface depend not only on wind direction but also on surface orientation.

The thermal properties of the surface are less significant for prediction of dynamic pressure than for most blast parameters. Dynamic pressure only appears to be strongly enhanced by dust loading (or, in the case of a water surface, spray loading) of the air, whether or not a precursor is formed. The dynamic pressure height of burst curves are therefore classed as ideal, "light dust," and "heavy dust" surface conditions. Light dust conditions usually may be taken to be equivalent to near-ideal surfaces, and heavy dust equivalent to thermally nonideal, but there are exceptions. For example, a surface covered by thick vegetation is expected to produce a precursor but little dust. Conversely, the interaction of a blast wave with very rough seas is expected to produce heavy spray loading but no precursor.

Figure 2-24 shows peak dynamic pressure at an ideal surface in the very high pressure region. It is based almost entirely on theory, and does not include dust loading effects (it should be noted that the 200 psi contour of Figure 2-23 does not agree with that in either Figure 2-25 or 2-26). Figure 2-25 shows peak dynamic pressure for light dust conditions, and Figure 2-26 shows peak dynamic pressure for heavy dust conditions. Since the latter is based on limited data, height of burst curves can be drawn only for scaled burst heights up to 300 feet. As a guide to the way in which the heavy dust curves might be extrapolated, portions of the light dust curves are shown for 1 kt burst heights between 330 feet and 600 feet. These latter curves do not represent heavy dust conditions. They should be used only as a guide to obtain rough estimates.

Figure 2-27 is presented to aid in the explanation of the effects of dust on peak dynamic pressure. The curves are drawn from data from Figures 2-25 and 2-26, and theoretical data for an ideal reflector. At a scaled distance of about 400 feet, the contribution of light dust to dynamic pressure is about twice that of heavy dust. This suggests that the inertia of heavy dust limits its velocity initially and probably also limits the velocity of the air in the blast wave by the drag force it exerts. After these inertial forces are overcome, heavy dust contributes strongly to dynamic pressure. At a scaled range of 900 feet, heavy dust exhibits its maximum effect, but the effect of light dust has diminished considerably. This also suggests an inertial effect acting to sustain the momentum of the air in the blast wave.

The explanation that has been given is only one of several possible explanations of Figure 2-27 and represents an oversimplification. For example, the explanation does not include the varying amount of dust that a given surface adds to the blast wave as a function of range. More detail may be found in DASA 1200 (see bibliography).

A large scatter exists in dynamic pressure data under heavy dust conditions. This is due to the nature and the varying amounts of particulate matter in the air. Fine grains of sand are readily carried by the air stream, flow with it as a part of a continuous fluid, and present a relatively small measurement problem. Larger

*This statement ignores the turbulence that is often associated with dynamic pressure. It is uncertain whether or not vertical components of air velocity contribute to dynamic pressure significantly. Gages used to measure dynamic pressure are usually mounted so as to be sensitive only to the horizontal force produced by dynamic pressure. For this reason curves such as those in Figures 2-24 through 2-26 are often labeled "horizontal component of dynamic pressure." It is desirable to avoid this phrase, because it tends to imply, incorrectly, that the forces produced by dynamic pressure may be resolved into components that can be treated by the ordinary rules of vector algebra.

particles tend to plug gage openings, and their effect is difficult to measure. Large objects picked up by the blast wave and thrown through the air can be very destructive, but they cannot be measured as part of a continuous pressure record. Arbitrarily, dynamic pressure has been defined as representing the effects of only those particles that are small enough to behave essentially as air particles. Dynamic pressure as thus idealized cannot fully account for the destructive effects of blast momentum.

2-26 Time of Arrival

Figures 2-28 through 2-32 show the time of arrival of the blast wave from a 1 kt explosion in a standard, homogeneous, sea level atmosphere as a function of height of burst and distance from ground zero.

2-27 Duration of the Positive Phase of Overpressure and Dynamic Pressure

Figures 2-33 and 2-34 present families of curves that show values of the positive phase overpressure duration (t_p^+) at points along the surface as a function of height of burst and ground distance from a 1 kt explosion in a sea level atmosphere.

Because of limited data, similar curves cannot be drawn for dynamic pressure; however, the data suggest that, as in the case of free air (paragraph 2-10 and Problem 2-4), the ratio of these two durations is a function of pressure level. Duration of dynamic pressure t_q^+ may be estimated by using the curves for positive overpressure duration and the relations shown in Table 2-4. If surface conditions are such that heavy dust (or spray) loading is predicted, the longer times found in Figure 2-34 probably provide a better basis for determining t_q^+ even if the surface is considered thermally near-ideal and Figure 2-33 is used to determine t_p^+.

Table 2-4. Relations Between the Positive Duration of the Overpressure Blast Wave (t_p^+) and the Positive Duration of the Dynamic Pressure (t_q^+) for a 1 kt Explosion

t_p^+ (sec)	t_q^+ (sec)
0.1	0.25
.15	.33
.2	.34
.25	.35
.3	.39
.35	.43
.4	.49

2-28 Overpressure Impulse

Figures 2-35 and 2-36 show the positive overpressure impulse (paragraph 2-11) at the surface as a function of height of burst and ground distance from a 1 kt explosion in a sea level atmosphere.

Formation of a Mach stem changes the shape of the overpressure waveform by increasing the amplitude of the shock front without changing the area under the waveform appreciably. Consequently, the HOB curves for overpressure impulse differ from the HOB curves for peak overpressure in that the impulse curves do not show a characteristic change where they cross the boundary separating the region of regular reflection from the region of Mach reflection. Overpressure impulse at the surface appears to be primarily a function of slant range; it only fluctuates strongly as a function of reflecting angle for low heights of burst.

Dynamic pressure impulse is another important blast-wave parameter, particularly under thermally nonideal conditions. Unfortun-

[redacted]

ately, it is a difficult parameter to measure, and there are not enough dependable data to allow HOB curves to be constructed.

2-29 Mach Stem Heights [redacted]

[redacted] The changes that occur in a blast wave as the incident and reflected waves fuse to form a Mach stem are among the changes associated with reflection from a surface. A target above the triple point, the top of the Mach stem (see paragraph 2-18), receives two shocks that correspond to the arrival of the incident and the reflected waves. A target at or below the triple point receives a single shock. As mentioned in paragraph 2-25, the reflection process transforms part of the incident dynamic pressure into overpressure. Thus, a target below the triple point is subjected to a higher overpressure impulse and a lower dynamic pressure impulse than a target above the triple point. Since a typical airborne target is more sensitive to dynamic pressure than to overpressure, such a target is usually safer below the triple point.

[redacted] The height of the Mach stem heigh affects tall structures on the ground. The nature of the response depends on whether the structure is more sensitive to overpressure or to dynamic pressure. The relative effects of a two shock front waveform and a single, nearly vertical shock wave also depend on the mechanical response properties of the target.

[redacted] Above the triple point, the strength of the first (or incident) shock wave may be found from free air data, and the time interval between the two shocks depends on the height of the target above the triple point. Below the triple point, shock parameters may be approximated best by data from the HOB charts, i.e., from data which, strictly speaking, apply only to targets at the surface. When the scaled height (that corresponding to a 1 kt burst) of the Mach stem is 50 feet or less, blast-wave properties anywhere on the stem are essentially the same as those at the surface. For taller Mach stems, the shock-front becomes curved. This modifies blast-wave properties along the stem. Pressure values decrease and arrival times increase with height above the surface. These variations have not been studied as thoroughly as blast-wave conditions at the surface have been, and data to describe them quantitatively are not presented here.

[redacted] The guidelines presented above must be applied with caution if a precursor is present. The two disturbing influences, dust and the thermal layer, are confined to a layer that is close to the ground. Above the region that is affected by the precursor, the near-ideal HOB curves are a better representation of the blast wave. The height above which the near-ideal curves apply is not known, but it is estimated to be between 50 and 300 feet (physical, not scaled height) under typical conditions.

[redacted] Although there are indications that the height of the Mach stem is affected by thermal effects and by surface hardness, these effects are not large, and the curves may be applied to both near-ideal and thermally nonideal surfaces. Both thermal effects and surface roughness will, however, make the position of the triple point less predictable.

[redacted] Figures 2-37 and 2-38 show the height of the Mach stem as a function of height of burst and ground distance from a 1 kt explosion in a sea level atmosphere.

[redacted]

[redacted]

Problem 2-9. Calculation of Peak Overpressure at the Surface

[redacted] Figures 2-17 through 2-22 show the peak overpressure as a function of height of burst and horizontal distance from ground zero for a 1 kt explosion in a sea level atmosphere. Figures 2-17 through 2-19 provide data for thermally near-ideal surfaces, while Figures 2-20 through 2-22 provide the same data for thermally nonideal surfaces. Figure 2-23 shows the peak overpressure as a function of horizontal distance from a contact surface burst. The data contained in the curves of Figure 2-23 could be obtained from points along the abscissas of Figures 2-17 through 2-19; however, for some applications, Figure 2-23 may be more convenient to use.

[redacted] *Scaling.* For yields other than 1 kt, the ground distance and height of burst for any specific overpressure scale as follows:

$$\frac{d}{d_1} = \frac{h}{h_1} = W^{1/3},$$

where d_1 and h_1 are the distance from ground zero and height of burst, respectively, for 1 kt, and d and h are the corresponding distance and height of burst for a yield of W kt.

[redacted] *Example 1* [redacted]

Given: An 80 kt explosion 2,580 feet above a thermally nonideal surface.

Find: The horizontal distance from ground zero beyond which the peak overpressure will not exceed 3 psi.

Solution: The corresponding height of burst for 1 kt is

$$h_1 = \frac{h}{W^{1/3}} = \frac{2{,}580}{(80)^{1/3}} = 600 \text{ feet.}$$

From Figure 2-22, a peak overpressure of 3 psi extends to a distance of 2,900 feet from a 1 kt explosion at a height of burst of 600 feet.

Answer: The corresponding distance for an 80 kt weapon at 2,500 feet height of burst is

$$d = d_1 W^{1/3} = (2{,}900)(80)^{1/3} = 12{,}500 \text{ feet.}$$

As a result of the ±15 percent uncertainty in this distance (see "Reliability" below), the range beyond which the peak overpressure will not exceed 3 psi is

$$12{,}500 + (0.15)(12{,}500) = 14{,}400 \text{ feet.}$$

[redacted] *Example 2* [redacted]

Given: A 100 kt explosion at a height of 2,320 feet above a near-ideal surface.

Find: The peak overpressure at a distance of 1,860 feet from ground zero.

Solution: The corresponding distance and ground zero and height of burst for a 1 kt weapon are

$$d_1 = \frac{d}{W^{1/3}} = \frac{1{,}860}{(100)^{1/3}} = 400 \text{ feet,}$$

$$h_1 = \frac{h}{W^{1/3}} = \frac{2{,}320}{(100)^{1/3}} = 500 \text{ feet.}$$

Answer: From Figure 2-18, the peak overpressure at a ground distance of 400 feet and a height of burst of 500 feet is 50 psi.

[redacted] *Reliability* [redacted]

Ground distances obtained from Figures 2-18, 2-19, and 2-22 are estimated to be reliable within ±15 percent of the indicated ground range (or HOB for points close to ground

[redacted]

zero – see paragraph 2-23). Figure 2-17 is based on theory, confirmed by only a few data points; it is estimated to be reliable within ±20 percent. Figure 2-20 is reliable within ±15 percent of the indicated ground range, but the 1/2 - 1/4 psi curves are subject to the additional uncertainty indicated by the shaded areas. Figure 2-21 is based on data subject to considerable scatter from thermal effects; it is estimated to be reliable within ±20 percent.

For near-ideal surface conditions, these reliability estimates apply to yields between 1 kt and 20 Mt; for thermally nonideal surface conditions, the estimates apply to yields between 1 kt and 50 kt. Outside this range of yields, these curves may be used with somewhat less confidence.

Related Material: See paragraphs 2-13, 2-14, 2-17 through 2-20, and 2-22 through 2-24. See also Tables 2-1 and 2-2 for surface conditions that differ from standard sea level atmospheric conditions.

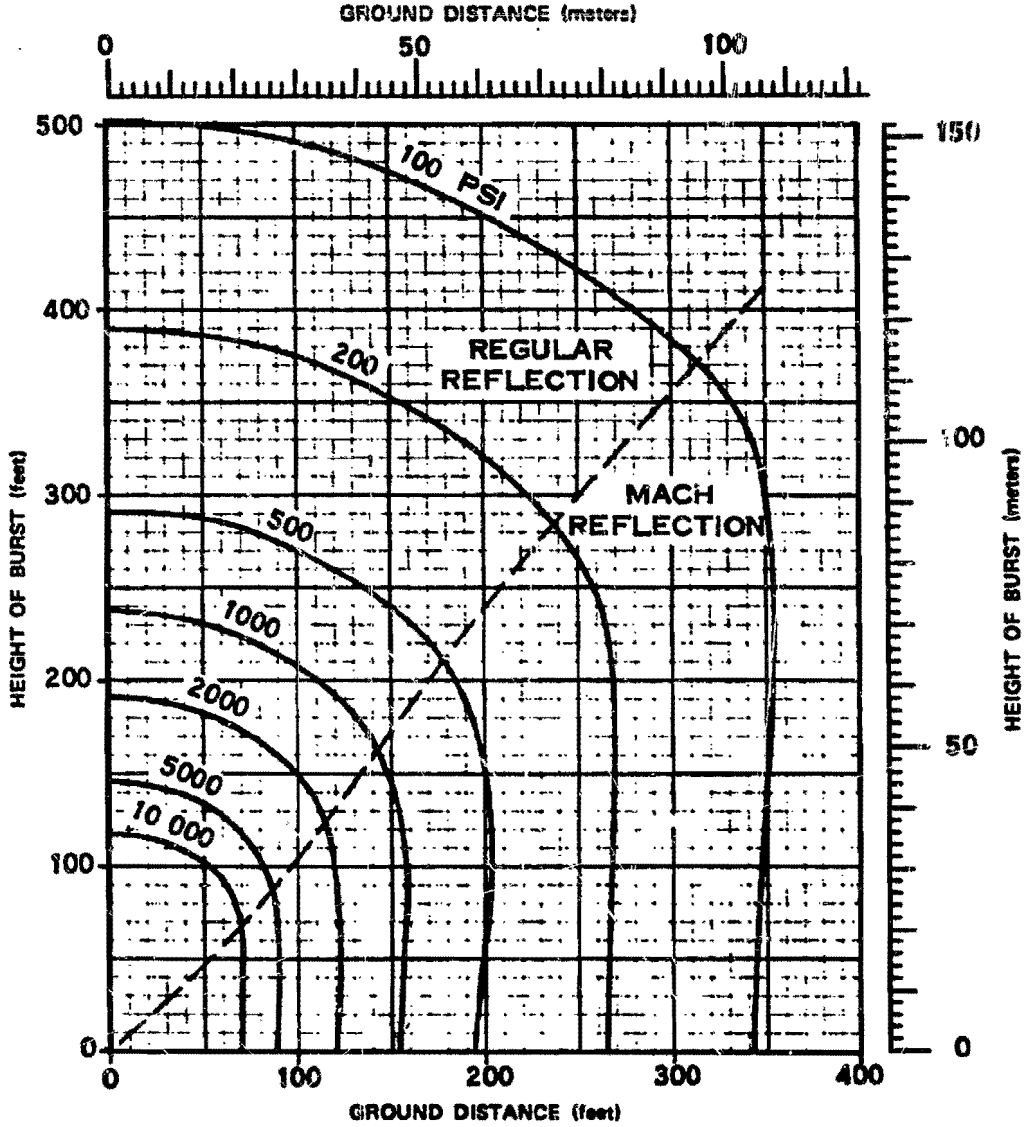

Figure 2-17. [redacted] Peak Overpressures at the Surface for a 1 kt Burst Over a Near-Ideal Surface, Very High Overpressure Region [redacted]

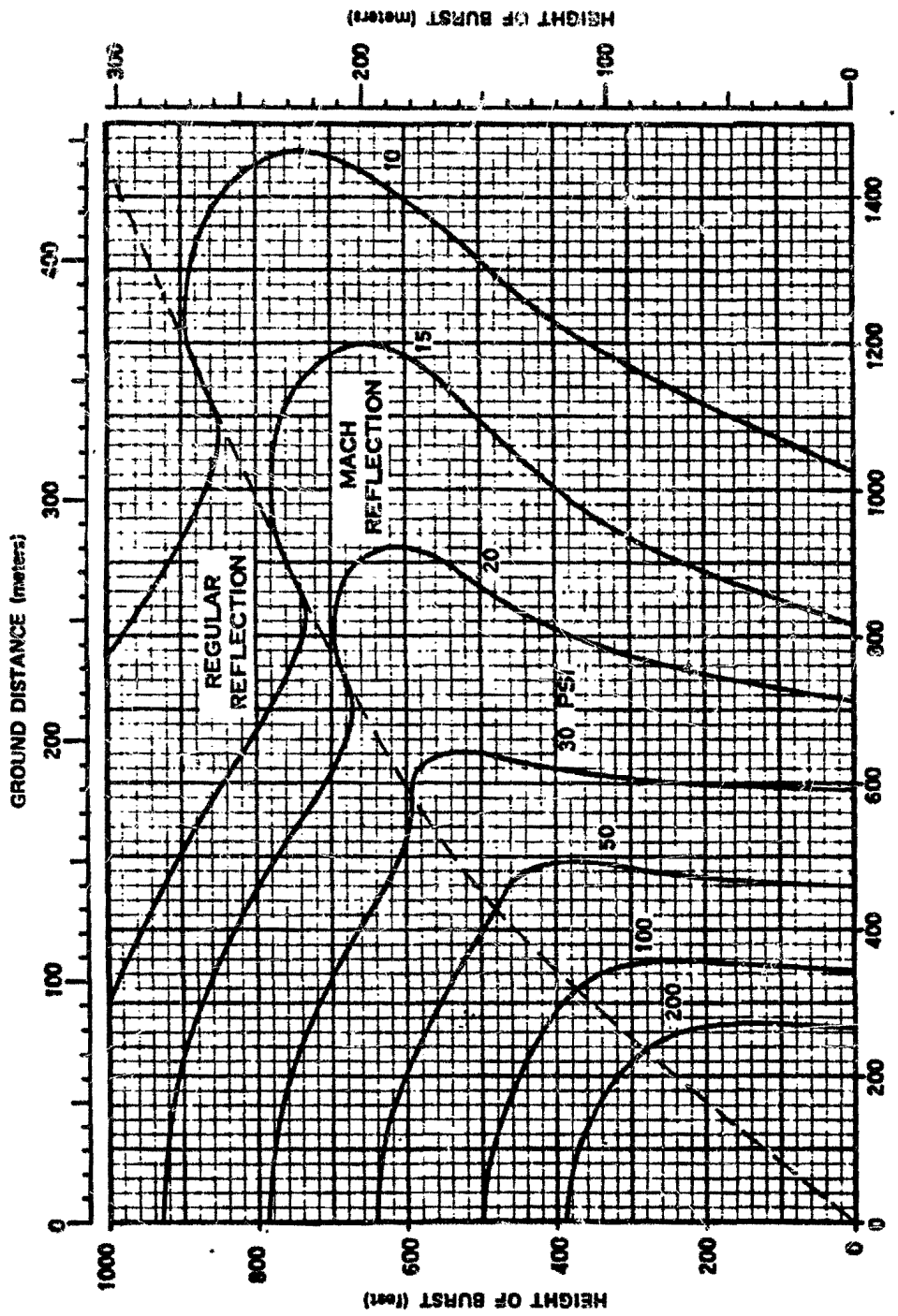

Figure 2-18. [redacted] Peak Overpressures at the Surface for a 1 kt Burst Over a Near-Ideal Surface, High Overpressure Region

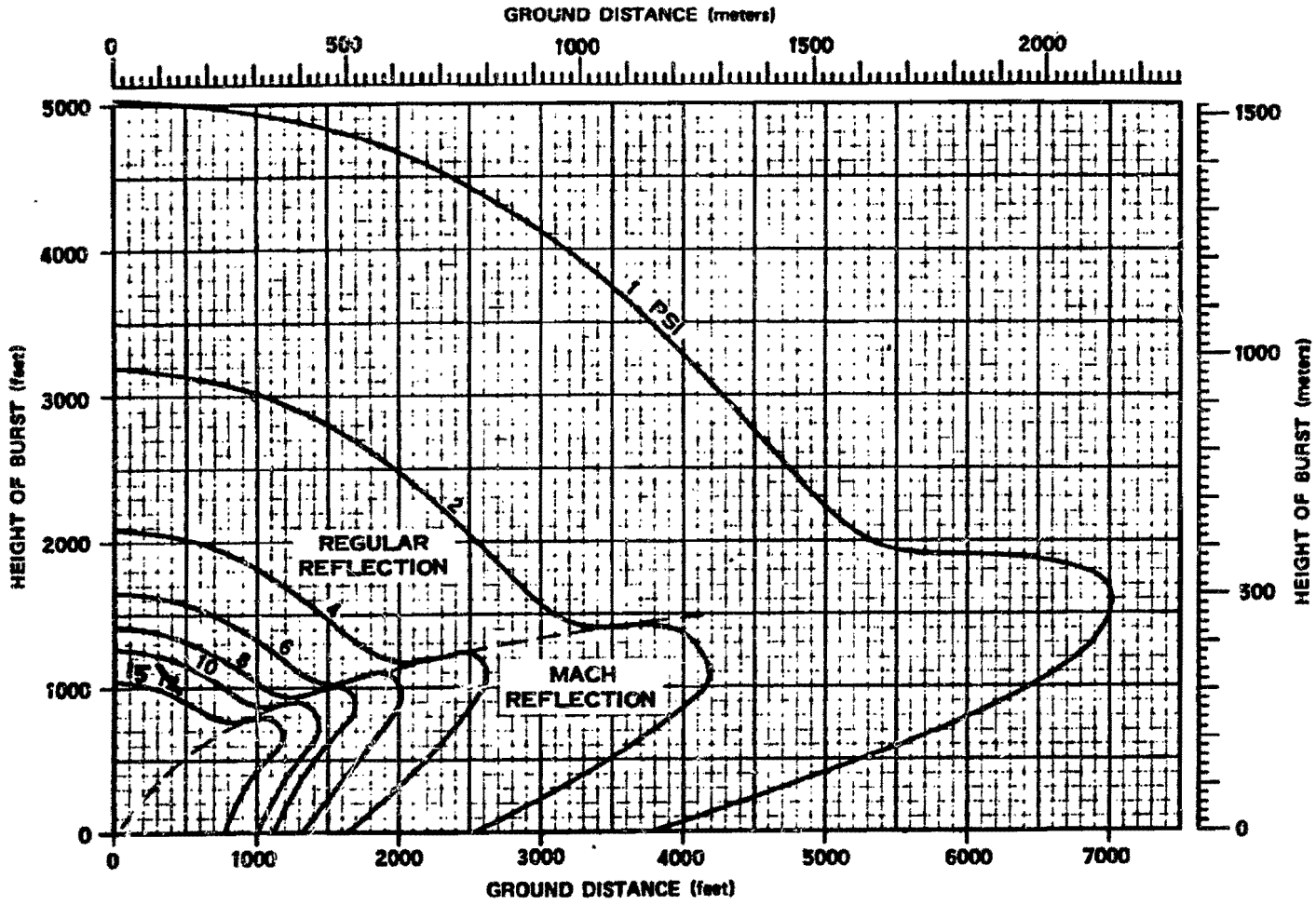

Figure 2-19. [redacted] Peak Overpressures at the Surface for a 1 kt Burst Over a Near-Ideal Surface, Low Overpressure Region [redacted]

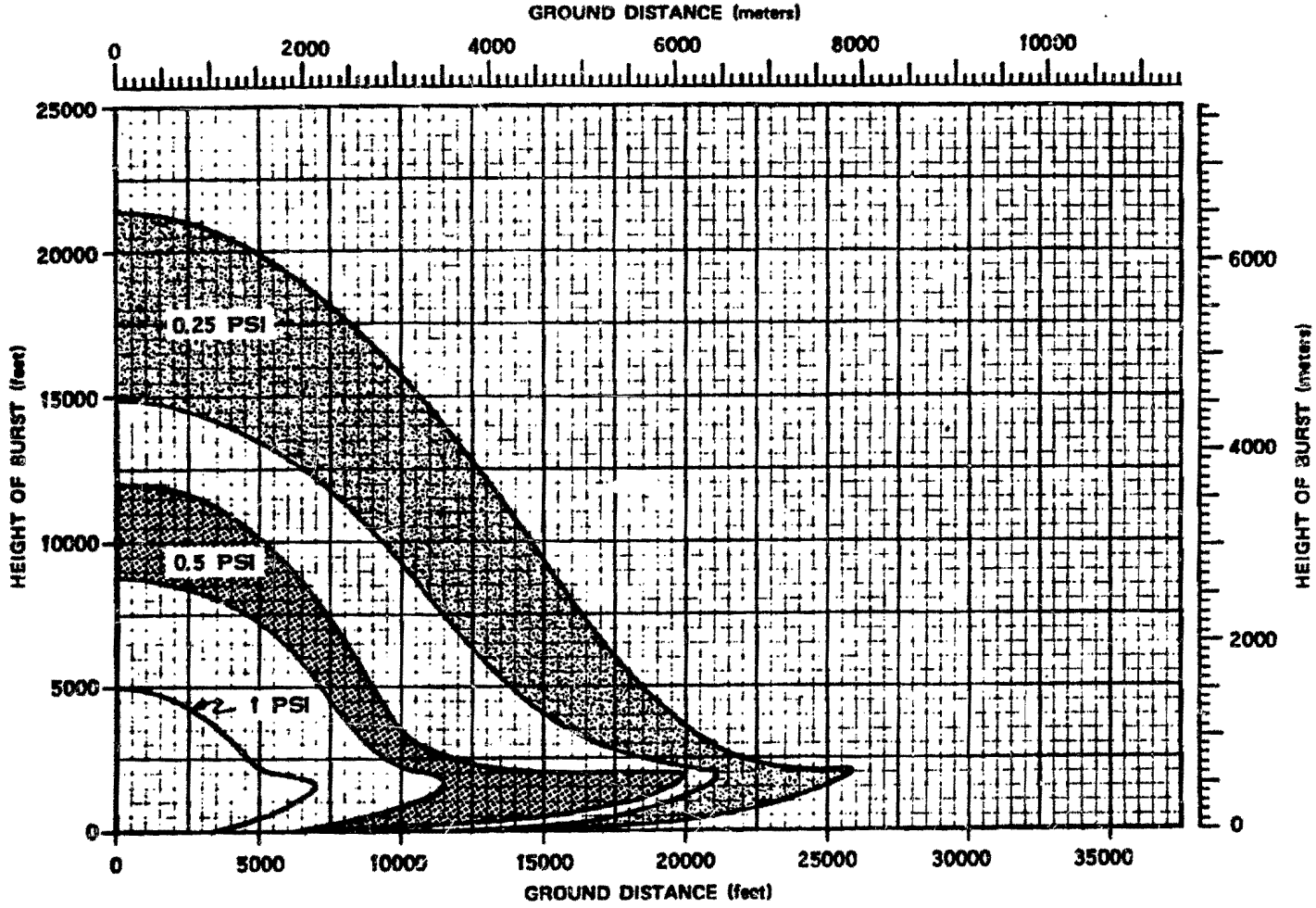

Figure 2-20. [redacted] Peak Overpressures at the Surface for a 1 kt Burst Over a Near-Ideal or Thermally Nonideal Surface, Very Low Overpressure Region [redacted]

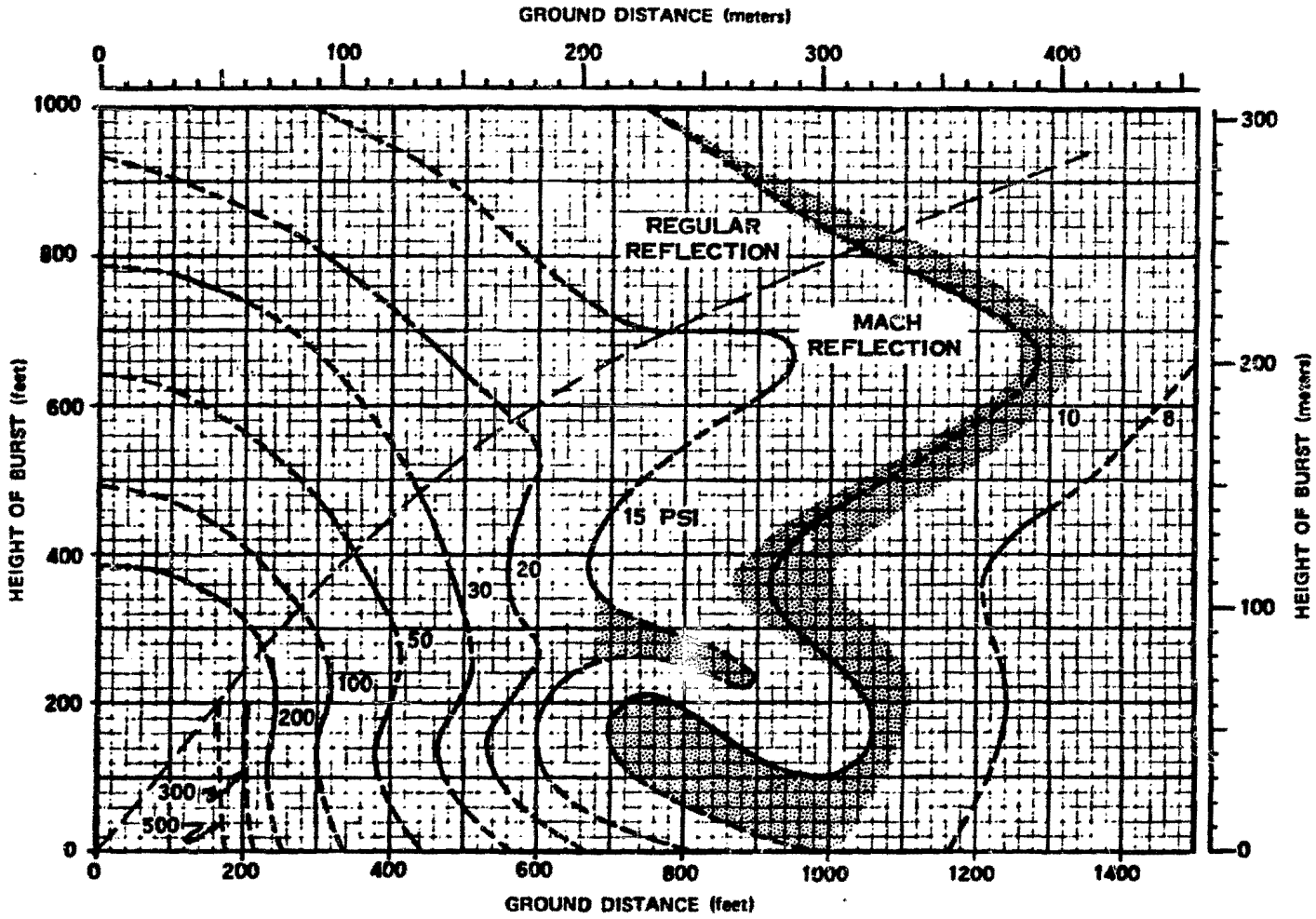

Figure 2-21. [redacted] Peak Overpressures at the Surface for a 1 kt Burst Over a Thermally Nonideal Surface, High Overpressure Region [redacted]

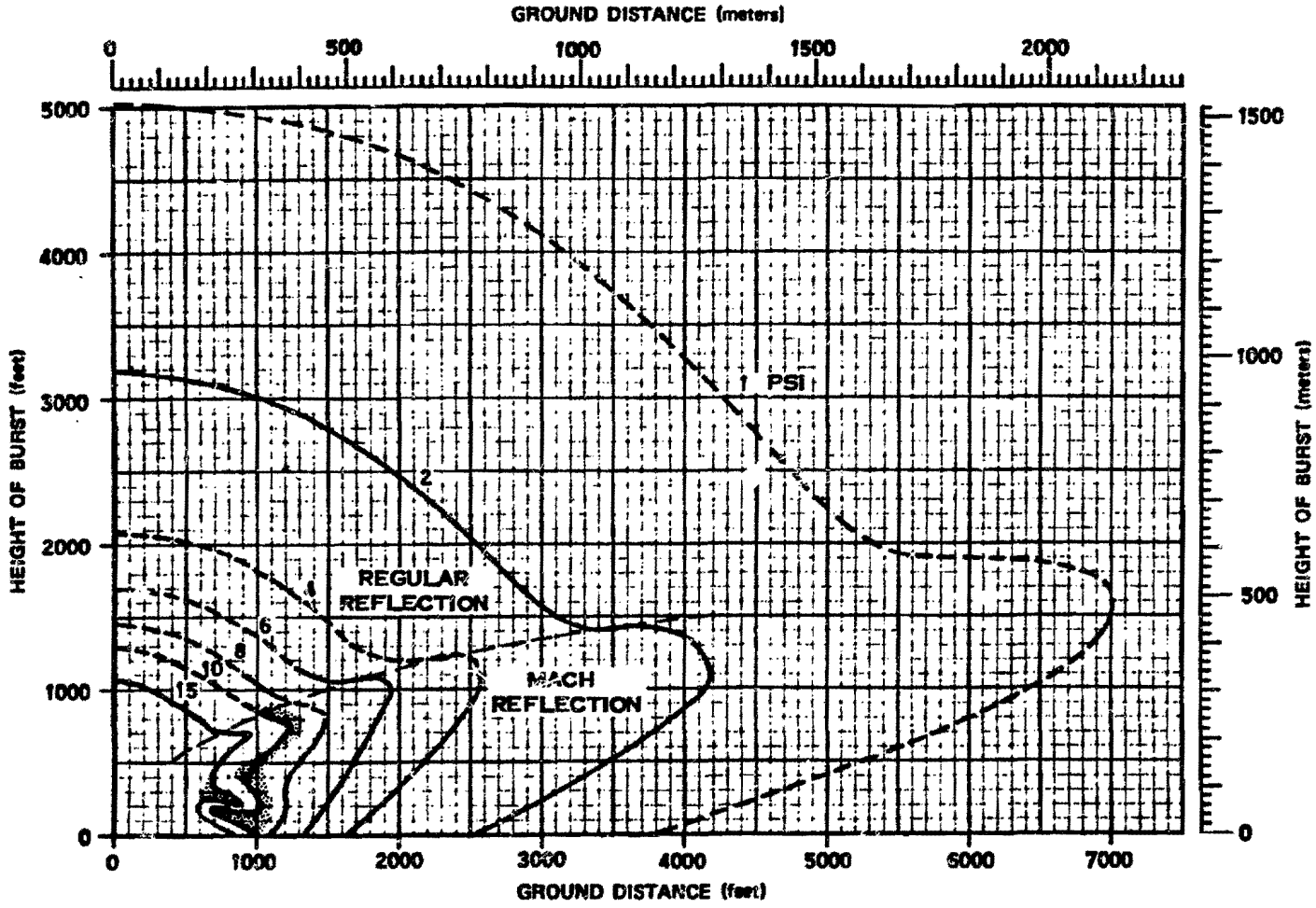

Figure 2-22. [redacted] Peak Overpressures at the Surface for a 1 kt Burst Over a Thermally Nonideal Surface, Low Overpressure Region [redacted]

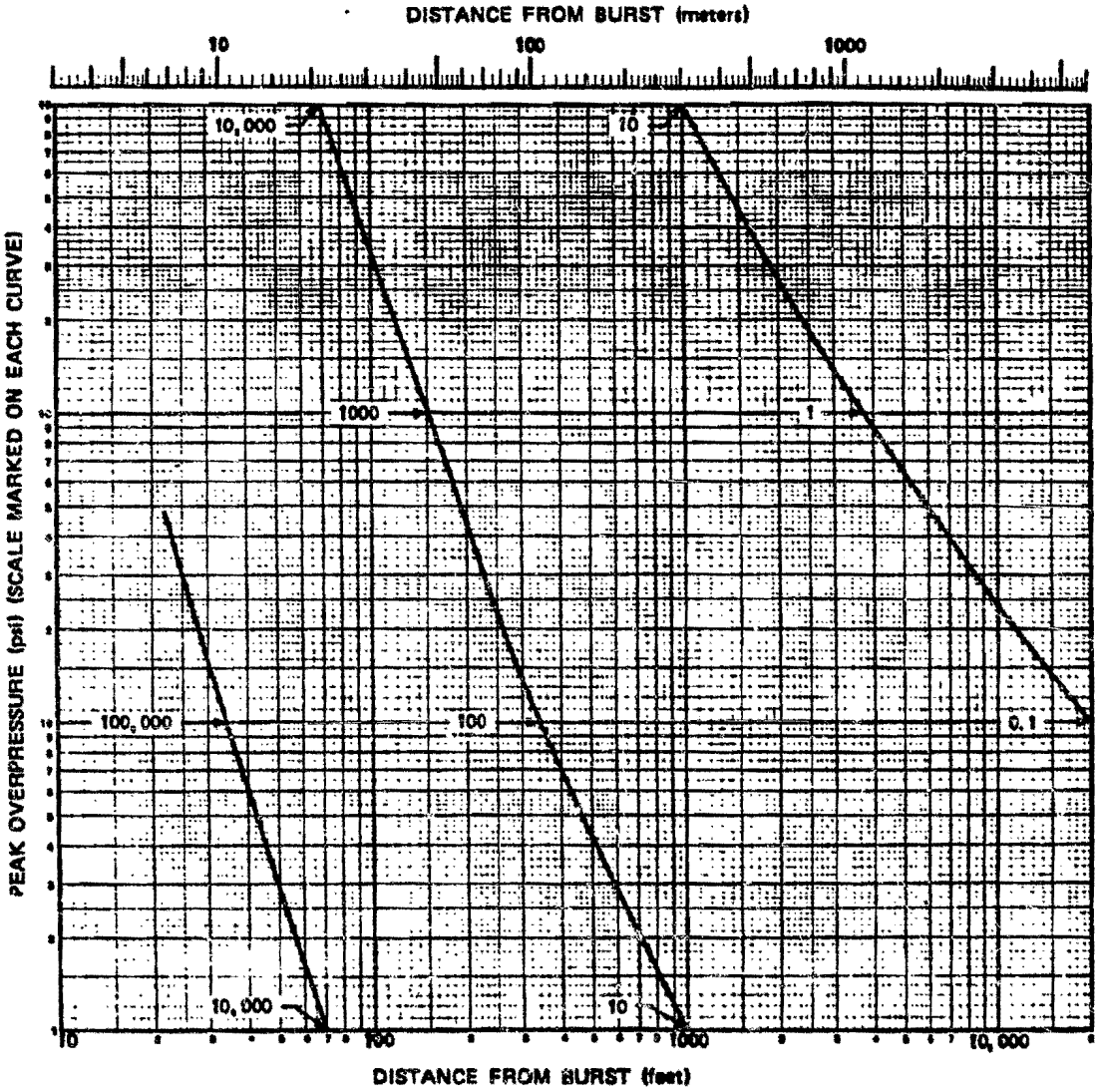

Figure 2-23. [redacted] Peak Overpressure from a Contact Surface Burst [redacted]

Problem 2-10. Calculation of Peak Dynamic Pressure at the Surface

[redacted] Figures 2-24 through 2-26 show peak dynamic pressure at the surface as a function of height of burst and horizontal distance from ground zero for a 1 kt explosion in a sea level atmosphere. Figure 2-24 is based almost entirely on theory and applies to peak dynamic pressure in the very high overpressure region at an ideal surface. Dust loading effects are not included in the curves of Figure 2-24. Figure 2-25 shows the peak dynamic pressure at the surface under light dust conditions, while Figure 2-26 shows similar data under heavy dust conditions. Figure 2-27 shows a comparison of the data from Figures 2-24 through 2-26 for a 1 kt explosion at a height of burst of 200 feet. A discussion of the comparisons is given in paragraph 2-25.

[redacted] *Scaling.* For yields other than 1 kt, the ground distance and height of burst for any specific peak dynamic pressure scale as follows:

$$\frac{d}{d_1} = \frac{h}{h_1} = W^{1/3},$$

where d_1 and h_1 are the distance from ground zero and height of burst, respectively, for 1 kt, and d and h are the corresponding distance and height of burst for a yield of W kt. If the surface is above 5,000 feet, or if the surface atmospheric conditions differ from standard, the altitude scaling procedures given in paragraph 2-14 should be used.

[redacted] *Example* [redacted]

Given: A 160 kt explosion 3,000 feet above a light dust surface.

Find: The peak dynamic pressure at a distance of 6,000 feet from ground zero.

Solution: The corresponding height of burst and ground distance from a 1 kt explosion are

$$h_1 = \frac{h}{W^{1/3}} = \frac{3{,}000}{(160)^{1/3}} = 550 \text{ feet},$$

$$d_1 = \frac{d}{W^{1/3}} = \frac{6{,}000}{(160)^{1/3}} = 1{,}100 \text{ feet}.$$

Answer: From Figure 2-25, the peak dynamic pressure corresponding to a height of burst of 550 feet and a distance of 1,100 feet is about 3 psi. Since this value of peak dynamic pressure is below 6 psi, the actual value (see "Reliability" below) may be between that shown for ground distances of 1,100 ±25 percent (1,375 and 825 feet) or between about 1.5 and 7 psi; however, since the reliability estimates do not extend to yields above 50 kt, the precise limits cannot be stated.

[redacted] *Reliability:* Distances for peak dynamic pressures below 6 psi are estimated to be reliable within ±25 percent. For dynamic pressures above 6 psi, the distances in Figure 2-25 (light dust) are estimated to be correct within ±50 percent; and distances in Figure 2-26 (heavy dust), to within +100 percent, or -50 percent. The reliability of Figure 2-24 has not been estimated. These reliability figures apply to yields between 1 and 50 kt. Outside this range of yields, scaling may introduce additional error.

[redacted] *Related Material:* See paragraphs 2-13 through 2-15, 2-17 through 2-23 and 2-25. See also Tables 2-1 and 2-2 when atmospheric conditions at the surface differ from standard sea level conditions.

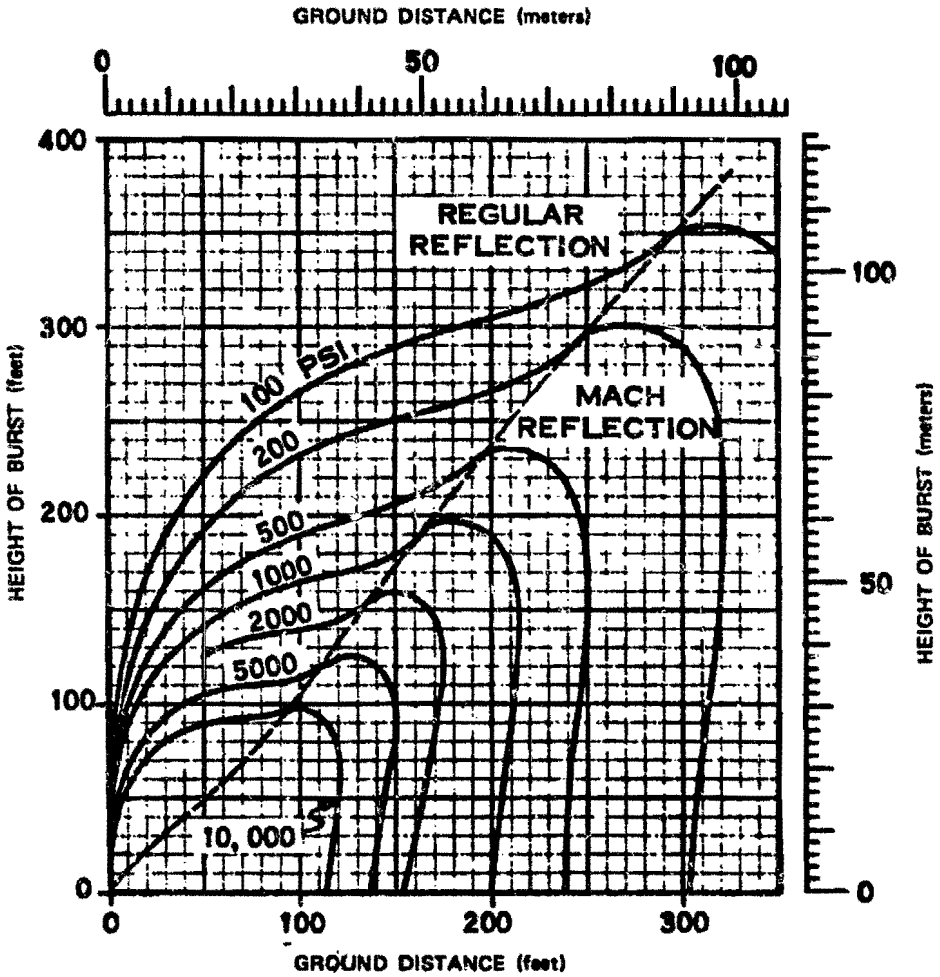

Figure 2-24. [redacted] Peak Dynamic Pressure at the Surface from a 1 kt Explosion Over an Ideal Surface [redacted]

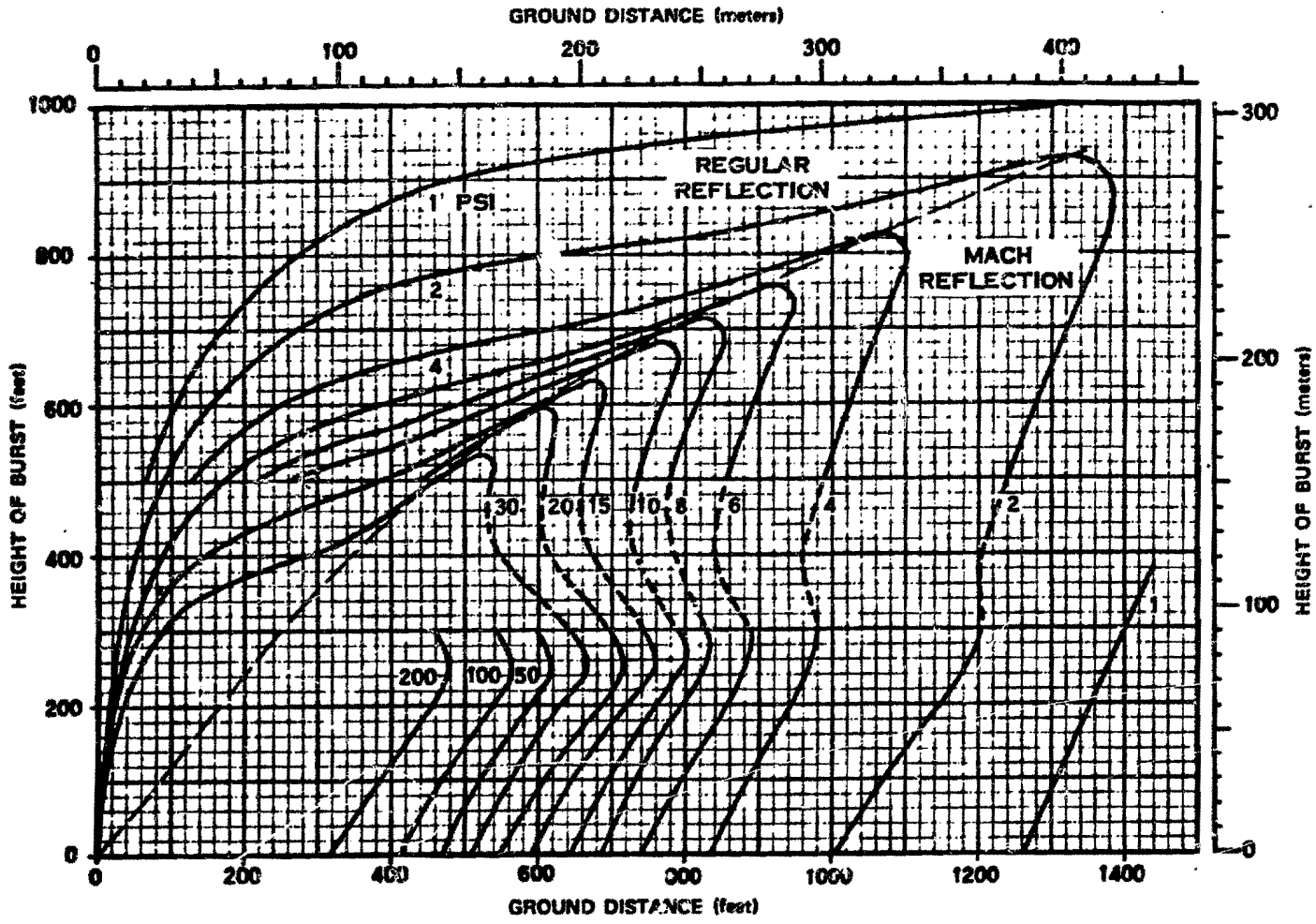

Figure 2-25. [redacted] Peak Dynamic Pressure at the Surface from a 1 kt Explosion [redacted]ver a Surface with Light Dust Conditions

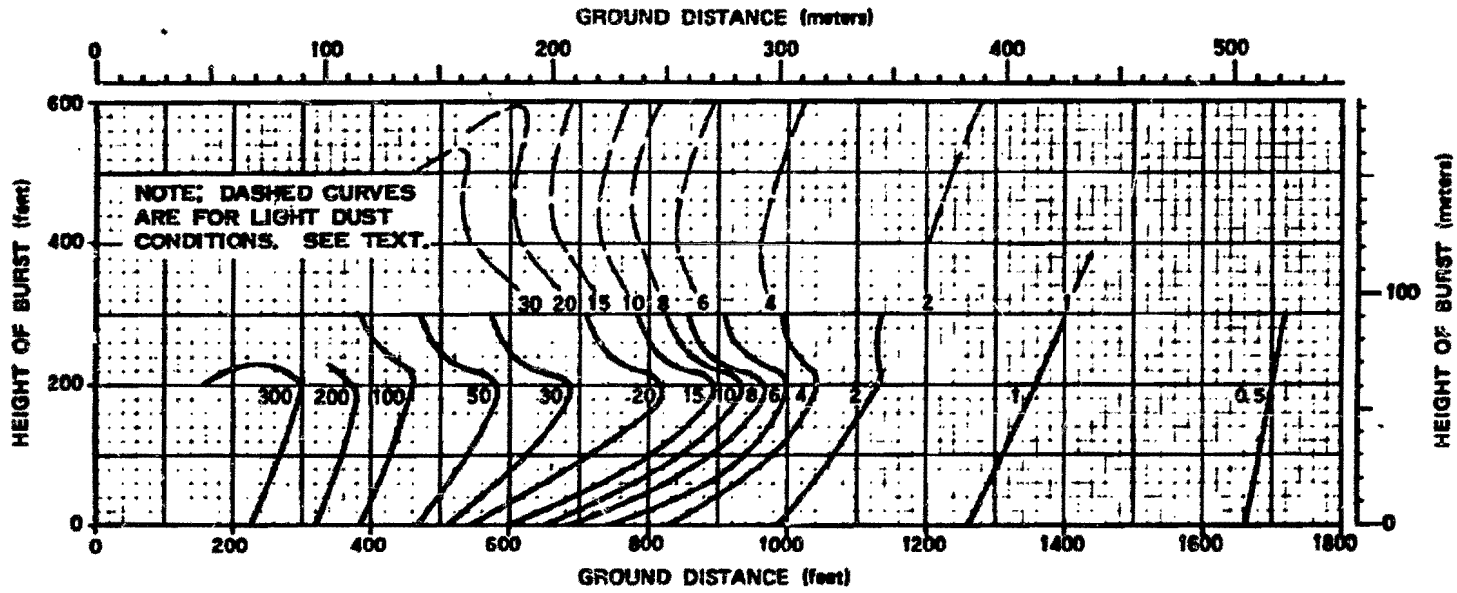

Figure 2-26. Peak Dynamic Pressure at the Surface from a 1 kt Explosion Over a Surface with Heavy Dust Conditions

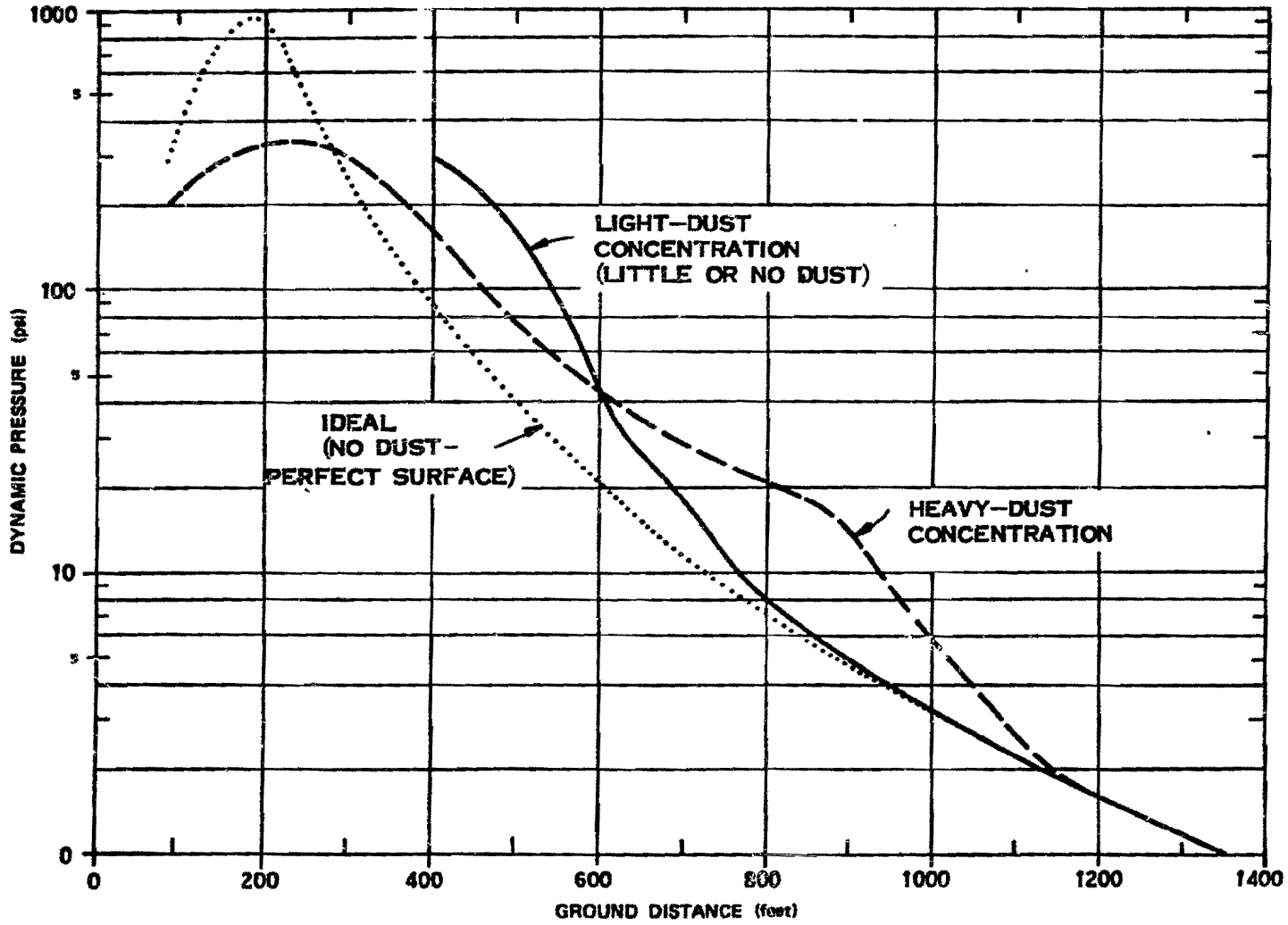

Figure 2-27. Comparison of Predicted Ideal, Light-Dust, and Heavy-Dust Dynamic Pressures for a 1 kt Explosion at a Height of Burst of 200 feet in a Sea Level Atmosphere

Problem 2-11. Calculation of the Time of Arrival of a Blast Wave at the Surface

Figures 2-28 through 2-32 show the time of arrival of a blast wave as a function of height of burst and horizontal distance from a 1 kt explosion in a sea level atmosphere. Figures 2-28 and 2-29 apply to bursts over thermally near-ideal surfaces while Figures 2-30 through 2-32 apply to bursts over thermally nonideal surfaces.

Scaling. For yields other than 1 kt, the time of arrival, ground distance, and height of burst scale as follows:

$$\frac{t}{t_1} = \frac{d}{d_1} = \frac{h}{h_1} = W^{1/3},$$

where t_1, d_1, and h_1 are the time of arrival, ground distance and height of burst, respectively for 1 kt and t, d, and h are the corresponding time and distances for a yield of W kt. If the surface is above 5,000 feet, or if the surface atmospheric conditions differ from standard, the altitude scaling procedures given in paragraph 2-14 should be used.

Example

Given: An 8 kt explosion 400 feet above a thermally nonideal surface.

Find: The time of arrival of the blast wave at a horizontal distance of 1,200 feet from ground zero.

Solution: The corresponding height of burst and ground distance for a 1 kt explosion are

$$h_1 = \frac{h}{W^{1/3}} = \frac{400}{(8)^{1/3}} = 200 \text{ feet.}$$

$$d_1 = \frac{d}{W^{1/3}} = \frac{1,200}{(8)^{1/3}} = 600 \text{ feet.}$$

From Figure 2-31, the time of arrival of a blast wave at a ground distance of 600 feet from a 1 kt explosion 200 feet above a thermally nonideal surface is 0.15 seconds.

Answer: The corresponding time of arrival for an 8 kt explosion is

$$t = t_1 W^{1/3} = (0.15)(8)^{1/3} = 0.30 \text{ sec.}$$

Under the specified conditions the ground range is reliable to within ±15 percent (see "Reliability" below), or the 1 kt ground distance could vary between 510 and 690 feet, providing arrival times from a 1 kt explosion of 0.12 and 0.19 seconds. The time of arrival from the 8 kt explosion may therefore be expected to fall between

$$t = t_1 W^{1/3} = (0.12)(8)^{1/3} = 0.24 \text{ sec, and}$$

$$t = t_1 W^{1/3} = (0.19)(8)^{1/3} = 0.38 \text{ sec,}$$

with an expected value of 0.30 seconds as previously calculated.

Reliability: Over near-ideal surfaces, the ground distance for a given arrival time is estimated to be reliable within ±10 percent. Over nonideal surfaces, two reliability estimates have been made: in the region of Mach reflection and for times less than about 0.8 sec per kt, the ground distances are estimated to be reliable within ±15 percent; at later times or in the region of regular reflection, the values are about ±10 percent. These reliability estimates apply to yields between 1 kt and 1 Mt. Outside this range of yields, the curves may be used with somewhat less confidence.

Related Material: See paragraphs 2-13 through 2-15 and paragraph 2-26. See also Tables 2-1 and 2-2.

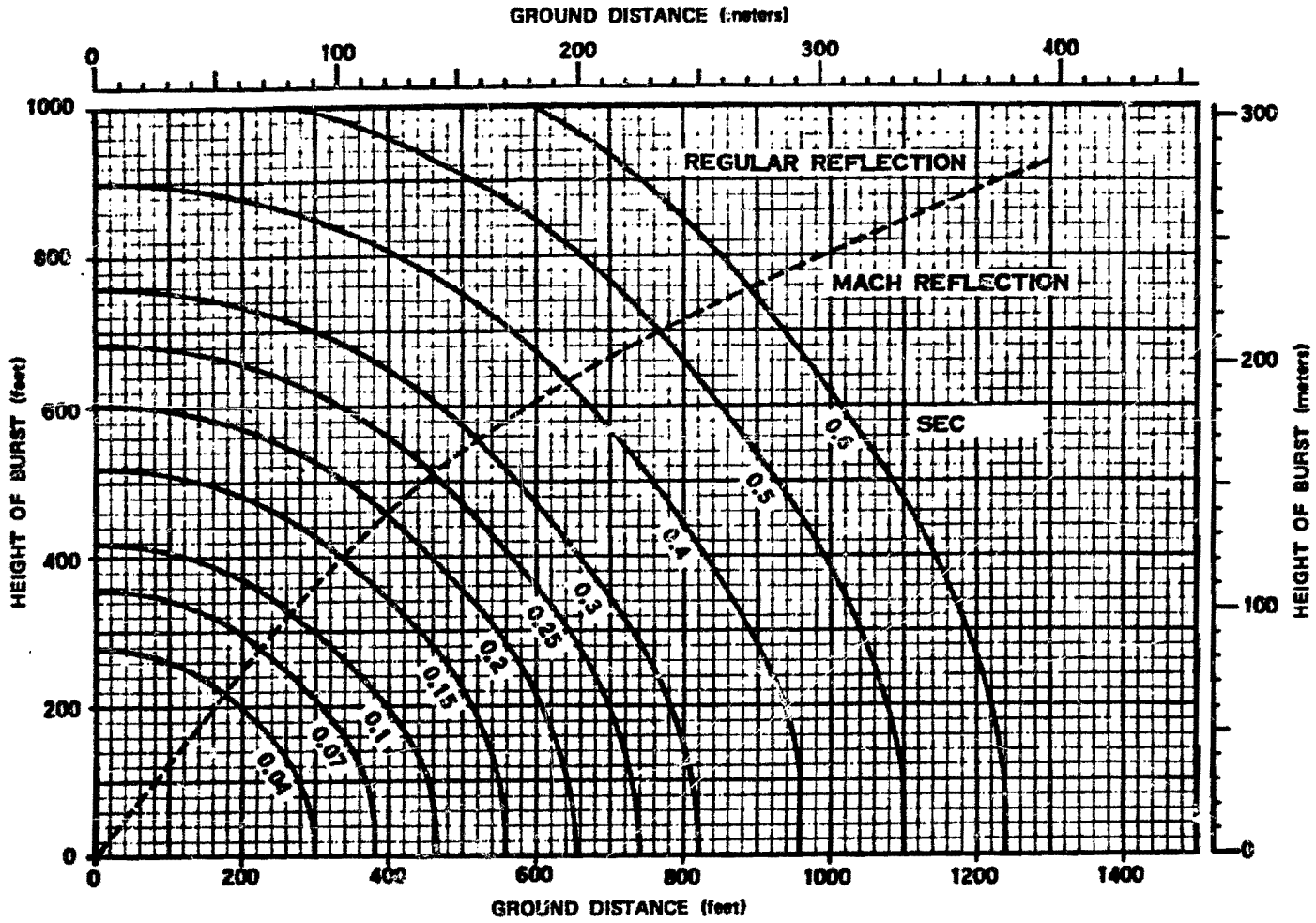

Figure 2-28. [redacted] Time of Arrival of the Blast Wave Along the Surface from a 1 kt Explosion Over a Near-Ideal Surface, High Overpressure Region [redacted]

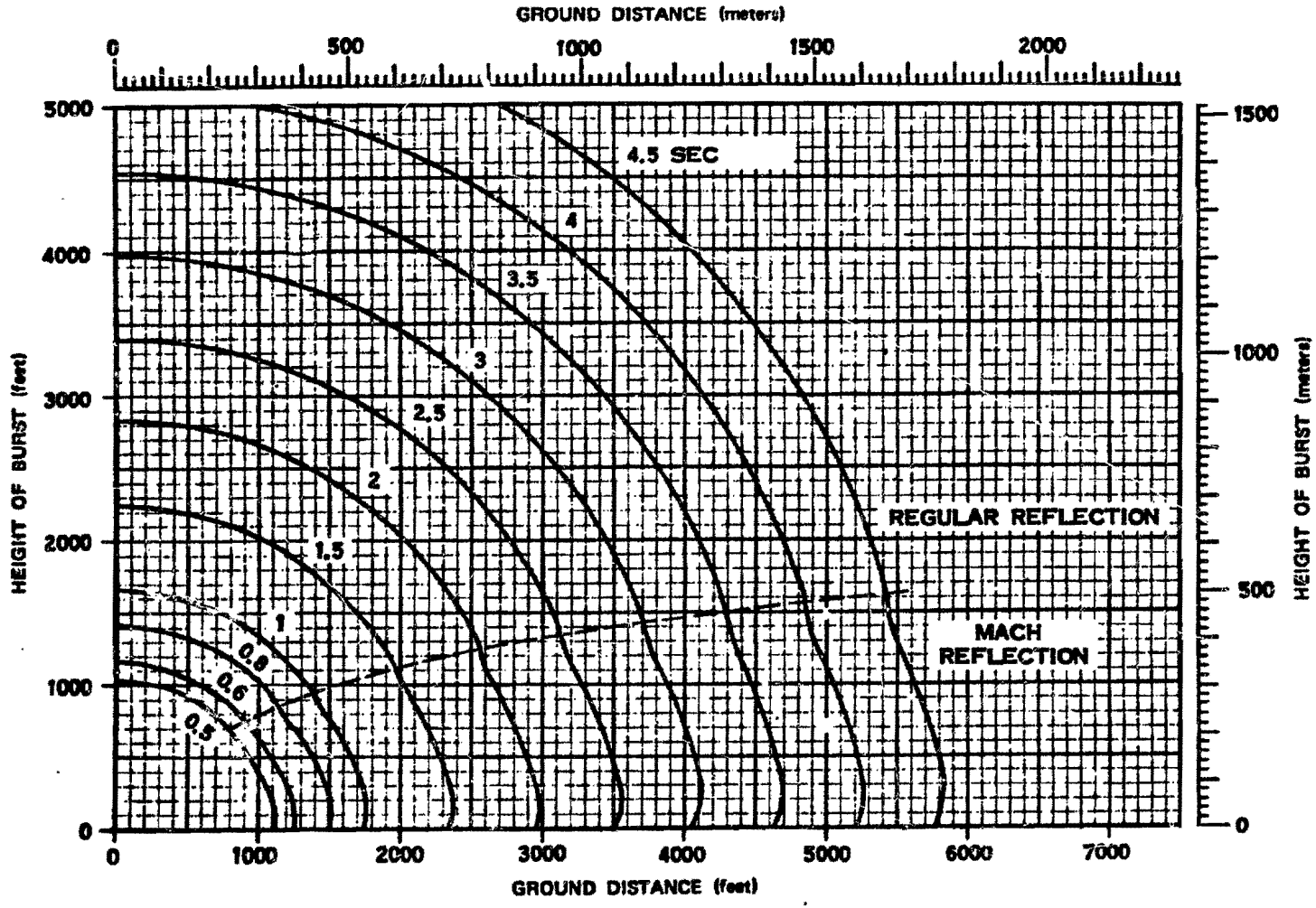

Figure 2-29. Time of Arrival of the Blast Wave Along the Surface from a 1 kt Explosion Over a Near-Ideal Surface, Low Overpressure Region

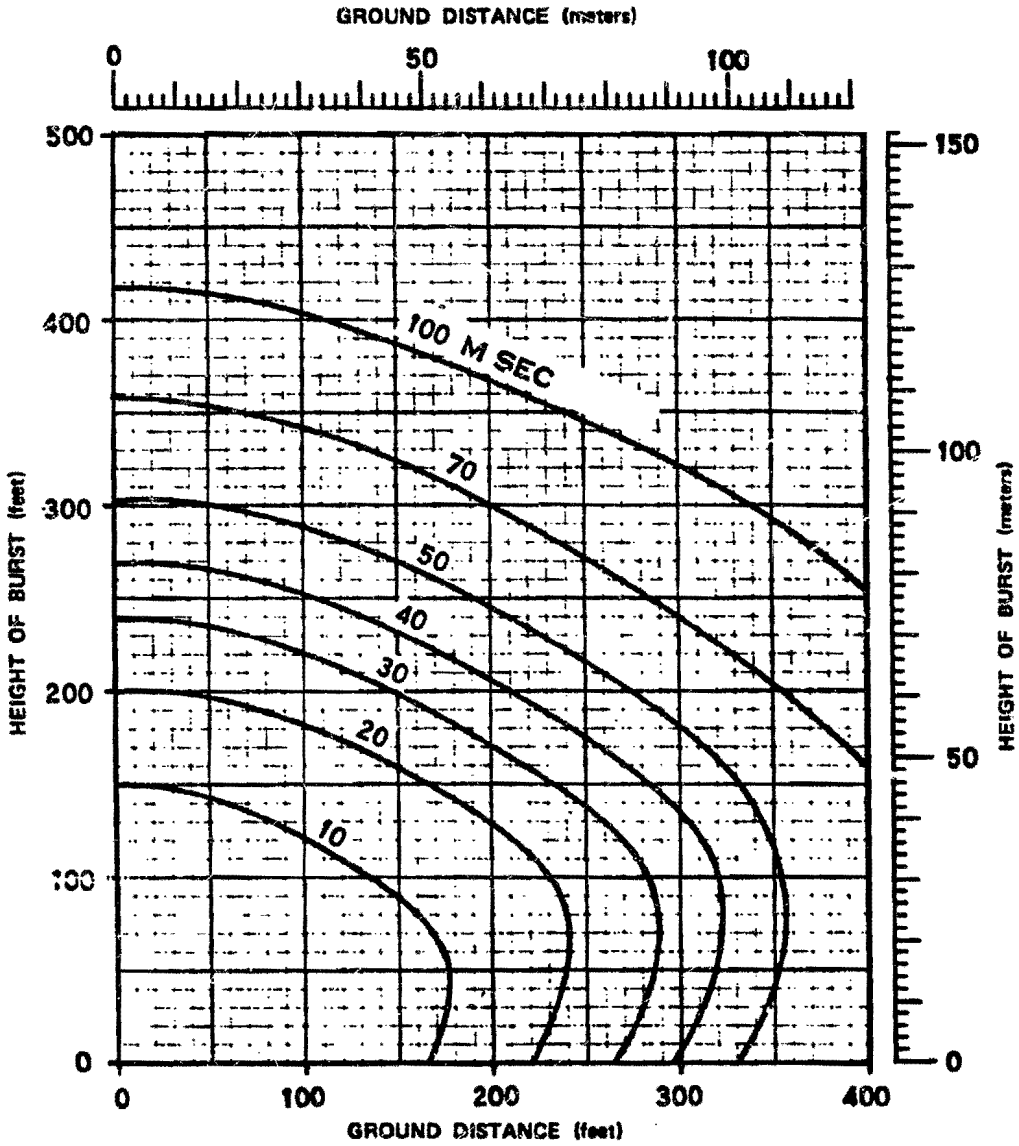

Figure 2-30. Time of Arrival of the Blast Wave Along the Surface from a 1 kt Explosion Over a Thermally Nonideal Surface, Very High Overpressure Region

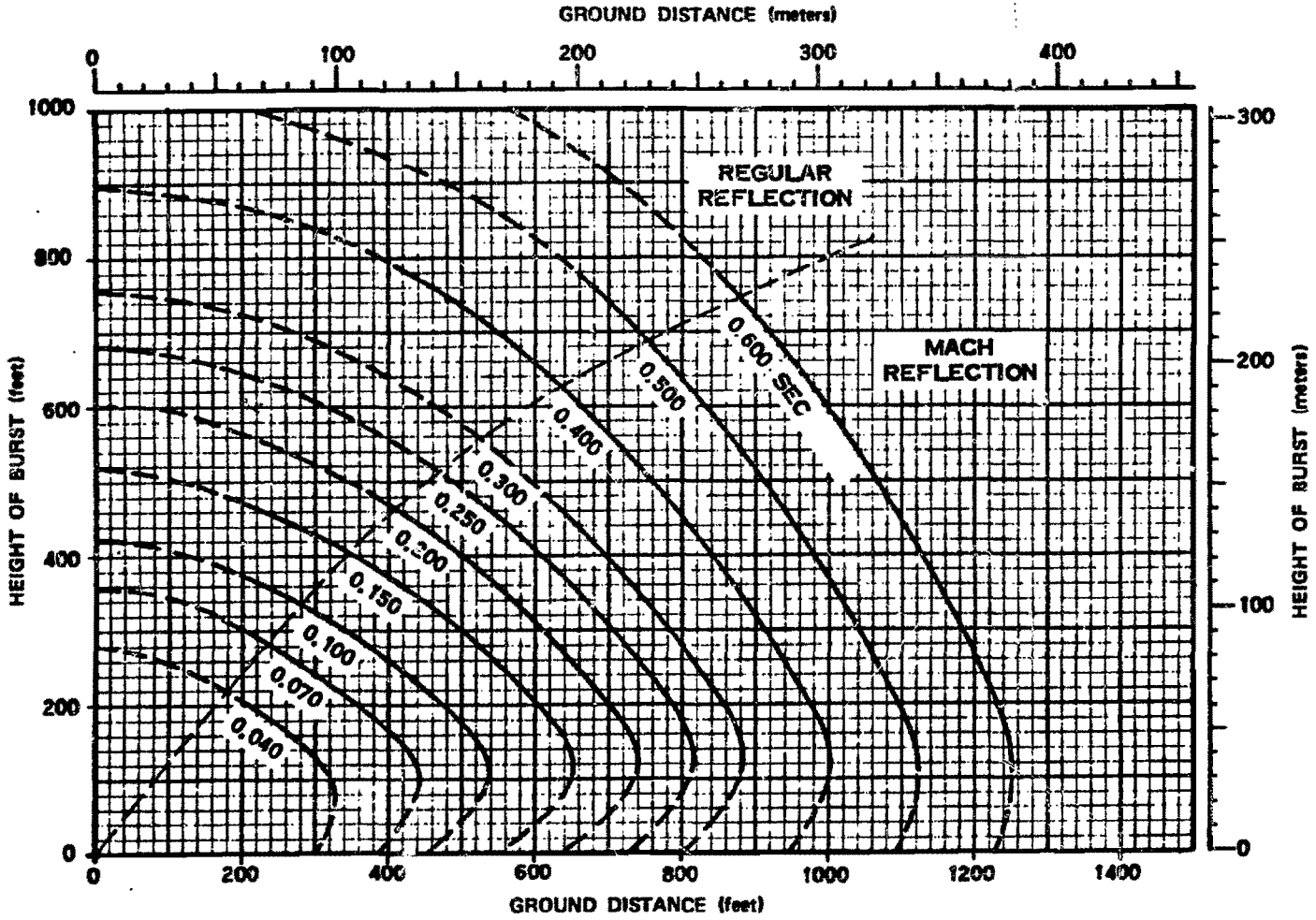

Figure 2-31. [redacted] Time of Arrival of the Blast Wave Along the Surface from a 1 kt Explosion Over a Thermally Nonideal Surface, High Overpressure Region [redacted]

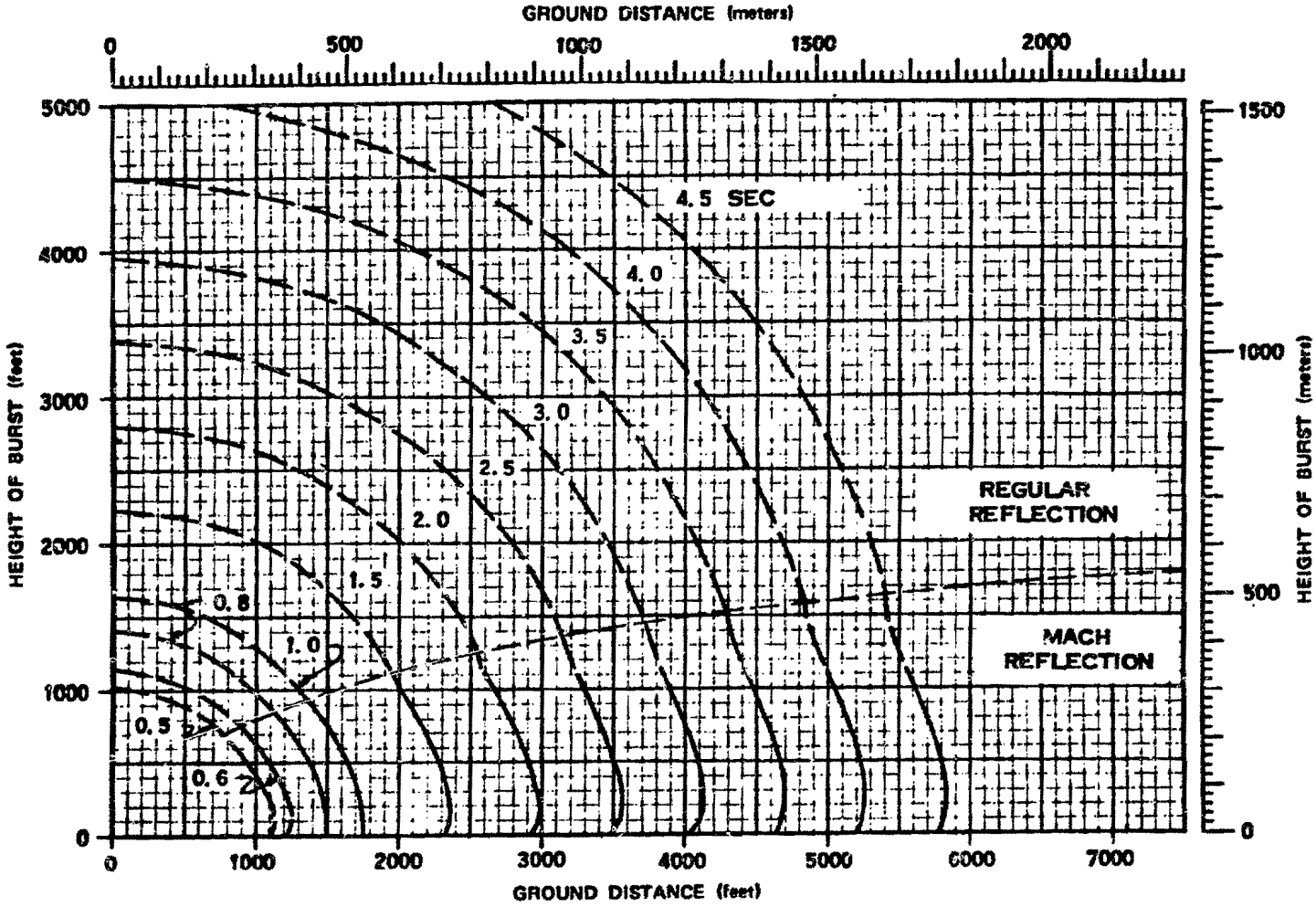

Figure 2-32. [redacted] Time of Arrival of the Blast Wave Along the Surface from a 1 kt Explosion Over a Thermally Nonideal Surface, Low Overpressure Region [redacted]

[redacted]

Problem 2-12. Calculation of Positive Phase Duration of the Blast Wave at the Surface

[redacted] Figures 2-33 and 2-34 show the duration of the positive phase of the overpressure pulse at the surface as a function of height of burst and horizontal distance from ground zero for a 1 kt explosion in a sea level atmosphere. The two figures are for near-ideal and thermally nonideal surface conditions, respectively. Positive phase duration of the dynamic pressure pulse may be estimated from data obtained from Figures 2-33 and 2-34, and Table 2-4.

[redacted] *Scaling.* For yields other than 1 kt, the duration of the positive overpressure, height of burst, and distance from ground zero scale as follows:

$$\frac{t_p^+}{t_{p1}^+} = \frac{h}{h_1} = \frac{d}{d_1} = W^{1/3},$$

where t_{p1}^+, h_1, and d_1 are the positive overpressure duration, height of burst, and ground distance for a 1 kt explosion, and t_p^+, h, and d are the corresponding time and distances for a yield of W kt. If the surface is above 5,000 feet, or if the atmospheric conditions at the surface differ from standard conditions, the altitude scaling procedures given in paragraph 2-14 should be used.

[redacted] *Example* [redacted]

Given: A 160 kt explosion 2,700 feet above a thermally nonideal surface.

Find: The positive overpressure and dynamic pressure durations at the surface 9,000 feet from ground zero.

Solution: The corresponding height of burst and ground distance for a 1 kt explosion are

$$h_1 = \frac{h}{W^{1/3}} = \frac{2{,}700}{(160)^{1/3}} = 500 \text{ feet},$$

$$d_1 = \frac{d}{W^{1/3}} = \frac{9{,}000}{(160)^{1/3}} = 1{,}660 \text{ feet}.$$

From Figure 2-34, the positive overpressure duration corresponding to a height of burst of 500 feet and a ground distance of 1,660 feet is about 0.3 seconds for a 1 kt explosion. From Table 2-4, the corresponding duration of the positive dynamic pressure is 0.39 seconds.

Answer: The corresponding positive overpressure and dynamic pressure durations for a 160 kt explosion are

$$t_p^+ = t_{p1}^+ W^{1/3} = (0.3)(160)^{1/3} = 1.6 \text{ seconds},$$

$$t_q^+ = t_{q1}^+ W^{1/3} = (0.39)(160)^{1/3} = 2.1 \text{ seconds}.$$

These are expected values. The range of possible values for the positive phase durations could be obtained by applying the uncertainties in ground distance given below in "Reliability" by methods similar to those illustrated for time of arrival in Problem 2-11. Since the uncertainties in t_q^+ are greater than for t_p^+, the smaller value of t_q^+ may be less than the smaller value of t_p^+. In this case, the smaller value of t_p^+ should be used as the lower limit for t_q^+ since the dynamic pressure positive phase is expected to last longer than the overpressure positive phase.

[redacted] *Reliability:* Figures 2-33 and 2-34 were constructed entirely from experimental data. Since overpressure usually is changing slowly

[redacted]

[redacted]

when it passes through zero, the exact time marking the end of the positive overpressure phase is difficult to determine experimentally, and the uncertainty of the curves, in terms of ground distance, is large. Ground distance for t_p^+ obtained from these curves is estimated to be reliable within ±25 percent for durations of 300 msec or less and within ±50 percent for longer durations. Use of Table 2-4 to obtain values for t_q^+ gives ground distances estimated to be within ±50 percent for durations of 390 msec or less and within ±100 percent for longer durations. *The positive dynamic pressure phase is expected to last longer than the positive overpressure phase. Therefore, the lower limit for t_q^+ should be no smaller than the lower limit calculated for t_p^+.* For near-ideal surface conditions, these estimates apply to a yield range between 1 kt and 20 Mt; for nonideal surface conditions, the estimates apply to a yield range between 1 kt and 50 kt. The curves may be used outside this range of yields with somewhat less confidence.

[redacted] *Related Material:* See paragraphs 2-13 through 2-15, 2-17 through 2-23 and 2-27. See also Tables 2-1 and 2-2 when atmospheric conditions at the surface differ from standard sea level conditions.

[redacted]

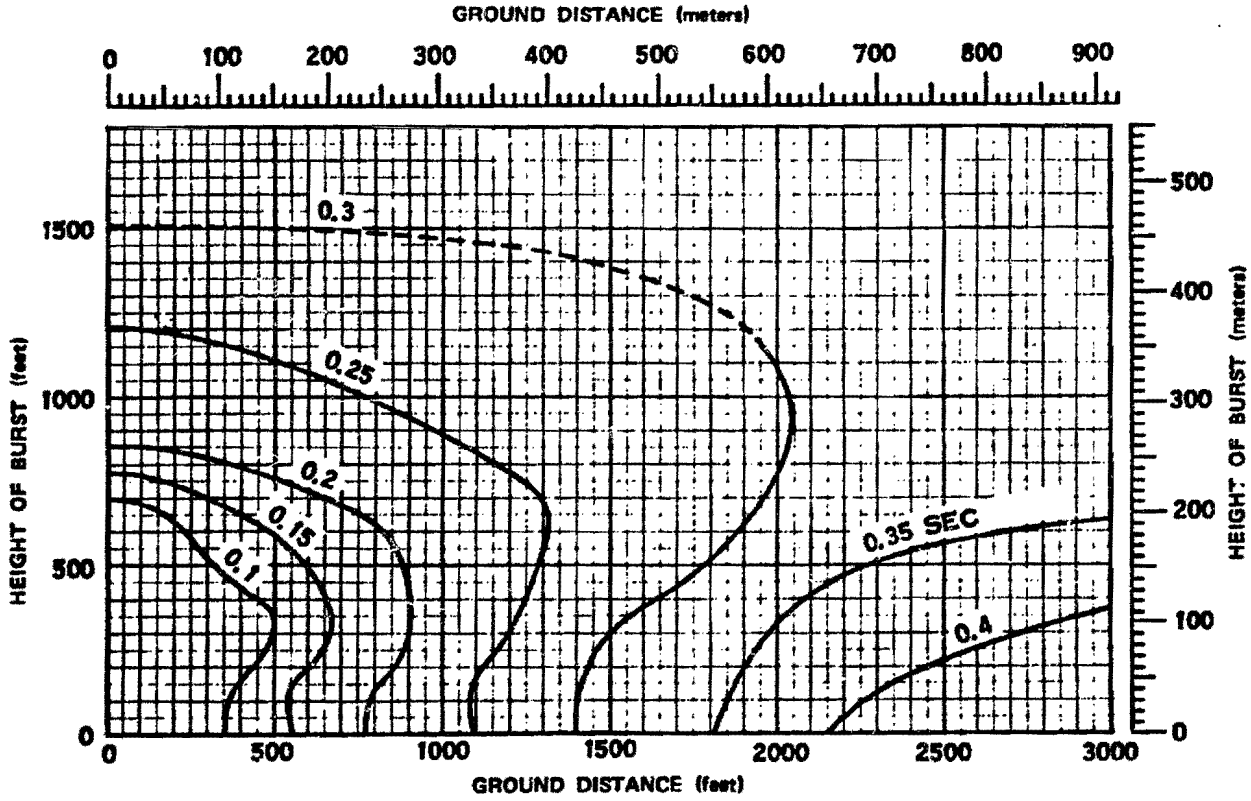

Figure 2-33. [redacted] Duration of Positive Overpressure at the Surface from a [redacted] kt Explosion Over a Near-Ideal Surface [redacted]

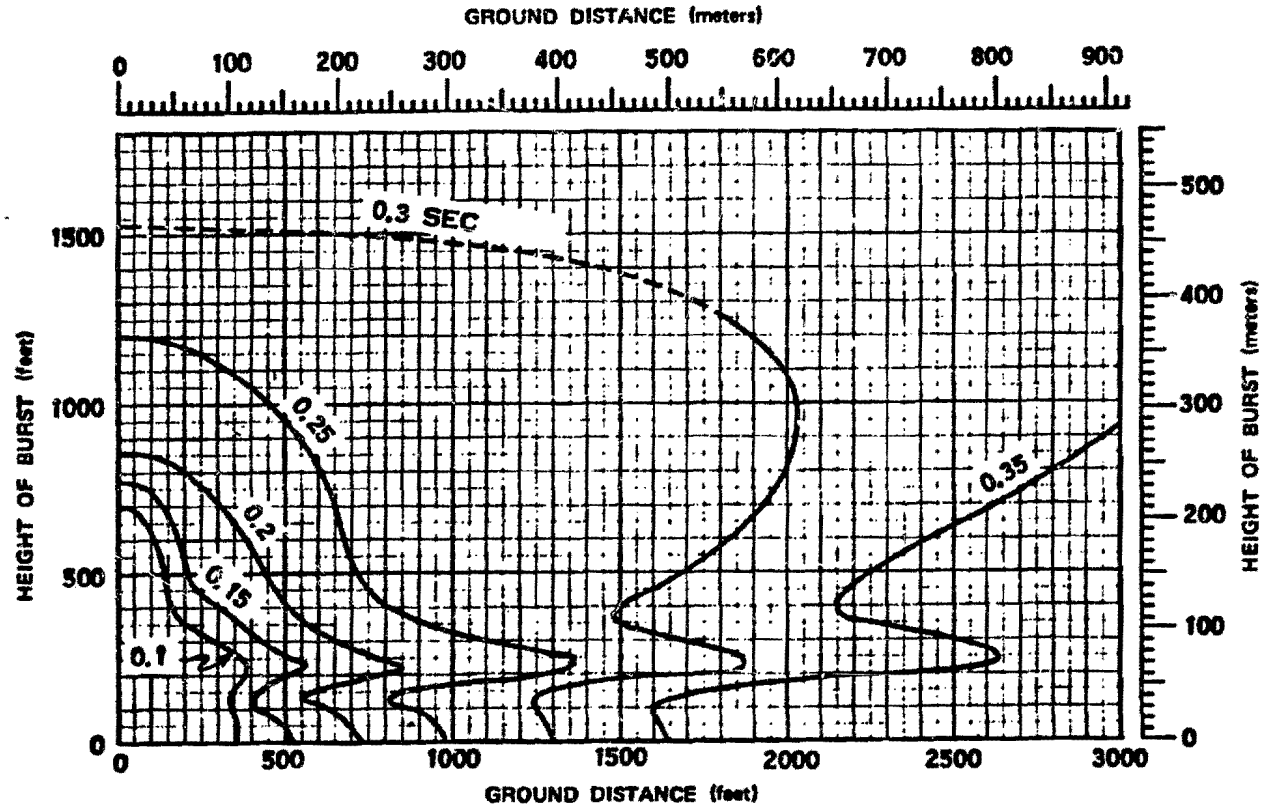

Figure 2-34. [redacted] Duration of Positive Overpressure at the Surface from a 1 kt Explosion Over a Thermally Nonideal Surface [redacted]

Problem 2-13. Calculation of Positive Overpressure Impulse at the Surface

Figures 2-35 and 2-36 show the positive overpressure impulse at the surface as a function of height of burst and the horizontal distance from ground zero for a 1 kt explosion in a sea level atmosphere. The two figures apply to near-ideal and thermally nonideal surface conditions, respectively.

Scaling. For yields other than 1 kt, the positive overpressure impulse, height of burst, and distance from ground zero scale as follows:

$$\frac{I}{I_1} = \frac{h}{h_1} = \frac{d}{d_1} = W^{1/3},$$

where I_1, h_1, and d_1 are the positive phase impulse at the surface, height of burst, and distance from ground zero, respectively, for a 1 kt explosion, and I, h, and d are the corresponding impulse and distances from a yield of W kt. If the surface is above 5,000 feet, or if the atmospheric conditions at the surface differ from standard conditions, the altitude scaling procedures given in paragraph 2-14 should be used.

Example

Given: A 30 kt explosion 1,000 feet above a thermally nonideal surface.

Find: The overpressure positive phase impulse along the surface 6,000 feet from ground zero.

Solution: The corresponding height of burst and ground distance for a 1 kt explosion are

$$h_1 = \frac{h}{W^{1/3}} = \frac{1{,}000}{(30)^{1/3}} = 320 \text{ feet},$$

$$d_1 = \frac{d}{W^{1/3}} = \frac{6{,}000}{(30)^{1/3}} = 1{,}930 \text{ feet}.$$

From Figure 2-36, the overpressure impulse 1,930 feet from ground zero of 1 kt explosion at 320 feet is 0.55 psi-sec. To account for unpredictable variations in overpressure impulse, the 1 kt ground distance should be taken to be 1,930 ±20 percent (see "Reliability" below), i.e., 1,540 to 2,320 feet. From Figure 2-36, the overpressure impulses at these distances are 0.70 and 0.45 psi-sec, respectively.

Answer: The overpressure positive phase impulse from the 30 kt explosion will be between

$$I = I_1 W^{1/3} = (0.70)(30)^{1/3} = 2.2 \text{ psi-sec},$$

and

$$W^{1/3} = (0.45)(30)^{1/3} = 1.4 \text{ psi-sec},$$

with an expected value of

$$I = I_1 W^{1/3} = (0.55)(30)^{1/3} = 1.7 \text{ psi-sec}.$$

Reliability: The overpressure impulse contours in Figures 2-35 and 2-36 are estimated to be reliable within ±20 percent of the indicated ground distance. For near-ideal surface conditions, this reliability estimate applies to yields between 1 kt and 20 Mt and burst heights for 1 kt below 1,000 feet; for nonideal surfaces, the estimates apply to yields between 1 kt and 50 kt and burst heights for 1 kt below 1,000 feet. Outside this range of yields and burst heights, these curves may be used with somewhat less confidence.

Related Material: See paragraphs 2-13 through 2-15, 2-17 through 2-23 and 2-28. See also Tables 2-1 and 2-2 when atmospheric conditions at the surface differ from standard sea level conditions.

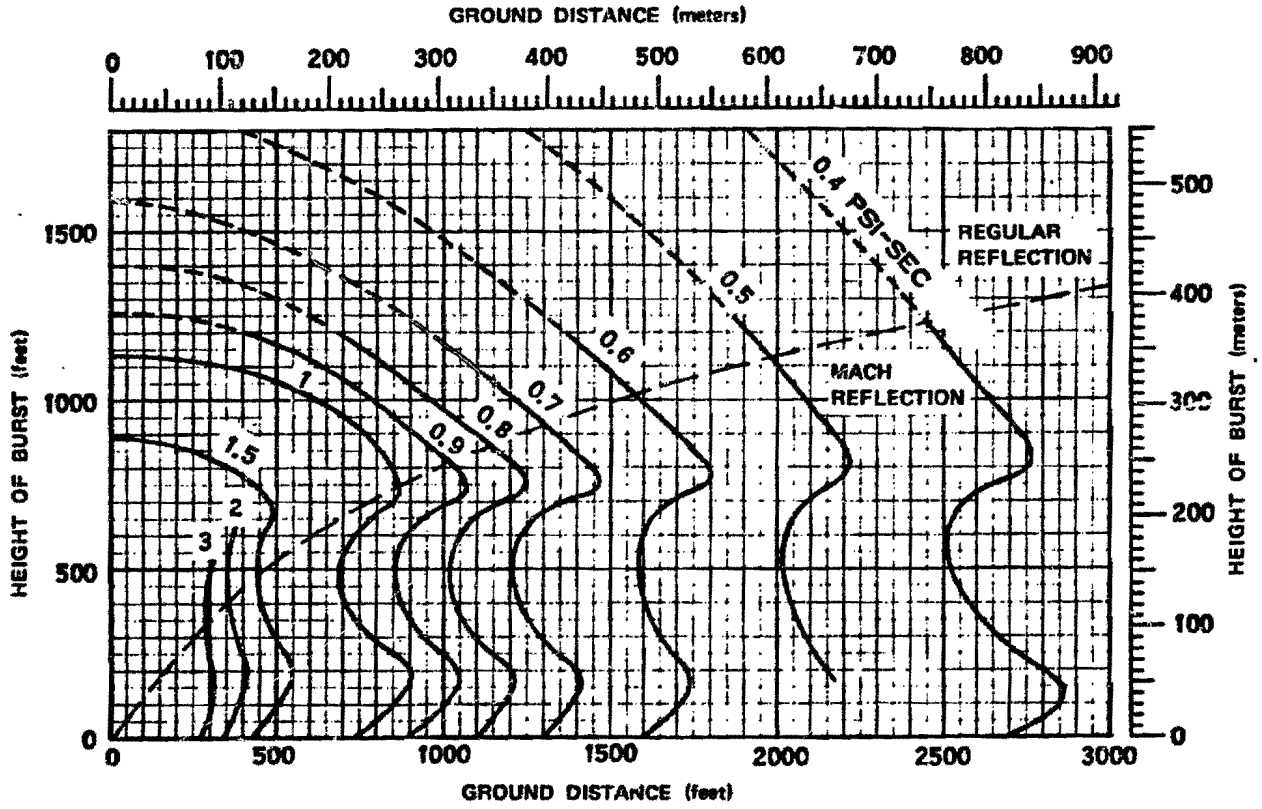

Figure 2-35. [redacted] Positive Overpressure Impulse at the Surface from a 1 kt Explosion Over a Near-Ideal Surface [redacted]

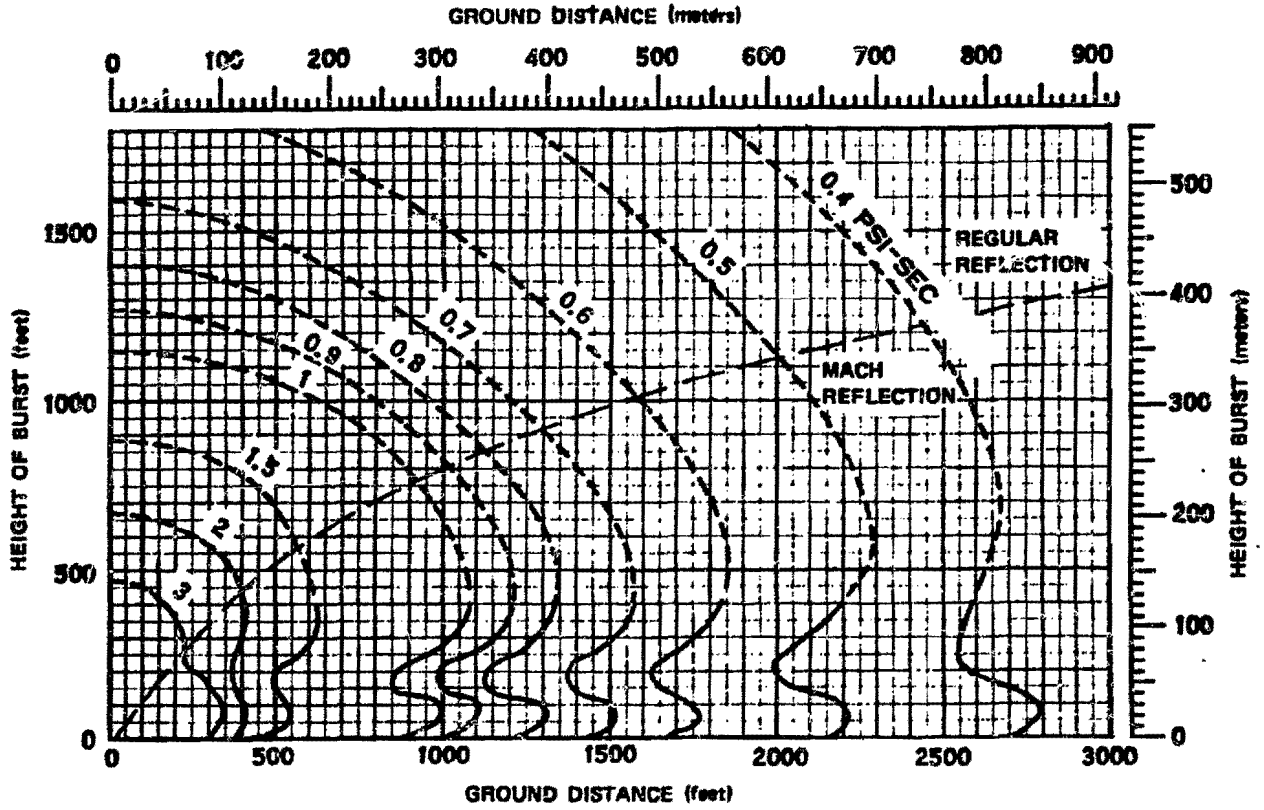

Figure 2-36. [redacted] Positive Overpressure Impulse at the Surface from a 1 kt Explosion Over a Thermally Nonideal Surface [redacted]

[redacted]

Problem 2-14. Calculation of Mach Stem Height

[redacted] Figures 2-37 and 2-38 show the height of the Mach stem as a function of horizontal distance from ground zero for several heights of burst for a 1 kt explosion in a sea level atmosphere. These curves, in effect, show the trajectory of the triple point (paragraph 2-18 and 2-29).

[redacted] *Scaling.* For yields other than 1 kt, the Mach stem height, height of burst, and ground distance scale as follows:

$$\frac{H}{H_1} = \frac{h}{h_1} = \frac{d}{d_1} = W^{1/3},$$

where H_1, h_1, and d_1 are the height of the Mach stem, the height of burst, and the distance from ground zero, respectively, for a 1 kt explosion, and H, h, and d are the corresponding distances for a yield of W kt. If the surface is above 5,000 feet, or if the atmospheric conditions at the surface differ from standard conditions, the altitude scaling procedures given in paragraph 2-14 should be used.

[redacted] *Example* [redacted]:

Given: A 55 kt explosion 1,000 feet above the surface.

Find: The ground distance beyond which an aircraft flying 500 feet above the surface will be in the Mach reflection region.

Solution: The corresponding height of burst and Mach stem height for a 1 kt explosion are

$$h_1 = \frac{h}{W^{1/3}} = \frac{1{,}000}{(55)^{1/3}} = 260 \text{ feet},$$

$$H_1 = \frac{H}{W^{1/3}} = \frac{500}{(55)^{1/3}} = 130 \text{ feet}.$$

Interpolation between the curves of Figure 2-37 shows that a 1 kt explosion burst at 260 feet will have a Mach stem height of 130 feet when the triple point is at a ground distance of about 750 feet.

Answer: The corresponding ground distance for a 55 kt explosion is

$$d = d_1 W^{1/3} = (750)(55)^{1/3} = 2{,}850 \text{ feet}.$$

Since this yield is close to the upper limit at which a ±10 percent tolerance applies (see "Reliability" below), the distance may reasonably be expected to be within about ±15 percent (± about 430 feet). Therefore the Mach stem height may reasonably be expected to exceed 500 feet at a ground range beyond about 3,300 feet.

[redacted] *Reliability:* The range at which a given Mach stem height is shown to occur in Figures 2-37 and 2-38 is considered reliable within ±10 percent for yields between 1 kt and 50 kt and within ±25 percent for yields up to 20 Mt. This decrease in confidence with increasing yield results from the lack of knowledge concerning the effect of atmospheric nonhomogeneity on the triple-point trajectory. It is suggested that no correction be made for *burst* altitude; however, when the data are applied to high-yield air bursts, the results should be treated with somewhat less confidence.

[redacted] *Related Material:* See paragraphs 2-13 through 2-15, 2-17 through 2-23, and 2-29. See also Tables 2-1 and 2-2 when atmospheric conditions at the surface differ from standard sea level conditions.

[redacted]

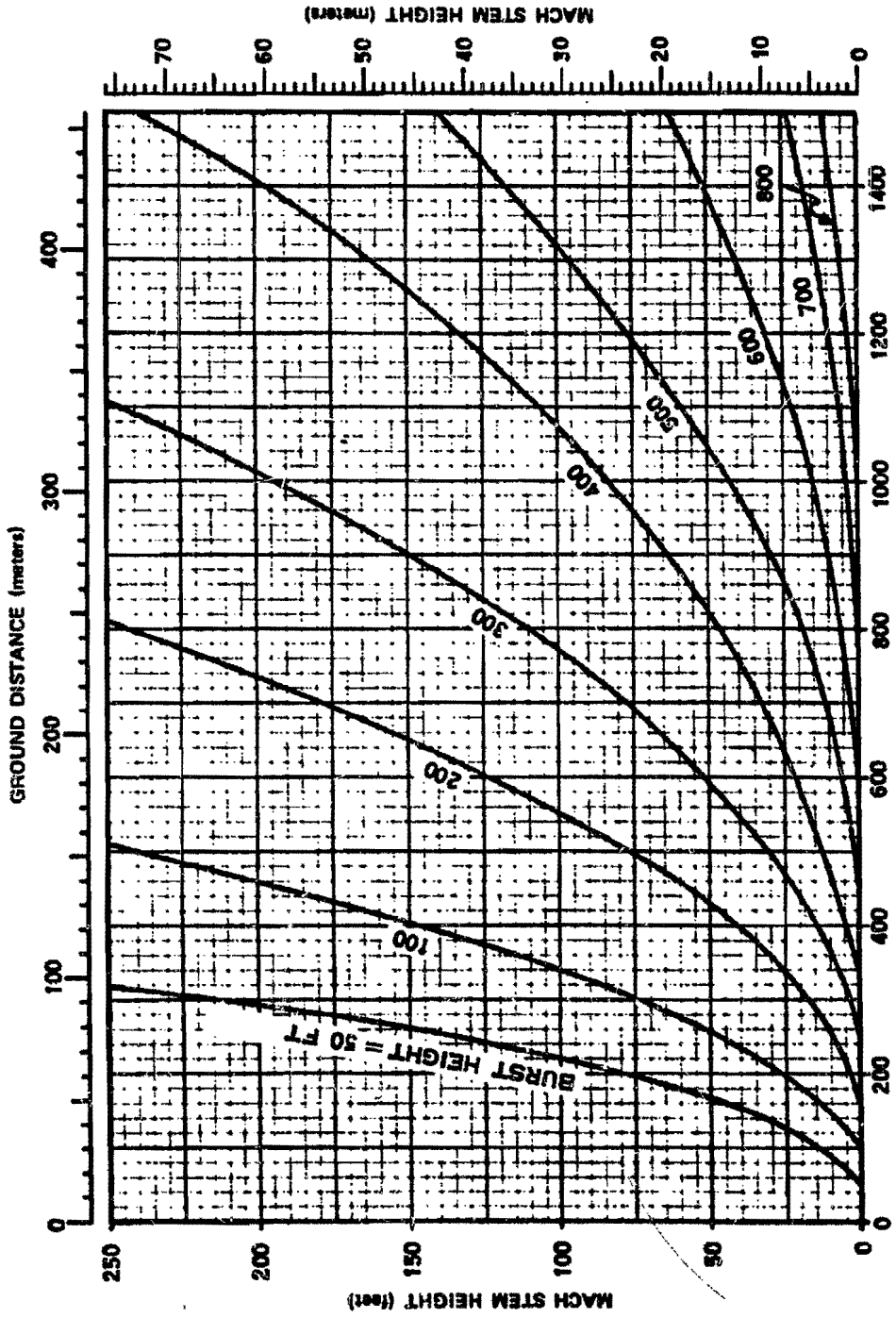

Figure 2-37. [redacted] Mach Stem Height for a 1 kt Explosion, High Overpressure Region

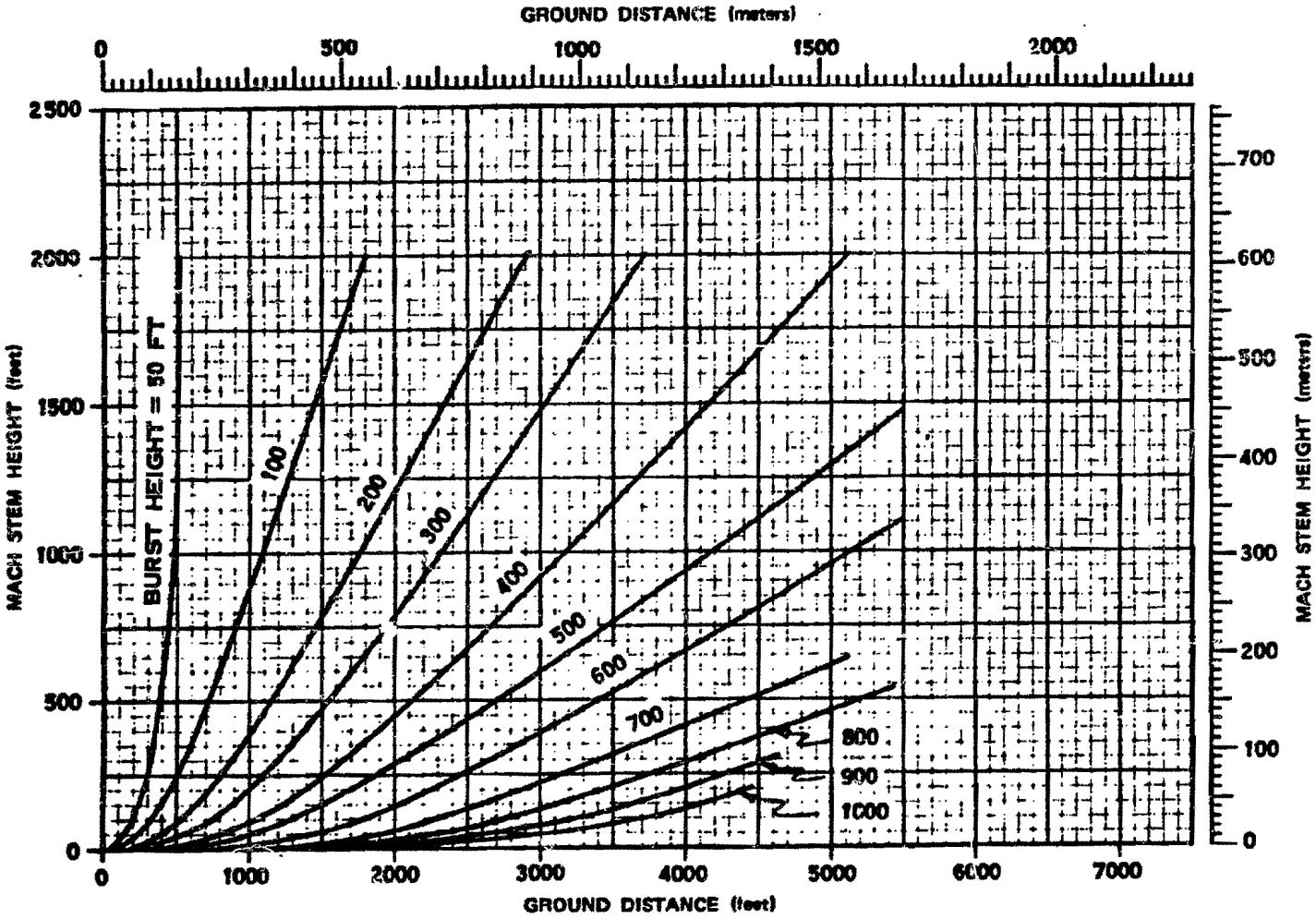

Figure 2-38. [redacted] Mach Stem Height for a 1 kt Explosion, Low Overpressure Region [redacted]

2-30 Criteria for Precursor Formation

Figure 2-39 shows heights of burst at which an explosion over a thermally nonideal surface is likely to produce a precursor. As indicated in Figure 2-39, bursts higher than 800 $W^{1/3}$ feet are not expected to form a precursor. This is the maximum height that will produce a precursor over asphalt, a surface that produces a precursor more readily than any other that has been tested. A burst below 650 $W^{1/3}$ feet will produce a precursor over desert sand. Since desert sand is considered a more typical nonideal surface than asphalt, it provides the basis for predicting precursors over most thermally nonideal surfaces.

Figure 2-39 also shows that a burst may be too low to produce a precursor as well as too high. At the ranges where a precursor might form, a contact surface burst of less than 30 kt is not expected to heat the surface sufficiently to produce a strong thermal layer; higher yields may create precursors over thermally nonideal surfaces.

Theories suggest that precursor formation depends not only on the amount of thermal energy absorbed by the surface, but also upon the time that is available for the thermal layer to form before the blast wave arrives. When time as well as thermal energy density is considered, theory indicates that the thermal layer and its influence on the blast wave might scale approximately as $W^{1/3}$, as indicated in Figure 2-39; however, no theory has yet been developed that explains the criteria for precursor formation in a completely satisfactory manner. For this reason, these criteria must be based on experimental data. Precursors have been observed from yields as high as 15 Mt; however, the yields that have been detonated between about 650 $W^{1/3}$ and 800 $W^{1/3}$ feet above the surface, and therefore the yields that are of value in confirming these criteria for precursor formation, are limited to the range of about 1 to 50 kt. Over this range of yields, the precursor seems to follow the cube root scaling; however, this may only result from the range of yields for which data are available being inadequate to reveal deviations. No reliability tolerances can be assigned to Figure 2-30, but if the surface is similar to desert sand, precursors may be predicted with reasonable accuracy for yields between 1 and 50 kt.

2-31 Overpressure Waveforms

The classical free air overpressure waveform (paragraph 2-12) is seldom found along the surface at overpressure levels above 6 psi. At higher overpressures, such waveforms approach the ideal for special surface conditions such as snow, ice, and water (where thermal effects are normally at a minimum). Even for these surfaces, minor mechanical effects may be present. For example, the rise time over water may not be instantaneous, and there may be a slight rounding of the peak of the overpressure waveform. When these near-ideal conditions exist, overpressure waveforms may be approximated by those for free air, shown in Figure 2-8.

In the simple case of ideal waveforms in free air, all of the properties of the blast wave, and therefore its damage potential, may be determined by specifying the ambient atmospheric conditions plus two blast parameters (for example, peak overpressure and positive overpressure impulse). When the blast wave loses its ideal characteristics, two other properties of the overpressure waveform become important: (1) for most overpressure-sensitive targets, a gradual rise to a given overpressure is less destructive than the abrupt rise of an ideal pulse; (2) as a result of the sustained overpressures often found in nonideal waveforms, a given peak overpressure may be associated with a much larger positive impulse than if overpressure pulse shape were ideal. Additional effects caused by changes in the dynamic pressure waveform are discussed in succeeding paragraphs.

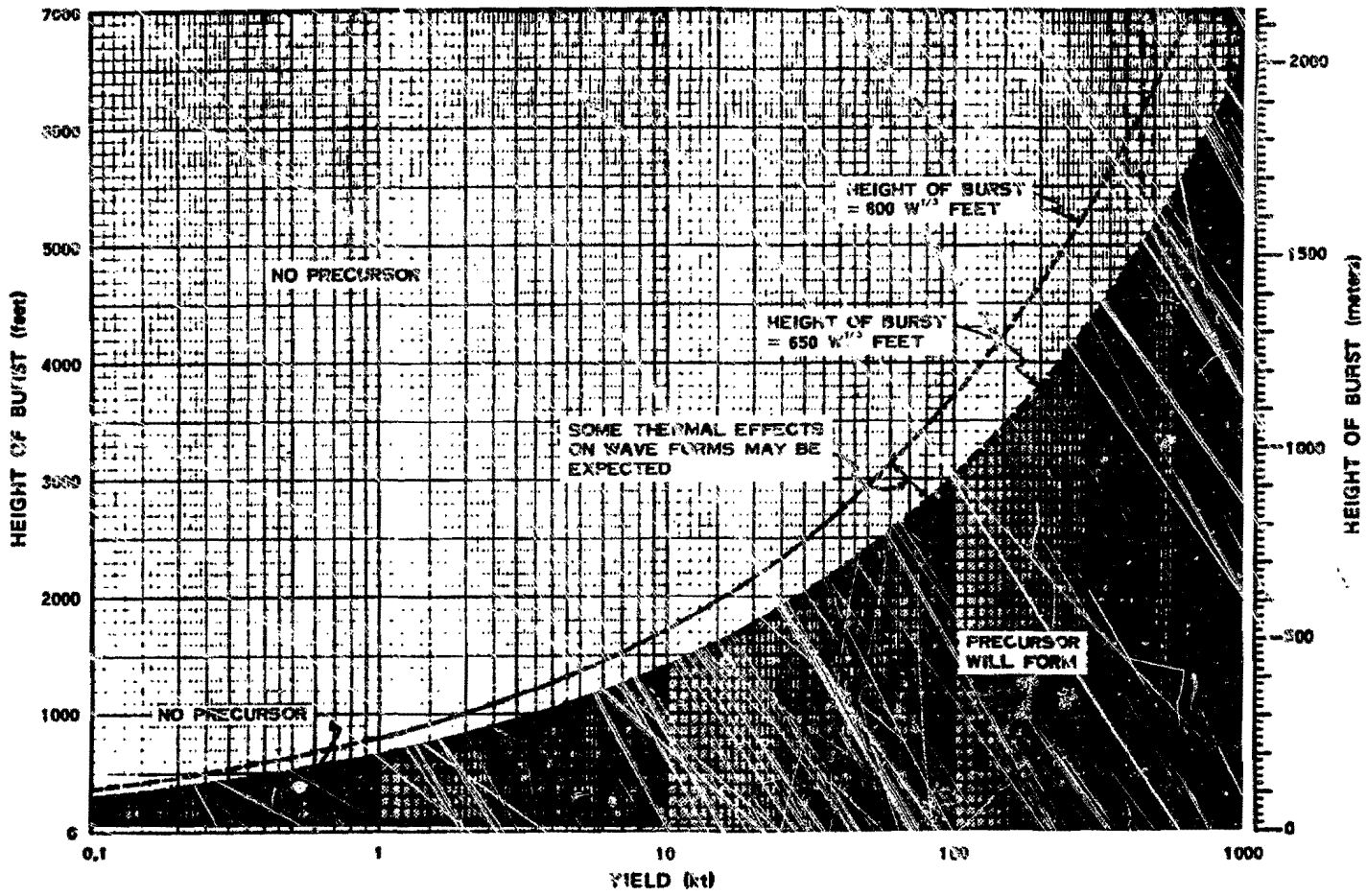

Figure 2-39. Criteria for Precursor Formation

A series of eleven waveforms characteristic of the blast wave over a thermally nonideal surface is shown in time sequence in Figure 2-40. Although the evolution of a precursor is a continuous process, the waveforms may be classified loosely into five types, according to the state of development of the precursor:

Type I: Waveform before precursor forms (a)
Type II: Development of the precursor (b, c, d)
Type III: Evolution of fully developed precursor (e, f, g)
Type IV: Decline of precursor (h, i, j)
Type V: Return to nearly ideal waveform (k)

The overpressure waveforms generated under any particular set of conditions depend strongly on the degree to which nonideal surface effects interact with the blast wave. In general, the more nonideal the surface conditions, the more nonideal will be waveforms near the surface. The waveforms shown in Figure 2-40 are typical for scaled heights of burst between 100 and 400 feet over flat desert surfaces. Characteristics of these waveforms are discussed below.

- Type I – Just before the precursor forms, the waveform *a* is relatively ideal.
- Type II – As the precursor starts to develop, a separate shock front forms in the thermal layer and moves out ahead of the main shock. In waveform *b* these two shock fronts are nearly ideal but, as the precursor develops, its diverging flow pattern weakens its own shock front. At the same time, the growing precursor interferes more strongly with the main blast wave, which apparently loses any semblance of a true shock front at the surface. Separation of the two peaks indicates the forward growth of the precursor; however, the second peak in waveforms *c* and *d* no longer marks the exact position of the main blast wave. Typical changes in Type II waveforms at early times are a rapid attenuation of the first peak and a rounding of the second peak. At later times, the second peak is attenuated more rapidly than the first, and the first loses its shock-like rise. The slow decay after the first peak in waveforms *c* and *d* is sometimes replaced by a plateau.
- Type III – As the distance from ground zero increases, the peaks and valleys become poorly defined. At close distances, the waveform *e* has a large rounded maximum followed by a slow decay, and a later and smaller second peak. At longer distances, the first peak is attenuated more rapidly than the second, and the two peaks become comparable in magnitude (f). The rise times also become longer. The second peak disappears at longer distances, leaving a low, rounded, flat-topped waveform *g* with a long initial rise and slow decay, during which there is considerable turbulence. This waveform is typical of strong precursor action.
- Type IV – Farther from ground zero, the thermal layer becomes less intense, and the precursor begins to weaken and lose forward speed. The second peak reappears, and both peaks become sharper. The rounded plateau in waveform *h* and the step-like appearance of *i* are typical. As the main shock overtakes the precursor, the waveform assumes an almost classical form *j* with a sharp rise to a more or less level plateau, followed by an essentially regular decay. This waveform is typical of the "clean-up" portion of the precursor cycle.
- Type V – After the precursor has disappeared, the pressure pulse again approaches a classical waveform *k*. This waveform is longer than it would be if a precursor had never formed.

Methods for determining ground dis-

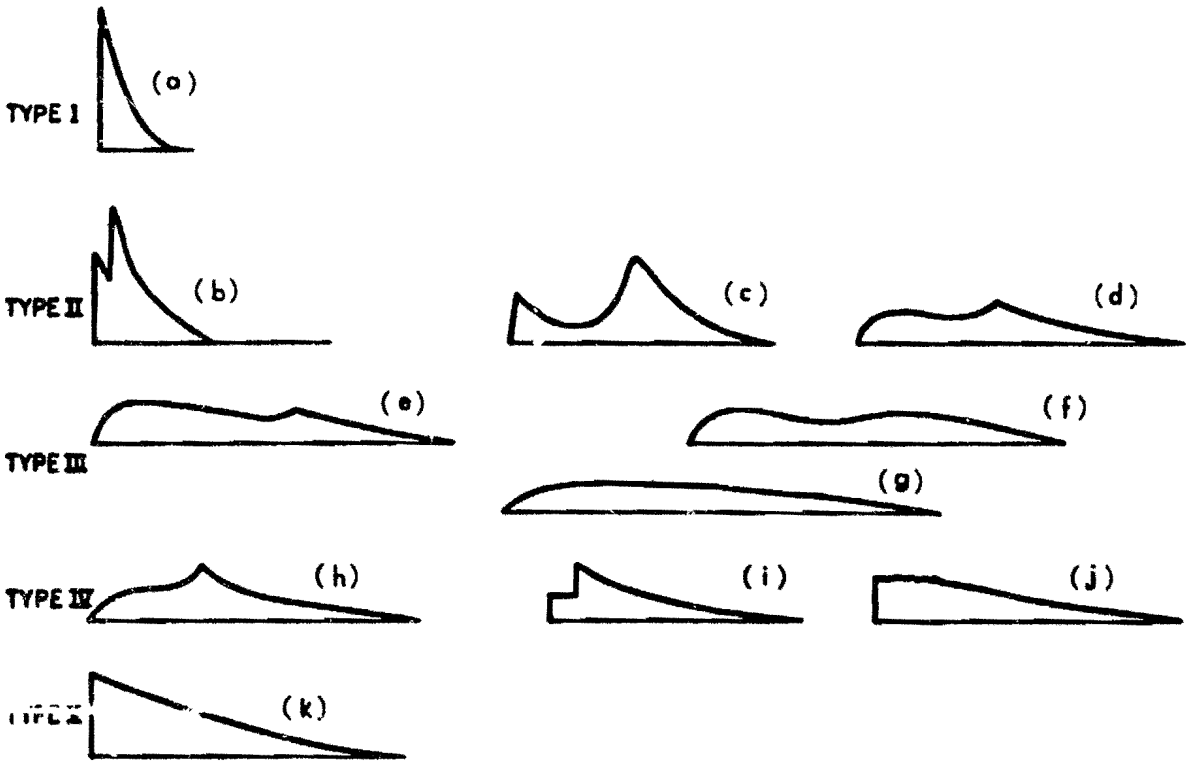

Figure 2-40. [redacted] Typical Sequence of Overpressure Waveforms Over Thermally Nonideal Surfaces [redacted]

tances at which the waveforms described above will occur are described in Problem 2-15.

2-32 Dynamic Pressure Waveforms

Dynamic pressure waveforms at the surface approach the classical shape shown in Figure 2-9 when the surface conditions are near-ideal. The conditions under which this occurs are more restricted than those for overpressure waveform. Differences result from surface conditions that do not lead to precursor formation but do lead to dust or spray loading of the air. Such surfaces are expected to modify the dynamic pressure waveform without changing the overpressure waveform to any great extent.

Dynamic pressure waveforms that appear over thermally nonideal surfaces are more difficult to measure than overpressure waveforms, and the measurements are subject to wider variations. For these reasons it is not possible at this time to provide a figure that shows zones in which various waveforms can be expected. However, representative waveforms have been constructed (Figure 2-41), and tentatively have been classified into five categories: A, B, C, D, and E (letters rather than Roman numerals are used with dynamic pressure waveforms to emphasize that the various types cannot be directly correlated with the waveform types used to classify overpressure waveforms). These waveforms are discussed below.

- Type A – Before the precursor forms, the waveform is relatively ideal (1).
- Type B – As the precursor starts to develop, the waveform shows two distinct peaks. The first, corresponding to the precursor, has a shock type rise in most cases. The second is larger than the first at close distances (waveforms 2 and 3), but at longer distances (waveform 4) it becomes comparable in magnitude to the first.
- Type C – As the precursor becomes fully developed, the waveform retains its double peak but loses its rapid initial rise time. Actual record traces have a very turbulent appearance. The second peak is smaller than the first (5) and tends to become indefinite with increasing distance (6).
- Type D – As the precursor becomes weaker, the waveform assumes an essentially single peaked form, characterized at close distances (waveform 7) by a low-amplitude plateau with a slow rise. Actual traces have a very turbulent appearance. As the distance from ground zero increases (waveform 8), the turbulence lessens, and the plateau develops a shock rise with either a flat top or a slow steady increase to a second shock rise, followed by a smooth decay. The second shock eventually overtakes the first (waveform 9), leaving a smooth, clean trace with a slight rounding after the initial shock type rise.
- Type E – After precursor cleanup, the waveform (10) resumes its approximately classical shape. Positive phase duration is longer than it would be at this distance if a precursor had not formed. This longer duration is more marked for dynamic pressure than for overpressure.

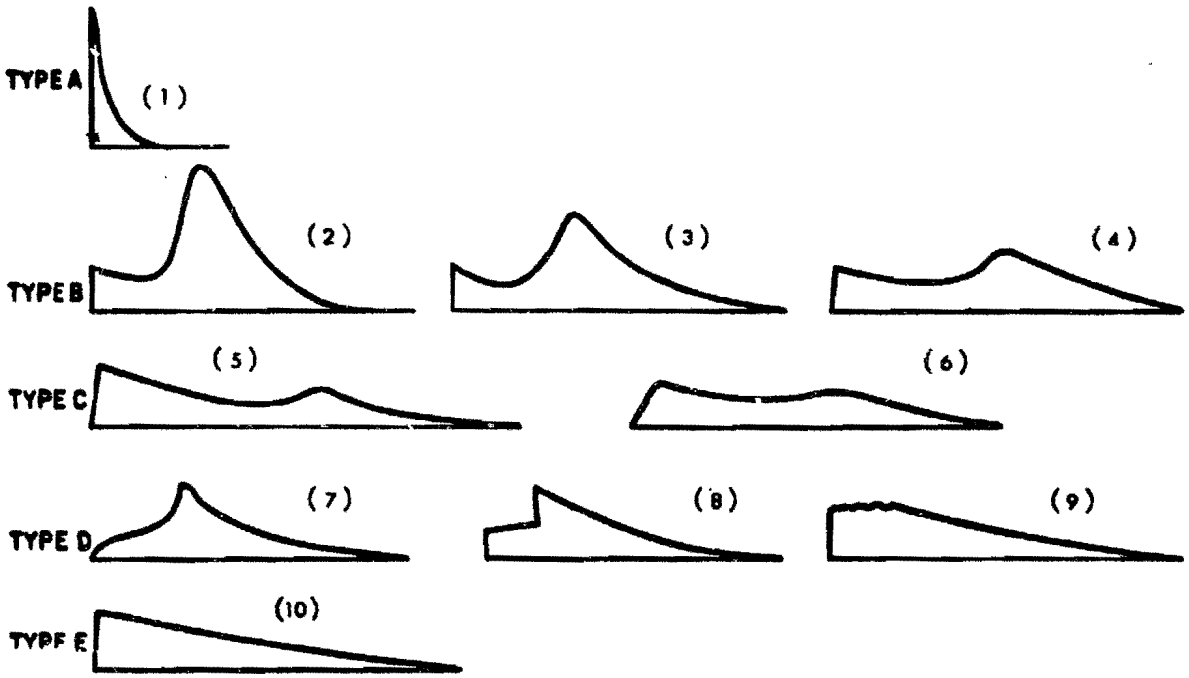

Figure 2-41. [redacted] Typical Sequence of Dynamic Pressure Waveforms Over Thermally Nonideal Surfaces [redacted]

Problem 2-15. Calculation of Distances for Overpressure Waveforms in the Precursor Region

Figure 2-42 shows zones, defined by height of burst and distance from ground zero, wherein overpressure waveforms depicted in Figure 2-40 might be expected to occur from a 1 kt explosion over a thermally nonideal surface. Neither the waveforms nor the ranges at which they occur can be predicted reliably for all conditions. The waveforms will be modified as height of burst changes; if the scaled height of burst is above 400 or below 100 feet, the waveforms may differ significantly from those shown in Figure 2-40. Any other surface effect that modifies the precursor also will modify the waveforms. For example, distortion of the overpressure waveform will be less severe if trees or shrubs decrease the velocity of the surface winds required for precursor formation (other surface interactions are discussed in paragraphs 2-20 through 2-22). Moderate thermal effects may produce disturbed waveforms that are neither ideal nor as extreme as those shown in Figure 2-40. Information from Figures 2-40 and 2-42 should be considered a useful guide, not an infallible prediction.

Scaling. For yields other than 1 kt, scale as follows:

$$\frac{h}{h_1} = \frac{d}{d_1} = W^{1/3},$$

where h_1 and d_1 are the height of burst and the ground distance for 1 kt, and h and d are the corresponding distances for a yield of W kt. If the surface is above 5,000 feet, or if atmospheric conditions at the surface differ from standard sea level conditions, the altitude scaling procedures described in paragraph 2-14 should be used.

Example

Given: A 100 kt explosion 600 feet above a thermally nonideal surface.

Find:

a. The ground distance to which a precursor may be expected to extend.

b. The waveform to be expected at the surface 1,800 feet from ground zero.

Solution: The corresponding height of burst for 1 kt is

$$h_1 = \frac{h}{W^{1/3}} = \frac{600}{(100)^{1/3}} = 130 \text{ feet.}$$

a. From Figure 2-42, the precursor zone extends to approximately 1,130 feet for a 1 kt explosion at a height of 130 feet (the zone indicating a Type V waveform shows the region where precursor characteristics disappear and the waveform approaches the classical shape (Figure 2-40)).

b. The ground distance for a 1 kt explosion corresponding to a distance of 1,800 feet for 100 kt is

$$d_1 = \frac{d}{W^{1/3}} = \frac{1{,}800}{(100)^{1/3}} = 390 \text{ feet.}$$

Answer:

a. The distance to which a precursor may be expected to extend from ground zero of a 100 kt explosion at a height of 600 feet is

$$d = d_1 W^{1/3} = (1{,}130)(100)^{1/3} = 5{,}240 \text{ feet.}$$

b. From Figure 2-42, a distance of 390 feet from ground zero of a 1 kt explosion at a

[redacted]

[redacted]

height of 130 feet falls within the zone corresponding to waveform II. This same waveform would be expected at a distance of 1,800 feet from a 100 kt burst at a height of 600 feet.

[redacted] *Reliability:* Specific reliability figures have not been set on the boundary positions in Figure 2-42. The zone boundaries are derived primarily from full scale tests over desert surfaces. Overpressure waveforms over other surfaces are subject to the variations noted above. Yield scaling is uncertain outside the range of 1 kt to 50 kt, but should be used in the absence of confirming experimental data. Altitude scaling is also a questionable procedure, but it should provide reasonable results for surface altitudes below 10,000 feet.

[redacted] *Related Material:* See paragraphs 2-12, 2-20 through 2-22, and 2-31.

[redacted]

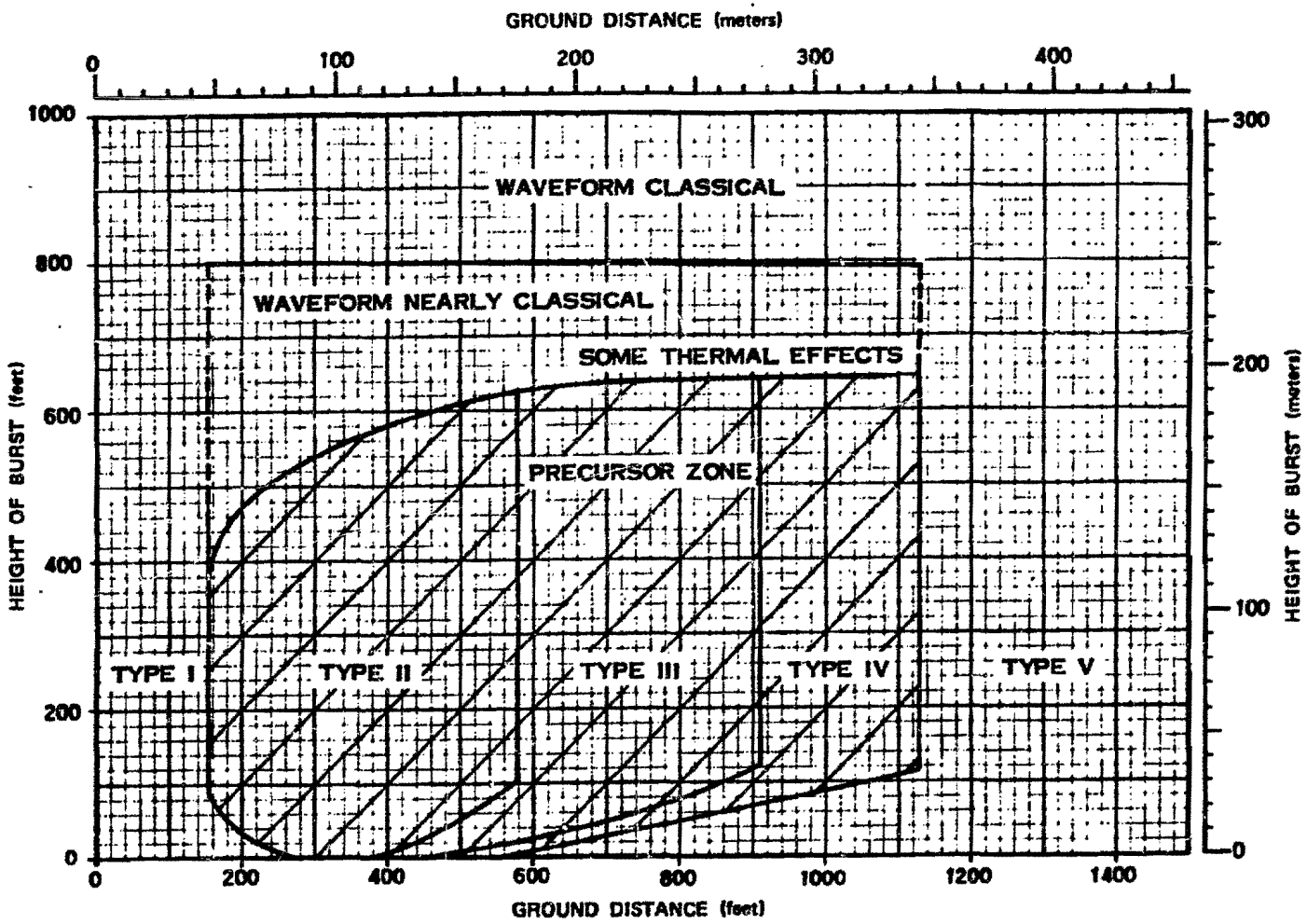

Figure 2-42. [redacted] Variation of Overpressure Waveform from a 1 kt Explosion Over a Thermally Nonideal Surface [redacted]

2-33 Effect of Rain and Fog on Overpressure

The effects of atmospheric moisture on blast propagation are not well known; however, theoretical studies agree qualitatively with the small amount of experimental data. As a strong blast wave propagates through air containing water droplets it vaporizes some or all of the water. Vaporization of the water absorbs energy that otherwise would be available for the blast wave to propagate through the air.* As a result, the blast wave is attenuated more rapidly in air that contains water droplets than in air that does not.

The effect of water droplets on peak overpressure may be calculated in terms of effective yield. This procedure is used to obtain lower calculated overpressures at some distance from the burst. Rain or fog has a negligible effect on the amount of available energy close to the nuclear source. The energy density within the fireball is orders of magnitude higher than the energy required to vaporize whatever water may be present, and the amount by which the suspended liquid increases effective air density, even under the extreme conditions within clouds producing severe thunderstorms, is not likely to exceed 2 percent.

Figure 2-43 shows the effective yield for three yields and two conditions of moisture content. Examination of these curves reveals several trends:

- The attenuation produced by heavy rain is greater than the attenuation produced by light rain or fog.
- Effective yield decreases as overpressure decreases, i.e., it decreases as distance (and, therefore, the amount of rain through which the blast wave must propagate) increases.
- At any overpressure level, the blast wave from a 1 kt burst is attenuated less than the blast wave from the two other yields. This difference results from the shorter distances for the 1 kt blast wave. Light rain or fog attenuates the blast wave from a 1 kt explosion to such a small extent that the curve is not included in Figure 2-43.
- At a given overpressure level, the blast wave from a 1 Mt burst is attenuated less than the blast wave from a 125 kt burst. This effect, opposite to that described above, probably results from the relatively large amount of hydrodynamic energy carried by the long-duration blast wave from a 1 Mt source.

The curves shown in Figure 2-43 are based on the assumption of uniform water content between the source and the target. In an actual rainstorm, this assumption is artificial. Typically, water content is several times as high within a rain cloud as it is below the cloud, but without such an assumption the analysis of rain effects would be unduly complex. Actual water distribution patterns are complex, different for different rainstorms, and generally unpredictable. The water densities used in the calculations correspond roughly to precipitation rates of 0.1 and 0.5 inches per hour.

*As a blast wave propagates through air, it continuously expends hydrodynamic energy at the shock front to compress and accelerate the air entering the blast wave. At the same time, the air behind the front expands and decelerates, thereby returning energy to the blast wave. The flow of energy in a weak shock wave resembles that in a sound wave. The expanding air returns nearly all of the energy that it received when it entered the shock front. Consequently, the attenuation of weak blast waves is due principally to spherical divergence. On the other hand, strong shock waves lose appreciable energy, because the sudden compression at the shock front is partially irreversible. Thus, the expanding air beyond the strong shock front returns less energy than was required to compress it, and the corresponding energy loss contributes to the attenuation of the blast wave. If the air contains water droplets, the energy extracted from the blast wave when the water evaporates is returned to the surrounding air when the water condenses; however, condensation occurs too slowly to contribute appreciable energy to the blast wave.

[redacted] Rain or fog effects should be evaluated only when the optimization of blast against soft targets is important, and then only if the rain or fog extends throughout a volume that includes both the target and the burst. HOB curves for thermally near-ideal surface conditions should be used with Figure 2-43 since thermal energy is attenuated by rain or fog and a wet surface is not expected to form a strong thermal layer.

[redacted] The effects of atmospheric moisture on other blast parameters, such as time of arrival, positive-phase duration, and dynamic pressure are not well known; however, theoretical considerations indicate that arrival times will remain essentially unchanged, positive-phase durations will be slightly reduced, and dynamic pressures will be slightly increased. Calculations for these other parameters should be made in the normal manner, without applying the yield correction factor obtained from Figure 2-43.

Problem 2-16. Calculation of Overpressure During a Rainstorm

Figure 2-43 shows the reduced yield in percentage of actual yield, that should be used for overpressure calculations under conditions of rain and fog. This figure should be used together with Figures 2-17 through 2-19 to obtain overpressure values under conditions of rain or fog.

Scaling. Interpolation between the curves of Figure 2-43 provides the only yield scaling available. After obtaining an effective yield from Figure 2-43, the scaling procedures described in Problem 2-9 are applicable.

Example

Given: A 50 kt explosion at a height of burst of 3,000 feet during a heavy rainstorm.

Find: The peak overpressure 4,000 feet from ground zero.

Solution: The corresponding height of burst and ground distance for a 1 kt explosion yield are

$$h_1 = \frac{h}{W^{1/3}} = \frac{3{,}000}{(50)^{1/3}} = 815 \text{ feet},$$

$$d_1 = \frac{d}{W^{1/3}} = \frac{4{,}000}{(50)^{1/3}} = 1{,}090 \text{ feet}.$$

From Figure 2-18, the peak overpressure expected in clear air is about 13 psi. At this peak overpressure, Figure 2-43 indicates that the effective yield during heavy rain is about 84 percent for 1 kt, 73 percent for a 125 kt burst. A probable effective yield for 50 kt should be between these values and may be about 77 percent. Uncertainty in the degree of attenuation produced by a rainstorm would cause the effective yield to vary according to the reliability estimates given below. This calculation will determine the most probable value of the peak overpressure rather than the upper and lower limits. The effective yield for further calculations is

$$50 \times 0.77 = 39 \text{ kt}.$$

The corresponding height of burst and ground distance for a 1 kt explosion are

$$h_1 = \frac{h}{W^{1/3}} = \frac{3{,}000}{(39)^{1/3}} = 885 \text{ feet},$$

$$d_1 = \frac{d}{W^{1/3}} = \frac{4{,}000}{(39)^{1/3}} = 1{,}180 \text{ feet}.$$

Answer: From Figure 2-18, the most probable peak overpressure is 10 psi.

Reliability: Figure 2-43 is based on theoretical calculations and a limited amount of data from small scale field tests and laboratory experiments. Thus, a high reliability cannot be assigned to the curves of Figure 2-43. The upper limit of the effective yield is 100 percent of the actual yield, while the lower limit is estimated to be 60 percent of the value obtained from Figure 2-43. If the burst is below or close to the cloud base in fairly uniform rainfall, somewhat greater reliability might be expected.

Related Material: See paragraphs 2-24 and 2-33. See also Problem 2-9.

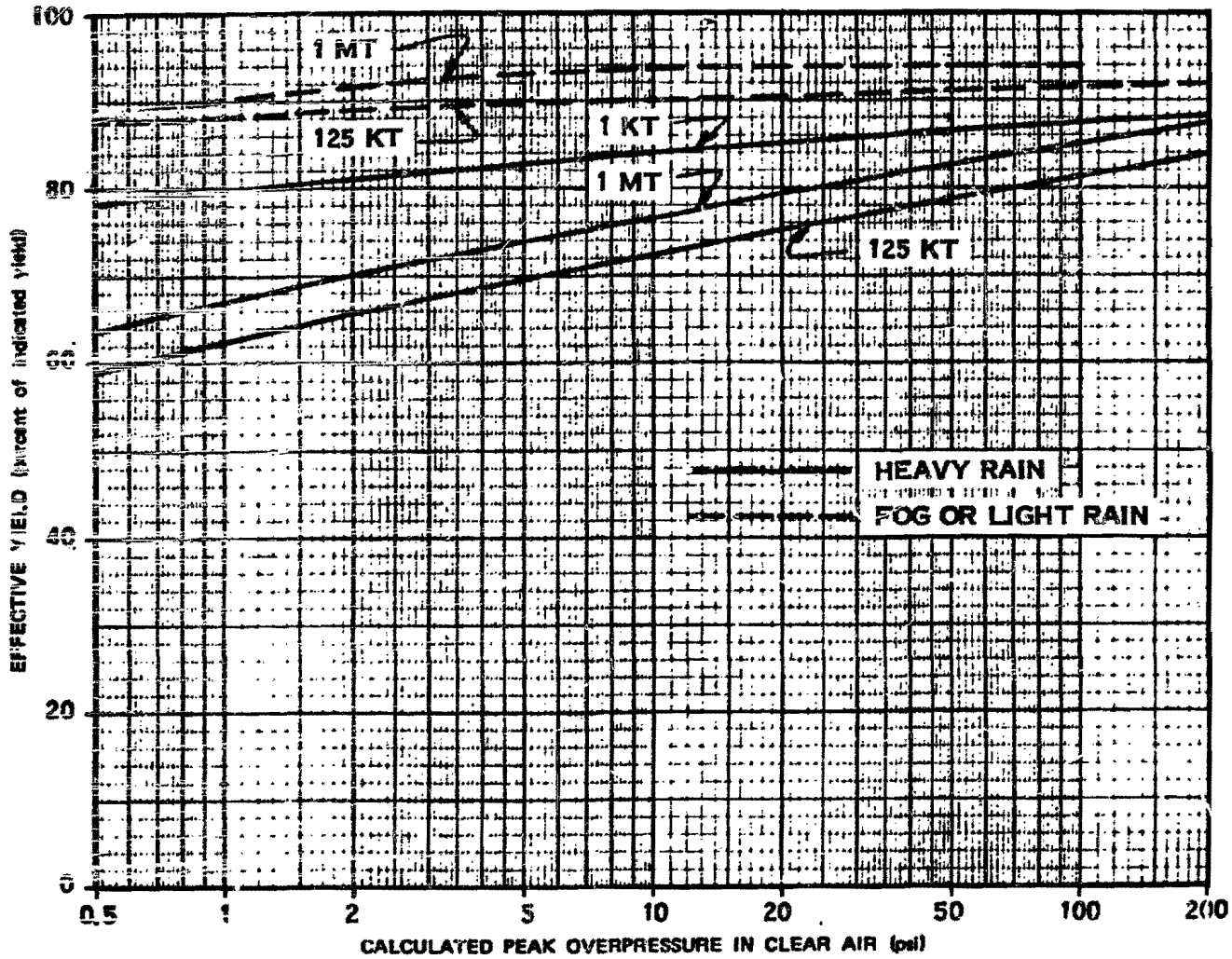

Figure 2-43. Reduction of Peak Overpressure at the Surface by Rain or Fog—Near-Ideal Surface Conditions

2-34 Peak Overpressure at the Surface of Deep Snow

When a shock front enters a layer of snow it is attenuated strongly. Drag forces on the snow crystals dissipate energy contained in the wind behind the shock front. The energy transmitted to the snow crystals is then consumed in compacting the snow layer.

Reflection occurs at the top surface of a deep snow layer just as it does at a ground surface. Momentum is conserved in the interaction, and, in the case of a ground surface, the process is analogous to a light, elastic object striking a heavy one. The light object bounces away, retaining most of the energy that it had before the collision. The heavy object receives a small amount of energy. A blast wave striking the earth transmits only a small fraction of its energy as ground shock; consequently, the earth's surface approximates an ideal reflector. A blast wave striking a snow surface is analogous to a ball bouncing from a heavy rug. The reflecting surface has a cushioning effect that makes it a poorer reflector.

In the case of a thin layer of snow, the cushioning effect ceases when the pressure wave penetrates the snow layer, reflects from the ground surface, and propagates back to the snow surface. At this time, the snow layer is supported by an internal pressure as high as the pressure produced by the blast wave reflecting from the surface; the reflecting qualities of the snow layer then approach the near-ideal reflecting qualities of the underlying surface.

Neither theoretical nor experimental data are available on the effects of thin snow layers on a blast wave, however, a rough calculation is enlightening. If a shock front in snow moves with a speed comparable to that of sound in air, a layer of snow one foot thick, struck by a normally incident blast wave, will absorb energy from the blast wave for about 2 milliseconds and will have the properties of a near-ideal reflecting surface after that time. This 2-millisecond interval is appreciably long only when compared with relatively sharp blast waves. For example, it might alter a 750 psi blast wave from a 1 kt source significantly. The overpressure pulse of this blast wave has an effective triangular duration (see Figure 2-10) of about 20 milliseconds. At lower overpressures, the pulse becomes broader. For a given overpressure, larger yields than 1 kt also produce broader pulses. This comparison indicates the following:

- If a blast wave with a very narrow pressure pulse strikes a thin layer of snow, the snow may alter the leading edge of the pressure pulse enough to reduce peak reflected overpressure.
- In a more typical situation, i.e., one for lower overpressures and yields greater than 1 kt, a thin snow cover affects such a small portion of the overpressure pulse that peak reflected overpressure is essentially the same as at a near-ideal surface.

Presently available experimental data on the properties of blast waves over deep snow surfaces are based on high-explosive (HE) experiments. In all of the tests, the snow layers were sufficiently thick to react as though they were infinitely thick. The thinnest snow layers tested (7 inches) correspond to snow layers about 60 $W^{1/3}$ feet thick (W in kt). For an 8 kt burst, this thickness is about 120 feet. Since snow layers thicker than about 120 feet compress to form glacial ice, the 7 inch snow layers have no real scaled counterpart for nuclear bursts larger than about 8 kt.

The available data for the effects of snow on the blast wave, when scaled for calculations of the blast wave from bursts larger than 1 kt may be applied with confidence only to regions such as the arctic, where large areas are covered by very thick snow layers.

[redacted] Scaling HE data over snow to the blast wave from a nuclear burst involves considerable uncertainty. Predictions of peak overpressure over a deep snow surface, are based on the following reasoning: (1) the HE studies show that snow reduces the ground distance to which a given peak overpressure extends by about 10 percent (this figure is never smaller than 0 percent or greater than 20 percent); (2) HE data over snow are not available at points near ground zero, and thus, the experimental data fail to show how much burst height should be changed for a given peak overpressure.

[redacted] Figures 2-18 and 2-19 may be used to predict peak overpressures over deep snow by reducing all ground distances by 10 percent.

[redacted] One significant effect of snow cover is that it forms a thermally near-ideal surface. Clean snow reflects most of the thermal radiation that strikes it. Dirty snow absorbs more energy than clean snow but it absorbs it in a way that is unlikely to produce a thermal layer. An experimental study indicates that thermal radiation from a nuclear burst will melt a negligible amount of a clean snow surface and that the water formed will be absorbed quickly by the remaining snow.

[redacted] An important unknown is the degree to which propagation through snow lengthens the rise time of the overpressure pulse. Even when snow cover is not thick enough to reduce peak reflected overpressure significantly, a layer of snow covering overpressure-sensitive targets may offer protection by reducing the sharpness of the overpressure pulse. This effect may be particularly important in evaluation of ground-shock damage to buried targets.

[redacted] In the absence of confirming data from nuclear tests over snow, use of the curves in Figures 2-18 and 2-19 must be regarded as tentative. Ground distances obtained from the curves are estimated to be reliable within ±25 percent for yields between 1 kt and 10 kt when used to predict peak overpressures over snow. Outside this range of yields, the curves may be used with somewhat less confidence.

2-35 Peak Overpressure at an Infinite Reflecting Surface [redacted]

[redacted] Curves showing peak reflected overpressure may apply to finite surfaces, such as the side of a building, or they may apply to the earth's surface, which is effectively infinite in extent. The two types of curves resemble one another except at angles of incidence close to 90°, i.e., at grazing incidence (see footnote to paragraph 2-17 for a summary of the conventions used in specifying the angular orientation of reflecting surfaces). At this grazing angle of incidence, a finite area produces no enhancement of the incident overpressure, the incident overpressure is sometimes called the "side-on" overpressure.

[redacted] A reflecting surface that is infinite in extent affects the blast wave differently. Figure 2-44 shows that the reflection coefficient $\Delta p_r/\Delta p$ of such a surface at grazing incidence is greater than 1. A blast wave having an angle of incidence of exactly 90° with a flat, infinite surface is, by definition, a contact surface burst. The surface of the earth confines the blast wave from a contact surface burst to half of the volume it would occupy in free air. As a result, peak overpressure is higher than it would be in free air; this fact is indicated by a reflection coefficient greater than 1.

[redacted] Figure 2-44 has two parts, corresponding to the regions of regular reflection and of Mach reflection. A peak occurs near the boundary between the two regions; at the lower incident overpressures, this peak shows a higher reflected overpressure than that produced by a blast wave striking a surface head-on. The same phenomenon appears in the height-of-burst charts as the knee of an overpressure curve.

[redacted] At incident overpressures greater than

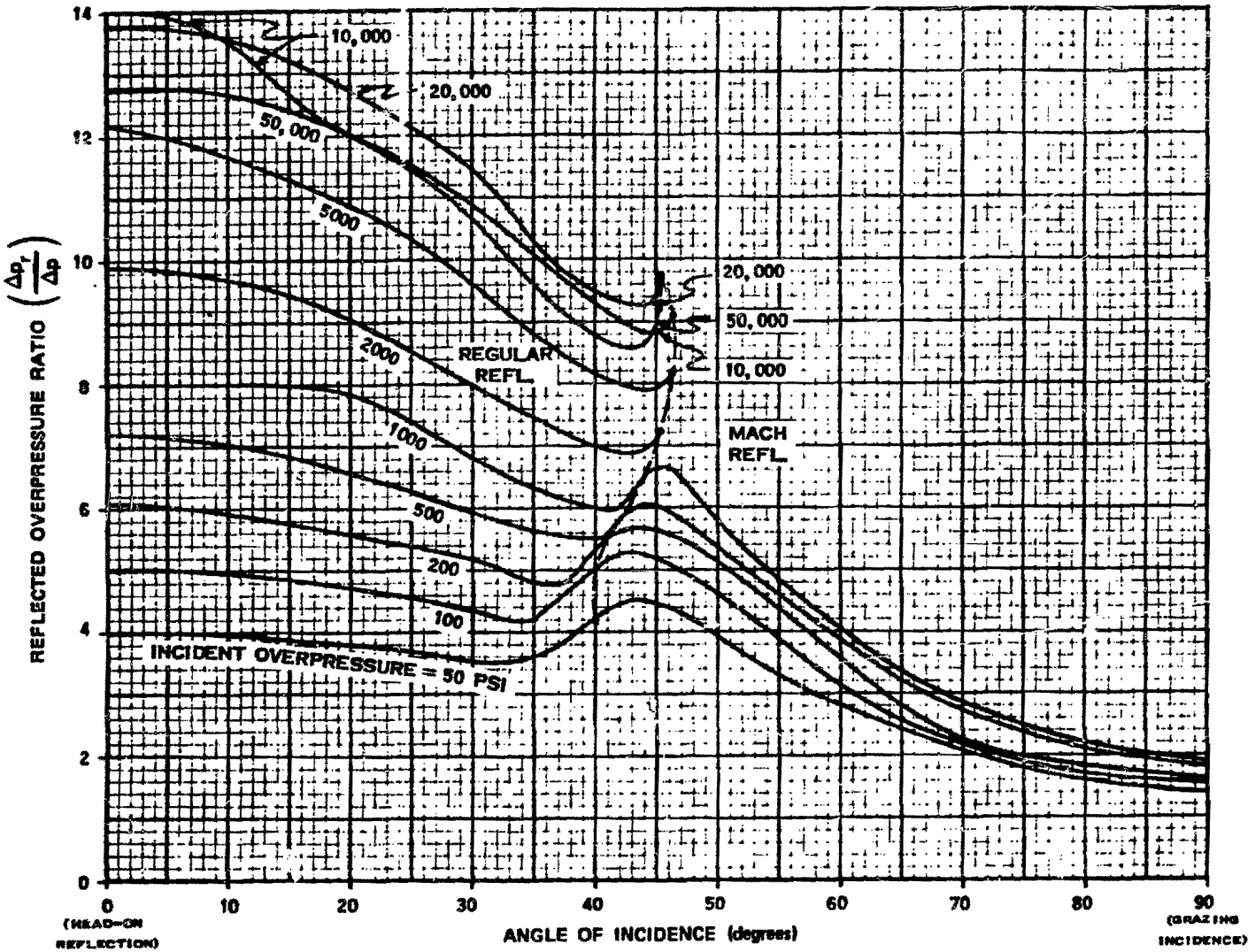

Figure 2-44. [redacted] Reflection Properties of Strong Shock Waves at an Infinite Surface [redacted]

5,000 psi, the curves in Figure 2-44 deviate from the regular pattern seen at lower incident overpressures. These deviations result from the high temperatures produced at the shock front, which cause dissociation and ionization of the air atoms to absorb energy that would otherwise increase the pressure of the gas.

The data in Figure 2-44 may be replotted to prepare a height of burst graph. An intermediate plot, consisting of a family of curves, each for a given angle of incidence should be plotted first. Figure 2-45 shows, as an example, the curve for an angle of incidence of 30°. Slant ranges for this intermediate plot are found as a function of incident overpressure from Figure 2-2, the overpressure-distance curve for free air. The data from the intermediate plot may be transferred to the HOB chart by plotting slant range and angle of incidence as shown in the inset of Figure 2-45.

Such a transformation should lead to the HOB chart shown in Figure 2-17; however, certain discrepancies exist between that HOB chart and the data in Figure 2-44. The principal difference is that the peaks shown at angles near 45° in Figure 2-44 have been rounded off in the HOB chart since it is uncertain how well the data in Figure 2-44 describe the actual reflecting properties of the surface of the earth for reasons described below. Although the peaks shown in Figure 2-44 probably occur, the angle at which they occur may be different from that indicated. Therefore, a transformation of every detail of the curves in Figure 2-44 to the HOB chart implies a more detailed knowledge of the shapes of the HOB curves than actually exists.

Uncertainty of the data in Figure 2-44 arises from the way in which these data had to be obtained. The Mach reflection portions of the curves in Figure 2-44 were obtained theoretically, using the shock-wave equations and the air equation of state given in Appendix A. The calculation is complex, involving successive approximations that are most appropriately handled on a computer.

A large portion of the regular reflection regions of the curves were obtained experimentally. Many data points from nuclear tests document the low pressure curves at angles close to 90°, and theory plus a few data points were used to extrapolate the data to smaller angles and to the highest overpressures shown.

Accuracy of the Mach reflection data is limited because the calculations for these data were based on an ideal reflecting surface. When the burst height is low, errors may result from the resiliency of the earth's surface (or, in the extreme case, cratering), and from thermal energy extracted from the fireball by absorption at the surface. Dirt thrown into the air may alter blast wave properties. Accuracy of the regular reflection data is limited by the difficulty of obtaining a large number of accurate blast wave data points at very high overpressures. These uncertainties are the reasons for smoothing the overpressure contours in Figure 2-17. They are also the reasons for omitting, as unrealistic, curves for peak reflected overpressures higher than 10,000 psi.

2-36 Peak Overpressure at a Finite Reflecting Surface

Since a finite surface may cause either regular or Mach reflection, the curves showing reflected overpressure at a finite surface resemble those showing reflected overpressure at an infinite surface.

Figure 2-46 shows curves of reflected overpressure as a function of peak incident overpressure. These curves apply directly to the reflection that occurs at flat surfaces (e.g., sides of buildings) when they are struck by the nearly vertical shock front which characterizes the Mach stem. Although the curves also may be used to determine peak reflected overpressure from the incident free air blast wave when regu-

[redacted]

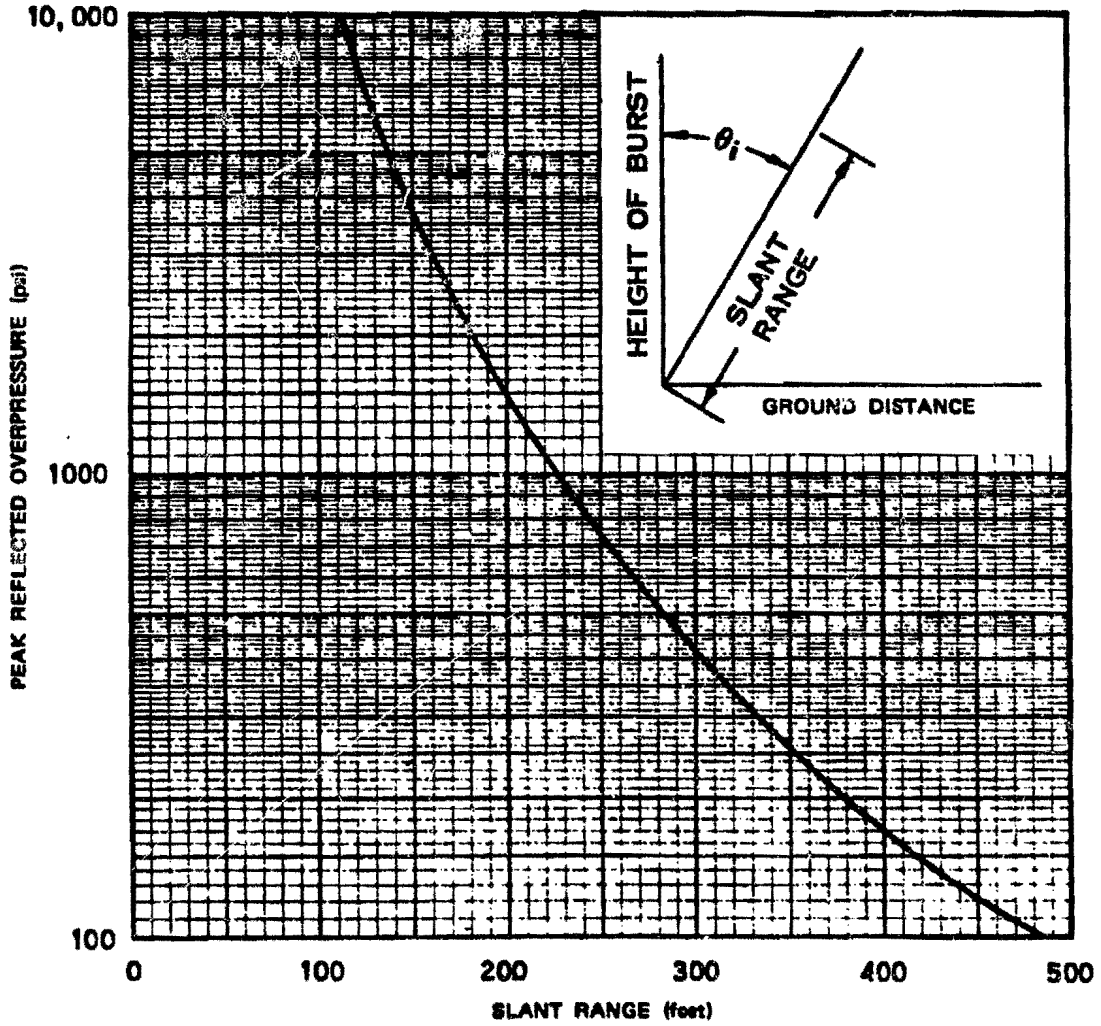

Figure 2-45. [redacted] Peak Reflected Overpressure Versus Slant Range for an Angle of Incidence θ_i of 30° [redacted]

[redacted]

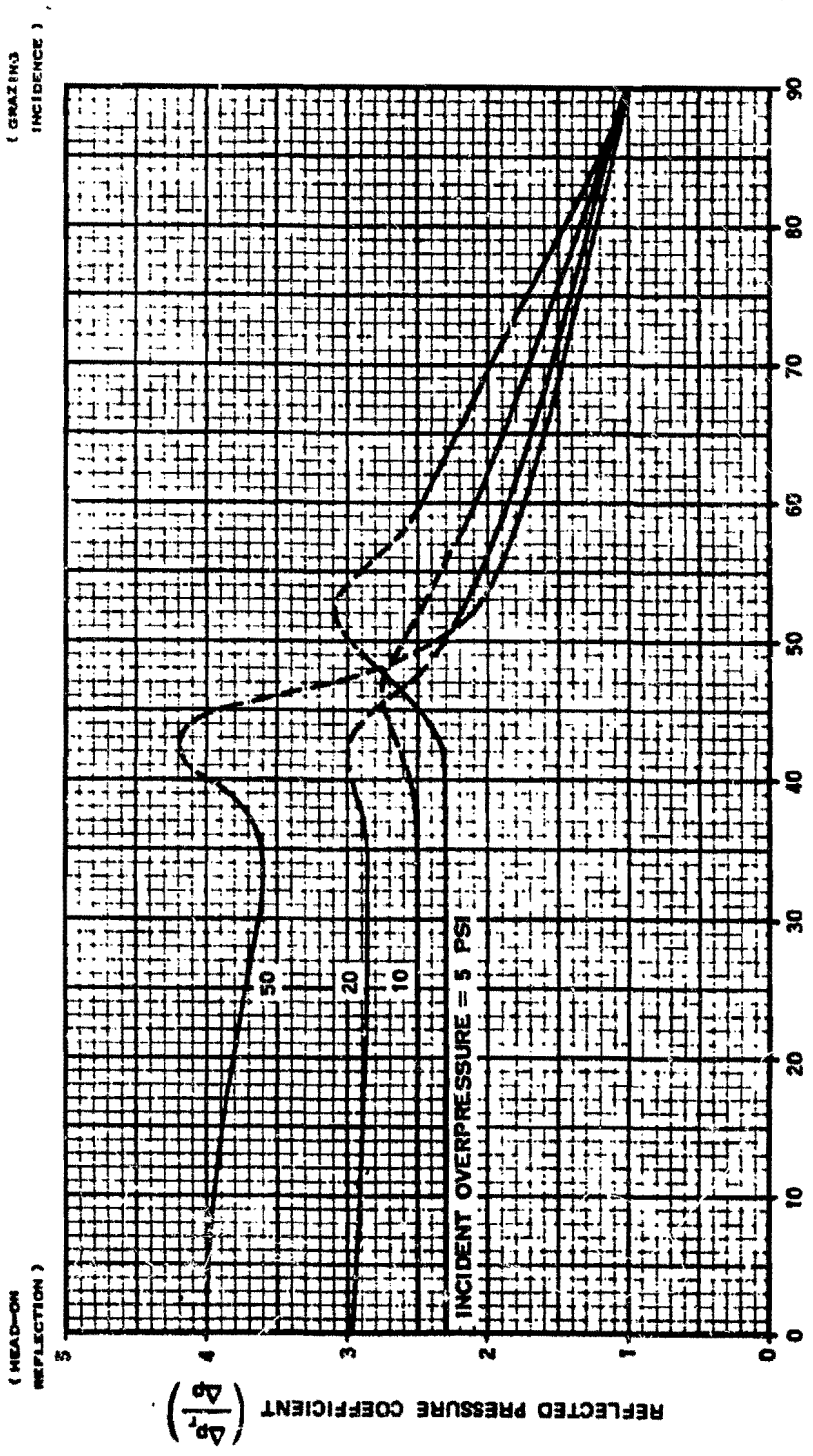

Figure 2-46. [redacted] Reflection Properties of Shock Waves at a Finite Surface

lar reflection is occurring at the surface of the earth, they do not represent the total effect of multiple reflections that occur when this direct wave strikes the angle formed by the earth and a vertical surface.

These curves only predict the peak overpressure produced when the shock front arrives. In many problems, the total waveform produced by the blast-target interaction also is important; however, the latter is a function of target dimensions as well as blast wave properties as discussed in Section II of Chapter 9 and Section I of Chapter 11.

2-37 Peak Overpressure at Rising and Falling Slopes (U)

If a shock wave that is travelling along the ground surface encounters a change in slope, the characteristics of the shock wave will change. If the terrain is characterized by large changes of slope, the changes in the blast wave can be significant. They can result in an overpressure increase by more than a factor of two or a decrease by more than a factor of three.

Interactions with real topography can be exceedingly complex. Therefore both experimental and theoretical studies have, for the most part, dealt with idealized, simplified terrain features. Techniques have been devised for predicting the characteristics of the shock waves that encounter changes in terrain, and methods for applying these techniques to real terrain have been devised.

If the level terrain in front of a slope is in the region of Mach reflection, the blast-wave incident on the slope will have a nearly vertical shock front, the Mach stem. (The nearly hemispherical shock front produced by a contact surface burst is considered a special case of an incident Mach stem.) If the level terrain in front of the slope is in the region of regular reflection, the first shock front striking the slope is the free air blast wave from the nuclear source. This shock front is not vertical, but forms an angle of less than 90° with the level ground in front of the slope.

When the nearly vertical Mach stem strikes a rising slope, the incident wave undergoes either regular (two-shock) or Mach (three-shock) reflection, depending on the angle that the slope makes with the surface over which the shock wave has been moving and on the strength of the incident shock. For a falling slope, diffraction always occurs; the shock wave curves to orient itself normal to the slope. Differences between regular and Mach reflection on a rising slope are illustrated in Figure 2-47. Diffraction on a falling slope is illustrated in Figure 2-48 (in these figures, the shock wave direction of propagation is assumed to be normal to the slope contours).

Similar interactions occur when the direction of shock wave motion makes an angle Φ with the line of steepest ascent or descent. The geometry of such an interaction is shown in Figures 2-49 and 2-50. In these figures, the angle that is important is θ, the effective slope angle. Its relationship to θ_s, the slope angle is

$$\sin \theta = \sin \theta_s \cos \Phi$$

This relationship is plotted in Figure 2-51. The relationship holds for both rising and falling slopes.

When a Mach stem encounters a rising slope, the incident overpressure and the effective slope angle determine whether regular or Mach reflection will occur. The conditions under which regular or Mach reflection occurs are shown in Figure 2-52.

Figure 2-53 shows how effective slope angle affects the peak overpressure produced by a 10-psi incident Mach stem. Similar data may be obtained from Figure 2-46 for other overpressures by noting that the angle of incidence to use with Figure 2-46 is equal to 90° minus the effective slope angle. The left-hand side of Fig-

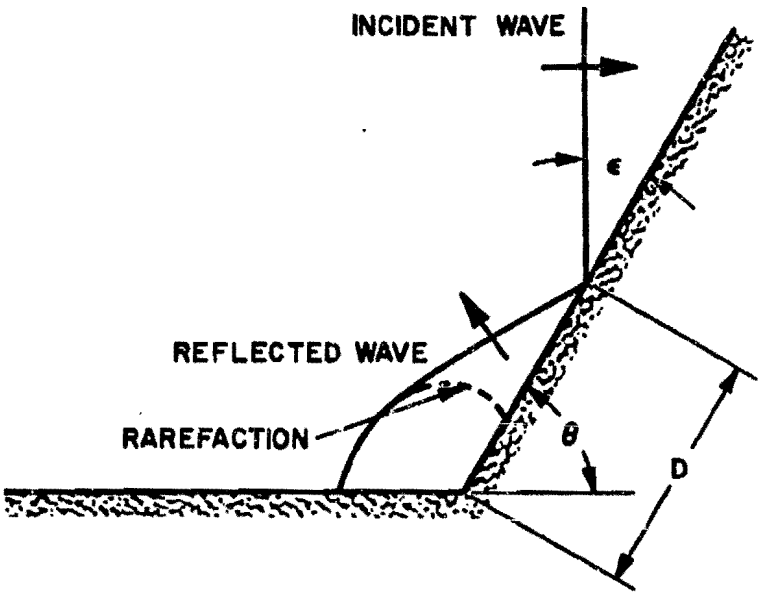

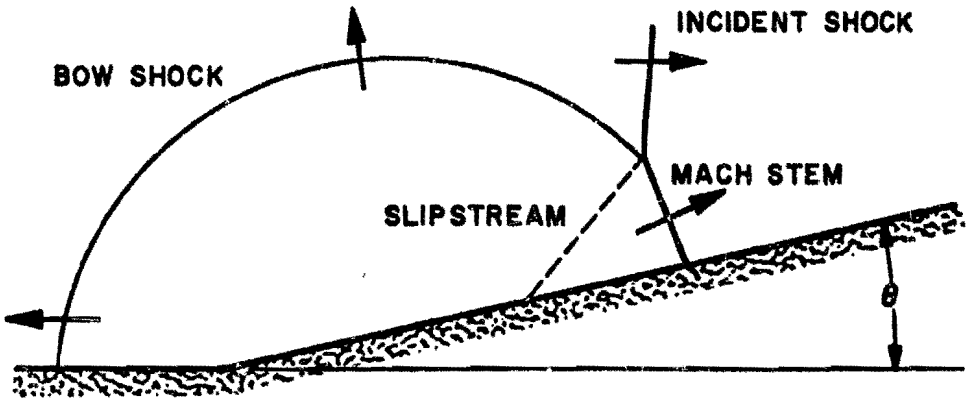

Figure 2-47. [redacted] Regular and Mach Reflection Patterns Formed by a Mach Stem Striking a Rising Slope [redacted]

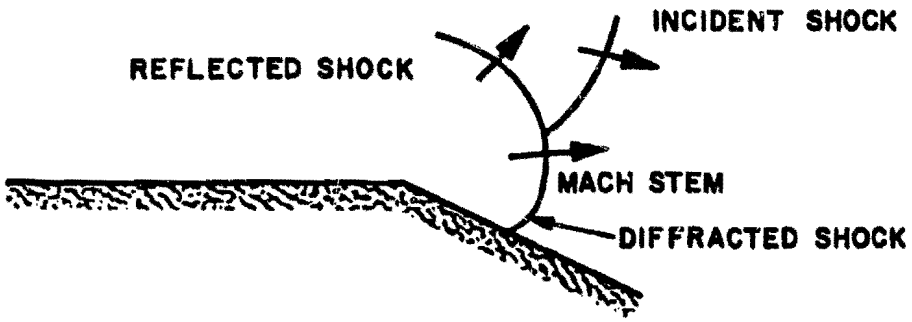

Figure 2-48. [redacted] Diffraction Shock Front Pattern Formed by a Mach Stem at a Falling Slope [redacted]

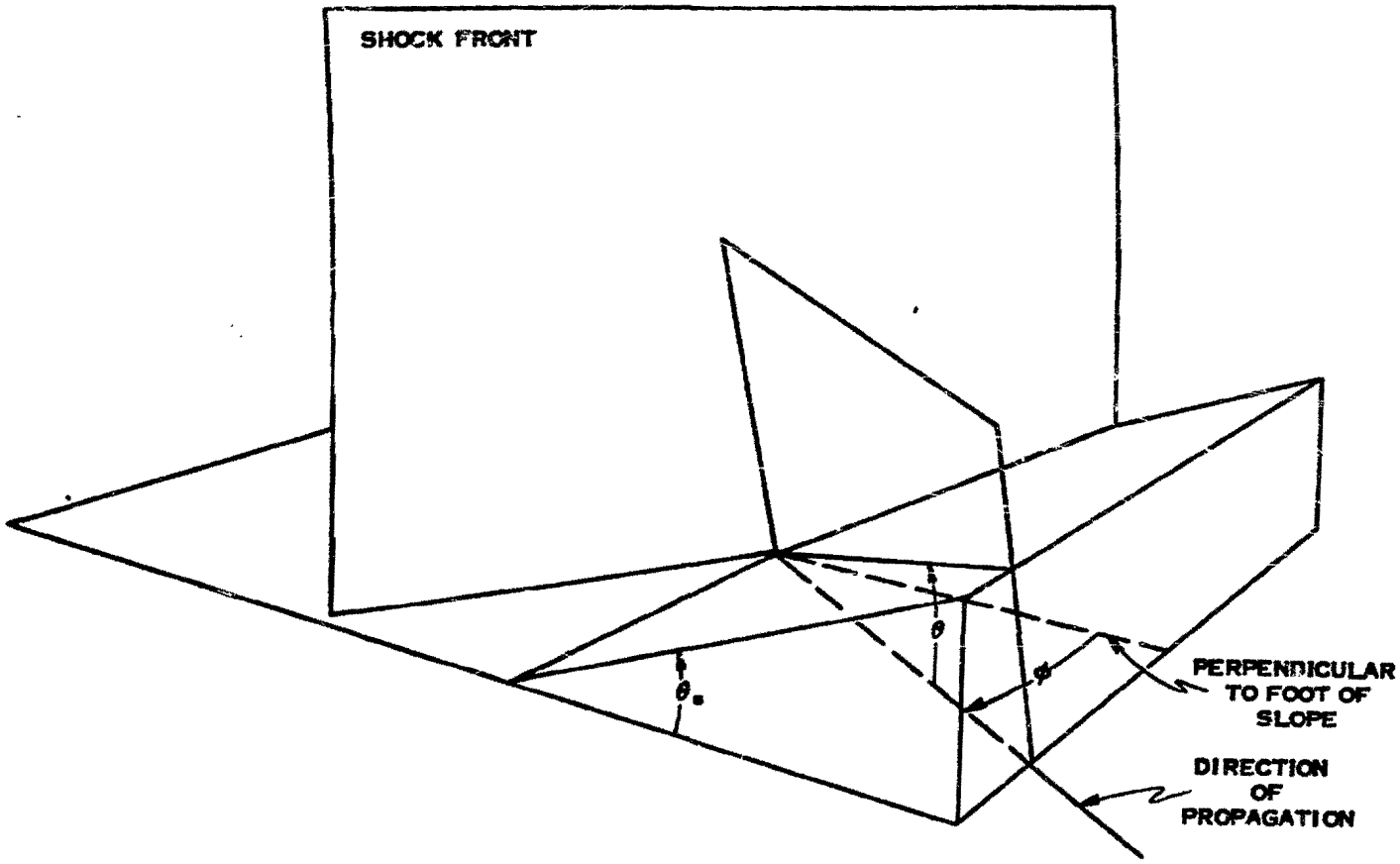

Figure 2-49. Mach Stem at a Rising Slope

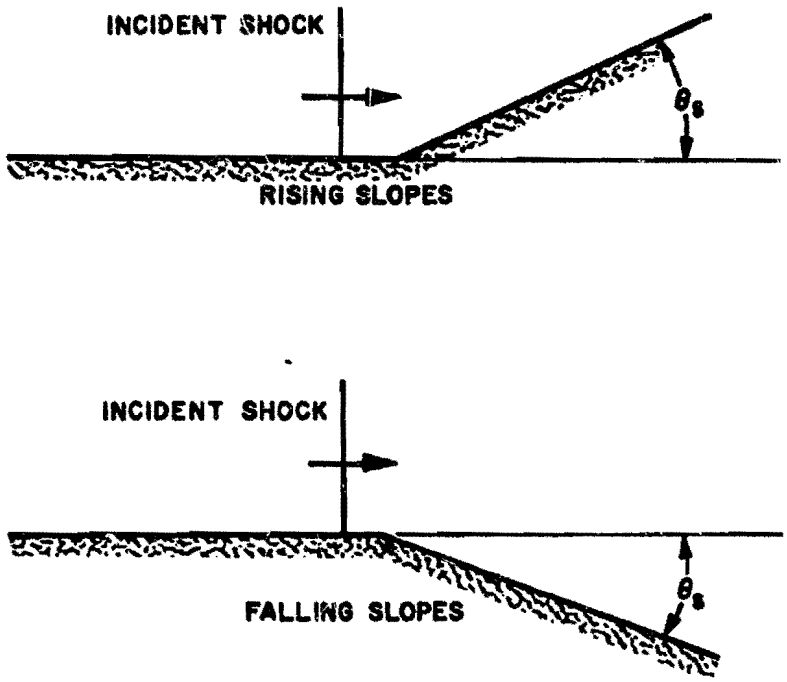

Figure 2-50. Sectional and Plan Views of a Shock Front Approaching a Slope

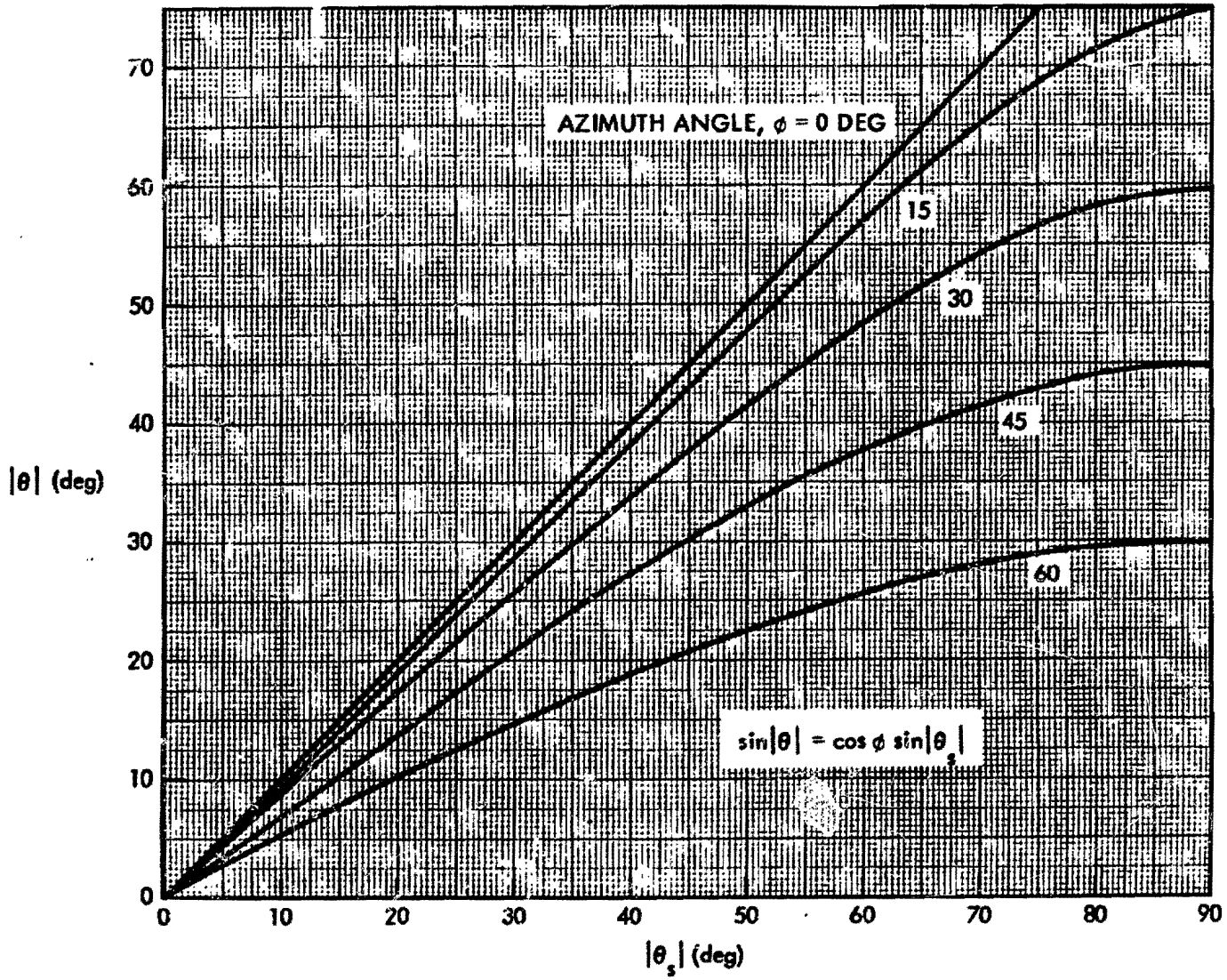

Figure 2-51. Effective Slope Angle θ as a Function of Slope Angle θ_s for Various Angles of Azimuth

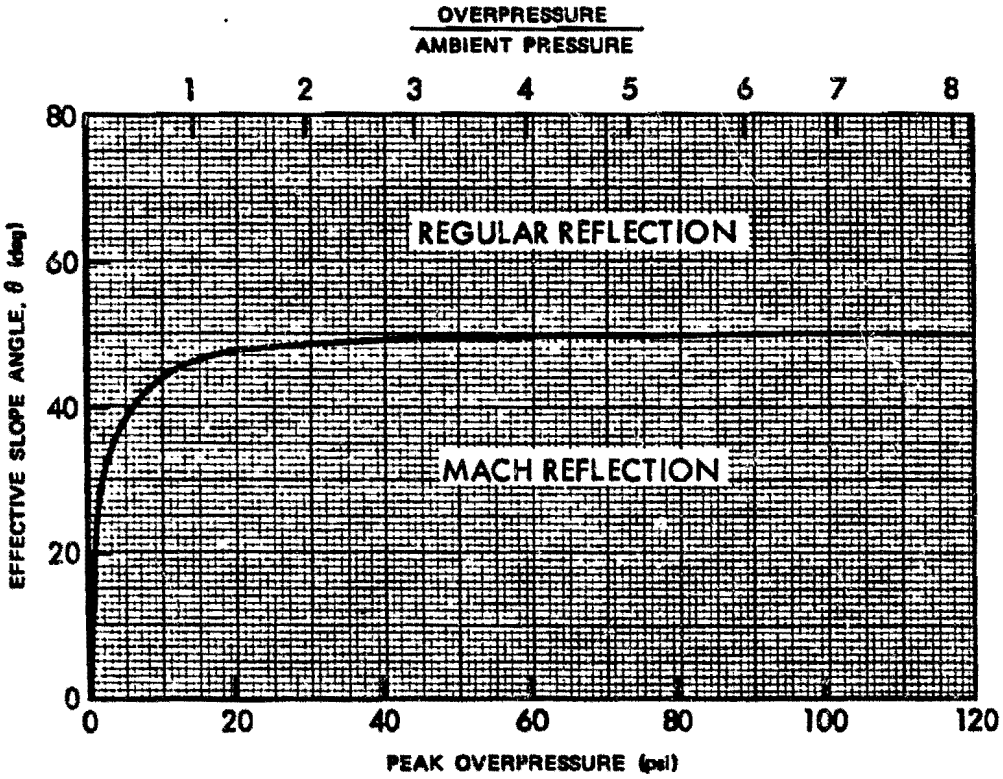

Figure 2-52. [redacted] Conditions for Regular or Mach Reflection of Incident Mach Stem [redacted]

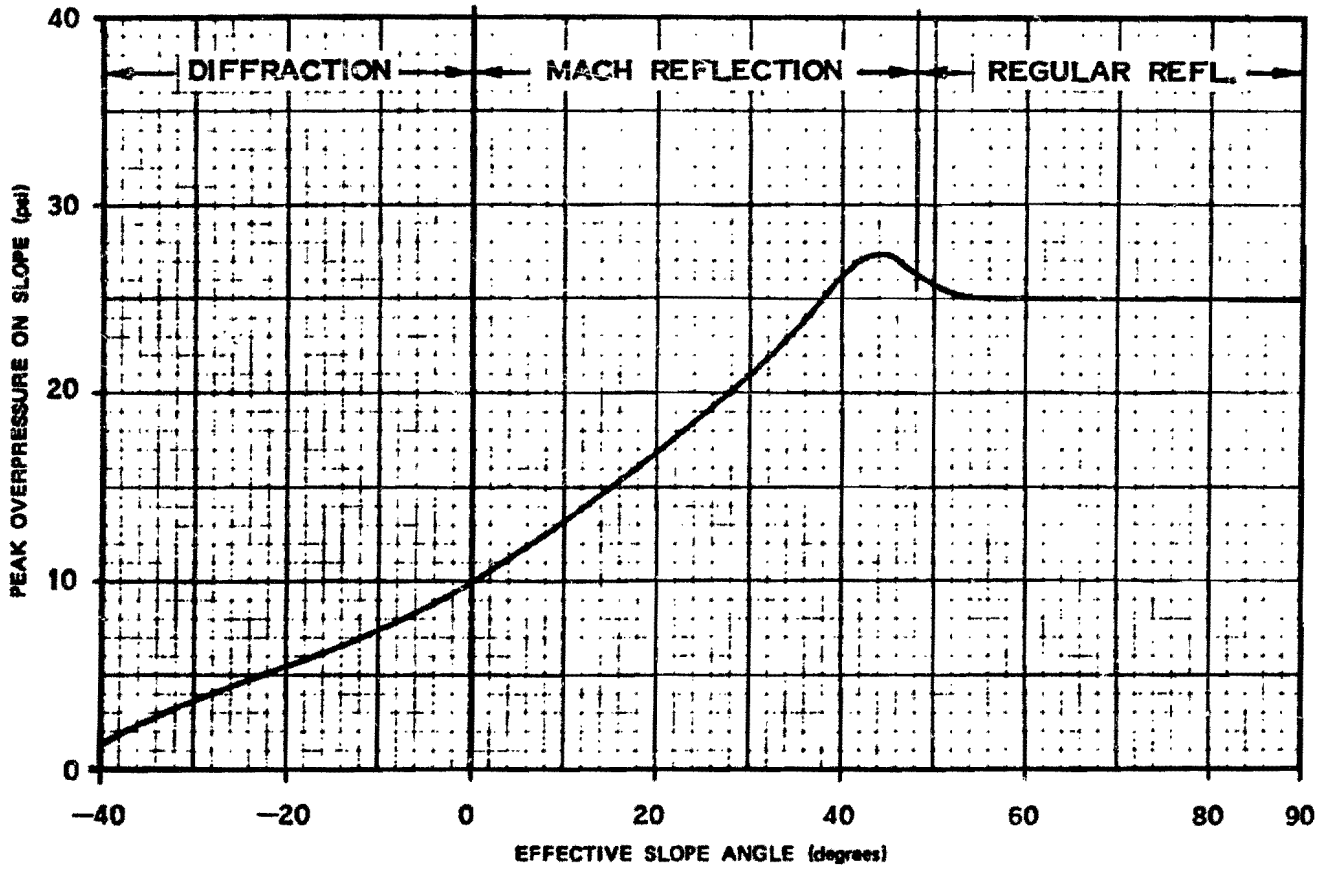

Figure 2-53. [redacted] Peak Overpressure Produced on a Slope by a 10-psi Incident Mach Stem as a Function of a Slope Angle [redacted]

ure 2-53 shows the effect of diffraction at a falling slope.

Figures 2-54, 2-55, and 2-56 show similar data in a more convenient form. The overpressure scales only apply to reflection of shock waves in a sea level atmosphere. At other ambient pressures, the scales marked "overpressure/ambient pressure" should be used. Note that Figure 2-54 is plotted for various values of the angle of incidence while Figures 2-55 and 2-56 are plotted for various values of the effective slope angle.

If the incident blast wave has been undergoing regular reflection before it encounters the rising or falling slope, approximate blast wave characteristics at the target can be determined by (1) constructing a sectional plot showing both the target area and the burst point, (2) drawing a "reference-plane line" through the target area showing the general plane in the vicinity of the target, and (3) drawing a line from the burst point perpendicular to the reference-plane line.

As Figure 2-57 shows, the length of the perpendicular is the effective height of burst; the length along the reference plane line between this perpendicular and the target area is the effective ground range or distance from ground zero, and shock-wave characteristics may be determined from height of burst charts. Although this technique does not take into account the effect of azimuth angle Φ (where the shock wave moves at an angle to the line of steepest ascent or descent), further refinement is rarely justified.

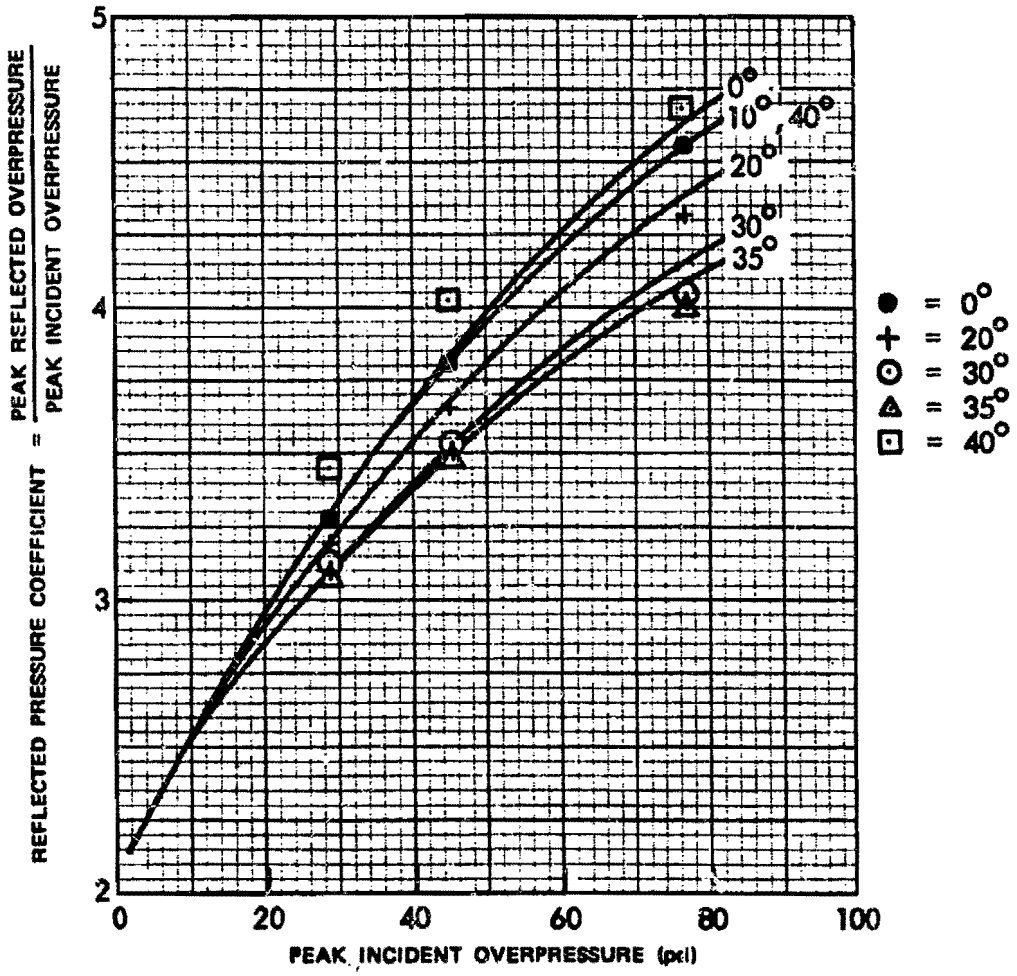

Figure 2-54. [redacted] Reflected Overpressure Coefficients for Regular Reflection as a Function Incident Overpressure for Various Angles of Incidence [redacted]

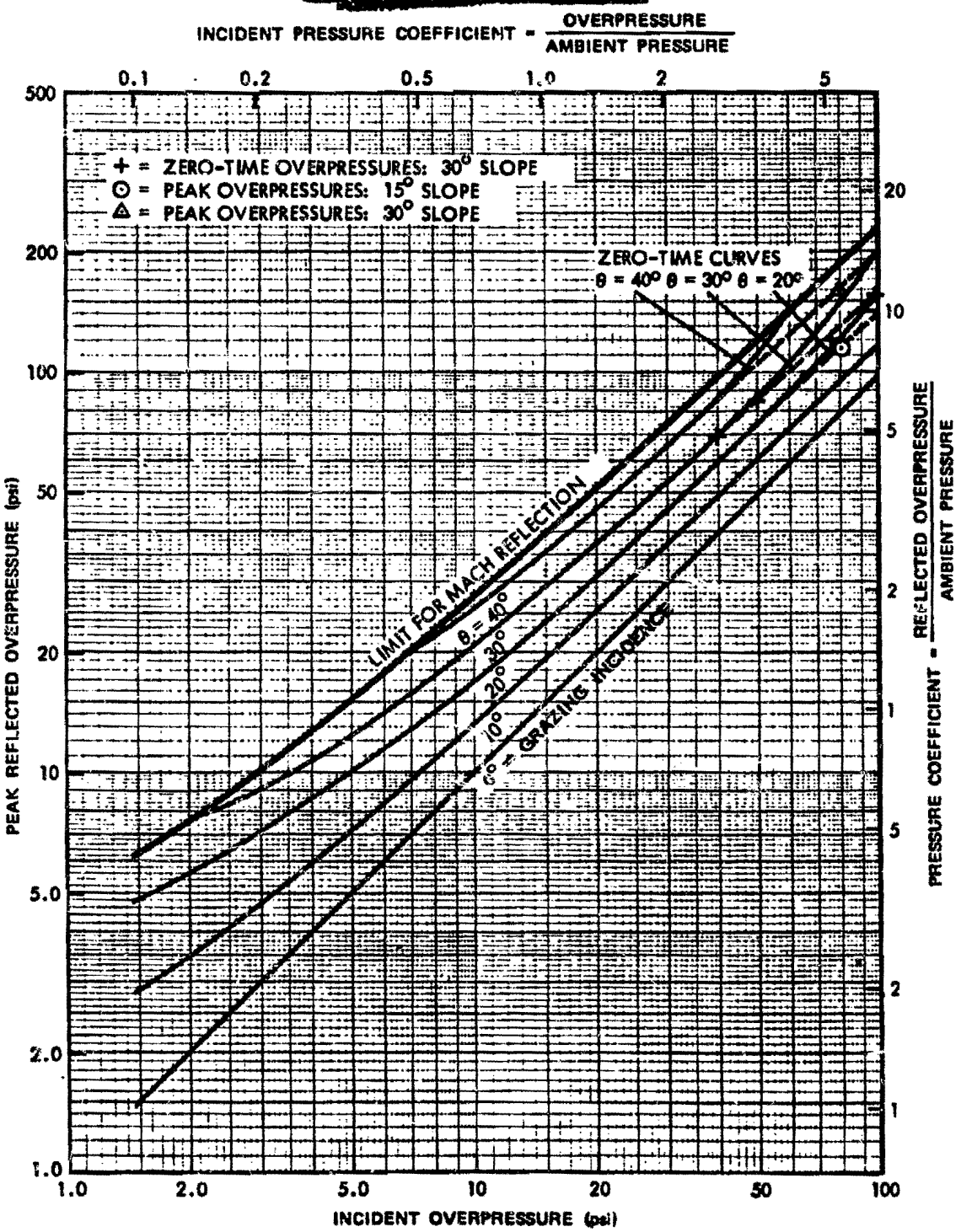

Figure 2-55. [redacted] Reflected Overpressure as a Function of Incident Mach-Stem Overpressure for Mach Reflection for Various Slope Angles [redacted]

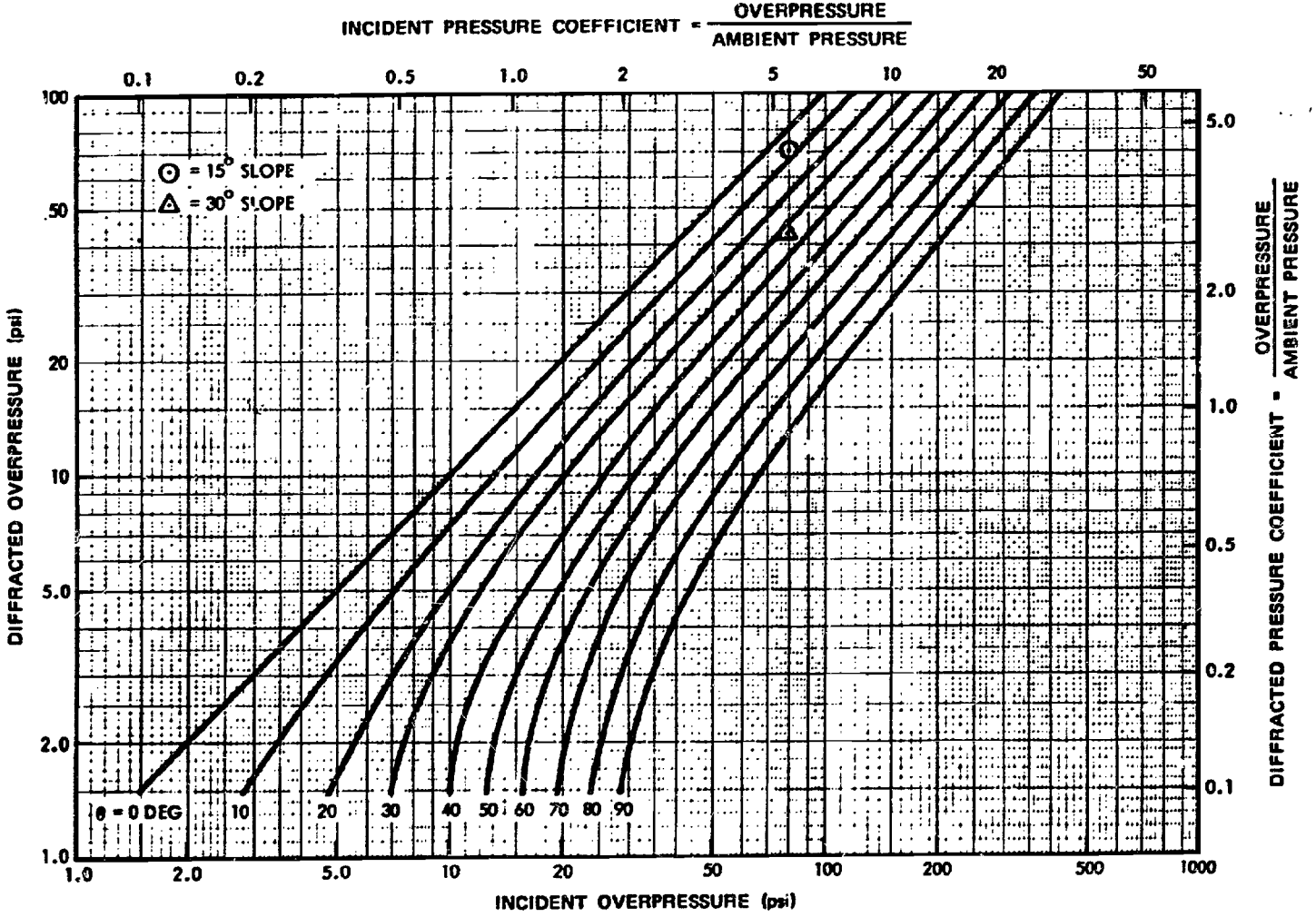

Figure 2-56. Diffracted Overpressure as a Function of Incident Mach-Stem Overpressure for Various Slope Angles

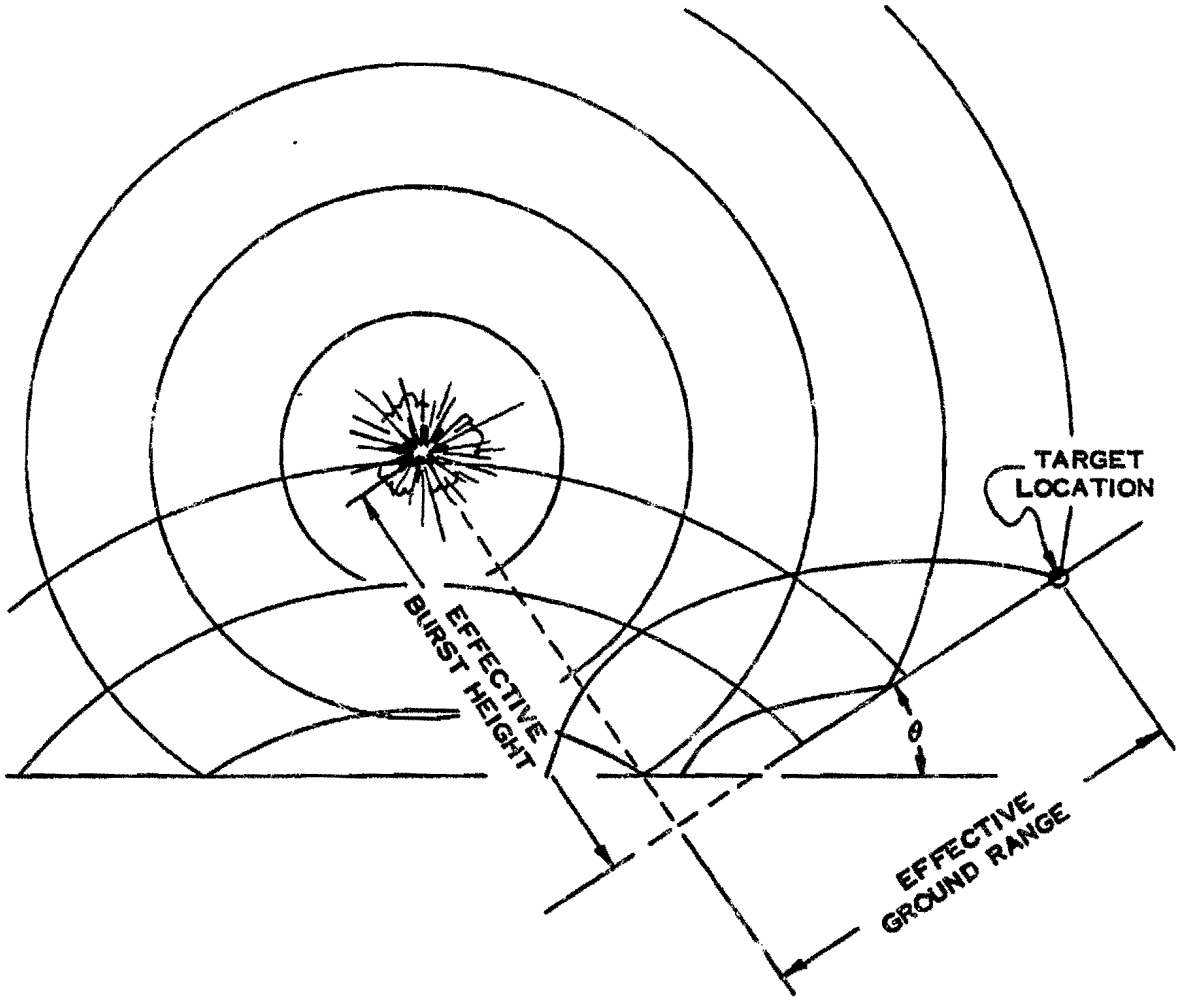

Figure 2-57. Construction Procedure Recommended When the Blast Wave Incident on a Slope Has Been Undergoing Regular Reflection on Level Ground

Problem 2-17. Calculation of Overpressure on a Slope

The information provided in paragraph 2-37 and in Figures 2-47 through 2-57 provides the data to calculate peak reflected overpressures when a blast wave encounters a rising or falling slope. The data are given relative to the incident overpressures that would be expected over flat terrain in a standard sea level atmosphere. These latter values may be obtained from Figures 2-17 through 2-22.

Scaling. For target altitudes above 5,000 feet, both the incident and the reflected overpressures scale according to the altitude scaling procedures described in paragraph 2-14, i.e.,

$$\frac{\Delta p_r}{\Delta p_{ro}} = \frac{\Delta p}{\Delta p_o} = S_p,$$

where Δp_{ro} and Δp_o are the reflected and incident peak overpressures, respectively, in a standard sea level atmosphere, Δp_r and Δp are the corresponding pressures at the desired altitude, and S_p is the pressure scaling factor described in paragraph 2-14 and tabulated in Tables 2-1 and 2-2.

Example

Given: A ridge with a slope angle of 27° on otherwise flat terrain at an altitude of 7,500 feet. For a particular set of burst conditions, the predicted blast wave in the absence of the ridge (but including altitude corrections) is a Mach stem with a peak overpressure between 10 and 15 psi. The direction of propagation of the blast wave makes an angle of 20° with the line of steepest ascent.

Find: The range of peak overpressures that may be expected on the side of the ridge facing the explosion.

Solution: From the equation given in paragraph 2-37 (or by interpolation in Figure 2-51), the effective slope angle is found as follows:

$$\sin \theta = \sin \theta_s \cos \Phi$$

$$= (\sin 27°)(\cos 20°)$$

$$= 0.427,$$

$$\theta = 25°.$$

From Table 2-1, the altitude scaling factor for pressure at 7,500 feet is

$$S_p = 0.76.$$

Under sea level conditions, the predicted value of the incident Mach stem overpressure would lie between

$$\Delta p_o = \frac{\Delta p}{S_p} = \frac{10}{0.76} = 13.2 \text{ psi, and}$$

$$\Delta p_o = \frac{15}{0.76} = 19.7 \text{ psi.}$$

Figure 2-55 shows that a rising slope will increase these sea level values to

$$\Delta p_{ro} = 19 \text{ psi, and}$$

$$\Delta p_{ro} = 28 \text{ psi, respectively.}$$

An uncertainty of about 20 percent exists in these values (see "Reliability" below). In order to bracket the range of expected values, the lower will be decreased by 20 percent, and the upper will be increased by 20 percent. The resulting sea level reflected overpressures are

[redacted]

Δp_{ro} = 15.2 psi, and

Δp_{ro} = 33.6 psi, respectively.

Answer: The corresponding values of reflected overpressure at an altitude of 7,500 feet are

$\Delta p_r = \Delta p_{ro} S_p$ = (15.2)(0.76) = 11.5 psi, and

Δp_r = (33.6)(0.76) = 25.5 psi, respectively.

[redacted] *Reliability:* Full scale nuclear tests indicate that the increase or decrease in peak overpressure at a rising or falling slope is generally within 10 or 20 percent of the predicted value. In the presence of a precursor, less accuracy may be expected. Accuracy also decreases if the slope angle is close to the critical angle that separates the regions of regular and Mach reflection.

[redacted] *Related Material:* See paragraphs 2-14, 2-17 through 2-20, 2-22 through 2-24, and 2-37. See also Tables 2-1 and 2-2.

[redacted]

2-38 Effects of Slopes on Other Blast-Wave Parameters

Methods for determining peak overpressures at rising and falling slopes are described in paragraph 2-37. This paragraph relates the peak dynamic pressure and the duration of the positive phases of the overpressure and the dynamic pressure to the expected overpressures that are determined by the methods described in paragraph 2-37. The relations of the dynamic pressure and positive phase durations to the overpressure will be discussed for three types of interactions of the blast wave with slopes: regular reflection of an incident Mach stem; Mach reflection of an incident Mach stem; and diffraction of an incident Mach stem.

Figure 2-58 shows the reflected dynamic pressure as a function of incident Mach stem overpressure in the regular reflection region for various effective slope angles. The duration of the positive phase overpressure after regular reflection can be considered to be the same as that of the incident pulse. The dynamic pressure pulse, on the other hand, changes as the shock wave proceeds up the slope as a result of the presence and growth of a rarefaction wave from the slope corner (see Figure 2-47). The dynamic pressure pulse effectively terminates where the rarefaction wave intersects the reflected wave. The effect depends on the distance up the slope that the shock wave has moved, the slope angle, and the overpressure coefficient in the manner shown in Figure 2-59. In this figure, the number 1116 is the velocity of sound (in feet/sec) for standard sea level conditions (15°C or 59°F). For different ambient temperatures, the appropriate sound speed should be used (see Tables 2-1 and 2-2).

In the case of Mach reflection of the incident Mach stem, the peak dynamic pressure at the shock front may be determined from Figure 2-13 once the reflected overpressure is determined as described in paragraph 2-37. Figure 2-13 is only valid when a single shock front is involved. If the rising slope is sufficiently steep to cause regular reflection (Figure 2-52), the peak dynamic pressure should be determined from Figure 2-58. The duration of the positive phase overpressure pulse in the Mach stem after Mach reflection can be assumed to be the same as that of the incident wave, while the positive phase dynamic pressure pulse is shorter than that of the incident wave. Over a range of overpressure coefficients from 2 to 11, and slope angles from 11.8 to 38 degrees, the reflected pulse after Mach reflection may be assumed to be 0.55 times as long as that of the incident blast wave.

Figure 2-13 also may be used to determine the peak dynamic pressure from the peak overpressure in a diffracted wave. Although the positive phase duration of both the overpressure and dynamic pressure pulses are known to decrease as a result of the formation of low pressure vortices at the slope change point, neither experiment nor theory is sufficiently extensive to provide a satisfactory prediction technique. As an approximation, the positive phase duration of the diffracted overpressure pulse may be taken to be the same as that of the incident pulse, and the duration of the diffracted dynamic pressure pulse may be shortened by the ratio of diffracted peak dynamic pressure to incident peak dynamic pressure.

2-39 Channeling of an Incident Mach Stem Along the Axis of a Valley

Figure 2-60 illustrates a third type of idealized topographic feature: an elongated valley. Shock waves reflecting from the walls of such a valley tend to enhance each other in the vicinity of the axis of the valley. The simple relations shown in Figure 2-61 have been shown to hold for a wide range of valley forms and for incident overpressures below about 60 psi. The relation for "flat-bottomed valleys" holds for

[redacted]

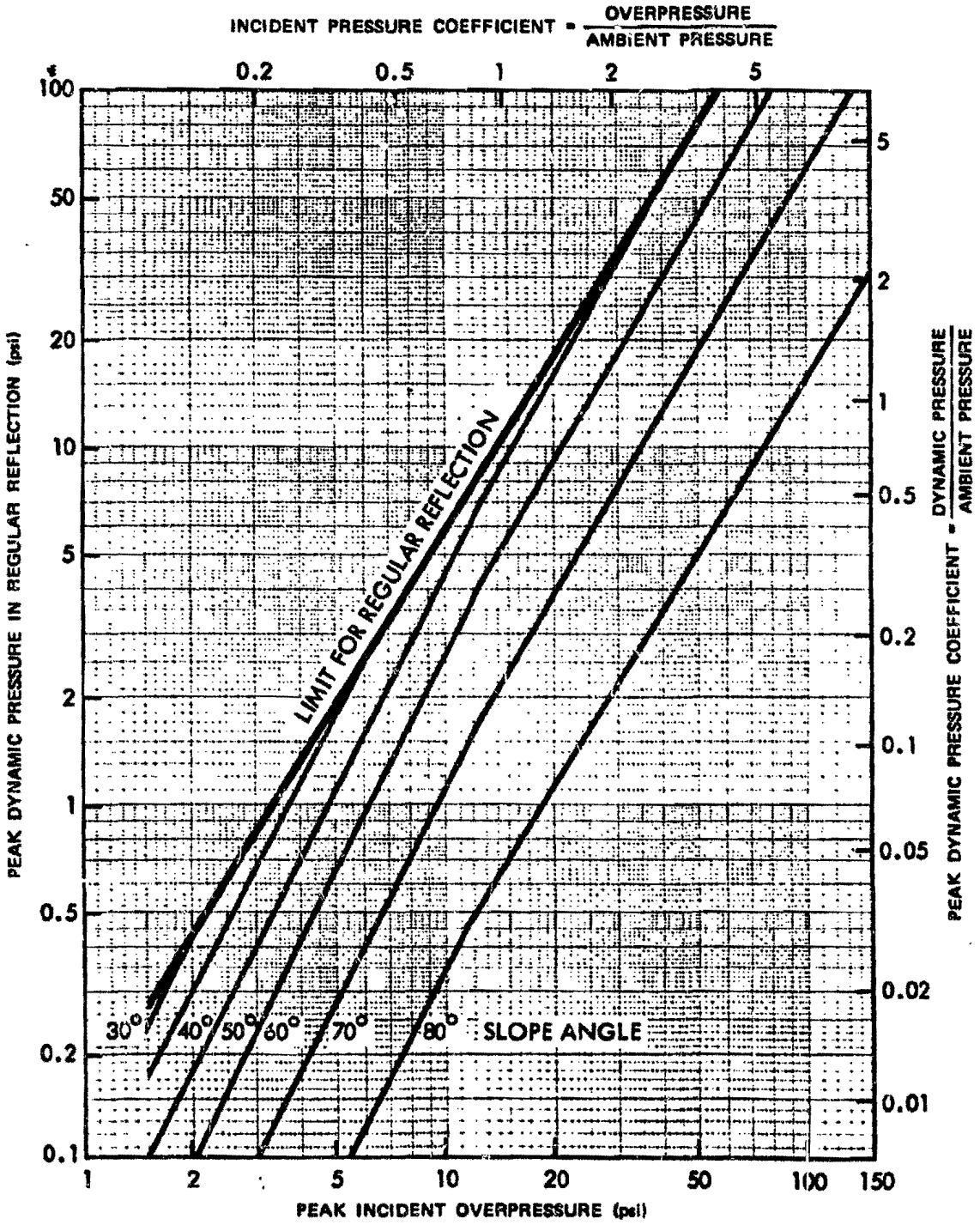

Figure 2-58. [redacted] Reflected Dynamic Pressure as a Function of Incident Mach Stem Overpressure for Regular Reflections for Various Effective Slope Angles [redacted]

[redacted]

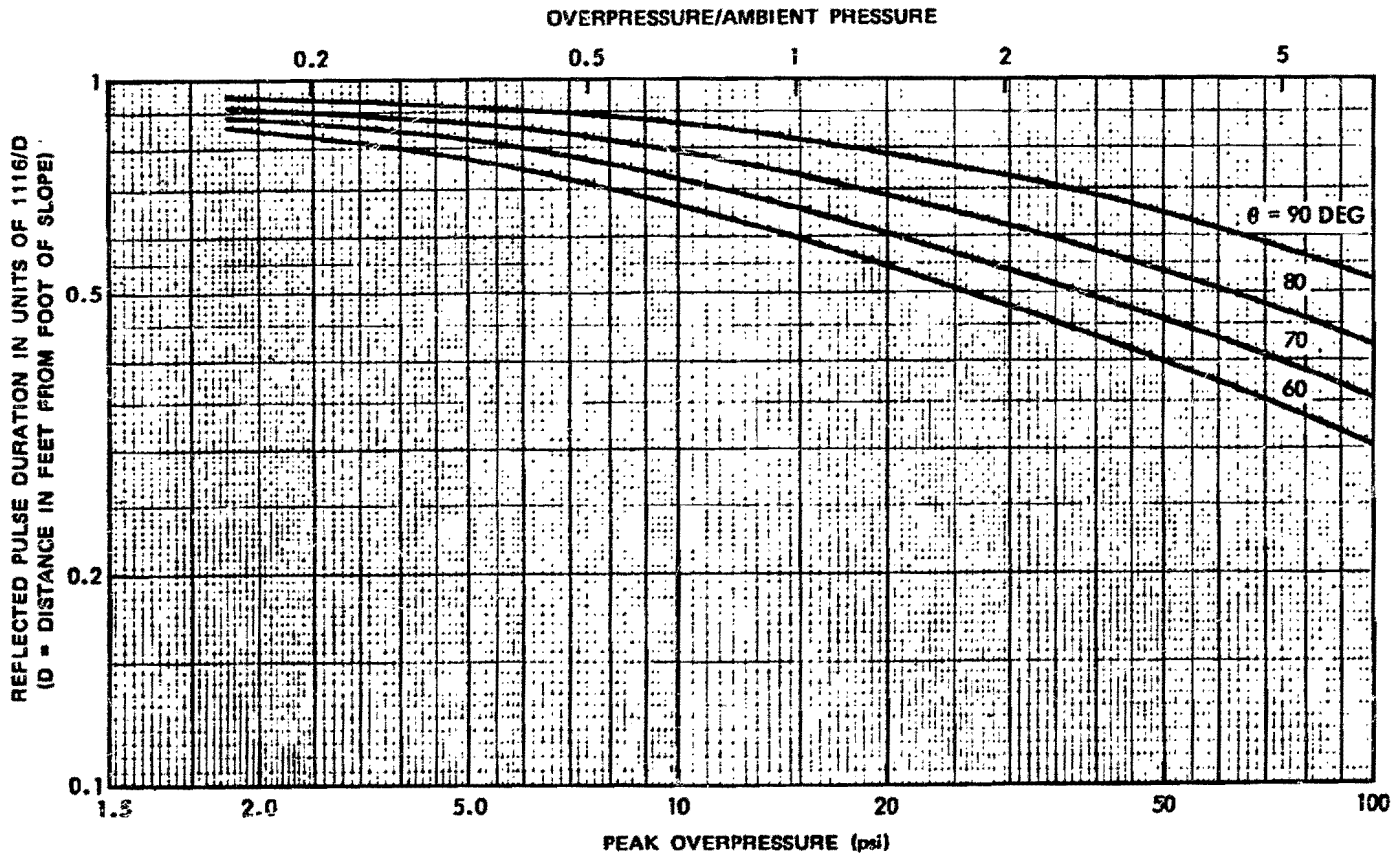

Figure 2-59. Duration of the Reflected Dynamic Pressure Pulse for Regular Reflection

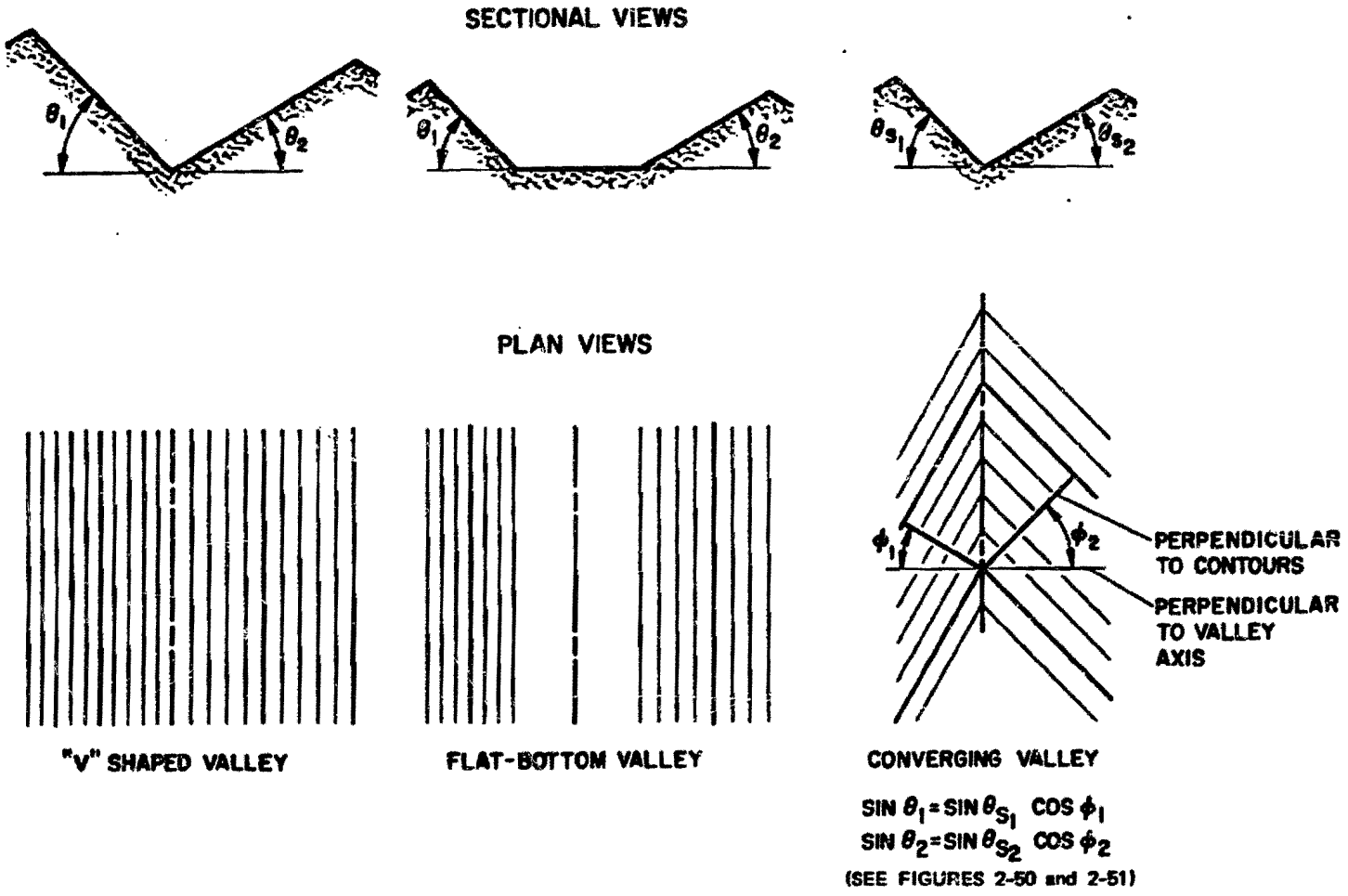

Figure 2-60. Sectional and Plan Views of Idealized Valley Shapes

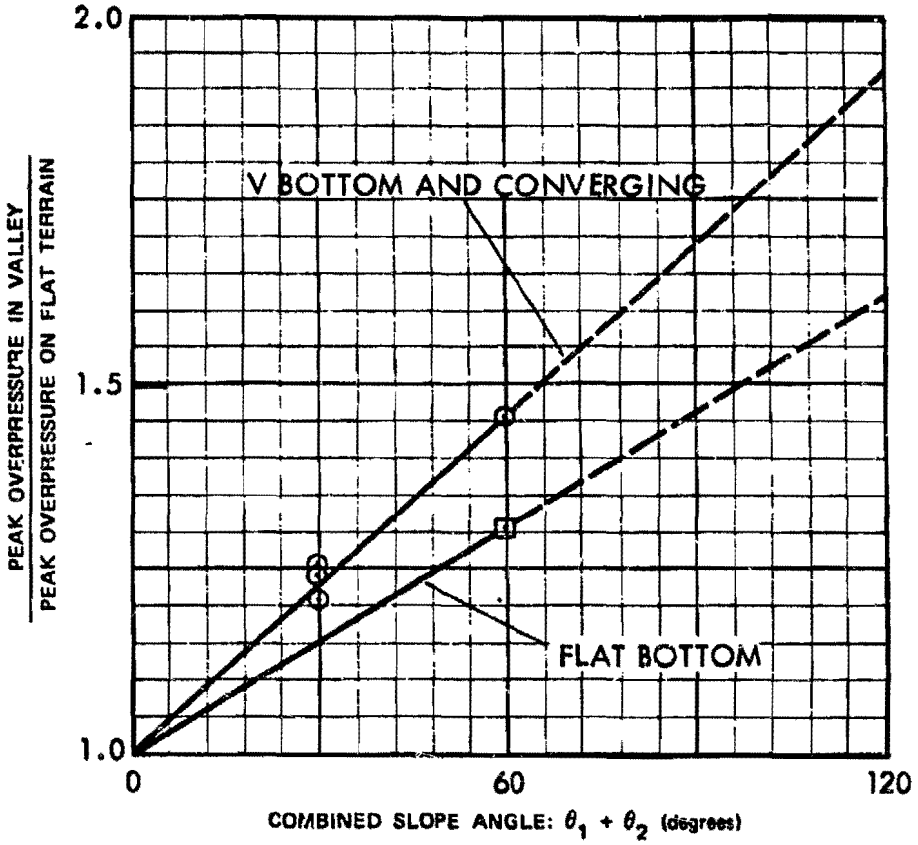

(SEE FIGURE 2-60)

Figure 2-61. [redacted] Average Peak Overpressure Amplification Factors at the Bottom of Valleys as a Function of Combined Slope Angle [redacted]

valleys whose floor widths (measured perpendicular to the valley axis) are of the same order as, or shorter than, the slope heights of the valley walls (also measured perpendicular to the valley axis). For wider flat-bottomed valleys, each side of the valley and a portion of the adjacent valley floor may be considered independently as a V-shaped valley.

2-40 General Application of Prediction Techniques to Actual Topographical Features

Paragraphs 2-37 and 2-38 provide data for only the most significant shock wave characteristics – peak pressures and positive phase durations. More detailed information, e.g., data on pressure waveforms, may be obtained from DASA 1200, "Nuclear Weapons Blast Phenomena" (see bibliography).

Applicability of the curves that have been presented depends largely on the size of a terrain feature relative to the size of the incident shock wave. If the incident shock is very much longer than a terrain feature of interest, the predicted changes in peak values of overpressure and dynamic pressure will occur on the slope; but the duration will not be affected greatly. The incident pulse length in feet is slightly more than 1116 times the incident pulse duration in seconds, and if this pulse length is more than about three times as long as the slope being considered, no changes in pulse duration can be expected.

Much of the complexity of actual terrain may be eliminated from blast wave calculations by application of the *local-slope* concept. This concept is based on the observation that, in many situations, a shock wave that has passed over a succession of terrain features (hills, valleys, etc.) before encountering a feature of interest interacts with that feature as if the shock wave had previously passed over flat terrain.

This trend was noted during testing programs and has been supported by theoretical inference. The Ranier nuclear test over fairly complex terrain, provided additional checks. Although much of the area around this explosion was subject to precursor type waves, sharp fronted waves traversed many regions that were protected from direct thermal radiation. Predictions of peak overpressures generally were within 10 to 20 percent of observed values.

Determining whether the local slope approximation will give reasonably accurate results requires application of judgment in an examination of the region between the target area and the presumed burst point to determine whether there are significant terrain features between the two, especially in the vicinity of the target. This examination is often based on a sectional plot of the terrain, made along a line between ground zero and the target. Although it is sometimes difficult to draw conclusions from this examination, the following criteria are helpful:

- Features that show slope angles of less than 10 degrees on a sectional plot of the terrain, i.e., about a 20 percent grade, will not create significant effects.
- Symmetrical features at an appreciable distance from the target generally can be ignored. Effects that occur on the front slope of such features compensate for effects that occur on the back slope.
- Terrain features near ground zero have a small effect on the blast wave at large ground distances.
- If the average slope of the terrain tends to follow a straight line, particularly if the deviations from this straight line are small or random, the local slope approximation is justified. However, if the average slope of the sectional plot clearly follows two straight lines, and the angle between these

lines exceeds 10 degrees, and if the break occurs in the region of Mach reflection, the blast wave calculations may have to treat the effects of two slopes in sequence.

Unless the average slope between ground zero and the target is essentially horizontal, use of the local slope concept requires establishment of the primary reference plane (PRP). Over complex terrain, the PRP often follows the average slope of the terrain between ground zero and the foot of the feature upon which the target lies. If the PRP does not seem clearly defined by this criterion, it is better to allow the terrain within the region of Mach reflection suggest the slope of the PRP. If the target is in the region of regular reflection, the average slope of the terrain near the target should be given more weight than the average slope of terrain closer to ground zero.

After the PRP has been established, effective burst height and ground distance *with respect to this plane* may be determined by means of a geometrical construction similar to that suggested by Figure 2-57. Properties of the blast wave incident on the terrain feature of interest may be read directly from height of burst curves in terms of these effective values of distance and height.

Although there are many cases in which the local slope concept will fail in detail if applied to features that are regular and uniform, ordinary terrain is so complex that the uncertainties engendered by terrain irregularities generally will exceed errors resulting from application of the local slope concept. Furthermore, the process of determining *approximate* terrain effects with the local slope concept is generally far simpler than that of obtaining more refined, *but still approximate*, effects with more rigorous techniques.

Once the blast wave properties are determined from height of burst curves, appropriate sectional plots should be made of the target area slope. Azimuth angle and valley slopes must be determined where appropriate.

2-41 Application of Prediction Techniques to Specific Topography

Figure 2-62 is a topographical map with a target area (designated by T) to be investigated. It is desired to determine the locus of ground zeros that would subject the target to an overpressure of 10 psi from a 1 Mt weapon burst at a height of 5,000 feet above the terrain.

Examination of Figure 2-62 shows that the highest point on the terrain around the target area is just over 4,000 feet (note that the grid lines and elevations are given in meters in Figure 2-62, and the highest point in the vicinity of the target is at an elevation of 1,243 meters), so altitude corrections are not required.

In accordance with the instructions in paragraph 2-20, the blast-wave parameters for explosions over mechanically nonideal surfaces are performed by first finding the desired blast parameters over a near-ideal surface. The results then are corrected for the change in the blast wave properties introduced by the mechanically nonideal features. The corresponding height of burst for a 1 kt explosion is

$$h_1 = \frac{h}{W^{1/3}} = \frac{5{,}000}{(1{,}000)^{1/3}} = 500 \text{ feet.}$$

From Figure 2-18, a 1 kt explosion at a height of burst of 500 feet will produce an overpressure of 10 psi at a ground distance of 1,315 feet (about 400 meters). The corresponding ground distance for a 1 Mt explosion is

$$d = d_1 W^{1/3} = (1{,}315)(1{,}000)^{1/3}$$

$$= 13{,}150 \text{ feet (or about 4,000 m).}$$

A circle, centered on the target, with this radius is shown in Figure 2-62. A 1 Mt explosion at a

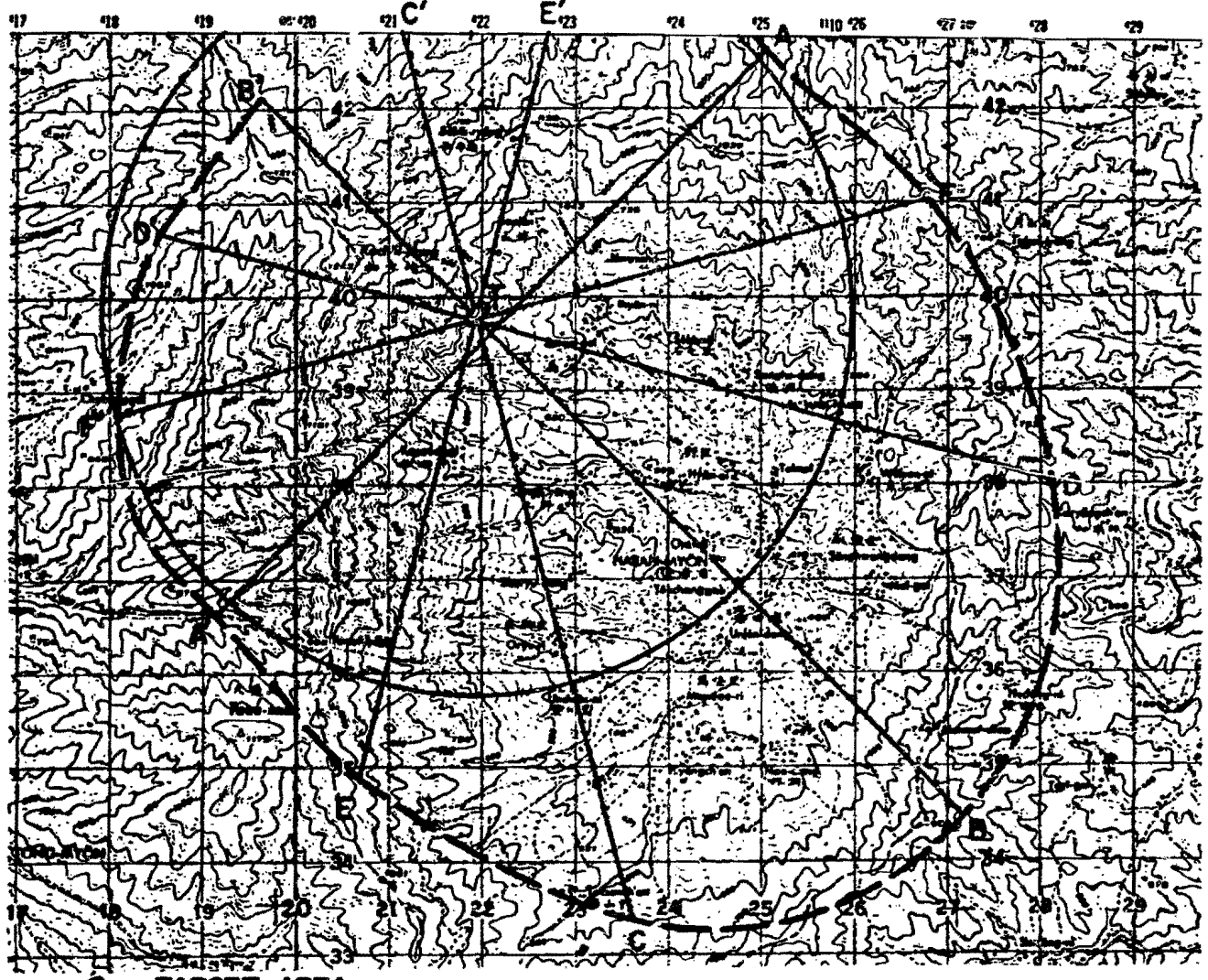

Figure 2-62. Terrain Map Used in Example

height of burst of 5,000 feet over any point on the circle would produce an overpressure of 10 psi at the target area (burst over points within the circle would produce overpressures in excess of 10 psi at the target).

The target area includes two small converging valleys that are relatively shallow and have relatively flat slopes normal to their axes. Figure 2-61 shows that relatively steep slopes are required to produce large effects in converging valleys, so these minor terrain irregularities may be ignored.

The general direction of the contours in the target area is established as being parallel to line AA'; and a sectional plot along line BB', perpendicular to AA' and through the target area, is constructed (this sectional plot is shown in Figure 2-63 with the distance scales in meters for ease in comparison with the map). The plot in Figure 2-63 is not extended to the ground-zero circle (though it could easily be), since inspection of the area between the target and this circle, and reference to Figure 2-15 shows that Mach reflection would take place long before the shock would arrive at the target area. Furthermore, inspection of the area within the ground zero line indicates that an assumption of a horizontal datum for the slope of the primary reference plane is fairly good.

From Figure 2-63, it can be determined that the tangent of the slope angle (vertical rise/horizontal distances) is 0.57. Thus, the slope angle is

$$\theta_s = 30°.$$

It is therefore necessary to determine the incident overpressure that will produce an overpressure of 10 psi when the shock wave encounters a 30 degree rising slope (along the line BT) or a 30 degree falling slope (along the line B'T). Figure 2-55 (Mach Reflection) gives an incident overpressure of 3.5 psi for the rising-slope condition, and Figure 2-56 (diffraction) shows an incident overpressure of 20 psi for the falling-slope condition. Figure 2-19 shows that 3.5 psi would occur at a ground distance of about 2,450 feet from a 1 kt burst or 24,500 feet (about 7,500 m) from a 1 Mt burst at heights of burst of 500 feet and 5,000 feet, respectively. Figure 2-18 shows that, for the same heights of burst, 20 psi occurs at a ground distance of 870 feet from a 1 kt burst or 8,700 feet (about 2,650 meters) from a 1 Mt burst.

Lines CC' and DD' are drawn at 30° to line BB'. For these lines, the angle between the direction of shock wave propagation and the angle of steepest ascent or descent is

$$\Phi = 30°,$$

and the effective slope angle is determined by

$$\sin \theta = \sin \Phi_s \cos \Phi$$

$$= \sin 30° \cos 30° = 0.43$$

which yields

$$\theta = 26°.$$

The angle Φ for lines EE' and FF' is 60°, from which $\theta = 14.5°$. Using these two values of θ with Figures 2-55, 2-56, 2-18, and 2-19 provides the results shown in Table 2-5.

Along line AA' the hill on which the target lies is, for all intents, a V-shaped valley with combined slope angle (see Figure 2-62) of 30°. Figure 2-60 indicates that an amplification factor of about 1.25 holds for such a valley, so an 8 psi incident overpressure (10/1.25) will yield 10 psi at the target area. Figure 2-19 shows that 8 psi would occur at a distance of approximately 1,375 feet for 1 kt or 13,750 feet for 1 Mt (about 4,200 meters for 1 Mt).

When the various distances given abov

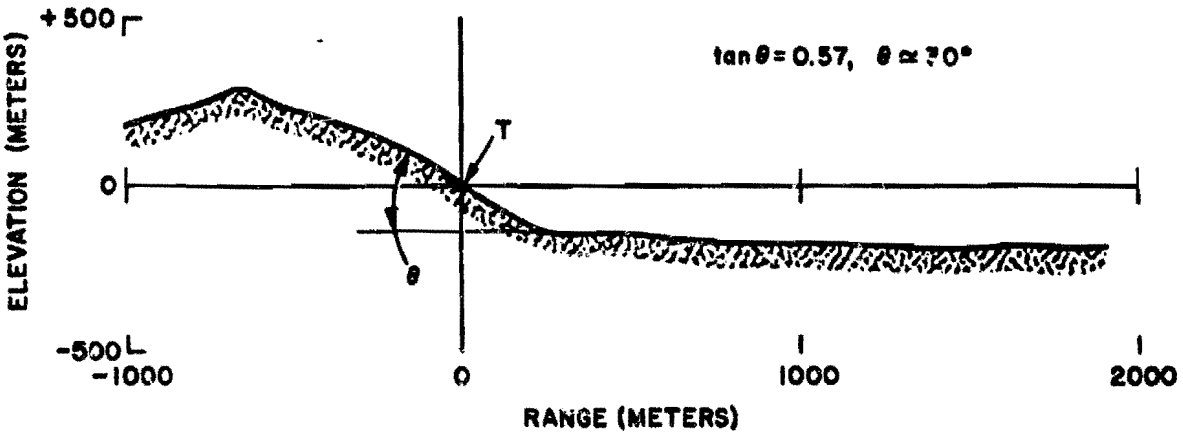

Figure 2-63. [redacted] Sectional Plot of the Terrain Along [redacted] in Figure 2-62

[redacted]

Table 2-5. [redacted] Incident Overpressure and Ranges [redacted]

Line	Φ	θ	Rising Slope Incident Overpressure (psi)	Approximate Distance	
				Feet	Meters
BT	0°	30°	3.5	24,500	7,500
CT, DT	30°	26°	4.1	21,500	6,600
ET, FT	60°	15°	6.0	17,000	5,000
			Falling Slope		
B'T	0°	30°	20.0	8,700	2,650
C'T, D'T	30°	26°	18.5	9,500	2,900
E'T, F'T	60°	15°	15.0	10,900	3,300

[redacted] are measured from the target area T along the appropriate lines, the points are connected, the dashed line shown in Figure 2-62 is the result. This line is the approximate locus of ground zeroes that will subject the target area to a peak overpressure of 10 psi.

[redacted] THE BLAST WAVE AT HIGH ALTITUDES [redacted]

[redacted] Nearly all of the energy from a nuclear burst detonated within the atmosphere is absorbed by air molecules. Within a few seconds, most of this energy evolves to three forms: blast energy, radiated thermal energy, and thermal energy retained in a large volume of air. The first two components of energy are useful nuclear effects; the third is harmlessly dissipated over a relatively long period of time. Deviations from Sachs' scaling laws (paragraphs 2-13 and 2-14) above 40,000 feet are caused principally by differences in the partitioning of these three energy components. Between sea level and 130,000 feet, blast energy decreases and radiated thermal energy increases with yield.

[redacted] These changes are, to a large degree, caused by changes in characteristic times. The blast wave develops more slowly at higher altitudes, and the thermal pulse radiates more rapidly. Thus, energy is radiated at high altitudes that would, at lower altitudes, have contributed to the blast wave. At altitudes higher than 130,000 feet, both blast and thermal* efficiencies drop.

2-42 Effective Blast Yield at High Altitudes [redacted]

[redacted] To account for the smaller fraction of the yield that appears as blast energy at higher altitudes, the actual yield is multiplied by the blast efficiency factor shown in Figure 2-64 to obtain the effective blast yield. Effective blast yield is that value of yield which, when used in Sachs' scaling laws, predicts the correct value of peak overpressure.

[redacted] Figure 2-64 shows approximate upper and lower limits rather than a single value for

*[redacted] Thermal radiation as used here includes ultraviolet through infrared, but excludes higher frequency radiations, e.g., X-rays. See Chapters 3 and 4.

[redacted]

[redacted]

[redacted]

the blast efficiency factor. At high altitudes, overpressure varies with distance in such a way that effective blast yield is different at different distances. For example, a 100 kt burst at 100,000 feet has an effective blast yield that varies from about 50 kt to 85 kt. It appears impossible to formulate simple rules that state where these numbers apply. It is preferable to consider the upper and lower effective blast yields as defining a range of uncertainty. Methods for making more detailed and complex calculations are suggested in DASA-1200 "Nuclear Weapons Blast Phenomena" (see bibliography).

[redacted] Although blast efficiency is a correction factor established to determine peak overpressure, it also may be used to calculate other blast-wave parameters. However, because of the nonlinear properties of air, blast waves with high shock strengths cannot be scaled exactly, and shock-front parameters other than peak overpressure are defined less accurately by effective blast yield. The waveform behind the shock front is subject to additional variations, and the blast efficiency is least dependable when applied to parameters such as impulse and positive phase duration.

[redacted]

Problem 2-18. Calculation of Peak Overpressure at High Altitudes

Figure 2-64 shows the blast efficiency factor as a function of height of burst. This efficiency factor when multiplied by the weapon yield provides the effective blast yield. The effective blast yield may then be used to obtain peak overpressure as a function of distance by the methods described in paragraph 2-7 and Problem 2-1 as modified by the altitude correction procedures described in paragraph 2-14. Other blast parameters may be obtained by using the effective blast yield in the manner described for total yield in paragraphs 2-8 through 2-11, as modified by the altitude scaling described in paragraph 2-14.

Scaling. After obtaining the effective blast yield, the various blast parameters are scaled according to the procedures described in Problems 2-1 through 2-5, as modified by the altitude scaling described in paragraph 2-14 and Problem 2-6.

Example

Given: A 200 kt explosion at an altitude of 100,000 feet.

Find: The highest value of peak overpressure that might be expected 5,000 feet below the explosion.

Solution: Since Figure 2-64 shows that the highest value of blast efficiency factor for a burst at 100,000 feet is 85 percent, the calculation is based on an effective yield, W_{eff}, of

$$W_{eff} = (0.85)(200) = 170 \text{ kt.}$$

While the blast efficiency factor is based on burst altitude, the altitude scaling factors are based on target altitude (paragraph 2-14). From Table 2-1, the distance and pressure scaling factors at 95,000 feet are

$$S_d \approx 4.2$$

$$S_p \approx 0.014.$$

The distance from a 1 kt explosion that corresponds to a distance of 5,000 feet from a 170 kt explosion is

$$d_1 = \frac{d}{S_d W^{1/3}} = \frac{5{,}000}{(4.2)(170)^{1/3}} = 215 \text{ feet.}$$

From Figure 2-2, the peak overpressure at this distance at sea level is 210 psi.

Answer: The corresponding peak overpressure at 95,000 feet is

$$\Delta p = \Delta p_0 S_p = (210)(0.014) = 2.9 \text{ psi.}$$

The reliability statement of Problem 2-1 indicates that for scaled distances (distances from a 1 kt explosion) less than 1,000 feet the values of peak overpressure obtained from Figure 2-2 are accurate to within ±15 percent. The probable upper limit of the required overpressure is

$$\Delta p = 2.9 + (0.15)(2.9) = 3.3 \text{ psi.}$$

Reliability: The data curves in Figure 2-64 are based on computer calculations supported by limited data from full-scale nuclear tests. As a result of the experimental checks, the computed data are believed to be accurate at high overpressures; however, this accuracy is not considered confirmed. At low overpressures (scaled radii under 300 feet, shock strengths less than 7), some of the numerical methods used by the computer introduce errors, and reliable esti-

[redacted]

[redacted]

mates of effective blast yield are not available; however, even at low shock strengths, the blast efficiency factor is believed to be approximately within the limits shown in Figure 2-64. Yield scaling appears to be relatively accurate, introducing errors of only a few percent. Uncertainties in the overpressure values obtained from Figure 2-2 are described in Problem 2-1.

[redacted] *Related Material:* See paragraph 2-41. See also paragraphs 2-7 through 2-11 and 2-14. See also Problems 2-1 through 2-6.

[redacted]

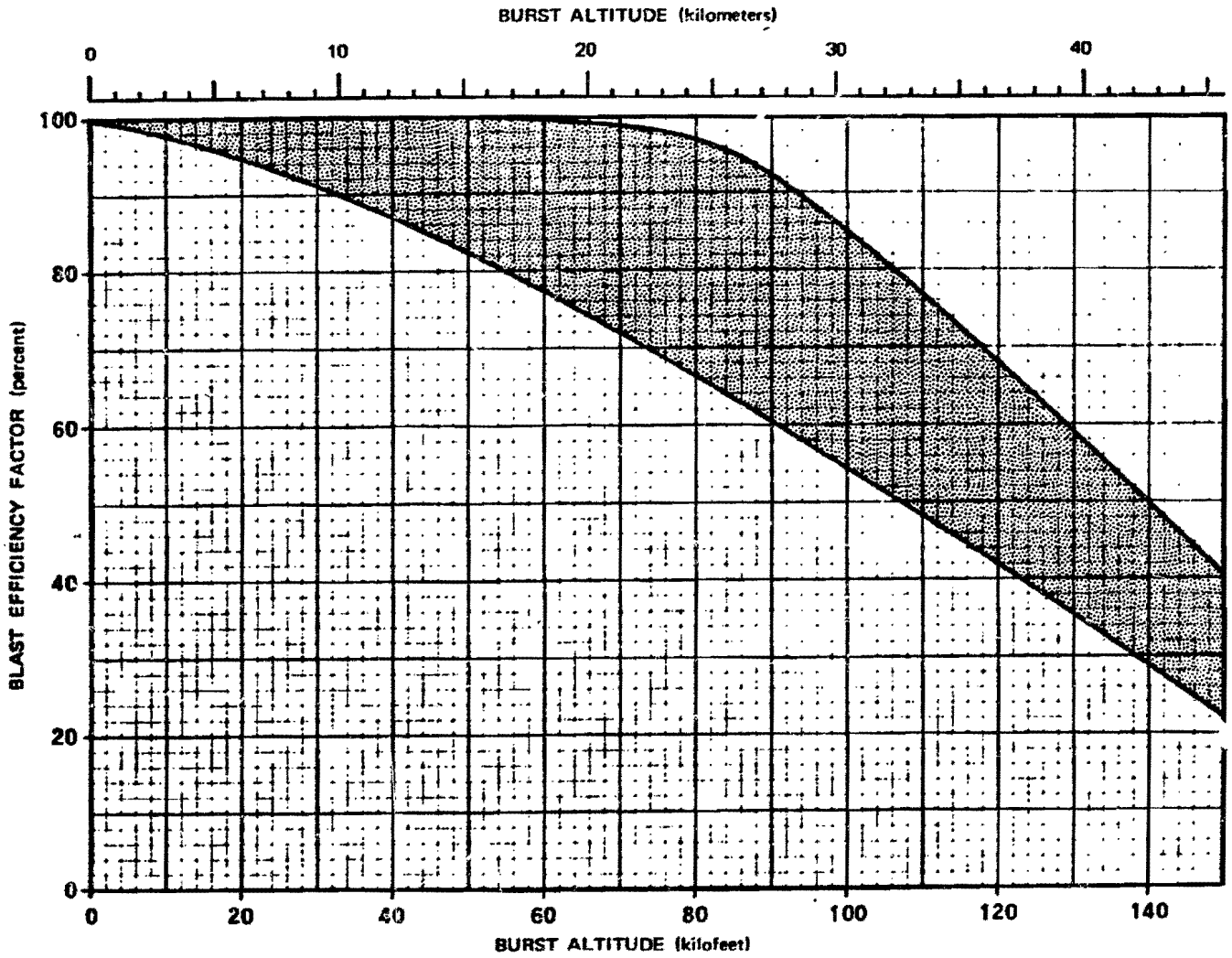

Figure 2-64. [redacted] Blast Efficiency Factor for High-Altitude Bursts [redacted]

2-43 Peak Overpressure on the Ground from High-Altitude Bursts

The conventional procedure for finding blast-wave parameters at one altitude produced by a burst at another altitude is modified Sachs' scaling (paragraph 2-14). Figure 2-65 uses this principle for the prediction of peak reflected overpressure at ground zero as a function of yield and burst altitude. The curves are based on computer calculations and are compatible with the curves in Figure 2-3, which show peak overpressure in free air.

The curves are drawn as though effective blast yield (paragraph 2-41) were always equal to actual weapon yield. If the burst is above 40,000 feet, a correction for effective blast yield is appropriate, and this reduced yield (rather than actual weapon yield) should be used to enter Figure 2-65.

Since the abscissa is slant range, Figure 2-65 may be used to predict peak reflected overpressure at locations other than at ground zero, provided the locations are within the region of regular reflection and are not too close to the range at which Mach reflection begins. Figure 2-46 may be used to determine the range over which the reflection coefficient has essentially the same value that it has at ground zero.

Since modified Sachs' scaling is an empirical method, there may be doubt as to its application over a wide altitude range. However, comparisons of reflected overpressures at ground zero from Figure 2-65 with calculations performed in a way that is independent of the technique of modified Sachs' scaling show substantial agreement up to burst altitudes of about 150,000 feet, the limit of the latter calculations.

2-44 Effects of Early Blast Phenomena

At the overpressures that are ordinarily of interest in blast calculations, the blast wave from a sea level burst has propagated well away from the region in which it originated. At high altitudes, however, the blast wave forms at relatively low overpressures and at long ranges. In making a blast calculation at these altitudes, a possibility exists that the range of interest is closer than that at which a scalable shock front forms.

The first stage of blast-wave formation occurs when the air around the burst, under high pressure because of its suddenly increased temperature, starts to move. In the analysis of computer runs, a convenient criterion for shock front formation is that the ratio of air density behind the shock to ambient air density (ρ_s/ρ) rises at some point to a value exceeding 1.5. This criterion indicates that the pressure waves originating in the air near the burst are starting to merge to form a shock front. Formation of the hydrodynamic shock front then proceeds rapidly, and the actual time and radius of shock formation are close to the values based on the $\rho_s/\rho = 1.5$ criterion.

[redacted]

Problem 2-19. Calculation of Peak Reflected Overpressure at Ground Zero from a High Altitude Explosion

[redacted] Figure 2-65 shows the peak reflected overpressure at the ground as a function of slant range for a selected family of weapon yields. The curves in Figure 2-65 are applicable at ground zero and at locations away from ground zero that are in the regular reflection region.

[redacted] *Scaling.* No scaling is required with Figure 2-65; however, for explosions above 40,000 feet, the effective yield obtained by use of Figure 2-64 should be used to enter Figure 2-65.

[redacted] *Example* [redacted]

Given: A 100 Mt explosion at an altitude of 120,000 feet.

Find: The maximum peak reflected overpressure expected at ground zero.

Solution: From Figure 2-64, the maximum blast efficiency factor for bursts at 120,000 feet is 68 percent. The effective yield is

$$W_{eff} = (0.68)(100) = 68 \text{ Mt}.$$

Answer: Interpolation in Figure 2-65 indicates that peak reflected overpressure at ground zero is about 2.5 psi.

[redacted] *Reliability* [redacted]

The few available experimental data points tend to substantiate the curves in Figure 2-65. A certain amount of uncertainty occurs at low overpressures because the overpressure distance curves in Figure 2-65 are not identical to the results of the calculations independent of Sachs' scaling that were mentioned in paragraph 2-42.

[redacted] No reliability estimate has been made for these curves; however, it should be observed that, for the extreme range of atmospheric conditions found along the path of the blast wave, overpressure values that are within a factor of 2 often represent satisfactory agreement.

[redacted] *Related Material:* See paragraphs 2-7, 2-13, 2-14, and 2-42. See also Tables 2-1 and 2-2.

[redacted]

[redacted]

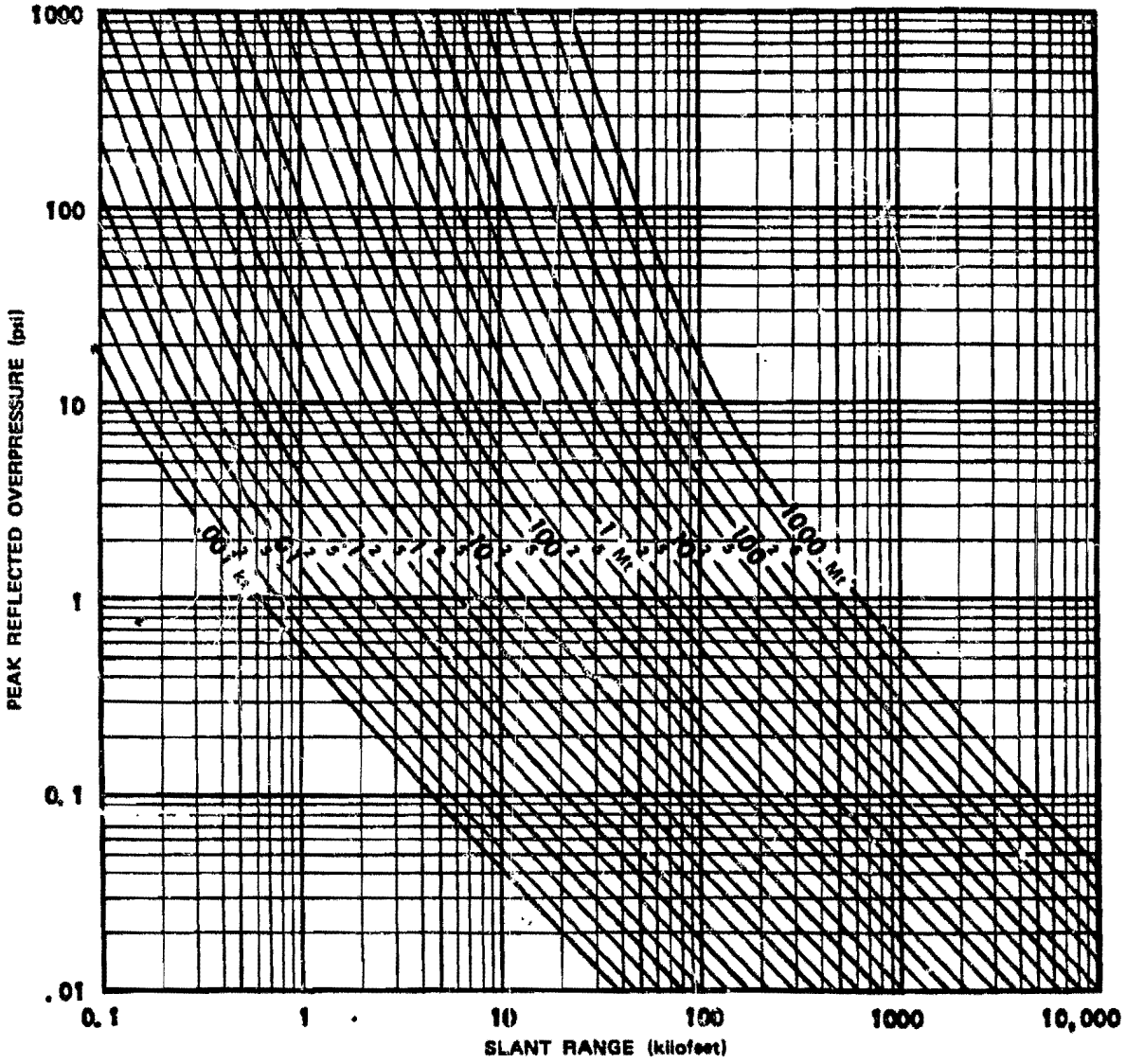

Figure 2-65. [redacted] Peak Reflected Overpressure at Ground Zero as a Function of Yield and Slant Range [redacted]

[redacted]

[redacted]

[redacted] The kinetic energy of the bomb debris, which is typically about 25 percent of the total yield, makes an important contribution to the strength of the blast wave. These high velocity debris atoms, pushing away the air surrounding the burst point, create a shock wave that is known as the nuclear shock or case shock. Until this shock front overtakes and merges with the hydrodynamic shock front, the blast wave will not have acquired its full energy. The fraction of the total energy carried by the debris is a function of weapon design. Therefore the arrival of the case shock at the hydrodynamic shock front, which marks the beginning of a scalable shock wave, also is a function of weapon design.

[redacted] Figure 2-66 shows the approximate ranges of shock-front formation and case-shock arrival as a function of burst altitude for a 1 kt explosion. These ranges were calculated for conventional nuclear devices. Different curves would be required to show these ranges accurately for weapons with enhanced radiation outputs (paragraph 2-45[redacted]

DNA (L)(3)

[redacted]

[redacted] Figure 2-66 also shows curves of blast-wave overpressure levels as a function of range and altitude. Since peak overpressure cannot be scaled accurately until the case-shock front joins the hydrodynamic shock front, the overpressure curves terminate on the curve for case-shock arrival. To emphasize the increasing uncertainty of peak overpressure data with increasing altitude, the overpressure contour lines are dashed above 100 kft.*

[redacted] These overpressure curves were obtained directly from Figure 2-2 and Sachs' scaling laws, including altitude corrections described in paragraph 2-14. However, correction for effective blast yield at high altitudes must be made, as illustrated in Problem 2-20.

[redacted] This procedure will give a reasonably accurate answer only if the range that is used exceeds the range for case-shock arrival. The latter range is obtained by multiplying range obtained from Figure 2-66 for case-shock arrival by $W'^{1/3}$ (note that actual yield W', not effective yield W'_{eff}, is required in this calculation). Similarly, the approximate range for shock front formation is obtained by multiplying the scaled range by $W'^{1/3}$.

[redacted] If a blast-wave calculation closer to the burst than the range of case-shock arrival is required, data from Figure 2-2 may be scaled to obtain a rough estimate of peak overpressure. If the calculation is for a range closer than the range for $\rho_s/\rho = 1.5$, the discrepancy between the actual overpressure and the calculated overpressure will probably be excessive. Requirement for a calculation of this type generally is a sign that other nuclear effects should be considered. Blast damage at ranges closer than shock-front formation usually is less serious than damage caused by neutrons, X-rays, gamma rays, and thermal energy.

[redacted] The stages of development of a nuclear blast wave are most accurately known in terms of time, because accurate comparisons can be made between experimental data and points in computer calculations. Approximate equations for determining three times of interest are given below.

[redacted]

DNA (W)(1)

[redacted] See NOTE in Reliability paragraph of Problem 2-20.

[redacted]

[redacted]

[redacted]

DNA (G)(1)

[redacted]

DNA (G)(1)

[redacted]

[redacted]

Problem 2-20. Calculation of Case-Shock Arrival and Peak Overpressure at High Altitudes

Figure 2-66 shows the approximate ranges of shock-front formation and case-shock arrival as a function of burst altitude and distance from a 1 kt explosion.

Scaling. For yields other than 1 kt, the range for case-shock arrival scales as follows:

$$\frac{d}{d_1} = W^{1/3},$$

where d_1 is the range for case-shock arrival for 1 kt (obtained from Figure 2-66), and d is the corresponding range for a yield of W kt. For heights of burst above 40,000 feet the range for a given *overpressure* scales as follows:

$$\frac{d}{d_1} = (W_{\text{eff}})^{1/3},$$

where d_1 is the range for the desired overpressure for a 1 kt explosion and d is the corresponding range for a yield of W_{eff} kt (W_{eff} is the effective yield for a high altitude burst obtained from Figure 2-64 as illustrated in Problem 2-18).

Example

Given: A 100 kt explosion at an altitude of 110 kilofeet above sea level.

Find: The peak overpressure at a range of 1,000 feet.

Solution: From Figure 2-66, the range for case shock arrival from a 1 kt burst at 110 kft is about 180 feet. The corresponding range for 100 kt is

$$d = d_1 W^{1/3} = (180)(100)^{1/3} = 835 \text{ feet.}$$

Since this is less than 1,000 feet, peak overpressure is scalable at the range of interest. From Figure 2-64, the blast efficiency for a burst at 110 kft is expected to be between 48 percent and 77 percent. The effective blast yield is therefore between 48 and 77 kt. The corresponding distances for a 1 kt explosion are

$$d_1 = \frac{d}{(W_{\text{eff}})^{1/3}} = \frac{1{,}000}{(48)^{1/3}} = 275 \text{ feet,}$$

and

$$d_1 = \frac{d}{(W_{\text{eff}})^{1/3}} = \frac{1{,}000}{(77)^{1/3}} = 235 \text{ feet.}$$

Answer: From Figure 2-66, the overpressures are 90 and 150 psi at these ranges from a 1 kt explosion at 110 kft. The 15 percent uncertainty in overpressure data (see "Reliability") extends the range of 1 kt overpressure values to between 75 and 170 psi.

Reliability

Ranges for shock formation and case-shock arrival were obtained from computer calculations. Case-shock arrival has been observed in nuclear tests, and the experimentally determined ranges substantiate the computer data. For conventional weapons (unconventional weapons are discussed in the following subsection), the range for case-shock arrival is believed correct within a few percent. Yield scaling appears to be fairly accurate for these phenomena.

Below 40,000 feet peak overpressure data are considered reliable within 15 percent for shock strengths greater than 1.5 (7 psi at sea level), within 20 percent for shock strengths between 1.5 and 1.03, and within 30 percent for shock strengths below 1.03 (~1/2 psi at sea

level). Above 40,000 feet, the additional uncertainty implied by Figure 2-64 should be considered.

Note: Although Figure 2-66 was used in this example to calculate peak overpressure, it is not the preferred source of overpressure data. More accurate values may be obtained by scaling data from Figure 2-2 and, at high altitudes, following the method of Problem 2-18. Figure 2-66 is convenient for rough calculations, because it eliminates the requirement for altitude scaling. However, the important information in this figure is given by the curves that show the approximate ranges of shock-front formation (ρ_s/ρ = 1.5) and the beginning of a scalable shock wave (case-shock arrival).

Related Material: See paragraphs 2-7, 2-41, and 2-43. See also Problem 2-18.

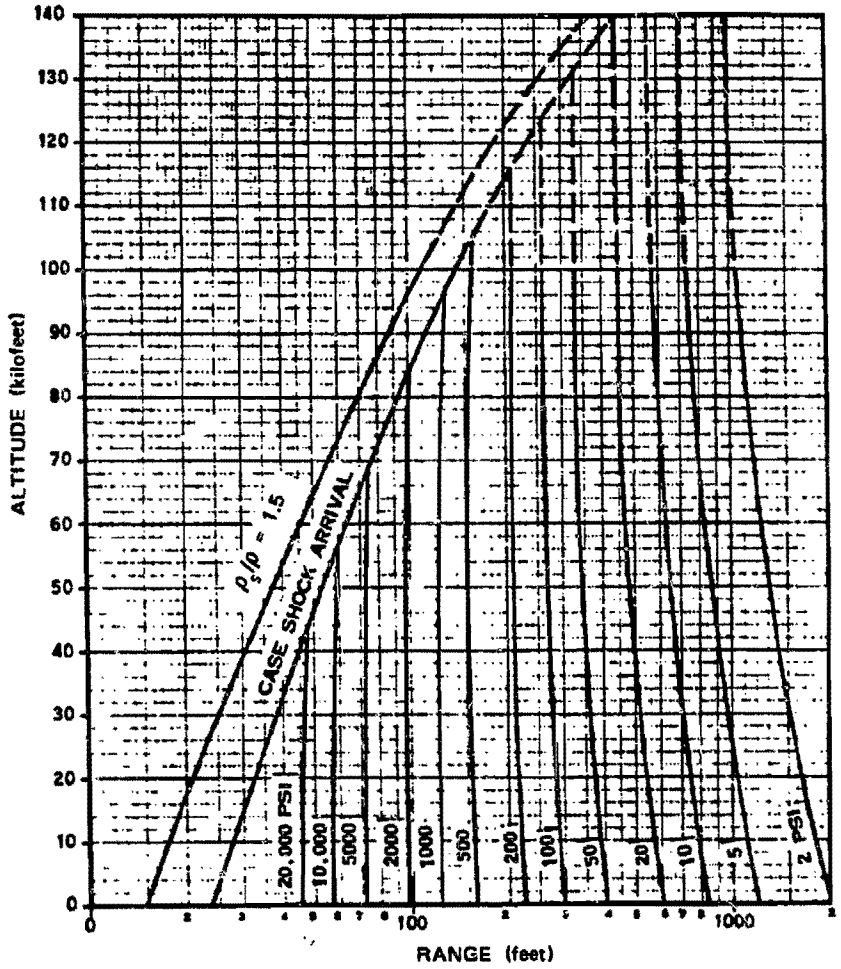

Figure 2-66. [redacted] Limits of Scalable Shock Wave and Calculated Peak Overpressure as a Function of Altitude as a Function of Distance from a 1 kt Explosion [redacted]

WEAPONS WITH ENHANCED OUTPUTS

The initial output energy of a conventional nuclear weapon consists mainly of black body radiation and kinetic energy of bomb debris as shown in Table 2-6. Table 2-7 shows the mean free path of various forms of energy that can be generated by a nuclear device. Most of the output of a conventional nuclear weapon interacts with air atoms near the burst.

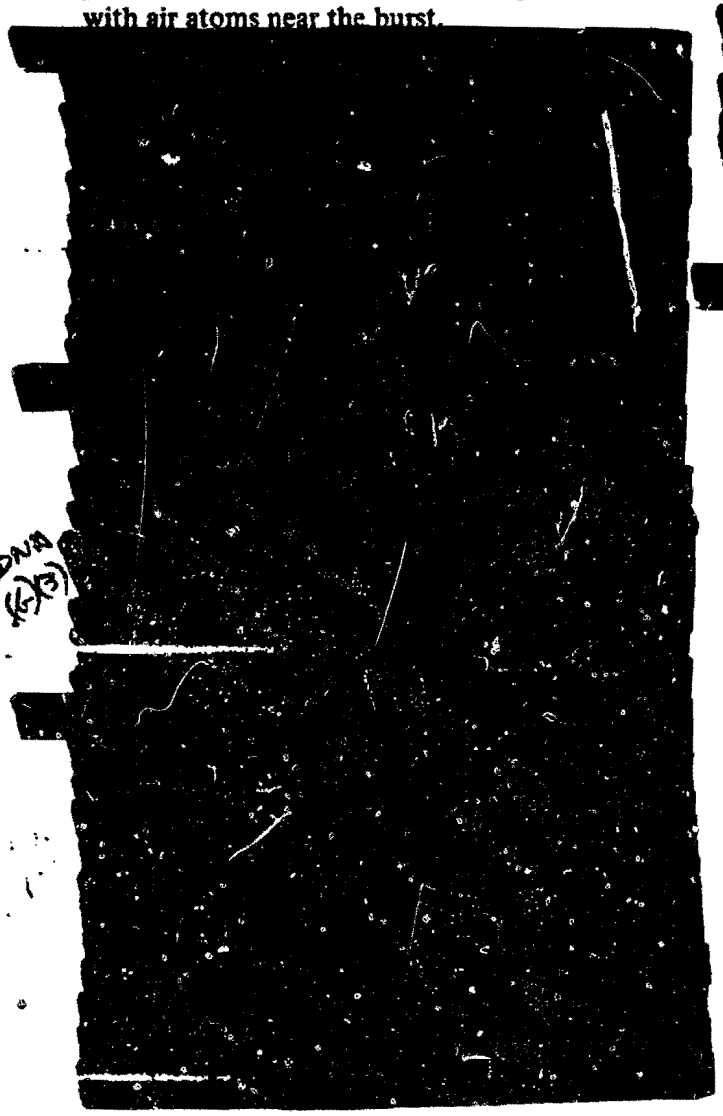

2-45 Air Blast from Weapons with Enhanced Radiation Outputs

The strength of the blast wave from enhanced radiation weapons is a complex function of the radiant energy distribution. Accurate blast wave calculations require detailed energy transport calculations, followed by hydrodynamic calculations to account for the motion of the heated air and the bomb debris. Frequently, the variation of ambient air density with altitude is sufficiently important to be included in the calculations. A large digital computer is required to account for all of these factors.

•The unit keV is commonly used in two senses. Strictly speaking, it is a unit of energy (1 keV = 1,000 electron volts = 1.602×10^{-9} erg) which has a magnitude that is convenient for specifying the energies of X-ray photons. However, by extension of its original meaning, the unit is used to define temperature (1 keV ≈ 11,600,000°K).

The term *1 keV spectrum* means the spectrum of thermal radiation from a black body, i.e., a perfect radiator of thermal energy, that has a temperature of 1 keV. Note, however, that an energy of 1 keV is not representative of the energy of the photons constituting such a spectrum: about 15 percent of the photons have energies of 1 keV or less, and these photons represent less than 3.5 percent of the total spectral energy. Half of the energy is carried by photons with energies greater than 3.5 keV. The spectrum extends roughly to 10 keV; photons with energies higher than this constitute only 1 percent of the spectral energy. See Chapter 4 for further discussion of black body radiators.

Table 2-7 Representative Mean Free Paths of Nuclear Weapon Radiation*

Source	Energy	Mean Free Path	
		Sea Level	80,000 ft
[redacted]			

*The mean free paths shown in this table are for individual particles in ambient air. Collectively, the particles may travel farther. Debris atoms, for example, assist one another in pushing the air atoms away from the burst point. X-ray photons completely ionize a small region of air near the burst, thus creating a nearly transparent region through which other X-ray photons can travel freely.

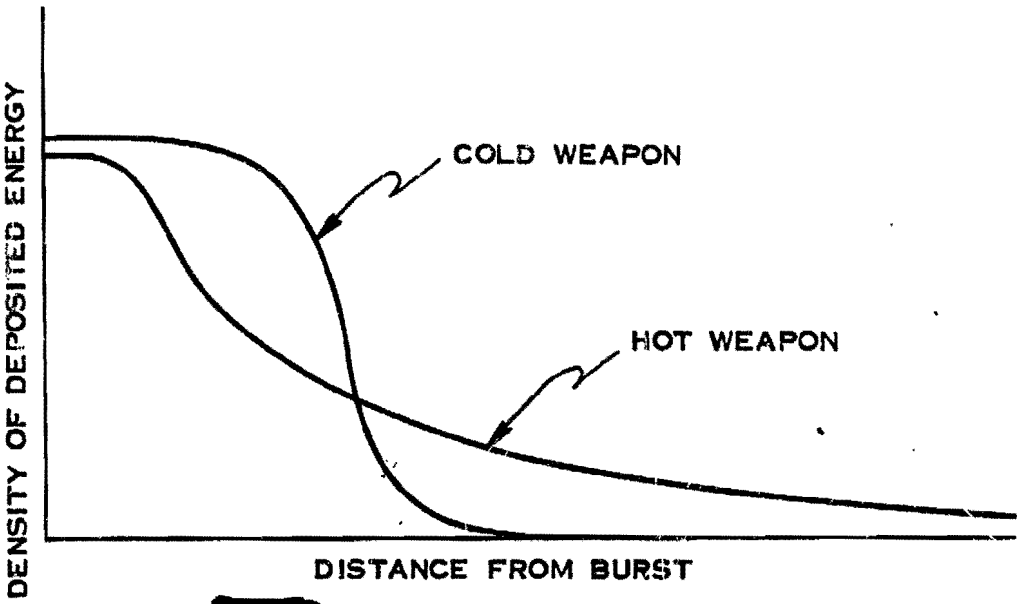

Figure 2-6 Energy Deposition in Air as a Function of Nuclear Source Characteristics (Not to Scale)

[redacted] Rough calculation may be made, however, by applying the following rule of thumb to weapons with enhanced outputs: blast calculations for a given radius may be based on a weapon yield that is equal to the amount of energy contained in the sphere defined by that radius. As this rule implies, the blast wave, as it propagates outward, picks up hydrodynamic energy from the heated air through which it passes.

DNA (6)(3)

DNA (6)(3)

[redacted]

Deleted

Figure 2-68. [redacted] Distribution of Deposited X-ray Energy in a Sea Level Atmosphere as a Function of Source Spectrum [redacted]

[redacted]

DNA (A)(3)

Deleted

Figure 2-69. [redacted] Density of Deposited Energy in Sea Level Air from Various Energy Sources [redacted]

[redacted]

[redacted]

[redacted] Many problems that require blast yield correction because of output spectrum will also require a blast yield correction because of altitude (paragraph 2-41). One correction factor does not replace the other, as illustrated in Problem 2-21.

[redacted] Effective blast yield, in percent, tends to increase with (1) increased range, (2) decreased radiating temperature, (3) increased yield, and (4) decreased altitude.

DNA (L)(3)

[redacted]

[redacted] As yield increases, the range for a given overpressure increases, but the distance that a given form of prompt energy can travel remains essentially the same; therefore, at a given overpressure level the blast wave from a higher yield encloses a greater fraction of the weapon output.

DNA (L)(

[redacted]

[redacted] As altitude decreases, the denser air confines the radiated energy to a smaller volume. Since the range for a given peak overpressure is relatively insensitive to altitude (Figure 2-66), the sphere defined by this range encloses an increasing fraction of the source energy as altitude decreases.

[redacted]

[redacted]

[redacted]

Problem 2-21. Calculation of Peak Overpressure from a Hot X-ray Warhead [redacted]

[redacted] Paragraph 2-44 describes the differences between the characteristics of blast waves from enhanced radiation weapons and the blast waves from conventional weapons. The following example will illustrate the use of the information discussed in paragraph 2-44.

[redacted] *Scaling.* Range is scaled in such a way that at a given scaled range the X-ray energy has passed through a given amount of air.

$$\frac{R_o}{R} = \frac{\rho}{\rho_o},$$

where R_o and ρ_o are range and ambient air density at sea level and R is range in air with an ambient density of ρ. The ordinate of Figure 2-68 (percent of radiated energy deposited) does not require scaling. Energy density added to the air is scaled in a way that accounts for spherical divergence and for yield.

$$\frac{\Delta E}{\Delta E_1} = \left(\frac{R_o}{R}\right)^2 W.$$

This equation is equivalent to:

$$\frac{\Delta E}{\Delta E_1} = \left(\frac{\rho}{\rho_o}\right)^2 W,$$

where ΔE_1 is the energy deposited by 1 kt, ΔE is the corresponding energy deposited by W kt, and the other terms are as previously defined. In addition to the scaling described above, Sachs' altitude scaling (paragraph 2-14) probably will be required.

DNA (b)(3)

[redacted]

[redacted]

DNA (b)(3)

Page 2-145 Deleted.

[redacted]

[redacted]

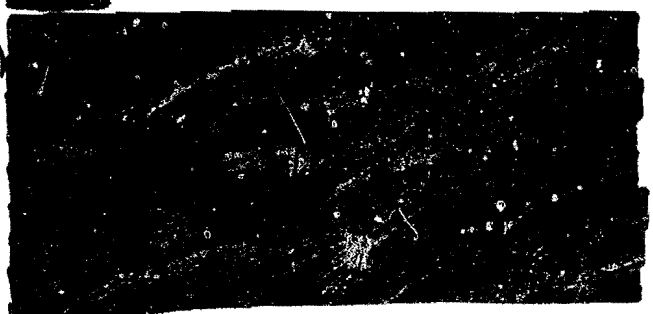

Reliability: The procedures described above have been substantiated by analysis of a limited number of computer calculations, and specific reliability estimates have not been made. The amount of error introduced by the procedures is expected to increase as the effective blast yield (in percent) decreases. In typical problems, the change in effective yield that the procedures predict is probably correct within about 25 percent.

Related Material: See paragraphs 2-7, 2-14, 2-41, and 2-44. See also Tables 2-1 and 2-2.

SECTION II
CRATERING PHENOMENA

A crater is formed when an explosion occurs at or near the ground surface. Figure 2-70a shows an idealized cross section of a crater formed by such an explosion. The diagram illustrates the dimensions that are commonly used to describe the crater, and the zones of subsurface deformation that typically surround a crater. The apparent crater is defined as the crater that is visible on the surface, the dimensions being measured between fallback and the original ground surface elevation. Fallback is material that was lifted or thrown out by the explosion and has fallen back within the true crater. The true crater is delineated by the approximate boundary between the fallback material and the rupture zone. The shape of the true crater is disguised by the fallback.*

The primary variables that affect the size and shape of the crater are the weapon yield and output characteristics, the height or depth of burst (HOB or DOB), the properties of the earth medium, and the geologic structure. As these variables change, the shape, characteristics, and actual dimensions of the crater change. Figure 2-70b illustrates the general cross sectional shapes of craters formed as a result of various burst positions.

*It is hypothesized by some that in certain geologies (notably those that are highly porous and water filled) the shock waves from the excavated crater may fracture the geological matrix. This could lead to late-time reconsolidation and liquefaction that could cause the apparent crater and the true crater to coincide and to be larger than the crater in a more competent geology. This theory is one that has been proposed to explain the large shallow craters produced at the Pacific Proving Ground.

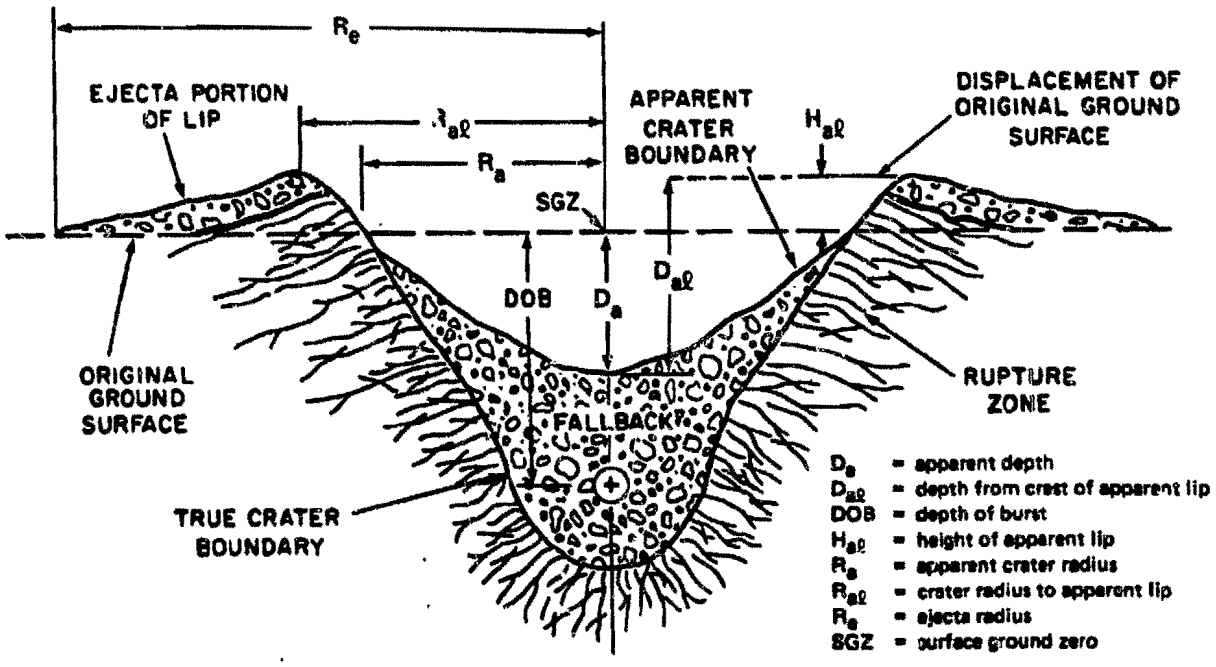

Figure 2-70a. Cross Section of a Crater from a Subsurface Nuclear Detonation

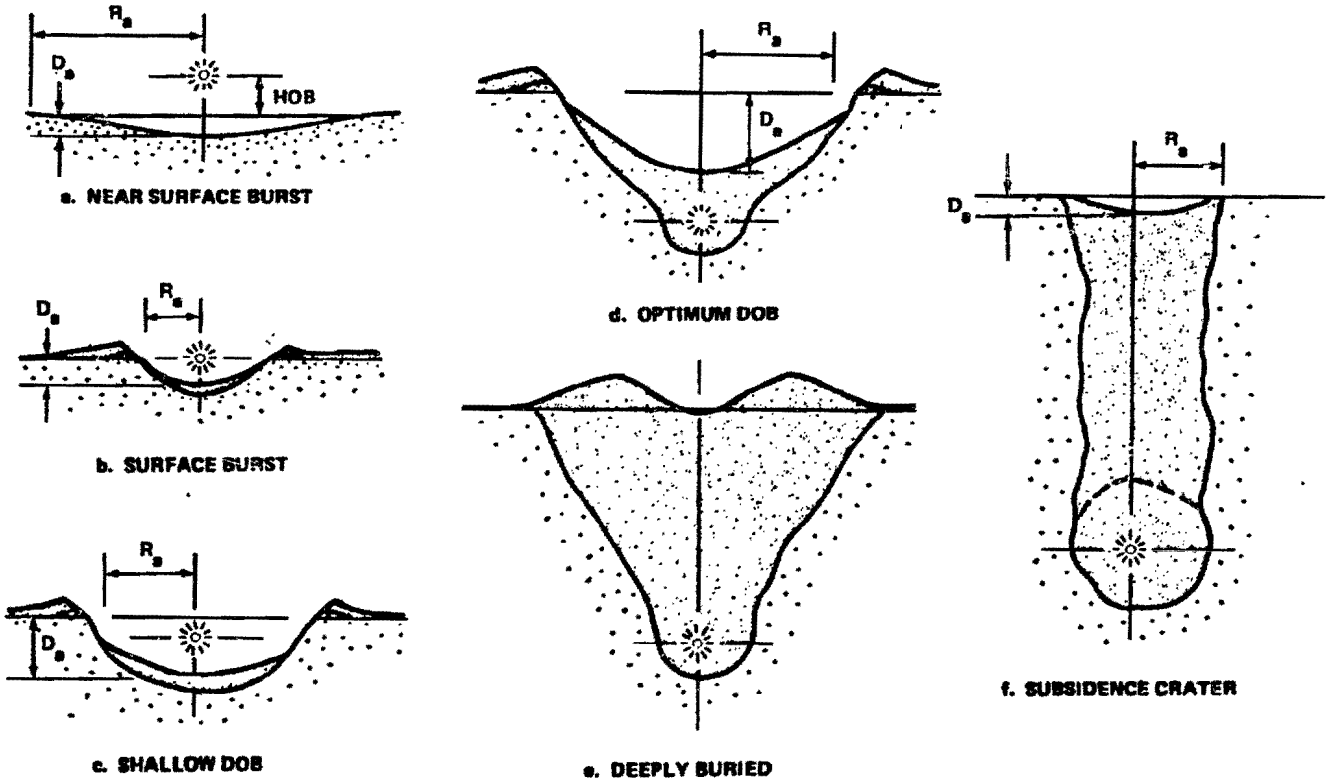

Figure 2-70b. Relative Crater Sizes and Shapes Resulting from Various Burst Positions

When a nuclear explosion occurs well above the surface, but low enough that the fireball still intersects the ground surface, a shallow crater is formed by compression of the earth beneath the explosion and no ejecta is produced. As the HOB decreases, the crater volume increases and the proportion of the crater volume that results from excavation and ejection also increases. This holds true in a continuum that includes surface bursts (HOB = 0) and buried bursts from the most shallow to the optimum DOB for the weapon being considered. If the burst takes place at the optimum depth of burial, i.e., at the depth that results in maximum apparent crater dimensions for the weapon being considered, the acceleration of the earth medium upward by the expanding explosion gases is the dominant feature of the cratering process. Figures 2.71a and 2.71b are photographs of apparent craters that occurred from nuclear explosions buried in soil and rock at depths near optimum for crater formation.

Finally, deeply buried explosions may lead to a subsidence crater, to a raised mound above the detonation point, or to no permanent displacement of the surface at all.

2-46 Energy coupling

When a nuclear weapon explodes at or above the surface of the earth, there are two phases in the process of energy flow into the ground. The initial phase is referred to as "radiation deposition." Part of the prompt radiation output from the weapon (x-rays; see Chapter 4) reaches the ground and is absorbed in a time that is so short (a fraction of a microsecond) that hydrodynamic motion in the ground will be negligible. The ground is heated rapidly, and most of the absorbed energy is reradiated back into the air above the surface.

In addition to the energy deposited directly in the ground, the atmosphere around the source is heated by radiation diffusion, producing a fireball that radiates energy into the ground. This creates a thin layer of very hot plasma. At this stage, before any significant mass motions have occurred, the plasma, a layer of very hot, high energy-density material, extends along the surface to a radius that depends on weapon yield (about 30 meters for a 1 Mt surface burst).

The radiative coupling is completed in approximately one to three tenths of a microsecond. The net energy permanently absorbed by the ground represents about 6 percent of the total explosive yield.

The second phase of the process of energy flow into the ground is the "debris impact" phase. Vaporized debris from the nuclear device and its associated material impact the ground surface and add more energy to the earth. This debris slap may last for 3 or 4 microseconds, depending on the height of burst, and may inhibit some reradiation out of the ground. The energy from the debris impact represents only about 2 percent of the nuclear warhead yield for a contact surface burst.

The radiation from the air in the fireball continues to add energy to the soil over a period of time that is much longer (up to several hundred microseconds) than the duration of the prompt-radiation deposition and debris impact phases. The amount of energy coupled by this process is very uncertain.

The height of burst has an important effect on the radiative coupling. The air acts as an energy sink for some of the downward directed x-rays, converting them into thermal energy. The radiative coupling of a 1 Mt burst at a height of burst of 5 meters could be a factor of two less than from a contact surface burst (HOB = 0 meters) of the same yield. Because of practical considerations, such as the location of the center of energy release in a reentry vehicle whose nose is just in contact with the ground, it is more likely that the HOB will be greater than zero.

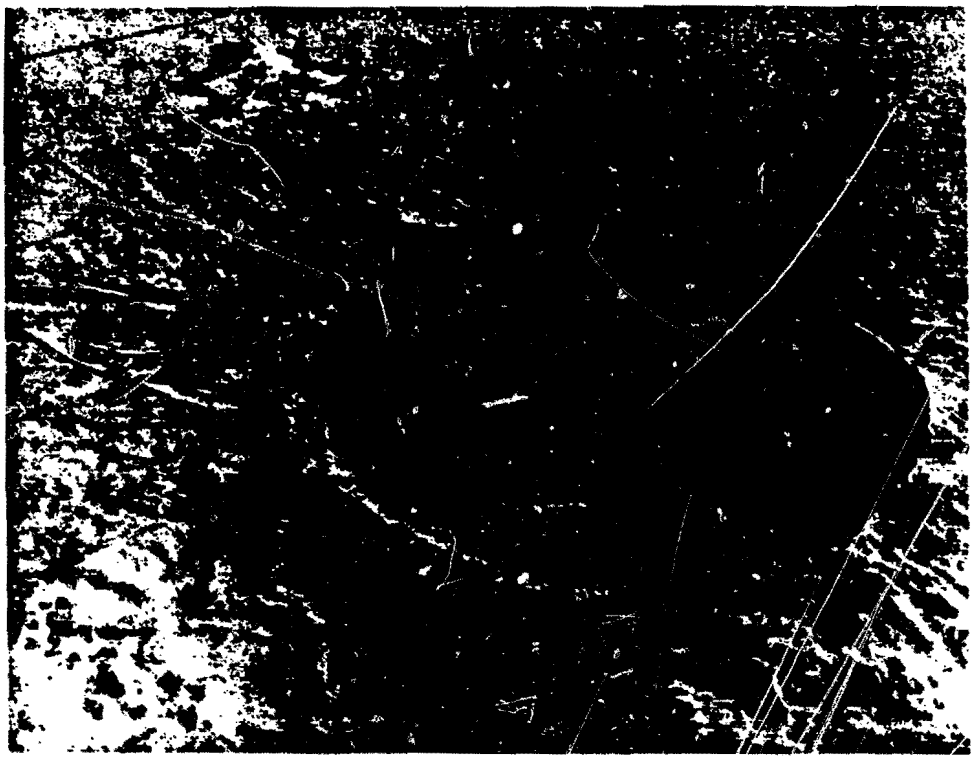

Figure 2-71a. SEDAN Event; Typical Crater Formed by a 100 kt Detonation in a Soil Medium at Optimum DOB: R_a = 186 m (611 ft.); D_a = 98.5 m (323 ft.); DOB = 194 m (635 ft.)

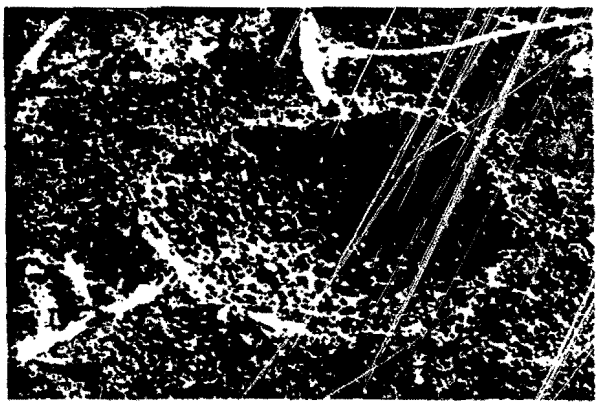

Figure 2-71b. DANNY BOY Event; Typical Crater Formed by a 0.43 kt Detonation in a Hard Rock Medium (Basalt) at Optimum DOB: R_a = 33.5 m (110 ft.); D_a = 18.9 m (62 ft.); DOB = 33.5 m (110 ft.)

ADA955386

CHAPTER 2 - PART 2
PAGES 2-151 through 2-303

Chapter 2

BLAST AND SHOCK PHENOMENA

AD-A955 386

DTIC
ELECTE
2 MAR 1989
S D
E

REPRODUCED BY
U.S. DEPARTMENT OF COMMERCE
NATIONAL TECHNICAL
INFORMATION SERVICE
SPRINGFIELD, VA 22161

On the other hand, the radiative coupling may be increased by as much as a factor of 5 compared to surface bursts if there is a slight penetration of the weapon into the surface of the ground (3 to 5 meters for a 1 Mt burst). This greater coupling is in addition to the well known increase in mechanical coupling, which is discussed in paragraph 2-47.

2-47 Mechanical Coupling

The preceding discussion outlined the flow of energy into the ground for cratering events that result from bursts at or above the surface. These processes take place during the first several milliseconds of actual crater formation. The hydrodynamic portion of crater formation may last for several seconds.

If the explosion occurs at a height-of-burst greater than 4 to 5 $m/kt^{1/3}$, the crater will be formed almost exclusively by compaction. Scouring, which results from airblast and airblast associated winds, contributes a small fraction of the crater volume. Since there is little fallback in such a crater, the true and apparent craters are essentially identical. As the height of burst is decreased, an increasing fraction of the crater is formed by excavation and ejection of ground material. In addition, compaction, plastic deformation and flow of the material in the rupture zone are principal mechanisms for crater formation of very near-surface bursts. These mechanisms produce a slight increase in material density as well as considerable brittle and plastic failure of the ground material. The mechanisms also cause a radial displacement with an overturning of crater material around the edge of the crater. The top of this mound is termed the crater lip. After detonation, the crater may be partially refilled by material falling back into the crater (fallback), by slumping, and by late-time rebound. The material thrown out beyond the crater lip (ejecta) forms a layer whose thickness diminishes with radial distance from the burst point.

The first diagram in Figure 2-70b illustrates the general crater shape that is expected from an above-surface burst. Despite many explosive cratering experiments with nuclear and high-explosive (HE) devices, the complex interrelationships that exist among the various mechanisms that could cause craters preclude the *quantitative* dynamics of crater formation by near-surface bursts from being well understood.

The size and shape of craters from subsurface detonations are affected significantly by the depth of burial. The dominant cratering mechanisms, which are discussed in succeeding paragraphs, will be related to the depths of burial shown in Figure 2-70b.

- *Crushing, Compaction, Plastic Deformation.* As the high pressure explosion gases expand against the surrounding medium, a spherical shock wave is generated. The initial shock pressures are as large as 10 to 100 million atmospheres. The medium surrounding a nuclear explosion is initially melted and vaporized as the shock passes through it. As the shock front moves outward in a spherically diverging shell, the medium behind the shock front is put into radial compression and tangential tension. The peak pressure in the shock front attenuates by spherical divergence and dissipative mechanisms in the medium. The material around the explosive charge (nuclear or HE) is crushed, heated, and physically displaced outward, forming a cavity. In regions outside this cavity, the shock wave will produce permanent deformation by plastic flow. This mechanism of crater formation is a significant contributor to crater size for bursts at or just below the ground surface (Figure 2-70b,(b)), and at depths of burial that result in subsidence craters (Figure 2-70b,(f)).

- *Spalling*. When an upward moving shock (compressive) front encounters the air-ground interface, the large mismatch of material properties results in the generation of a negative stress (rarefaction) wave. The refraction wave propagates back into the medium in which the burst occurred, and puts the medium (originally under high compression) into tension (or less compression). This phenomenon causes the medium to break up and move upward with a velocity characteristic of the total momentum imparted to it. In a loose soil material, this spalling ejects individual particles of similar size into the air. In a rock medium, however, the thickness and size of the spalled material generally is determined by the presence of pre-existing fracture patterns and zones of weakness. The velocity of the spalled material decreases in proportion to the decrease in peak compressive stress. The spall mechanism produces an extended rupture and plastic zone near the ground surface and contributes significantly to the true lip height of the crater. This mechanism appears to be dominant in determining crater size at shallow depths of burial (Figure 2-70b,(c)).
- *Gas Acceleration*. Gases are produced in the material surrounding the explosion by vaporization and chemical changes induced by heat and pressure. The near-adiabatic expansion of the gases imparts motion to the medium. At depths of burial at which crater dimensions are maximized (optimum DOB), the cavity gases produce appreciable acceleration in overlaying material before they escape (vent) through cracks extending from the cavity to the surface. Gas acceleration is the dominant crater producing mechanism at optimum DOB (Figure 2-70b,(d)). At shallow depths of burial the gases cannot exert significant pressure before venting occurs. In the case of very deep explosions, the weight of the overburden precludes any significant gas induced acceleration of the overlying material.
- *Overburden Collapse*. At depths of burial that are large (two or more times) compared to the optimum, the mechanism of overburden collapse (subsidence) becomes dominant. This effect is closely linked to the crushing, compaction and plastic deformation mechanism that produces an underground cavity. At these large depths of burial, spall and gas acceleration will not impart sufficient velocity to the overlying material to eject it physically from the crater. It would be expected that the crater volume would be determined largely by the underground cavity formed by the detonation. In a rock medium, however, material that is fractured and displaced from its original position tends to take up more space than it occupied in its natural state. This bulking action could result in no crater or, indeed, even a mound above the ground. A mound was produced after the SULKY detonation, as shown in Figure 2-72a.

  In certain geologic materials yet another type of subsidence occurs. When the pressure in the cavity decreases below overburden pressure, the roof of the cavity begins to collapse. In most media, this collapse will continue upward and will form a "chimney" of collapsed material. In a soil medium, where the density of the material will not change significantly after it has fallen, the volume of the cavity will be transmitted to the surface, forming a "subsidence crater" on the surface (Figure 2-70b,(f)). This phenomenon is illustrated in Figure 2-72b.

Figure 2-72a. SULKY Event; Mound Created by the Bulking of Rock Material in a Deeply Buried 0.087 kt Nuclear Detonation:
Mound Diameter = 48.8 m (160 ft.); Mound Height = 7.6 m (25 ft.); DOB = 27 m (90 ft.)

Reproduced from best available copy.

Reproduced from best available copy.

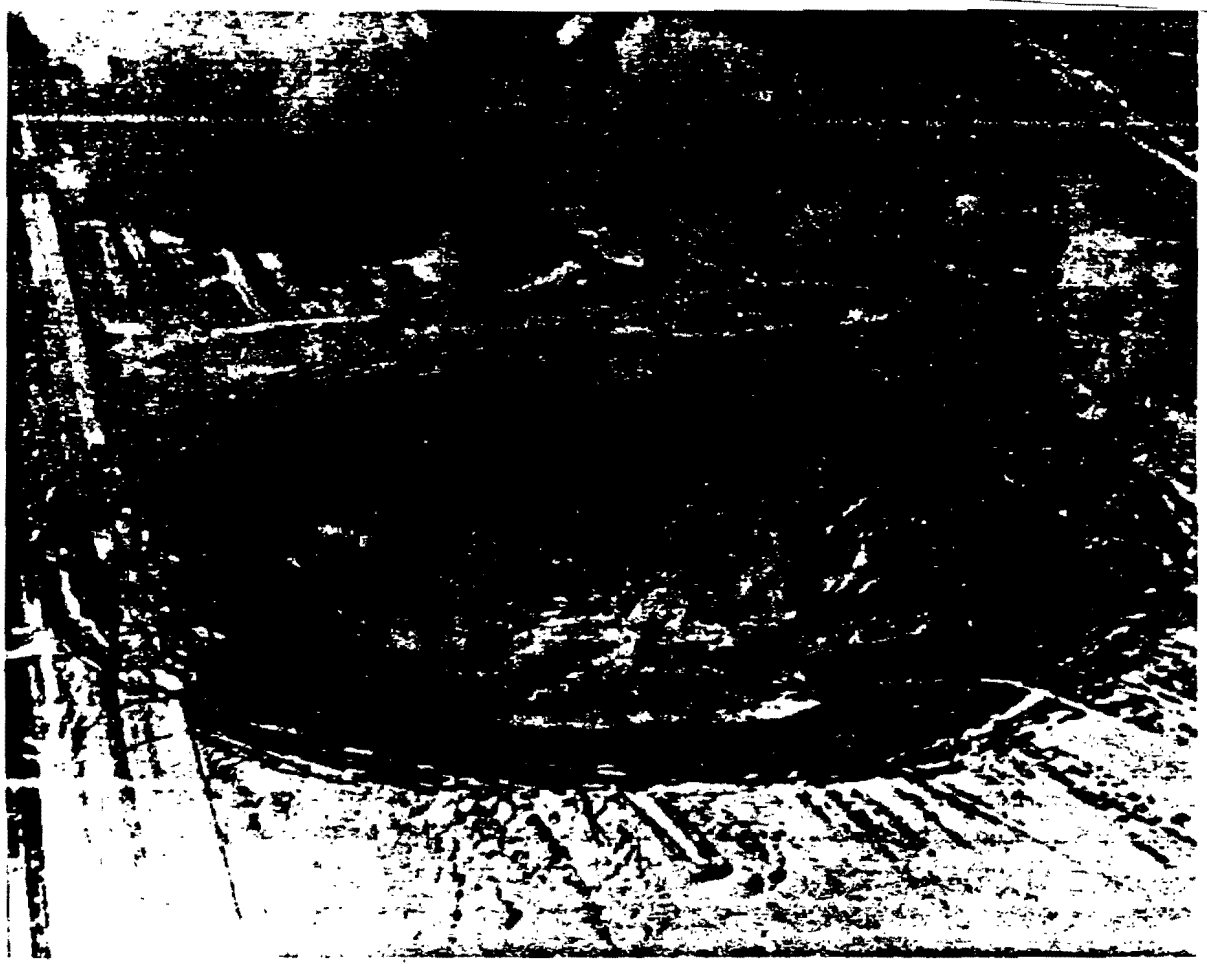

Figure 2-72b. PASSAIC Event; Subsidence Crater Produced by a Deeply Buried Nuclear Detonation in a Soil Medium

PREDICTION OF CRATER DIMENSIONS

The present prediction of crater dimensions for above-surface, surface, and shallow-buried bursts is based on the nuclear tests conducted in dry alluvial soil at the Nevada Test Site and the saturated coral at the Pacific Proving Ground. Extrapolation to other geologies is made on the basis of HE spherical-charge events. There have been no high-yield near-surface nuclear experiments in dry soil or rock. It is assumed that the influence of geology can be separated from that of the energy source. However, the nuclear tests conducted at the Pacific Proving Ground (saturated coral) and HE tests conducted at the Suffield Experiment Station (wet soil) suggest that the influence of geology is not *entirely* independent of the source. This fact is illustrated in Figure 2-73.

The dimensions of the crater vary in a complex manner as the HOB approaches the ground surface; but with lower HOBs the apparent depth of the crater generally increases and the ratio of the apparent radius to depth decreases. When crater dimensions for surface, above-surface, and shallow-buried bursts are scaled to yields much greater than 1 kt (for example, 1 Mt), the calculated change in the shape of the apparent crater as the yield increases is also an important consideration. This phenomenon, unfortunately, has not been observed in dry media.

2-48 Crater Dimension Scaling

The results of cratering explosions of various yields and burst geometries have been correlated by empirical scaling laws that express crater dimensions in terms of a standard yield of one kiloton. Crater dimensions for any other yield can be predicted by application of an empirical yield scaling exponent, as will be described in the succeeding paragraphs. The dimensions for which curves and scaling procedures will be presented are the radius of the apparent crater, R_a, the depth of the apparent crater, D_a, and the apparent volume V_a. Other pertinent crater dimensions such as the radius to the crest of the apparent lip and the height of the apparent lip, may be related to the above dimensions by scaling laws that will be described.

Several burst geometries will be considered: above-surface (near and contact), surface, shallow-buried, and deep-buried bursts. The actual height of burst (HOB) or depth of burst (DOB) is measured from the original ground surface to the *center of energy* of the weapon. The scaled HOB or DOB is the actual dimension divided by the scaled yield (described below). Of the *above-surface* bursts ($\mathrm{HOB}/W^{1/3} > 0$), the lower bursts are of most significance to cratering, i.e., $\mathrm{HOB}/W^{1/3} \leq 3$ m/kt$^{1/3}$. A *contact* burst is considered to be one wherein the weapon is in contact with the ground surface, and therefore has an actual HOB of approximately 0.5 m. A *surface* burst is one in which the HOB as defined above, is exactly zero. A *shallow-buried* burst has a $\mathrm{DOB}/W^{1/3} \leq 5$ m/kt$^{1/3}$ and the *deep-buried* burst has a $\mathrm{DOB}/W^{1/3} > 5$ m/kt$^{1/3}$.

No single yield scaling exponent has been found to be valid for scaling apparent crater dimensions over a wide range of yield, geology, and HOB or DOB. However, the following yield scaling exponents, α, (yield, W (kt), to the α power) have been found to be approximately correct for scaling the apparent crater dimensions for surface/above-surface bursts and for deep-buried bursts:

$$\alpha = 1/3 \text{ for } 0 \leq \frac{\mathrm{HOB}}{W^{1/3}} \leq 3 \text{ m/kt}^{1/3},$$

$$\alpha = 1/3.4 \text{ for } \frac{\mathrm{DOB}}{W^{1/3}} > 5 \text{ m/kt}^{1/3}.$$

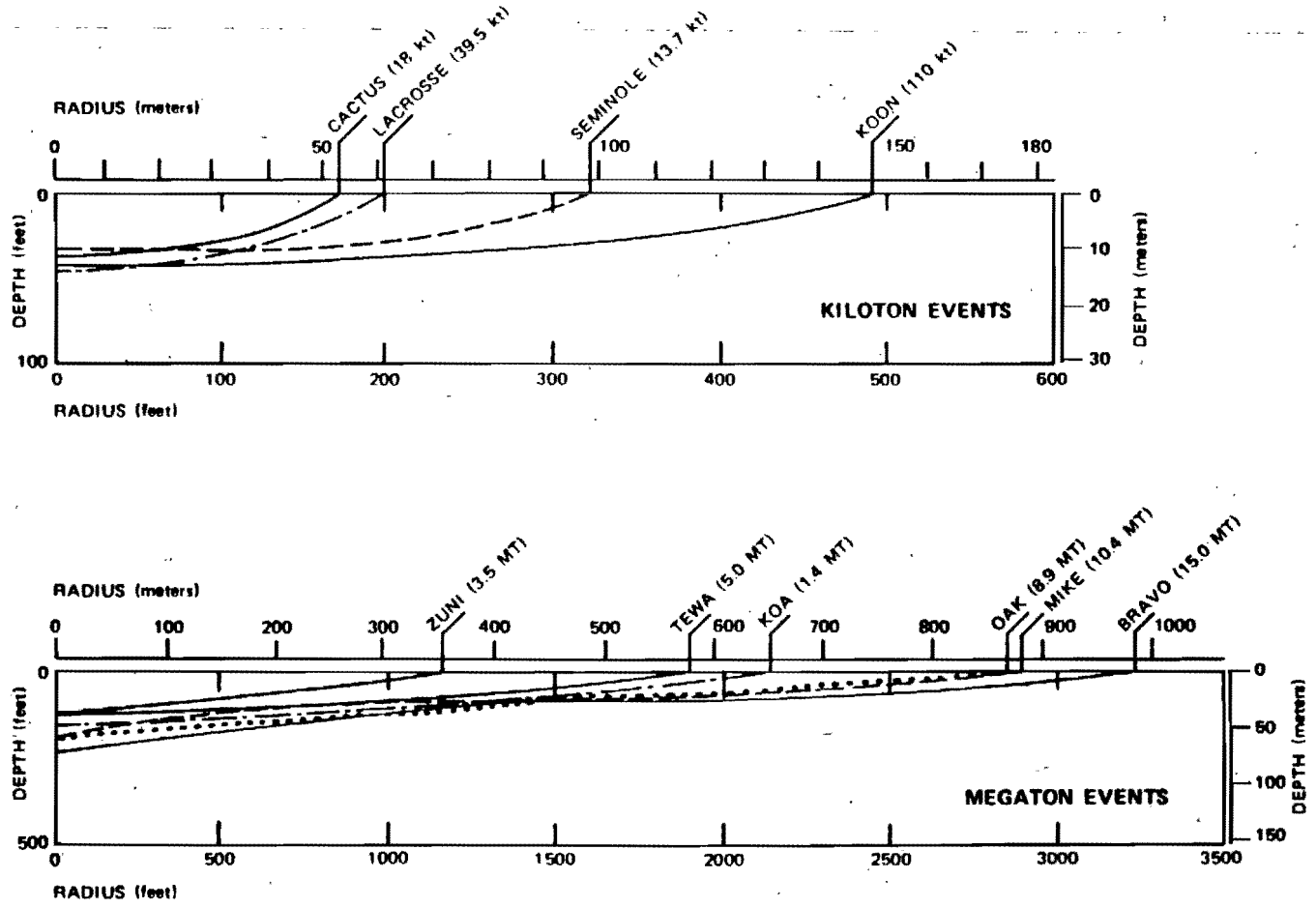

Figure 2-73. Typical Pacific Proving Ground Crater Profiles

In the shallow-buried region where the DOB/$W^{1/3}$ is less than 5 m/kt$^{1/3}$, the yield scaling exponent, a, is a function of depth of burial.* It is in this region that an interpolation procedure is required to determine a, as will be discussed in paragraph 2-49.

The near-surface region (HOB/$W^{1/3} \leq 3$ m/kt$^{1/3}$ to DOB/$W^{1/3} \leq 5$ m/kt$^{1/3}$) and the buried burst (DOB/$W^{1/3} > 5$ m/kt$^{1/3}$) region will be examined separately in the succeeding paragraphs. Five generic geologies have been chosen to describe the effect of various homogeneous media on cratering efficiency.

2-49 Volume of Craters from Surface and Near-Surface Bursts (HOB/$W^{1/3} \leq 3$ m/kt$^{1/3}$ to DOB/$W^{1/3} \leq 5$ m/kt$^{1/3}$)

Figures 2-74a through 2-75e show the apparent crater volume, as a function of height of burst,† for a near-surface 1 kt explosion in various homogeneous generic geologies. Figures 2-74a through 2-74e are valid for yields less than or equal to 1 kt and Figures 2-75a through 2-75e are valid for yields greater than 10 kt.

For yields between 1 and 10 kt, the crater volume may be estimated by using the best estimate curve of the appropriate geology for either 1 kt or 10 kt or a weighted average, depending upon the output characteristics of the warhead. The higher the radiative fraction, the closer the crater volume will be to the $W > 10$ kt curve. If, for example, it is known that a 3 kt weapon of interest has a high radiative output, the $W > 10$ kt curve should be used to determine the apparent crater volume. If, however, no information is available concerning the radiative output, the crater volume should be determined by interpolation, assigning a 60 percent weight to the $W \leq 1$ kt curve and 40 percent weight to the $W > 10$ kt curve, i.e., for a 3 kt weapon with no further information

$$V_a(3) = 0.6V_a(W \leq 1) + 0.4\ V_a(W > 10).$$

The yield scaling parameter, a, for near-surface bursts is determined as follows:

$$\frac{\text{HOB}}{W^{1/3}} \geq 0; a = 0.333$$

$$-5 \leq \frac{\text{HOB}}{W^{1/3}} < 0\ (\text{m/kt}^{1/3}); a = \text{(see Figure 2-76a)}.$$

Once the value of a is known, the apparent scaled crater volume can be obtained from Figures 2-74a through 2-75e for a specified yield (W) and HOB/W^a in the appropriate geology. The value obtained by this procedure is the "best estimate" of the apparent crater volume for a 1 kt explosion (V_{a1}).

The crater volume for yields other than 1 kt may be obtained by the following scaling relation:

$$\frac{V_a}{V_{a1}} = W^{3a},$$

where V_{a1} is the apparent crater volume for a 1 kt explosion, and V_a is the corresponding volume for a yield of W kt. The height of burst scaling relation is

$$\frac{\text{HOB}}{\text{HOB}_1} = W^a,$$

where HOB_1 is the height of burst for a 1 kt explosion, and HOB is the corresponding height of burst for a yield of W kt.

*Craters from detonations on the islands of the Pacific Proving Ground (Eniwetok and Bikini atolls) indicate that, for a saturated coral medium, the scaling exponent for the apparent crater radius may be greater than 1/3 and for the crater depth, smaller than 1/3. Until the reason that it is necessary to depart from cube-root scaling in saturated coral is understood, it will not be possible to determine similar departures in other media.

†In this group of figures, HOB is used to indicate both HOB and DOB, i.e., buried bursts are shown with a negative HOB.

The uncertainty in the crater volume for $W \leq 1$ kt is based on HE cratering results. It is assumed that the uncertainty is independent of geology and yield. The bounds shown in Figures 2-74a through 2-74e are not the results of a detailed statistical analysis. These bounds contain 95 percent of the experimental data, but statistical implications should not be drawn from this fact.

The best estimate for the $W > 10$ kt curve was determined by nuclear data from the Pacific Proving Ground. The lower bound was suggested by calculations. and was influenced by the fact that all the nuclear data were obtained from devices that were *very* dissimilar to modern weapons.

2-50 Crater Shapes and Dimensions for Surface and near-Surface Bursts

The shape of the crater from a near-surface burst must be known to determine the radius and depth from the crater volume and the explosive yield. The shape depends mainly on the yield, the scaled height of burst, and the geology Table 2-8 shows the shape to be expected as a function of these three variables. The succeeding discussion provides the necessary scaling relationships to determine the dimensions for the various shapes. Separate procedures are provided for each of the yield/HOB combinations shown in Table 2-8.

Table 2-8. Classification of Crater Shapes from Near Surface Bursts as a Function of Yield, Height of Burst, and Geology

Yield	Scaled HOB ($m/kt^{1/3}$)	Geology	Crater Shape
$W \leq 1$ kt	All	All	Bowl
$W > 1$ kt	$HOB/W^{1/3} \geq 0$	All	Dish
$W > 1$ kt	$-5 \leq HOB/W^{1/3} < 0$	Unsaturated	Dish/Bowl
		Saturated	Dish

a. $W \leq 1$ kt

The crater shape for near-surface bursts (-5 $m/kt^{1/3} \leq HOB/W^{1/3} \leq 3$ $m/kt^{1/3}$) in *all* geologies for $W \leq 1$ kt is best described as bowl-shaped. The dimensions of the apparent crater radius, R_a, and apparent crater depth (D_a) for these bursts are given by the following expressions:

$$1.1\ V_a^{1/3} \leq R_a \leq 1.4\ V_a^{1/3},$$
$$0.35\ V_a^{1/3} \leq D_a \leq 0.7\ V_a^{1/3}.$$

The best estimates for R_a and D_a are

$$R_a = 1.2\ V_a^{1/3},$$
$$D_a = 0.5\ V_a^{1/3},$$

where V_a = the best estimate apparent volume.

b. $W > 1$ kt

The crater shape for near-surface bursts in which $W > 1$ kt depends on the yield and HOB.

(1) $HOB/W^{1/3} \geq 0$.

For above-surface bursts ($HOB/W^{1/3} \geq 0$), in which $W > 1$ kt, the crater shape is best described as dish-shaped and the crater dimensions are determined by the expressions

$$1.1\ W^{0.08} \leq \frac{R_a}{V_a^{1/3}} \leq 1.4\ W^{0.08},$$

$$0.35\ W^{-0.12} \leq \frac{D_a}{V_a^{1/3}} \leq 0.7\ W^{-0.12}.$$

The best estimates for R_a and D_a are

$$\frac{R_a}{V_a^{1/3}} = 1.2\ W^{0.08},$$

$$\frac{D_a}{V_a^{1/3}} = 0.5\ W^{-0.12}.$$

where V_a = the best estimate apparent volume.

(2) $HOB/W^{1/3} < 0$

For near-surface buried events

$$\left(0 < \frac{DOB}{Wa} \leq 5 \text{ m/kt}^a\right),$$

in which $W > kt$, the shape of the crater may be either "bowl" or "dish" in nature or some combination of the two extremes. Mechanisms such as compaction, rebound, bulking, slumping and layering effects play a significant role in the final crater shape. Cratering experience to date is not sufficient to make quantitative judgments regarding the impact of each mechanism.

The apparent crater dimensions for near-surface buried events are determined by the expressions

$$\frac{R_a}{V_a^{1/3}} = 1.2\ W'^b \text{ meters},$$

$$\frac{D_a}{V_a^{1/3}} = 0.5\ W'^{-c} \text{ meters}.$$

The values of the exponents (b, c), as a function of DOB, are found in Figures 2-76b and 2-76c. These exponents are necessary to ensure a smooth continuous curve for the radii of large yield (1 Mt) bursts as the depth of burial increases. Existing data indicate that above-surface bursts of high yield nuclear explosions produce dish-shaped craters and buried nuclear explosions produce bowl-shaped craters. However, since no data exist in the region

$$0 < \frac{DOB}{Wa} \leq 5 \text{ (m/kt}^a\text{)},$$

it is necessary to provide a transition region in which the crater produced is neither dish-shaped nor bowl-shaped, but some intermediate of the two extremes. The above equations produce this smooth transition region for the crater dimensions.

It has been noted, however, that in highly saturated media slope failure and/or liquefaction can produce a shallow crater for buried events. High explosive tests conducted at Fort Polk, Louisiana are good examples of these phenomena.

Other pertinent crater dimensions may be related to the above dimensions as follows:

- The radius to the crater lip crest is

$$R_{a\ell} = 1.25R_a.$$

- The height of the apparent lip is

$$.25D_a \leq H_{a\ell} \leq .33D_a$$

(near-surface bursts).

A summary of the procedures for calculating craters from near-surface bursts is given on page 2-161, immediately preceding the applicable figures.

2-51 Dimensions of Craters from Deep-Buried Explosions

Cratering experiments with chemical explosives (HE) and nuclear explosions (NE) suggest that linear dimensions of craters from buried explosions scale according to a modified overburden rule. This scaling rule is somewhat cumbersome to use for the computation of crater dimensions, and the available data do not conclusively prove the validity of any single scaling rule. Therefore, a simplified yield scaling exponent, yield (kt) to the 1/3.4 power, has been chosen for scaling apparent crater dimensions for scaled DOBs greater than 5 $m/kt^{1/3}$. Figures 2-77 through 2-81 may be used to obtain apparent crater volumes for buried bursts in each of the soil types indicated. The curves in these figures are valid for *all* yields. The uncertainty in crater volume is independent of geology and yield, and is based on HE cratering results.

Crater radius and depth are given by the following expressions

$$1.1\ V_a^{1/3} \leq R_a \leq 1.4\ V_a^{1/3},$$

$$0.35\ V_a^{1/3} \leq D_a \leq 0.7\ V_a^{1/3}.$$

These expressions are valid for deep-buried bursts in *all* geologies for *all* yields. The best estimates for the crater dimensions are

$$R_a = 1.2\ V_a^{1/3},$$

$$D_a = 0.5\ V_a^{1/3},$$

where V_a is the best estimate of the apparent volume.

It is possible that slumping of the walls will produce a wide, shallow crater for some yield-DOB combinations in a saturated geology. The resulting crater shape is neither "bowl" nor "dish" in nature; it is some combination of the two. The only explosions to date that resulted in such occurrences in the craters have been in a very wet clay soil with the explosive charge at or near the optimum depth of burial.

The uncertainty in crater dimensions obtained from the expressions given above is, however, approximately correct for any specified crater volume. If the crater volume is chosen as the lower or upper uncertainty band from Figures 2-77 through 2-81, then the expressions for the radius and depth are still valid. A new range of crater dimensions is determined by using the equations and the chosen volume.

Figure 2-82 contains the best estimate prediction for high-explosive detonations in the five generic homogeneous geologies. These curves show the relative crater volumes for the geologies. The curves can be used as a guide as to the proper nuclear curve to use for a new or unknown geology. If some HE cratering data are available, the curves of Figure 2-82 can be used to determine which homogeneous geology is best for the problem. This figure should not be used to calculate crater volume for nuclear explosions.

Other pertinent crater dimensions may be related to the above dimensions as follows:

- The radius to the crater lip crest is

$$R_{a\ell} = 1.25R_a.$$

- The height of the apparent lip is

$$.20D_a \leq H_{a\ell} \leq .25D_a$$
(deep-buried bursts).

A summary of the procedures for calculating craters from deep-buried bursts is given on page 2-179, immediately preceding the applicable figures.

SUMMARY OF PROCEDURES FOR CALCULATING CRATERS FROM NEAR-SURFACE BURSTS ($-5\ m/kt^{1/3} \leq HOB/W^{1/3} \leq 3\ m/kt^{1/3}$)

Figures 2-74a through 2-75e and 2-76a, b and c, together with appropriate scaling laws, may be used to obtain crater volumes and dimensions from near-surface bursts in a variety of situations. The following summary provides a step-by-step procedure for obtaining such information. Example problems are provided on the pages immediately following the figures.

Required (either given or estimated)

Yield (W) in kt

Actual HOB or DOB (may be zero if required)

Soil type (one of the five generic types or a combination; see Figure 2-86b).

1. Determine yield scaling parameter, a, for burst position:
   a. $HOB/W^{1/3} \geq 0 \rightarrow a = 1/3 \equiv 0.333$,
   b. $0 < DOB/W^{1/3} \leq 5\ m/kt^{1/3} \rightarrow a$ from Figure 2-76a.

2. Compute HOB_1 (HOB for 1 kt) $= \dfrac{\text{Actual HOB}}{W^a}$

   or DOB_1 (DOB for 1 kt) $= \dfrac{\text{Actual DOB}}{W^a}$

3. Determine V_{a1} (apparent-crater volume for 1 kt):
   a. If $W \leq 1$ kt, use curve for given soil type from Figures 2-74a through 2-74e.
   b. If $W > 10$ kt, use curve for given soil type from Figures 2-75a through 2-75e.
   c. If $1\ kt < W \leq 10$ kt, with *low or unknown* radiative output, interpolate using $V_{a1} = 0.6\ V_{a1}$ (from $W \leq 1$ kt curve) $+ 0.4\ V_{a1}$ (from $W > 10$ kt curve).
   d. If $1\ kt < W \leq 10$ kt with *known high* radiative output, use curve for given soil type from Figures 2-75a to 2-75e.

4. Compute V_a (actual crater volume for yield other than 1 kt):

   $$V_a \text{ (actual volume)} = V_{a1}\ (W^{3a}).$$

   These curves are provided for each soil type: best estimate, upper bound, and lower bound. Using the following guidelines, select the curve most appropriate to the problem.
   a. Use *best estimate* V_{a1} if no specific geologic data are given. If actual HE tests are available for a specific site, compare them with the HE curves in Figure 2-82, and move toward the upper or lower bound NE curve to adjust for these data, depending on where the data are grouped.
   b. Use *lower bound* V_{a1} (if desirable) for target-oriented calculations (offensive-conservative) to calculate R_a or D_a. Consider lower-bound V_{a1} for targeting when calculating crater volume-related phenomena, such as ejecta, transient velocity or displacement.*
   c. Use *upper-bound* V_{a1} (if desirable) for design-oriented calculations (defense-conservative) to calculate R_a or D_a. Consider upper bound V_{a1} for design when calculating crater-related phenomena affected by volume.
   d. For $W > 10$ kt, the discrepancy between the theoretical calculations and the empirical data in our understanding of the energy coupling produced by modern weapons detonated at low HOBs or in contact with the earth (HOB = 0.5 m)

*In all instances it is recommended that upper and lower bound values be calculated in order to gain an appreciation of the effects of uncertainties on the particular problem under consideration.

must be considered. (See paragraph 2-49.) Since this discrepancy only occurs in the lower-bound V_a values, it principally influences targeting, or offensive-conservative, problems.

It is recommended that the lower-bound V_a values be considered in calculating kill probabilities (P_k) due to the crater, but that high credence in cratering P_k not be used in assessing overall system P_k.

Note: This cratering discrepancy is a systematic uncertainty and should not be treated as a random uncertainty.

5. Calculate R_a and D_a using the expression from the following table that fits the yield and HOB and inserting the appropriate V_a:

Yield	Near-Surface Bursts: Above Surface ($\frac{HOB}{W^{1/3}} \geq 0$)	Near-Surface Bursts: Below Surface ($\frac{DOB}{W^{1/3}} \leq 5$ m/kt$^{1/3}$)
$W \leq k$t	$R_a = 1.2\, V_a^{1/3}$	same
	$D_a = 0.5\, V_a^{1/3}$	same
$W > 1$ kt*	$R_a = 1.2\, W^{0.08}\, V_a^{1/3}$	$R_a = 1.2\, W^{b}\, V_a^{1/3}$
	$D_a = 0.5\, W^{-0.12} V_a^{1/3}$	$D_a = 0.5\, W^{-c}\, V_a^{1/3}$

*See Figures 2-76b and 2-76c for determining b and c.

The dimensions R_a, D_a, and V_a can be related to other pertinent crater dimensions as follows:

- The radius to the crest of the apparent-crater lip is

$$R_{a\ell} = 1.25\, R_a.$$

- The height of the apparent lip is

$$0.25\, D_a \leq H_{a\ell} \leq 0.33\, D_a$$

for near-surface bursts.†

Variations in the thickness of the ejecta as a function of range from the surface ground zero (SGZ) are discussed in paragraphs 2-52 and 2-53.

†An exception to this is a similar crater formed by an explosion at the Pacific Proving Ground. The crater had no lip and greatly reduced ejecta. It is thought that such a crater shape may have been the result of a late-time reconsolidation/liquefaction process, which caused the crater lip to be below the water surface.

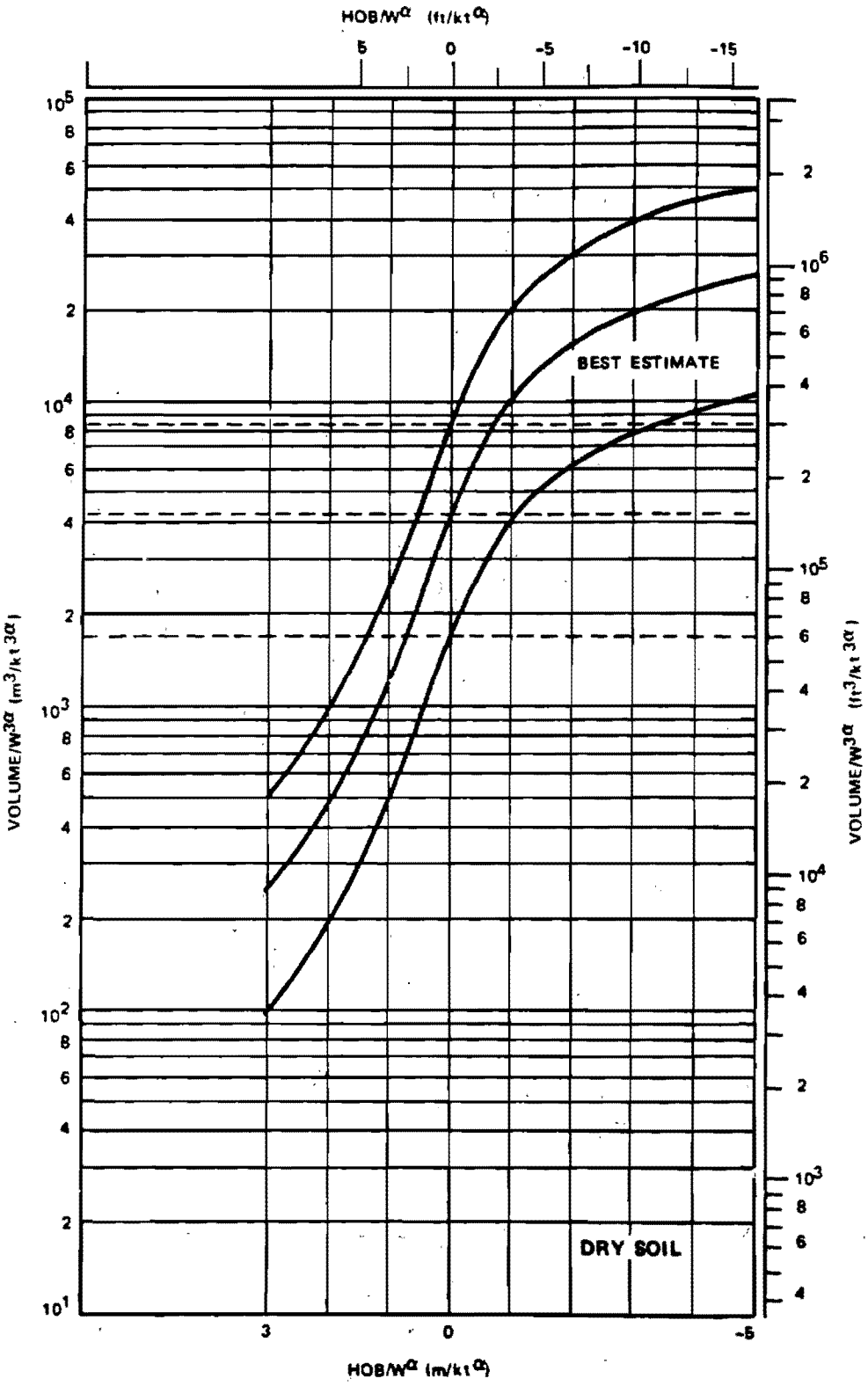

Figure 2-74a. Apparent Crater Volume for a 1-Kiloton Near-Surface Explosion in Dry Soil; Applicable for W ≤ 1 kt

[redacted]

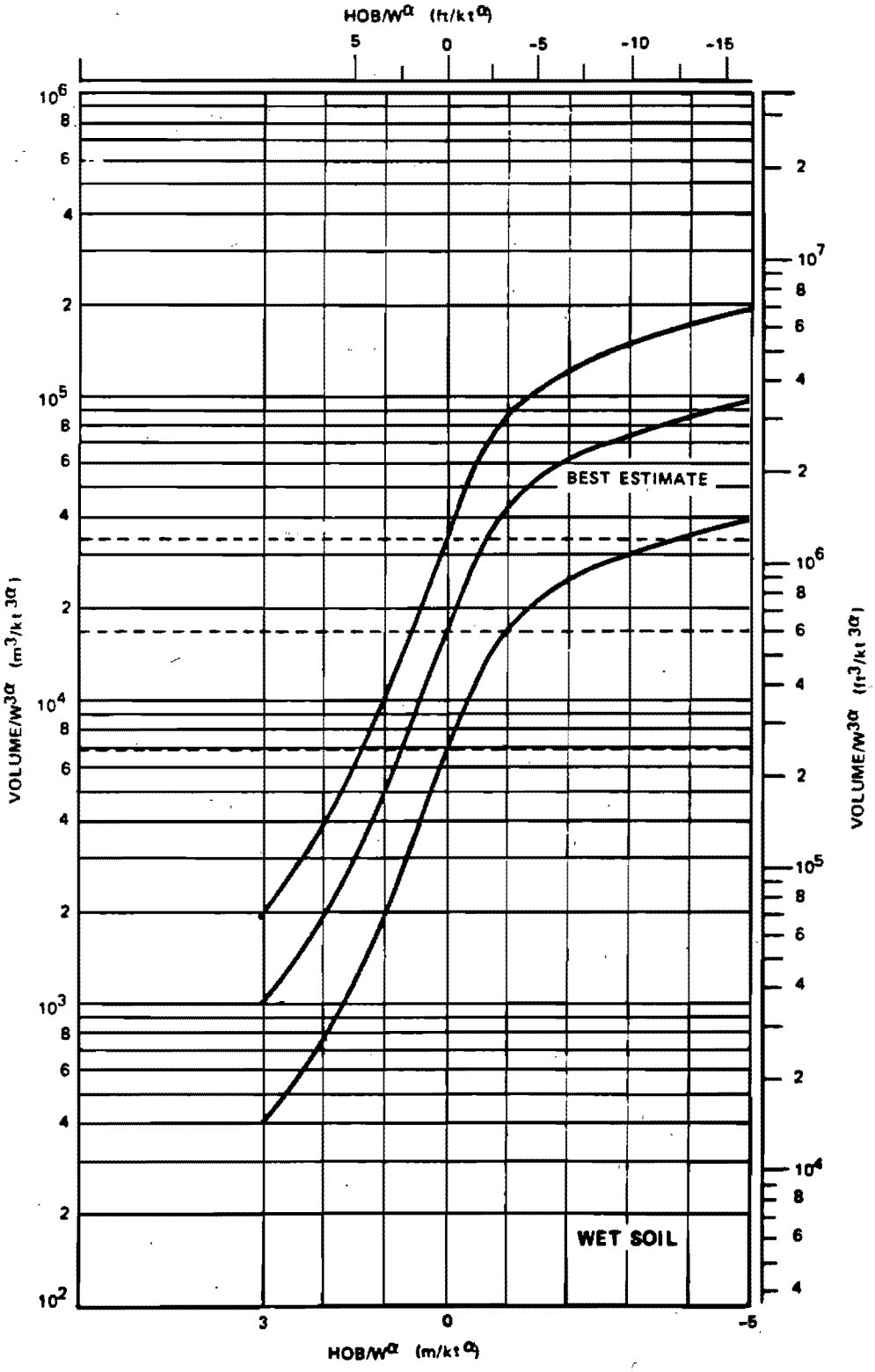

Figure 2-74b. Apparent Crater Volume for a 1-Kiloton Near-Surface Explosion in Wet Soil; Applicable for W ≤ 1 kt

[redacted]

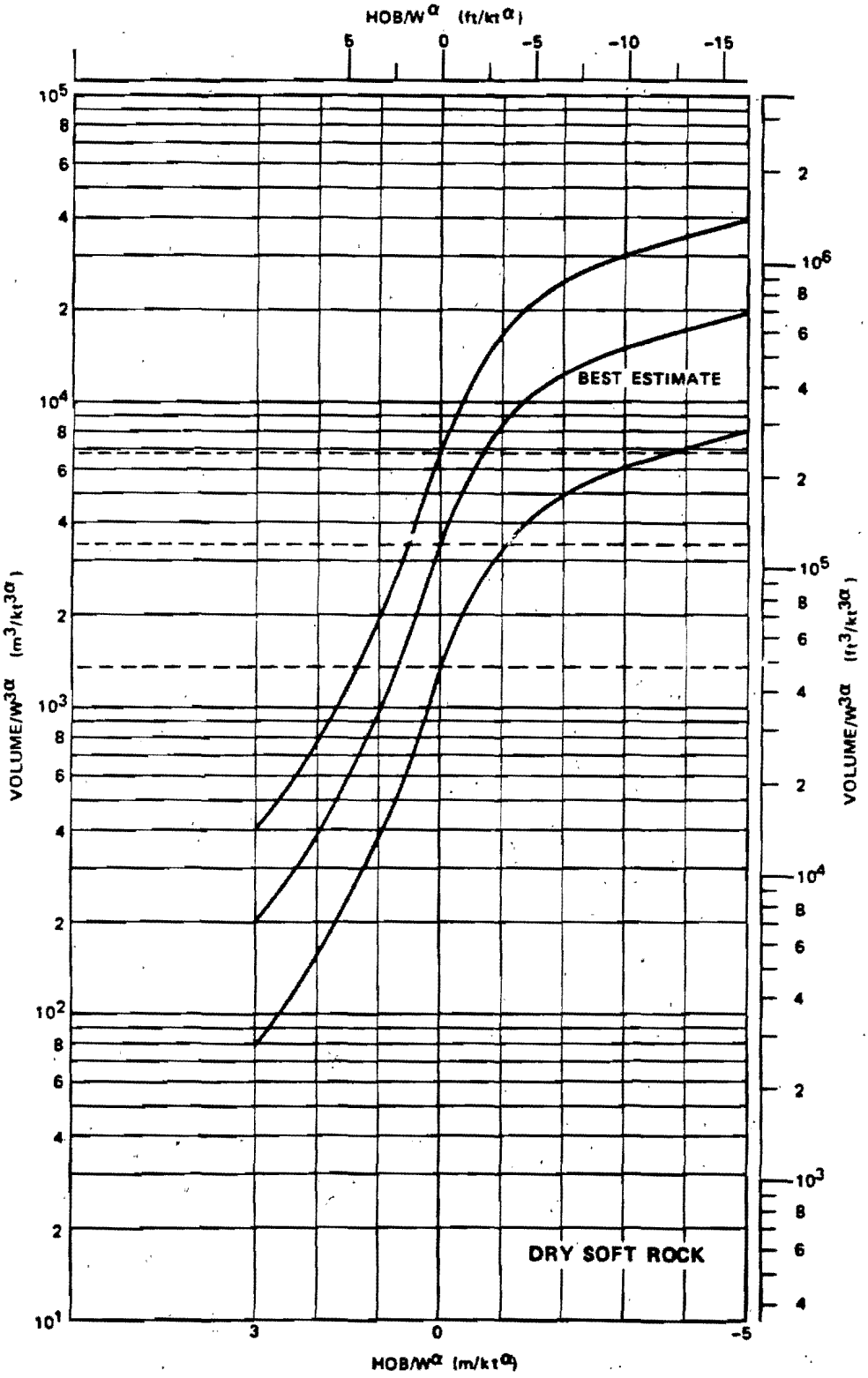

Figure 2-74c. Apparent Crater Volume for a 1 Kiloton Near-Surface Explosion in Dry Soft Rock; Applicable for W ≤ 1 kt

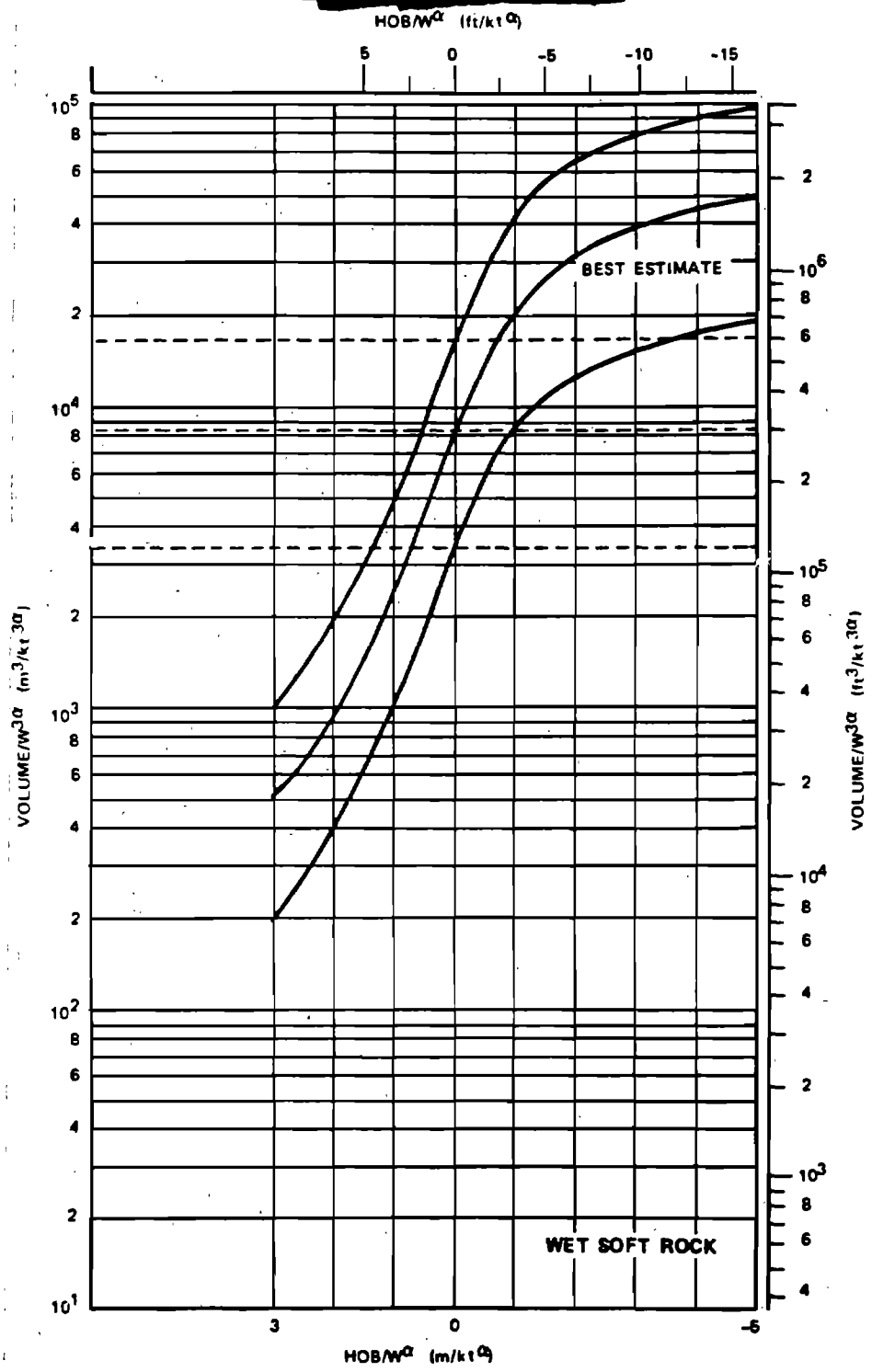

Figure 2-74d. Apparent Crater Volume for a 1-Kiloton Near-Surface Explosion in Wet Soft Rock; Applicable for W ≤ 1 kt

[redacted]

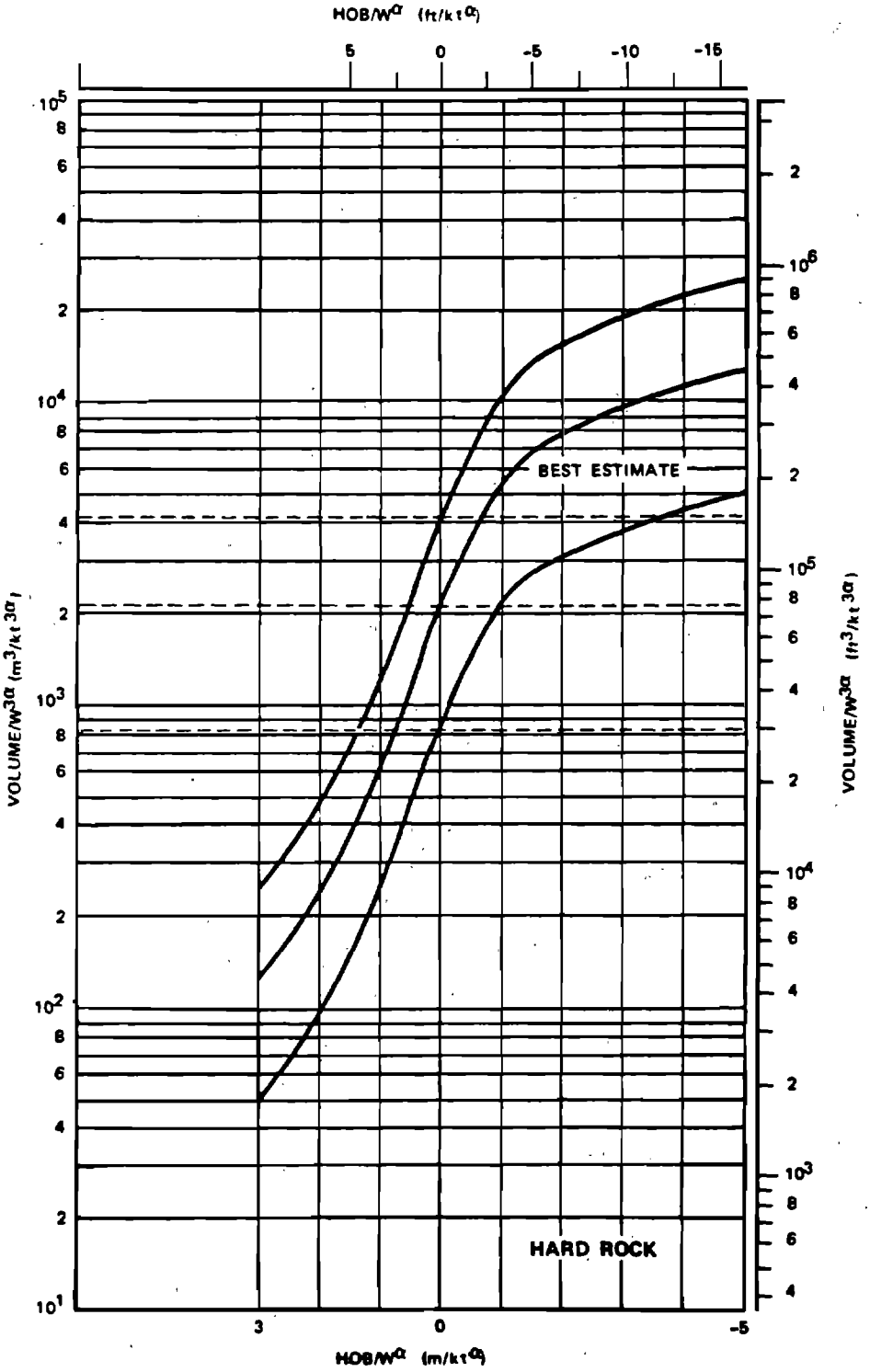

Figure 2-74e. Apparent Crater Volume for a 1 Kiloton Near-Surface Explosion in Hard Rock; Applicable for W ≤ 1 kt

[redacted]

[redacted]

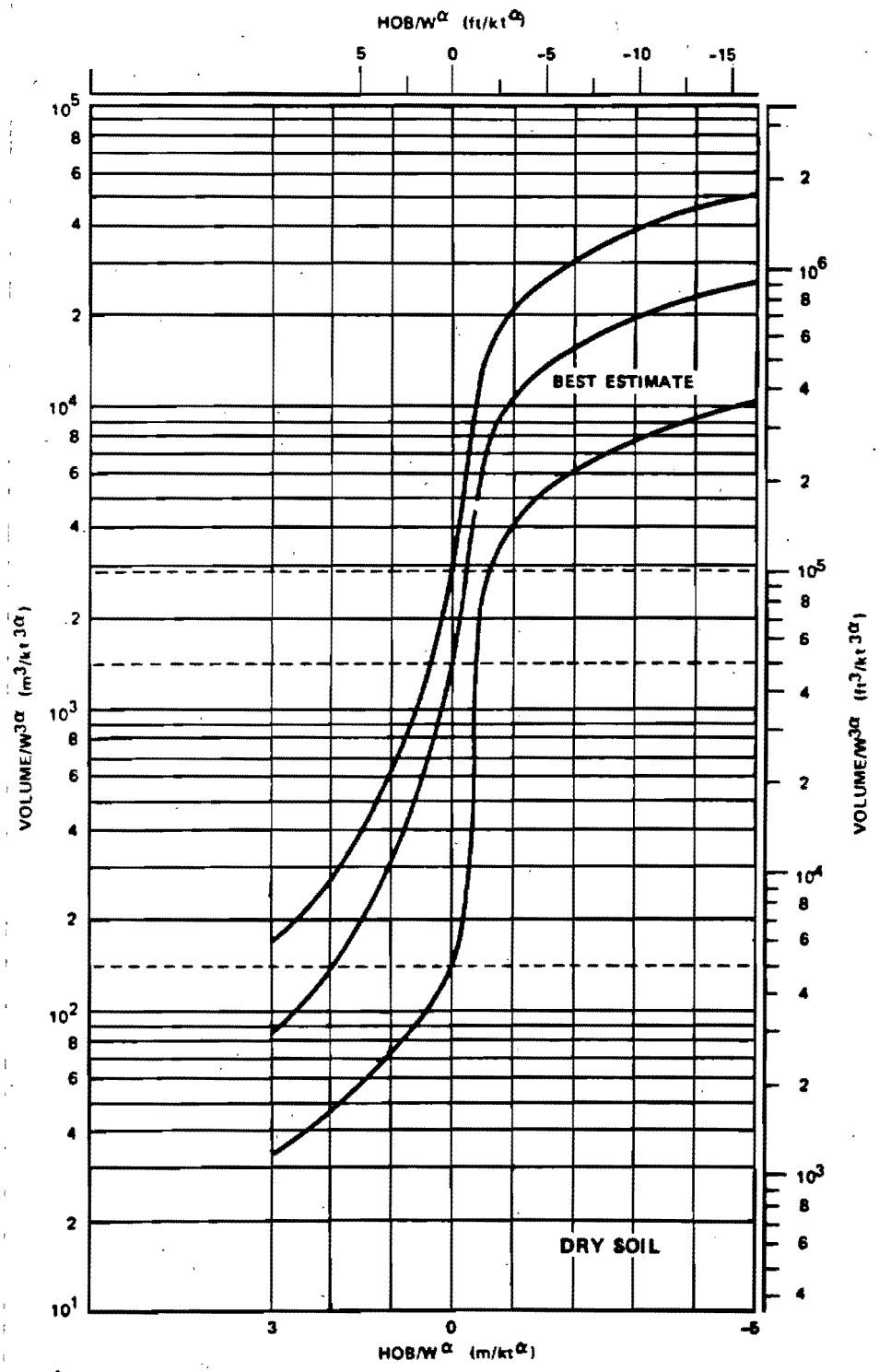

Figure 2-75a. Apparent Crater Volume for a 1 Kiloton Near-Surface Explosion in Dry Soil; Applicable for W > 10 kt

[redacted]

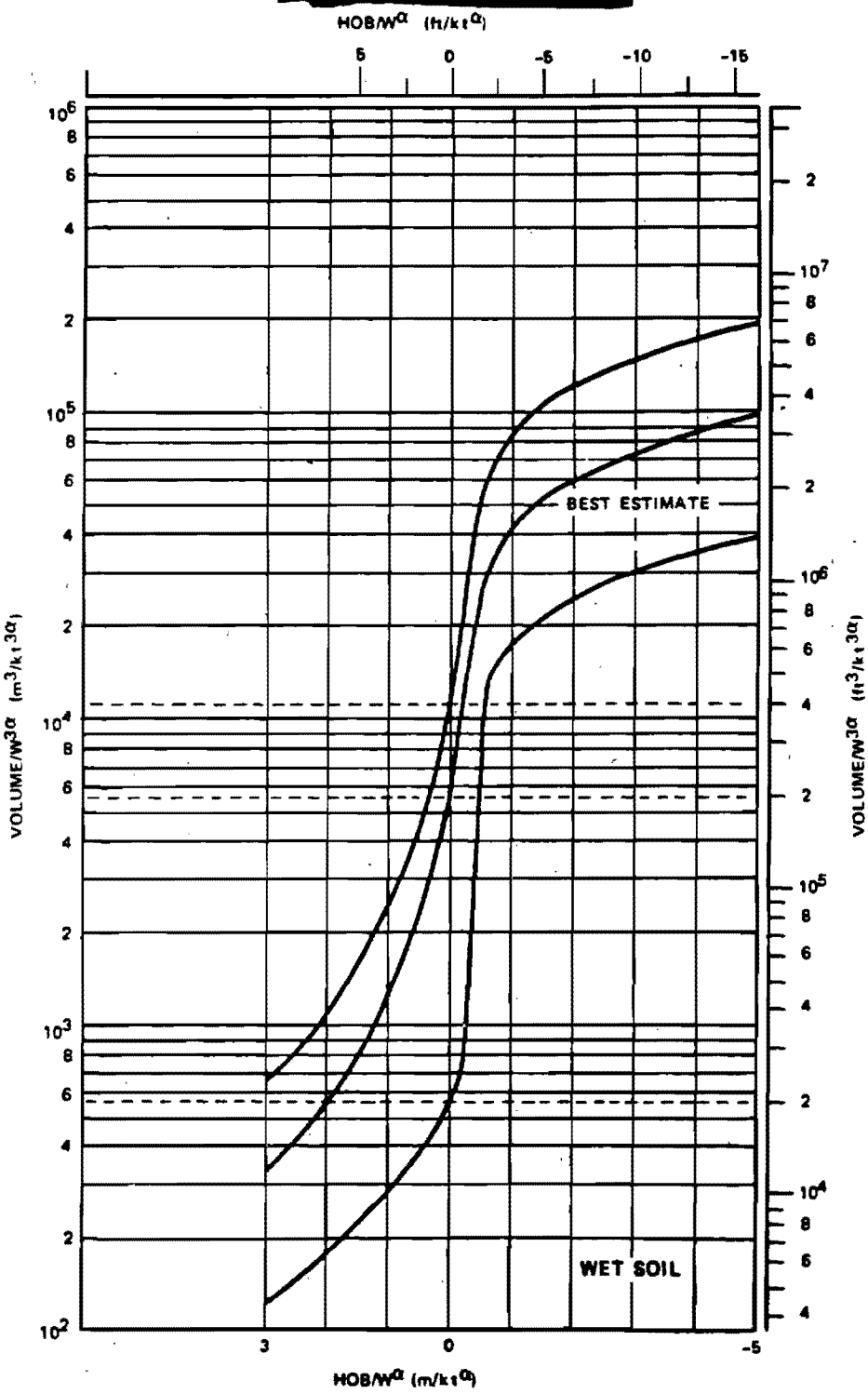

Figure 2-75b. Apparent Crater Volume for a 1 Kiloton Near-Surface Explosion in Wet Soil; Applicable for W > 10 kt

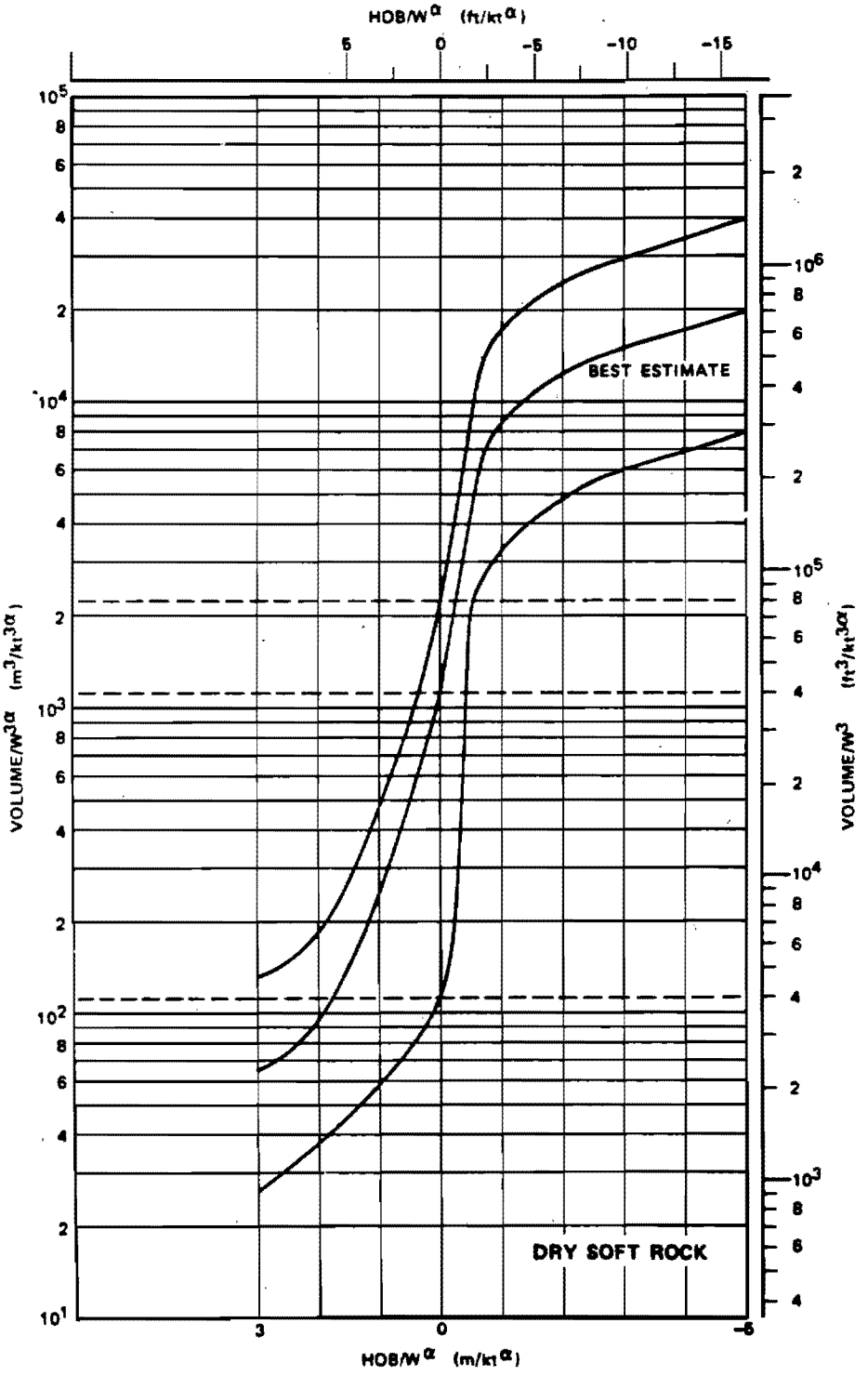

Figure 2-75c. Apparent Crater Volume for a 1 Kiloton Near-Surface Explosion in Dry Soft Rock; Applicable for W > 10 kt

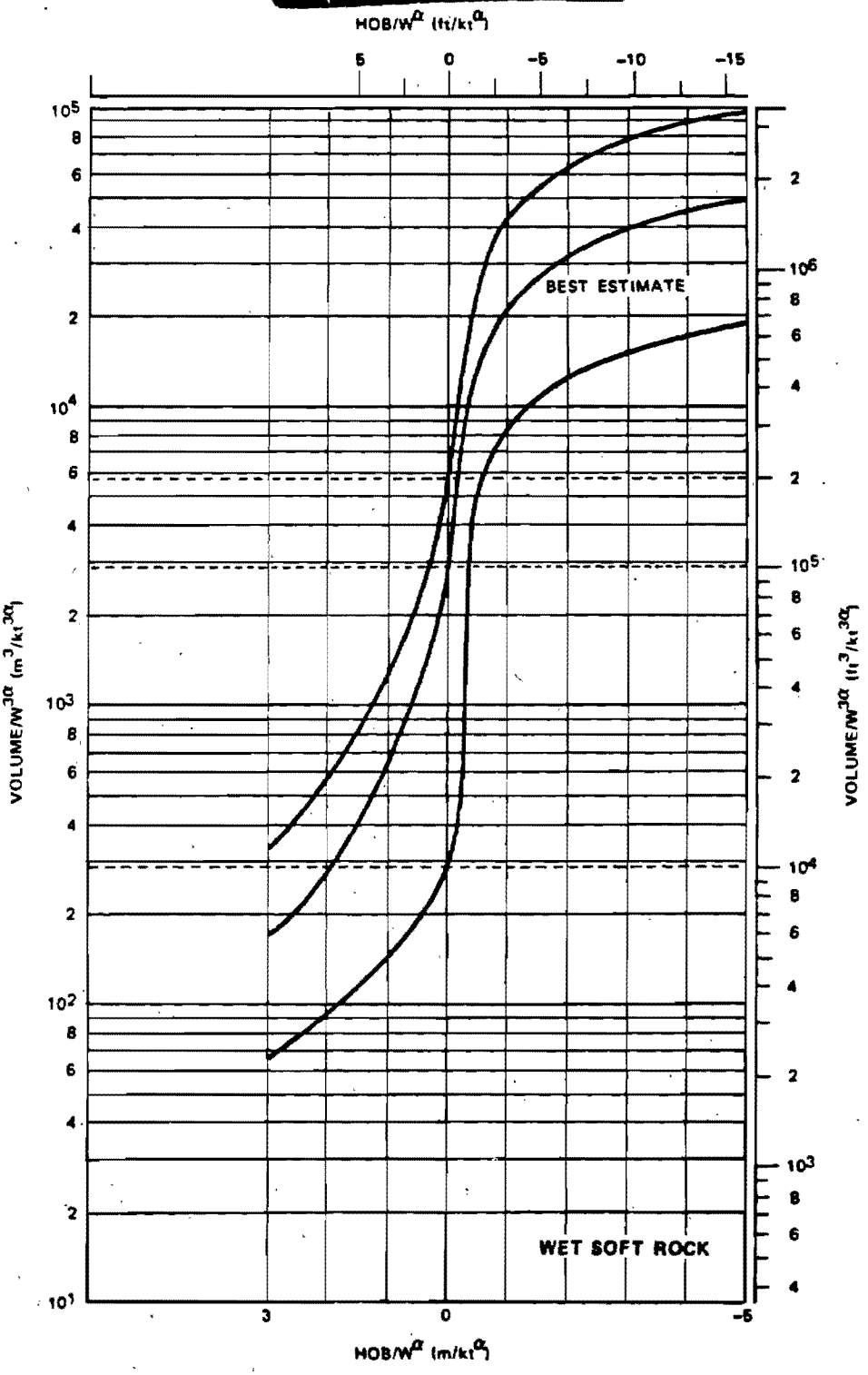

Figure 2-75d. Apparent Crater Volume for a 1-Kiloton Near-Surface Explosion in Wet Soft Rock; Applicable for W > 10 kt

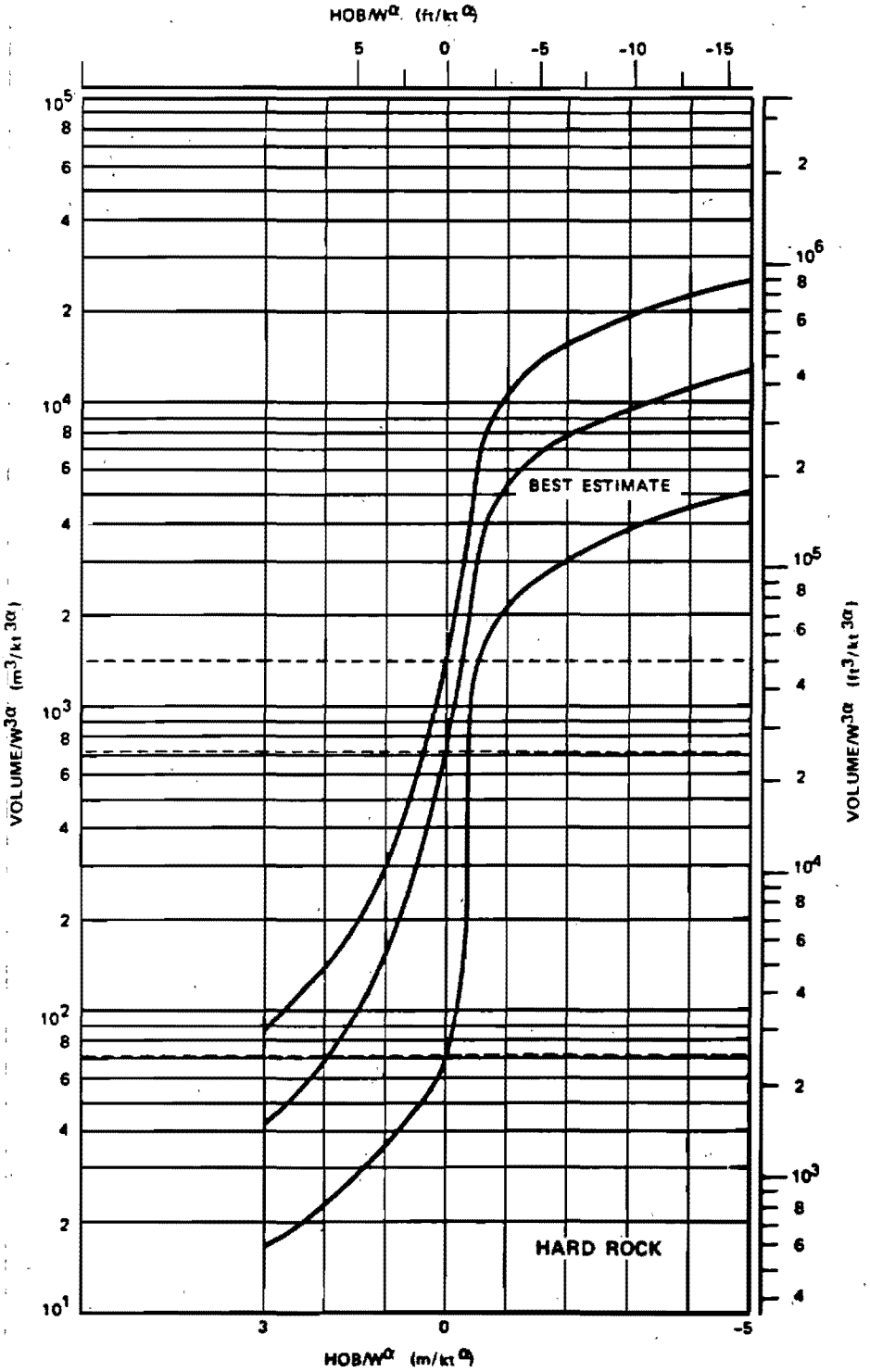

Figure 2-75e. Apparent Crater Volume for a 1 Kiloton Near-Surface Explosion in Hard Rock; Applicable for W > 10 kt

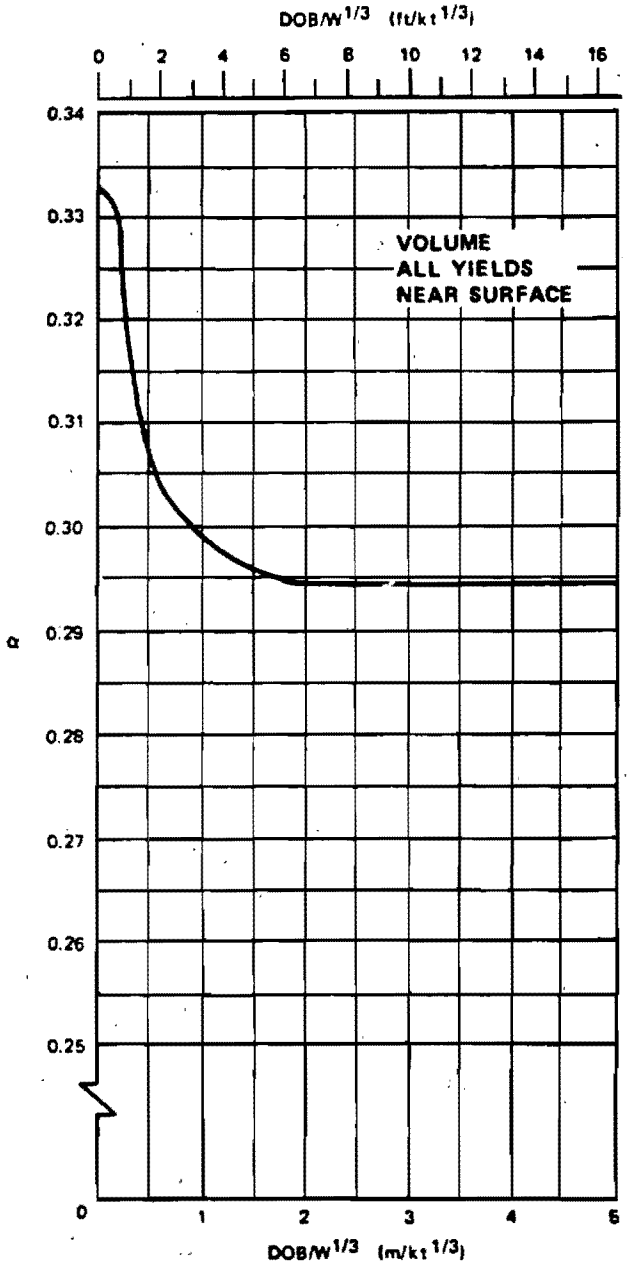

Figure 2-76a. Volume Scaling Exponent, α, as a Function of Scaled DOB for Near-Surface Explosions, All Yields

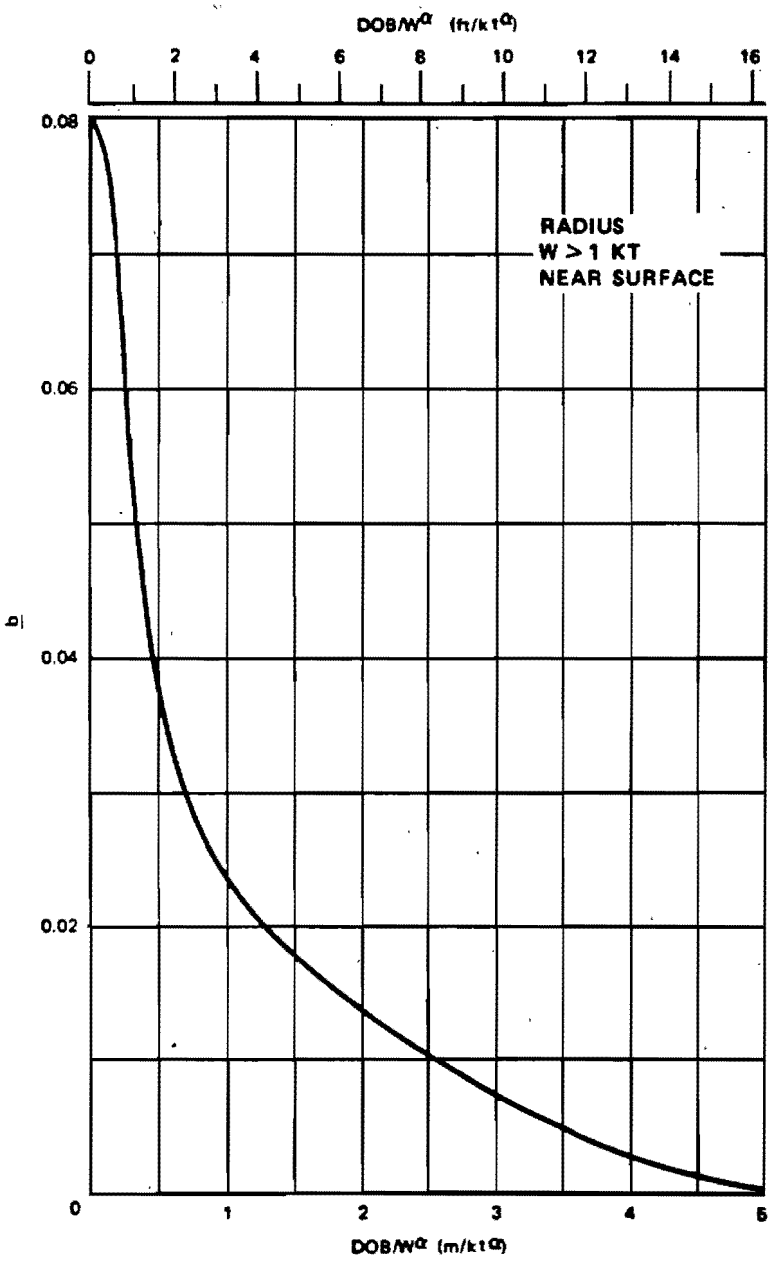

Figure 2-76b. Yield Transition Exponent, b, for Calculation of the Radius of Near-Surface, Buried Explosions W > 1 kt

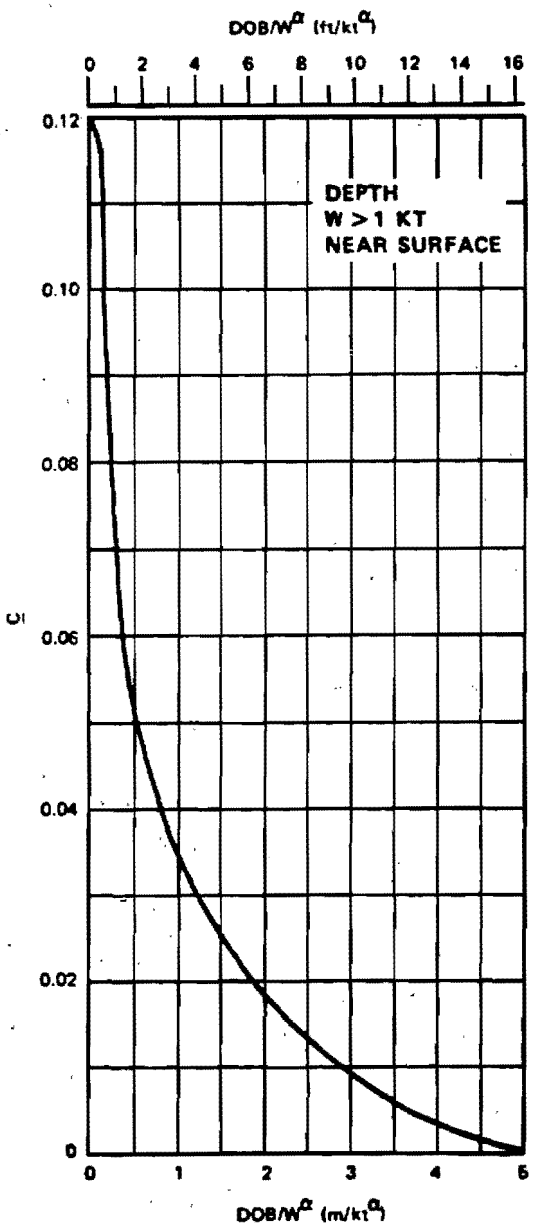

Figure 2-76c. Yield Transition Exponent, c, for Calculation of the Depth of Near-Surface, Buried Explosions, W > 1 kt

Problem 2-22. Crater Dimensions for Above-Surface Bursts (HOB > 0)

Figures 2-74a through 2-75e include curves that indicate the apparent crater volume as a function of HOB for a 1 kt explosion in various homogeneous media.

Scaling. For yields other than 1 kt, the crater volume scales as follows:

$$V_{a1} = W^{3\alpha},$$

where V_{a1} is the apparent crater volume for a 1 kt explosion, and V_a is the corresponding volume for a yield of W kt. The height of burst scales as

$$\frac{\text{HOB}}{\text{HOB}_1} = W^{\alpha}$$

Example:

Given: A hypothetical 300 kt contact burst on dry soil.

Find. The apparent crater radius and depth.

Solution: The HOB for a contact nuclear explosion is 0.5 meters. From paragraph 2-49,

$$\alpha = 0.3333$$

for HOB $\geq$ 0. Therefore,

$$\text{HOB}_1 = \frac{\text{HOB}}{W^{\alpha}} = \frac{0.5}{(300)^{1/3}} = 0.075 \text{ m/kt}^{1/3}.$$

From Figure 2-75a, the apparent crater volume for a 1 kt explosion at a scaled HOB of 0.075 m/kt$^{1/3}$ in dry soil is

$$V_{a1} = 1.25 \times 10^3 \text{ m}^3/\text{kt}^{3\alpha}$$

$$V_a = V_{a1} (W)^{3\alpha} = 1.25 \times 10^3 (300)^{1.0}$$
$$= 3.75 \times 10^5 \text{ m}^3.$$

Answer: The dimensions of the crater for a 300 kt contact burst are

$$\frac{R_a}{V_a^{1/3}} = 1.2\, W^{0.08} = 1.2\,(300)^{0.08} = 1.89,$$

$$R_a = 1.89\,(V_a)^{1/3} = 1.89\,(3.75 \times 10^5)^{1/3}$$
$$= 137 \text{ meters},$$

and

$$\frac{D_a}{V_a^{1/3}} = 0.5\, W^{-0.12} = 0.5\,(300)^{-0.12} = 0.252,$$

$$D_a = 0.252\,(V_a)^{1/3} = 0.252\,(3.75 \times 10^5)^{1/3}$$
$$= 18.2 \text{ meters}.$$

Uncertainty. The dimensions of the apparent crater obtained for the above problem have a range of uncertainties that are defined by the following:

$$1.1\, W^{0.08} \leq \frac{R_a}{V_a^{1/3}} \leq 1.4\, W^{0.08}$$

$$125 \leq R_a \leq 159 \text{ meters},$$

and

$$0.35\, W^{-0.12} \leq \frac{D_a}{V_a^{1/3}} \leq 0.7\, W^{-0.12}$$

$$13 \leq \frac{D_a}{V_a^{1/3}} \leq 25 \text{ meters}.$$

The characteristics of the medium represent a major uncertainty in the crater data presented in Figure 2-74a through 2-75e. Details concerning material properties and geologic structure are not usually known about any particular site, but, in many cases small changes in these media characteristics can cause large changes in crater dimensions. The largest changes usually occur in the presence of an intersecting water table or a layered medium. Therefore, the range of uncertainty for a generic geology such as "wet soil" can be quite large, especially in the prediction of the apparent crater depth.

Related Material: See paragraphs 2-46 through 2-50; see also paragraphs 1-14 and 1-33.

Problem 2-23. Crater Dimensions for a Shallow Buried Burst

Figures 2-74a through 2-75e include curves that indicate the apparent crater volume as a function of HOB for 1 kt explosion in various homogeneous media.

Scaling. For yields other than 1 kt, the crater volume scales as follows:

$$\frac{V_a}{V_{a1}} = W^{3a}.$$

where V_{a1} is the apparent crater volume for a 1 kt explosion, and V_a is the corresponding volume for a yield of W kt. The height of burst scales as

$$\frac{\text{HOB}}{\text{HOB}_1} = W^a.$$

Example:

Given. A hypothetical 30 kt burst in wet soft rock at a depth of burial of 3 meters.

Find. The apparent crater radius and depth.

Solution: The value of a is obtained from Figure 2-76a, which must be entered with the scaled DOB.

The scaled DOB is

$$\frac{\text{DOB}}{W^{1/3}} = \frac{3}{(30)^{1/3}} = 0.965 \text{ m/kt}^{1/3}.$$

From Figure 2-76a,

$$a = 0.299.$$

The scaled HOB is

$$\text{HOB}_1 = \frac{\text{HOB}}{W^a} = \frac{-3}{(30)^{0.299}} = -1.09 \text{ m/kt}^a.*$$

From Figure 2-75d,, the apparent crater volume for a 1 kt explosion, at HOB = -1.09 m/kt^a in wet soft rock, is,

$$V_{a1} = 2.20 \times 10^4 \text{ m}^3/\text{kt}^{3a},$$

and

$$V_a = V_{a1} (W)^{3a} = 2.20 \times 10^4 (30)^{0.897}$$
$$= 4.65 \times 10^5 \text{ m}^3.$$

The dimensions for the 30 kt explosion are determined from the following expressions:

$$\frac{R_a}{V_a^{1/3}} = 1.2 W^b,$$

$$\frac{D_a}{V_a^{1/3}} = 0.5 W^{-c}.$$

From Figures 2-76b and 2-76c the values of the yield transition exponents, b and c, at a scaled DOB of 1.09 m/kt^a (HOB = -1.09 m/kt^a) are:

$$b = 0.023,$$

$$c = 0.033.$$

Answer: The dimensions of the crater for a 30 kt explosion at a DOB of 3 meters are:

$$\frac{R_a}{V_a^{1/3}} = 1.2 W^{0.023} = 1.2 (30)^{0.023} = 1.30,$$

$$R_a = 1.30 (4.65 \times 10^5)^{1/3} = 101 \text{ meters},$$

and

$$\frac{D_a}{V_a^{1/3}} = 0.5 W^{-0.033} = 0.5 (30)^{-0.033} = 0.447,$$

$$D_a = 0.447 (4.65 \times 10^5)^{1/3} = 34.6 \text{ meters}.$$

Uncertainty. The ranges of uncertainty for the radius and the depth are

$$1.1 W^{0.023} \leq \frac{R_a}{V_a^{1/3}} \leq 1.4 W^{0.023},$$

$$92 \leq R_a \leq 117 \text{ meters},$$

and

$$0.35 W^{-0.033} \leq \frac{D_a}{V_a^{1/3}} \leq 0.7 W^{-0.033},$$

$$24 \leq D_a \leq 49 \text{ meters}.$$

Related Material: See paragraphs 2-46 through 2-50; see also paragraphs 1-14 and 1-33.

*This could be written $\text{DOB}_1 = \frac{\text{DOB}}{W^a} = \frac{3}{(30)^{0.299}} = 1.09 \text{ m/kt}^a$, i.e., HOB = -1.09 is equivalent to DOB = 1.09.

Problem 2-24. Crater Dimensions for a Low Yield Near-Surface Explosion

Figures 2-74a through 2-75e include curves that indicate the apparent crater volume as a function of HOB for 1 kt explosion in various homogeneous media.

Scaling. For yields other than 1 kt, the crater volume scales as follows

$$\frac{V_a}{V_{a1}} = W^{3\alpha},$$

where V_{a1} is the apparent crater volume for a 1 kt explosion, and V_a is the corresponding volume for a yield of W kt. The height of burst scales as

$$\frac{\text{HOB}}{\text{HOB}_1} = W^{\alpha}.$$

Example:

Given: A hypothetical 3 kt burst over wet soil at a height of burst of 1 meter.

Find: The apparent crater radius and depth.

Solution: From paragraph 2-49,

$$\text{HOB}_1 = \frac{\text{HOB}}{W^{\alpha}} = \frac{1.0}{(3)^{1/3}} = 0.693 \text{ m/kt}^{1/3}.$$

The apparent crater volume for a 3 kt burst will be determined by interpolating between the best estimate values from Figures 2-74b and 2-75b.

$$V_a\,(3) = 0.6\,V_a\,(W \leq 1) + 0.4\,V_a\,(W > 10).$$

From Figure 2-74b, the apparent crater volume for a 1 kt explosion (for $W \leq 1$), at a scaled HOB = 0.693 m/kt$^{1/3}$, in wet soil is

$$V_{a1} = 7.00 \times 10^3 \text{ m}^3/\text{kt}^{3\alpha},$$

and

$$V_a\,(W \leq 1) = V_{a1}\,(W)^{3\alpha} = 7.00 \times 10^3\,(3)^{1.0} = 2.10 \times 10^4 \text{ m}^3.$$

From Figure 2-75b, the apparent crater volume for a 1 kt explosion ($W > 10$), at a scaled HOB = 0.693 m/kt$^{1/3}$, in wet soil is

$$V_{a1} = 1.80 \times 10^3 \text{ m}^3/\text{kt}^{3\alpha},$$

and

$$V_a\,(W > 10) = V_{a1}\,(W)^{3\alpha} = 1.80 \times 10^3\,(3)^{1.0} = 5.40 \times 10^3 \text{ m}^3.$$

Therefore, for a 3 kt burst

$$V_a = 0.6\,(2.10 \times 10^4) + 0.4\,(5.40 \times 10^3) = 1.48 \times 10^4 \text{ m}^3.$$

Answer: The apparent crater dimensions for a 3 kt explosion with HOB of 1 meter are:

$$\frac{R_a}{V_a^{1/3}} = 1.2\,W^{0.08} = 1.2\,(3)^{0.08} = 1.31,$$

$$R_a = 1.31\,(V_a)^{1/3} = 32.2 \text{ meters},$$

and

$$\frac{D_a}{V_a^{1/3}} = 0.5\,W^{-0.12} = 0.5\,(3)^{-0.12} = 0.438,$$

$$D_a = 0.438\,(V_a)^{1/3} = 10.8 \text{ meters}.$$

Uncertainty. The dimensions of the apparent crater obtained for the above problem have a range of uncertainty that is defined by the following:

$$1.1\,W^{0.08} \leq \frac{R_a}{V_a^{1/3}} \leq 1.4\,W^{0.08}$$

$$29 \leq R_a \leq 38 \text{ meters}$$

and

$$0.35\,W^{-0.12} \leq \frac{D_a}{V_a^{1/3}} \leq 0.7\,W^{-0.12}$$

$$8 \leq D_a \leq 15 \text{ meters}.$$

If the 3 kt weapon in the preceding example were known to have a high radiative output, similar to weapons of larger yield (10 kt), then the best estimate for the apparent crater volume would be found using only Figure 2-75b. Therefore, V_a would be given by

$$V_a = 5.40 \times 10^3 \text{ m}^3,$$

and

$$R_a = 1.31\,(V_a)^{1/3} = 23.0 \text{ meters},$$

$$D_a = 0.438\,(V_a)^{1/3} = 7.7 \text{ meters}$$

Related Material: See paragraphs 2-46 through 2-50; see also paragraphs 1-14 and 1-33.

SUMMARY OF PROCEDURES FOR CALCULATING CRATERS FROM DEEP-BURIED BURSTS (DOB/$W^{1/3}$ > 5 m/kt $^{1/3}$)

Figures 2-77 through 2-81, together with appropriate scaling laws may be used to obtain crater volumes from deep-buried bursts in a variety of situations. The following summary provides a step-by-step procedure for obtaining such information. An example problem is provided immediately following the figures.

Required (either given or estimated):
Yield (W) in kt
Actual DOB
Soil Type (one of the five generic types or a combination; (see Figures 2-82 and 2-86b).
Yield-scaling parameters, α, for burst position:
DOB/$W^{1/3}$ > 5 m/kt$^{1/3}$ → α = 1/3.4

1. Compute DOB_1

$$(\text{DOB for 1 kt}) = \frac{\text{Actual DOB}}{W^{\alpha}}$$

2. Determine V_{a1} (apparent-crater volume for 1 kt), using curve for given soil type from Figures 2-77 to 2-81.

3. Compute V_a (actual crater volume for yield other than 1 kt):

$$V_a \text{ (actual volume)} = V_{a1}\ (W^{3\alpha}).$$

Three curves are provided for each soil type: best estimate, upper bound, and lower bound. Using the following guidelines, select the curve most appropriate to the problem.

a. Use *best estimate* V_{a1} if no specific geologic data are given. If actual HE test are available for specific site, compare them with the HE curves in Figure 2-82, and move toward the upper or lower bound NE curve to adjust for these data, depending on where the data are grouped.

b. Use *lower-bound* V_{a1} (if desirable) for target-oriented calculations (offensive-conservative) and to calculate R_a or D_a. Consider *lower-bound* V_{a1} for targeting when calculating crater-volume-related phenomena such as ejecta, transient velocity, or displacement.*

c. Use *upper-bound* V_{a1} (if desirable) for design-oriented calculations (defense-conservative) and to calculate R_a or D_a. Consider *upper-bound* V_{a1} for design when calculating crater-related phenomena affected by volume.

4. Calculate R_a and D_a using the following expressions:

$$R_a = 1.2\ V_a^{1/3}$$

$$D_a = 0.5\ V_a^{1/3}$$

The dimensions R_a, D_a, and V_a can be related to other pertinent crater dimensions as follows:

- The radius to the crest of the apparent-crater lip is

$$R_{a\ell} = 1.25\ R_a.$$

- The height of the apparent lip is

$$0.20 D_a \leq H_{a\ell} \leq 0.25\ D_a$$

for deep-buried bursts.

Variations in the thickness of the ejecta as a function of range from the surface ground zero (SGZ) are discussed in paragraphs 2-52 and 2-53.

*In all instances it is recommended that upper and lower bound values be calculated in order to gain an appreciation of the effects of uncertainties on the particular problem under consideration.

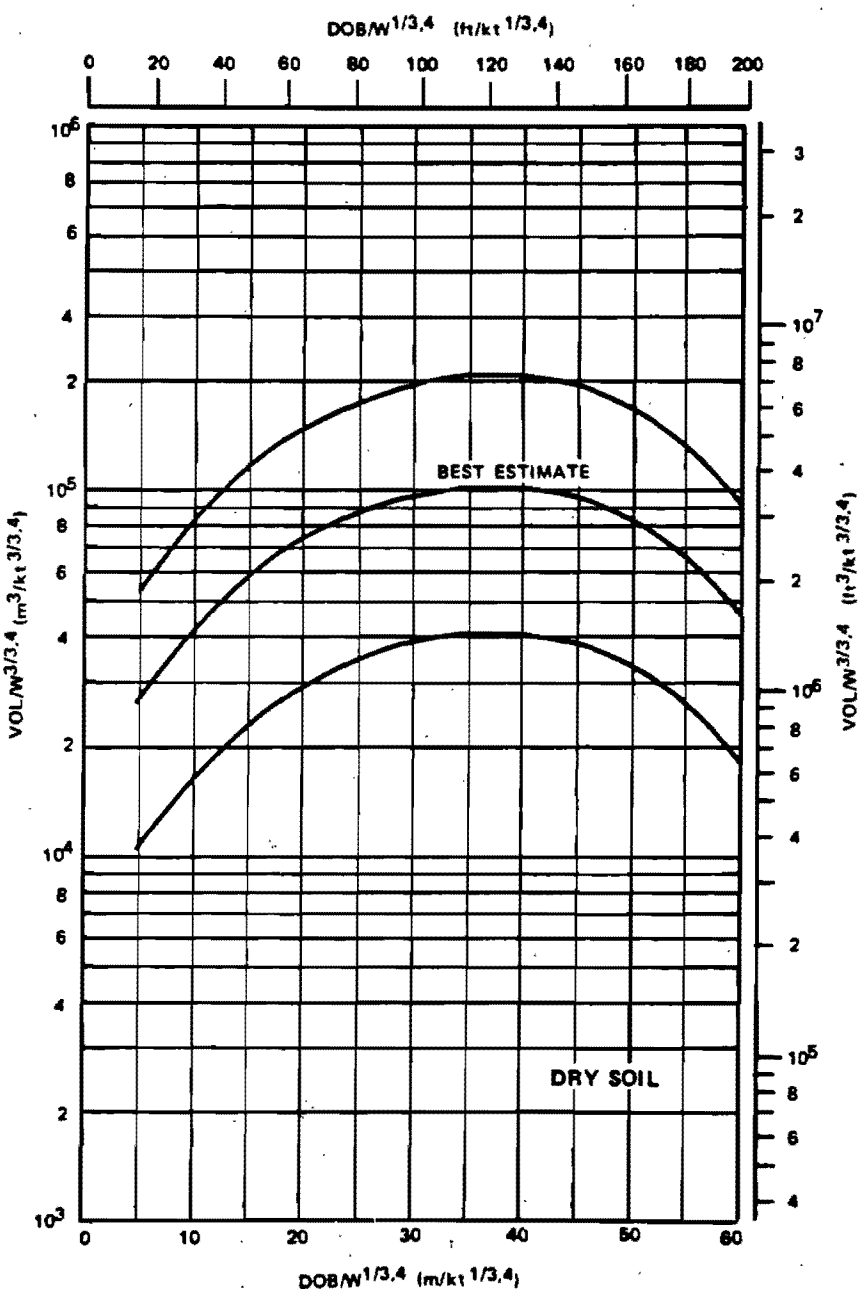

Figure 2-77. Crater Volume as a Function of Depth of Burial for a 1 Kiloton Explosion Buried in Dry Soil

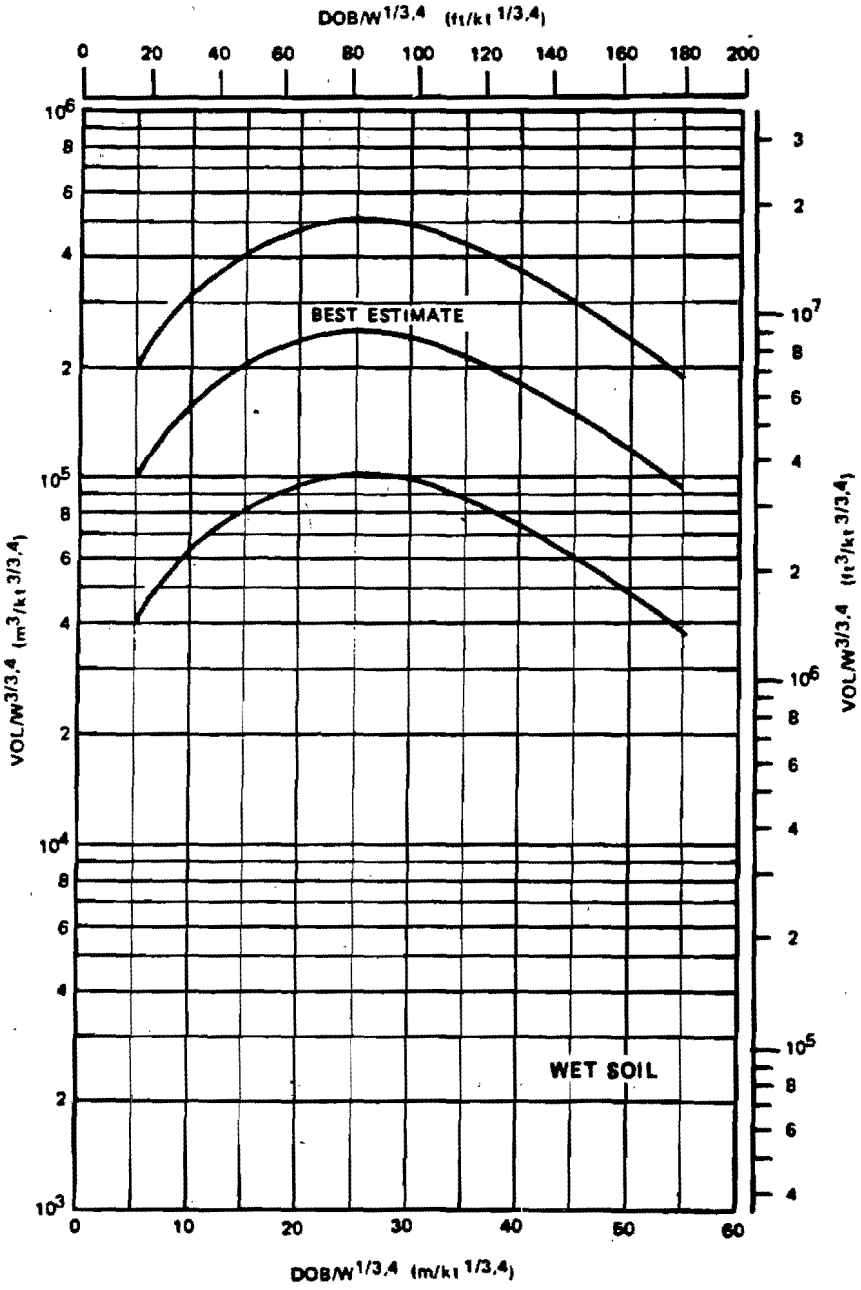

Figure 2-78. Crater Volume as a Function of Depth of Burial for a 1 Kiloton Explosion Buried in Wet Soil

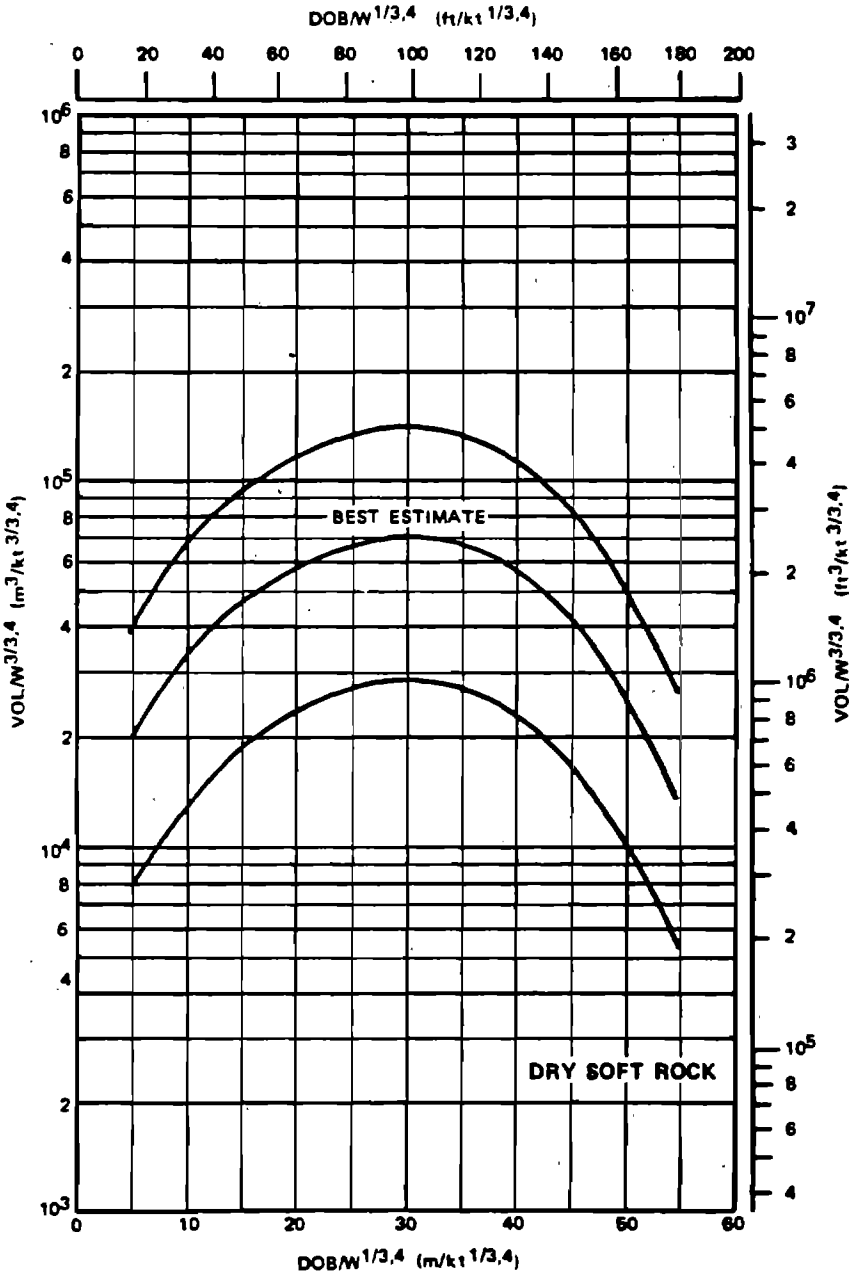

Figure 2-79. Crater Volume as a Function of Depth of Burial for a 1 Kiloton Explosion Buried in Dry Soft Rock

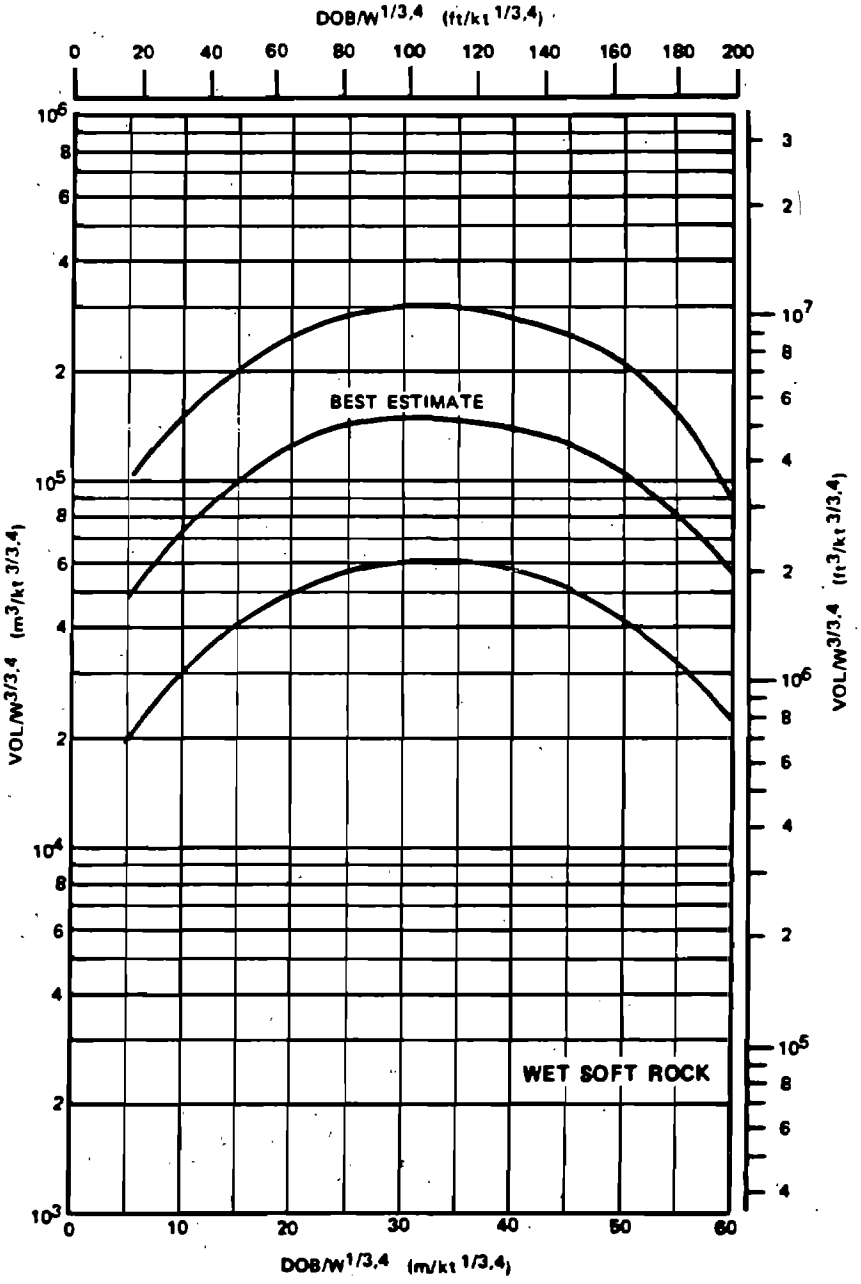

Figure 2-80. Crater Volume as a Function of Depth of Burial for a 1 Kiloton Explosion Buried in Wet Soft Rock

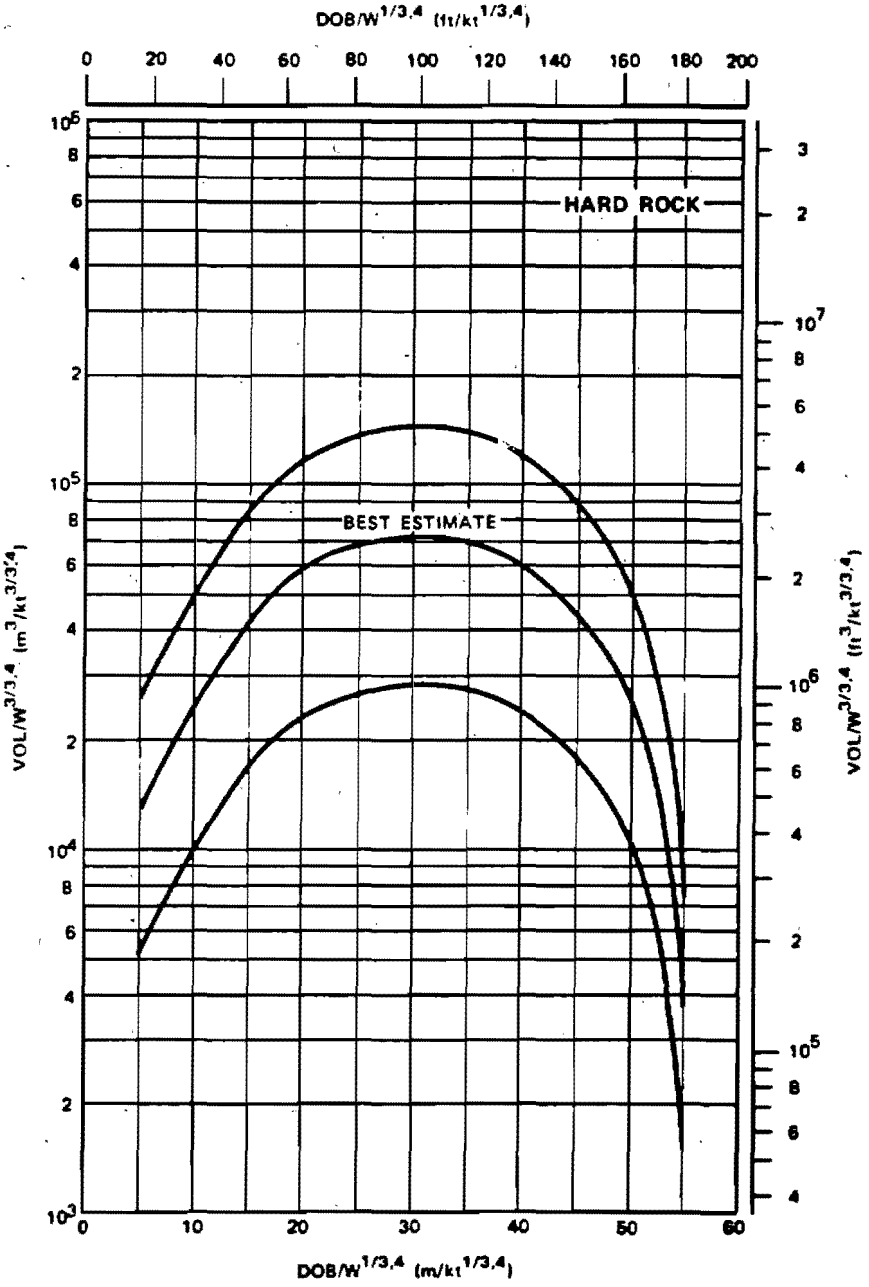

Figure 2-81. Crater Volume as a Function of Depth of Burial for a 1 Kiloton Explosion Buried in Hard Rock

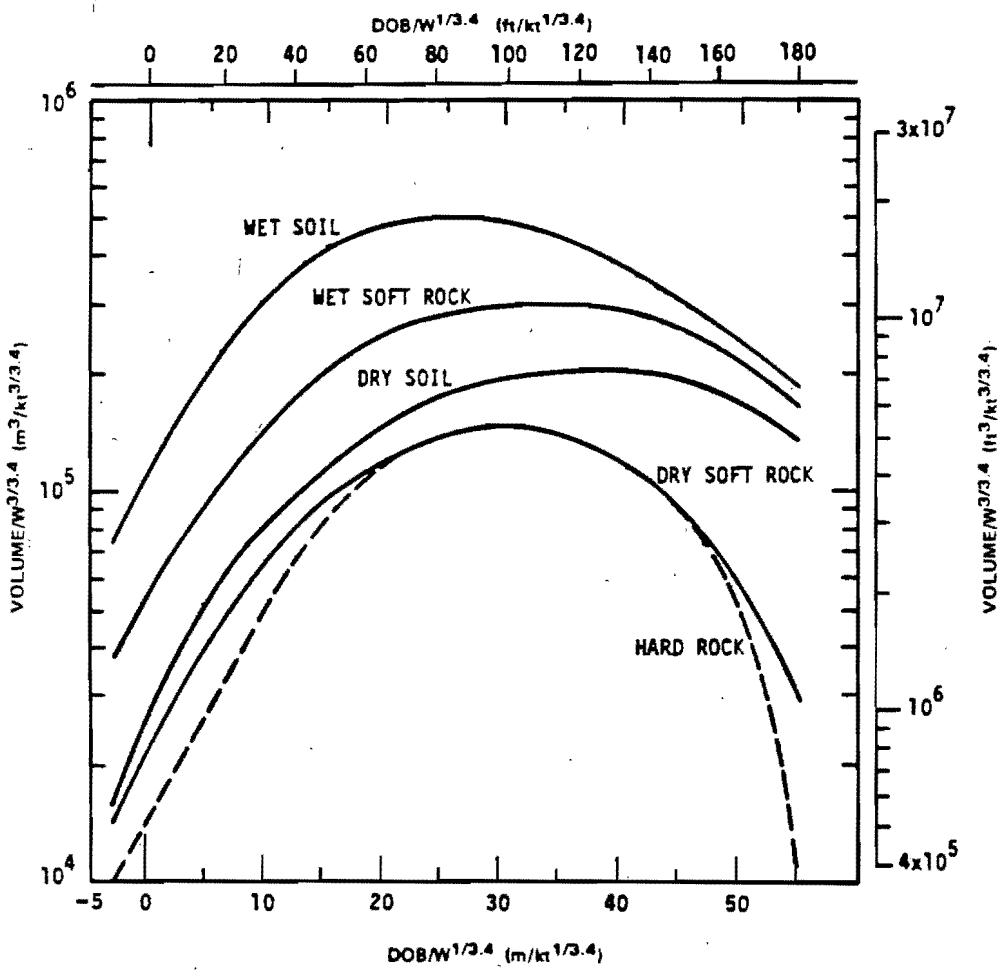

Figure 2-82. Crater Volume as a Function of Depth of Burst for HE Explosions in Five Homogenous Geologies

[redacted]

(This page is intentionally blank)

[redacted]

Problem 2-25. Calculation of Depth of Burial for Optimum Crater

Figures 2-77 through 2-81 show curves that indicate the apparent crater volume as a function of DOB for a 1 kt explosion in various media which are indicated in each figure.

Scaling. For yields other than 1 kt the crater volume and depth of burial scale as

$$\frac{DOB}{DOB_1} = W^{1/3.4},$$

$$\frac{V_a}{V_{a1}} = W^{3/3.4},$$

where DOB_1 and V_{a1} are the depth of burst and apparent crater volume for a 1 kt explosion, and DOB and V_a are the corresponding quantities for a yield of W kt.

Example:

Given: A hypothetical 3 kt explosion in hard rock.

Find: The depth of burst at which the maximum apparent crater will occur, and the dimensions of the apparent crater at this depth of burst.

Solution: From Figure 2-81, the maximum crater volume from a 1 kt explosion in hard rock occurs at a DOB_1 of 30.5 meters (note that the curve is flat in this region, and a variation of a few meters in DOB will have a small effect on V). The apparent volume of the crater from such a burst is

$$V_1 = 7.20 \times 10^4 \text{ m}^3.$$

Answer: The corresponding depth of burst and crater volume for a 3 kt explosion are

$$DOB = (DOB_1)(W)^{1/3.4} = 30.5\ (3)^{1/3.4}$$
$$= 42.1 \text{ meters},$$
$$V_a = (V_{a1})(W)^{3/3.4} = 7.20 \times 10^4\ (3)^{3/3.4}$$
$$= 1.90 \times 10^5 \text{ m}^3.$$

The apparent crater dimensions are defined by the expressions

$$R_a = 1.2\ V_a^{1/3} = 1.2\ (1.90 \times 10^5)^{1/3}$$
$$= 69.0 \text{ meters},$$
$$D_a = 0.5\ V_a^{1/3} = 0.5\ (1.90 \times 10^5)^{1/3}$$
$$= 28.7 \text{ meters}.$$

Uncertainty: The dimensions of the apparent crater have a range of uncertainty that is defined by the expressions

$$1.1\ V_a^{1/3} \leq R_a \leq 1.4\ V_a^{1/3},$$
$$63 \leq R_a \leq 80 \text{ meters},$$
$$0.35\ V_a^{1/3} \leq D_a \leq 0.70\ V_a^{1/3},$$
$$20 \leq D_a \leq 40 \text{ meters}.$$

In addition, the uncertainty in crater volume is given by

$$V_a \text{ (min)} = V_{a1} \text{ (min)}\ W^{3/3.4},$$
$$V_a \text{ (min)} = 2.80 \times 10^4\ (3)^{3/3.4},$$
$$= 7.38 \times 10^4 \text{ m}^3,$$
$$V_a \text{ (max)} = V_{a1} \text{ (max)}\ W^{3/3.4},$$
$$V_a \text{ (max)} = 1.45 \times 10^5\ (3)^{3/3.4},$$
$$= 3.82 \times 10^5 \text{ m}^3.$$

Related Material: See paragraph 2-51; see also paragraph 1-14 and 1-33.

EJECTA

Crater ejecta consists of soil or rock debris that is thrown beyond the boundaries of the apparent crater by an explosion. Together with the fallback, which lies between the true and apparent crater boundaries, ejecta comprises all material that is completely dissociated from the parent medium by the explosion. The ejecta field is divided into two zones:

- The crater lip, including the continuous ejecta surrounding the apparent crater.
- The discontinuous ejecta, comprised of the discrete natural missiles that fall beyond the limit of continuous ejecta.

The principal parameters used to describe the ejecta are:

- The average lip crest height.
- The radius to the crest of the crater lip from surface ground zero (SGZ).
- The depth of deposition.
- The ejecta mass density.
- The missile size distribution, which is a function of the azimuthal and radial distance from SGZ, the radius to the outer boundary of continuous ejecta, and the maximum missile range.

The principal variables that control the ejecta parameters are the yield and geometry, and the physical characteristics of the earth medium. Figure 2-83a shows the throwout of ejecta from the SEDAN Event, a 100 kt explosion at a depth of 635 feet.

2-52 Ejecta Thickness

The amount and linear extent of the continuously deposited ejecta in the crater lip are determined primarily by the yield. The radial limit of continuous ejecta, which is the outer edge of the lip, will usually vary between 2 and 3 times the apparent crater radius. The lip crest height above the original surface is estimated to be one-fourth of the apparent crater depth ($H_{ag} = 0.25\ D_a$, paragraphs 2-50 and 2-51). The depth of ejecta decreases rapidly in an exponential fashion as the distance from SGZ increases. About 80 to 90 percent of the entire ejecta volume generally is deposited within the area of continuous ejecta. Analysis of data for craters formed by near-surface bursts over soil indicates that ejecta mass represents approximately 55 percent of the apparent crater mass (the remainder being found in fallback, compaction, and the dust cloud, which is blown away). When the same yields explode at successively greater depths, ejecta mass increases significantly until the optimum DOB is reached. Ejecta thickness can be estimated for soil as follows (all dimensions are in feet):

$$t_e = 0.9V_a^{1.6}\ R^{-3.86},\ \text{for } R > 2.2V_a^{1/3}$$

where t_e is the ejecta thickness, V_a is the apparent crater volume, and R is the distance from SGZ to the point of interest. This formula for ejecta thickness assumes that the ejecta mass density will be approximately equal to the original in-situ density of the medium. The equation may be considered valid for a soil medium; however, the bulking, which is inherent in a disturbed rock medium would result in greater ejecta thicknesses than predicted by the formula. Therefore, in a rock medium, the ejecta thickness should be increased by 30 percent to account for the bulking, i.e., the formula for a rock medium is

$$t_e = 1.17V_a^{1.6}R^{-3.86},\ \text{for } R > 2.2V_a^{1/3}$$

2-53 Maximum Missile Range

Figure 2-83b shows the maximum missile range as a function of depth of burst for a 1 kt explosion in two soil types. These data are based on empirical results from several nuclear explosions.

Figure 2-83a. Throwout of Ejecta from the 100-kt SEDAN Event

Reproduced from best available copy.

Problem 2-26a. Calculation of Ejecta Thickness

Paragraph 2-52 provides formulas for the prediction of ejecta thickness as a function of distance from surface ground zero and the apparent crater volume (V_a). V_a may be obtained from Figures 2-74a through 2-76c for near surface bursts and 2-77 through 2-81 for deep-buried bursts by the methods described in paragraphs 2-49 through 2-51.

Example:

Given: A hypothetical 300 kt contact surface burst (center of gravity of the weapon 0.5 meters above the surface) will produce a crater predicted to have an apparent radius of 137 meters, an apparent depth of 18.2 meters and an apparent volume of 3.75×10^5 cubic meters in dry soil. (See problem 2-22).

Find: The thickness of the ejecta at a distance of 300 meters from SGZ.

Solution:

R = 300 meters,

$2.2V_a^{1/3} = 2.2(3.75 \times 10^5)^{1/3} = 159$ meters

$R > 2.2V_a^{1/3}$

Therefore the equation for soil given in paragraph 2-52 applies.

Answer: The ejecta thickness is

$$t_e = 0.9V_a^{1.6} R^{-3.86}$$

$$t_e = 0.9 (3.75 \times 10^5)^{1.6} (300)^{-3.86} =$$

0.20 meters

Reliability: Based on empirical formulas derived from high explosive and nuclear burst. Specific reliability has not been estimated.

Related Material: See paragraph 2-49 through 2-52. See also Problem 2-22.

[redacted]

Problem 2-26b. Calculation of Maximum Missile Range

Figure 2-83b shows the maximum range to which missiles might be expected from a 1 kt explosion as a function of depth of burial in two soil types.

Scaling. For yields other than 1 kt, the maximum missile range and depth of burst scale as follows:

$$\frac{R_m}{R_{m1}} = \frac{DOB}{DOB_1} = W^{0.3}$$

where R_{m1} is the maximum missile range for 1 kt, DOB_1 is the depth of burst for 1 kt, and R_m and DOB are the corresponding range and burial depth for W kt.

Example:

Given: A hypothetical 3 kt explosion at a depth of 85 meters in hard rock.

Find: The maximum missile range for the explosion.

Solution: The corresponding depth of burst for a 1 kt explosion is

$$DOB_1 = \frac{DOB}{W^{0.3}} = \frac{85}{(3)^{0.3}} = 61 \text{ meters.}$$

From Figure 2-83b, the maximum missile range for a 1 kt explosion at a depth of 61 meters in hard rock is 440 meters.

Answer: The corresponding maximum missile range for a 3 kt explosion at a depth of 85 meters in hard rock is

$$R_m = R_{m1}\, W^{0.3} = (440)\,(3)^{0.3} = 612 \text{ meters.}$$

Reliability: Based on empirical results from several nuclear explosions, but no specific reliability has been estimated.

Related Material: See paragraphs 2-46 through 2-52.

[redacted]

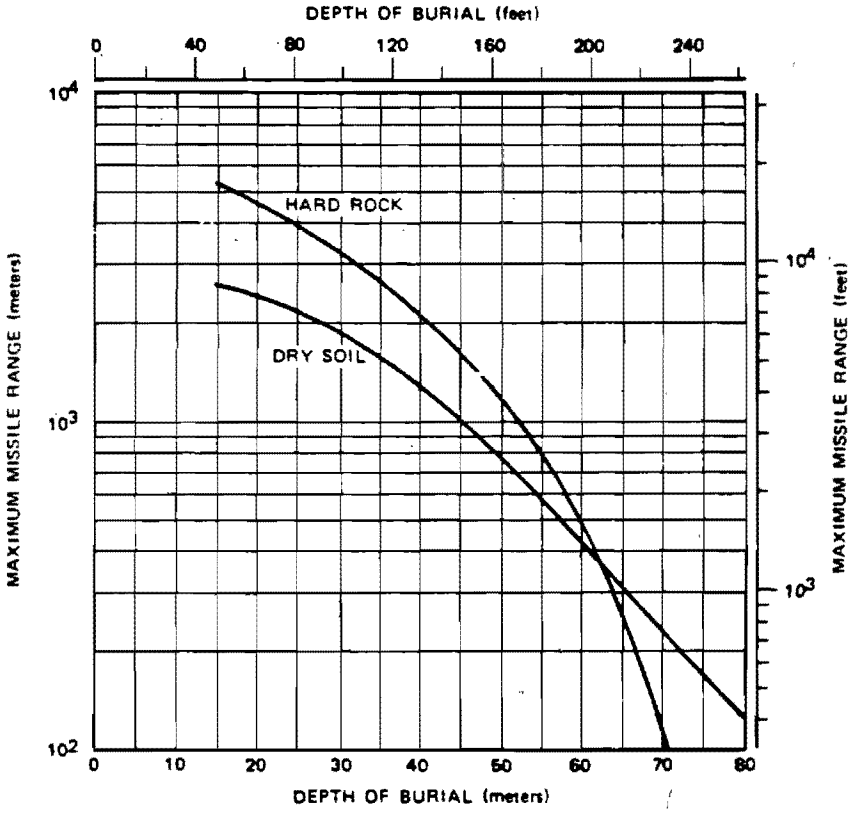

Figure 2-83b. Maximum Missile Range as a Function of Depth of Burial for a 1 kt Explosion

CHARGE STEMMING

The term charge stemming refers to the backfilling of material in the charge-emplacement hole. Ideally, charges should be completely stemmed and tamped to contain the explosive energy temporarily, which increases its coupling with the medium. Typical stemming materials are concrete, gravel, sand and water. The cratering curves shown in preceding paragraphs provide predictions for fully stemmed charges. There are, however, operational considerations that may require reduced stemming or the capability to emplace or remove the stemming material in a short period of time. Therefore, modified stemming geometries, including various degrees of stemming or no stemming at all, are important considerations in the evaluation of nuclear cratering phenomena.

The following changes in cratering phenomena generally may be expected when less than full stemming is used:

- Air blast and the fraction of radioactive materials that vents will be increased.
- Energy loss out of the emplacement hole will reduce the coupling effectiveness of the explosion. This will result in crater dimensions that are smaller than those from fully stemmed explosions.
- Energy deposited in the emplacement hole will cause a modification to the energy deposition pattern in the medium. The source will appear to be a distorted cylindrical source rather than a concentrated spherical source. Lip height, ejecta distribution, and maximum missile range will vary from those of a fully stemmed explosion.

2-54 Guidelines for Assessing the Effect of Stemming

The crater dimensions from a partially stemmed or an unstemmed emplacement hole will be affected primarily by the amount of stemming, the diameter of the emplacement hole, and the depth of burial. The following are some general conclusions concerning stemming that are based largely on HE experiments.

- The crater radius, which is the dimension of greatest military importance, does not increase significantly with increased stemming.
- Stemming about one-half of the emplacement hole (50% stemming) provides most of the crater depth that would be expected from a fully stemmed charge.
- Water appears to be a very efficient stemming material.

Figures 2-84a, b, and c illustrate the HE experimental results concerning the effect of stemming on crater volume, diameter, and depth, respectively.

EFFECTS OF GEOLOGICAL FACTORS

In most situations a weapon will *not* be burst in a homogeneous medium such as dry soil or wet soft rock. Instead, typical geologies may contain a water table at a shallow depth, a layering of one type of media over another (e.g., soil over rock), parallel planes of distant jointing in rock, or a steeply sloping ground surface. All of these factors can influence the formation of a crater and, in some cases, can change the size or characteristics of the crater significantly. The following paragraphs describe the general effects of geologic variations on cratering phenomena.

2-55 Sloping Topography

Terrain slopes of about five degrees or more will affect the geometry of a crater formed by either a surface or buried explosion. The ejecta distribution will also be affected. If the slope is gentle, the crater volume will be comparable

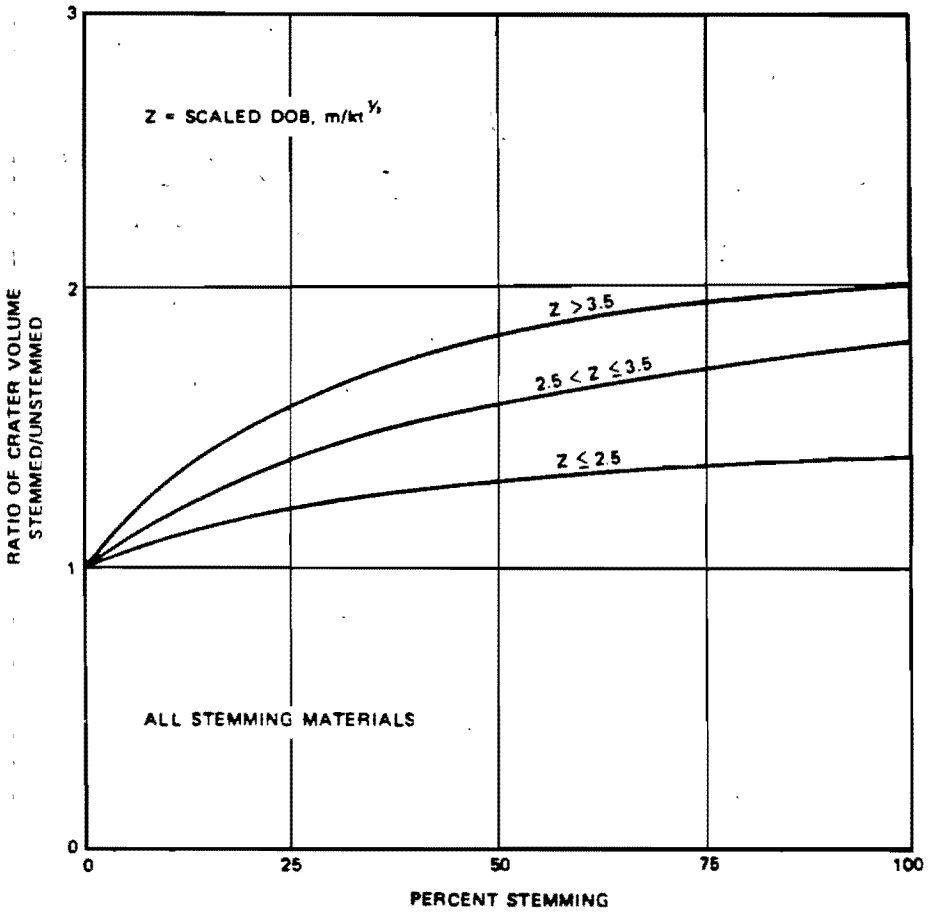

Figure 2-84a. Increase in HE Crater Volume as a Function of Stemming for Various DOBs

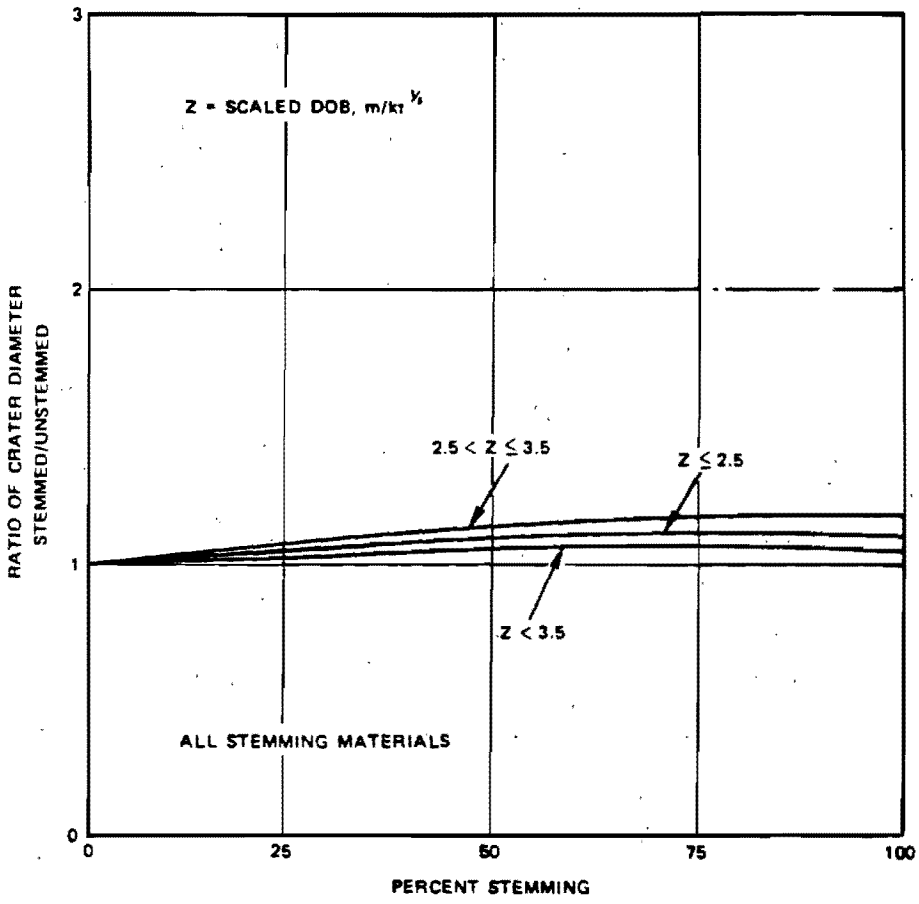

Figure 2-84b. Increase in HE Crater Diameter as a function of Stemming for Various DOBs

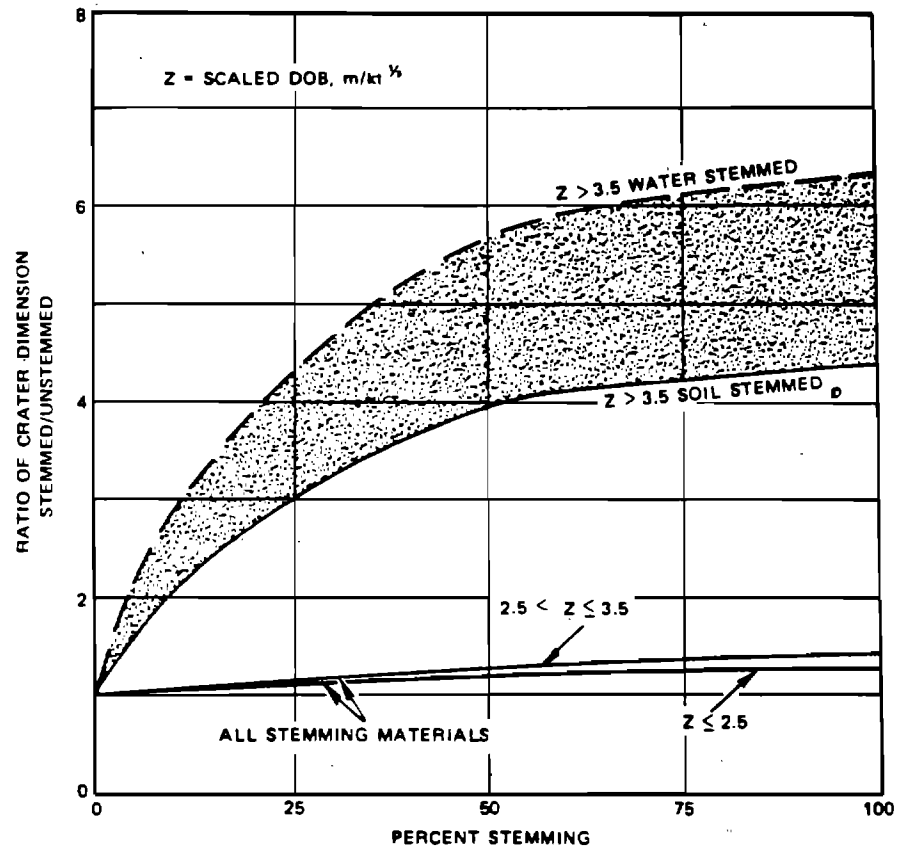

Figure 2-84c. Increase in HE Crater Depth as a Function of Stemming for Various DOBs

with that of craters on level ground, but the resulting crater will be asymmetrical; it will be wider up-slope and will have a larger lip down-slope. Figures 2-85a and b show a photograph and a schematic drawing, respectively, of the crater from a nuclear event buried 30 meters below a 30 degree slope in tuff. The shape of the crater formed by this explosion was influenced by the slope of the surface because almost all the debris formed a rock slide originating at the lower edge of the crater and terminating about 240 meters down the slope.

Limited small-scale cratering experiments have been conducted in moist, sandy soil and in desert alluvium on slopes ranging from 40 degrees to vertical wedges. For charges buried on severe but nonvertical slopes, with DOB measured normal to the sloping surface and with the vertical depth of overburden being greater than containment depth, crater dimensions decrease with increasing slope. Optimum vertical DOB appears larger by about one-third than optimum DOB on level terrain.

2-56 Water Tables

A subsurface ground water table in a soil medium will begin to influence the size and shape of the crater when its depth below the surface is equal to or less than three-fourths the predicted apparent crater depth. Its effect is to flatten and widen the crater. Figure 2-86a illustrates the effect of a shallow water table on the shape of the crater. As the water table depth decreases, its effect becomes more evident. Based upon HE experiments, it can be concluded that for a surface detonation, the influence of the water table is not significant for scaled water table depths greater than about 3.5 m/kt$^{1/3}$, and the apparent radius, volume and lip height increase exponentially as the water table approaches the ground surface. For shallow buried bursts (DOB/$W^{1/3}$ < 3 m/kt$^{1/3}$) the final crater radius may be as much as 50 percent greater than the predicted value and the depth as little as one-third that of the predicted value.

Figure 2-86b shows a normalization technique that has been developed for plotting crater volume for surface and shallow buried explosions in a layered geology. A shallow water table effectively causes a homogeneous medium to act as a two layered medium

d = depth to water table (thickness of upper layer)

V_a = apparent crater volume

V_u = apparent crater volume predicted in the upper layer alone (usually dry soil)

V_L = apparent crater volume predicted in the lower layer alone (usually wet soil).

The curve fitted to the water table crater volume data in Figure 2-86b is given by the expression

$$\frac{V_a - V_L}{V_u - V_L} = 1 - \exp\left(-5.4\, d/V_a^{1/3}\right).$$

Iteration is required to solve this expression for V_a; however, the technique converges very rapidly. It is recommended that the curve in Figure 2-86b be used to predict crater volume for sites having a shallow water table.

2-57 Bedrock

The influence of a bedrock layer below a soil medium is similar to that of a water table, though somewhat less pronounced. For surface explosions it appears that a hard layer may limit the crater depth while causing the crater shape to be more nearly trapezoidal than parabolic or conical (see Figure 2-86c). The bedrock layer may increase the crater radius slightly (5 to 10

[redacted]

Figure 2-85a. NEPTUNE Crater and its Position on Slope of Mesa

Reproduced from best available copy.

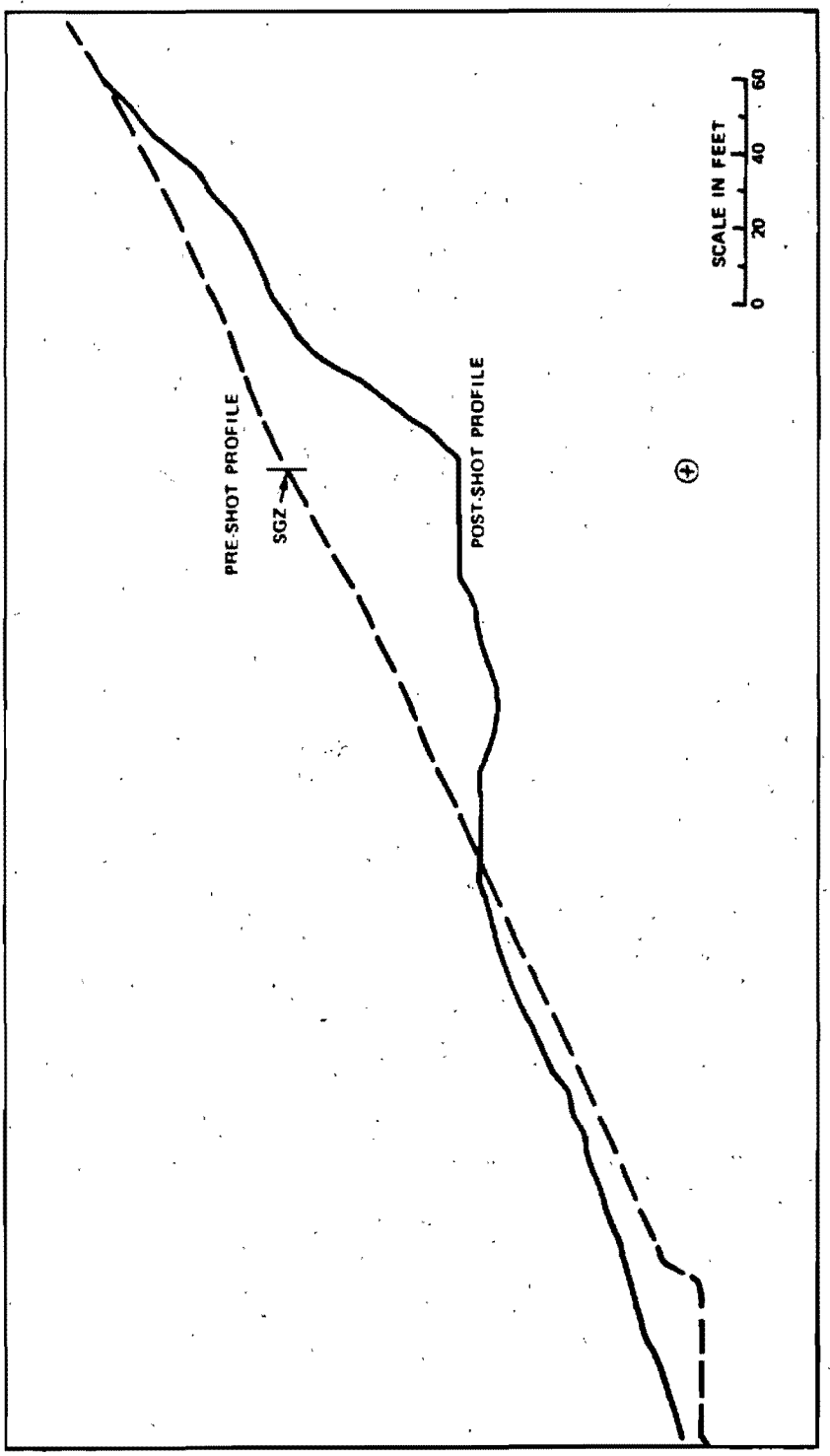

Figure 2-85b. Section of NEPTUNE Crater Normal to Slope Contours

Reproduced from best available copy.

Figure 2-88a. Crater Formed by a Surface Detonation of a 0.5 kt High Explosive Charge in a Wet Soil Medium with a Shallow Water Table (DIAL PACK Event); a 8.2 m (27 ft.) Diameter Sphere with the Bottom Tangent to the Ground: R_s = 30.48 m (100 ft.); D_s = 4.6 m (15 ft.)

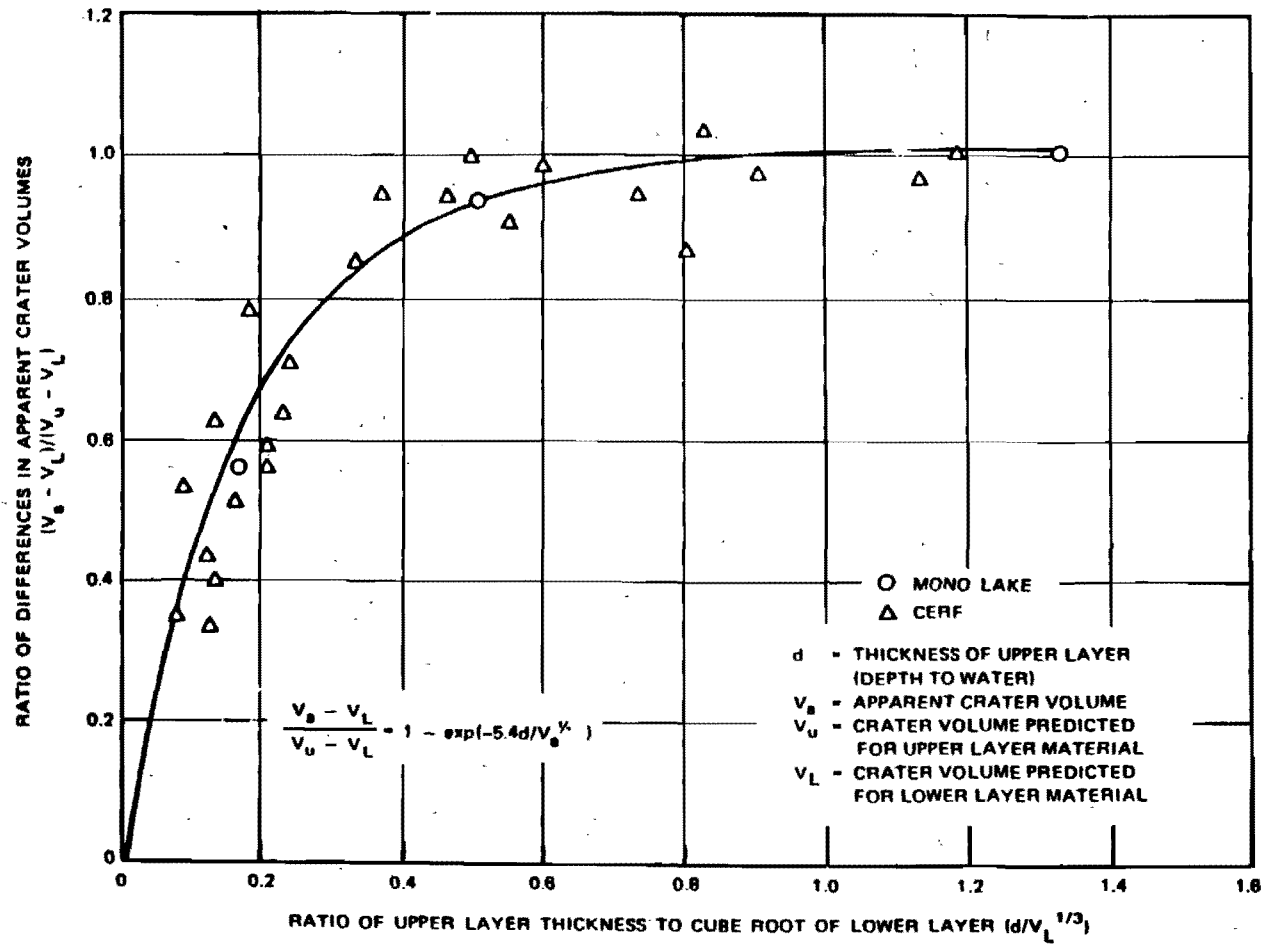

Figure 2-86b. Cratering Data for Dry Soil over Wet Soil

percent). The layer may decrease the final crater depth by as much as one-third when the overburden layer is as shallow as one-fourth the predicted apparent crater depth.

Although the effect of a water table and the effect of a hard layer are different, the water table curve is a good approximation for predicting the crater volume in a layered geology involving a gradual transition to rock. The water table curve should *not* be used for geologies involving a sharp transition to rock.

The two-layer problem can be generalized to three layers. Let V_1, V_2, and V_3 be the crater volume associated with the top, middle, and bottom materials considered separately. Then, V_{23} is the crater volume associated with the middle layer and bottom layer, and V is the crater volume in the total layered medium.

V_{23} is calculated by neglecting the top layer and then solving a two-layer problem with V_2 as the upper layer and V_3 as the lower layer. The thickness of the middle layer d_2 is used as the depth to the lower layer. This gives

$$\frac{V_{23} - V_3}{V_2 - V_3} = 1 - \exp\left(-5.4\, d_2 / V_{23}^{1/3}\right)$$

V is then calculated by solving another two-layer problem with V_1 as the upper layer and V_{23} as the lower layer. The thickness of the upper layer d_1 is used as the depth of the lower layer. This gives

$$\frac{V - V_{23}}{V_1 - V_{23}} = 1 - \exp\left(-5.4\, d_1 / V^{1/3}\right).$$

2-58 Rock Bedding/Jointing

If a low-yield explosion occurs at or very near the surface, the bedding or jointing planes in rock can influence the shape of the crater produced. The direction of the ejection process will also be affected. The formation of the crater will tend to follow the direction of the predominant joints, and the crater radius will be increased by as much as one-third in the direction parallel to the joints and decreased by as much as one-third in the direction normal to the joints. The magnitude of the crater depth is usually not affected significantly, but the deepest point may be shifted to one side of the crater. As the yield or the DOB is increased, the influence of rock jointing is reduced.

The dip of bedding planes will influence energy propagation, and this will cause the maximum crater depth to be offset in the down-dip direction. Little overall effect is noted on the size of the crater radius, but differences in ejection angles cause the maximum lip height and ejecta radius to occur down-dip.

2-59 Snow and Ice

Measured craters in snow or ice are a rarity; however, data for a few craters have been recorded for surface HE explosions. In general, these craters are larger than would be predicted in soil and they are characteristically wide and flat. The trends in crater size and shape for a surface explosion in a snow/ice medium are given by the expressions

$$R_a = 38.8\, W^{0.26} \text{ meters}$$

$$D_a = 5.75\, W^{0.15} \text{ meters}$$

where W is the yield in kilotons.

MULTIPLE BURST GEOMETRIES

Nuclear weapons may be detonated in close proximity to each other to create a linear crater or a series of interconnected craters. When simultaneous explosions are sufficiently close to cause interactions, the shot geometry is termed "multiple burst." A linear array of this nature is referred to as a row crater, as illustrated in Figure 2-87.

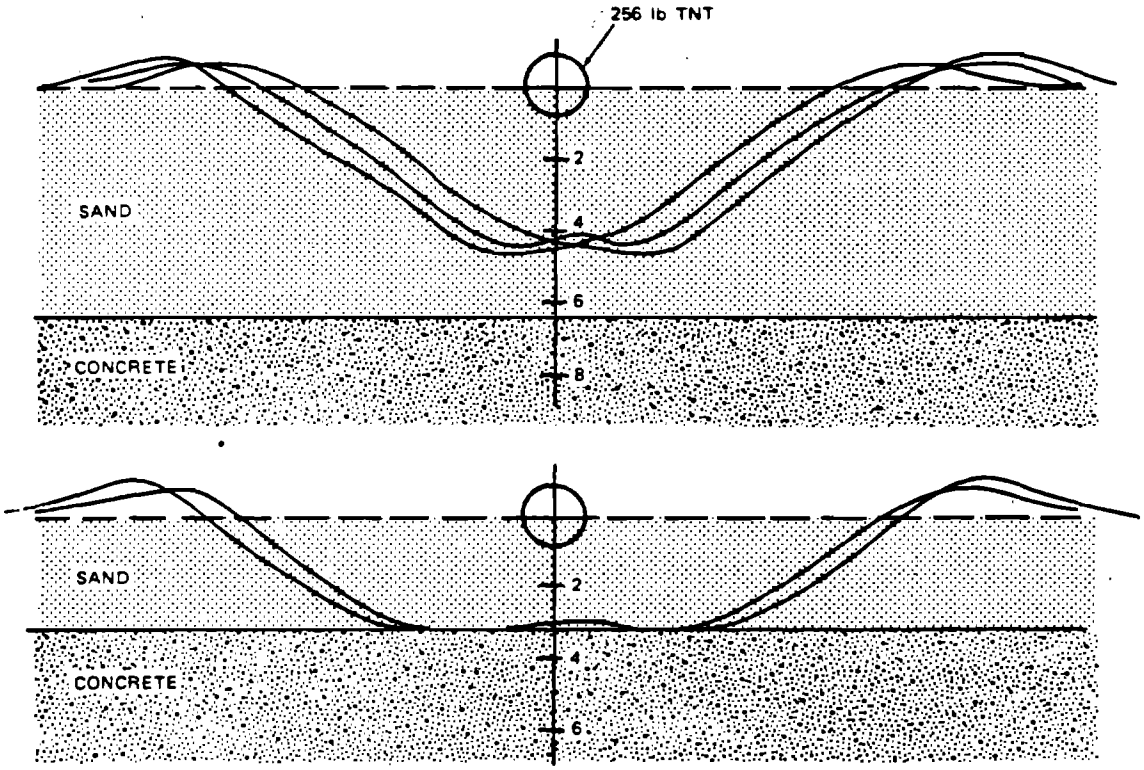

Figure 2-86c. Effects of a Hard Near-Surface Layer on Cratering

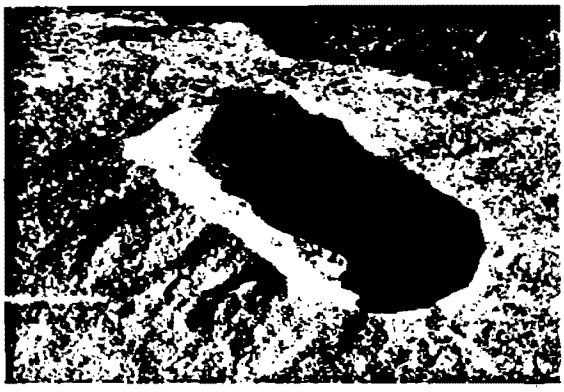

Figure 2-87. A Row Crater Produced by Simultaneous Explosions of Five 1.1 kt Nuclear Devices at Optimum DOB (BUGGY Event) in Basalt: DOB = 41 m (135 ft.); Spacing = 45.7 m (150 ft.); Width = 76.2 m (250 ft.); Depth = 19.8 m (65 ft.); Length = 262 m (860 ft.)

In addition to the parameters normally associated with an underground explosion, the results of a row charge also depend upon the spacing between charges (s) and the degree of simultaneity of the explosions. Differences of only a few milliseconds in the times of explosion of adjacent charges can result in significantly degraded row charge crater dimensions. Close spacing of weapons (less than 1.4 times a single weapon crater radius) increases both the crater radius and depth compared to single weapon craters at the same scaled DOB. Experience has shown that a spacing of 1.0 R_a (for explosions at optimum DOB) results in a smooth channel with crater depth and radius approximately 20 percent greater than those of single explosions. A spacing of 1.25 R_a will still form a smooth channel, but with less enhancement of crater dimensions, while spacing of 1.5 R_a will provide an adequate linear obstacle. The length of a row crater L can be found in the equation:

$$L = s(n - 1) + 2R_a,$$

where n is the number of charges in the row, and s is the spacing between charges.

SECTION III
GROUND SHOCK PHENOMENA

2-60 General Nature of Free-Field Effects

The position of the weapon at the time of detonation has a marked influence on the amount and nature of the energy transfer into the ground. The effects at depths below the surface from a high air burst will be primarily of the air-induced type. For surface or near surface bursts, both air-induced and direct-transmitted ground shock effects are produced, and both may be of importance. Deep underground bursts cause direct-transmitted effects almost exclusively.

The nuclear field tests of the past several decades involving air, surface, and fully contained bursts have provided the data that permit development of the expressions for predicting the peak values of air-induced and direct-transmitted acceleration, velocity, and displacement. Field observations for regions where the air blast overpressures are less than 1,000 psi generally indicate that, within about 50 to 100 feet of the surface, ground motions are predominantly air-induced. The relatively few measurements of acceleration and displacement that have been made at significant distances below the ground surface show the effects of attenuation and dispersion as the air-induced pulse travels through the ground.

A typical acceleration-time record from a gage mounted near the surface of the ground

Reproduced from best available copy.

[redacted]

exhibits a systematic pulse shape corresponding to the passage of the shock wave, with a random type disturbance often superimposed on this systematic pulse. In the superseismic case, when the air blast propagation velocity is greater than the ground seismic velocity, the downward acceleration is large compared with the following upward acceleration. The velocity-time record is similar in shape to the overpressure-time pulse, at least in the early stages. In cases in which the ground motion outruns the air blast, there is a slower rise in the acceleration; it may even be reversed in direction initially, i.e., upward rather than downward. In such cases, the signals may last for a longer time than the positive phase overpressure duration. The associated velocity wave form usually exhibits a velocity jump as the air-shock wave passes over the position, but the overall record is characterized by a considerable degree of oscillation. When precursors are present, the acceleration and velocity records may exhibit higher frequency components and more random type of oscillation. Wave front diagrams for the superseismic and outrunning cases are shown in Figure 2-88.

[redacted] Most values of velocity have been obtained by integrating acceleration records. In general, velocities appear to be more predictable quantities than accelerations or displacements. Displacement data are even scarcer than velocity data, and only a few direct measurements have been made. For the most part, displacement data consist of integrated acceleration records or extrapolation of displacement spectra to zero frequency.

[redacted] Knowledge of direct-transmitted ground shock effects is limited. Those data that exist were obtained from buried high explosive shots, from several surface and near surface nuclear detonations, and from a number of fully contained bursts. For a completely buried shot, measurements indicate that at any particular range R, the strain or velocity pulse rises in a parabolic manner to a peak value in a time roughly corresponding to $T_r = R/6c_p$ to $R/12c_p$, where R is the range from the explosion, and c_p

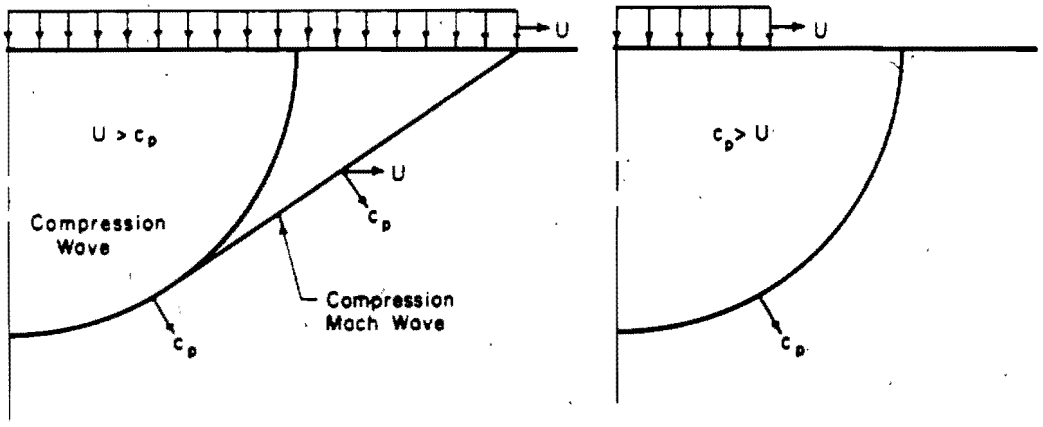

(A) Superseismic Blast Wave (B) Outrunning Ground Wave

Figure 2-88. [redacted] Wave Front Diagram for Superseismic Air Blast and Outrunning Ground Wave [redacted]

[redacted]

is the effective seismic velocity of the medium. The signal then drops slowly with a total positive phase duration corresponding approximately to $T_o = R/2c_p$ to R/c_p. The effects of layering, reflection, and refraction, tend to introduce high frequency and random components of motion.

2-61 Types of Effects

It is convenient to consider the earth shock resulting from a nuclear explosion as producing both systematic and random effects. Systematic effects can be divided further into two major types:

- Air-induced shock associated with the passage of an air shock wave over the surface of the ground, and the overpressure at the surface above the structure transmitted downward with such attenuation and dispersion as may be consistent with the physical conditions at the site.
- Direct-transmitted ground shock that arises from direct energy transfer from surface, near surface, or underground bursts.

Random effects include high frequency ground-transmitted shock, surface-wave effects, reflections, refractions, etc. The dominant effect depends on such factors as weapon yield, point of detonation with respect to the ground surface, range from ground zero, depth of the measurement, and, in particular, the geologic conditions.

Reasonable estimates can be made of the maximum values of displacement, velocity, and acceleration associated with the air-induced shock and in more restricted cases for the direct-transmitted ground shock under more or less uniform geologic conditions.

2-62 Air-Induced Effects

At the surface in a homogeneous medium the maximum transient elastic vertical displacement may be expressed as

$$d_{ae} = \frac{Hp_{so}}{2\bar{E}},$$

where H is the depth to which the air-induced shock wave extends during the effective duration of the shock, t_i, p_{so} is the side-on overpressure at the surface, and $\bar{E}$ is the restrained modulus. The duration of the shock may be approximated by

$$t_i \approx 0.37 \left(\frac{100}{p_{so}}\right)^{1/2} \left(W(\mathrm{Mt})\right)^{1/3}$$

for

$$2 \leq p_{so} \leq 10{,}000 \text{ psi.}$$

Thus,

$$H = c_p t_i = 0.37 \left(\frac{100}{p_{so}}\right)^{1/2} \left(W(\mathrm{Mt})\right)^{1/3} c_p.$$

The restrained modulus is related to the effective seismic velocity, the mass density, and Young's modulus of elasticity of the medium as follows:

$$\frac{\bar{E}}{\rho} = c_p^2 = \left(\frac{E}{\rho}\right)\left(\frac{1-\nu}{(1+\nu)(1-2\nu)}\right),$$

where E is the Young's modulus of elasticity (psi), ρ is the mass density of the medium ($\rho = \gamma/g$ lb sec^2/ft^4, where γ is the unit weight of the medium in pounds per cubic foot and g is the gravitational acceleration constant), and ν is Poisson's ratio. For values of ν of 0.25 or less, the relation may be approximated by:

$$\bar{E} = \rho c_p^2 \approx E.$$

If the unit weight of the soil is about 115 lb/ft^3,

an approximate value of $\bar{E}$ is

$$\bar{E} = 25{,}000 \left(\frac{c_p}{1{,}000}\right)^2, \text{ psi.}^*$$

Substituting the values for H and $\bar{E}$ gives

$$d_{se} = 9 \left(\frac{p_{so}}{100}\right)^{0.5} \left(\frac{1{,}000}{c_p}\right) \left(W(\text{Mt})\right)^{1/3} \text{ inches.}$$

The permanent vertical displacement is not so easily estimated; at present the best estimates can be made by considering the static stress-strain properties of the soil. In the absence of better information, it is suggested that the permanent displacement at the surface be taken to be the following for overpressures greater than 40 psi:

$$d_{sp} = \frac{p_{so} - 40}{30} \left(\frac{1{,}000}{c_p}\right)^2 \text{ inches,}$$

where c_p is the seismic velocity of the material *near the surface.*

From wave propagation theory it may be demonstrated that the following relationship exists for particle velocities in terms of the dimensional units defined above.

$$v = c_p \frac{p_{so}}{\bar{E}} = c_p \epsilon,$$

where ϵ is the strain. Upon substitution this gives the maximum velocity

$$v_s = 50 \left(\frac{p_{so}}{100}\right) \left(\frac{1{,}000}{c_p}\right) \text{ in./sec.}$$

For a rise time of velocity of about 0.002 seconds, and considering a parabolic rise with a 20 percent increase for nonlinearity, the maximum acceleration at the surface, computed as a rate of change of velocity, may be expressed by

$$a_s \approx 150 \left(\frac{p_{so}}{100}\right) \left(\frac{1{,}000}{c_p}\right), g.$$

Since the surface acceleration is not related solely to the maximum velocity, but is partially dependent on the weapon yield and other factors, it is recommended that a value of c_p no greater than 2,000 fps be used in this expression, regardless of the actual surface seismic velocity.

Horizontal effects data are lacking for the surface. At present, it is recommended that the maximum horizontal deflection be taken as one-third the vertical, the maximum horizontal velocity as two-thirds the vertical, and the maximum horizontal acceleration as equal to the vertical.

The same type of reasoning can be followed in arriving at maximum values of acceleration, velocity, and displacement at depths below the surface. The difference in deflection between the surface and some point at a depth y beneath the surface cannot exceed the surface stress divided by the lower restrained modulus of deformation, $\bar{E}$, in the interval y, and multiplied by the depth y. Thus between the surface and a depth y, not greater than 100 ft, assuming no attenuation of pressure with depth, an upper limit of the elastic component of differential displacement is given by

$$d_s - d_y \approx \frac{p_{so}}{\bar{E}} y.$$

The actual difference in deflection i more likely to be one-half this value, and may be

* If the unit weight of the medium differs significantly from 175 lb/ft^3, a representative value of $\bar{E}$ should be used rather than the approximation given here.

considered to vary linearly to a depth of 100 ft, which results in the following expression

$$d_{se} - d_{ye} = 2.4\left(\frac{p_{so}}{100}\right)\left(\frac{1{,}000}{c_p}\right)^2\left(\frac{y^*}{100\text{ ft}}\right)\text{inches}$$

where $y^* = y$ for depths of 0 to 100 ft, and $y^* = 100$ ft for depths greater than 100 ft.

It is not generally considered desirable to assume any attenuation of displacement, except for very soft soils. Since total impulse must be preserved, the wavelength of the strain pulse probably increases with depth, and, therefore, it does not seem reasonable that there should be a reduction in elastic component of displacement consistent with the reduction in peak stress, as given by the attenuation relationships for stress or velocity with depth.

It is recommended that the permanent displacement of soils at depths below the surface be determined by multiplying the permanent displacement at the surface by $(100 - y^*)/100$, i.e.,

$$d_{yp} = d_{sp}\left(\frac{100 - y^*}{100}\right)$$

$$= \frac{p_{so} - 40}{30}\left(\frac{1{,}000}{c_p}\right)^2\left(\frac{100 - y^*}{100}\right)\text{inches.}$$

Thus, permanent displacements below 100 feet would be taken to be zero. At depths less than 100 feet, the total displacement should be taken as the sum of the elastic displacement at the surface, d_{se}, shown previously, and the permanent displacement, d_{yp}, given above.

The value of maximum stress below the surface is given approximately, for any yield or overpressure, by the following expression

$$p_y = \alpha p_{so}$$

where

$$\alpha = \frac{1}{1 + \frac{y}{H}},$$

and for depths that are not near the surface

$$H = 230\left(\frac{100}{p_{so}}\right)^{0.5}\left(W(\text{Mt})\right)^{1/3}.$$

Note: The attenuation factor, α, that is used in this section is different than the corresponding attenuation factor $1/\beta$ that is used in Section II, "Damage to Belowground Structures," of Chapter 11, "Damage to Structures." The attenuation factor given in Figure 11-29, Section II of Chapter 11 is the result of more recent studies. It reflects the influence of soil type (as represented by its seismic velocity) on peak pressure or soil particle velocity attenuation. The disparity between the two factors increases as the peak overpressure and/or the soil seismic velocity increase, but the disparity is relatively insensitive to variations in weapon yield. As a result of the influence of seismic velocity, the difference between the two factors also increases as the depth below ground surface increases. The factor given in Figure 11-29 gives substantially smaller attenuation rates under high overpressures and high seismic velocities than does the factor used in this section. Consequently, from the "vulnerability analysis" point of view, the factor of Figure 11-29 is more conservative, and its use in shock analysis studies is generally recommended. The attenuation factor obtained from Figure 11-29 may be introduced into the equations of this section by simply replacing "α" of this section with "$1/\beta$," where "β" is obtained from Figure 11-29. As mentioned previously, it is recommended that this replacement be made, in general; however, there is

one important exception. The factor $1/\beta$ is not compatible with the shortcut vulnerability curves shown in Figures 11-48 through 11-50, and calculations of similar curves that are compatible with the $1/\beta$ attenuation factor have not been performed at this time. It is for this reason that the α attenuation factor is introduced here, and its use will be illustrated in Problem 2-27. The use of the $1/\beta$ attenuation factor is illustrated in Problems 11-3 and 11-4.

At depths below the surface, it is recommended that velocities be attenuated in about the same manner as the maximum stress. Thus, the vertical velocity at any depth y is given by

$$v_y = \alpha v_s.$$

The peak downward acceleration attenuates sharply with depth, especially near the surface. The sharp attenuation is caused primarily by the increase of rise time in the stress or velocity with depth.

The time of rise of the maximum velocity from an initial zero value can be taken as one-half the transit time of the shock wave from the surface to depth considered. For a parabolic rise in velocity the acceleration can be considered to be twice the value for a linear rise, which leads to the expression

$$a_y = 2\frac{v_y}{t_r} = 5\left(\frac{p_{so}}{100}\right)\frac{100}{y}\alpha\, g,$$

where t_r is the effective velocity pulse rise time. This expression gives values which appear to agree well with test data for depths greater than 10 ft.

In the absence of better information at depths below the surface, it is recommended that the ratios of horizontal to vertical effects be taken equal to those previously specified for the surface, i.e., horizontal deflection is one-third the vertical, the maximum horizontal velocity is two-thirds the vertical, and the maximum horizontal acceleration is equal to the vertical.

Layered media pose a complicated situation, but with care and judgment, reasonable estimates of acceleration, velocity, and displacement can be made. A convenient method is to use the stepwise passage of a stress wave downward through the medium. In general, the basic concepts governing the computation of displacement, velocity, and acceleration are the same as those described for a uniform medium. The displacements at any particular time may be computed by dividing the average pressure in an interval by the modulus of elasticity to obtain the strain and then multiplying by the length of the interval to obtain the displacement; the total displacement occurring over the length of the pulse is the sum of the incremental displacements.

Complications arise at the interface of two media because of stress transmission and reflection. For soil and rock, the interface may not be sharply defined and the reflected and transmitted stresses probably do not follow the laws governing purely elastic media. If it is known that the interface is fairly sharp, an estimate of the reflected and transmitted stresses can be made from the following relationships:

$$p_r = \frac{1-\psi}{1+\psi}p_i$$

$$p_t = \frac{2}{1+\psi}p_i$$

where ψ is the ratio of the impedances of the two media. The stresses at the interface must be taken as equal, and, from considerations of continuity, the displacements also are equal.

2-63 Outrunning Ground Motion

Outrunning ground motion occurs when the air-shock velocity U decays below the seis-

mic wave velocity c of the medium. In the most general sense, outrunning ground motions and direct-transmitted ground shock are different phenomena. Direct-transmitted ground shock is ground motion propagated through the ground media from the region of the crater (this is often denoted outrunning when it clearly arrives, as reflected or refracted waves from deep-seated layers, ahead of the blast front). Outrunning ground motion occurs when the air-induced ground motion begins to propagate more rapidly than the air blast shock front, as illustrated in Figure 2-88. In actual fact, the motion-time history at a point in the medium can be quite complicated, even random in nature, when air-induced, outrunning, and direct-transmitted effects all arrive at about the same time.

Some information on outrunning motions observed in field tests can be found in "Nuclear Geoplosics" (see bibliography). Computer codes that are presently being developed should provide guides to even better estimates or outrunning motions.

2-64 Direct-Transmitted Ground Shock

The energy transmitted directly to the earth from a surface or near-surface burst can be propagated effectively through competent material for long distances. Experimental data that demonstrate this are available from buried high explosive shots and from surface and contained nuclear weapon tests.

For a completely buried shot, the first portion of the strain or velocity record at a distance R from the point of burst has the form described in paragraph 2-60, i.e.,

$$T_R = \frac{R}{6c_p} \text{ to } \frac{R}{12c_p} \quad \text{and} \quad T_o = \frac{R}{2c_p} \text{ to } \frac{R}{c_p}$$

Without serious error, the relation between peak strain ϵ and peak particle velocity v is given by the equation previously shown in paragraph 2-62, i.e.,

$$v = c_p \frac{p_{so}}{E} = c_p \epsilon.$$

Assuming that the steepest part of the velocity-time curve has a slope that is twice the average slope during the rise phase leads to the following relationship between the range of peak acceleration, peak velocity, and strain, all in the radial direction.

$$a_r = \frac{2v_r}{T_r} \approx \frac{12c_p^2}{R} \epsilon \text{ to } \frac{24c_p^2}{R} \epsilon.$$

An estimate of the maximum displacement d_r in the radial direction may be obtained by integrating the area under the positive phase of the velocity curve. If the velocity waveform is parabolic, then

$$d_r = \frac{2}{3} v_r T_o \approx \frac{1}{3} R\epsilon \text{ to } \frac{2}{3} R\epsilon.$$

If data for strain, acceleration, or displacement are available, approximate relations for the other quantities may be obtained. In general, the seismic velocity enters into the relationships as indicated in equations shown above.

Most of the available test data from which direct-transmitted shock effects may be estimated were obtained from buried nuclear and high explosive detonations. To extrapolate from the test data to estimate shock effects produced by surface nuclear detonations requires establishment of the equivalence factor relating buried HE to buried nuclear yield, and also establishment of the equivalence of fully buried detonations to surface detonations of the same type of explosive.

A yield effectiveness factor of 0.2 to 0.5 has been used to relate fully contained nuclear

[redacted]

explosions to fully contained HE explosions. To relate a surface nuclear burst to a fully contained nuclear burst, factors of 0.02 for a burst slightly above the surface to 0.05 for a burst slightly below the surface are recommended. Significant uncertainties exist regarding these equivalence factors.

Expressions for acceleration, velocity, and displacement have been derived on the basis of test data available for accelerations from shot RAINIER in Operation HARDTACK in volcanic tuff with a seismic velocity of 6,000 fps. For scaled ranges of 2,500 ft/Mt$^{1/3}$ and closer, and an equivalence factor of 0.05 as just discussed, the acceleration may be expressed as follows:

$$a_r = 0.4 \left(W(\mathrm{Mt})\right)^{5/6} \left(\frac{1{,}000}{R}\right)^{3.5} \left(\frac{c_p}{1{,}000}\right)^2, \ g.$$

Using the relations between acceleration, velocity, and displacement, and choosing the equations with coefficients of 12 and 1/3, respectively, this equation for acceleration may be used to arrive at the following equations for radial velocity and displacement for materials with seismic velocities less than 10,000 feet per second:

$$v_r = 12 \left(W(\mathrm{Mt})\right)^{5/6} \left(\frac{1{,}000}{R}\right)^{2.5} \left(\frac{c_p}{1{,}000}\right) \text{in./sec}$$

$$d_r = 4 \left(W(\mathrm{Mt})\right)^{5/6} \left(\frac{1{,}000}{R}\right)^{1.5} \text{inches.}$$

There is little or no information on tangential motions, and until additional information becomes available, it is recommended that maximum values of tangential acceleration, velocity, and displacement be taken as 1, 2/3, and 1/3 times the corresponding radial values.

It is desirable to consider the direct-transmitted effects as being applicable only at some distance below ground surface, except possibly at close in ranges. At scaled distances greater than 2,500 ft/Mt$^{1/3}$, the limited available data suggest a decrease in the rate of decay of motion with distance. Approximate expressions for radial acceleration, velocity, and displacement for materials with an average seismic velocity less than 10,000 fps are as follows:

$$a_r = 0.081 \left(W(\mathrm{Mt})\right)^{0.25} \left(\frac{1{,}000}{R}\right)^{1.75} \left(\frac{c_p}{1{,}000}\right)^2, \ g.$$

$$v_r = 4.8 \left(W(\mathrm{Mt})\right)^{0.5} \left(\frac{1{,}000}{R}\right)^{1.5} \left(\frac{c_p}{1{,}000}\right) \text{in./sec}$$

$$d_r = 3.19 \left(W(\mathrm{Mt})\right)^{0.75} \left(\frac{1{,}000}{R}\right)^{1.25} \text{inches.}$$

These expressions give only very approximate values. Geologic conditions can produce large and random variations in the motions at large distances. For materials with seismic velocities greater than 10,000 fps, e.g., granite rock materials, the field test data suggest the following relationships as being applicable at scaled ranges of about 2,700 ft/Mt$^{1/3}$ and closer.

$$a_r = 180 \left(W(\mathrm{Mt})\right)^{5/6} \left(\frac{1{,}000}{R}\right)^{7/2} \left(\frac{165}{\gamma}\right)^{5/6} \left(\frac{c_p}{18{,}000}\right)^{1/3}, \ g,$$

$$v_r = 30 \left(W(\mathrm{Mt})\right)^{5/6} \left(\frac{1{,}000}{R}\right)^{5/2} \left(\frac{165}{\gamma}\right)^{5/6} \left(\frac{18{,}000}{c_p}\right)^{2/3}, \ \text{ft/sec,}$$

[redacted]

[redacted]

(U)

$$d_I = 12 \left(\frac{W(\mathrm{Mt})}{}\right)^{5/6} \left(\frac{1{,}000}{R}\right)^{3/2} \left(\frac{165}{\gamma}\right)^{5/6} \left(\frac{18{,}000}{c_p}\right)^{5/3}, \text{ inches.}$$

As would be expected from the different scaling relationships, the expression for materials with seismic velocities less than 10,000 feet per second and those for materials with seismic velocities greater than 10,000 feet per second show lack of agreement at a seismic velocity of 10,000 feet per second, which divides the areas of applicability. This matter is currently receiving further attention, but in the interim it is believed that the expressions provide the best estimates of such motions.

No expressions exist for motions at large distances in hard materials that are comparable to the expressions presented above for soft materials. It was necessary to make approximate estimates to develop the relationships presented in Section III, Chapter 11.

2-65 Spectrum Concepts — Simple Systems

When structural systems or equipment are subject to a base disturbance, such as that arising from the ground motion associated with a nuclear explosion, the response of the system is governed by the distribution and magnitudes of the masses and resistance elements. A knowledge of the response of systems subjected to such loadings is extremely important from the standpoint of design in order to proportion the structure so that it will not undergo complete collapse, and to protect the structure, equipment, and personnel from shock damage. One of the simplest interpretations of ground motion data involves the concept of the response spectrum, which is a plot of the maximum response of a simple linear oscillator subjected to a given input motion as a function of frequency.

The time history of the actual motions of the earth caused by the passage of a shock wave over the surface is complex and is subject to considerable uncertainty. However, the principal effects on equipment and structural components can be described by use of the concept of the shock-response spectrum.

Consider a piece of equipment or an internal element of a structure supported at a point on an underground structure that is subjected to motion from blast. The equipment or element can be represented as a simple oscillator, consisting of a mass m attached by a linear spring of spring constant k to the base as shown in Figure 2-89(a). The natural frequency f of the oscillator is

$$f = \omega/2\pi = \frac{1}{2\pi}\sqrt{\frac{k}{m}}.$$

For a given transient ground motion x, the mass m will be set into motion. If the motion of the mass m is designated by the coordinate y and the motion of the base by the coordinate x, the deformation in the spring u is $(y\text{-}x)$ and is positive when y exceeds x. For such a system the most useful spectra are found to be the following: the maximum relative displacement u of the system; the maximum relative velocity $\dot{u}$; the maximum pseudo relative velocity or the quantity ωu, the circular frequency ω times the displacement u, which is not quite the same as $\dot{u}$ and differs considerably from $\dot{u}$ at low frequencies; and the absolute acceleration of the mass, $\omega^2 u$, which is nearly the same as $\ddot{y}$. A plot of the maximum values (denoted D, $\overline{V}$, V, and Ag, respectively) as a function of the frequency of the system for a given type of input constitutes a response spectrum for the particular function. These quantities are defined as follows:

$$Ag = \left|\omega^2 D\right| = (2\pi f)^2 D$$

$$V = \left|\omega D\right| = 2\pi f D$$

[redacted]

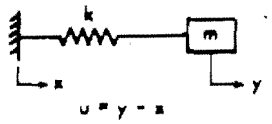

(a) SINGLE-DEGREE-OF-FREEDOM SYSTEM

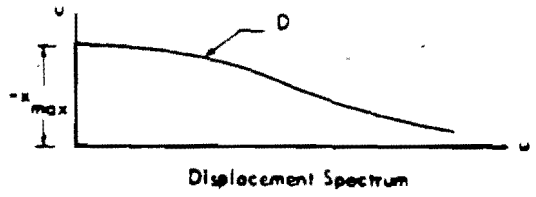

Displacement Spectrum

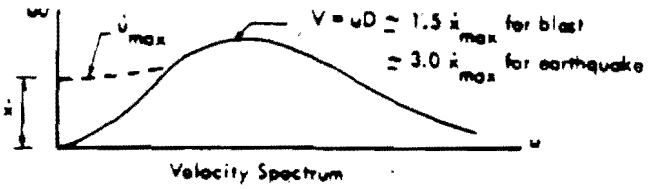

Velocity Spectrum

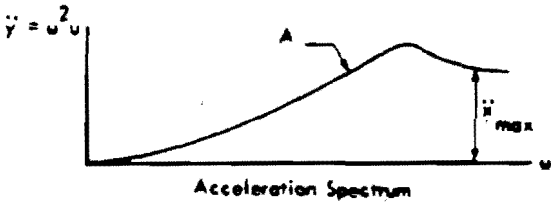

Acceleration Spectrum

(b) TYPICAL SPECTRA

Figure 2-89. [redacted] Single-Degree-of-Freedom System and Typical Response Spectra [redacted]

The maximum energy absorbed in the spring is associated with V. The quantity $\bar{V}$ is not particularly useful.

For inputs of the type associated with air-induced or direct-transmitted ground shock, the spectra for a simple system will have the characteristic appearances shown in Figure 2-89(b). The limiting conditions that apply to the spectra illustrated in Figure 2-89(b) are of particular interest. For example, as the frequency of the system approaches zero, the mass m does not move when the base of the system has a given motion applied. Then the relative displacement u is equal to the negative value of x, and the relative velocity $\dot{u}$ is equal to minus the maximum base velocity $\dot{x}$. The dotted line in Figure 2-89(b) indicates the difference between $\dot{u}_{max}$ and V that may be observed in the region of low frequencies; likewise, there is some difference between $\dot{u}_{max}$ and V at the high frequency end, but these differences are of a smaller order of magnitude. Typical values of V that might be expected for blast conditions are shown in Figure 2-89(b). An additional control is that as the frequency of the system becomes large, the displacement y approaches the displacement x, i.e., u approaches zero, and the acceleration $\ddot{y}_{max}$ approaches $\ddot{x}_{max}$. These controls are of special importance in arriving at design shock spectra.

Ordinarily, the input for ground motion consists of two parts, a systematic portion on which is superimposed a series of random oscillations. The magnitude of the peaks of the random components may be either small or large compared to the systematic portion. The random part may exist over the entire range of the systematic portion, over only part of the range, or even may be prior to the systematic portion.

For a random series of pulses, the relative velocity peak of the spectrum compared with the maximum input velocity can be high, but it is not likely to be much higher than about 3, unless an almost resonant condition is obtained with several pulses of alternate positive and negative signs of exactly the same shape and duration. Such a resonant condition for velocity is extremely unlikely from blast loading, although it has been observed in long duration earthquake phenomena. Even if, for some reason, partial resonance is achieved, the dampening in the system being excited will reduce the peaks considerably.

In general, the combined effect of the two input motions, systematic and random, depends on their individual effects. It can be shown that the combined spectrum will be either equal to or less than the sum of the absolute values of the spectra corresponding to the individual inputs. It also appears reasonable that the combined spectrum can be expected to be approximately equal to the square root of the sum of the squares of the individual spectra, point by point. In most practical cases of the type under consideration, the frequencies for which the spectrum values are important differ by a considerable amount, and the sums of the spectra or the square root of the sums of the squares are nearly the same as the maximum individual modal value.

2-66 Shock Spectra for Free Field Ground Motion

Using the concepts discussed above, it is possible to derive shock spectra that can be used in design to assess the relative effects in a structure (above or below ground) or the effects on equipment within a structure. Such spectra can be described best by the use of a logarithmic plot that permits values of displacement, pseudo-velocity, and acceleration to be read versus frequency in accordance with the relations given by the equations in paragraph 2-65.

In accordance with the limiting conditions discussed for Figure 2-89, the response spectrum can be represented by three regions, each region defined by a straight line constituting an envelope to the actual spectrum. An

example of such a spectrum for air-induced shock for conditions of 100 psi surface pressure, 5 Mt yield, and an acoustic velocity of 2,500 ft/sec is shown in Figure 2-90 for situations at the surface and at a depth of 100 ft. The left hand region, at the low frequency side, is influenced primarily by the maximum elastic transient displacement. The intermediate part of the spectrum (horizontal line) is a function of the maximum velocity reached in the free field. The right hand side depends on the maximum acceleration. In brief, the approximate response spectrum "envelope" is described by three straight lines (actually there are discrepancies that may be as high as a factor of 2 in some areas, but the actual ground motions are now known even this accurately, and the simplification of the spectrum in this way is permissible).

- A line D = constant, parallel to the displacement scales, drawn with a magnitude equal to the maximum ground displacement.
- A line V = constant, drawn with a magnitude of 1.5 times the maximum ground velocity.
- A line A = constant, parallel to the acceleration scales, drawn with a magnitude equal to twice the maximum ground acceleration.

Spectra may be sketched for horizontal and vertical motions at various depths and employed as appropriate. Detailed procedures for constructing more accurate spectra may be found in "Effect of Inelastic Behavior on the Response of Simple Systems to Earthquake Motions," A. S. Veletsos and N. M. Newmark, and "Response Spectra Approach to Behavior of Shock Isolation Systems," A. S. Veletsos and N. M. Newmark (see bibliography). In general, the air-induced and direct-transmitted ground motions, as well as the out-running ground motions, if applicable, are computed. The spectra of each are plotted, and the design is made according to the envelop of the spectra. If it is known that the motions will arrive at significantly different times, the design or analysis is only made for the worst case.

The response spectrum, such as that shown in Figure 2-90, may be used directly for elastic systems. If the frequency of equipment within a structure and its type and mode of support are known, it is possible to ascertain certain results in terms of the response of the system. For example, for a single-degree-of-freedom system, the number of gravities of acceleration corresponding to the natural frequencies may be considered as applied to the body to ascertain the dynamic stresses. For more complex systems, the analysis is more difficult, although consideration of the most significant mode will lead to useful estimates of dynamic loadings in many cases.

For purposes of comparison and interest, three shock spectra determined from reed gages or ground motion records in atomic field tests are shown in Figure 2-91. The Operation HARDTACK spectra exhibit high accelerations; this is likely to be the result of the high water table that tends to emphasize the high frequency end of the spectrum. The maximum velocity is much higher than would be expected in a typical soil site. The Operation PLUMBBOB data approximate the type of response that would be expected for more normal soil conditions.

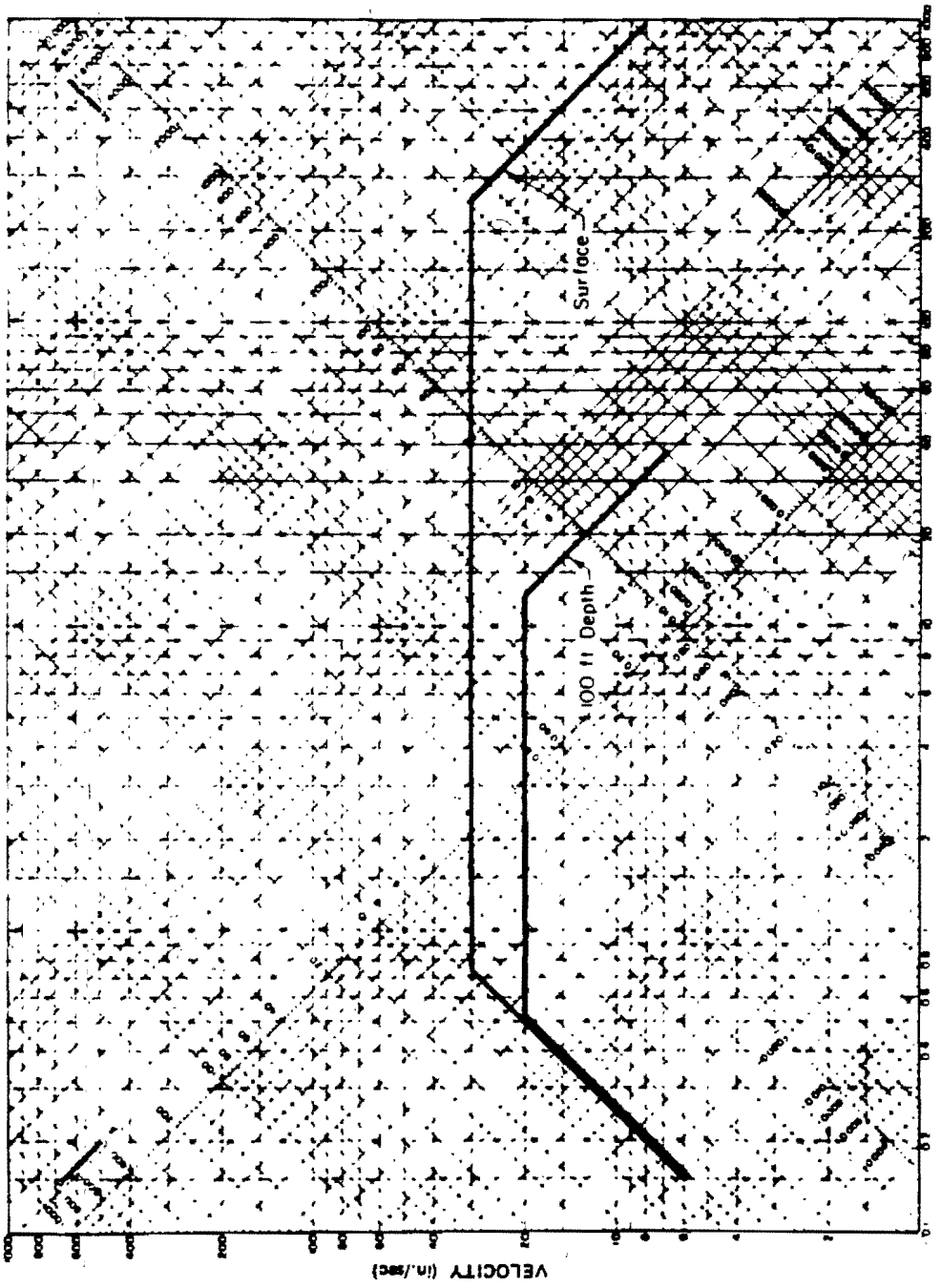

Figure 2-90. [redacted] Response Shock Spectra, 100 psi Overpressure, 5 Mt Yield, c = 2,500 fps (Vertical Motion – Air-Induced Effects)

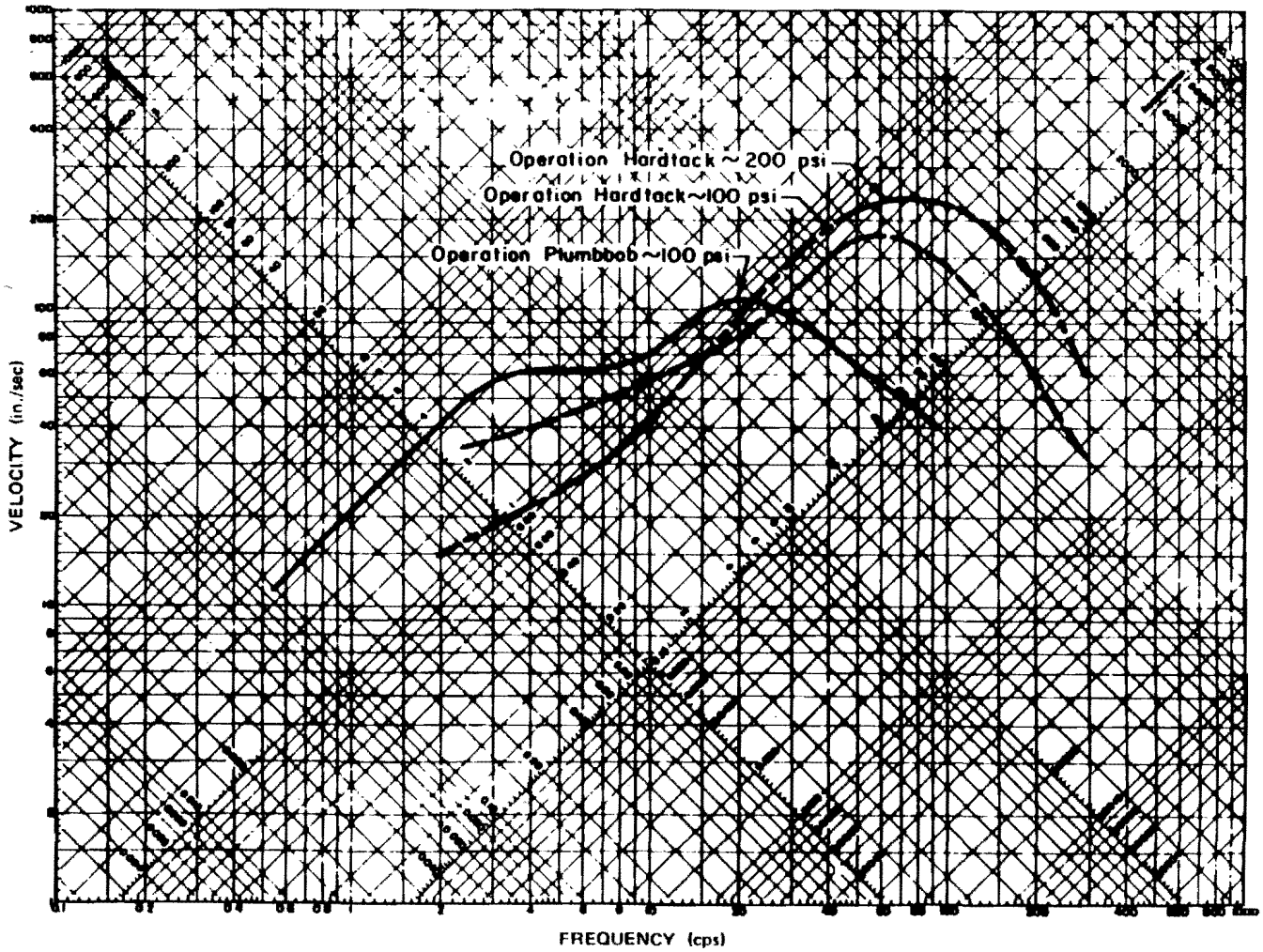

Figure 2-91. Typical Shock Spectra from Field Tests – Surface Data

Problem 2-27. Calculation of the Ground Motions from a Nuclear Explosion at the Surface

The nature of the free field effects of ground motion are described in paragraphs 2-60 through 2-66. The attenuation factor α that is defined in paragraph 2-62 is used in the example presented below. As noted in paragraph 2-62, it generally is preferable to use the factor $1/\beta$ for attenuation, where β is described in Section II of Chapter 11, and more specifically in Figure 11-29. However, $1/\beta$ attenuation is not compatible with the equipment vulnerability curves in Figures 11-48 through 11-50. Therefore, the following example illustrates the use of the attenuation factor described in paragraph 2-62; use of the $1/\beta$ attenuation is illustrated in Problems 11-3 and 11-4.

Example

Given: A 1 Mt weapon burst on the surface of a medium that has a seismic velocity of 5,000 ft/sec.

Find: The vertical and horizontal displacement, velocity, and acceleration at a point 50 feet below the surface and at a ground distance of 1,500 feet from the explosion.

Solution: The equivalent distance for 1 kt is

$$d_1 = \frac{d}{\left(W(\text{kt})\right)^{1/3}} = \frac{1{,}500}{(1{,}000)^{1/3}} = 150 \text{ feet.}$$

From Figure 2-17, the overpressure at the surface is about 1,000 psi.

a. *Air Induced Motions:* The maximum elastic vertical displacement at the ground surface is given by the equation shown in paragraph 2-62:

$$d_{se} = 9\left(\frac{P_{so}}{100}\right)^{0.5}\left(\frac{1{,}000}{c_p}\right)\left(W(\text{Mt})\right)^{1/3}$$

$$= 9\left(\frac{1{,}000}{100}\right)^{0.5}\left(\frac{1{,}000}{5{,}000}\right)(1)^{1/3} = 5.7 \text{ inches.}$$

It is reasonable to assume that impulse is preserved in the stiff medium described in this case. Therefore, the vertical elastic displacement at a depth of 50 feet will be the same as that at the surface, i.e., 5.7 inches. As described in paragraph 2-62, the permanent displacement at a depth of 50 feet is

$$d_{yp} = \frac{P_{so} - 40}{30}\left(\frac{1{,}000}{c_p}\right)^2\left(\frac{100 - y^*}{100}\right)$$

$$= \left(\frac{1{,}000 - 40}{30}\right)\left(\frac{1{,}000}{5{,}000}\right)^2\left(\frac{100 - 50}{100}\right)$$

$$= 0.6 \text{ inches.}$$

Thus, from paragraph 2-62 the total vertical displacement is

$$d_y = d_{se} + d_{yp} = 5.7 + 0.6 = 6.3 \text{ inches.}$$

The peak vertical velocity given in paragraph 2-62 is:

$$v_y = \alpha v_s,$$

where

$$v_s = 50\left(\frac{P_{so}}{100}\right)\left(\frac{1{,}000}{c_p}\right),$$

$$\alpha = \frac{1}{1 + \frac{y}{H}},$$

[redacted]

and

$$H = 230 \left(\frac{100}{p_{so}}\right)^{0.5} \left(W(\mathrm{Mt})\right)^{1/3}.$$

This gives

$$H = (230) \left(\frac{100}{1{,}000}\right)^{0.5} (1)^{1/3} = 73$$

$$\alpha = \frac{1}{1 + \frac{50}{73}} = 0.59$$

$$v_s = 50 \left(\frac{1{,}000}{100}\right)\left(\frac{1{,}000}{5{,}000}\right) = 100 \text{ in./sec},$$

$$v_y = (0.59)(100) = 59 \text{ in./sec}.$$

The vertical acceleration is given by the equation in paragraph 2-62 as:

$$a_y = 5 \left(\frac{p_{so}}{100}\right)\left(\frac{100}{y}\right) \alpha$$

$$= (5) \left(\frac{1{,}000}{100}\right)\left(\frac{100}{50}\right) (0.59) = 59 \text{ g}.$$

As described in paragraph 2-62, the horizontal values of the motions are taken to be 1/3, 2/3, and 1 times the vertical displacement, velocity and acceleration, respectively, i.e.,

$$d_x = 1/3\ d_y = \left(\frac{1}{3}\right)(6.3) = 2.1 \text{ inches},$$

$$v_x = \frac{2}{3} v_y = \left(\frac{2}{3}\right)(59) = 39 \text{ in./sec},$$

$$a_x = a_y = 59 \text{ g}.$$

b. *Direct Transmitted Motions:* The expressions given in paragraph 2-64 are applicable for direct transmitted motions. The radial motions are essentially horizontal for the distance and depth of this example. These are (note the distance is less than 2,500 ft/$\mathrm{Mt}^{1/3}$):

$$d_r = 4 \left(W(\mathrm{Mt})\right)^{5/6} \left(\frac{1{,}000}{R}\right)^{1.5}$$

$$= (4)\ (1)^{5/6} \left(\frac{1{,}000}{1{,}500}\right)^{1.5} = 2.2 \text{ inches}.$$

$$v_r = 12 \left(W(\mathrm{Mt})\right)^{5/6} \left(\frac{1{,}000}{R}\right)^{2.5} \left(\frac{c_p}{1{,}000}\right)$$

$$= 12\ (1)^{5/6} \left(\frac{1{,}000}{1{,}500}\right)^{2.5} \left(\frac{5{,}000}{1{,}000}\right)$$

$$= 22 \text{ in./sec},$$

$$a_r = 0.4 \left(W(\mathrm{Mt})\right)^{5/6} \left(\frac{1{,}000}{R}\right)^{3.5} \left(\frac{c_p}{1{,}000}\right)^2$$

$$= (0.4)\ (1)^{5/6} \left(\frac{1{,}000}{1{,}500}\right)^{3.5} \left(\frac{5{,}000}{1{,}000}\right)^2$$

$$= 2.4 \text{ g}.$$

In this case, the motions normal to the radial motions may be taken to be vertical. These are 1/3, 2/3, and 1 times the corresponding radial values of displacement, velocity and acceleration, i.e.,

$$d_y = \frac{1}{3} d_r = \left(\frac{1}{3}\right)(2.2) = 0.7 \text{ inches},$$

$$v_y = \frac{2}{3} v_r = \left(\frac{2}{3}\right)(22) = 15 \text{ in./sec},$$

$$a_y = a_r = 2.4 \text{ g}.$$

[redacted]

[redacted]

Answer: The peak values of both horizontal and vertical motions, for air-induced and direct-transmitted shocks are:

	d(in.)	v(in./sec)	a(g)
Vertical			
Air-induced	6.3	59	59
Direct-transmitted	0.7	15	2.4
Horizontal			
Air-induced	2.1	39	59
Direct-transmitted	2.2	22	2.4

In this particular example the air-induced motions, with the exception of the horizontal displacement, are the largest values for both the vertical and horizontal directions. In the horizontal direction, the direct-transmitted value of displacement is nearly equal to that of the air-induced value. In many cases, especially at short range and for stiff media, it will be found that the direct-transmitted motions will be the largest, and will control the analysis. From paragraph 2-66, the bounds for the shock response spectra are obtained by multiplying the controlling displacement, velocity, and acceleration values by 1, 1.5, and 2.0, respectively.

Vertical Response Spectrum Bounds:

$D = 1.0d = 6.3$ in.

$V = 1.5v = 89$ in./sec

$A = 2.0a = 118g$

Horizontal Response Spectrum Bounds:

$D = 1.0d = 2.2$ in.

$V = 1.5v = 59$ in./sec

$A = 2.0a = 118g$

These spectra bounds are shown in Figure 11-51. They show the response spectra for a single-degree-of-freedom system. These bounds are used in the analysis of the vulnerability of equipment mounted in an underground structure in Problem 11-8.

[redacted] *Related Material:* See paragraphs 2-24, 2-60 through 2-66, and Sections II and III of Chapter 11.

[redacted]

SECTION IV

UNDERWATER EXPLOSION PHENOMENA

An underwater nuclear explosion is characterized initially by the formation and propagation of an underwater shock wave. The dissipation of heat at the shock front causes the water to vaporize in the vicinity of the explosion and results in the formation of a large bubble of steam. The interaction of the bubble and the shock wave with the air-water interface produces various surface phenomena, including spray domes, columns, plumes, base surges, radioactive pools and surface waves. If the explosion is on or near the bottom, a crater is formed.

An underwater nuclear explosion also can result in thermal, nuclear, and electromagnetic radiation above the surface, but these phenomena are insignificant, except in the case of a shallow burst. These phenomena, when caused by a shallow burst, should approximate those from a shallow underground explosion.

2-67 Underwater Bubble

An underwater nuclear explosion releases large amounts of thermal and nuclear radiation, essentially all of which is absorbed by the surrounding water within several feet of the explosion (some radiation in the visible spectrum can be radiated to greater distances, depending on the transparency of the water).

During the early stages of the explosion, the warhead materials attain a very high temperature (tens of millions of degrees) and a very high pressure (on the order of millions of atmospheres). Energy acquired by these materials is transferred to the layer of water nearest the bomb, which is heated and compressed and which, then, heats and compresses the next outward layer. A compression wave (or hydrodynamic shock front) is formed by this mechanism, and this wave moves outward from the explosion at a speed greater than that of sound. This shock front expands faster than the material that it engulfs, which also moves outward, but at a slower rate.

As the shock front moves away from the point of explosion, energy is dissipated as heat, which raises the temperature of the water engulfed by the shock front. The largest temperature increase occurs near the center of the explosion, where the water is not only vaporized but dissociated as well. At greater distances, the water is vaporized and turned to steam at the shock front. At still greater distances, the water is not heated by the shock front sufficiently to boil. The bubble that is formed does not have a clearly defined "surface." Figure 2-92 shows this progression in a highly stylized form.

Thus, shortly after an underwater burst an expanding bubble is formed, which is composed largely of vaporized water with radioactive bomb debris at its center, surrounded by heated water. Large quantities of neutron-activated elements in the sea water are also present in the steam and layer of surrounding water; however, the total induced radioactivity is relatively small compared to the fission product radioactivity. Continued expansion of this bubble reduces the pressure within it. As the bubble pressure falls below the vapor pressure of the heated water, additional water flashes to steam at the interface of the bubble and the water.

If the explosion is deep underwater, the bubble continues to expand at a decreasing rate until a maximum size is reached. If it is not too near the surface or the bottom, the bubble remains nearly spherical to this point. As a result of the inertia of the water surrounding the expanding bubble, the bubble actually overexpands, i.e., when it attains its maximum size, its pressure is below the ambient water pressure. The high pressure around the bubble then causes it to contract with an increase in its pressure and

[redacted]

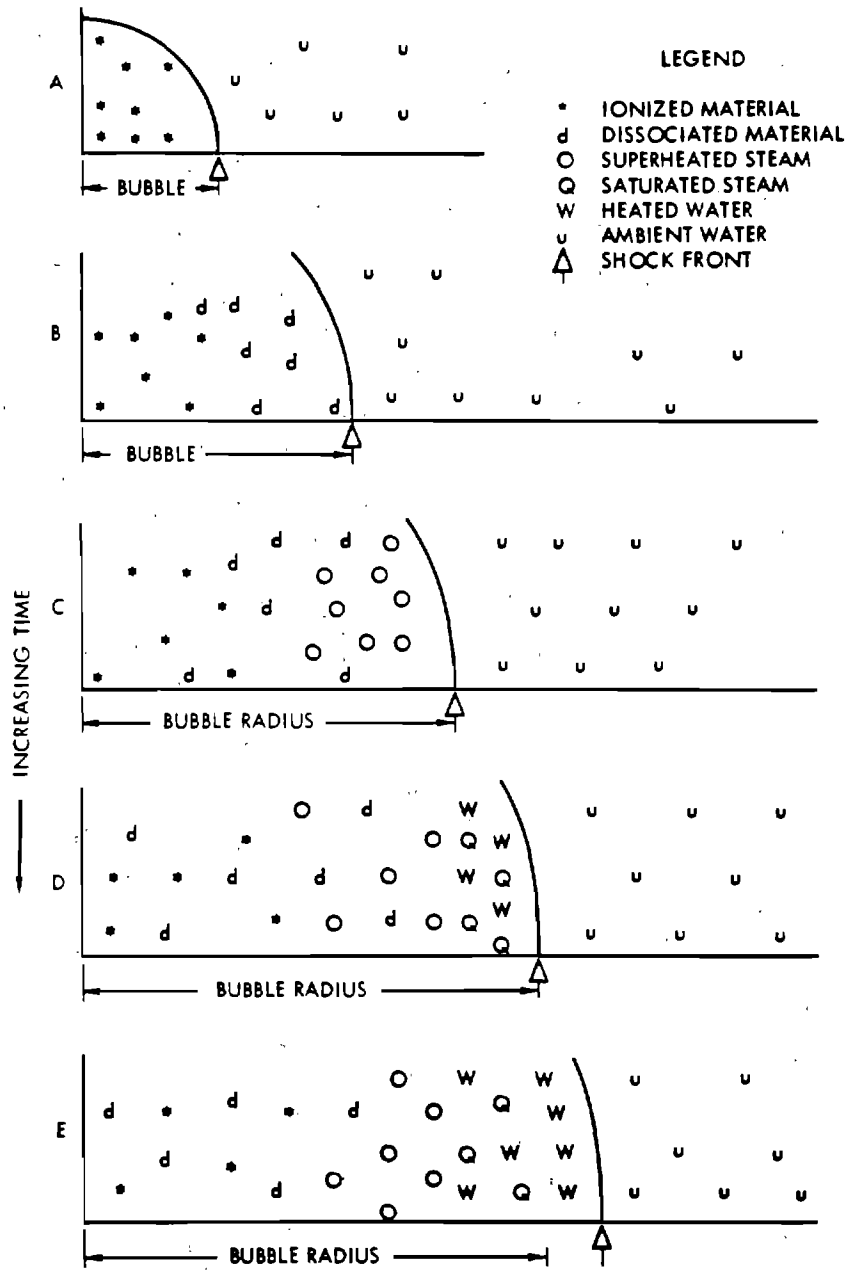

Figure 2-92. [redacted] Representation of Bubble Development [redacted]

[redacted]

condensation of some of its steam. Since the hydrostatic pressure is larger at the bottom of the bubble than at the top, the bubble does not remain spherical during the contracting phase. The bottom moves upward faster than the top (which may even remain stationary) and contacts the top to form a toroidal, or doughnut-shaped, bubble as viewed from above. This causes turbulence and mixing of the bubble contents with the surrounding water.

The inertia of the water set in motion by the bubble contraction causes it to overcontract, and its internal pressure becomes very much higher than the ambient water pressure. A second compression wave (the first bubble pulse) commences when the bubble reaches its minimum volume. This wave has a lower peak pressure, but a longer duration, than the initial shock. A second cycle of bubble expansion and contraction begins.

When the bubble pulse is emitted, the bubble surface becomes exceedingly unstable; a multitude of water spray jets shoot inward, thereby condensing much of the steam and degrading the bubble energy. Figure 2-93 shows the relative partitioning of the energy of the explosion with time qualitatively.

The bubble is relatively stationary during the initial expansion cycle, but upon contracting, it begins to migrate upward under the action of buoyant forces. The rate of upward migration is greatest when it is contracted and nearly zero when it is expanded.

If the bubble is far enough below the surface, it continues to pulsate and rise, though after three complete cycles enough steam will have condensed to make additional pulsations unlikely. During the pulsation and upward motion of the bubble, the water surrounding the bubble acquires considerable upward momentum and eventually breaks through the surface with a high velocity (about 200 mph for Wigwam, a deep underwater shot) thereby creating a large plume.

If the explosion is at a shallow depth, the bubble may break through the surface during one of the early pulsations, or even during the first pulsation cycle. If such a breakthrough occurs when the bubble pressure is higher than ambient (as with a very shallow explosion), a phenomenon known as a "blowout" occurs. If a breakthrough occurs when bubble pressure is below ambient, "blowin" occurs. The surface effects differ markedly for the two phenomena (see Figures 2-100 and 2-101 and accompanying text). A migrating bubble will not produce a bubble pulse if the bubble minimum occurs at or above the original water surface.

A strongly migrating bubble might continue to expand and not pass through a maximum size, somewhat like a balloon rising through the atmosphere. This is the balloon effect. A bubble migrating in this manner will not emit any bubble pulses. The conditions that cause a nuclear bubble to balloon rather than to pulsate are still subject to speculation; however, the absence of an expected bubble pulse might be explained by the balloon effect.

The maximum bubble radius and the first bubble period (time between burst and first minimum) are related to yield and depth of burst, as illustrated by the following two equations, which pertain to submerged bursts, i.e., the depth of burst, d_b is greater than A_{max}:

$$A_{max} = J' \frac{W^{1/3}}{Z^{1/3}},$$

$$T_1 = K' \frac{W^{1/3}}{Z^{5/6}},$$

where

A_{max} = Maximum bubble radius (ft),

[redacted]

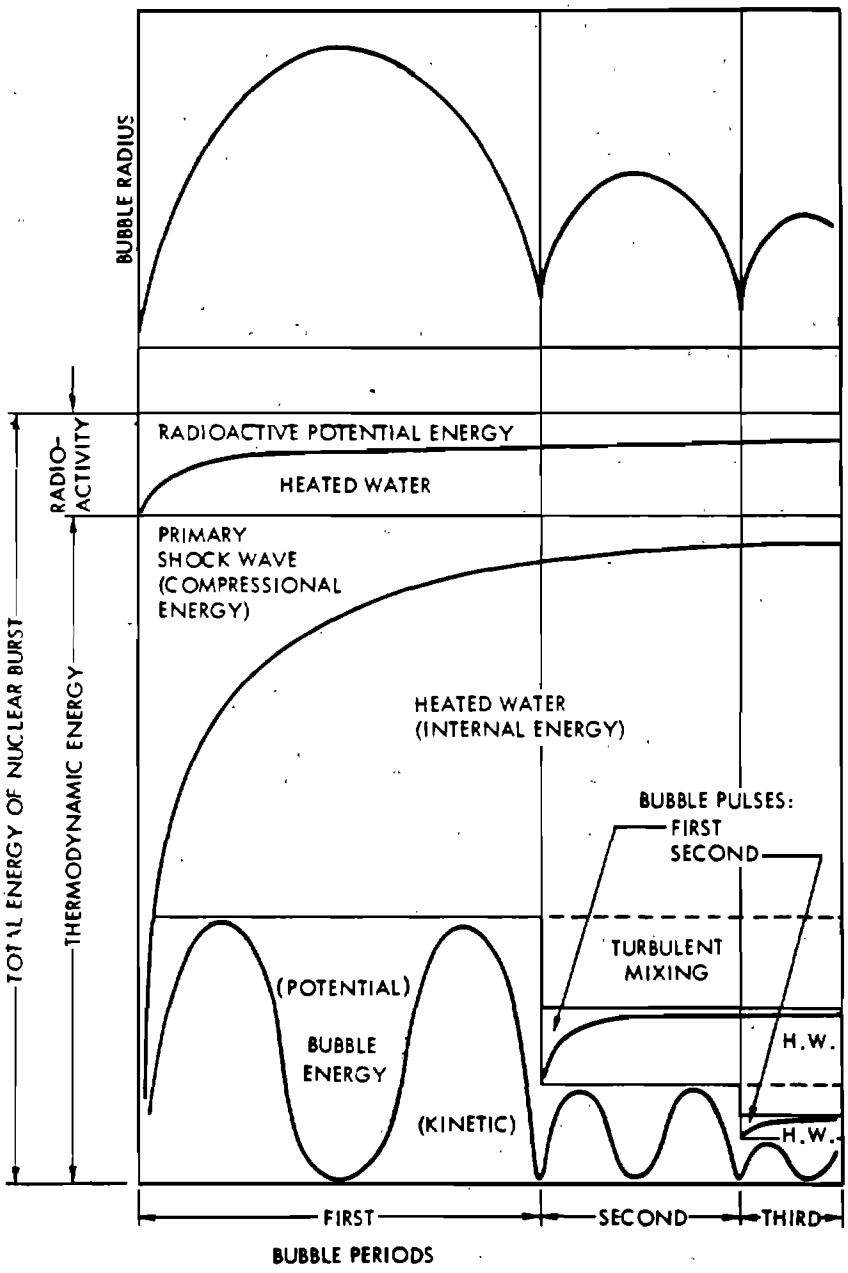

Figure 2-93. [redacted] Energy Distribution Following an Underwater Nuclear Burst [redacted]

[redacted]

[redacted]

J' = Empirical constant, 1500,

K' = Empirical constant, 515,

T_1 = First bubble period (sec),

W = Yield (kt),

Z = Hydrostatic head (d_b + 33) (ft).

The form of the equations is the same as those given by Cole for high explosives. The constants, J' and K', are slightly different because an underwater nuclear burst forms a steam bubble rather than gas bubble (as do high explosives) and because of other differences, mainly the distribution of total energy between bubble energy, shock wave energy, and residual radioactive energy.

[redacted] It is likely that the constants J' and K' are actually somewhat dependent on depth. This can be understood qualitatively as follows: J' and K' implicitly include the fraction of explosion energy included in the bubble. As the depth of burst is increased, a smaller fraction of explosion energy is converted to steam by the expanding shock wave (and more energy goes into heating water) because of the greater hydrostatic pressure that must be overcome to boil water.

[redacted] The second and third bubble maximum radii, the periods between minima, and the migration between periods, depend on the fraction of bubble energy that remains following succeeding bubble minima. The energy loss that occurs is due primarily to steam condensation at bubble minima as previously described, but the amount of energy loss is influenced by the depth at which the minimum occurs. An analytical representation of the energy as a function of bubble migration, which is best solved by use of a high-speed computer, has been developed,* however, satisfactory solutions to bubble problems can be obtained by use of curves derived from the representation, as illustrated in Problem 2-28.

[redacted] WATER SHOCK WAVE AND OTHER PRESSURE PULSES [redacted]

[redacted] The initial shock wave from an underwater explosion propagates radially from the source. This shock wave is characterized by an abrupt, virtually instantaneous, increase in pressure followed by a decrease that is approximately exponential. Near the explosion, the peak shock wave pressure is extremely high, but energy losses to the water cause the pressure to decrease somewhat faster than inversely with radius. Similarly, early shock wave propagation velocities are high, but by the time the peak pressure falls to about 3,000 psi, the propagation velocity becomes nearly equal to the acoustic speed in water (about 5,000 ft/sec), and the energy losses become small.

[redacted] If an explosion takes place far from either the surface or the bottom, the shock wave remains spherical as long as it propagates into water having constant acoustic velocity. This velocity depends on temperature, hydrostatic pressure, and salinity, however, and in regions of the ocean in which significant sound velocity gradients exist, the shock wave can be bent or refracted. Refraction can either increase or decrease the shock wave pressures locally, depending on ambient water conditions. No general prediction techniques can be given, but the subject is discussed further in paragraph 2-71.

[redacted] When a shock wave moving in water encounters another medium, it may be reflected as a tensile or rarefaction wave, as in the case of a water-air boundary; a compression or shock wave, as in the case of a water-bottom interface if the angle of incidence is not too far from the normal; or a distorted pulse having in general

* [redacted] This expression is described in "The Parameters of Underwater Nuclear Explosion Bubbles" (see bibliography).

[redacted]

both a positive and a negative phase, as in the case of more glancing incidence at the bottom. These are discussed separately in the following paragraphs.

2-68 Surface Reflection

The rarefaction wave, generated by the reflection of the primary shock wave from the surface, propagates downward and relieves the pressure behind the primary shock wave. If the shock wave is treated as a weak (acoustic) wave, this interaction instantaneously decreases the pressure in the primary shock wave to a value that might be well below the vapor pressure of the water, as shown by the broken line in Figure 2-94, Point A. Cavitation occurs in seawater when its pressure decreases to a value somewhat below its vapor pressure. The pressure of the primary shock wave is, therefore, reduced to a value which, when compared with the peak pressure, is usually so close to ambient water pressure that the shock wave pulse appears to have been truncated, i.e., reduced to ambient pressure.

For a strong primary shock wave, the reflected rarefaction wave propagates into water that has already been set in motion by the shock wave. Therefore, the rarefaction wave arrives earlier than predicted from the acoustic approximation, and the pressure cutoff is not instantaneous. This effect typically gives a pulse shape shown by the solid line for Point A of Figure 2-94. The shallower the point at which pressure measurements are made, the sooner the primary shock pulse is "cut off" and, hence, the shorter its duration (see Figure 2-94, Point B). At sufficiently shallow locations, the rarefaction wave interacts with the shock front and reduces the peak pressure (see Figure 2-94, Points C and D). The region in which peak pressure is reduced is known as the "anomalous region."

The effects of surface reflection decrease rapidly with increased depth of either the explosion or the point of measurement. Conversely, as the depth of burst is decreased (or the yield increased for a given depth of burst), the effects increase. The size of the anomalous region increases with decreased depth of burst until, for a surface burst, the anomalous region ~~increases~~ includes all points beneath the water surface except those close to the explosion and directly under it.

A limited amount of data are available concerning the reflection of shock waves from an ice layer. To date all tests have been with relatively small explosive charges (a majority of the test shots have been in the 1- to 40-lb range, with one shot of 630 lb). The situation is complicated by reflection and refractions at both the water-ice boundary and the ice-air boundary.

2-69 Bottom Reflection

Under certain circumstances, the shock wave from the bottom can be more damaging to surface ships and shallow submarines than the primary shock. Although the peak pressure of the reflected wave is usually smaller, the wave arrives at a steeper angle, and therefore may induce more damaging shock motion to a target at or near the surface.

2-70 Secondary Shocks and Pressure Waves

An underwater burst can cause compression waves in addition to those described above, but these effects are usually negligible. These waves include retransmitted pulses, cavitation pulses, bubble pulses, and others that are described briefly below.

- *Retransmitted Pulses.* Upon reflecting from the surface and bottom, some primary shock energy is transmitted into the air or bottom material, and some of this energy can be retransmitted back into the water.
- *Cavitation Effects.* As noted earlier, the reflection of the shock wave from the sur-

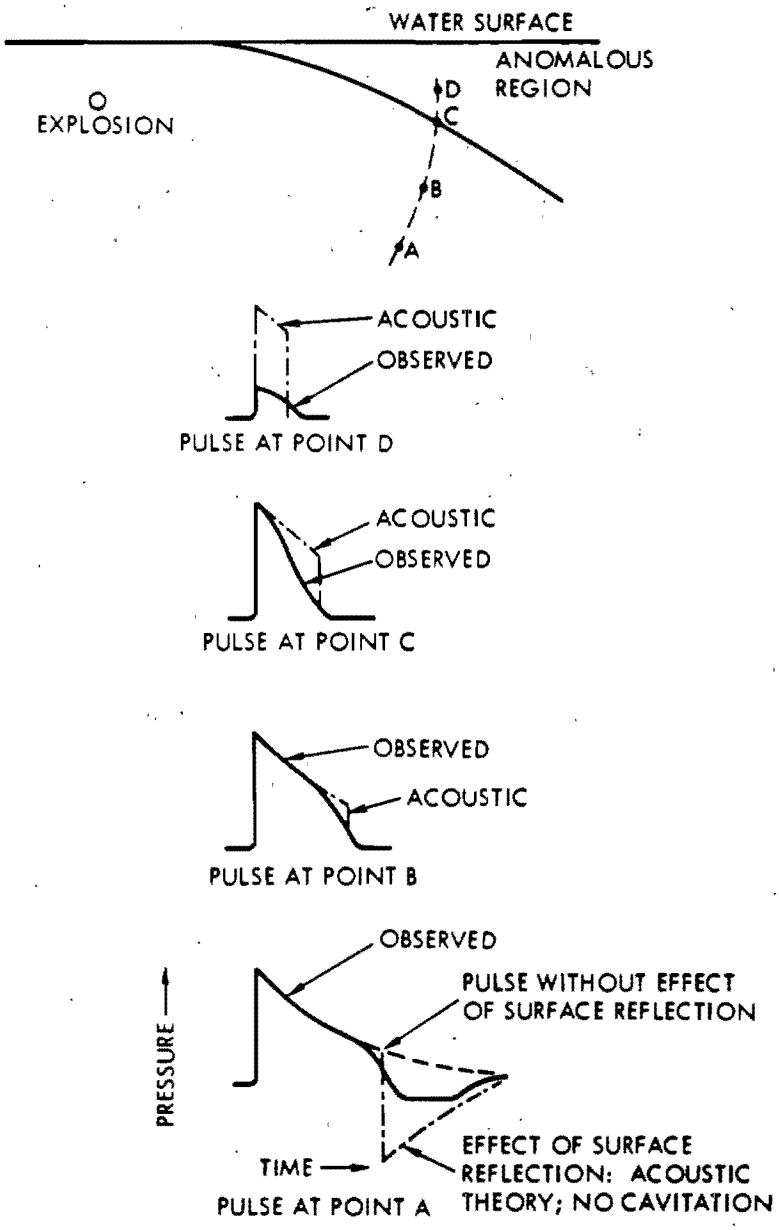

Figure 2-94. [redacted] Typical Pressure Pulses Affected by Surface Reflection [redacted]

face can lead to bulk cavitation below the surface. During the period of cavitation, the cavitated region can absorb further shock waves impinging on it. In the formation of the cavitation region, the rupture of the water by the shock wave causes a liquid surface layer (sometimes called "spall") to project upward in almost a ballistic trajectory. The impact of this spall when it returns to the surface can lead to further secondary shock waves. These shock waves account for the occasional larger damage to ships at intermediate ranges compared with the damage at shorter or longer ranges.

- *Bubble Pulses.* If an explosion is deep enough for one or more bubble pulsations to occur, compression waves are generated at the time of each bubble minimum.
- *Other Pulses.* All pressure waves are subject to multiple reflection from the surface and bottom. Also, in areas of irregular bottom topography, more than one reflected pulse can be generated.

Figure 2-95 shows typical shock wave and pressure pulse patterns for various burst and measurement conditions.

2-71 Refraction of Shock Waves

The shock front from an explosion far from a boundary (surface, bottom, etc.) remains spherical provided that it expands into water having constant acoustic velocity (isovelocity). However, the acoustic velocity in water depends on the temperature, salinity, and hydrostatic pressure, and these properties are not necessarily constant throughout a large body of water. As a result of variations in these properties, generally in horizontal layers, a region of water can have a characteristic acoustic velocity profile (sound velocity vs depth). Under such conditions, the shock wave is bent (refracted) because one part of the wave moves faster than another.

Refraction of the shock wave can result in convergence and reinforcement of the shock wave. This reinforcement commonly occurs along a surface called a "caustic." This effect may be illustrated by the use of a ray diagram* (Figure 2-96). The acoustic velocity profile that corresponds to the ray diagram is also shown in the figure. The formation of several caustics for one burst is observed frequently. Regions of relatively low pressure also occur, such as the "shadow zone" above the caustic in the figure.

The caustic can reinforce the peak pressure by a factor of five or more over the isovelocity value, while the pressure observed deep in the shadow zone can be essentially negligible. Shock wave impulse amplification factors do not go through a maximum at the caustic position. They remain much closer to unity than do peak pressure and energy factors.

As a result of ocean currents and underwater swells, the acoustic velocity profile in the ocean is rarely stable. Thus, the location of the caustics can shift rather quickly and unpredictably (similar to optic mirages).

Common types of sound velocity profiles can give rise to caustics at various distances greater than about one mile. In particular, in about half of the areas of the oceans, a caustic occurs at what is known as the convergence zone, typically 30 (10 to 40) miles from an underwater burst. Therefore, it is conceivable that a submarine might suffer damage from its own multi-kiloton weapon detonated at a distance of about 30 miles if it happened to lie on the caustic of its shot.

In Figure 2-96, sound speed is considered to vary with depth only. Actually this would rarely happen. The velocity can vary considerably across the ocean within the range of interest. Generally, the region of focusing is sharper

* A ray is generated by a curve that is always perpendicular to the expanding shock front.

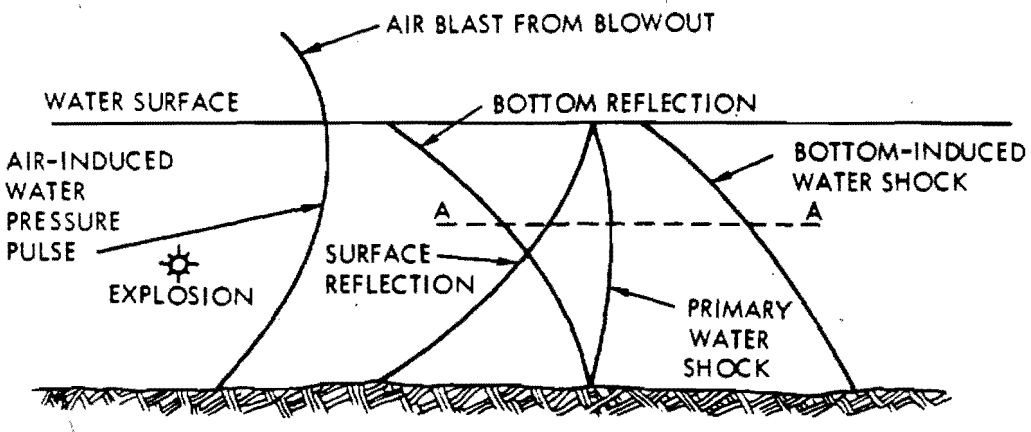

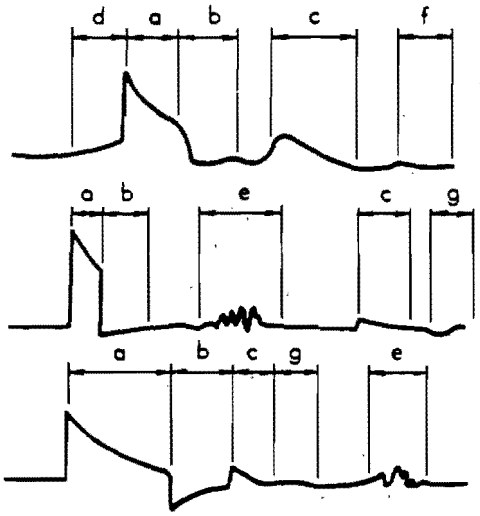

1. SHALLOW EXPLOSION IN SHALLOW WATER MEASUREMENT IN SHALLOW WATER
2. DEEP EXPLOSION IN MUCH DEEPER WATER MEASUREMENT AT SHALLOW DEPTH
3. DEEP EXPLOSION IN MUCH DEEPER WATER MEASUREMENT AT DEEP DEPTH

a. PRIMARY SHOCK WAVE
b. SURFACE REFLECTION
c. BOTTOM REFLECTION
d. BOTTOM-INDUCED PRESSURE PULSE
e. SHOCK FROM CAVITATION COLLAPSE
f. AIR-INDUCED WATER SHOCK
g. OTHER

Figure 2-95. [redacted] Typical Shock Wave Patterns Along Line A-A [redacted]

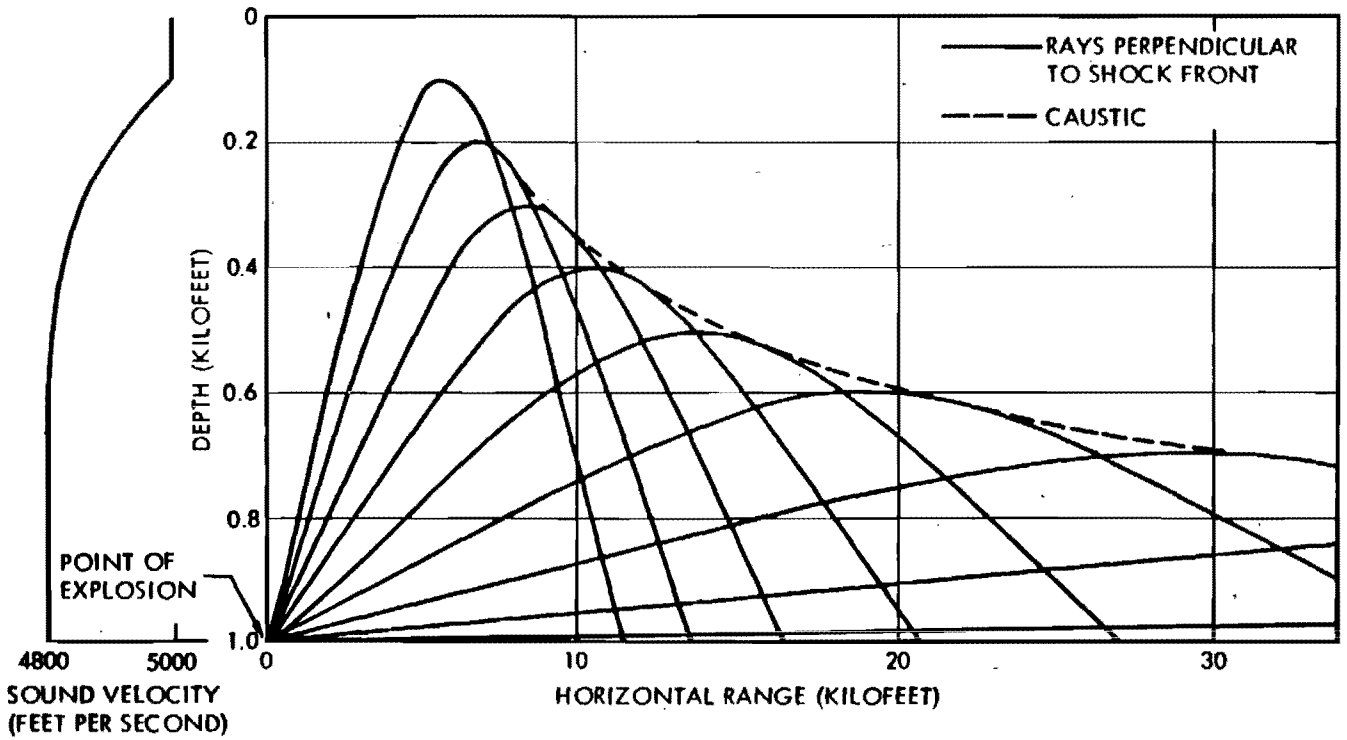

Figure 2-96. [redacted] Ray Diagram for an Idealized Velocity Profile [redacted]

and the maximum value of the amplification is greater for smaller yields.

2.72 Air Blast

The air blast wave has one to three pulses of various amplitudes, depending on the burst depth and the location of the observation point with reference to surface zero. These pulses are generated by two underwater explosion mechanisms. One is the underwater shock wave that transmits a portion of its energy across the water-air interface. The other is the underwater explosion bubble, which manifests itself in two ways: for burst depths shallower than about $35W^{1/3}$ feet, the bubble vents, causing an air pressure pulse; for burst depths deeper than $35W^{1/3}$ feet, a spray dome is pushed up by the expanding bubble, causing a bow wave.

For burst depths shallower than about $50W^{1/3}$ feet the transmitted pulse and the bubble generated pulse are formed almost simultaneously, resulting in a single intense pressure pulse over surface zero. For burst depths between $50W^{1/3}$ feet and about $150W^{1/3}$ feet, up to three pulses can be seen. The transmitted shock in air bifurcates near surface zero to form two air pulses, and the bow shock causes the third air pulse. For burst depths deeper than about $150W^{1/3}$ feet, the spray dome rises so slowly that no bow shock is formed and only the air pulse from the transmitted shock is important.

This discussion of the generation of air blast from underwater bursts is a simplified discussion of a complex subject. Much analytical, theoretical, and experimental work has been done to understand the physics of air blast generation. More complete discussions of the subject are given in Malme, Carbonell and Dyer (1966); Peckham and Pittman (1968); Pittman (1968); and Rudlin and Silva (1960) (see bibliography). Only a limited number of air blast measurements are available from nuclear weapon tests. The data are not sufficient to form a basis for predicting air blast for a spectrum of burst depths and pressure levels. The available predictive measures are based mainly on high explosive tests as described in Problem 2-31.

SURFACE EFFECTS OTHER THAN WAVES

The first surface effect of an underwater burst is caused by the intersection of the primary shock wave and the surface. Viewed from above, the effect frequently appears to be a rapidly expanding ring of darkened water, often called the "slick" (Figure 2-97). A white circular patch (the "crack") follows closely behind the darkened region. The crack probably is caused by underwater cavitation produced by the reflected rarefaction wave. Shortly after appearance of the crack, the water above the explosion rises vertically and forms a white mound of spray, called the "spray dome" (Figure 2-98). This dome is caused by the velocity imparted to the water near the surface by the reflection of the shock wave and the subsequent breakup of the surface layer into drops of spray. Additional slick, crack, and spray dome phenomena may result if the bottom-reflected shock waves and bubble-pulse compression waves reach the surface with sufficient intensity (Figure 2-99).

The spray dome from a shallow burst changes rapidly to a shallow column formed by the upward and outward motion of the water surrounding the explosion bubble. If blowout occurs, the upper part of the column is likely to resemble a crown, which contains explosion products blown out of the column (Figure 2-100). If blowin occurs, the crown is likely to be absent (Figure 2-101a). In its later stages, the column may break up into column jets (relatively broad spouts of water that disintegrate into spray as they travel through the air) (Figure 2-101b).

If the burst is sufficiently deep to prevent blowout, but shallow enough for the bubble to continue to oscillate as it approaches the

2-264
232

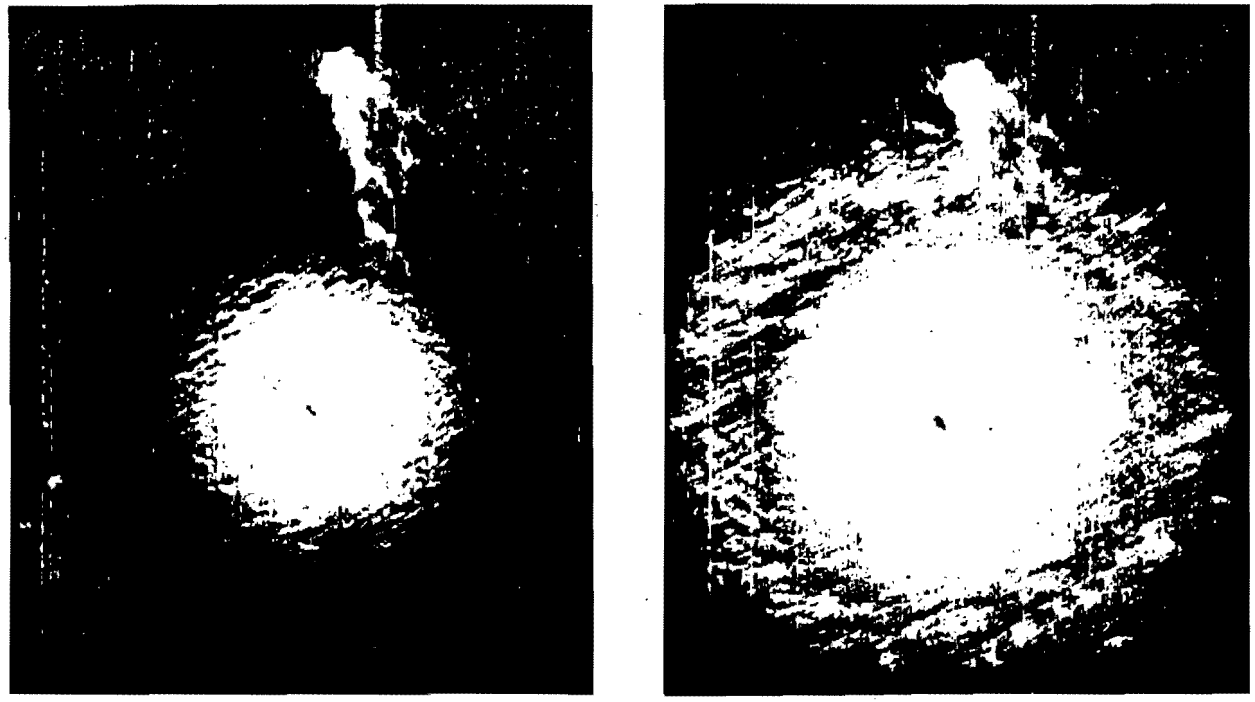

(a) PRIMARY SHOCK WAVE
Slick and Spray Dome
(0.28 sec after burst)

(b) CAVITATION PULSE
Slick and Spray Ring
(0.73 sec after burst)

Figure 2-97. [redacted] Slick Spray Dome and Cavitation Pulse Spray Ring (aerial view) [redacted]

Reproduced from best available copy.

[redacted]

Figure 2-98. [redacted] Spray Dome (3.3 sec after burst) [redacted]

[redacted]

Reproduced from
best available copy.

[redacted]

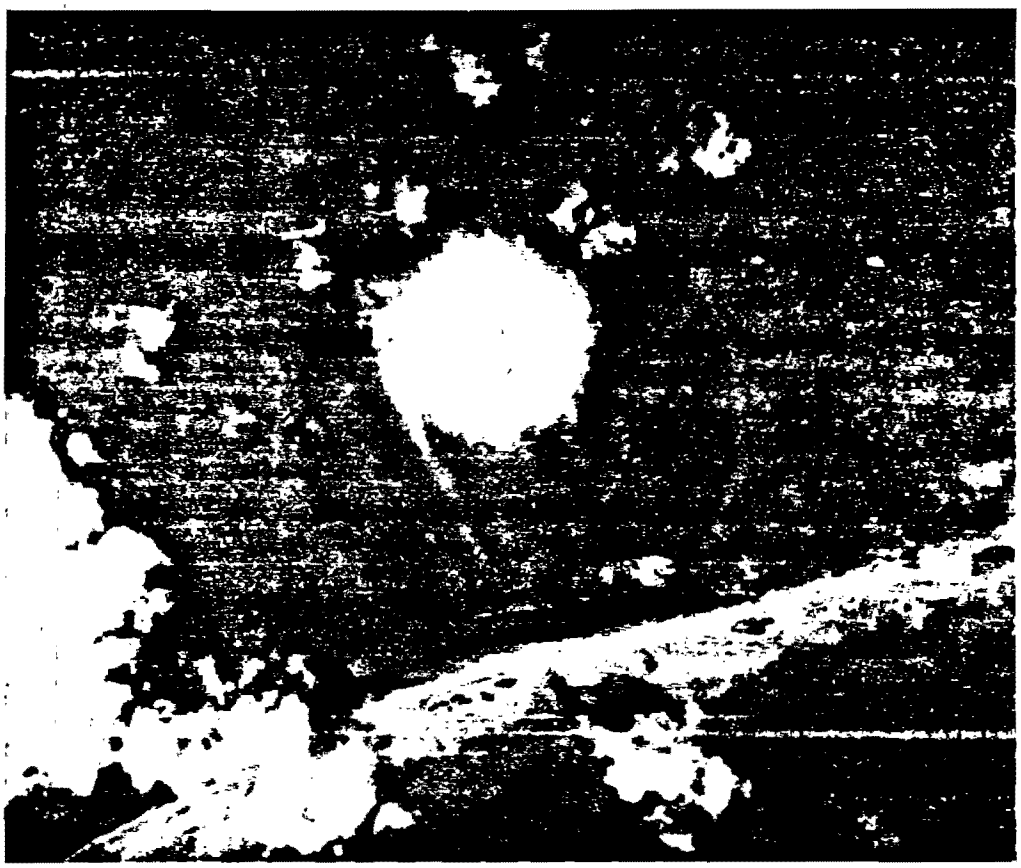

Figure 2-99. [redacted] Bottom-Reflected Shock Wave Slick
(aerial view 1.38 sec after burst) [redacted]

[redacted]

Reproduced from
best available copy.

[redacted]

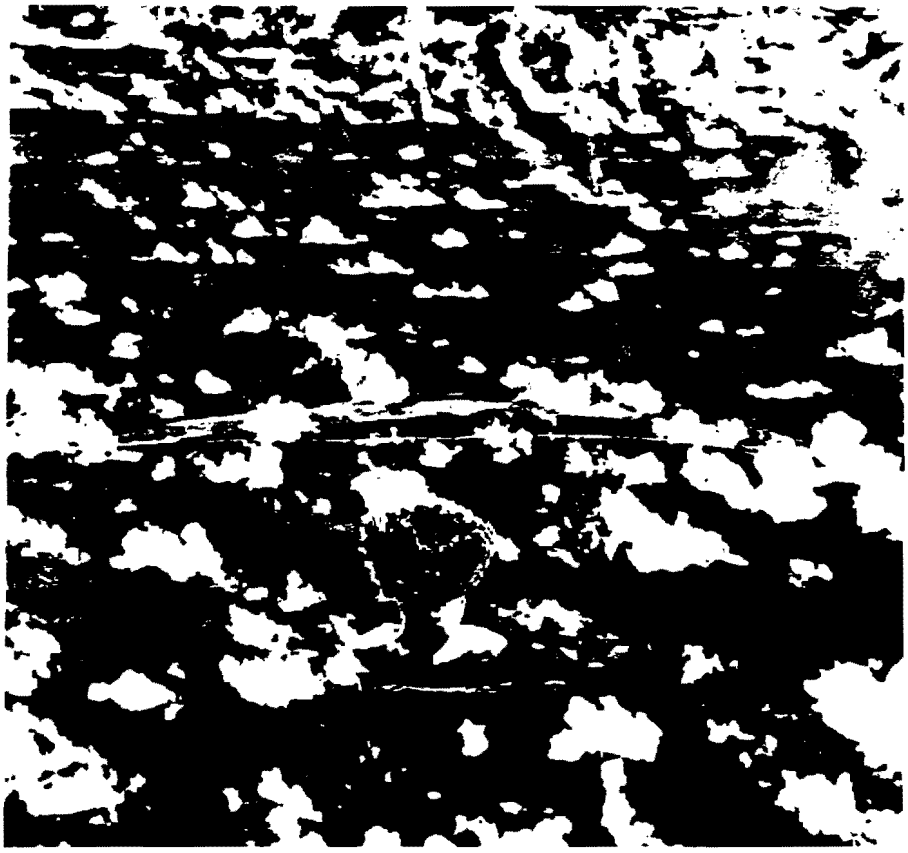

Figure 2-100. [redacted] Very Shallow Burst Showing Crown of Explosion Products on Column (oblique aerial view 0.7 sec after burst) [redacted]

[redacted]

Reproduced from best available copy.

Reproduced from best available copy.

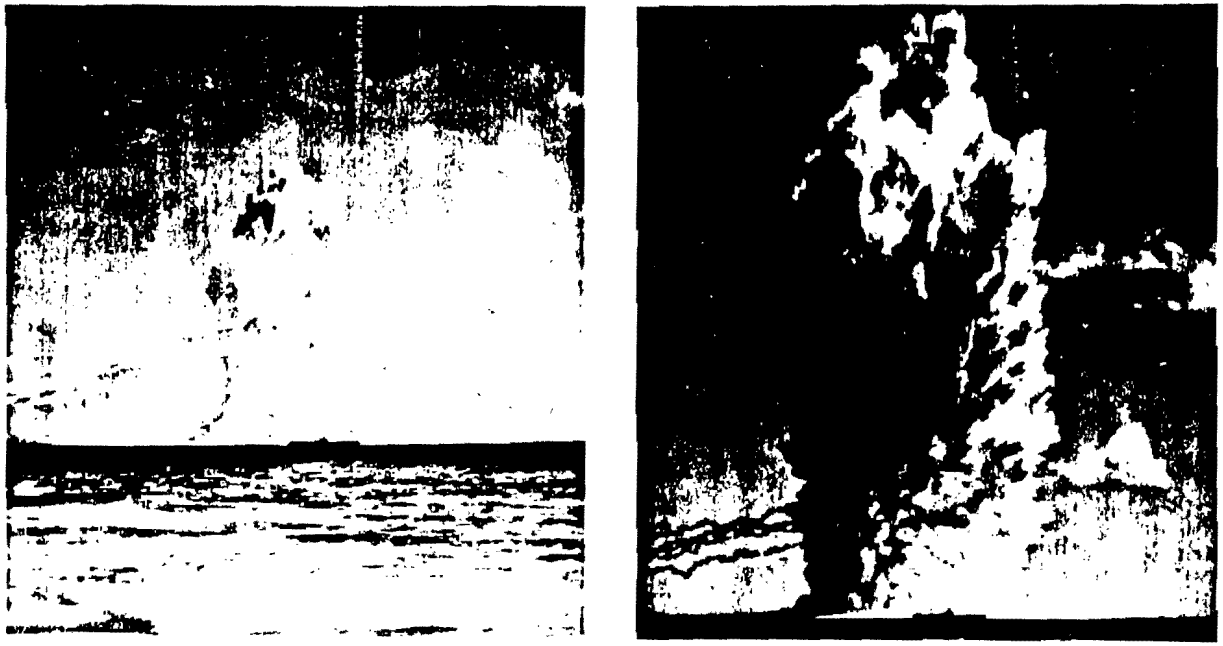

(a) EARLY STAGE (2.5 sec after burst)

(b) LATER STAGE SHOWING COLUMN JETS (8.2 sec after burst)

Figure 2-101. [redacted] Column from Shallow Underwater Burst (no blowout) [redacted]

surface, plumes of upwelled water and steam can occur (Figure 2-102).

Upon subsidence of the column and plumes from an underwater explosion, a "doughnut-shaped ring" of mist is formed, which is called the base surge and which is highly radioactive (Figure 2-103). This ring, or series of rings, expands radially in the absence of wind, but in the presence of wind, it elongates and drifts with the wind until it dissipates. A train of surface waves also expands radially from the explosion.

After dissipation of the base surge, the water surface around the explosion appears white (Figure 2-104). This "foam-patch" results from the upward motion of water and gaseous explosion products in the vicinity of the bubble, their spreading over the surface of the patch, and their downward motion at the edge of the patch. During its later stages, the foam-patch appears as a ring of foam and debris that is left floating where the water circulates downward.

As previously noted, the surface phenomena described above vary with the weapon yield and the depth of burst. Although clear-cut distinctions cannot be made in all cases, six explosion categories have been established to aid in establishing safe weapon delivery criteria. These categories are defined in Table 2-8. The classifications have been tested at yields as large as 30 kt, but they probably are valid for yields up to about 100 kt.

The limits of the relations given in Table 2-8 are plotted in Figure 2-105, and the phenomena that establish the categories are described below.

- *Near-surface bursts.* The layer of water above the burst is vaporized by the explosion. The surface phenomena for this type of burst and the associated hazards are unknown. The radiological hazard of the base surge is considered to be unimportant compared with air blast and fallout hazards.
- *Very shallow bursts.* The bubble vents early during the first expansion cycle, i.e., when the bubble pressure is greater than ambient, and fission products are blown out at that time.
- *Shallow bursts.* The bubble vents late during the first cycle, after the bubble pressure has dropped below ambient, and fission products are blown in.
- *Deep bursts.* The depth of burst is equal to or greater than the radius of the fully expanded bubble, but not as deep as the very deep burst described below.
- *Very deep burst.* The explosion is at sufficient depth that the bubble breaks up, becomes a vortex ring, or loses its identity before reaching the surface.

The surface radioactivity from a very deep burst is operationally insignificant within about an hour and may be faint enough to escape detection.

Table 2-8. Classification of Burst Depth Categories

Classification	Definition
Near surface	$0 < d_b < 21W^{1/3}$
Very shallow	$21W^{1/3} < d_b < 75W^{1/3}$
Shallow	$75W^{1/3} < d_b < 240W^{1/4}$
Deep	$240W^{1/4} < d_b < 700W^{1/4}$
Very deep	$700W^{1/4} < d_b$
Contained*	$1550W^{1/4} < d_b$
No spray dome*	$2500W^{1/3} < d_b$

* These values are derived from H.E. tests. They have not been confirmed by nuclear tests; therefore, they are to be interpreted as "containment *possible*" and "*possible* limiting depth for spray dome formation."

[redacted]

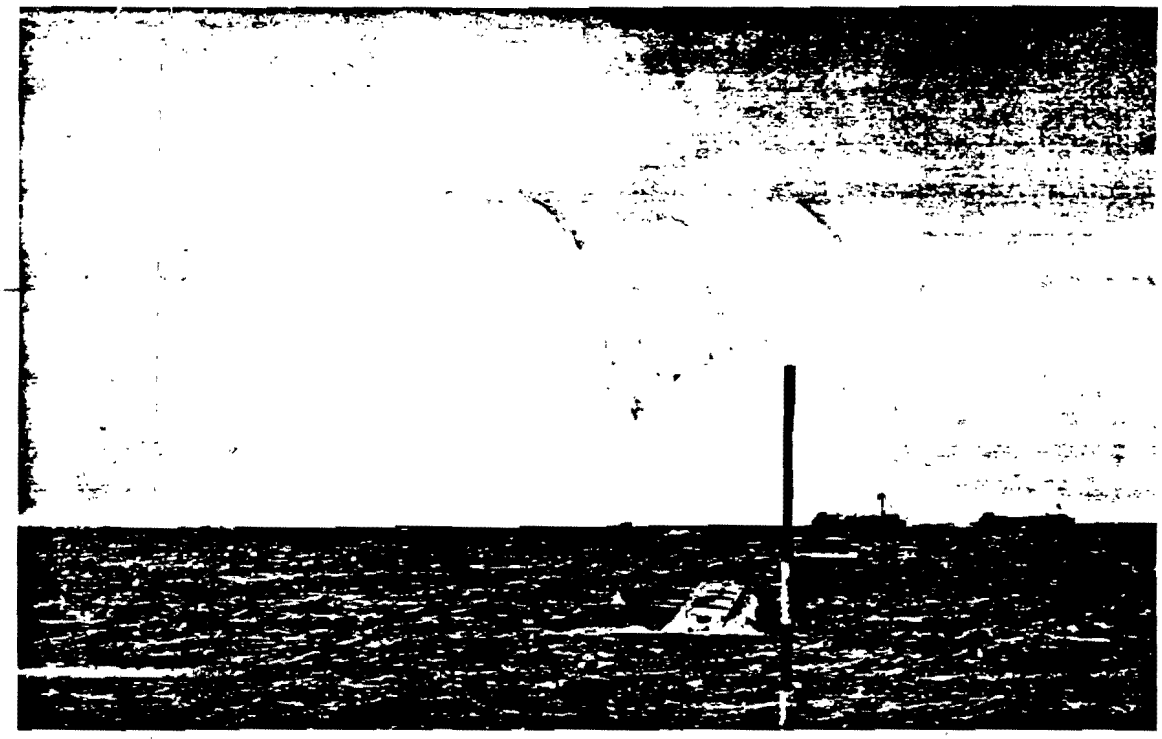

Figure 2-102. [redacted] Plume from Upwelling of Water from Very Deep Burst (24 sec after burst) [redacted]

[redacted] Reproduced from best available copy.

Reproduced from
best available copy.

Figure 2-103. [redacted] Base Surge "Doughnut-Shaped" Ring (oblique aerial view 100 sec after burst) [redacted]

Figure 2-104. [redacted] Foam Patch (oblique aerial view 6.3 min after burst)

Reproduced from best available copy.

[redacted]

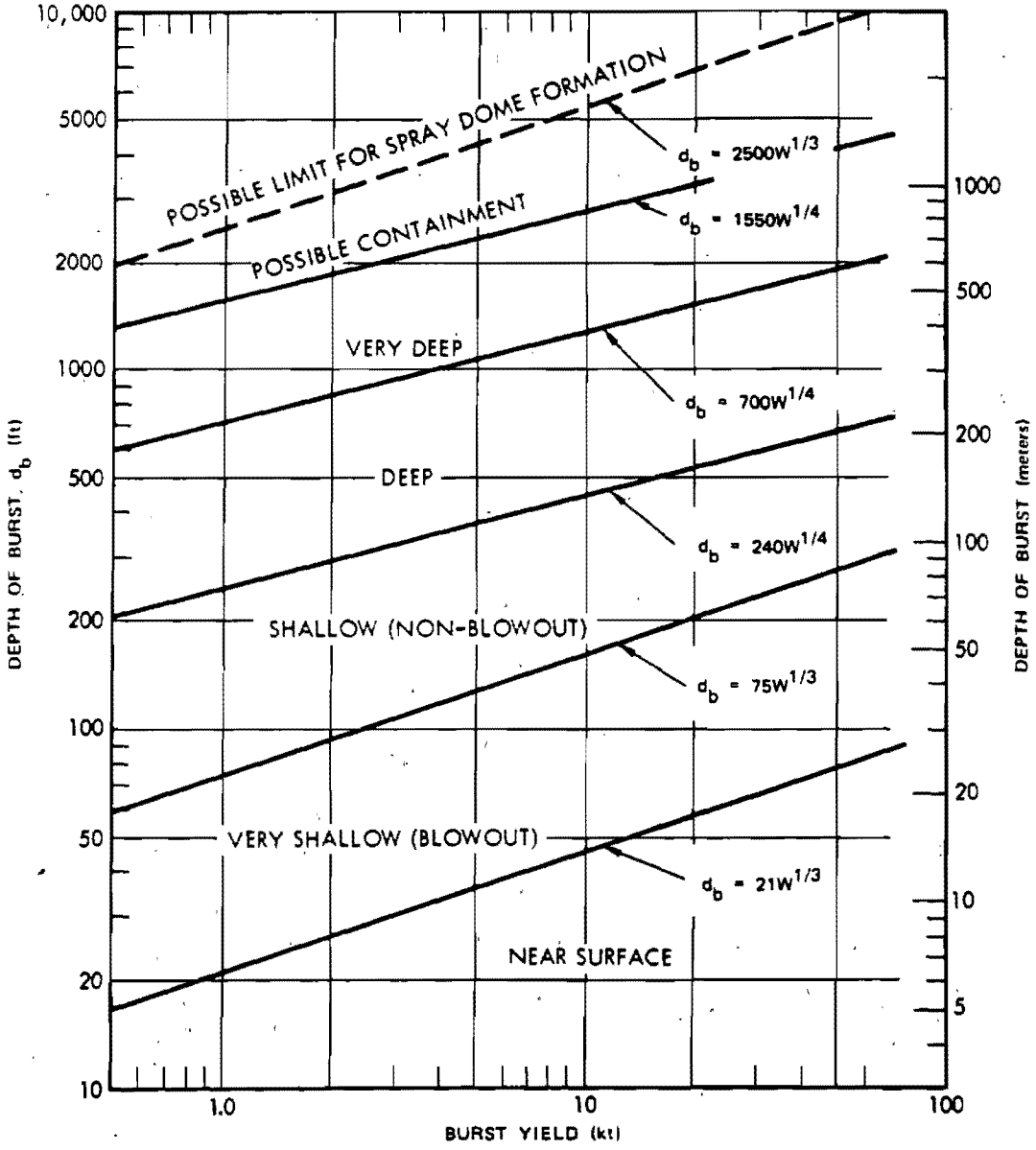

Figure 2-105. [redacted] Classification of Underwater Nuclear Bursts [redacted]

[redacted]

[redacted]

[redacted] No radioactive debris would be observed on the surface from contained bursts. The probability of containment of the radioactive debris is a function of the oceanic density profile. The relation in Figure 2-105 probably is valid in certain tropical waters, but bursts at these same depths in northerly latitudes probably would not be contained.

[redacted] No surface effects due to bubble pulsation or migration occur as a result of bursts that do not produce a spray dome.

[redacted] Although water depths may also influence surface phenomena, and consequently burst classification, the mathematical definitions in Table 2-8 do not include this influence.

[redacted] The various surface phenomena can be divided into two categories according to their origin, i.e., those produced by shock waves and those produced by the water motion accompanying bubble pulsation and rise. In the former category, the slick, crack, and spray dome are of operational importance. In the latter category, columns, plumes, base surge, and the long-lasting foam patch can be significant. More detailed descriptions of the surface phenomena are given in the following paragraphs.

2-73 Spray Dome [redacted]

[redacted] The spray dome (or spall), is formed by the acceleration and breakup of the surface water layer. The initial surface velocity directly above the burst is the sum of the water particle velocities imparted by the incident and reflected waves; elsewhere, the initial velocity is approximately the sum of the vertical components of these velocities (some initial surface velocities have been observed to be higher than so calculated). The height of the spray dome is limited by deceleration of gravity and air drag.

[redacted] If the depth of burst is sufficiently deep for one or more bubble oscillations to occur before venting, there may be secondary spray domes from reflection of compression waves emitted by the later bubble expansions. These can be several times higher than the primary dome from very deep bursts.

[redacted] The calculations of spray dome extent, vertical water velocity, and spray height are described in Problem 2-32. Plumes appear over the central portion of the spray dome from shallow bursts; therefore, a calculation of spray dome height may have little value.

2-74 Plumes, Column, Cauliflower Cloud [redacted]

[redacted] If the burst is deep enough to prevent blowout (shallow to very deep bursts), expansion, pulsation, and rise of the bubble produce a violent upheaval and expansion of water above the surface to form plumes. In those deep explosions where the bubble collapses just beneath the surface, the rising bottom of the bubble jets through the layer of water above the bubble and probably will form a plume. In deep and very deep explosions, the upward motion of the water about the rising bubble also forms a plume.

[redacted] The water displaced by the expanding bubble from very shallow bursts forms a dome-shaped shell of water over the bubble. Later, this shell ruptures and blows out the bubble constituents. For a very shallow nuclear explosion, blowout is accompanied by the formation of a "cauliflower cloud" at the top of the plume.

[redacted] Since there are insufficient data for a comprehensive prediction technique, predictions of plumes, columns, and clouds are based on direct scaling from four nuclear bursts. Predictive relationships and examples of their use are given in Problem 2-33.

2-75 Base Surge [redacted]

[redacted] As the plume from a deep burst or the column from a shallow burst falls back to the surface, it generates a cloud of fine spray, or aerosol, called "base surge," which usually is a

[redacted]

radiation hazard. The base surge expands and circulates as a toroidal cloud under the influence of the collapsing water plume. The expansion is rapid at first (exceeding 100 ft/sec); however, it decelerates upon mixing with the ambient air. During this period, part of the cloud evaporates and cools the air. As its kinetic energy dissipates and the cloud reaches its maximum diameter, it tends to thin out, and it may even become invisible as a consequence of diffusion and continued evaporation. In a sense, the base surge still exists, because some ocean salts and detonation products remain airborne.

Two types of base surge have been encountered during weapon tests:

- "Doughnut-shaped" clouds from very shallow and shallow detonations
- "Disc-shaped" clouds or, more properly, a series of concentric "doughnut-shaped" clouds from deep and very deep detonations.

Although visible configurations are actually quite irregular, the base surge configuration for very shallow and shallow detonations can be represented as a hollow cylinder or a hollow truncated cone for radiation exposure estimates. The inner diameter of the cylinder is approximately two-thirds the outer diameter. For very deep and deep bursts, a cylinder or truncated cone are adequate model configurations. The height of the visible base surge clouds at various weapon tests have varied between about 1,000 and 2,000 ft, probably as a result of turbulence and meteorological conditions.

A base surge is transported by the wind during its formation and growth. As a general rule, the transport should depend upon the wind speeds at altitudes between the surface and the maximum surge height. The downwind growth curve may be predicted by adding the highest wind speed reported between these levels to the average growth curves. The upwind growth should lie between a predicted curve based on subtracting half the surface wind speed (a rule-of-thumb to account for friction with the surface) and a curve obtained by subtracting the wind speed used for the downwind curve. At early times the former would be more accurate while at later times the latter would be more correct. Base surge prediction relationships and an example of their use are given in Problem 2-34.

2-76 Foam Patch and Ring

After subsidence of the plume, column, and base surge, a roughly circular area of disturbed water is still visible. This area is primarily defined by its white color and indications of turbulence at the perimeter. In the case of deep explosions, the patch can result from an upsurge of water caused by bubble migration. This water spreads out and then sinks, the overall motion being somewhat toroidal. Foam and flotsam tend to collect at the edge of the patch.

The whiteness from deep shots is believed to be caused by foam generated by the agitation of the water, particularly as the plumes fall back. Similar foam patches occur from shallow detonations, but their whiteness is caused partly by suspended bottom material. The foam patch contains appreciable quantities of weapon debris and presents a potential radiation hazard to personnel in small boats or ships.

The foam patches developing from test explosion have been on the order of 1.5 to 2.5 miles in diameter about 15 min after detonation, but they continued to expand slowly and irregularly with water currents and diffusion into the water, until the last visible manifestation was a ring of foam and debris. Their radioactivity could be traced for many days, although they had been invisible for quite some time.

WATER SURFACE WAVES

2-77 Generation and Propagation of Water Surface Waves

A submerged nuclear explosion, like any other physical event that produces a localized disturbance on the water surface, generates a group of surface waves that expand radially. The characteristics of explosively generated waves depend upon the yield, the depth of burst, and the range to the point of observation. If the water is sufficiently shallow, the bottom contour also can affect the generation and propagation of the waves.

The following physical description of the wave generation process and the succeeding prediction technique are based on:

- Laboratory experiments with small H.E. charges
- Wave data for the nine nuclear shots that have been fired on or in the lagoons at Eniwetok and Bikini, as listed in Table 2-9.
- Wave data for all the known tests in water with H.E. charges larger than 10 lb, as listed and referenced in Table 2-10.

Surface waves produced by an underwater explosion are generated by pulsations of the cavity formed at the surface when the oscillating bubble breaks through the surface (vents).

At a short range, within a few cavity radii, the first wave crest is so high and steep that it is unstable, and it spills forward turbulently and dissipates much of its energy. However, as the wave train expands and attenuates, the waves become shallow and smooth, their number increases, their energy remains nearly constant, and the highest wave appears successively later in the train. A wave gage record for such an expanded wave train is shown in Figure 2-106. The height H of the highest wave (trough-to-crest) decreases nearly inversely with range R; but the length, speed, and period all remain nearly constant for this peak wave, which is the one temporarily located at the first anti-node of the wave envelope as the waves move back in the envelope.

An approximate mathematical theory has been developed for shallow waves propagating from a shallow disturbance on the surface of water with constant depth. The results of this theory compare well with measured wave trains when a motionless "pseudo-cavity" is selected to approximate the wave generator or initial conditions. The "pseudo-cavity" is a shallow motionless depression of the water surface near the explosion. Its shape is derived empirically to correspond with the waves measured far from an explosion, but it does not necessarily correspond accurately with the actual shape of the water surface at any time.

All of the known measurements of peak wave height over deep water for charges greater than 10 lb are plotted in Figure 2-107. The vertical bars indicate the variation of HR for repeated shots and/or various gage ranges R. There is little discernible effect of depth of burst except near the "upper critical depth," where the H.E. charges were only partially submerged and where the peak wave height nearly doubled. Although current studies indicate that the upper critical depth effect may exist for nuclear as well as for H.E. charges, there is no firm evidence to support the inference as yet.

A plot comparable with Figure 2-107 of the data for H.E. charges smaller than 10 lb exhibits a pronounced upward hump in wave height versus depth of burst at $d_b \approx 3W_{HE}^{0.3}$ (and possibly also at $d_b \approx 8W_{HE}^{0.3}$). This increase in wave generation efficiency at the "lower critical depth" occurs when the expanding underwater cavity ruptures the layer of water above it (or vents) just before it becomes fully expanded. For large submerged explosions, the expanded bubble becomes tangent to the surface when the

[redacted]

Table 2-9. [redacted] Measured Wave Data from Nuclear Tests [redacted]

NUMBER SERIES SHOT	YIELD W (kt) $100(W)^{1/4}$	WATER DEPTH AT CHARGE d_w (ft)	DEPTH OF BURST d_b (ft)	PEAK WAVE* HEIGHT x RANGE HR/2,000 (ft)† min - max	CAVITY RADIUS R_c (ft)	$d_w/100(W)^{1/4}$	$HR/2 \times 10^4 \sqrt{W}$ min - max
1 HARDTACK UMBRELLA	[redacted]	140	140	[redacted]	[redacted]	[redacted]	[redacted]
2 HARDTACK WAHOO	[redacted]	3,000	500	[redacted]	[redacted]	[redacted]	[redacted]
3 CROSSROADS BAKER	23.5 220	180	90	36 - 60	1,000‡	0.82 Shallow	0.74 - 1.24
4 WIGWAM	32 238	15,000	2,000	118	490†	63 Very Deep	2.08
5 REDWING FLATHEAD	[redacted]	120	0	[redacted]	[redacted]	[redacted]	[redacted]
6 REDWING DAKOTA	[redacted]	140	0	[redacted]	[redacted]	[redacted]	[redacted]
7 REDWING NAVAHO	[redacted]	230	0	[redacted]	[redacted]	[redacted]	[redacted]
8 CASTLE UNION	7,000 916	145	7	232 - 312	1,000†	0.16 Shallow	0.16 - 0.28
9 CASTLE YANKEE	13,500 1,080	220	7	426 - 438	1,000†	0.20 Shallow	0.37 - 0.38

*H is twice the measured height of the peak crest except for shots 8 and 9 where H is the measured height of the first crest from the following trough. H is corrected for uniform water depth = d_b by Green's law.

†Value deduced from measured surface wave train (Kaplan and Wallace, see bibliography) is a lower limit considerably smaller than actual values, which are unknown.

‡Measured values of the column radius (Young, DASA 1240–1(9)), see bibliography.

[redacted]

[redacted]

[redacted]

Table 2-10. [redacted] Measured Wave Data from Large H.E. Tests [redacted]

SHOT	YIELD	WATER DEPTH	DEPTH OF BURST	PEAK WAVE HEIGHT	CAVITY RADIUS	$d_w/100(W)^{1/4}$	$HR/2 \times 10^4\sqrt{W}$
	W (kt)	d_w (ft)	d_b (ft)	HR/2 $(ft)^2$	R_C (ft)		min - max
WES Test Series at Lake Ouachita (from Pinkston and from Whalin)							
125 lb	0.625×10^{-4}	100	0 - 25	80 - 110		22.5	.90 - 1.24
385 lb	1.97×10^{-4}	100	0 - 36	147 - 225		17.0	1.25 - 1.91
WES Test Series at Mono Lake (1965 - 1966) (Preliminary data by private communication with R. Whalin and M. Pinkston and from Walter)							
1965 - 6	0.46×10^{-2} (9,200 lb)	130	0	1650 - 1900	68	5.2	2.4 - 2.8
- 2			.67	2100 - 3900	69		3.1 - 5.7
- 4			1.04	2100 - 2850	71		3.1 - 4.2
- 3			1.40	1750 - 3000	74		2.6 - 4.4
-5, 7, 8, 9			9 - 51		61 - 80		
1966 - 3		≈130	5.2	1150 - 1250			1.7 - 1.8
- 2			23	850 - 1200			1.2 - 1.8
- 1			60	1300 - 1400			1.9 - 2.1
HYDRA 11a (Van Dorn) W = 10^4 lb HBX							
- 7	0.723×10^{-2} (14,450 lb)	300	140	1650 - 1970		10.3	1.94 - 2.31
- 8			80	975 - 1340			1.15 - 1.55
- 9			35.5	1260 - 1590			1.48 - 1.87
- 10			7.1	1610			1.88
- 11			15.9	1510 - 1840			1.77 - 2.16
- 12			15.9	1490			1.75
- 13			17.7	1450			1.71

[redacted]

[redacted]

[redacted]

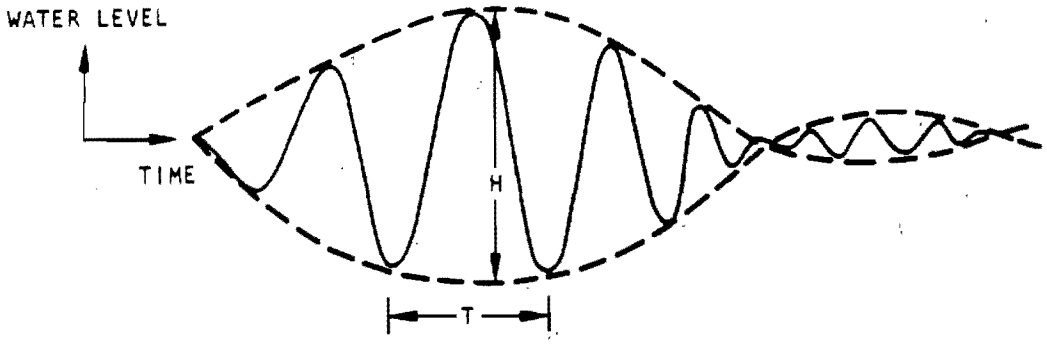

Figure 2-106. [redacted] Wave Gage Record for an Explosion-Generated Wave Train [redacted]

[redacted]

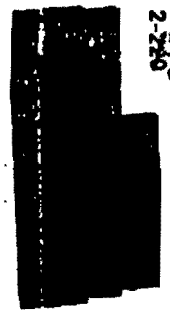

Deleted

Figure 2-107. [redacted] Peak Wave Height vs Depth of Burst for Shots in Deep Water [redacted]

burst depth d_b equals $240W^{1/4}$. The lower critical depth is somewhat smaller at about $d_b = 170W^{1/4}$. However, the effect on wave generation is much smaller for the larger charges in Figure 2-107, and the height of the peak wave generated by large explosions in "deep" water can be approximated simply by

$$HR/W_{HE}^{0.54} = 16 \pm 4,$$

where H is the amplitude of the maximum of the first envelope trough-to-crest in feet, R is the radial distance from the explosion in feet, and W_{HE} is the charge weight in equivalent pounds of TNT. An equivalent approximation is

$$HR = 40{,}500\ (W)^{0.54} \pm 25 \text{ percent},$$

where W is the yield in kilotons and the other symbols are as defined above. Similarly, the length and period of the peak wave can be approximated by

$$L = 15.5 \left(W_{HE}\right)^{0.288} \text{ ft},$$

$$T = 1.74 \left(W_{HE}\right)^{0.144} \text{ sec}.$$

These three relationships were derived empirically from test data for 125- and 385-lb H.E. charges and the two nuclear explosions shown in Figure 2-107. For a pseudo-cavity of a given shape, which has a potential (gravitational) energy comprising a fixed fraction of the explosive yield, all the dimensions of the cavity and the wave train are proportional to $W_{HE}^{1/4}$ or $W^{1/4}$ (Froude scaling), and the exponents in the three equations given above are 1/2, 1/4, and 1/8, respectively. Since the empirical exponent in the first equation was found to be 0.62 for small H.E. charges, it seems reasonable to suppose that the "theoretical" value of 1/2 may be the best value to use for extrapolation to large yields (the high kiloton and megaton range). With this exponent, the data in Figure 2-107 have been replotted as a function of reduced water depth (rather than charge depth) for use in Problem 2-35 (Figure 2-128).

The horizontal line in Figure 2-128 can be used to predict the peak wave height in deep water. However, it can be derived by the following simple procedure to illustrate qualitatively the physical process of wave generation in "deep" water to define "deep." The approximation is made that an explosion in deep water at any depth of burst above the lower critical depth generates a parabolic (nearly hemispherical) cavity upon venting, and that the potential energy of this cavity E_c is equal to 5 percent of the explosive yield E_o. That is:

$$E_c = \frac{\pi}{6}\rho_w g R_c^4 = 0.05E_o$$

$$= 0.05 \times 2.86 \times 10^{12}\ W \text{ ft-lb}.$$

This gives the following cavity radius, which is taken equal to the cavity depth and the radius of the plume (or column) of water projected upward:

$$R_c = 256\ (W)^{1/4} \text{ ft}.$$

if $d_w \geq R_c$,

and if the density of seawater and the hydrodynamic yield of the explosion are taken as

$$\rho_w g = 65 \frac{\text{lb}}{\text{ft}^3}, \text{ and } e_o = 1{,}025 \frac{\text{cal}}{\text{gm}}.$$

This cavity radius is not much larger than the bubble radius and depth of burst corresponding to the lower critical depth. The restriction on

[redacted]

water depth d_w in the equation for R_c is taken as the minimum water depth that can be considered "deep" i.e., the depth for which the assumed cavity shape touches bottom as it vents.

[redacted] The dissipative effects close to the cavity are approximated by the assumption that the leading peak wave crest spills forward and breaks turbulently at $R = 2R_c$ to the limiting height of a wave that can propagate in a stable manner over deep water (the Michell limit, or $H_{max} = 0.14L$). Finally it is assumed that the amplitude of the wave envelope H is attenuated inversely with range R as it continues to expand without dissipation. This gives the "predicted" peak wave height when the water depth at the charge location is "deep" ($d_w \geq 256W^{1/4}$) as

$$HR = 49{,}000\sqrt{W},$$

which corresponds to the horizontal line in Figure 2-128. This "predicted" value can be used for depths of burst ranging from zero to at least five times the lower critical depth (at $d = 170W^{1/4}$) judging by the comparison with WIGWAM data, even though the cavity radius becomes too large for depths of burst much below the lower critical depth.

[redacted] The line in Figure 2-128 can be extended into "shallow" water by a comparable simple procedure. In shallow water the cavity both touches bottom and vents to the atmosphere early during its expansion. Hence, much less work is done on the water by the expanding gaseous bubble, and much less energy is propagated as water surface waves over shallow water. Experimental data indicate that explosions in shallow water generate a dry cavity surrounded by a nearly vertical wall of water which extends upward as a thin lip to form the "column." A lower limit for the maximum radius of this cavity (or column) is given by the following relationship, which was derived from the energy calculated from measured wave trains over *shallow* water (Table 2-9) and which will be discussed in succeeding paragraphs.

$$R_c = 100\ (W)^{1/4} \text{ if } d_w < R_c$$

Once again, the dissipative effects close to the cavity are approximated by the assumption that the leading peak wave breaks down to the limiting height of a stable progressive wave, but, for shallow water, the approximation is that $H_{max} = (3/4)\,d_w$ = Miche limit at $R = 2R_c$. If this peak wave height is then attenuated inversely with range R, the "predicted" peak wave height when the water depth at the charge location is "shallow," ($d_w < 100W^{1/4}$), becomes

$$HR = 150\ d_w W^{1/4},$$

which gives the line with the 45 degree slope in Figure 2-128. This "prediction" can be used for any depth of burst ($0 < d_b < d_w$) as shown by measured data for H.E. charges in shallow water. As shown in Figure 2-128, there is much scatter in the nuclear wave data in shallow water and some of the measured peak wave heights are more than twice as large as "predicted" by the foregoing equation, which should be regarded only as a rough rule-of-thumb for correlating the measured data in Figure 2-128.

[redacted] The only actual measured data for the radii of the water columns (or cavities) for nuclear bursts near the surface of water are for shots BAKER and UMBRELLA (Table 2-9). These values of R_c and those measured for submerged H.E. explosives are roughly equal to the value given by the equation for maximum bubble radius in paragraph 2-67, which gives a burst estimate for R_c [redacted]

DNA (6)(3)

[redacted]

[redacted]

DNA (2)(3)

[redacted] In soil, TNT charges detonated at the surface generate crater radii approximately twice as large as nuclear explosions of the same yield, so the nuclear-TNT equivalence is only about 10 percent. The *column* radii observed for TNT detonations near the surface of the water are roughly equal to $470W^{1/3}$, which is the bubble radius given by the equation in paragraph 2-67 for a surface burst. This occurs even when the bubble radii exceed the water depth by a factor of 5. Therefore, it might be expected that a nuclear burst at the surface of water would produce a column radius about half as large as the H.E. value, or $240W^{1/3}$. This latter value is much larger than the lower limit estimated above ($R_c = 100W^{1/4}$). This lower limit is also exceeded by the crater radii measured in the bottom after explosions in shallow water, and the water column radii probably exceed the crater radii. Although there are no substantiating data, nuclear explosions at the surface of water of any depth probably generate water columns with radii between $100W^{1/4}$ and $240W^{1/3}$ feet.

2-78 Refraction and Shoaling

[redacted] Explosion-generated waves, in common with wind waves and tsunami (earthquake-generated) waves, are affected by changes in the depth over which they propagate. As the waves move into water shallower than about one-third their length (or shoal), their period remains fixed, but both their speed and their length decrease (between successive crests) and their height first decreases about 10 percent and then begins to increase. Because of the change in speed, a wave bends or refracts if it moves into shallow water at an angle to the bottom contours. Refraction can increase or decrease the localized wave height, depending on the hydrography over which the wave moves. No general methods for determining refraction effects are given here; however, such techniques for calculating these effects are available ("Oceanographical Engineering," R. L. Wiegel, see bibliography).

[redacted] The increase in height of a wave relative to its length (steepening) continues until the wave becomes unstable and breaks, unless the bottom slope is so shallow that bottom friction dissipates the wave before it breaks. In shallow water without dissipation, steepening increases the wave height as the inverse fourth root of the water depth. Many types of waves become unstable and break (or spill) when their height exceeds either 75 percent of the water depth (the Miche limit) or 14 percent of the wave length over deep water (the Michell limit) as described by Weigel (see bibliography).

[redacted] UNDERWATER CRATERING [redacted]

[redacted] If an explosion occurs in or even close to a layer of water overlaying bottom material, a significant crater forms in the bottom material whenever the gaseous bubble or water cavity formed by the explosion contacts the bottom. An underwater crater is similar to an onshore crater formed by an explosion near the ground since both are characterized by a dish-shaped depression, wider than it is deep, and surrounded by a lip raised above the undisturbed surface. In the case of most underwater craters, however, the observed ratio of crater radius to depth is larger and the lip height is smaller than for craters from comparable bursts in similar bottom materials onshore. These differences are caused by water displaced by the explosion washing back over the crater. This flow increases the crater radius by as much as 10 percent and decreases the crater depth by as much as 30 percent. An exception to this general rule occurs when the water layer is so shallow that the lip formed by the initial cratering extends above the surface of the water. Such craters (termed "un-

[redacted]

[redacted]

washed craters") approach onshore craters in appearance, with higher lips and larger depth-to-radius ratios than washed craters. This section describes only the crater characteristics directly related to the explosion. The effects of tidal currents and the collapse of unwashed crater lips by hydrostatic forces are not considered.

[redacted] The characteristics of underwater craters can be predicted at least qualitatively from the depth of burst, water depth, bottom composition, and weapon yield. The use of empirical curves relating the depth and radius of the crater for surface and bottom bursts over a clayey-sand bottom is described in Problem 2-36. Predictions for other bottom materials can be made by applying tabulated factors to the values predicted for clayey sand, as described in Problem 2-36. It is evident that larger craters are produced by moving the charge toward the bottom; increasing the water depth above a bottom burst (up to a point); or decreasing the water depth beneath a surface burst.

[redacted] A very large yield is required to form an unwashed crater in water having a depth that is common to most harbors. For example, with 30 ft of water over clayey-sand, 4 Mt would be required on the bottom to produce a dry crater lip. It is quite unlikely that materials that tend to flow, such as oceanic ooze or fine-grained silt, could support the hydrostatic pressure exerted on a dry crater lip.

[redacted]

Problem 2-28. Calculations of Underwater Explosion Phenomena

Calculations can be performed to determine bubble characteristics described in paragraph 2-67. The characteristics include the maximum radii, bubble periods, and migration between maxima for events to the end of the second bubble period. The calculation methods do not apply to cases where the bubble touches the bottom, and the methods contain uncertainties not yet fully resolved when the bubble center is very close to or above the surface. Furthermore, predictions that are made for events increasingly removed in time from the first maximum have increasing uncertainty. Two methods for calculating these bubble characteristics are demonstrated in the example. The first method uses the equations given in paragraph 2-67 and Figures 2-108 through 2-110. The second method uses equations introduced in the example and Figure 2-111. The first method is graphical and is less accurate than the second, but it provides a quick estimate.

Example

Given: 32 kt fired at a depth of 2,000 ft in very deep water.

Find:

a. The initial bubble period and radius,

b. The depth of the second maximum radius,

c. The second bubble period,

d. The radius at second maximum,

e. The depth of third maximum radius,

f. The third bubble period and radius at third maximum.

Solution (Method 1):

a. Calculate the initial radius A_1 and the period T_1, by using equations given in paragraph 2-67:

$$A_1 = J' \frac{W^{1/3}}{Z^{1/3}},$$

$$A_1 = (1{,}500)\left(\frac{(32)^{1/3}}{(2{,}000 + 33)^{1/3}}\right) = 376 \text{ ft.}$$

$$T_1 = K' \frac{W^{1/3}}{Z^{5/6}},$$

$$T_1 = (515)\left(\frac{(32)^{1/3}}{(2{,}033)^{5/6}}\right) = 2.86 \text{ sec.}$$

b. Find the reduced hydrostatic head:

$$\frac{Z_1}{A_1} = \frac{2{,}033}{376} = 5.41.$$

From Figure 2-108, for $n = 1$,

$$\frac{\Delta Z_1}{Z_1} = 0.28,$$

$\Delta Z_1 = (0.28)(2{,}033) = 569$ ft (migration during first period),

$$d_2 = d_b - \Delta Z_1,$$

$$d_2 = 2{,}000 - 569 = 1{,}431 \text{ ft.}^*$$

* Note that results are sensitive to graph readings.

c. From Figure 2-109, for $n = 2$,

$$T_2 = 0.90\ T_1,$$

$$T_2 = (0.90)(2.86) = 2.57 \text{ sec.}$$

d. From Figure 2-110, for $n = 2$,

$$A_2 = 0.77\ A_1 = (0.77)(376) = 290 \text{ ft.}$$

e. From Figure 2-108, using $Z_1/A_1 = 5.41$ and $n = 2$,

$$\frac{\Delta Z_2}{Z_1} = 0.23,$$

$$\Delta Z_2 = 0.23\ Z_1 = (0.23)(2{,}033) = 468 \text{ ft},$$

$$d_3 = d_2 - \Delta Z_2,$$

$$d_3 = 1{,}431 - 468 = 963 \text{ ft.}$$

f. From Figure 2-109, for $n = 3$,

$$T_3 = 0.66\ T_1,$$

$$T_3 = (0.66)(2.86) = 1.89 \text{ sec.}$$

From Figure 2-110, for $n = 3$,

$$\frac{A_3}{A_1} = 0.47,$$

$$A_3 = 0.47\ A_1 = (0.47)(376) = 177 \text{ ft.}$$

Solution (Method 2): This method uses Figure 2-111 to obtain values for bubble energy ratio, r_n/r_{n-1}, and the following reduced equations:

$$\left(\frac{\Delta Z_n}{Z_n}\right) = 3.5\left(\frac{A_1}{Z_1}\right)^{3/2}\left(\frac{r_n}{r_1}\right)^{1/2}\left(\frac{Z_1}{Z_n}\right)^2,$$

$$\left(\frac{A_n}{A_1}\right) = \left(\frac{Z_1}{Z_n}\right)^{1/3}\left(\frac{r_n}{r_1}\right)^{1/3},$$

$$\left(\frac{T_n}{T_1}\right) = \left(\frac{Z_1}{Z_n}\right)^{5/6}\left(\frac{r_n}{r_1}\right)^{1/3}.$$

a. By the same procedures used in Method 1,

$$A_1 = 376 \text{ ft},$$

$$T_1 = 2.86 \text{ sec.}$$

b. Using the first reduced equation given above,

$$\left(\frac{\Delta Z_1}{Z_1}\right) = 3.5\left(\frac{A_1}{Z_1}\right)^{3/2}\left(\frac{r_1}{r_1}\right)^{1/2}\left(\frac{Z_1}{Z_1}\right)^2,$$

$$\left(\frac{\Delta Z_1}{Z_1}\right) = 3.5\left(\frac{375}{2{,}033}\right)^{3/2}(1)^{1/2}(1)^2 = 0.277,$$

$$\Delta Z_1 = 0.277\ Z_1,$$

$$\Delta Z_1 = (0.277)(2{,}033) = 564,$$

$$d_2 = d_b - \Delta Z_1,$$

$$d_2 = 2{,}000 - 564 = 1{,}436 \text{ ft.}$$

c. The second bubble period T_2 can be obtained from the third reduced equation given above, and T_1 from (a) after finding the energy

ratio between the first and second bubbles. Using the reduced migration $\Delta Z_1/Z_1 = 0.277$ to enter Figure 2-111, the energy ratio is $r_2/r_1 = 0.324$. Thus,

$$\left(\frac{T_2}{T_1}\right) = \left(\frac{Z_1}{Z_2}\right)^{5/6}\left(\frac{r_2}{r_1}\right)^{1/3},$$

$$\left(\frac{T_2}{T_1}\right) = \left(\frac{2{,}033}{1{,}469}\right)^{5/6}(0.324)^{1/3},$$

$$\frac{T_2}{T_1} = 0.90,$$

$$T_2 = (0.90)(2.86) = 2.57 \text{ sec.}$$

d. The radius of the second maximum is obtained from the second reduced equation given above.

$$\left(\frac{A_2}{A_1}\right) = \left(\frac{Z_1}{Z_2}\right)^{1/3}\left(\frac{r_2}{r_1}\right)^{1/3},$$

$$\left(\frac{A_2}{A_1}\right) = \left(\frac{2{,}033}{1{,}469}\right)^{1/3}(0.324)^{1/3},$$

$$\left(\frac{A_2}{A_1}\right) = 0.765,$$

$$A_2 = 0.765\ A_1 = (0.765)(376) = 288 \text{ ft.}$$

e. To calculate the depth of the third maximum, it is first necessary to find the reduced migration $\Delta Z_2/Z_2$. From the first reduced equation,

$$\left(\frac{\Delta Z_2}{Z_2}\right) = 3.5\left(\frac{A_1}{Z_1}\right)^{3/2}\left(\frac{r_2}{r_1}\right)^{1/2}\left(\frac{Z_1}{Z_2}\right)^2,$$

$$\left(\frac{\Delta Z_2}{Z_2}\right) = 3.5\left(\frac{376}{2{,}033}\right)^{3/2}(0.324)^{1/2}\left(\frac{2{,}033}{1{,}469}\right)^2,$$

$$\left(\frac{\Delta Z_2}{Z_2}\right) = 0.303,$$

$$\Delta Z_2 = 0.303\ Z_2 = (0.303)(1{,}469) = 445 \text{ ft},$$

$$d_3 = d_2 - \Delta Z_2,$$

$$d_3 = 1{,}436 - 445 = 991 \text{ ft.}$$

f. From c., $r_2/r_1 = 0.324$. Using the reduced migration $\Delta Z_2/Z_2 = 0.303$ to enter Figure 2-111, the energy ratio $r_3/r_2 = 0.158$.

$$\left(\frac{r_3}{r_1}\right) = \left(\frac{r_2}{r_1}\right)\left(\frac{r_3}{r_2}\right),$$

$$\left(\frac{r_3}{r_1}\right) = (0.324)(0.158) = 0.0512.$$

From the third reduced equation

$$\left(\frac{T_3}{T_1}\right) = \left(\frac{Z_1}{Z_3}\right)^{5/6}\left(\frac{r_3}{r_1}\right)^{1/3},$$

$$\left(\frac{T_3}{T_1}\right) = \left(\frac{2{,}033}{1{,}024}\right)^{5/6}(0.0512)^{1/3} = 0.658,$$

$$T_3 = 0.658\ T_1$$

$$T_3 = (0.658)(2.86) = 1.88 \text{ sec.}$$

[redacted]

From the second reduced equation,

$$\left(\frac{A_3}{A_1}\right) = \left(\frac{Z_1}{Z_3}\right)^{1/3}\left(\frac{r_3}{r_1}\right)^{1/3}$$

$$\left(\frac{A_3}{A_1}\right) = \left(\frac{2{,}033}{1{,}024}\right)^{1/3} (0.0512)^{1/3} = 0.467$$

$$A_3 = 0.467\ A_1$$

$$A_3 = (0.467)(376) = 176 \text{ ft.}$$

Answer:	*Method 1*	*Method 2*
a. The initial bubble period and radius	A_1 = 376 ft T_1 = 2.86 sec	376 ft 2.86 sec
b. The depth of the second maximum radius	d_2 = 1,431 ft	1,436 ft
c. The second bubble period	T_2 = 2.57 sec	2.57 sec
d. The radius at second maximum	A_2 = 290 ft	288 ft
e. The depth of third maximum radius	d_3 = 963 ft	991 ft
f. The third bubble period and radius at third maximum	T_3 = 1.89 sec A_3 = 177 ft	1.88 sec 176 ft

[redacted] *Reliability:* The uncertainty in the values for maximum radii calculated by the methods described above are about +20 percent and -35 percent, based on very limited information.

[redacted] *Related Material:* See paragraph 2-67.

[redacted]

[redacted]

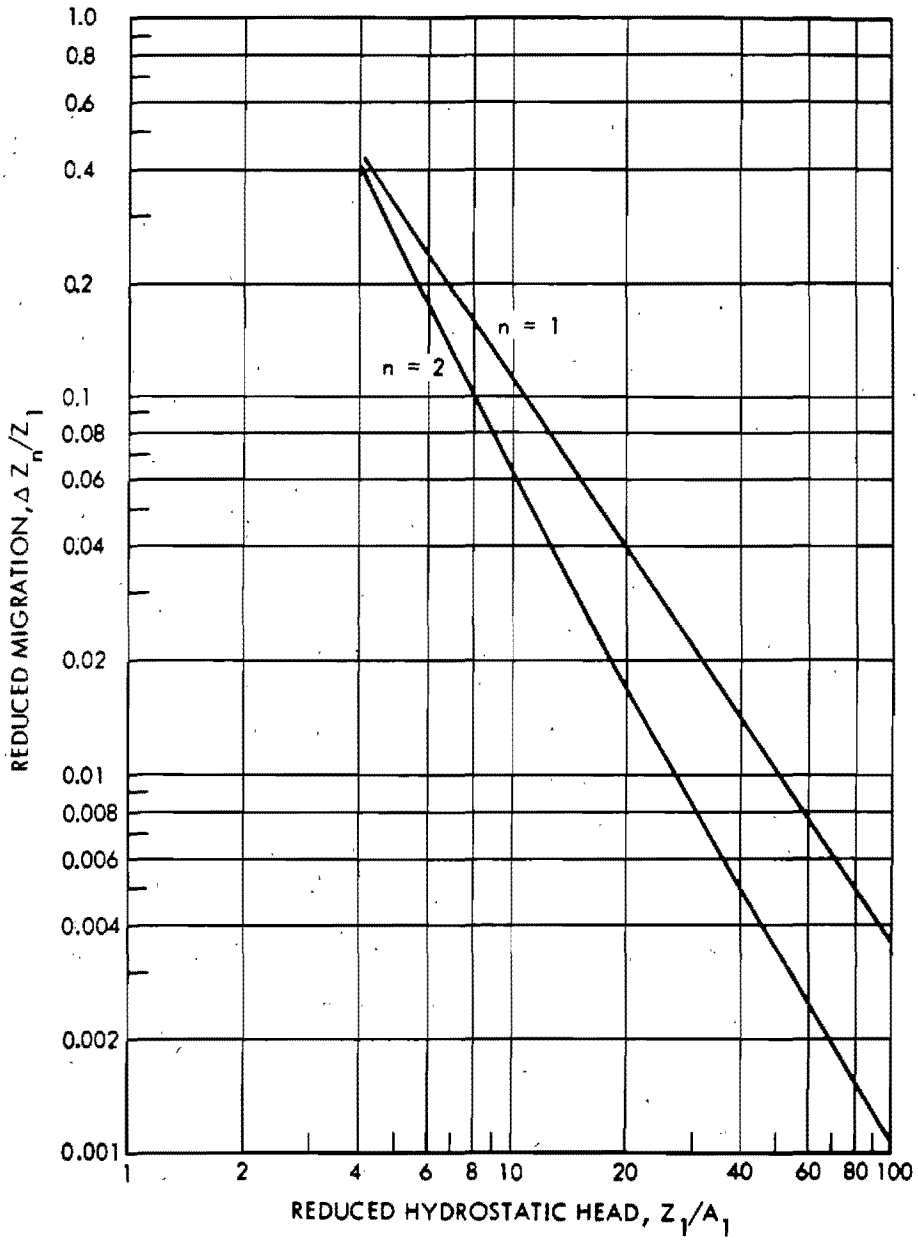

Figure 2-108. [redacted] Reduced Nuclear Bubble Migration [redacted]

[redacted]

[redacted]

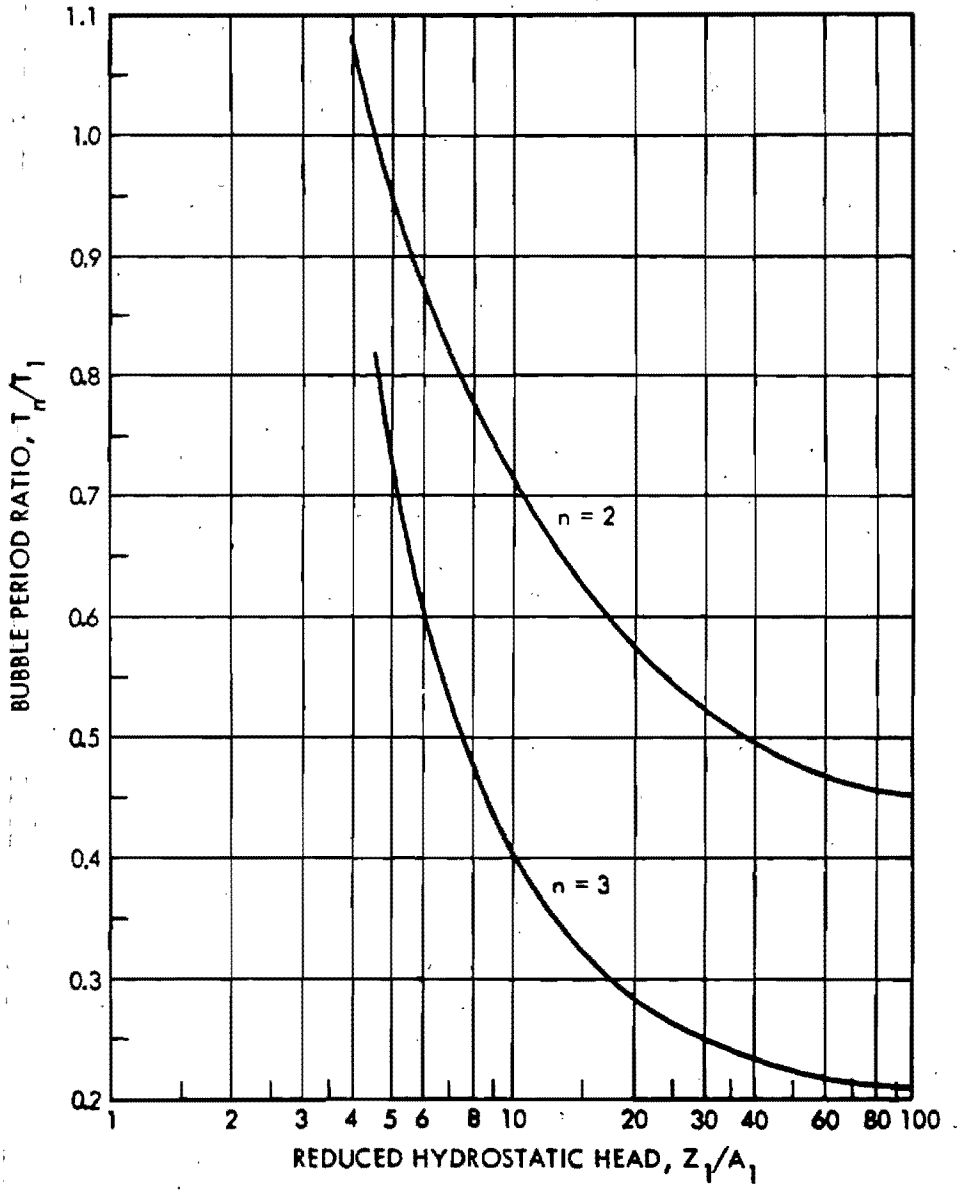

Figure 2-109. [redacted] Successive Nuclear Bubble Period Ratios [redacted]

[redacted]

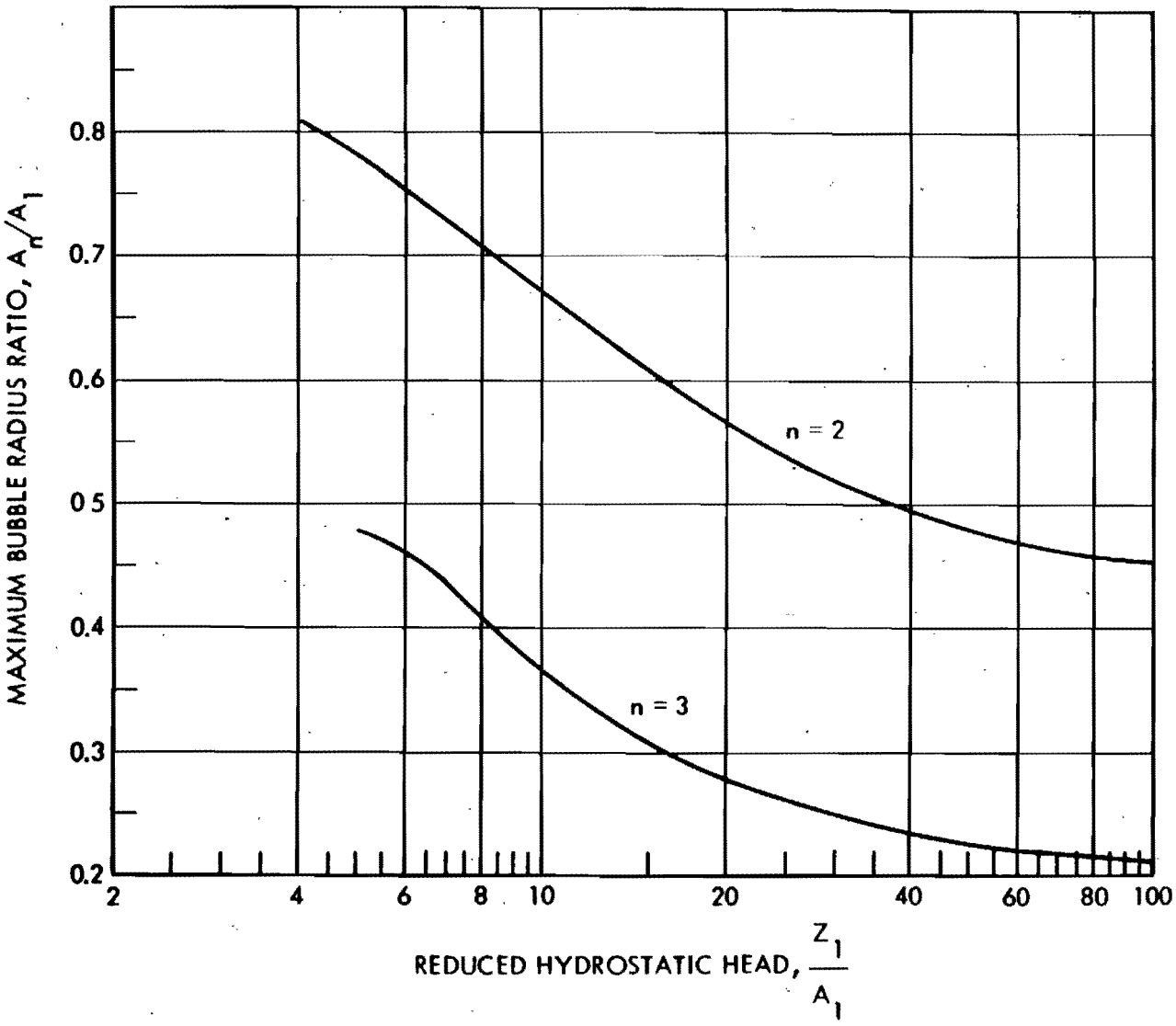

Figure 2-110. [redacted] Successive Nuclear Maximum Bubble Radius Ratios [redacted]

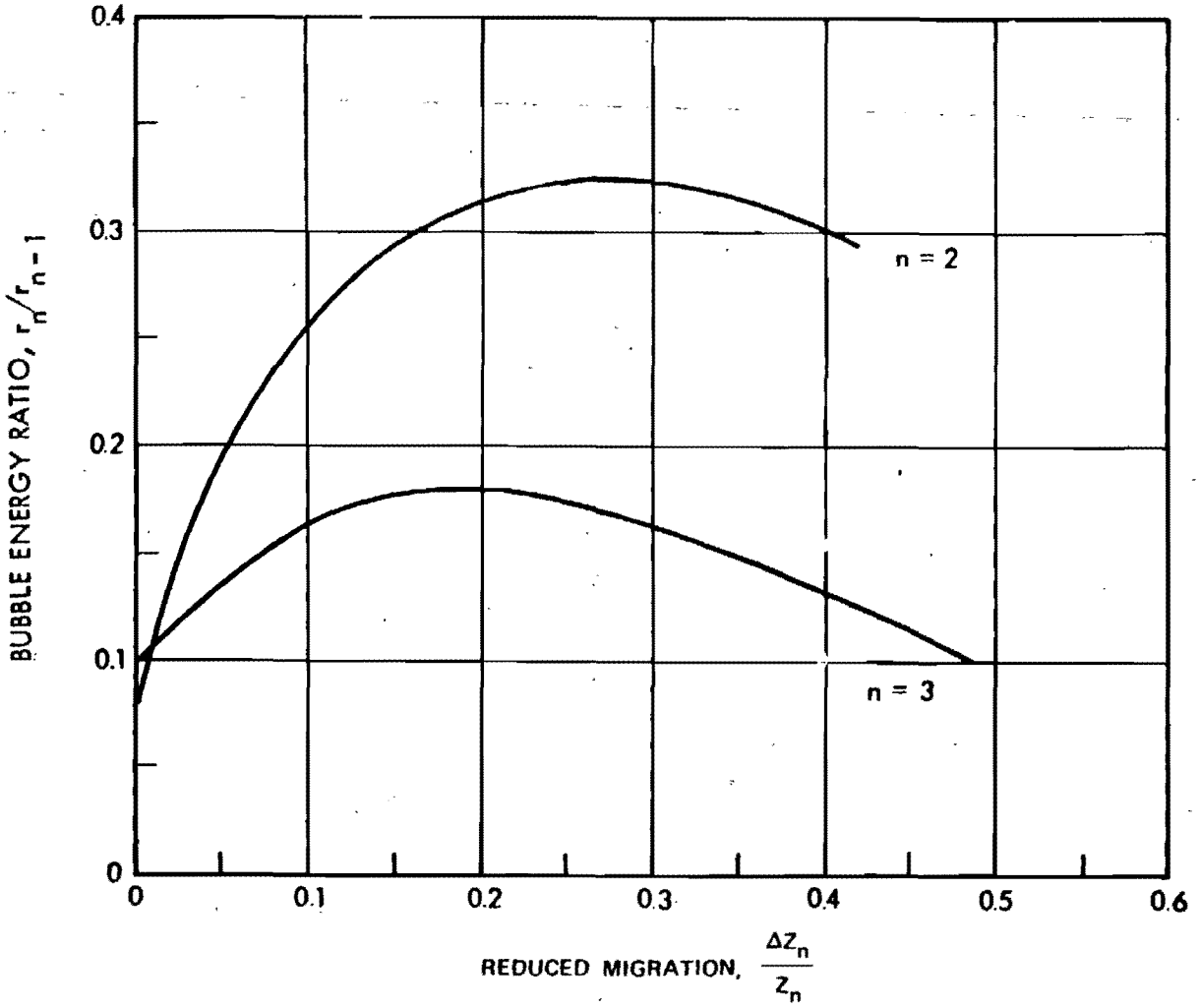

Figure 2-111. [redacted] Nuclear Bubble Energy Ratios [redacted]

[redacted]

Problem 2-29. Calculation of Shock Wave Parameters for Free Water (Deep Bursts)

[redacted] Figures 2-112 through 2-116 show the parameters for the primary shock wave from an underwater explosion in free, isovelocity water (no reflections, no refractions). Figure 2-112 shows the peak pressure as a function of slant range for various yields, where the peak pressure is lower than 3,000 psi, and as a function of reduced slant range ($R/W^{1/3}$) for peak pressures above 3,000 psi. Figure 2-113 shows the shock wave impulse as a function of slant range for various yields, while Figure 2-114 shows the shock wave energy flux as a function of slant range for the same yields. These latter two families of curves show values of impulse and energy flux integrated to a time of 6.7θ, where θ is the time constant for the shock wave, which is defined as the time for the shock wave pressure to fall to approximately 37 percent of its peak value.

[redacted] The time constant θ is shown in Figure 2-115 as a function of slant range for the same family of yields shown in Figures 2-113 and 2-114. Figure 2-116 shows a dimensionless pressure-time curve. Using values of θ from Figure 2-115 and values of p_m from Figure 2-112, Figure 2-116 may be used to construct the pressure-time shape of the shock wave in free water at various ranges from underwater explosions of various yields.

[redacted] *Scaling.* For yields other than those shown in Figure 2-112 through 2-115, use linear interpolation between appropriate curves.

[redacted] *Example* [redacted]

Given: A 50 kt burst at a depth of 1,000 ft in deep water.

Find. The peak shock pressure p_m, the shock wave impulse I, energy flux E, and time constant θ at a 1,000 ft depth, 4,000 yd from the burst.

Solution: The desired shock wave parameters can be read directly from Figures 2-112 through 2-115.

Answer:

$$p_m \approx 470 \text{ psi},$$

$$I \approx 28 \text{ psi-sec},$$

$$E \approx 10^3 \text{ in.-lb/in.}^2,$$

$$\theta \approx 50 \text{ msec}.$$

[redacted] *Reliability:* Values shown in Figures 2-112 through 2-115 are estimated to be accurate within ±10 percent for shock pressure, and ±20 percent for the other parameters for yields between 1 kt and 1 Mt. For yields below 1 kt or above 1 Mt, the values are more uncertain. The assumption of isovelocity water becomes increasingly uncertain for ranges beyond a few kiloyards in the ocean.

[redacted] *Related Material:*

See paragraphs 2-68 through 2-72.

Figures 2-112 through 2-115 are based on the following equations:

$$p_m = 4.38 \times 10^6 \left(\frac{W^{1/3}}{R}\right)^{1.13} \text{ psi}$$

$$I \text{ (to } 6.7\theta) = 1.176 \times 10^4 \; W^{1/3} \left(\frac{W^{1/3}}{R}\right)^{0.91} \text{ psi-sec}$$

$$E \text{ (to } 6.7\theta) = 3.976 \times 10^9 \; W^{1/3} \left(\frac{W^{1/3}}{R}\right)^{2.04} \frac{\text{in.-lb}}{\text{in.}^2}$$

[redacted]

[redacted]

$$\theta = 2.274\ W^{1/3} \left(\frac{W^{1/3}}{R}\right)^{-0.22} \text{ msec.}$$

The values of these parameters are related to those for TNT (Cole, 1948) by an approximate equivalence factor. Snay and Butler (1957) (see bibliography) report that an underwater nuclear burst with a radiochemical yield of 1 kt gives approximately the same shock wave parameters at the same distance as a TNT charge weighing 0.67 kiloton (where 1 ton = 2,000 lbs).

[redacted]

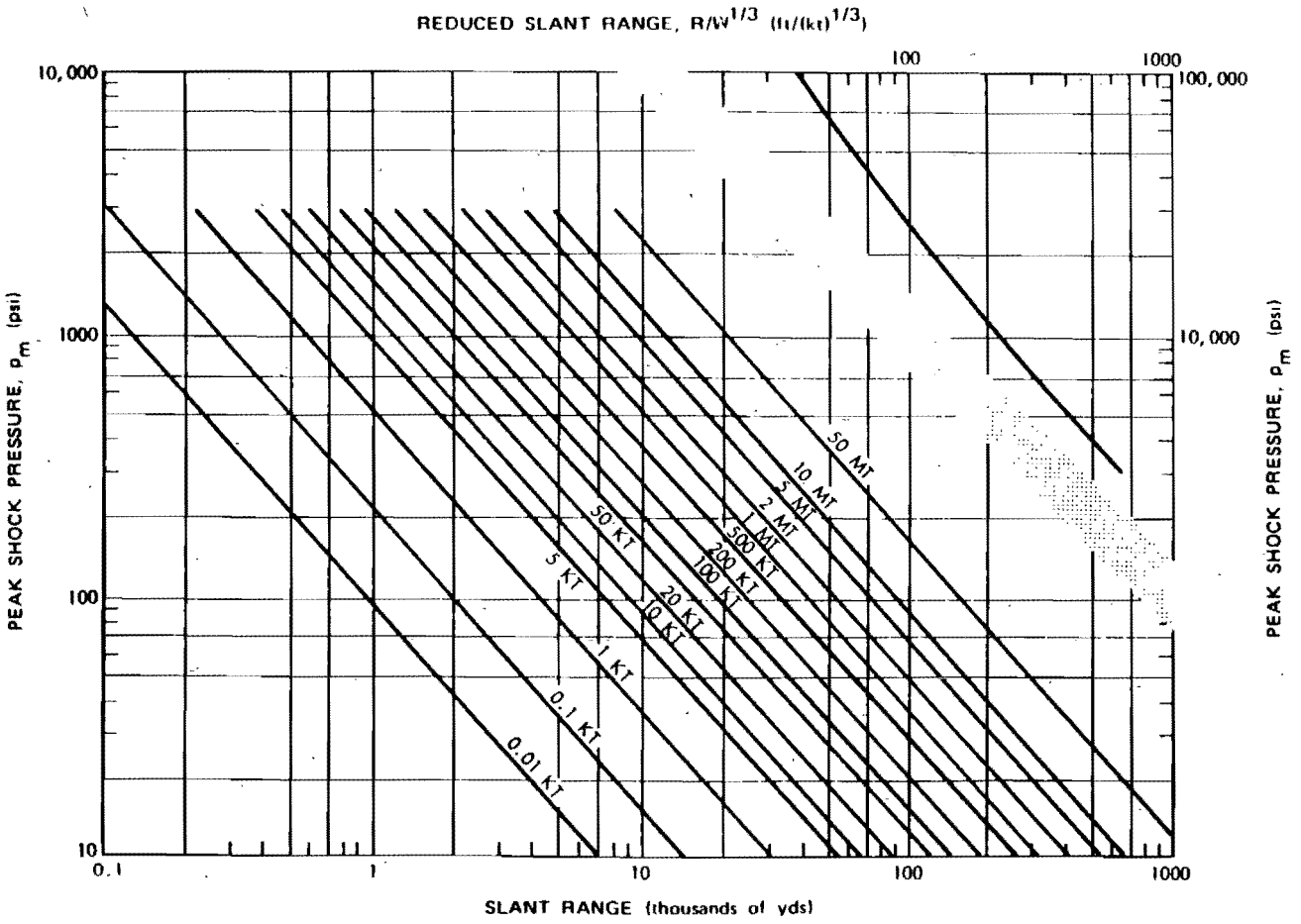

Figure 2-112. [redacted] Shock Wave Peak Pressure in Free Isovelocity Water [redacted]

[redacted]

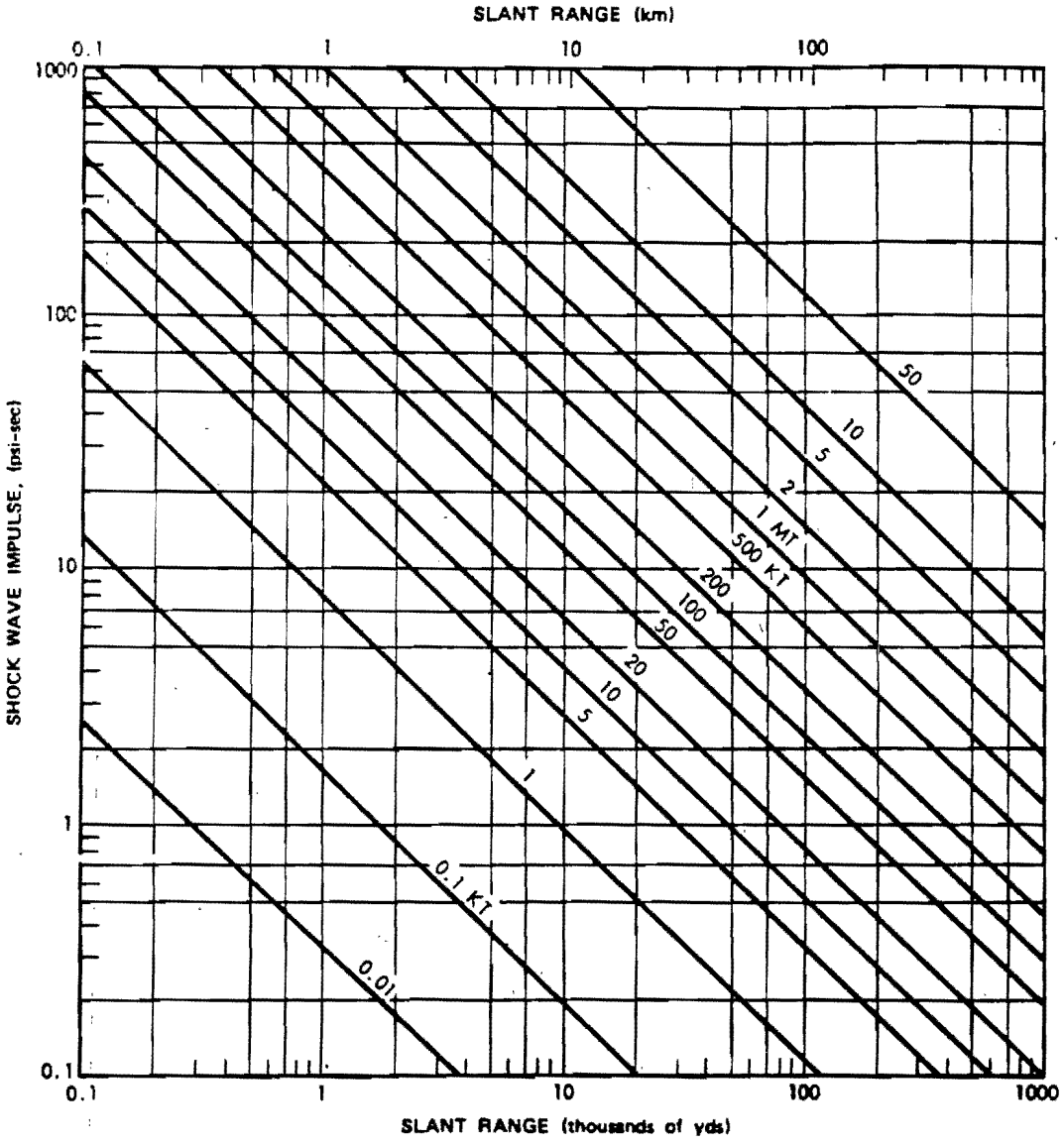

Figure 2-113. [redacted] Shock Wave Impulse vs Slant Range in Free Isovelocity Water [redacted]

[redacted]

[redacted]

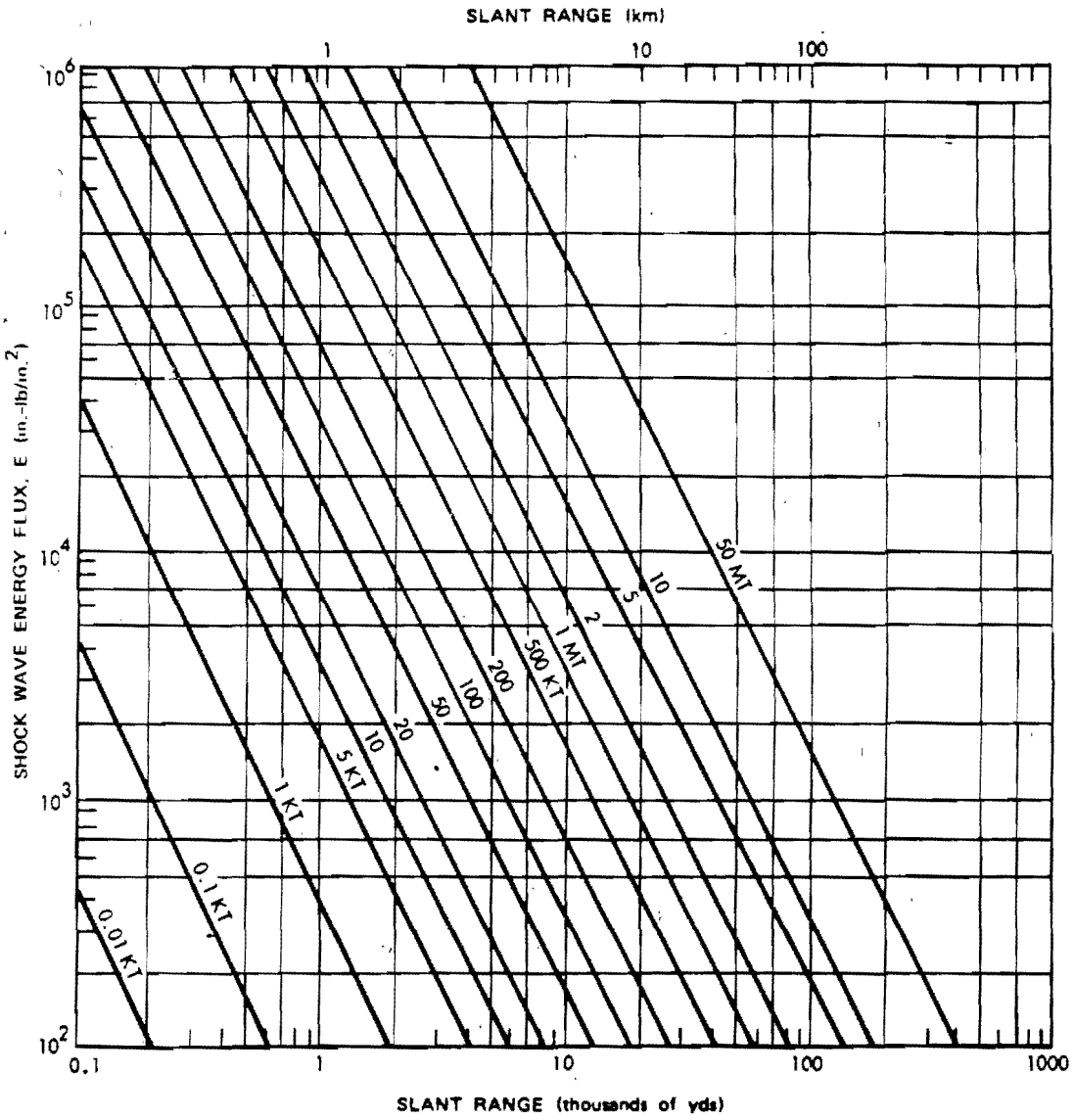

Figure 2-114. [redacted] Shock Wave Energy Flux vs Slant Range in Free Isovelocity Water [redacted]

[redacted]

[redacted]

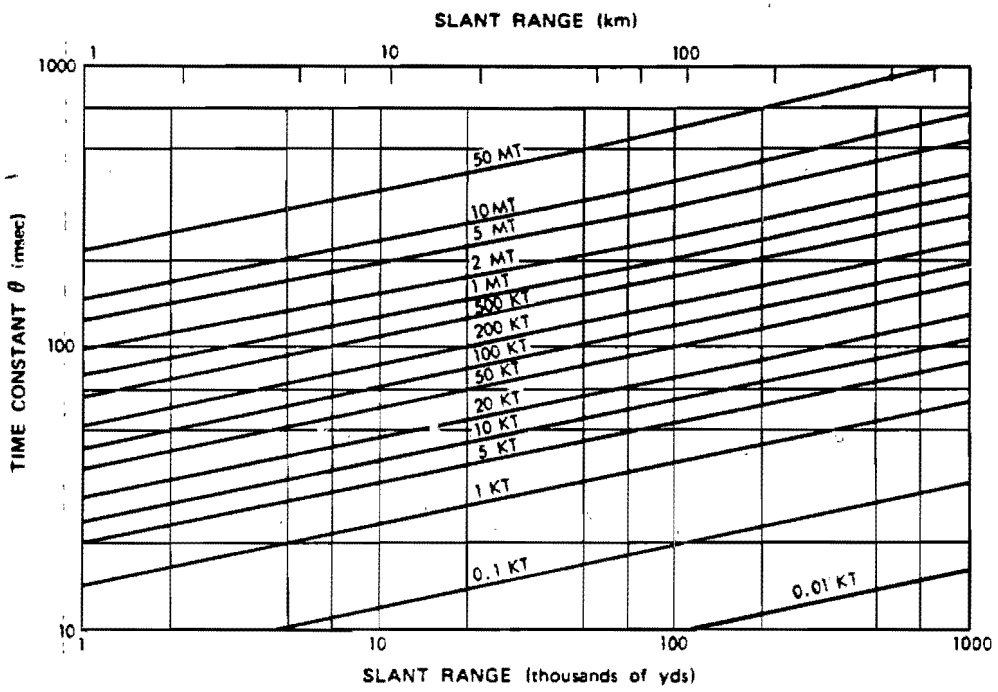

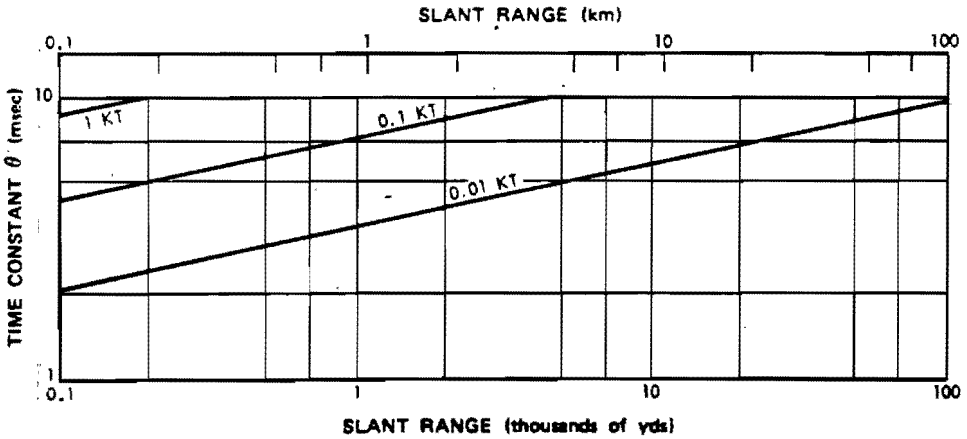

Figure 2-115. [redacted] Shock Wave Time Constant in Free Isovelocity Water vs Slant Range [redacted]

[redacted]

[redacted]

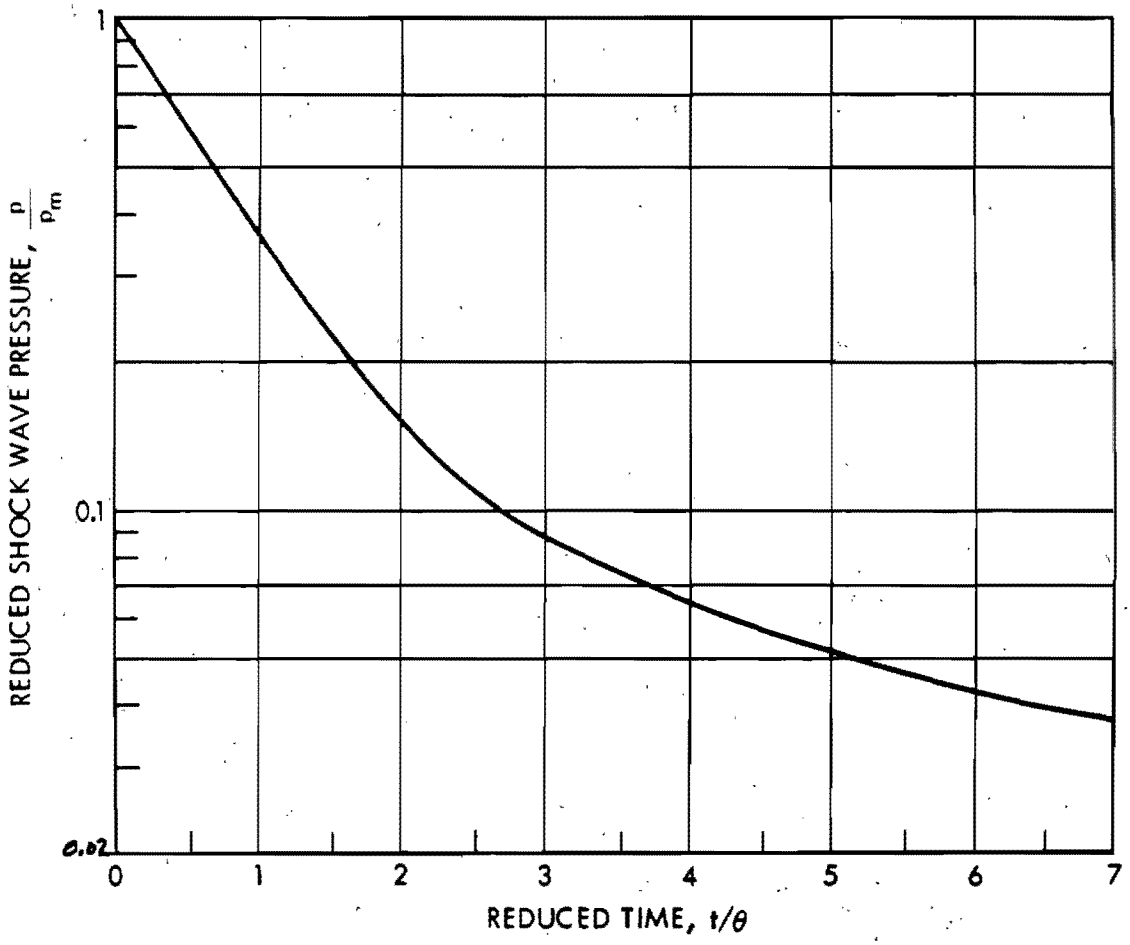

Figure 2-116. [redacted] Pressure-Time for Free Isovelocity Water Shock Waves from Nuclear Explosion [redacted]

[redacted]

[redacted]

Problem 2-30. Calculation of Shock Wave Parameters for Reduced Water Depths, $d_w/W^{1/3} \leq 2{,}000$ ft/kt$^{1/3}$

[redacted] Figures 2-117 through 2-120 show the influence of surface and bottom reflection on the primary shock wave. The curves are drawn through values of peak pressure and impulse at mid-depth both for explosions at mid-depth (Figures 2-117 and 2-118) and at the bottom (Figures 2-119 and 2-120). The solid curves indicate the approximate coverage of the data. As the water depth approaches zero the dashed curves approach the values for air blast at ground level. Transition to the free-water shock parameters (Figures 2-112 through 2-116) occurs as the water depth increases. In the anomalous region near the water surface, the reflected tension waves lead to a sharp reduction of pressure and impulse (Figure 2-94).

[redacted] The curves in Figures 2-117 through 2-120 were derived mainly from H.E. data; however, they were shifted to agree with nuclear data for the limit of free isovelocity water. In most instances, the shift (or conversion factor) was in agreement with the factors determined separately for converting from H.E. to nuclear data in deep water. Most of the data were obtained for the mid-depth location of both the charge and the pressure gauges. All of the curves pertain to either a coral sand or an ordinary sand bottom material.

DNA (6)(3)

[redacted]

[redacted] Detailed shock wave measurements have been made over concrete, sand, and clayey-silt bottoms to assess the effects of shock reflection from various bottom materials. Measurements were made within 48 ft from 10-lb TNT charges in 20 ft of water. Both the charge and gauges were placed deeper than mid-depth to minimize the effects of surface reflection.

[redacted] Briefly, the following effects were observed for the shock strength, impulse, and energy flux as compared with values at the same range in free water. Near the bottom and away from the charge, the pressure fronts of the incident and reflected shocks were nearly equal. Near the charge and away from the bottom, the reflected shock was about one-fifth as strong as the incident shock. The impulse of the shock wave increased as much as 100 percent near the charge over concrete, but there was little change at the greatest range from the charge. The impulse increased near the charge but decreased further away from it over clayey-silt and sand. The increase was as much as 40 percent over silt and 20 percent over sand. The decrease was as much as 50 percent over silt and 30 percent over sand. The observed changes in energy flux were roughly comparable with those for impulse, although the energy decreased as much as 30 percent away from the charge over concrete.

[redacted] The shock wave duration T in milliseconds can be approximated with

$$T = \frac{KI}{p_m}$$

$$K \approx 1.8 + 0.0021 \left(d_w/W^{1/3}\right)$$

$$\text{for } 2{,}000 > \left(d_w/W^{1/3}\right) > 100$$

$$K \approx 3.0 - 0.01 \left(d_w/W^{1/3}\right)$$

2-8
2-240

[redacted]

[redacted]

for $\left(d_w/W^{1/3}\right) < 100$

where

d_w = water depth (ft)

I = shock wave impulse (psi-msec)

p_m = peak shock pressure (psi).

[redacted] The shock wave energy flux for an explosion at a reduced depth of approximately 250 ft/(kt)$^{1/3}$ is related to the shock wave impulse I, and peak pressure by

$$E_{250} \approx 1.2 \times 10^{-4} p_m I \text{ in.-lb/in.}^2,$$

and at reduced depths equal to or greater than 2,000 ft/(kt)$^{1/3}$ by

$$E_{2,000} \approx 9.0 \times 10^{-5} p_m I \text{ in.-lb/in.}^2.$$

For intermediate depths, a linear interpolation between the two values can be adopted.

[redacted] The following approximations can be used to estimate the shock parameters at various gauge depths when the charge is at mid-depth, when $250 < R/W^{1/3} < 2{,}500$ and when $70 < d_w/W^{1/3} < 200$.

Gauge Depth Water Depth	*Fraction of Value at Mid-Depth*
3/4 to 1	0.9 for peak pressure 0.8 for impulse 0.7 for energy impulse
1/4	0.8 for peak pressure 0.7 for impulse 0.6 for energy flux
0	Use air blast loading

[redacted] *Example* [redacted]

Given: A 1 Mt explosion at a depth 2,500 ft in water having a depth of 5,000 ft.

Find: The peak pressure, the impulse, shock wave duration, and the energy flux depth of 2,500 ft and a horizontal rang 20,000 ft.

Solution: The reduced water depth is

$$\frac{d_w}{W^{1/3}} = \frac{5{,}000}{(1{,}000)^{1/3}} = 500 \text{ ft.}$$

The reduced burst depth is

$$\frac{d_b}{W^{1/3}} = \frac{2{,}500}{(1{,}000)^{1/3}} = 250 \text{ ft.}$$

The reduced range is

$$\frac{R}{W^{1/3}} = \frac{20{,}000}{(1{,}000)^{1/3}} = 2{,}000 \text{ ft.}$$

Since the explosion is at mid-depth, Fig 2-117 and 2-118 apply. From Figure 2-117, peak pressure is

$$p_m = 700 \text{ psi.}$$

From Figure 2-118, the reduced positive imp is

$$\frac{I}{W^{1/3}} = 9{,}000 \text{ psi-msec/(kt)}^{1/3}.$$

Since $2{,}000 > \left(d_w/W^{1/3}\right) > 100$, the shock v duration equations give

$$K = 1.8 + 0.0021 \left(d_w/W^{1/3}\right)$$

[redacted]

[redacted]

[redacted]

$$K = 1.8 + (0.0021)(500) = 2.85$$

Answer: The peak pressure is

$$p_m = 700 \text{ psi.}$$

The positive impulse is

$$I = (9{,}000)(W^{1/3}) = 90{,}000 \text{ psi-msec}$$

The shock wave duration is

$$T = \frac{KI}{p_m} = \frac{(2.85)(9 \times 10^4)}{700} = 366 \text{ msec.}$$

The shock wave energy flux is

$$E_{250} = 1.2 \times 10^{-4} p_m I$$

$$E_{250} = (1.2 \times 10^{-4})(700)(9 \times 10^4)$$

$$= 7.6 \times 10^3 \text{ in. lb/in.}^2.$$

[redacted] *Reliability:* Peak pressures obtained from Figures 2-117 and 2-119 are estimated to be reliable within about ±30 percent. Impulses obtained from Figures 2-118 and 2-120, and energy fluxes are estimated to be reliable to within about ±50 percent.

[redacted] *Related Material:* See paragraphs 2-68 through 2-72.

[redacted]

[redacted]

[redacted]

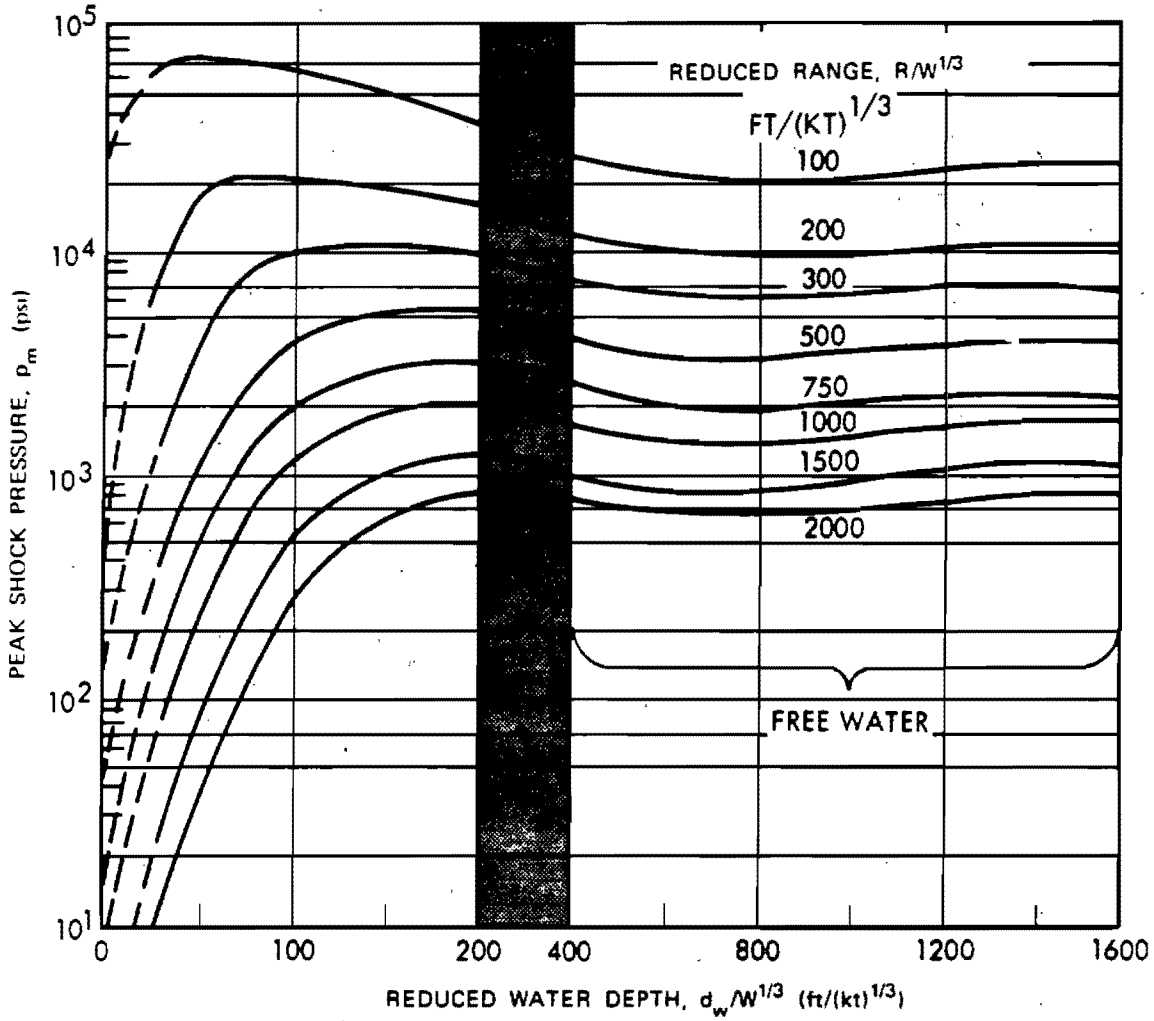

Figure 2-117. [redacted] Peak Shock Pressure vs Reduced Water Depth. Explosion and Gauges at Mid-Depth. [redacted]

[redacted]

[redacted]

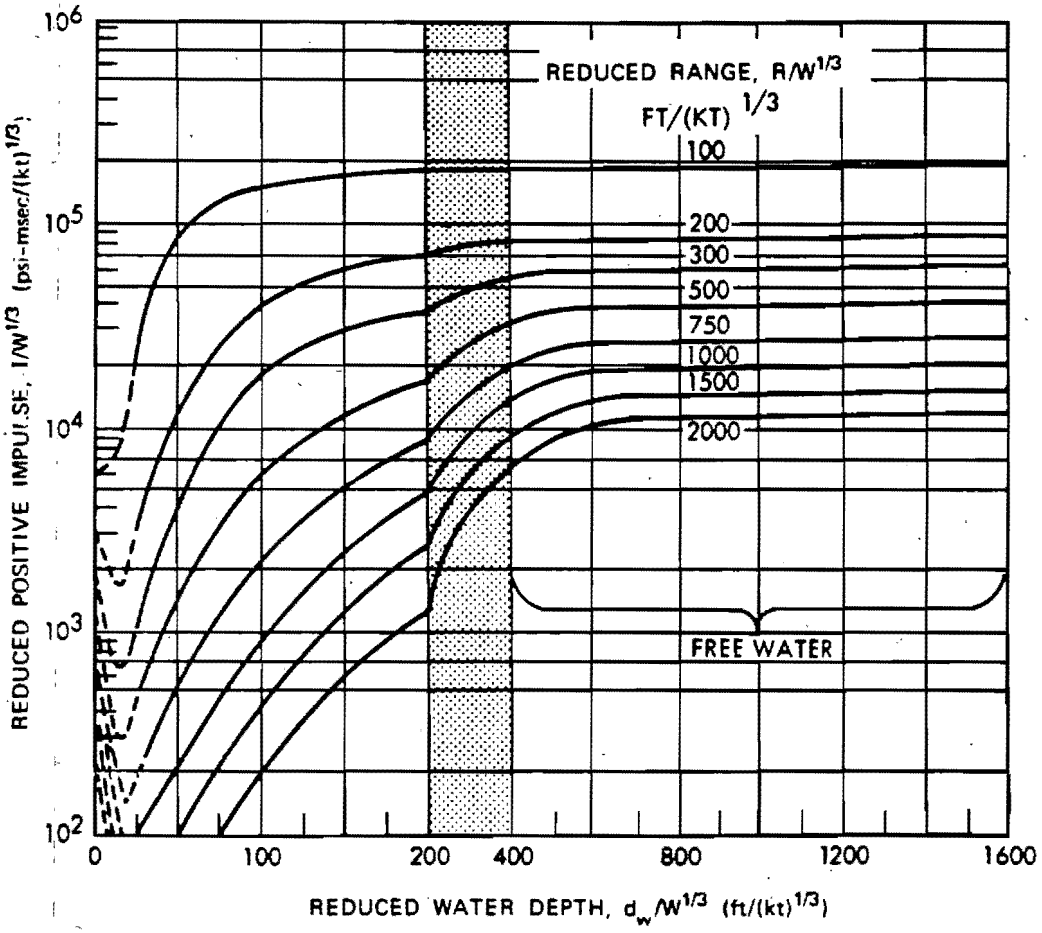

Figure 2-118. [redacted] Reduced Positive Impulse of Shock Wave vs Reduced Water Depth. Explosion and Gauges at Mid-Depth. [redacted]

[redacted]

[redacted]

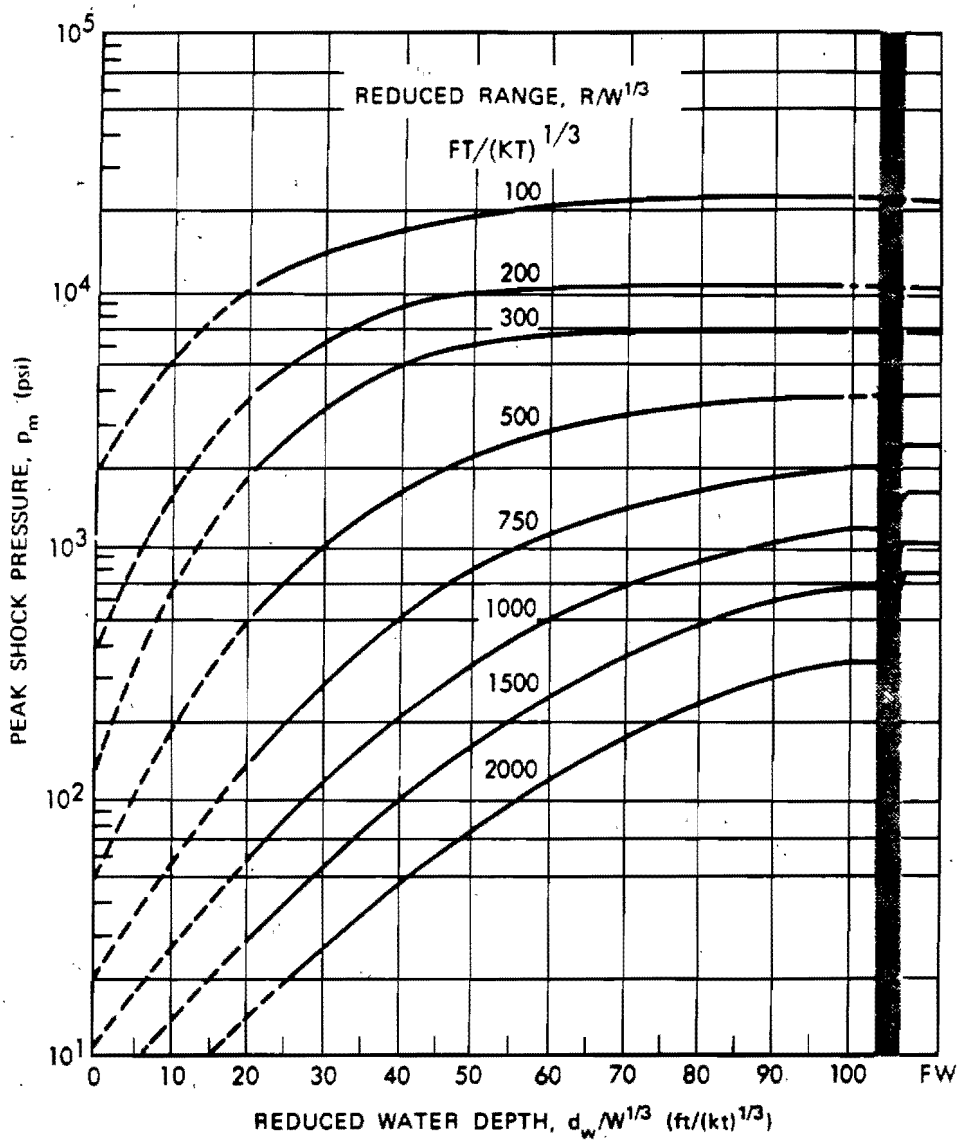

Figure 2-119. [redacted] Peak Shock Pressure vs Reduced Water Depth. Explosion on Bottom, Gauges at Mid-Depth. [redacted]

[redacted]

[redacted]

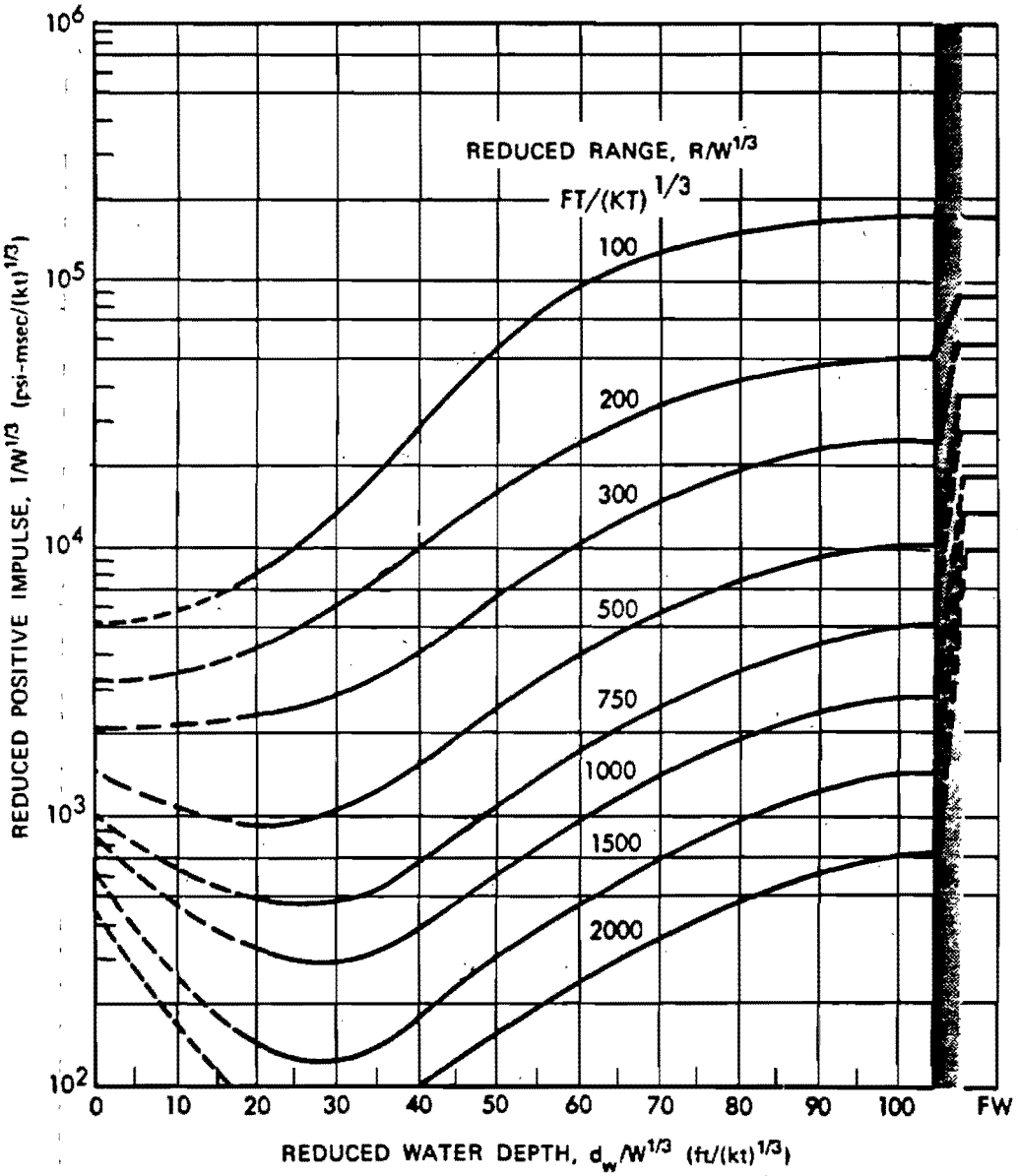

Figure 2-120. [redacted] Reduced Positive Impulse vs Reduced Water Depth. Explosion on Bottom, Gauges at Mid-Depth. [redacted]

[redacted]

[redacted]

Problem 2-31. Calculation of Peak Overpressure Along the Water Surface as a Function of Underwater Burst Depth

[redacted] Figure 2-121 shows the relations to obtain the maximum air blast overpressure from a scaled underwater explosion as a function of depth of burst and horizontal distance. The air blast is for an altitude just above the surface of the water. To determine the air blast at other altitudes, see the references listed in paragraph 2-72.

[redacted] *Example*

Given: A 10 kt explosion at a depth of 500 ft in deep water.

Find:

a. The horizontal distance at which a 0.5 psi peak air blast overpressure would be predicted.

b. The upper and lower limits of the range for item a. that would cover the estimated accuracy.

Solution: The reduced depth of burst is

$$\frac{d_b}{W^{1/3}} = \frac{500}{(10)^{1/3}} = 232 \text{ ft/(kt)}^{1/3}.$$

From Figure 2-121, the intersection of the 0.5 psi curve with a reduced depth of 232 ft/(kt)$^{1/3}$ occurs at a reduced horizontal distance of 0.7 kft/(kt)$^{1/3}$.

Answer:

a. The predicted horizontal distance at which 0.5 psi will occur is

$$d = 0.7\ W^{1/3} = (0.9)(10)^{1/3}$$

$$d = 1.50 \text{ kilofeet} = 1{,}500 \text{ feet}.$$

b. The estimated accuracy in predicting the distance for a given overpressure is ±30 percent (see "Reliability" below). Thus, the limits are

$$d = 1{,}500 \times 1.3 = 1{,}950 \text{ ft (upper limit)}.$$

$$d = 1{,}500 \times 0.7 = 1{,}050 \text{ ft (lower limit)}.$$

[redacted] *Reliability:* The accuracy of the relation in Figure 2-121 has not been tested rigorously. The relations provide an approximation based on high-explosive underwater tests and confirmed by a few measurements made at nuclear underwater tests. However, it is felt that ±30 percent in predicting the distances for maximum overpressure is a realistic accuracy estimate.

[redacted] *Related Material:* See paragraph 2-72.

[redacted]

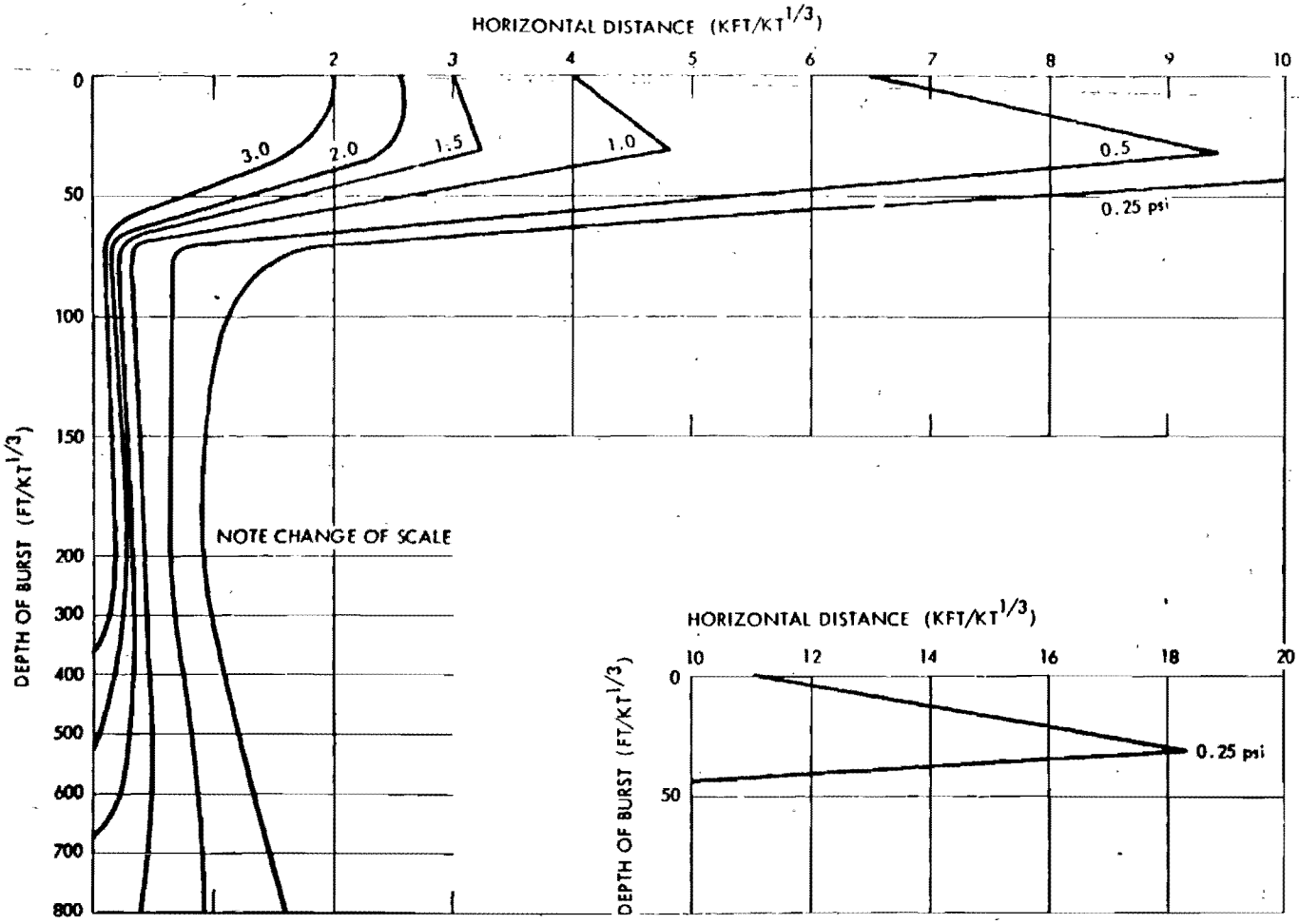

Figure 2-121. [redacted] Peak Air Blast Overpressure Along the Water Surface from Underwater Nuclear Explosions [redacted]

[redacted]

Problem 2-32. Calculation of the Extent, Initial Vertical Velocity, and Approximate Height of the Spray Dome

[redacted] The maximum extent of the spray dome can be estimated with the following relations, which are valid for reduced depths of burst as large as:

$$d_b/W^{1/3} \leq 1{,}260 \text{ ft/(kt)}^{1/3}$$

$$r_{sd} = d_b \tan \delta_{max}$$

$$\delta_{max} = 85.3 - 0.021\ (d_b/W^{1/3})$$

where (as shown in the following sketch):

r_{sd} = the horizontal extent of the spray dome (ft).

δ = the spray dome angle, the angle between a vertical line passing through the center of the burst and a line passing through the point of interest on the surface and the center of the burst (degrees).

d_b = the burst depth (ft).

W = the weapon yield (kt).

h = maximum spray dome height (ft).

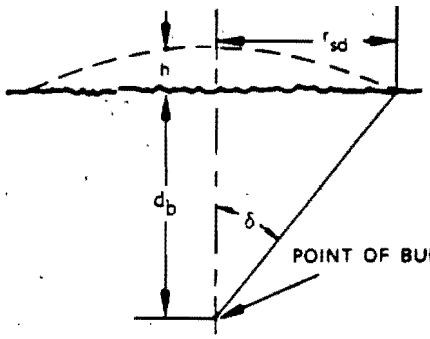

[redacted] Initial spray velocities can be calculated from:

$$V_o = (144 \cos \delta)\frac{p_m}{U}$$

where at a point on the surface,

p_m = peak shock pressure (psi).

U = shock front propagation velocity (ft/sec).

V_o = initial spray velocity (ft/sec.)

[redacted] Values of p_m are given in Figure 2-112. Values of U are given in Figure 2-122 as a function of p_m. In practice, the presence of the bottom does not appear to have an influence upon the value for the spray velocity. However, for bursts on the bottom, the yield should be doubled (as an upper limit estimate) when calculating spray velocities.

[redacted] Higher velocities than given by the above equation have been observed for deep bursts,* therefore a 50 percent safety factor should be added to calculate values of initial dome velocity.

[redacted] An upper limit of dome height h can be derived from:

$$h = V_o t - (f)t^2$$

where

t = time (sec),

f = retardation factor (ft/sec^2),

[redacted] Choppy sea, together with "Taylor instability" appear to account qualitatively for this observation.

[redacted]

[redacted]

by assuming that gravity is the only retarding force and, therefore, that f = 16 ft/sec^2. The time that the upper limit height is reached can be determined that the first derivative of h with respect to time (that is, dome velocity) = zero at that time. Therefore,

$$\frac{dh}{dt} = 0 = V_o - 2(f)t$$

[redacted] *Example*

Given:

DNA (G)(3)

[redacted]

DNA (G)(3)

[redacted]

Reliability: Spray dome angles are estimated to be reliable to within ±10 percent for $d_b/W^{1/3} < 1{,}260$ ft/(kt)$^{1/3}$. Initial vertical velocities that are calculated by the equations given above might be low by as much as 50 percent, therefore, a safety factor is included in the method. The retardation factor f is taken to be 16 ft/sec^2 to obtain an upper limit for dome height. Actual retardation factors as large as 30 ft/sec^2 have been observed during nuclear tests.

[redacted] *Related Material:* See paragraph 2-73.

278

2-250

[redacted]

[redacted]

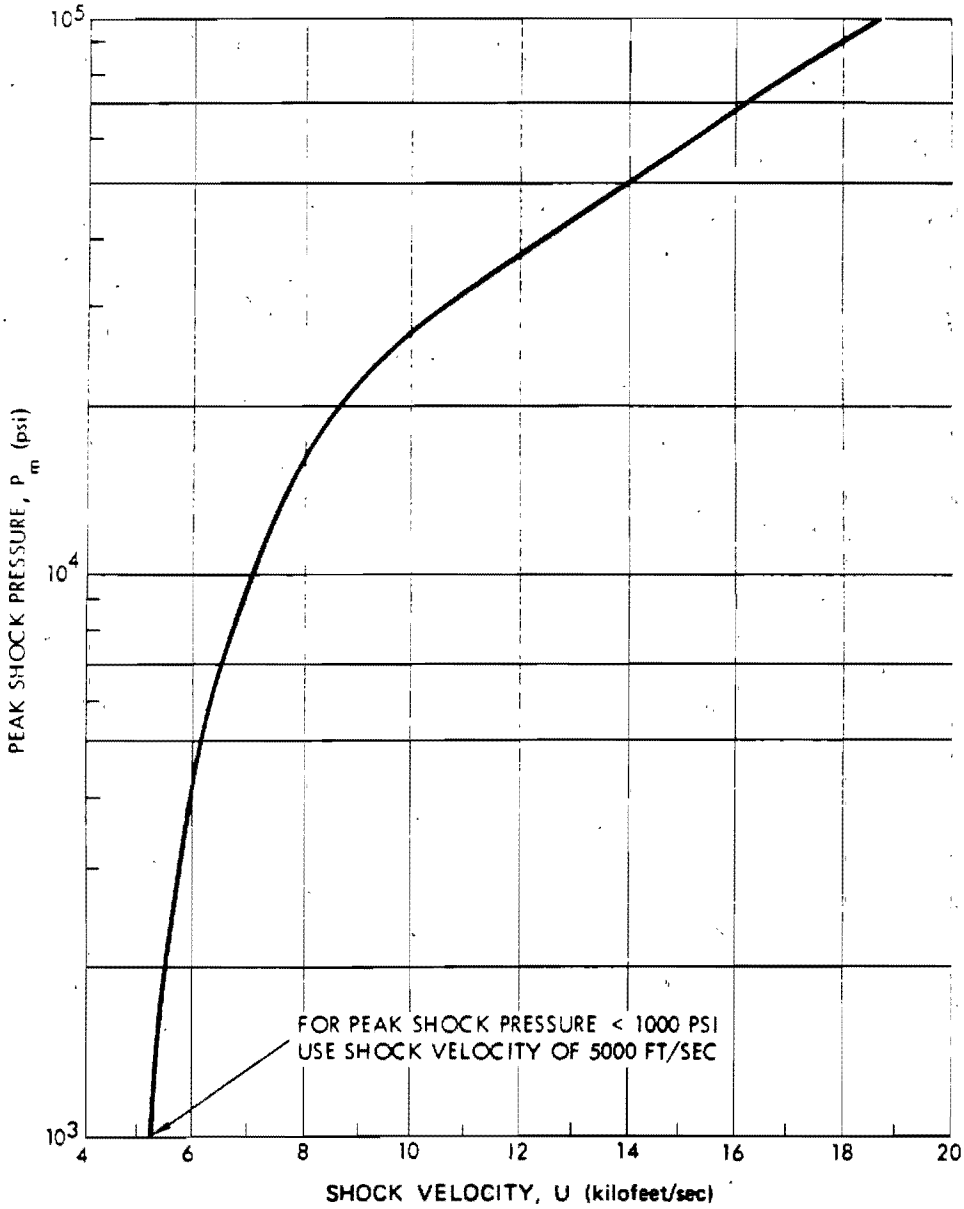

Figure 2-122. [redacted] Velocity of Shock Wave in Free Water vs Peak Shock Pressure [redacted]

[redacted]

[redacted]

Problem 2-33. Calculation of Plume, Column, and Cauliflower Formation

[redacted] Figure 2-123 shows reduced plume dimensions as a function of reduced time for very deep and deep explosions. Figure 2-124 shows reduced plume dimensions for shallow bursts and cloud dimensions. The criteria for determining the explosion categories as a function of depth of burst and weapon yield are given in Figure 2-105 and Table 2-8. The accuracy of the predictions obtained from Figures 2-123 and 2-124 has not been established firmly because of the limited number of nuclear tests upon which they are based.

[redacted] *Example* [redacted]

Given: A 10 kt explosion at a depth of 500 ft in deep water.

Find: The plume radius and plume height 15 seconds after the explosion.

Solution:

$$240\ W^{1/4} = 427\ \text{ft}$$

$$700\ W^{1/4} = 1{,}245\ \text{ft}.$$

Since $240\ W^{1/4} < d_b < 700\ W^{1/4}$, this is a deep burst. The reduced time is

$$\frac{t}{W^{1/3}} = \frac{15}{(10)^{1/3}} \approx 7\ \text{sec/(kt)}^{1/3}.$$

From Figure 2-123, the reduced plume height is about 800 $\text{ft/(kt)}^{1/3}$, and the reduced plume radius is about 700 $\text{ft/(kt)}^{1/3}$.

Answer:

$$\text{Plume height} \approx 800\ W^{1/3} \approx (800)(10)^{1/3} \approx 1{,}700\ \text{ft},$$

$$\text{Plume radius} \approx 700\ W^{1/3} \approx (700)(10)^{1/3} \approx 1{,}500\ \text{ft}.$$

[redacted] *Reliability:* The curves in Figures 2-123 and 2-124 are estimated to be reliable to within ±30 percent. For safety considerations, multiply the radius and the height by 1.3. For assurance of damage, multiply the values obtained from the figures by 0.7.

[redacted] *Related Material:* See "SURFACE EFFECTS OTHER THAN WAVES," in particular paragraph 2-74. See also Table 2-8 and Figure 2-105.

[redacted]

[redacted]

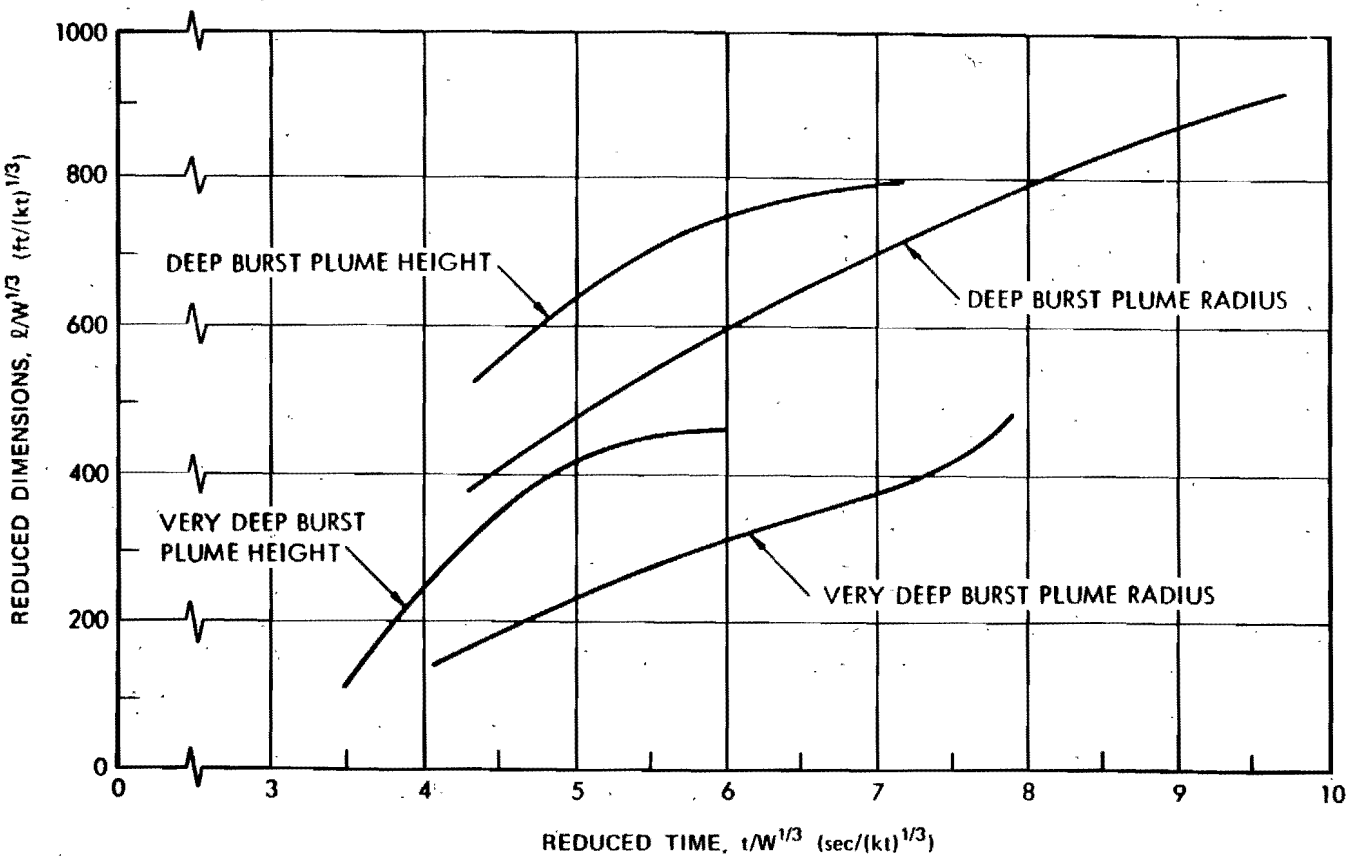

Figure 2-123. [redacted] Plume Dimensions for Deep and Very Deep Underwater Bursts [redacted]

[redacted]

[redacted]

[redacted]

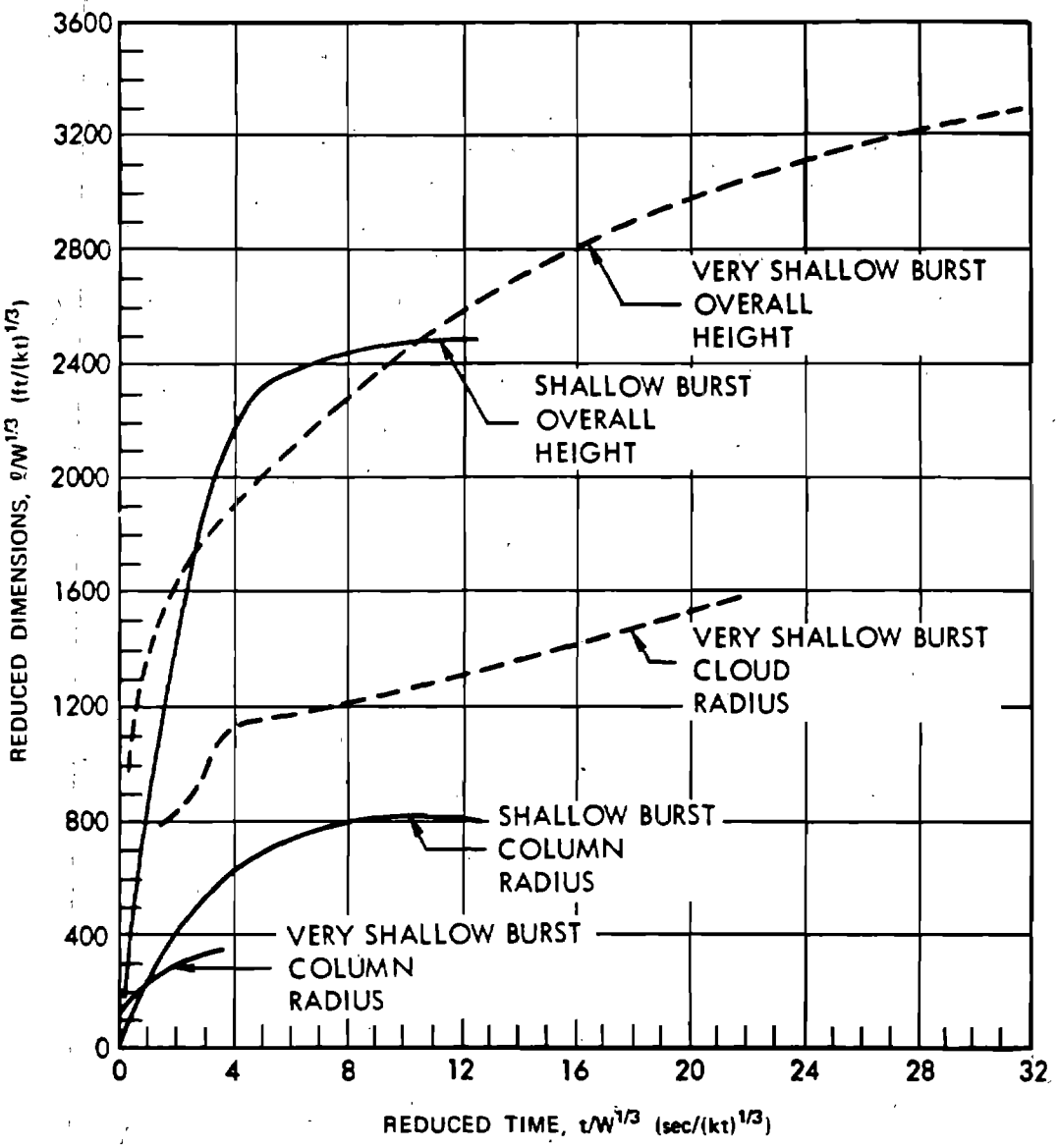

Figure 2-124. [redacted] Column and Cloud Dimensions for Shallow and Very Shallow Bursts [redacted]

[redacted]

[redacted]

Problem 2-34. Calculation of Base Surge Growth and Cloud Height

[redacted] The reduced outside radius of various base surge clouds is shown in Figures 2-126 and 2-127 as a function of reduced time after burst. Figure 2-126 shows a curve that is applicable to shallow and very shallow bursts, while Figure 2-127 shows separate curves for deep and very deep bursts (see Table 2-8 and Figure 2-105 for burst depth categories). Equations that relate the reduced radii and times to actual radii and times for various explosion conditions are shown below:

Burst Classification	Reduced Radius, R_s (Dimensionless)	Reduced Time, t_s ($sec/ft^{1/2}$)	Equation for Estimated* D_{max} (ft) or A_{max}	Applicable Figure
Very shallow	R_s/D_{max}	$t_s(D_{max})^{1/2}$	$D_{max} = 710\ W^{1/3}$*	2-125
Shallow	R_s/D_{max}	$t_s(D_{max})^{1/2}$	$D_{max} = 377\ W^{1/3}\ (d_b/W^{1/3})^{1/6}$	2-125
Deep and very deep	R_s/A_{max}	$t_s(A_{max})^{1/2}$	$A_{max} = 1{,}500\ (W/Z)^{1/3}$	2-126

[redacted] The equation $D_{max} = 710\ W^{1/3}$ is valid for very shallow explosions off the bottom. The equation $D_{max} = 377\ W^{1/3}\ (d_b/W^{1/3})^{1/6}$ is valid for very shallow and shallow explosions on a bottom.

[redacted]

[redacted]

where

W = yield of the weapon (kt)

R_s = radius of the base surge (ft)

t_s = time after explosion (sec)

d_b = depth of the explosion (ft)

Z = $d_b + 33$ = total hydrostatic pressure at d_b (ft of water)

D_{max} = estimated maximum column radius (ft)

A_{max} = estimated maximum bubble radius (ft).

[redacted] Figure 2-125 was developed to approximate the height of the visible base surge for use with radiation exposure calculations. The curve in Figure 2-125 was drawn under the assumption that the height is not a function of yield or depth of burst. This assumption probably is not correct, but there is not sufficient information to incorporate these parameters.

[redacted] *Example (U):*

Given: A 40 kt explosion at a depth of 200 feet.

Find:

a. The base surge radius R_s.

b. The height of the visible cloud h_c 10 minutes after burst.

Solution: Refer to Table 2-8:

$$21\ W^{1/3} = (21)(40)^{1/3} = 72 \text{ ft},$$

$$75\ W^{1/3} = (75)(40)^{1/3} = 256 \text{ ft},$$

therefore, a 40 kt explosion at a depth of 200 feet is a very shallow explosion. From the relations given above (since the burst was not described as being on the bottom)

$$D_{max} = 710\ W^{1/3} = (710)(40)^{1/3} = 2{,}430 \text{ ft},$$

and

$$t_{sr} = \frac{t_s}{(D_{max})^{1/2}} = \frac{600}{(2{,}430)^{1/2}} = 12.2 \text{ sec}.$$

From Figure 2-126, the reduced base surge radius is about 7.

Answer:

a. $R_s \approx R_{sr} \times D_{max} = (7)(2{,}430)$

$$R_s \approx 17{,}000 \text{ ft}.$$

b. From Figure 2-125, the height of the base surge cloud is

$$h_c \approx 2{,}000 \text{ ft}.$$

[redacted] *Reliability:* Base surge radii obtained from Figures 2-125 and 2-126 are estimated to be reliable to within ±20 percent. No estimate can be made of the reliability of the height of the base surge cloud obtained from Figure 2-127.

[redacted] *Related Material:* See paragraph 2-75. See also Table 2-8 and Figure 2-105.

[redacted]

[redacted]

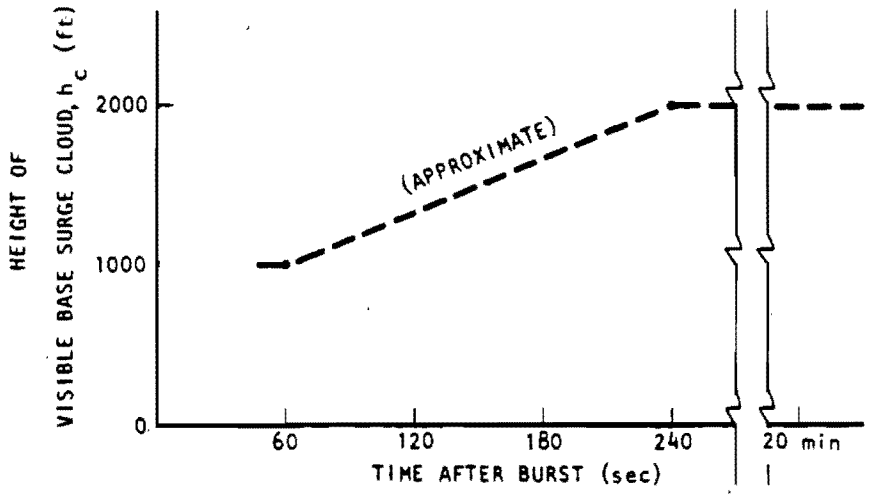

Figure 2-125. [redacted] Height of Visible Base Surge Cloud as a Function of Time After Burst [redacted]

[redacted]

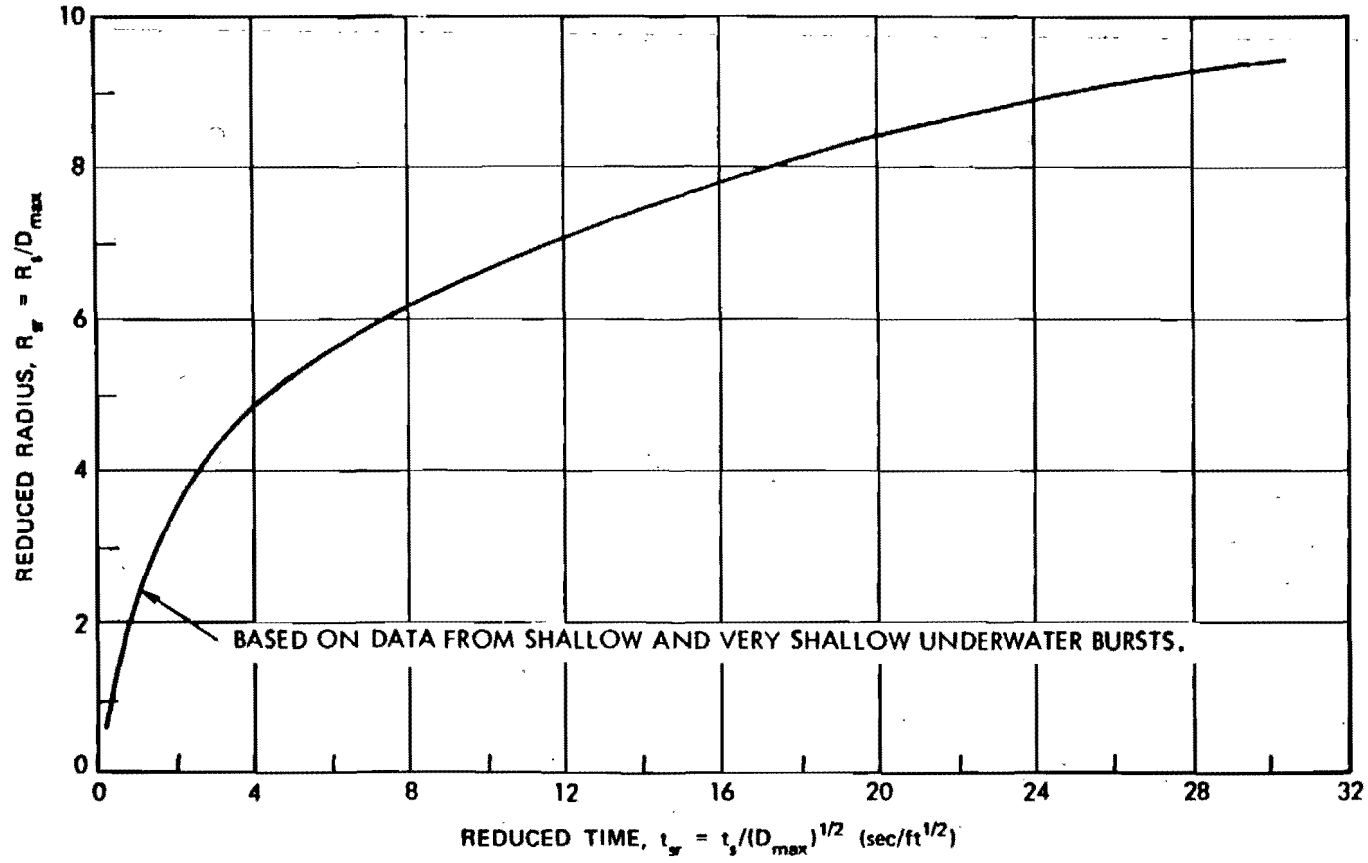

Figure 2-126. [redacted] Reduced Base Surge Radius vs Reduced Time for Shallow and Very Shallow Bursts [redacted]

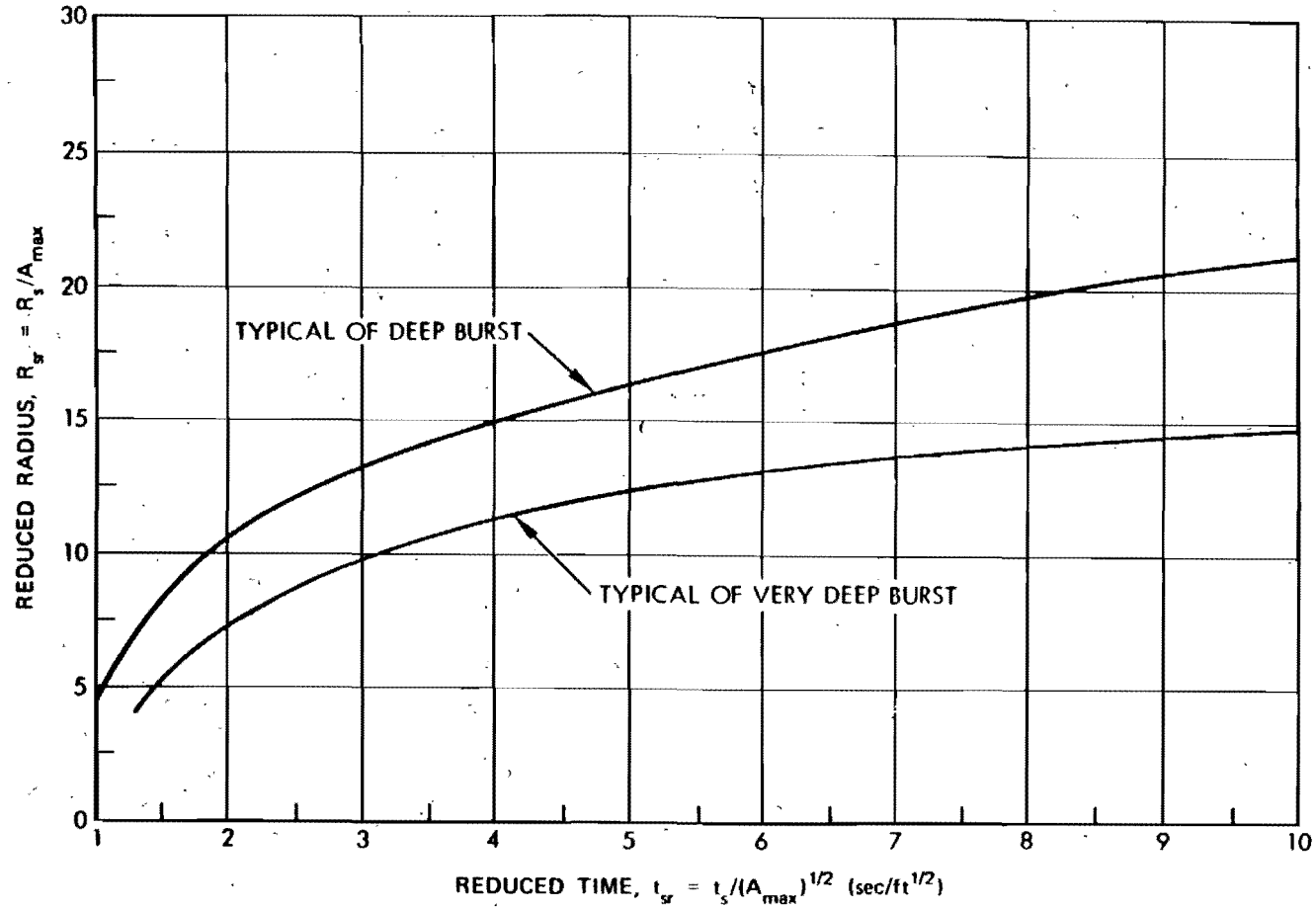

Figure 2-127. [redacted] Reduced Base Surge Radius vs Reduced Time for Deep and Very Deep Bursts [redacted]

[redacted]

Problem 2-35. Calculation of the Properties of Water Surface Waves

[redacted] Figure 2-128 shows the peak wave height (crest to trough) for any depth of burst in shallow water (for waves, shallow water is $0 \leq d_w \leq 100\ W^{1/4}$, see paragraph 2-77), and for any depth of burst not greater than five times the lower critical depth ($0 \leq d_b/5 \leq 170\ W^{1/4}$, see paragraph 2-77) in deep water (for waves $d_w \geq 256\ W^{1/4}$). The dashed transitional curve in Figure 2-128 can be used for intermediate depths. For any depth of burst in shallow water, and for bursts as low as the lower critical depth ($d_b = 170\ W^{1/4}$) in deep water, the foregoing limits on water depth are also the estimated cavity radii as shown in Figure 2-128. For nuclear explosions in deep water at shallow depths of burst near the upper critical depth ($d_b \approx 8.6\ W^{1/3}$), the peak wave height may be nearly twice as large as predicted in Figure 2-128 (see Figure 2-107).

DNA (L)(3)

Example

[redacted]

DNA (L)(3)

[redacted]

Reliability

1. Deep water.
   a. The cavity radius given by the equation

[redacted]

[redacted]

in paragraph 2-77 agrees within [redacted] percent with the measured values shown in Table 2-10 for the H.E. tests at Mono Lake (for which the predicted value is 66.5 ft). [redacted]

DNA (L-)(3)

b. The peak wave height given in Figure 2-128 and the equation in paragraph 2-77 agrees with the measured H.E. data within a factor of two, and within [redacted] percent of the measured data of the two nuclear explosions. [redacted]

DNA (L-)(3)

2. Shallow water.

a. The cavity radius given by the equation in paragraph 2-77 (and Figure 2-128) provides a lower limit for explosions in shallow water. An upper limit is probably half the maximum bubble radius given by the equation in paragraph 2-67.

b. The peak wave height given by the equation in paragraph 2-77 (and in Figure 2-128) agrees with the measured values within about a factor of 2, which is roughly the uncertainty of the data. [redacted]

Related Material: See paragraphs 2-67 and 2-77. See also Tables 2-9 and 2-10.

[redacted]

[redacted]

[redacted]

[redacted]

Deleted

Figure 2-128. [redacted] Peak Wave Height H as a Function of Yield W Range R and Water Depth d_w [redacted]

[redacted]

Problem 2-36. Calculation of Underwater Crater Dimensions

[redacted] Figures 2-129 through 2-131 show the apparent crater radius, the apparent crater depth, and the average height of the crater lip, respectively, as a function of weapon yield. Figures 2-129a, 2-130a, and 2-131a are for surface bursts. Figures 2-129b, 2-130b, and 2-131b are for bursts near a clayey sand bottom. Linear interpolation between the curves may be used for bursts between the surface and the bottom. [redacted] The curves in Figures 2-129 through 2-131 were developed from nuclear cratering data; however, H.E. data were used to obtain scaling laws and the shape of the curves for bottom placement. Data from about 600 H.E. and [redacted] nuclear explosions were used in the preparation of the curves. The nuclear data are shown in Table 2-11, [redacted]

DNA (2)(3)

[redacted]

[redacted] The critical water depth dividing washed and unwashed craters can be found from Figure 2-132 for a clayey-sand bottom. An unwashed crater results when the water depth is less than the minimum height of the irregular cavity lip and when the lip does not fail. For other bottom materials, the critical water depth can be found by multiplying the value of d_c by the appropriate soil factor for crater lip height in Table 2-12.

[redacted] *Example* [redacted]

Given: A 40 kt explosion on the bottom, which consists of oceanic ooze, in 60 feet of water.

Find: The radius, depth, and lip height of the apparent crater.

Solution: From Figures 2-129, 2-130, and 2-131, the crater dimensions in clayey sand are

[redacted]

[redacted]

Table 2-11. [redacted] Partial Compilation of Nuclear Cratering Data [redacted]

Deleted

[redacted]

Table 2-12. [redacted] Soil Factors for Cratering in Various Materials as Compared with Clayey Sand [redacted]

Material	Soil Factors: Crater Radius	Crater Depth	Crater Lip Height
Clayey sand	1.0	1.0	1.0
Sand	1.1	0.8	0.7
Loess	0.9	1.3	1.2
Muck*	1.5	0.5	0.4
Clayey silt	1.1	1.1	1.0
Coral sand	0.9	0.8	0.7
Clay	0.9	1.4	1.3
Soft rock	0.8	0.6	0.6
Hard rock*	0.6	0.4	0.4
Oceanic ooze*	1.7	0.2	0.1

*([redacted] Soil Factors estimated or interpolated from the others based on experimental data.

[redacted]

radius, r_{ac} $\approx$ 750 ft,

depth, d_{ac} $\approx$ 42 ft,

lip height, h_ℓ $\approx$ 1.7 ft.

Answer: The corresponding dimensions for oceanic ooze are (Table 2-12)

$$r_{ac} \approx (1.7)(750) \approx 1{,}275 \text{ ft},$$

$$d_{ac} \approx (0.2)(42) \approx 8 \text{ ft},$$

$$h_\ell \approx (0.1)(1.7) \approx 0.2 \text{ ft}.$$

DNA

[redacted] *Reliability* [redacted]

[redacted] Dimensions from these curves are considered to have the following reliabilities:

radius	+150%–50%
depth	+150%–50%
lip height	+160%–60%

The accuracy of the soil factors shown in Table 2-12 is unknown.

[redacted] *Related Material:* See "UNDERWATER CRATERING," page 2-223.

[redacted]

[redacted]

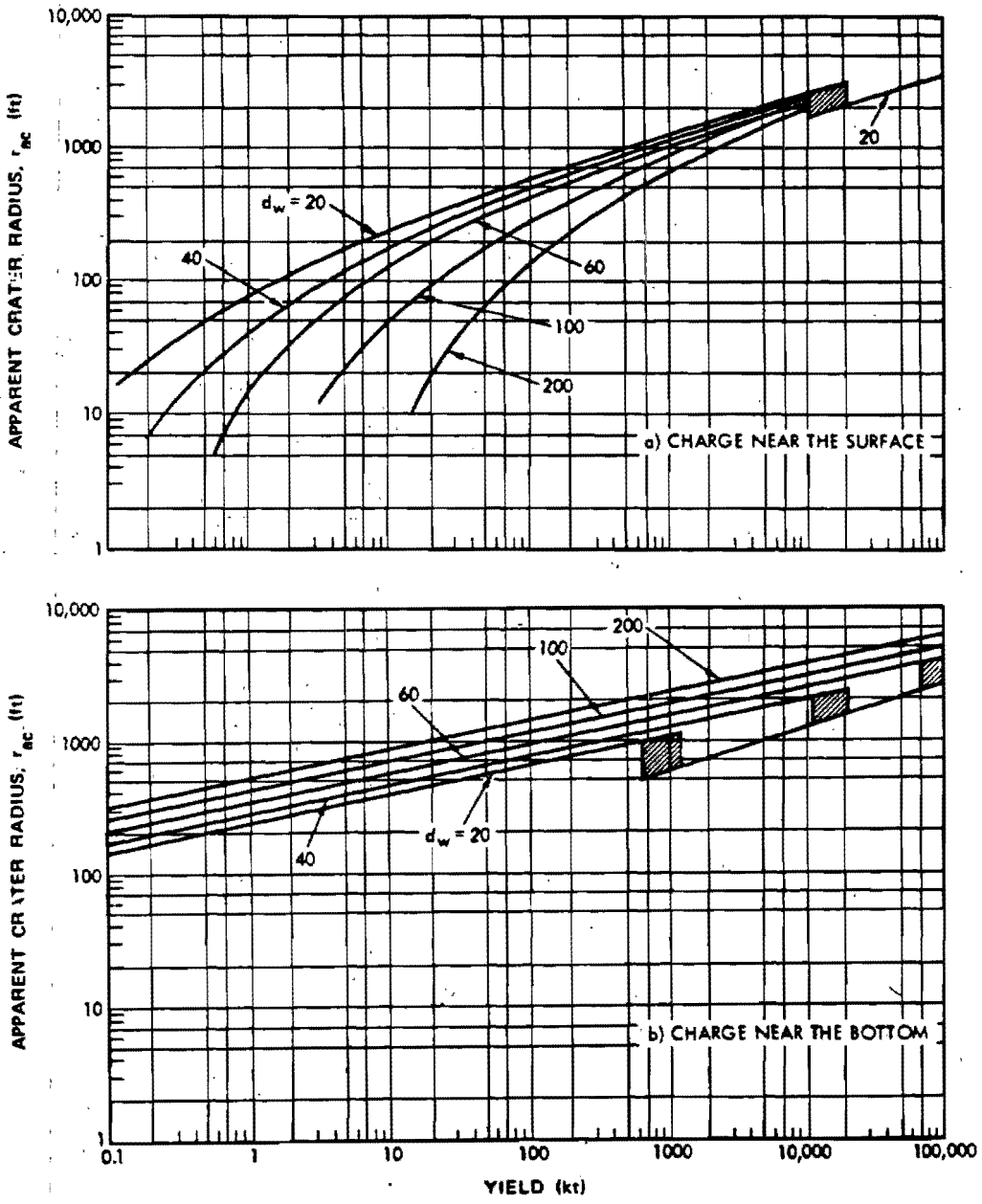

Figure 2-129. [redacted] Apparent Crater Radius as a Function of Yield for Various Water Depths Over a Clayey Sand Bottom, where d_w = Water Depth in Feet. Shaded Areas Denote Possible Transition Regions from a Washed to an Unwashed Crater for d_w = 20, 40, and 60. [redacted]

[redacted]

[redacted]

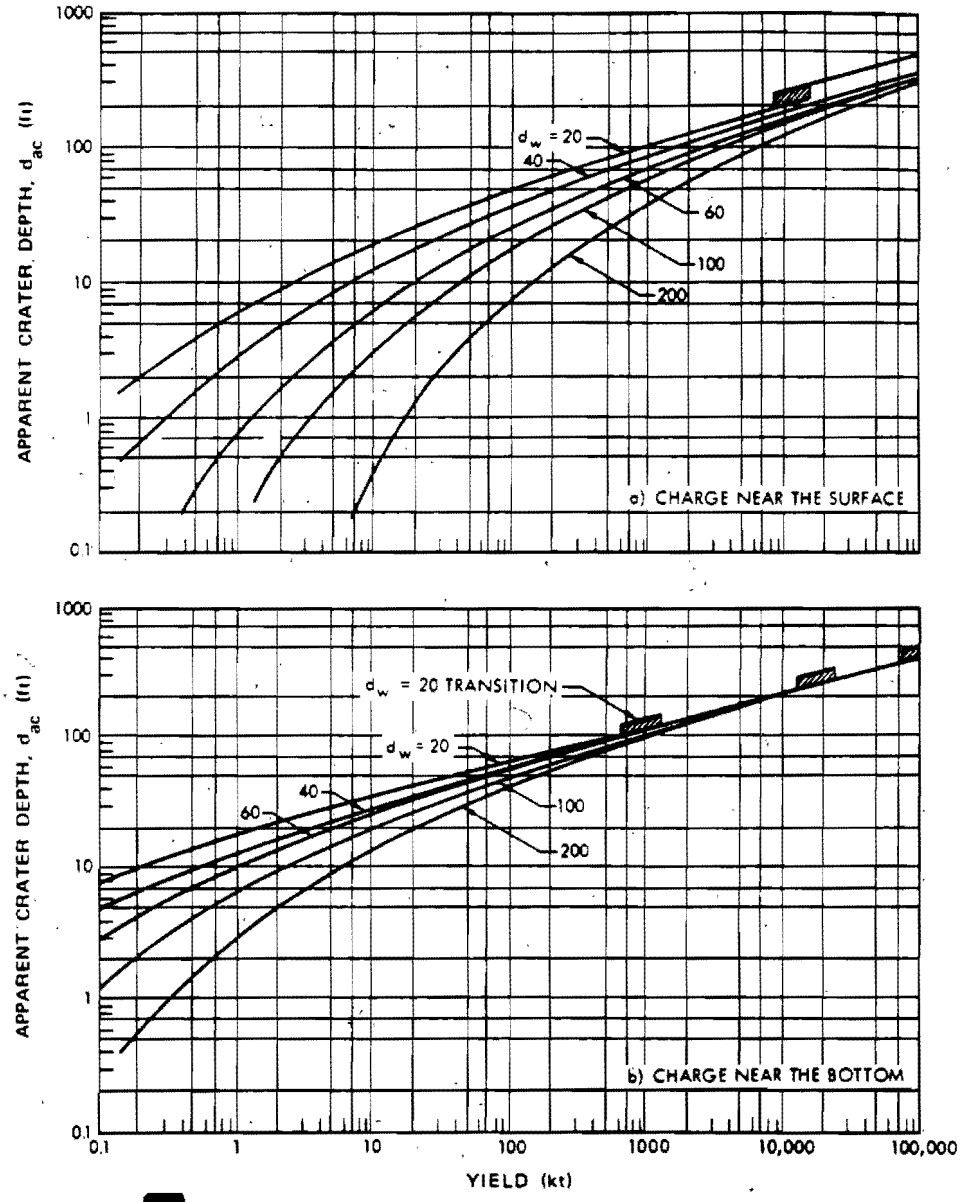

Figure 2-130. [redacted] Apparent Crater Depth as a Function of Yield for Various Water Depths Over a Clayey Sand Bottom, where d_w = Water Depth in Feet. Shaded Areas Denote Possible Transition Regions from a Washed to an Unwashed Crater for d_w = 20, 40, and 60. [redacted]

[redacted]

[redacted]

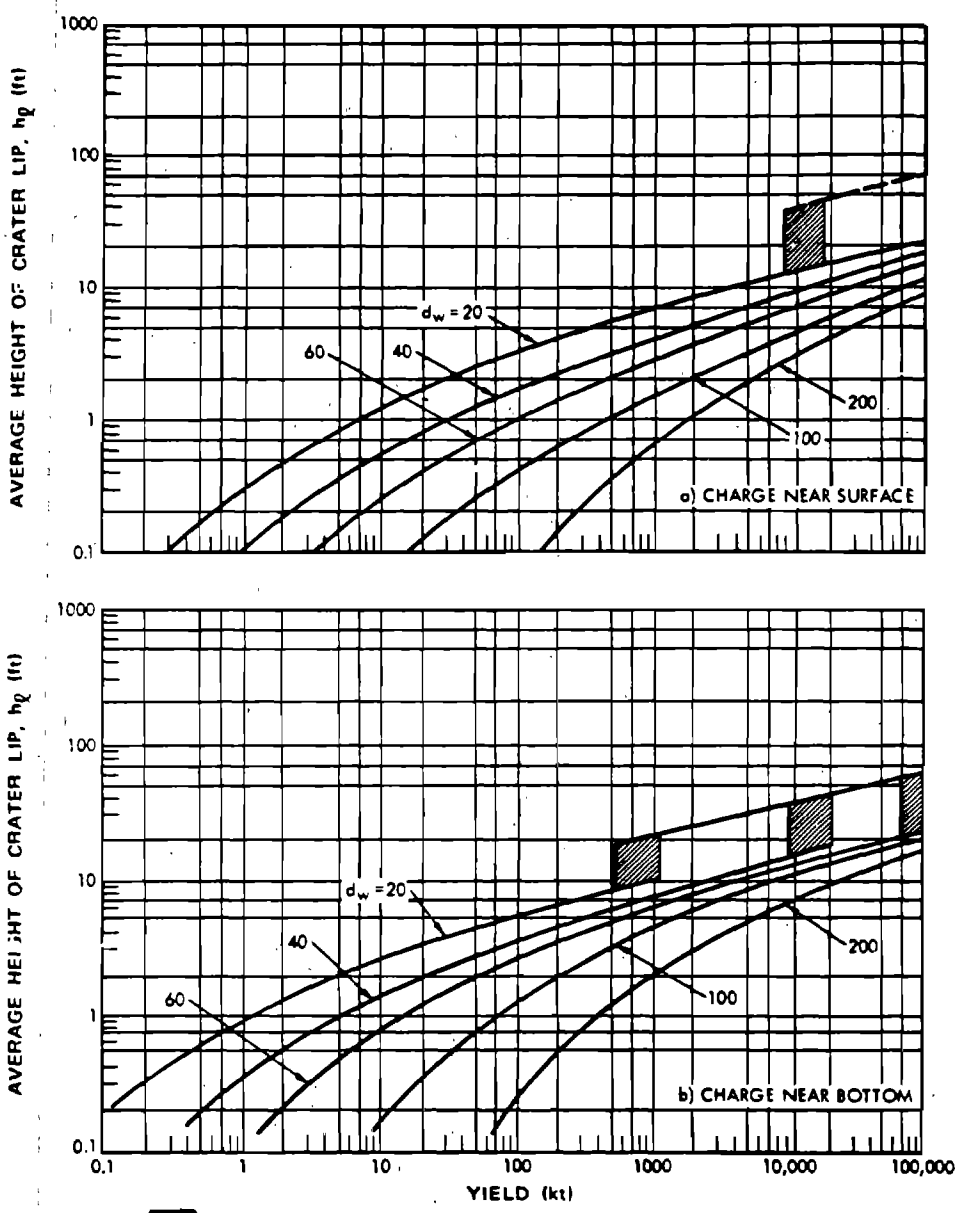

Figure 2-131. [redacted] Average Height of Crater Lip as a Function of Yield for Various Water Depths with the Charge Near a Clayey Sand Bottom, where d_w = Water Depth in Feet. Shaded Areas Denote Possible Transition Regions from Crater for d_w = 20, 40, and 60. [redacted]

[redacted]

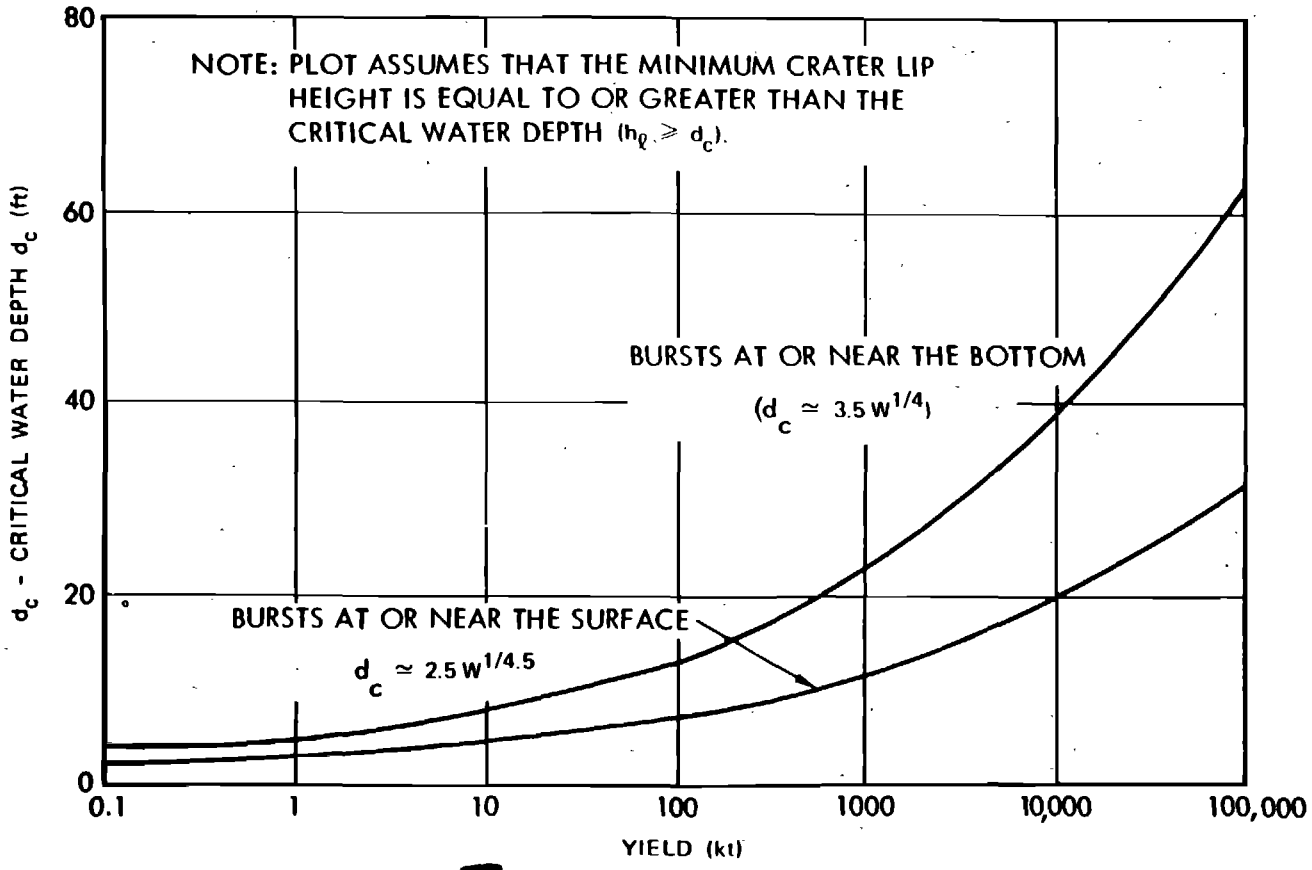

Figure 2-132. [redacted] Estimated Critical Water Depth as a Function of Yield for a Clayey Sand Bottom [redacted]

[redacted]

[redacted] BIBLIOGRAPHY [redacted]

Allen, R. T., *The Effect of an Open Emplacement Hole on Crater Formation near Optimum Depth of Burial* [redacted], DASA 2680, Systems, Science, and Software, La Jolla, California, 23 March 1971 [redacted]

Barash, R. M., and H. G. Snay, *Effect of Refraction on Safe Delivery Ranges for Submarine-Launched Underwater Nuclear Weapons* [redacted], NOLTR-62-199, U.S. Naval Ordnance Laboratory, White Oak, Silver Spring, Maryland, June 1963 [redacted]

Barash, R. M., and J. A. Goertner, *Refraction of Underwater Explosion Shock Waves: Pressure Histories Measured at Caustics in a Flooded Quarry*, NOLTR-67-9, U.S. Naval Ordnance Laboratory, White Oak, Silver Spring, Maryland, 19 April 1967 [redacted]

Blake, T. R., and D. E. Wilkins, *The Effect of an Open Emplacement Hole on the Crater Produced at Shallow Depth of Burial* [redacted], DNA 2813T, 3SCR-841, Systems, Science, and Software, La Jolla, California, October 1971 [redacted]

Carlson, R. H., and W. A. Roberts, *Project SEDAN, Mass Distribution and Throwout Studies*, PNE-217E, The Boeing Company, Seattle, Washington, August 1963 [redacted]

Circeo, L. J., and M. D. Nordyke, *Nuclear Cratering Experience at the Pacific Proving Grounds*, UCRL-12172, University of California Lawrence Radiation Laboratory, Livermore, California, November 1964 [redacted]

Cole, R. H., *Underwater Explosions*, Dover Publications, Inc., New York, N.Y., 1965 [redacted]

Cooper, H. F., Jr., *Free-Field Ground Motions from Surface Bursts on Rock* [redacted], AFWL-TR-67-94, Air Force Weapons Laboratory, Kirtland Air Force Base, Albuquerque, New Mexico, December 1967 [redacted]

Davis, L. K., and A. D. Rooke, Jr., *Project DANNY BOY, Mass Distribution Measurements of Crater Ejecta and Dust; Appendix B: Volumetric Equalities of the Crater* [redacted], Miscellaneous Paper No. 1-754, U.S. Army Waterways Experiment Station, Vicksburg, Mississippi, February 1965 [redacted]

Davis, L. K., and J. V. Strange, *Cratering Experiments at Mono Lake*, U.S. Army Engineer Waterways Experiment Station, Vicksburg, Mississippi, November 1966 [redacted]

Davis, L. K., *MINE SHAFT Series, Events MINE UNDER and MINE ORE, Subtask, N121, Crater Investigations*, Technical Report N-70-8, U.S. Army Engineer Waterways Experiment Station, Vicksburg, Mississippi, March 1970 [redacted]

[redacted]

Davis, L. K., *Effects of a Near-Surface Water Table on Crater Dimensions*, Miscellaneous Paper No. 1-939, U.S. Army Engineer Waterways Experiment Station, Vicksburg, Mississippi, October 1967

Divoky, D. J., and B. LeMéhaute, *Handbook of Explosion-Generated Water Waves, Vol. II – Applications* Report No. TC-130C, Tetra Tech, Inc., Pasadena, California, December 1969

Dodge, Carl, Jr., *A Photographic Investigation of the Spray Dome Produced by Shallow Underwater Explosions* NOLTR-63-273, U.S. Naval Ordnance Laboratory, White Oak, Silver Spring, Maryland, 13 March 1964

Fisher, P. R., R. J. Kley, and H. A. Jack, *Geologic Investigations and Engineering Properties of Craters*, PNE-1103, U.S. Army Engineer Nuclear Cratering Group, Livermore, California, May 1969

Fitchett, D. J., *MIDDLE COURSE I Cratering Series*, Technical Report 35, U.S. Army Engineer Nuclear Cratering Group, Livermore, California, June 1971

Frandsen, A. D., *Project CABRIOLET, Engineering Properties Investigations of the CABRIOLET Crater*, PNE-957, U.S. Army Engineer Nuclear Cratering Group, Livermore, California, March 1970

Kaplan, K., and O. H. Criner, *A Study of Explosion-Generated Surface Water Waves* URS 162-8, URS Corporation, Burlingame, California, December 1963

Kaplan, K., and N. R. Wallace, *Surface Waves from Nuclear Explosions* URS 190-1, DASA 1240(8), URS Corporation, Burlingame, California, March 1962

Kaplan, K., C. Wiehle, *Air Blast Loading in the High Shock Strength Region* Part II, Prediction Methods and Examples, URS 633-3, DASA 1460-1, URS Corporation, Burlingame, California, February 1965

Kaulum, K. W., and M. A. Olson, *Containment of Explosion Products from a Deep Underwater Explosion (Chase V) – Final Report* USNRDL-TR-67-60, U.S. Naval Radiological Defense Laboratory, San Francisco, California, 5 May 1967

Kot, C. A., *Hydra Program: Theoretical Study of Bubble Behavior in Underwater Explosions*, USNRDL-TR-747, U.S. Naval Radiological Defense Laboratory, San Francisco, California, 15 April 1964

Kranzer, H. C., and J. B. Keller, "Water Waves Produced by Explosions," *J. Appl. Phys.*, Vol. 30, No. 3, March 1959, pp. 398-407

Kriebel, A. R., *Analysis of Water Waves Generated Explosively at the Upper Critical Depth* URS 679-1, 2, 3, URS Corporation, Burlingame, California, January 1968

Lewis, J. G., *Ground Shock and Survival or Kill of Military Systems* DASA 1836, Defense Atomic Support Agency, Washington, D.C., October 1966

Maine, C. I., J. R. Carbonell, and I. Dyer, *Mechanisms in the Generation of Airblast by Underwater Explosions*, Bolt, Beranek and Newman Report No. 1434, NOLTR-66-88, U.S. Naval Ordnance Laboratory, White Oak, Silver Spring, Maryland, 23 September 1966

Moulton, J. F., Jr., *Height-of-Burst Curves Above 100 psi, Shock, Vibration, and Associated Environments, Protective Construction* Part I, DDR&E Bulletin-32, U.S. Naval Ordnance Laboratory, White Oak, Silver Spring, Maryland, November 1963

Military Engineering with Nuclear Explosives, DASA 1669, U.S. Army Engineer Nuclear Cratering Group, Livermore, California, June 1966

Newmark, N. M., and W. J. Hall, *Preliminary Design Methods for Underground Protective Structures*, AFSWC-TDR-62-6, University of Illinois, Urbana, Illinois, June 1962

Newmark, N. M., *Notes on Shock Isolation Concepts*, Vibration and Civil Engineering Proceedings of Symposium of British National Section International Association for Earthquake Engineering, pp. 71-82, Butterworths, London, 1966

Nuclear Weapons Blast Phenomena DASA 1200-I, -II, -III, -IV, Defense Atomic Support Agency, Washington, D.C., Vol. I, March 1971, Vol. II, December 1970, Vol. III, 1 March 1970. Vol. IV, to be issued during calendar year 1972

Peckham, P. and J. F. Pittman, *Airblast from Lithanol Charges Fired Underwater* NOLTR-68-174, U.S. Naval Ordnance Laboratory, White Oak, Silver Spring, Maryland, 2 December 1968

Phillips, D. E., and T. B. Heathcote, *Underwater Explosion Tests of Two Steam Producing Explosives, I. Small Charge Tests*, NOLTR-66-79, U.S. Naval Ordnance Laboratory, White Oak, Silver Spring, Maryland, 23 May 1966

Phillips, D. E., and H. G. Snay, *The Parameters of Underwater Nuclear Explosion Bubbles* NOLTR-68-63, U.S. Naval Ordnance Laboratory, White Oak, Silver Spring, Maryland, 26 June 1968

Phillips, D. E., and R. L. Willey, *Underwater Explosion Tests of Two Steam Producing Explosives, II. 50- and 300-lb Charge Tests* NOLTR-67-7, U.S. Naval Ordnance Laboratory, White Oak, Silver Spring, Maryland, 22 March 1967

Pinkston, J. M., Jr., *Surface Waves Resulting from Explosions in Deep Water Report 2, Summary of Experimental Procedures and Results of Tests at Lake Ouachita, Arkansas* DASA 1482-2, WES-TR-1-647, U.S. Army Engineer Waterways Experiment Station, Vicksburg, Mississippi, April 1966

Pittman, J. F., *Airblast from Shallow Underwater HBX-1 Explosions* NOLTR-68-45, U.S. Naval Ordnance Laboratory, White Oak, Silver Spring, Maryland, 3 April 1968

Pyatt, D. E., *A Short Summary of Radiative Ground Coupling* General Atomics, Inc., San Diego, California, April 1967

Rooke, A. D., Jr., G. B. Clark, and J. N. Strange, *Shot JOHNNY BOY, Mass Distribution Measurements,* POR-2282, U.S. Army Engineer Waterways Experiment Station, Vicksburg, Mississippi

Rooke, A. D., Jr., and L. K. Davis, *FERRIS WHEEL Series, FLAT TOP Event, Crater Measurements,* POR-3008, U.S. Army Engineer Waterways Experiment Station, Vicksburg, Mississippi, 9 August 1966

Rudlin, L., and J. C. Silva, *Airblast from Underwater Nuclear Explosions* NAVORD Report 6714, U.S. Naval Ordnance Laboratory, White Oak, Silver Spring, Maryland, 1 February 1960

Sauer, F. M., et al., *Nuclear Geoplosics, A Sourcebook of Underground Phenomena and Effects of Nuclear Explosions – Part Four, Empirical Analysis of Ground Motion and Cratering,* DASA 1285 (IV), 1964

Shelton, A. V., M. D. Nordyke, and R. H. Goerchermann, *The NEPTUNE Event, A Nuclear Explosive Cratering Experiment,* UCRL-5766, Lawrence Radiation Laboratory, Livermore, California, 19 April 1960

Shelton, F. H., B. S. Evans, and D. C. Sachs, *A Study of Air Blast Phenomenology in the Very High Pressure Region* DASA-1331, Kaman Nuclear, Colorado Springs, Colorado, 31 December 1962

Snay, H. G., *The Hydrodynamic Background of the Radiological Effects of Underwater Nuclear Explosions* NAVWEPS Report 7323, U.S. Naval Ordnance Laboratory, White Oak, Silver Spring, Maryland, 29 September 1960

Snay, H. G., *Underwater Explosion Phenomena: The Parameters of Migrating Bubbles,* NAVORD Report 4185, U.S. Naval Ordnance Laboratory, White Oak, Silver Spring, Maryland, 12 October 1962

Snay, H. G., *Hydrodynamic Concepts Selected Topics for Underwater Nuclear Explosions*, NOLTR-65-52, DASA-1240-1(2), U.S. Naval Ordnance Laboratory, White Oak, Silver Spring, Maryland, 15 September 1966

Snay, H. G., and J. F. Butler, *Shock Wave Parameters for Nuclear Explosions Under Water*, NAVORD Report 4500, U.S. Naval Ordnance Laboratory, White Oak, Silver Spring, Maryland, 1 May 1957

Snay, H. G., J. F. Butler, and A. N. Gleyzal, *Predictions of Underwater Explosion Phenomena*, WT-1004 (NOLR-1213), U.S. Naval Ordnance Laboratory, White Oak, Silver Spring, Maryland, May 1956

Strange, J. N., *Underwater Cratering*, Miscellaneous Paper No. 1-598, DASA-1240, Chapter VII, Part I, U.S. Army Engineer Waterways Experiment Station, Vicksburg, Mississippi, September 1963

Strange, J. N., *Water Shock-Wave Reflection Properties of Various Bottom Materials*, Miscellaneous Paper No. 1-826, U.S. Army Engineer Waterways Experiment Station, Vicksburg, Mississippi, June 1966

Strange, J. N., and S. H. Halper, *A Quantitative Evaluation of the Underwater Shock Wave Resulting from Surface and Underwater Explosions*, TR No. 2-615, U.S. Army Engineer Waterways Experiment Station, Vicksburg, Mississippi, February 1963

Strange, J. N., and L. Miller, *Blast Phenomena from Explosions at an Air-Water Interface*, Rept. 1, Miscellaneous Paper No. 1-814, U.S. Army Engineer Waterways Experiment Station, Vicksburg, Mississippi, June 1966

Taylor, G. I., "The Instability of Liquid Surfaces When Accelerated in a Direction Perpendicular to their Planes, Part I," *Proceedings of the Royal Society*, London, Volume A 201, pp. 192-196

U.S. Army Special Text 5-26, ADM Employment, U.S. Army Engineer School, Fort Belvoir, Virginia, November 1969

U.S. Standard Atmosphere, 1962, U.S. Committee on Extension to the Standard Atmosphere, available through the U.S. Government Printing Office, December 1962

U.S. Standard Atmosphere Supplements, 1966, U.S. Committee on Extension to the Standard Atmosphere, available through the U.S. Government Printing Office

Van Dorn, W. G., B. LeMéhaute, and L. Hwang, *Handbook of Explosion-Generated Water Waves, Vol. I – State of the Art*, Report No. TC-130, Tetra Tech, Inc., Pasadena, California, October 1968

[redacted]

Van Dorn, W. G., and W. S. Montgomery, *Water Waves from 10,000-lb High-Explosive Charges*, Final Report Operation HYDRA II-A, S10 63-20, Scripps Institution of Oceanography, La Jolla, California, 1 June 196[redacted]

Veletsos, A. S., and N. M. Newmark, *Effect of Inelastic Behavior on the Response of Simple Systems to Earthquake Motions*, Ill. U. SRS 219, University of Illinois, Urbana, Illinois, 1960[redacted]

Veletsos, A. S., and N. M. Newmark, *Response Spectra Approach to Behavior of Shock Isolation Systems*, Volume 2, Newmark, Hansen and Associates, Urbana, Illinois, June 1963[redacted]

Vulnerability Handbook for Hardened Installations, Volume I Revised, Response to Large-Yield Nuclear Weapons [redacted] Newmark, Hansen and Associates, Urbana, Illinois, 1965 [redacted]

Walter, D., *Explosion-Generated Wave Tests, Mono Lake, California, Ground and Aerial Photography*, URS 654-2, URS Corporation, Burlingame, California, January 1966 [redacted]

Whalin, R. W., and R. Kent, *Water Waves Produced by Impulsive Energy Sources (U), Part VI: Data Analysis* [redacted] NMC-ONR-62, National Marine Consultants, Anaheim, California, December 196[redacted]

Whalin, R. W., and D. J. Divoky, *Water Waves Generated by Shallow Water Explosions*, Report No. S-359, National Engineering Science Co., Pasadena, California, September 1966[redacted]

Wiegel, R. L., *Oceanographical Engineering*, Prentice Hall, 1964[redacted]

Wilton, C., K. Kaplan, and N. R. Wallace, *Study of Channeling of Air Blast Waves*, URS 170-19, DASA 1605, URS Corporation, Burlingame, California, December 1964 [redacted]

Young, G. A., *The Physics of the Base Surge*, NOLTR-64-103, U.S. Naval Ordnance Laboratory, White Oak, Silver Spring, Maryland, 17 June 1965[redacted]

Young, G. A., *Surface Phenomena of Underwater Nuclear Explosions* [redacted] NOLTR-63-111, DASA 1240-1(9), U.S. Naval Ordnance Laboratory, White Oak, Silver Spring, Maryland, 22 September 196[redacted]

Young, G. A., and B. W. Scott, *Explosion Debris Distributions Following Large Lithanol Underwater Explosions* [redacted] NOLTR-68-162, U.S. Naval Ordnance Laboratory, White Oak, Silver Spring, Maryland, 6 November 1968[redacted]

[redacted]

DTIC FILE COPY

DTIC ELECTE S 2 MAR 1989 D E

AD-A955 387

Chapter 3

THERMAL RADIATION PHENOMENA

Within a few seconds after the explosion a typical low altitude nuclear fireball emits about a third of the weapon yield as infrared, visible, and ultraviolet radiation (see Figure 4-1). This sudden pulse of thermal energy may damage any target that is susceptible to high temperatures. The damage may take many forms, but the effects that are most frequently of concern are fires that start as the result of ignition of thin combustible materials (e.g., paper or dried leaves) and injuries to personnel, in the form of burns.

The thermal pulse decays as the fireball fades, but there is no specific time that marks the end of the thermal radiation from the fireball. At late times, as the radioactive cloud rises, the heated air in the nuclear cloud still radiates some thermal energy; however, this radiant energy is released so slowly that it has little military importance. Therefore, in this chapter, the terms "thermal radiation phenomena," "thermal effects," and "thermal pulse" only pertain to that portion of the radiated energy that could be termed the "prompt thermal pulse."

This restriction in the meanings of terms such as "thermal effects" excludes a number of nuclear burst phenomena that are thermal in the broader sense. For example, fireball rise is a thermal effect; the fireball is buoyant for the same reason that a hot-air balloon is buoyant. Another effect that properly could be termed thermal is the radiation of X-ray energy by the nuclear source. The X-ray energy is the thermal radiation that is characteristic of an extremely high temperature source (see Chapter 4). In many situations, e.g., low altitude bursts, this radiation has no direct effect on targets, because it is absorbed by air close to the source. In other situations, notably aerospace vehicles exposed to high altitude detonations, this X-ray energy becomes one of the most important direct damage mechanisms. This damage mechanism is discussed in Section V, Chapter 9.

RADIANT EXPOSURE

Four variables determine the effects of the thermal pulse on a target:

- The amount of energy that is incident on the target.
- The time history of the thermal pulse.
- The spectral distribution of the radiant energy.
- The directional characteristics of the incident radiation, e.g., does it come directly from the source, or is it scattered and therefore arrives from many directions.

In most cases of military interest the first of the variables is dominant. A careful analysis cannot ignore the other three, but a *preliminary* evaluation of a thermal environment, for example, a calculation to determine whether a thermal problem exists, often can be based on the total energy received.

The energy delivered by the thermal pulse usually is specified in terms of *radiant exposure*, the energy per unit area incident on the target surface. It is denoted by the symbol Q and is conventionally measured in units of calories per square centimeter (cal/cm^2). The factors that affect the radiant exposure are discussed separately in the following paragraphs.

This document has been approved for public release and sale; its distribution is unlimited.

89 3 02 046

[redacted]

3-1 Thermal Partition [redacted]

[redacted] The ratio of the thermal energy radiated by the fireball of a nuclear explosion to the total yield is *thermal partition* (sometimes called *thermal efficiency*), denoted by the symbol f. For burst altitudes below 100,000 feet and yields between 1 kt and 10 Mt, values of thermal partition may be determined from Figure 3-1. For higher burst altitudes, thermal partition must be determined by the method described in paragraph 3-19. If the burst is below $180W^{0.4}$ feet (where W is the yield in kilotons), it is classed as a surface burst and the thermal partition should be determined by the method described in paragraph 3-9.

[redacted]

[redacted]

DNA 6(X3)

Accession For	
NTIS GRA&I	☒
DTIC TAB	☐
Unannounced	☐
Justification	per telecon
By	
Distribution/	
Availability Codes	
Dist	Avail and/or Special
A-1	

QUALITY INSPECTED 4

UNANNOUNCED

[redacted]

[redacted]

Problem 3-1. Calculation of Thermal Partition

[redacted] Figure 3-1 contains a family of curves that show the thermal partition as a function of yield and height of burst. The data in Figure 3-1 apply to yields between 1 kt and 10 Mt and to burst altitudes from $180W^{0.4}$ feet (where W is the yield in kt) to 100,000 feet.

[redacted] *Example* [redacted]

Given: A 10 Mt explosion at an altitude of 39,000 feet.

Find: The thermal energy that is radiated.

Solution: From Figure 3-1, the thermal partition is [redacted]

Answer: The thermal energy radiated is [redacted]

[redacted]

[redacted] *Reliability* [redacted]

[redacted] The shapes of the contour lines in Figure 3-1, and the precision with which values may be read from these lines suggest clearly established relations between yield, altitude, and thermal partition; however, the contour lines were obtained by fitting curves to the results of computer code calculations. Although many aspects of the computed results have been compared to experimental data, and the comparisons were favorable, the thermal partitions that the code predicts have not been confirmed definitely.

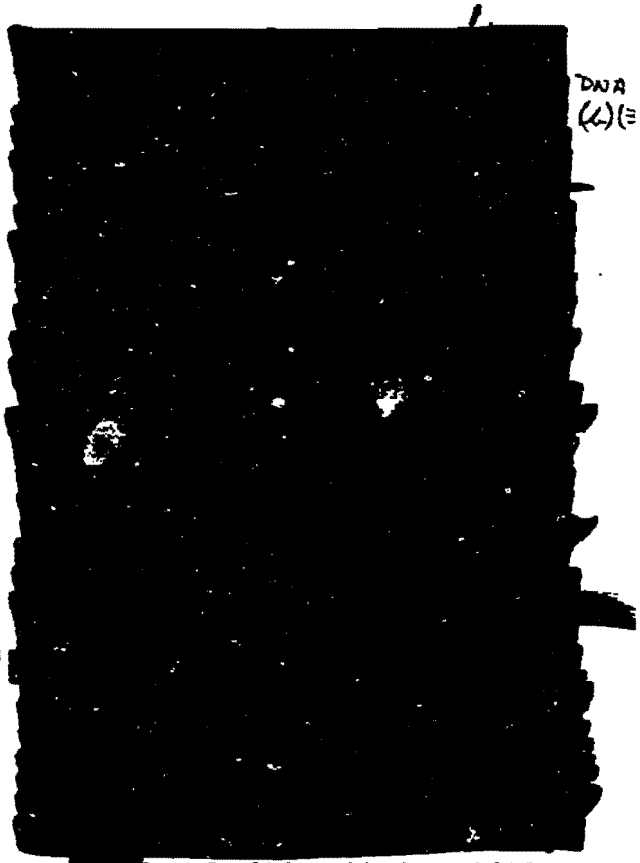

[redacted] Data for higher altitudes and higher yields are discussed in paragraph 3-19; data for surface bursts are described in paragraph 3-9, and data for special types of weapons are described in paragraph 3-17.

[redacted] *Related Material:* See paragraph 3-1. See also paragraphs 3-9 and 3-19.

Page 3-4 deleted.

[redacted]

3-2 Range Effects

As the thermal energy propagates away from the fireball, the divergence that results from the increasing area through which it passes causes the radiant exposure to decrease as the inverse square of the slant range. At a slant range R centimeters from the source, the thermal energy is distributed over a spherical area of $4\pi R^2$. Since the thermal yield in calories is 10^{12} Wf*, where W is the yield in kilotons, the radiant exposure at a distance R cm in a clear atmosphere is

$$Q = \frac{10^{12} Wf}{4\pi R^2} \text{ cal/cm}^2.$$

Kilofeet and kilometers are more convenient units than centimeters for measuring the range from a nuclear burst. Appropriate conversion factors change the form of the equation to

$$Q = \frac{100\ Wf}{4\pi R_{km}^2} = 7.96\ Wf/R_{km}^2 \text{ cal/cm}^2,$$

and

$$Q = 85.7\ Wf/R_{kft}^2 \text{ cal/cm}^2,$$

where R_{km} and R_{kft} are slant ranges in kilometers and kilofeet, respectively.

TRANSMITTANCE

The equations presented above ignored the attenuation by the atmosphere that would affect the thermal energy received by a target. In many cases, particularly when the air is clear and the range is short, atmospheric attenuation is not important. In other situations, scattering and absorption of thermal energy by the atmosphere can reduce the amount of thermal energy reaching the target significantly.

In addition to atmospheric attenuation, other effects also must be considered. A cloud layer above a fireball can scatter radiation downward and can increase the thermal energy that reaches the ground. If the ground also is highly reflecting, e.g., if the ground is covered by a layer of snow, further enhancement of the thermal radiation may result.

All of these effects are approximated by one factor, the transmittance T. Transmittance is the ratio of the radiant exposure at a target facing the fireball to the radiant exposure that the target would receive if the intervening atmosphere were perfectly transparent.

Adding the transmittance factor to the equations given in paragraph 3-2 gives

$$Q = \frac{7.96\ WfT}{R_{km}^2} \text{ cal/cm}^2,$$

and

$$Q = \frac{85.7\ WfT}{R_{kft}^2} \text{ cal/cm}^2.$$

The corresponding expressions for slant range in terms of yield and transmittance are†

$$R_{km} = 2.82\ \sqrt{WfT/Q}$$

$$R_{kft} = 9.26\ \sqrt{WfT/Q}$$

3-3 Specification of Transmittance

A difficult task in applying transmittance data to a thermal problem is deciding which model atmosphere to use. Various model

---

* One kiloton equals 10^{12} calories (see Table 1-2).

† A relationship that is easy to remember and that is reasonably correct if it is assumed that the thermal partition, $f = 1/3$, and the transmittance, $T = 1.0$, is that the radiant exposure at one statute mile is about $Q = 1$ cal/cm^2 per kt.

[redacted]

atmospheres are identified in terms of parameters that can be measured without special instruments. The first of these is visual range, a parameter that indicates the light transmission properties of the layer of air near the surface. A second is the appearance of the sky, which can be used to indicate the amount of haze or fog that thermal radiation from a high altitude burst must penetrate to reach a target at the surface.

[redacted] Although transmittance can be calculated between any two points in space, a large number of thermal problems involve ground targets. The material presented in this paragraph has been developed primarily to calculate transmittance between the point of burst and a target on the ground. These methods may be extended to calculate transmittance to airborne targets, but the validity of such calculations has not been checked as carefully as has the validity of transmittance calculations for ground targets.

[redacted] Whether or not a particular transmittance calculation is useful depends on the nature of the problem. If the burst is a specific test, the weather at the particular time can be determined, and appropriate transmittances can be assigned. If the burst involves a hypothetical attack at some unknown date, a reliable prediction of the transmittance, and, as a result, the extent of the thermal damage from a particular explosion, is impossible. The atmosphere could be clear or foggy; light combustibles such as leaves or paper could be wet or dry. Yield and position of the weapon are unknown and can only be estimated.

[redacted] Two types of problems provide answers that are sufficiently reliable to be useful. A calculation intended to be conservative from the point of view of the defense indicates the level of damage that an explosion could inflict on a day when the air is clear and the ground is dry. This type of calculation is useful for designating safe areas or designing defense systems. Useful answers also can be obtained in tactical situations. The minimum intercept altitude of a defensive missile might be lowered on a foggy day, and an attacking force might use current weather conditions to determine whether their weapon would produce significant thermal damage or whether they must rely primarily on other effects.

3-4 Model Atmospheres [redacted]

[redacted] The typical cloudless atmosphere has a haze layer near the surface. Often this haze layer is relatively uniform, with a sharply defined upper boundary; when cumulus clouds are present, the bases of these clouds may mark the top of the haze layer.

[redacted] At higher altitudes, the air usually is clearer, and, in the absence of clouds, about 80 percent of the attenuation of radiation from a high altitude source occurs at altitudes below 3 miles. The low density air several miles above the surface offers almost no interference to radiation in the visible and infrared regions of the spectrum.

[redacted] A set of cloudless model atmospheres provides an approximate representation of the optical properties of real atmospheres. These models only represent the atmosphere in a general way, but they form a basis for transmittance calculations. They have the advantage that selection of the appropriate model is based on the simple criterion of daytime visual range. The model atmospheres are cloudless; correction factors introduced into the transmittance calculations account for the effects of clouds. These model atmospheres and the empirical equations that are used with them give reasonably accurate estimates of transmittance if the transmittance is above about 0.1.

[redacted] Current reports consistently use visibility, which is called "visual range" in this chapter, as one means for classifying model atmospheres; however, no standard definition of visibility is adopted consistently. The atmo-

[redacted]

sphere described in this chapter as having a visual range of 16 miles would be assigned a visibility of 12 miles by at least one author and a visibility of 24 miles by some others.

The extent to which the atmosphere impedes the flow of thermal energy and limits visibility depends largely on the amount of scattering of radiant energy by atmospheric particles. Absorption of energy also affects radiative transport, but absorption usually is less important than scattering. A description of these phenomena is the first step in explaining visual range and transmittance.

The thermal radiation of concern in this chapter consists of electromagnetic radiations from the ultraviolet to the infrared. The photons that make up electromagnetic radiations can react with matter in many complex ways, but the photons that constitute the thermal radiation spectrum of a nuclear fireball interact almost exclusively by being absorbed or elastically scattered. If the photon is absorbed, it gives up its energy to the absorbing particle, and this energy ultimately appears as heat. Scattering may be thought of as reflection from a small particle. Its effect is to change the direction in which the photon is traveling. The term "elastic" means that the photon does not lose energy during the scattering process. Other interactions of electromagnetic radiations with matter that are more probable for higher frequency (shorter wavelength) radiations than those of the thermal radiation are described in paragraph 4-3, Chapter 4.

The scattering and absorption properties of the atmosphere depend partly on the wavelength of the radiant energy. Wavelength is often measured in microns (1 micron = 10^{-6} meter), for which the symbol is μ. Wavelengths in the visible spectrum may be identified by the relation between wavelength and color: light with a wavelength of 0.7 μ is red; 0.58 μ light is yellow; and 0.48 μ light is blue. White light is a mixture containing all wavelengths in the visible spectrum, which extends from 0.38 to 0.78 μ. The infrared spectrum consists of radiant energy at wavelengths longer than 0.78 μ, and the ultraviolet spectrum consists of radiant energy at wavelengths shorter than 0.38 μ.

The energy transport properties of atmospheric particles may be expressed in terms of scattering and absorption cross sections, which are fictitious areas that are a measure of the probability that scattering or absorption will occur. Particles that are small compared to the wavelength of light have scattering cross sections that are inversely proportional to the fourth power of the wavelength. Therefore, air molecules scatter light from the extreme blue end of the visible spectrum (wavelength = 0.38 μ) about 16 times as effectively as they scatter light from the red end of the spectrum (wavelength = 0.78 μ). Blue smoke, which consists of very small particles, has similar scattering properties. Particles that are large compared to the wavelength of light (e.g., haze or fog particles) have scattering cross sections that are much less dependent on wavelength. Individual particles have a scattering cross section that varies somewhat with wavelength, but the mixture of particle sizes found in a haze or fog usually results in an average cross section that is nearly independent of wavelength.

The sky is blue because most of the scattering at high altitudes is by air molecules, which scatter blue light more efficiently than they scatter other colors of the visible spectrum. A distant mountain appears blue on a clear day for the same reason.

The scattering properties of larger airborne particles may be observed on days when a very light haze reduces visibility to about 10 miles or less. Near the surface, scattering by haze particles contributes more to the light in the air than does scattering by air molecules. The sky still appears blue, but the color is not as deep as

[redacted]

it would be on a clearer day. Distant hills and the sky near the horizon appear to be more gray than blue, which indicates that the lower atmosphere is scattering all wavelengths of light about equally.

[redacted] Water droplets cause nearly all of the scattering that occurs in a fog or a thick cloud. Consequently, clouds are white and fogs tend to wash out all impressions of color.

[redacted] Absorption usually has little effect on visible light, but it can affect the infrared and ultraviolet portions of the spectrum significantly. The principal absorber of thermal energy usually is water vapor, which has strong absorption bands in the infrared spectrum. Dry air transmits infrared energy more efficiently than humid air. Carbon dioxide and other gases present in the atmosphere in small amounts also absorb infrared energy.

[redacted] Ultraviolet energy is absorbed most strongly at the shorter wavelengths: the limiting wavelength that air in the lower atmosphere will transmit is about 0.2 micron. Ozone, appreciable quantities of which are found between roughly 60,000 and 80,000 feet, absorbs ultraviolet radiation with wavelengths shorter than 0.29 micron. As a result of these absorption bands ultraviolet energy that reaches the earth from the sun is almost entirely limited to the spectral band between 0.38 micron (the violet edge of the visible spectrum) and 0.29 micron.

[redacted] Dark colored particles absorb appreciable energy in all regions of the thermal spectrum. Dust, smoke, and the smoky haze from large cities fall into this category.

[redacted] Detailed calculations of the complex scattering and absorption processes that can occur between a nuclear explosion and a target require computer codes that are capable of considering detailed changes in the atmosphere and the effect that these changes can have on the entire spectrum of frequencies emitted by the fireball. Monte Carlo calculations have been performed for several model atmospheres and for several discrete wavelengths; however, as of this time, these calculations have not been generalized into a form that is suitable for inclusion in this manual. Therefore, the formulas and curves for atmospheric transmittance that are given below are based on a simplified model based on the concept of effective optical height for single wavelengths.

[redacted] One way to specify the attenuating properties of the atmosphere as a function of altitude is to assume that the transmittance between the point of burst and ground zero follows an equation of the form

$$T = e^{-\tau(h)},$$

where T is transmittance and $\tau(h)$ is the *effective optical height* of the burst height h. This concept was applied in 1966 to specify one particular model atmosphere for which the visual range is 16 miles.* The attenuation for light of 0.65 micron wavelength was used to specify $\tau(h)$. This choice was a purely empirical one, used because it brought the calculated values of transmittance into general agreement with experimentally determined values. The wavelength that was selected is attenuated less than is the thermal radiation spectrum as a whole;

*[redacted] "Transmissivity of the Atmosphere for Thermal Radiation from Nuclear Weapons" (see bibliography). A 12 mile visual range was assigned to this model atmosphere. This choice was based on a comparison between a large number of visual range estimates at an airport weather station and simultaneous measurements with instruments designed to measure meteorological range. The 16 mile figure is used here because it is consistent with the definition of visual range given in this chapter. Qualitatively, this range is defined as the distance at which a dark object silhouetted against the sky is visible and recognizable. This range is more specifically defined in paragraph 3-7.

[redacted] Although the specification for this model atmosphere has been changed, the reason for having assigned the 12 mile figure carries a useful warning. There is no assurance that even trained meteorologists will make estimates that are consistent with a precise mathematical definition of visual range.

[redacted]

[redacted]

[redacted]

therefore, this choice makes allowance for additional energy that reaches the target by scattering. For bursts below one-quarter mile and surface targets, a wavelength of 0.55 microns was used together with a buildup factor, as described below.

[redacted] Figure 3-2 shows $\tau(h)$ as a function of altitude for this particular model atmosphere. This model shows no attempt to represent an abrupt increase in transparency at the top of the haze layer; optical height is a smoothly varying function of altitude. This approximation to the actual atmosphere does not appear to introduce serious error into the calculations, and it is more convenient then a model atmosphere that requires an estimate of the height of the haze layer as well as an estimate of visual range.

[redacted] When visual range is different from 16 miles, the model atmosphere is specified by multiplying the values of effective optical height in Figure 3-2 by $16/V$, where V is visual range in miles. For example, if the visibility is 8 miles, all values of optical height are doubled, indicating that transparency at all altitudes is reduced by a factor of 2. This transformation may be stated mathematically as

$$\tau(h)_V = \tau(h)_{16} \frac{16}{V}$$

where $\tau(h)_V$ is the effective optical height at a given altitude for the model atmosphere for which visual range is V and $\tau(h)_{16}$ is the effective optical height of the 16 mile model atmosphere at the same altitude.

[redacted] Visual range, a surface measurement, is a poor criterion for predicting the clarity of the air a few miles up. Although there is some correlation between these two quantities, the main justification for this somewhat arbitrary procedure is that the optical thickness assigned to the upper atmosphere, since it is a small fraction of the total optical thickness, has little influence on the calculated transmittance to targets on the ground.

[redacted] If the burst height is less than about one-quarter mile, the line-of-sight path from the burst to the target passes through air which, in most cases, has optical properties that are fairly uniform. In a uniform atmosphere, the attenuation of a direct beam of thermal energy may be related to the visibility of distant objects by the equation.

$$T_d = e^{-2.9\ R/V},$$

where T_d is the transmission coefficient for *direct* flux over a path of slant range R, and V is visual range. As mentioned above, scattered as well as direct flux must be considered. Consequently, transmittance is larger than the transmission coefficient for direct flux and is given approximately by the following empirical equation:

$$T = e^{-2.9\ R/V}\ (1 + 1.9\ R/V).$$

[redacted] The exponential factor in this equation accounts for energy loss from the direct beam by scattering. The expression in brackets is a buildup factor that accounts for energy scattered toward the target. This equation does not specifically involve any property of the model atmosphere other than visual range; however, the properties of the model atmosphere are involved implicitly, because the rate at which transparency changes with altitude helps determine the magnitude of the coefficient 1.9 in the buildup factor. Figure 3-3 shows this relation in graphical form.

[redacted] When the burst height h is greater than about one-quarter mile, transmittance may be calculated from

$$T = e^{-\tau(h)\ \frac{16}{V}\ \frac{R}{h}}$$

[redacted]

[redacted]

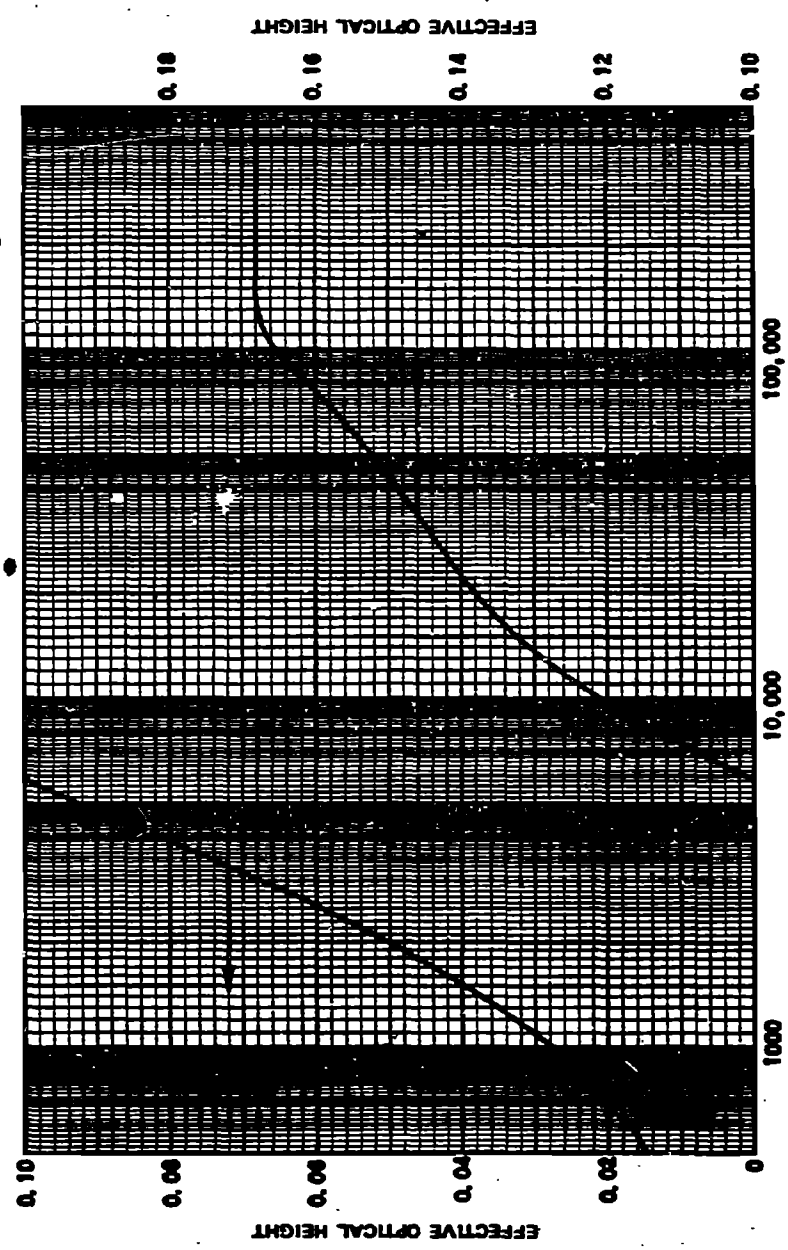

Figure 3-2. [redacted] Effective Height of Model Atmosphere (Visual Range = 10 Miles)

[redacted]

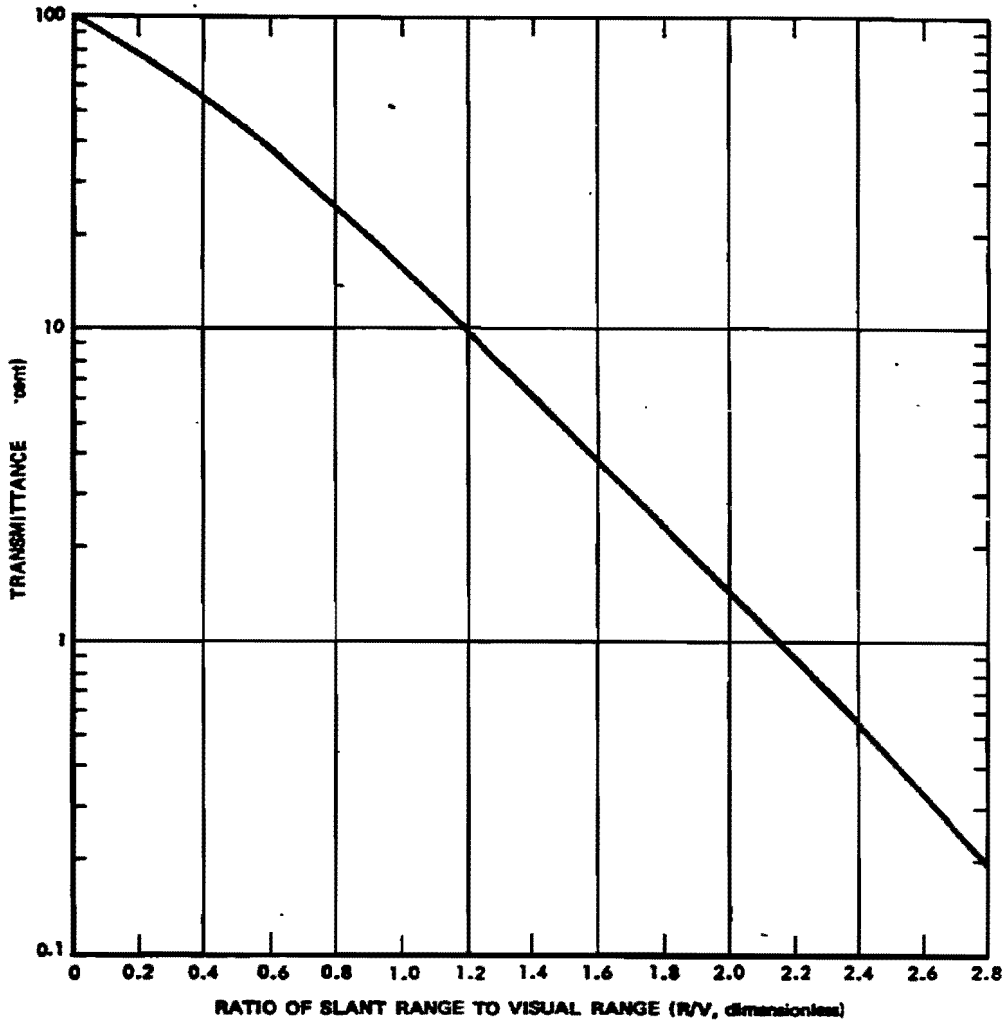

Figure 3-3. [redacted] Transmittance Between a Burst Within 1/4 Mile of the Surface and a Target on the Ground [redacted]

where $\tau(h)$ (from Figure 3-2) is the effective optical height of the model atmosphere with 16 mile visual range, and $\tau(h)\ 16/V$ is the effective optical height in the model atmosphere for which visual range is V. The factor R/h converts effective optical height to the effective optical distance measured along the slant path of length R, where h is the height of burst.

The two equations just given are for cloudless (but not necessarily clear) atmospheres. The effects of cloud layers are considered later in this subsection.

Height-of-burst curves provide a convenient means for applying these transmittance equations to thermal effects calculations. Figures 3-4 through 3-14 are a series of such curves.

The height-of-burst curves do not show transmittance data for bursts above 100,000 feet (with the exception of Figure 3-13a). Transmittance above this altitude depends only on elevation angle. If the burst is above 130 kilofeet, the transmittance is independent of altitude, and the contours become straight lines. This is illustrated for a 16 mile visual range in Figure 3-13a, in which the height of burst is extended to 250,000 feet. As mentioned above, these curves are based on two empirical equations, one of which applies when the burst height exceeds one-quarter mile (1.32 kilofeet) and the other of which applies to lower bursts. The discontinuities that occur where these two families of curves meet has no particular significance other than to suggest the degree of uncertainty inherent in any transmittance data. The discontinuities have been allowed to remain; joining the contour lines would produce shapes that may have no physical basis (for example, the curves should not be interpreted to imply that for short ground ranges the optimum burst height for thermal effects on the ground is necessarily below 1/4 mile).

[redacted]

Problem 3-2. Calculation of Radiant Exposure

[redacted] Figures 3-4 through 3-14 show atmospheric transmittance as a function of height of burst and ground distance for various visual ranges. These curves, together with the equations given in paragraph 3-2 allow the calculation of radiant exposure for a variety of circumstances.

[redacted] For bursts above one-fourth mile height of burst, interpolation between the figures (to obtain data for visual ranges other than those for which curves are provided) may be accomplished as follows:

$$T_2 = T_1^{\,V_1/V_2}$$

where T_1 is the label of a given contour line on a figure for a visual range of V_1 and T_2 is the label that this same curve would have if the figure were for a visual range of V_2. If the height of burst is below one-fourth mile, the transmittance may be obtained from Figure 3-3 for any combination of slant range and visual range.

[redacted] *Example 1* [redacted]:

Given: A 5 kt nuclear warhead is being considered for a defensive missile warhead.

Find: The minimum burst altitude such that the radiant exposure on the ground will not exceed 1 cal/cm^2.

DNA (6)(3)

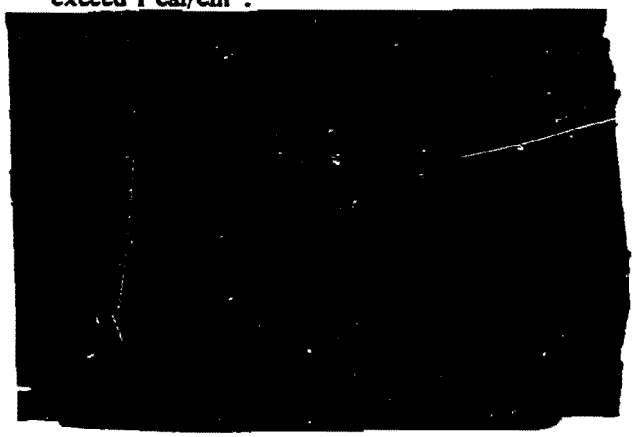

DNA (6)(3)

[redacted] *Example 2* [redacted]

Given: A 100 kt explosion at an altitude of 10,000 feet at a location where the visual range is 16 miles.

Find: The thermal radiant energy incident on a target at a ground distance of 9,000 feet from ground zero.

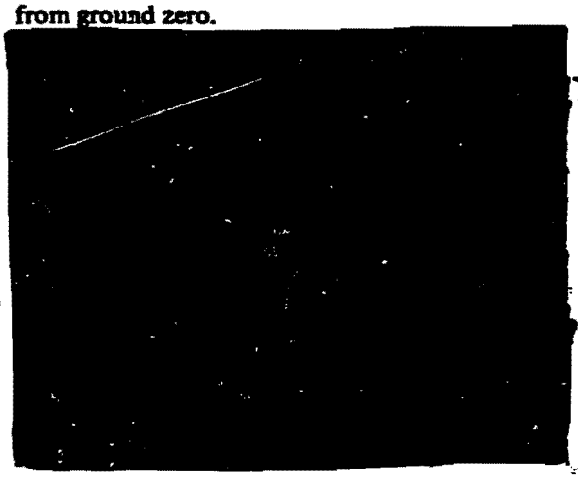

DNA (4)(

[redacted]

[redacted]

Reliability: The calculated transmittances exceeding 0.1 are believed to be correct to ±30 percent; however, this tolerance is seldom required in practical problems. When transmittance exceeds 0.1, the product fT is believed to be within the range obtained by setting upper and lower limits on f as specified in "Reliability" in Problem 3-1. The reliability of transmittance calculations decreases as transmittance decreases. Transmittances below 0.1 are very uncertain, and errors that amount to a factor of 2 to 10 are not unusual. When correction factors for reflecting surfaces are required, an additional tolerance of ±30 percent should be applied to the fT product.

Related Material: See paragraphs 3-2 through 3-6.

[redacted]

[redacted]

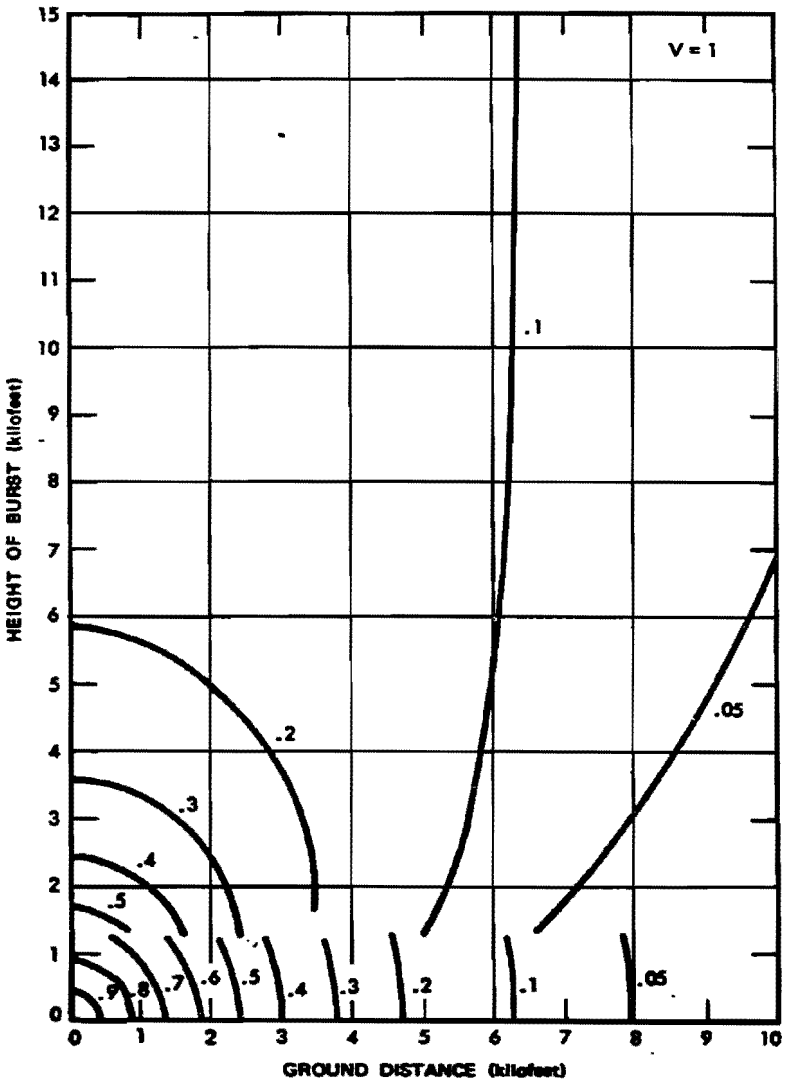

Figure 3-4. [redacted] Transmittance to a Target on the Ground on a Clear Day (Visual Range = 1 Mile) [redacted]

[redacted]

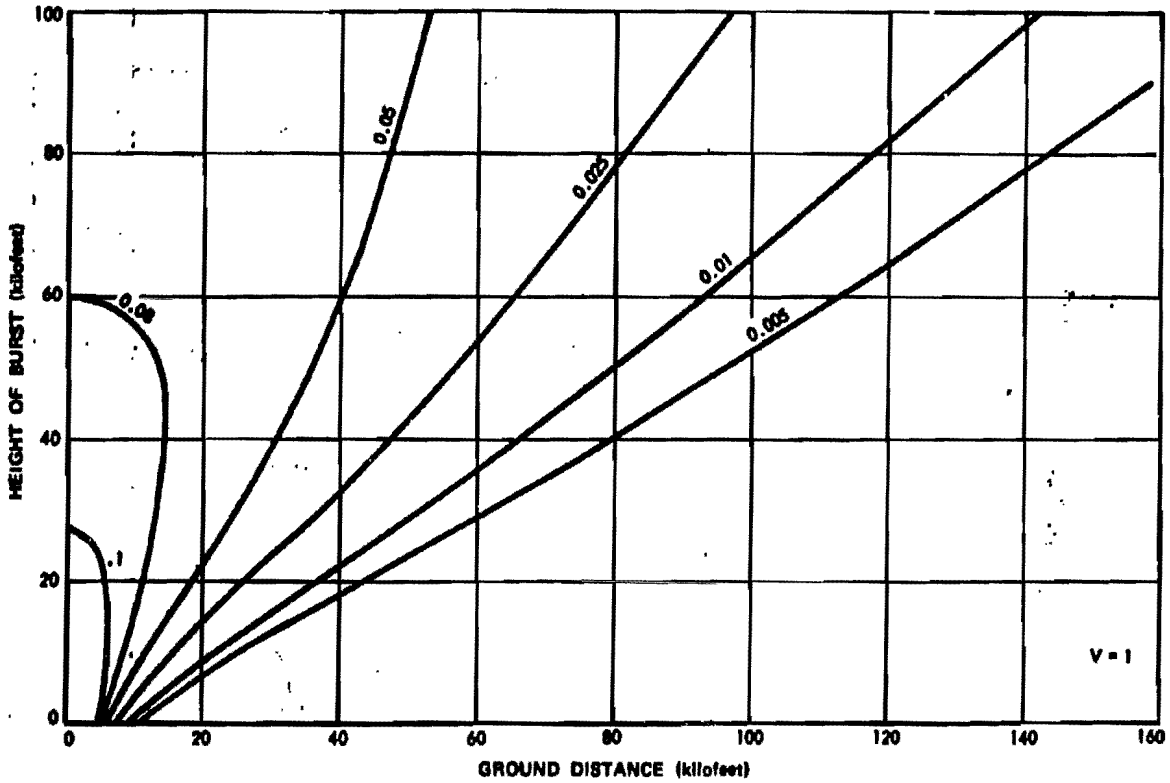

Figure 3-5. [redacted] Transmittance to a Target on the Ground on a Clear Day (Visual Range = 1 Mile) [redacted]

[redacted]

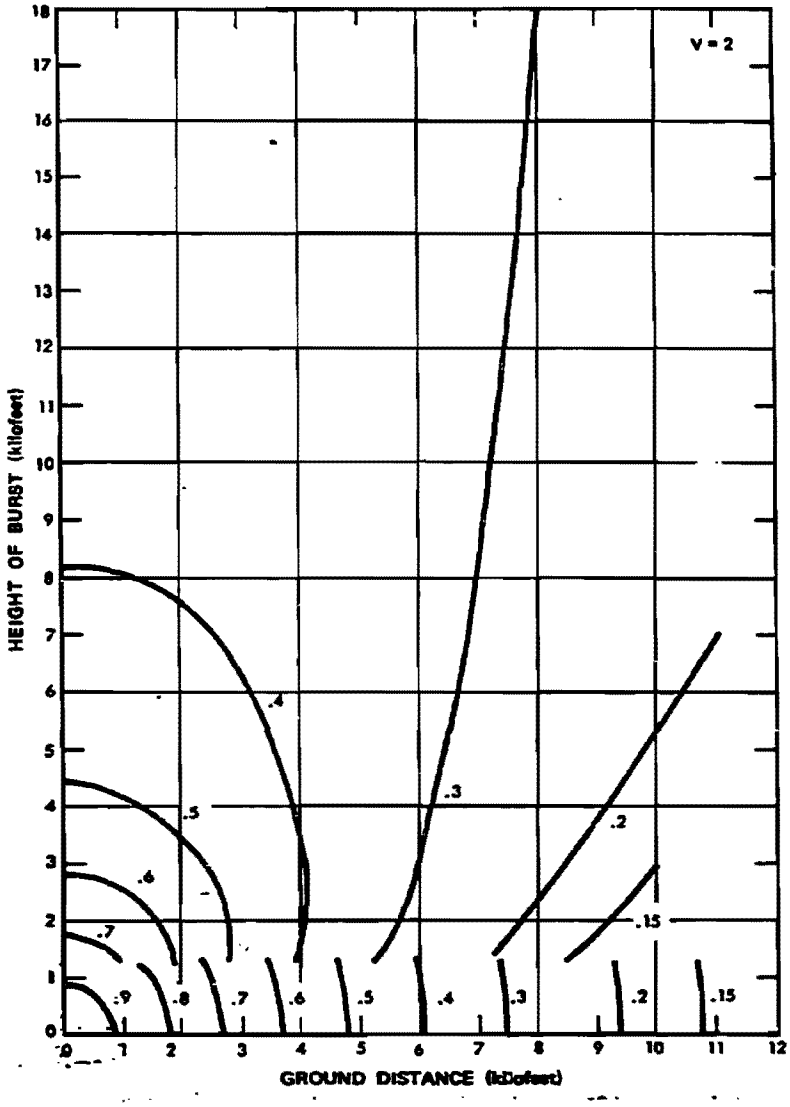

Figure 3-6. [redacted] Transmittance to a Target on the Ground on a Clear Day (Visual Range = 2 Miles) [redacted]

[redacted]

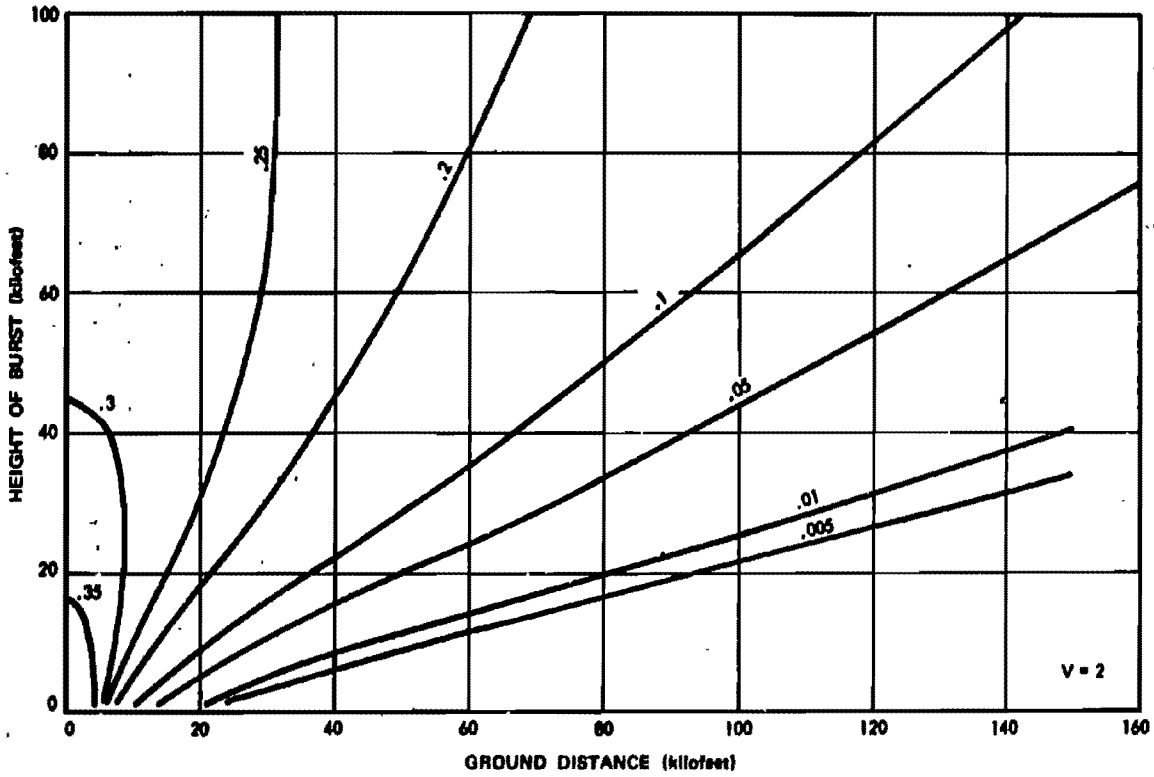

Figure 3-7. [redacted] Transmittance to a Target on the Ground on a Clear Day (Visual Range = 2 Miles) [redacted]

[redacted]

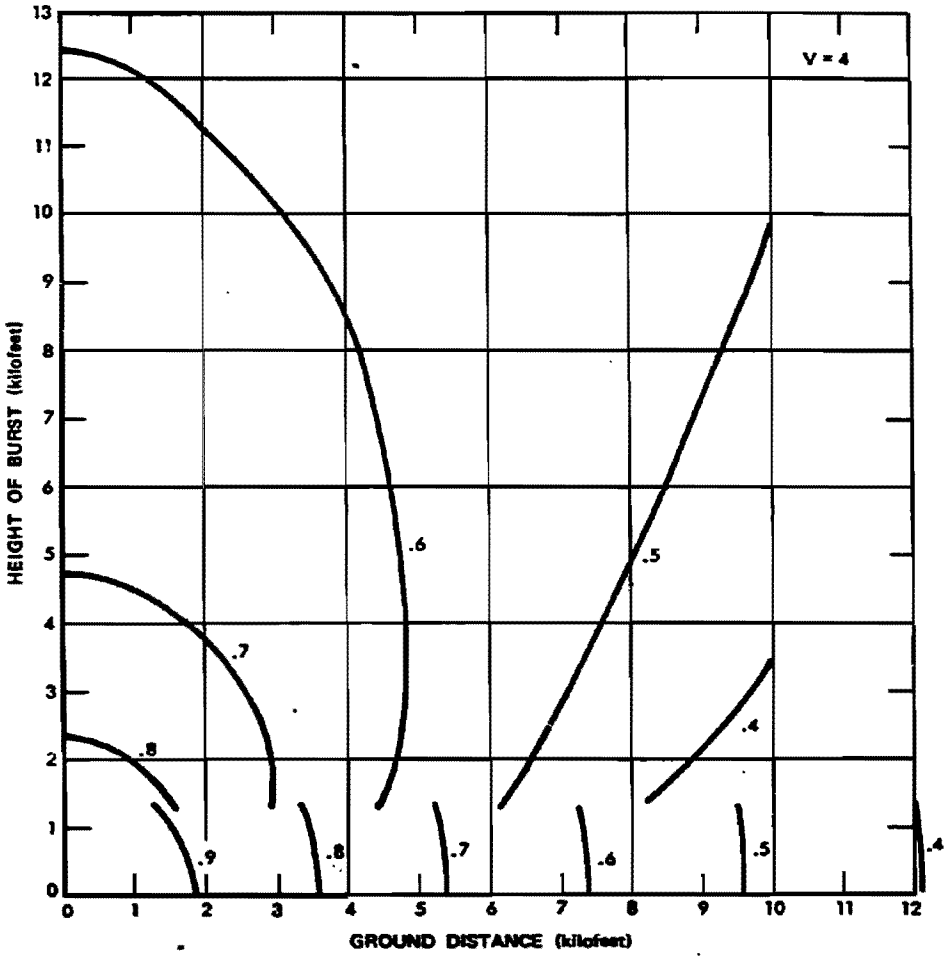

Figure 3-8. [redacted] Transmittance to a Target on the Ground on a Clear Day (Visual Range = 4 Miles) [redacted]

[redacted]

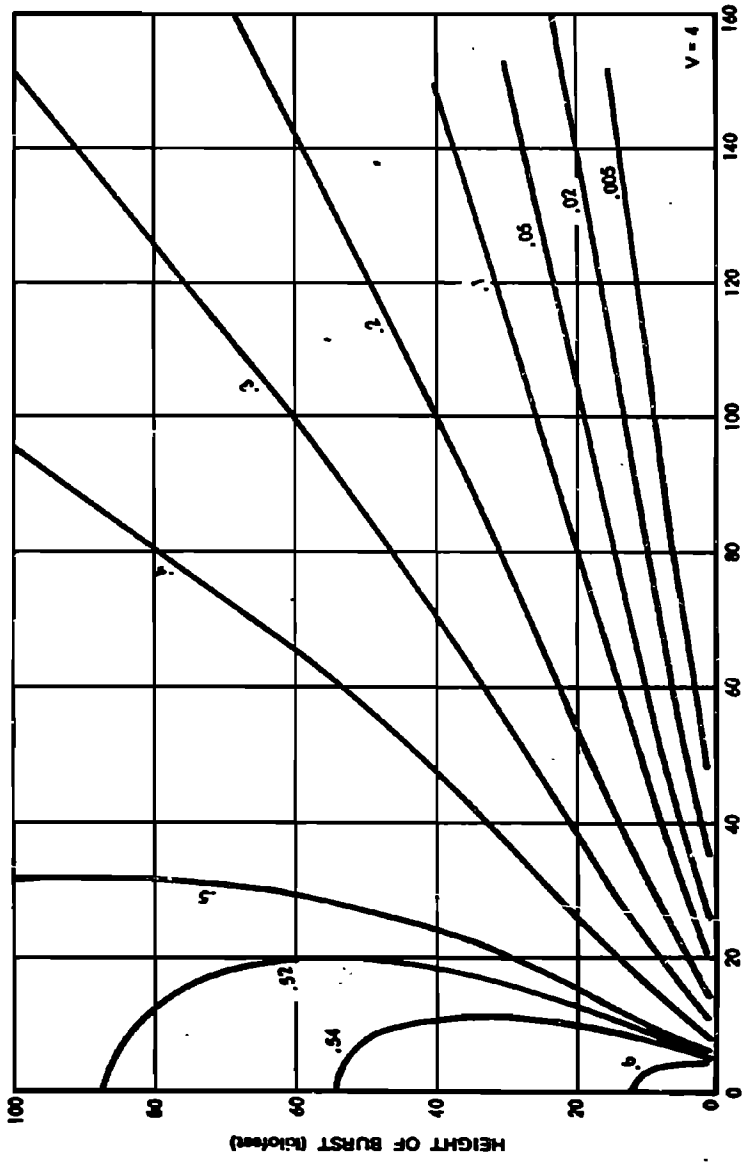

Figure 3-9. [redacted] Transmittance to a Target on the Ground on a Clear Day (Visual Range = 4 Miles)

[redacted]

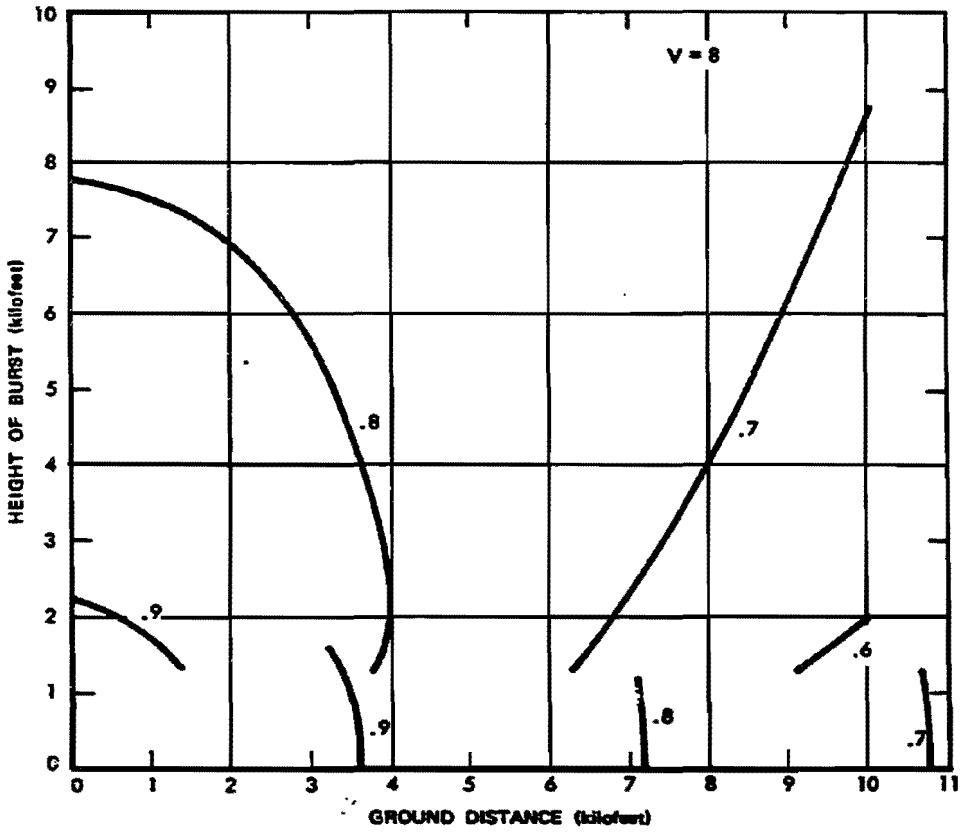

Figure 3-10. [redacted] Transmittance to a Target on the Ground on a Clear Day (Visual Range = 8 Miles) [redacted]

[redacted]

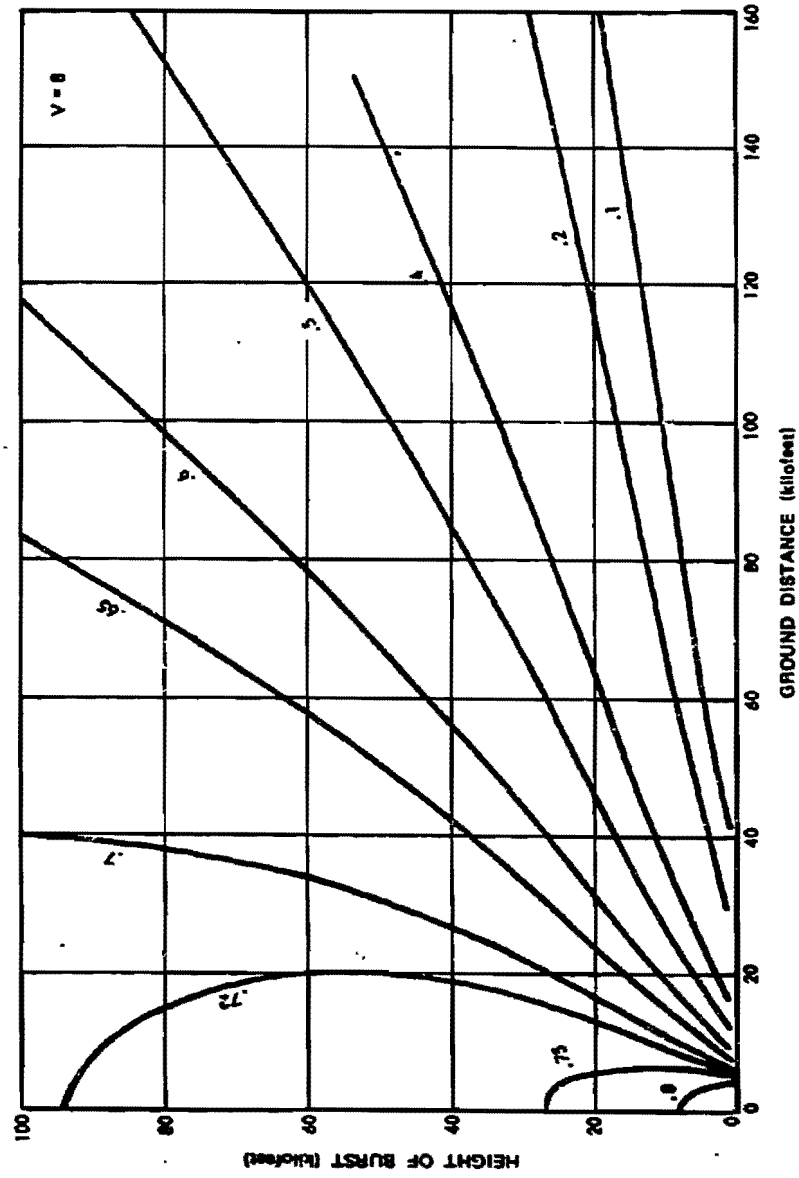

Figure 3-11. [redacted] Transmittance to a Target on the Ground on a Clear Day (Visual Range = 8 Miles) [redacted]

[redacted]

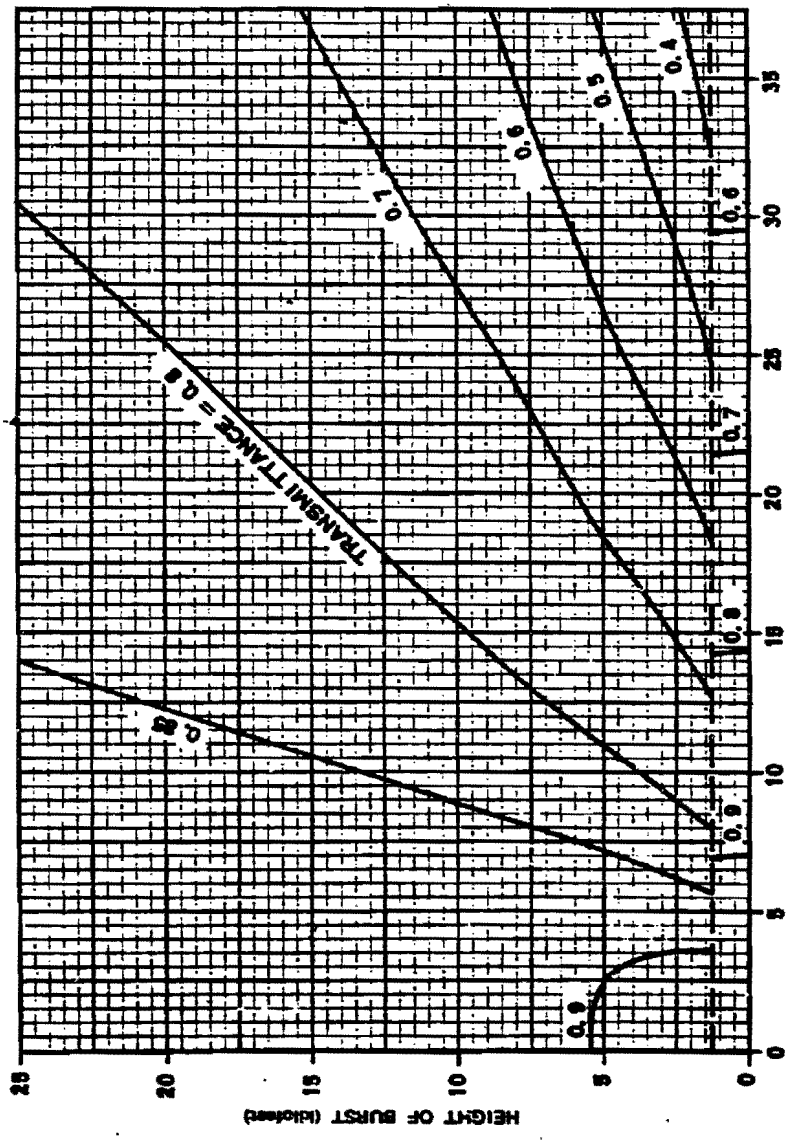

Figure 3-12. [redacted] Transmittance to a Target on the Ground on a Clear Day (Visual Range = 16 Miles)

[redacted]

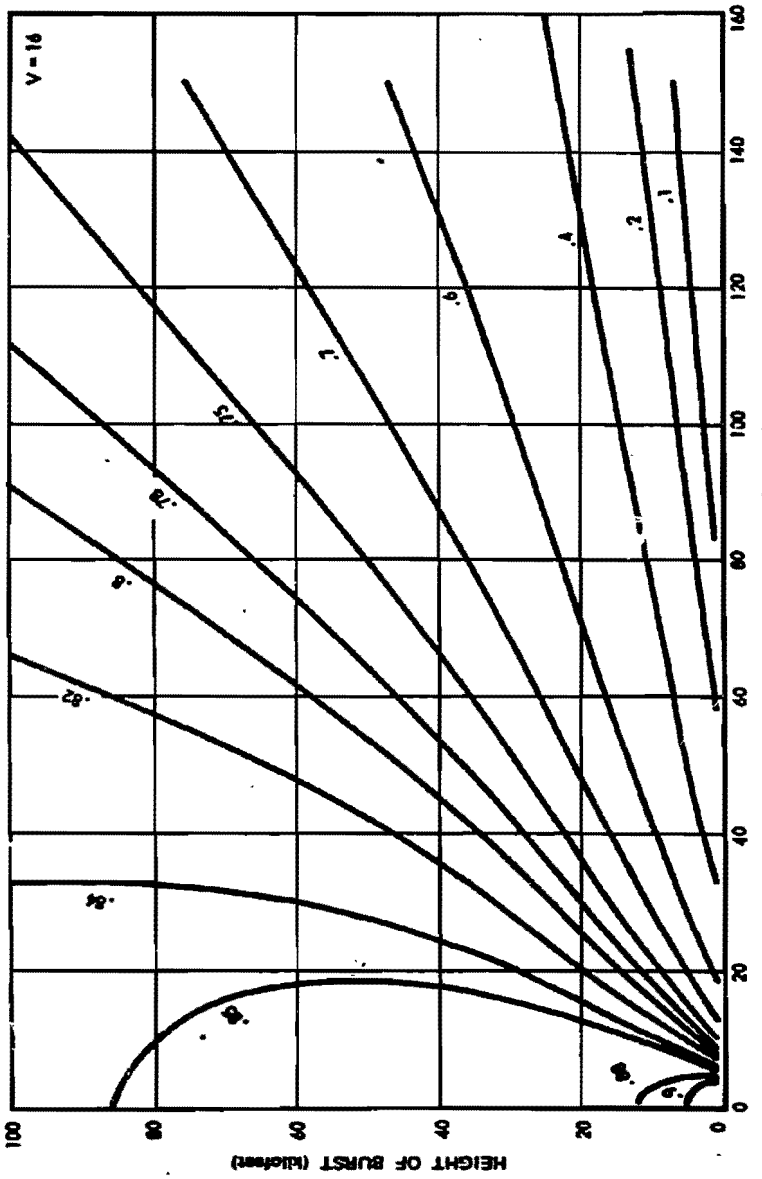

Figure 3-13. [redacted] Transmittance to a Target on the Ground on a Clear Day (Visual Range = 16 Miles)

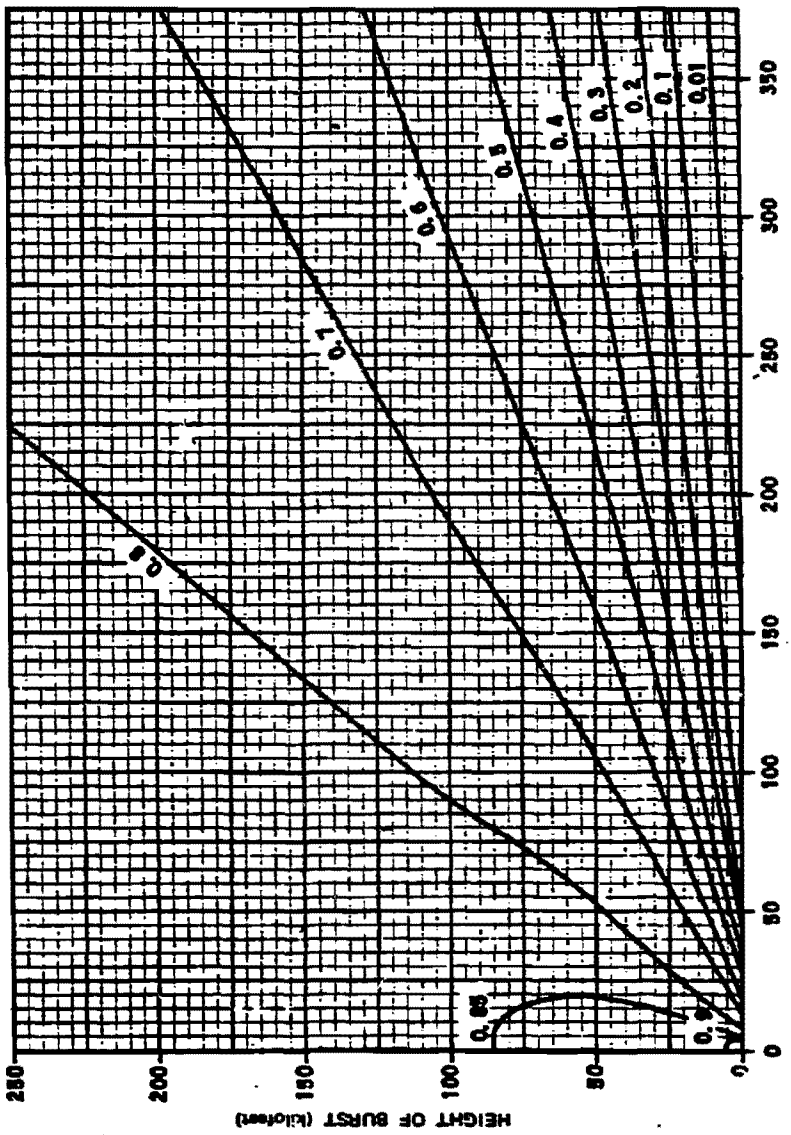

Figure 3-13a. [redacted] Transmittance to a Target on the Ground on a Clear Day (Visual Range = 18 Miles)

[redacted]

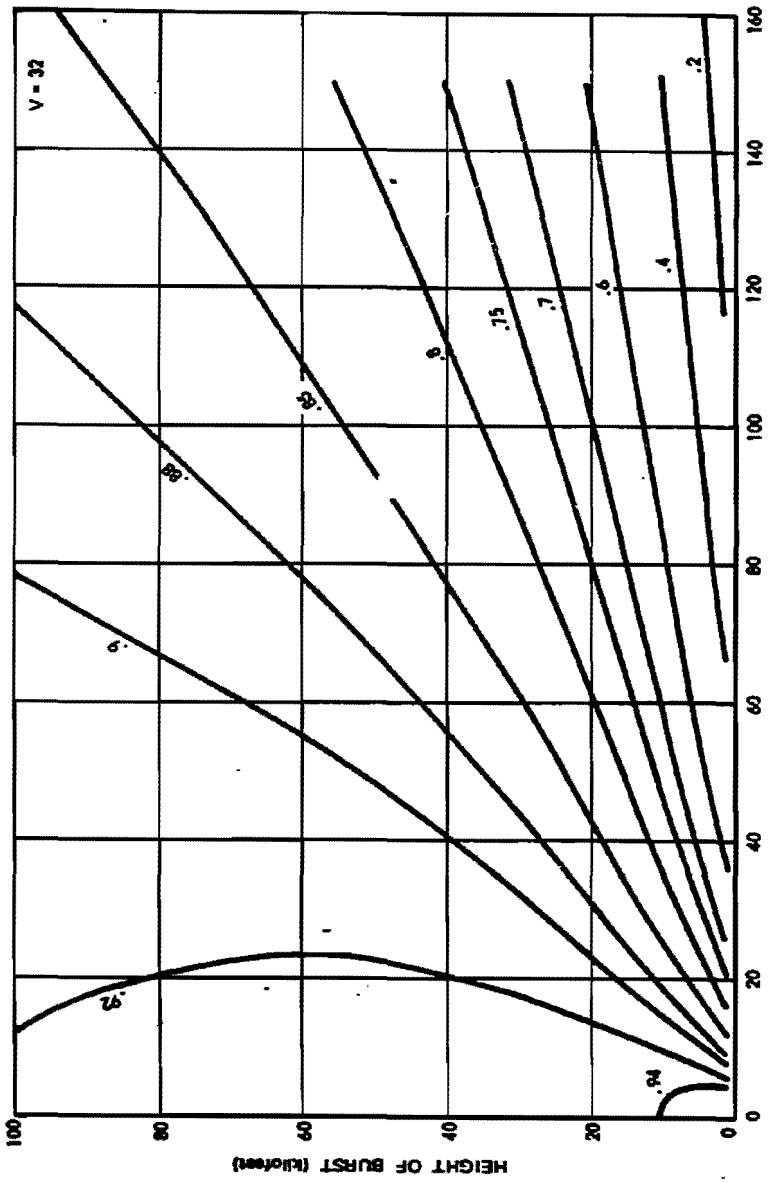

Figure 3-14. [redacted] Transmittance to a Target on the Ground on a Clear Day (Visual Range = 32 Miles) [redacted]

[redacted]

[redacted]

Figure 3-15 shows transmittance data for bursts above 100,000 feet. As mentioned above, transmittance above this altitude depends only on the elevation angle. For convenience, Figure 3-15 shows the transmittance as a function of the ratio of slant range to height of burst as well as the elevation angle.

3-5 Effects of Clouds and Reflecting Surfaces

The model atmospheres are cloudless, and all have the same basic pattern of transparency as a function of altitude. When the actual atmosphere does not conform to these limitations, the calculation procedure must be modified.

If a cloud layer is present and the burst is above the clouds, a transmission modifying factor is used to account for the attenuation produced by the cloud layer. Table 3-1 provides a list of transmission correction factors in terms of the appearance of the daytime sky. Transmittance is calculated as though the air were clear and no cloud layer were present, and the result is multiplied by the correction factor obtained from the table.*

Table 3-1 suggests two ways to calculate the transmittance for a high-altitude burst (high enough to be in clear air, above the haze and clouds) when the haze (or fog) extends to the ground. For example, if a medium haze exists, a 4 mile visual range could be assumed, and from Figure 3-9 the transmittance of a high altitude overhead burst would be 0.51. Alternatively, the transmittance of a typical clear day (visual range = 16 miles), 0.85, could be used as a starting point. This with the modifying factor for medium haze, 0.5, gives a transmittance value of about 0.43. The discrepancy is within the uncertainty of the calculation.

Judgment must be used to determine whether a transmittance calculation should be based on visual range or on sky appearance. If the burst is directly over the target and high enough to be above cloudy or hazy air, sky conditions provide the better basis for the calculation. If the burst is at a low height and the target is at a long ground distance, visual range is preferred. When the situation is less clear, looking through the atmosphere may suggest which criterion is the more representative of conditions along the path from the burst to the target.

The transmission modifying factors ordinarily should be used with the HOB curves for 16 mile visual range, otherwise the attenuation of the atmosphere is counted twice.

Since a cloud layer appears thicker when the sun is low in the sky, cloud cover estimates made under this condition should be modified by taking the type listed just above the cloud description that fits the observed conditions best. Similarly, when the elevation angle of the burst is below 30°, the effect of a given cloud cover will be greater than if the burst were more nearly above the target area. In this case it is appropriate to take the transmission modifying factor just below the one that would ordinarily be selected.

This procedure is based on the similarity between the solar spectrum and the spectrum of thermal radiation from a fireball. Although the spectra are by no means identical, the ability of the atmosphere to transmit solar radiation often is the best available indication of its ability to transmit thermal energy. The appearance of the sky is, of course, an indication of its effect on light from the sun.

---

* It might appear that thermal radiation that passes through a cloud at an angle with the vertical would be attenuated more than the same radiation would be if it passed through the cloud vertically; however, the radiation does not follow a line-of-sight path but follows randomly directed paths characteristic of diffusion. The attenuation depends on the angle of the line-of-sight path to some extent, but the dependence is not strong, and radiation will penetrate a thick cloud about equally well regardless of the angle at which it enters.

[redacted]

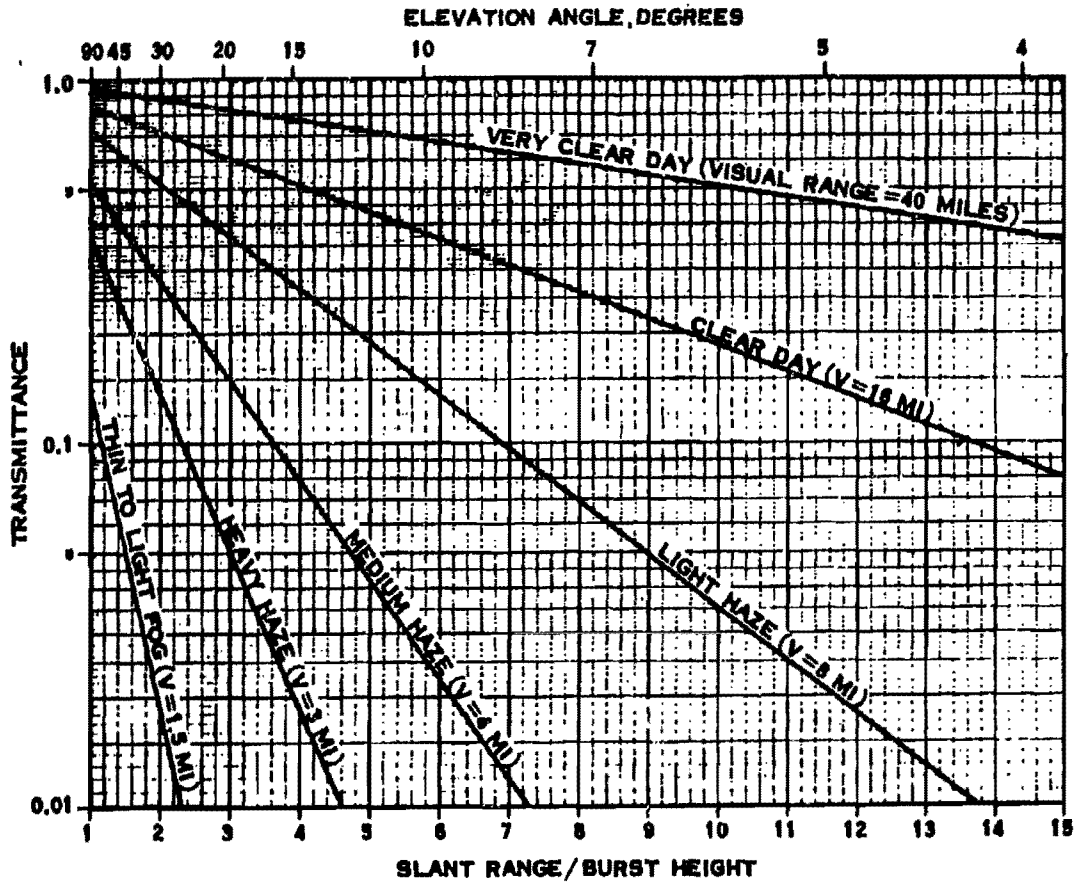
ELEVATION ANGLE, DEGREES
90 45 30 20 15 10 7 5 4
1.0
0.1
0.01
TRANSMITTANCE
VERY CLEAR DAY (VISUAL RANGE = 40 MILES)
CLEAR DAY (V = 16 MI)
LIGHT HAZE (V = 8 MI)
MEDIUM HAZE (V = 4 MI)
HEAVY HAZE (V = 2 MI)
THIN TO LIGHT FOG (V = 1.5 MI)
1 2 3 4 5 6 7 8 9 10 11 12 13 14 15
SLANT RANGE/BURST HEIGHT

Figure 3-15. [redacted] Atmospheric Transmittance for Thermal Radiation from High Altitude Nuclear Bursts (Height of Burst > 100 kft) [redacted]

[redacted]

Table 3-1. [redacted] Modifying Factors for Transmission Under Various Atmospheric Conditions [redacted]

If Haze or Fog Layer Extends to the Surface		If Haze or Cloud Layer is Overhead		
Type	Probable Visual Range (miles)	Type	Description	Transmission Modifying Factor
Very clear	32.0	Very clear	This condition rare except at high-altitude locations.	1.1–1.0
Clear	16.0	Clear	Sky deep blue. Shadows distinct, dark.	1.0–0.9
Light haze	8.0	Light haze	Sky white; dazzling near sun. Shadows visible, gray.	0.9–0.6
Medium haze	4.0	Medium haze	Sky bright grayish-white. View sun without serious discomfort. Shadows visible but faint.	0.6–0.4
Heavy haze	3.0	Heavy haze	Sky dull gray-white. Sun's disc just visible. Shadows barely discernible.	0.5–0.3
Thin fog	1.5	Light cloud	Sky light gray with maximum luminance around sun. Sun's disc not visible, no shadows.	0.4–0.2
Light fog	0.8	Medium cloud	Sky dull gray with maximum luminance at zenith.	0.3–0.1
–	–	Heavy cloud	Sky dark gray; brightness pattern gives no indication of sun's position.	0.2–0.06
–	–	Dense cloud	The low luminance level suggests the approach of nightfall. Gloomy.	0.1–0.02

[redacted]

[redacted]

If a cloud layer lies above the burst, it will scatter thermal energy toward the ground. The calculated value of transmittance should be multiplied by the modifying factor 1.5 when a cloud layer is above the explosion.

If the burst is between cloud layers, the upper layer will act as a reflector and the lower layer as an attenuator. If the two layers are equally thick, as much thermal energy will emerge from the bottom of the lower cloud layer as will emerge from the top of the upper layer. In most situations of this type, the cloud structure cannot be determined well enough to make detailed transport calculations meaningful; consequently, systematic calculation procedures for this case have not been developed. However, the procedures already described may be used to set approximate limits on the values of transmittance that may apply.

Similar problems arise when a broken cloud cover lies between the burst and the target. Whether the target will be in the shadow of a cloud at the time of burst is, in most practical situations, impossible to determine, and the results of transmittance calculation become much more uncertain. If the individual clouds are sufficiently thick that they do not reveal the location of the sun by a local bright area, and if they are spaced sufficiently close that they shade each other (i.e., so that some of the cloud areas appear dark gray), transmittance to targets shaded from direct radiation from the fireball will be roughly 20 percent of the transmittance calculated for a cloudless atmosphere.

When any cloud or haze layer listed in Table 3-1 is in contact with the surface, that layer has a most probable value of visual range associated with it. Under these conditions, the appearance of the sky may be used, in the absence of more direct measurements, to estimate visual range. Table 3-1 includes a rough assignment of visual range values in terms of the appearance of the sky.

An additional modifying factor relates to surface albedo, which is the reflection coefficient of the surface of the earth. Most surfaces, including water and desert areas, have low albedos (usually 25 percent or less). Only surfaces such as snow and white sand are in the high albedo class. These latter surfaces enhance thermal radiation because they can reflect energy directly toward the target and also because they reflect energy into the atmosphere, where some of it is scattered back toward the target. When such a surface is present, the calculated transmittance is multiplied by 1.5. If the burst is between a cloud layer and a high albedo surface, the enhancement factor is applied twice, giving a factor of 2.25.

3-6 Transmittance to Targets Above the Surface [redacted]

Transmittance to targets above the surface (e.g., aircraft in flight) may be calculated by using an equation similar to that given in paragraph 3-4 for the model atmosphere above one-quarter mile,

$$T = e^{-\Delta\tau(h)\ \frac{16}{V}\frac{R}{\Delta h}}$$

where $\Delta\tau(h)$ is the absolute value of the difference between $\tau(h)$ at burst altitude and $\tau(h)$ at target altitude (values of $\tau(h)$ can be obtained from Figure 3-2), Δh is the absolute value of the altitude difference between the burst and the target, V is visual range at the surface, and R is slant range between burst and target.

If the burst and target altitudes are equal, the exponent in the equation becomes indeterminate. An estimate may be obtained in this case by increasing burst altitude a small amount, decreasing target altitude the same amount, and holding slant range constant. Estimates obtained from this equation must be regarded as very rough approximations to actual transmittance.

[redacted]

[redacted]

Problem 3-3. Calculation of Transmittance

[redacted] Table 3-1 provides descriptions of various atmospheric conditions from which visual range may be estimated. The table also provides transmission modifying factors to be applied to the transmittance values for a 16 mile visual range when appropriate. Conditions under which the appearance of the sky should be used rather than the measured or estimated ground level visual range to determine transmittance are described in paragraph 3-5.

[redacted] *Example 1* [redacted]

Given: A nuclear explosion at an altitude of 5,000 feet. The appearance of the sky suggests a light haze atmosphere.

Find: The transmittance to a target on the surface 50,000 feet from ground zero.

Solution: Since the line of sight from the burst to the target is low and nearly horizontal, visual range rather than sky appearance would provide a better criterion for selecting a model atmosphere. Nevertheless, this problem must be solved on the basis of sky appearance, because a direct visual range measurement is not available. From Table 3-1, a light haze condition corresponds to a visual range of 8 miles.

Answer: From Figure 3-11, the transmittance is 0.15. No definite tolerance can be placed on this value of transmittance, and it must be regarded as a rough estimate.

[redacted] *Example 2* [redacted]

Given: A nuclear explosion at an altitude of 30,000 feet. The visual range is 6 miles, and the sky appearance fits the medium cloud condition. The time is one hour before sunset, and the ground is covered with snow.

Find: The transmittance to a target on the surface 10,000 feet from ground zero.

Solution: Since the burst is nearly over the target and is sufficiently high that it probably is above most of the haze and clouds, the sky conditions provide the best indication of transmittance. Therefore, the visual range will be ignored in the solution. As a result of the low elevation angle of the sun, the cloud layer appears to be thicker than it actually is. Therefore, the transmission modifying factor for light cloud conditions should be used rather than medium cloud conditions.

Answer: From Figure 3-13, transmittance on a clear day (16 mile visual range) would be 0.86. From Table 3-1, the transmission modifying factor for light cloud conditions is between 0.2 and 0.4. Reflection from the snow covered surface requires an additional correction factor of 1.5. The calculated transmittance therefore lies between

$$(0.2)(1.5)(0.86) = 0.26,$$

and

$$(0.4)(1.5)(0.86) = 0.52.$$

[redacted] *Reliability* [redacted]

In general, transmittance calculations are most reliable when transmittance is high and when the atmosphere is relatively clear. A tolerance of ±30 percent is assigned when transmittance exceeds 0.1 and when visual range is 5 miles or greater. This tolerance is based on comparisons between transmittance calculations made by the methods of several different investigators. When reflection from snow cover or an overhead cloud cover must be considered, the uncertainty rises to ±60 percent.

[redacted] Comparisons of calculated values with data from full scale nuclear tests show uncertainty that basically relates to the product fT, since thermal partition and transmittance cannot be measured independently. When transmittance

[redacted]

exceeds 0.1 and visual range exceeds 5 miles, the tolerance on thermal partition f accounts for all of the uncertainty in the fT product. No additional tolerance on T is required. When reflecting surfaces are present or when visual range drops below 5 miles, an additional ±30 percent tolerance should be applied.

No reliability estimate is assigned to calculated transmittances below 0.1. At these low values, transmittance estimates become increasingly uncertain, and errors may rise to factors of 2-10.

Errors in the estimation of visual range also can affect the error in the calculation of transmittance. If a visual range of 3 miles is estimated as 2 miles, which is not an unreasonable error, the percent error in transmittance rises rapidly as the transmittance drops to low values.

Additional errors are produced by approximations in the calculation procedure. These errors tend to be small when transmittance is high and large when transmittance is low. Three approximations are made in transmittance calculations.

First, a single parameter, visual range, serves as the basis for transmittance calculations in cloudless atmospheres. Although visual range at the surface is only one of the parameters required to specify the transmitting properties of the region between the burst and the target, it is one of the very few parameters that can be observed directly from the ground. Other parameters necessary to define the atmosphere completely are supplied by a set of model atmospheres that include the measured visual range at the surface and an increasing transparency with increasing altitude. This change in transparency with altitude is chosen to match the changes that occur in real atmospheres under typical conditions; however, there is no assurance that the model atmosphere is a particularly good match to any single real atmosphere.

Second, the transport of thermal energy through these model atmospheres is calculated from empirical equations confirmed by experimental data. The results of more accurate computational procedures are expected at some future date.

Third, the model atmospheres are cloudless. Cloud effects are accounted for by correction factors that modify the transmittance calculated for a cloudless atmosphere. An empirical treatment of some kind is unavoidable; cloud effects are too complex to be treated rigorously.

Any of these sources of error can, under certain conditions, cause the calculated transmittance to be wrong by a factor of 10 or more, but these extremely high errors appear when the atmosphere attenuates thermal energy from the fireball strongly and therefore when thermal effects are unlikely to be as important as other effects such as blast.

3-7 Visual Range

Ordinarily, the purpose of visibility measurements is to determine the ability of an observer to see through the atmosphere; such a measurement may determine the approximate distance at which a pilot can recognize a runway. In the study of thermal effects, visibility measurements are useful because they indicate the transparency of the atmosphere and its ability to transmit thermal radiation. The model atmosphere that should be used in a particular transmittance calculation is selected on the basis of daytime visual range.

The term *visual range* as used in this chapter is synonymous with *daytime visibility* as commonly measured at weather stations. Although "visibility" is a more widely used term than "visual range," the latter is used in this chapter because it indicates that the quantity being discussed is a distance and not a measure of the clarity with which a particular object can be seen. Visual range is defined as the distance at which a dark object silhouetted against the sky is visible and recognizable. It is commonly measured in statute miles.

Two factors make it advisable for the person who must develop the ability to make weapon effects calculations in tactical situations to understand the procedures for measuring visual range. First, he will not always have access to weather station information. Second, he may wish to question the information he obtains from weather stations. For the usual purposes of visual range measurements, underestimates of this range are less serious errors than are overestimates. For troop safety calculations, the opposite is true. Some meteorologists, not in the habit of thinking in terms of weapons effects, may shade their estimates incorrectly.

At the visual range, all objects appear so nearly alike in both brightness and color that a dark object silhouetted against the sky is barely recognizable. This reduction in contrast may be described quantitatively in terms of the brightness B of an object and the brightness of B' of the background. Contrast is defined as the ratio

$$C = \frac{B - B'}{B'}$$

If the object is darker than its background, the contrast is negative, reaching -1 for a perfectly black object. On the other hand, lights have very large positive values of contrast at night.

A hypothetical example illustrates the problems of estimating visual range and the accuracy that may be expected from such estimates. Table 3-2 shows a series of values calculated for the condition that the fifth pole of a row of telephone poles closely spaced in a uniform fog is at the visual range as it would be

Table 3-2. Contrast Ratio for a Series of Black Telephone Poles in a Fog: Visual Range = 500 Feet

Pole Number	Distance (feet)	Contrast Ratio
1	100	0.56
2	200	0.31
3	300	0.18
4	400	0.098
5	500	0.055
6	600	0.031
7	700	0.017
8	800	0.010

[redacted]

measured by a transmissometer.* If the poles have a dark color, the inherent contrast of each pole with its background may be assumed to be nearly 100 percent. The contrast, as seen by the observer is given in the last column, and is, by definition, 0.055 at the visual range.†

[redacted] What an observer sees may be affected by factors such as the uniformity of the fog layer. The first three or four poles are distinct, the fog has changed the apparent color of even the first pole to gray. The fourth pole is sufficiently distinct that if the cross arms are of lighter wood than the pole itself the difference in color is discernible. The fifth pole, at the visual range, is little more than a shadow, but it would be visible instantly and would be recognized as a telephone pole even if it were standing alone.

[redacted] An observer looking at the sixth pole standing alone probably would see it if he knew where to look, but he might question its identity. Although the line separating the image of the pole from its background is sharp, the faintness of the contrast makes the outline appear slightly blurred.

[redacted] The seventh pole is at approximately the distance known as the *meteorological range*, which is the range that gives a contrast of 0.02 between a black object and the sky. If the pole were standing alone and the observer did not know where to look for it, he very likely would miss it. Meteorological range has often been used as a measure of visual range; it corresponds more closely to the threshold of detection than to the implications of the presently used standard of "visible and recognizable."

[redacted] The eighth pole probably is not visible because of its size. A car parked beside it might be visible, but only if the observer, looking down the row of poles, knows exactly where to look for it. Detection at this contrast level requires a background uniformity that is rare except under laboratory conditions.

[redacted] Many observers would estimate visual range as the distance to the fourth or sixth pole; a few might select the seventh; still fewer, the third. As Table 3-2 shows, the error in range that this uncertainty produces is not excessive.

[redacted] The factors that would lead some observers to select the fourth pole may include more than overly conscientious application of the "visible and recognizable" rule. The fifth pole is only about 1/4 as wide as the ideal distance marker (which should subtend an angle of

---

*[redacted] A transmissometer is an instrument designed to measure light transmission characteristics of the atmosphere. It consists of a light and a detector separated by a baseline of either 500 or 750 feet. The transmissometer reading is called transmissivity. It is the ratio of the light received at the detector to the light that would be received if the air were perfectly transparent. The transmissivity defines the ability of a direct beam of light to penetrate a specified distance (the transmissometer baseline) through the atmosphere. The transmittance, as used in this chapter, defines the ability of radiant energy to pass through the atmosphere between a nuclear explosion and a target either directly or by scattering.

†[redacted] The visual range may be defined as the range at which the apparent contrast between a black object and its sky background is reduced to 5-1/2 percent or as the range at which a beam of light is reduced to 5-1/2 percent of the intensity it would have in a transparent atmosphere. Light from the sky generally appears to come from the region behind objects on the horizon, but air light originating beyond an object at the visual range actually contributes little to the sky brightness that the observer sees. All but 5-1/2 percent of this distant light is scattered out of the line of sight before it reaches the observer. The air between the object and the observer contributes as much to the apparent brightness of the object as it does to the brightness of the sky, but, if the object is black, it fails to contribute the 5-1/2 percent of total sky brightness that reaches the observer from the air beyond the object. The contrast to the observer is reduced from 100 percent to 5-1/2 percent. These conclusions are strictly correct: if the brightness and color of the sky as seen at the object is the same as the brightness and color of the sky as the observer sees it; if the atmosphere is not hazy, i.e., if the atmosphere is clear enough that the scattering cross section varies appreciably with wavelength and contrast is reduced to 5-1/2 percent for all colors; absorption of light is assumed negligible.

[redacted] In practice, these three restrictions usually may be ignored. The errors they introduce are in most cases no more serious than other problems (such as nonuniformities in the atmosphere) that limit the precision of visual range measurements.

[redacted]

at least 1/2°), and for this reason it may not appear to be as distinct as a larger object would.

Additional factors that could cause an observer to underestimate visual range can occur when the seeing conditions are different from those assumed in this example. For example, the fog was assumed to be perfectly uniform. Actually, the atmosphere near the surface over land is rarely uniform, and patches of haze that can be misjudged for distant objects are common. Shimmer, an optical effect similar to the heat waves observed over a metal object on a sunny summer day, can distort images of distant objects and can reduce the apparent visual range even though the air is clear.

An observer who uses a distant hill for a range marker may be inclined to overestimate visual range. This is particularly true if he knows, perhaps from the pattern formed by closer hills, exactly where to look. Aided by such landmarks, he may detect so many details of the familiar outline that, to him, the hill is definitely "visible and recognizable." The observer, if he is unsure of the mark, should ask himself whether he sees the hill clearly enough that *conspicuous* surface features (e.g., patches of trees separated by large areas of light-colored, vegetation-free rock) would be faintly discernible, even though such features may not actually be present. He should also ask whether an observer unfamiliar with the terrain would be reasonably sure that he was looking at a hill instead of cloud structure near the horizon. If the answers to these questions are "yes," he should judge the hill within the visual range.

Distance markers that are appreciably easier or harder to see than the standard dark-colored marker should be avoided if possible, since they lead to inaccurate measurements of visual range. A snow-covered mountain is likely to be an unreliable marker for two reasons: If the peak is at a high altitude, the observer sees it through air that is usually clearer than the air along a line of sight closer to the surface. Also, under strong illumination the snow is visible from a greater distance than darker portions of the mountain would be. Either effect can cause an artificially high measured value of visual range, implying a clearer atmosphere than actually exists. On the other hand, the tree-covered base of a mountain is an excellent marker for long visual ranges.

Surfaces with high reflection coefficients are not always more easily seen than dark objects. An observer looking in the general direction of the sun may see a white object as darker than the horizon sky, because the side of the object facing the observer is not illuminated strongly. If the angle of the sun is just right, there may be virtually no brightness contrast between a white object and its sky background. On the other hand, the inherent contrast between a very dark object and the sky never varies greatly from 100 percent; therefore, the use of dark objects as distance markers results in reasonably consistent visual range measurements.

The observer should be aware of phenomena related to lighting effects. If he is looking at a distance marker that is in the general direction of the sun, the strong forward scattering property of haze particles will make the air light between him and the marker will appear to be particularly bright. This does not affect the distance at which a dark marker can be seen. The sky behind the marker is similarly bright, and the apparent contrast between the marker and its background is no different than if, for example, the sun were overhead.

The preceding discussion provides the user with information that will help him to make accurate estimates of visual range. Much of this information can be condensed to a set of rules.

- Range markers should be as dark as possible. If the reflection coefficient of the

marker is more than 30 percent and the sun is behind the plane of the observer, the marker should be avoided.*

- The range marker should be silhouetted against the sky, or its background should be at least half again as far from the observer as is the marker itself. When such a marker is at the visual range, the background will be so nearly obscured that it is indistinguishable from the sky.
- The distance marker should be sufficiently large that increasing its size would not increase the range at which it can be recognized. This requirement is met if the angular size of the marker (vertically and horizontally) is 1/2°, which is the diameter of the full moon. A distance of 5/16 inch on a ruler held at arm's length is an approximate measure of this angle. If shimmer is not a serious problem (if the image is steady), binoculars may make a smaller distance marker usable.
- Distance markers should be available in several directions so that nonuniformities in the atmosphere can be detected.
- When a requirement for visual range measurements in a given area can be anticipated, a map showing usable distance markers should be prepared. It should indicate the range, direction, and identification of each marker. (Heights of hills or tall buildings should also be recorded, because such objects sometimes provide useful indications of cloud height.)
- The altitude of distance markers should be such as to place the line of sight as close as possible to the average ground level.

Usually it is necessary to use some markers that fall short of these standards. The markers may be too small or the wrong color, and often no marker will exist at the visual range. In this case the observer must use judgment to decide the visual range that ideal markers would indicate. One important clue is the apparent color of markers that are within the visual range. Clear, undistorted colors indicate that the amount of air light from the intervening air is small, and that objects at considerably greater ranges would be clearly visible.

3-8 Nighttime Visual Range

The distance at which a person can see a light depends partly on the transparency of the atmosphere. However, it also depends on the state of dark adaptation of the observer, the brightness of the light, and the amount of background produced by whatever other lights may be illuminating the air. Only the first of these four factors concerns the ability of the atmosphere to transmit thermal energy. In general, the variations caused by the last three factors make measurements of nighttime visual range a poorer indication of the transport properties of the atmosphere than measurements of daytime visual range.

In the absence of definite changes in the weather, the transparency of the air usually does not change much from day to night. Daytime visual range, which usually can be measured more readily than nighttime visual range, is often the most satisfactory means for estimating the transport properties of the atmosphere the following night.

Exceptions occur in regions where the relative humidity exceeds 90 percent in polar regions, and in areas subject to air pollution. In the latter case, the source of pollution (e.g., domestic heating or cooking and industrial exhausts) are likely to vary from day to night. Polluted atmospheres also often produce a haze

*The reflection coefficient is about 4 percent for a pine woods and about twice that amount for a deciduous woods. A grassy field, for which the reflection coefficient may exceed 20 percent, is a much less reliable mark.

[redacted]

layer near dawn, particularly when a steep temperature inversion forms near the surface. Such a haze layer may be dense enough to offer some protection from thermal radiation.

If nighttime visual ranges must be measured, these ranges should be converted to the equivalent daytime visual ranges. This is necessary because daytime visual range is the parameter on which transmittance calculations are based. Figure 3-16 may be used to convert nighttime ranges to equivalent daytime ranges.

Figure 3-16 is based on a large number of observations to determine the distance that a 25 candlepower light (25 candlepower is approximately the output of a 25 watt incandescent lamp) can be seen through various atmospheres. The data were originally taken to correlate transmissometer data with visual range measurements; therefore the seeing conditions would be similar to those existing at airport weather stations.

In practice, the 25 candlepower source can be replaced by any light of moderate intensity. In a transparent atmosphere, a 100 watt lamp could be seen about twice as far as a 25 watt lamp, but in an attenuating atmosphere the difference is less. When nighttime visual range is 50,000 feet, the 100 watt lamp could be seen from about 65,000 feet. When nighttime visual range is 5,000 feet, the 100 watt lamp can be seen from about 6,000 feet.

APPROXIMATE CALCULATIONS OF RADIANT EXPOSURE

The procedures described in the preceding subsections permit the calculation of radiant exposure by methods that are as accurate as present knowledge of thermal partition and transmittance allows the information to be presented in a manner suitable for this manual. In many cases, a quicker but less accurate estimation of radiant exposure is desirable. Such an estimate may indicate whether more time consuming calculations are necessary. Figures 3-17a and b are intended for use in such cases.

These figures are based on transmittance values for a moderately clear, cloudless atmosphere (visual range = 16 miles) and on thermal partition values for an intermediate value of yield, 200 kt. Transmittances were calculated using the high altitude equation only, and some loss in accuracy is expected for burst heights below 1/4 mile.

[redacted]

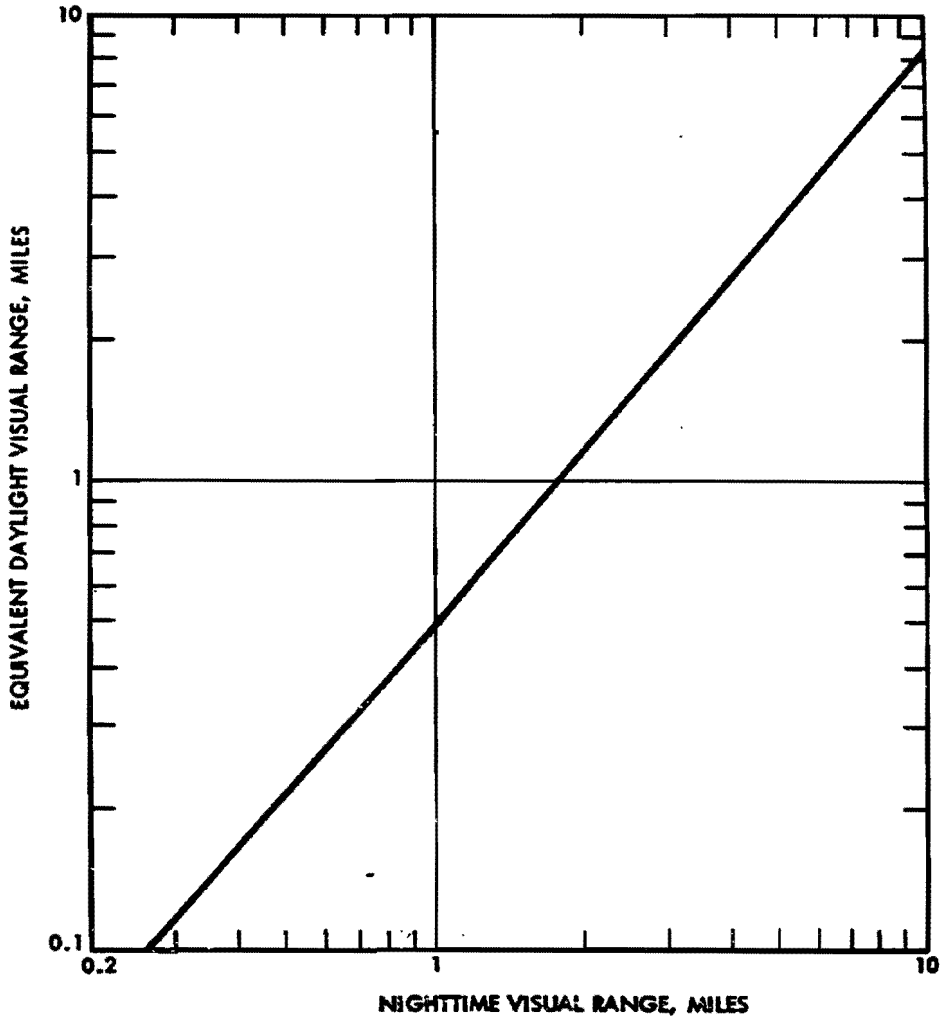

Figure 3-16. [redacted] Equivalent Daytime Visual Range as a Function of Nighttime Visual Range [redacted]

[redacted]

Problem 3-4. Approximate Calculation of Radiant Exposure

[redacted] Figures 3-17a and b show approximate radiant exposure to targets on the surface from a 1 kt explosion as a function of distance from ground zero and height of burst. These curves are based on calculations for a 200 kt explosion under the assumption that the radiant exposure could be scaled to 1 kt directly with yield. Visual range was assumed to be 16 miles.

[redacted] *Scaling.* For yields other than 1 kt, the radiant exposure is

$$Q = Q_1 W,$$

where Q_1 is the radiant exposure for 1 kt obtained from Figure 3-17a or b for the height of burst and ground distance of interest, and Q is the corresponding exposure for W kt.

[redacted] *Example* [redacted]

Given: A 500 kt explosion at an altitude of 30,000 feet.

Find: The radiant exposure on the surface 150,000 feet from ground zero.

Solution: From Figure 3-17b, a 1 kt explosion at an altitude of 30,000 feet will produce a radiant exposure 150,000 feet from ground zero

$$Q_1 = 0.0007 \text{ cal/cm}^2.$$

Answer: The radiant exposure from a 500 kt explosion is

$$Q = Q_1 W = (0.0007)(500) = 0.35 \text{ cal/cm}^2.$$

[redacted] *Reliability:* Radiant exposures from Figures 3-17a and b are approximations. For the assumed atmospheric conditions and burst altitudes below 100 kilofeet, values of radiant exposure obtained from Figures 3-17a and b are estimated to be reliable within ±40 percent. Additional loss of accuracy is expected for bursts below one-quarter mile altitude since the transmittances were calculated with the high altitude equations. The reliability also drops for bursts above 100,000 feet as a result of the uncertainty in the values assumed for thermal partition.

[redacted] *Related Material:* See paragraphs 3-1 through 3-8.

[redacted]

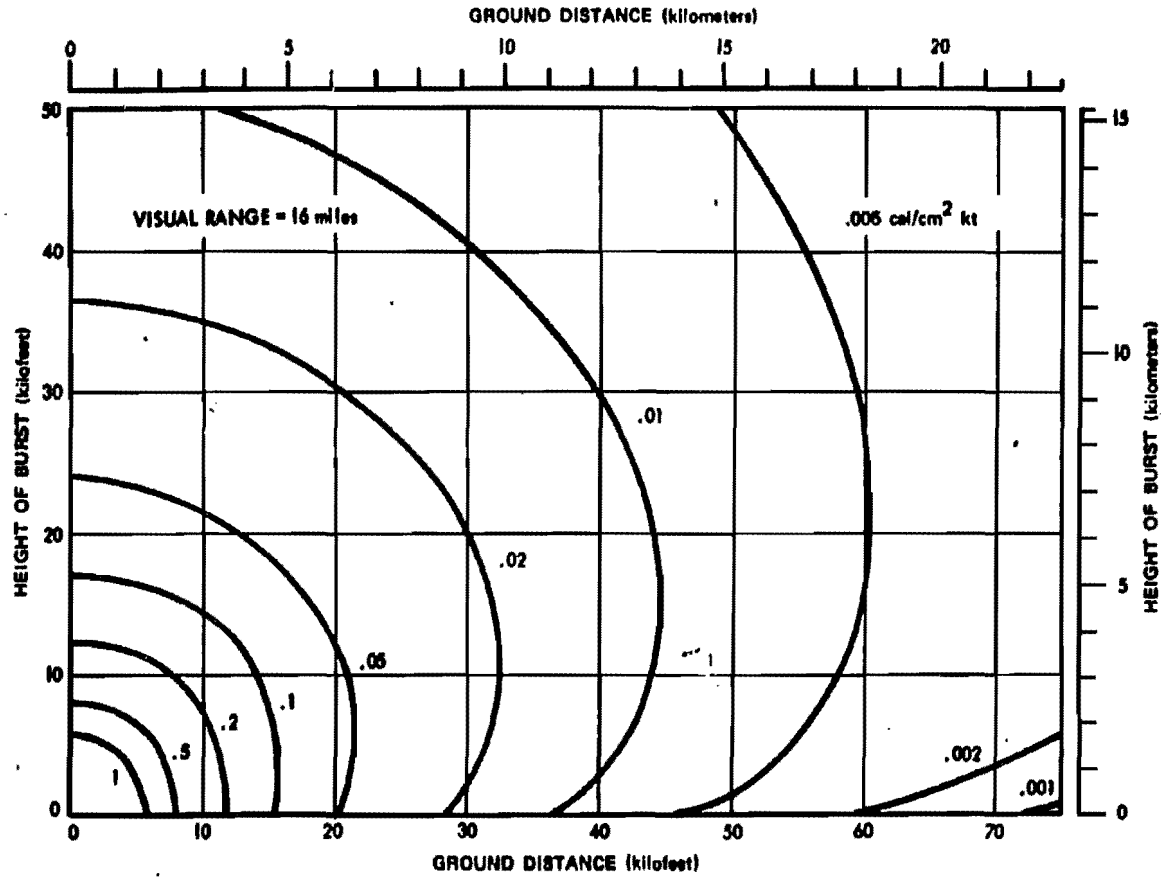

Figure 3-17a. [redacted] Approximate Values of Radiant Exposure Through a Clear Atmosphere [redacted]

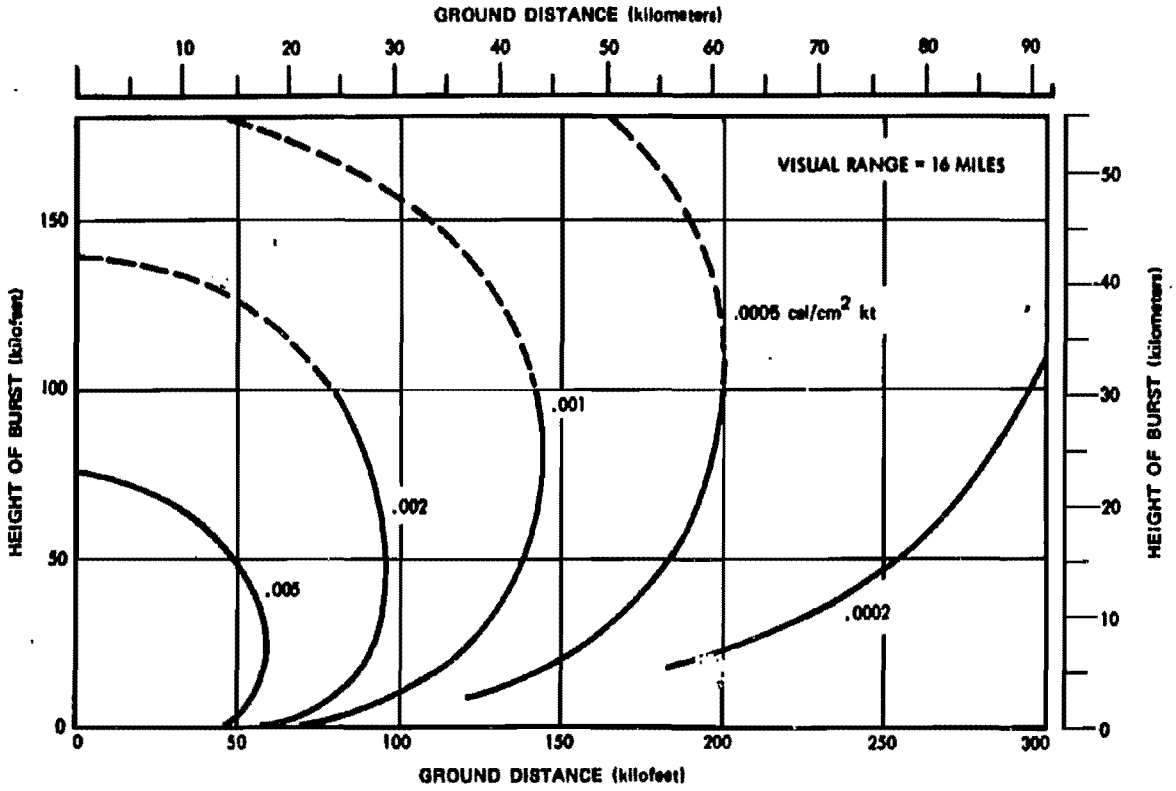

Figure 3-17b. [redacted] Approximate Values of Radiant Exposure Through a Clear Atmosphere [redacted]

SURFACE AND SUBSURFACE BURSTS

Clouds of dust (or spray) partly obscure the fireball of surface bursts and reduce the thermal radiation received by targets on the ground. Even less thermal radiation escapes from underground and underwater bursts. If the burst is deep enough, the earth or water absorbs almost all of the thermal energy; the amount of radiated thermal energy is insignificant.

3-9 Surface Bursts

The terms contact surface burst, surface burst, and air burst, when used in connection with thermal effects, have meanings similar to those assigned to the same terms in Chapter 2 (see paragraph 2-19). A contact surface burst is one that is no more than 5 $W^{0.3}$ feet above or below the surface. The region between 5 $W^{0.3}$ and 180 $W^{0.4}$ feet (±20 percent for yields between 10 and 100 kt, and ±30 percent for other yields) is called the transition zone, and a burst within this region is a surface burst for purposes of thermal radiation phenomena. Since the fireball is approximately 180 $W^{0.4}$ feet in radius for explosions in the lower atmosphere, a surface burst is any burst above 5 $W^{0.3}$ feet but low enough that the fireball will interact strongly with the surface of the earth. As mentioned in paragraph 3-1, an air burst occurs above 180 $W^{0.4}$ feet.

Experimental data indicate that the thermal partition of contact surface bursts is about 0.21. Figure 3-18 assumes a thermal partition of 0.21 for a contact surface burst, assigns the air burst partition (Figure 3-1) to a burst at 180 $W^{0.4}$ feet, and provides intermediate values by linear interpolation. This procedure is arbitrary and is only supported in a general way by experimental data. Points above the dashed line in Figure 3-18 represent air bursts; points below the dashed line are surface bursts. The radiant exposure from surface bursts may be calculated by the formulas given in paragraph 3-2 with the values of thermal partition, f, taken from Figure 3-18.

Figure 3-18 describes the fireball as it would be seen by targets on the surface. Clouds of dust would not obscure the fireball from above; consequently, radiant exposure of airborne targets should be calculated on the basis of the thermal partition of free air bursts given in Figure 3-1.

Since confinement of the fireball by the surface is roughly equivalent to reflection, the fireball radius for a contact surface burst is larger than that for the same burst in free air. Blast wave theory suggests that the fireball of a contact surface burst as viewed from above might resemble that of a free air burst with a yield of 2.0 W. In fact, determination of fireball yield by hydrodynamic scaling uses the 2.0 W assumption.

3-10 Subsurface Bursts

Two effects reduce the amount of thermal energy radiated by the nuclear explosions below the surface of the earth: a large amount of thermal energy is absorbed in fusing and vaporizing the earth; and the fireball that does develop above the surface is obscured to a great extent by earth that is thrown from the crater. Even relatively shallow underground bursts throw dirt up as a cone shaped cloud that screens surface targets from thermal radiation effectively.

Since surface reactions are complex and different types of surfaces react in different ways, the effects of underground bursts are extremely variable. As a result of these complexities as well as the fact that thermal effects from underground bursts usually are unimportant compared to other effects, methods for predicting thermal partition have not been developed for underground bursts.

[redacted]

Underwater bursts are similar to underground bursts in that thermal radiation is greatly reduced by the heat absorbed by the water and by the screening effect of water thrown from the crater. Thermal effects usually are insignificant. For example, a 20 kt burst in 90 feet of water produced negligible thermal radiation.

[redacted]

Problem 3-5. Calculation of Thermal Partition for a Surface Burst

Figure 3-18 contains a family of curves that provide an effective thermal partition for surface targets from nuclear explosions that occur at heights of burst greater than 5 $W^{0.3}$ feet and less than 180 $W^{0.4}$ feet. A thermal partition of 0.21 should be used for surface targets for bursts 5 $W^{0.3}$ feet above or below the surface. Thermal partition for targets directly above the burst should be obtained from Figure 3-1 or from the upper portion (above the dashed line) of Figure 3-18.

Example

Given: A 500 kt explosion at a height of burst of 300 feet.

Find: The effective thermal partition.

Solution: From Figure 3-18, the effective thermal partition is 0.24.

Answer: The effective thermal partition for a surface target is 0.24. The effective thermal partition for a target directly above the burst is 0.45 (from Figure 3-1, or from the intersection of the dashed line in Figure 3-18 with a yield of 500 kt). The thermal partition for targets at intermediate altitudes would fall between these values. As a result of the uncertainties (see Reliability), the thermal partition for surface targets could fall between 0.44 and 0.1, and the thermal partition for targets directly over the burst could fall between 0.65 and 0.25.

Reliability: Interaction of the fireball with the surface produces complex effects, and thermal radiation from surface bursts cannot be predicted as reliably as thermal radiation from air bursts. Values of effective thermal partition obtained from Figure 3-18 are estimated to be reliable within ±0.20 if the value is greater than 0.33. If the value that is read is less than 0.33, the lower limit of the expected range of values is 40 percent of the value that is read. The same tolerance is estimated for the effective thermal partition of the fireball as seen from above.

Related Material: See paragraphs 3-1 through 3-3. See also Figure 3-1.

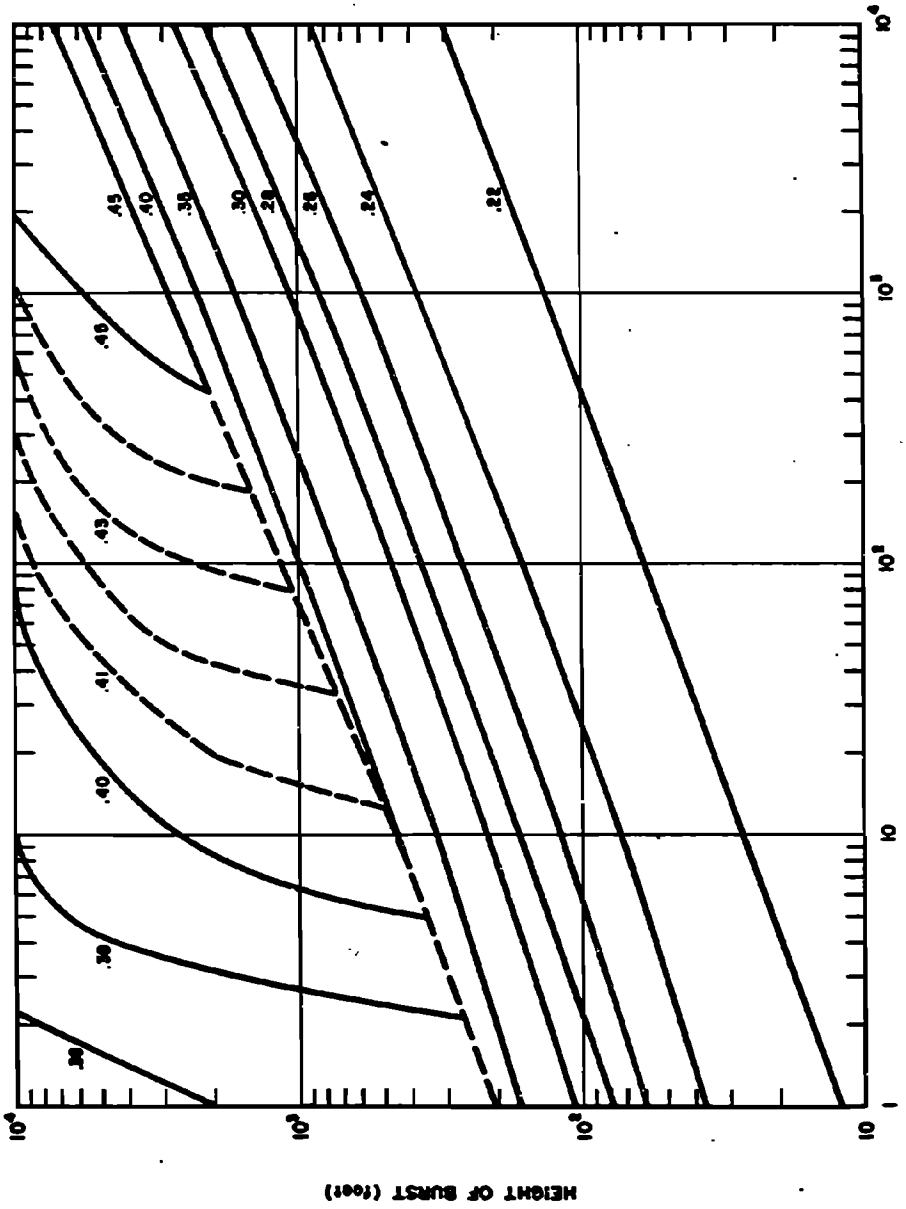

Figure 3-18. [redacted] Thermal Partition for Surface Bursts

THE THERMAL PULSE

Next in importance to the radiant energy incident on a target is the rate at which the energy is delivered. Dry leaves that receive a radiant exposure of 5 cal/cm^2 within a fraction of a second would ignite, but bright sunshine produces the same radiant exposure within about 3 minutes without producing ignition.

3-11 Thermal Power-Time Curve

Figure 3-19 shows the power-time curve for a 200 kt burst at an altitude of 5,000 feet. The shape is complex, with three peaks showing the results of competing processes (largely associated with the changing optical effects produced by the shock front) that alter the level of thermal radiation as the fireball evolves. Changes in burst altitude and weapon design can change the number and sizes of the peaks, therefore a complete, general description of thermal pulses is complex.

If the curve of Figure 3-19 is normalized and plotted on linear graph paper it becomes much simpler, as shown in Figure 3-20. Also, since equal areas on the linear graph represent equal amounts of energy, the curve in Figure 3-20 is a more realistic indication of the amount of thermal damage that each portion of the pulse can produce. The first peak, which lasts only a fraction of a millisecond and which contains slightly over 0.1 percent of the energy of the pulse, cannot be seen. Even the second peak is so compressed by the linear time scale that most of it shows up as only a vertical line.

When the features of the thermal pulse were first named, little more was known about the pulse than is shown in Figure 3-20; consequently, these two peaks and the valley were called *first maximum*, *light minimum*, and *second maximum*. Since the earlier features of the pulse produce negligible damage, many discussions ignore them; consequently, the names originally assigned to the later features still tend to be used even though these names are not strictly appropriate. In most of this chapter, the features shown in Figure 3-20 are called first maximum, principal minimum, and final maximum (i.e., the first maximum and first minimum shown in Figure 3-19 are ignored). The first maximum of low altitude bursts is sometimes called the shock exposure maximum, a name that suggests its physical origin. However, this name does not apply at all altitudes: above about 60,000 feet, the mechanism responsible for the first maximum changes.

3-12 Energy-Time Curve

The energy curve in Figure 3-20 shows the fraction of the thermal pulse energy that is radiated by a given normalized time. For example, it shows that 0.5 percent of the energy is radiated prior to principal minimum, that about 28 percent has been radiated by the time of final maximum, and that 15 percent is radiated at times later than are shown on the graph.

3-13 The Standard Thermal Pulse

Analysis of thermal radiation phenomena may be simplified by selecting the curves in Figure 3-20 as being representative of thermal pulses in general. Since changes in yield, altitude, and weapon design affect the shape of the pulse, use of such a standard is an approximation. Fortunately, this approximation is reasonably accurate for most bursts below 100,000 feet. The 200 kt burst at 5,000 feet was chosen as the basis for the standard thermal pulse for this manual because both yield and altitude have midrange values for typical thermal problems.

Both of the curves in Figure 3-20 appear in dimensionless form. The normalizing parameters are t_{max}, the time of final maximum, and P_{max}, the radiated power at final maximum. Of these parameters, the more frequently calculated is t_{max}, which specifies the time scale of the entire thermal pulse. Values of t_{max} may be

[redacted]

Deleted

[redacted]

Figure 3-19. [redacted] Calculated Power-Time Curve for a 200 kiloton Burst at 5,000 feet [redacted]

(b)(3) DNA

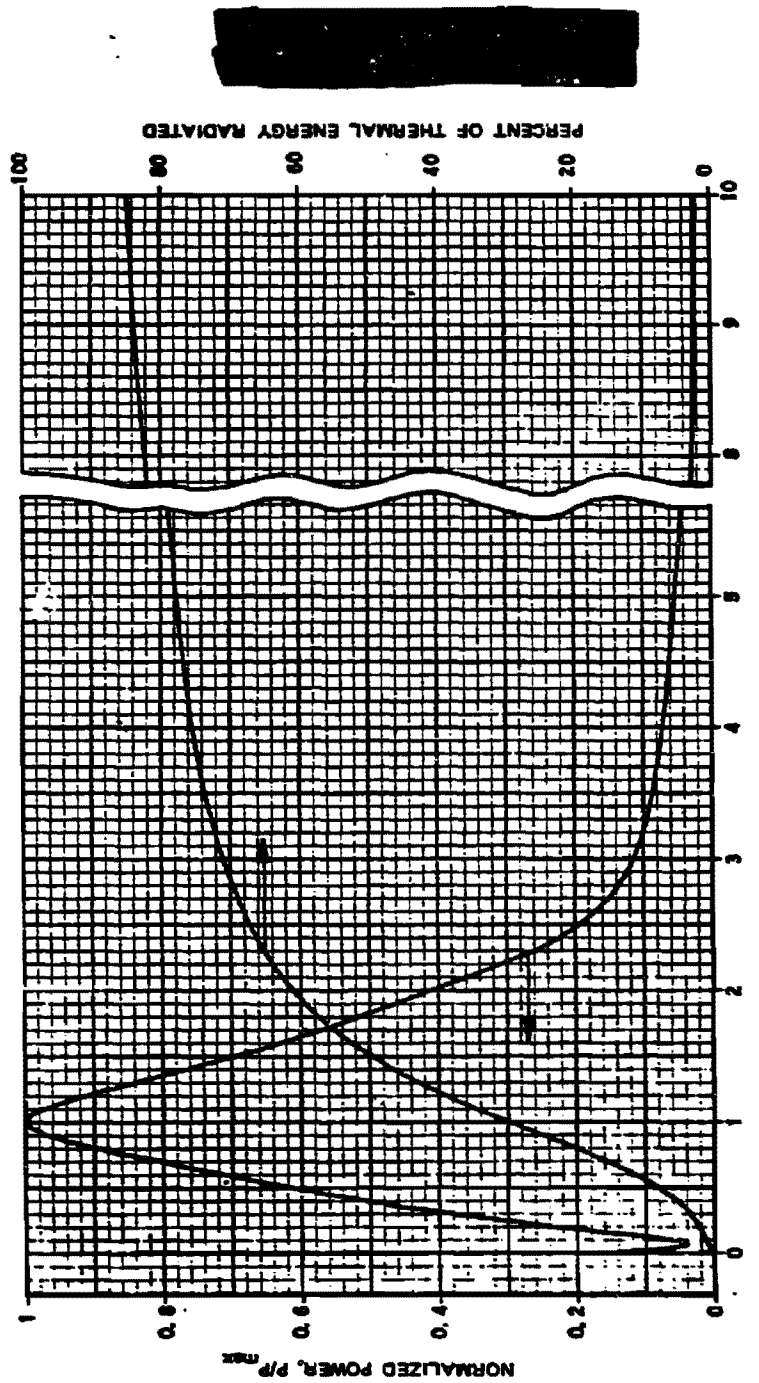

Figure 3-20. [redacted] Power-Time and Energy-Time Curves for a 200 kiloton Burst at 5,000 feet [redacted]

[redacted]

obtained from Figure 3-21. Data for altitudes above 100,000 feet should not be used without consulting paragraph 3-19. Values of t_{max} also may be obtained from the equation

$$t_{max} = 0.043\ W^{0.43}\ (\rho/\rho_o)^{0.42}\ \text{sec},$$

where W is the yield in kilotons and ρ/ρ_o is the ratio of the air density at the altitude of interest to the air density at sea level. Equations for various thermal phenomena (including P_{max}) are summarized in paragraph 3-25. Table 3-4 shows values of ρ/ρ_o as a function of altitude.

[redacted]

[redacted]

Problem 3-6. Calculation of Time to Final Maximum

[redacted] Figure 3-21 shows the time to final maximum as a function of weapon yield and burst altitude. Values of t_{max} obtained from Figure 3-21 can be used to convert the normalized time scale in Figure 3-20 to actual time after burst.

[redacted] *Example* [redacted]

Given: A 25 kiloton explosion at an altitude of 50,000 feet.

Find: The time of the final maximum.

Solution: The value of t_{max} may be obtained directly by interpolation in Figure 3-21, or it may be calculated from the equation given in paragraph 3-13.

Answer: From Figure 3-21,

$$t_{max} \approx 0.078 \text{ sec.}$$

From the equation

$$t_{max} = 0.043\ (W)^{0.43}\ (\rho/\rho_o)^{0.42}.$$

From Table 3-4, $\rho/\rho_o = 0.153$ at an altitude of 50,000 feet in a standard atmosphere. Therefore,

$$t_{max} = (0.043)(25)^{0.43}\ (0.153)^{0.42}$$

$$= 0.078 \text{ sec.}$$

[redacted] *Reliability:* Figure 3-21 was obtained from a combination of theoretical and experimental data. A description of the manner by which these numbers were derived is given in paragraph 3-25. Additional comments on the reliability are given in the subsection RELIABILITY OF THERMAL SOURCE DATA. Times given by this figure are estimated to be reliable within ±25 percent.

[redacted] *Related Material:* See paragraphs 3-11 through 3-13. See also paragraphs 3-24 and 3-25 and Table 3-4.

[redacted]

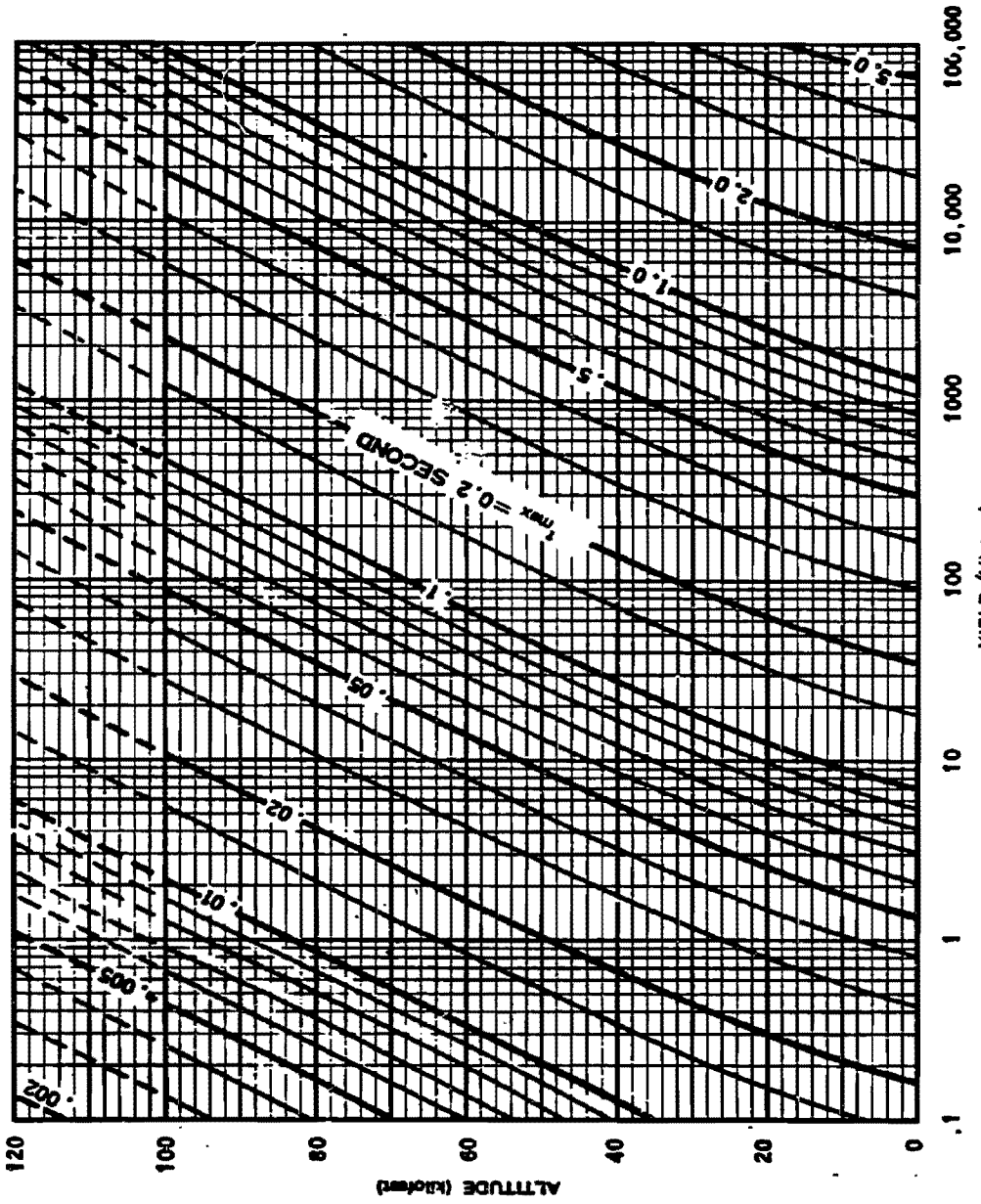

Figure 3-21. [redacted] Time of Final Maximum as a Function of Yield and Altitude

[redacted]

3-14 Effect of Thermal Pulse Duration [redacted]

[redacted] For most target materials and a particular level of radiant exposure, there is a value of thermal pulse length that will produce maximum damage. If the pulse is too short, there will be too little time for the energy to penetrate the material of an opaque target. Consequently, the heat is confined to a thin surface layer. This layer will vaporize rapidly, and will carry the deposited energy away with it. Often, this vapor will be in the form of smoke, which will shield the target from later portions of the thermal pulse. If the pulse is too long, a thin target (e.g., paper) will dissipate the heat as it is received or a thick target will absorb the energy harmlessly in a thick layer of material.

[redacted] For the types of damage that receive the most attention – ignition of waste materials and skin burns – most nuclear bursts produce thermal pulses that are longer than the pulse that would produce maximum damage. Consequently, in almost every situation a short thermal pulse is more damaging than a long one. Short thermal pulses are produced by low yields and high burst altitudes.

[redacted] The reasoning that has been applied to different thermal pulses also can be applied to different portions of the same pulse. The first pulse is unimportant because of the small total energy that it contains. The final pulse radiates about 70 percent of the total pulse energy by 3 t_{max}, and this portion of the pulse produces most of the thermal damage. Another 15 percent of the pulse energy is radiated between 3 t_{max} and 10 t_{max}. This also contributes to thermal damage, but with reduced effectiveness because of the lower power level. The remaining 15 percent of the pulse is released after 10 t_{max} so slowly that it fails to add significantly to the total thermal damage.

3-15 Effect of Altitude on Pulse Shape [redacted]

[redacted] Although both yield and altitude affect the shape of the thermal pulse, the effect of altitude is the more severe. Below 100,000 feet, the changes are relatively minor. As illustrated in Figure 3-22, higher altitudes increase the relative width of the "first" pulse, which now contains sufficient energy to produce significant damage in some situations. The higher altitudes also decrease the depth of the principal minimum. The width of the final pulse on the dimensionless plot remains about the same, and the standard pulse shape is still a fair representation of the ability of the thermal pulse from a burst at 100,000 feet to produce damage. Thermal radiation damage to materials is discussed in Section III, Chapter 9, and thermal injuries are discussed in Section II, Chapter 10.

[redacted] Figure 3-23 shows a thermal pulse that was calculated for a 200 kt burst at an altitude of 40 km (131,000 feet). Between 100,000 feet and 131,000 feet, the pulse shape changes drastically. The principal minimum has disappeared, and even a logarithmic plot of this power-time curve would show only a single maximum. These differences in shape are caused by low air density (about 0.33 percent of sea level density) and the resulting weakness of shock wave effects. (As discussed in paragraph 3-25, the oscillations in the power-time curves of low altitude bursts depend strongly on the optical properties of the shock wave.)

3-16 The Effects of Thermal Pulse Specifications on Thermal Partition [redacted]

[redacted] The time at which the prompt thermal pulse ends must be specified in order to define the total energy of the thermal pulse. Among the logical choices are the following:

[redacted]

Deleted

Figure 3-22. [redacted] Power-Time Curve for a 200 kiloton Burst at 100,000 feet [redacted]

[redacted]

DNA (4)(3)

Deleted

Figure 3-23. [redacted] Power-Time Curve for a 200 kiloton Burst at 40 kilometers [redacted]

[redacted]

- Since the energy radiated after about 10 t_{max} produces little damage, 10 t_{max} is a logical cutoff time. This choice would have the effect of increasing the height of the energy curve so that it reaches 100 percent at 10 t_{max} in Figure 3-20.
- At times on the order of 20 or 30 t_{max}, fireball radiation becomes difficult to measure; therefore, the experimentally measured thermal pulse typically ends in this time range.

Precedent may be found for either alternative. The definition selected in this chapter is approximately equivalent to the second choice listed above: the portion of the pulse after 10 t_{max} is assigned a value of 15 percent of the total pulse energy. This definition of the prompt thermal pulse agrees within a few percent with the thermal pulse as described in most reports on thermal pulse measurements and on thermal damage effects.

Reports of theoretical calculations of the thermal pulse usually define the pulse energy in a way that corresponds roughly to the first alternative. The reason is a purely practical one: since calculation of the pulse beyond 10 t_{max} is neither accurate nor economical, the calculations usually are terminated at about 10 t_{max}. The reported energy content of the pulse is the energy contained in that portion of the pulse covered by the calculation. In reports describing these calculated results, a radiant exposure of 8.5 cal/cm^2 may imply the identical thermal pulse that is implied in this chapter by a radiant exposure of 10 cal/cm^2. Similarly, a thermal partition of 0.34 as reported, for example, in DASA 1589 (see bibliography) is reported in this chapter as approximately 0.40.

The use of a standard thermal pulse introduces another problem. Since different thermal pulses have different shapes, the convenience of a standard pulse requires some sacrifice in accuracy. To minimize the effects of this loss in accuracy, the most damaging portion of the pulse is matched carefully but substantial errors are tolerated where power levels are low. Comparison of the pulse for 200 kt at 100,000 feet (Figure 3-22) with the standard pulse (Figure 3-20) shows that the two pulses are nearly equivalent near the time of final maximum but quite different at late times.

To achieve this match, all parameters, including thermal partition, are chosen to give the correct power level and time scale at the time of final maximum. For the burst at 100,000 feet, the value of thermal partition so chosen is a few percent higher than a value based solely on total thermal energy. The standard pulse shape implies a level of late time radiation that the calculated thermal pulse for 100,000 feet fails to maintain. To match the high power portions of the calculated pulse to the standard pulse shape, thermal partition must be made artificially high.

These matters of definition present no particular problem within this manual. Thermal pulses below 100,000 feet are specified so that the standard pulse shape, the assigned value of thermal energy, and the time of final maximum imply a pulse that provides a close match to the actual pulse in its ability to produce thermal damage. On the other hand, the user must keep these details in mind if he wishes to compare thermal data as given in this chapter with similar data from other sources.

FIREBALL BRIGHTNESS

The surface of a nuclear fireball is many times brighter than the surface of the sun. The image of the fireball, brought to a focus on the retina of the eye, can produce burns and permanently damage the area covered by that image (see paragraph 10-20, Chapter 10). Fireball brightness is therefore one of the important parameters of the thermal source.

A detailed study of eye damage also re-

quires knowledge of the spectral distribution of thermal radiation and the transport properties of the air as a function of wavelength; however, the present discussion is limited to the most important and most easily used parameter, surface brightness. This quantity may be measured in terms of the total power per unit area radiated by the fireball. Convenient units are watts/cm^2. Brightness of the sun provides a useful standard for comparison. As viewed from outside of the atmosphere, the surface brightness of the sun is 6,350 watts/cm^2.

For bursts below 100,000 feet, the approximate brightness of the fireball at final maximum is

$$B = \frac{2.7 \times 10^4}{W^{0.14}(\rho/\rho_o)^{0.42}} \text{ watts/cm}^2,$$

where W is yield in kilotons and ρ/ρ_o is the ratio of ambient air density at burst altitude to ambient air density at sea level. This equation gives a rough approximation of fireball brightness: more complete and accurate data for a particular yield and altitude may be found from the equation.

$$B = \frac{P}{4 \times 10^4 \pi R_f^2}$$

where P is power in watts radiated by the fireball and R_f is fireball radius in meters. Values of P and R_f as functions of time may be found for a wide range of yields and altitudes in "Theoretical Models for Nuclear Fireballs," DASA 1589 (see bibliography).

Scattered light from a nuclear fireball can contribute to temporary flashblindness, but it is too diffuse to produce retinal burns. Consequently, the direct flux from the nuclear fireball is the only parameter of interest in the study of eye damage. Transmittance calculations are not appropriate, because they include scattered as well as direct flux.

The direct flux received from a low altitude burst (burst height about 1/4 mile or less) is attenuated by the factor

$$T_d = e^{-2.9R/V}$$

where T_d is the transmission coefficient of the atmosphere for direct flux, R is the slant range, and V is visual range. For higher altitude bursts, the transmission coefficient is

$$T_d = e^{-\tau(h)\,\frac{R}{h}\,\frac{16}{V}}$$

where $\tau(h)$ is optical thickness of the model atmosphere with 16-mile visual range (Figure 3-2), and h is the height of burst.

These equations give average attenuation for the entire fireball spectrum and underestimate the amount of infrared energy that the atmosphere can transmit. Since infrared contributes substantially to eye damage, exposure to fireball radiation may be somewhat more serious than the equations given above would indicate. Figures 10-6 through 10-10 provide estimates of safe separation distances for eye damage for various observer and burst altitudes.

Cloud layers attenuate direct flux more than they attenuate radiant exposure. A cloud layer between the burst and the ground will produce the approximate attenuations shown in Table 3-3. The transmission coefficients shown in Table 3-3 are based on visible light, but they are expected to apply to the entire fireball spectrum within the limits to which a transmission coefficient can be matched to a particular sky condition.

THE THERMAL PULSE FROM SPECIAL WEAPONS

As stated in paragraph 2-45, Chapter 2, weapons that have enhanced radiation out-

[redacted]

Table 3-3. [redacted] Attenuation of Direct Thermal Radiation by a Cloud or Haze Layer [redacted]

Type of Atmosphere	Description of Sky	Transmission Coefficient for Direct Flux
Very clear	Visual range is 25 miles or more. This condition is rare except at high altitude locations.	90.0%
Clear	Sky deep blue. Shadows are distinct and dark.	80.0%
Light haze	Sky white; dazzling near the sun. Shadows visible, gray.	3.0%
Medium haze	Sky bright grayish white. Can view sun without discomfort. Shadows are visible but faint.	0.1%
Heavy haze	Sky dull gray-white. The sun's disk is just visible. Shadows are barely discernible.	0.003%

[redacted]

puts, i.e., weapons that produce a large fraction of their output in the form of neutrons, gamma rays, or X-rays [redacted] will, in most cases, generate a weaker blast wave than a nominal weapon of the same yield. Similarly, the thermal pulse from such special weapons may be weaker than that from a nominal weapon. The explanation for the reduced thermal output is the same as the explanation for a weaker blast wave: neutrons, gamma rays, and ...gh energy X-rays travel much farther through the atmosphere than the energy from a conventional weapon; therefore, a large portion of the weapon energy may be absorbed by air far from the burst. This air will not become sufficiently hot to contribute effectively to either the blast wave or to the thermal pulse.

[redacted] The terms "nominal weapon" and "conventional weapon" used in the preceding paragraph refer to a nuclear weapon that radiates 70 to 80 percent of its energy as X-rays [redacted] and retains nearly all of the remaining energy as thermal and kinetic energy of the weapon debris (see paragraph 4-4, Chapter 4). Such a source serves as a convenient starting point for calculations involving weapons with other characteristics. The procedures described in this subsection apply to burst altitudes of 100,000 feet and lower.

3-17 Effective Thermal Yield of Special Weapons [redacted]

[redacted] The modified thermal effects produced by weapons with enhanced outputs may be calculated in terms of an effective thermal yield. This is defined as the yield that a nominal warhead would have in order to radiate the same thermal energy as the special weapon. Effective thermal yield should not be interpreted to mean

[redacted]

thermal energy radiated (a quantity sometimes assigned to the term "thermal yield"). Effective thermal yield means *the effective value of total yield to be used in thermal calculations.*

The concept of effective thermal yield is an oversimplification, and it cannot describe the performance of special weapons precisely. For example, the effective thermal yield calculated on the basis of time of final maximum will, in general, be slightly different from the effective thermal yield that gives the correct value of total thermal energy radiated. A still different effective thermal yield would predict the correct power at final maximum.

In this subsection, effective thermal yield is the value that gives the correct value for thermal energy radiated, because, in most applications, this is the most important of the thermal parameters. Other parameters may be calculated by using this same value of effective thermal yield, but the calculation will be somewhat less accurate than if the procedure had been designed to calculate those parameters.

Effective thermal yield is roughly the amount of energy that the nuclear source deposits within a sphere the size of the fireball at the time of the principal minimum. This radius is

$$R_{min} = \frac{95\ W^{0.36}}{(\rho/\rho_o)^{0.22}} \text{ feet}$$

$$= \frac{29\ W^{0.36}}{(\rho/\rho_o)^{0.22}} \text{ meters,}$$

where W is the weapon yield in kilotons, ρ is the ambient air density at the burst altitude, and ρ_o is the ambient density at sea level. Table 3-4 shows the ratio ρ/ρ_o as a function of altitude. Energy that is deposited beyond the radius R_{min} is assumed to make a negligible contribution to the energy radiated by the fireball.

Table 3-4. Relative Air Density as a Function of Altitude

Altitude (feet)	Relative Density,* ρ/ρ_o	Altitude (feet)	Relative Density,* ρ/ρ_o
0	1.000	80,000	0.0361
1,000	0.971	85,000	0.0284
2,000	0.943	90,000	0.0224
3,000	0.915	95,000	0.0176
4,000	0.888	100,000	0.0140
5,000	0.862	110,000	8.69-3†
10,000	0.739	120,000	5.43
15,000	0.629	130,000	3.45
20,000	0.533	140,000	2.22
25,000	0.449	150,000	1.45
30,000	0.375	160,000	9.77-4
35,000	0.311	170,000	6.69
40,000	0.247	180,000	4.65
45,000	0.194	190,000	3.22
50,000	0.153	200,000	2.22
55,000	0.121	210,000	1.54
60,000	0.0949	220,000	1.05
65,000	0.0747	230,000	7.05-5
70,000	0.0586	240,000	4.62
75,000	0.0459	250,000	2.60

* $\rho_o = 2.38 \times 10^{-3}$ slugs/ft^3 = 1.225 gm/cm^3.
† 8.69-3 means 8.69×10^{-3}.

Since the size of the fireball is determined by the thermal energy it contains, it would be logical to let W represent effective thermal yield rather than total weapon yield. To do this requires a trial-and-error approach. Effective yield is unknown until the equation given above has been solved and the energy deposited within R_{min} has been determined. In practice, the accuracy of this method for calculating effective thermal yield is sufficiently uncertain that this refinement is seldom justified. Unless

[redacted]

the effective thermal yield is less than half of the total yield, it is recommended that W be equated to total yield in the equation.

[redacted] To determine the amount of energy deposited within a radius R_{min} of the burst, the form of the energy emitted by the weapon must be determined.

DNA (4-X(3)

[redacted]

[redacted] The steps in calculating the energy contained within R_{min} are:

1. Find the scaled radius

$$(\rho/\rho_o)\ R_{min} = 95\ W^{0.36}\ (\rho/\rho_o)^{0.78} \text{ feet}$$

$$= 29\ W^{0.36}\ (\rho/\rho_o)^{0.78} \text{ meters.}$$

This is the path length at sea level that passes through the same amount of air that a path of length R_{min} passes through at the burst altitude. Use of this scaled radius makes further scaling unnecessary.

2. Assume that 100 percent of the debris is contained within the radius.

3. [redacted]

DNA (4-X(3)

4. In a similar manner, find the amount of gamma ray energy that is deposited within R_{min} of the burst. The 1 MeV gamma photon curve in Figure 3-24 is approximately representative of the energy deposition properties of the gamma spectrum of a nuclear weapon.

5. [redacted]

DN (4-

6. The components of energy deposited within R_{min} of the burst are added together to obtain the effective thermal yiel[redacted]

(4-

The calculation is then repeated on the basis of this new value of scaled radius.

[redacted] The effective thermal yield calculated by the procedures described above may be used to calculate other thermal parameters by the methods described in preceding paragraphs. For example, the effective thermal yield may be used as the weapon yield to calculate thermal partition as described in paragraph 3-1.

3-18 Thermal Pulse Shape from Special Weapons [redacted]

[redacted] The two properties that characterize special weapons (in the sense that the term is used in this chapter) are that the initial deposition of energy fills a large volume and that the density of the deposited energy drops gradually with distance from the point of burst when compared to nominal weapons. The early fireball of a conventional weapon rapidly develops a sharply defined edge, formed by the shock front. The sharply defined edge results in a very bright fireball; the diffuse fireball from an enhanced weapon is relatively dim, becoming bright only when the shock wave propagates through the incandescent region of the initial fireball and reaches cooler air.

[redacted]

[redacted]

[redacted]

DNA (6)(3)

The thermal pulse assumes its conventional appearance at a time that depends on yield, altitude, and output properties of the nuclear device.

[redacted]

DNA (6)(3)

[redacted]

DNA (6)(3)

[redacted]

[redacted]

Problem 3-7. Calculation of the Effective Thermal Yield of a Hot X-ray Warhead [redacted]

[redacted] Paragraph 3-17 outlines six steps to be used together with Figure 3-24 to determine the effective thermal yield of weapons with enhanced radiation outputs. The effective thermal yield thus obtained is used in place of the weapon yield to calculate the various thermal parameters as described in preceding paragraphs of this chapter.

[redacted] *Example*

[redacted] ***Related Material:*** See paragraphs 3-1 through 3-6, 3-17 and 3-18. See also paragraphs 4-4 through 4-8, Chapter 4.

[redacted]

[redacted]

DNA (1)(3)

[redacted]

Deleted

Figure 3-24. [redacted] Distribution of Deposited X-ray Energy in a Sea Level Atmosphere as a Function of Source Spectrum [redacted]

[redacted]

[redacted] HIGH ALTITUDE THERMAL PHENOMENA

DNA (G)(3)

[redacted]

[redacted] Both experimental and theoretical data are very limited, so the methods described are based on information that is sketchy at b[redacted]. An additional problem affects theoretical data: the approximations necessary to limit computer programs to a usable size become poorer at higher altitudes. Although many points of agreement exist between experimental data and the corresponding computer calculations, the confidence that can be placed on theoretical results is less at high altitudes than at low altitudes.

3-19 Thermal Partition [redacted]

[redacted] Two factors affect thermal partition at high altitudes. First, shock waves form much less readily in the thinner air; consequently the fireball is able to radiate thermal energy that would have been transformed to hydrodynamic energy of the blast wave at lower altitudes. Second, the thinner air allows energy from the nuclear source to travel much farther than is possible at sea level. Some of this energy travels so far from the source that it makes no contribution to the energy contained in the fireball.

[redacted] In general, the first of these factors becomes effective between about 100,000 and 140,000 feet, and, as a result, thermal efficiency rises. Above 140,000 feet, the second factor becomes the more important and efficiency drops.

[redacted] DNA (G)(3)

[redacted] As in the previous subsection on special weapons, this method requires that the X-ray output of the weapon be represented by the sum of several black body spectra. The energy density deposited at a given range may then be obtained from Figure 3-25a or 3-25b. Briefly, the scaling procedure is the following: the energy ΔE_2 = 2,500 cal/gm is scaled by the equation

$$\frac{\Delta E_2}{\Delta E_1} = \left(\frac{\rho}{\rho_o}\right)^2 \frac{W_2}{W_1}$$

This equation is solved for ΔE_1, the value of energy to be read directly from Figure 3-25a or 3-25b. In this equation, ρ/ρ_o is the ratio of ambient air density at burst altitude to ambient

[redacted]

[redacted]

density at sea level (Table 3-4), W_1 is a reference yield of 1 kt and W_2 is the energy, in kilotons, contained in a particular black body temperature component of the nuclear source.

[redacted] The scaled radius R_1 is read directly from the horizontal axis of Figure 3-25a or 3-25b. This radius is related to the actual radius R_2 by the scaling equation

$$\frac{R_1}{R_2} = \frac{\rho}{\rho_o}.$$

However, the rest of the problem does not require that R_2 be known; the calculation is based only on the scaled radius R_1. In general, R_1 is determined by more than a single spectral component; the way in which this calculation is performed is made clear in Problem 3-7.

[redacted] The method of treating debris, gamma, and neutron energy is identical to that described in paragraph 3-17.

DNA (6)(3)

[redacted]

[redacted] The procedures described above apply to burst altitudes up to about 250,000 feet.

3-20 High Altitude Thermal Pulse Duration [redacted]

[redacted] Since the thermal pulse from a high altitude explosion rises to its maximum in an extremely short time and declines from that time (see Figure 3-23), pulse duration no longer can be specified in terms of the time to final maximum. A number that is useful in many applications is t_{70}, the time required for a pulse to deliver 70 percent of the total energy. At low altitudes,

$$t_{70} \approx 2.9\ t_{max}$$

and it follows that at high altitudes it might be possible to assign an effective time of final maximum such that

$$t_{max}\ (\text{effective}) = t_{70}/2.9.$$

DNA (6)(3)

[redacted]

[redacted] Analyses of a limited number of computer calculations of high altitude burst phenomena show the following trends: below 80,000 feet, the equation holds within the scatter of the data; above 80,000 feet, the thermal pulse is delivered more rapidly than this equation predicts, until at 160,000 feet the pulse is only about a third as long as predicted by the equation, above 200,000 feet, the pulse approaches and, in one case, exceeds the predicted value. This behavior is shown in Figure 3-26.

[redacted]

Problem 3-8. Calculation of Thermal Energy Radiated from a High Altitude Explosion

Figures 3-25a and 3-25b show the density of deposited energy from various energy sources as a function of range from a 1 kiloton explosion at sea level. These figures, together with the equations given in paragraph 3-19 provide the means to determine the thermal energy radiated by various yields at burst altitudes between about 120,000 feet and 250,000 feet. If the burst altitude is between 100 kft and 120 kft, thermal partition should be obtained by interpolation between the thermal partition obtained for 100 kft by the methods described in paragraph 3-1 and the thermal partition determined by the methods illustrated below. If the burst altitude is above 250,000 feet, refer to paragraph 3-21.

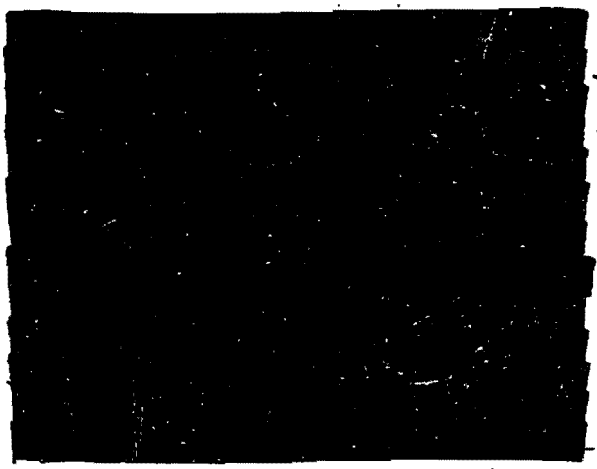

Example 1

Example 2

[redacted]

DNA
(b)(3)

Related Material: See paragraphs 3-1 through 3-6 and 3-19 through 3-21. See also Table 3-4.

[redacted]

[redacted]

DNA
(LX3)

Deleted

Figure 3-25a. [redacted] Density of Deposited Energy from Various Energy Sources [redacted]

[redacted]

[redacted]

DNA
(b)(3)

Deleted

Figure 3-25b. [redacted] Density of Deposited Energy from Various Energy Sources [redacted]

[redacted]

Deleted

Figure 3-28. [redacted] A Comparison of Calculated Effective Times of Final Maximum with Predictions from the Simplified Equation [redacted]

3-21 Bursts Above 250 Kilofeet

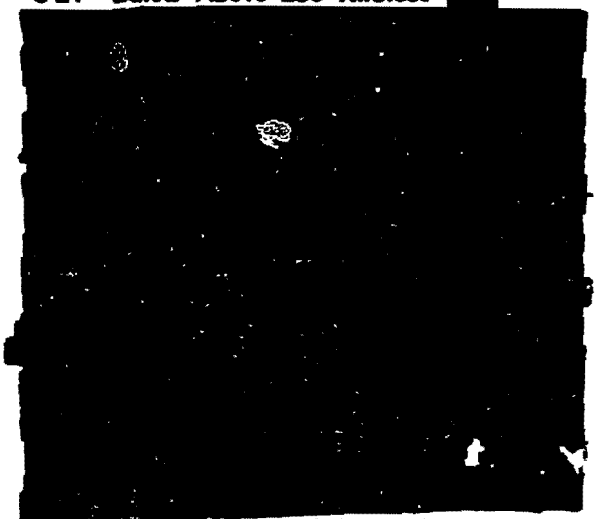

The calculations indicate that at heights of burst at or above about 290,000 feet the incandescent air heated by absorption of X-rays from the explosion is approximately at the same altitude, regardless of the actual height of burst. The heated region then reradiates at the longer wavelengths which could reach the ground. The reradiating region is in the form of a frustum of a cone, pointing upward, with a vertical thickness of approximately 45,000 feet and a mean altitude of 270,000. At this altitude, the radius of the frustum is roughly equal to the difference between the height of burst h and 270,000 feet, i.e., h - 270,000 feet. Consequently, as the burst altitude increases, the radius of the radiating region becomes greater but its thickness and altitude remain roughly constant. The shape of the region thus approaches a thick disk centered at about 270,000 feet altitude. The debris energy still is contained fairly locally until the height of burst reaches the debris stopping altitude of about 380,000 feet (see Table 8-1, Chapter 8), but the main effects of thermal energy delivered as a result of debris deposition at these altitudes are flashblindness or retinal burns (see Section II, Chapter 10). The total thermal energy emitted as a result of the debris deposition is masked by that energy emitted at lower altitudes as a result of X-ray deposition insofar as total energy that reaches the earth is concerned.

About one-fourth of the X-ray energy from the explosion is absorbed in the low density air of the reradiating region, and only a small fraction, which decreases with the height of burst, is reradiated as secondary radiation. Consequently, only a few percent of the weapon energy is emitted as radiation capable of causing damage at the earth's surface. In fact, for bursts at altitudes exceeding about 330,000 feet the thermal radiation from a nuclear explosion even in the megaton range is essentially ineffective on the ground.

If the horizontal distance d from ground zero, i.e., from the point on the ground immediately below the center of the disk-like region, to the position where the incident thermal energy is to be calculated is less than the height of burst, h, the source may be regarded as being located at the median radius of the disk in an altitude of 270,000 feet; this is indicated by the point S in Figure 3-27. Hence, for the target point X, the appropriate slant range is given by

$$R\ (\text{kilofeet}) = \left\{(270)^2 + [1/2\ (h - 270) - d]^2\right\}^{1/2},$$

with d and h in kilofeet. This expression holds even when d is greater than 1/2 (h - 270); although the quantity in the square brackets is then negative, the square is positive. The slant range, R_o, for ground zero is obtained by setting d equal to zero; thus,

$$R_o\ (\text{kilofeet}) = [(270)^2 + 1/2\ (h - 270)^2]^{1/2}.$$

If the distance d is greater than the height of burst, and equivalent point source is located at

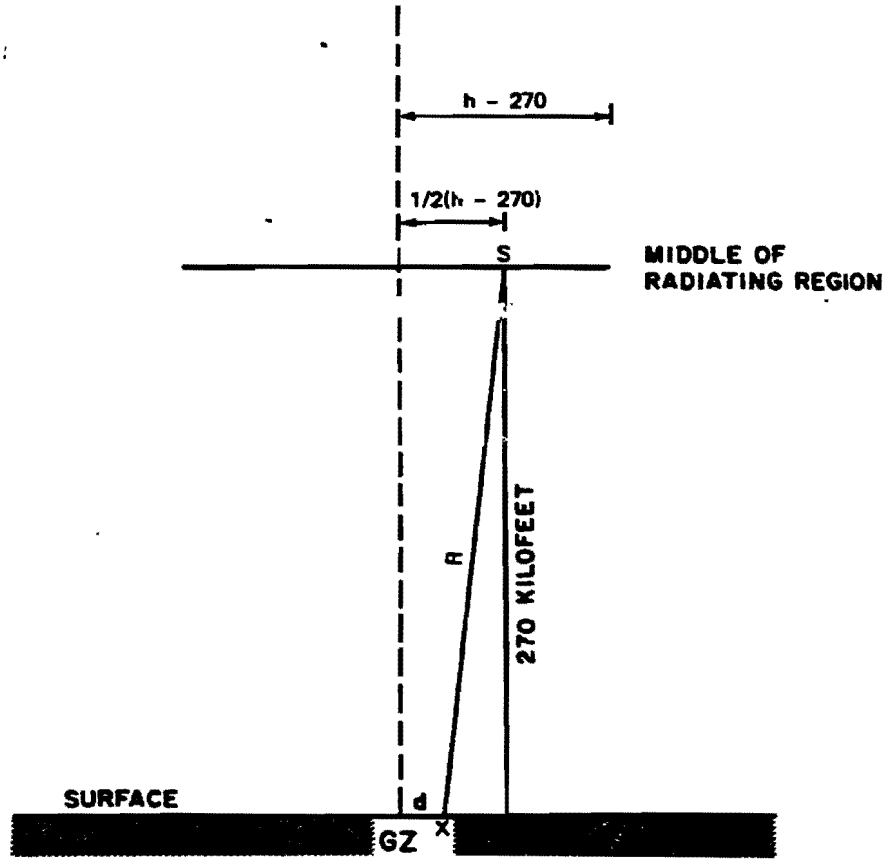

Figure 3-27. [redacted] Equivalent Point Source at Median Radius When Height of Burst Exceeds Distance of Target, X, from Ground Zero [redacted]

the center of the radiating disk at 270,000 feet altitude; then

$$R \text{ (kilofeet)} = [(270)^2 + d^2]^{1/2}.$$

The calculations assumed that 80 percent of the total yield is emitted as X-ray energy and that 25 percent of this energy is absorbed in the radiating disk region. Hence, 0.8 x 0.25 = 0.2 of the total yield is absorbed. For calculating the radiant exposure, the total yield W in the equations in paragraph 3-2 is consequently replaced by 0.2 W. Furthermore, the equivalent of the thermal partition is called the "thermal efficiency," ϵ, defined as the effective fraction of the absorbed energy that is reradiated. Hence, if R is in kilofeet, the equation for radiant exposure given in paragraph 3-2 becomes

$$Q = \frac{17.1\epsilon\, WT}{R^2} \text{ cal/cm}^2.$$

The values of ϵ given in Figure 3-28 as a function of height of burst and yield were obtained by the theoretical calculations mentioned previously. The transmittance may be estimated from Figure 3-15, but no serious error would be involved by setting it equal to unity for the large burst heights involved. No attempt should be made to interpolate between values of radiant exposure obtained for a burst height of 250,000 feet by the method described in paragraph 3-19 and the values obtained for 290,000 feet by the method described in this paragraph. If values of radiant exposure from bursts between these altitudes are desired, it is recommended that the radiant exposure be calculated for each altitude (250,000 feet and 290,000 feet) and that the higher or lower value be taken as an estimate, depending on the direction of conservatism that is desired.

RELIABILITY OF THERMAL SOURCE DATA

Most of the thermal radiation source data presented in this chapter were obtained from the series of computer runs reported in DASA 1589, "Theoretical Models for Nuclear Fireballs" (see bibliography). These data are not purely theoretical: development of the computer code included comparisons of calculated results with experimental data, and adjustments in the assumed weapon characteristics were made as a result of these comparisons.

The advantages of computer data (provided that this choice can be justified) are:

(1) This method eliminates many random errors that are inherent in experimental data. These random errors include uncertainty in the exact value of nuclear yield, instrument errors, uncertainty in atmospheric transmittances, blurring of some results as a result of finite time resolution of certain instruments, and uncertainty in the methods for transforming measured data to the parameters required for thermal calculations.

(2) Computer calculations can generate a large amount of data for a wide range of yields and altitudes that are not available from experiments.

(3) Errors that appear in the code results are likely to be consistent; therefore, the code probably predicts the trends produced by changes in yield or altitude more accurately than it predicts the results of any individual burst.

The disadvantage of using the code is that at best it gives only an approximation of the many processes that determine, directly or indirectly, the amount of thermal energy radiated. The method of accounting for spectral absorption lines is an example of the approximations that are required. A subroutine stores data for 151,528 different spectral lines, yet this is a small fraction of the number of lines that affect

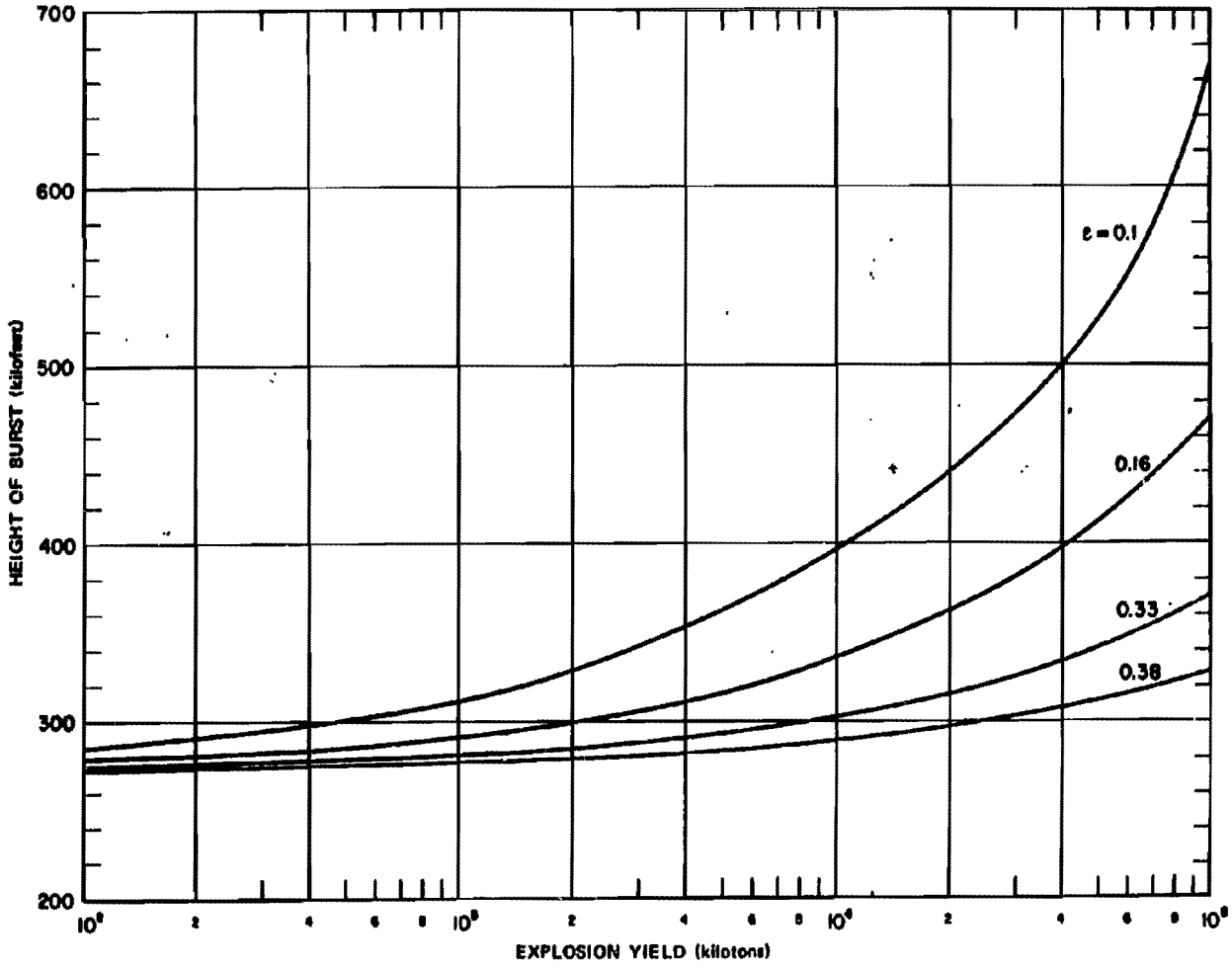

Figure 3-28. [redacted] Fraction of Absorbed X-ray Energy Reradiated [redacted]

radiative transport within the fireball.

Justification for using the code is the agreement between code results and measured data. The most striking areas of agreement are: (1) radius-time data, which are the most accurate experimental data, and (2) the ability of the code to reproduce intricate details of fireball evolution such as the fluctuations of the power-time curve (Figure 3-19) and the complex structure observed in high altitude fireballs.

Unfortunately, the code-calculated parameters that are of more direct interest in this chapter (e.g., thermal partition) cannot be confirmed as accurately by experimental data. Since uncertainty in the experimental data generally is as great as the discrepancy between theory and experiment, the experimental data provide no clear indication of the reliability of the code results, e.g., the code reproduces observed fireball phenomena within the accuracy of most test measurements.

This agreement has been obtained by comparisons of early code results with experimental data; however, changes in the code have never taken the form of arbitrary correction factors. Two examples illustrate the procedure used to correct the code.

The code, as originally written, did not predict the correct level of radiation during the first maximum. Analysis of the radiative properties of the shock front revealed that a shock precursor (discussed in paragraph 3-25), a very thin layer of heated air ahead of the shock front, determines the radiative properties of the fireball during this interval. The fine structure of this precursor was lost by the approximate methods that were required to represent the shock front on the computer. A possible solution, much finer zoning in the region of the shock front, was rejected as uneconomical; however, a separate program to calculate shock-wave properties gave results that agree with the observed first maximum. This separate program was used to correct the radiation level that was calculated by the main computer program.

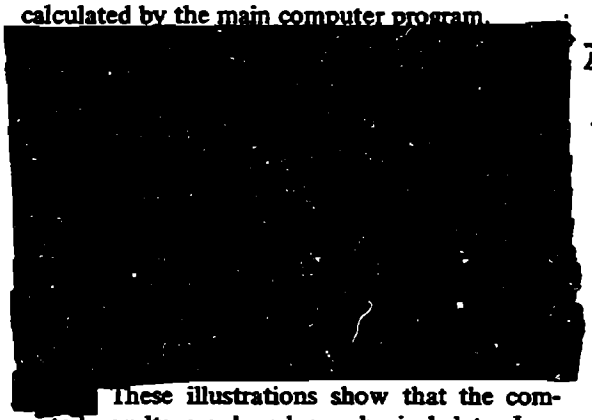

DNA (6X3)

These illustrations show that the computed results are based on physical data. In a sense, experimental data are represented indirectly because they indicated the parts of the computer program that should be examined more closely. Nevertheless, agreement between code results and observations indicate that the physics of radiative transport and hydrodynamic motion is understood well enough that the computer program is an adequate representation of the fireball itself. Therefore, in this chapter these code results are tentatively accepted as the preferred source of data concerning the source of thermal radiation from nuclear fireballs.

RELATION OF RADIANT EXPOSURE TO PEAK OVERPRESSURE

In many weapons effects problems, the first step is to determine which nuclear effect establishes the damage radius for a given burst. The series of figures in this subsection (Figure 3-29 through 3-56) show radiant exposure and peak overpressure as a function of height of burst and ground distance for 7 yields. The curves in these figures provide an aid in the determination of whether blast or thermal effects will be more important for specific situations. Four families of curves are presented for each yield. In each case the first two families of

[redacted]

curves are for no atmospheric attenuation of the thermal radiation, i.e., the worst case thermal exposure, and the second two families of curves are for a visual range of 16 miles (a clear day). Table 3-5 shows a summary of the data presented in the figures.

[redacted] These curves reflect the data presented in preceding paragraphs of this chapter and the free field air blast data from Chapter 2 accurately for the yields and conditions shown on each figure; however, they do not provide the answers to all potential problems, e.g., only 7 yields are included, and no data are presented for visual ranges less than 16 miles. The curves are intended to be used as an aid in determining the relative importance of blast and thermal radiation. Their use can be extended beyond the particular values that are plotted. For instance, the value of radiant exposure obtained from the curves for no atmospheric attenuation may be converted to the value for any visual range by multiplying by the transmittance appropriate to the given conditions. Interpolation between yields will provide a first order, and frequently sufficient, estimate of the more important effect.

Table 3-5. [redacted] Summary of Blast-Thermal Curves [redacted]

Figure Number	Yield (kt)	Atmospheric Attenuation	Blast Values (psi)
3-29	0.01	None	10-50
3-30	0.01	None	1- 4
3-31	0.01	16 Mile Visual Range	10-50
3-32	0.01	16 Mile Visual Range	1- 4
3-33	0.1	None	10-50
3-34	0.1	None	1- 4
3-35	0.1	16 Mile Visual Range	10-50
3-36	0.1	16 Mile Visual Range	1- 4
3-37	1.0	None	10-50
3-38	1.0	None	1- 4
3-39	1.0	16 Mile Visual Range	10-50
3-40	1.0	16 Mile Visual Range	1- 4
3-41	10	None	10-50
3-42	10	None	1- 4
3-43	10	16 Mile Visual Range	10-50
3-44	10	16 Mile Visual Range	1- 4
3-45	100	None	10-50
3-46	100	None	1- 4
3-47	100	16 Mile Visual Range	10-50
3-48	100	16 Mile Visual Range	1- 4
3-49	1,000	None	10-50
3-50	1,000	None	1- 4
3-51	1,000	16 Mile Visual Range	10-50
3-52	1,000	16 Mile Visual Range	1- 4
3-53	10,000	None	10-50
3-54	10,000	None	1- 4
3-55	10,000	16 Mile Visual Range	10-50
3-56	10,000	16 Mile Visual Range	1- 4

[redacted]

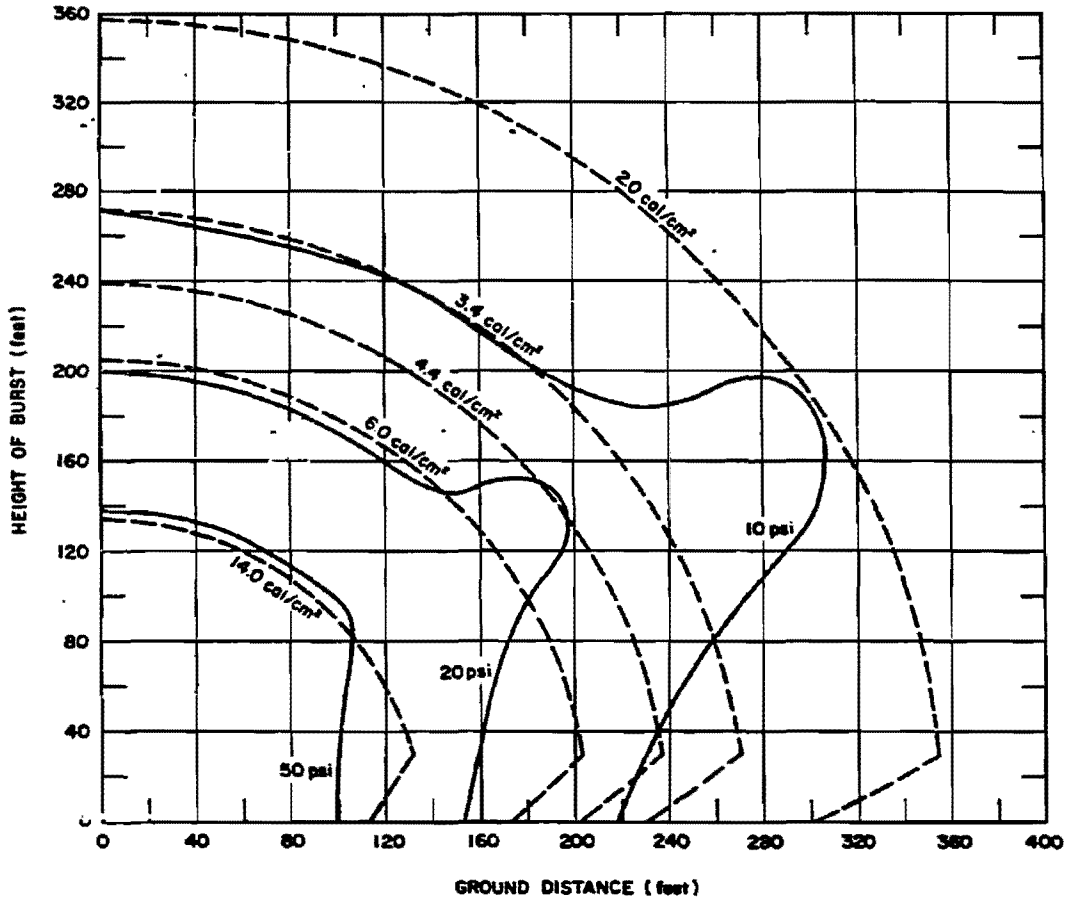

Figure 3-29. [redacted] Free Field Radiant Exposure and Air Blast Overpressure at the Surface, as a Function of Height of Burst and Ground Distance, for 0.01 kilotons, No Atmospheric Attenuation, High Overpressure Region [redacted]

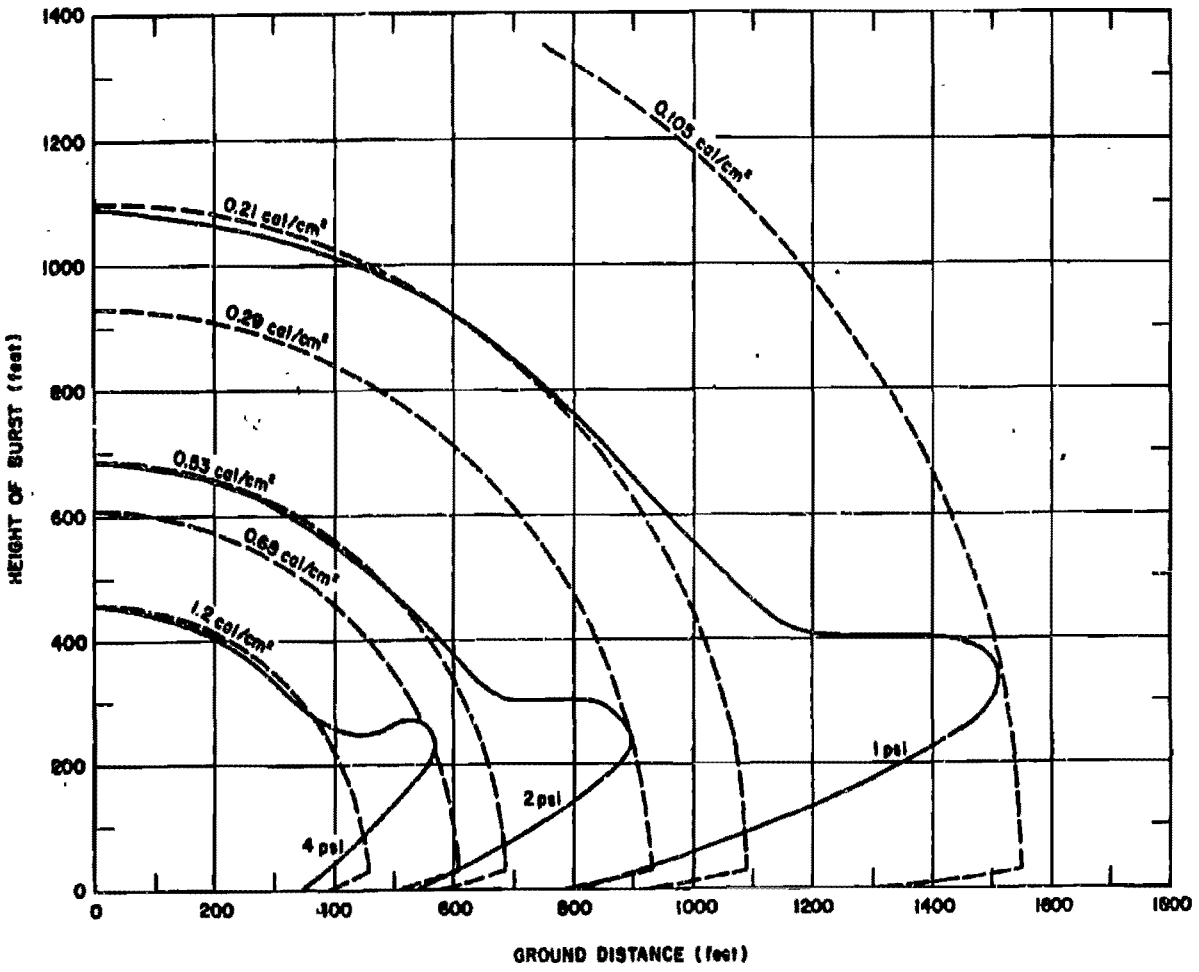

Figure 3-30. [redacted] Free Field Radiant Exposure and Air Blast Overpressure at the Surface, as a Function of Height of Burst and Ground Distance, for 0.01 kilotons, No Atmospheric Attenuation, Low Overpressure Region [redacted]

[redacted]

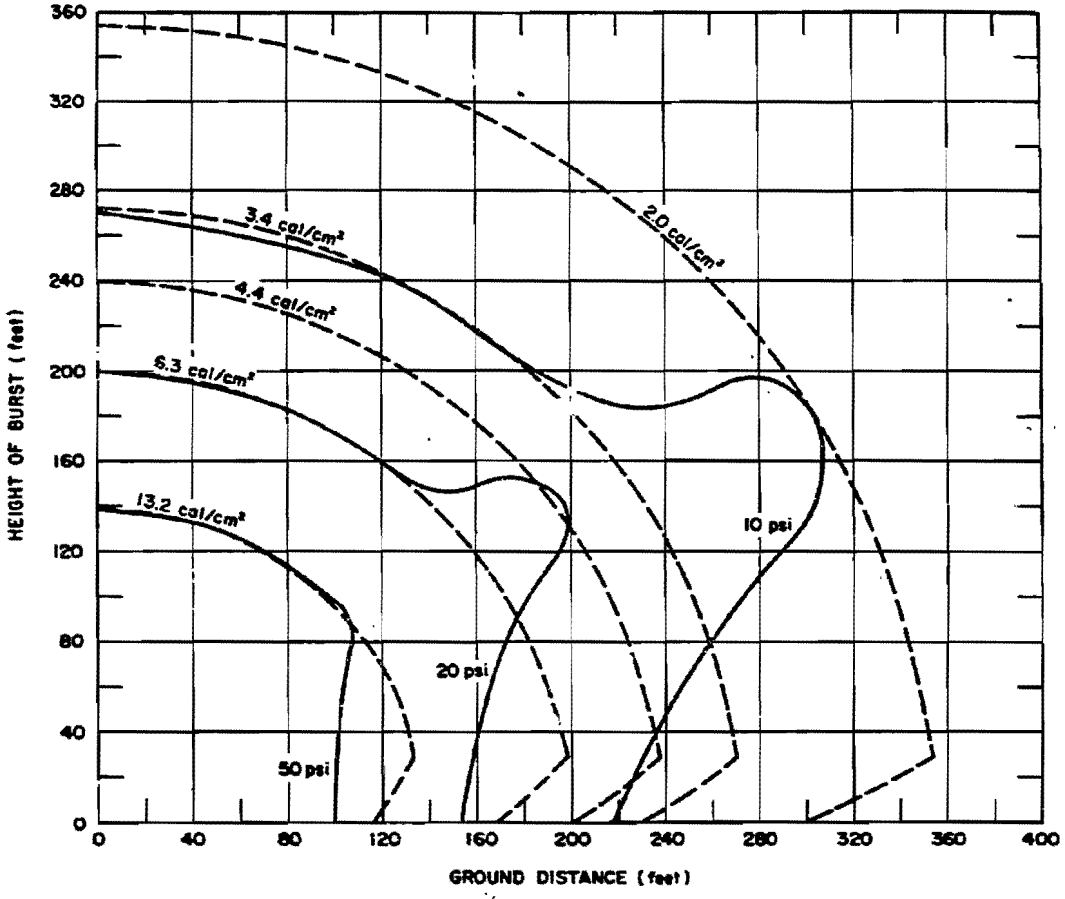

Figure 3-31. [redacted] Free Field Radiant Exposure and Air Blast Overpressure at the Surface, as a Function of Height of Burst and Ground Distance, for 0.01 kilotons, 16 Mile Visual Range, High Overpressure Region: [redacted]

[redacted]

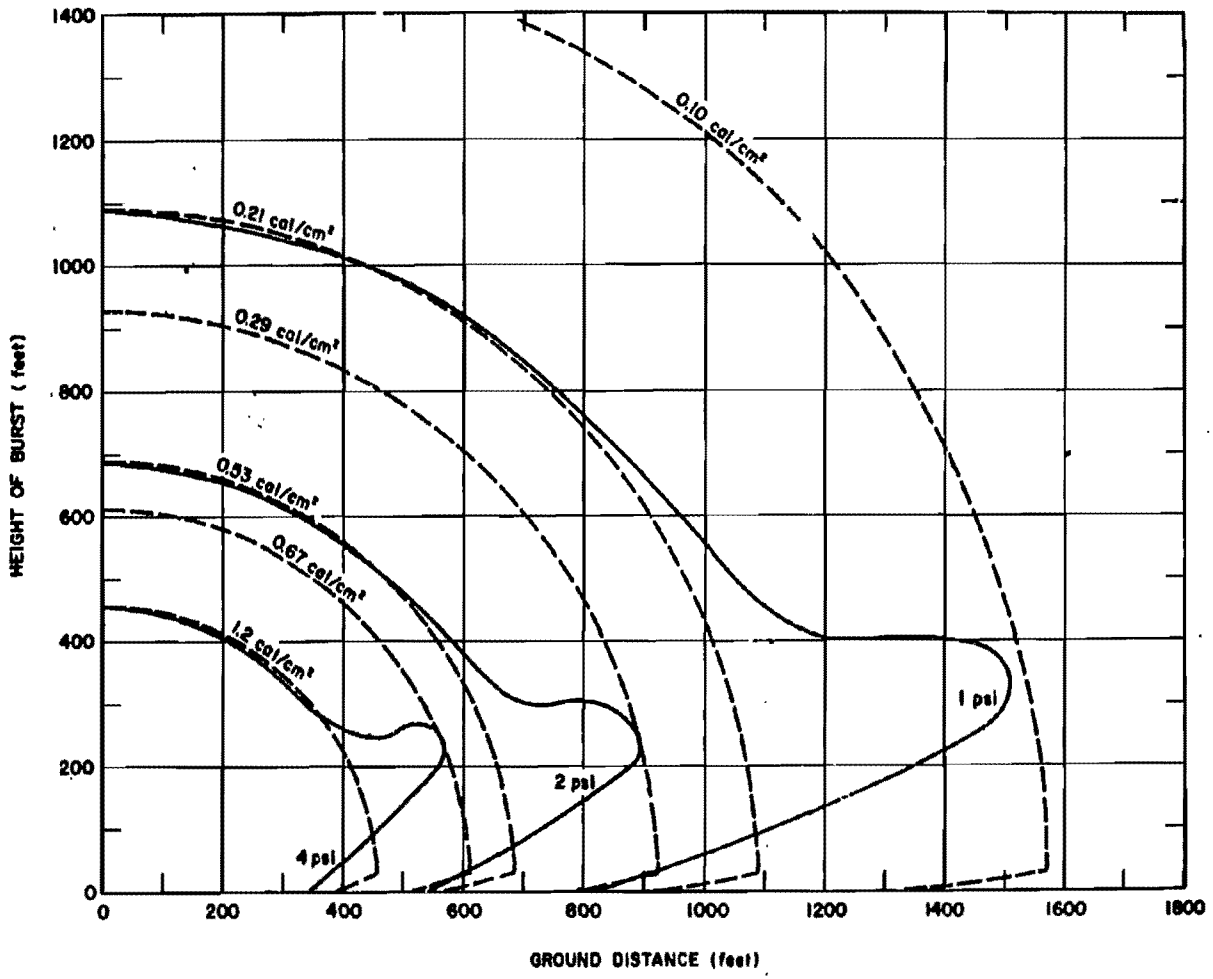

Figure 3-32. [redacted] Free Field Radiant Exposure and Air Blast Overpressure at the Surface, as a Function of Height of Burst and Ground Distance, 0.01 kilotons, 16 Mile Visual Range, Low Overpressure Region [redacted]

[redacted]

[redacted]

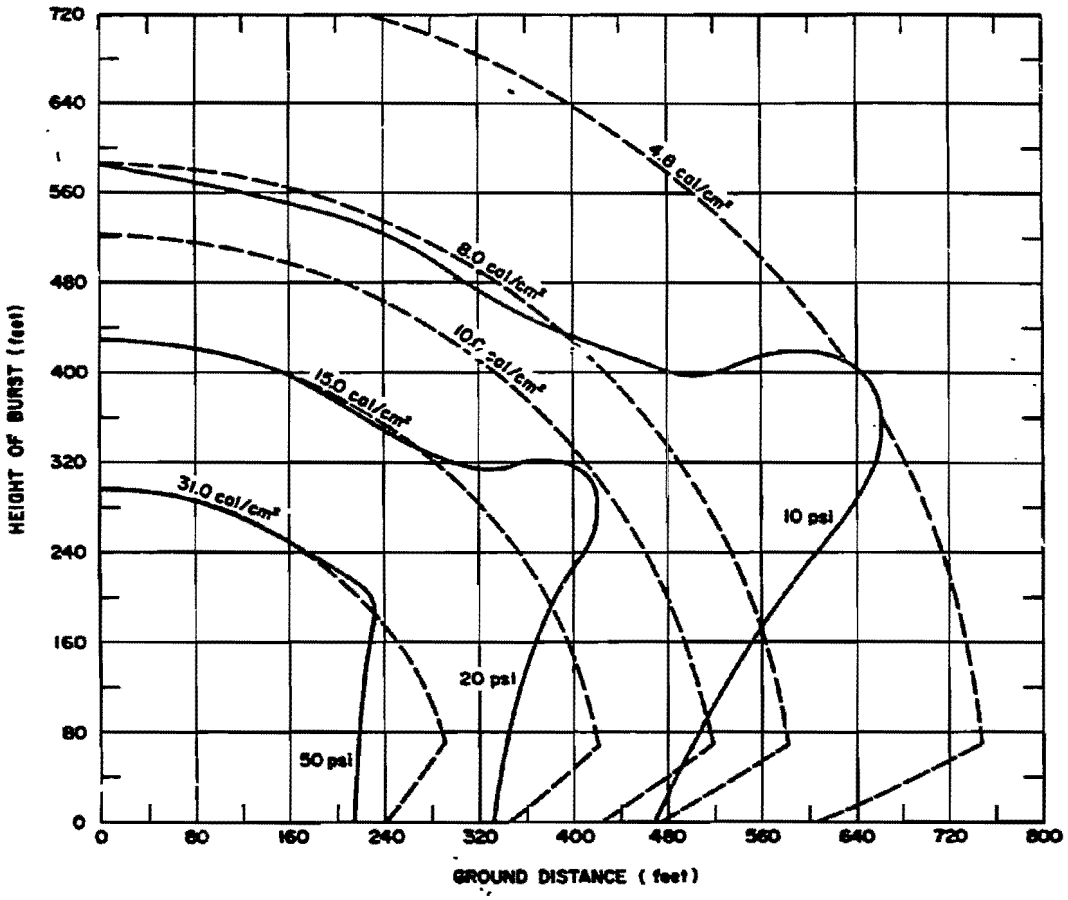

Figure 3-33. [redacted] Free Field Radiant Exposure and Air Blast Overpressure at the Surface, as a Function of Height of Burst and Ground Distance, for 0.1 kilotons, No Atmospheric Attenuation, High Overpressure Region [redacted]

[redacted]

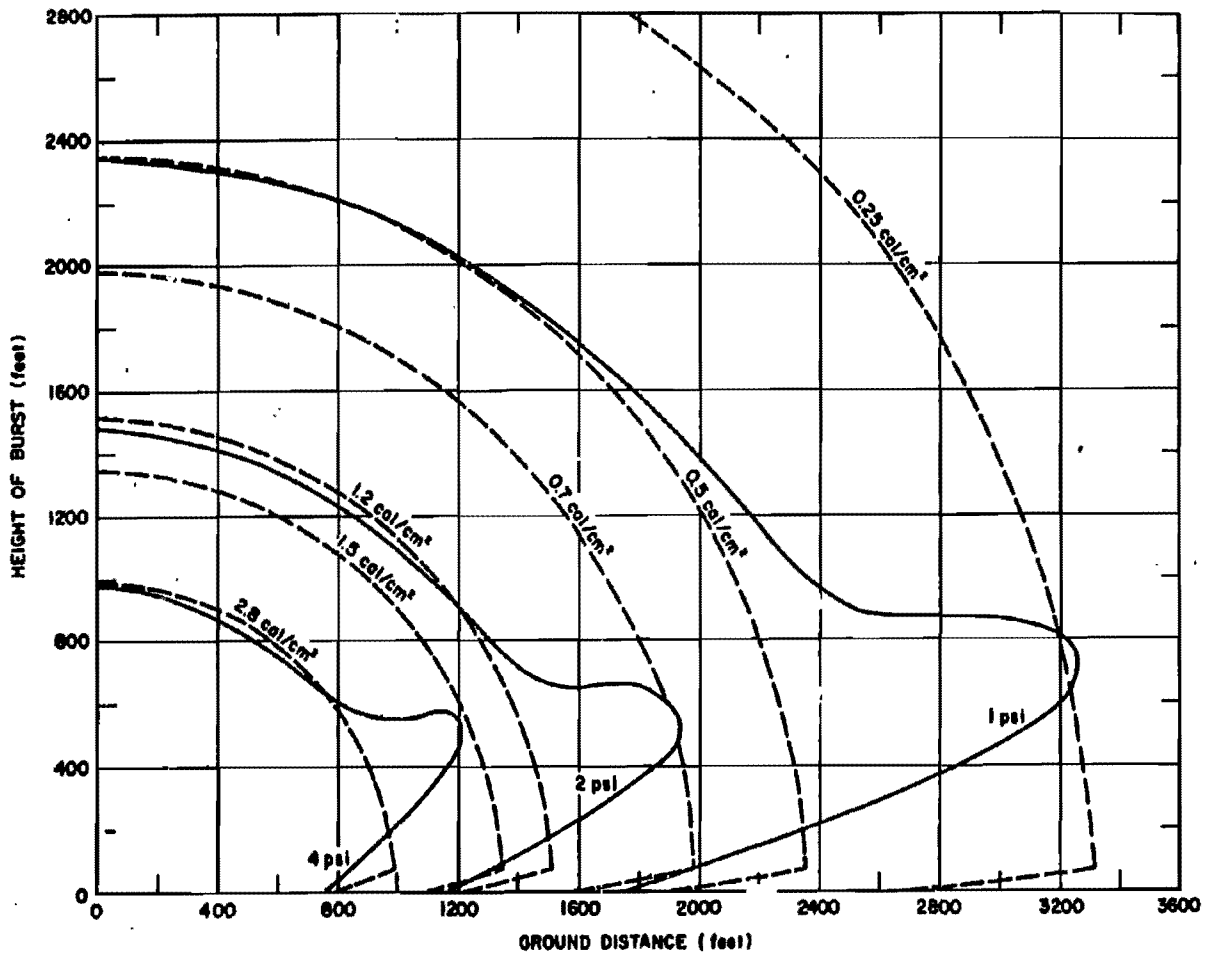

Figure 3-34. [redacted] Free Field Radiant Exposure and Air Blast Overpressure at the Surface, as a Function of Height of Burst and Ground Distance, for 0.1 kilotons, No Atmospheric Attenuation, Low Overpressure Region [redacted]

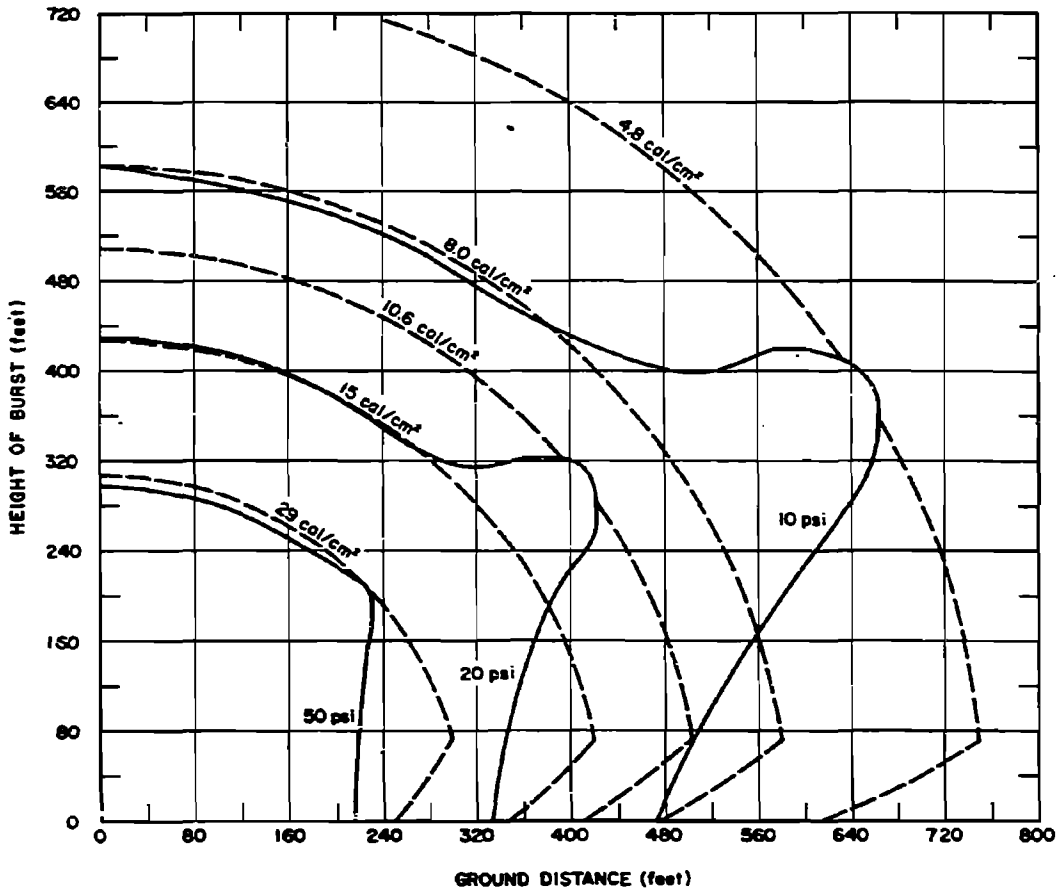

Figure 3-35. [redacted] Free Field Radiant Exposure and Air Blast Overpressure at the Surface, as a Function of Height of Burst and Ground Distance, for 0.1 kilotons, 16 Mile Visual Range, High Overpressure Region [redacted]

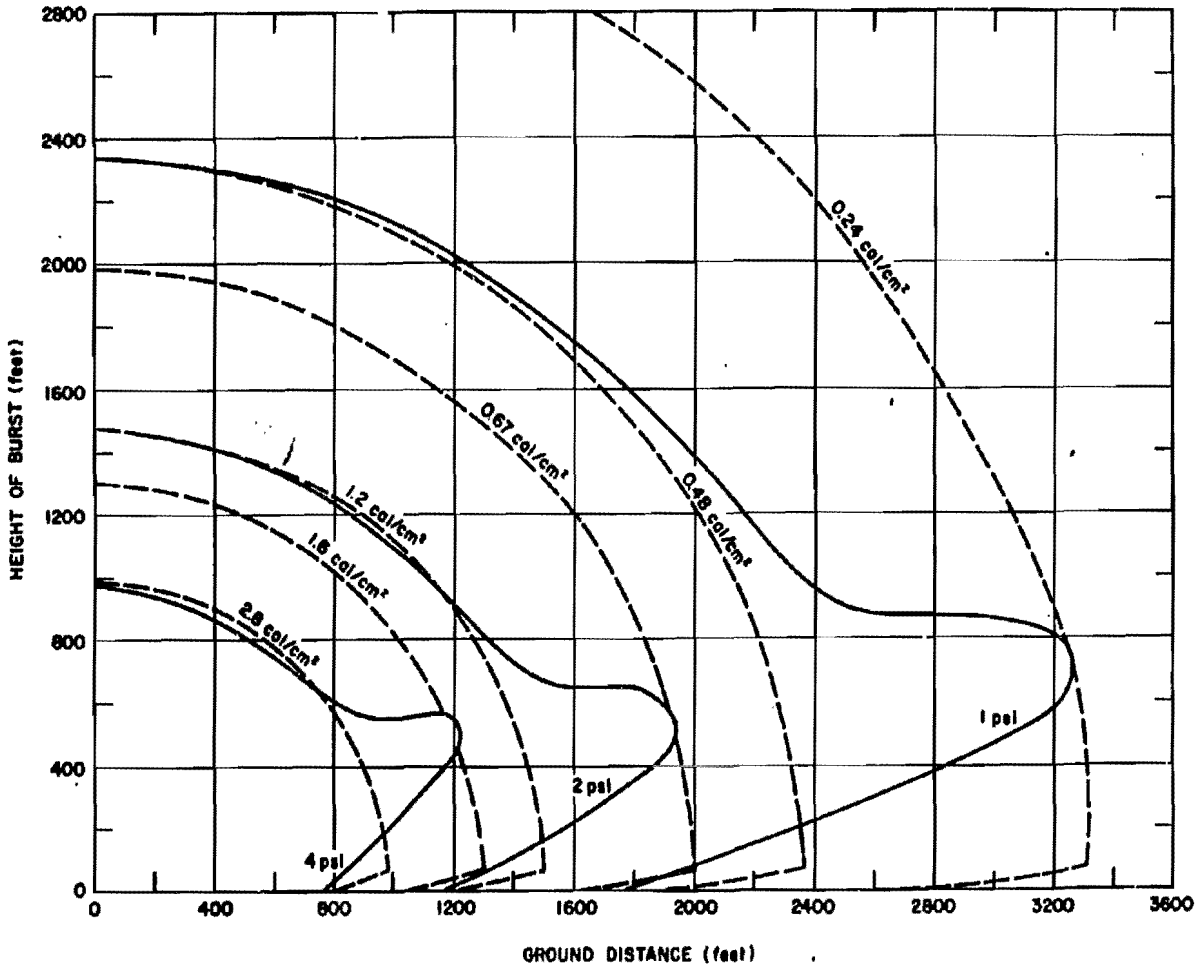

Figure 3-36. [redacted] Free Field Radiant Exposure and Air Blast Overpressure at the Surface, as a Function of Height of Burst and Ground Distance, for 0.1 kilotons, 16 Mile Visual Range, Low Overpressure Region [redacted]

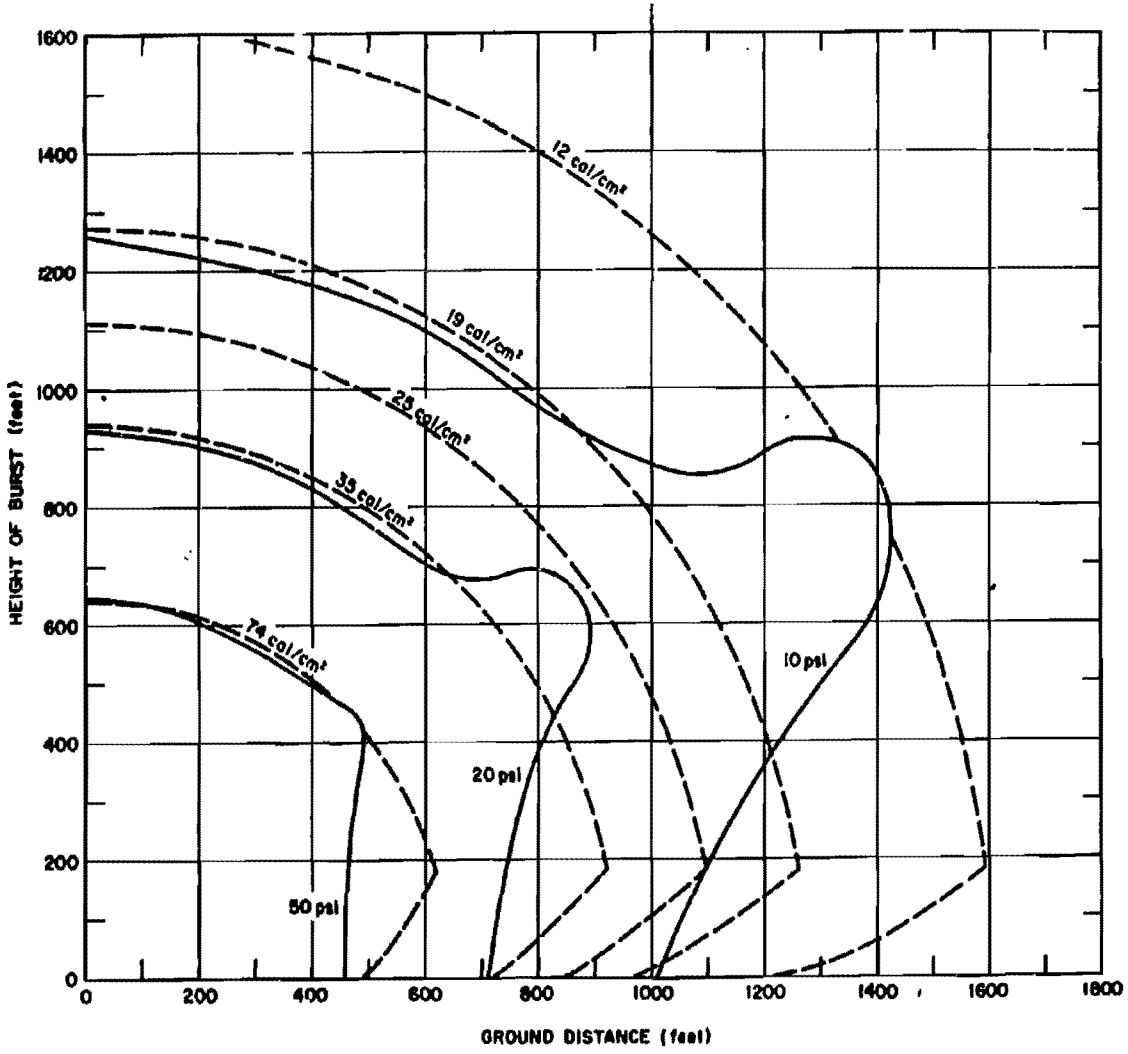

Figure 3-37. [redacted] Free Field Radiant Exposure and Air Blast Overpressure at the Surface, as a Function of Height of Burst and Ground Distance, for 1 kiloton, No Atmospheric Attenuation, High Overpressure Region [redacted]

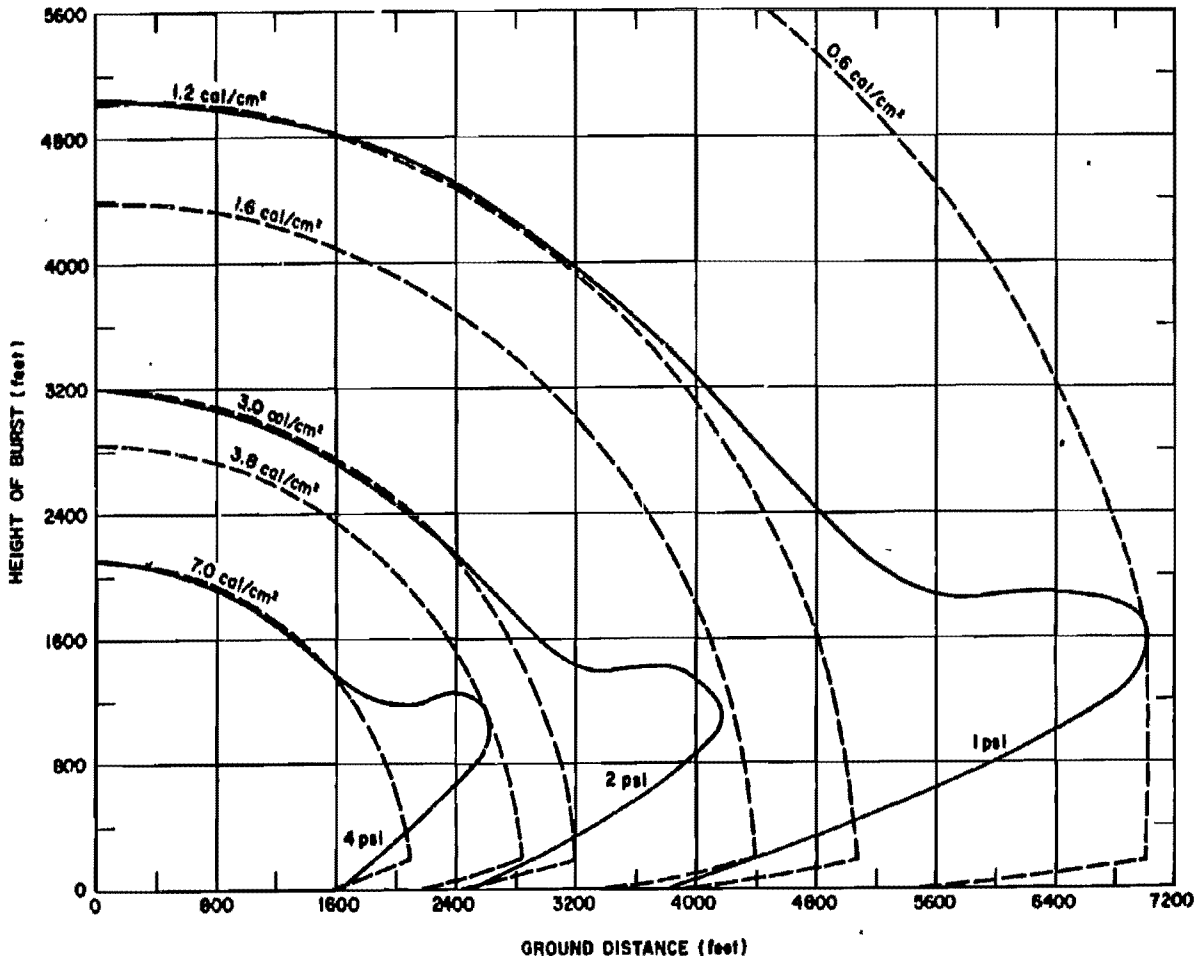

Figure 3-38. [redacted] Free Field Radiant Exposure and Air Blast Overpressure at the Surface, as a Function of Height of Burst and Ground Distance, for 1 kiloton, No Atmospheric Attenuation, Low Overpressure Region [redacted]

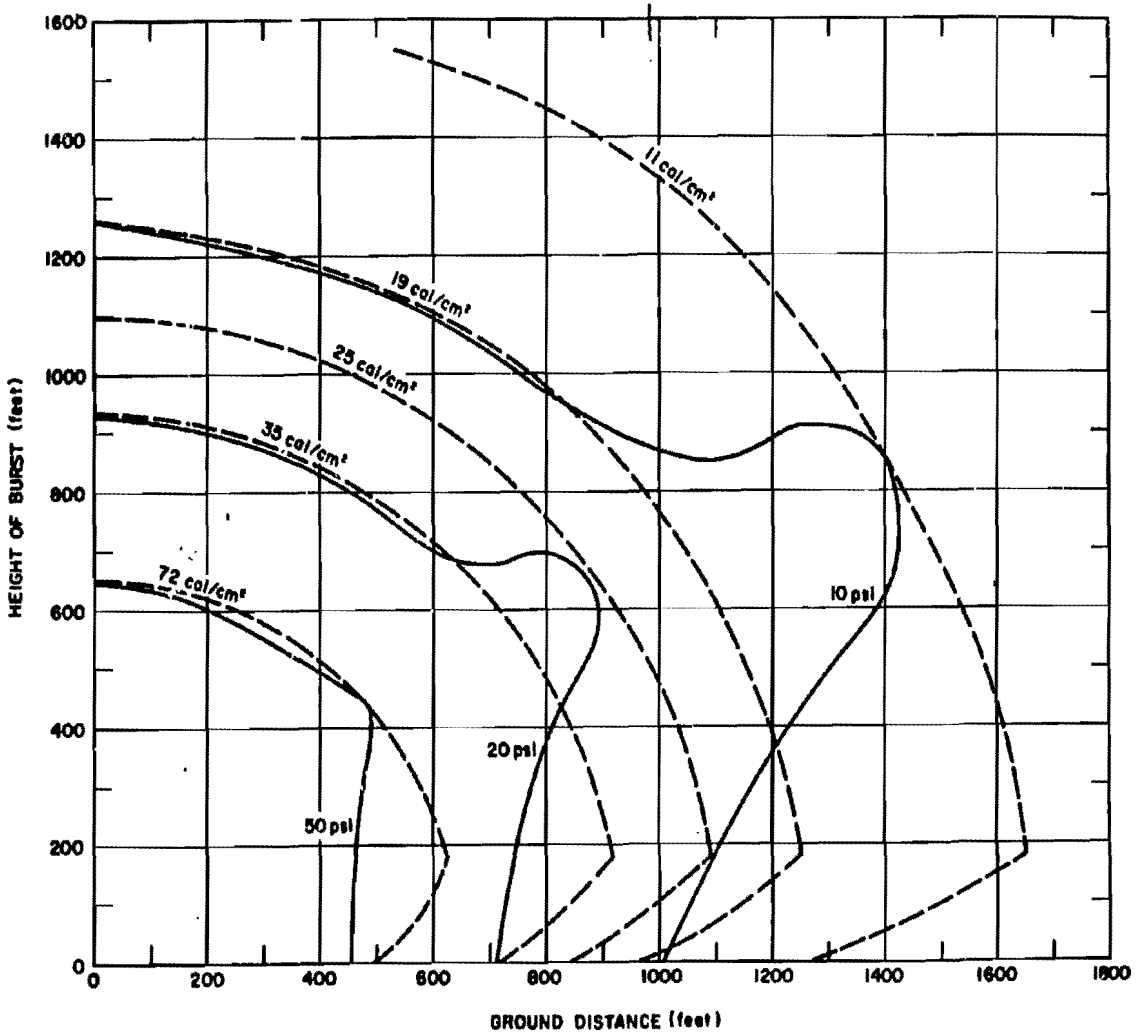

Figure 3-39. [redacted] Free Field Radiant Exposure and Air Blast Overpressure at the Surface, as a Function of Height of Burst and Ground Distance, for 1 kiloton, 16 Mile Visual Range, High Overpressure Region [redacted]

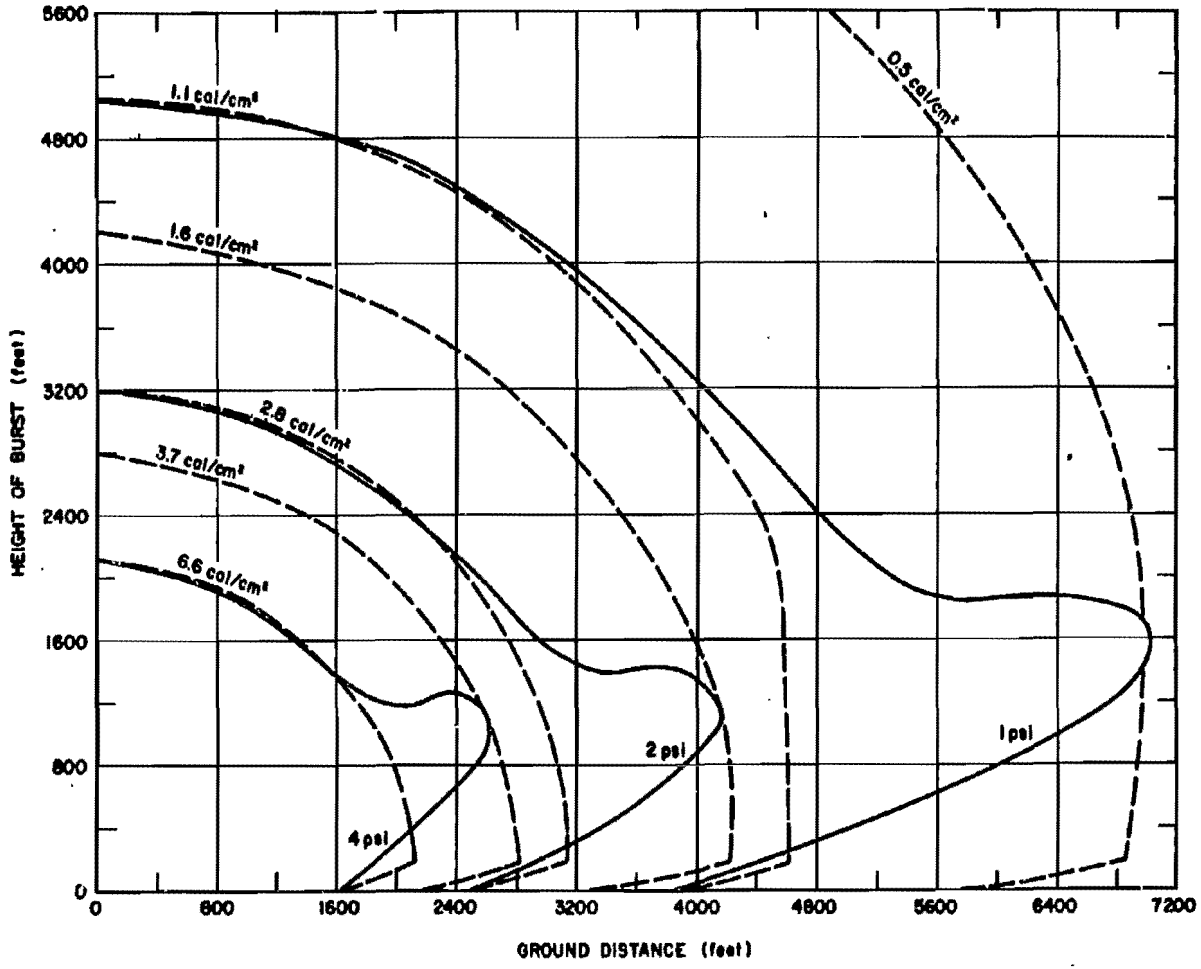

Figure 3-40. [redacted] Free Field Radiant Exposure and Air Blast Overpressure at the Surface, as a Function of Height of Burst and Ground Distance, for 1 kiloton, 16 Mile Visual Range, Low Overpressure Region [redacted]

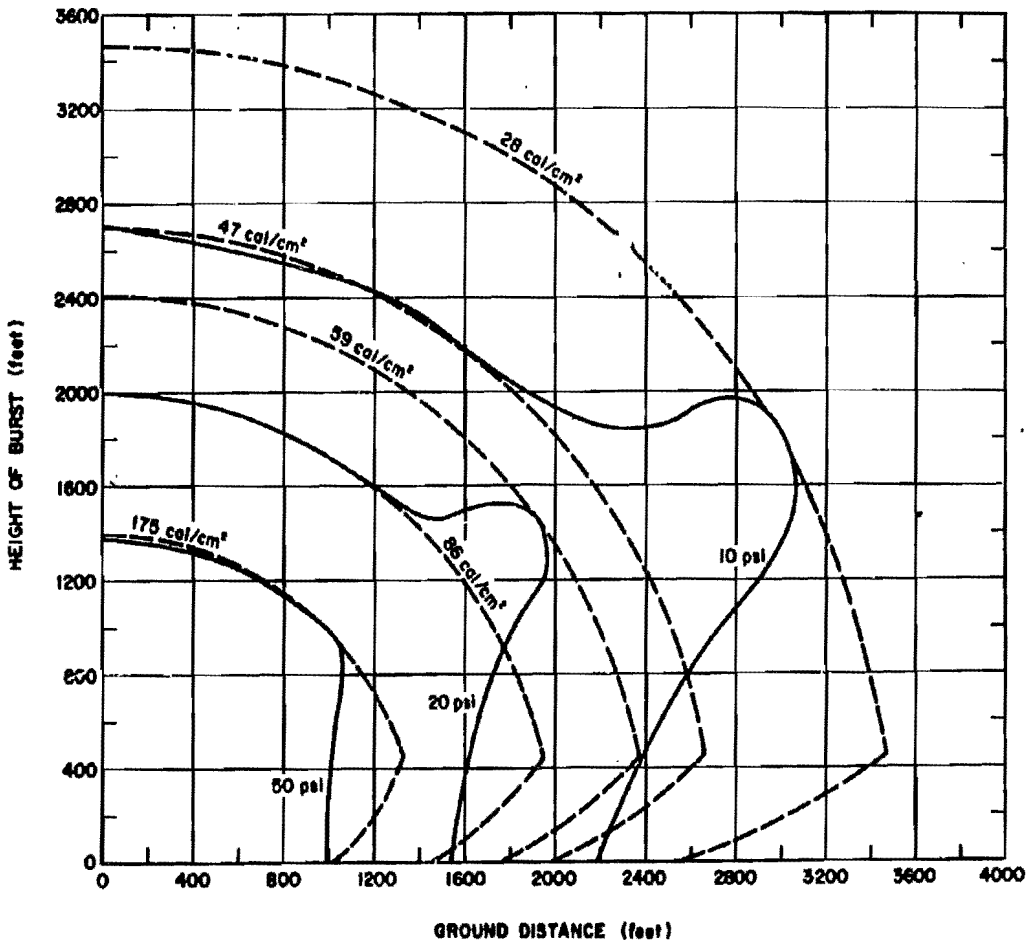

Figure 3-41. [redacted] Free Field Radiant Exposure and Air Blast Overpressure at the Surface, as a Function of Height of Burst and Ground Distance, for 10 kilotons, No Atmospheric Attenuation, High Overpressure Region [redacted]

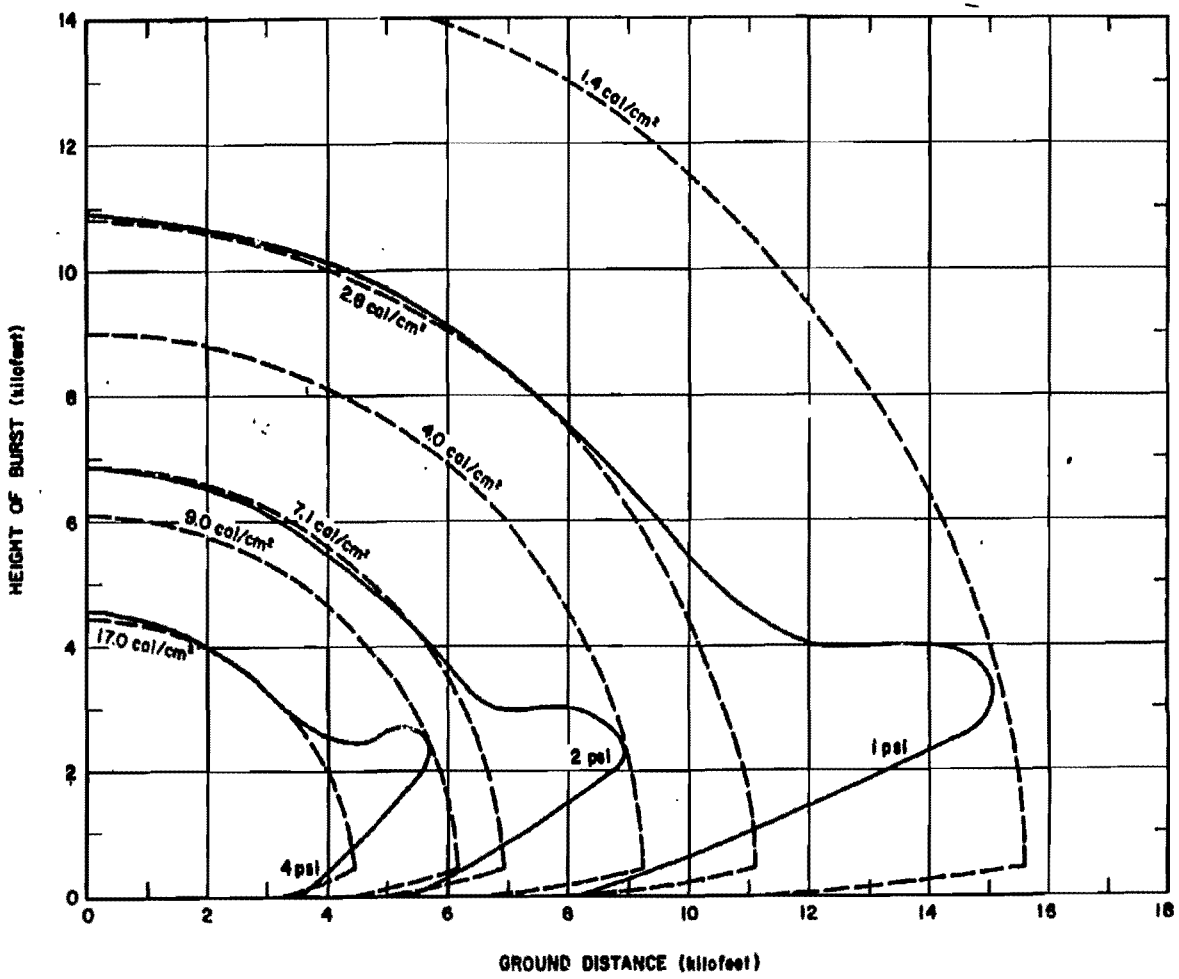

Figure 3-42. [redacted] Free Field Radiant Exposure and Air Blast Overpressure at the Surface, as a Function of Height of Burst and Ground Distance, for 10 kilotons, No Atmospheric Attenuation, Low Overpressure Region [redacted]

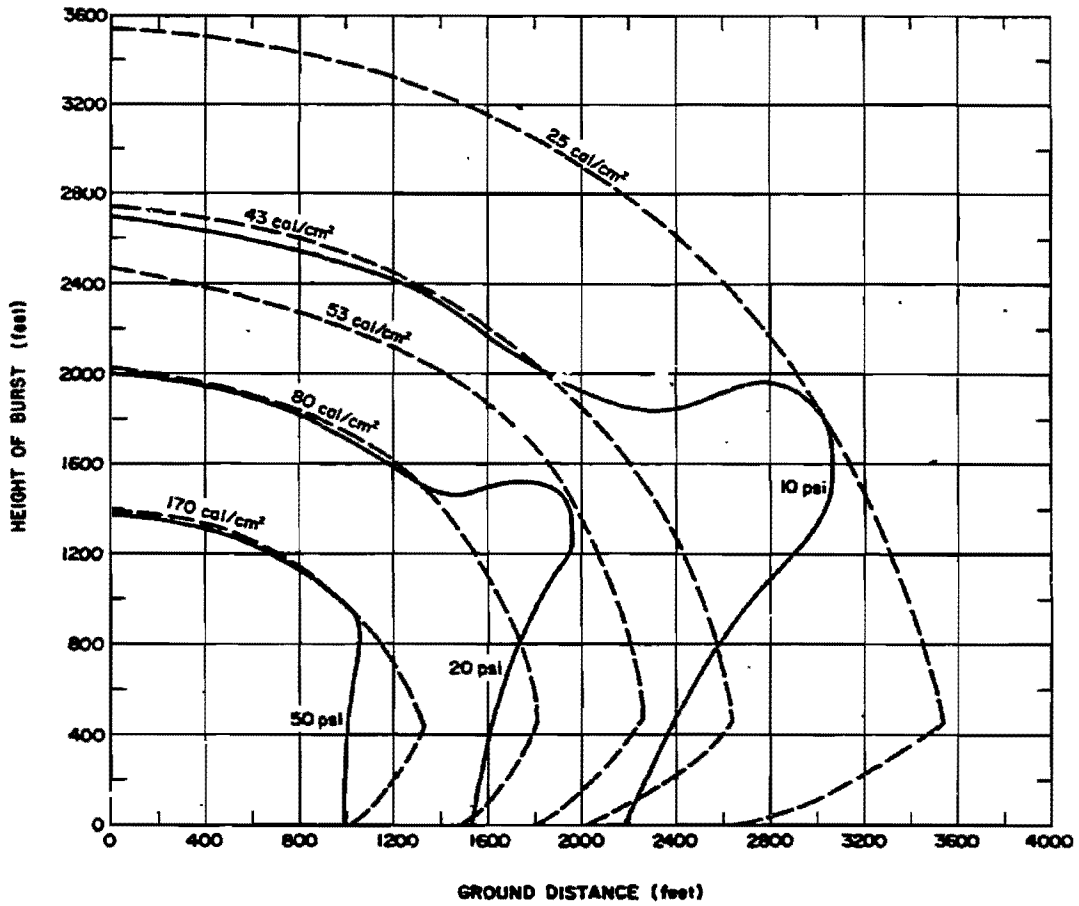

Figure 3-43. [redacted] Free Field Radiant Exposure and Air Blast Overpressure at the Surface, as a Function of Height of Burst and Ground Distance, for 10 kilotons, 16 Mile Visual Range, High Overpressure Region [redacted]

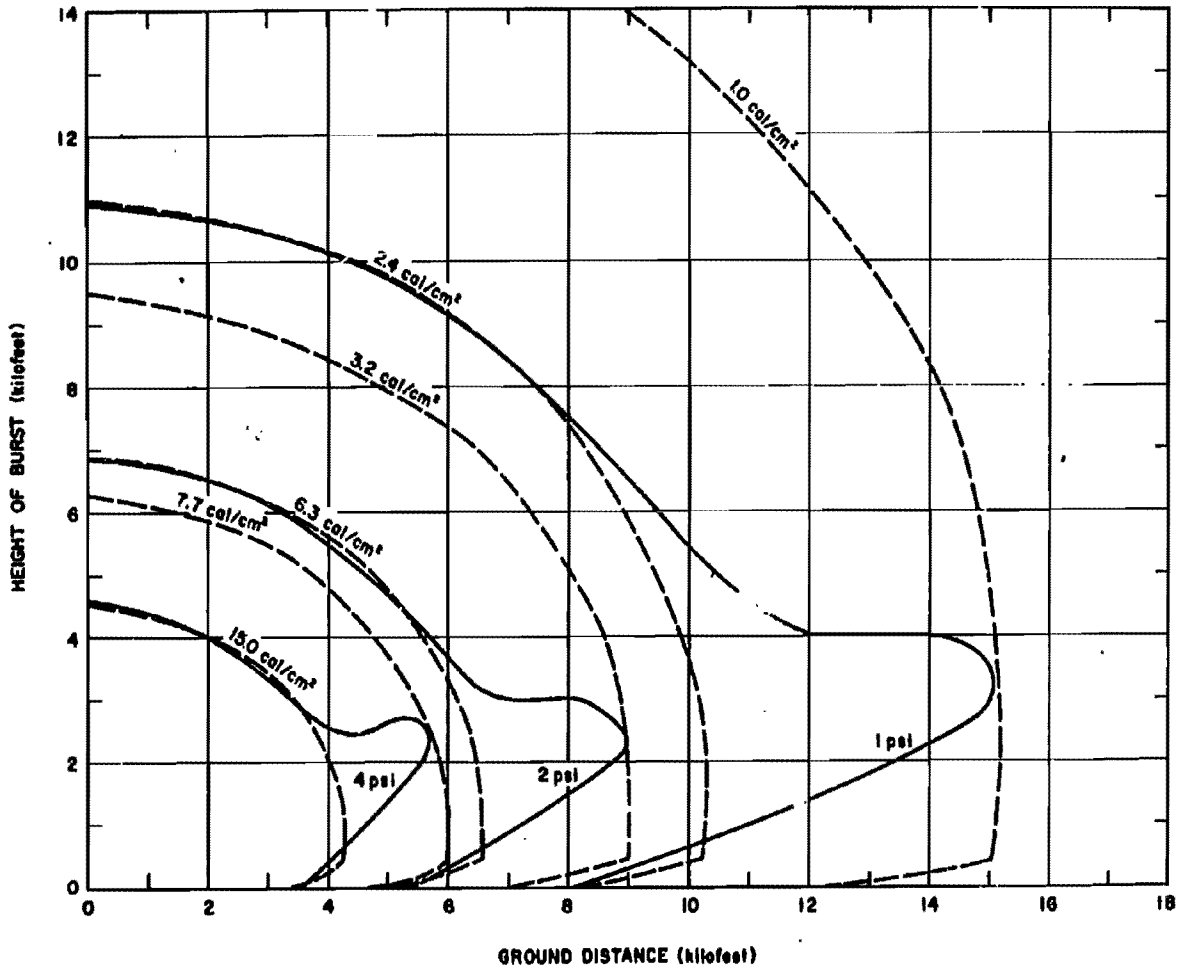

Figure 3-44. [redacted] Free Field Radiant Exposure and Air Blast Overpressure at the Surface, as a Function of Height of Burst and Ground Distance, for 10 kilotons, 16 Mile Visual Range, Low Overpressure Region [redacted]

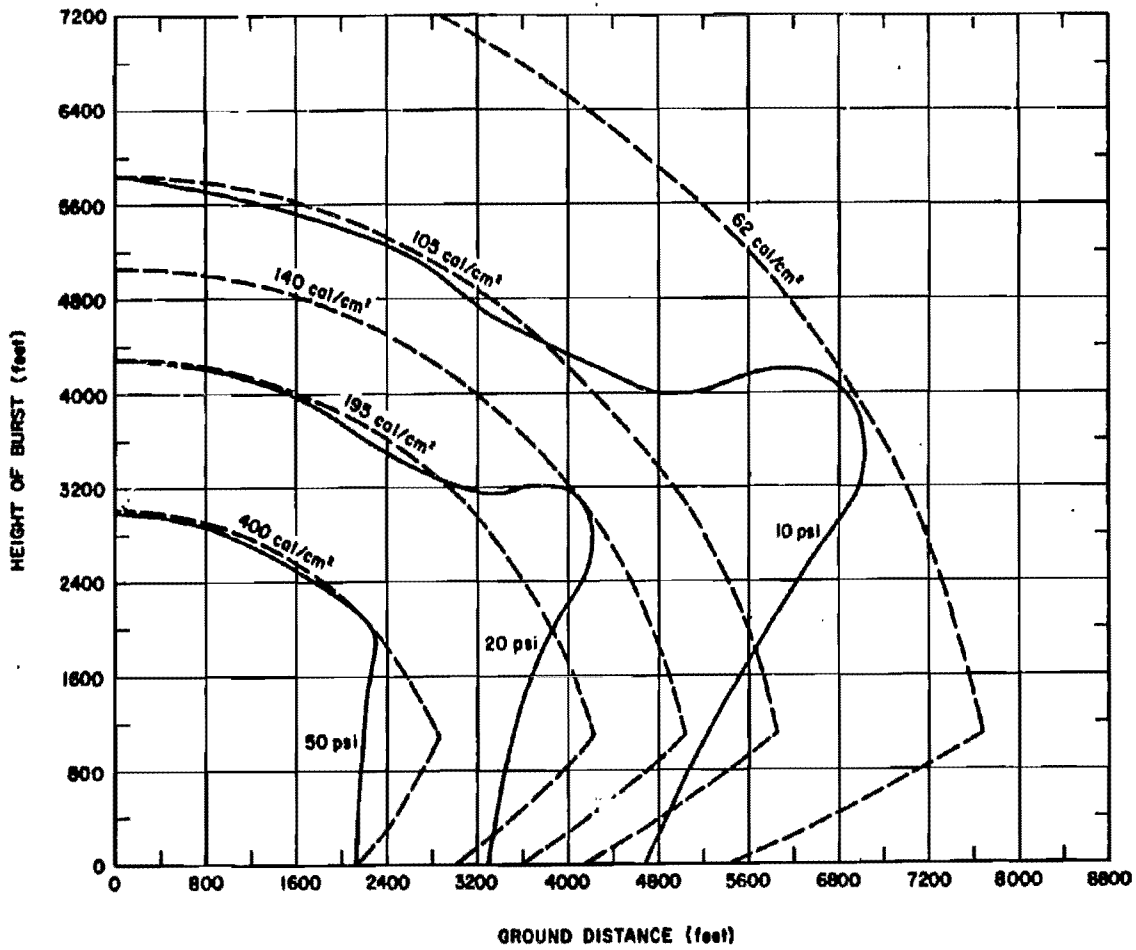

Figure 3-45. [redacted] Free Field Radiant Exposure and Air Blast Overpressure at the Surface, as a Function of Height of Burst and Ground Distance, for 100 kilotons, No Atmospheric Attenuation, High Overpressure Region [redacted]

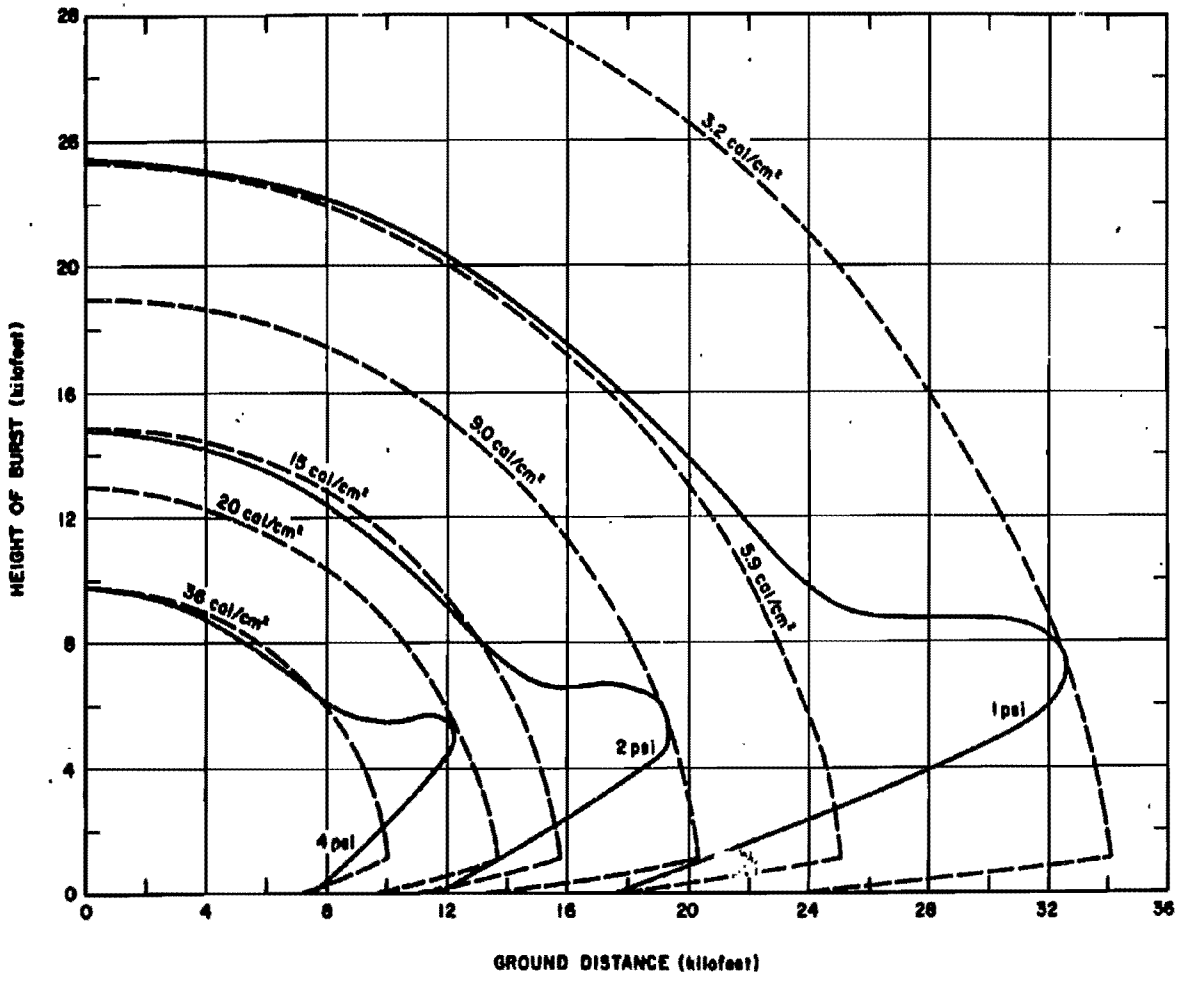

Figure 3-46. [redacted] Free Field Radiant Exposure and Air Blast Overpressure at the Surface, as a Function of Height of Burst and Ground Distance, for 100 kilotons, No Atmospheric Attenuation, Low Overpressure Region [redacted]

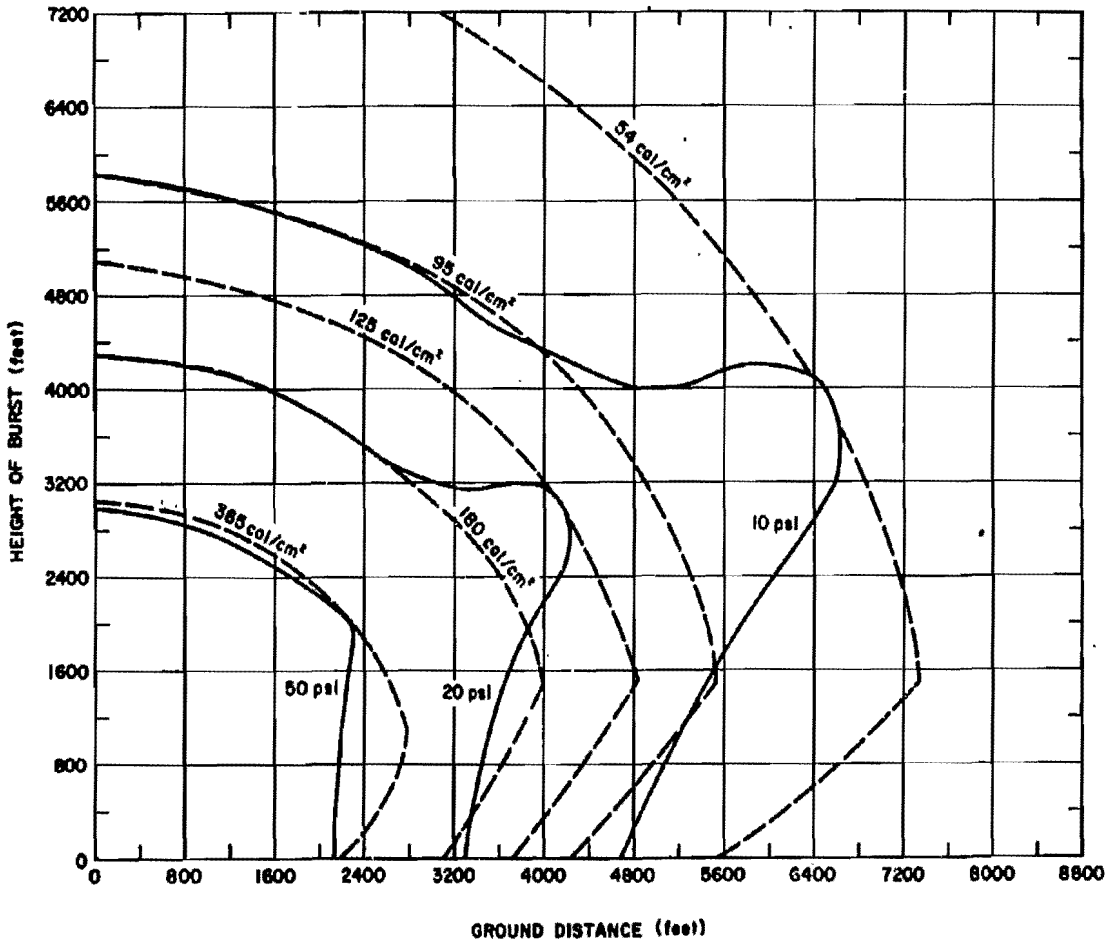

Figure 3-47. [redacted] Free Field Radiant Exposure and Air Blast Overpressure at the Surface, as a Function of Height of Burst and Ground Distance, for 100 kilotons, 16 Mile Visual Range, High Overpressure Region [redacted]

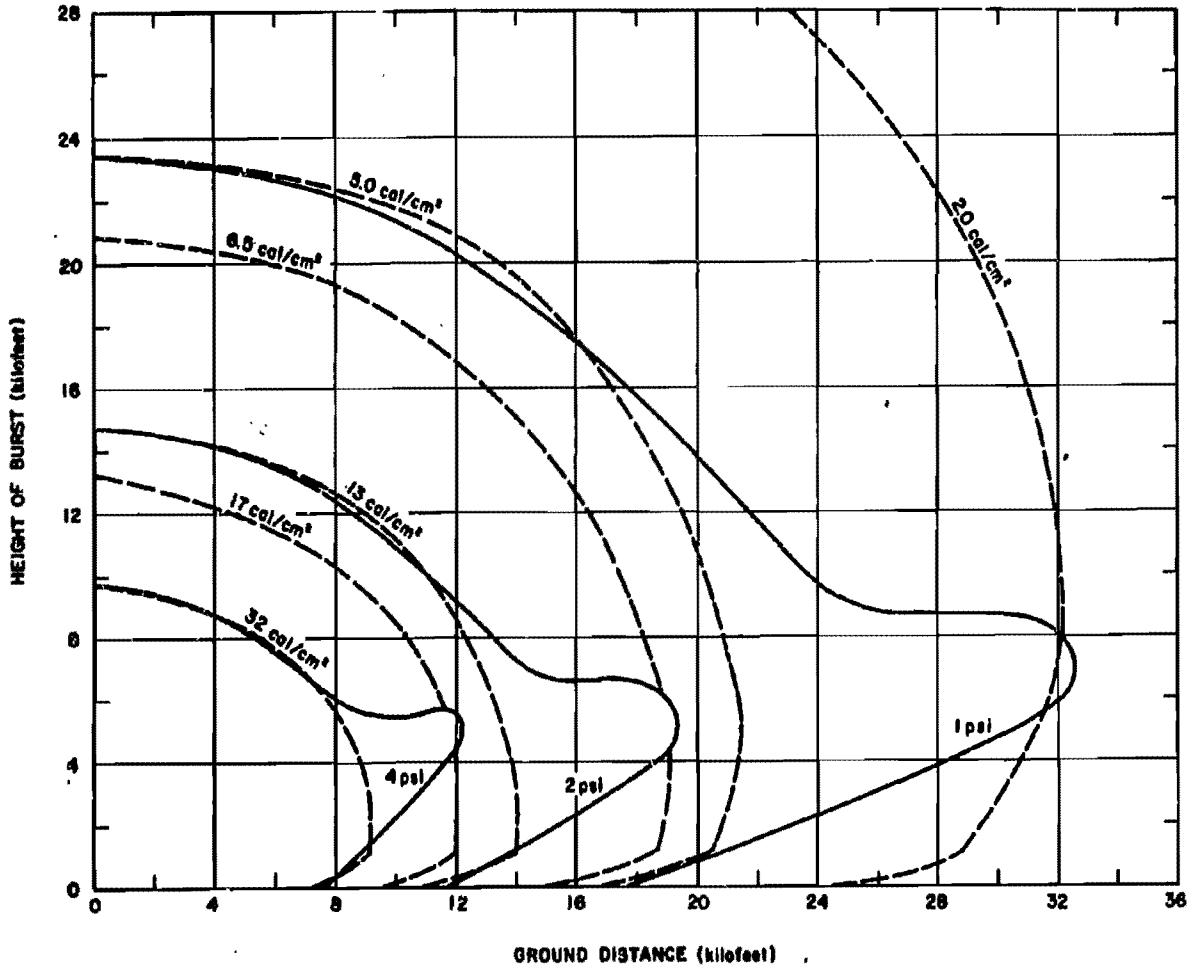

Figure 3-48. [redacted] Free Field Radiant Exposure and Air Blast Overpressure at the Surface, as a Function of Height of Burst and Ground Distance, for 100 kilotons, 16 Mile Visual Range, Low Overpressure Region [redacted]

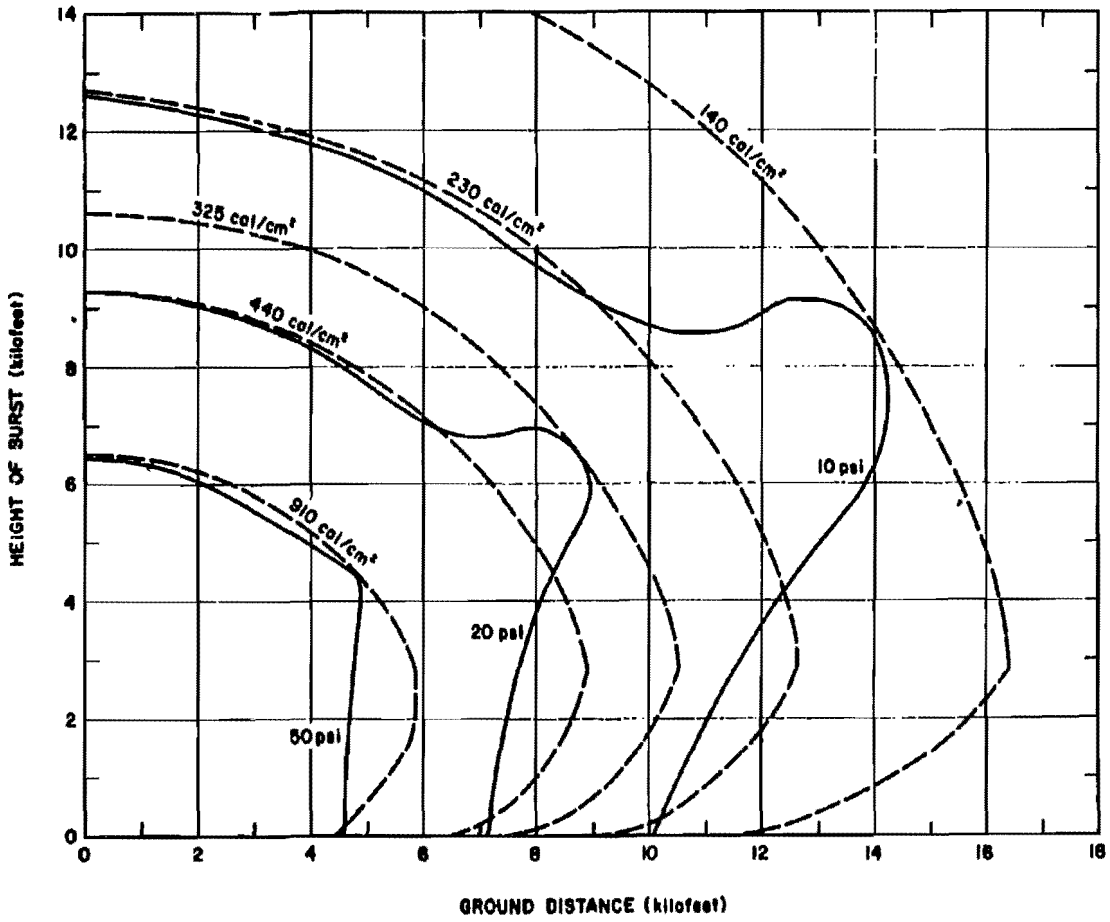

Figure 3-49. [redacted] Free Field Radiant Exposure and Air Blast Overpressure at the Surface, as a Function of Height of Burst and Ground Distance, for 1 megaton, No Atmospheric Attenuation, High Overpressure Region [redacted]

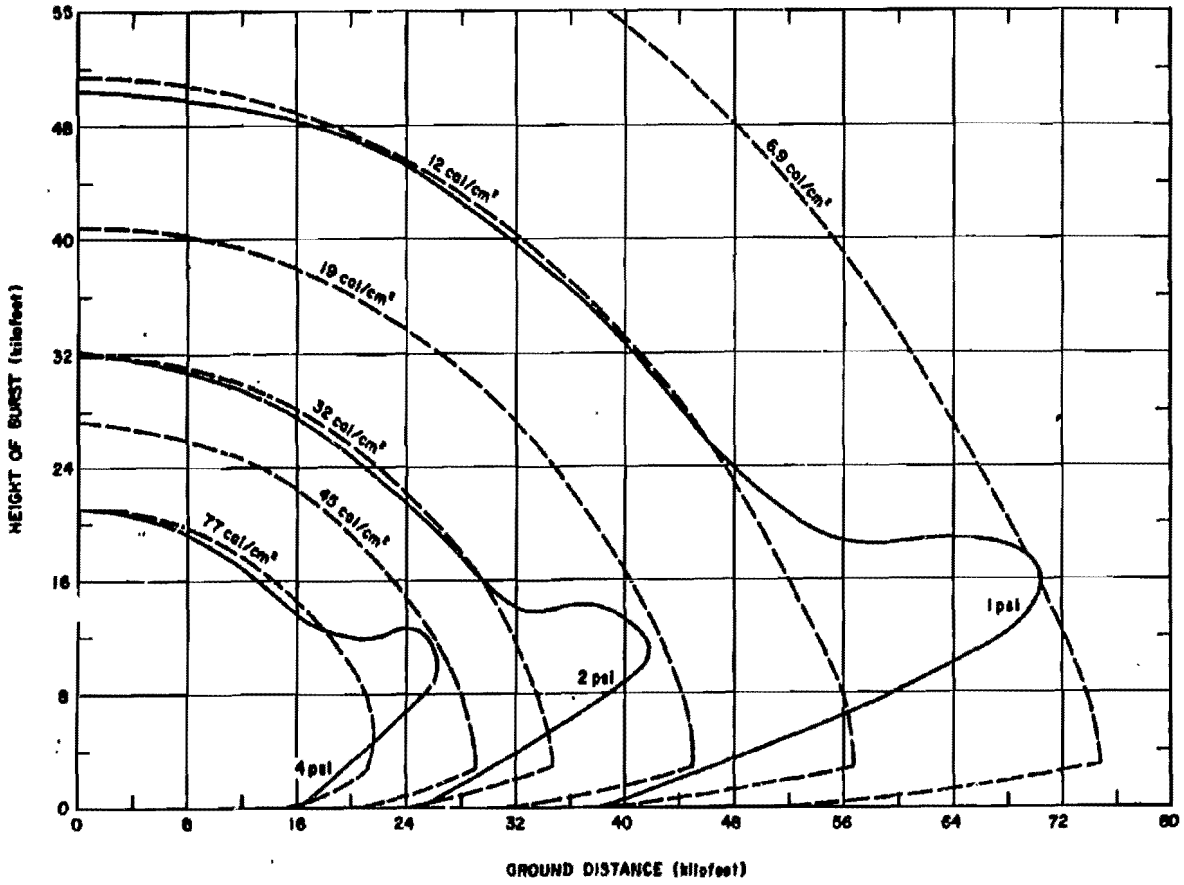

Figure 3-50. [redacted] Free Field Radiant Exposure and Air Blast Overpressure at the Surface, as a Function of Height of Burst and Ground Distance, for 1 megaton, No Atmospheric Attenuation, Low Overpressure Region [redacted]

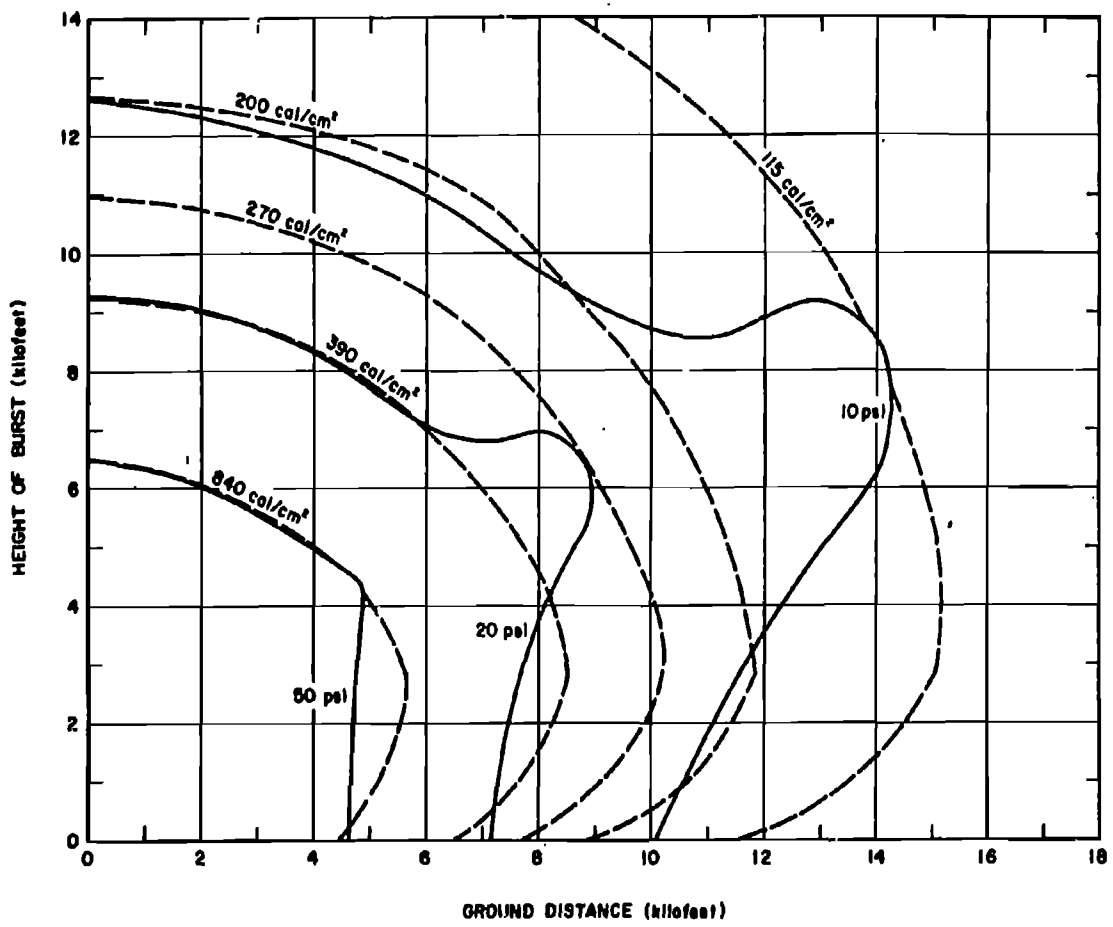

Figure 3-51. [redacted] Free Field Radiant Exposure and Air Blast Overpressure at the Surface, a Function of Height of Burst and Ground Distance, for 1 megaton, 16 Mile Visual Range, High Overpressure Region [redacted]

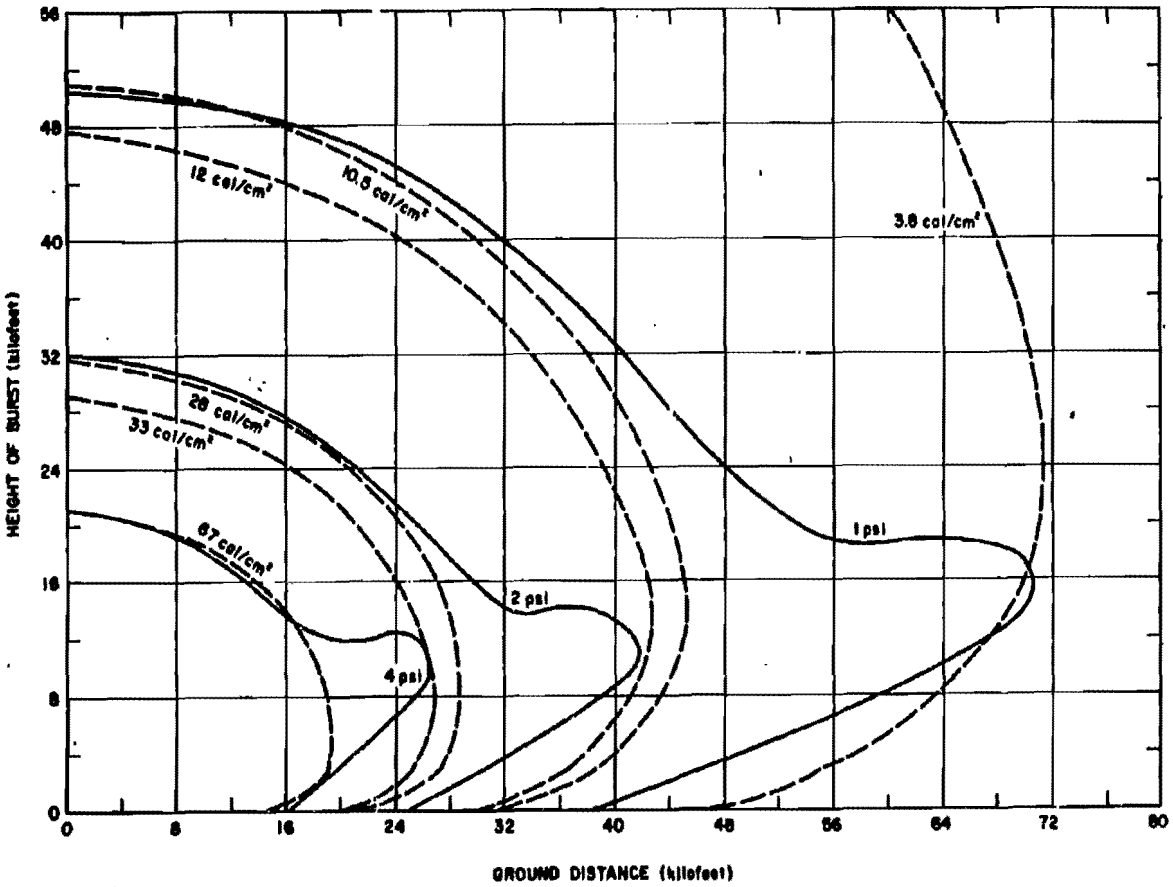

Figure 3-52. [redacted] Free Field Radiant Exposure and Air Blast Overpressure at the Surface, as a Function of Height of Burst and Ground Distance, for 1 megaton, 16 Mile Visual Range, Low Overpressure Region [redacted]

[redacted]

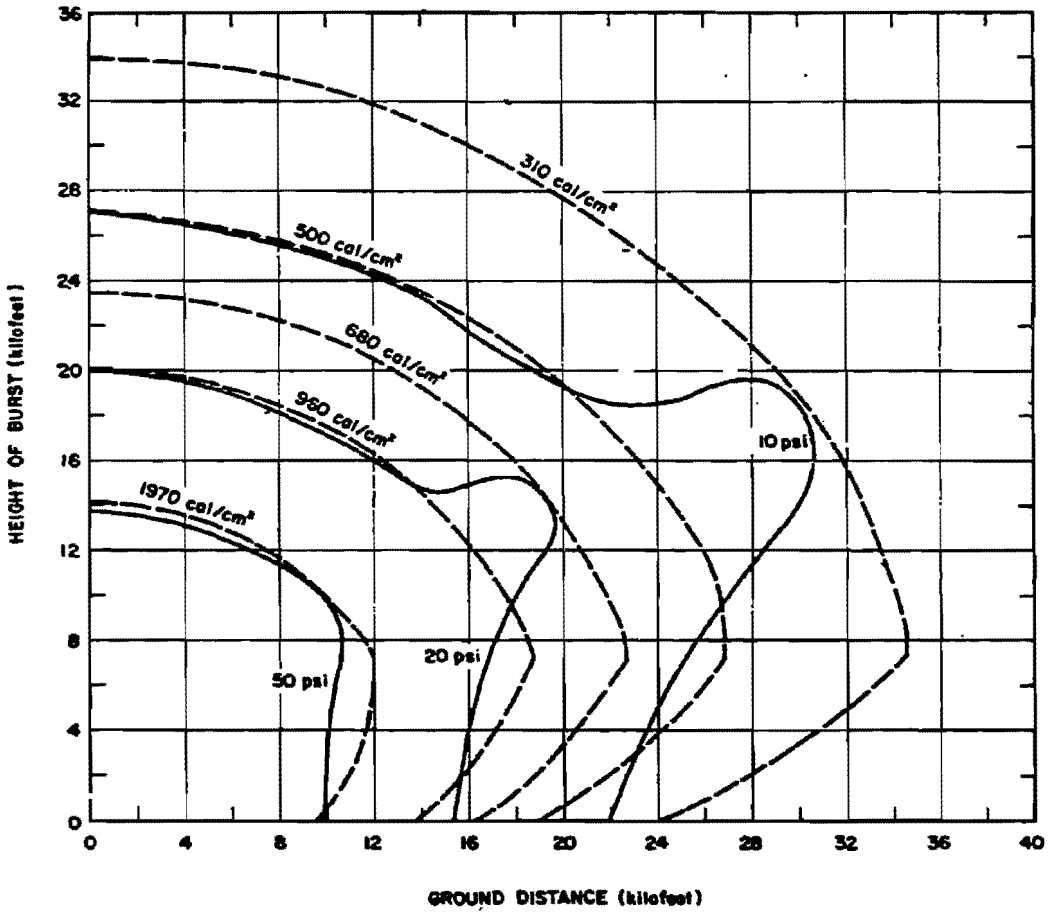

Figure 3-53. [redacted] Free Field Radiant Exposure and Air Blast Overpressure at the Surface, as a Function of Height of Burst and Ground Distance, for 10 megatons, No Atmospheric Attenuation, High Overpressure Region [redacted]

[redacted]

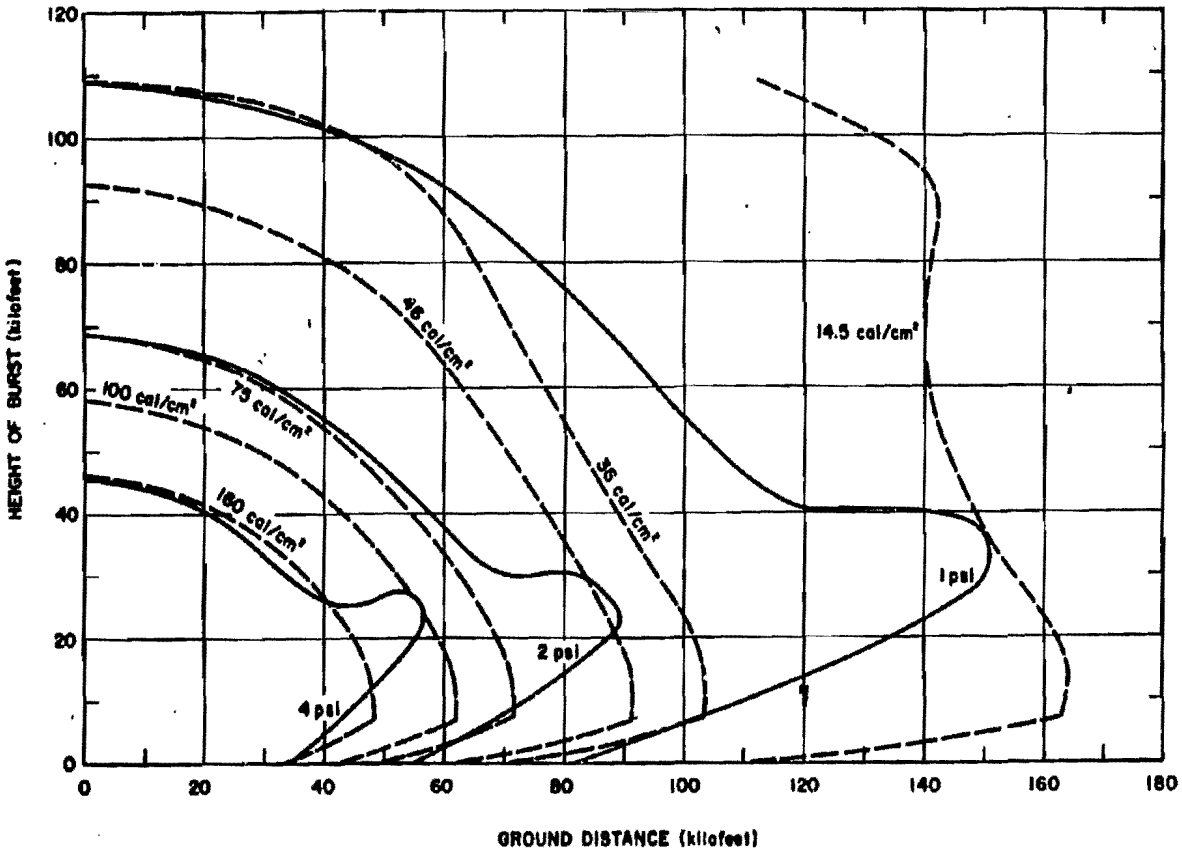

Figure 3-54. [redacted] Free Field Radiant Exposure and Air Blast Overpressure at the Surface, as a Function of Height of Burst and Ground Distance, for 10 megatons, No Atmospheric Attenuation, Low Overpressure Region [redacted].

[redacted]

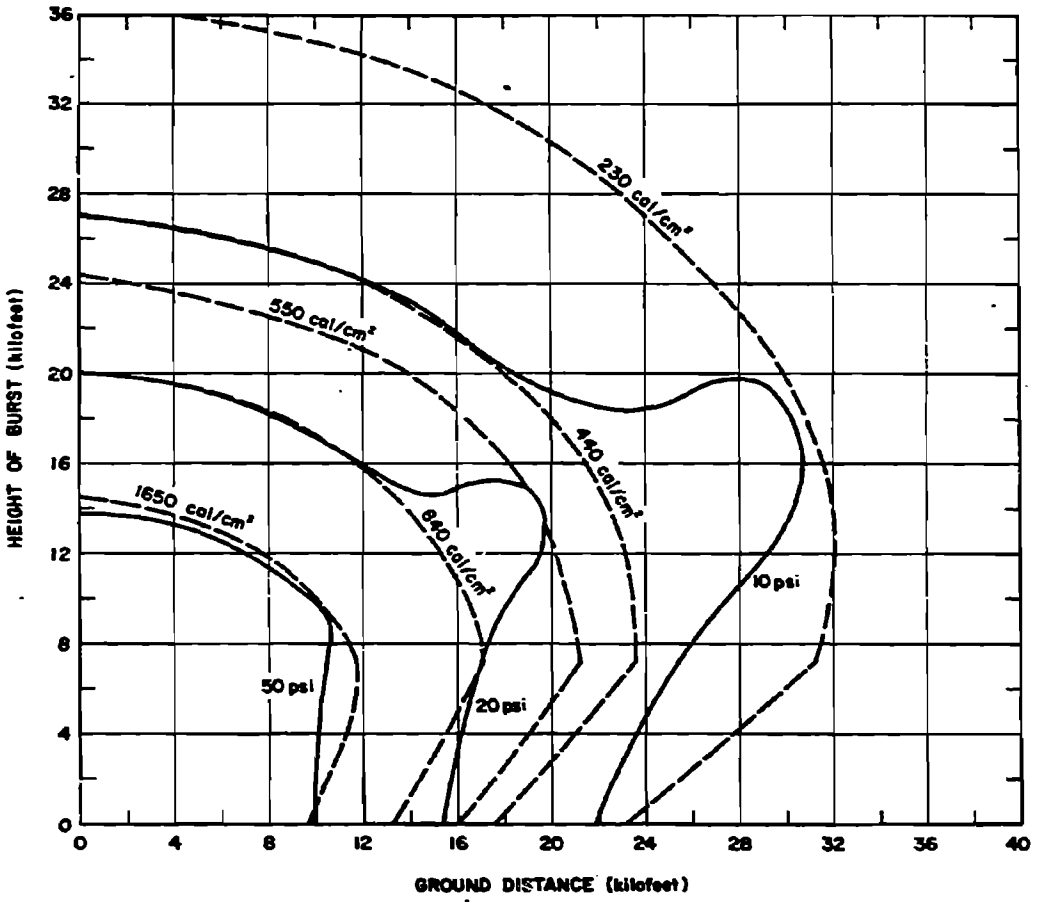

Figure 3-55. [redacted] Free Field Radiant Exposure and Air Blast Overpressure at the Surface, as a Function of Height of Burst and Ground Distance, for 10 megatons, 16 Mile Visual Range, High Overpressure Region [redacted]

[redacted]

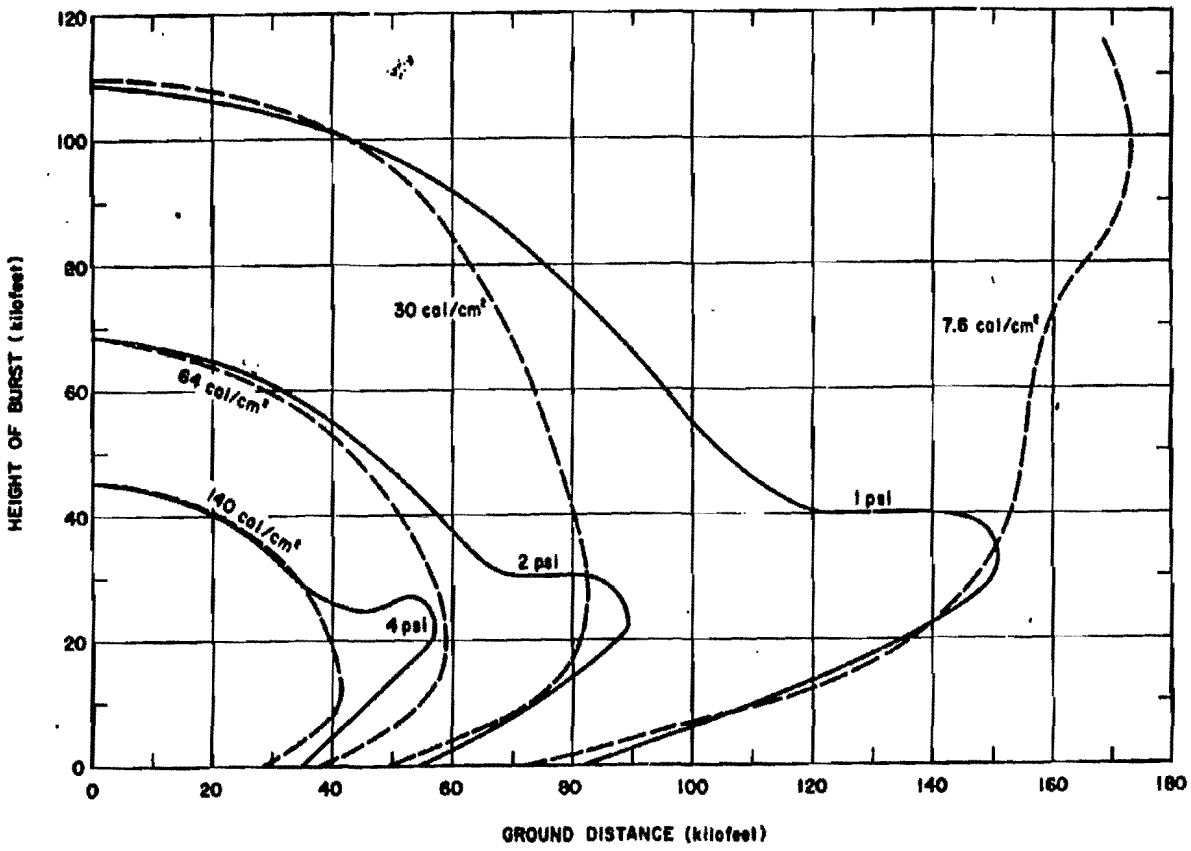

Figure 3-56. [redacted] Free Field Radiant Exposure and Air Blast Overpressure at the Surface, as a Function of Height of Burst and Ground Distance, for 10 megatons, 16 Mile Visual Range, Low Overpressure Region [redacted]

PHYSICS OF FIREBALL DEVELOPMENT

It is not necessary to understand the physics that govern fireball evolution to perform the calculations of the thermal environment that are described in the preceding paragraphs. The following discussion is an introduction to the subject of fireball physics that is intended to introduce certain additional fireball phenomena and to serve as a bridge to more advanced discussions found in the references.

3-22 Black Body Radiation

A basic principal of physics is that a good radiator is also a good absorber of radiation. Thus, a perfectly black object, i.e., one that absorbs all of the radiation that is incident on it, is an ideal radiator of thermal radiation. Consequently, black body radiation is a convenient standard to which thermal radiation from actual sources can be compared.

The radiation properties of nuclear weapons frequently may be described as a black body source of a given temperature or as a combination of several such sources. Paragraph 4-2, Chapter 4, describes the properties of an ideal black body source. Paragraphs 4-4 through 4-7, Chapter 4, describe the spectral characteristics of nuclear weapons in terms of black body sources.

3-23 Opacity

The flow of energy through a nuclear fireball is strongly affected by the opacity of heated air. The term opacity correctly suggests impedance to the flow of radiation, i.e., energy flows more slowly through those parts of the fireball in which the opacity of the air is high. A less obvious but equally important effect of opacity arises from the physical principle described in paragraph 3-22: in order to be a good radiator of thermal energy a material must also be a good absorber. For this reason the late time fireball cannot radiate effectively. The gas becomes relatively transparent and, as a result, radiates its energy so slowly that it produces negligible thermal damage.

In radiation transport theory, the term opacity is assigned a more specific meaning than it has as a nontechnical world. In a medium that absorbs much more radiation than it scatters (this is generally true of the hot gases that constitute the fireball), opacity is the reciprocal of the mean free path, the average distance that a photon travels before it is absorbed. Thus, the units of opacity are reciprocal distance, and values given in the following discussion are in $meters^{-1}$.

The terms "opaque" and "transparent" are used in a less specific sense. A zone of air is opaque if it is thick compared to the mean free path of the radiation passing through it. For example, if a region 1 meter thick has an opacity of 10 $meter^{-1}$ (mean free path = 1/10 meter), it is definitely opaque; if its opacity is 0.01 $meter^{-1}$ (mean free path = 100 meters), it is quite transparent.

The opacity of a gas is different for photons of different energy; therefore, the radiation to which the value of opacity applies must be specified. Normally, opacity is given as an average value that represents the transport properties of that black body spectrum which corresponds to the temperature of the gas.

There is an optimum value of opacity that allows the fireball to radiate at the highest possible rate. This value is low enough to permit rapid flow of thermal energy from the hot interior of the fireball to the cooler surface layers, but it is high enough that all regions of the fireball are able to radiate the thermal energy that they contain.

The physical processes that determine opacity over the range of temperature and photon energies that are of interest are changes in the energy levels of atoms or molecules. At

photon energies of a few eV* or higher, these processes involve absorption of the photon energy by the electrons of the atom or molecule. At the lower photon energies characteristic of infrared photons, the interactions may involve changes in the vibrational states of atoms. All of these interactions involve changes between two allowable energy states of the atom or molecule. In many cases the photon encounters an atom that has no allowable energy level that exceeds its present energy level by exactly the photon energy. In these cases, absorption of the photon is impossible. Photons of visible light propagating through air illustrate this condition. The photon energy is too high to excite the small changes in molecular energy that certain infrared photons can produce, and it is too low to produce the electronic excitation or ionization that certain photons in the ultraviolet region can produce. Consequently, pure air is transparent to these photons, affecting them only by infrequent scattering interactions.

The radiating properties of the fireball and the surrounding air are strongly affected by a particular absorption band of the oxygen molecule, the Schumann-Runge band. Although several mechanisms render air opaque to photons with energies of the order of 10 eV, the Schumann-Runge band is parficularly important because it is effective at lower values of photon energy than other strong absorption bands. For this reason, it determines the cutoff energy of the spectrum of transmitted photon energies.

The Schumann-Runge band normally absorbs only those photons with energies greater than about 6.7 eV. However, when air is heated to temperatures of a few thousand degrees, oxygen molecules are excited to high vibrational energy levels, with reduces the energy gap between the equilibrium molecular states and the Schumann-Runge continuum. This smaller energy gap reduces the energy that a photon must have in order to induce a transition, and air at 4,000°K absorbs photons with energies as low as 3 eV strongly. This is the photon energy that is associated with violet lights. Thus, the hot layer of air surrounding the luminous region of the fireball removes most ultraviolet energy from thermal radiation, causing fireball radiation to contain a much lower fraction of ultraviolet energy than does sunlight.

3-24 The Fireball Before Final Maximum

A discussion of a low altitude fireball close to the final maximum is valuable for two reasons: this stage of development is of practical interest because the bulk of the thermal pulse is emitted during this final pulse; it is of theoretical interest because most of the physical phenomena affecting all stages of fireball development are active at the time of final maximum. Figure 3-57 shows the opacity properties of a particular fireball in terms of four zones.

- *Zone I:* The hot core of the fireball has a relatively uniform temperature. For this reason, it is called the "isothermal sphere." Since this zone is fairly transparent at most stages of fireball development, thermal energy flows rapidly from hotter regions to cooler ones, and large temperature differences cannot form. At the time shown in Figure 3-57, the opacity is about 1 meter.
- *Zone II:* At the edge of the isothermal sphere, opacity rises rapidly because of increasing air density. Air in this zone not only is more opaque to its own radiation (the mean free path drops to about 12 cm); it has much higher opacity to the higher temperature radiation from the isothermal sphere. Zone I is expanding by heating the air in Zone II; as a result, Zone II has a high temperature gradient. The outer edge of

*1 eV = 1.6×10^{-12} erg.

[redacted]

DNA
(b)(3)

Deleted

Figure 3-57. [redacted] Fireball Properties after Breakaway [redacted]

[redacted]

[redacted]

Zone II forms the radiating surface of the visible fireball.

- *Zone III:* Between the fireball and the shock front, air is too cool to radiate energy efficiently. The low opacity of this region to its own radiation reflects this property. This region is, however, opaque to portions of the radiation from Zone II. It absorbs the blue and ultraviolet regions of the spectrum. As a result, it intercepts part of the energy radiated by the fireball and changes the spectral distribution of fireball radiation as seen from a distance.
- *Zone IV:* Ambient air is relatively transparent to infrared, visible, and near-ultraviolet radiation, and will transmit that portion of the fireball radiation that is emitted in this spectral region.

3-25 History of Fireball Evolution [redacted]

[redacted] Most of the stages of fireball development are of little interest in connection with thermal damage, but, for some purposes, the entire sequence of observable phenomena provides useful information. The most obvious application is the comparison of computer calculations with experimental data. This comparison is an excellent indication of the degree to which the computer program simulates actual fireball phenomena.

[redacted] It is not the purpose of this discussion to consider phenomena that contribute only minutely to the total thermal output in detail. The user who desires such detail should consult "Theoretical Models for Nuclear Fireballs [redacted]" DASA 1589, or "Thermal Radiation Phenomena," DASA 1917 (see bibliography).

[redacted] Figure 3-58 shows a calculated power-time curve for a 200 kt burst at 5,000 feet (this curve was presented previously in Figure 3-19 and forms the basis for the standard therm pulse in Figure 3-20). The labeled points correspond to the following events:

1. Deposition of the X-ray energy from the nuclear source produces an extremely hot zone of completely ionized air surrounded by a transition region in which the temperature drops to the ambient value. This transition region is produced by the higher energy X-ray photons radiated by the source. It is hot (and therefore

DNA
4)(3

Deleted

Figure 3-58. [redacted] Calculated Power-Time Curves for a 200 kiloton Burst at 5,000 feet [redacted]

[redacted]

[redacted]

opaque) enough to obscure visible radiation from the central zone. The radiation that is seen is produced by this so-called X-ray veil.

2. The isothermal sphere continually expands as radiation from the hot plasma is absorbed by the cooler, opaque gases at the edge of the sphere. The jump in radiated power at point 2 occurs as this hot sphere breaks through the X-ray veil and the brightness suddenly increases.

3. As the fireball continues to grow by radiative expansion, it engulfs more and more of the partially opaque air surrounding the veil itself.

4. Hydrodynamic motion, delayed by the inertia of the strongly heated air, has developed to the point that a shock front has formed at the surface of the fireball. The abrupt temperature rise created by the shock front produces a sudden brightening of the fireball surface. This event is partially obscured by the shock precursor, a thin zone of air ahead of the shock front that has been heated by radiation from the shock front. It is similar to the X-ray veil formed at earlier times. The peak at 4 is called the shock formation maximum.

5. As the shock front is attenuated by its expansion, both the shock temperature and the shock precursor temperature fall, and radiated power declines. At 5, the shock precursor is becoming transparent; power starts to increase as radiation from the shock front penetrates beyond the edge of the fireball. This point is called the shock precursor minimum.

6. At some altitudes, a peak known as the debris shock maximum occurs as the shock wave produced by bomb debris overtakes and intensifies the main shock wave. In this case, this event happens to coincide with the shock precursor minimum; therefore, it is not evident on the power-time curve.

7. As the shock precursor continues to cool, radiation from the shock front is transmitted increasingly well, and the traditional first maximum occurs. Power then falls as the shock front drops in temperature. Point 7 is more descriptively termed the shock exposure maximum.

8. The air heated by the shock front, screening the hot regions deeper in the fireball, produces essentially the same phenomenon that was produced at point 5 by the shock precursor. As the air behind the front cools and starts to become transparent, the radiated power first drops and then levels off at the principal minimum as radiation from the hotter inner regions of the fireball begins to penetrate to the outside.

9. During the final maximum (traditionally, the second maximum), the fireball radiates the bulk of the thermal energy. The air behind the shock front continues to become more transparent, and the radiated power comes from the large volume of hot air that constitutes the fireball. As each zone of air radiates its energy and cools below about 6,000°K, it becomes transparent and transmits radiation from a zone closer to the center. Power output drops as the so-called radiative cooling wave propagates inward and the area of the radiating surface decreases.

10. The fireball becomes largely transparent, but is still capable of radiating energy as spectral lines. This final phase of fireball evolution is called the late time radiative phase.

[redacted]

DNA 4(a)(3)

[redacted]

Figure 3-59 shows the way in which the relative timing of some of these events changes with altitude for a 200 kt burst. The numbers in circles are the same numbers that appear in Figure 3-58 to label various events.

From the point of view of thermal damage, the most important change that Figure 3-59 shows is that the principal minimum weakens and finally disappears as it merges with the debris-air shock catch-up and the final maximum at high altitudes. This effect changes the shape of the main thermal pulse and is the reason that the standard thermal pulse is roughly representative of thermal pulses only at altitudes below about 100,000 feet.

3-26 Comparison with Recent Analysis of Experiments

Although, as mentioned previously, the computer calculations agreed well with the experimental data with which they were compared, and the calculations form the basis for a complete set of data that is compatible and can be put into a form that is suitable for this manual, they do not necessarily represent the ultimate answers. A set of semi-empirical equations has recently been developed that give t_{max} and t_{min} of the thermal pulses produced by bursts up to 100 kilometers. These equations are

$$t_{max} = 0.042\ (\rho W)^{0.44}\ (\rho_s/\rho)^{-\rho_s/\rho}\ \text{sec},$$

Deleted

Figure 3-59. Altitude Variation of Phenomena for a 200 kiloton Burst

where ρ is the atmospheric density at burst altitude, and ρ_s is the density at the "singular" altitude for the yield being considered, which is the altitude at which the thermal pulse changes from a two peaked pulse to a single peaked pulse, and which is given by

$$\rho_s = 0.033\ W^{-1/2},$$

and

$$t_{min} = 0.00365\ (\rho W)^{0.44}\ \text{sec.}$$

For comparative purposes, these values are plotted together with the equations given previously for t_{max} and t_{min} as a function of yield for scaled burst heights of 180 $W^{0.4}$ feet, i.e., low air bursts, in Figure 3-60. This one comparison is presented only to show some of the uncertainty associated with the prediction of the thermal radiation environment. As pointed out previously, the computer calculations were used as the basis for the prediction of the thermal environment in this manual for several reasons, one being that they provide a complete description of all of the various phenomena in a compatible format. Further investigations may reveal that changes in the presentation of the data are required.

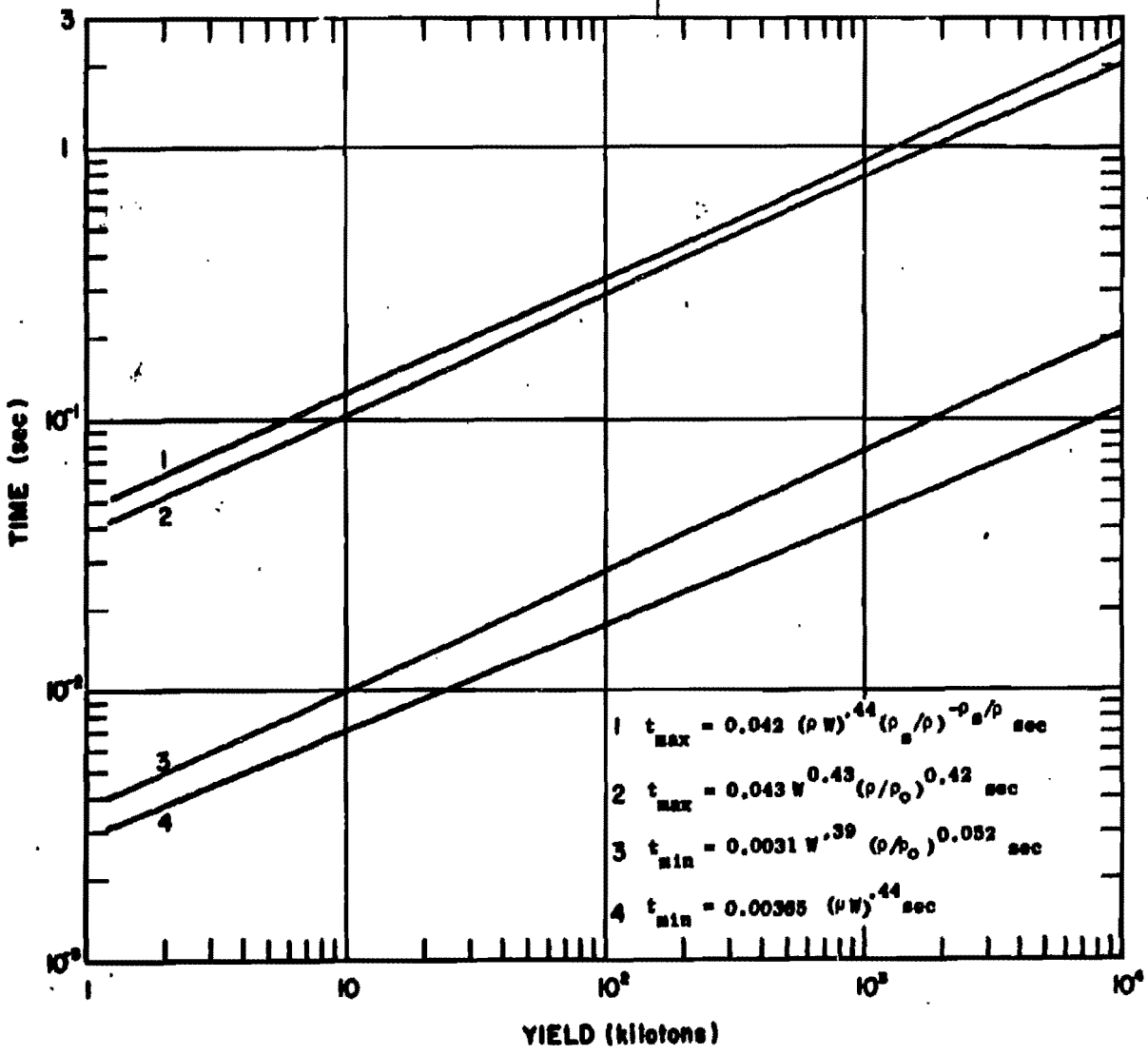
TIME (sec)
YIELD (kilotons)
1 $t_{max} = 0.042\ (\rho W)^{.44} (\rho_s/\rho)^{-\rho_s/\rho}$ sec
2 $t_{max} = 0.043\ W^{0.43} (\rho/\rho_o)^{0.42}$ sec
3 $t_{min} = 0.0031\ W^{.39}\ (\rho/\rho_o)^{0.052}$ sec
4 $t_{min} = 0.00365\ (\rho W)^{.44}$ sec

Figure 3-60. Comparison of Equations for t_{min} and t_{max}, $HOB = 180\ W^{0.4}$ feet

[redacted]

[redacted] BIBLIOGRAPHY [redacted]

Duntley, S. O., *The Visibility of Distant Objects*, Journal of the Optical Society of America, 38, 237-249, 1948 [redacted]

Ellis, P. A., *A Note on the Prediction of Thermal Pulse from Special Nuclear Weapons* [redacted] DASA 2097, KN-717-68-3, Kaman Nuclear, Colorado Springs, Colorado, 20 March 1968 [redacted]

Gibbons, M. G., *Transmissivity of the Atmosphere for Thermal Radiation from Nuclear Weapons*, USNRDL-TR-1060, U.S. Naval Radiological Defense Laboratory, San Francisco, California, 12 August 1966 [redacted]

Hillendahl, R. W., *Theoretical Models for Nuclear Fireballs* [redacted] (41 Volumes) DASA 1589, Lockheed Missiles and Space Company, Sunnyvale, California, 1965-1968 (Part A, [redacted] Part B, [redacted] Volumes 1-39, [redacted]

Landshoff, R. M., *Thermal Radiation Phenomena* [redacted] (6 Volumes), DASA 1917, Lockheed Missiles and Space Company, Palo Alto, California, 1967 (Volumes 1-5, [redacted] Volume 6, [redacted].

Manual of Surface Observations (WBAN), 7th Edition, Circular N., U.S. Government Printing Office, Washington, D.C., 1966 [redacted].

Middleton, W. E. Knowles, *Vision Through the Atmosphere*, University of Toronto Press, 1958 [redacted]

Passell, T. O., and R. I. Miller, *Radiative Transfer from Nuclear Detonations Above 50-km Altitude*, Fire Research Abstracts and Reviews, Vol. 6, No. 2, 1964 [redacted]

Shnider, R. W., *A Compilation and Semi-Emperical Analysis of Thermal Pulse Times* [redacted] URS 7007, DASA 2677, URS Research Company, San Mateo, California, September 1970 [redacted]

Wells, P. B., J. R. Keith, R. E. Wellck, and D. C. Sachs, *Air Blast from Special Weapons* [redacted] (3 Volumes) KN-68-168(R), Kaman Nuclear, Colorado Springs, Colorado, October 1968 (Volume 1, [redacted] Volume 2, [redacted] Volume 3, [redacted]

[redacted]

[redacted]

(This page intentionally left blank)

[redacted]

ADA955388

Chapter 4

X-RAY RADIATION PHENOMENA

INTRODUCTION

4-1 Production of X-Rays

X-rays are electromagnetic radiations of frequencies from about 10^{16} Hz* to about 10^{20} Hz, overlapping ultraviolet radiation at the low frequency end of the spectrum and gamma rays at the high end (see Figure 4-1). The wavelengths of the radiations are given by

$$\lambda = c/\nu \text{ cm},$$

where ν is the frequency in Hz, and c is the velocity of light (3×10^{10} cm per sec). X-rays exhibit particle-like properties as well as wave-like properties, and are absorbed or emitted in quanta, or photons, of energy

$$E = h\nu \text{ ergs},$$

where h is Planck's constant (6.625×10^{-27} erg-sec). This energy is ordinarily expressed in kiloelectron-volts (keV).† Figure 4-2 shows X-ray wavelength and frequency as a function of photon energy. The more energetic X-rays of higher frequency are commonly known as "hard" X-rays, and the less energetic ones are correspondingly "soft."

The distinction between X-rays and other electromagnetic radiations is not made in terms of their respective frequencies but in terms of their method of production. Gamma rays, for instance, are those photons produced as a result of nuclear forces, whereas production of X-rays is associated with electromagnetic forces acting on electrons. Two basic physical mechanisms are principally responsible for X-ray production; the corresponding emissions are bremsstrahlung (braking radiation) and the characteristic radiation.

Bremsstrahlung is a result principally of inelastic (or radiative) scattering of fast electrons by atoms. If a beam of monoenergetic electrons impinges on a thick target, a spectrum of X-rays is produced with maximum energy equal to that of the electrons and a spectral distribution that depends on the atomic number, Z, of the target.

The spectrum of X-rays from such an experiment will contain (in addition to the bremsstrahlung spectrum) a number of intense, fairly sharp spectral lines. These lines are characteristic of the material being bombarded and result from X-rays that are emitted when the atomic electrons rearrange themselves into states of lower energy after one or more electrons have been knocked out of the atom by the bombarding electrons. Since the atomic electrons must be in one of a number of discrete energy stages, transitions between the states are accomplished by emissions of photons of discrete energies. If the initial beam has sufficient energy to remove the most tightly bound (K-shell) electrons from the atom, all possible transitions between states will result in X-rays and all of the characteristic spectral lines will be seen. At slightly lower incident beam energies, the K X-ray lines will disappear but the other lines will still be observed, and so on. The frequencies of the characteristic radiation depend on the atomic numbers of the

*1 Hz (Hertz) = 1 cycle per second.

†1 keV = 10^3 ev; 1 ev = 1.6×10^{-12} erg.

This document has been approved for public release and sale; its distribution is unlimited.

[redacted]

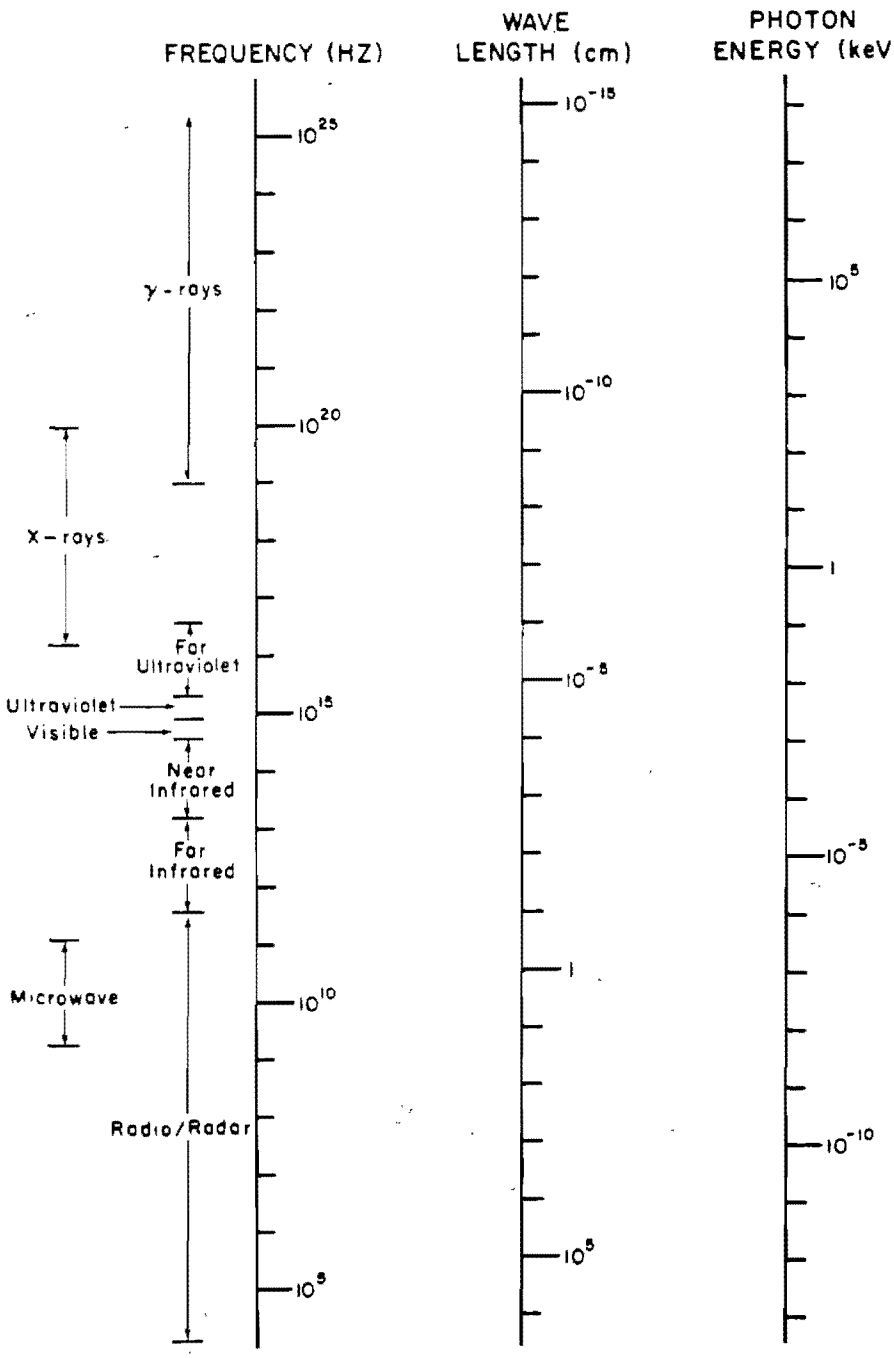

Figure 4-1. [redacted] Properties of Electromagnetic Radiation [redacted]

Accession For
NTIS GRA&I
DTIC TAB
Unannounced
Justification
By
Distribution/
Availability Codes
Dist | Avail and/or Special
A-1

UNANNOUNCED

[redacted]

QUALITY INSPECTED 4

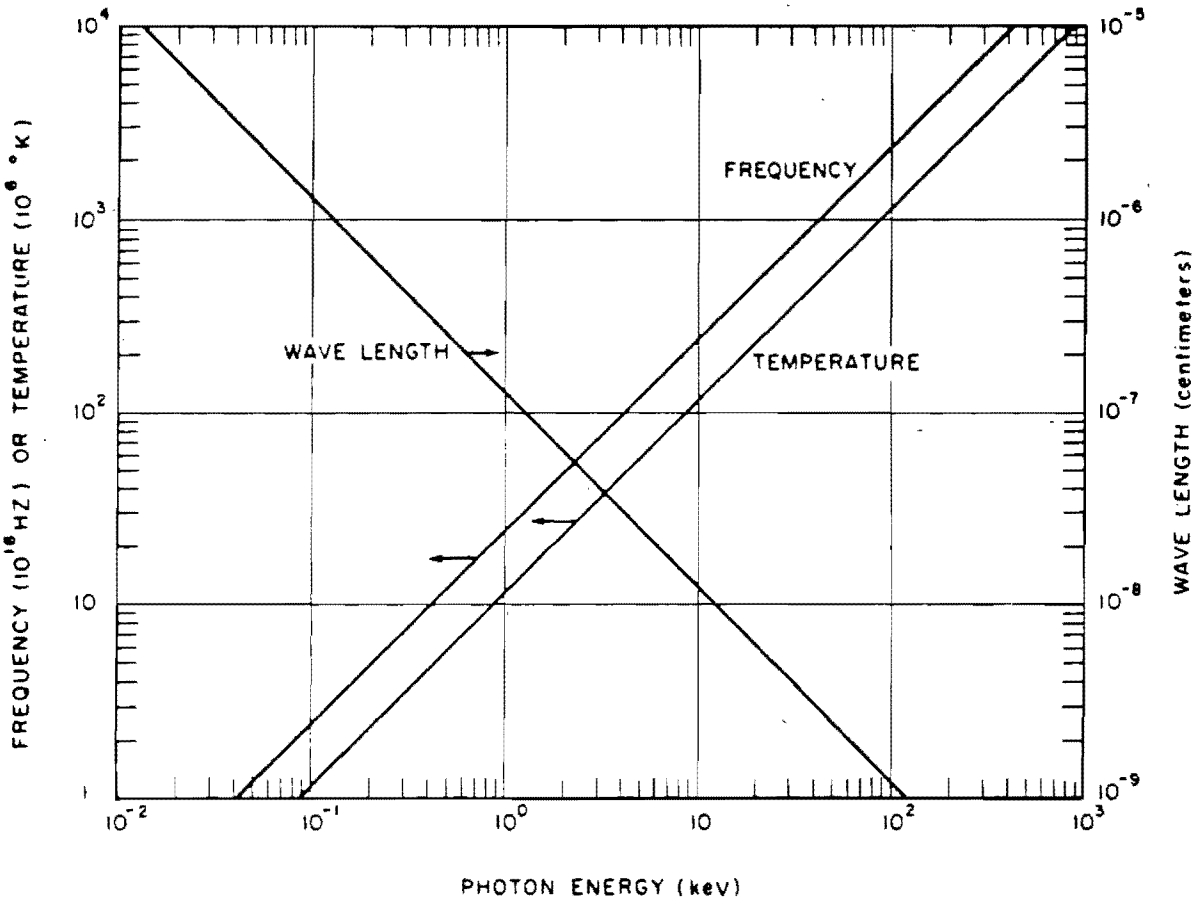

Figure 4-2. [redacted] Wavelength, Frequency, and Temperature as a Function of Electromagnetic Photon Energy [redacted]

[redacted]

target materials: the higher the atomic number, the higher is the frequency and energy of the hardest characteristic X-ray.

4-2 Black Body Radiation [redacted]

[redacted] The mechanism whereby an atom is ionized (loses one or several electrons) does not alter the characteristics of the X-rays emitted as the ionized atom deexcites (recaptures electrons). An X-ray can be produced no matter whether the ionization is produced by an incident fast electron or by any other process leaving an unfilled energy level. Similarly, any process whereby fast electrons are decelerated rapidly can produce X-ray bremsstrahlung. Both types of conditions are found in high temperature plasmas, which are composed of molecules, atoms, ions, electrons, and accompanying electromagnetic radiation, all in a state of thermal excitation corresponding to the temperature of the plasma. The hotter the plasma, the less likely it is that nonionized atoms and molecules will be

[redacted]

present, and the more likely will be the presence of multiply ionized atoms. At very high temperatures, the atoms can become completely ionized, leaving only bare nuclei and electrons in the plasma. Under such conditions, the possible frequencies of "characteristic" X-rays become essentially a continuum, both because so many energy states are unfilled and because the thermal motions of the nuclei cause Doppler shifts in the frequencies of the emitted lines. The resultant radiation is similar to that from any hot gas, except that the plasma can be enormously hotter and therefore can emit much higher frequencies, including X-rays, as well as ultraviolet, visible, and infrared radiations.

Plasmas are, in general, very complex, and the spectral distributions of the radiation emitted from them are correspondingly complex. However, much insight can be gained by studying a simpler, idealized thermal radiator, the black body. This does not mean that radiation from a plasma can be characterized by a black body, but in some cases a black body provides a rough approximation. Black body radiation is that seen emerging through a small hole in the wall of a hollow body at a constant temperature. It is also known as isothermal cavity radiation. Black body radiation has been studied extensively both experimentally and theoretically, and the following results are of interest.

(U) The total power emitted per unit area of a black body at absolute temperature T is

$$\Phi_s = \sigma T^4 \text{ erg-sec}^{-1}\text{-cm}^{-2}$$

where the Stefan-Boltzmann constant σ is equal to 5.67×10^{-5} erg sec^{-1} cm^{-2} °K^{-4}.

The theoretical explanation of the observed distribution of the frequencies of the radiation depended on the quantum hypothesis advanced by Planck, and the energy spectrum is generally referred to as a Planck spectrum. The Planck spectrum, in terms of the energy density radiated between wavelengths λ and $\lambda + d\lambda$, is

$$\Psi(\lambda)d\lambda = \frac{8\pi ch}{\lambda^5} \frac{d\lambda}{e^{(ch/\lambda kT)} - 1}$$

where all symbols are as previously defined, except that k is the Boltzmann constant and is equal to 1.38×10^{-16} erg/°K. The Planck spectrum can also be expressed in terms of the power emitted per unit area per unit frequency for photons with frequencies between ν and $\nu + d\nu$ as

$$\Phi_s(\nu)d\nu = \frac{2\pi\nu^2 d\nu}{c^2} \frac{h\nu}{e^{(h\nu/kT)} - 1}$$

Since both $h\nu$ and kT have the dimensions of energy (and can be expressed in keV), the spectral distribution can be expressed in terms of the normalized energy (a dimensionless parameter) $u = h\nu/kT$ as

$$\Phi_s(u)du = \sigma T^4 F(u)du$$

where use has been made of the Stefan-Boltzman equation, and

$$F(u) = \frac{15\pi^{-4}u^3}{e^u - 1}$$

is called the density function of the normalized Planck distribution. The quantity $F(u)du$ is the fraction of the total radiation emitted by a black body at temperature T between the frequencies ν and $\nu + d\nu$, where $\nu = u(kT/h)$.

The fraction of photons with energies less than $h\nu$ is therefore

$$G(u) = \int_0^u F(u')du'$$

$G(u)$ is called the cumulative distribution func-

[redacted]

Table 4-1. [redacted] Normalized Planck Distribution [redacted]

Normalized Energy, u	Density Function, F(u)	Cumulative Distribution Function, G(u)
0.5	2.9674×10^{-2}	5.2932×10^{-3}
1.0	8.9627×10^{-2}	3.4618×10^{-2}
1.5	1.4928×10^{-1}	9.4780×10^{-2}
2.0	1.9283×10^{-1}	1.8114×10^{-1}
2.5	2.1519×10^{-1}	2.8402×10^{-1}
2.82 (u_{max})	2.1890×10^{-1}	3.5368×10^{-1}
3.0	2.1787×10^{-1}	3.9301×10^{-1}
4.0	1.8389×10^{-1}	5.9702×10^{-1}
5.0	1.3059×10^{-1}	7.5453×10^{-1}
6.0	8.2660×10^{-2}	8.6016×10^{-1}
7.0	4.8212×10^{-2}	9.2442×10^{-1}
8.0	2.6459×10^{-2}	9.6084×10^{-1}
9.0	1.3857×10^{-2}	9.8038×10^{-1}
10.0	6.9920×10^{-3}	9.9045×10^{-1}

[redacted]tion (note that $G(\infty) = 1$ for all temperatures). The functions $F(u)$ and $G(u)$ are tabulated in Table 4-1 and plotted in Figure 4-3. The maximum of the density function occurs at $u_{max} = 2.82144$. Other useful relationships are that only about three and a half percent of the radiation occurs at energies below kT ($u = 1$), and only about thirty-five percent below the peak of the spectrum ($u = 2.82$). Only one percent of the energy is radiated in photons with energies greater than ten times the black body temperature (kT), i.e., for $u \geq 10$. The median energy is at about $u = 3.5$.

[redacted] Ideal black bodies produce some radiation at all frequencies. In order for significant quantities of X-rays to be produced, however, the temperature of the black body must be great enough that u_{max} occurs in the X-ray region, i.e., for the $h\nu \sim .3$ keV or greater. This implies that $kT > 0.1$ keV or that T must be greater than about a million degrees Kelvin.

[redacted]

[redacted]

Problem 4-1. Calculation of Spectral Distribution and Cumulative Emissions from Black Body Sources

[redacted] Figure 4-3 and Table 4-1 show the normalized energy distribution and the normalized cumulative energy function for black body radiators. These normalized functions may be applied to black body radiators of various temperatures expressed in any unit of temperature measure. The common unit of temperature measure for high temperature plasmas is keV.

[redacted] *Scaling*

a. To find the fraction of total energy emitted at a specified photon energy, $h\nu$, divide the specified photon energy by the black body source temperature, kT, to obtain the normalized energy, u,

$$u = \frac{h\nu}{kT}.$$

Enter Figure 4-3 with the normalized energy, and read the fraction of the total energy emitted at the specified energy from the density function curve.

b. To find the cumulative fraction of energy emitted at or below a specified photon energy, $h\nu$, divide the specified photon energy by the black body source temperature, kT, to obtain the normalized energy, u,

$$u = \frac{h\nu}{kT}.$$

Enter Figure 4-3 with the normalized energy, and read the cumulative fraction of energy emitted at or below the specified photon energy from the cumulative distribution function curve.

[redacted] *Example* [redacted]

Given:

a. A black body radiating at a temperature of 2 keV.

b. A black body radiating at a temperature of 3 keV.

Find:

a. The photon energy that is emitted with the greatest frequency from the 2 keV black body.

b. The photon energy at which 65 percent of the total energy emitted contains photons of that energy or lower from the 3 keV black body.

Solution:

a. From Figure 4-3 (or Table 4-1), the peak emission occurs at a normalized energy of

$$u = 2.82.$$

b. From Figure 4-3, 65 percent of the energy is emitted at normalized energies equal or less than

$$u = 4.3.$$

Answer:

a. The photon energy that is emitted with greatest frequency from a 2 keV black body radiator is

$$h\nu = 2.82\ kT = (2.82)(2) = 5.64 \text{ keV}.$$

b. Sixty-five percent of the photons from a 3 keV black body radiator have energies equal to or less than

$$h\nu = 4.3\ kT = (4.3)(3) = 12.9 \text{ keV}$$

(Thirty-five percent of the photons will have energies greater than 12.9 keV.)

Reliability: Figure 4-3 represents the density function and cumulative distribution function of theoretically ideal black body radiators. Actual radiators will deviate from the ideal.

Related Material: See paragraphs 4-1 and 4-2.

[redacted]

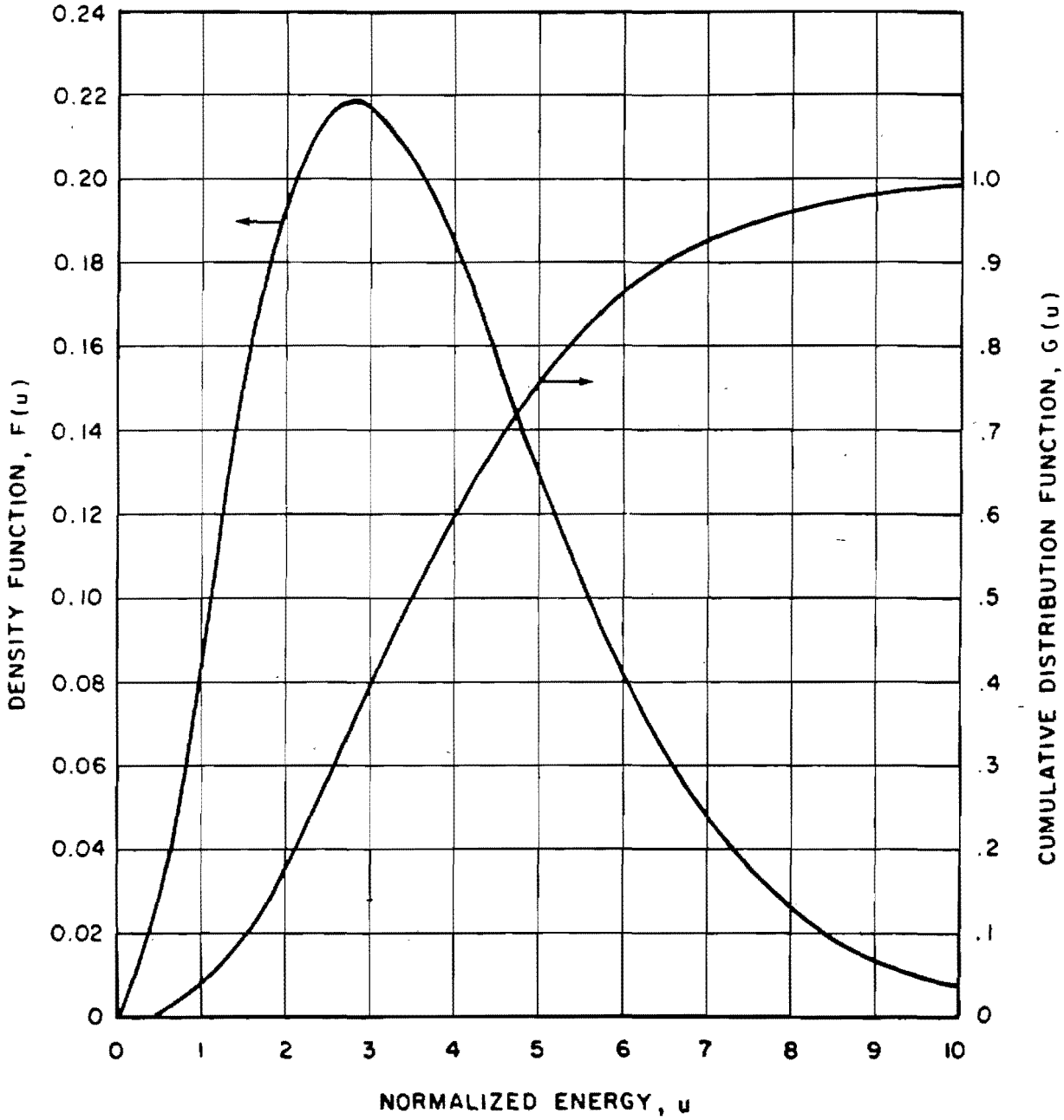

Figure 4-3. [redacted] Spectral Distribution of a Black Body Source [redacted]

4-3 Interactions of X-Rays with Matter

Just as X-rays are produced principally by phenomena involving electrons, the principal interactions of X-rays with matter also depend on atomic electrons.

In the photoelectric effect, an X-ray is totally absorbed; its energy is partly used in overcoming the binding energy of an atomic electron, and the remainder is imparted as kinetic energy to the electron and (to a much lesser extent) to the recoiling ion. No scattered X-ray is observed; however, the deexcitation of the ionized atom can result in secondary X-ray, ultraviolet, or optical radiation. This phenomenon is known as fluorescence. Photoelectric absorption is most probable when the X-ray energy just exceeds the binding energy of a particular electron. Thus, as the wavelength of the incident X-ray increases (the energy decreases), the probability of absorption gradually rises until the binding energy of the K-shell electron is reached. It then abruptly drops (the "K-absorption edge"), and then begins rising again until the next absorption edge is reached, and so on.

Another effect is Compton (inelastic) scattering. When an X-ray collides with an electron, it is possible that, not only a resultant energetic electron, but also a scattered X-ray photon of lower frequency (longer wavelength) will be observed. This usually happens when the target electron is free or very loosely bound. If it is assumed that the electron is free, the interaction can be analyzed as collision between two particles. Conservation of momentum and energy then yield the relation

$$\lambda' - \lambda = \frac{h}{m_o c}(1 - \cos\theta)$$

where λ is the wavelength of the incident photon, λ' that of the scattered photon, θ the angle of scattering, and m_o the mass of the electron (9.1×10^{-28} g).

A third effect is elastic scattering. If an electron is excited by an electromagnetic wave, it will gain energy and oscillate. As a moving charge, it will then reradiate the energy as electromagnetic radiation of the same frequency, which appear as scattered photons. The scattered photons may be coherent (in phase) or incoherent (random phases).

The probability that any of the above scattering or photoelectric processes will take place is given in terms of a cross-section σ (so called because it has units of area), which is the probability of a given interaction taking place under the condition that one interaction per unit area is possible.

If the medium with which the X-rays interact is characterized by an electron density ρ_e, then for every centimeter an X-ray traverses, there are ρ_e electrons within a cross-sectional area of one cm^2 with which it can interact. The probability of interaction per centimeter is therefore $\mu = \rho_e \sigma$. Since this is also the probability that an X-ray disappears from the incident beam, the beam intensity falls by a factor $e^{-\mu x}$ after having penetrated a distance x into the material. It is often convenient to express the penetration in terms of the total amount of material "seen" by the beam, ρx, where ρ is the mass density of the material. In this case, the mass attenuation coefficient $\kappa = \mu/\rho$ is used. The mass attenuation coefficients for air are shown as a function of X-ray photon energy in Table 4-2 and in Figure 4-4.

If the X-rays radiate isotropically from a point source rather than in a narrow beam, the flux, Φ, of X-rays (photons per unit area per unit time) at any point depends not only on the exponential attenuation described above but also on the spherical attenuation, so that

$$\Phi = Ne^{-\kappa(\rho R)}/4\pi R^2$$

where R is the radial distance from the source

[redacted]

Table 4-2. [redacted] Mass Attenuation Coefficients for Air [redacted]

Photon Energy (keV)	Total Scatter (cm^2/g)	Photoelectric (cm^2/g)	Total Attenuation (cm^2/g)
2	9.791×10^{-1}	4.95×10^{2}	4.960×10^{2}
3.2*	7.754×10^{-1}	1.34×10^{2}	1.348×10^{2}
3.2*	7.754×10^{-1}	1.56×10^{2}	1.568×10^{2}
4	6.707×10^{-1}	8.27×10^{1}	8.337×10^{1}
6	5.070×10^{-1}	2.30×10^{1}	2.351×10^{1}
8	4.126×10^{-1}	9.54×10^{0}	9.953×10^{0}
10	3.529×10^{-1}	4.57×10^{0}	4.923×10^{0}
20	2.409×10^{-1}	4.96×10^{-1}	7.369×10^{-1}
40	1.885×10^{-1}	5.07×10^{-2}	2.393×10^{-1}
60	1.690×10^{-1}	1.33×10^{-2}	1.823×10^{-1}
80	1.569×10^{-1}	5.29×10^{-3}	1.622×10^{-1}
100	1.480×10^{-1}	2.61×10^{-3}	1.506×10^{-1}
200	1.210×10^{-1}	1.68×10^{-4}	1.212×10^{-1}
400	9.468×10^{-2}	9.80×10^{-6}	9.469×10^{-2}
600	8.014×10^{-2}	3.92×10^{-6}	8.014×10^{-2}

*Argon K-Absorption Edge.

[redacted]

and N is the total number of photons emitted by the source per unit time. This, however, is only the component that reaches the point directly from the source. Scattered photons (coherent, incoherent, and Compton) originating at other points also reach the point. The result is that the flux of that point is larger by a buildup factor B. The magnitude of B depends on the distance from the source, the energy spectrum of the X-rays, and properties of the scattering material in complex ways. It is ordinarily calculated by computer codes. The integral of the flux over time, or the total number of X-ray photons per unit area reaching a point, is known as the fluence. *Flux and fluence are also commonly described in terms of the energy carried by the photons instead of their number.*

SECTION I [redacted] NUCLEAR WEAPONS AS X-RAY SOURCES [redacted]

4-4 X-Ray Production in Nuclear Weapons [redacted]

[redacted] The multitude of processes that occur very early in the detonation of a nuclear weapon are described in Chapter 1. The result,

[redacted]

[redacted]

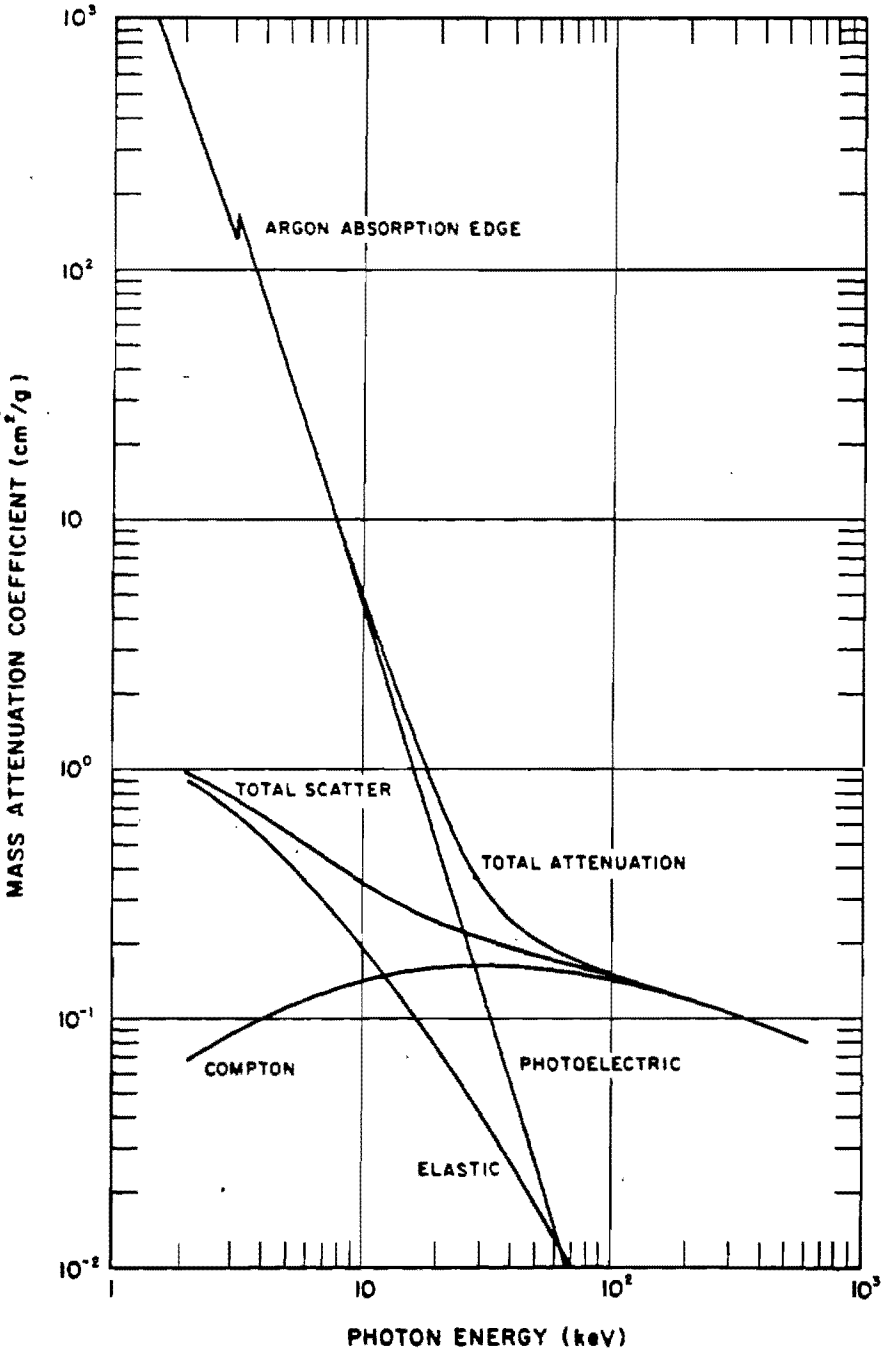

Figure 4-4. [redacted] Mass Attenuation Coefficients for Air [redacted]

[redacted]

[redacted]

as far as X-ray production is concerned, is that a very hot (tens of millions of degrees Kelvin) plasma is formed, consisting of electrons and the stripped nuclei of the fission and fusion products, of the elements in the casing materials, and of any other elements in the immediate vicinity of the detonation, such as nitrogen and oxygen in the air. Although the spectrum of emissions from this plasma is not that of a black body, particularly because the temperature is by no means uniform, it often approximates a black body spectrum, or a combination of two or more such spectra. The disposition of X-rays is further complicated by interactions with the atmosphere.

[redacted] Approximately 70 to 80 percent of the total prompt yield of many nuclear weapons is radiated in the form of X-rays. [redacted] In recent years, considerable attention has been devoted to designing "hot" nuclear weapons with effective radiation temperatures greater than [redacted]

DNA (L-)(3)

DNA (L-)(3)

4-5 X-Ray Energy Emitted [redacted]

[redacted] A temperature gradient, decreasing outward, exists between the enormously hot interior nuclear materials and the somewhat cooler exterior bomb casing materials of the nuclear weapon. The X-rays, of course, are continuously being absorbed and reradiated, but with a temperature gradient, the conditions for an ideal black body with isotropic radiation at every point do not exist, and there is a net flow of energy outward from the point of detonation. The outward flux at the surface is, in fact, about twice what would be implied by black body radiation at the temperature of the surface because of X-rays from the interior escaping without interaction at the surface. If the actual surface temperature is T_s, then the surface energy flux is given by

$$\Phi_s = \sigma T_e^4$$

where

$$T_e = 2^{1/4} T_s = 1.19 T_s .$$

The effective temperature, T_e, will be used in the succeeding discussions.

4-6 Rate of X-Ray Emission [redacted]

[redacted]

DNA (L-)(3)

[redacted]

[redacted]

DNA (L)(3)

[redacted] Actually, radiation cannot continue at the peak emission rate because the loss of energy cools the plasma and it radiates correspondingly less rapidly as time goes on. The time necessary to radiate a given fraction (about 90 percent) of the weapon energy increases with the size of the emitting sphere *(r)*, and of course is larger than the time calculated from the peak emission rate; however, it is still generally measured in shakes or tenths of a shake for most weapons.

4-7 Spectral Distribution of X-Rays [redacted]

[redacted] An approximation of the X-ray spectra from nuclear weapons can be obtained from the normalized Planck distribution by applying the appropriate multiplicative factors to the independent *(u)* and dependent *(F* and *G)* variables for the black body temperature indicated (see paragraph 4-2). [redacted]

DNA (L)(3)

[redacted] Similarly, the effective X-ray temperature and equivalent black body fluence may be obtained from experimental measurements [redacted]

DNA (L)(3)

[redacted] This example is given in more detail in Problem 4-3. The equivalent black body spectrum can now be constructed and compared with the rest of the measured spectrum. Some examples of such comparisons will be shown in subsequent paragraphs.

[redacted] For the purpose of calculating X-ray effects, the spectrum is most useful if tabulated by intervals in u enclosing approximately equal energy increments of the cumulative distribution function. In such computations, each increment is treated as being composed of monoenergetic photons of the central energy. Table 4-3 shows the boundaries of the energy intervals for approximately five percent increments of the normalized cumulative distribution function and the corresponding boundaries of photon energies for several source temperatures. Five percent increments may be too coarse for estimating effects both at the very low and very high ends of the spectrum. For these regions, the one percent increments shown in Table 4-4 may be useful.

4-8 Real Nuclear Weapons as X-Ray Sources [redacted]

[redacted] Since X-rays are attenuated rapidly by air, very little can be ascertained about the initial properties of nuclear weapons as X-ray sources from atmospheric weapons tests. However, X-ray effects may constitute the principal kill mechanism for high altitude interception of ballistic missiles [redacted]

DNA (L)(3)

[redacted]

Page 4-13 is deleted.

[redacted]

[redacted]

Table 4-3. [redacted] Five Percent Energy Intervals for a Planck Spectrum [redacted]

Cumulative Distribution Function	Photon Energy in keV for Various Black Body Temperatures			
	1 keV	2 keV	8 keV	10 keV
0	0	0	0	0
0.0506	1.16	2.32	9.28	11.60
0.1008	1.54	3.08	12.32	15.40
0.1511	1.84	3.68	14.72	18.40
0.2007	2.10	4.20	16.80	21.00
0.2500	2.34	4.68	18.72	23.40
0.3013	2.58	5.16	20.64	25.80
0.3493	2.80	5.60	22.40	28.00
0.4017	3.04	6.08	24.32	30.40
0.4491	3.26	6.52	26.08	32.60
0.4994	3.50	7.00	28.00	35.00
0.5515	3.76	7.52	30.08	37.60
0.6007	4.02	8.04	32.16	40.20
0.6499	4.30	8.60	34.40	43.00
0.7010	4.62	9.24	36.96	46.20
0.7519	4.98	9.96	39.84	49.80
0.8004	5.34	10.68	42.62	53.80
0.8499	5.88	11.76	47.04	58.80
0.9003	6.56	13.12	52.48	65.60
0.9502	7.64	15.28	61.12	76.40

DNA (L)(3)

[redacted]

DNA (L)(3)

[redacted]

Figures 4-6 through 4-11 show some X-ray spectra from real nuclear weapons, both observed and predicted. Figure 4-6 shows the observed spectrum of a warm X-ray weapon.

DNA (L)(3)

[redacted]

[redacted]

[redacted]

Table 4-4. [redacted] One Percent Energy Intervals for a Planck Spectrum [redacted]

Cumulative Distribution Function	Photon Energy in keV for Various Black Body Temperatures			
	1 keV	2 keV	8 keV	10 keV
0.0105	0.64	1.28	5.12	6.40
0.0205	0.82	1.64	6.56	8.20
0.0295	0.94	1.88	7.52	9.40
0.0402	1.06	2.12	8.48	10.60
0.0506	1.16	2.32	9.28	11.60
0.0597	1.24	2.48	9.92	12.40
0.0697	1.32	2.64	10.56	13.20
0.0804	1.40	2.80	11.20	14.00
0.0903	1.47	2.94	11.76	14.70
0.1008	1.54	3.08	12.32	15.40
0.9003	6.56	13.12	52.48	65.60
0.9098	6.72	13.44	53.76	67.20
0.9200	6.91	13.82	55.28	69.10
0.9300	7.12	14.24	56.96	71.20
0.9401	7.36	14.72	58.88	73.60
0.9502	7.64	15.28	61.12	76.40
0.9598	7.96	15.92	63.68	79.60
0.9700	8.39	16.78	67.12	83.90
0.9801	8.98	17.96	71.84	89.80
0.9900	9.94	19.88	79.52	99.40

[redacted]

DNA (k)(3)

DNA (k)(3)

Pages 4-16 through 4-24 are deleted.

[redacted]

[redacted]

[redacted]

SECTION II

[redacted] X-RAY ENVIRONMENTS PRODUCED BY NUCLEAR WEAPONS [redacted]

4-9 Exoatmospheric (Vacuum) Detonations [redacted]

[redacted] X-ray environments from nuclear detonations are completely specified by the magnitude of the source and the distance from the source to the point of interest if the detonation occurs in a vacuum. If the detonation occurs at an altitude sufficiently high that essentially vacuum conditions prevail, it is designated an exoatmospheric detonation. Since, in any case, the vacuum will be less than perfect, the distinction between exoatmospheric and endoatmospheric detonations will depend on the degree to which effects vary from those predicted for a vacuum. This will depend on weapon design features, particularly whether the X-ray spectrum is hot or cold.

[redacted] For perfect vacuum conditions, the X-ray energy fluence at a range R from the point of detonation is

$$\varphi = \frac{E_o}{4\pi R^2} \text{ cal/cm}^2$$

where E_o is the X-ray yield of the weapon in calories and R is the distance in centimeters. If E_o is not known, it may be estimated as 75 percent of the total yield of the weapon. Using the relationship that 1 kt = 10^{12} calories, the vacuum fluence is shown as a function of distance from detonations of various x-ray yields in Figure 4-12. The fluence may also be calculated from the equation

$$\varphi = \frac{85.7\ W'_x}{R_f^2}$$

where W'_x is the X-ray yield in kilotons and R_f is the range in kilofeet.

[redacted] Since no interactions can take place in an empty medium, no changes in the spectral distribution of X-rays occurs in exoatmospheric detonations. For the same reason, the time dependence of X-ray energy flux is unchanged, and the time of arrival of the pulse at range R is R/c, where c is the velocity of light. Since, for the calculation of effects, only times relative to the arrival time are important, the only variation of effects with range is due to the variation in total fluence.

4-10 Endoatmospheric Detonations [redacted]

[redacted] The X-ray environment produced by nuclear detonations within the atmosphere are much more complicated because of the many interactions that can take place between the X-rays and the atmospheric constituents. Photoelectric absorption, elastic scattering, and inelastic (Compton) scattering all play a part in altering the total X-ray fluence that reaches a given range, the spectral distribution at that point, and the time rate of energy delivery. Density gradients and other inhomogeneities in the atmosphere cause the X-ray environment to deviate from the spherical symmetry exhibited in vacuum detonations. Because of scattering, the X-ray photons arriving at a given point do not all arrive from the direction of the detonation; in fact, some may arrive from precisely the opposite direction.

4-11 The Standard Atmosphere [redacted]

[redacted] The estimation of X-ray environments around an endoatmospheric nuclear detonation requires a knowledge of the atmospheric properties along any path that an X-ray photon might traverse from the weapon to the point of interest. Although atmospheric properties can change somewhat from day to day and place to place, most calculations are based on a standard atmosphere such as the one described by the National Bureau of Standards in 1962. The im-

[redacted]

[redacted]

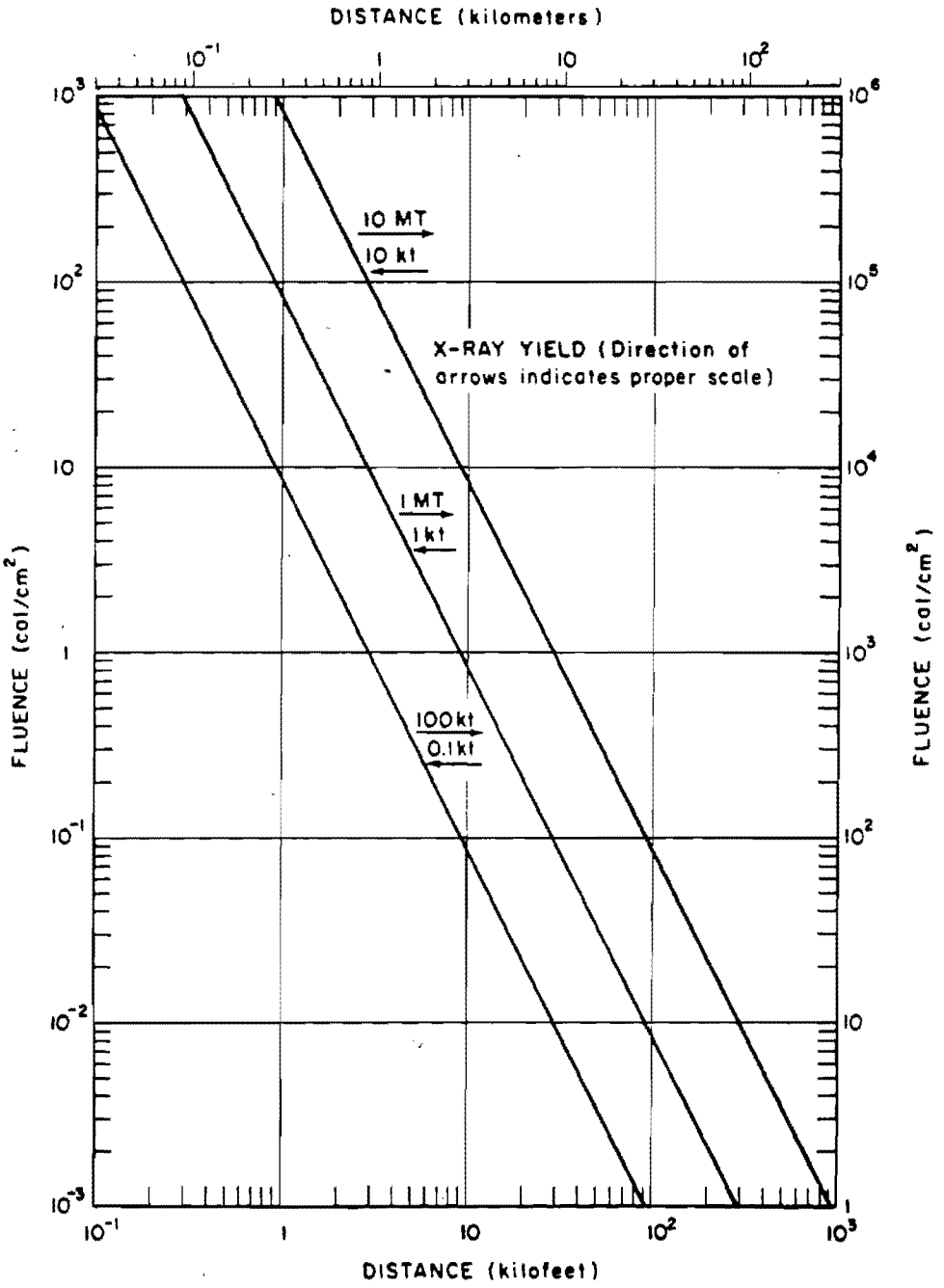

Figure 4-12. [redacted] X-Ray Fluence in a Vacuum [redacted]

[redacted]

portant atmospheric constituents are

	Fraction by Weight
Nitrogen	0.7553
Oxygen	0.2318
Argon	0.0129

Argon is included because its photoelectric absorption cross section for X-rays is large and serious errors can be made if it is neglected. The other minor components of the atmosphere, however, can be neglected without serious loss of accuracy.

The other principal feature of the standard atmosphere is its variation in density with altitude. The density, ρ, falls approximately exponentially with increasing altitude, as is shown in Table 4-5 and Figure 4-13. Also shown is the quantity of air above a given altitude, h, which is given by the mass integral

$$q(h) = \int_h^\infty \rho(h')dh'$$

Table 4-5 also shows the density normalized to the sea level density, ρ_o.

If two points are at altitudes h_1 and h_2 and are separated by a horizontal distance, d, then the slant range R is given by

$$R = \sqrt{d^2 + (h_2 - h_1)^2}$$

and the mass integral between them is given by

$$q(R) = \int_o^R \rho(h')ds' = R\,\frac{q(h_2) - q(h_1)}{h_2 - h_1}$$

This expression reduces to

$$q(R) = q(h_2) - q(h_1)$$

when $d = 0$ and (in the limit) to

$$q(R) = \rho(h)R$$

when $h_1 = h_2$ (the coaltitude case).

These values for the mass integral between the source of X-rays and the point of observation are to be used for the quantity ρR in the flux or fluence attenuation equations as described in paragraph 4-3. When the mass integral is used instead of the absolute range, the X-ray environment is substantially independent of other parameters; this property is known as mass integral scaling.

4-12 Direct X-Ray Fluence in the Atmosphere

If the attenuation equations are combined with the results for vacuum fluence, the direct fluence from a weapon with W_x kilotons of X-ray yield is

$$\varphi_{dir} = \frac{85.7\ W_x}{R_f^2}\, e^{-\kappa q(R)}$$

at a range R, where q is the mass integral calculated along R and κ is the mass attenuation coefficient. Notice that q will not be the same for different directions of R unless the atmosphere is essentially uniform, so that contours of constant fluence usually are not spherically symmetric about the burst point, although they usually are cylindrically symmetric about a vertical axis.

Moreover, the value of the mass attenuation coefficient κ varies with X-ray photon energy according to the curve shown in Figure 4-4, so that the direct fluence must be calculated by weighting monoenergetic calculations by the spectral distribution. For a given penetration of the atmosphere, $q(R)$, this weighting process can be replaced by using an effective κ, but the value of this effective κ will change with $q(R)$. Similar-

[redacted]

Table 4-5. [redacted] The Standard Atmosphere [redacted]

Altitude (kft)	Air Density (g/cm^3)	Mass Integral Above Altitude (g/cm^2)	Density Normalized to Sea Level
0	1.2250×10^{-3}	1.0331×10^{3}	1.0000×10^{0}
5	1.0556×10^{-3}	8.5967×10^{2}	8.6170×10^{-1}
10	9.0477×10^{-4}	7.1059×10^{2}	7.3859×10^{-1}
20	6.5312×10^{-4}	4.7525×10^{2}	5.3316×10^{-1}
30	4.5904×10^{-4}	3.0749×10^{2}	3.7473×10^{-1}
40	3.0267×10^{-4}	1.9305×10^{2}	2.4708×10^{-1}
50	1.8756×10^{-4}	1.1973×10^{2}	1.5311×10^{-1}
60	1.1628×10^{-4}	7.4292×10^{1}	9.4919×10^{-2}
70	7.1742×10^{-5}	4.6182×10^{1}	5.8565×10^{-2}
80	4.4174×10^{-5}	2.8855×10^{1}	3.6060×10^{-2}
90	2.7391×10^{-5}	1.8151×10^{1}	2.2360×10^{-2}
100	1.7101×10^{-5}	1.1493×10^{1}	1.3960×10^{-2}
110	1.0647×10^{-5}	7.3417×10^{0}	8.6918×10^{-3}
120	6.6487×10^{-6}	4.7534×10^{0}	5.4275×10^{-3}
130	4.2214×10^{-6}	3.1247×10^{0}	3.4460×10^{-3}
140	2.7222×10^{-6}	2.0831×10^{0}	2.2222×10^{-3}
150	1.7810×10^{-6}	1.4070×10^{0}	1.4539×10^{-3}
160	1.1968×10^{-6}	9.5903×10^{-1}	9.7697×10^{-4}
180	5.6991×10^{-7}	4.4396×10^{-1}	4.6523×10^{-4}
200	2.7163×10^{-7}	1.9859×10^{-1}	2.2174×10^{-4}
250	3.6248×10^{-8}	2.0476×10^{-2}	2.9590×10^{-5}
300	2.3839×10^{-9}	1.5137×10^{-3}	1.9460×10^{-6}
400	1.8645×10^{-11}	2.7532×10^{-5}	1.5220×10^{-8}
500	1.6329×10^{-12}	6.2391×10^{-6}	1.3330×10^{-9}
1,000	3.2769×10^{-14}	0	2.6750×10^{-11}

[redacted]

ly, the spectrum changes as matter is traversed because of the varying proportions of photons absorbed or scattered out of the flux at varying photon energies.

[redacted] In practice, the most accurate method for calculating fluences uses Monte Carlo computer codes with accurate photon cross sections for each energy group and each scattering or absorbing process. This technique is also essential for following those X-ray photons scattered out of the direct fluence, as will be discussed subsequently.

[redacted]

[redacted]

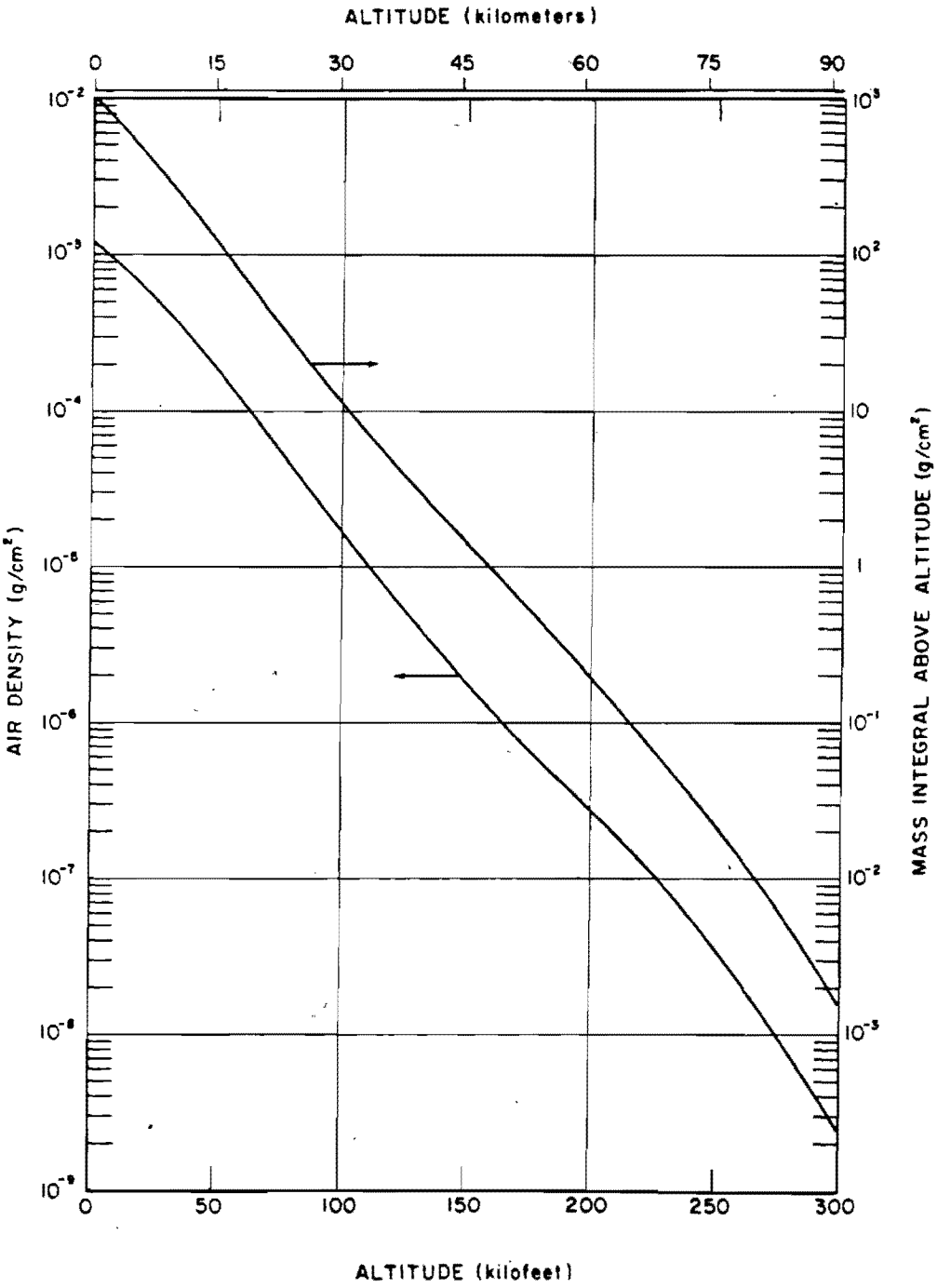

Figure 4-13. [redacted] The Standard Atmosphere [redacted]

[redacted]

[redacted]

DNA (L)(3)

addition to the spherical divergence, which is not included since the fraction of vacuum fluence is the quantity shown). The build-up factor, which includes photons of degraded energy, rises so rapidly that the total fluence for short ranges actually exceeds that expected for the vacuum case, in which only spherical divergence would be operating. Figure 4-15 and 4-16 show results for black body source spectra, also normalized to the vacuum fluence. Notice that the direct fluences are no longer exponential, although in the latter case a mass attenuation coefficient corresponding to about five times the black body temperature gives reasonable results. The normalized fluences for the latter two cases are also tabulated in Table 4-6.

4-13 Scattered X-Ray Fluence [redacted]

[redacted] The X-rays arriving at a given point come not only directly from the source but also indirectly (and usually from other directions) after one or more scattering events. The probabilities of scattered photons contributing to the flux depends on the total cross sections for scattering and the differential cross sections for scattering at specific angles. The flux of scattered photons is usually computed by a Monte Carlo simulation of the paths taken by a representative sample of photons, taking into account also the possibility of degradation of energy in Compton scattering. The resultant flux adds to that penetrating directly from the source, and the ratio of the total fluence to the direct fluence is known as the build-up factor. The build-up factor increases from unity very near the source to more than one hundred for longer ranges.

[redacted] No simple analytic expression gives the build-up factor, but Figures 4-14 through 4-16 give direct and total fluences and the build-up factor for three representative X-ray sources. In the monoenergetic source case (Figure 4-14), the direct fluence is attenuated exponentially (in

[redacted] The cold X-rays are attenuated much more quickly in air, because the mass attenuation coefficient is so much larger for lower energies [redacted]

DNA (L)(3)

DNA (L)(3)

4-14 Low Altitude Endoatmospheric Detonations [redacted]

[redacted] Low altitude (deep) endoatmospheric detonations are the next simplest case – after vacuum detonations – because the air density is sufficiently high that most of the attenuation occurs close to the burst point. Therefore, there are no large variations in density to affect critically the computation of fluences. In particular, the density of air through which the scattered X-rays reach a given point does not differ greatly from that through which the direct X-rays penetrate. Although whether or not altitudes are low (detonations are deep) depends on the energy

[redacted]

[redacted]

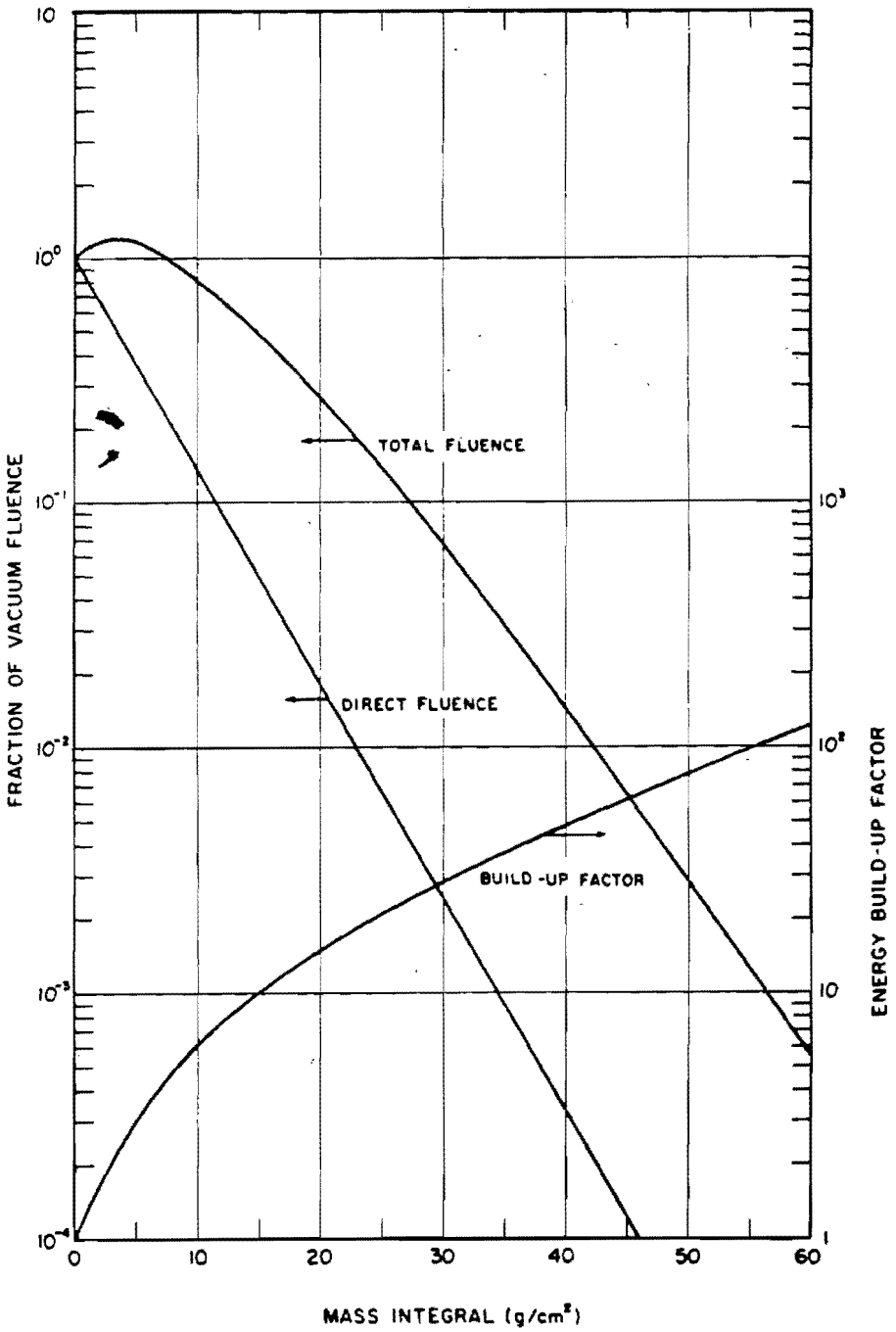

Figure 4-14. [redacted] Energy Fluence and Build-up Factor for a 50 keV Monoenergetic Source in Homogeneous Air [redacted]

Pages 4-32 + 4-33 are deleted. 4-31

[redacted]

[redacted]

Table 4-6. [redacted] X-Ray Fluences for Black Body Sources [redacted]

DNA (A)(3)

[redacted]

spectrum of the weapon, if deep endoatmospheric conditions do prevail, the X-ray environment can be approximated by mass integral scaling. The total quantity of air (the mass integral) between the source and the point of interest is computed as described in paragraph 4-11, and then the appropriate direct and scattered fluences for the given energy spectrum are calculated as described in paragraphs 4-12 and 4-13. Examples of such calculations are provided in Problems 4-5 and 4-6. Less detailed examples are discussed in the following paragraphs.

[redacted]

DNA (L)(3)

[redacted] The fluences for the same mass-integrally scaled distances in directions other than horizontal are approximately the same. For instance, the actual distance to the 10 cal/cm^2 contour will be somewhat larger vertically upward than horizontally because the air is somewhat less dense; conversely, the distance vertically downward will be somewhat smaller. The resulting fluence contours are egg-shaped.

[redacted] Furthermore, the computed fluences will be even more accurate at the same mass-integrally scaled distances as the burst point falls lower in the atmosphere. The X-ray fluence contours will tend to become more spherical and contract because of the increasing air density. On the other hand, the reliability of the computations decreases as the burst altitude increases above 100 kilofeet.

[redacted]

DNA (L)(3)

[redacted]

[redacted]

[redacted]

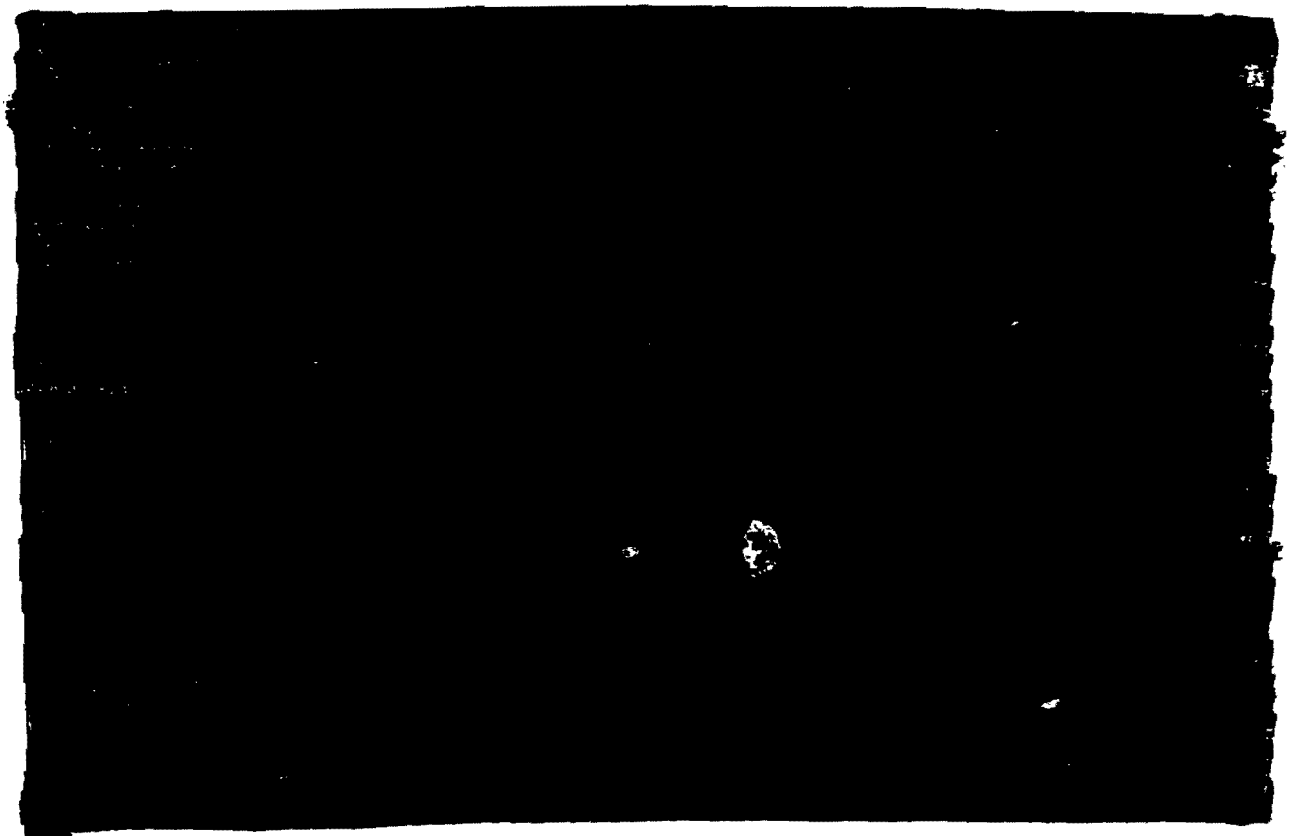

DNA (L)(3)

DNA (L)(3)

[redacted] X-ray effects on materials may depend on several variables in the X-ray environment

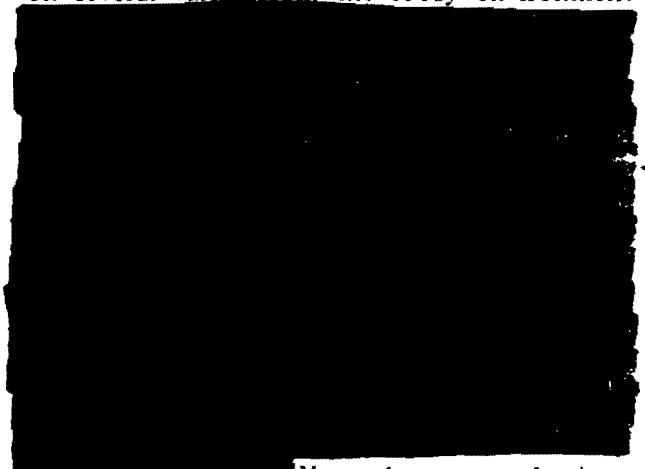

DNA (L)(3)

[redacted] X-ray damage mechanisms are discussed in Section V of Chapter 9.

[redacted] The spectrum of the direct fluence tends to become harder – that is, its proportion of

[redacted]

[redacted]

[redacted]

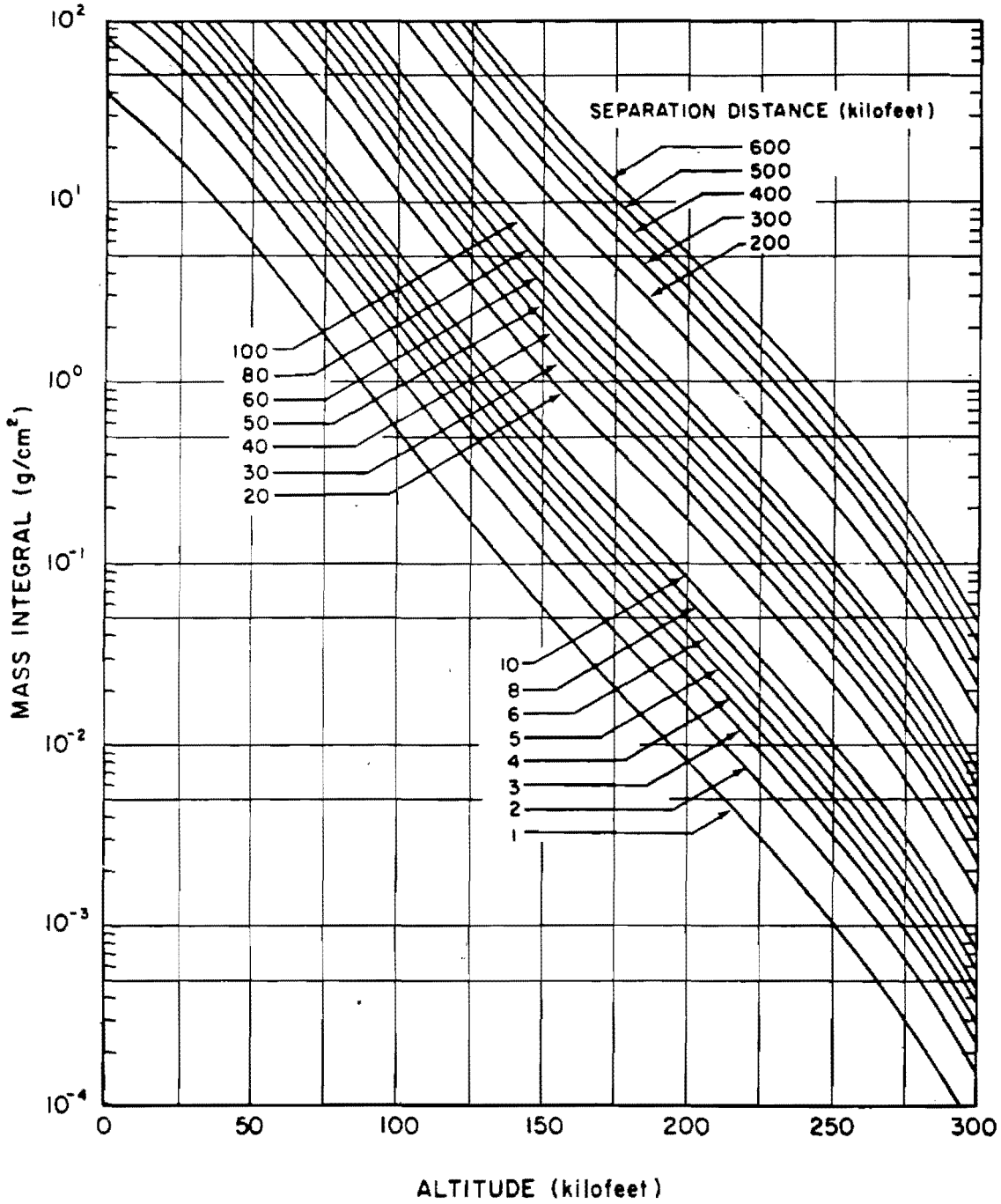

Figure 4-17 [redacted] Mass Integral for Specified Coaltitude Separation Distances as a Function of Altitude [redacted]

[redacted]

[redacted]

DNA
(L)(3)

Deleted

Figure 4-18. [redacted] Transmission of Direct X-Ray Fluence Through Air for Various Black Body Sources

[redacted]

[redacted]

[redacted]

DNA
(L)(3)

Deleted

Figure 4-19. [redacted] X-Ray Fluence Through Air for Various Black Body Sources

[redacted]

[redacted]

high energy X-rays increases – as the mass of air penetrated increases. This phenomenon occurs because the higher cross sections, particularly for photoelectric absorption, occur at lower energies and preferentially remove low energy X-rays from the direct fluence. However, every Compton scattering process degrades the energy of the scattered photon, and the scattered component of the fluence tends to become increasingly soft as the penetration increases. These two effects partially compensate for one another, and the typical black body spectrum is little affected by passage through air.

[redacted] The rate of X-ray production from nuclear weapons as sources has already been discussed in paragraph 4-6.

DNA (L)(3)

[redacted]

[redacted] Because the scattered component is softer than the direct component and arrives later, the spectrum of X-rays incident also varies with time in a complex fashion, and the dependence varies with the quantity of air traversed. Similarly, the direct fluence is all moving radially outward from the source, whereas the scattered photons can be incident from all directions, even from directly opposite the source. Thus the fraction of the energy flux moving outward (angles less than 90° from the radial vector) varies with time and location. In general, the fraction decreases from unity as time increases. However, when all times are considered, about 80 percent of the total fluence is outward for most ranges, and the fact that a portion of the fluence is backscattered can be neglected for most applications.

4-15 High Altitude Endoatmospheric Detonations [redacted]

[redacted] When nuclear detonations are so high that mass integral scaling is not correct, but yet sufficiently endoatmospheric that vacuum conditions are not satisfied, special and detailed calculations must be made for each case of interest. Although mass integral scaling is applicable for the direct fluence, the scattered component traverses paths of varying composition, and detailed Monte Carlo computer codes are necessary to describe the interactions.

[redacted]

DNA (L)(3)

The spectrum of Figure 4-10 was used. In computing horizontal ranges, the curvature of the earth was considered. The resulting total fluence contours are shown in Figure 4-21. Contours for the mass integral are also shown. Vacuum fluences and attenuation factors can be computed and direct fluences predicted from these contours.

Pages 4-40 through 4-44 are deleted.

[redacted]

[redacted]

Problem 4-5. Calculation of Direct Fluence in the Atmosphere

[redacted] Because every interaction of a photon with the material it traverses takes it out of the beam, the attenuation of *direct* fluence is exponential with the mass integral traversed, for a given energy of X-ray photon. Changes in spectral shape can be computed by calculating the contributions of the various energy components as the atmosphere is penetrated. As discussed in paragraph 4-12, the weighting of monoenergetic components becomes laborious for complex spectra, and these calculations usually are performed with computer codes. For this reason, a very simple example has been chosen to illustrate the procedures.

Example

[redacted]

Pages 4-46 and 4-47 are deleted.

[redacted]

[redacted]

[redacted] BIBLIOGRAPHY [redacted]

Christian, R. H., and P. G. Fischer, *Phenomenology Estimates and a Proposed Experimental Program for Sentinel Environment Tests* [redacted] DASA 2116, 68TMP-30, General Electric Company, TEMPO, Santa Barbara, California, 29 February 1968 [redacted]

Evans, B. S. and F. H. Shelton, *A Table of the Planck Radiation Function and Its Integral*, KN-770-70-36, Kaman Nuclear, Colorado Springs, Colorado, 2 February 1970 [redacted]

Gilmore, F. R., *A Table of the Planck Radiation Function and Its Integral*, RM-1743, RAND Corporation, Santa Monica, California, 2 July 1956 [redacted]

Latter, A. L., *Another Vulnerability* [redacted] RM-3981-PR, RAND Corporation, January 1964 [redacted]

Latter, A. L., *A High Temperature Nuclear Weapon* [redacted] RM-3978-AEC, RAND Corporation, Santa Monica, California, 23 December 1963 [redacted]

LRL Warheads for Advanced Spartan [redacted] LRL-CMA 68-154, Lawrence Radiation Laboratory, Livermore, California, 31 October 1968 [redacted]

Shelton, F. H., *Some Notes on the Spectral Distribution of Blackbody Sources* [redacted] KN-655-65-12, Kaman Nuclear, Colorado Springs, Colorado, 31 March 1965 [redacted]

Shelton, F. H., and J. R. Keith, *X-Ray Air Transport* [redacted] DASA 1981, KN-717-67-1, Kaman Nuclear, Colorado Springs, Colorado, 1 July 1967 [redacted]

Shelton, F. H., and J. R. Keith, *Time Dependent X-Ray Air Transport* [redacted] DASA 2138, KN-717-68-4, Kaman Nuclear, Colorado Springs, Colorado, 31 May 1968 [redacted]

Shelton, F. H., and J. R. Keith, *Initial Radiation Environments Produced by SPARTAN Events and Some of Their Aerospace Systems Effects* [redacted] DASA 2371, KN-774-69-4, Kaman Nuclear, Colorado Springs, Colorado, 24 July 1969 [redacted]

Shelton, F. H., *Nuclear Weapons as X-Ray Sources, the Environments They Produce, and Some Effects on Aerospace Systems* [redacted] *Volume I – X-Ray Sources and the Environments They Produce* [redacted] DASA 2397-1, KN-770-69-30, Kaman Nuclear, Colorado Springs, Colorado, September 1969 [redacted]

[redacted]

[redacted]

U.S. Standard Atmosphere, 1962, U.S. Committee on Extension to the Standard Atmosphere, available through the U.S. Government Printing Office, December 1962[redacted]

U.S. Standard Atmosphere Supplements, 1966, U.S. Committee on Extension to the Standard Atmosphere, available through the U.S. Government Printing Office, 196[redacted]

[redacted]

[redacted]

This page intentionally left blank

[redacted]

DTIC FILE COPY

DTIC ELECTE S D & E

Chapter 5

NUCLEAR RADIATION PHENOMENA

AD-A955 389

INTRODUCTION

As described in Chapter 1, one of the special features of a nuclear explosion is the fact that it is accompanied by the emission of nuclear radiations. These radiations consist of gamma rays, neutrons, beta particles, and a small proportion of alpha particles. Most of the neutrons and part of the gamma rays are emitted during the actual fission or fusion processes (see paragraphs 1-1 and 1-2, Chapter 1). The remainder of the gamma rays are produced in various secondary nuclear processes, including decay of the fission products. The beta particles are also emitted as the fission products decay. Some of the alpha particles result from the normal radioactive decay of the uranium or plutonium that does not fission in the weapon, and others are formed during the fusion reactions (paragraph 1-2).

As a result of the nature of the phenomena associated with a nuclear explosion, it is convenient to consider the nuclear radiations as being divided into two categories; initial and residual. The line of demarcation is somewhat arbitrary, but it is generally accepted to be about 1 minute after the explosion. The initial nuclear radiations consequently refer to the radiations emitted within 1 minute of the explosion. These radiations are discussed in Section I of this chapter. The residual radiations are further subdivided into neutron induced activity, which results from neutron activation of the earth below an air burst, and fallout, which is the deposition of radioactive residues following a surface or near-surface burst. These latter two forms of nuclear radiation are discussed in Sections II and III of this chapter, respectively.

The ranges of alpha and beta particles are short, and they can be neglected in the consideration of initial radiation. The beta particles, however, may be a hazard to personnel if fallout particles are in contact with the skin for protracted periods of time. The beta particles emitted by radioactive debris from high altitude explosions also may cause intense patches of ionization in the atmosphere that can interfere with, or disrupt, radio or radar communications as described in Chapter 8.

SECTION I
INITIAL NUCLEAR RADIATION

From the standpoint of total energy delivered, the principal sources of initial nuclear radiation (that delivered within 1 minute) are prompt neutrons (those emitted simultaneously with the fission or fusion events), gamma rays from the decay of fission products, and (in the case of an atmospheric burst) secondary gamma rays from neutron interactions with nuclei of the air and ground. Sources of lesser importance from the standpoint of energy delivered are delayed neutrons emitted by some fission products, secondary gamma rays from neutron interactions with the materials of the device, and gamma rays that are emitted simultaneously with fission. These latter components normally may be neglected in predicting total doses or exposures; however, the gamma components may be important for electronic components whose vulnerability is determined by dose rate rather than total dose.

This document has been approved for public release and sale; its distribution is unlimited.

89 3 02 044

NEUTRONS

5-1 Neutron Source

As mentioned previously, the neutrons of interest originate during the fission and fusion processes. The neutron source of interest is that which exists at the weapon case, i.e., the source of interest consists of those neutrons that escape from the exploding weapon. Both the number of neutrons and their spectrum are altered during transit through the weapon materials. Thus, the source of interest may be quite different from the source of origin (fission or fusion). The neutron source can be defined properly only by considering the actual design of a specific weapon. No average source can be defined that will represent most weapons with any degree of accuracy. It is beyond the scope of this manual to describe the output of a sufficient number of weapon types to present the user with adequate information concerning the neutron output for any possible specific situation. The examples that are presented in succeeding paragraphs are truly examples and should not be taken to be representative for purposes of generalization. Further information concerning nuclear weapons as neutron sources may be obtained from "Status of Neutron and Gamma Output from Nuclear Weapons," DASA 2567 (see bibliography). On the other hand, the curves shown in Figures 5-9 through 5-13 that provide the total dose to personnel on or near the surface of the earth were calculated for eight specific sources. It is believed that, with the descriptions of the eight sources provided in Table 5-3, one of the eight sources may be selected that will represent a reasonable estimate of the total dose to personnel on or near the surface of the earth for most situations.

Table 5-1 shows the spectra for two weapons, one pure fission and one thermonuclear, for which calculations are available.* These spectra are also shown in Figure 5-1 and 5-2.

As mentioned before, the spectra shown in Table 5-1 should not be construed as

*These spectra are those that were used in the calculation of dose to personnel from weapon types II and VIII, respectively, as shown in Figures 5-9 through 5-13.

Table 5-1. Weapon Neutron Output Spectra

Neutron Energy (MeV)	Fission Weapon (neutrons/kt)	Thermonuclear Weapon (neutrons/kt)
12.2 -15.0		1.62×10^{22}
10.0 -12.2		8.53×10^{21}
8.18 -10.0	7.32×10^{20}	6.08×10^{21}
6.36 - 8.18	1.27×10^{21}	5.46×10^{21}
4.06 - 6.36	3.00×10^{21}	6.41×10^{21}
2.35 - 4.06	8.90×10^{21}	1.22×10^{22}
1.11 - 2.35	2.52×10^{22}	2.84×10^{22}
0.111 - 1.11	3.84×10^{22}	6.18×10^{22}
0.0033- 0.111	2.22×10^{22}	1.71×10^{23}
Total	9.97×10^{22}	3.16×10^{23}

[redacted]

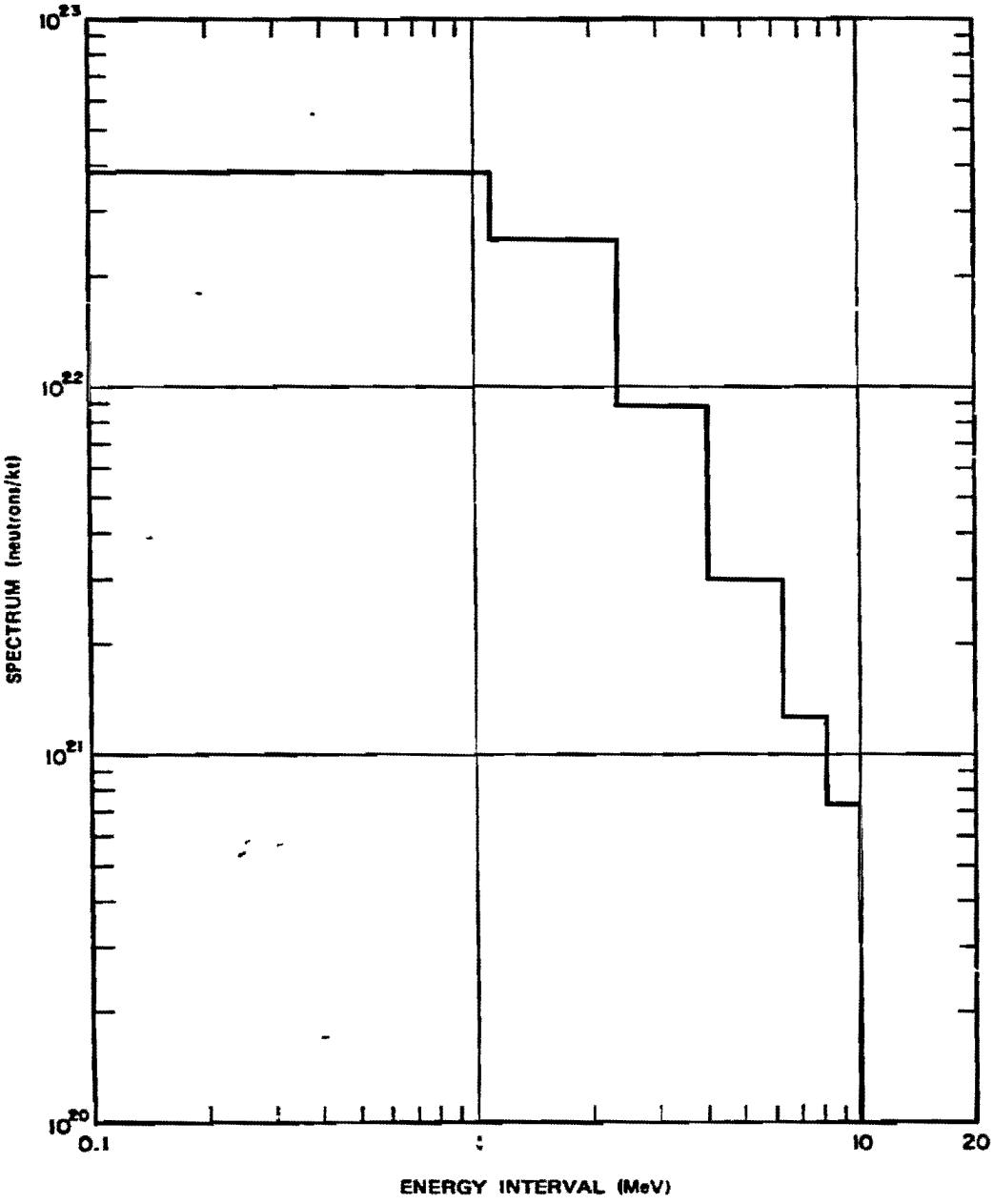

Figure 5-1. [redacted] Spectrum for a Fission Weapon (Normalized to 1 kt) [redacted]

Accession For
NTIS GRA&I
DTIC TAB
Unannounced
Justification
By
Distribution/
Availability Codes
Dist | Avail and/or Special
A-1

[redacted]

UNANNOUNCED
QUALITY INSPECTED

[redacted]

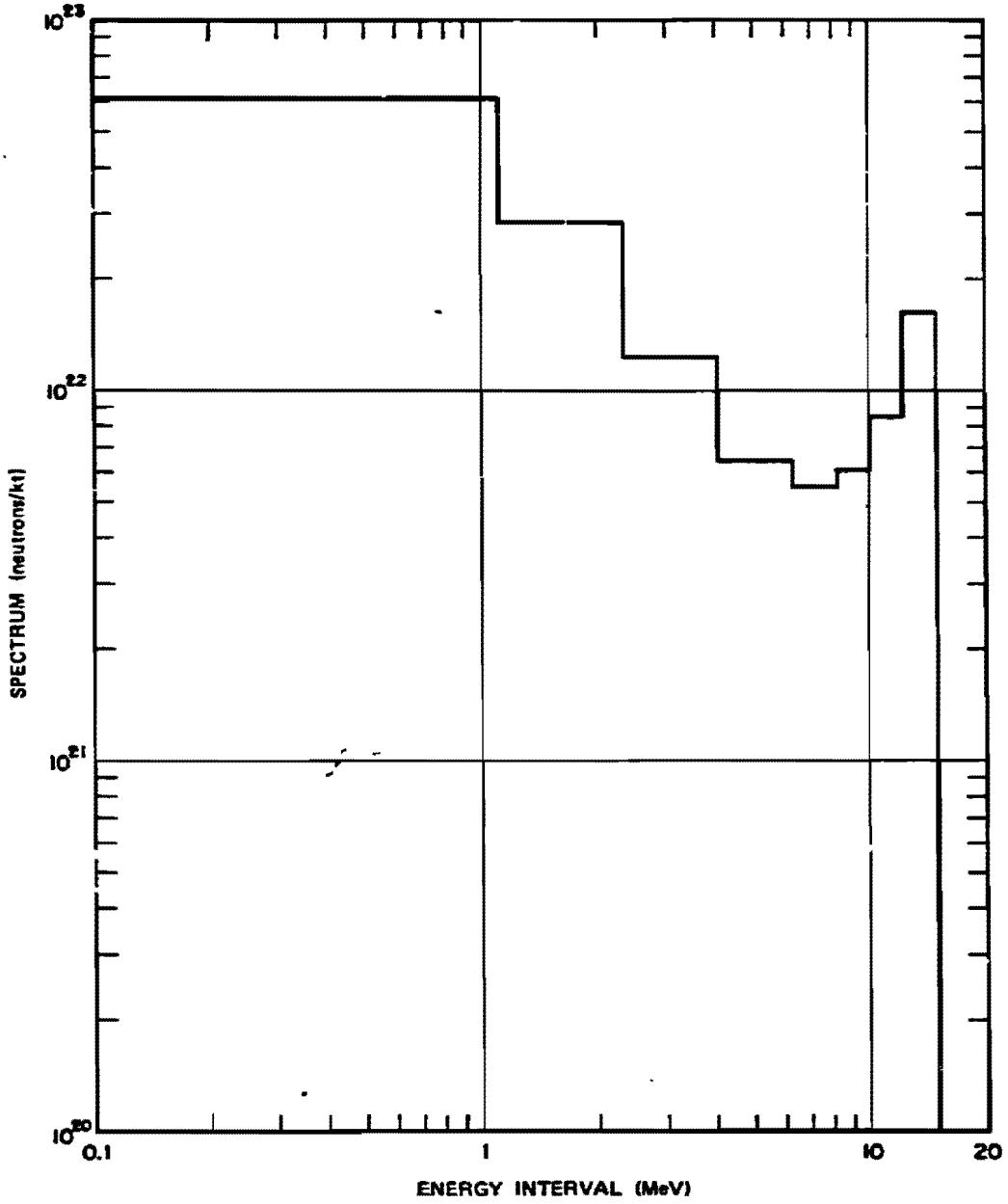

Figure 5–2. [redacted] Spectrum for a Thermonuclear Weapon (Normalized to 1 kt) [redacted]

[redacted]

being representative. They are merely examples.

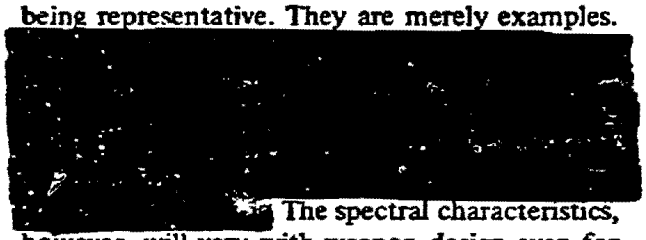

The spectral characteristics, however, will vary with weapon design even for weapons with the same total neutron output per kiloton.

5-2 Exoatmospheric (Vacuum) Transport

Neutron environments are completely specified by the description of the source and the distance from the source to the point of interest if the explosion occurs in a vacuum. If an explosion occurs sufficiently high that essentially vacuum conditions prevail, it is designated an exoatmospheric explosion. Since in any case, the vacuum will be less than perfect, the distinction between exoatmospheric and endoatmospheric explosions will depend on the degree to which effects vary from those predicted for a vacuum.

For perfect vacuum conditions, the neutron fluence is given by

$$\varphi = \frac{N_o}{4\pi R^2} \text{ n/cm}^2$$

where N_o is the total number of neutrons emitted by the weapon and R is the distance in centimeters. Under these conditions the spectrum will remain constant, since no interactions can take place in a vacuum. However, as a result of the energy differences the flux (neutrons cm^{-2} sec^{-1}) will be a function of the distance from the source, i.e., the more energetic neutrons will arrive ahead of the less energetic ones. The energies associated with neutrons produced by nuclear explosions are sufficiently low compared to their rest mass energy that their velocities may be determined from their kinetic energy by non-relativistic mechanics, i.e.,

$$\frac{1}{2}Mv^2 = \text{K.E.},$$

where M is the neutron mass, 1.67×10^{-24} gm, v is the velocity, cm/sec, and K.E. is the kinetic energy in ergs. Using the relationship

$$1 \text{ MeV} = 1.6 \times 10^{-6} \text{ ergs},$$

the velocity is related to the kinetic energy in MeV as follows

$$v = 1.38 \times 10^9 \sqrt{\text{K.E. (MeV)}} \text{ cm/sec},$$

or

$$v = 1.38 \times 10^4 \sqrt{\text{K.E. (MeV)}} \text{ km/sec}.$$

Thus the velocities of 14 MeV, 4 MeV, and 1 MeV neutrons are

$$v_{14} = 1.38 \times 10^4 \sqrt{14} = 5.16 \times 10^4 \text{ km/sec},$$

$$v_4 = 1.38 \times 10^4 \sqrt{4} = 2.76 \times 10^4 \text{ km/sec},$$

$$v_1 = 1.38 \times 10^4 \sqrt{1} = 1.38 \times 10^4 \text{ km/sec}.$$

Expressed in a different manner, the times of flight will be 19.3, 36.2, and 72.4 μ sec/km for the 14 MeV, 4 MeV, and 1 MeV neutrons, respectively. Thus, although the spectrum will remain unchanged, the neutrons will arrive at points several kilometers from the explosion over periods of tens of microseconds.

5-3 Neutron Transport Through Materials

Neutrons undergo three main types of reactions when traversing matter: elastic scatter-

ing; inelastic scattering; and capture. In the elastic scattering process, the neutron interacts with the nucleus of an atom and is scattered away from its original line of flight. If the nucleus is light (e.g., the proton that constitutes a hydrogen nucleus), the neutron may transmit a significant amount of its energy to the nucleus, and the scattered neutron will be less energetic than the incident neutron. If the nucleus is heavy, however, the energy transmitted to the nucleus will be insignificant, and the neutron will continue in a new direction with essentially the same energy as before the collision. In the inelastic scattering process, the neutron interacts with the nucleus with the subsequent emission of a gamma ray and a neutron with degraded energy. There are a variety of capture reactions, most of which result in the subsequent emission of a charged particle (generally a proton or alpha particle) and/or a gamma ray. When the reaction results solely in the emission of a gamma ray, it is generally referred to as a radiative capture reaction. As a rule, the probability for capture reactions is small compared to elastic and inelastic scattering when the neutron energy exceeds a few keV. The nuclei remaining after neutron capture are frequently radioactive. The fission process described in paragraph 1-1 is a special case of neutron-induced reactions. Neutrons that do not undergo any of the reactions described above will decay into a proton and an electron with a half life of about 12.8 minutes. The same is true of neutrons that undergo scattering, if they do not undergo some other reaction prior to decaying. The probabilities of the various reactions are such that the decay process is most important for neutrons traveling upwards from a relatively high altitude burst.

[redacted] The primary reactions that occur during neutron transport through air are elastic scattering, inelastic scattering, and capture by nitrogen nuclei. These latter two reactions provide a source of secondary gamma rays that can be important in some cases, as will be discussed in subsequent paragraphs.

[redacted] The neutron environment produced by nuclear explosions within the atmosphere are much more complicated than those described in paragraph 5-2 for exoatmospheric cases because of the interactions that take place with the atmospheric constituents. Even for a monoenergetic source the interactions described above alter the total neutron fluence that reaches a given range, result in a spectral distribution at that point, and change the time rate and direction of arrival at the point. As a result of scattering, the neutrons may arrive at a given point from any direction. If the source consists of a spectrum such as those shown in Figures 5-1 and 5-2, the situation is even more complex. In practice, the calculation of neutron fluences, fluxes, and spectra at some point distant from an endoatmospheric nuclear explosion, or for the interior of a system that is operating exoatmospherically, is performed by complex computer codes. It is beyond the scope of this manual to provide the means for calculating all of these quantities or even to provide a description of the methodology. The latter is contained in Volume III of the "Weapons Radiation Shielding Handbook," DASA 1892-3 (see bibliography). Selected examples of the change in fluence and spectrum will be provided in succeeding paragraphs and figures.

[redacted] An extensive set of tabulated results of computer calculations of neutron fluxes and doses is contained in "Time-Dependent Neutron and Secondary Gamma-Ray Transport in an Air-Over-Ground Geometry," ORNL-4289, Vol. II, (see bibliography). These data were used to obtain the spectra that would result from the source spectra shown in Figures 5-1 and 5-2 at slant ranges of 390, 1,050, and 1,500 meters. The resulting spectra are shown in Figures 5-3 and 5-4, respectively. Note that the spectra in Figures 5-3 and 5-4 show 4π (slant range)^2 x

fluence. This does not mean that the spectra will be the same in all directions. The spectra shown in Figures 5-3 and 5-4 only apply to low air bursts and to *targets located on or near the surface of the earth.* The units for the ordinates in Figures 5-3 and 5-4 were chosen to allow a convenient visual comparison with Figures 5-1 and 5-2, respectively. Inspection of Figures 5-1 through 5-4 indicates that the shape of the fission source spectrum is not changed appreciably during transit through 1,500 meters of air (the relative abundance of extremely low energy neutrons, much lower energies than shown in Figures 5-1 through 5-4, will increase, however). The shape of the thermonuclear spectrum, on the other hand, does change as the neutrons penetrate air. The peak that exists at 14 MeV at the source becomes lower relative to the total, and the valley between about 8 and 12 MeV at the source becomes filled in as the higher energy neutrons are degraded to the 8 to 12 MeV range.

Figures 5-5 and 5-6 show the neutron fluence for a receiver located on or near the surface of the earth as a function of slant range for the source spectra shown in Table 5-1. The fluence is shown for each of the energy intervals in Table 5-1. The total number fluence for neutron energies above 3.3 keV is also shown for each source. Once again the user is cautioned that these fluences should not be considered representative. They are presented as illustrative examples. Changes in weapon design will change the source spectrum, and this will modify the spectrum as well as the total number fluence at some distance from the explosion. Figures 5-5 and 5-6 also illustrate the large change in the spectral characteristics of the thermonuclear spectrum when compared to the variations in the fission spectrum with slant range.

The preceding paragraphs have provided estimates of neutron fluences and spectra from low air bursts for detectors on or near the surface of the ground. The presence of an air-ground interface can increase or decrease the neutron intensities by as much as an order of magnitude compared to intensities at corresponding distances in an infinite air medium as a result of reflections and absorption by the ground. For source detector separation distances less than a mean-free path,* localized reflection from the ground generally tends to increase the intensity of high energy neutrons; however, initial nuclear radiation is only of interest for very low yields at such short distances since other weapon effects normally will be dominant. At longer distances, the high energy neutron intensity may be reduced by a factor of five or more compared to infinite air when both the source and the detector are at the ground surface. These effects have been included in the calculations from which the preceding figures were derived.

The estimation of neutron environments around an endoatmospheric nuclear explosion for receivers away from the surface of the earth requires a knowledge of the atmospheric properties along any path that a neutron might traverse from the weapon to the point of interest. Although atmospheric properties can change from day to day and from place to place, most calculations are based on a standard atmosphere such as the one described by the National Bureau of Standards in 1962. The important atmospheric constituents that affect neutron transport are

	Fraction by Weight
Nitrogen	0.7553,
Oxygen	0.2318.

* A mean-free path is the distance in which the radiation intensity is decreased by a factor of e, where e is the base of the natural logarithms (about 2.718). The length of a mean-free path depends on the neutron energy and on whether only the direct fluence or the total (direct plus scattered) fluence is being considered.

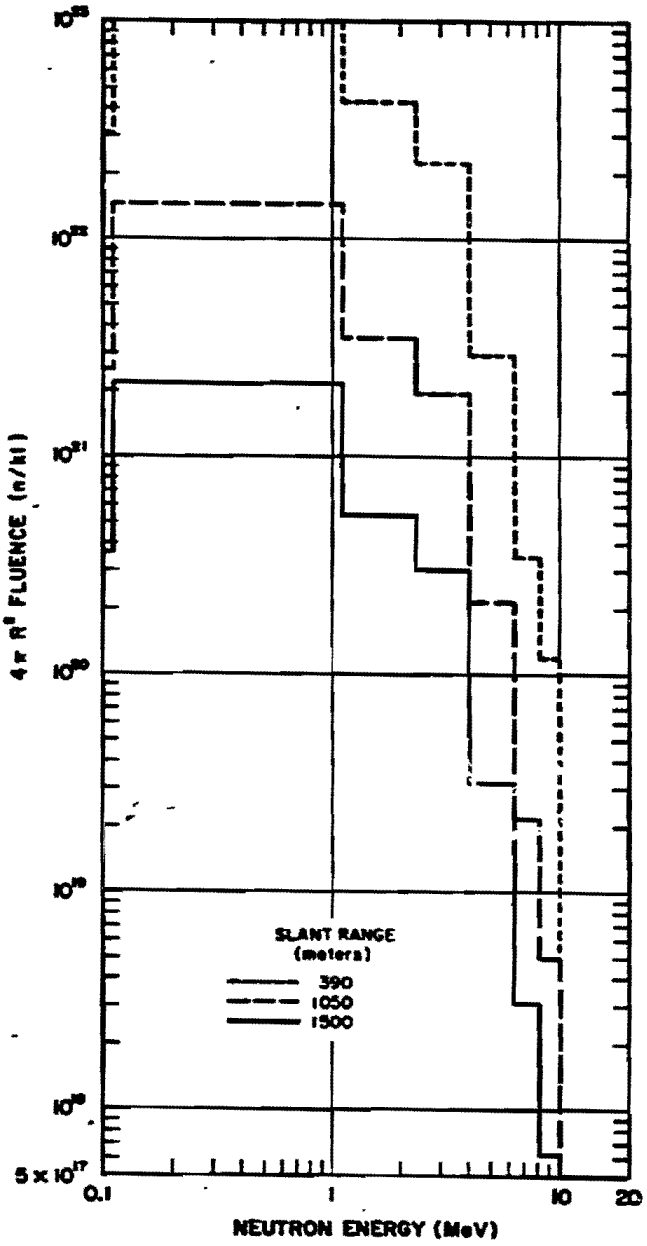

Figure 5-3. [redacted] Spectra from the Fission Source of Figure 5-1 with the Receiver On or Near the Surface of the Earth at Various Slant Ranges [redacted]

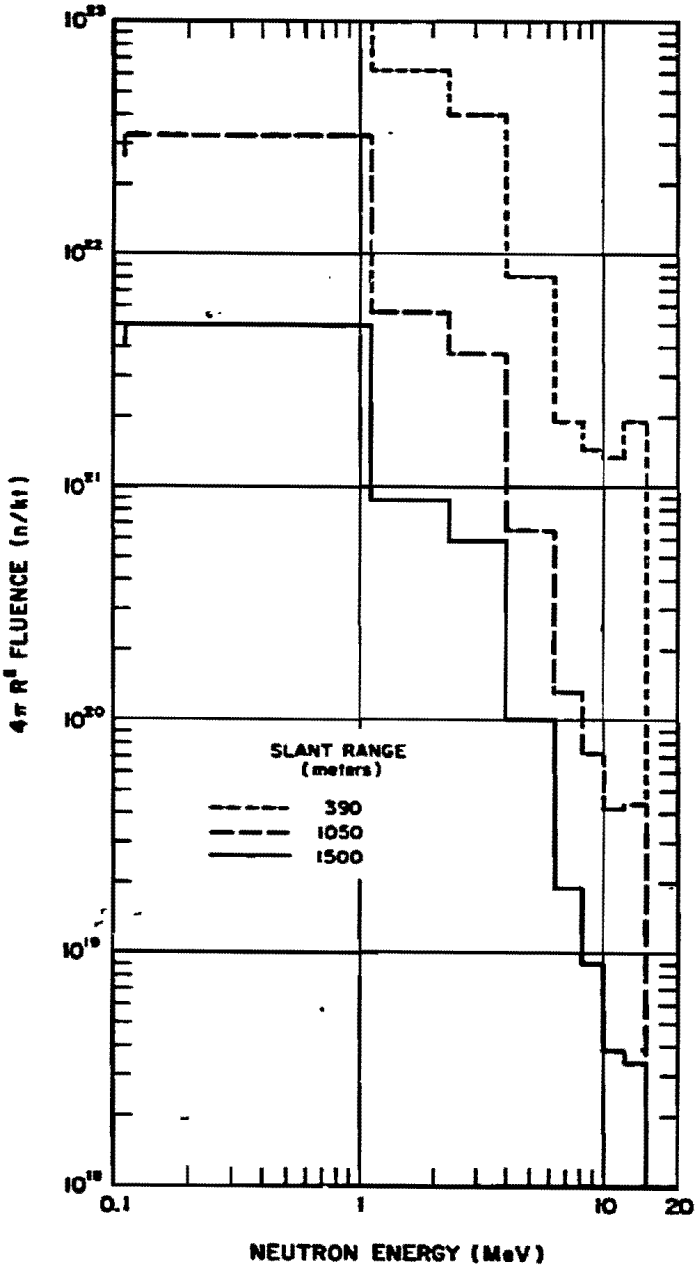

Figure 5-4. [redacted] Spectra from the Thermonuclear Source of Figure 5-2 with the Receiver On or Near the Surface of the Earth at Various Slant Ranges [redacted]

[redacted]

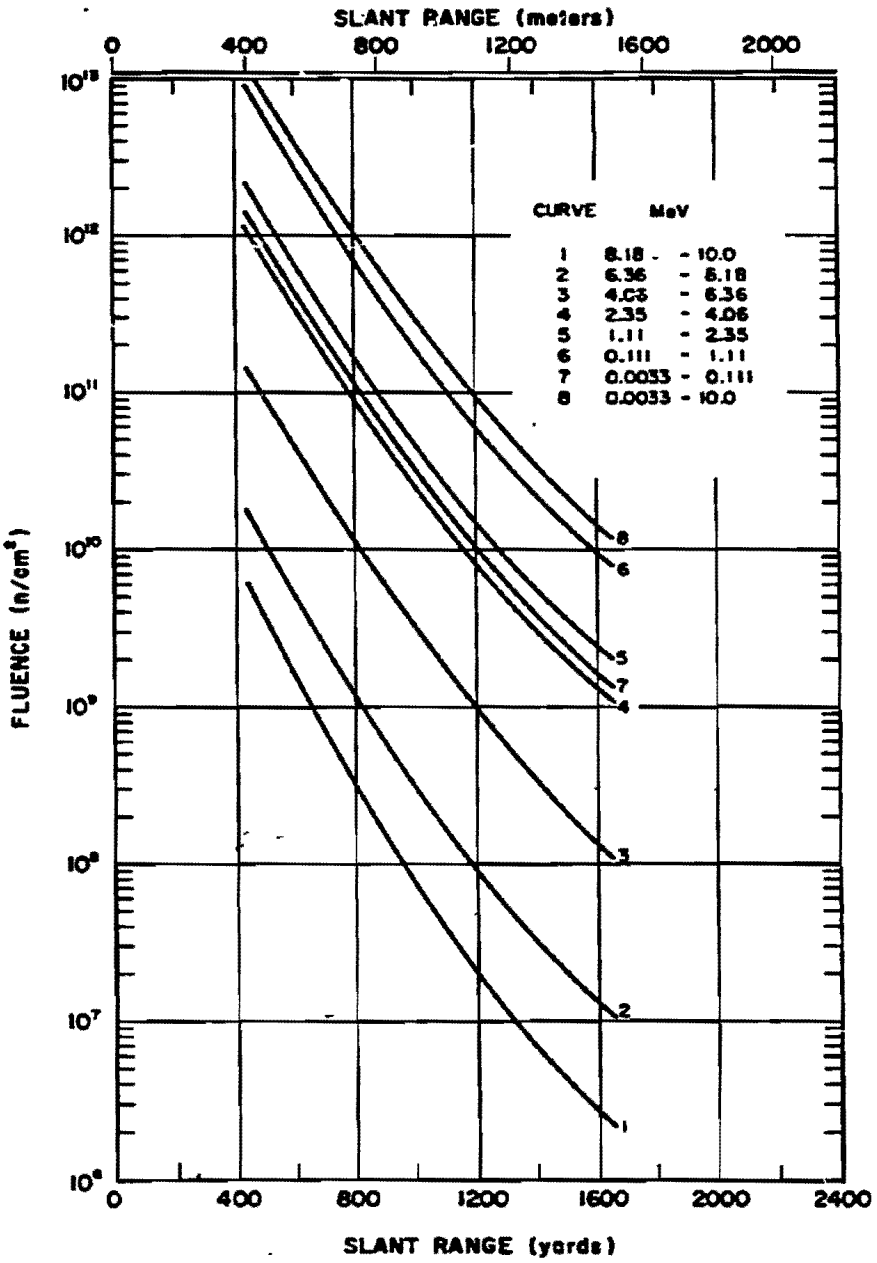

Figure 5-5. [redacted] Neutron Fluence Incident on a Receiver Located On or Near the Surface of the Earth from the Fission Spectrum Shown in Table 5-1 and Figure 5-1 [redacted]

[redacted]

[redacted]

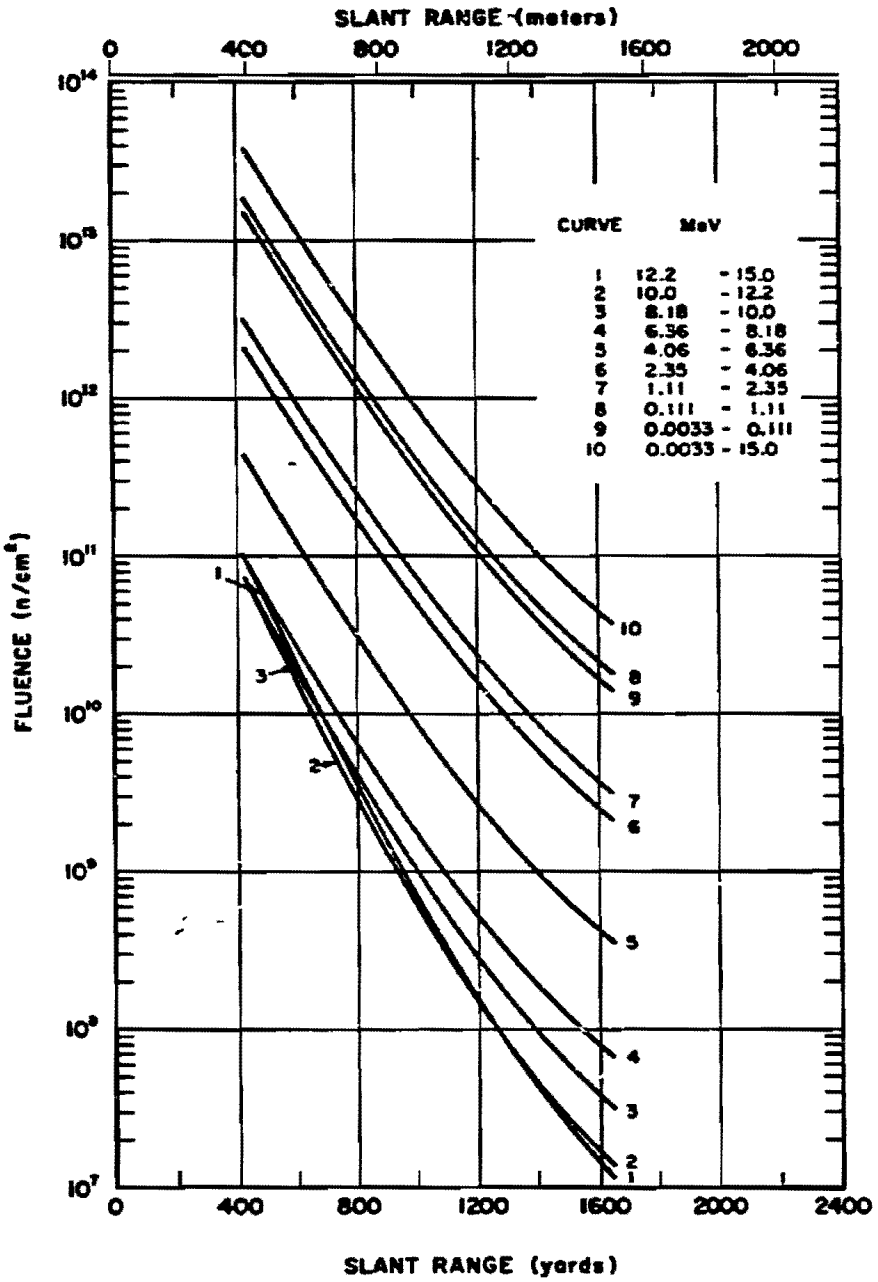

Figure 5-6. [redacted] Neutron Fluence Incident on a Receiver Located On or Near the Surface of the Earth from the Thermonuclear Spectrum Shown in Table 5-1 and Figure 5-2 [redacted]

[redacted]

[redacted]

Other minor components of the atmosphere can be neglected without serious loss of accuracy.

[redacted] The other principal feature of the standard atmosphere is its variation in density with altitude. The density, ρ, falls approximately exponentially with increasing altitude, as is shown in Table 5-2. Also shown is the quantity of air above a given altitude, h, which is given by the mass integral

$$q(h) = \int_h^\infty \rho(h')dh'.$$

Table 5-2 also shows the density normalized to the sea level density, ρ_o.

[redacted] If two points are at altitudes h_1 and h_2 and are separated by a horizontal distance, d, then the slant range R is given by

$$R = \sqrt{d^2 + (h_2 - h_1)^2}$$

and the mass integral between them is given by

$$q(R) = \int_o^R \rho(h')ds' = R\,\frac{q(h_2) - q(h_1)}{h_2 - h_1}.$$

(U) This expression reduces to

$$q(R) = q(h_2) - q(h_1)$$

when $d = 0$ and (in the limit) to

$$q(R) = \rho(h)R$$

when $h_1 = h_2$ (the coaltitude case).*

[redacted] If the air is characterized by an atomic density ρ_i for each important constituent, then

* The value of the mass integral as a function of altitude is shown in Figure 4-17 for various coaltitude separation distances.

Table 5-2. [redacted] The Standard Atmosphere [redacted]

Altitude (kft)	Air Density (g/cm^3)	Mass Integral Above Altitude (g/cm^2)	Density Normalized to Sea Level (ρ/ρ_o)
0	1.2250×10^{-3}	1.0331×10^{3}	1.0000×10^{0}
5	1.0556×10^{-3}	8.5967×10^{2}	8.6170×10^{-1}
10	9.0477×10^{-4}	7.1059×10^{2}	7.3859×10^{-1}
20	6.5312×10^{-4}	4.7525×10^{2}	5.3316×10^{-1}
30	4.5904×10^{-4}	3.0749×10^{2}	3.7473×10^{-1}
40	3.0267×10^{-4}	1.9305×10^{2}	2.4708×10^{-1}
50	1.8756×10^{-4}	1.1973×10^{2}	1.5311×10^{-1}
60	1.1628×10^{-4}	7.4292×10^{1}	9.4919×10^{-2}
70	7.1742×10^{-5}	4.6182×10^{1}	5.8565×10^{-2}
80	4.4174×10^{-5}	2.8855×10^{1}	3.6060×10^{-2}
90	2.7391×10^{-5}	1.8151×10^{1}	2.2360×10^{-2}

[redacted]

for every centimeter that a neutron traverses, there are ρ_i atoms of that type within a cross-sectional area of one cm^2 with which the neutron can interact. The probability that any reaction (elastic or inelastic scattering or neutron induced reaction) will occur is given in terms of a cross section $\sigma_{i,n}$ (so called because it has units of area), which is the probability of a given interaction (n) taking place with a given type of atom (i) under the condition that one interaction per unit area is possible. The probability of interaction per centimeter is therefore $\mu = \sum_{i,n} \rho_i \sigma_{i,n}$. Since this is also the probability that a neutron disappears from the incident beam, the beam intensity falls by a factor $e^{-\mu x}$ after having penetrated a distance x into the material. It is often convenient to express the penetration in terms of the total amount of material "seen" by a beam of neutrons, ρx, where ρ is the mass density of the material. In this case, the mass attenuation coefficient $\kappa = \mu/\rho$ is used. Thus, in the endoatmospheric case, the neutron fluence at a point depends not only on the spherical divergence described in paragraph 5-2 for the exoatmospheric case but also on exponential attenuation, so that

$$\varphi = \frac{N_o e^{-\kappa \rho R}}{4\pi R^2} \text{ n/cm}^2,$$

where R is the radial distance from the source in centimeters and N_o is the total number of neutrons emitted.

[redacted] It is frequently convenient to replace the quantity ρR by the mass integral $q(R)$ described above, so that the equation for fluence becomes

$$\varphi = \frac{N_o e^{-\kappa q(R)}}{4\pi R^2} \text{ n/cm}^2.$$

This procedure is known as mass integral scaling. Notice that q will be different for different directions of R unless the atmosphere is essentially uniform, so that contours of constant fluence usually are not spherically symmetric about the burst point, although they usually are cylindrically symmetric about a vertical axis unless asymmetries are introduced by the weapon.

[redacted] The expressions given above, however, only represent the component that reaches the point directly from the source. Scattered neutrons also reach the point from other directions. The result is that the fluence at that point is larger by a buildup factor B. The magnitude of B depends on the distance from the source, the energy spectrum of the neutrons, and the properties of the scattering material in complex ways. The flux of neutrons (neutrons/cm^2-sec) is altered as a result of the fact that scattered neutrons travel longer paths and neutrons of any given energy will arrive at the point over a finite time span even after undergoing only elastic scatterings. This alteration of the flux with distance is in addition to the alterations resulting from differences in time of flight of different energy neutrons discussed for exoatmospheric transport in paragraph 5-2, and further alterations will result from the changes in the spectral distribution during endoatmospheric transport. Moreover, the value of the mass attenuation coefficient κ varies with neutron energy so that even the direct fluence must be calculated by weighting monoenergetic calculations by the spectral distribution. For a given penetration distance, this weighting process can be replaced by using an effective κ, but the value of the effective κ will change with distance as a result of spectral changes.

[redacted] In practice, the most accurate method for calculating neutron fluences uses computer codes with accurate neutron cross-section for each energy group and each scattering or interaction process. This technique is also essential for following neutrons out of the direct fluence as well as for calculating the flux. It is beyond the

[redacted]

[redacted]

scope of this manual to provide methods for calculating all of these quantities. Moreover, the vulnerability criteria of electronic components and systems to neutrons that are given in Section VII of Chapter 9 and in Section IV of Chapter 14 are given in terms of fluence (>10 keV fission). While these vulnerability criteria imply a knowledge of the spectrum, the calculation of the spectrum at the point of interest for any situation would require more information concerning source spectra than is provided herein. Therefore, the following discussion will be limited to the calculation of total number fluence for low altitude (deep) endoatmospheric bursts. It should be noted that the calculations of the curves shown in Figures 5-3 through 5-6 did make use of the results of computer calculations, and these curves are accurate representations of the spectra shown in Table 5-1 at various distances from an explosion. They are, however, limited to low air bursts and receivers on or near the surface. Likewise, the calculations of neutron dose presented in a later subsection are based on computer code transport calculations.

[redacted] Low altitude (deep) endoatmospheric explosions are the next simplest case — after vacuum detonations — because the air density is sufficiently high that most of the attenuation occurs close to the burst point. Therefore, there are no large variations in density to affect critically the computation of fluences. In particular, the density of air through which the scattered neutrons reach a given point does not differ greatly from that through which the direct neutrons penetrate. Although whether or not altitudes are low (explosions are deep) depends on the energy spectrum of the weapon, if deep endoatmospheric conditions do prevail, the neutron fluence can be approximated by mass integral scaling. The total quantity of air (the mass integral) between the source and the point of interest is computed as described above, and then the appropriate buildup factors are applied to the vacuum fluences calculated for the given energy spectrum as described in paragraph 5-2. Examples of such calculations are provided below.

[redacted] No simple analytic expression gives the build-up factor, but Figure 5-7 shows the build-up in neutron fluences for various monoenergetic neutron sources. The curves in Figure 5-7 are based on Monte Carlo transport calculations in uniform air. Use of the curves in Figure 5-7 will provide reasonably accurate results up to burst altitude of about 60 kilofeet. The build-up factors in Figure 5-7 may be used with somewhat less confidence up to burst altitudes of 85 kilofeet. The effects of a non-uniform atmosphere become significant above 85 kilofeet, and computer calculations should be made for each burst altitude and spectrum of interest for burst altitudes between 85 and 200 kilofeet. It is beyond the scope of this manual to provide neutron environments for bursts in this altitude regime. For bursts above about 200 kilofeet, the vacuum calculations described in paragraph 5-2 may be used. Note that the build-up factors in Figure 5-7 are given as fractions of the vacuum fluence.

[redacted] The source energy intervals used in the Monte Carlo calculations from which the curves in Figure 5-7 were derived are shown below:

Nominal Source Energy (MeV)	Source Energy Interval (MeV)
14.1	12.5 -16.0
10.0	9.0 -12.5
7.5	6.0 - 9.0
4.0	3.0 - 6.0
1.3	0.7 - 3.0
0.5	0.3 - 0.7
0.1	0.09- 0.3
0.03	0.01- 0.09

[redacted] It is unfortunate that the source energy intervals used in the Monte Carlo calculations

[redacted]

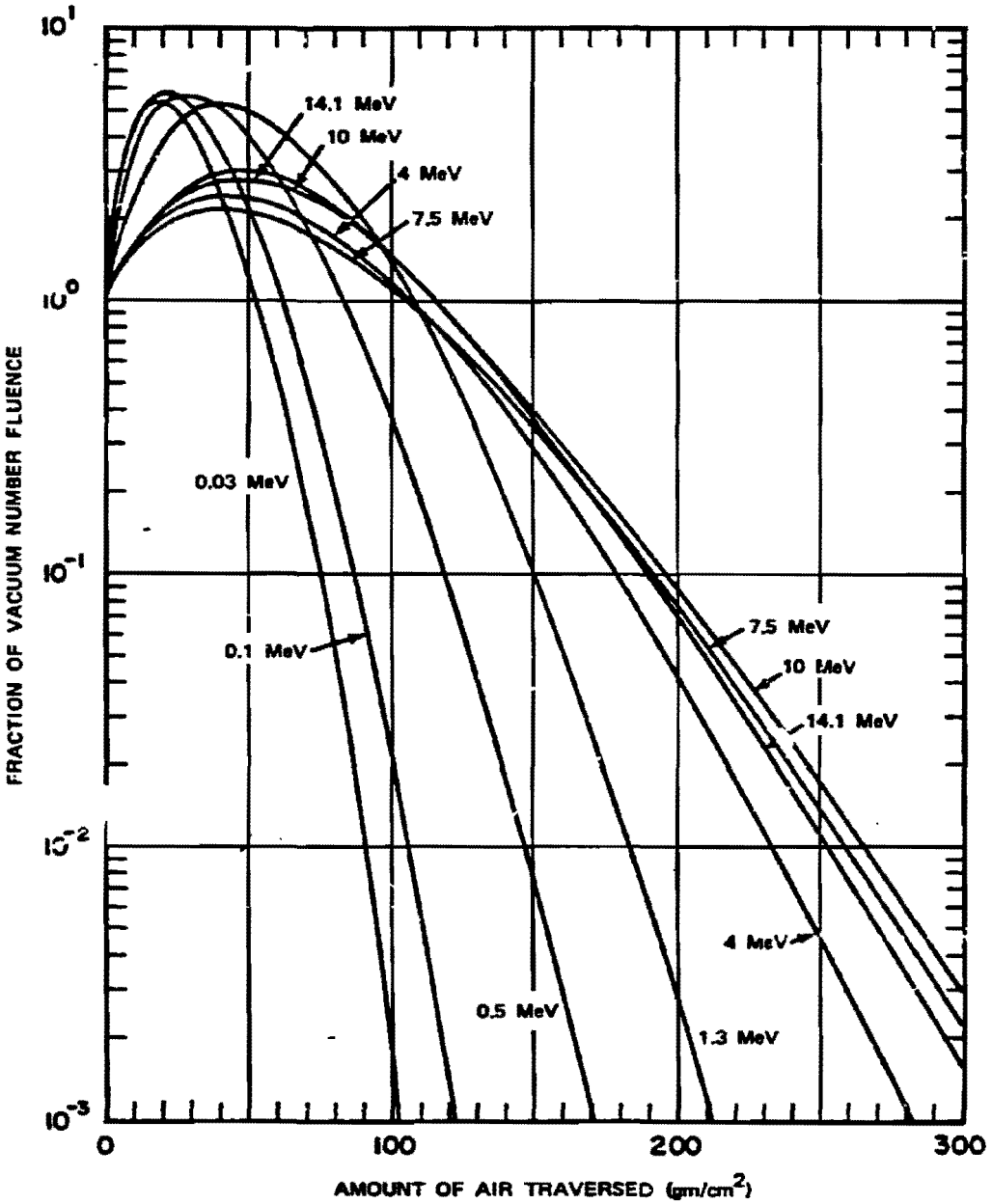

Figure 5-7. Neutron Energy Build-Up Factors for Various Monoenergetic Sources in Homogeneous Air

differ from those shown in Table 5-1. However, many different source energy intervals will be found in reported weapon spectra. Most of the reported spectra will contain a uniform distribution (neutrons per MeV) within an energy band; however, some will contain an uneven distribution for the lower energies, e.g., 1/energy for energies below 0.1 MeV. In any case, it generally will be possible to divide the spectrum into energy groups that correspond roughly to those used in the preparation of Figure 5-7. Interpolation between the curves in Figure 5-7 should not be attempted; the spectral intervals should be adjusted to use the curves.

As an example of the use of Figure 5-7, consider a hypothetical weapon with the following spectrum:

Nominal Source Energy (MeV)	Neutrons per kt
14.1	1.23×10^{22}
10.0	3.00×10^{21}
7.5	3.80×10^{21}
4.0	1.36×10^{22}
1.3	4.25×10^{22}
0.5	1.72×10^{22}
0.1	2.74×10^{22}
0.03	8.24×10^{22}
Total	2.02×10^{23}

Assume that the neutron number fluence coaltitude at a distance of one mile from a 1 Mt explosion of such a weapon at a burst altitude of 60,000 feet is desired. The distance in centimeters is

$$1 \text{ (mile)} \times 1.609 \times 10^5 \text{ cm/mile}$$
$$= 1.609 \times 10^5 \text{ cm.}$$

The vacuum fluence, φ_i, for each of the monoenergetic neutron sources, N_{oi}, is

$$\varphi_i = \frac{N_{oi}}{4\pi R^2} = \frac{N_{oi}}{4\pi(1.609 \times 10^5)^2} = \frac{N_{oi}}{3.25 \times 10^{11}},$$

e.g., for the 14.1 nominal source energy, the vacuum fluence is

$$\varphi_{14.1} = \frac{(1.23 \times 10^{22} \text{ n/kt})\ (10^3 \text{ kt/Mt})}{3.25 \times 10^{11}}$$

$$\varphi_{14.1} = 3.78 \times 10^{13} \text{ n/cm}^2.$$

In the same manner, the vacuum fluences for remaining source energies are determined to be

Nominal Source Energy (MeV)	Vacuum Fluence (n/cm^2)
14.1	3.78×10^{13}
10.0	9.22×10^{12}
7.5	1.17×10^{13}
4.0	4.18×10^{13}
1.3	1.31×10^{14}
0.5	5.29×10^{13}
0.1	8.42×10^{13}
0.03	2.53×10^{14}
Total	6.22×10^{14}

From Table 5-2, the ambient air density at 60 kilofeet is 1.1628×10^{-4} gm/cm^3. The mass integral at a coaltitude distance of one mile is

$$q(R) = \rho(h)R,$$

$$q(R) = (1.1628 \times 10^{-4})(1.609 \times 10^5),$$

$$q(R) = 18.7 \text{ gm/cm}^2.$$

From Figure 5-7, the build-up factors corresponding to traversal of 18.7 gm/cm^2 are

Nominal Source Energy (MeV)	Build-Up Factor (fraction of vacuum fluence)
14.1	2.0
10.0	2.0
7.5	1.75
4.0	1.9
1.3	3.5
0.5	5.0
0.1	5.6
0.03	5.2

The neutron fluences in air are obtained by multiplying the vacuum fluences by the build-up factors:

Nominal Source Energy (MeV)	Neutron Fluence in Air (n/cm^2)
14.1	7.56×10^{13}
10.0	1.84×10^{13}
7.5	2.05×10^{13}
4.0	7.94×10^{13}
1.3	4.59×10^{14}
0.5	2.64×10^{14}
0.1	4.72×10^{14}
0.03	1.32×10^{15}
Total	2.71×10^{15}

Thus, 2.71×10^{15} neutrons/cm^2 are incident at a point coaltitude at a distance of 1 mile from a 1 Mt explosion of the hypothetical weapon described above burst at 60,000 feet. The corresponding vacuum fluence at the same distance would have been 6.22×10^{14} neutrons/cm^2. Thus, there is a factor of

$$\frac{2.71 \times 10^{15}}{6.22 \times 10^{14}} = 4.36$$

in the number of fluence for the explosion at 60,000 feet compared to the same distance from the same explosion in a vacuum. Note that the only meaningful fluence in air is the *total* number of fluences. Fluences shown for each nominal source energy represent number fluence *resulting* from that source energy, but any given source energy fluence would contain a spectrum of energies at the receiver. No information concerning the spectrum at the receiver can be obtained by the mass integral scaling demonstrated above.

If the point of interest is at an altitude that differs from that of the burst, but is still below 85 kilofeet, the only change in the procedure for determining the neutron fluence in air is in the determination of $q(R)$ to enter Figure 5-7. The appropriate value may be determined by the equations given previously together with the tabulated values in Table 5-2. Examples of the calculation of $q(R)$ for other than coaltitude cases are given in Problems 4-5 and 4-6, Chapter 4, which deal with mass integral scaling of X-rays. The same procedures for determining $q(R)$ apply to mass integral scaling of neutron fluences.

GAMMA RAYS

5-4 Gamma Ray Sources

As mentioned in the introductory paragraph to this section, there are several sources for the gamma rays that contribute to the initial nuclear radiation (that radiation delivered within 1 minute) from a nuclear explosion. These sources include the gamma rays that are released essentially simultaneously with the fission process, gamma rays resulting from non-fission interactions with weapon materials, gamma ray resulting from inelastic scattering of neutrons by atoms of the air (paragraph 5-3), gamma rays resulting from isomeric decays of weapon materials,* gamma rays resulting from neutron capture in nitrogen, and finally, gamma rays emitted during the decay of the fission products. Figure 5-8 provides an illustration of the time dependence of these various sources of gamma rays in terms of energy released per unit time

* Isotopes that have the same atomic number and the same atomic weight may differ in some property of their nuclei; these isotopes are called isomers. The nuclear property by which isomers may differ may be the type of particle emitted, the half-life or energy of the particle or the presence or absence of radioactivity. Here the interest is in those that emit gamma rays, either with or without accompanying particulate emissions. The gamma may be emitted by nuclei of weapon materials that have simply been raised to energy states above their normal state and return to their ground state by emitting one or more gamma rays.

[redacted]

per kt from a large yield weapon. The dotted curves in Figure 5-8 show the source as it would exist in a vacuum, i.e., the gammas resulting from inelastic scattering and neutron capture in the air would not be present under vacuum conditions. Not shown in Figure 5-8, but of potential importance for receivers near the surface of the earth in the vicinity of a low air burst are gammas that result from neutron interactions with the ground. It is convenient to divide the initial gamma radiation into two components: prompt gamma rays that result from the fission process and some neutron interactions with weapon materials, and are generally emitted within 1 to 2 shakes;* and delayed gamma radiation which originates from the sources described above subsequent to the prompt gamma ray emission and up to 1 minute after burst.

5-5 Prompt Gamma Rays [redacted]

[redacted] Prompt fission gamma rays are released essentially simultaneously with the fission process and thus their source rate behavior is determined by the rate profile of fission events in the weapon. These gamma rays escape before the detonation has appreciably deformed the weapon case or perturbed the atmosphere. The energy distribution of the fission gamma rays has been investigated using small samples of fissionable material; however, extrapolation of the small sample information to a weapon source involves considerable uncertainty because of the requirements to define the fission rate profile and to evaluate the attenuation provided by weapon materials as a function of time.

[redacted] Another source of very early gamma rays that contributes to the prompt pulse results from the non-fission interaction of neutrons with weapon materials.† These two sources combine to form a pulse of extremely short duration. Although the total amount of radiation given off during this period is small relative to the total, the peak rate of the pulse is extremely high. In some cases, such as for high altitude systems, the high ionization rate produced by this pulse may be the damage mechanism extending to the greatest range from the explosion. At low altitudes, the peak rate is attenuated rapidly, as a result of gamma ray absorption and scattering out of the time region of the peak rate.

[redacted] The prompt gamma environment is very sensitive to weapon design and to weapon yield. Moreover, comparison of theory and experiment for specific weapons is poor. Most calculations and experiments agree that the prompt gamma yield ranges between 0.1 and 0.3 percent of the total yield. The prompt gamma energy output rate may be expressed as

$$\Phi_{\gamma p} = \frac{2.6 \times 10^{25}\ fW}{\tau}\ \text{MeV/sec},$$

where f is the fraction of the weapon energy emitted as prompt gamma, W is the weapon yield in kt, and τ is the emission time (2.6×10^{25} is the energy equivalent of 1 kt in MeV; see paragraph 1-1). Using the limits quoted above for f and τ would lead to

$$\frac{(2.6 \times 10^{25})(10^{-3})}{2 \times 10^{-8}} < \Phi_{\gamma p}\ (\text{MeV/sec/kt}) < \frac{(2.6 \times 10^{25})(3 \times 10^{-3})}{10^{-8}}$$

$$1.3 \times 10^{30} < \Phi_{\gamma p}\ (\text{MeV/sec/kt}) < 7.8 \times 10^{30}.$$

* [redacted] A shake is 10^{-8} seconds.

† [redacted] Gamma rays from these interactions may continue to times on the order of 10 microseconds, but their contribution is generally small compared to other sources after one or two shakes beyond the time of peak gamma emission.

[redacted]

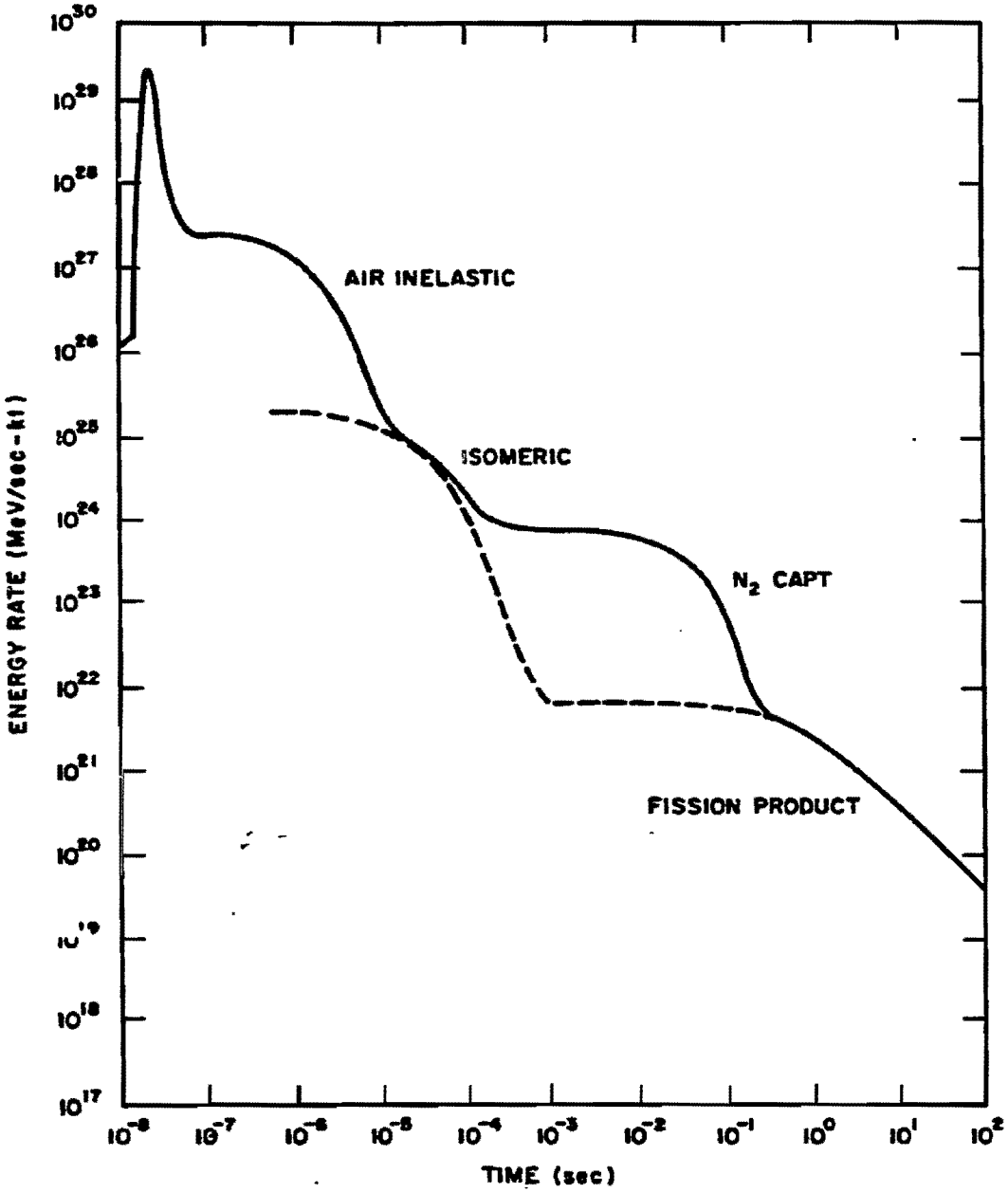

Figure 5-8. [redacted] Calculated Time Dependence of the Gamma Ray Output from a Large Yield Explosion, Normalized to 1 kt [redacted]

[redacted]

However, results of calculations and experiments indicate that the peak gamma energy output rate is more likely to lie between 5×10^{29} MeV/sec/kt and 1×10^{31} MeV/sec/kt. As mentioned previously, the peak gamma energy output rate depends on yield and on weapon design. The yield dependence shows a rough correlation as follows

$$\Phi_{\gamma p} = (W)^{-0.29} \times 10^{31} \text{ MeV/sec/kt},$$

at least between about 2 kt and 10 Mt. However, this does not account for the variation with weapon design, which might introduce differences on the order of plus or minus a factor of 3. Therefore, rather than use the yield dependent expression given above, it is recommended that the upper and lower limits given above be used for defensive and offensive estimates of the peak gamma energy output rate, respectively. Since no interactions take place in a vacuum, the peak prompt gamma exposure for exoatmospheric conditions should lie between

$$\Phi_{\gamma p} = \frac{10^{31} W}{4\pi R^2} \text{ MeV/cm}^2\text{/sec, and}$$

$$\Phi_{\gamma p} = \frac{3 \times 10^{30} W}{4\pi R^2} \text{ MeV/cm}^2\text{/sec,}$$

where W is the yield in kilotons, and R is the slant range in centimeters. These expressions are equivalent to

$$\Phi_{\gamma p} = \frac{8.57 \times 10^{20} W}{R_f^2} \text{ MeV/cm}^2\text{/sec, and}$$

$$\Phi_{\gamma p} = \frac{4.28 \times 10^{19} W}{R_f^2} \text{ MeV/cm}^2\text{/sec,}$$

where R_f is the slant range in kilofeet.

[redacted] Gamma rays interact with matter in three ways. The first is called the Compton effect. In this type of interaction, a gamma ray (primary photon) collides with an electron, and its energy is transferred to the electron. A secondary photon, with less energy, is created and departs in a direction at an angle to the direction of motion of the primary photon. The second type of interaction of gamma rays with matter is the photoelectric effect. A gamma ray with energy somewhat greater than the binding energy of an electron in an atom, transfers all its energy to the electron, which is consequently ejected from the atom. Since the photon involved in the photoelectric effect transfers all of its energy, it ceases to exist and is said to be absorbed. The third type of interaction is pair production. When a gamma ray photon with energy in excess of 1.02 MeV passes near the nucleus of an atom, the photon may be converted into matter with the formation of a pair of electrons, equally but oppositely charged. The positive electron soon annihilates with a negative electron to form two photons, each having an energy of at least 0.51 MeV. In some cases, if the interaction takes place near the nucleus of a heavy atom, only one photon of about 1.02 MeV energy may be created. Figure 6-1, Chapter 6, illustrates the three processes qualitatively.

[redacted] Any photon (e.g., an X-ray or a gamma ray) can produce ionization in a material by these processes of creating secondary electrons that deposit their kinetic energy by ionizing the medium in which they are created. The relative importance or frequency with which each process occurs depends upon the photon energy and the characteristics of the material. The Compton process is the dominant ionization mechanism for most gamma rays of interest, particularly in electronic materials such as silicon, of which many solid-state devices are fabricated.

[redacted] The spectra of the prompt gamma rays are sensitive to weapon design and yield, just as

[redacted]

the gamma energy output rate is. It is beyond the scope of this manual to provide spectral information concerning sufficient samples of weapons spectra to be of general use (some such samples are provided in "Status of Neutron and Gamma Output from Nuclear Weapons (U)," DASA 2567 (see bibliography)). Moreover, with the wide range of prompt gamma output energy rates provided above, precise spectral data would be of little use. However, most of the prompt gamma rays lie in the energy range between 0.2 and 2 MeV, and in this energy range the Compton fractional energy loss is relatively constant. As mentioned above, the Compton process is the dominant energy transfer process for most electronic materials of interest (atomic number less than 20). These facts lead to a simplification in the relations between the incident prompt gamma energy fluence or energy flux and the energy absorbed by the material.

The unit of the absorbed energy, or dose, is the rad. One rad is the absorption of 100 ergs per gram of material being irradiated. Thus, the rad is independent of the type of radiation (e.g., gamma rays, neutrons, X-rays), but the material absorbing the radiation must be specified (e.g., rad (Si), rad (Ge), rad (tissue)). However, in view of the simplification mentioned above, in the case of *prompt gamma rays* and *materials with atomic numbers less than 20*, a simple conversion is possible, i.e.,

$$1 \text{ rad} = 2 \times 10^9 \text{ MeV/cm}^2, \text{ or}$$

$$1 \text{ rad/sec} = 2 \times 10^9 \text{ MeV/cm}^2\text{/sec}.$$

These are, of course, approximations. However, in view of the approximate nature of the prompt gamma energy flux that has been provided, and in view of the fact that effects of the prompt gamma dose rates on electronics given in Section VII of Chapter 9 and Section 4 of Chapter 14 are not provided for system design or for specific system vulnerability analyses but only as a general guide to vulnerability, the approximation is considered to be adequate.

As an example of the use of the dose conversion, consider a system with essentially no shielding for gamma rays that is operating exoatmospherically and that is 2,000 feet from a 100 kt explosion. It is desired to determine the peak gamma dose rate to a silicon transistor within the system. From the equations given previously, the maximum peak gamma energy flux incident on the system is expected to be

$$\Phi_{\gamma p} = \frac{8.57 \times 10^{20} W}{R_f^2},$$

$$\Phi_{\gamma p} = \frac{(8.57 \times 10^{20})(100)}{(2)^2}$$

$$\approx 2 \times 10^{22} \text{ MeV/cm}^2\text{/sec},$$

and the minimum energy flux is expected to be

$$\Phi_{\gamma p} = \frac{4.28 \times 10^{19} W}{R_f^2},$$

$$\Phi_{\gamma p} = \frac{(4.28 \times 10^{19})(100)}{(2)^2}$$

$$\approx 1 \times 10^{21} \text{ MeV/cm}^2\text{/sec}.$$

Thus the peak dose rate is expected to lie between

$$\dot{D}_{\gamma p} = \frac{2 \times 10^{22}}{2 \times 10^9} = 10^{13} \text{ rads (Si)/sec, and}$$

$$\dot{D}_{\gamma p} = \frac{10^{21}}{2 \times 10^9} = 5 \times 10^{11} \text{ rads (Si)/sec.}$$

In view of the lack of spectral data that has been provided, the prompt gamma ener-

gy flux for endoatmospheric can only be determined by use of an effective mass attenuation coefficient (see the discussion of neutron transport in paragraph 5-3). A reasonable effective mass attenuation coefficient for prompt gammas is about 2.8 x 10^{-2} cm^2/gm. Combining this with the exoatmospheric equations given previously, the direct peak prompt gamma ray energy flux may be *estimated* to lie between

$$\Phi_{\gamma p} = \frac{10^{31} W}{4\pi R^2} e^{-(2.8 \times 10^{-2})\rho R} \text{ MeV/cm}^2\text{/sec, and}$$

$$\Phi_{\gamma p} = \frac{5 \times 10^{29} W}{4\pi R^2} e^{-(2.8 \times 10^{-2})\rho R} \text{ MeV/cm}^2\text{/sec,}$$

where W is the yield in kt, ρ is the density in gm/cm^3, and R is the range in centimeters. As in the case for neutrons, the quantity ρR may be replaced by the mass integral $q(R)$. The mass integral may be determined from the equations given in paragraph 5-3 and the data tabulated in Table 5-2.

[redacted] The prompt gamma dose may be bounded by multiplying the minimum and maximum dose rates by 1 and 2 shakes, respectively.

5-6 Air-Ground Secondary Gamma Rays [redacted]

[redacted] Potentially important sources of secondary gamma rays result from the inelastic scattering of high-energy neutrons by the nuclei of the air and ground, and the capture of thermal neutrons by the nitrogen-14 in the air and by various elements in the ground. The relative importance of the inelastic and capture gamma rays depends strongly upon the neutron spectrum of the source.

[redacted] Most of these gamma rays are produced near the neutron source where the neutron fluence is highest. The short neutron flight time to the regions of most intense interaction, and the practically instantaneous character of the nuclear interaction accounts for the early ($10^{-7} < t < 10^{-5}$ sec) appearance of the secondary gamma components. The number of inelastic-scattering gamma rays relative to the total depends directly on the relative abundance of high-energy neutrons. The fraction of the total may be negligible in fission warheads or in large thermonuclear warheads. As the fusion yield fraction is increased the importance of the inelastic component will increase.

[redacted] Any determination of the intensity of inelastic-scattering gamma rays must rely primarily upon analysis because of the difficulty in distinguishing the source of the different gamma rays measured in field tests. The first step in the analysis is that of neutron transport calculations. The local source strength of inelastic gamma rays is an energy dependent response to the local fluence of neutrons. Once the source intensity resulting from neutron interactions in air and ground is known, a gamma ray transport calculation must be performed to obtain the intensity at points of interest.

[redacted] The energy spectrum of the gamma rays evolved in elastic scattering depends on the energy of the neutrons and the energy level structure of the nuclei with which the neutrons interact. However, the inelastic gamma rays are generally high in energy and, consequently, take on added significance when the target is behind a shield such as in a hardened military installation. Even though only a few percent of the gamma radiation incident on the shield results from inelastic scattering, it may be the source that is responsible for the maximum rate experienced by equipment inside the shielded installation since prompt gamma rays are attenuated more rapidly by shielding materials than the inelastic scattered gamma rays. Thus, where hardened installations are concerned, the inelastic gamma rays should be evaluated even in cases where they do not constitute a large fraction of the total free-field exposure. Methods for calculating the

tissue dose from secondary gamma rays are provided in the following subsection.

5-7 Fission Product Gamma Rays

Gamma rays produced by the decay of fission products following a fission detonation are an important source of radiation during the initial radiation time regime (the first minute following the explosion). The intensity of fission product gamma rays reaching a location of interest is affected by the complex source and media dynamics consisting of the formation and evolution of the fireball, the cloud expansion and rise, and the decay of the fission products with time. The fission products disperse throughout the cloud with the passage of time and the shape of the cloud may vary from spherical to toroidal as the materials forming the cloud rise through the atmosphere.

The formation of the fireball and the expansion and rise of the cloud depends upon weapon yield, weapon design, atmospheric conditions, and other parameters. The distribution of fission products in the cloud as a function of time is not well known, and, consequently, the attenuation of fission-product gamma rays within the cloud can only be approximated.

Atmospheric perturbation caused by the passage of the shock front also has a pronounced effect on the transport of fission-product gamma rays. The distribution of energy from a low altitude conventional fission weapon is such that roughly 50 percent of the energy is released in the form of blast and shock. The actual percentage depends on the weapon design and yield and on the nature of the surrounding environment (see Section I, Chapter 2). The percentage decreases for neutron enhanced weapons.

The sudden release of energy in the form of blast and shock produces an immediate increase in temperature and pressure thus producing hot, compressed gases from the weapon material. A pressure wave is initiated in the surrounding medium (paragraphs 1-4 through 1-6, 1-8, and Section I, Chapter 2). The characteristics of a shock wave is that there is a sudden increase of pressure at the front with a gradual decrease behind it. A severe change in the density of the heated air behind the shock front is associated with the pressure change. The large reduction in the air density, or optical depth, between the rising source and the receiver produces an enhancement of gamma ray intensities from hydrodynamic effects that is known as "hydrodynamic enhancement." These effects may last for several minutes and may extend to large distances from the explosion. The intensity and duration of hydrodynamic effects are yield dependent.

At early times when the shock front is located between the cloud and the receiver, the gamma ray intensity may increase because of the geometric displacement of the air. After the blast wave has passed the receiver, the gamma ray intensity is enhanced as a result of the reduced air density. This hydrodynamic enhancement becomes increasingly more important with higher weapon yields. For high yield weapons (in the megaton range), hydrodynamic enhancement can increase the fission-product gamma ray intensity by several orders of magnitude, with the result that fission product gamma rays can become the most important of all initial radiation sources.

With minimal hydrodynamic enhancement, as in the case of very low-yield weapons, the intensity of fission product gamma rays reaching a given point may be of approximately the same magnitude as that resulting from the secondary gamma ray sources. However, the average energy of the fission product gamma rays is considerably less than that of the secondary gamma rays, and the angle distribution of the fission product gamma rays is diffused by

the rise of the cloud. Each of these factors tends to reduce the penetrating power of fission product gamma rays relative to secondary gamma rays.

A reasonably accurate calculation of the transport of fission product gamma rays must consider such time-dependent parameters as cloud rise, source decay, and hydrodynamic enhancement. The curves presented in the following subsection that show tissue dose from fission product gamma rays were constructed by the use of such a model.*

INITIAL RADIATION DOSE TO PERSONNEL

The preceding paragraphs have described the complexity of the calculations of the source and environments produced by the initial nuclear radiations. Simplified, but reasonably accurate, methods have been developed to predict the dose to personnel located on or near the surface of the earth. These methods are described in the succeeding paragraphs and figures, and illustrations of their use are provided in four problems.†

Various units have been used to describe the radiation dose to personnel. One of the earliest originally used to describe X-ray environments, is the roentgen, which is defined in terms of ionization produced in air. In view of the long history of the roentgen, various attempts have been made to develop units that described the response of living creatures or physical objects in terms of "roentgen equivalent" units. None of these was completely satisfactory since they depended strongly on the type and energy of the radiation, and their relationship to an exposure measured in roentgens was not always descriptive of the response of the target. Since the response of a target to radiation generally can be related to the energy absorbed, the rad has come into general use for the description of dose to any target. As previously defined in paragraph 5-5, one rad is the absorption of 100 ergs per gram of material being irradiated. Thus, the rad is independent of the type of radiation, but the material absorbing the radiation must be specified. The curves provided in this subsection provide a methodology for determining the dose in rads (tissue) for the various components of the initial nuclear radiation. The response of personnel, as a function of absorbed dose, is given in Section III of Chapter 10.

In view of the strong dependence of the neutron and secondary gamma ray environments on weapon design, no one representative weapon could be chosen to provide a basis for calculating dose to humans. The fission product dose is relatively independent of design specifics, but it is strongly dependent on total yield and the ratio of fission yield to total yield. Consequently, eight different weapons, for which case output data were available, were selected to perform the basic calculations from which the curves presented below were developed. It is believed that these eight weapons provide a sufficiently wide spectrum of designs that one of the eight will represent a given weapon of interest in a reasonable manner. The eight weapons are described in Table 5-3.

5-8 Initial Neutron Dose

Figures 5-9 through 5-11 provide all of the information necessary to calculate the contribution of neutrons to the initial nuclear radiation dose from each of the weapon types listed

* The development of this model is explained in "Improved Models for Predicting Nuclear Weapon Initial Radiation Environments (U)," DASA 2615 (see bibliography).

† ATR, which stands for Atmospheric Radiation Transport library, may be used to obtain exact answers to problems involving radiation transport in the atmosphere without the necessity of making specific transport calculations. ATR is documented in DNA 2803I, "Models of Radiation Transport in Air – the ATR Code" (see bibliography). The Code itself may be obtained from the Radiation Shielding Information Center (RSIC), Oak Ridge, Tennessee.

[redacted]

Table 5-3. [redacted] Representative Types of Nuclear Weapons [redacted]

Type	Description	Representative Yield Range
I	Subkiloton Fission	[redacted]
II	Pure Fission Implosion	
III	Large (physically) Boosted Fission	
IV	Small (physically) Boosted Fission	
V	Enhanced Neutron Weapon	
VI	Gun-Assembly Fission Weapon	
VII	Thermonuclear Weapon	
VIII	Thermonuclear Weapon	

DNA (4)(3)

[redacted]

in Table 5-3. Problem 5-1 describes the use of these figures to obtain the neutron dose.

5-9 Air-Ground Secondary Gamma Ray Dose [redacted]

[redacted] Figures 5-11 through 5-13 provide all of the information necessary to calculate the contribution of air-ground secondary gamma rays to the initial nuclear radiation dose from each of the weapon types listed in Table 5-3. Problem 5-2 describes the use of these figures to obtain the air-ground secondary gamma ray dose.

5-10 Fission Product Gamma Ray Dose [redacted]

[redacted] Figures 5-14 through 5-17 provide all of the information necessary to calculate the contribution of fission product gamma rays to the initial nuclear radiation dose. Problem 5-3 describes the procedures for obtaining the fission product dose from these figures. Note the caution given in Problem 5-3 concerning interpolation between the hydrodynamic enhancement curves.

5-11 Total Dose [redacted]

[redacted] The total initial radiation dose is simply the sum of the contributions of the neutrons, the secondary gamma rays, and the fission product gamma rays. Problem 5-4 illustrates the calculation of total initial radiation dose.

[redacted]

[redacted]

Problem 5-1. Calculation of Neutron Radiation Dose

[redacted] The spectrum and intensity of neutron radiation depends strongly upon the details of design of a nuclear weapon; however, it is possible to obtain neutron dose to personnel from a weapon of interest with reasonable accuracy if it is "similar" to one for which detailed calculations have been made. Eight "representative" types of weapons, listed in Table 5-3, provide the basis for such calculations within the following constraints:

- The weapon of interest must be similar to one of the representative types,
- The range of interest must lie between 400 and 5,000 yards,
- The detonation takes place in the "lower atmosphere," and
- The target is located on or near the surface of the earth.

[redacted] Within the constraints listed above, Figures 5-9 through 5-11 provide the information necessary to obtain the dose to personnel located on or near the surface of the earth. If the air density is $\rho_o = 1.225 \times 10^{-3}$ gm/cm^3, the neutron dose is

$$D_N = \frac{WF_N H_1}{R^2}$$

where

D_N is the total neutron dose (rads (tissue)),

R is the slant range (yards)

F_N is the value taken from Figure 5-9a or b or from Figure 5-10a or b for the most representative weapon type (yards^2 rads/kt).

W is the weapon yield (kt), and

H_1 is the detonation height correction factor from Figure 5-11 (dimensionless).

[redacted] If the air density differs from ρ_o, Figures 5-9 or 5-10 are entered with a scaled range R_ρ which is given by

$$R_\rho = \frac{\rho}{\rho_o} R = \bar{\rho} R,$$

where $\bar{\rho}$ is the relative air density. Values of ρ/ρ_o are given in Table 5-2, and with smaller altitude increments in Table 2-1, Chapter 2. If the values of ρ/ρ_o are different at the burst and the receiver, the average value should be used for $\bar{\rho}$. Note that R, not R_ρ, is still used in the denominator of the equation given above for D_N.

[redacted] *Example 1* [redacted]:

Given: A 30 kt surface burst of a weapon similar to type IV in air of average relative density $\bar{\rho} = 1.0$.

Find: The neutron dose delivered to a surface target 1,500 yards from the burst.

Solution: From Figure 5-9a, $F_N = 8.5 \times 10^6$ yards^2 rad (tissue)/kt for a type IV weapon at 1,500 yards.

Answer: The neutron dose delivered to a surface target 1,500 yards from a 30 kt surface burst of a type IV weapon is:

$$D_N = \frac{(30)(8.5 \times 10^6)(1.0)}{(1{,}500)^2},$$

$$D_N = 113 \text{ rads (tissue)},$$

[redacted] *Example 2* [redacted]

Given: A 500 kt burst at a height of 100 yards of a weapon similar to type IV in air of average relative density $\bar{\rho} = 0.9$.

Find: The neutron dose delivered to a target near the surface 2,000 yards from the burst.

[redacted]

Solution: The scaled range R_ρ = (0.9)(2,000) = 1,800 yards. From Figure 5-10a, $F_N = 1.6 \times 10^6$ yards^2 rads (tissue)/kt for a type VII weapon at 1,800 yards. From Figure 5-11, $H_1 = 2.07$ for type VII at 100 yards *HOB*.

Answer: The neutron dose delivered to a target near the surface 2,000 yards from a type VII weapon at 100 yards *HOB* is:

$$D_N = \frac{(500)(1.6 \times 10^6)(2.07)}{(2,000)^2}$$

$$D_N = 414 \text{ rads (tissue)}.$$

Reliability. For weapons closely similar to one of the eight representative types, the predicted neutron dose is estimated to be correct within ±25 percent.

Related Material. See paragraphs 5-1 through 5-3. See also Tables 5-2 and 5-3.

Problem 5-2. Calculation of Secondary Gamma Ray Dose

[redacted] Secondary gamma rays are those that result from neutron interactions, primarily with nitrogen in the air, as described in paragraph 5-6. Since the neutron output is strongly dependent upon details of weapon design, the secondary gamma ray output also depends upon weapon design; however, it is possible to obtain the secondary gamma ray dose to personnel from a weapon of interest if it is "similar" to one for which detailed calculations have been made. Eight "representative" types of weapons, listed in Table 5-3, provide the basis for such calculations within the following constraints:

- The weapon of interest must be similar to one of the representative types,
- The range of interest must lie between 400 and 5,000 yards,
- The detonation takes place in the "lower atmosphere," and
- The target is located on or near the surface of the earth.

[redacted] Within the constraints listed above, Figures 5-11 through 5-13 provide the information necessary to obtain the secondary gamma dose to personnel located on or near the surface of the earth. If the air density is $\rho_o = 1.225 \times 10^{-3}$ gm/cm^3, the secondary gamma dose is

$$D_{\gamma s} = \frac{W\ F_{\gamma s}\ H_1}{R^2}$$

where

$D_{\gamma s}$ is the secondary gamma ray dose (rads (tissue)),

R is the slant range (yards),

$F_{\gamma s}$ is the value taken from Figure 5-12a or b or from Figure 5-13a or b for the most representative weapon type (yards^2 rads/kt),

W is the weapon yield (kt), and

H_1 is the detonation height correction factor from Figure 5-11 (dimensionless).

[redacted] If the air density differs from ρ_o, Figures 5-12 or 5-13 are entered with a scaled range R_ρ.

$$R_\rho = \frac{\rho}{\rho_o} R = \bar{\rho} R,$$

where $\bar{\rho}$ is the relative air density. Values of ρ/ρ_o are given in Table 5-2, and with smaller altitude increments in Table 2-1, Chapter 2. If the values of ρ/ρ_o are different at the burst and the receiver, the average value should be used for $\bar{\rho}$. Note that R, not R_ρ, *is still used in the denominator of the equation given above for* $D_{\gamma s}$.

[redacted] *Example 1* [redacted]

Given: A 15 kt explosion at a height of 150 yards of a weapon similar to weapon type VI, in air of average relative density $\bar{\rho} = 1.0$.

Find: The secondary gamma ray dose delivered to personnel on the surface 1,500 yards from the burst.

Solution: From Figure 5-13a, $F_{\gamma s} = 3.7 \times 10^6$ yards^2 rads (tissue)/kt for a type VI weapon at 1,500 yards. From Figure 5-11, $H_1 = 2.03$ for a type VI weapon burst at 150 yards.

Answer: The secondary gamma ray dose delivered to a surface target 1,500 yards from a 15 kt burst of weapon type VI at 150 yards *HOB* is:

$$D_{\gamma s} = \frac{(15)(3.7 \times 10^6)(2.03)}{(1,500)^2}$$

$$D_{\gamma s} = 50 \text{ rads (tissue)}$$

[redacted] *Example 2* [redacted]

Given: A 0.08 kt burst at a height of 20

[redacted]

yards of a weapon similar to type I in average air density of $\bar{\rho} = 0.9$.

Find: The secondary gamma ray dose delivered to personnel on the surface 500 yards from the burst.

Solution: From Figure 5-12a, $F_{\gamma s} = 1.6 \times 10^8$ yards^2 rads/kt for a type 1 weapon at 500 yards. From Figure 5-11, $H_1 = 1.52$ for a type I weapon burst at 20 yards.

Answer: The secondary gamma ray dose delivered to a target near the surface 500 yards from a 0.08 kt burst of a type I weapon at 20 yards *HOB* is

$$D_{\gamma s} = \frac{(0.08)(1.6 \times 10^8)(1.52)}{(500)^2}$$

$$D_{\gamma s} = 78 \text{ rads (tissue)}.$$

Reliability. For weapons closely similar to one of the eight representative types, the predicted secondary gamma ray dose is estimated to be correct to within ±25 percent for slant ranges up to 1,500 yards. At longer ranges, the predicted values might be high although a precise estimate cannot be made.

Related Material. See paragraph 5-6. See also Tables 5-2 and 5-3.

[redacted]

Problem 5-3. Calculation of Fission Product Gamma Ray Dose

[redacted] Figures 5-14 through 5-17 provide the information necessary to calculate the fission product contribution to the initial nuclear radiation dose to personnel on or near the surface of the earth. Figures 5-14a through c provide the nominal dose per kt fission yield as a function of slant range for several relative air densities. The gamma dose as a function of slant range depends on cloud rise, which depends on weapon yield. The effects of cloud rise on exposure for a given yield depends on the burst height, and, to a slight extent, on the ambient air density. Analysis of the interdependence of these parameters has shown that reasonable accuracy can be retained by the use of two independent burst height adjustment factors, one associated with slant range, as shown in Figure 5-15, and the other associated with weapon yield, as shown in Figure 5-16. Figures 5-17a through e show hydrodynamic enhancement factors as a function of slant range for selected yields and several air densities. In using Figures 5-17a through e, no attempt should be made to perform a visual interpolation of the hydrodynamic enhancement factor between yields that are shown. Rather, a plot of the hydrodynamic enhancement factor as a function of yield should be made at the slant range and relative air density of interest, and the hydrodynamic enhancement factor should be obtained from this plot for the desired yield.

[redacted] The tissue dose from fission product gamma rays is obtained as follows:

$$D_{\gamma f} = W_f F_{\gamma f} H_R H_W E$$

where

$D_{\gamma f}$ is the fission product gamma ray dose at slant range R (rads (tissue)),

W_f is the fission yield (kt),

$F_{\gamma f}$ is the value taken from Figures 5-14a through c (rads (tissue)/kt),

H_R is the range dependent burst height adjustment factor from Figure 5-15 (dimensionless),

H_W is the yield dependent burst height adjustment factor from Figure 5-16 (dimensionless), and

E is the hydrodynamic enhancement factor from Figures 5-17a through e (dimensionless).

[redacted] Note that *fission* yield is used in the equation given above for fission product gamma ray dose; however, *total* yield is used to enter Figure 5-16 and Figures 5-17a through e.

[redacted] *Example 1* [redacted]

Given: A 50 kt pure fission weapon burst at a height of 100 yards in air of relative air density $\bar{\rho} = 0.8$.

Find: The fission product gamma ray dose to personnel on the ground at a slant range of 2,000 yards from the burst.

Solution: From Figure 5-14a, $F_{\gamma f} = 1.5$ rads (tissue)/kt for $\bar{\rho} = 0.8$ at 2,000 yards. From Figure 5-15, $H_R = 0.94$ for a height of burst of 100 yards and a slant range of 2,000 yards. From Figure 5-16, $H_W = 0.71$ for 50 kt total yield at a height of burst of 100 yards. From Figure 5-17d ($\bar{\rho} = 0.8$), $E = 6$ for a 50 kt total yield at 2,000 yards.

Answer:

$$D_{\gamma f} = (50)(1.5)(0.94)(0.71)(6),$$

$$D_{\gamma f} = 300 \text{ rads (tissue)}.$$

[redacted] *Example 2* [redacted]

Given: A 200 kt, 1:1 fission/fusion ratio

[redacted]

(i.e., 1/2 fission, 1/2 fusion) surface burst in air of average relative density $\bar{\rho} = 1.1$.

Find: The fission product gamma ray dose delivered to a target near the ground 1,000 yards from the burst.

Solution: The fission yield $W_f = (1/2)(200) = 100$ kt for a 1:1 fission/fusion ratio. From Figure 5-14a, $F_{\gamma f} = 17$ rads (tissue)/kt for $\bar{\rho} = 1.1$ at 1,000 yards. From Figure 5-15, $H_R = 0.94$ for a surface burst at 1,000 yards range. From Figure 5-16, $H_W = 0.63$ for a surface burst at 200 kt total yield. From Figure 5-17a, $E \simeq 24$ for 200 kt total yield at 1,000 yards (the best interpolation scheme for this figure is to make a plot on linear paper of E vs W at a constant R, and draw a smooth curve through the points).

Answer: The fission product gamma ray dose delivered to a target near the ground 1,000 yards from a 200 kt (1:1 fission/fusion) surface burst in air of average relative density 1.1 is:

$$D_{\gamma f} = (100)(17)(0.94)(0.63)(24)$$

$$D_{\gamma f} = 2.4 \times 10^4 \text{ rads (tissue)}.$$

Reliability. For submegaton yields the radiation dose predicted by equation 5.4 will be within 15 percent of the values calculated by the most sophisticated methods. The variations may approach 40 percent for megaton yields at ranges less than 1,000 yards; however, these are generally not interesting combinations. The total gamma ray dose predicted by the methods illustrated in Problems 5-2 and 5-3 when added together generally agrees with weapons test data within 50 percent and seldom disagrees by more than a factor of 2.

Related Material. See paragraph 5-7. See also Table 5-2.

[redacted]

Problem 5-4. Calculation of Total Initial Radiation Dose

[redacted] The total initial radiation dose may be determined by calculating the neutron dose, the secondary gamma ray dose, and the fission product gamma ray dose separately, as described in Problems 5-1, 5-2, and 5-3 and summing the individual results.

[redacted] *Example*

Given: A 10 Mt burst, 2:3 fission/fusion ratio (i.e., 2/5 fission, 3/5 fusion), of a weapon similar to type VIII at a height of 2,000 yards in air of average relative density $\bar{\rho} = 0.8$.

Find: The total radiation dose delivered to a target near the surface at a slant range of 4,000 yards from the burst.

Solution: For the neutron dose, the scaled range is $R_\rho = (0.8)(4{,}000) = 3{,}200$ yards. From Figure 5-10b, $F_N = 5 \times 10^3$ yards^2 rads (tissue)/kt for type VIII at 3,200 yards. From Figure 5-11, $H_1 = 2.16$ for type VIII over 200 yards *HOB*. For the secondary gamma ray dose, the same scaled range and height correction factors apply. From Figure 5-13b, $F_{\gamma s} = 5 \times 10^4$ yards^2 rads (tissue)/kt for type VIII at 3,200 yards. For the fission product gamma ray dose, the fission yield is $W_f = (2/5)(10{,}000) = 4{,}000$ kt for a 2:3 fission/fusion ratio. From Figure 5-14b, $F_{\gamma f} = 1.3 \times 10^{-3}$ rads (tissue)/kt for $\bar{\rho} = 0.8$ at 4,000 yards. From Figure 5-15, $H_R = 0.62$ for a 2,000 yard *HOB* and a slant range of 4,000 yards. From Figure 5-16, $H_W = 0.24$ for a 2,000 yard *HOB* and a total yield of 10 Mt. From Figure 5-17d, $E = 4.1 \times 10^3$ for 10-Mt total yield at 4,000 yards.

Answer:

$$D_N = \frac{WF_N H_1}{R^2}$$

$$D_N = \frac{(10{,}000)(5 \times 10^3)(2.16)}{(4{,}000)^2}$$

$$D_N = 6.8 \text{ rads (tissue)}$$

$$D_{\gamma s} = \frac{WF_{\gamma s} H_1}{R^2}$$

$$D_{\gamma s} = \frac{(10{,}000)(5 \times 10^4)(2.16)}{(4{,}000)^2}$$

$$D_{\gamma s} = 68 \text{ rads (tissue)}$$

$$D_{\gamma f} = W_f F_{\gamma f} H_R H_W E$$

$$D_{\gamma f} = (4{,}000)(1.3 \times 10^{-3})(0.62)(0.24)(4.1 \times 10^3)$$

$$D_{\gamma f} = 3{,}170 \text{ rads (tissue)}$$

$$\text{Total Dose} = D_N + D_{\gamma s} + D_{\gamma p}$$

Total Dose = 6.8 + 68 + 3,170 = 3,245 rads (tissue).

[redacted] *Reliability.* See problems 5-1, 5-2, and 5-3 for reliability statements for the individual components of the total dose. There are no corroborating data; however, it is estimated that the total dose prediction would fall within ±25 percent of the true value, except for megaton yield weapons at slant ranges less than 1,000 yards, where the error is likely to be ±50 percent.

[redacted] *Related Material.* See paragraphs 5-5 through 5-7. See also Tables 5-2 and 5-3.

[redacted]

[redacted]

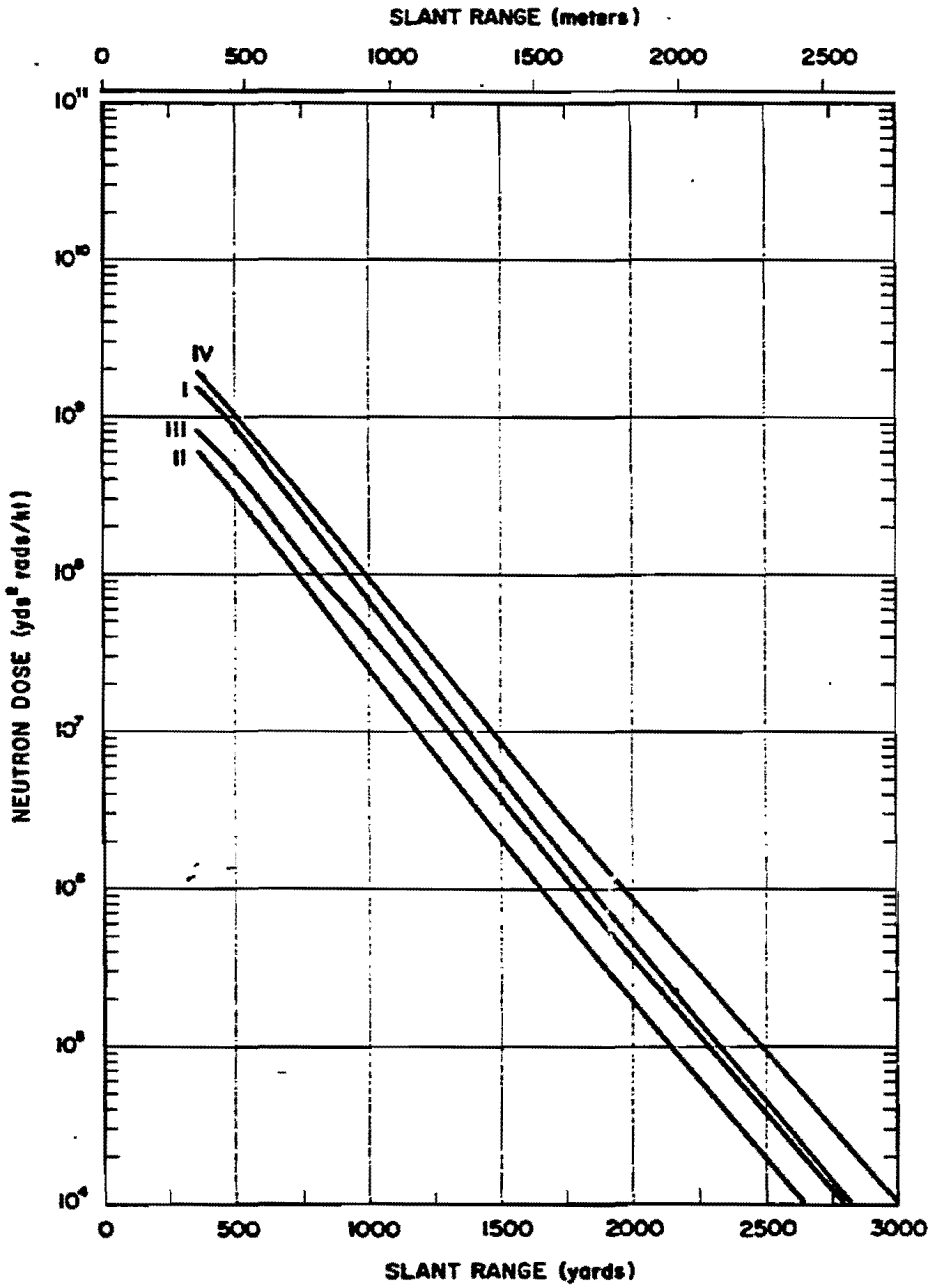

Figure 5-9a. [redacted] Neutron Dose as a Function of Slant Range from a 1 kt Surface Burst, Weapon Types I through IV, Short Ranges [redacted]

[redacted]

[redacted]

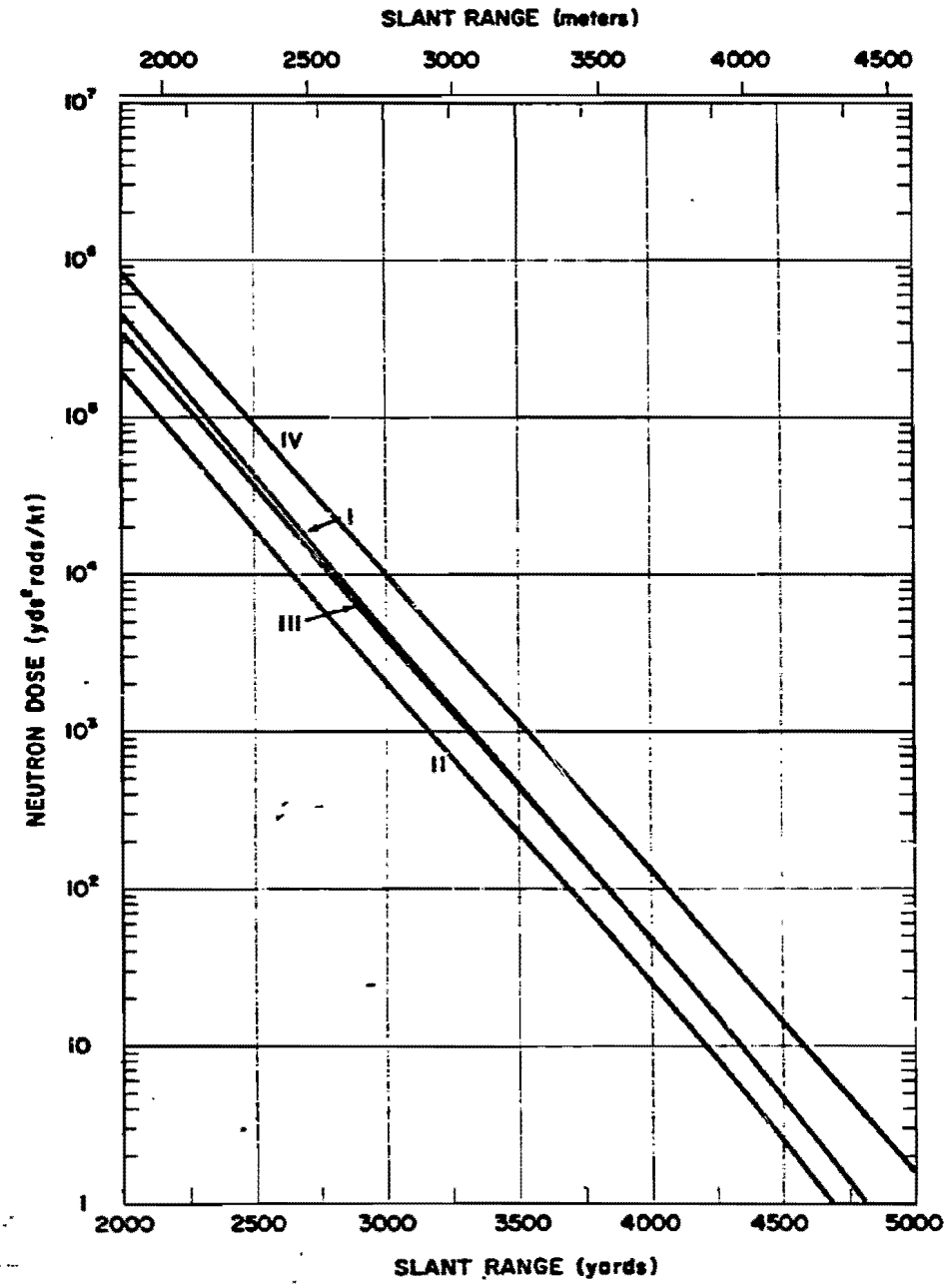

Figure 5-9b. [redacted] Neutron Dose as a Function of Slant Range from a 1 kt Surface Burst, Weapon Types I through IV, Long Ranges [redacted]

[redacted]

[redacted]

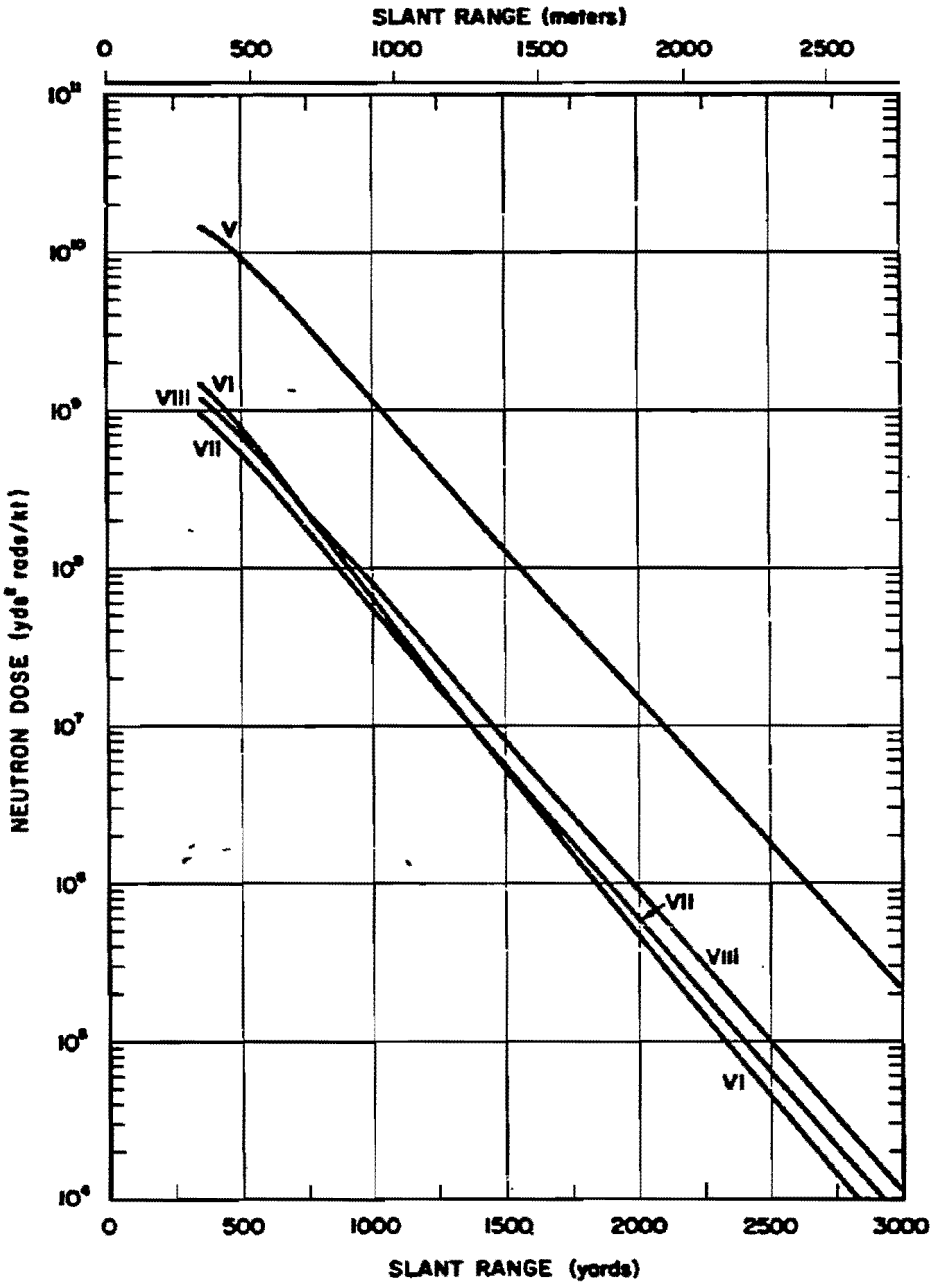

Figure 5-10a. [redacted] Neutron Dose as a Function of Slant Range from a 1 kt Surface Burst, Weapon Types V through VIII, Short Ranges [redacted]

[redacted]

[redacted]

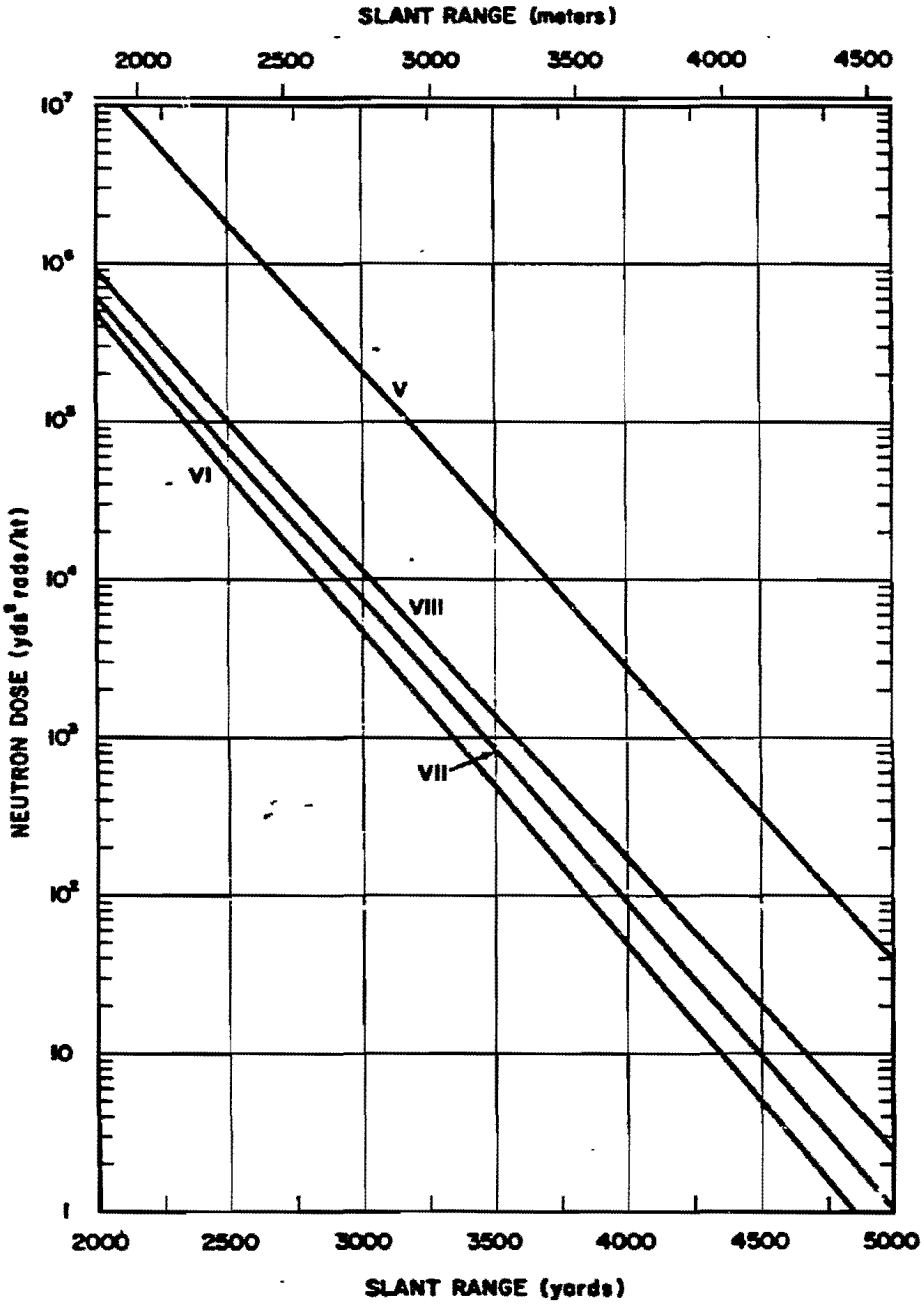

Figure 5-10b. [redacted] Neutron Dose as a Function of Slant Range from a 1 kt Surface Burst, Weapon Types V through VIII, Long Ranges [redacted]

[redacted]

[redacted]

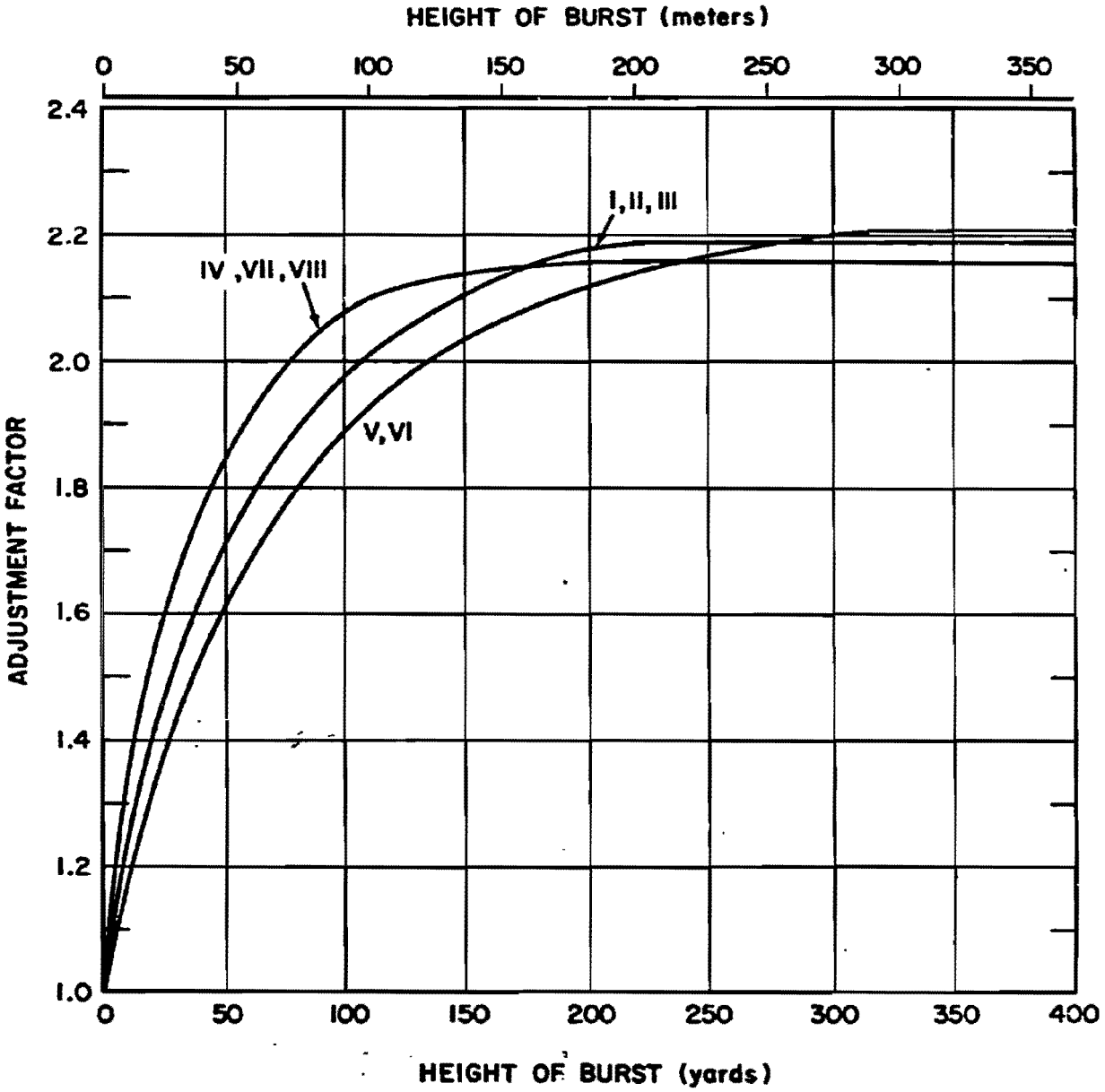

Figure 5-11. [redacted] Burst Height Adjustment Factors for Neutrons and Secondary Gamma Rays [redacted]

[redacted]

[redacted]

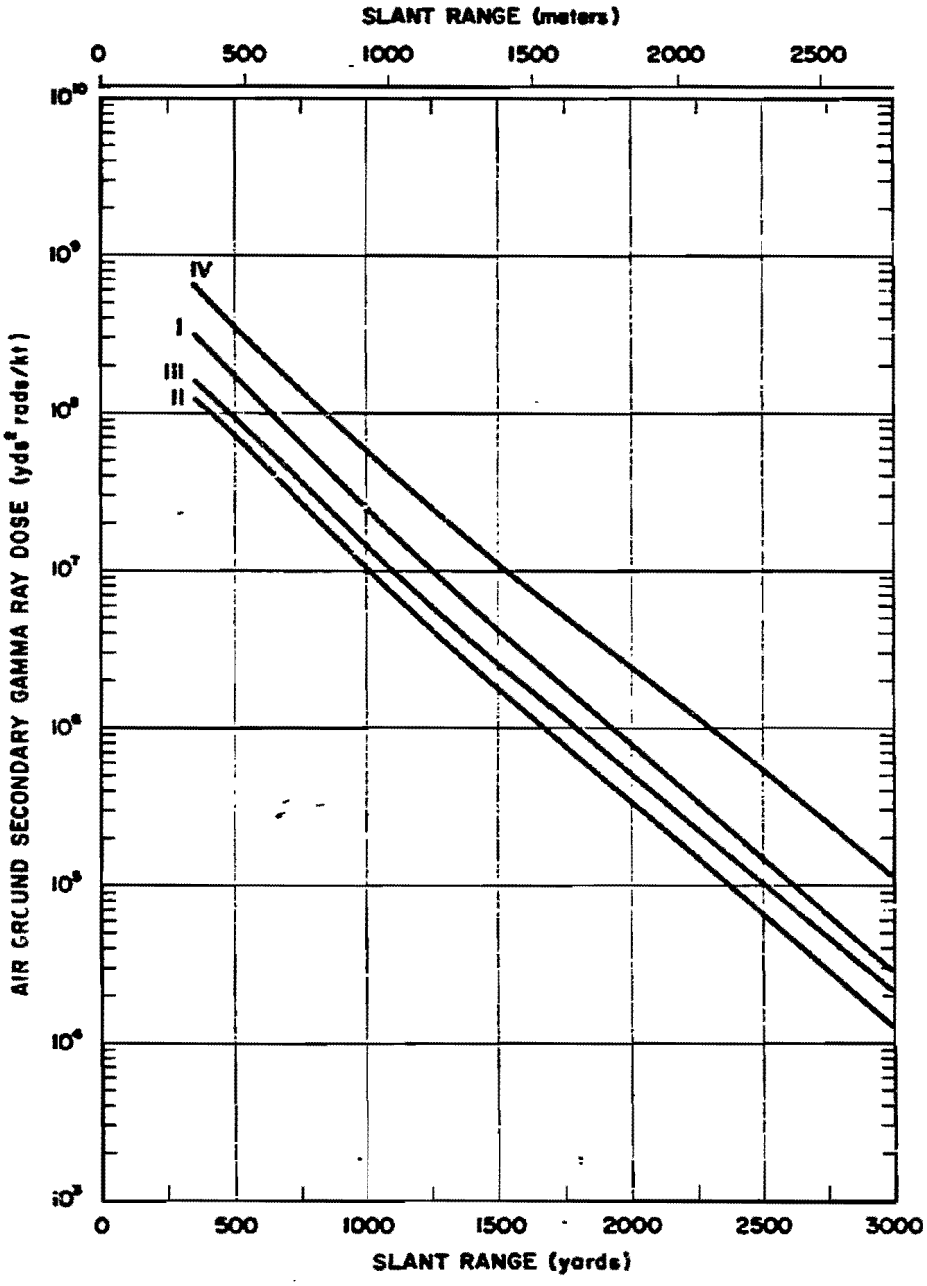

Figure 5-12a. [redacted] Secondary Gamma Ray Dose as a Function of Slant Range from a 1 kt Surface Burst, Weapon Types I through IV, Short Ranges [redacted]

[redacted]

[redacted]

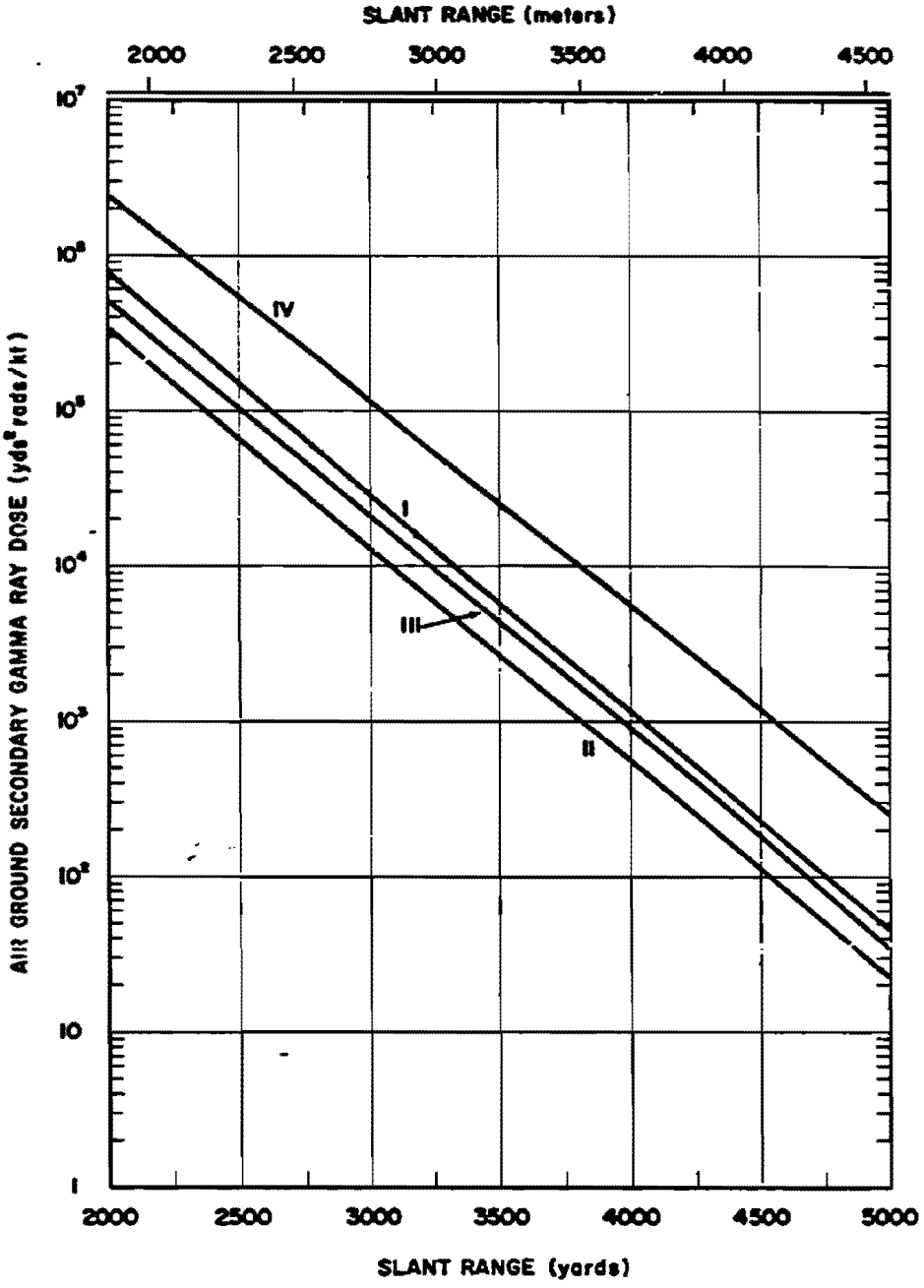

Figure 5-12b. [redacted] Secondary Gamma Ray Dose as a Function of Slant Range from a 1 kt Surface Burst, Weapon Types I through IV, Long Ranges [redacted]

[redacted]

[redacted]

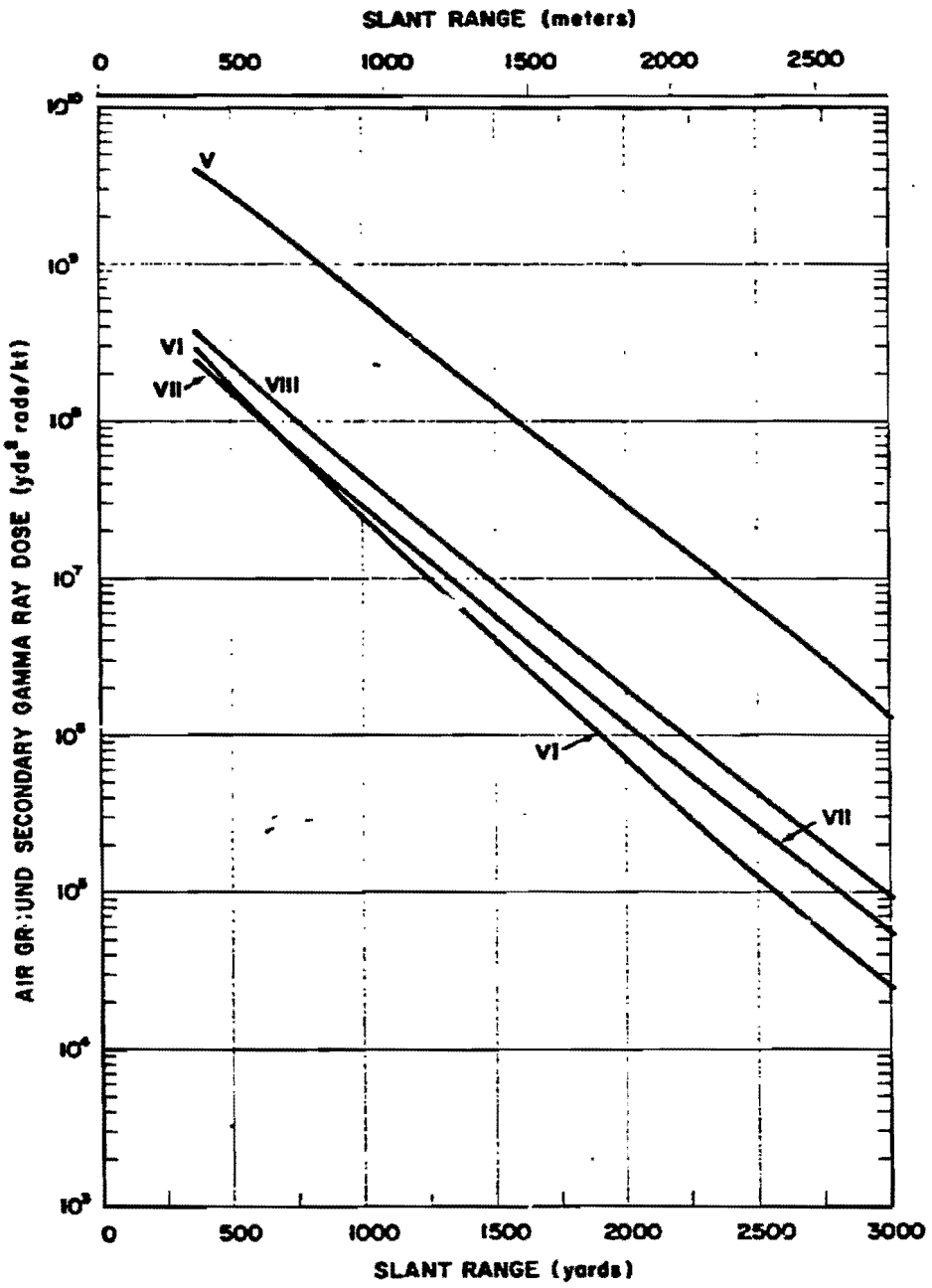

Figure 5-13a. [redacted] Secondary Gamma Ray Dose as a Function of Slant Range from a 1 kt Surface Burst, Weapon Types V through VIII, Short Ranges [redacted]

[redacted]

[redacted]

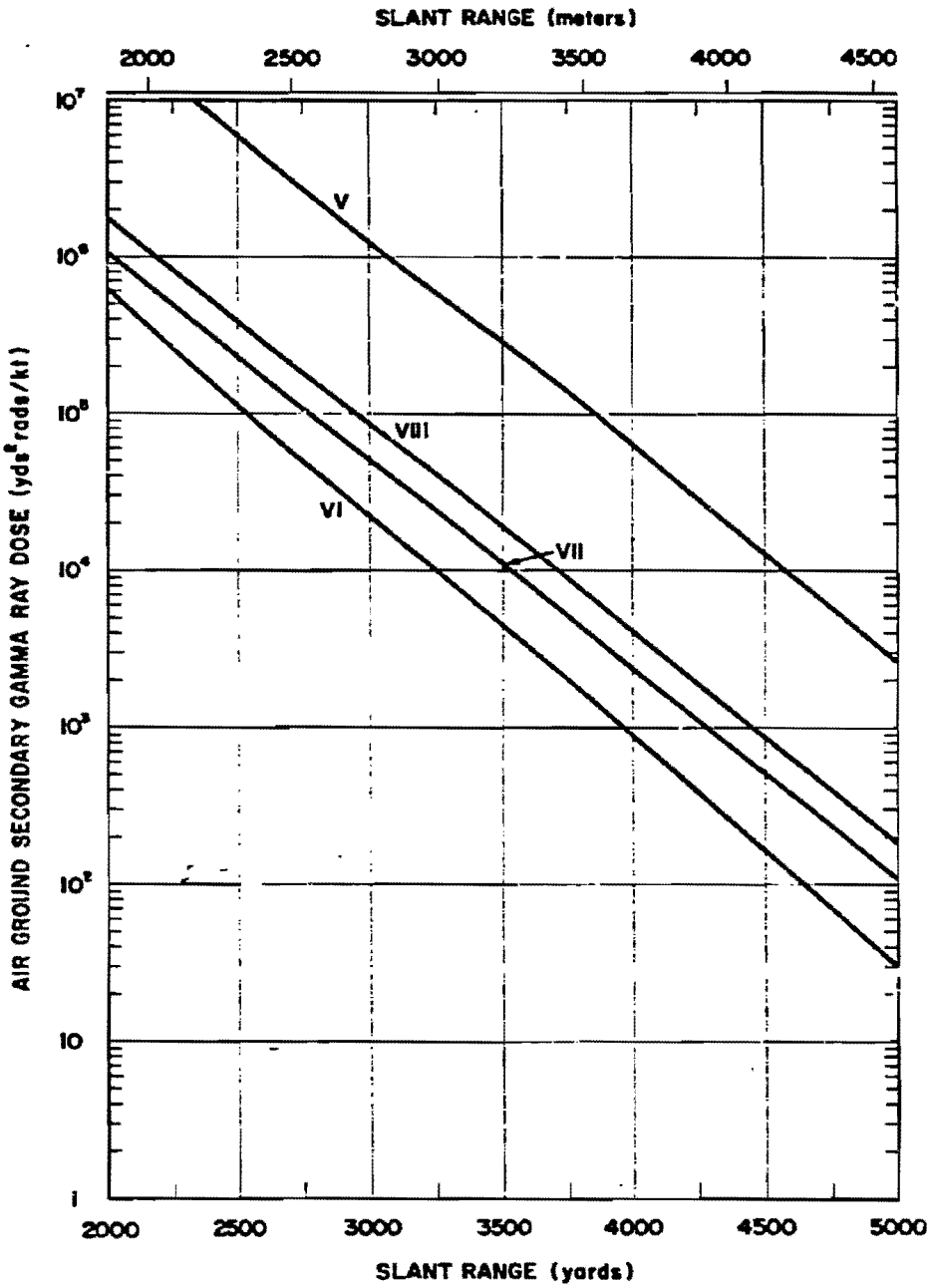

Figure 5-13b. [redacted] Secondary Gamma Ray Dose as a Function of Slant Range from a 1 kt Surface Burst, Weapon Types V through VIII, Long Ranges [redacted]

[redacted]

[redacted]

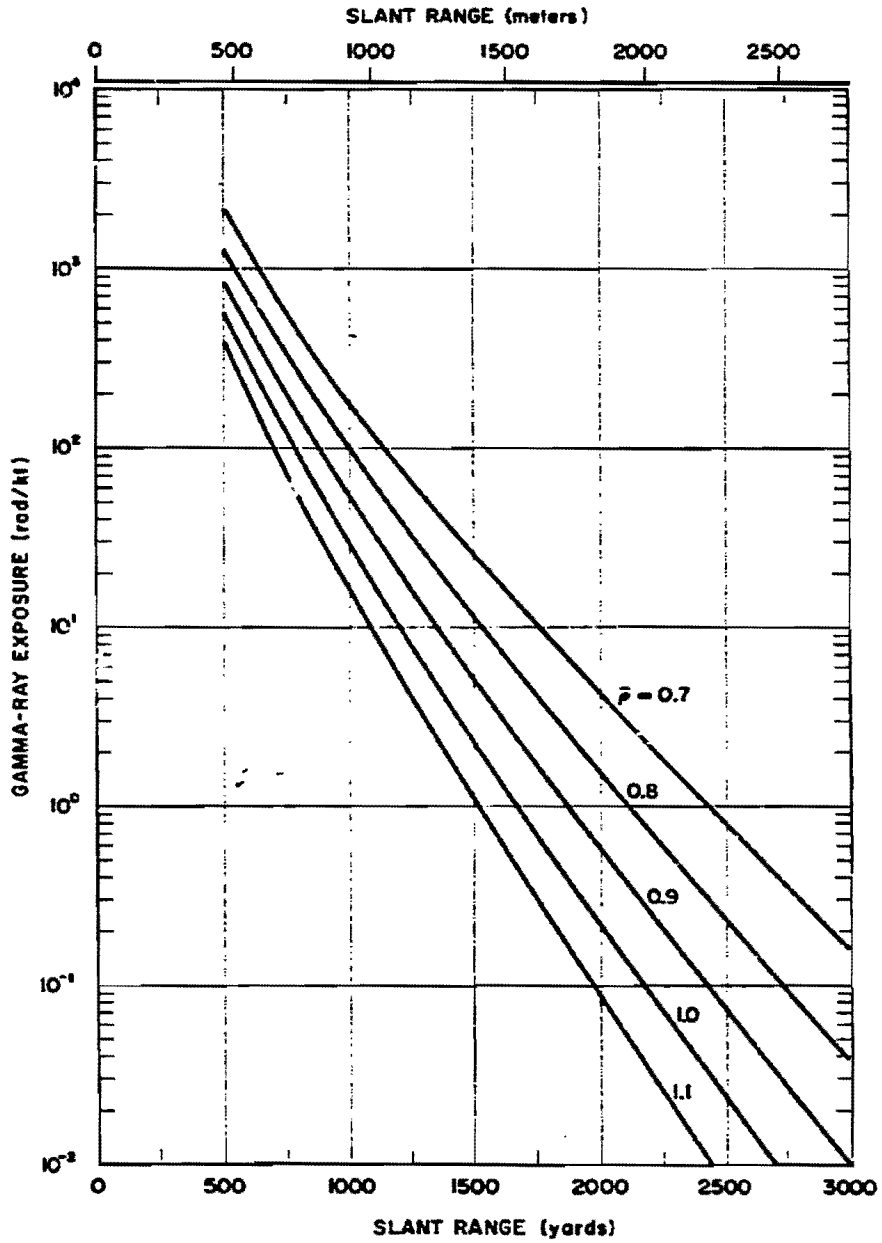

Figure 5-14a. [redacted] Fission Product Gamma Ray Dose as a Function of Slant Range from a 1 kt (Fission Yield) Surface Burst, Short Ranges [redacted]

[redacted]

[redacted]

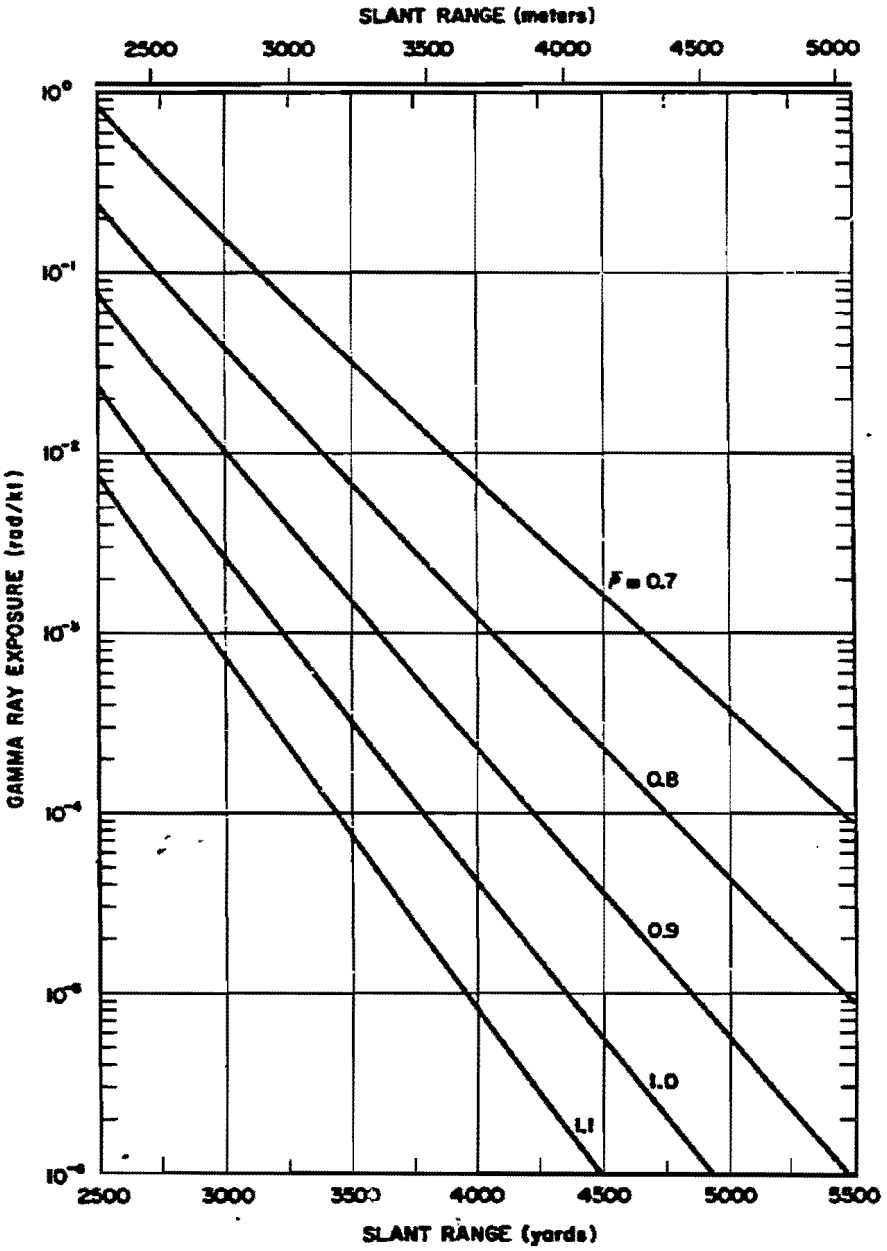

Figure 5–14b. [redacted] Fission Product Gamma Ray Dose as a Function of Slant Range from a 1 kt (Fission Yield) Surface Burst, Intermediate Ranges [redacted]

[redacted]

[redacted]

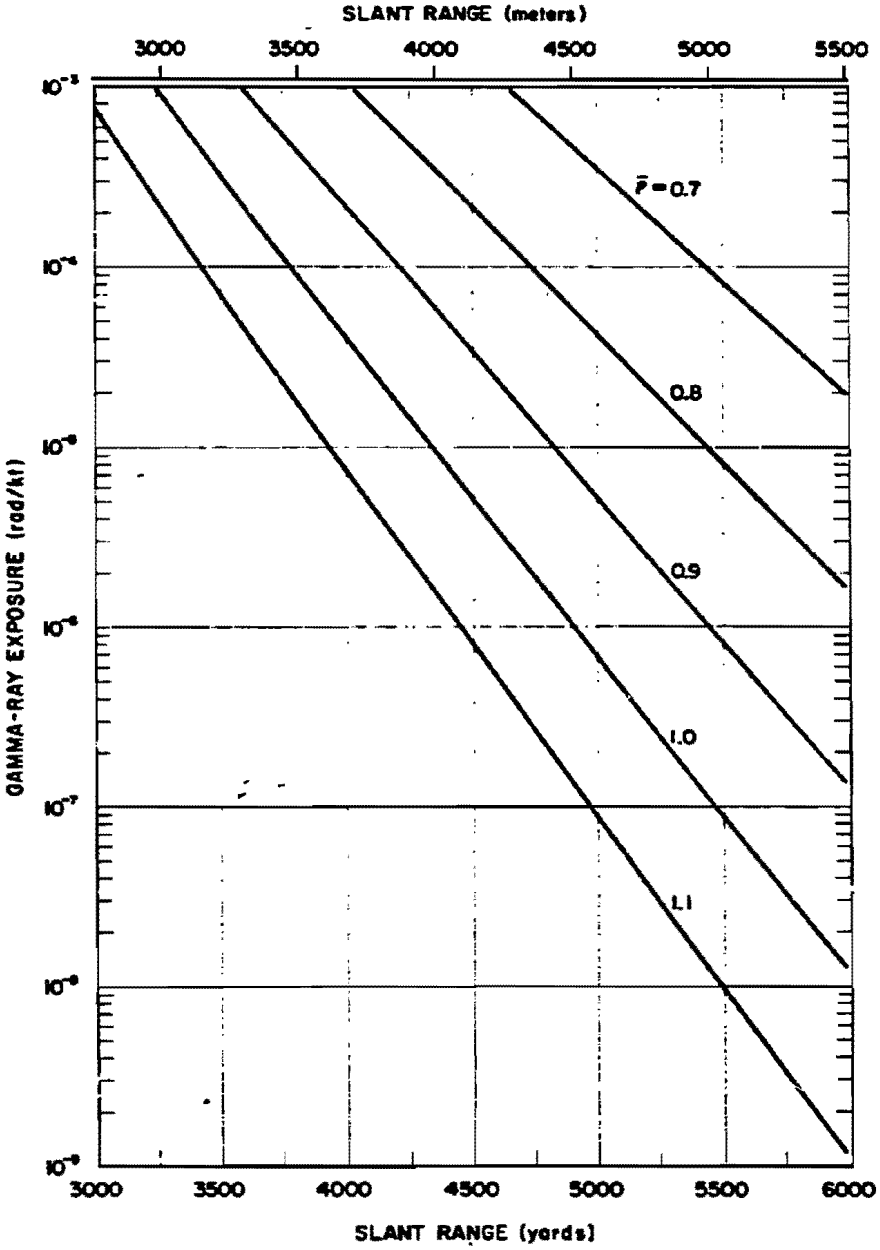

Figure 5-14c. [redacted] Fission Product Gamma Ray Dose as a Function of Slant Range from a 1 kt (Fission Yield) Surface Burst, Long Ranges [redacted]

[redacted]

[redacted]

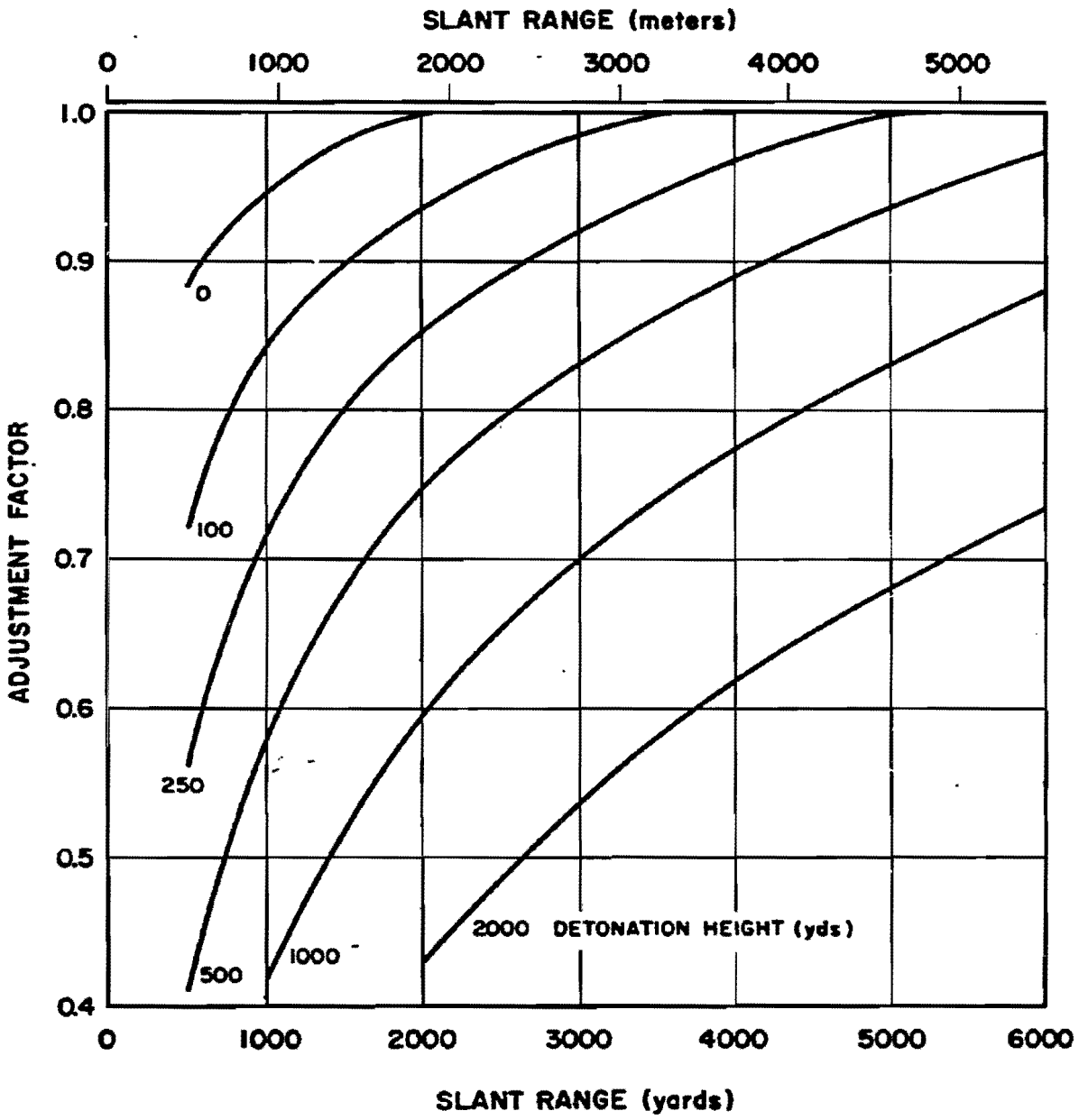

Figure 5-15. [redacted] Range Dependent Burst Height Adjustment Factors for Fission Product Gamma Rays [redacted]

[redacted]

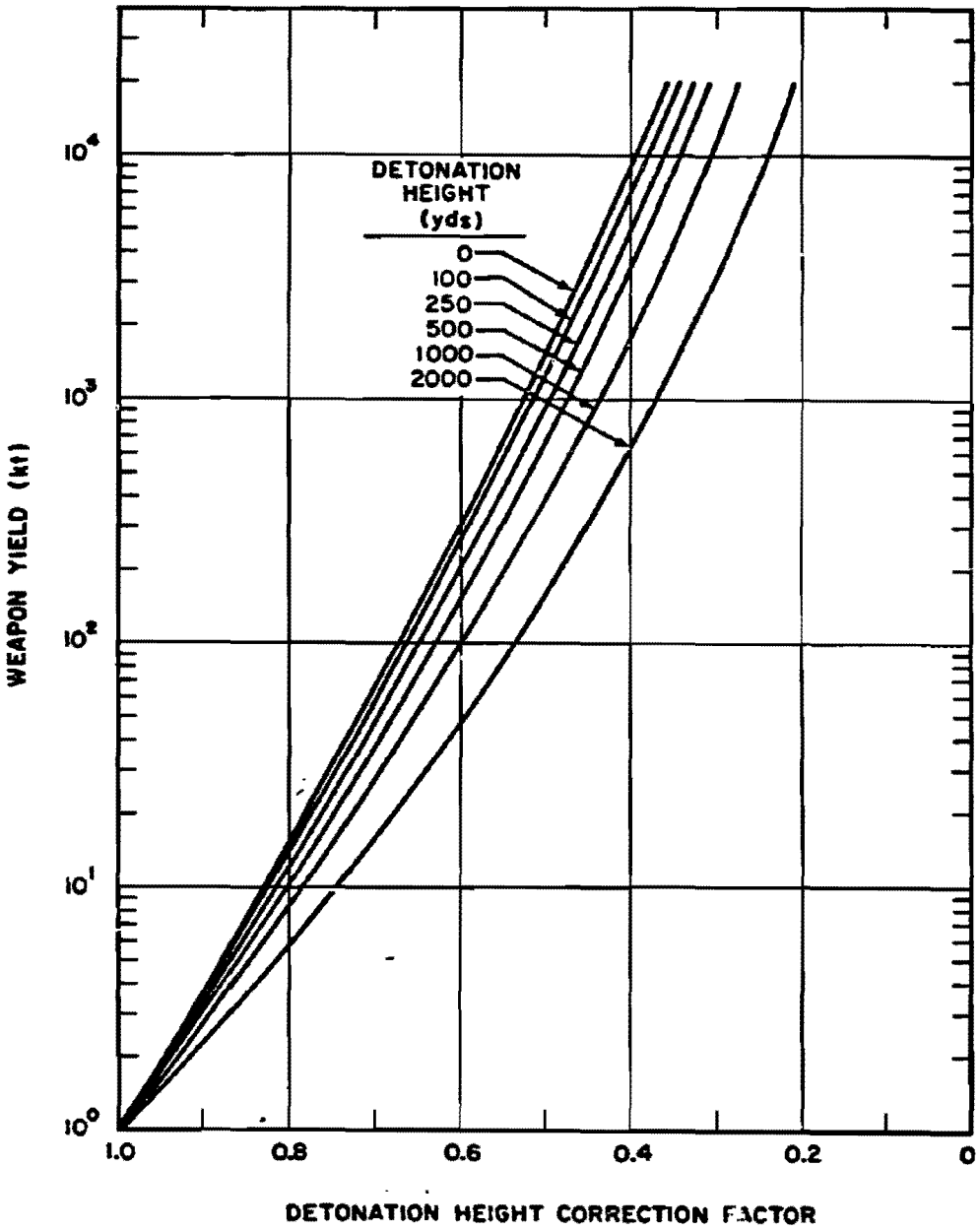

Figure 5-16. [redacted] Yield Dependent Burst Height Adjustment Factors for Fission Product Gamma Rays [redacted]

[redacted]

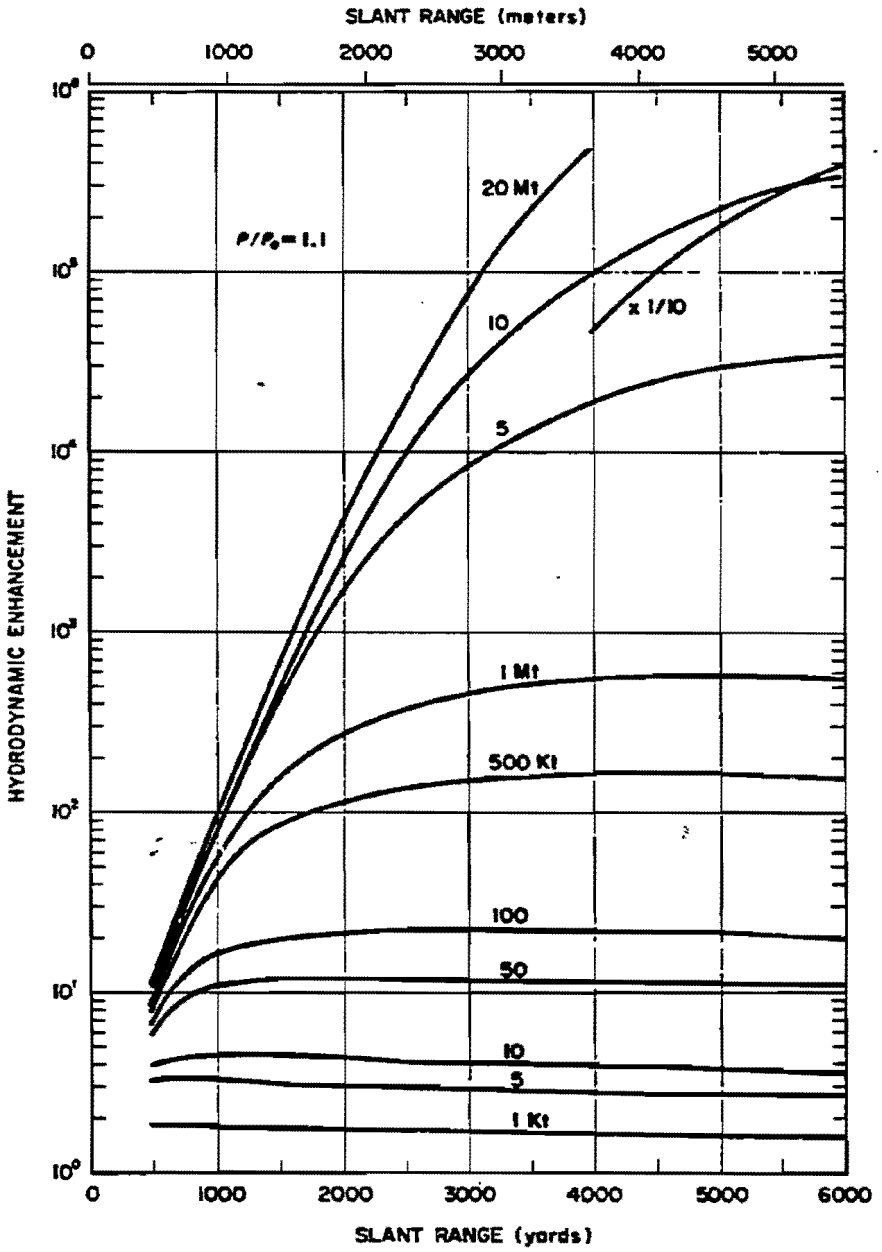

Figure 5-17a. [redacted] Fission Product Gamma Ray Hydrodynamic Enhancement Factors as a Function of Slant Range for Relative Air Density of 1.1 [redacted]

[redacted]

[redacted]

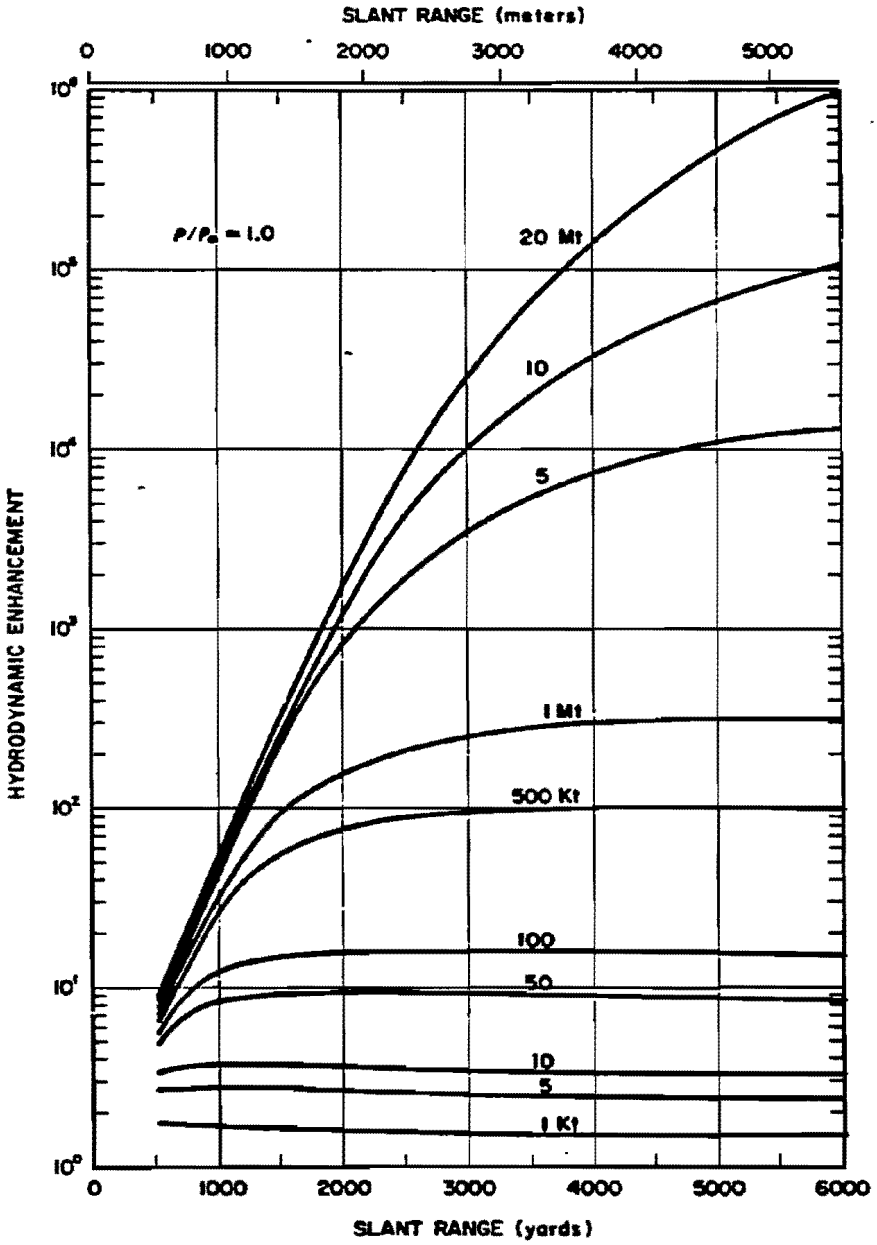

Figure 5-17b. [redacted] Fission Product Gamma Ray Hydrodynamic Enhancement Factors as a Function of Slant Range for Relative Air Density of 1.0 [redacted]

[redacted]

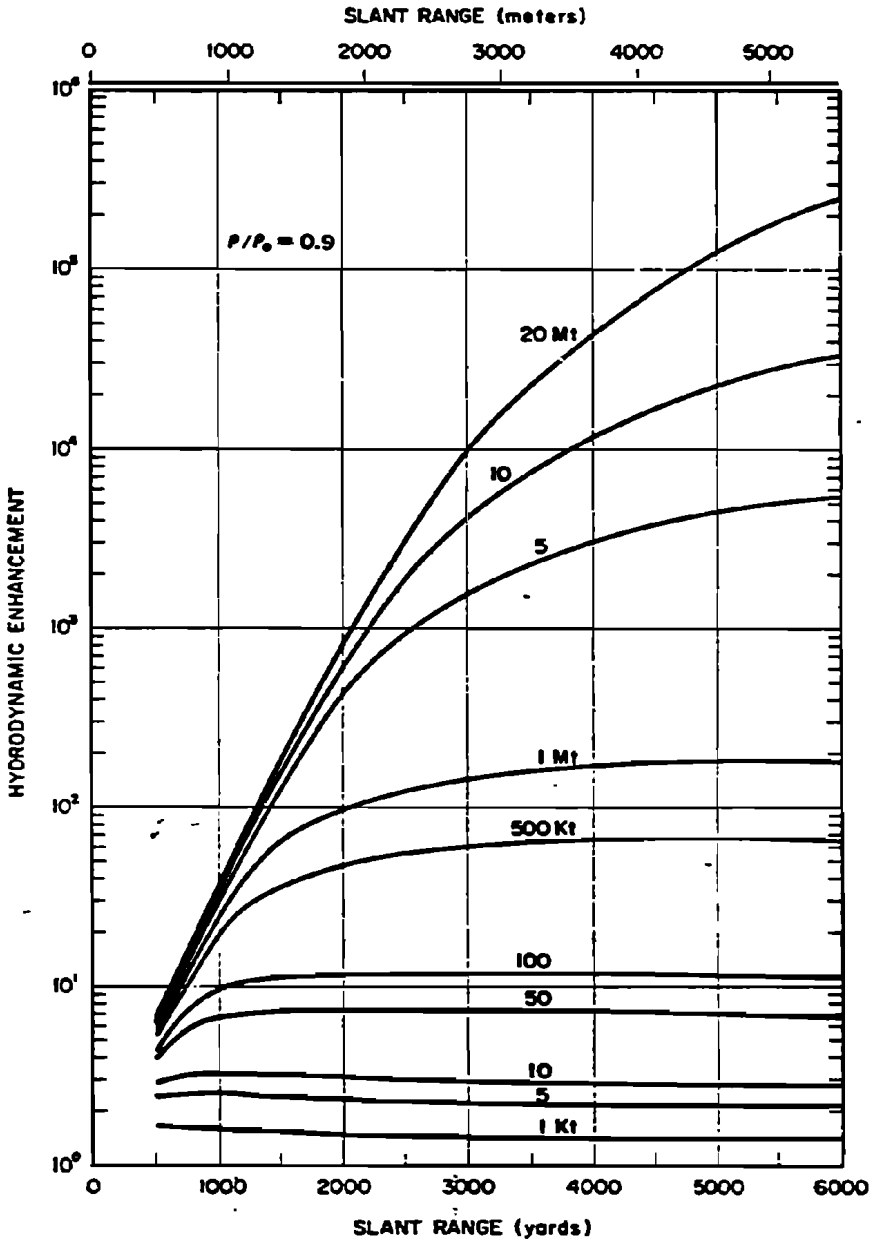

Figure 5-17c. [redacted] Fission Product Gamma Ray Hydrodynamic Enhancement Factors as a Function of Slant Ranges for Relative Air Density of 0.9 [redacted]

[redacted]

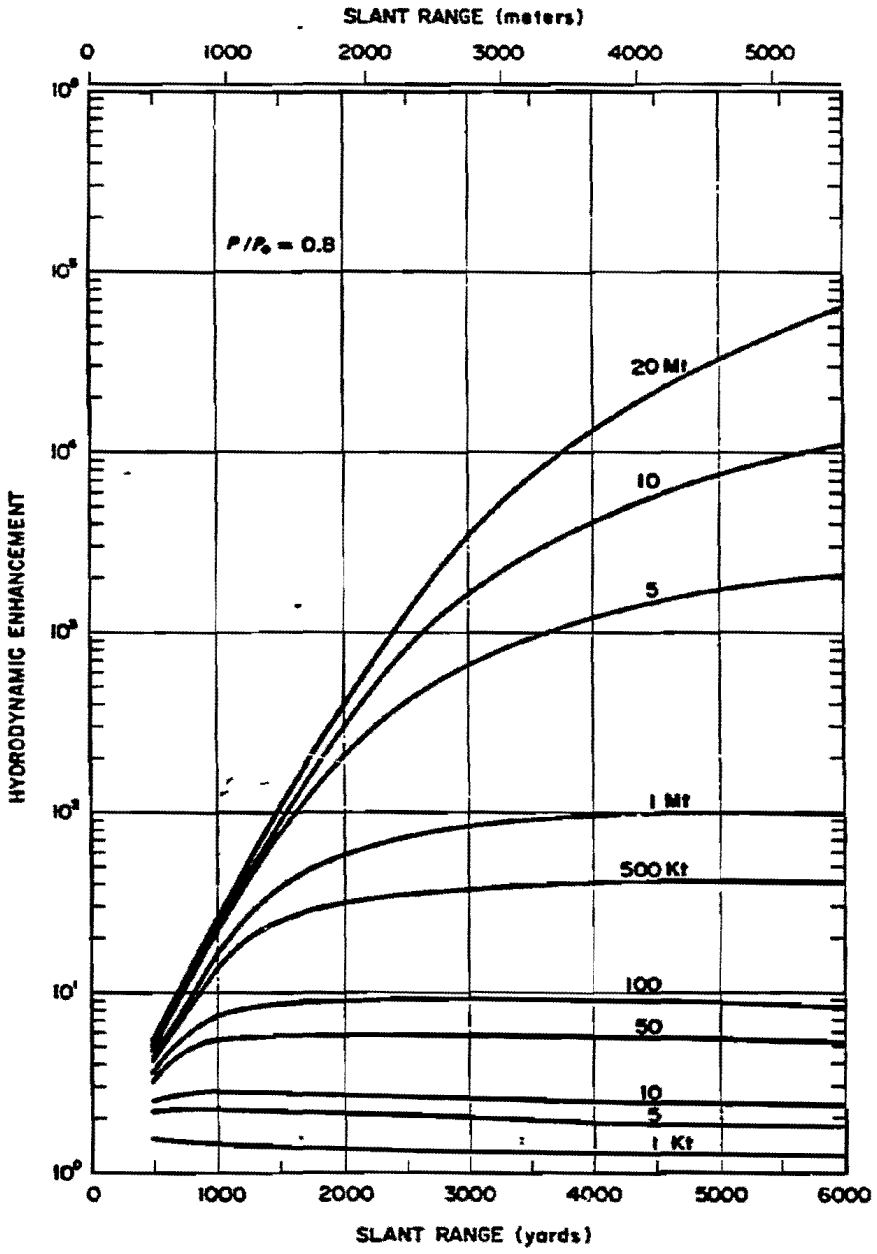

Figure 5-17d. [redacted] Fission Product Gamma Ray Hydrodynamic Enhancement Factors as a Function of Slant Range for Relative Air Density of 0.8 [redacted]

[redacted]

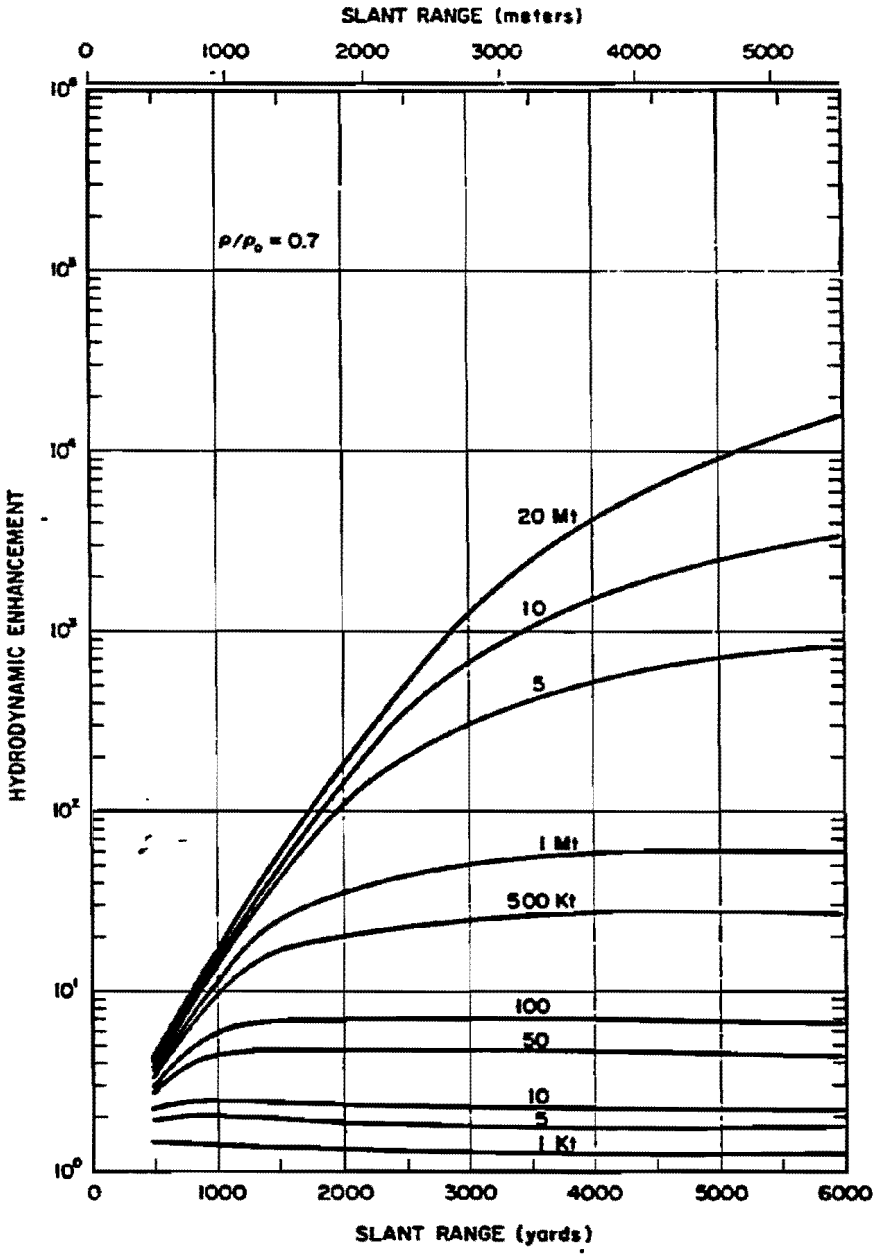

Figure 5-17e. [redacted] Fission Product Gamma Ray Hydrodynamic Enhancement Factors as a Function of Slant Range for Relative Air Density of 0.7 [redacted]

SECTION II
NEUTRON-INDUCED ACTIVITY IN SOILS

As mentioned in paragraph 5-3, the neutrons emitted during a nuclear explosion undergo three main types of reactions when traversing matter: elastic scattering; inelastic scattering; and neutron capture. There are a variety of capture reactions, most of which result in the subsequent emission of a charged particle (generally a proton or alpha particle) and/or a gamma ray. When the reaction results solely in the emission of a gamma ray, it is generally referred to as radiative capture. As a rule, the probability for capture reactions is small compared to elastic and inelastic scattering when the neutron energy exceeds a few keV. The nuclei remaining after neutron capture are frequently radioactive, generally emitting a beta particle, a gamma ray(s), or both. The extent of the hazard to personnel that results from radioactivity induced in the soil by neutrons from a nuclear explosion is described in this section.

5-12 Height of Burst

The residual radioactive contamination (fallout) that results from fission products that are distributed subsequent to a contact surface or subsurface burst (Section III of this chapter) is much greater than the radioactive contamination that results from the neutron activity discussed in this section. Thus, the neutron-induced activity may be neglected for contact surface and subsurface bursts.* If a weapon is burst at such a height as to be in the transition zone as far as fallout is concerned, the neutron-induced activity generally can be neglected if the burst height is in the lower three-quarters of the fallout transition zone, i.e., if the burst is below about $75W^{0.35}$ feet (see Section III). If the height of burst is in the upper quarter of the transition zone (between about $75W^{0.35}$ feet and $100W^{0.35}$ feet), the neutron-induced activity may not be negligible compared to fallout. When fallout dose rate contours determined by the methods described in Section III are much smaller than those for a surface burst, the neutron-induced activity should be obtained by the methods described below. The overall contour values may be obtained by summing the dose rate values for induced activity and fallout at a particular time; however, as will be shown in succeeding paragraphs of this chapter, the radioactivity from fallout and that from neutron-induced activity decay at different rates. Therefore, the dose rate from each source must be determined separately for each time of interest, or the total doses over some period of time must be determined separately, and then the appropriate summing may be performed.

For burst heights that are sufficiently high, the various forms of attenuation described in paragraph 5-3 will result in a neutron fluence at the surface of the earth that is too small to produce significant induced activity. Since the neutron-induced gamma radiation depends on soil type as well as weapon type and yield, a height of burst above which neutron-induced activity will cease to be important cannot be defined. In general, however, this effect will only be important for low air bursts (just above the height of burst at which fallout ceases to be important).

5-13 Soil Types

The type, intensity, and energy distribution of the induced activity produced by the neutrons will depend on which isotopes are produced and in what quantity. These factors depend on the number and energy distribution of the incident neutrons and the chemical composi-

*The induced activity contribution may, however, assume more importance if Plowshare type nuclear devices are adapted for military use.

tion of the soil. Induced contamination contours are independent of wind, except for some wind redistribution of the surface contaminant. The contours can be expected to be roughly circular.

Examination of several thousand analyses of the chemical composition of soils and the relative probabilities of neutron capture by the various elements present in the various samples has indicated that sodium, manganese, and aluminum generally will contribute most of the induced radioactivity. Small changes in the quantities of these materials can change the activity significantly. Other elements can also influence the radioactivity. Some elements have a relatively high probability for capturing neutrons (cross section), but the isotope that is formed after the capture either is not radioactive, does not emit gamma rays, or has such a long half life that the low activity does not produce a hazardous dose rate. The presence of such elements in the soil will tend to lower the hazard from neutron-induced activity.

As described in paragraph 5-3, scattering of neutrons from light elements may cause the neutron to transmit a significant amount of its energy to the nucleus, and the scattered neutron will be less energetic than the incident neutron. Since the probability of neutron capture generally increases as the neutron energy decreases (in particular, this is true for sodium, manganese, and aluminum), the presence of light elements in the soil will tend to cause a larger number of neutrons to be captured near the surface rather than at some depth (the peak intensity from neutron activated radionuclides generally is two to three inches below the surface). Thus, it might be expected that the presence of light elements might increase the hazard from neutron-induced activity by raising the primary gamma ray source to a level nearer the surface, where attenuation of the earth above the source would be less. A study of many soil samples indicates that the light element that is most likely to cause such an effect is hydrogen that might be present in moisture (water) in the soil.* Thus, it might be expected that soil saturated with water might be more hazardous from neutron-induced activity than the same soil when dry. However, competing effects occur because the hydrogen absorbs neutrons to form nonradioactive deuterium. These neutrons otherwise could produce gamma ray emitters. Experiments have confirmed that moisture content does increase the hazard from neutron-induced activity; however, this effect does not appear to be of major importance in view of the uncertainties in soil composition and variations in possible weapon neutron outputs.

Four soils have been chosen to illustrate the extent of the hazard that may be expected from induced activity. These soils were selected to show wide variations in predicted dose rates; the activity from most other soils should fall within the range of activities presented for these soils. Table 5-4 shows the chemical composition of the selected soils. The elements listed in Table 5-4 are in the order of probable importance so far as induced activity is concerned.

When applying the data presented in this section to soils other than the four types shown, the activity should be estimated by using the data for the type that most closely resembles the soil in question in chemical composition. If none of the four types resembles the soil in question very closely, the following points should be kept in mind. For times less than $H + 1/2$ hour, aluminum is the most important contributor. Between $H + 1/2$ hour and $H + 5$ hours, manganese is generally the most important element. In the

* Hydrogen, being the lightest element, will have many more atoms per unit volume for the same percentage concentration by weight. It is also the most effective element in reducing the energy of the neutron, since its nucleus (a proton) has essentially the same mass as a neutron and energy transfer by elastic collision is very effective.

Table 5-4. [redacted] Chemical Composition of Illustrative Soils [redacted]

Element	Percentage of Soil Type (by weight)			
	Type I (Liberia, Africa)	Type II (Nevada desert)	Type III (lava, clay, Hawaii)	Type IV (beach, sand, Pensacola, Florida)
Sodium	–	1.30	0.16	0.001
Manganese	0.008	0.04	2.94	–
Aluminum	7.89	6.90	18.79	0.006
Iron	3.75	2.20	10.64	0.005
Silicon	33.10	32.00	10.23	46.65
Titanium	0.39	0.27	1.26	0.004
Calcium	0.08	2.40	0.45	–
Potassium	–	2.70	0.88	–
Hydrogen	0.39	0.70	0.94	0.001
Boron	–	–	–	0.001
Nitrogen	0.065	–	0.26	–
Sulfur	0.07	0.03	0.26	–
Magnesium	0.05	0.60	0.34	–
Chromium	–	–	0.04	–
Phosphorous	0.008	0.04	0.13	–
Carbon	3.87	–	9.36	–
Oxygen	50.33	50.82	43.32	53.332

[redacted]

absence of manganese, the sodium content will probably govern the activity for this period. Between H +5 hours and H + 10 hours, sodium and manganese content are both important. After H + 10 hours, sodium will generally be the only large contributor. If the sodium, manganese, and aluminum contents are low, the neutron-induced activity generally will be low. Soil type IV is an example of such a soil. Using these guidelines, it may be possible to obtain better data for a given soil by using data for a different illustrative soil at each of several times of interest. A word of caution is in order, however. While the content of sodium and aluminum will generally be relatively constant over fairly large areas, manganese generally is a trace element and the content may vary by an order of magnitude over a few hundred yards. Between H + 1/2 hour and H + 5 hours, the dose rate will vary almost directly in proportion to the magnitude of the variation in manganese content. In view of the uncertainty in the soil composition at any location under

[redacted]

operational conditions, and the possibility of variations in composition over short distances, the data presented herein should only be used for rough estimates and should not be used as the basis for operational planning.

5-14 Dose Rate and Dose Predictions

As described in paragraph 5-1, both the spectrum and the total number of neutrons emitted during a nuclear explosion are sensitive functions of weapon design. Thus, no "representative" weapon was used for the prediction of neutron-induced activity, and, in view of the other uncertainties discussed above, presentation of prediction techniques for several weapon designs is not warranted. Figure 5-18 shows a broad band that indicates the variation of neutron-induced gamma activity as a function of slant range from the explosion. It is believed that the activity produced by most weapons will fall within the band.* Dose rates at $H + 1$ hour after burst may be obtained by multiplying the dose rates from Figure 5-18 by the multiplying factors given in Problem 5-5.

Figure 5-19 represents the radioactive decay characteristics of the four soil types shown in Table 5-4. The decay factors taken from Figure 5-19 are multiplied by the $H + 1$ hour dose rate for a particular soil to give the dose rate for that soil at any other time.

Figures 5-20 through 5-23 are presented to facilitate the computation of total dose. Multiplying factors may be obtained from these figures, which, when applied to the $H + 1$ hour dose rate for the particular soil, will give the dose accumulated over any of several periods of time for various times of entry into the contaminated area.

*This band considers the representative types of nuclear weapons shown in Table 5-3 with the exception of Type V.

[redacted]

Problem 5-5. Calculation of Neutron-Induced Activity at 1 Hour After Explosion

[redacted] Figure 5-18 shows a range of normalized neutron-induced dose rates as a function of slant range from a 1 kt explosion. To estimate the $H+1$ hour dose rate, enter the slant range axis with the slant range in yards and read the range of normalized dose rates. Multiply these dose rates by the appropriate factor for the soil type of interest from the following list.

Soil Type	Multiplying Factor
I	1.0
II	9.1
III	109.0
IV	0.024

[redacted] *Scaling.* For yields other than 1 kt, multiply the dose rates obtained from Figure 5-19 by the weapon yield in kt.

[redacted] *Example*

Given: A 50 kt explosion at a height of burst of 900 feet above soil type III.

Find: The range of $H+1$ hour dose rates that might be expected: at ground zero and at a ground distance of 950 yards from ground zero.

Solution: The corresponding slant ranges are 300 yards to ground zero and 996 yards to a point at a ground distance of 950 yards from ground zero. From Figure 5-18, the normalized $H+1$ hour dose rate at a slant range of 300 yards from ground zero are expected to be between 0.8 rad/hr/kt and 1.8 rads/hr/kt. The corresponding dose rates at a slant range of 996 yards are 1.6×10^{-2} rad/hr/kt and 5×10^{-2} rad/hr/kt. The multiplying factor for soil type III is 109.

Answer: The $H+1$ hour dose rates at ground zero should be between

$$50 \times 109 \times 0.8 = 4{,}360 \text{ rads/hr},$$

and

$$50 \times 109 \times 1.8 = 9{,}800 \text{ rads/hr}.$$

The $H+1$ hour dose rates at a ground distance of 950 yards from ground zero should be between

$$50 \times 109 \times 1.6 \times 10^{-2} = 87 \text{ rads/hr},$$

and

$$50 \times 109 \times 5 \times 10^{-2} = 272 \text{ rads/hr}.$$

[redacted] *Reliability.* $H+1$ hour dose rates are expected to fall within the limits of the band shown in Figure 5-19 for the specific soils shown. For other soils, even with small variations in the content of sodium and manganese, the data merely will furnish an estimate of the magnitude of the hazard.

[redacted] *Related Material.* See paragraphs 5-1 through 5-3, and paragraphs 5-12 through 5-14.

[redacted]

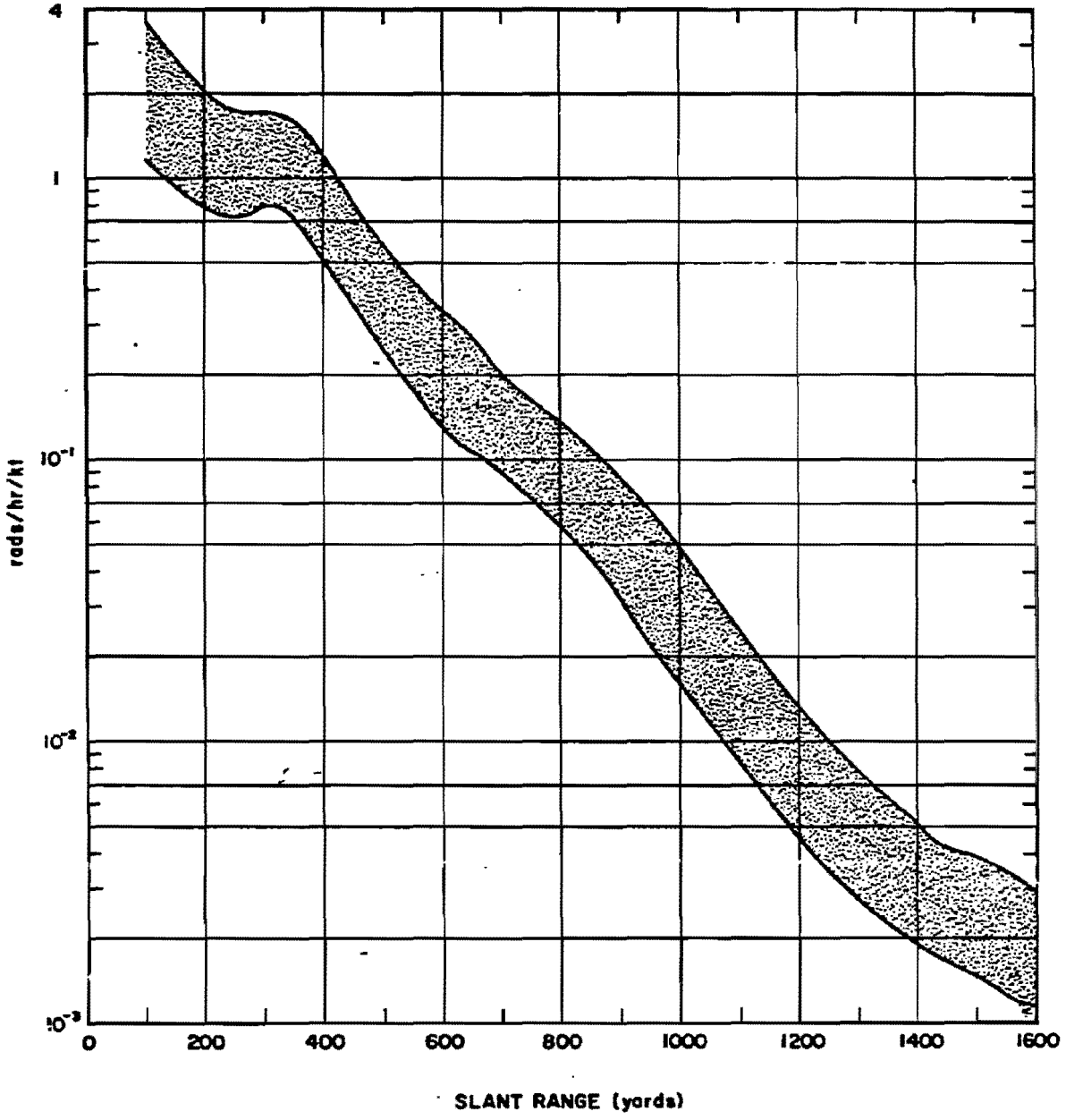

Figure 5-18. [redacted] Neutron-Induced Gamma Dose Rate as a Function of Slant Range at a Reference Time of 1 Hour After Burst [redacted]

[redacted]

Problem 5-6. Calculation of Neutron-Induced Gamma Activity at Times Other than $H + 1$ Hour

[redacted] The dose rate at any time after burst may be determined by multiplying the $H + 1$ hour dose rate by the decay factor appropriate to the soil of interest from Figure 5-19. The decay curves may also be used to determine the value of the dose rate at $H + 1$ hour from the dose rate at a later time. In this case, the measured dose rate is divided by the appropriate decay factor. The dose rate at any other time then may be determined from the $H + 1$ hour dose rate.

[redacted] *Example 1* [redacted]

Given: The dose rate at a given point on soil type I is 30 rads/hr at $H + 1$ hour.

Find: The dose rate at that point at $H + 1/2$ hour and at $H + 10$ hour.

Solution: From Figure 5-19, the decay factors for soil type I for 1/2 hour and 10 hours are 3 and 0.083, respectively.

Answer: The dose rate at 1/2 hour is:

$$30 \times 3 = 90 \text{ rads/hr}$$

and the dose rate at 10 hours is

$$30 \times 0.083 = 2.5 \text{ rads/hr.}$$

[redacted] *Example 2* [redacted]

Given: The measured dose rate at a point over type II soil is 375 rads/hr 3 hours after the explosion.

Find: The dose rate at the same point 50 hours after the explosion.

Solution: From Figure 5-19, the decay factors for soil type II are 0.75 and 0.06 for times of $H + 3$ and $H + 50$ hours, respectively. The $H + 1$ hour dose rate at the point is

$$\frac{375}{0.75} = 500 \text{ rads/hr.}$$

Answer: The $H + 50$ hours dose rate at the point is

$$(500)(0.06) = 30 \text{ rads/hr.}$$

[redacted] *Reliability.* The curves of Figure 5-19 are estimated to represent the decay of the soil compositions shown in Table 5-4 to within ±10 percent; however, small changes in the chemical composition of the soil, particularly in the content of sodium, manganese, and aluminum, may change the decay characteristics drastically. Uncertainties associated with the *prediction* of $H + 1$ hour dose rates will affect the prediction of dose rates at any other time.

[redacted] *Related Material.* See paragraphs 5-13 and 5-14. See also Problem 5-5.

[redacted]

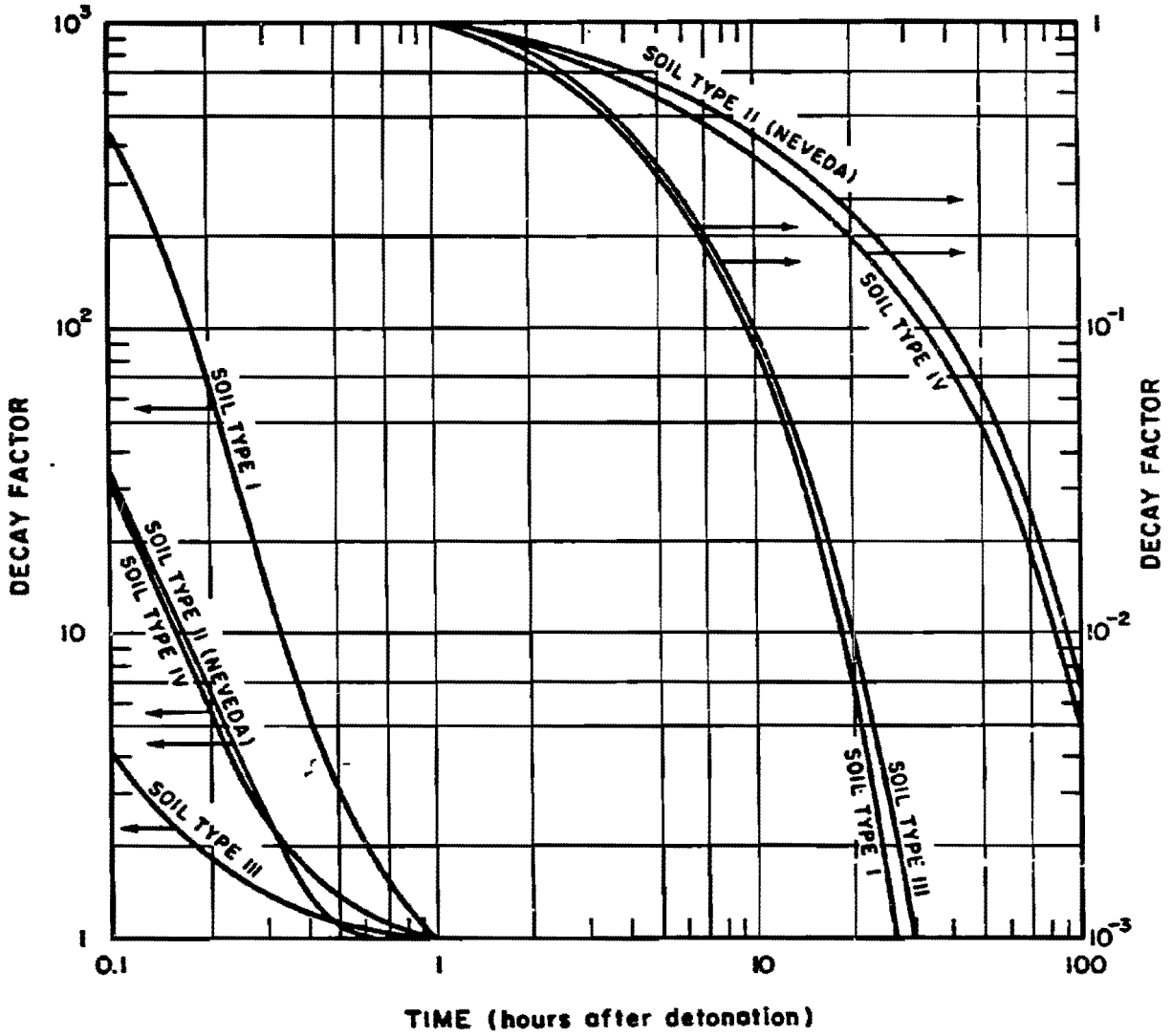

Figure 5-19. [redacted] Decay Factors for Neutron-Induced Gamma Activity [redacted]

[redacted]

[redacted]

Problem 5-7. Calculation of Total Dose from Neutron-Induced Activity

[redacted] Figures 5-20 through 5-23 provide the means to obtain the total dose received when entering an area contaminated with neutron-induced activity and remaining for a specified interval of time. The various curves represent times that an individual remains in the contaminated area. To determine the dose, obtain the multiplying factor from the vertical axis that corresponds to the time of entry on the horizontal axis and the stay time from the appropriate curve (or by interpolation between curves).

[redacted] *Example*

Given: A dose rate of 105 rads/hr was measured on entering a contaminated area of soil type III 5 hours after an air burst nuclear explosion.

Find: The total dose that would be received by an individual who remained in that area for 1 hour.

Solution: From Figure 5-19, the decay factor for soil type III at $H + 5$ hours is 0.35. The 1 hour dose rate is therefore

$$\frac{105}{0.35} = 300 \text{ rads/hr.}$$

Figure 5-22 is the appropriate figure from which the dose multiplying factor should be obtained for soil type III. From this figure, the intersection of the line for a time of entry of 5 hours after burst with the 1 hour stay time curve gives a factor of 0.32.

Answer: If the individual remains in the area for 1 hour, the accumulated dose will be

$$(0.32)(300) = 96 \text{ rads.}$$

[redacted] *Reliability.* Figures 5-20 through 5-23 are integrals of the curves in Figure 5–19. The same reliability statement given in Problem 5-6 applies.

[redacted] *Related Material.* See paragraphs 5-13 and 5-14. See also Problems 5-5 and 5-6.

[redacted]

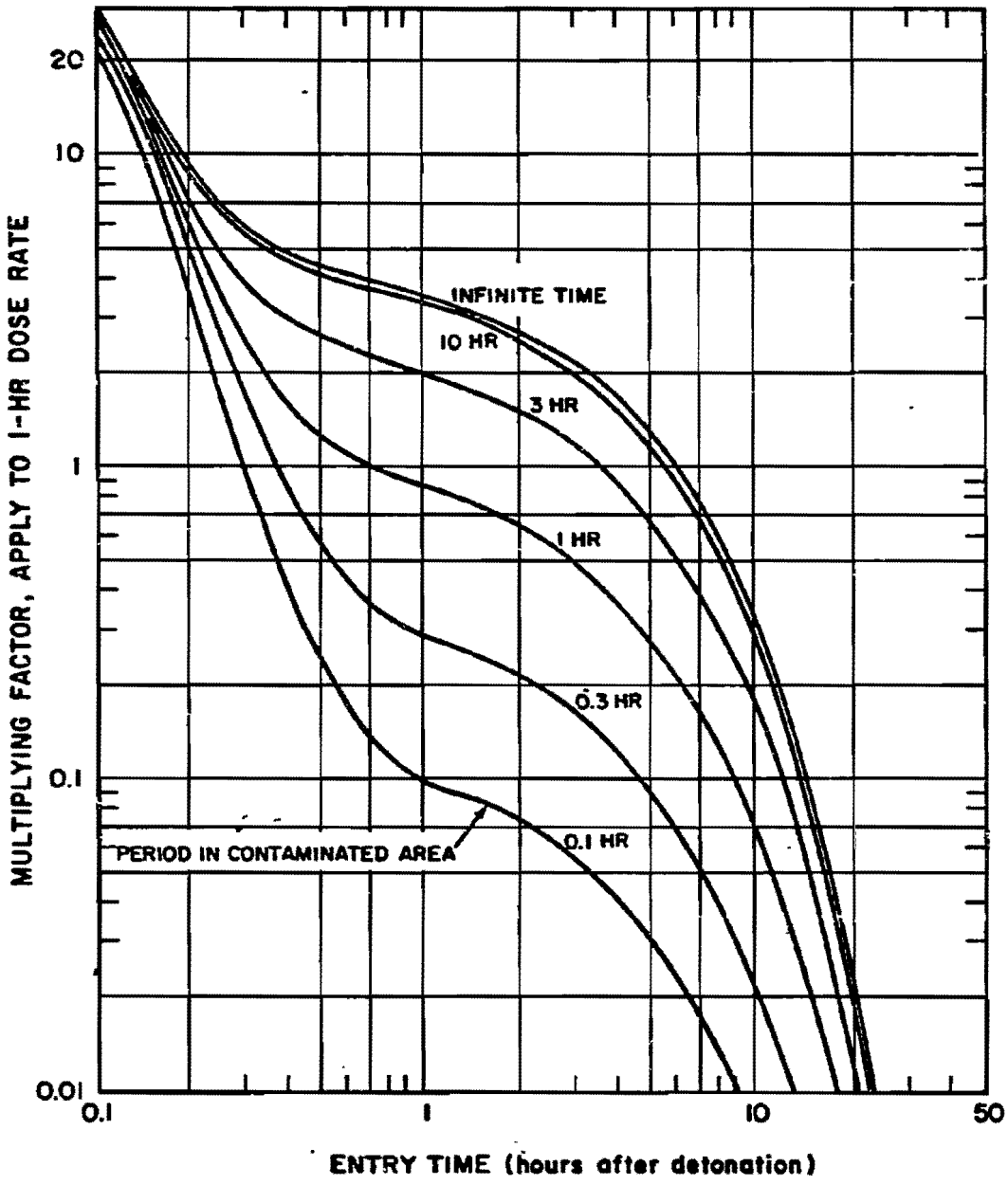

Figure 5-20. [redacted] Total Radiation Dose Received in an Area Contaminated by Neutron-Induced Gamma Activity, Soil Type I [redacted]

[redacted]

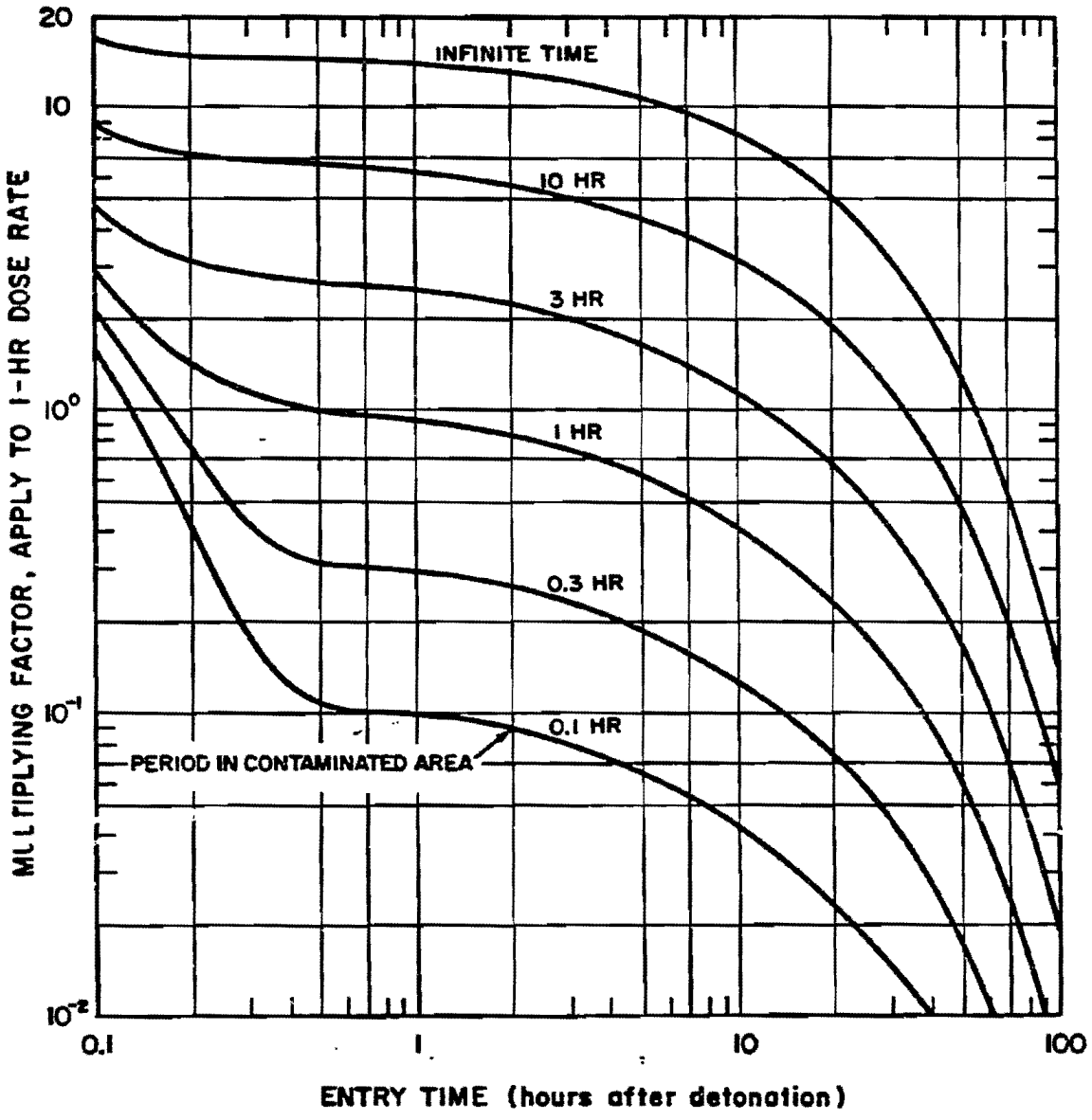

Figure 5-21. [redacted] Total Radiation Dose Received in an Area Contaminated by Neutron-Induced Gamma Activity, Soil Type II [redacted]

[redacted]

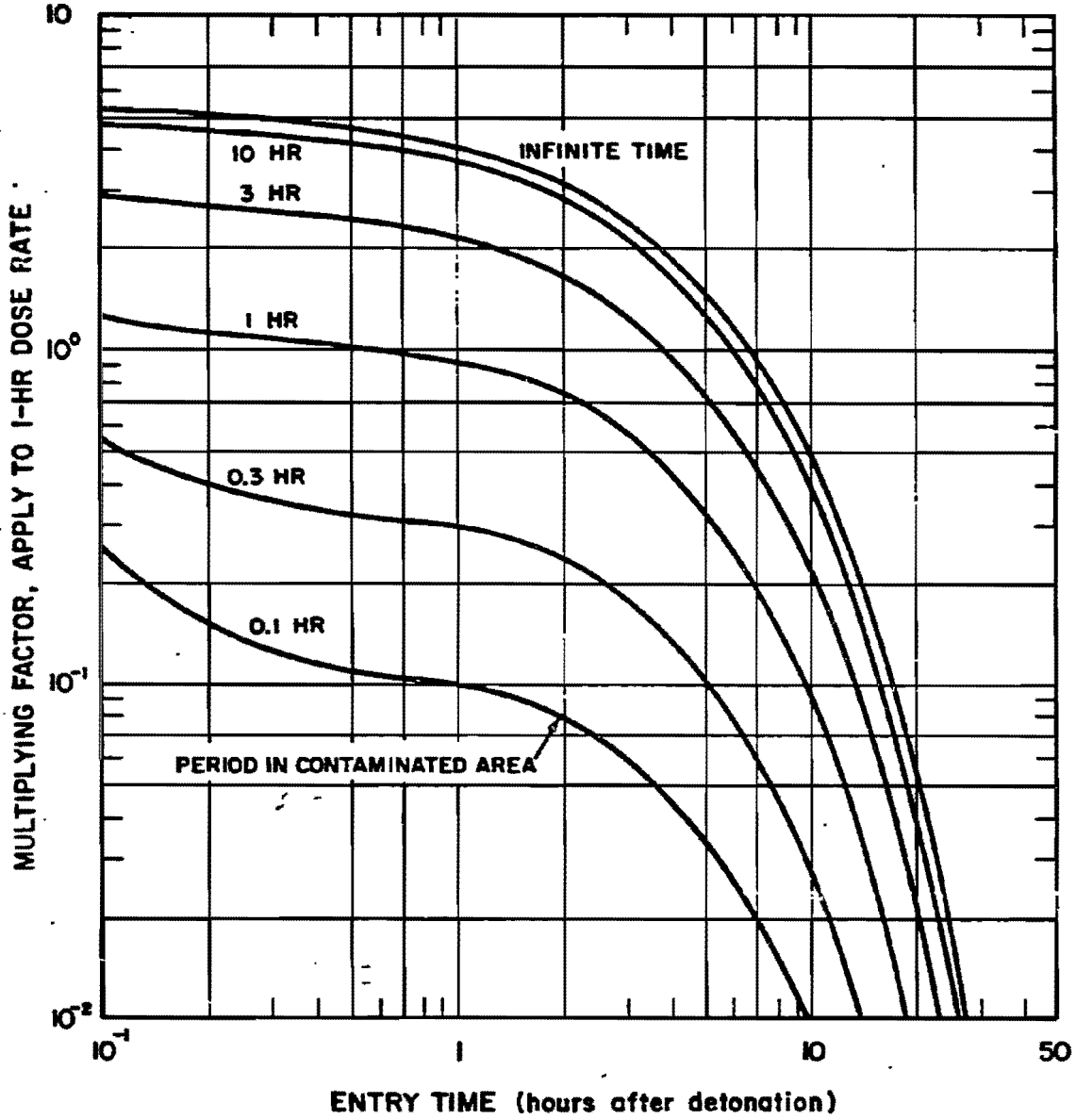

Figure 5-22. [redacted] Total Radiation Dose Received in an Area Contaminated by Neutron-Induced Gamma Activity, Soil Type III [redacted]

[redacted]

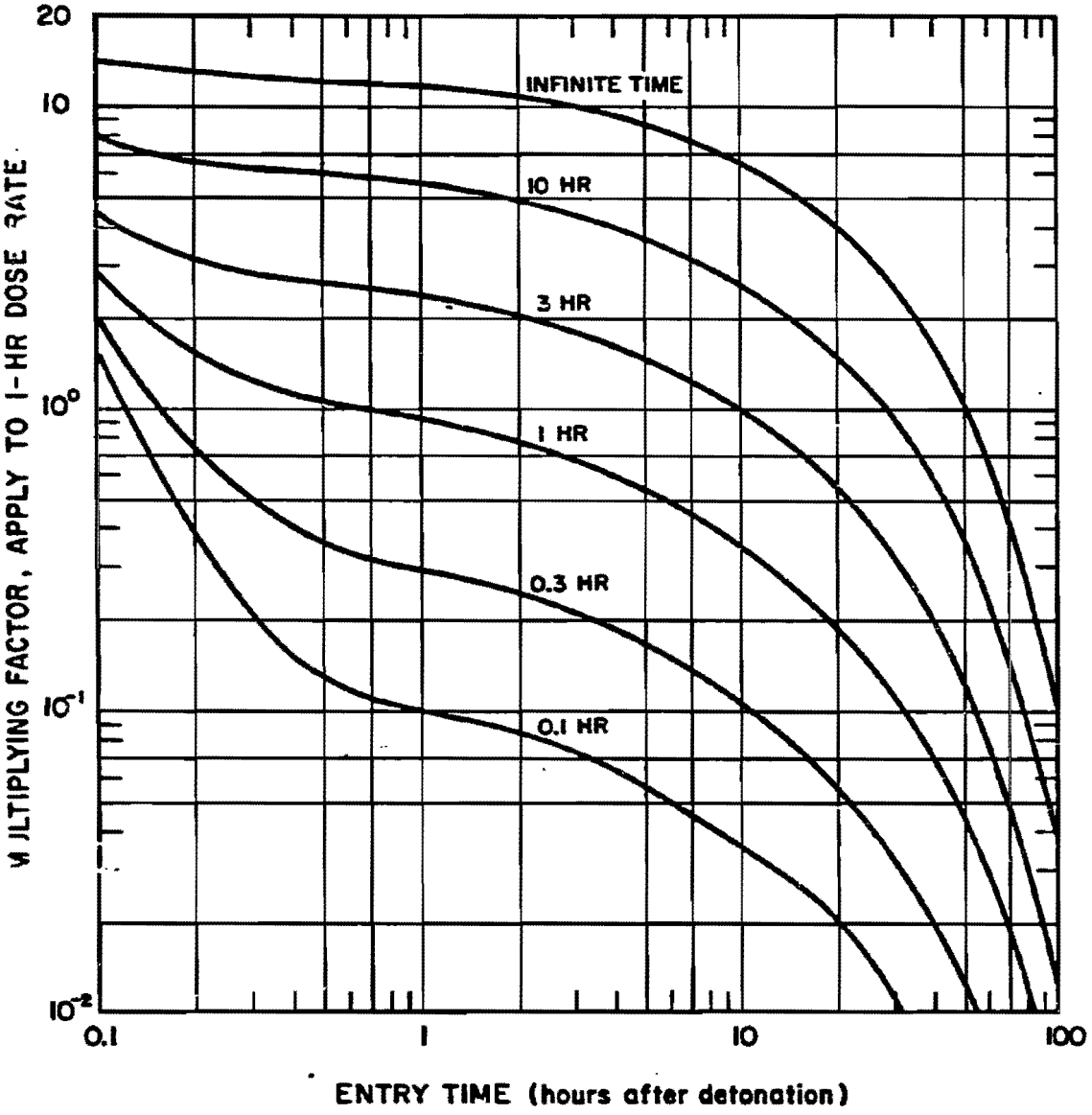

Figure 5-23. [redacted] Total Radiation Dose Received in an Area Contaminated by Neutron-Induced Gamma Activity, Soil Type IV [redacted]

[redacted]

SECTION III
RESIDUAL RADIATION

Residual radiation is that radiation that is emitted later than one minute after the explosion. The sources and characteristics of this radiation vary depending on the extent to which fission and fusion reactions contribute to the energy of the weapon. Residual radiation from a fission weapon arises mainly from fission products and, to a lesser extent, from radioactive isotopes formed by neutron reactions in weapon materials and from uranium and/or plutonium that have escaped fission. Other sources of residual radiation hazard are the activity induced by neutrons that interact with various elements present in the earth, sea, air, or other substances in the explosion environment. The most important of these sources is the neutron-induced activity in soils that is discussed in Section II of this chapter. The radioactivity from a thermonuclear weapon will not contain the same quantity of fission products that are associated with a pure fission weapon of the same yield; however the large number of high energy neutrons will produce larger quantities of neutron-induced activity in weapon components and the surroundings. The total radioactivity from such a weapon will, however, generally be less than from a pure fission weapon of the same yield.

FALLOUT

The main hazard of residual radiation results from the creation of fallout particles that incorporate the radioactive weapon residues and the induced activity in the soil, water, and other materials in the vicinity of the explosion that are sucked up from the earth's surface into the rising fireball. The wind disperses these particles over large areas. Another hazard may arise from neutron-induced activity on the earth's surface in the immediate neighborhood of the burst point. Both the absolute and relative contributions of the fission product and induced radioactivity will depend on the total yield and fission yield of weapon, the height of burst, the nature of the surface at the burst point, and the time after the explosion.

Two phases of fallout may be considered: early (local) and delayed (worldwide). Early fallout reaches the ground during the first 24 hours following a nuclear explosion. It is th early fallout from surface, subsurface, or low a.. bursts that produces radioactive contamination over large areas, with an intensity great enough to represent an immediate biological hazard. Delayed fallout, which arrives after the first day, consists of very fine, invisible particles that settle in low concentrations over a considerable part of the earth's surface. Radioactive decay during the relatively long time the delayed fallout remains suspended in the atmosphere reduces the radiation intensity from the fission products and other substances significantly. Because of these characteristics, the radiations from the delayed fallout pose no significant military effect and are not considered here.

5-15 Early Fallout

The early fallout from a nuclear weapon consists of fission products and neutron activation products in quantities that are related to the fission and total yields of the weapon, respectively. In the case of a weapon in which large quantity of the energy is derived from fusion reactions, and especially for bursts high in the transition zone between surface (fallout producing) bursts and air bursts where little soil mixes with bomb debris to form fallout, the induced activity can be more important than that from fission products (see Section II). The relative importance of these two sources of residual radiation depends upon the fission-fusion ratio, type and composition of the surface material under the detonation and the height of burst.

[redacted] For detonations over land, where the particles consist mainly of soil minerals, the fission-product vapors condense onto solid and diffuse into molten soil particles and other particles that may be present. The vapors of the fission products also may condense with vapors of other substances to form mixed solid particles of small size.

[redacted] The fact that different materials condense at different temperatures, and at different times after detonation, changes the composition of fallout particles, giving rise to the phenomenon known as "fractionation." The occurrence of fractionation is shown, for example, by the fact that in a land surface burst the larger particles, which fall out of the fireball early and are found near ground zero, have radioactive compositions different from the smaller particles that leave the cloud later and reach the ground some distance downwind. The phenomena that account for fractionation are not all completely understood, but models have been developed to explain the phenomena reasonably satisfactorily. An example of fractionation is the change in physical state of fission products, such as krypton and xenon, as they decay. These two example products are gaseous in their normal state and do not combine with other elements to form compounds. During their radioactive decay, however, they form rubidium and cesium, respectively. These decay products can condense onto solid particles. In early fallout, the solid particles will be depleted not only in krypton and xenon, but also in their various decay (or daughter) products. In delayed fallout, small particles that have remained in the cloud for some time will have rubidium and cesium, and their daughters, strontium and barium, condensed upon them. Hence, the delayed fallout will be relatively richer in these elements.

5-16 Air Bursts [redacted]

[redacted] The surface contamination effects of fallout from an air-burst weapon are militarily insignificant in most cases, because the cloud carries most of the radioactive weapon debris to high altitudes. In general, by the time this material can fall back to earth, dilution and radioactive decay decreases the activity to levels that are no longer militarily important. An exception may occur in the case of a nuclear weapon cloud that is intercepted by a rainstorm from above. This special case of fallout, called "rainout" is discussed in a subsequent subsection.

5-17 Land Surface Bursts [redacted]

[redacted] The activity available from a nuclear explosion at a reference time of 1 hour after burst corresponds roughly to 450 megacuries per kiloton of fission yield.*

[redacted] Roughly half of the available activity is deposited as early fallout during the first 24 hours following a surface burst. This deposited radioactivity can extend several hundred miles from the burst point, depending on the yield and the prevailing winds. The winds of the upper atmosphere (the stratosphere) slowly deposit the remainder of the activity, or the delayed fallout, over the earth's surface, mainly in the hemisphere of detonation. The land surface burst is used as the standard for the development of deposition patterns and idealized contours that are discussed below. Adjustments to correct these idealized contours for bursts in the transition zone (heights of burst between an air burst and a surface burst) and for underground bursts are described in paragraphs 5-22 and 5-23.

* [redacted] This value approximates the activity per kiloton in disintegrations per second at one hour. Actual values may range from about 430 to about 460 megacuries, depending on the fissile material and the neutron spectrum that causes the fission. The user may encounter other values in various sources, e.g., 550 gamma-megacuries per kiloton at 1 hour after explosion. This latter is a fictitious, but useful, relationship that relates the fission product gamma source to an equivalent monoenergetic source with an energy equal to the average photon energy of the fission products at 1 hour after the explosion.

5-18 Deposition Patterns

In a complete calm, the fallout contamination would form a roughly circular pattern around the point of detonation. Wind leads to an elongated area, the exact nature of which depends upon the speed and direction of the wind from the surface up to the altitude of the top of the stabilized cloud. If the direction of the wind does not vary excessively from the surface up to the top of the cloud, the ground fallout contours may be characterized by a semicircular pattern upwind from ground zero and an elliptical pattern downwind. The upwind pattern is formed by the rapid settling of the heavier particulate matter in the stem and ejecta from the crater, whereas the downwind elliptical pattern is formed by fallout of smaller and lighter particles from the cloud.

Complicated wind patterns (wind shear) as well as variations of the wind pattern in time and space may cause extreme departures from a simple elliptical pattern. Also, the measured dose-rate contours have frequently been observed to occur in patterns that are best described as a series of islands of relatively high activity surrounded by areas of lower activity. The most common pattern of this type has been one in which the higher dose rate contours appear around two major areas and one or more smaller areas. One of the larger areas is in the immediate vicinity of ground zero; the other is in the general downwind direction from ground zero. The locations of the smaller areas of high activity have not demonstrated patterns that can be described simply in terms of the wind structure. The dose rates observed within these high activity areas have been of comparable magnitude when extrapolated back to some early time after detonation, such as $H + 1$ hour. Because of the earlier arrival of the contaminant, however, the activities actually observed near ground zero have been higher than in the areas away from ground zero. A quantitative treatment of such complicated deposition patterns is possible only through use of a complex computational model. The simplified method for obtaining deposition patterns presented below will not predict these islands of relatively high activity.

The area covered and the degree of localization of the contamination also depend to some extent on the character of the soil at the burst point. For example, a surface detonation over dry soil with small particle sizes probably would result in a larger area enclosed by low dose rate contours and a smaller area enclosed by high dose rate contours than for the average case. A similar detonation over water covered, finely divided soil such as clay probably would result in relatively high dose rate contours over larger areas close to the detonation, with a corresponding reduction in the areas of the lower dose rate contours farther out.

5-19 Idealized Contours

In any simplified discussion of the areas affected by residual contamination from fallout, it is convenient to set up a system of contamination dose rate contours which, although simplified and idealized, fit actual contours measured in the field as closely as possible. Figure 5-24 illustrates such a contour system. The idealized contour shown consists of a nearly semicircular upwind portion and a roughly elliptical continuation of the contour in the downwind direction. The radioactivity in the vicinity of ground zero is deposited soon after the detonation, largely from heavy particulate matter, ejecta from the crater, and soil made radioactive by neutron-capture reactions. The parameters that define the contour extent in this region are the upwind distance and ground zero width. The parameters that determine the shape of the downwind contours are the downwind distance, maximum width, and distance to the maximum width. To define the downward axis, it is assumed that the downwind direction and extent are determined by a single wind of constant velocity, the so-

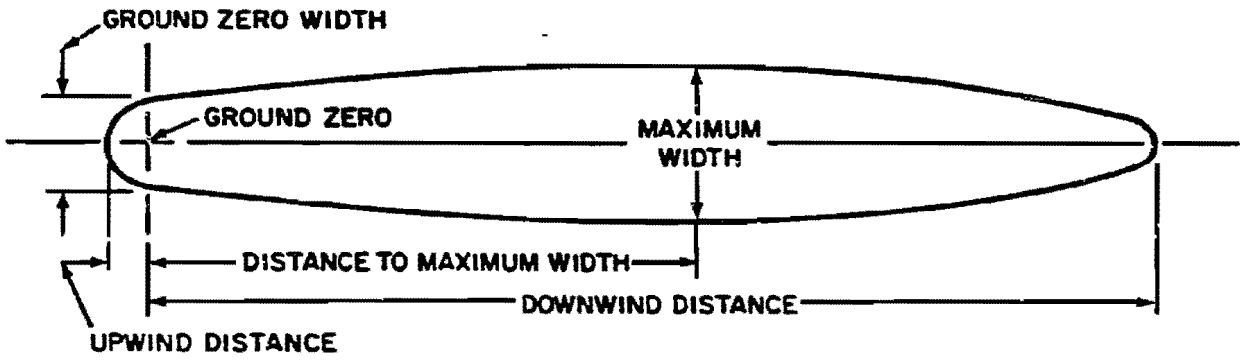

Figure 5-24. (U) Idealized Early Fallout Dose Rate Contour (U)

called effective wind, as described in paragraph 5-20. Usually wide discrepancy from the idealized pattern will result if there are large directional shears in the winds from the surface up to the altitudes of the stabilized cloud. Such shears can distort the idealized pattern seriously, so that, in practice, radical departures from the idealized patterns can be expected. Figure 5-25 compares the idealized dose rate contour pattern to the observed pattern normalized to 1 hour after shot SMALL BOY, a low yield shot in Nevada during which the wind shear was not [illegible]. The actual winds had an effective velocity of about 8 knots and an effective shear of about 30 degrees (effective velocity and effective shear are defined in paragraph 5-20). The idealized pattern is shown for an effective velocity of 10 knots and an effective shear of 15 degrees, for the reasons explained in paragraph 5-20. The downwind distance is expected to increase and the crosswind distance to decrease both with an increase in velocity and with a decrease in shear. These tendencies are noticeable in Figure 5-25; however, for this case of low yield and minimal shear, the idealized contours represent a reasonable approximation of the observed contours.

Figure 5-26 shows a hodograph of a typical summer wind structure over Fort Worth, Texas. This is an example of a severely sheared wind structure. The average wind speed to altitudes of the stabilized cloud from a 2 Mt burst is about 10 knots, but, as a result of directional changes, the effective velocity is only 2.5 knots. The direction of this effective wind is 43.5 degrees east of north.

Figure 5-27 shows a comparison of the idealized dose rate contours for a 2 Mt explosion on the surface and the contours computed by the "Defense Land Fallout Interpretive Code (DELFIC)" (see bibliography) for the wind hodograph shown in Figure 5-26 assuming that the winds stayed constant in time and distance. While this comparison is not a comparison with actual data, it is a comparison with the results of a complex computer code that was developed independent of empirical data and which has demonstrated a very good agreement with available data. The general direction as well as the areas of the two patterns are quite divergent. This comparison is intended to illustrate the lack of confidence that can be placed in the idealized contours for prediction of a fallout pattern for a particular explosion, even if meteorological data

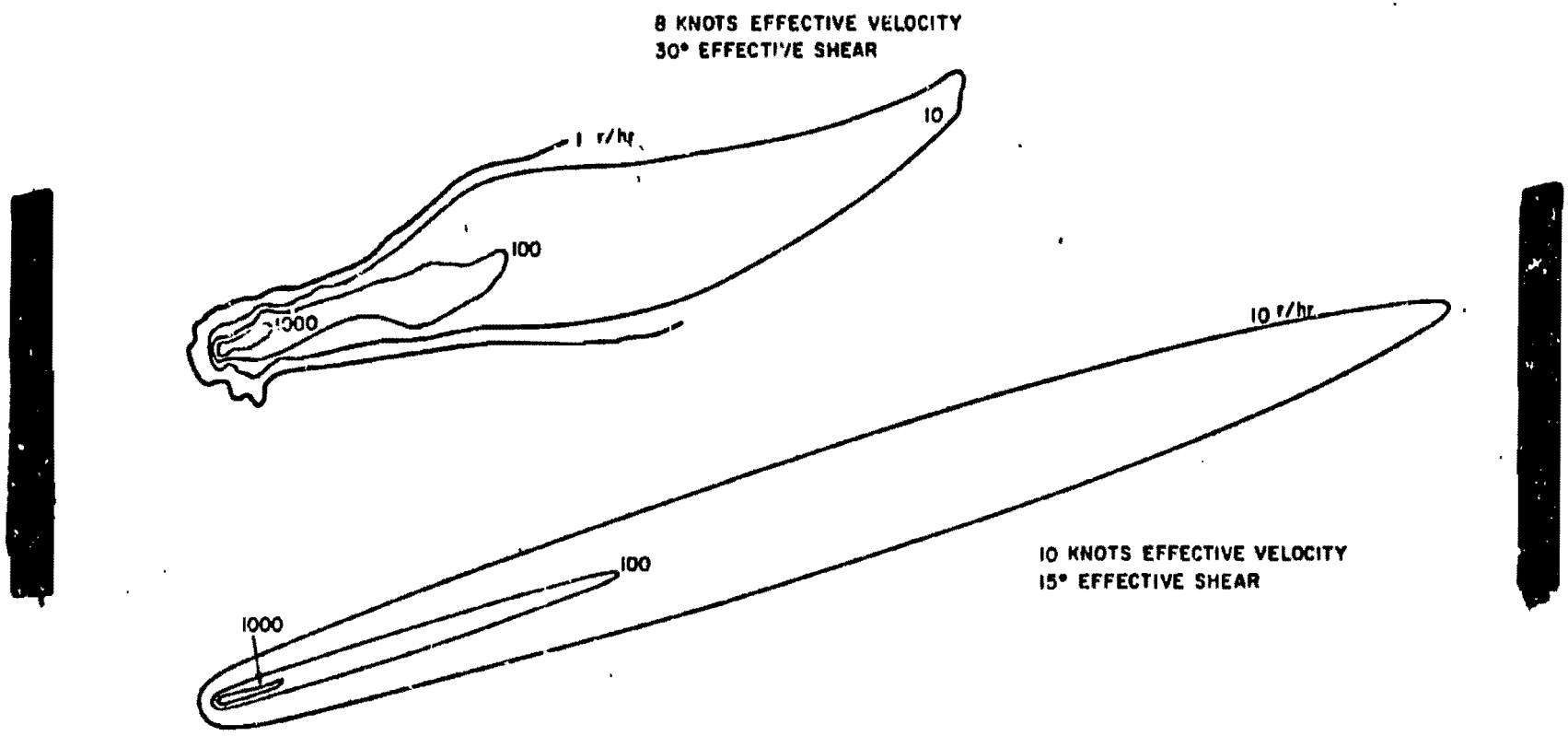

Figure 5-25. [redacted] Comparison of Idealized Dose Rate Contours with Observed Contours from a Low Yield Explosion [redacted]

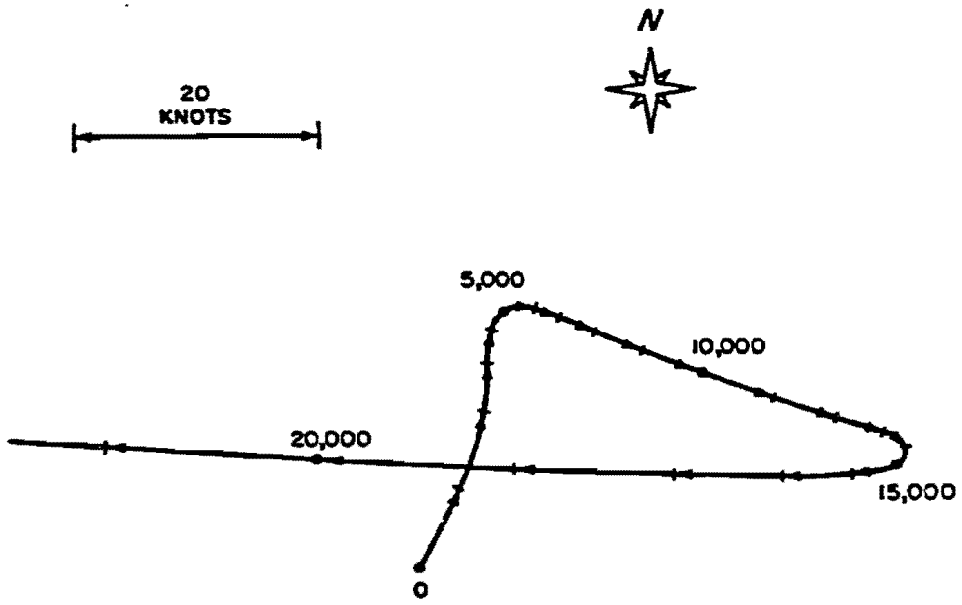

NOTE: NUMBERS ARE METERS OF ALTITUDE.

Figure 5-26. Hodograph of a Typical Summer Wind Structure Over Fort Worth, Texas

at the burst point are known. The contours for the idealized curves were extrapolated to a speed of 2.5 knots even though extrapolation below 10 knots is not recommended. On the other hand, for small yields, or for the case of many weapons, the total dose predicted by the idealized contours over large areas probably would provide a reasonable basis upon which to base casualty predictions.

5-20 Dose Rate Contour Dimensions

Figures 5-28 through 5-37 may be used to draw idealized dose rate contours for land surface explosions with yields between 0.01 kt and 30 Mt. Separate sets of curves are provided for downwind distance, maximum width, and downwind distance to maximum width for effective wind speeds of 10, 20, and 40 knots. Since actual winds are seldom unidirectional and since the radioactive particles that cover the area around ground zero include many that were not carried to high altitudes, the ground zero width is presented independent of wind velocity in Figure 5-37. The upwind distance is estimated to be one-half the ground zero contour widths, i.e., they may be represented by a semi-circle, centered at ground zero, with a radius equal to one-half the ground zero width. The dose rate values obtained from the curves correspond to the values existing at a reference time of 1 hour after burst, 3 feet above a hypothetical smooth, infinite plane; therefore, they must be reduced to account for ground roughness. A reduction

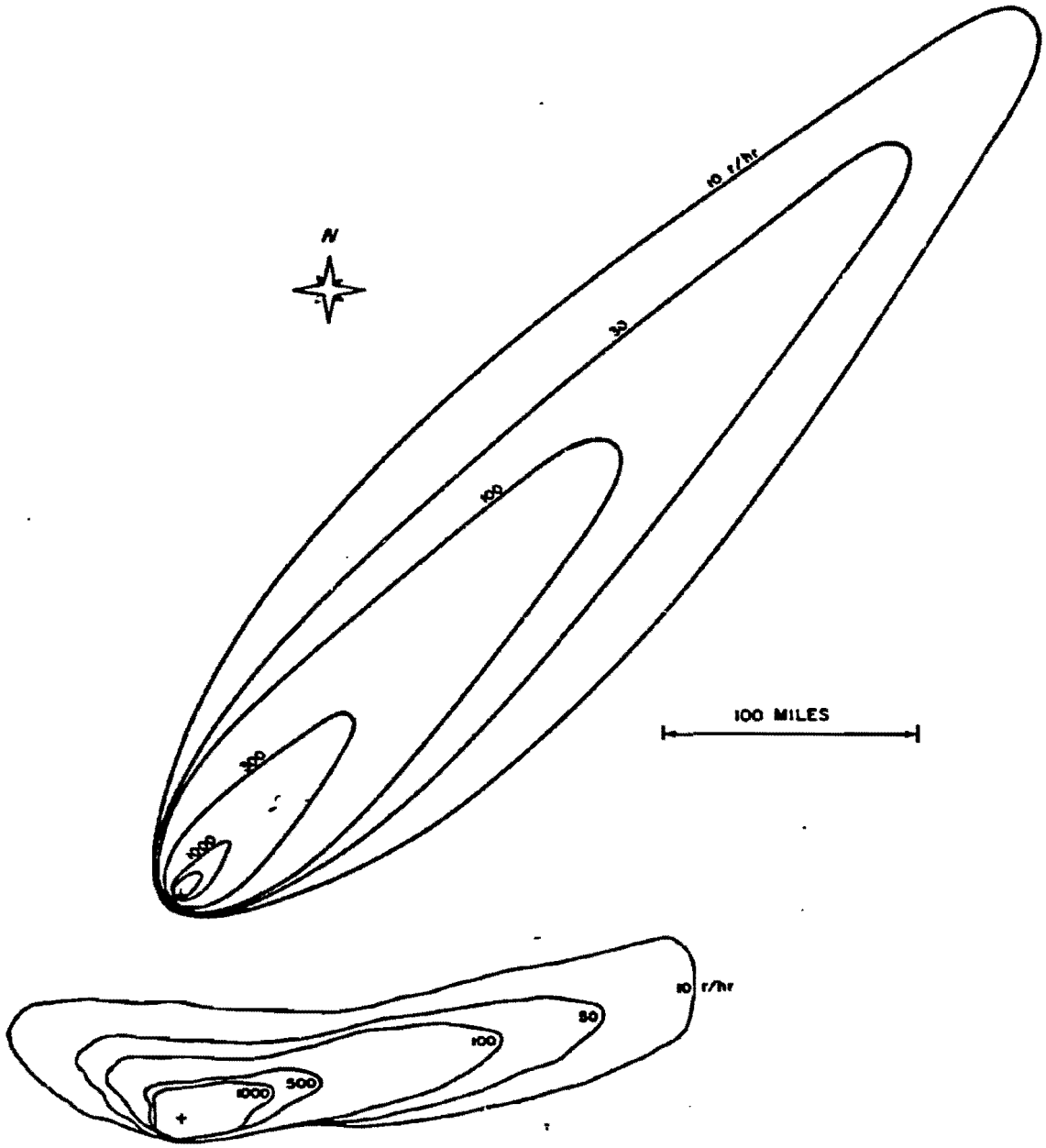

Figure 5-27. [redacted] Comparison of Idealized Dose Rate Contours with Those Calculated by a Complex Computer Code for a 2 Mt Explosion and the Winds of Figure 5-25 [redacted]

factor of 0.7 is appropriate for reasonably level terrain. A factor of 0.5 to 0.6 would be more appropriate for rough and hilly terrain. If additional shielding exists (e.g., foxholes, buildings, tanks), additional shielding factors should be obtained from Section VI, Chapter 9.

To obtain the effective wind for use with Figures 5-28 through 5-36, a wind hodograph similar to that shown in Figure 5-26 should be prepared. The vector averages of the winds from ground zero to the base of the stabilized cloud and to the top of the stabilized cloud should then be obtained. The average of these two average vectors is the effective wind for use with Figures 5-28 through 5-36. The heights of the bottom and top of the stabilized cloud are shown as a function of yield in Figures 5-38 and 5-39, respectively. For wind speeds between the values of 10, 20, and 40 knots that are shown in Figures 5-28 through 5-36, contour values may be obtained by linear interpolation. Extrapolation to values below 10 knots or above 40 knots is not recommended.

As used herein the term "effective shear" refers to the angle between the average vectors to the bottom and top of the stabilized cloud. In the absence of a sufficient quantity of test data with which empirical curves for determining the idealized contours could be constructed, data were generated by use of the Defense Land Fallout Interpretive Code (DELFIC) (see bibliography). An effective shear of 15 degrees was used in the computer calculations from which the curves of Figures 5-28 through 5-36 were derived. In general, increased wind velocity tends to lengthen and narrow the pattern, while increased directional shear tends to shorten and widen the pattern. An effective velocity and an effective directional shear do not define a unique wind structure, i.e., different wind structures could have the same effective velocity and directional shear. It is not recommended that any attempt be made to change the contour values for effective directional shears different from 15 degrees; however, the user should be aware that differences from this value are more likely to result in idealized contours that are farther from reality than if the shear is nearly equal to 15 degrees.

5-21 Decay of Early Fallout

Fission products are composed of a complex mixture of over 200 different forms (isotopes) of 36 elements. Most of these isotopes are radioactive, decaying by the emission of beta particles, frequently accompanied by gamma radiation. About 2 ounces of fission products are formed for each kiloton (or 125 lb/Mt) of fission energy yield. The total radioactivity of the fission products initially is extremely large but it falls off rapidly as the result of radioactive decay.

At 1 minute after a nuclear explosion, when the residual nuclear radiation is postulated to begin, the gamma ray activity of the 2 ounces of fission products from a 1 kt fission yield explosion is comparable with that of about 30,000 tons of radium. For explosions in the megaton-energy range the amount of radioactivity produced is enormous. Although there is a decrease from the 1 minute value by a factor of over 6,000 by the end of a day, the radiation intensity still will be large.

Early fallout consists mainly, but not entirely, of fission products. The following rule indicates how the dose rate of the actual mixture decreases with time: for every seven-fold increase in time after the explosion, the dose rate decreases by a factor of 10. For example, if the radiation dose rate at 1 hour after the explosion is taken as a reference point, then at 7 hours after the explosion the dose rate will have decreased to 1/10; at 7 x 7 = 49 hours (or roughly 2 days) it will be 1/100; and at 7 x 49 = 343 hr (or roughly 2 weeks) the dose rate will be 1/1,000 of that at 1 hour after the burst.

Another aspect of the rule is that at the end of 1 week (7 days), the radiation dose rate will be 1/10 of the value after 1 day. This rule is accurate to within about 25 percent up to 2 weeks or so, and is applicable to within a factor of 2 up to roughly 6 months after the nuclear detonation. After 6 months, the dose rate decreases at a much more rapid rate than predicted by this rule.

Information concerning the decrease of dose rate in the early fallout can be obtained from the continuous curve in Figure 5-40, in which the ratio of the approximate exposure dose rate at any time after the explosion to a convenient reference value, called the 1 hour reference dose rate, is plotted as a function of time in hours.

Table 5-5 gives the results of Figure 5-40 in more convenient, although somewhat less complete, form. The dose rate, in any suitable units, is taken as 1,000 at 1 hour after a nuclear explosion; the expected dose rate in the same units at a number of subsequent times, for the same quantity of early fallout, is then as shown in the table. If the actual dose rate at 1 hour (or any other time) after the explosion is known, the value at any specified time, up to 1,000 hours, can be obtained by simple proportion.

It should be noted that Figure 5-40 and Table 5-5 are used for calculations of dose *rates*. To determine the total radiation dose received it is necessary to multiply the average dose rate by the exposure time. Since the dose rate is decreasing steadily during the exposure, however, appropriate allowance for this must be made. The results of the calculations based on Figure 5-40 are expressed by the curve in Figure 5-41, which gives the total dose received from early fallout, between 1 hour and any other specified time after the explosion, in terms of the 1 hour reference dose rate.

The continuous curve in Figure 5-40, which represents the decrease in dose rate due to gamma radiation from radioactive fallout, sums up the contributions of the more than 200 isotopes in the fission products and in the activity induced by neutrons in the weapons materials for various times after fission. The effects of fractionation, resulting from the partial loss of gaseous krypton and xenon (and their daughter elements), and from other circumstances, have also been taken into account (see paragraph 5-15). The dose rates calculated in this manner vary with the nature of the weapon, but the values plotted in Figure 5-40 are reasonable averages when the fallout activity arises mainly from fission products. The decrease in the dose rate with time cannot be represented by a simple equation that is valid at all times, but it can be approximated to within 25 percent by the straight dashed lines labeled $t^{-1.2}$ for times between 30 minutes to about 5000 hours (about 200 days) after the explosion. After 200 days, the fallout decays more rapidly than indicated by the $t^{-1.2}$ (broken) line, so the continuous

Table 5-5. Relative Theoretical Dose Rates from Early Fallout at Various Times After a Nuclear Explosion

Time (hr)	Relative Dose Rate	Time (hr)	Relative Dose Rate
1	1,000	36	14.0
1-1/2	615	48	9.6
2	435	72	5.9
3	268	100	4.0
5	145	200	1.7
6	116	400	0.75
10	63	600	0.46
15	40	800	0.33
24	22	1,000	0.25

curve should be used to estimate dose rates from fallout at these times.

(U) While the approximation is applicable, the decay of fallout activity at a given location may be represented by the simple expression

$$\dot{D}_t = \dot{D}_1 \, t^{-1.2},$$

where $\dot{D}_t$ is the gamma radiation dose rate at time t after the explosion, and $\dot{D}_1$ is the 1 hour dose rate, which is also the reference dose rate that is used in Figures 5-28 through 5-37. The actual value of $\dot{D}_1$ will depend on the time units, that is, minutes, hours, days, and so on. In this chapter, time is generally expressed in hours, so that the unit time for the reference dose rate $\dot{D}_1$ is 1 hour.

The curves in Figure 5-40 and the equation given above apply so long as there is no change in the quantity of fallout during the time interval under consideration. Therefore, it cannot be used while the fallout is still descending, but only after it is essentially complete, at the particular location. If during the time t, any fallout material is removed, for example, by weathering or by washing away, or if any additional material is brought to the given point by wind or by another nuclear explosion, neither the curves nor the equation will predict the decay of the fallout activity correctly.

Measurements made on actual fallout from weapons tests indicate that, although the $t^{-1.2}$ decay represents a reasonable average, exponents in the range of -0.2 to -2, rather than -1.2, are sometimes needed to represent the rate of decay. In fact, different exponents are sometimes needed for different times after the explosion. These anomalies, which apparently arise from the particular circumstances of the explosion, are very difficult to predict, except in cases where a large quantity of neutron-induced activity is known to have been produced, either in the ground or in weapon components or both. Furthermore, fallout from two or more explosions occurring at different times will change the observed decay rate completely. For measurements made over a long period of time after the burst, weathering will tend to alter the dose rates unpredictably. In an actual situation following a nuclear detonation, estimates based on either the $t^{-1.2}$ decay rule or even on the continuous curves in Figures 5-40 and 5-41 must be used with caution and should be verified by actual measurements as frequently as possible.

In principal, either Figures 5-40 and 5-41, or the $t^{-1.2}$ decay equation could be used to estimate the total dose received from fallout in a contaminated area, provided that all of the fallout arrives in a short time. Actually, the contaminated particles may descend for several hours, and without knowing the rate at which the fission products reach the ground, useful calculations cannot be made. However, after the fallout has ceased to arrive, either the figures or the equation will provide rough estimates of radiation doses up to about 200 days after the explosion, provided one measurement of the dose rate is available. After 200 days, the solid curve of Figure 5-40 together with Figure 5-41 should be used. However, at such long times after the explosion, it is not likely that the standard decay pattern will persist. It is advisable to make frequent measurements and to derive an appropriate decay scheme.

Table 5-6 shows the percentage of the infinity (residual radiation) dose that would be received from a given quantity of early fallout, computed from 1 hour to various times after a nuclear explosion. The infinity dose is that which would be received as a result of continued exposure to a certain quantity of early fallout for many years. These data can be used to determine the proportion of the infinity dose received during any specified period following the complete deposition of the early fallout from a nuclear explosion. If the decay followed the

Table 5-6. [redacted] Percentage of the Infinite Residence Dose Received from 1 Hour to Various Times After Explosion [redacted]

Time (hr)	Percent of Infinite Dose	Time (hr)	Percent of Infinite Dose
2	15	72	68
4	28	200	78
6	33	500	85
12	44	1,000	89
24	53	2,000	93
48	63	5,000	98

[redacted] $t^{-1.2}$ decay law given above beyond 200 days, the infinite residence dose, starting at 1 hour, would be equal to 5 times the $H + 1$ hour dose rate, and this convenient rule of thumb has been used frequently. However, in view of the more rapid decay of the actual fission product mix after about 5,000 hours (see Figure 5-40), a better rule of thumb is that the infinite residence dose is equal to 4 times the $H + 1$ hour dose rate.

[redacted] Figure 5-42 provides a convenient means for determining the total dose received during various times of occupancy of a contaminated area as a function of time of entry. For purposes of prediction, the time of entry may be taken to be the time of arrival of the fallout. Within the accuracy of Figures 5-28 through 5-37, this time may be taken to be equal to the distance from ground zero divided by the effective wind speed, i.e., the buildup of activity during the finite arrival time is neglected.

5-22 Bursts in the Transition Zone [redacted]

[redacted] The deposition patterns and decay rate of the contamination from weapons that are burst very close to the surface will be similar to those for a weapon of the same yield burst on the surface. However, as the height of burst increases, the activity deposited locally as fallout decreases, and the residual contamination resulting from the neutron-induced activity becomes more important. The exact scaling of the fallout dose rate contour values with height of burst is uncertain. Residual contamination from tests at heights of burst immediately above or below $100W^{0.35}$ feet has been small enough to permit approach to ground zero within the first 24 to 48 hours after detonation without exceeding reasonable peacetime dosages. In these tests the mass of the tower, special shielding, and other test equipment contributed to considerable part of the fallout actually experienced, and neutron-induced activity in the soil added further to the total contamination. Thus, for heights of burst of $100W^{0.35}$ feet or greater, contamination from fallout will probably not be sufficiently extensive to affect military operations materially. Figure 5-43 shows this relation plotted as minimum height of burst versus weapon yield. It must not be assumed that even low to intermediate yields will never present a residual radiation problem when burst above $100W^{0.35}$ feet. The neutron-induced gamma activity can be intense in a relatively small area around ground zero. A better idea of the contamination pattern, dose rate contour values, and decay rate of the residual radiation from the above types of explosions generally will be obtained by basing the predictions on the induced activity as described in Section II of this chapter. In view of the uncertainty involved and the lack of experimental data for high yields burst over land at heights of burst near $100W^{0.35}$ feet, a more conservative estimate of $180W^{0.4}$ feet may be desirable for use under some circumstances as the height at which fallout becomes negligible.

[redacted] A rough estimate of the dose rate contour values for bursts in the transition zone may

be obtained by applying an adjustment factor from Figure 5-44 to the dose rate contour values obtained from Figures 5-28 through 5-37. For bursts in the upper quarter of the fallout transition zone, neutron-induced activity must also be considered. For bursts in the lower three-quarters of the transition zone the neutron-induced gamma activity generally can be neglected compared to the fallout activity.

5-23 Underground Bursts

A large amount of residual contamination is deposited in the immediate vicinity of the burst point after an underground detonation, because most of the radioactive material falls from the column and cloud to the surface rapidly. A very shallow underground burst conforms closely to the contamination mechanisms and patterns described in paragraphs 5-19 and 5-20 for land surface bursts. As depth of burst increases, a greater percentage of the total available contaminant is deposited as local fallout, until for the case of no surface venting, all of the contamination is contained in the volume of ruptured earth surrounding the point of detonation.

Figure 5-45 shows a depth multiplication factor as a function of scaled depth of burst for yields between 1 kt and 1 Mt. These factors are applied to the linear dimensions of the dose rate contours for a land surface burst of the same yield, which must be obtained from Figures 5-28 through 5-37. This treatment yields dose rate contours for underground bursts that have shapes similar to the comparable surface burst dose rate contours. Although there is some reason to believe that this is not a valid representation, this treatment does yield a fair representation of the total activity deposited in early fallout patterns. Variations in soil type and other factors introduce additional uncertainties, which are reflected by the broad band in Figure 5-45.

5-24 Beta Radiation

The hazard from the gamma rays of the residual radiation generally will exceed that from beta particles, except in those cases where intimate contact with beta emitting particles occurs. Such contact may result when an individual lies prone in a contaminated area, or when particles fall directly on the scalp. Burns that range from being superficial to severe may result from such exposures (see paragraph 10-27, Chapter 10). The severity of the burn will depend both on the intensity of the radiation source in contact with the body and on the promptness with which the particles are washed from the skin, i.e., the length of exposure.

Problem 5-8. Calculation of Fallout Gamma Radiation Dose Rate Contours for Surface Bursts

[redacted] Figures 5-28 through 5-37 show idealized dose rate contour parameters for residual fallout radiation from surface bursts of weapons with yields between 0.01 kt and 30 Mt. The dose rates are given in terms of exposure rate in roentgens per hour as calculated by the DELFIC computer code for a receiver 3 feet above an infinite plane surface. Within the accuracy of the data, 1 roentgen may be taken to be equal to 1 rad. The actual exposure will be about 0.7 times that shown for the plane surface if the terrain is smooth, and 0.5 to 0.6 times the values for the plane surface if the terrain is rough or hilly. The basic data are presented for weapons from which all the yield results from fission; but, as described below, the data can also be used to obtain fallout contours for weapons for which the fission yield is only a fraction of the total yield, and for which essentially all of the contamination produced (90 percent or more) results from fission products. The dose rate values are given for a reference time of $H + 1$ hour. The more distant parts of the larger contours do not exist at $H + 1$ hour, because the fallout that eventually reaches some of these more distant areas is still airborne at that time. The dose rate contours do exist at later times when fallout is complete, but with dose rate contour values reduced according to the appropriate decay factor from Figure 5-40. Visual interpolation may be used for dose rate contour values between those for which curves are given. Extrapolation to dose rate contour values higher or lower than those shown in the families of curves cannot be done accurately and should not be attempted.

[redacted] An approximate estimate of the area within particular dose rate contour may be calculated by assuming that the roughly elliptical contour obtained by plotting the parameters given in Figures 5-28 through 5-37 is an ellipse. The formula for this area is: Area = $\pi ab/4$ where a is downwind distance plus upwind distance, and b is maximum crosswind distance. It must be realized that the dose rate contours are not true ellipses, and that this formula is only an approximation.

[redacted] The decay factors from Figure 5-40 should be used to obtain dose rate values for times other than $H + 1$ hour. To obtain contour values for effective winds other than those given in the curves, that is, 10, 20, and 40 knots, linear interpolation may be used. Thus, the downward distance for a 30 knot effective wind speed would be midway between the 20 knot and 40 knot downwind distances.

[redacted] Contour shapes and sizes are a function of the total yield of the weapon, whereas the dose rate contour values are determined by the fission yield. Thus, if only a fraction of the total yield of the weapon results from fission, and this fraction is known, Figures 5-28 through 5-37 may be used to estimate fallout contours resulting from the detonation of such a weapon. The dose rate for the dimension of interest as read from the figures opposite the total yield must be multiplied by the ratio of fission yield to total yield to obtain the true dose rate value for that dimension. Similarly, to obtain contour dimensions for a particular dose rate, the value of the desired dose rate must be divided by the ratio of fission to total yield, and the dimension of the resultant dose rate read from the figure opposite the total yield.

[redacted] *Example* [redacted]

Given: A hypothetical weapon with a total yield of 600 kt, of which 200 kt results from fission, is detonated on a land surface with 10 knot effective wind conditions.

[redacted]

[redacted]

Find: The contour parameters for a dose rate of 50 rads/hr at $H + 1$ hour reference time over rough, hilly terrain.

Solution: The 50 rads/hr contour for a fission yield to total yield ratio of 200/600 = 1/3 corresponds to the contour of 50 ÷ 1/3 = 150 rads/hr for a weapon for 600 kt fission yield. The dose rate above contaminated rough and hilly terrain is about one-half that above an ideal smooth plane. Thus the desired contour parameters can be obtained by entering Figures 5-28, 5-31, 5-34, and 5-37 with a yield of 600 kt and reading the parameter values corresponding to an $H + 1$ hour dose rate of 2 x 150 = 300 rads/hr (the factor 2 corrects for the rough, hilly terrain).

Answer: The $H + 1$ hour dose rate parameter values are shown below.

[redacted] *Reliability.* The degree to which wind and other meteorological conditions affect these contour parameters cannot be overemphasized. The contours presented in these curves have been idealized in order to make it possible to present average, representative values for planning purposes. Due to these limitations, a meaningful percentage reliability figure cannot be assigned to the idealized fallout pattern.

[redacted] *Related Material.* See paragraphs 5-17 through 5-20.

Parameter	Source Figure	Parameter Value for a 10 Knot Effective Wind (miles)
Downwind Distance	5-28	80.0
Maximum Width	5-31	9.0
Distance to Maximum Width	5-34	25.0
Ground Zero Width	5-37	4.4
Upwind Distance	5-37*	2.2

*[redacted] Upwind distance equals one-half the ground zero width.

[redacted]

[redacted]

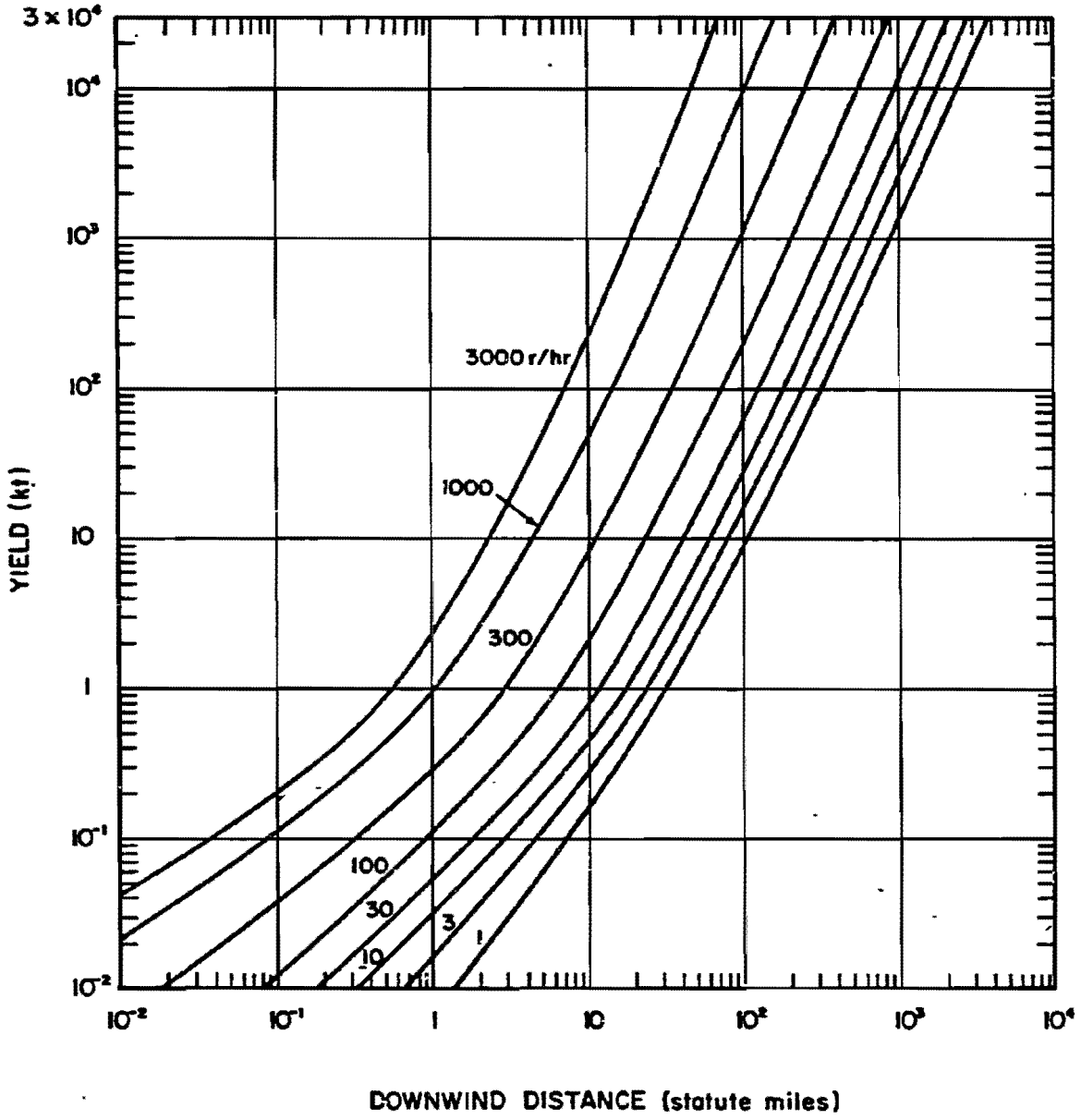

Figure 5-28. [redacted] Downwind Distance as a Function of Yield, .10 Knot Effective Wind [redacted]

[redacted]

[redacted]

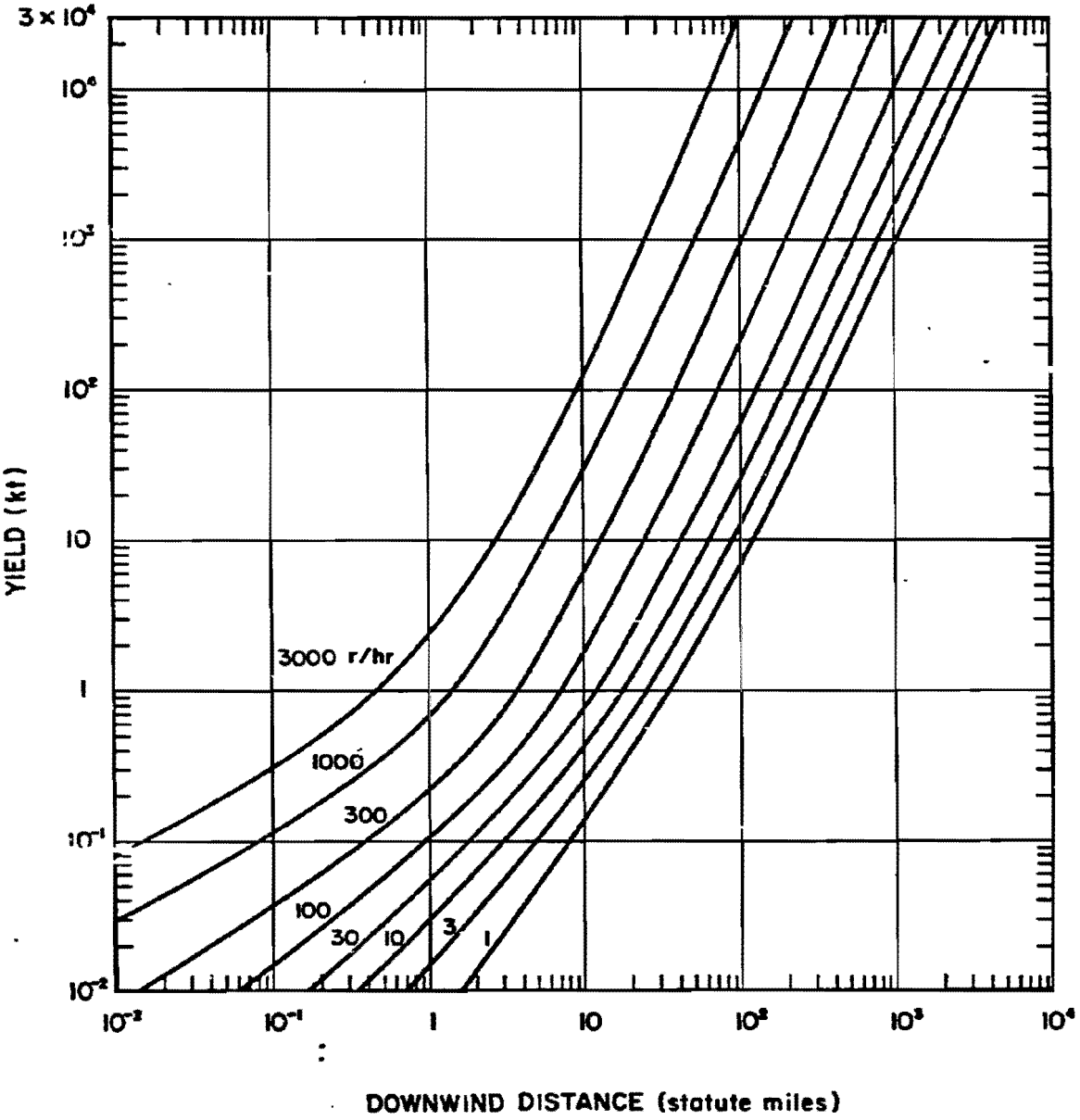

Figure 5-29. [redacted] Downwind Distance as a Function of Yield, 20 Knot Effective Wind [redacted]

[redacted]

[redacted]

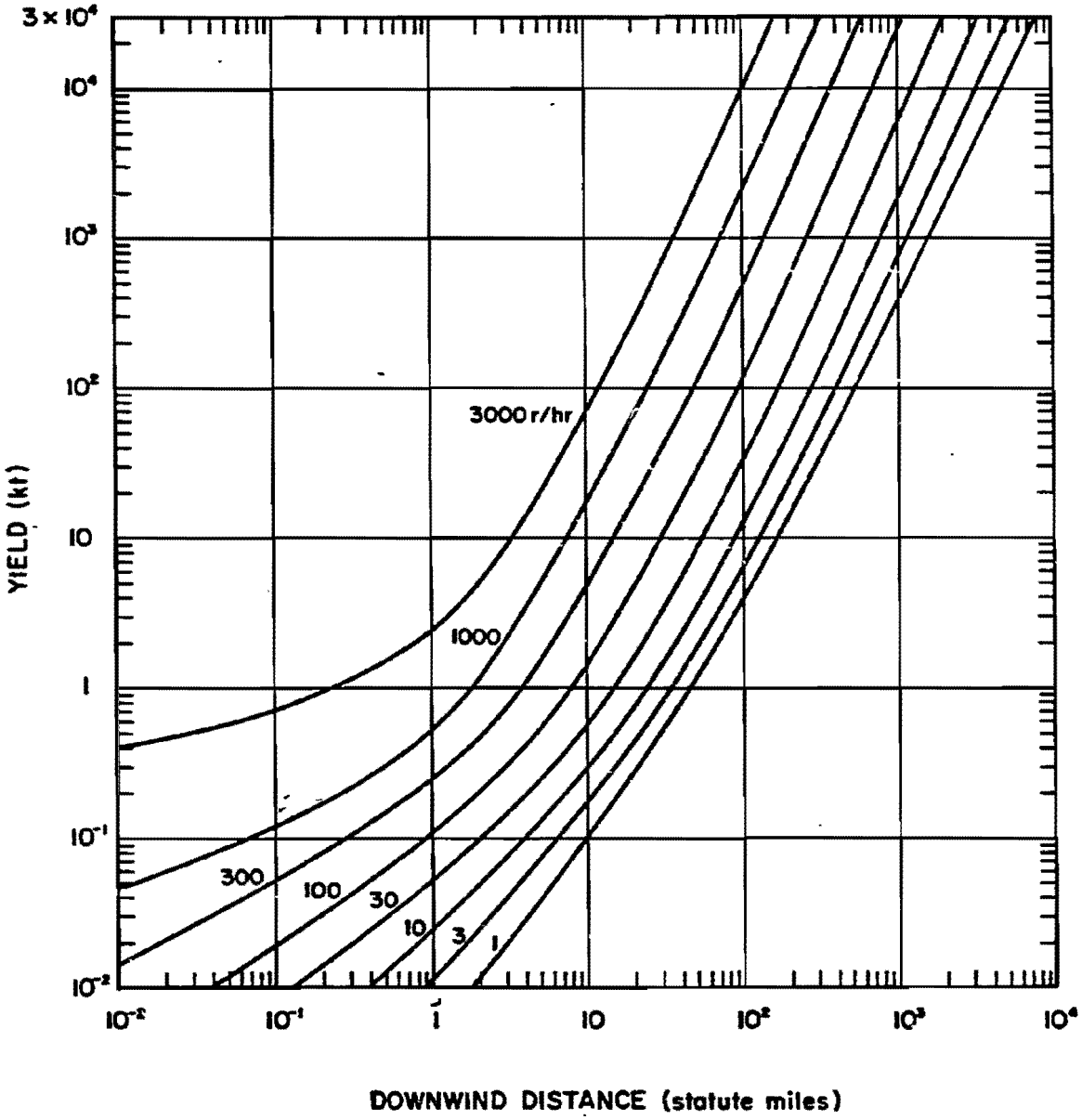

Figure 5-30. [redacted] Downwind Distance as a Function of Yield, 40 Knot Effective Wind [redacted]

[redacted]

[redacted]

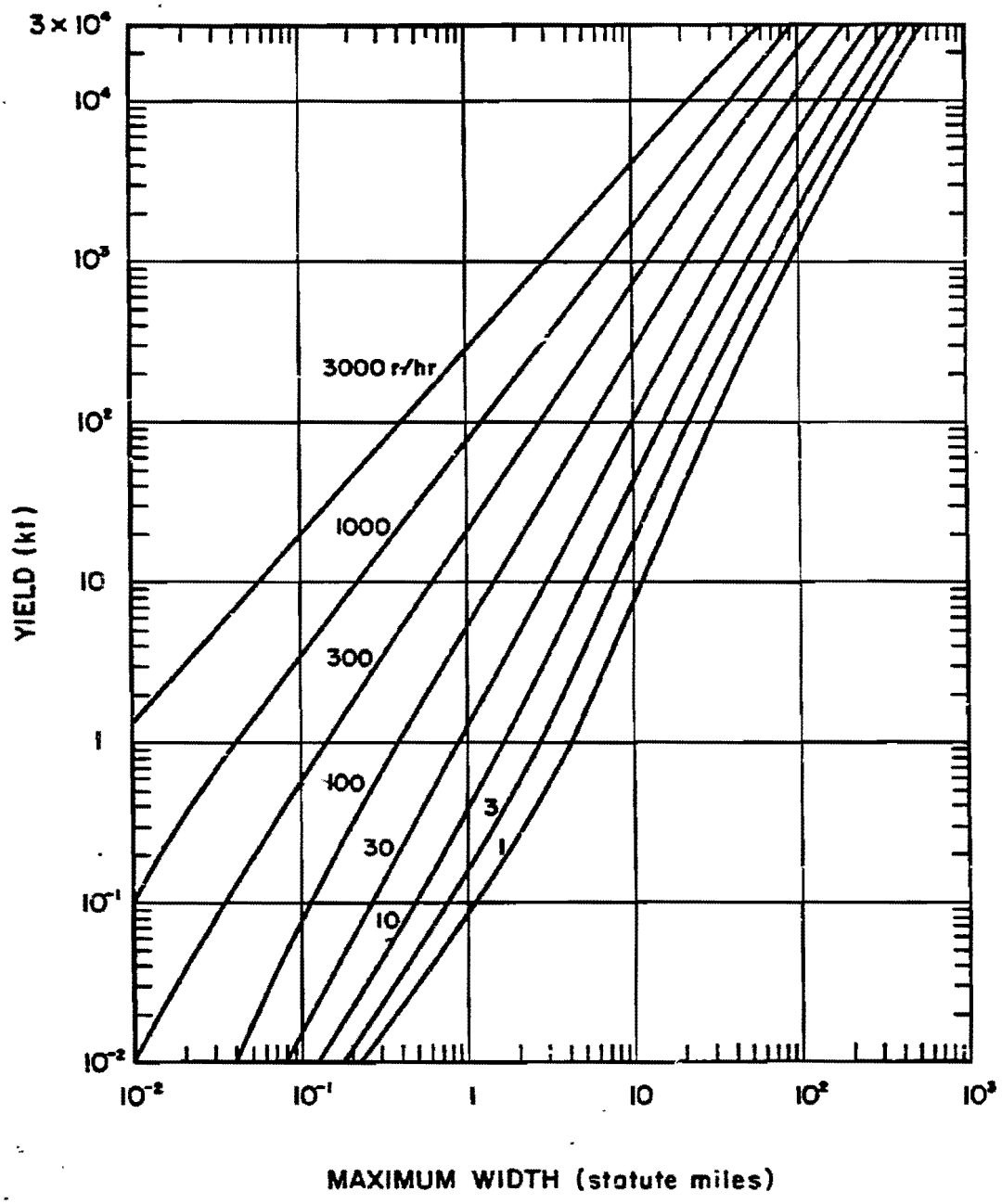

Figure 5-31. [redacted] Maximum Width as a Function of Yield, 10 Knot Effective Wind [redacted]

[redacted]

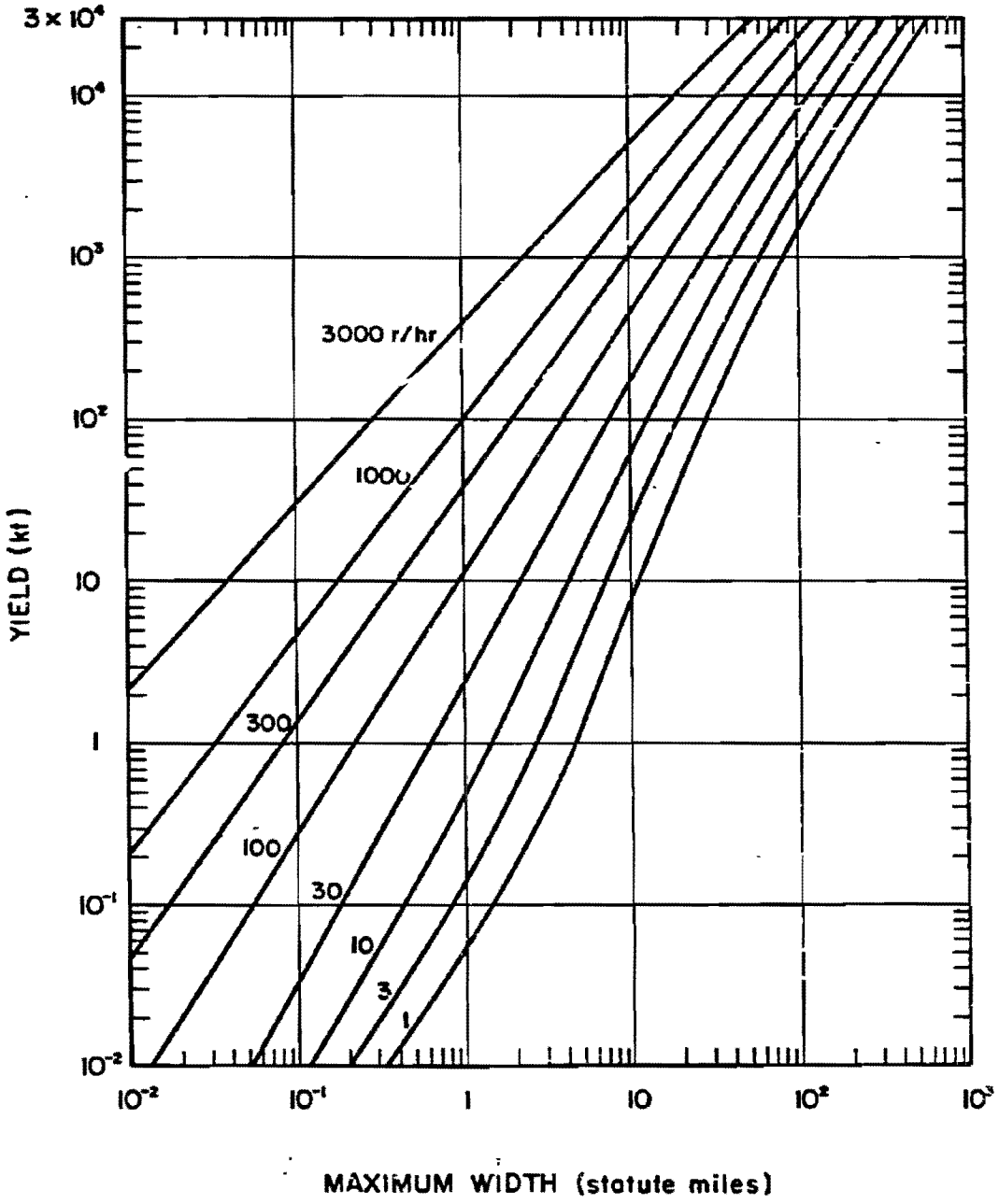

Figure 5-32. [redacted] Maximum Width as a Function of Yield, 20 Knot Effective Wind [redacted]

[redacted]

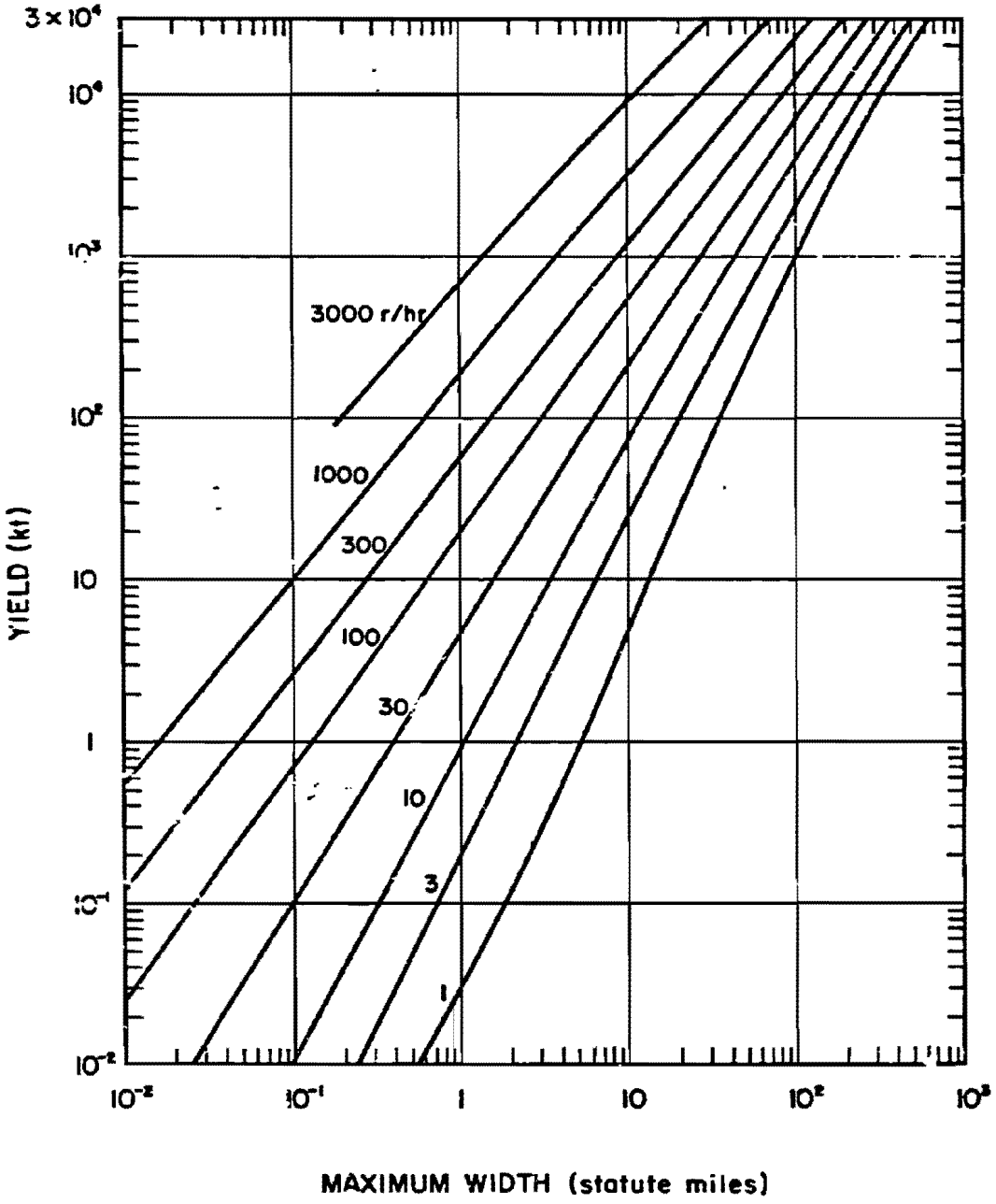

Figure 5-33. [redacted] Maximum Width as a Function of Yield, 40 Knot Effective Wind [redacted]

[redacted]

[redacted]

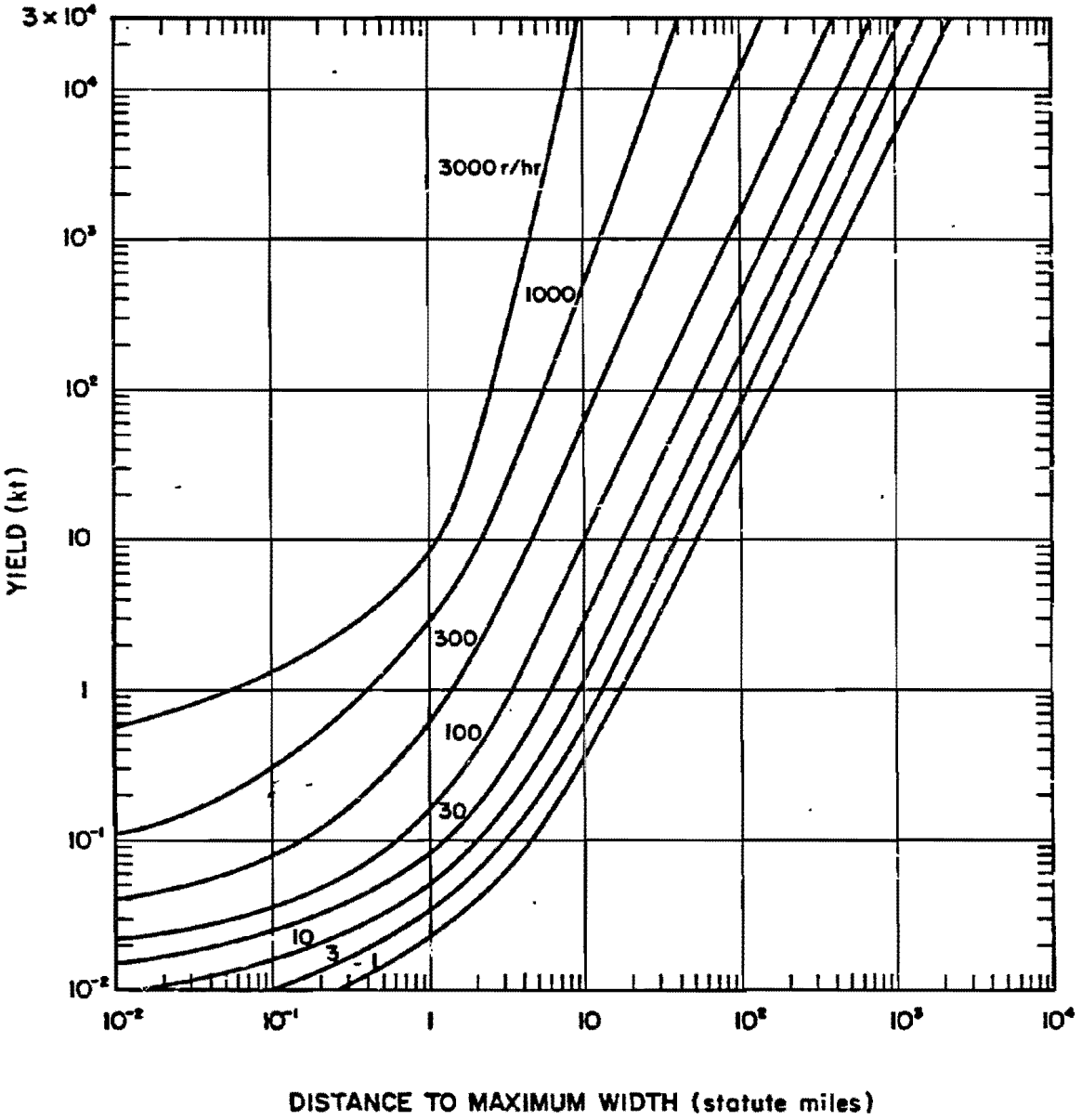

Figure 5-34. [redacted] Distance to Maximum Width as a Function of Yield, 10 Knot Effective Wind [redacted]

[redacted]

[redacted]

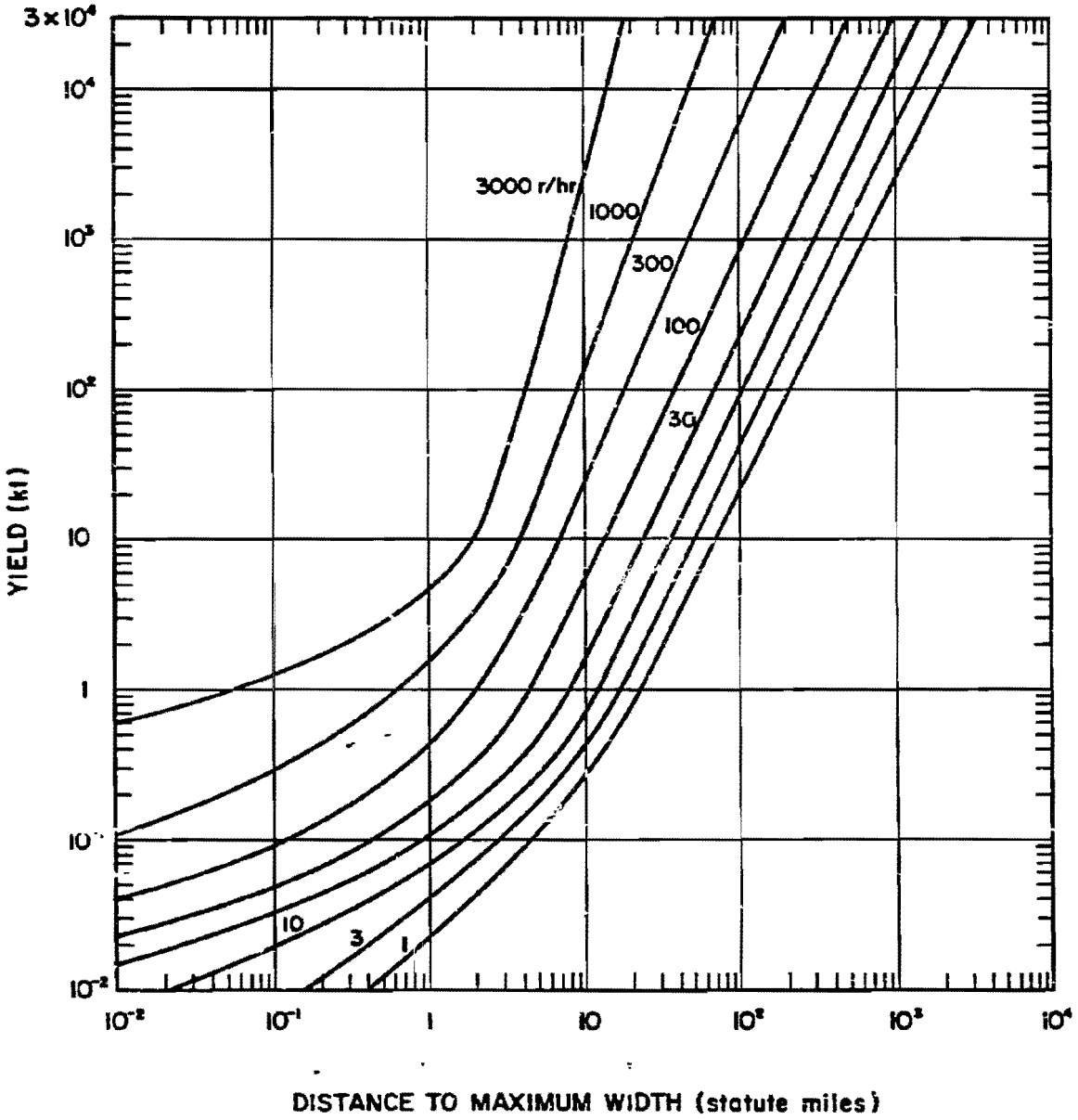

Figure 5-35. [redacted] Distance to Maximum Width as a Function of Yield, 20 Knot Effective Wind [redacted]

[redacted]

[redacted]

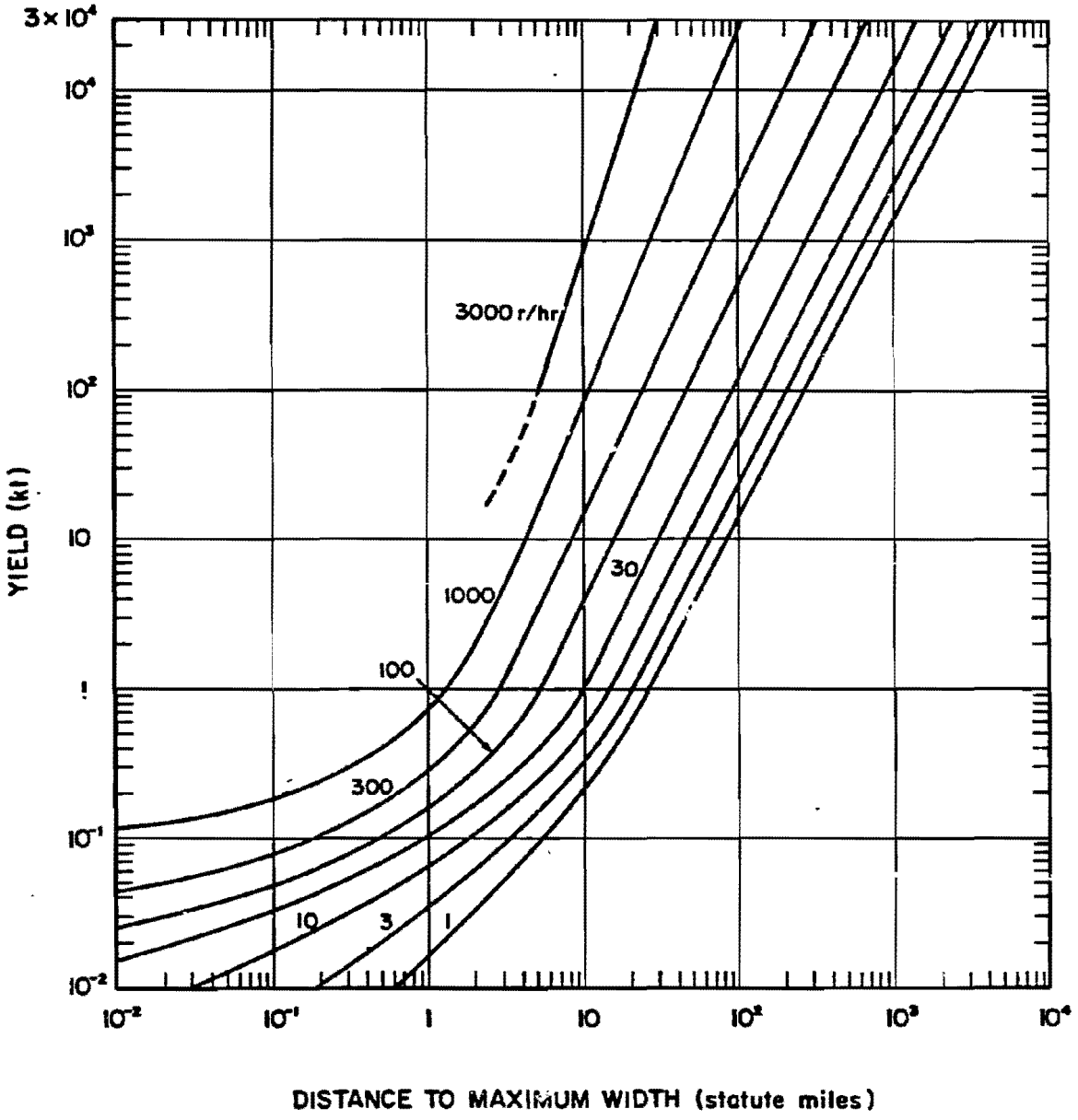

Figure 5-36. [redacted] Distance to Maximum Width as a Function of Yield, 40 Knot Effective Wind [redacted]

[redacted]

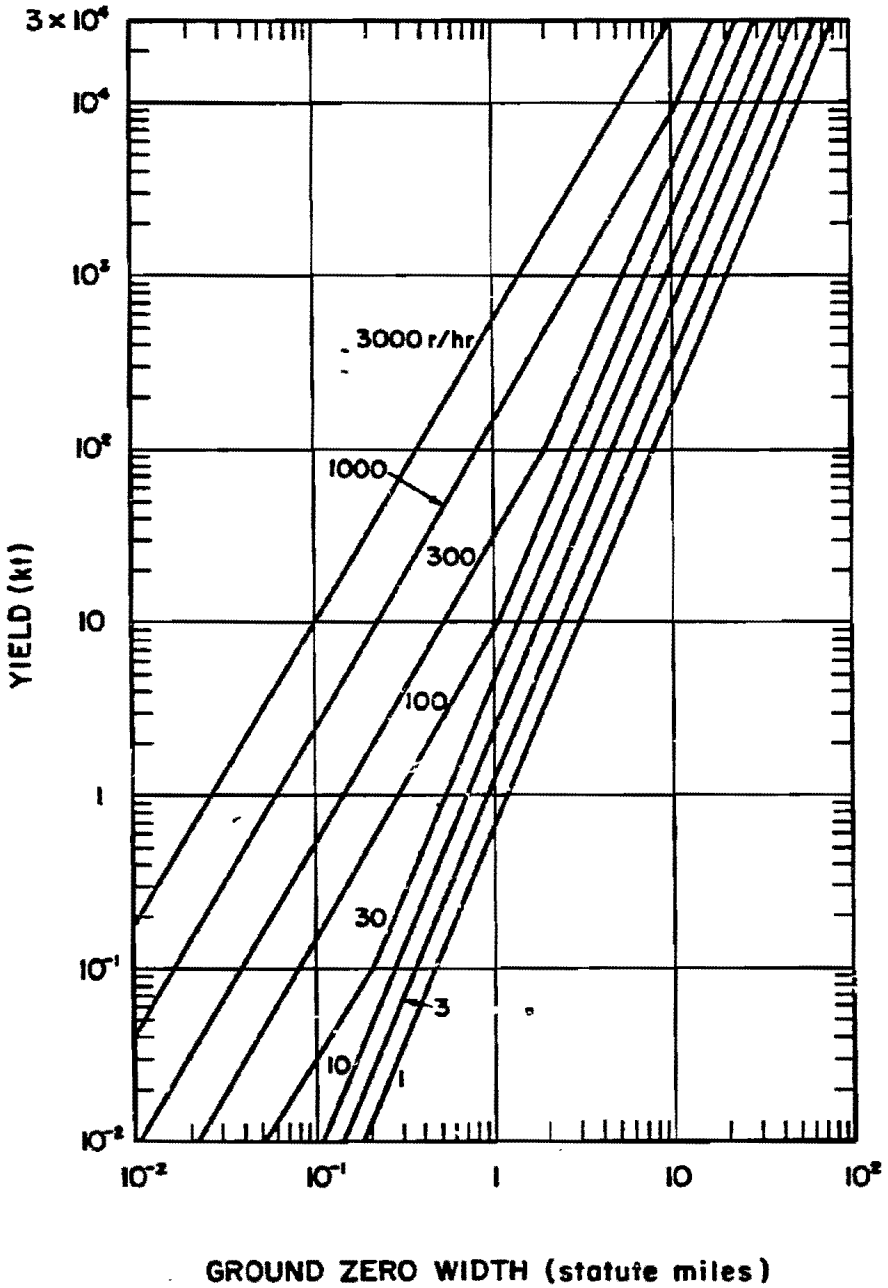

Figure 5-37. [redacted] Ground Zero Width as a Function of Yield [redacted]

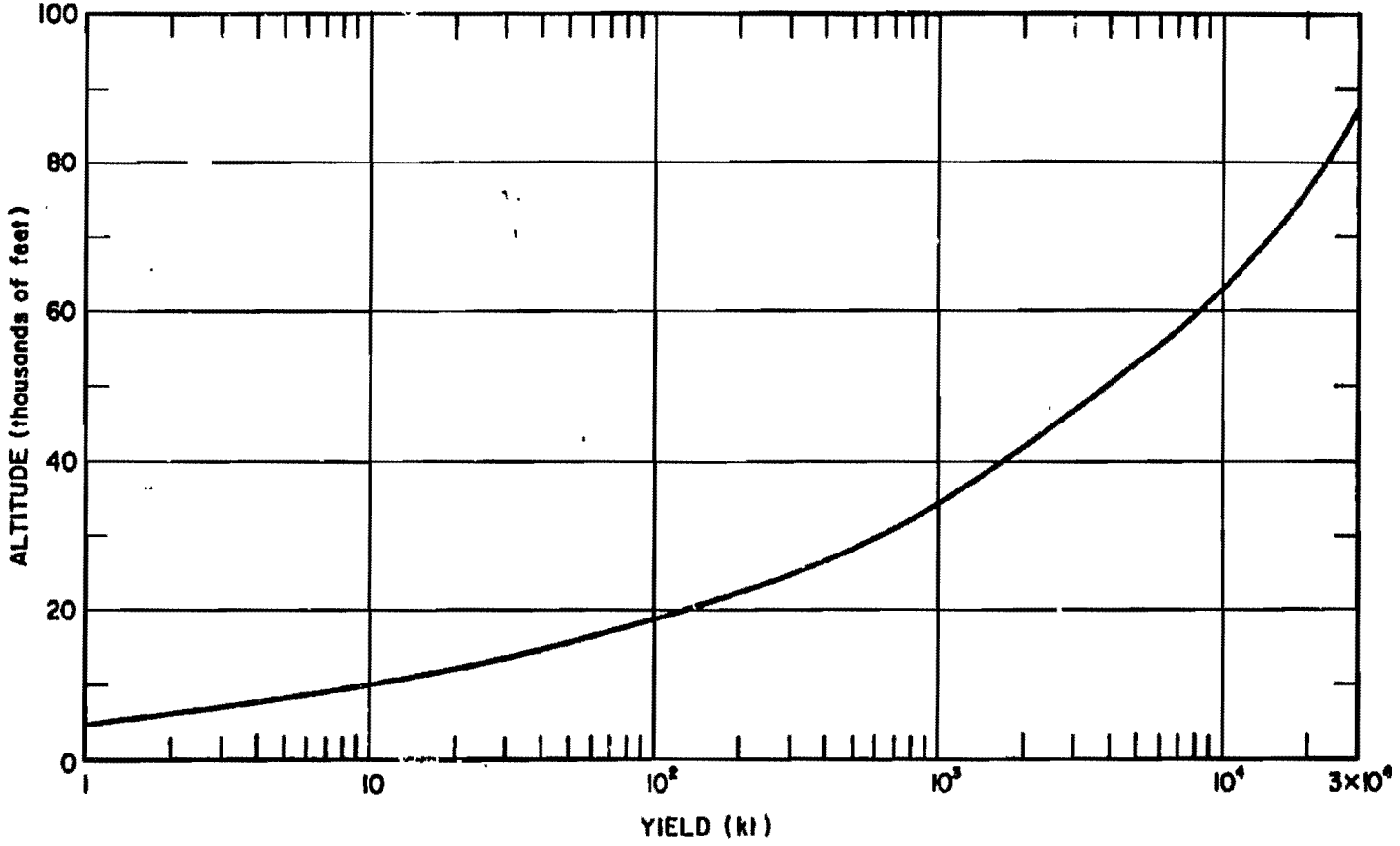

Figure 5-38. [redacted] Height of the Stabilized Cloud Bottom as a Function of Yield [redacted]

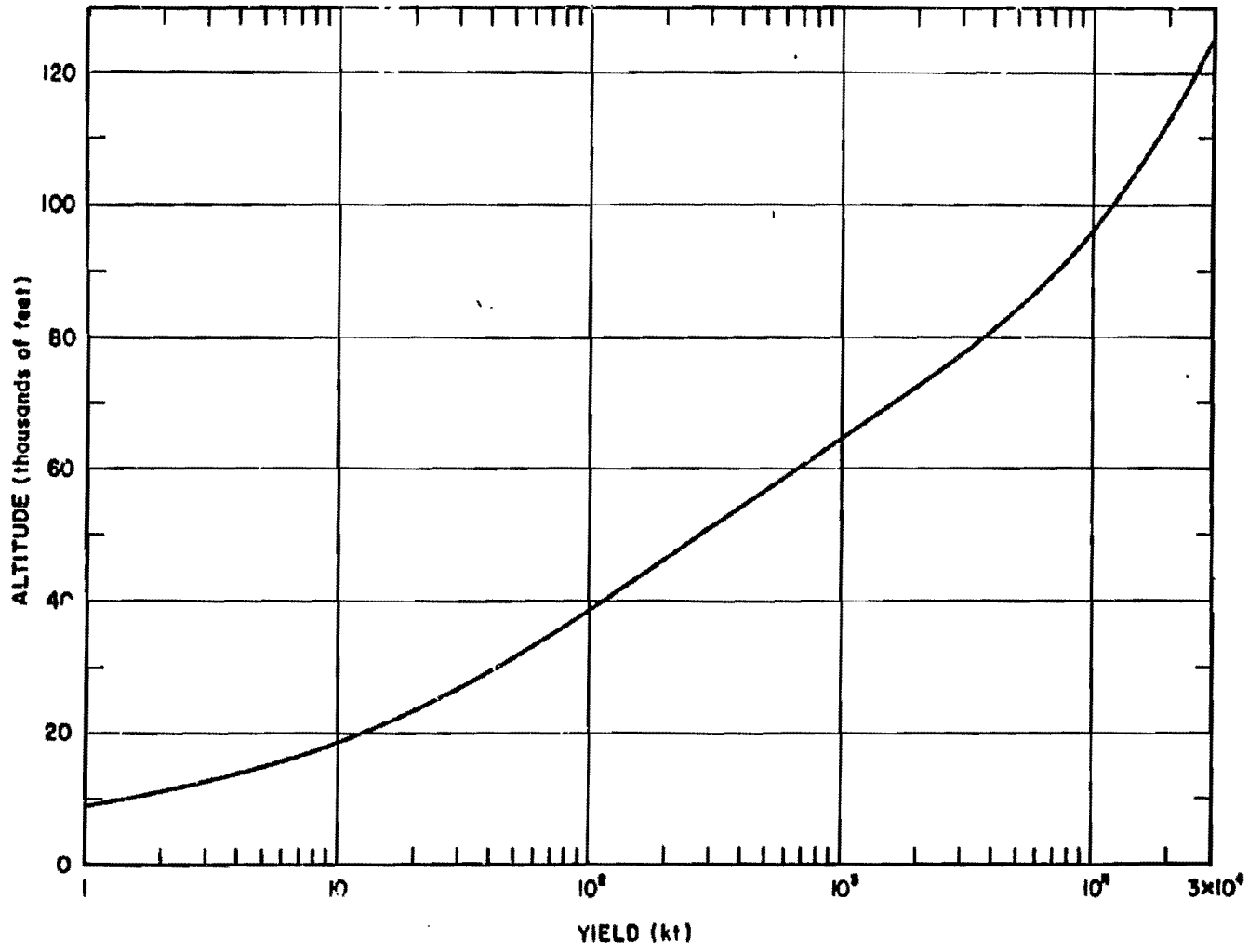

Figure 6-39. [redacted] Height of the Stabilized Cloud Top as a Function of Yield [redacted]

[redacted]

Problem 5-9. Calculation of Fission Product Decay

[redacted] Figure 5-40 provides fission product decay factors as a function of time after burst. The dose rate at any time can be obtained by multiplying the $H + 1$ hour dose rate by the appropriate decay factor from Figure 5-40. The decay curve also may be used to determine the value of the $H + 1$ hour dose rate from the dose rate measured at a later time. In this case the measured dose rate is divided by the appropriate decay factor.

[redacted] *Example 1* [redacted]

Given: The dose rate at a given point at 1 hour after a nuclear explosion is 500 rads/hr.

Find: The dose rate at that point 12 hours after the explosion.

Solution: From Figure 5-40, the decay factor at 12 hours is 0.05.

Answer: The dose rate at 12 hours is

$$500 \times 0.05 = 25 \text{ rads/hr.}$$

[redacted] *Example 2* [redacted]

Given: The dose rate at a given point 10 hours after detonation is 72 rads/hr.

Find: The dose rate at the same point 1 hour after the detonation.

Solution: From Figure 5-40, the decay factor at 10 hours is 0.06.

Answer: The dose rate at 1 hour is

$$\frac{72}{0.06} = 1{,}200 \text{ rads/hr.}$$

[redacted] *Related Material.* See paragraph 5-21. See also Figure 5-42.

[redacted]

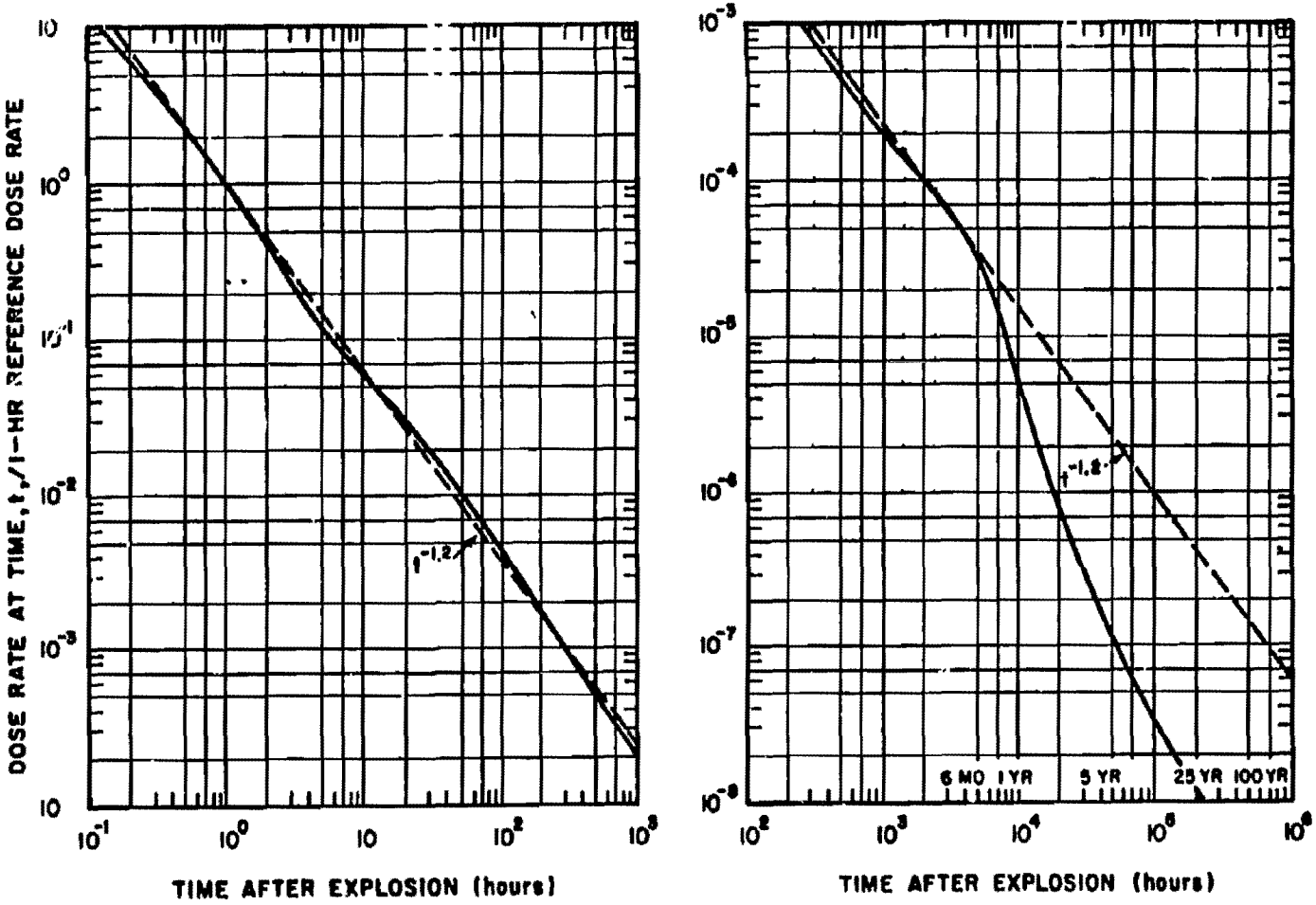

Figure 5-40. [redacted] Fission Product Decay Factors Normalized to Unity at 1 Hour After Detonation [redacted]

Problem 5-10. Calculation of Gamma Radiation Dose as a Function of Time

Figure 5-41 shows the integrated gamma dose received in a fallout-contaminated area as a function of time after $H + 1$ hour (~0.042 day). This curve was generated by integrating the solid curve of Figure 5-40. If the true dose rate at some time between $H + 1$ hour and $H + 1{,}000$ days is known, Figure 5-41 can be used to estimate the dose accumulated during any time interval in this time range, *provided* the fallout decays as shown in Figure 5-40.

Example

Given: A dose rate of 20 rads/hr is measured in a fallout contaminated area 4 hours after the explosion (fallout had ceased to arrive at this time).

Find: The dose received by personnel who enter the area at $H + 4.8$ hours and remain for 2.5 hours before leaving the area.

Solution:

$$H + 4.8 \text{ hr} = H + 0.2 \text{ day}$$

$$(H + 4.8 + 2.5) \text{ hr} = H + 7.3 \text{ hr}$$

$$= H + 0.304 \text{ day}$$

From Figure 5-41, the normalized dose that would be received between $H + 1$ hour and $H + 0.304$ day is 1.55. Similarly, the normalized dose received between $H + 1$ hour and $H + 0.2$ day is 1.3. Therefore, the *normalized* dose received by these personnel between $H + 0.2$ and $H + 0.304$ day would be:

$$1.55 - 1.3 = 0.25$$

To convert this to actual dose received, use is made of the $H + 4$ hour dose rate (20 rads/hr). From Figure 5-40, the normalized dose rate at $H + 4$ hour is found to be 0.18. The $H + 1$ hour dose rate is

$$\frac{20}{0.18} = 111 \text{ rads/hr.}$$

Answer: The dose that the personnel can expect to receive is found by multiplying the $H + 1$ hour dose rate by the normalized dose obtained from Figure 5-41:

$$111 \times 0.25 \approx 28 \text{ rads.}$$

NOTE: The dose calculated above is only the dose received during the stay at the particular spot in question. Additional dose would be accumulated during entry and exit. The amount of the additional dose would depend on the means of transportation and the size of the contaminated area.

Related Material. See paragraph 5-21. See also Figure 5-42.

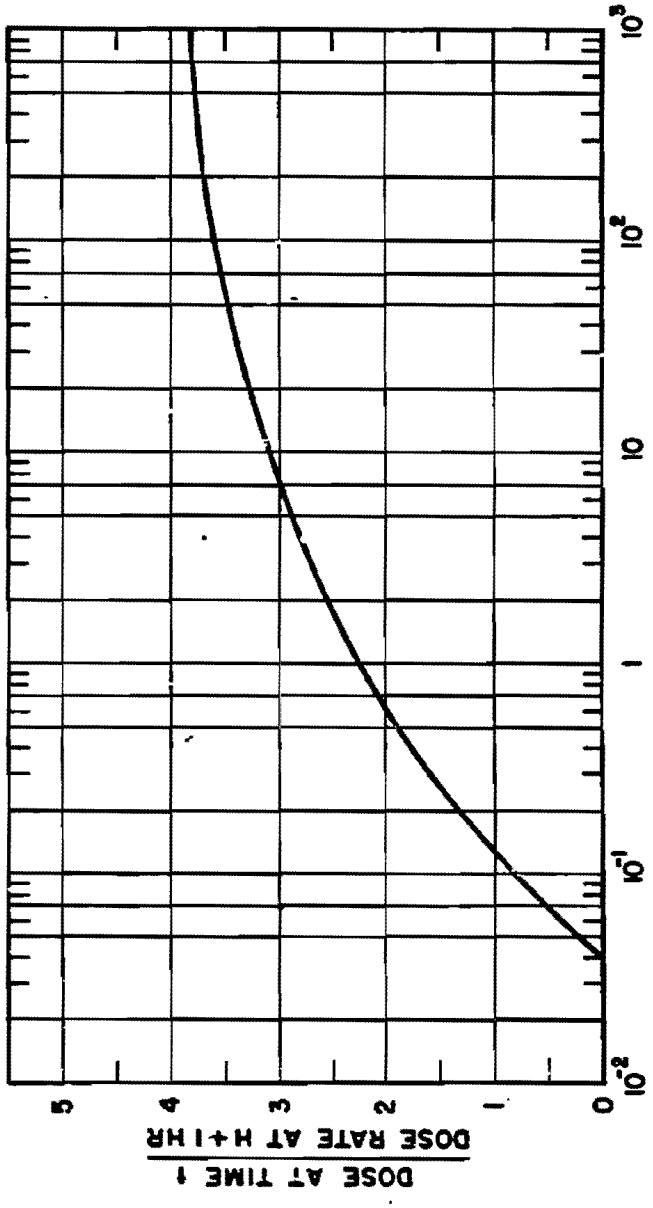

Figure 6-41. [redacted] Normalized Dose Accumulated in a Fallout Contaminated Area from $H + 1$ Hour to $H + 1{,}000$ Days

[redacted]

Problem 5-11. Calculation of Total Gamma Radiation Dose Received in a Contaminated Area

[redacted] Figure 5-42 gives the total dose received if a contaminated area is entered at a specified time and occupied for a specified interval of time. The vertical axis gives the accumulated dose for each unit (rads/hr) of dose rate at one hour after the detonation. The various curves represent time of stay in the contaminated area. To determine the accumulated dose, a factor is taken from the vertical axis corresponding to the time of entry and the time of stay. The product of this factor and the dose rate at one hour is the accumulated dose.

[redacted] *Example* [redacted]:

Given: The dose rate in a given area at 1 hour after a nuclear explosion is 500 rads/hr.

Find: The total dose received by a man who enters the area 2 hours after the explosion and remains 4 hours.

Solution: From Figure 5-42, the intersection of the line for a time of entry of 2 hours after burst with the 4 hour curve gives a factor of 0.8.

Answer: The accumulated dose is:

$$500 \times 0.8 = 400 \text{ rads.}$$

[redacted] *Related Material.* See paragraphs 5-21. See also Figures 5-40 and 5-41.

[redacted]

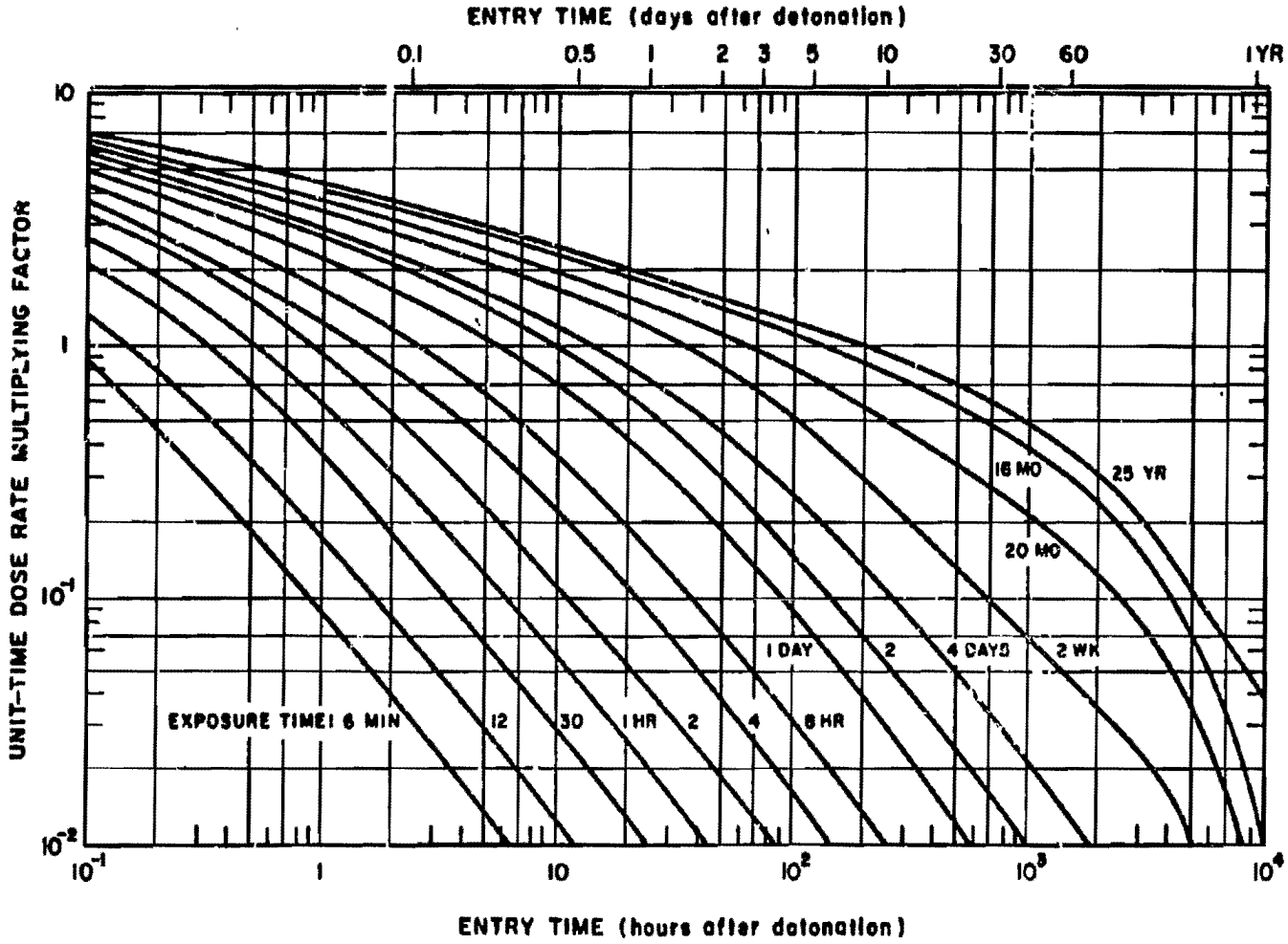

Figure 6-42. [redacted] Total Radiation Dose from Early Fallout as a Function of Entry Time and Stay Time, Normalized to Unit Time Reference Dose Rate [redacted]

Problem 5-12. Calculation of Fallout Gamma Radiation Dose Rate Contours for Bursts in the Transition Zone

[redacted] Figure 5-43 may be used to determine whether or not a burst is in the transition zone, i.e., below a height of burst of $100W^{0.35}$ feet. Burst heights below the curve in Figure 5-43 are in the transition zone. Burst heights above the curve are air bursts. In some situations, it may be desirable to consider bursts below $180W^{0.4}$ feet to be in the transition zone for conservative estimates. The means for doing this are discussed below. When a burst occurs in the transition zone, an approximation of the resulting fallout contamination patterns may be obtained by multiplying the dose rate contour values for a contact surface burst weapon of the same yield by an adjustment factor from Figure 5-44. The curves of Figure 5-44 were constructed under the assumption that the ratio of the dose rate values from a burst in the transition zone to the dose rate values for the same contour from a surface burst are proportional to the ratio of the volume of a segment of a sphere intercepted by the ground surface to the volume of the hemisphere, where the radius of the sphere is $100W^{0.35}$ feet, i.e.,

$$\text{Adjustment Factor} = \frac{\left(100 - \frac{h}{W^{0.35}}\right)^2 \left(200 + \frac{h}{W^{0.35}}\right)}{2 \times 10^6},$$

where h is the actual height of burst in feet, and W is the total weapon yield in kilotons.

[redacted] In view of the lack of data from bursts in the transition zone over a land surface, a more conservative estimate may be desired. In this case, the height of burst for the upper limit of the transition zone is taken to be $180W^{0.4}$ feet. The adjustment factor to be applied to dose rate values for the same contours from a surface burst of the same yield can be calculated from:

$$\text{Adjustment Factor} = \frac{\left(180 - \frac{h}{W^{0.4}}\right)^2 \left(360 + \frac{h}{W^{0.4}}\right)}{1.17 \times 10^7}.$$

[redacted] *Example* [redacted]

Given: A hypothetical weapon with a total yield of 600 kt, of which 200 kt results from fission, is burst 560 feet over a land surface with 10 knot effective wind conditions.

Find: The contour parameters for a dose rate of 15 rads/hr at $H + 1$ hour reference time over smooth terrain.

Solution: From Figure 5-43, a 600 kt weapon burst below about 940 feet would be in the transition zone. A height of burst of 560 feet is less than three quarters of the limiting altitude of the transition, so fallout is the only residual radiation to be considered. The 15 rads/hr contour for a fission yield to total yield ratio of 200/600 = 1/3 corresponds to the contour for 15 ÷ 1/3 = 45 rads/hr for a weapon of 600 kt fission yield. The dose rate over reasonably level terrain is about 70 percent of that over an ideal smooth plane. Thus, the ideal smooth plane contour parameters for this weapon burst on the surface would correspond to

$$\frac{45}{0.7} = 64 \text{ rads/hr}.$$

From Figure 5-44 (or from the normal adjustment factor equation given above) the height of burst adjustment factor for a 600 kt weapon burst at 560 feet is 0.21. Therefore, the desired contour parameters can be obtained by entering Figures 5-28, 5-31, 5-34, and 5-37 with a yield of 600 kt and reading the parameter values corresponding to an $H + 1$ hour dose rate of

$$\frac{64}{0.21} = 300 \text{ rads/hr}.$$

[redacted]

[redacted]

Answer: The $H + 1$ hour dose rate parameter values are shown below:

Parameter	Source Figure	Parameter Value for a 10 Knot Effective Wind (miles)
Downwind Distance	5-28	80.0
Maximum Width	5-31	9.0
Distance to Maximum Width	5-34	25.0
Ground Zero Width	5-37	4.4
Upwind Distance	5-37*	2.2

*[redacted] Upwind distance equals one-half the ground zero width.

NOTE: These are the same dose rate contour parameters that were obtained in Problem 5-8 for the 50 rad/hr contour from an identical weapon burst on the surface of rough, hilly terrain.

[redacted] *Reliability.* There is little data to support the height of burst correction factors. Additionally, the degree to which wind and other meteorological conditions affect these contour parameters cannot be overemphasized. The contours presented in these curves have been idealized in order to make it possible to present average, representative values for planning purposes. Due to these limitations, a meaningful percentage reliability figure cannot be assigned to the idealized fallout pattern.

[redacted] *Related Material.* See paragraphs 5-17 through 5-22.

[redacted]

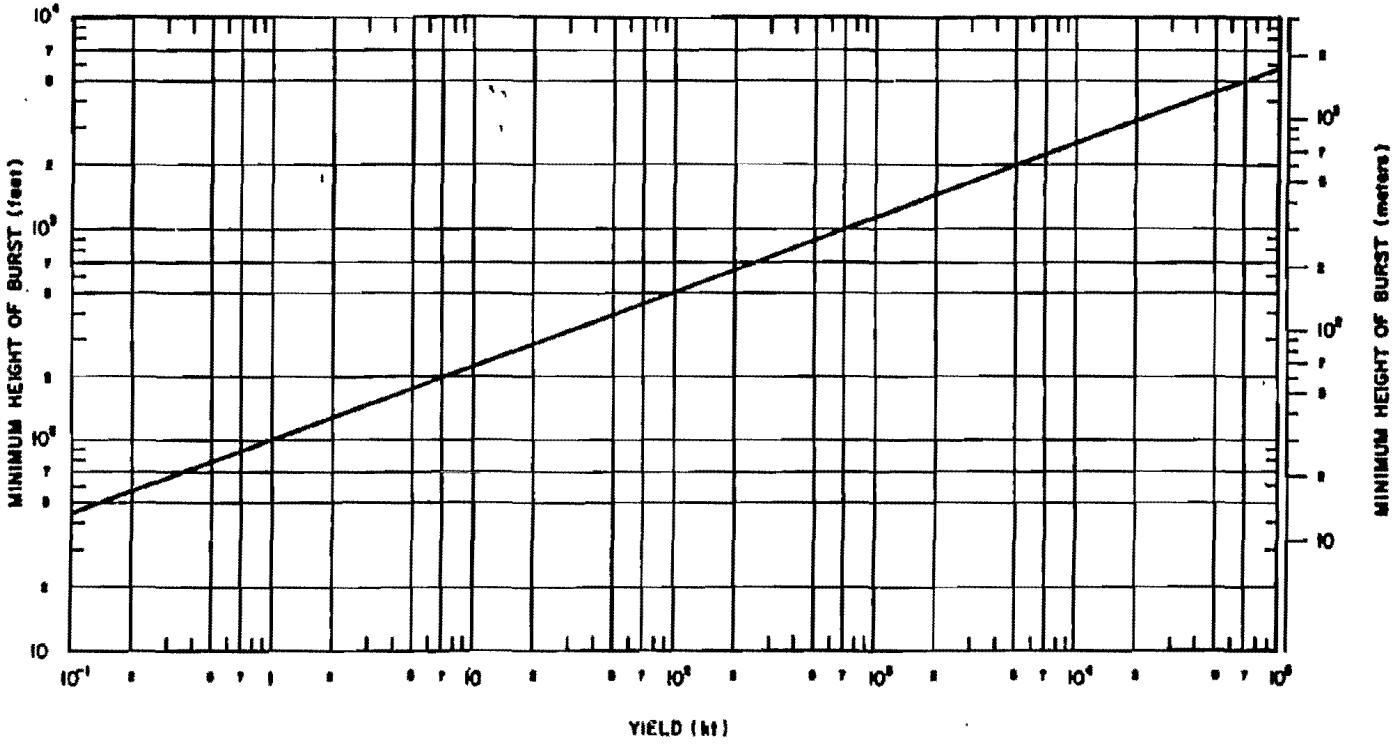

Figure 6-43. [redacted] Minimum Height of Burst for No Fallout as a Function of Yield [redacted]

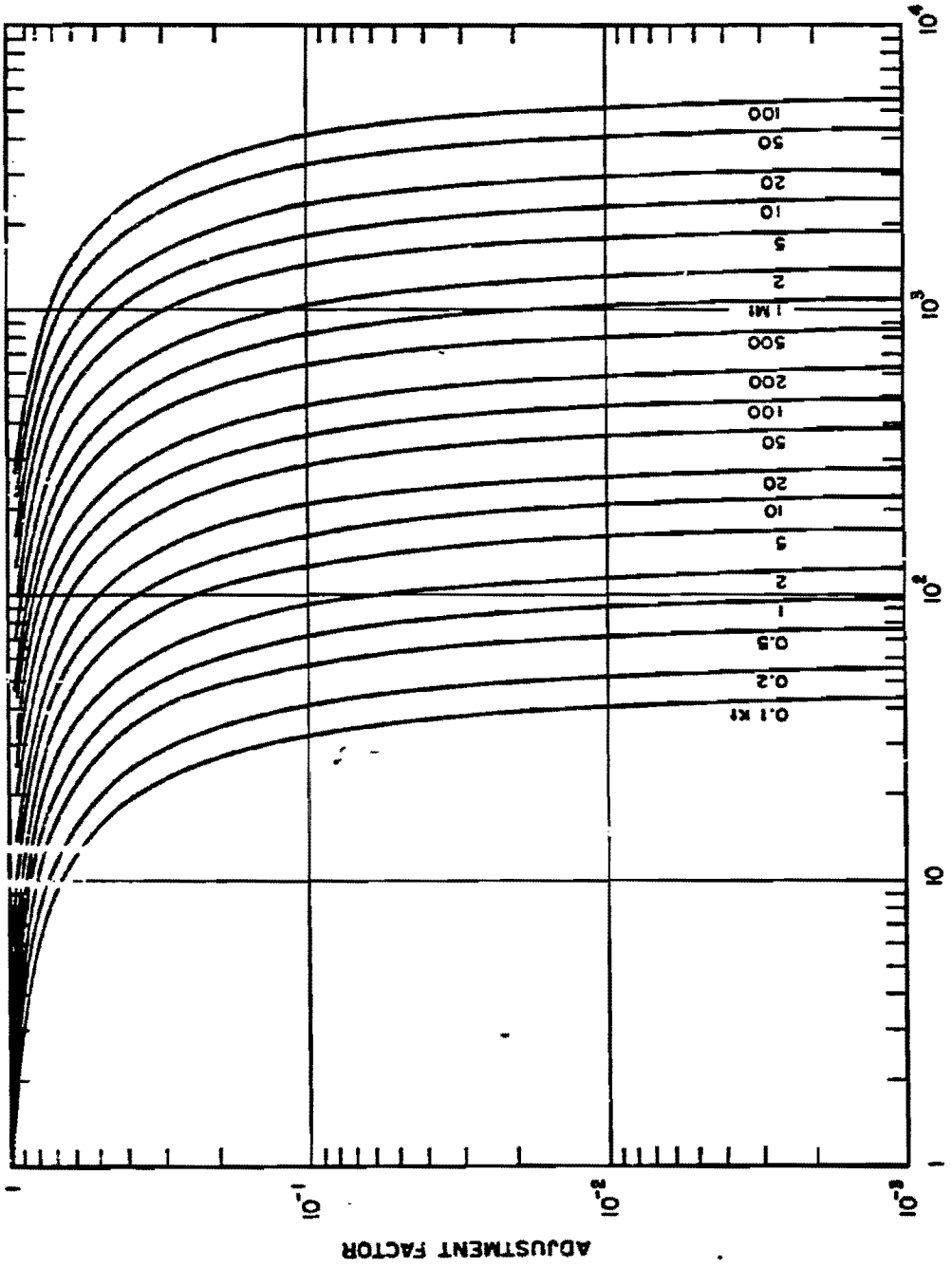

Figure 5-44. [redacted] Height of Burst Adjustment Factors for Various Yields

Problem 5-13. Calculation of Fallout Gamma Ray Dose Rate Contours for Underground Bursts

[redacted] Figure 5-45 presents depth multiplication factors for the surface burst contour parameters in Figures 5-28 through 5-37. If the weapon yield and depth of burst in land are known, a multiplication factor can be determined from this curve, or a range of values can be determined for deep bursts. The idealized contour parameters of a surface burst of the same yield are multiplied by this factor to obtain idealized contour parameters for the underground burst.

[redacted] Figures 5-28 through 5-37 must be used to obtain surface burst parameters. These curves present idealized contour parameters for various effective wind speeds and for yields from 0.01 kt to 30 Mt. These parameters are for a *reference* time of one hour after detonation on an infinite smooth plane. Since these surface burst parameters must be used to determine contours for underground bursts, all conditions that apply to Figures 5-28 through 5-37 also apply to the resulting underground burst contours. For example, to obtain dose rate values for times other than $H + 1$ hour, adjustment procedures are the same for underground bursts as those for surface bursts as discussed in the explanatory text for those figures.

[redacted] Figure 5-45 shows the depth multiplication factor as a function of depth of burst for a 1 kt explosion. Factors may be obtained for other yields by the scaling procedures.

[redacted] *Scaling.* For yields other than 1 kt, scale as follows:

$$db_1 = \frac{db}{W^{1/3}},$$

where db_1 is the depth of burst for 1 kt and db is the depth of burst for a yield of W kt. Once the equivalent depth of burst for 1 kt has been determined, the depth multiplication factor may be read from Figure 5-45. This factor is applied to dose rate contour values obtained from Figures 5-28 through 5-37 for a yield of W kt.

[redacted] *Example* [redacted]:

Given: A 20 kt explosion at a depth of 135 feet under 20 knot effective wind conditions.

Find: The idealized dose rate contour parameters for a dose rate of 100 rads/hr at 1 hour after the explosion.

Solution: The equivalent depth of burst for a 1 kt explosion is

$$db_1 = \frac{db}{W^{1/3}} = \frac{135}{(20)^{1/3}} = 50 \text{ ft.}$$

From Figure 5-45, the depth multiplication factor corresponding to this depth of burst for a 1 kt explosion is 1.2.

Answer: The $H + 1$ hour dose rate parameters for a 20 kt explosion at a depth of 135 feet are shown below:

Parameter	Source Figure	Surface Burst Value (statute miles)	Depth Multiplication Factor	Underground Burst Value (statute miles)
Downwind Distance	5-29	35.0	1.2	42.0
Maximum Width	5-32	1.4	1.2	1.7
Distance to Maximum Width	5-35	18.0	1.2	21.6
Ground Zero Width	5-37	1.4	1.2	1.7
Upwind Distance	5-37	0.7	1.2	0.8

[redacted]

[redacted] *Reliability.* The limitations present in Figures 5-28 through 5-37 and the treatment of surface bursts apply to this treatment of underground bursts. Also, more stringent restrictions must be placed on the use of this treatment of underground bursts. In the absence of sufficient data, the results of a complex computer code were used to generate the idealized dose rate parameter contour values for surface bursts. The results of an equivalent code are not available for underground bursts. Thus, the dependence of the size and shape of a particular contour on depth of burst cannot be predicted in detail, even under the restrictions of the idealized model presented here. Variations in soil type also are expected to affect the fallout pattern of underground bursts to a greater degree than surface bursts, but there are little data to substantiate this belief. Some of the uncertainties are reflected by the shaded region in Figure 5-45. Although the predictions cannot be considered reliable, this treatment should give a rough picture of the general behavior of the fallout pattern.

[redacted] *Related Material.* See paragraphs 5-18 through 5-21 and paragraph 5-23. See also Problem 5-8 and Figures 5-28 through 5-37.

[redacted]

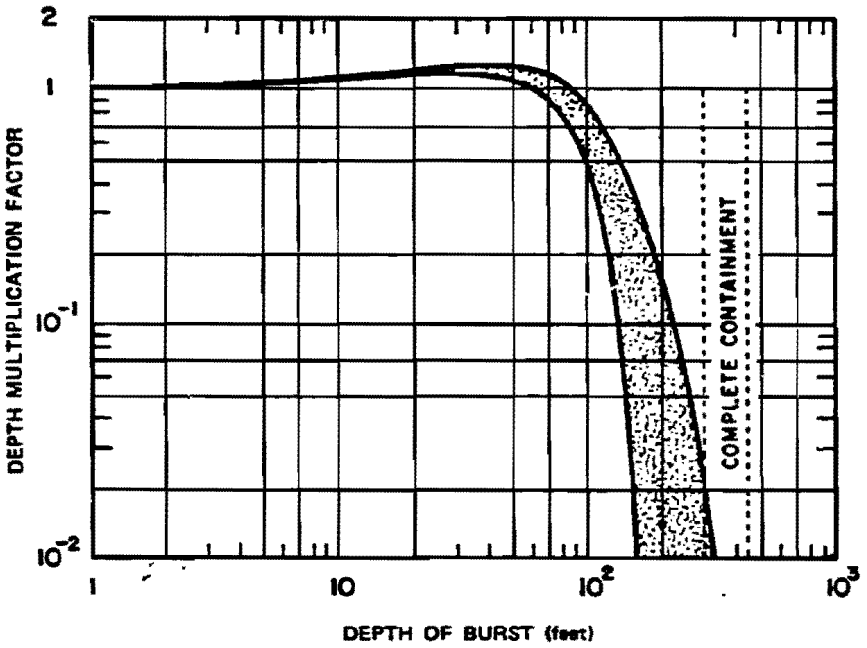

Figure 5–45. [redacted] Depth Multiplication Factor for Linear Dimensions of the Fallout Pattern from a 1 kt Explosion as a Function of Depth of Burst [redacted]

RESIDUAL RADIATION FROM WATER SURFACE AND UNDERWATER BURSTS

The distinction between initial and residual radiation from underwater bursts is much less distinct than it is for air bursts or land surface or subsurface bursts. The radiation accompanying the base surge expands sufficiently rapidly as to become merged with what is normally considered initial radiation. In the case of water surface bursts, the distinction between initial and residual radiation is somewhat more clear cut, but in most cases the residual radiation will not be of great significance.

5-25 Water Surface Bursts

A base surge (paragraph 2-75, Chapter 2) is not expected to form as a result of a water surface burst, consequently a separation between initial and residual nuclear radiation can be made as in the case of a land surface explosion. An approximation of the initial nuclear radiation dose may be obtained from Figures 5-9 through 5-17 in Section I of this chapter. It must be emphasized, however, that the dose so obtained will be an approximation. The curves of Figures 5-9 through 5-17 are based on extensive computer calculations for a receiver on or near a *land* surface. These calculations included the effect of the ground-air interface, and a number of comparisons with measured data have substantiated the validity of the calculations. A limited number of comparisons of the same computer calculations have also indicated good agreement with initial gamma ray dose measurements made near a water surface after high yield explosions; however, these were not true water surface explosions, and no comparisons with neutron dose are available. Thus, in the absence of data and in the absence of comprehensive computer calculations, the curves of Figures 5-9 through 5-17 provide the best available data for simplified calculations of initial nuclear radiation dose from water surface bursts.

For yields of more than a few kilotons, the cloud from a sea water surface burst is similar to that from a land surface or low air burst of the same yield. The cloud height and horizontal extent are determined primarily by the yield and by atmospheric conditions. For megaton yields, the maximum cloud height may be somewhat greater than that for a land surface burst, as a result of the release of latent heat from condensation of vaporized sea water. For very low yields, it is possible that the maximum cloud height may be less than for a land or low air burst, as a result of interference from the disturbed water. It is also possible, under certain atmospheric conditions, that the sea salt raised and dispersed in the atmosphere by low yield explosions may have a cloud-seeding effect. In this event, the water burst could produce a larger, higher cloud than a land burst, and the dispersion of salt would trigger a rainout of radioactivity.

The possible cloud seeding described above is only one example of the extreme sensitivity of fallout from water surface bursts to atmospheric conditions, especially relative humidity. This sensitivity results from the hygroscopic (water-absorbing) nature of the fallout particles. These particles consist mainly of sea salt and water. When dry, they are generally much smaller and lighter than fallout particles from land surface bursts. Because water burst particles are smaller than those from land bursts, water bursts produce less close-in fallout than land bursts. In particular, water bursts, unlike land bursts, generally will not produce a region of intense fallout (several thousand r/hr) near surface zero. The one possible exception is a water burst in an extremely humid atmosphere.

Water surface bursts are even less likely to produce regular cigar-shaped fallout patterns than land surface bursts. The effect of atmo-

spheric humidity introduces further irregularities in fallout patterns. Also, because water surface burst particles take longer to fall than particles from land surface bursts, wind and weather conditions are more likely to change during the time of fallout transport and deposition. It is often difficult to define a downwind direction in the fallout pattern. The apparent downwind direction may vary with yield and with time after burst at which the pattern is observed or calculated.

In almost all cases, the region of maximum deposit intensity is not around surface zero but considerably downwind. Thus, for a 10 Mt burst, the calculated region of a normalized dose rate of at least 300 r/hr at 1 hour extends from about 125 to 300 miles from surface zero. The dose rate would, of course, be much lower at the time of arrival and would vary throughout the area as a result of varying arrival times.

As material in the cloud rises, it cools by entraining ambient air, and by expanding with increasing altitude. Fallout particles form by condensation of vapor and grow by coagulation; that is, by collision and adhesion of smaller particles to form larger particles. The vapor condensation may be considered a 3-stage process.

In the first stage, calcium and magnesium from the sea water and iron, and other metals from the weapon condense as oxides. In the second stage sodium chloride, which is about 90 percent of dried sea salt, condenses on the nuclei provided by the stage 1 particles. In the third stage, water vapor condenses to liquid water or to ice, on the stage 2 particles.

The median diameter of the stage 1 particles is about 1 micron contrasted to a few hundred microns for a land surface burst. The size is expected to increase slightly with yield, because the particles are formed by diffusion onto nuclei while the fireball is cooling by thermal radiation. The larger the fireball, the slower the cooling rate. The slower the cooling rate, the more time is available for diffusive growth.

During and after the three condensation stages, coagulation causes particle growth. Particles of sub-micron size coagulate as a result of Brownian motion. Somewhat larger particles coagulate due to turbulent accelerations in the cloud. Turbulent coagulation only appears to be of importance in clouds from megaton bursts. Even larger particles grow by gravitational coagulation; that is, as they fall through the cloud they overtake and capture smaller particles. Gravitational coagulation is particularly important for low-yield bursts in humid atmospheres. The process is similar to one of the mechanisms for growth of ordinary raindrops. The largest particles formed, i.e., those from low yield bursts in a humid atmosphere, may have actual diameters of 2,000 microns. Particles of this size fall out of the cloud rapidly. Thus, there is a practical limit on the growth of particles in the cloud.

Moisture effects play a dominant part in water surface burst fallout. In general, the more humid the atmosphere, the more radioactivity is deposited as close-in fallout. Most of the moisture contained in the clouds of low yield bursts comes from entrained air. Consequently, the higher the humidity, the greater the cloud moisture content. In turn, the salt particles absorb more water, and, as they get larger, gravitational coagulation proceeds faster.

Moisture not only has a direct effect on particle formation, but also has an indirect effect on cloud height. The top of the cloud from a 20 kt water surface burst in a very humid tropical atmosphere may reach the tropopause at about 55,000 feet. In a less humid atmosphere, the cloud from a burst of the same yield may rise less than half as high (see Figure 5-39). Salt particles absorb moisture from humid air; the moisture evaporates when the particles are exposed to relatively dry air. Consequently the

size, falling rate, and time and place of deposit of water surface burst fallout particles vary with the atmospheric humidity the particles encounter during their trajectories. As the particles fall, they usually shrink by evaporation and may become completely dry, with a diameter of at most 100 to 200 microns. They then fall very slowly, and move large horizontal distances as a result of the forces exerted by the wind. Finally, the particles reach the more humid air near sea level, begin to grow by absorbing moisture, and fall faster. Thus, although particles from a megaton burst may leave the cloud with a water content almost entirely derived from sea water, this water may evaporate completely during fall, and the water content of the particles that reach the surface is entirely atmospheric moisture. An exception to this situation could occur for a burst in an arctic atmosphere. The cold air retards evaporation, even if humidity is low, and some of the original sea water could remain on the particles.

Maximum fallout intensity, as well as the area covered by fallout from a water surface burst increases with weapon yield. For yields between 1 kt and 100 kt, the normalized $H + 1$ hour exposure rates are expected to be negligible. The highest normalized intensities from a 100 kt explosion are expected to be more than 50 roentgens per hour (r/hr), but less than 100 r/hr. The highest intensities from a 1 Mt burst are expected to be over 100 r/hr but less than 300 r/hr. Finally, a 10 Mt burst is expected to produce intensities over 300 r/hr, but less than 1,000 r/hr. Since all of these exposure intensities are normalized to $H + 1$ hour, and the fallout will arrive at significantly longer times after burst for the larger yields (depending upon the wind), the radioactivity will have decayed to much smaller levels prior to the time of arrival and fallout generally is not expected to be a governing effect from water surface bursts.

5-26 Underwater Bursts

An underwater burst creates a highly energetic bubble, whose history determines the major above-surface effects. For very shallow explosions, the bubble expands through the water surface with a high internal pressure, and develops a hollow column through which the bubble blows out into the atmosphere in the form of a cloud at the column top. For a somewhat greater depth, the bubble expands through the water surface at lower internal pressure and a column again forms, but no blowout occurs. Transition from columnar formations to plume-like eruptions, hemispherical in shape, takes place as the depth increases. The migration of the underwater bubble through the surface near its minimal phase at or shortly after its maximum-expansion phase creates the plumes. For deep explosions, the bubble may experience several oscillations as it migrates upwards. If the explosion is very deep, the bubble will degenerate and break up before reaching the surface. It is possible that an explosion may take place at such a great depth that little, if any, disturbance will be noted on the surface.

The ejected water, whether a column or a plume, will fall back to the surface rapidly. This massive subsidence creates a radially expanding aerosol cloud, or base surge, at the water surface. The base surge expands as a ring or disk until it dissipates energy received from the subsidiary plumes or columns. After expanding, it drifts with the surface winds. Some evidence suggests the base surge has the same initial bulk density as that of the plumes or columns from which it is formed, being several times the density of air. As it travels downwind, it will react to the existing atmospheric conditions; e.g., evaporating or developing into low-cloud formations. These physical phenomena are described in more detail in Section IV, Chapter 2.

Three sources of radioactivity are the

major contributors to the radiation above the surface subsequent to an underwater explosion: initial, above surface nuclear radiation; base surge; and residual radioactivity deposited in the mixed layer of the ocean. These sources are very time dependent, and they are affected by atmospheric and oceanic variables.

Even for a shallow underwater explosion the neutron and secondary gamma portions of the initial nuclear radiation are essentially negligible. The initial above-surface source includes the fission product activity contained in the visible column and crown, or plume. This source contains radioactivity ejected into the atmosphere as a result of underwater hydrodynamic phenomena. The scaled depth of burst is a major factor in determining the extent to which this initial radiation contributes to the total above surface exposure. The rapid development and spread of the base surge (paragraph 2-75, Chapter 2) causes the initial and residual radioactivity from an underwater burst to merge into one more or less continuous source.

The base surge develops as a result of both underwater flow phenomena and the collapse of the water masses associated with the initial source. This radially expanding surge grows to large dimensions as a dense, fog-like aerosol carrying with it a substantial fraction of suspended fission products. This source is either annular or disk-shaped in geometry and extends from the ocean surface to a height of several thousand feet. The base surge is influenced strongly by the wind, moving as an entity at the existing wind speed and direction. Initially it is highly radioactive; however, as it expands and dilutes, the concentration of the fission products decreases. This dispersion, coupled with rapid radioactivity decay, results in comparatively low exposure rates by the first half-hour after burst.

The residual radioactivity in the surface layer of the ocean is the third, and final, major source of radiation. This radioactive pool is moved by the local currents, which depend on the existing oceanographic conditions. The pool is initially a disk which upon expansion approximates an annulus, although at times significantly later than a half-hour, it reverts to an irregular disk shape. Eventual mixing down to the top of the thermocline and the action of horizontal turbulent diffusion result in rapid dilution of the pool, reducing its hazard as time progresses.

The gamma radiation hazard created by the initial source, base surge, and pool resulting from an underwater nuclear explosion varies significantly with weapon yield and burst depth, proximity of the ocean bottom to the point of detonation, wind velocity and current velocity. Consequently, a description of the radiation fields (exposure rate and total exposure) associated with an underwater burst is complex, and no simplified prediction system suitable for general application has been developed.

A prediction system, DAEDALUS, has been developed to compute the radiological effects of underwater nuclear bursts. In this system, all above-surface sources, as well as the radioactive pool, are approximated by cylinders homogeneously contaminated with mixed fission products. The dimensions, water concentrations, and fission product contents of these cylindrical sources are estimated from empirical and theoretical considerations. Having defined the radioactive sources, DAEDALUS calculates, for each time of interest, exposure rates from these sources at specified detector locations. At each location the exposure rates are summed over time and the total exposure is thus cumulated. In the absence of a simple prediction system suitable for inclusion in this manual, examples of the results of DAEDALUS calculations are presented to provide an appreciation of the potential magnitude of the problems associated with radioactivity from underwater nuclear bursts.

[redacted]

Table 5-7. [redacted] Examples Selected for Base Surge and Pool Exposure Rates [redacted]

Yield (kt)	Explosion Depth (ft)	Depth of Water (ft)	Base Surge Figure Number	Pool Figure Number
10	65	5,000	5-46	5-52
10	65	65	5-47	5-53
10	150	5,000	5-48	5-54
10	500	5,000	5-49	5-55
10	1,000	5,000	5-50	5-56
10	1,500	5,000	5-51	5-57

[redacted] A yield of 10 kt was selected to illustrate the effects of depth of burst and water depth on the time dependence of the gamma ray exposure rates from the base surge and the pool. Table 5-7 shows combinations of depth of burst and water depth that were selected. Table 5-7 also indicates the corresponding figures that show exposure rates as a function of time and radial distance from the source for the base surge and the pool respectively. A no-wind environment was chosen for these examples, and, in the case of the pools, a no-current environment was assumed.

[redacted] Figures 5-58 through 5-75 show the accumulated exposures for two scaled depths ($d_b \approx 30W^{1/3}$ and $d_b \approx 280W^{1/4}$), corresponding to very shallow and deep explosions, respectively (Figure 2-105, Chapter 2). The doses are shown for 1, 10, and 100 kt explosions at each scaled depth. Two minute, 10 minute, and 30 minute exposures are shown for each yield at each scaled depth. In all cases it was assumed that the depth of the water was 5,000 feet, the effective wind was 15 knots, and a no-current condition existed. Table 5-8 identifies the figure for each combination of yield, burst depth, and exposure time.

Table 5-8. [redacted] Examples Selected for Total Exposure [redacted]

Yield (kt)	Explosion Depth (ft)	Exposure Time		
		2 Minutes	10 Minutes	30 Minutes
1	30	Fig. 5-58	Fig. 5-59	Fig. 5-60
10	65	Fig. 5-61	Fig. 5-62	Fig. 5-63
100	140	Fig. 5-64	Fig. 5-65	Fig. 5-66
1	280	Fig. 5-67	Fig. 5-68	Fig. 5-69
10	500	Fig. 5-70	Fig. 5-71	Fig. 5-72
100	890	Fig. 5-73	Fig. 5-74	Fig. 5-75

[redacted]

[redacted]

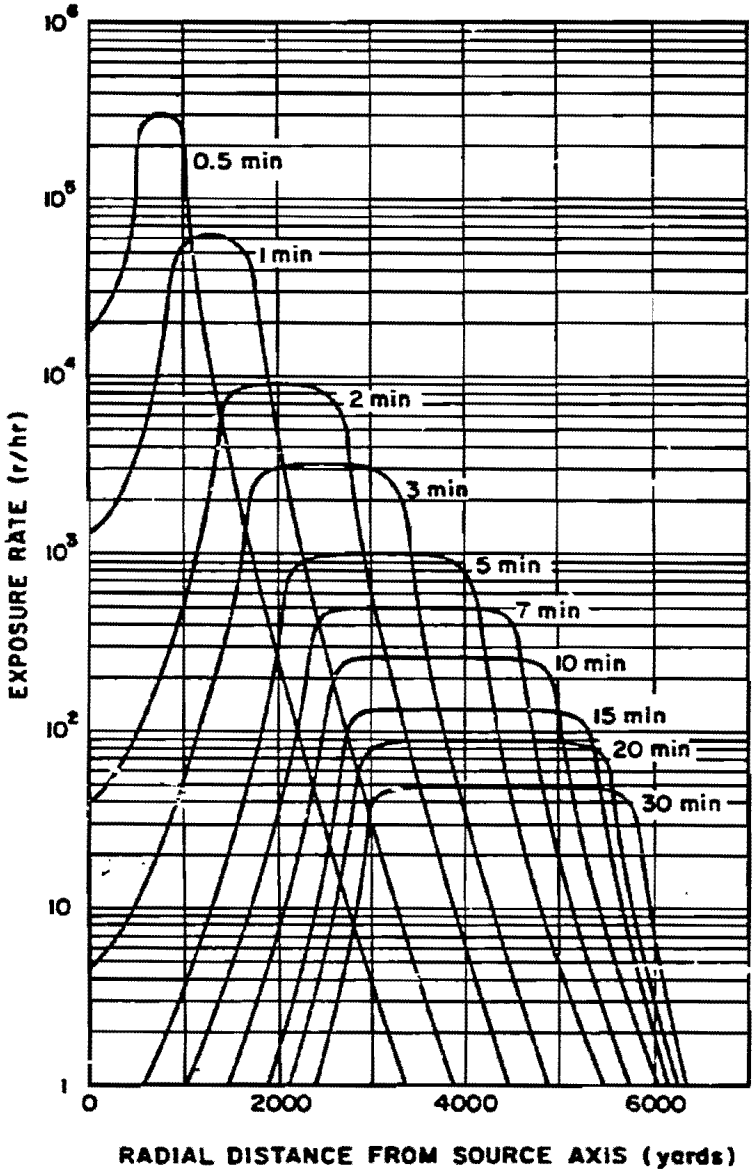

Figure 5-46. [redacted] Base Surge Radiation Exposure Rate 15 Feet Above the Water Surface from a 10 kt Explosion at a Depth of 65 Feet in 5,000 Feet of Water, No-Wind Environment [redacted]

[redacted]

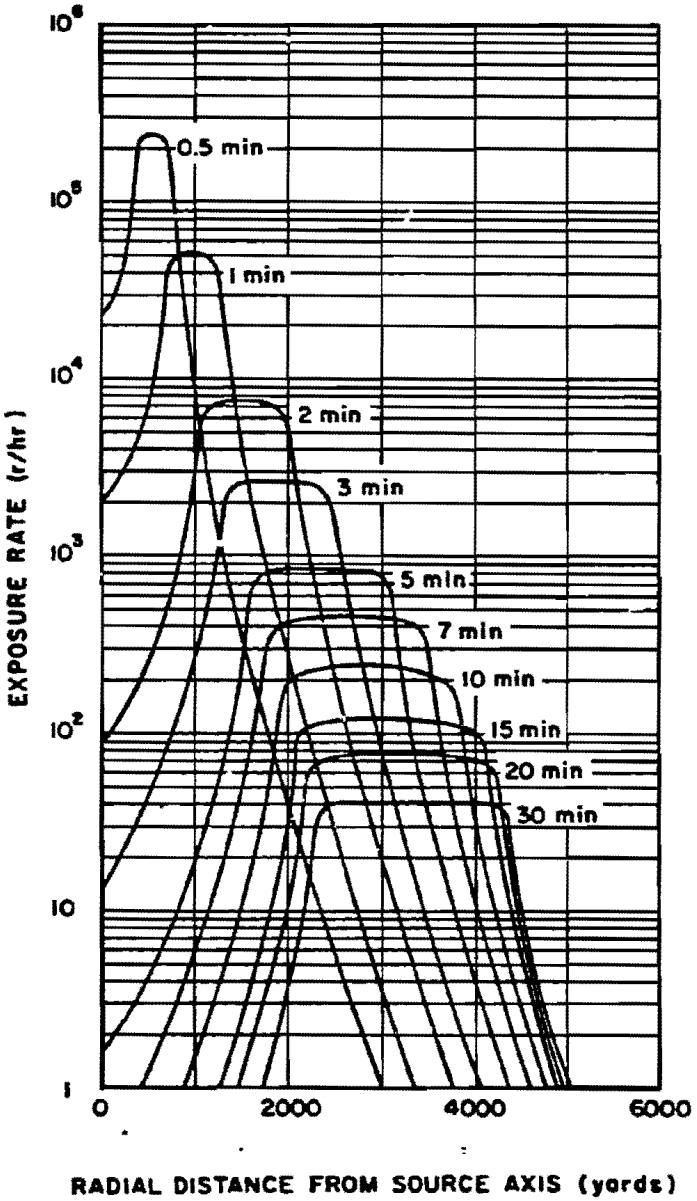

Figure 5-47. [redacted] Base Surge Radiation Exposure Rate 15 Feet Above the Water Surface from a 10 kt Explosion on the Bottom in 65 Feet of Water, No-Wind Environment [redacted]

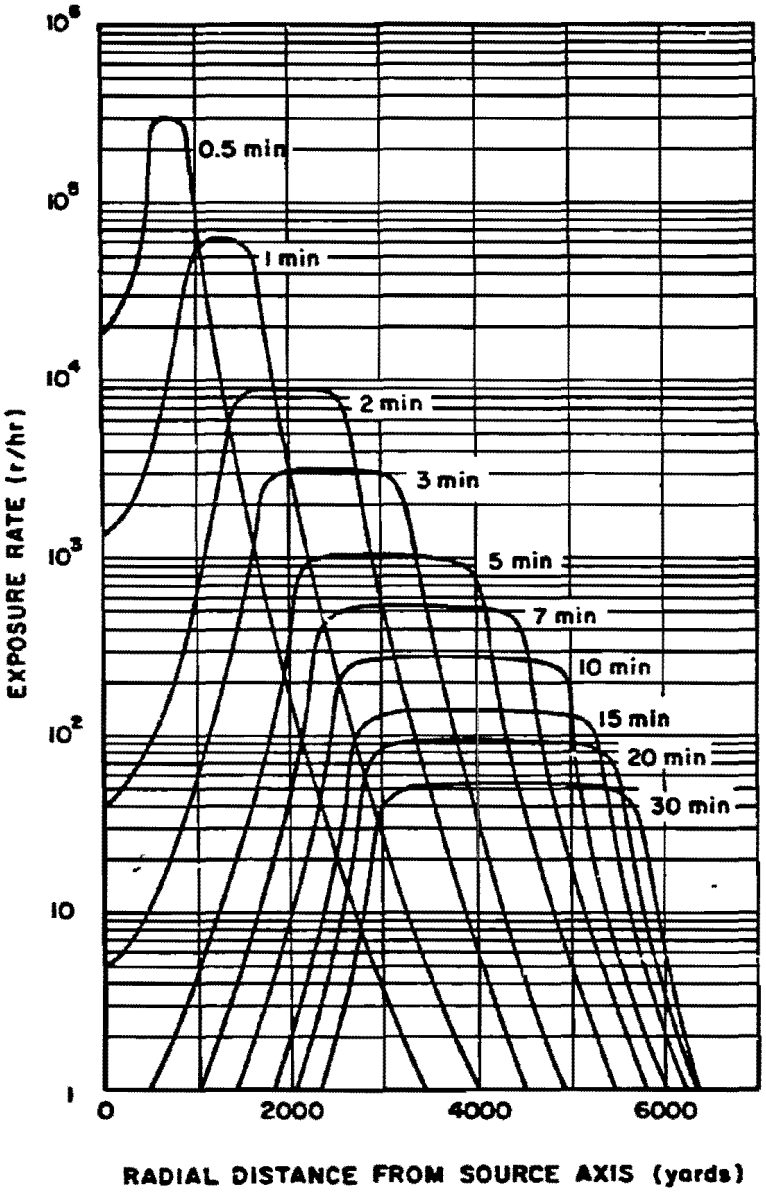

Figure 5-48. [redacted] Base Surge Radiation Exposure Rate 15 Feet Above the Water Surface from a 10 kt Explosion at a Depth of 150 Feet in 5,000 Feet of Water, No-Wind Environment [redacted]

[redacted]

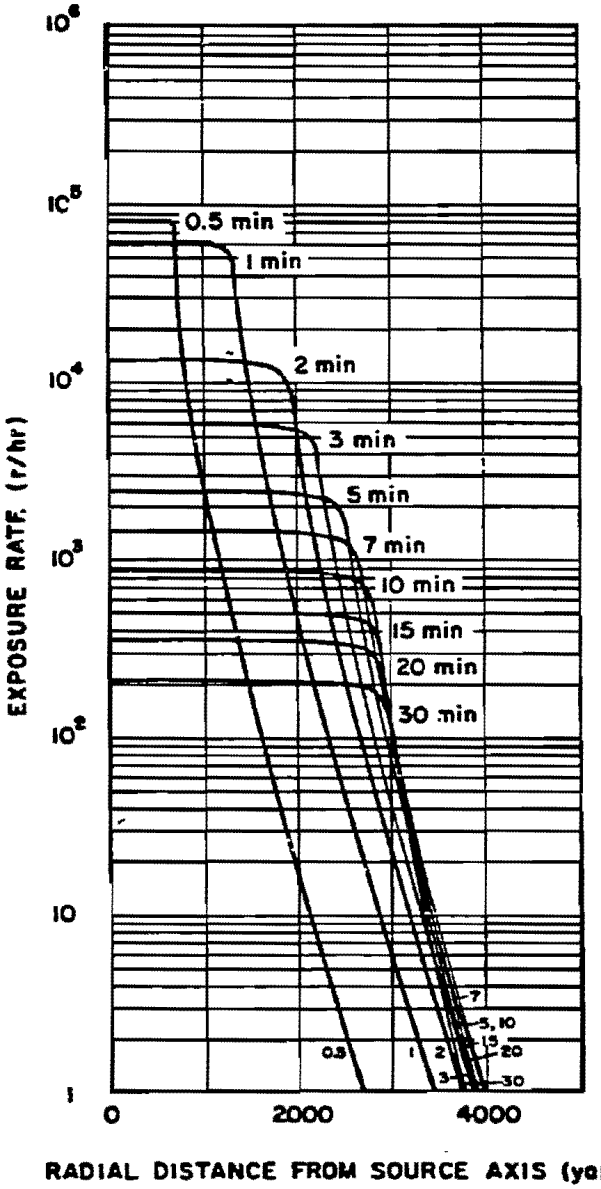

Figure 5-49. [redacted] Base Surge Radiation Exposure Rate 15 Feet Above the Water Surface from a 10 kt Explosion at a Depth of 500 Feet in 5,000 Feet of Water, No-Wind Environment [redacted]

[redacted]

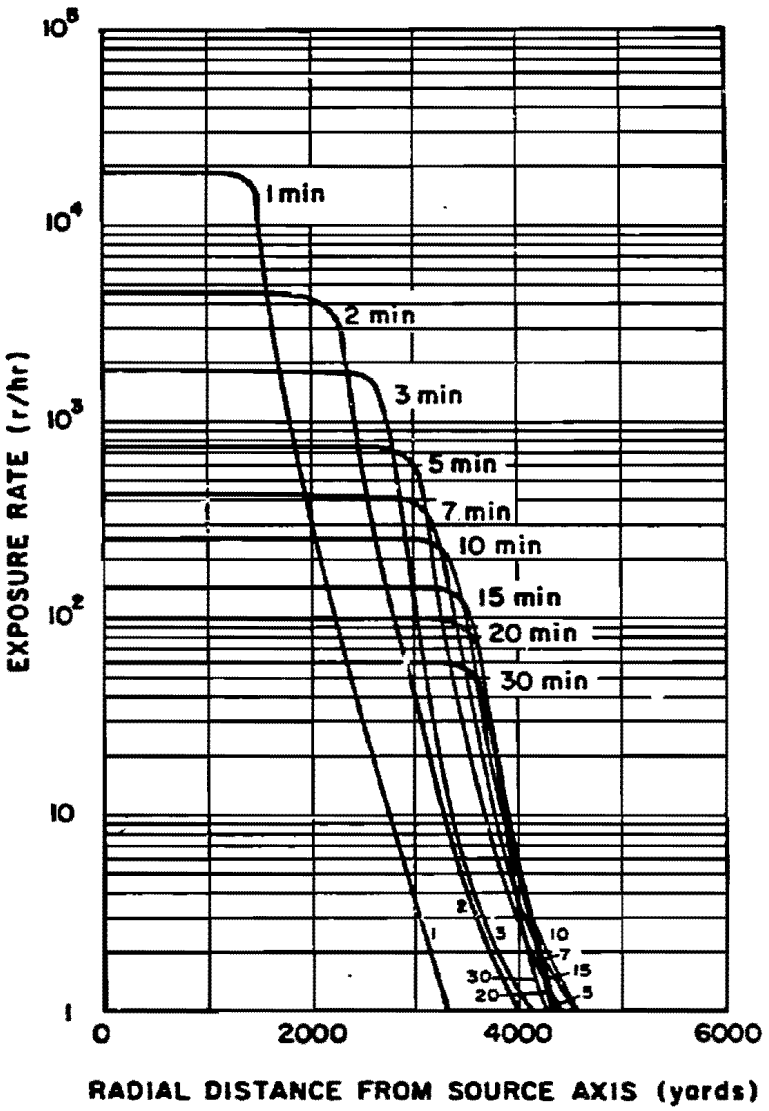

Figure 5-50. [redacted] Base Surge Radiation Exposure Rate 15 Feet Above the Water Surface from a 10 kt Explosion at a Depth of 1,000 Feet in 5,000 Feet of Water, No-Wind Environment [redacted]

[redacted]

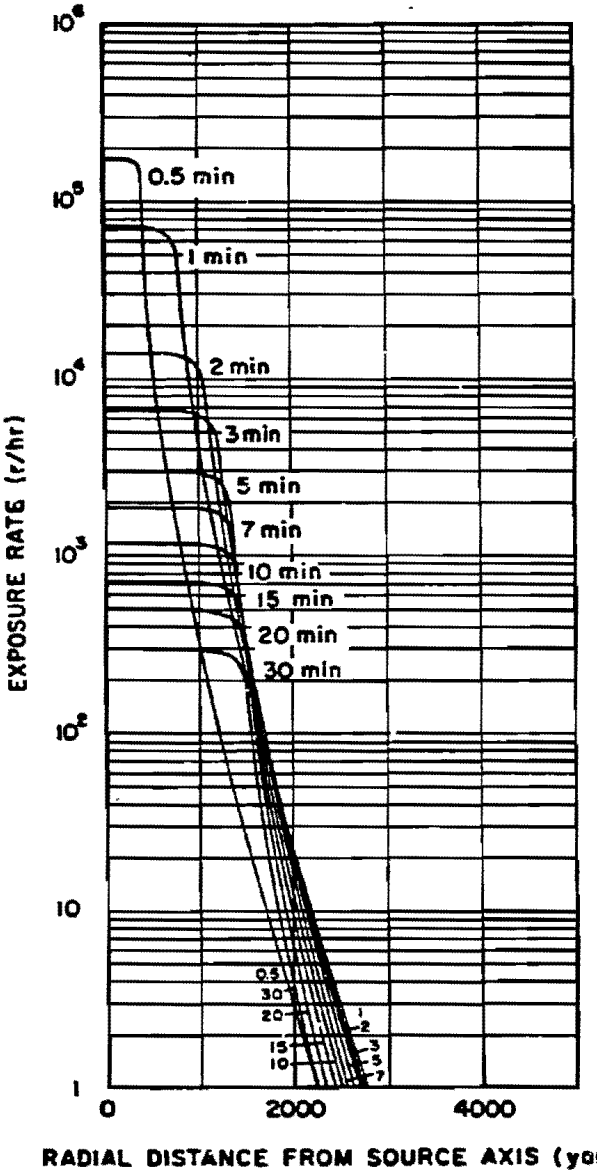

Figure 5-51. [redacted] Base Surge Radiation Exposure Rate 15 Feet Above the Water Surface from a 10 kt Explosion at a Depth of 1,500 Feet in 5,000 Feet of Water, No-Wind Environment [redacted]

[redacted]

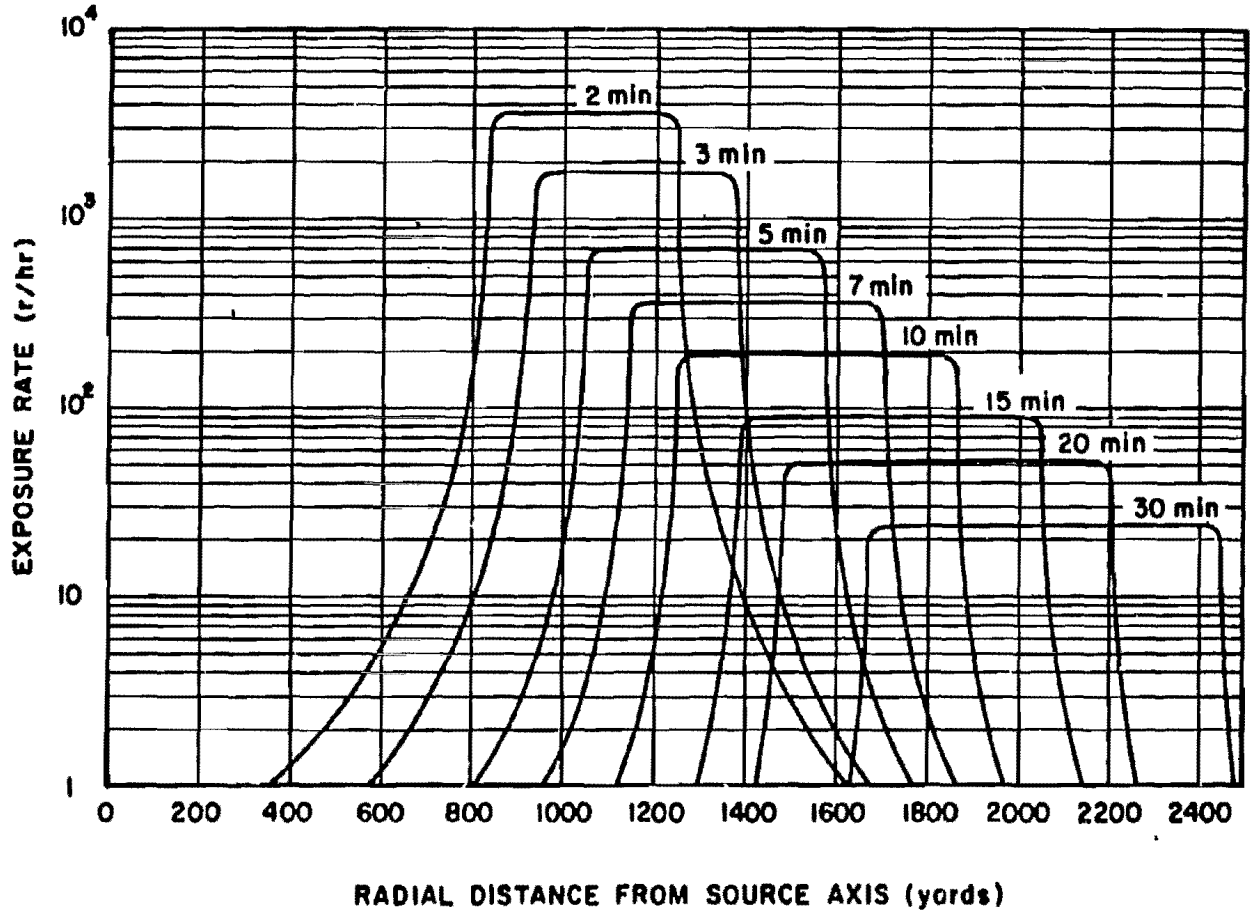

Figure 5-52. [redacted] Pool Radiation Exposure Rate 15 Feet Above the Water Surface from a 10 kt Explosion at a Depth of 65 Feet in 5,000 Feet of Water, No-Current Environment [redacted]

[redacted]

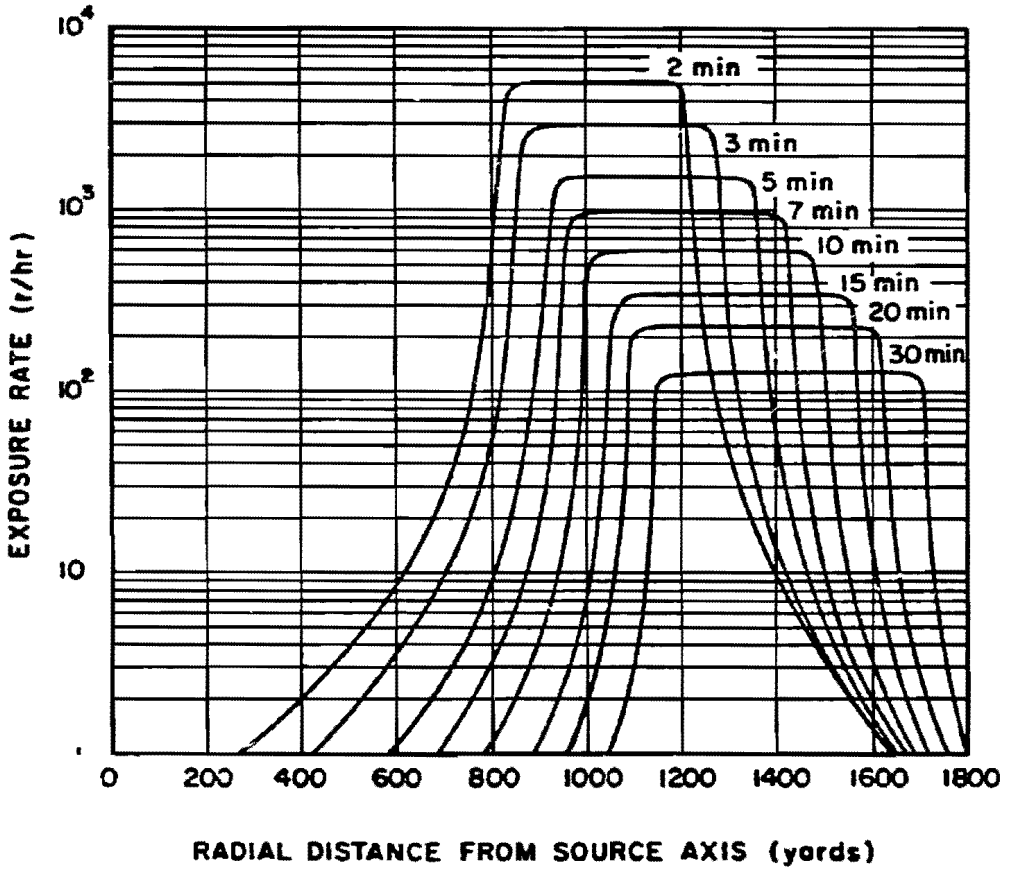

Figure 5-53. [redacted] Pool Radiation Exposure Rate 15 Feet Above the Water Surface from a 10 kt Explosion on the Bottom in 65 Feet of Water, No-Current Environment [redacted]

[redacted]

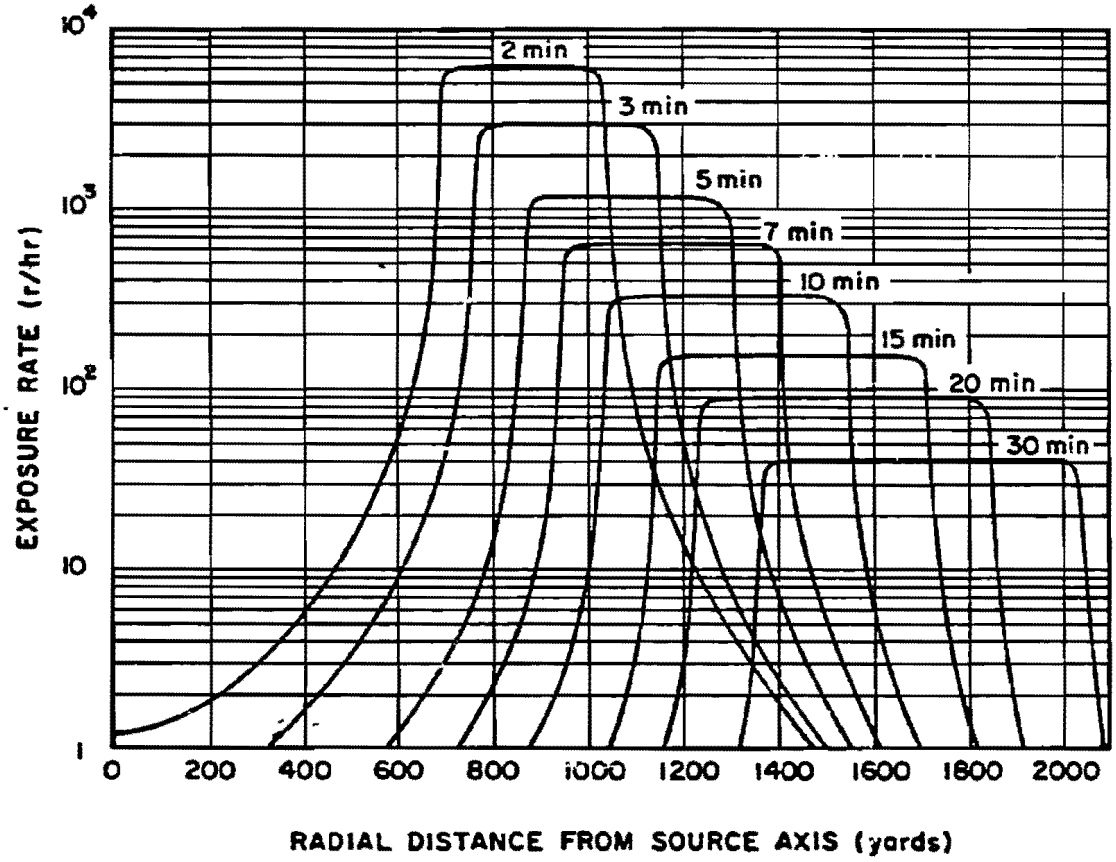

Figure 5-54. [redacted] Pool Radiation Exposure Rate 15 Feet Above the Water Surface from a 10 kt Explosion at a Depth of 150 Feet in 5,000 Feet of Water, No-Current Environment [redacted]

[redacted]

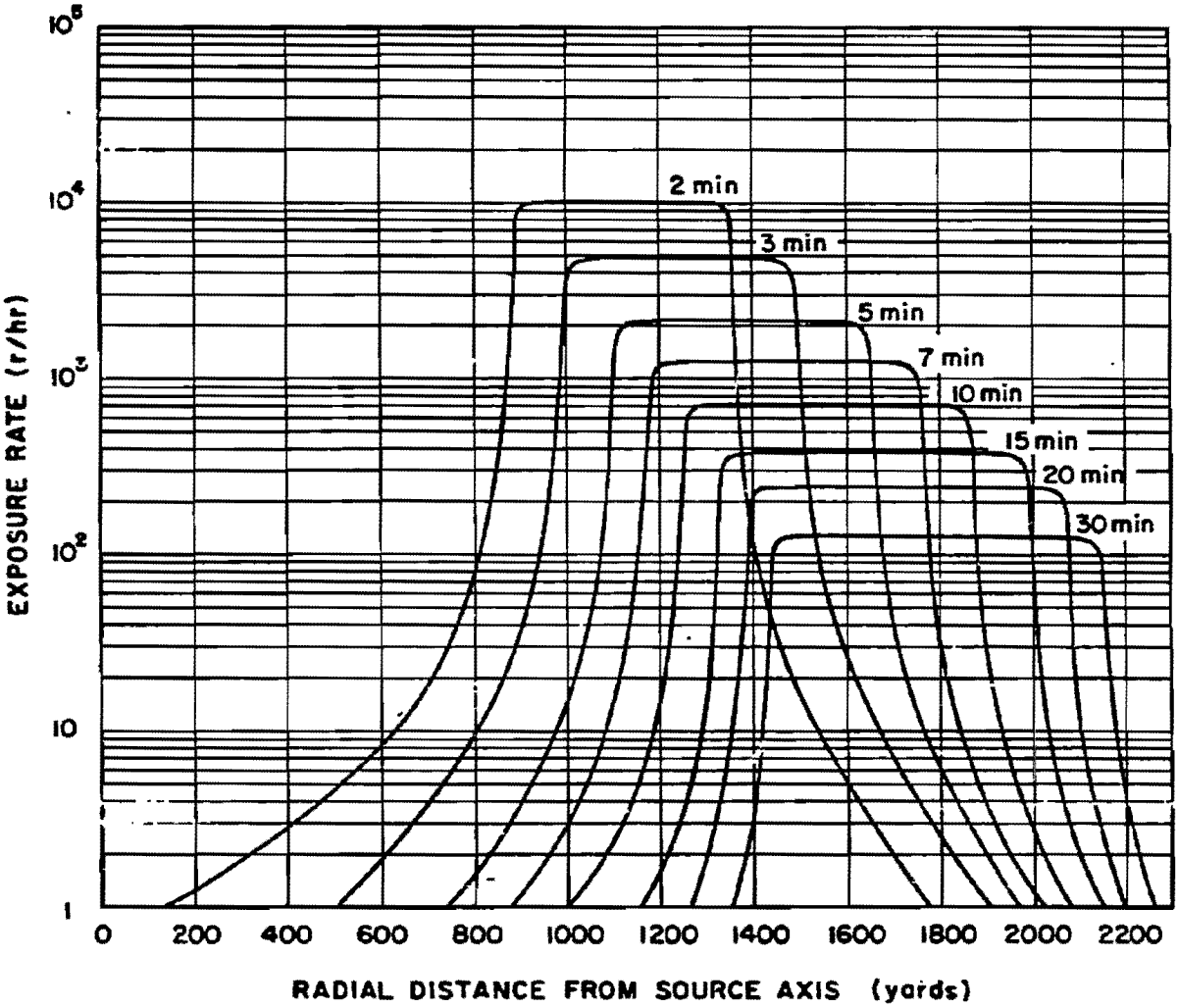

Figure 5-55. [redacted] Pool Radiation Exposure Rate 15 Feet Above the Water Surface from a 10 kt Explosion at a Depth of 500 Feet in 5,000 Feet of Water, No-Current Environment [redacted]

[redacted]

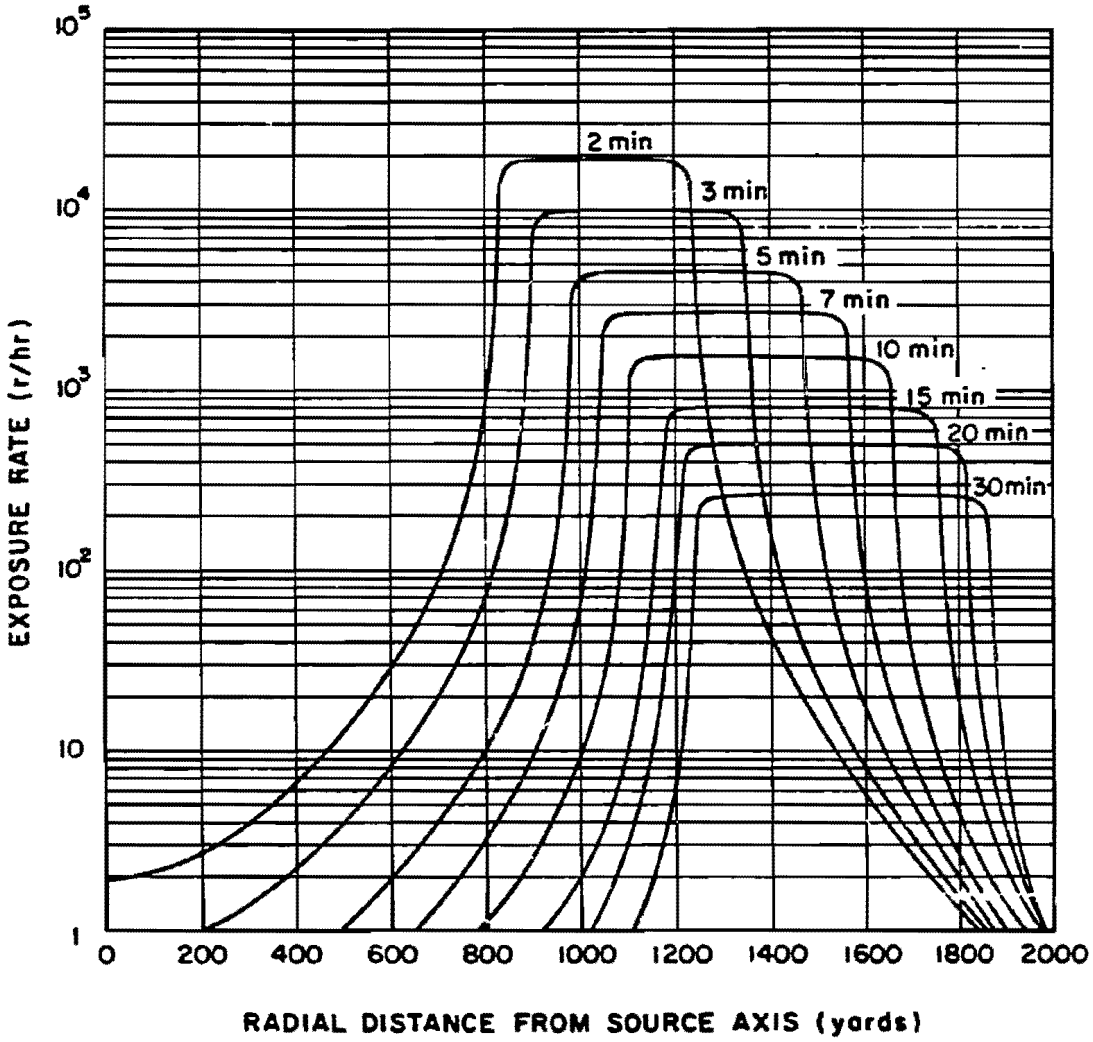

Figure 5-56. [redacted] Pool Radiation Exposure Rate 15 Feet Above the Water Surface from a 10 kt Explosion at a Depth of 1,000 Feet in 5,000 Feet of Water, No-Current Environment [redacted]

[redacted]

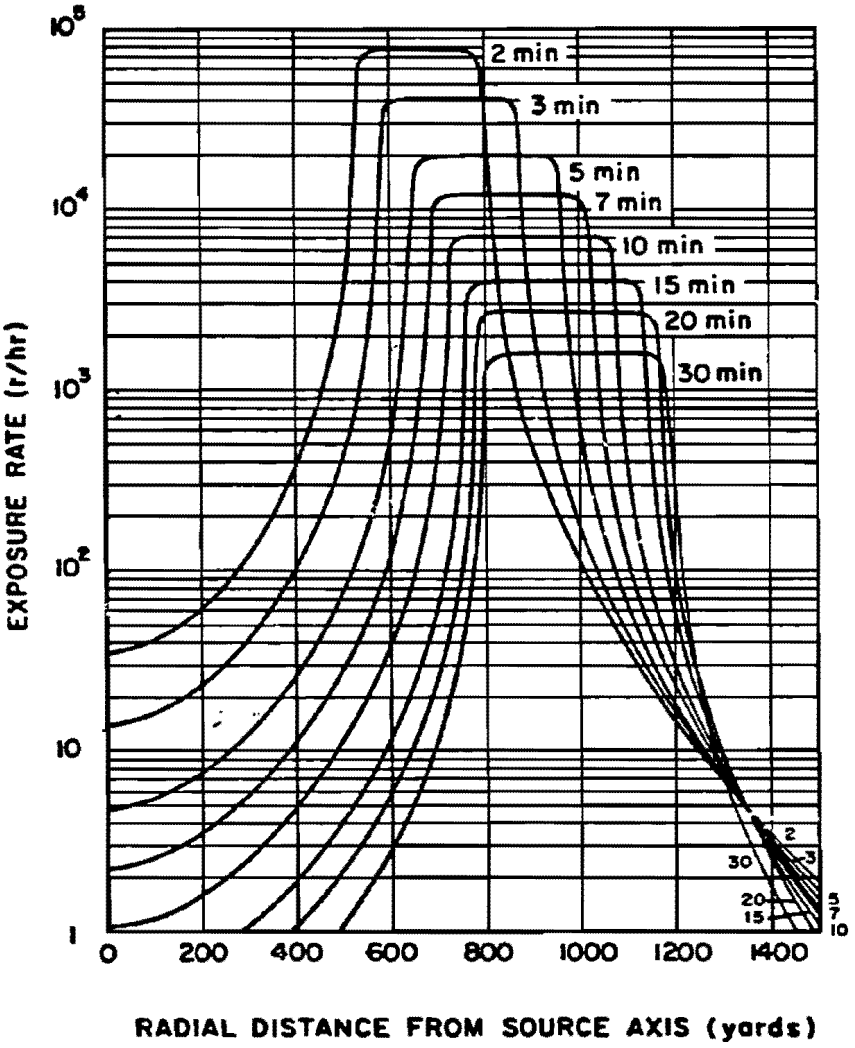

Figure 5-57. [redacted] Pool Radiation Exposure Rate 15 Feet Above the Water Surface from a 10 kt Explosion at a Depth of 1,500 Feet in 5,000 Feet of Water, No-Current Environment [redacted]

[redacted]

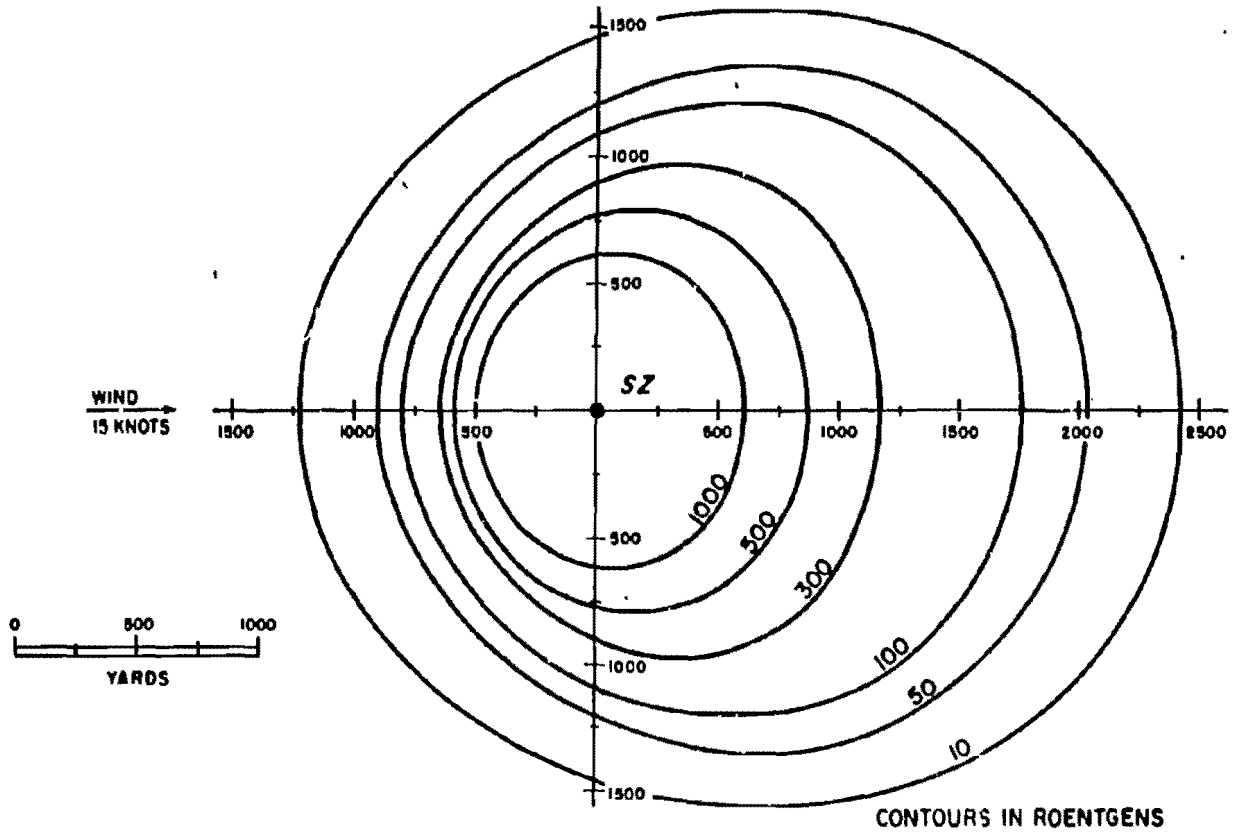

Figure 5-58. [redacted] Two-Minute Total Exposure 15 Feet Above the Water Surface from a 1 kt Explosion at a Depth of 30 Feet in 5,000 Feet of Water, 15 Knot Wind, No-Current Environment [redacted]

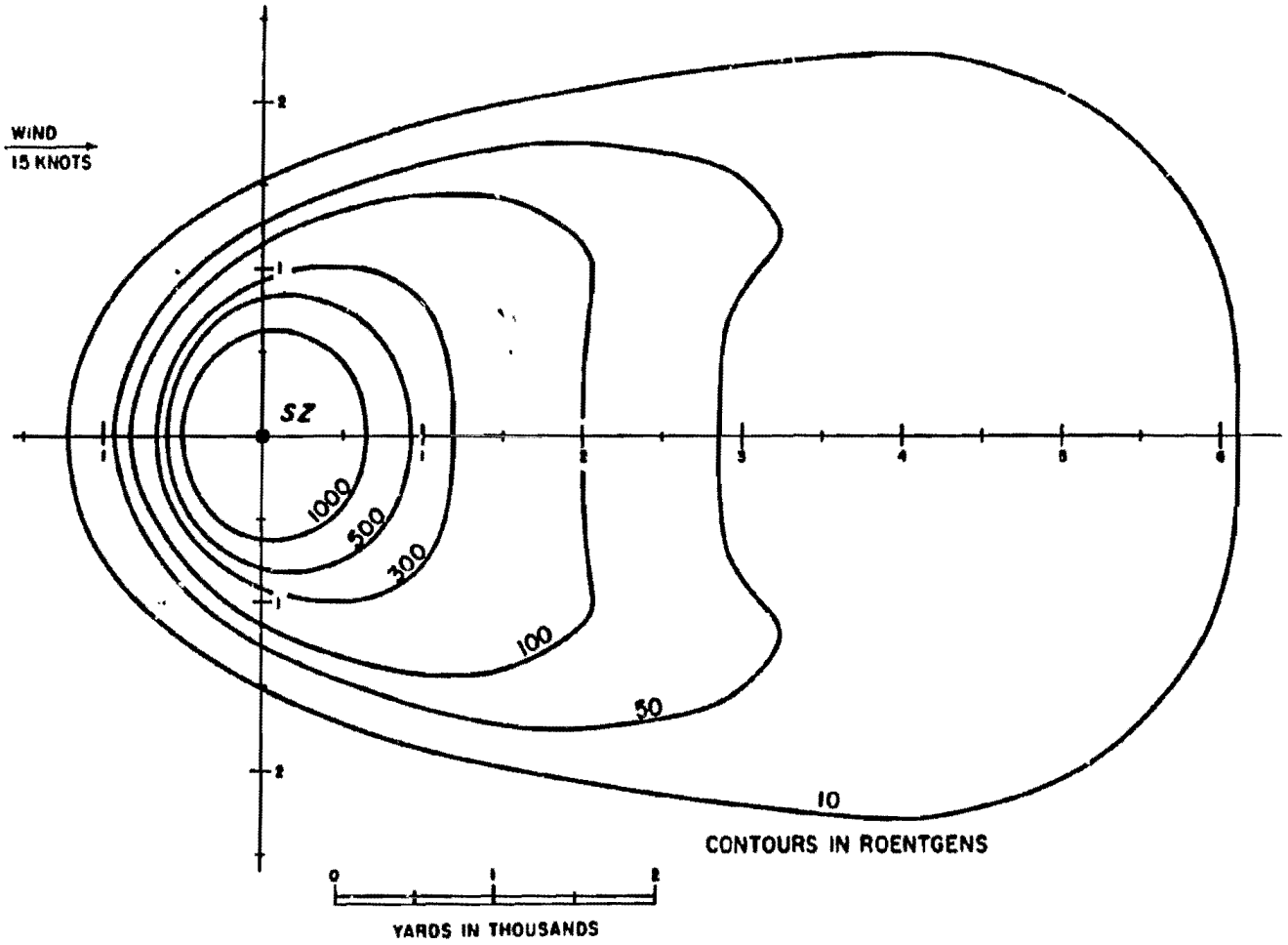

Figure 5-59. [redacted] Ten-Minute Total Exposure 15 Feet Above the Water Surface from a 1 kt Explosion at a Depth of 30 Feet in 5,000 Feet of Water, 15 Knot Wind, No-Current Environment [redacted]

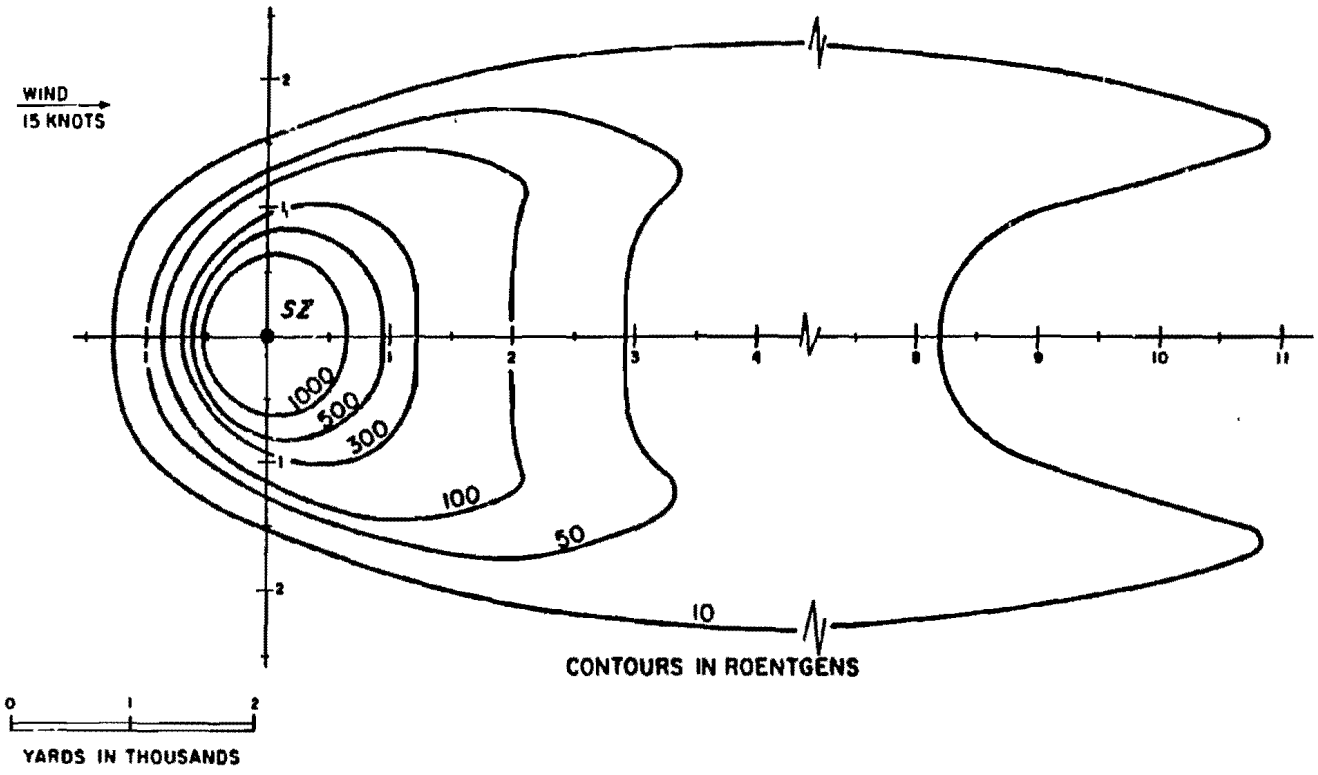

Figure 5-60. [redacted] Thirty-Minute Total Exposure 15 Feet Above the Water Surface from a 1 kt Explosion at a Depth of 30 Feet in 5,000 Feet of Water, 15 Knot Wind, No-Current Environment [redacted]

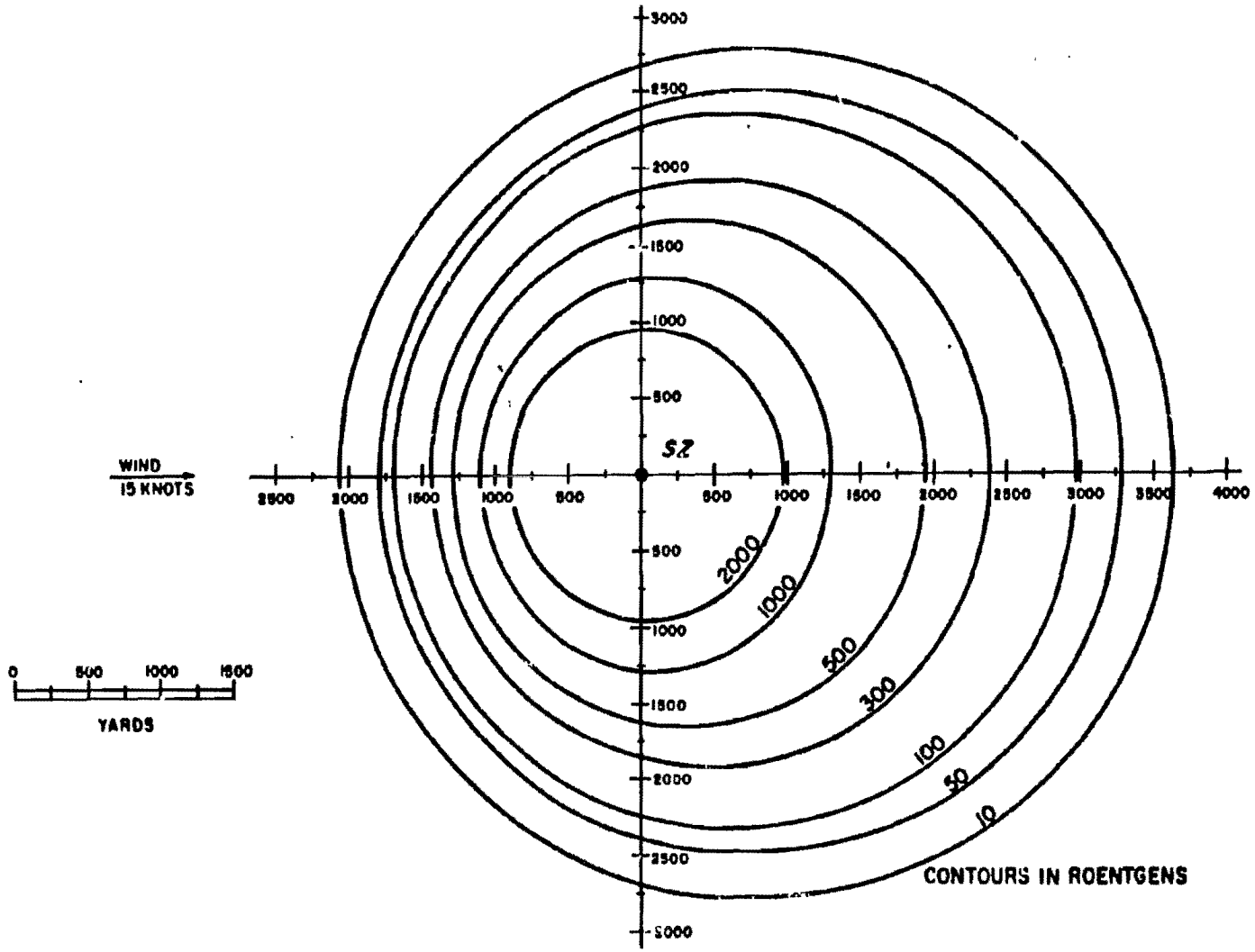

Figure 5-61. [redacted] Two-Minute Total Exposure 15 Feet Above the Water Surface from a 10 kt Explosion at a Depth of 65 Feet in 5,000 Feet of Water, 15 Knot Wind, No-Current Environment [redacted]

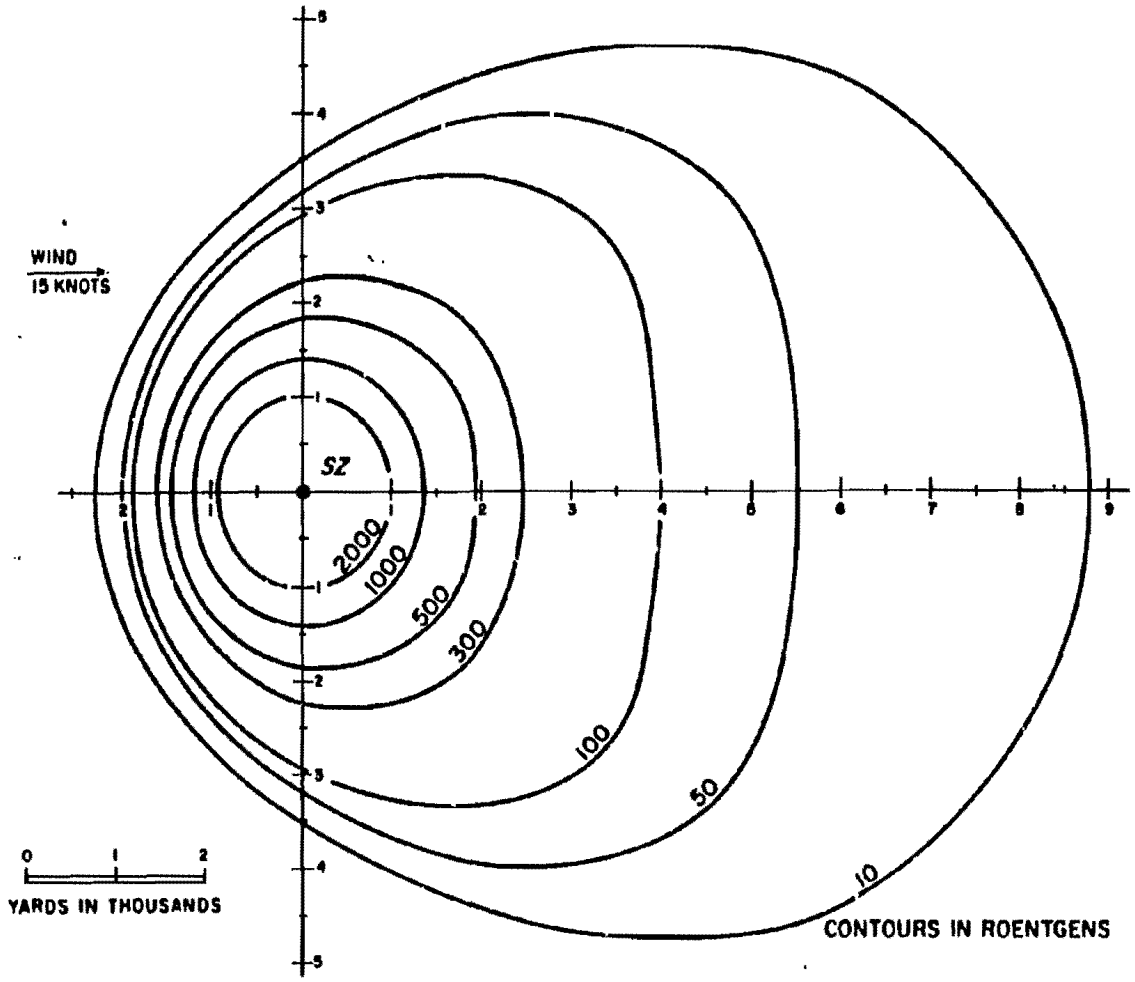

Figure 5-62. [redacted] Ten-Minute Total Exposure 15 Feet Above the Water Surface from a 10 kt Explosion at a Depth of 65 Feet In 6,000 Feet of Water, 15 Knot Wind, No-Current Environment [redacted]

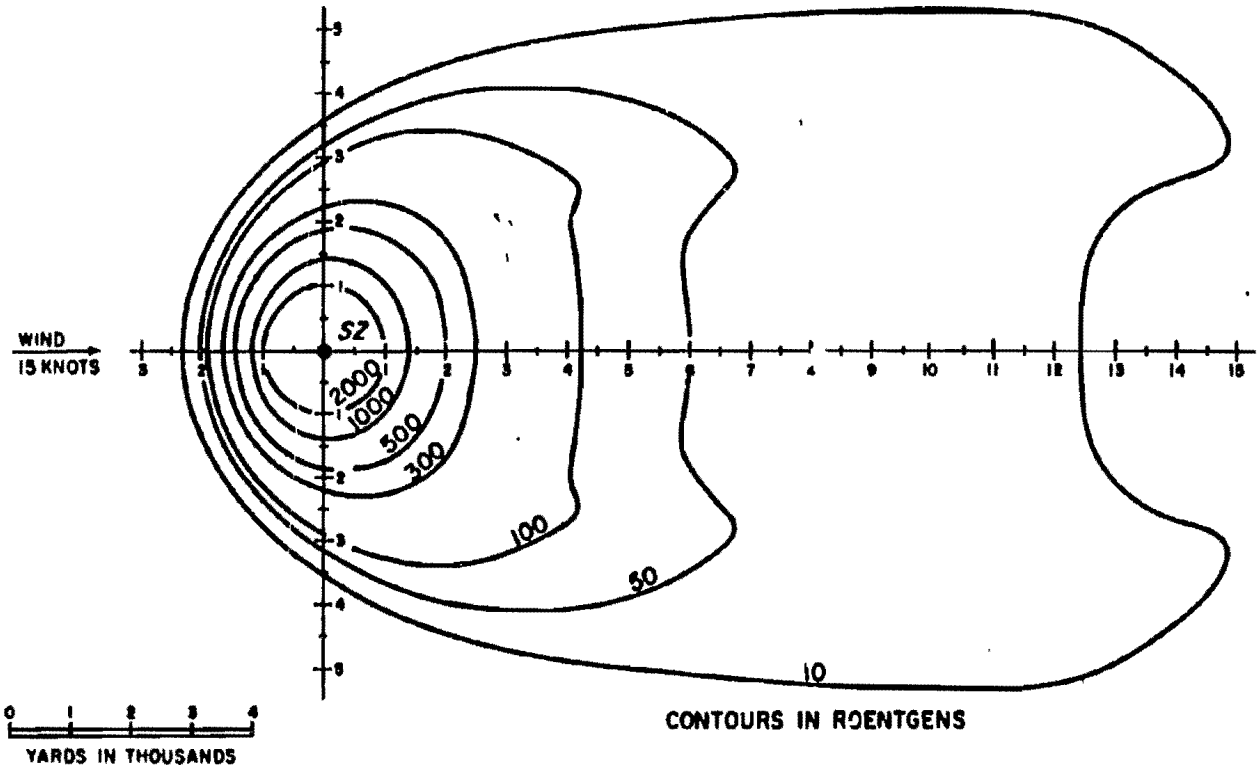

Figure 5-63. [redacted] Thirty-Minute Total Exposure 15 Feet Above the Water Surface from a 10 kt Explosion at a Depth of 65 Feet in 5,000 Feet of Water, 15 Knot Wind, No-Current Environment [redacted]

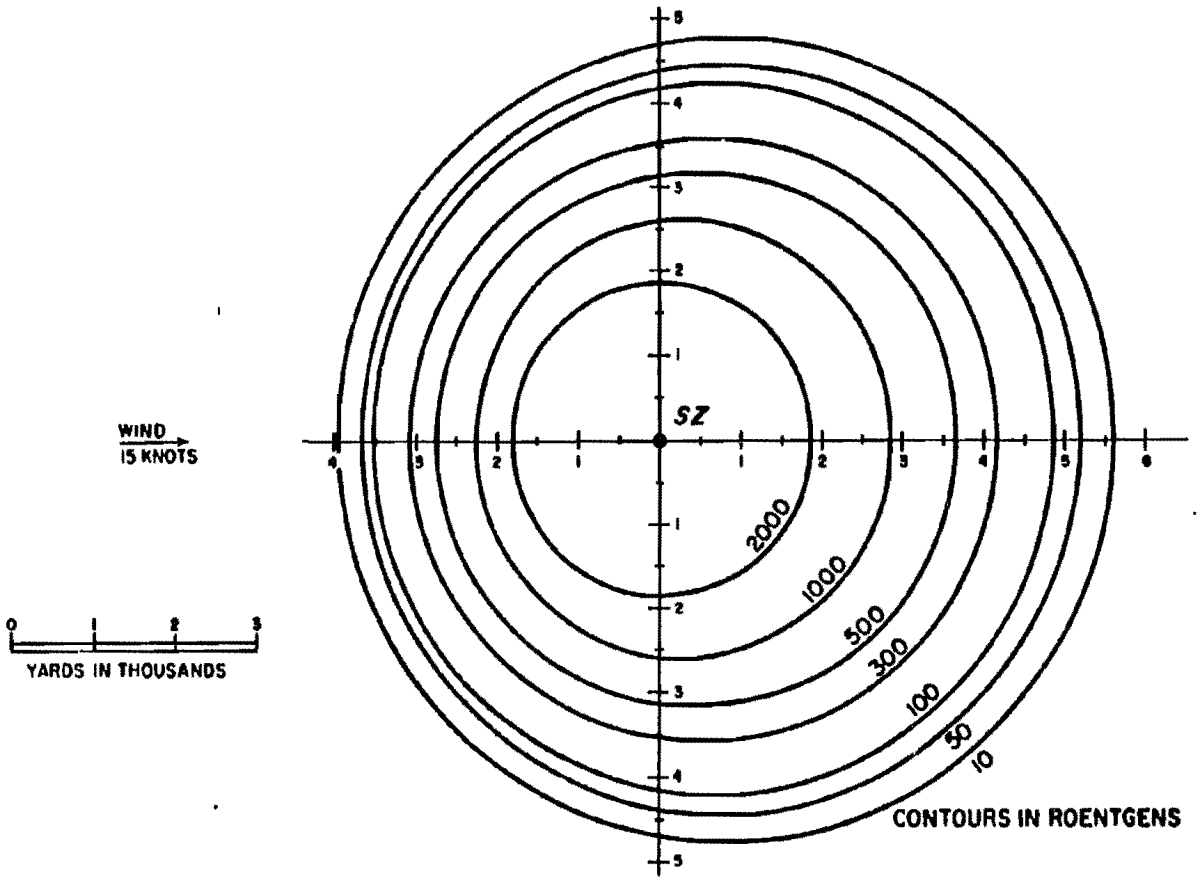

Figure 5-64. [redacted] Two-Minute Total Exposure 15 Feet Above the Water Surface from a 100 kt Explosion at a Depth of 140 Feet in 5,000 Feet of Water, 15 Knot Wind, No-Current Environment [redacted]

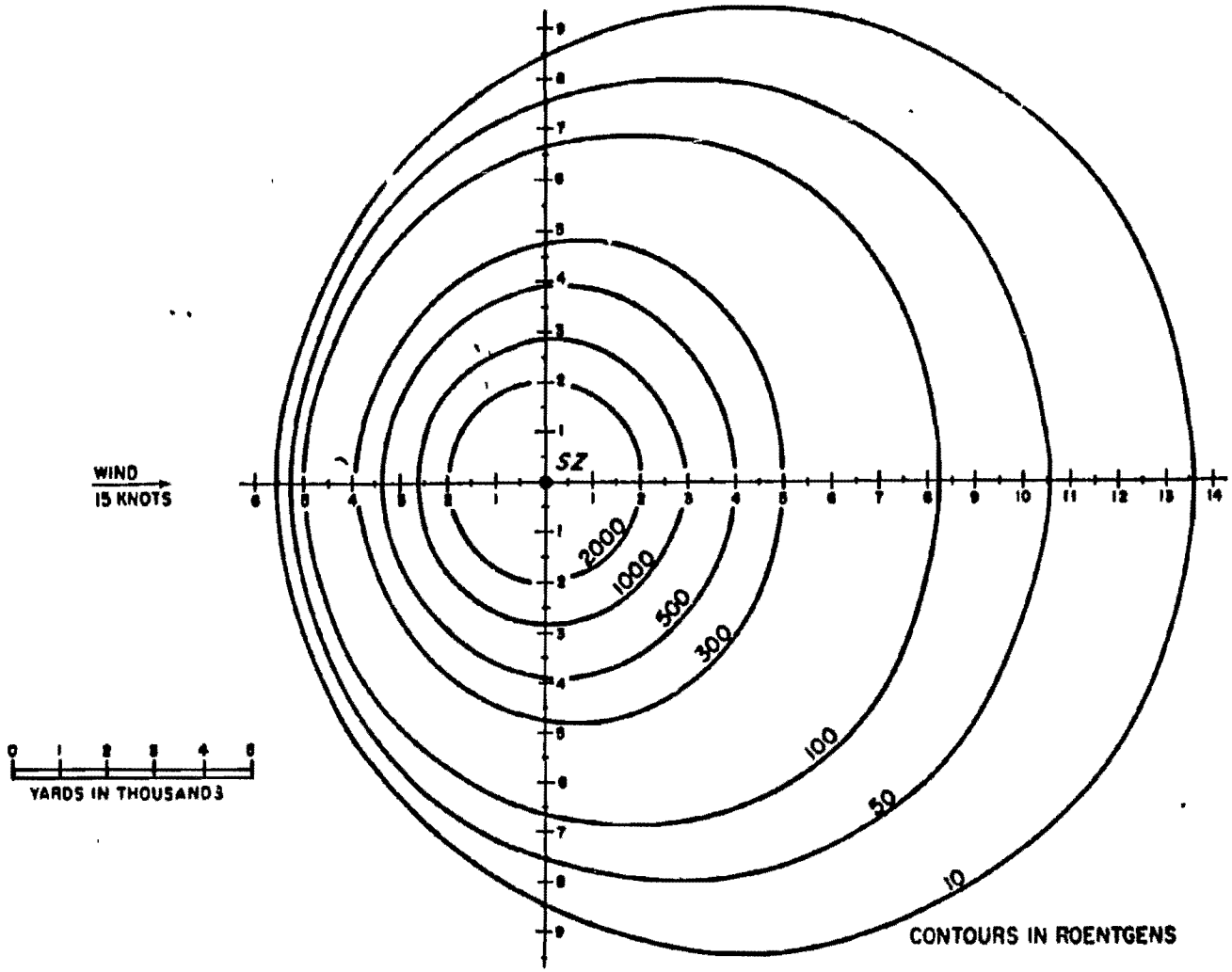

Figure 5-65. [redacted] Ten-Minute Total Exposure 15 Feet Above the Water Surface from a 100 kt Explosion at a Depth of 140 Feet in 5,000 Feet of Water, 15 Knot Wind, No-Current Environment [redacted]

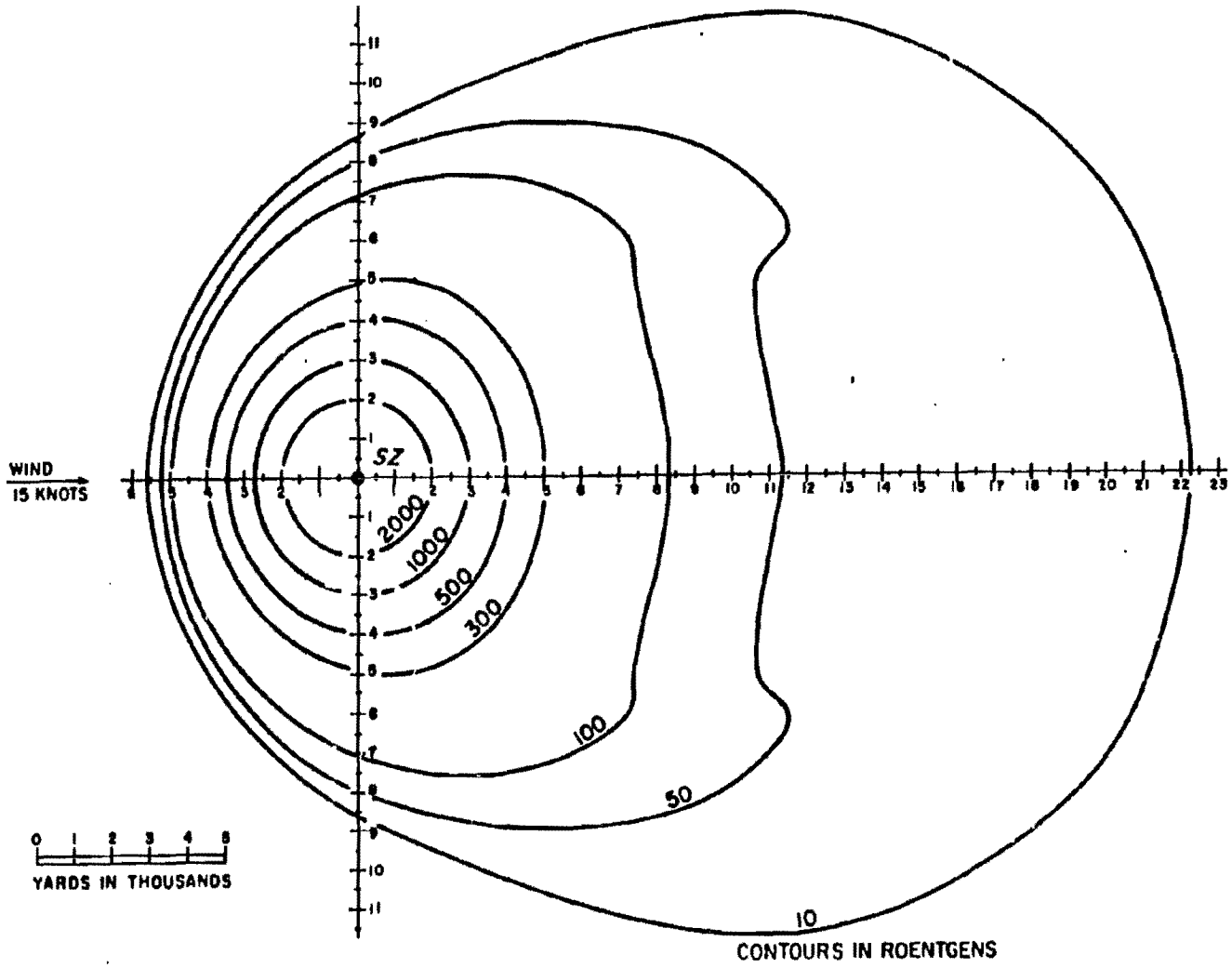

Figure 5-66. [redacted] Thirty-Minute Total Exposure 15 Feet Above the Water Surface from a 100 kt Explosion at a Depth of 140 Feet in 5,000 Feet of Water, 15 Knot Wind, No-Current Environment [redacted]

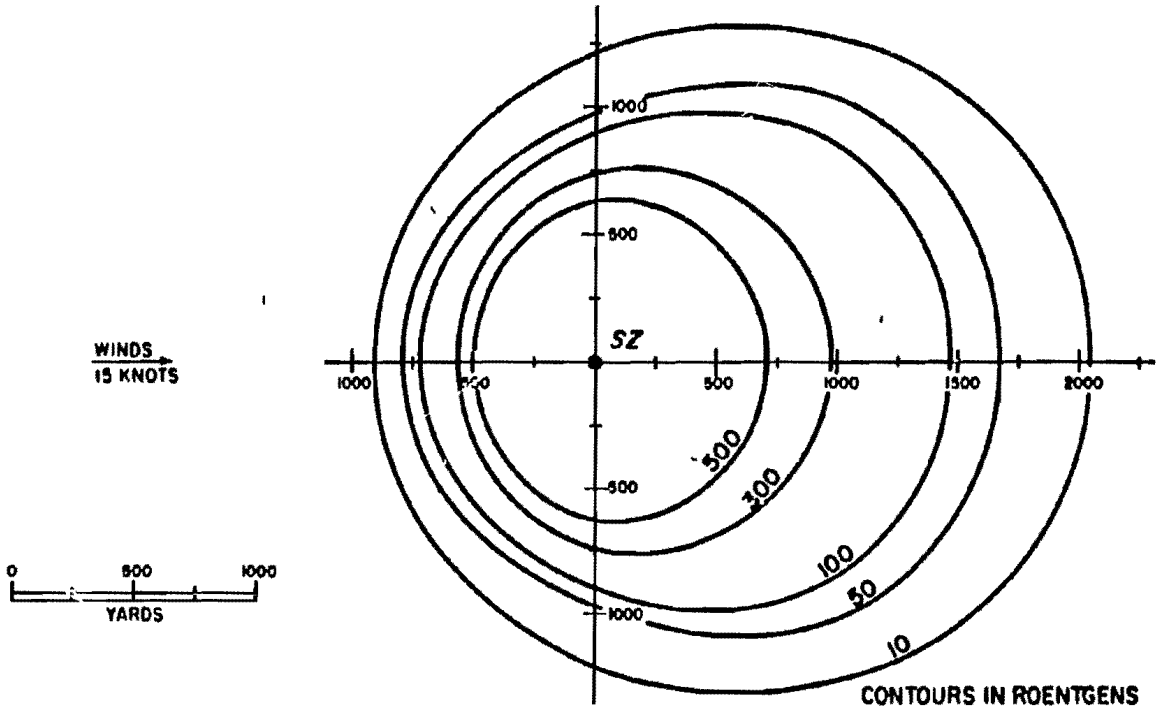

Figure 5-67. [redacted] Two-Minute Total Exposure 15 Feet Above the Water Surface from a 1 kt Explosion at a Depth of 280 Feet in 5,000 Feet of Water, 15 Knot Wind, No-Current Environment [redacted]

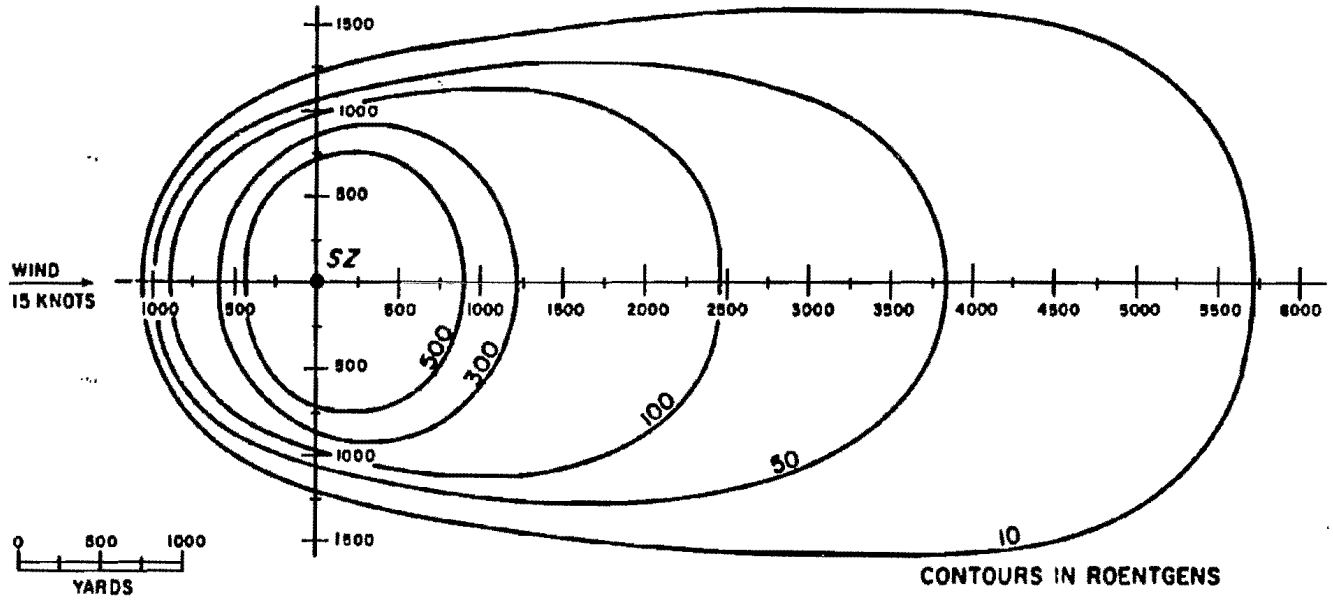

Figure 5-68. [redacted] Ten-Minute Total Exposure 15 Feet Above the Water Surface from a 1 kt Explosion at a Depth of 280 Feet in 5,000 Feet of Water, 15 Knot Wind, No-Current Environment [redacted]

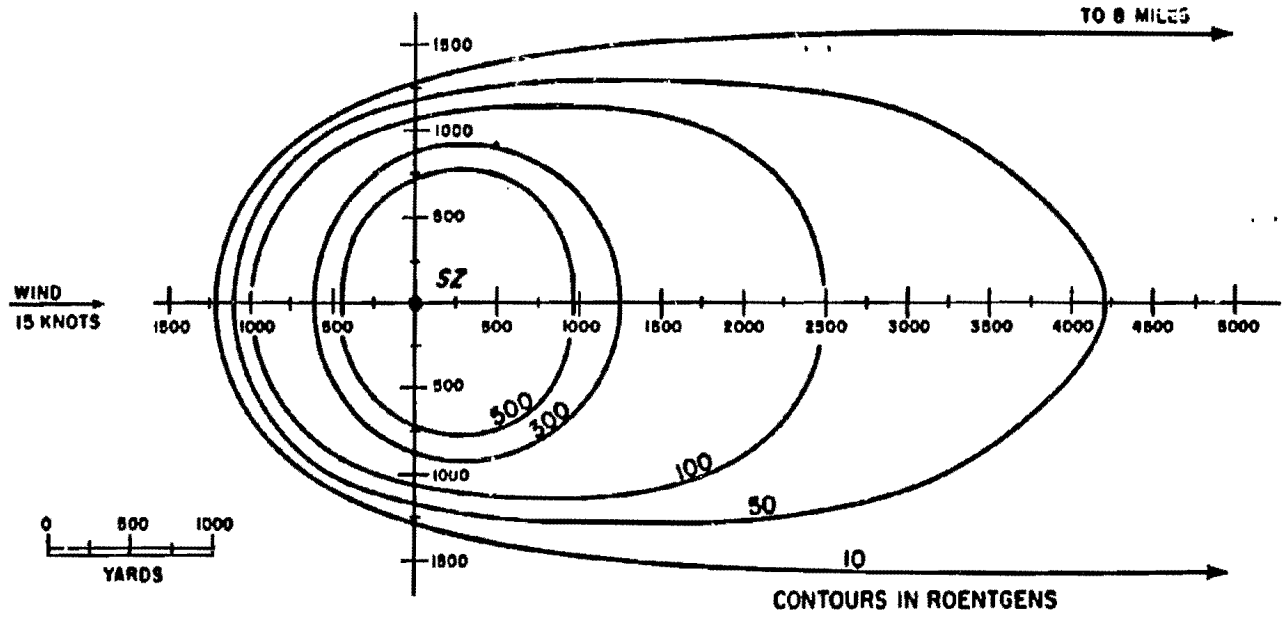

Figure 6-69. [redacted] Thirty-Minute Total Exposure 15 Feet Above the Water Surface from a 1 kt Explosion at a Depth of 280 Feet in 5,000 Feet of Water, 15 Knot Wind, No-Current Environment [redacted]

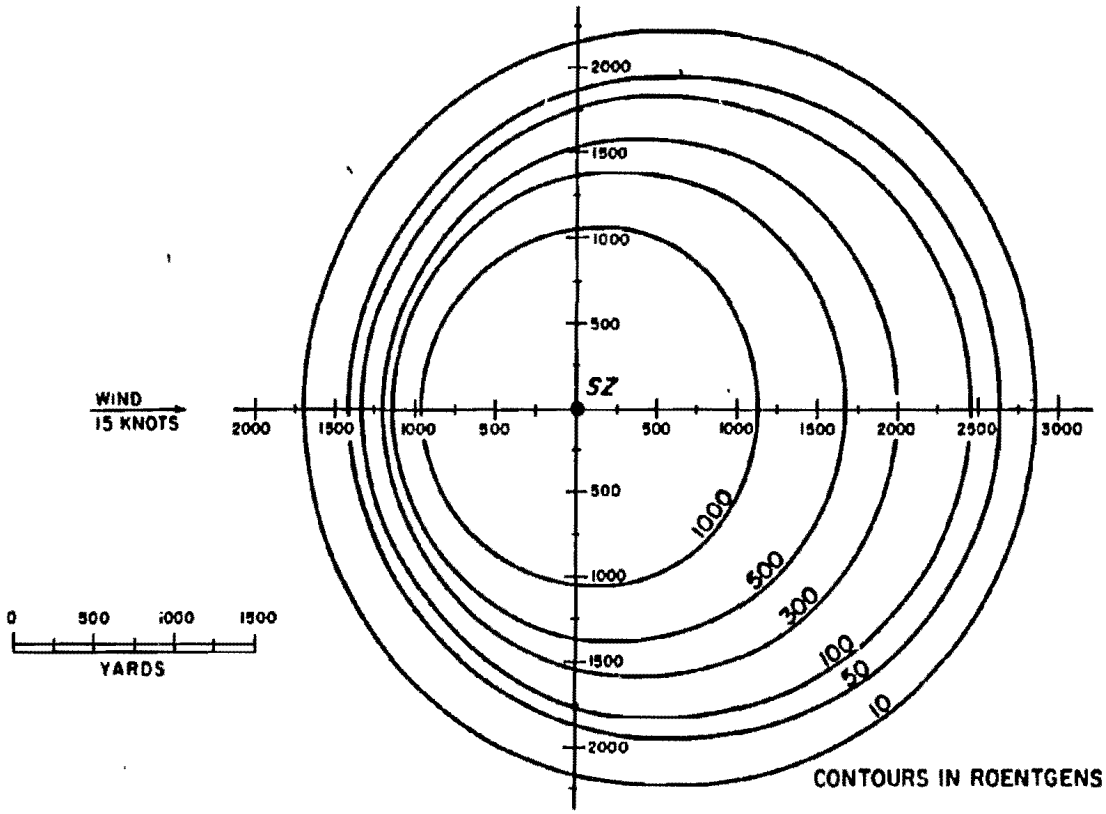

Figure 5-70. [redacted] Two-Minute Total Exposure 15 Feet Above the Water Surface from 10 kt Explosion at a Depth of 600 Feet in 6,000 Feet of Water, 15 Knot Wind, No-Current Environment [redacted]

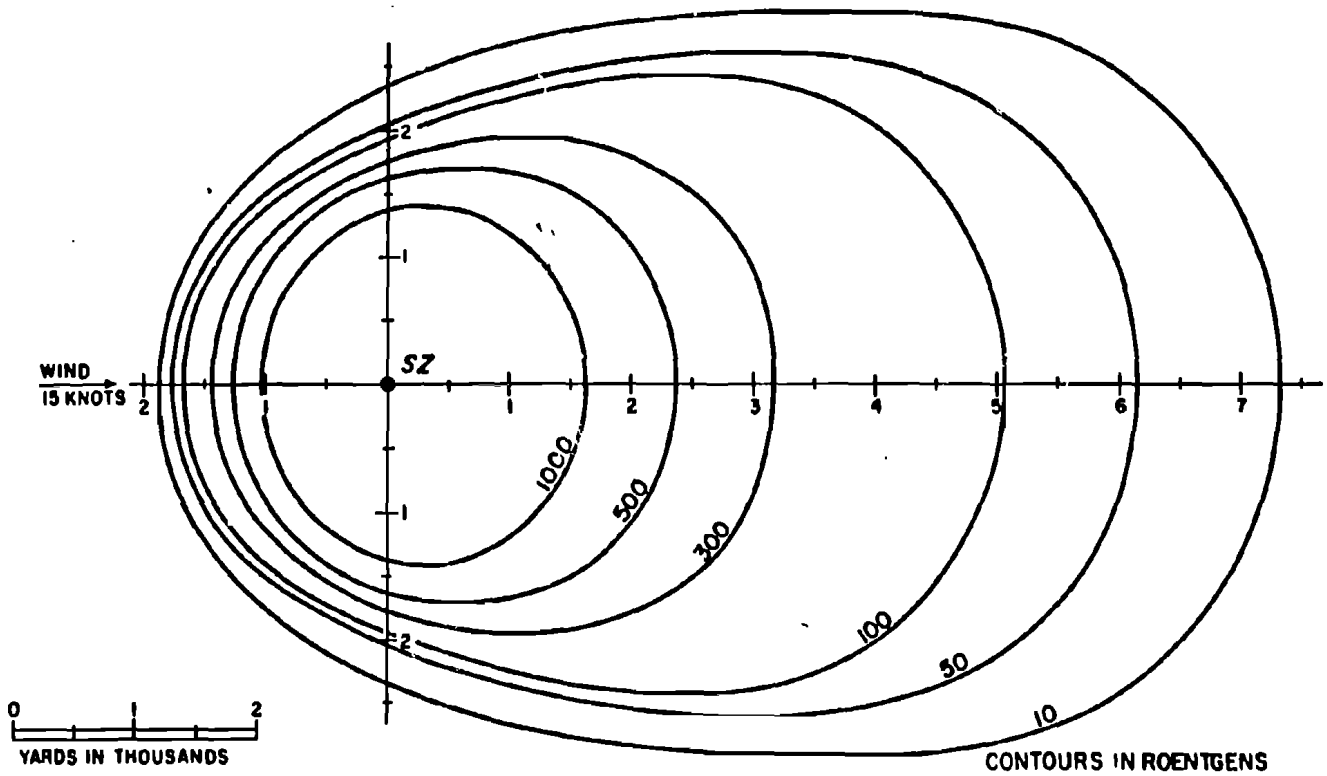

Figure 5-71. [redacted] Ten-Minute Total Exposure 15 Feet Above the Water Surface from a 10 kt Explosion at a Depth of 500 Feet in 5,000 Feet of Water, 15 Knot Wind, No-Current Environment [redacted]

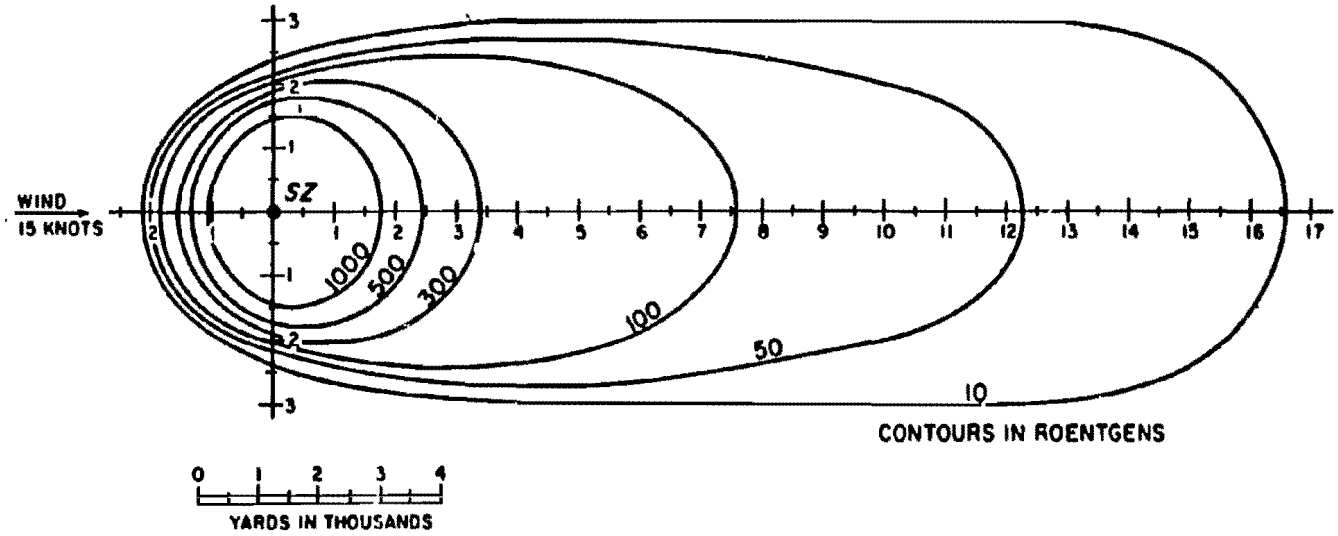

Figure 5-72. [redacted] Thirty-Minute Total Exposure 15 Feet Above the Water Surface from a 10 kt Explosion at a Depth of 500 Feet in 5,000 Feet of Water, 15 Knot Wind, No-Current Environment [redacted]

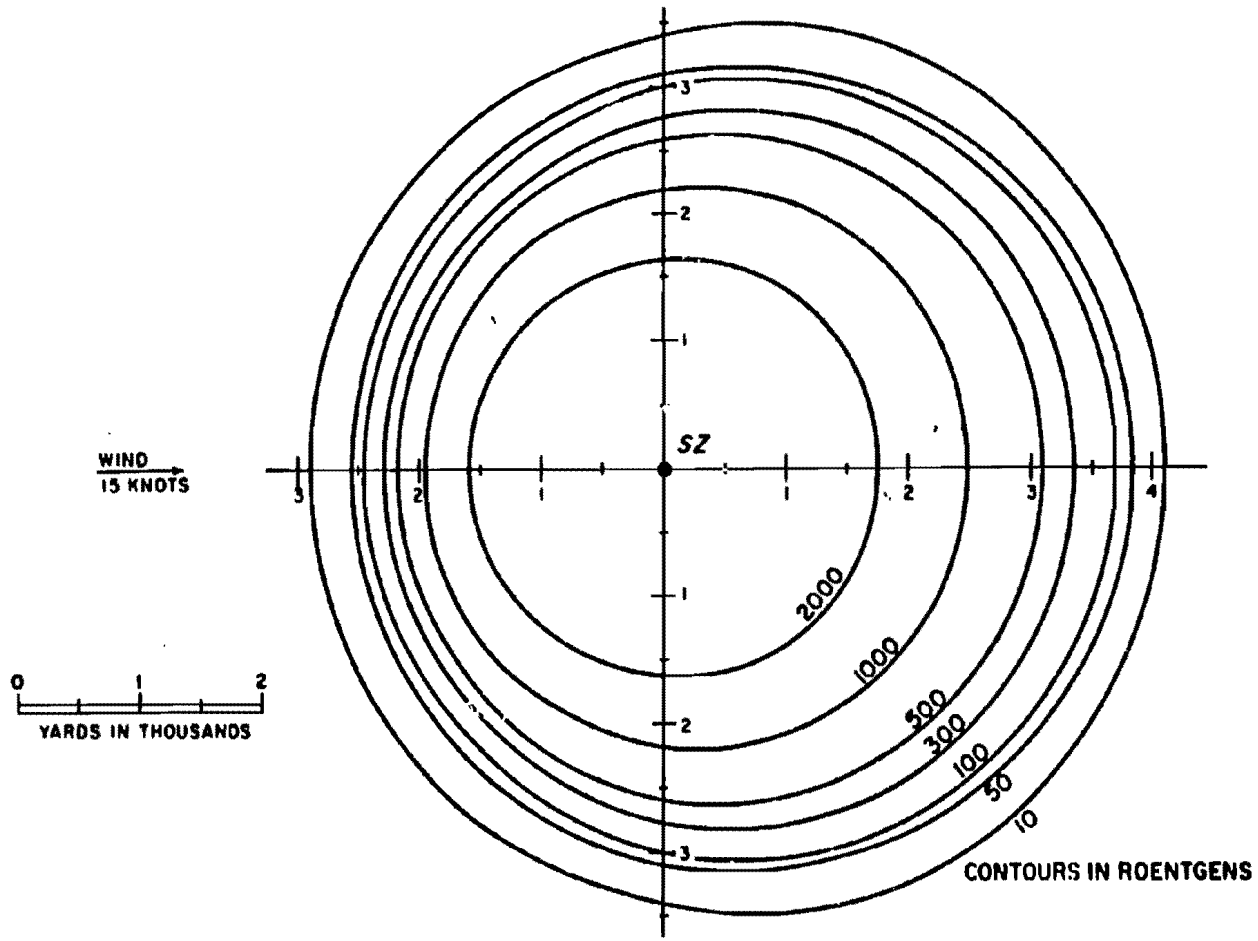

Figure 5-73. [redacted] Two-Minute Total Exposure 15 Feet Above the Water Surface from a 100 kt Explosion at a Depth of 890 Feet in 5,000 Feet of Water, 15 Knot Wind, No-Current Environment [redacted]

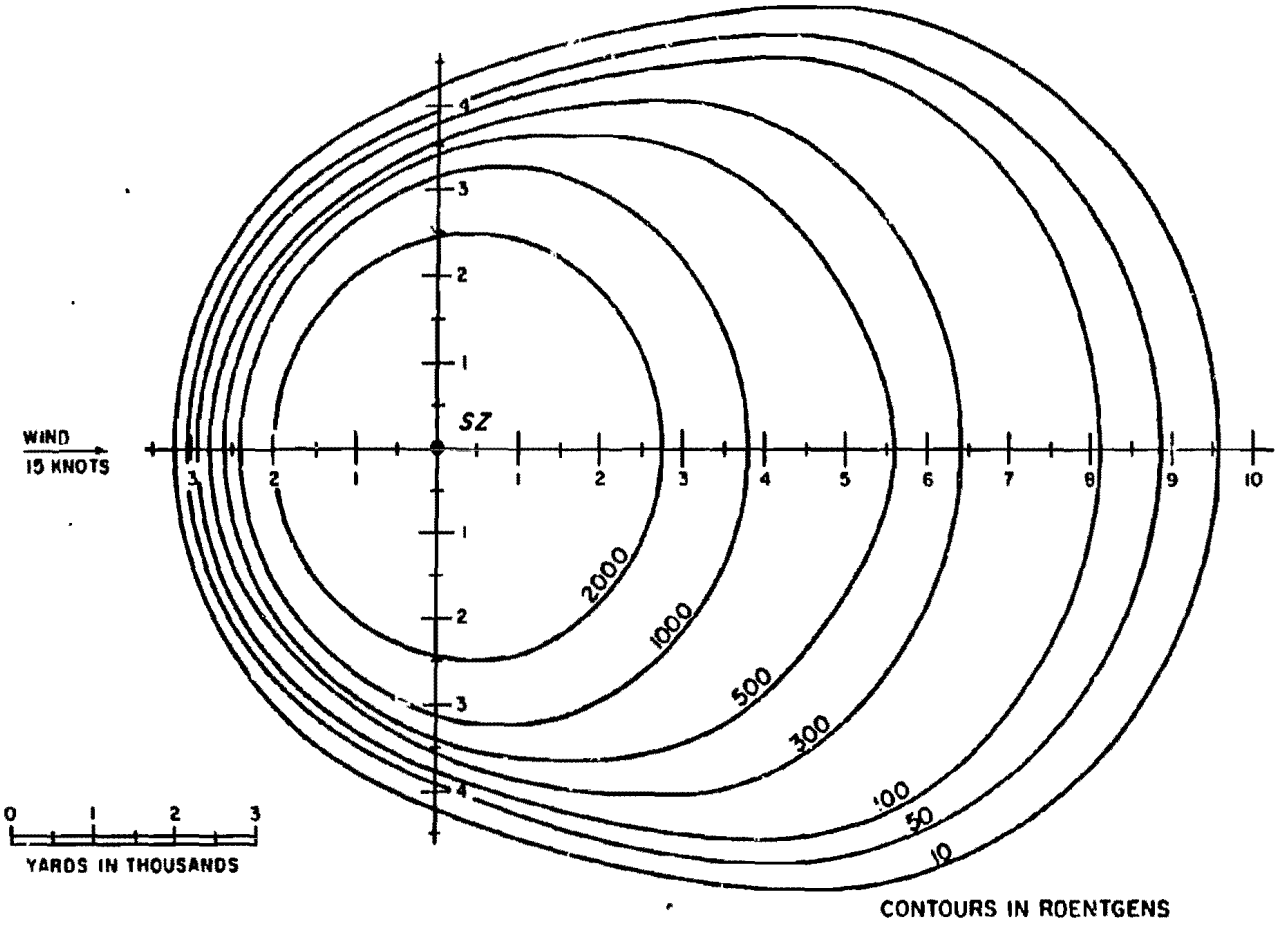

Figure 5-74. [redacted] Ten-Minute Total Exposure 15 Feet Above the Water Surface from a 100 kt Explosion at a Depth of 890 Feet in 5,000 Feet of Water, 15 Knot Wind, No-Current Environment [redacted]

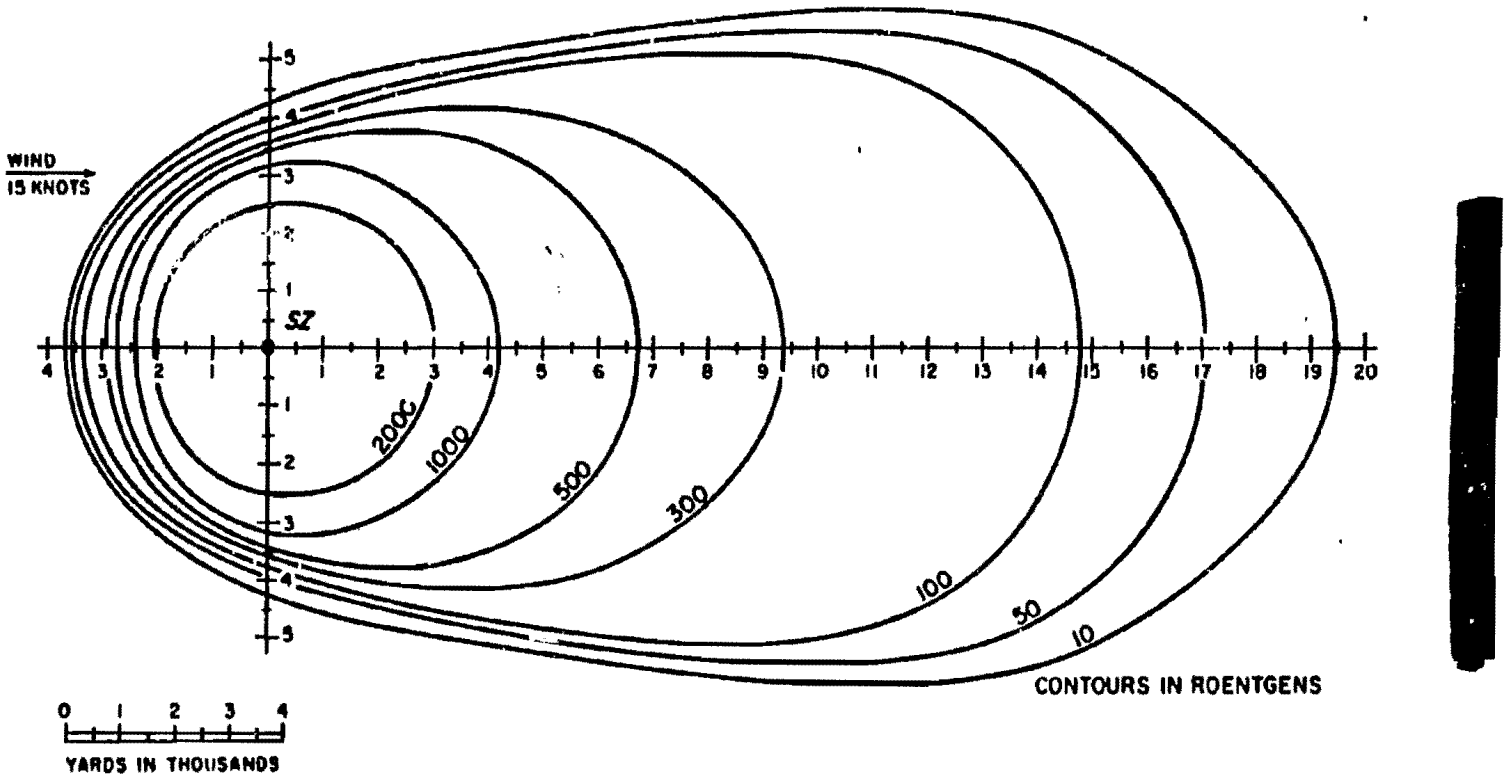

Figure 5-75. [redacted] Thirty-Minute Total Exposure 15 Feet Above the Water Surface from a 100 kt Explosion at a Depth of 890 Feet in 5,000 Feet of Water, 15 Knot Wind, No-Current Environment [redacted]

[redacted]

[redacted] DOSE RECEIVED WHILE FLYING THROUGH A NUCLEAR CLOUD [redacted]

[redacted] The radioactive nuclear cloud represents a potential hazard to crews of aircraft that fly through the cloud. The dose that a crew might receive will depend upon many variables including the time after burst (which determines the intensity of the radiation as well as the size of the cloud), the portion of the cloud traversed, and the length of transit time through the cloud.

[redacted] After stabilization, the particles that make up the radioactive cloud will travel with the winds as they fall, and, since the wind speed and direction are both likely to vary with altitude and time, the size and shape of the cloud can only be described by complex computer codes that can accept temporal and spatial variations in weather data. No simple idealized shape can describe the cloud adequately. Even during the time of cloud rise, the winds will act on the particles, and the cloud probably will not stabilize directly above ground zero; however, the shape can be approximated roughly by a right circular cylinder, with a stem of smaller diameter below it, at the time of stabilization. Figures 5-76 through 5-78 show the cloud diameter, the height of the cloud bottom, and the height of the cloud top, respectively, as functions of time after burst for various yields. These figures allow approximations of the cloud dimensions during the first few minutes after an explosion.

[redacted] Even if the cloud geometry were known, no satisfactory model exists from which simple scaling procedures could be developed to predict the dose received while flying through the cloud. Figure 5-79 shows estimates of the transit dose as a function of transit time for several entry times. These estimates were extrapolated from a limited amount of test data. The relative hazard for flight through the stem is even less certain, but it is believed to be less than that from flight through the center of the cloud.

[redacted]

[redacted]

Problem 5-14. Calculation of Dose Received While Flying Through a Nuclear Cloud

[redacted] The curves in Figure 5-79 show the total dose received while passing through nuclear clouds at various times after burst. Figures 5-76 through 5-78 provide the dimensions of the cloud as a function of time after burst.

[redacted] *Example* [redacted]

Given: An aircraft flying at 235 knots at an altitude of 23,000 feet passes through a nuclear cloud from a 50 kt weapon 5 minutes after the explosion.

Find: The probable maximum exposure of the crew, assuming that the shielding of the aircraft structure is negligible.

Solution: From Figure 5-77, the height of the cloud bottom will be about 16,000 feet 5 minutes after a 50 kt explosion, and from Figure 5-78, the corresponding height of the cloud top is 30,000 feet. Thus, the aircraft is flying at an altitude corresponding to the vertical center of the cloud. The maximum dose (corresponding to maximum transit time) will occur if the aircraft flies through the horizontal center of the cloud, i.e., if the aircraft traverses the entire diameter. From Figure 5-76, the diameter of a cloud from a 50 kt explosion will be 2.7 miles at 5 minutes after the burst. The aircraft speed is

$$235 \times 1.15 = 270 \text{ mph.}$$

The transit time is

$$\frac{2.7}{270} = 0.01 \text{ hr}$$

$$= 0.6 \text{ min.}$$

Answer: From Figure 5-79, with an entry time of 5 minutes and a transit time of 0.6 minutes, the expected dose is 37 rads. The maximum dose might be twice this value (see Reliability below), or

$$2 \times 37 = 74 \text{ rads.}$$

[redacted] *Reliability.* The doses obtained from Figure 5-79 are estimated to be accurate within a factor of 2 for flight paths that pass near the cloud center. If the path is near the cloud boundary, the predicted dose probably will be higher than the actual dose, although the magnitude of the error is unknown. Additional uncertainties of unknown magnitude are introduced by the prediction of the cloud size, but these uncertainties are not believed to be large for times of entry soon after burst and for short transit times.

[redacted] *Related Material:* See paragraphs 5-15 through 5-19.

[redacted]

[redacted]

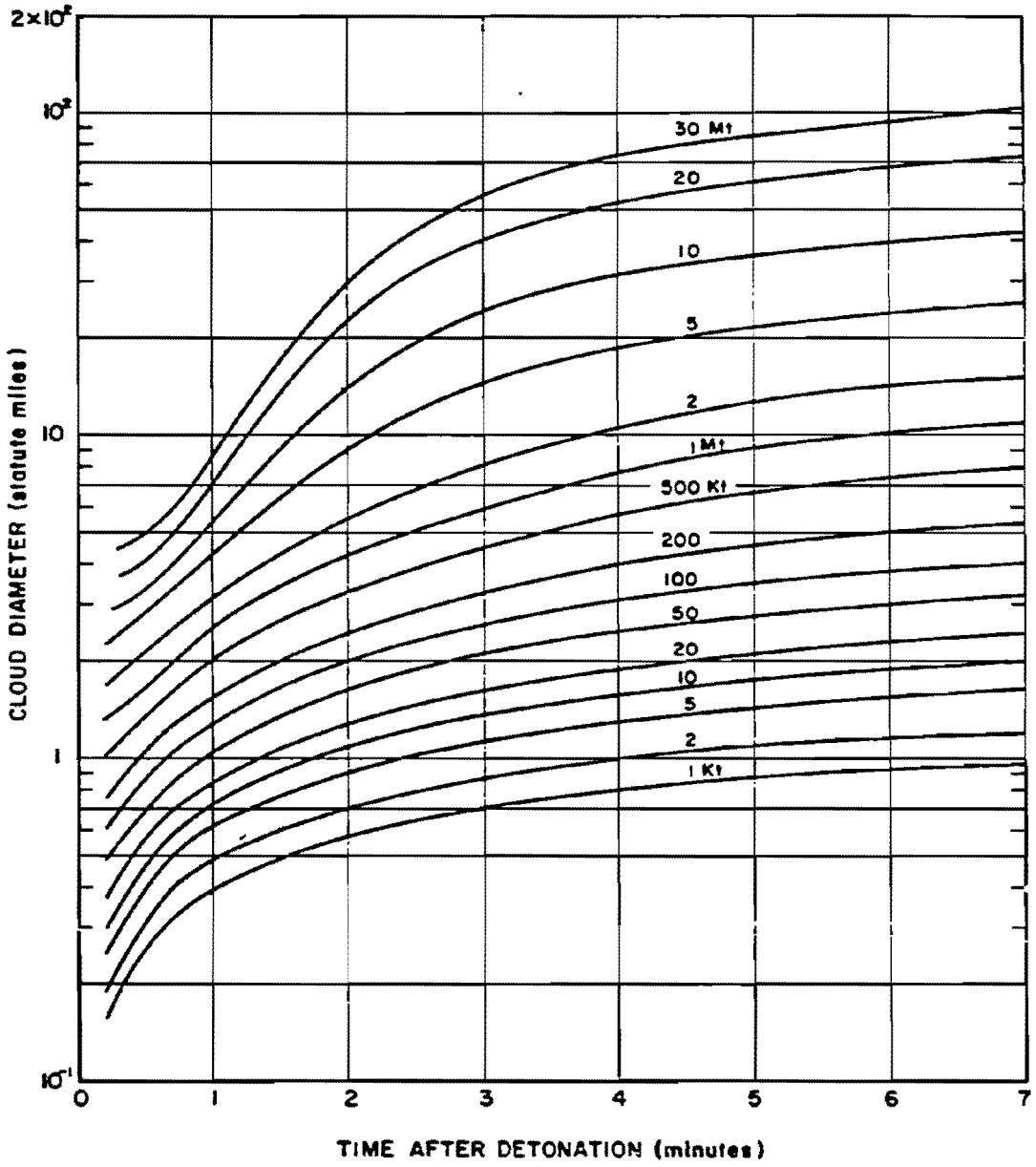

Figure 5-76. [redacted] Cloud Diameter as a Function of Time After Burst for Various Weapon Yields [redacted]

[redacted]

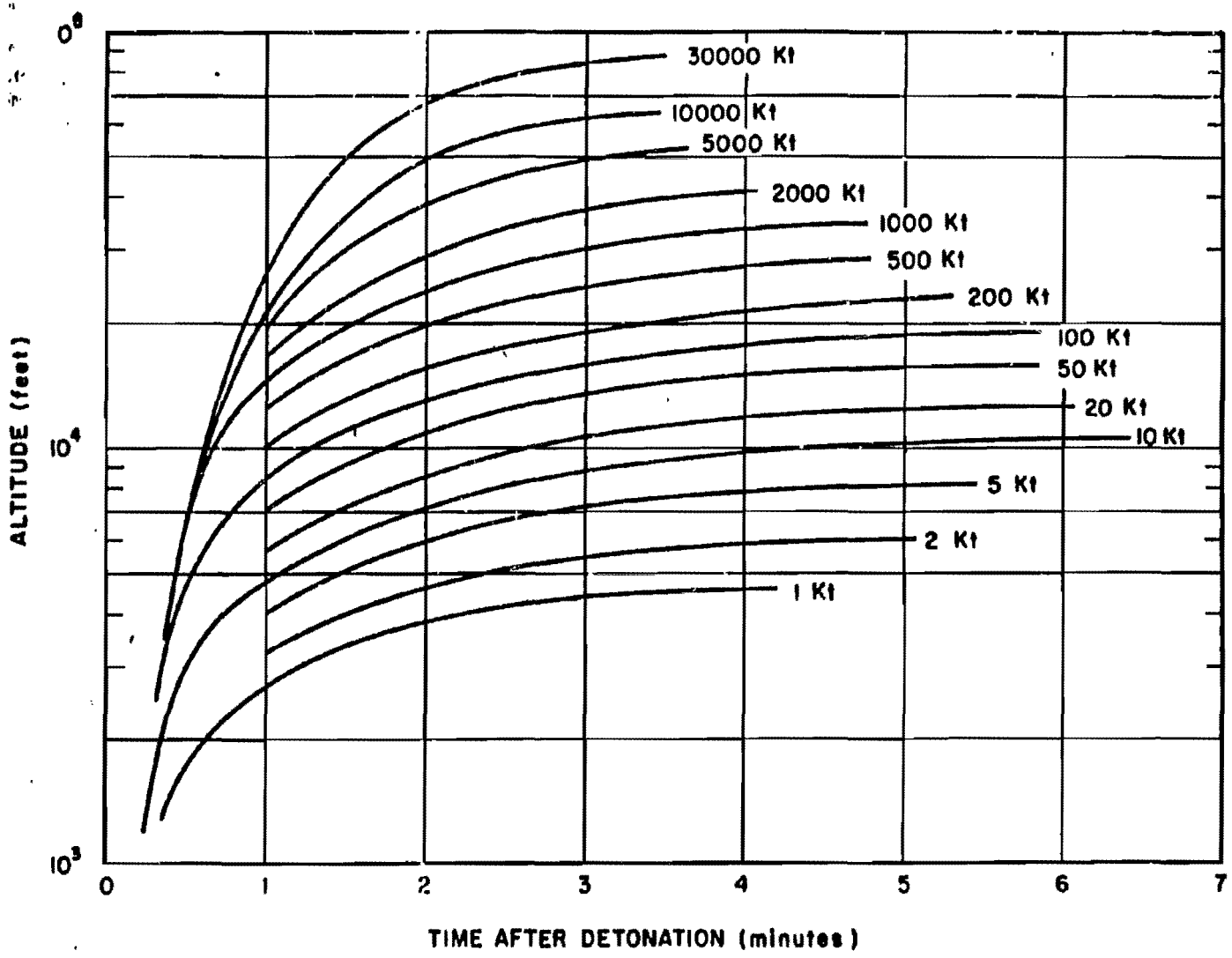

Figure 5-77. [redacted] Height of Cloud Bottom as a Function of Time for Various Weapon Yields [redacted]

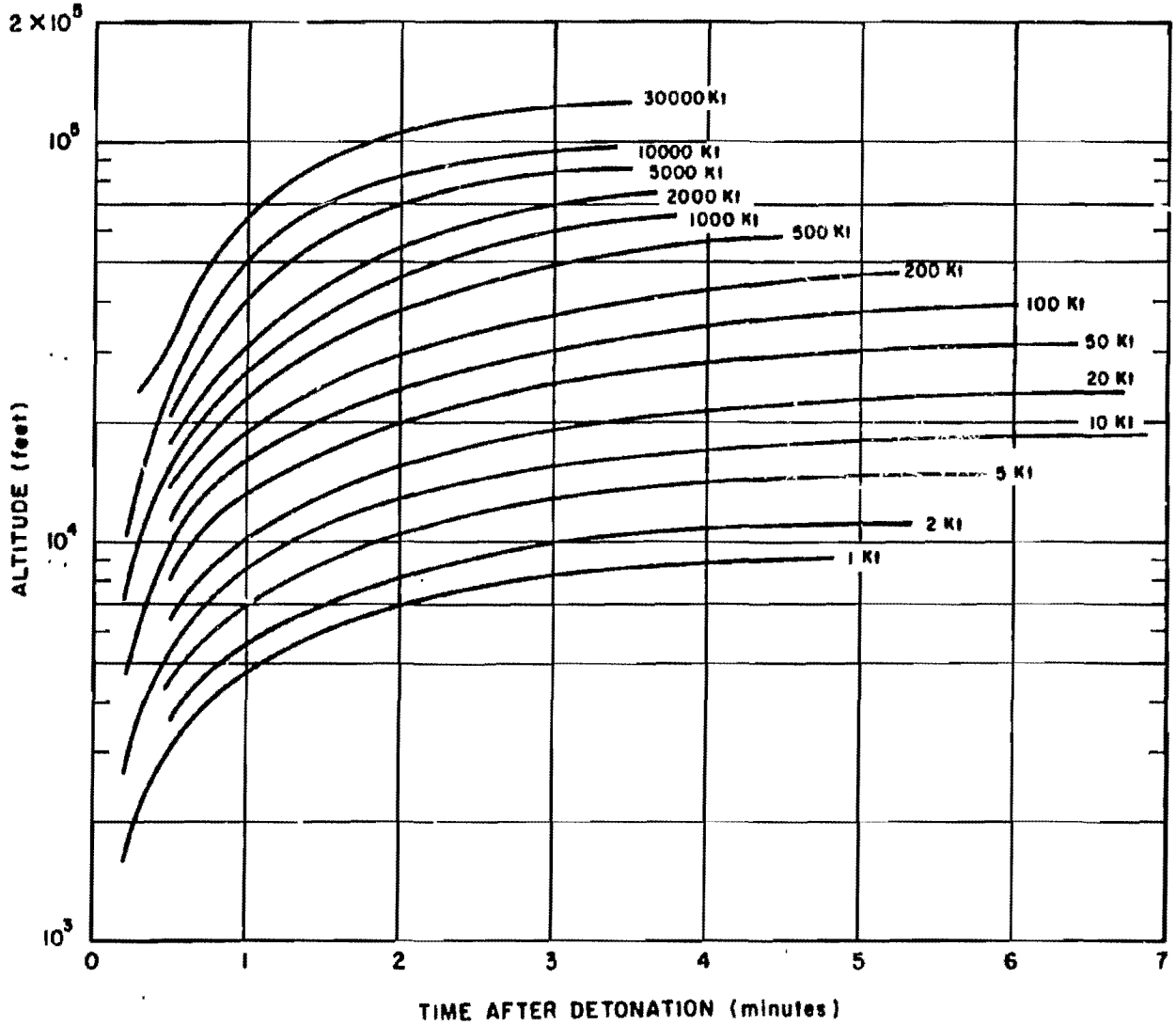

Figure 5-78. [redacted] Height of Cloud Top as a Function of Time for Various Weapon Yields [redacted]

[redacted]

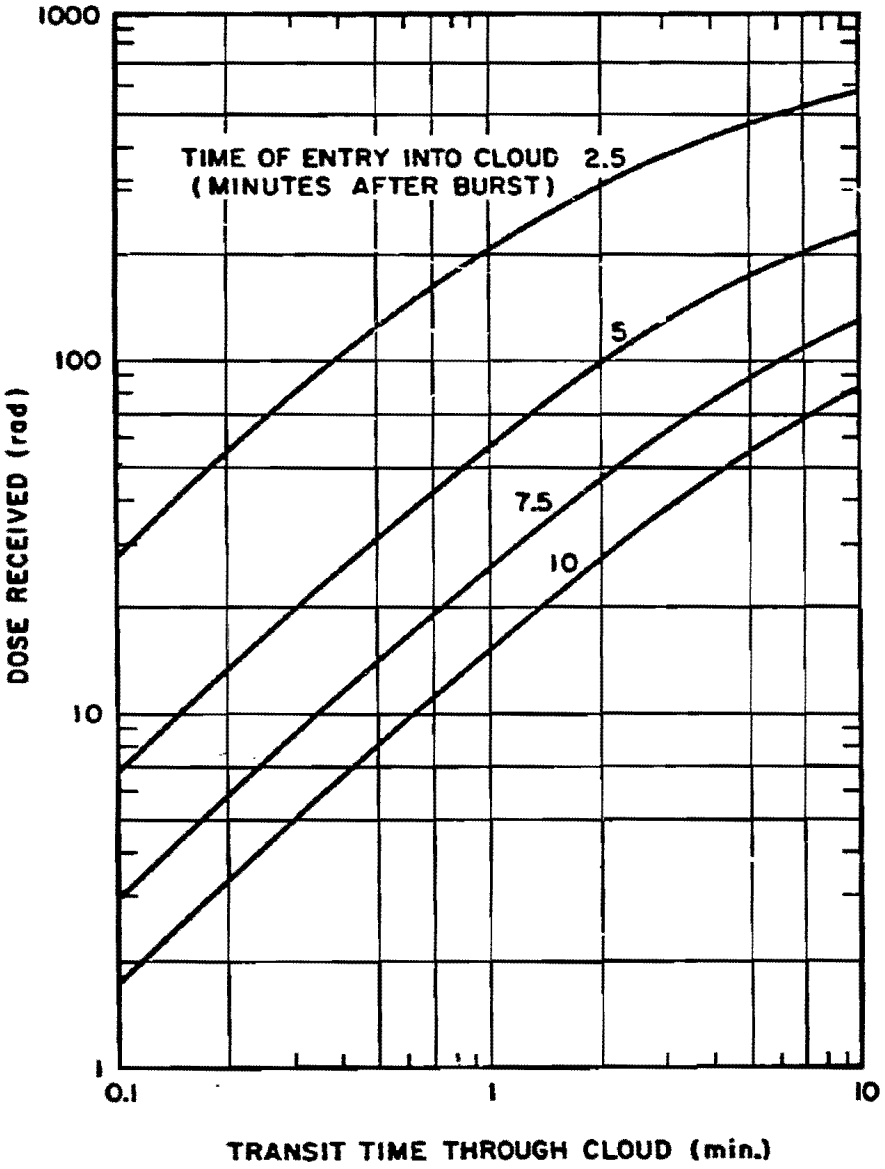

Figure 5-79. [redacted] Dose Received While Flying Through a Nuclear Cloud as a Function of Transit Time Through the Cloud [redacted]

[redacted]

PRECIPITATION EFFECTS

As mentioned in paragraph 5-16, the surface contamination from an air burst weapon will be militarily insignificant in most cases. The radioactive particles remaining from the weapon debris are extremely small, having diameters that range roughly between 0.01 and 20 micrometers. The weapon cloud carries these particles to high altitudes, with the exact altitude being dependent on the weapon yield and atmospheric conditions. These particles are too small to fall, but they can diffuse downward and can be deposited by atmospheric turbulence processes. In the absence of precipitation, the deposition process takes place over sufficiently long periods of time that the cloud will have spread over a large volume as a result of diffusion and the action of winds at different levels, thereby reducing the particle concentration. Over this same period of time the radioactive decay decreases the activity levels. The net result is that dry deposition of particles from air burst weapons will not be militarily significant although there may be some long-term effects, e.g., thyroid exposures from radioactive iodine. If precipitation occurs in or above the nuclear cloud, however, there is a possibility that contamination that could be considered militarily significant may be deposited on the ground as a result of scavenging of the radioactive particles by the rain or snow. Precipitation also can affect the fallout from a surface or subsurface burst, but contamination is expected from these bursts with or without precipitation. The primary effect of precipitation on the contamination resulting from surface or subsurface bursts would be to change the location and shape of the militarily significant fallout contours. If precipitation scavenges and deposits that portion of the radioactive debris from surface or subsurface bursts that would have been delayed fallout rather than early fallout (see Section III, "RESIDUAL RADIATION," "FALLOUT"), the resulting contamination on the ground is not expected to be militarily significant.

5-27 Precipitation Scavenging

Precipitation scavenging may be divided into two types: scavenging when the nuclear cloud is within the rain cloud, usually called rainout or snowout; and scavenging when the nuclear cloud is below the rain (snow) cloud, usually called washout. Rainout is generally considered to be a much more efficient form of scavenging than washout, but there are many factors that affect precipitation scavenging and the ground contamination resulting therefrom. These factors are discussed in the succeeding paragraph.

5-28 Factors Affecting the Prediction of Ground Contamination from Precipitation Effects

The prediction of the contamination patterns that may result from precipitation scavenging of air burst nuclear weapons is complicated by many factors. Some of the important factors are discussed below.

- *The burst occurs during precipitation.* If the burst occurs during heavy precipitation, or if heavy precipitation begins at the burst location during stabilization time, the pattern will be roughly circular around ground zero, and will be roughly the size of the nuclear cloud (if the rain cloud extends to distances beyond the nuclear cloud radius).

- *The weapon yield.* The cloud from low yield weapons will be completely contained beneath the rain layers; as the yield is increased, the percentage of the nuclear cloud beneath the rain layer decreases; at a sufficiently high

yield, the entire stabilized cloud will be above the rain layers. Specific yields will, of course, depend upon the height of the rain layer.

- *The size and shape of the nuclear cloud.* If no precipitation occurs during or very soon after burst, the nuclear cloud will reach its stabilized altitude. The size and shape of the radioactive cloud will depend upon the meteorological conditions after the stabilization time (the stabilization altitudes of both the top and bottom of the cloud will depend on the atmosphere within which the explosion occurs, and the position of the stabilized cloud will depend upon the winds that act on it during its rise, but these effects are generally small compared to the changes in cloud shape and size after stabilization). In the absence of precipitation or velocity shear in the wind, the dominant physical phenomena responsible for reducing the activity concentration in a nuclear cloud is diffusion produced by turbulent eddies in the atmosphere. Reasonable estimates of the diffusion in a horizontal plane exist. Less is known about vertical diffusion; however, unless the vertical diffusion causes the particles to enter a zone where the wind speed or direction changes, it will not affect the horizontal concentration. Changes in wind speed and direction can have a significant effect on the size and shape of the nuclear cloud. Since the particles from an air burst are so small that they will not actually "fall," they will be acted on by winds within a specific altitude layer. Frequently, several such layers will exist within the thickness of the cloud at stabilization, each having a different speed and/or direction. Changes in both speed and direction of the wind are likely to occur as a function of time and space. Since most of the particles within any one altitude layer will remain in that layer for long periods of time, differences in wind velocity (speed and direction) between layers, as well as changes within a layer, generally will tend to decrease the horizontal concentration as viewed from above (exceptions may occur, of course, e.g., changes in direction may cause two layer that have separated to overlap after some time). The net result of all of the factors acting on the nuclear cloud from a low altitude air burst is that it generally will tend to increase in size horizontally without drastic changes in the vertical dimension for relatively long periods of time, unless precipitation scavenging occurs. This increase in horizontal dimensions will decrease the concentration of radioactive particles available for scavenging.
- *Radioactive decay.* While the nuclear cloud is drifting, the radioactive isotopes decay continuously. Thus, the longer the time between the explosion and the time that the nuclear cloud encounters precipitation, the smaller the total intensity of radiation that will be available (see Problem 5-9 and Figure 5-40). This, together with the general decrease in horizontal concentration described above, reduces the potential hazard with increasing time.
- *The rain cloud size, and the type and during of the precipitation.* If the rain cloud is smaller than the nuclear cloud, only that portion of the nuclear cloud that is in or below the rain cloud will be available for scavenging (any part of the nuclear cloud that is above the rain cloud is not available, as discussed under the effects of yield above). If the rain cloud is larger than the nuclear cloud in horizontal dimensions, any portion of the nuclear cloud that is in or below the rain cloud will be available for scavenging. The length of time during which the nuclear cloud is available for scavenging will depend on the relative directions and speed of travel of the nuclear and

rain clouds. The efficiency of the scavenging process will depend on the debris characteristics, scavenging mechanisms, and the type of rain. Heavy precipitation generally is considered to be more efficient in the scavenging process than light rainfall. Finally, strong updrafts and downdrafts of wind are frequently found around and within a rain cloud. These vertical air motions could prevent the intersection of the nuclear cloud and the rain cloud, but under some circumstances the air motions could enchance the mixing of the two clouds.

- *The effects of precipitation on the contamination once it reaches the ground.* After radioactive particles are brought to the ground by precipitation, they may or may not stay in place. There is a possibility that water run-off will create hot spots in some areas while decreasing the activity in other areas. Some of the radioactive particles may be leached into the ground and, as a result of the attenuation by the ground between the particle and the ground-air surface, the dose rate above the ground will be reduced.

[redacted] There are no data concerning precipitation effects where the resulting contamination was militarily significant. Also, no computer model has been developed that can include all of the factors described above either on a deterministic or a statistical basis. The results of theoretical studies, field simulations, and laboratory experiments have, however, provided some general conclusions concerning the importance of precipitation effects. First, contamination resulting from precipitation scavenging is *not* considered to be a major problem from the standpoint of effects on military operations. Second, weapons may be separated into three groups according to their relative importance with regard to precipitation effects: 1. weapons in the yield range from 1 to 10 kt are most likely to have an effect on military operations, if any such effect occurs; 2. weapons with yields greater than 10 kt and less than about 60 kt may have some effect on military operations, with the probability of such an effect decreasing with increasing yield; 3. weapons with yields greater than 60 kt or less than 1 kt are not expected to have any effect on military operations. The potential hazard may be reduced by making use of available shelter.

[redacted]

[redacted]

BIBLIOGRAPHY

Baum, S., P. W. Wong, and P. J. Dolan, *NUCROM: A Model of Rainout from Nuclear Clouds*, DNA 3389F, Stanford Research Institute, Menlo Park, California, August 1974 [redacted]

Biggers, W. A., and K. C. Kohr, *Neutron Outputs from Selected LASL Nuclear Devices* [redacted] LA 3688, Los Alamos Scientific Laboratory, Los Alamos, New Mexico, April 1967 [redacted]

Beyster, J. R., et al., *Status of Neutron and Gamma Output from Nuclear Weapons* [redacted] SAI 70-205, DASA 2567, Science Applications Incorporated, La Jolla, California, May 1971 [redacted]

Bunney, L. R., and D. Sam, *Gamma-Ray Spectra of Fractionated Fission Products*, NOLTR 71-103, Naval Ordnance Laboratory, White Oak, Silver Spring, Maryland, 18 June 1971 [redacted]

Canu, J. F., and P. J. Dolan, *Prediction of Neutron Induced Activity in Soils* [redacted] Technical Analysis Report AFSWP 518, Headquarters, Armed Forces Special Weapons Project, Washington, D.C., 4 June 1957 [redacted]

Crawford, T. V., and K. R. Peterson, *BANEBERRY – Discussion of Diffusion Calculations Including Potential Exposure to Child's Thyroid from I-131 Via the Forage-Cow-Milk Pathway* [redacted] COPK 71-20, Lawrence Radiation Laboratory, Livermore, California, 3 March 1971 [redacted]

Crawford, T. V., *Precipitation Scavenging and 2BPUFF*, UOPKA 71-14, Lawrence Livermore Laboratory, Livermore, California, 6 December 1971 [redacted]

Crocker, G. R., *Fission Product Decay Chains: Schematics with Branching Fractions, Half-Lives, and Literature References*, USNRDL-TR-67-111, U.S. Naval Radiological Defense Laboratory, San Francisco, California, 24 June 1967 [redacted]

Crocker, G. R., and T. Turner, *Calculated Activities, Exposure Rates, and Gamma Spectra for Unfractionated Fission Products*, USNRDL-TR-1009, U.S. Naval Radiological Defense Laboratory, San Francisco, California, 28 December 1965 [redacted]

Crocker, G. R., and M. A. Connors, *Gamma-Emission Data for the Calculation of Exposure Rates from Nuclear Debris, Volume I, Fission Products*, USNRDL-TR-876, U.S. Naval Radiological Defense Laboratory, San Francisco, California, 10 June 1965 [redacted]

Crocker, G. R., J. D. O'Connor, and E. C. Freiling, *Physical and Radiochemical Properties of Fallout Particles*, NRDL-TR-899, Naval Radiological Defense Laboratory, San Francisco, California, 15 June 1965 [redacted]

Department of Defense Land Fallout Prediction System, DASA 1800-I through 1800-VII, Defense Atomic Support Agency, Washington, D.C.; U.S. Army Nuclear Defense Laboratory, Edgewood Arsenal, Maryland; U.S. Naval Radiological Defense Laboratory, San Francisco, California; Technical Operations Research, Burlington, Massachusetts; 1966 [redacted]

[redacted]

Dolan, P. J., *Gamma Spectra of Uranium-235 Fission Products at Various Times After Fission*, AFSWP 524, Headquarters, Armed Forces Special Weapons Project, Washington, D.C., March 1959

Dolan, P. J., *Gamma Spectra of Uranium-238 Fission Products at Various Times After Fission*, DASA 526, Headquarters, Defense Atomic Support Agency, Washington, D.C., May 1959

Dolan, P. J., *Theoretical Dose Rate Decay Curves for Contamination Resulting from Land Surface Burst Nuclear Weapons*, DASA 528, Defense Atomic Support Agency, Washington, D.C., 6 August 1959

Englemann, R. J., and W. G. N. Slinn, *Precipitation Scavenging (1970)*, AEC Symposium Series, U.S. Atomic Energy Commission, Washington, D.C., 22 December 1970

Englemann, R. J., *Priorities in Scavenging Research*, AEC Symposium Series U.S. Atomic Energy Commission, Washington, D.C., 22 December 1970

French, R. L., *A First-Last Collision Model of the Air/Ground Interface Effects on Fast-Neutron Distributions*, *Nucl. Sci. Engr.*, *19*, 151-157, 1964

Freiling, E. C., and N. E. Ballou, *Nature of Nuclear Debris in Sea Water*, *Nature 195*, No. 4848, pp. 1283-1287, 29 September 1962

Fritzsche, A. E., N. E. Lorimier, and Z. G. Burson, *Measured Low-Altitude Neutron and Gamma Dose Distributions Due to a 14-MeV Neutron Source*, *EGG 1183-1449*, *E. G., and G., Inc.*, *1969*

Fritzsche, A. E., N. E. Lorimier, and Z. G. Burson, *Measured High-Altitude Neutron and Gamma Dose Distributions Due to a 14-MeV Neutron Source*, EGG 1183-1438, E. G., and G., Inc., 1969

Harris, R. J., Jr., et al., *Models of Radiation in Air – The ATR Code*, DNA 2803I, SAI-71-557.LV, Science Applications Incorporated, La Jolla, California, May 1972

Huebsch, I. O., *Fallout Predictions for Water-Surface Nuclear Bursts*, USNRDL-TR-67-147, U.S. Naval Radiological Defense Laboratory, San Francisco, California, 28 November 1967

Heubsch, I. O., *Development of a Water-Surface-Burst Fallout Model: The Formation, Dispersion and Deposition of Fallout Particles*, USNRDL Technical Report, U.S. Naval Radiological Defense Laboratory, San Francisco, California

Keith, J. R., and F. H. Shelton, *Neutron Transport in Non-Uniform Air by Monte Carlo Calculation, Volume I*, DASA 2236-I KN-774-69-1, Kaman Nuclear, Colorado Springs, Colorado, 15 January 1969

Keith, J. R., and F. H. Shelton, *Neutron Transport in Non-Uniform Air by Monte Carlo Calculation* Volume II, KN-774-69-1, DASA 2236-II, Kaman Nuclear, Colorado Springs, Colorado, 15 January 196

Knox, J. G., and A. L. Williams, *Rainout Studies at Lawrence Livermore Laboratory*, UCRL 51530, Lawrence Livermore Laboratory, University of California/Livermore, Livermore, California, 11 February 197

Krey, P. W., et al., *Soil Activation by Neutrons* Project 2.1, WT-1410, U.S. Army Chemical Warfare Laboratories, Army Chemical Center, Maryland, 16 May 1960

Lee, H., P. W. Wong, and S. L. Brown, SEER II: *A New Damage Assessment Fallout Model*, DNA 3008F, Stanford Research Institute, Menlo Park, California, May 1972

Marshall, J. D., and M. B. Wells, *The Effects of Cut-Off Energy on Monte Carlo Caiculated Gamma-Ray Dose Rates in Air*, RRA-M67, Radiation Research Associates, Fort Worth, Texas, 1966

Mooney, L. G., and R. L. French, *Improved Models for Predicting Nuclear Weapon Initial Radiation Environments* RRA-T93, DASA 2615, Radiation Research Associates, Fort Worth, Texas, 31 December 1969

Norment, H. G., and E. J. Tichovolsky, *A New Fallout Transport Code for the DELFIC System: The Diffusive Transport Module*, DASA 2669, Arcon Corporation, Wakefield, Massachusetts, 1 March 1971

Norment, H. G., *A Precipitation Scavenging Model for Studies of Tactical Nuclear Operations, Volume I – Theory and Preliminary Results, Volume II – The DELFIC-PSM Code*, DNA 3661F-1, -2, Mt. Auburn Research Associates, Inc., Newton, Massachusetts, 18 June 1975

Read, P. A., *Neutron Induced Activity on a Beach: A Method for Calculating the Dose Rate*, USNRDL-TR-67-133, U.S. Naval Radiological Defense Laboratory, San Francisco, California, 27 October 1967

Ritchie, R. H., and V. E. Anderson, *Some Monte Carlo Results on the Penetration of Neutrons from Weapons in an Air-Over-Ground Geometry* ORNL-3116, Oak Ridge National Laboratory, Oak Ridge, Tennessee, 26 July 1962

Schuert, E. A., *Distribution of the Radioactive Debris and Associated Nuclear Radiation from Underwater Nuclear Explosions* USNRDL-TR-67-28, DASA 1240, Part I, Chapter 11, U.S. Naval Radiological Defense Laboratory, San Francisco, California, 15 December 1966

Selph, W. E., and M. B. Wells, *Weapons Radiation Shielding Handbook, Chapter 6, Methods for Predicting Radiation Fields Produced by Nuclear Weapons*, DASA-1892-4, Oak Ridge National Laboratory, Oak Ridge, Tennessee, December 1969 [redacted]

Shelton, F. H., *Nuclear Weapons as Neutron Sources, The Neutron Environments They Produce, and Some Neutron Effects on Aerospace Systems*, DASA-2383-1, Volume I, Neutron Sources, KN 774-69-6, Kaman Nuclear, Colorado Springs, Colorado, October 1969 [redacted]

Shelton, F. H., and J. R. Keith, *Nuclear Weapons as Neutron Sources, The Neutron Environments They Produce, and Some Neutron Effects on Aerospace Systems*, *Volume II, Neutron Environments and Some Effects*, DASA 2383-2, KN 774-69-6, October 1969 [redacted]

Slade, D. H. (Ed.), *Meteorology and Atomic Energy — 1968*, USAEC Report TID-24190, Environmental Science Services Administration, Washington, D.C., July 1968 [redacted]

Smith, R. J., R. F. Benck, and E. E. Lissak, *Initial Gamma Data from Nuclear Weapon Tests, 1948 Through 1962*, NDL-TR-53, U.S. Army Nuclear Defense Laboratory, Edgewood Arsenal, Maryland, July 1965 [redacted]

Snay, H. G., *The Hydrodynamic Background of the Radiological Effects of Underwater Nuclear Explosions*, Proceedings of the Tripartite Symposium on the Technical Status of Radiological Defense in the Fleets, U.S. Naval Radiological Defense Laboratory, San Francisco, California, 16-20 May 1960, Vol. II, USNRDL Reviews and Lectures, No. 103 [redacted]

Stensland, G. J., *Further Numerical Model Studies of the Washout of Hygroscopic Particles in the Atmosphere*, UCRL-51614, Lawrence Radiation Laboratory, University of California/Livermore, Livermore, California, 2 July 1974 [redacted]

Straker, E. A., *Time-Dependent Neutron and Secondary Gamma-Ray Transport in an Air-Over-Ground Geometry, Volume II. Tabulated Data*, ORNL 4289, Vol. II, Oak Ridge National Laboratory, Oak Ridge, Tennessee, September 1968 [redacted]

Williams, A. L., *Rain Scavenging of Radioactive Particles*, UCRL-517765, Lawrence Radiation Laboratory, University of California/Livermore, Livermore, California, 28 February 1975 [redacted]

Wong, P. W., and H. Lee, *Utilization of the SEER Fallout Model in a Damage Assessment Computer Program (DACOMP)*, DNA 3608F, Stanford Research Institute, Menlo Park, California, 27 February 1975 [redacted]

Young, F. H., et al., *The Radiological Effects from Underwater Nuclear Explosions*, USNRDL-TR-68-1, U.S. Naval Radiological Defense Laboratory, San Francisco, California, 17 October 1967 [redacted]

[redacted]

(This page intentionally left blank)

[redacted]

[redacted]

Chapter 6

TRANSIENT-RADIATION EFFECTS ON ELECTRONICS (TREE) PHENOMENA

INTRODUCTION

This chapter introduces the subject of transient-radiation effects on electronics and provides a basic description of the interaction of nuclear radiation with matter as it applies to electronic components. The response of electronics to the radiation from a nuclear weapon burst depends not only on the radiation present at the electronics but also depends on the specific operating state of the electronics at the time of the radiation exposure and on the specific electronics in the system. A knowledge of the individual characteristics of the circuits contained in an electronics package, of the exact electronic components used in the circuits, and of the specific construction techniques and materials used in making the electronic components constitutes the necessary background for determining the radiation response of the electronic system. This chapter explains how the radiation interacts with different materials to produce a wide variety of effects. These material effects are used in the discussions of the component-part responses in Section VII of Chapter 9. Section IV of Chapter 14 contains a brief discussion of circuit and electronic-system response supplemented with discussions of general electrical responses of classes of systems (radios, radar, etc.).

The cumbersome name applied to the class of effects that are the subject of this chapter, transient-radiation effects on electronics, is generally abbreviated to the acronym TREE. In general, TREE means those effects occurring in electronics as a result of the transient radiation from a nuclear weapon explosion or as a result of an environment designed to simulate that radiation. It should be understood that the transient-radiation from a nuclear explosion can be and is simulated by the use of controlled sources of steady-state and transient radiation since the environment produced can be correlated to the actual environment of interest, and thereby the effects on electronics can be studied.

Although the weapons radiation environment lasts for a very short time, its effect on electronics can be both short or long term. For emphasis, it must be stated that the word transient in TREE modifies the word radiation and does not modify the word effects: the effects may be transient, semipermanent, or permanent.

The term electronics means any one or all of the following: electronic component parts, electronic component parts assembled into a circuit, and circuits assembled into a system. TREE studies also may include the response of electromechanical components connected to the electronics, e.g., gyros, inertial instruments, etc. TREE does, however, specifically exclude other types of component parts or systems such as hydraulic cylinders and hydraulic systems, fuel lines and fuel systems, etc. This exclusion is made since electronics as a group or as part of a hybrid system are one of the most radiation-sensitive portions of a system.

There are several points to be emphasized about TREE. The TREE interest is in the environment at the electronics produced by the

AD-A955 390

[redacted]

This document has been approved for public release and sale; its distribution is unlimited.

89 3 02 043

[redacted]

[redacted] ENVIRONMENT [redacted]

[redacted] In order to specify the hardness required of an electronic system, or to formulate an analysis or test program on which its hardness level will be established, it is necessary to describe the radiation environment to which the electronic systems may be exposed. Since the multitude of components of this environment leads to confusion in understanding the variety of mechanisms whereby a nuclear explosion can affect the operation of electronic systems, the primary outputs of a nuclear weapon and the mechanisms whereby secondary radiation are generated will be reviewed. In quantifying the environment to which the electronics are exposed, it is first necessary to treat the primary output of the nuclear explosion, then transport this radiation through the atmosphere and generate secondary radiations by interaction with the atmosphere. At this point, the radiation incident at the system of interest can be quantified. Since most of the electronics are enclosed by some structural material, there is the additional effect of transport through such shields, and it becomes necessary to describe the radiation field as it interacts with the affected part.

[redacted] This step-wise description of the radiation explains the variety of methods and units by which the radiation field is described. The weapon designer usually describes the output from the nuclear explosion-total energy output, total number of neutrons emitted, total gamma-ray energy, and reaction pulse shape. The person who formulates specifications for system design usually describes the radiation field as it impinges on the system, e.g., energy per unit area, neutron fluence, gamma exposure, pulse shape as affected by radiation transport through intervening material. Finally, the designer of the individual electronic piece-part or circuit is concerned with describing the radiation in units that are convenient for quantifying the radiation effect that he has to take into account, e.g., energy deposition per unit mass or volume, 1-MeV equivalent neutron fluence, gamma dose, radiation pulse shape at the device.

6-1 Weapon Output [redacted]

[redacted] The weapon radiation output and its interaction with the atmosphere will be summarized in succeeding paragraphs, together with the units in which these radiations are usually described. Following this summary, the individual radiation effects of concern will be discussed, and the appropriate methods of describing the radiation at the affected parts or circuits will be described for each type of effect.

[redacted] The majority of the energy released in a nuclear explosion heats the material of which the nuclear device was composed, to temperatures of tens and hundreds of millions of degrees. A smaller fraction (0.1 to 10%) escapes promptly in the form of fast neutrons and prompt gamma rays (see Chapters 4 and 5). The intense thermal source radiates most of its energy in the form of X-rays. If the explosion occurs in a vacuum, or, if the weapon is a "hot" X-ray device (see Section II, Chapter 4) that explodes in relatively thin atmosphere, these X-rays can produce important TREE effects. Depending upon the specific temperature of the source, the X-rays have energies varying from a few to a few hundred kilovolts. One method by which the energy spectrum from such a source is frequently described is by specifying the temperature of a black body which would emit a spectrum that approximates the observed X-ray spectrum (Chapter 4). It should be noted that even though the temperature is usually specified as a number in units of keV (kilo-electron-Volts), this unit describes a spectrum of photon energies extending significantly below and above the quoted number [redacted] DNA (6)(3)

[redacted]

[redacted]

initial nuclear radiation (i.e., that radiation emitted within 1 minute following the burst) which, in turn, consists of both prompt and delayed radiation. The weapon-burst radiations of interest are neutrons, gamma rays, X-rays, and to a much less extent, electrons. The effects of interest are both temporary and permanent even though the radiation persists only for a short time.

[redacted] Examples of system responses to TREE and their consequences are given below. These examples represent only a small sample and are not necessarily representative of present day problems.

Effect in System Due to Temporary Disturbances of the Electronics	Typical Consequence
Change in logic state in missile-borne guidance computer	Program jump or disturbance of key data causing mission failure
Spurious (ill-timed) fuzing signal	Warhead dudding or premature detonation
Excess currents in transistors and capacitors in servo control loop	Excessive steering maneuvers causing structural instability
Excess currents in memory write circuits	Writing erroneous data in memory, usually causing mission failure
Microcircuit latchup following ionization pulse	Functional disabling of microcircuit until power is cycled off and on

Effect in System Due to Permanent Degradation of the Electronics	Typical Consequence
Neutron-induced loss of gain in lower-frequency transistors	Loss of power supply regulation; decreased servo-loop gain
Delamination of semiconductor wire bonds due to thermomechanical shock	Functional failure of the affected device, usually leading to mission failure
Neutron-induced loss of gain in higher-frequency transistor structures	Decreased fan-out capability in computer logic
Metallization burnout due to excess ionization-induced currents	Functional failure of affected device, usually causing mission failure

[redacted]

[redacted]

After the prompt radiations have been emitted from the nuclear explosion, a residue of hot and radioactive debris remains. Some of its energy continues to be irradiated as thermal energy in the ultra violet and visual regions of the spectrum. Subsequent radioactive decay of the debris produces lower intensity gamma rays as well as emitting high energy electrons. These electrons are particularly important for high altitude nuclear detonations, which may inject the electrons into orbits trapped by the earth's magnetic field. These electrons are of particular concern to space vehicles whose orbits intercept the earth's radiation belts, because continued exposure to the electrons can cause significant permanent degradation.

If the explosion occurs within or near the atmosphere, the prompt radiations interact with the constituents of the atmosphere, producing secondary effects. The X-rays are absorbed most strongly and, depending upon altitude, the air is heated by the interaction to produce an intense thermal source and a blast wave in the air (Chapters 1 through 4). The gamma rays interact to produce secondary electrons. In concert with the earth's magnetic field and/or inhomogeneities, such as the surface of the earth, these electrons create a radiating electromagnetic pulse (EMP) (Chapter 7). The neutrons interact with the atmosphere to produce secondary gamma rays (Chapter 5).

6-2 Time Considerations [redacted]

The general time frame for the arrival of the various radiation components at the electronics package is sometimes important. In general, for the purposes of electronic vulnerability, the prompt gamma radiation can be considered as a single pulse. Since the flight time for X-rays and gamma rays of all energies equals the speed of light, *unscattered* photons arrive at the equipment with the same time distribution they had at the source, with a time delay of 3.33 μsec/km from the weapon burst. The arrival of the gamma pulse approximately coincides with the unscattered prompt X-rays.

The neutrons arrive after the initiation of the gamma- and X-radiation. Their arrival time depends on the neutron energy and the range to the receiver. The first neutrons to arrive will be the unscattered 14-MeV neutrons. Their time of flight is 19.3 μsec/km, therefore, they will arrive 16 μsec/km after photon arrival. The photons resulting from neutron inelastic-scattering (Chapter 5) will also begin to arrive at about this time. Within 32.8 μsec/km (the arrival time after photon arrival for 4-MeV neutrons), the photons resulting from neutron inelastic-scattering will be completed, since the inelastic-scatter contribution is negligible for lower energy neutrons. Within 69.0 μsec/km, the bulk of the unscattered 1-MeV neutrons will have been deposited. The photons resulting from neutron capture (or thermalization) typically will peak shortly after the arrival of the 1-MeV neutrons depending on the system configuration being studied. Both the thermalization time and the capture time following thermalization depend strongly on the interacting materials and the system configuration. The radiation of interest to TREE is complete in less than 1 minute.

6-3 Description of Radiation Fields [redacted]

A complete description of the radiation field produced at the system should include the time dependence, angular distribution, and energy spectrum of each of the components. Of course, this should be done for a wide variety of conditions to cover all possible interaction scenarios. In practice, it is not necessary to be so thorough, and the following approximations are usually made:

- A worst case radiation environment is spe-

[redacted]

cified and the objective is to have the system tolerate all combinations of environments that are less stringent than the specification.

- The incident radiation is assumed to be unidirectional. This is usually the worst case angular distribution, and it represents a reasonable approximation to reality.
- Where possible, the individual radiation fields are specified in units that facilitate conversion to those units that are convenient for describing the effect.

For example, it is possible to specify the time dependent neutron energy spectrum incident on the system. Since the time dependence of arrival of unscattered neutrons is correlated with neutron energy, as discussed above, specifying the neutron energy spectrum, and the range of distances between nuclear explosion and the irradiated system, also is equivalent to specifying the time dependence. Finally, if the only effect of interest is permanent neutron-induced displacement effects, the spectrum can be replaced by a single quantity such as the 1-MeV damage equivalent neutron fluence. The meaning of these units and the method of calculating them will be discussed in following paragraphs. It must be emphasized, however, that such convenient units are intended for simplification only. They are useful only if the assumptions underlying their use are valid. In the foregoing example, specifying only the 1-MeV damage equivalent neutron fluence is useless for determining the magnitude of neutron-induced ionization effects quantitatively.

The degree to which such simplifications can be used depends in large measure upon the simplicity of the interaction of the incident radiation with the target materials. A particularly simple case is the description of the gamma-ray environment. High energy gamma rays suffer negligible attenuation in passing through significant quantities of material, and they interact with matter to produce approximately the same energy deposition, independent of atomic composition of the target. Therefore, it has been possible to describe the gamma ray environment fairly simply and this has frequently led to carelessness. A more complicated situation, in which carelessness cannot be tolerated, is represented by the X-ray interactions. X-rays of energies of tens to a few hundred kilovolts are attenuated significantly even by thin missile skins and electronic subsystem boxes, and the energy deposition produced by such X-rays is a strong function of the atomic number of the target material. For this reason, it is invariably necessary to specify not only the total X-ray energy fluence incident on the system (usually given in calories/cm^2), its pulse width (usually given in nanoseconds), but also a range of possible energy spectra (sometimes given as explicit spectra, and at other times specified by a range of characteristic black body temperatures). The relating of such an exposure to the intensity of the radiation present at the affected area, such as the junction region of a transistor, requires detailed and specific calculations of the transport of the spectrum through the intervening material and the resultant energy deposition in the affected volume.

The transport of the various radiation components to the site of the equipment of interest is discussed in Chapters 4 and 5. It is of value, however, to note that typical electronic packaging materials will not produce significant attenuation of the neutron and gamma ray components of the environment. They do represent significant shields of X-rays, particularly if high-Z materials are used for electronic envelopes. Only the higher energy photons penetrate to the electronics of interest. Since the lower energy photons produce the highest energy deposition per unit volume when they interact, such shielding is especially useful because it removes preferentially that portion of the photon energy spectrum that would be most damaging if it were

allowed to penetrate to the sensitive devices. This fact reinforces the observation that is necessary to specify both the X-ray energy fluence and its spectrum outside and inside the shield. Indicating only the energy-fluence attenuation factor of a shield would ignore the fact that remaining photons are less effective in producing damage.

INTERACTIONS BASIC TO TREE

6-4 Ionization

Ionization is that process by which electrons are freed from their parent atoms in a material. A free electron carries a negative charge. After losing an electron, the atom (then called an ion) carries a net positive charge. Thus, the process of ionization results in the formation of electron-ion pairs in a material. If none of the electrons or ions leave the material, the material remains electrically neutral, since the positive and negative charges balance one another. Nevertheless, characteristics of the material may be altered considerably by ionization. The number of electron-ion pairs formed and their subsequent behavior are of prime interest in determining the effects of ionization.

Gamma rays interact with matter in three ways. The first is called the Compton effect. In this type of interaction, a gamma ray (primary photon) collides with an electron, and some of its energy is transferred to the electron (see Figure 6-1a). A secondary photon, with less energy, is created and departs in a direction at an angle to the direction of motion of the primary photon. The second type of interaction of gamma rays with matter is the photoelectric effect (see Figure 6-1b). A gamma ray, with energy somewhat greater than the binding energy of an electron in an atom, transfers all its energy to the electron, which is consequently ejected from the atom. Since the photon involved in the photoelectric effect transfers all of its energy, it ceases to exist and is said to be absorbed. The third type of interaction is pair production (see Figure 6-1c). When a gamma ray photon with energy in excess of 1.02 MeV passes near the nucleus of an atom, the photon may be converted into matter with the formation of a pair of electrons, equally but oppositely charged. The positive electron soon annihilates with a negative electron to form two photons, each having an energy of at least 0.51 MeV. In some cases, if the interaction takes place near the nucleus of a heavy atom, only one photon of about 1.02 MeV energy may be created.

Any photon (e.g., an X-ray or a gamma ray) can produce ionization in a material by these processes of creating secondary electrons that deposit their kinetic energy by ionizing the medium in which they are created. The relative importance or frequency with which each process occurs depends upon the photon energy and the characteristics of the material. The Compton process is the dominant ionization mechanism for most gamma rays of interest, particularly in electronic materials such as silicon, of which many solid-state devices are fabricated.

Fast neutrons can produce ionization indirectly. As neutrons undergo inelastic scattering and capture in a material (see Section I, Chapter 5), gamma rays that are emitted can cause ionization. In addition, collision of a neutron with an atom may impart sufficient energy to the atom for it to cause ionization. Only high-energy neutrons ($E > 1$ MeV) contribute significantly to ionization. The 14-MeV neutrons arising from fusion reactions in a weapon are particularly important.

The types of radiation that cause ionization in materials – namely, gamma rays, electrons, X-rays, and, to a lesser extent, fast neutrons – are known collectively as ionizing radiation.

Once created by the ionization processes (either primary or secondary), the charged par-

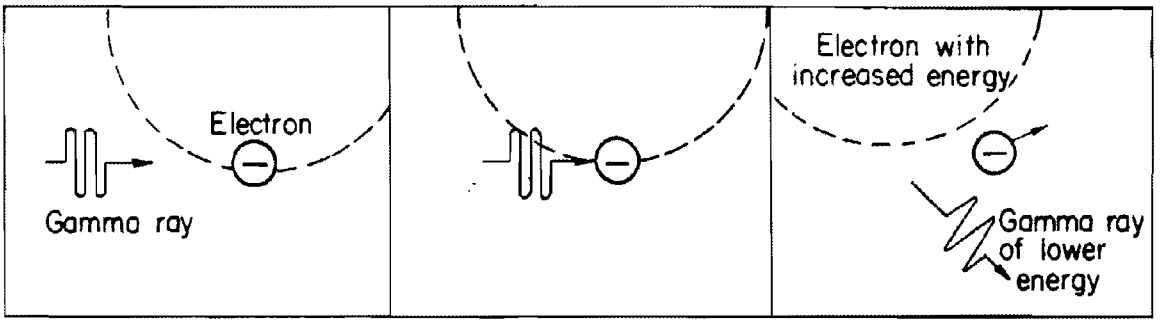

a. Compton Effect

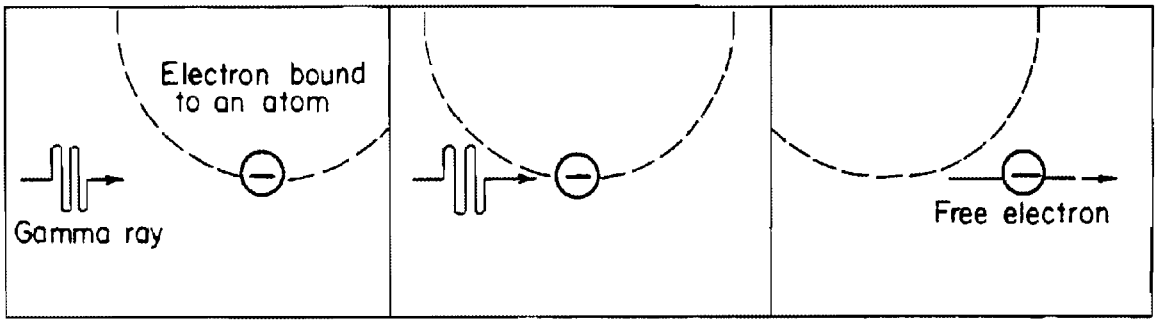

b. Photoelectric Effect

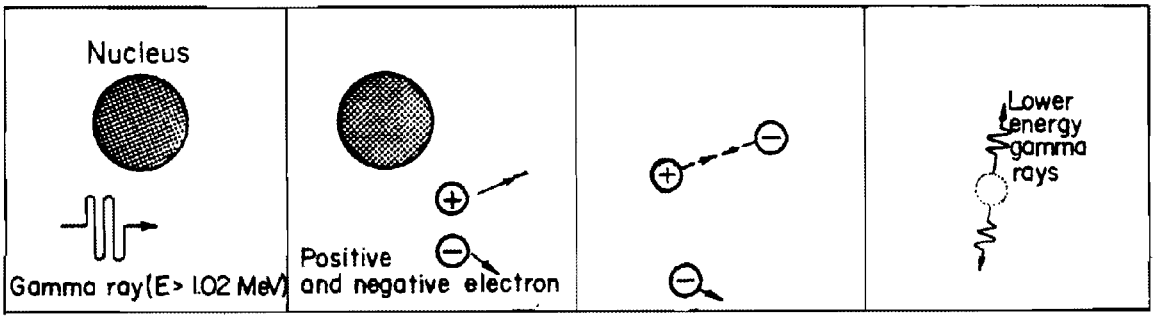

c. Pair Production

Figure 6-1. [redacted] Gamma Ray Interaction with Matter [redacted]

[redacted]

[redacted]

ticles (electrons or ions) are free to move in a material, scattering frequently and following a random-walk pattern. If the concentration of electric charge carriers throughout the material is not uniform, and if no externally applied electric field is present, the carriers will move from regions of high concentration to regions of low concentration. This movement is known as diffusion and it would be superimposed on the normal random-movement. If an electric field is present (e.g., as a result of an intentionally applied voltage), the carriers drift in the electric field while they undergo a predominantly random scattering. If impurities are present in the material (as they always are in solid-state devices, such as transistors and diodes), carriers may be captured (trapped) and immobilized by impurity atoms (traps). Eventually, the trapped carriers will be annihilated by their mates (oppositely-charged carriers) in a process called recombination. The net result of these processes is that the carriers diffuse and/or drift until they are trapped and usually recombined.

6-5 Displacement [redacted]

[redacted] As described above, ionization involves the movement of electrically charged electrons and ions in a material. Displacement involves the movement of atoms (which are electrically neutral).

[redacted] Any material may be described as being either crystalline or amorphous. The atoms of a crystalline material (a crystal) are arranged in a definite, repeated, three-dimensional pattern called a lattice; the atoms of an amorphous material have no definite arrangement. Displacement is an important phenomenon in crystalline materials, and it is a very important phenomenon in TREE because many electronic devices (e.g., transistors, diodes, integrated circuits) are constructed from crystalline semiconductors – primarily silicon and germanium. Lattice defects result from the displacement of atoms from their usual sites in crystal lattices. The simplest lattice defects are extra atoms inserted between lattice positions (interstitials) and unoccupied lattice positions (vacancies). At least part of the resultant damage to the material is stable and accounts for permanent property changes of irradiated crystalline materials.

[redacted] The production of displacement damage in a crystalline solid is a complex process. An abbreviated history of this process follows.

(1) Radiation of an appropriate form enters the material, interacts with a lattice atom, and imparts to it a certain energy.

(2) The target (recoil) atom leaves its lattice site, thus creating a vacancy, and collides with other lattice atoms (see Figure 6-2).

(3) Other atoms are displaced from their sites, creating more vacancies.

(4) Eventually, most recoil atoms come to rest in interstitial positions, while a few fall into vacancies. Some of the interstitials and vacancies may be isolated, but most of them will be associated with other defects in cluster formations.

(5) The simple defects and defect clusters migrate through the crystal.

(6) Eventually, the mobile defects are annihilated by recombination of vacancy-interstitial pairs, are immobilized by the formation of stable defect clusters with other impurities of lattice defects (either present in the original material or created by the irradiation), or escape to a free surface.

(7) Meanwhile, the physical properties of the material are changed by the presence of the defects.

[redacted] Fast neutrons are very effective in producing displacement damage. Energetic electrons can also produce displacement damage; however, their displacement effects are negligible compared to those of fast neutrons.

[redacted]

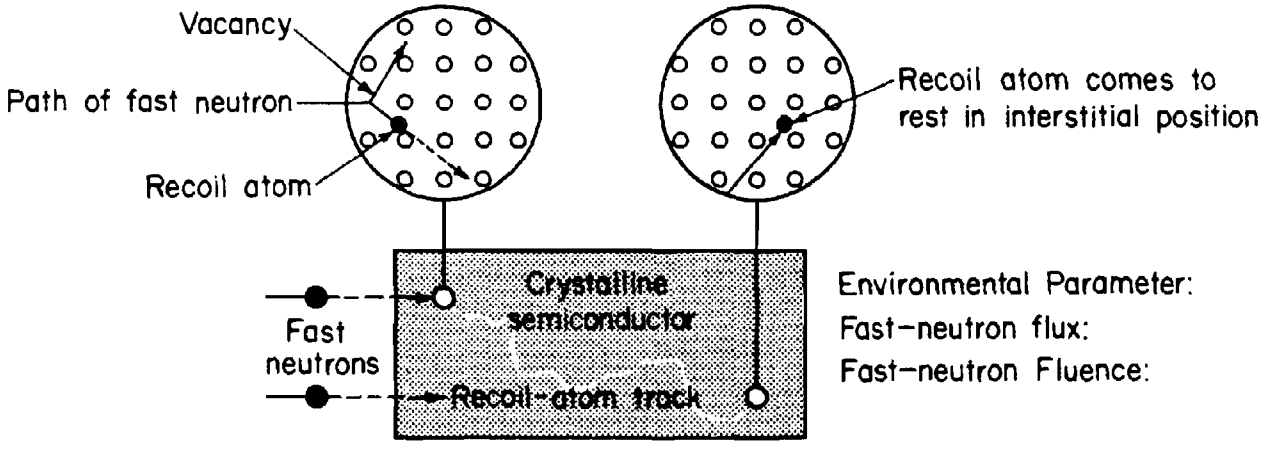

Figure 6-2. Displacement Damage in a Crystalline Solid

The absolute magnitude of damage in a material caused by neutrons is difficult to predict because some of the defects that are produced will effectively disappear at room temperature, that is, anneal. However, much useful information can be gained from the relative value of the concentration of defects produced before annealing. Assuming the same fraction anneals, the relative concentration of stable defects would be in the same ratio. It has been found that the number of unannealed defects that are generated depends on the energy of the impinging neutron. The number of unannealed defects generated by a 14-MeV neutron (one from a fusion weapon) is about 2.5 times the number of unannealed defects generated by a 1-MeV neutron (roughly the average energy for a neutron from a fission weapon). As will be discussed below, the number of defects generated in semiconductor materials is directly related to the change in semiconductor device parameters.

Not all of the defects produced in the displacement process are stable. Some defects are annihilated by recombination of vacancy-interstitial pairs, some combine with pre-existing lattice defects, and some eventually escape to a free surface of the material. The stable defects contribute to the permanent damage of the material. The unstable defects are said to disappear, or anneal, with time. In practice, this means that the degree of displacement damage in a crystalline semiconductor varies with time, reaching a peak rapidly and then partially annealing with time. The temperature of the material exerts a considerable influence on the amount of annealing that takes place. More annealing is observed at elevated temperatures.

Annealing may be divided roughly into two time frames. Rapid, or short term, annealing occurs in times of the order of hundredths of a second. Long term annealing continues at a slower rate for times of the order of tens of seconds (see Figure 6-3). If the temperature remains constant, annealing will be essentially complete after one-half hour. The ratio of the damage observed at early times (number of defects present) to the damage after a very long time is called the annealing factor, which is a function of the time of measurement and other parameters. The maximum damage created at short times following the fast-neutron burst frequently is important to electron-system perfor-

mance. Therefore, the maximum annealing factor is an important quantity, because it indicates the peak damage that must be tolerated above the permanent damage in the steady state. Values of the annealing factor depend on the temperature and on the electrical condition of the material. An annealing factor of three is commonly used for room temperature at ~10 msec. Larger factors have been observed at shorter times, or low injection conditions (e.g., cut-off transistors).

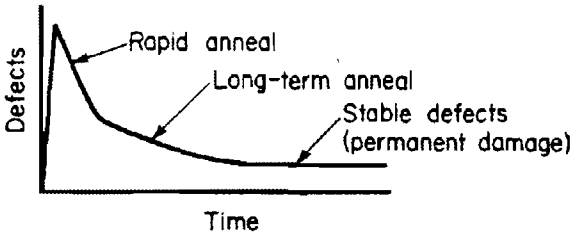

Environmental Parameters:
Fast-neutron flux:
Fast-neutron Fluence:

Figure 6-3. Annealing Due to Vacancy-Interstitial Recombination and Escape of Defects from Semiconductor

6-6 Heating

Whenever a material absorbs energy from its surroundings and cannot instantaneously dissipate that energy, the temperature of the material will rise, i.e., the material will be heated. The temperature will return to ambient at a rate determined by the efficiency with which the material can dissipate heat to its surroundings. If the energy deposition is great, and the mechanisms for heat dissipation are inadequate, the temperature rise will be significant and will persist for a considerable time (see Figure 6-4).

X-rays are the primary contributors to heating. Therefore, the relevant environmental parameters are the X-ray dose rate, and the X-ray dose. Predictions of the X-ray environment from nuclear weapon bursts and the X-ray absorption mechanisms are discussed in Chapter 4. Responses of electronic components to heating are discussed in Section VII, Chapter 9.

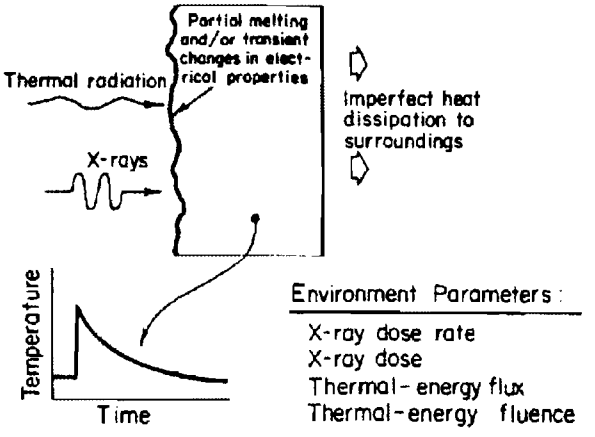

Figure 6-4. Heating

MANIFESTATIONS OF TREE IN MATERIALS

6-7 Ionization Effects

The important manifestations of ionization include (1) charge transfers, (2) bulk-conductivity increases, (3) excess minority-carrier generation, (4) charge trapping, and (5) chemical effects.

Charge transfer results from the escape of some electrons produced during ionization from the surface of the material being ionized. If the net flow of electrons is out of the material, the material will be left with a net positive charge. If these electrons are stopped in an adjacent material, a transfer of charge will have occurred from one material to the other, and a difference of potential (or voltage) will exist between the two materials.

[redacted]

The transfer of charge from one material to another can have a number of effects. The most obvious one is that a current will flow through any electrical circuit connecting the two materials to restore charge neutrality. The charge will produce electric and magnetic fields during transit. If there is matter in the gap between the materials, the charge transfer also will produce ionization and conduction in response to local electrical fields. Finally, if the charge either originates or embeds itself in an insulator, a long-lived local space charge may result. Charge transfer, therefore, may result in either a temporary or a semipermanent effect.

The free carriers produced during ionization respond to an applied electric field by producing a net drift current. This is precisely the mechanism by which a material conducts electricity. Therefore, ionization induces a transient increase in conductivity. An example of a detrimental effect to the operation of electronic equipment resulting from an increase in bulk conductivity occurs in a capacitor exposed to a weapon burst environment. The ability of a capacitor to retain, or restore, electrical charge is dependent upon the low conductivity of the dielectric, or insulating material, that is contained within the capacitor. In an ionizing environment the increase in bulk conductivity results in a decrease of stored charge in the capacitor.

The ionization effect of excess minority carriers is a prime concern in many semiconductors and is usually the most important manifestation of TREE. Semiconductor devices, such as transistors and diodes, employ both positive and negative charge carriers, either of which may be in the minority with respect to concentration. The characteristics of many such devices depend strongly upon the instantaneous concentration of minority carriers in various regions of the device. Since ionizing radiation creates large (and equal) numbers of positive and negative charge carriers, the concentration of minority carriers in the device is temporarily enhanced by a large percentage, and the electrical operation of the device may be affected adversely. The most familiar example of this effect is the current flow across a reverse-biased PN junction, such as those that are found in a diode or the base-collector junction of a transistor (see Section VII, Chapter 9).

When free carriers are created in insulating materials, and are trapped at impurity sites, many may not undergo recombination with their mates, which may be trapped elsewhere. In these cases, the material properties may be altered semipermanently, even though there is no net charge in the material. This ionization effect is known as charge trapping.

Trapped charge can change the optical properties of materials (e.g., F centers in alkali halides, coloration of glasses). The trapped carriers may be released thermally, either at the irradiation temperature or by elevating the temperature. In either case the resultant creation of some free carriers is manifested by an increase in conductivity and sometimes by the emission of light.

The chemical effects of ionization occur during the processes of trapping and recombination when sufficient energy is available to disrupt chemical bonds. At the completion of the ionization cycle (i.e., after recombination is complete), the material may return to electrical inactivity, but its chemical composition may be altered permanently. The resulting chemical changes may be manifested as permanent changes in physical and/or electrical properties of the material. The radiation dose required to cause such effects is larger than normally will be encountered; therefore, the effect will not be discussed further.

Since ionization effects do not occur and/or recover in the same time period, the time domain for their occurrence and recovery must be considered. There are three categories of time

[redacted]

[redacted]

dependence – prompt, delayed, and long term.

[redacted] Prompt effects are those in which the width of the ionization pulse is longer than the times required for atoms or electrons within the material being exposed to make a specified amount of recovery. The magnitude of the effect is a function of the density of the positive and negative particles created during the ionization, which in turn is a function of the dose rate. Examples of prompt effects are charge transfer and prompt bulk-conductivity increases in insulating and semiconductor materials.

[redacted] Delayed effects are those in which the width of the ionization pulse is shorter than the times required for atoms or electrons within the material being exposed to make a specified amount of recovery. The initial response of the material or device is a function of dose, and its persistence is determined by the length of the specified recovery time. An example of this effect is delayed bulk conductivity of insulator materials. In this particular example the recovery times for the prompt and delayed effects are based on different mechanisms of carrier generation (ionization induced or thermal trapping) and, hence, they have very different time periods.

[redacted] Long-term effects are those which persist for periods longer than minutes. These effects can be, but are not necessarily, permanent. Recovery may be so slow that it takes days, months, or years for apparent complete recovery. Examples of long-term effects are some cases of trapped charge and chemical effects.

[redacted] An important point, emphasized here, is that a general class of materials or devices (plastics, transistors, etc.) could be both dose and dose-rate sensitive with respect to the ionization effects observed.

[redacted] It has been established that, with the exception of charge transfer, the magnitude of the ionization effects is primarily a function of the total concentration of thermalized charge carriers (electrons and holes). These carriers are generated at a rate proportional to the instantaneous ionization energy deposition and independent of the nature of the radiation producing that energy deposition. Therefore, it is appropriate to use units that quantify the energy deposition in the material of interest when describing the radiation field at the responding device. Such units include ergs/gram (material), rads (material), and calories/gram (material). Since these are descriptions of energy deposition in a given material, they are called units of dose. The time dependence of energy deposition can be specified by these same units per second, and are called dose rate.

[redacted] Unfortunately, the magnitude of charge transfer depends not only on the energy deposition but the spectrum of the secondary electrons. Therefore, quantitative evaluations of systems in which charge transfer represents a significant vulnerability mode must use a more complex characterization of the spectrum of the incident photons, together with a calculation of the photon interactions, to produce the spectrum of secondary electrons.

[redacted] In some materials, particularly insulators, the ionization effects are also a weak function of the microscopic concentration of the ionization around individual particle tracks. For example, neutron-induced ionization created by intensively ionizing recoil atom may be less effective in producing conductivity in an insulator than the same dose or dose rate imparted by lightly ionizing gamma rays. Units for describing this process include specific ionization (ratios of ionization to the minimum level of ionization at high velocities of a singly charged particle), and linear energy transfer (MeV/cm or MeV cm^2/gram). Fortunately, these effects are of second order importance for most TREE applications. A specification of dose rate and dose is adequate in the majority of applications.

[redacted] The gamma-ray field incident on a

[redacted]

[redacted]

system is frequently described by its exposure measure in roentgens. The roentgen is determined by specifying the energy deposition in a standard material (dry air under standard temperature and pressure conditions). For high energy gamma rays that interact primarily via the Compton process, exposure of almost any material to one roentgen of gamma rays produce (within 20%) approximately one rad of energy deposition in any material. This factor has enabled the users of these units to become somewhat careless, without serious consequence, so long as only high-energy photons are of interest. However, these relations do not carry over into photons of lower energies (200 kilovolts or less in medium atomic-number materials) and careful treatment of the units is required. One way of minimizing the chances of misinterpretation is to use units of calories/cm^2 with a defined spectrum for external exposure and units of cal/gram (material) for dose.

6-8 Displacement Effects

[redacted] The displacement effects of prime concern to TREE are those generated in semiconductor materials. The lattice damage resulting from displacement degrades the electrical characteristics of semiconductor devices by increasing the number of trapping, scattering, and recombination centers. The effect of displacement in semiconductors is, therefore, threefold: (1) the trapping centers remove charge carriers from the electrical conduction process (reduces electrical current flow), (2) the additional scattering centers reduce the capability of the charge carriers to move through the semiconductor material (reduces charge-carrier mobility), and (3) the recombination centers reduce the time that the minority charge carriers are available for electrical conduction (reduces the lifetime of the minority-charge carriers). This last effect is most important for prediction of semiconductor device performance in radiation environments that cause displacement. The decrease in minority-carrier lifetime (τ) is predicted according to the relationship

$$\frac{1}{\tau_\varphi} = \frac{1}{\tau_0} + K\varphi ,$$

where

τ_φ = minority-carrier lifetime at fluence φ in seconds,

τ_0 = initial minority-carrier lifetime in seconds

K = lifetime damage constant, cm^2/(neutron · second)

φ = total fast-neutron fluence, neutrons/cm^2.

[redacted] Typical values for τ_0 in device materials of interest are 10^{-8} to 10^{-4} seconds. The value of the lifetime damage constant, K, is dependent on the type of material, the type and amount of impurities in the material, the operating voltage applied to the material, the temperature, the energy spectrum of incident neutrons, and, because of defect annealing, the time after the nuclear radiation is incident on the material. A general value for silicon, the prime material used in transistors, diodes, and integrated circuits, is $K \approx 1 \times 10^{-6}$ cm^2/(n · sec).

[redacted] To illustrate the magnitude of displacement effects that occur in semiconductors compared to those that occur in other materials, a comparison of neutron fluences that will cause significant effects is made in the following paragraph. Interest is focused only on those property changes that affect the normal use of the materials being compared.

[redacted] Semiconductor lifetime can begin to show significant effects in devices at a fluence of 10^{11} n/cm^2 (Pu, fission)* and by 10^{16} n/cm^2

*Accurate neutron dosimetry requires that the foil used for making the neutron measurement and the energy spectrum of the neutrons be specified with the value measured. Therefore, in the example presented here, 10^{11} neutrons per square centimeter were detected with a plutonium foil and the energy spectrum of the neutrons was a nominal fission spectrum.

[redacted]

[redacted]

(Pu, fission) the lifetime in most semiconductor devices is so short that the device is no longer useful. Metals such as nickel and copper start to show effects in material strength at a fluence of 10^{18} n/cm^2 (Pu, fission). As a general rule, the electrical properties will not start to change in structural materials until the material properties change. Glasses and ceramics are much less susceptible to neutron damage than semiconductors, but they are more susceptible than metals. The point that is emphasized is that semiconductors are among the devices that are most susceptible to displacement effects.

[redacted] It is frequently desirable to express neutron effects data observed by different experimenters using different neutron-energy spectra in terms of an equivalence fluence unit in addition to the measured flux and fluence units. This permits easy comparison of damage levels obtained from different neutron test facilities. Since silicon is the material of most interest to displacement effects, the equivalence is usually based upon damage in silicon. The energy spectrum typically used as a standard for comparison is a hypothetical 1-MeV monoenergetic neutron source. The damage caused by the neutrons (of some known spectrum) is compared to the damage done by the neutron spectrum which is used as a standard. The neutron fluence of the standard which would cause the same damage in the given material as observed for the known spectrum is then specified as the damage equivalent fluence for that material. An example of this equivalence unit for 1-MeV neutrons standard spectrum and silicon material is: 10^{13} n/cm^2 (1-MeV damage equivalence in silicon). The procedures for obtaining a 1-MeV equivalent fluence for any known neutron spectrum are specified in the TREE Handbook (see bibliography).

6-9 Heating Effects [redacted]

[redacted] The radiation environment, especially the X-rays, produced by nuclear weapons can deposit considerable energy in electronic materials. The energy deposited is sufficient to heat some materials to such an extent as to cause partial melting, and it is sufficient to change electrical properties in other materials. These temperature transients may last from fractions of a second to minutes. If the energy is deposited in the material in a very short time (deposition time is typically 10^{-8} seconds for a nuclear weapon) an additional effect is observed; the material is heated very rapidly but does not have time to expand. The result is the instantaneous creation of a shock wave, or pressure pulse, which tends to compress the material. This compression wave starts at the point of energy absorption, typically close to the material's front surface upon which the incident energy impinges, and quickly propagates to the back surface. When it reaches the back surface, it is reflected, becomes a tension wave, and propagates toward the front surface. For energy deposition of sufficient magnitude delivered in a sufficiently short interval, the tension wave can be intense enough to exceed the strength of the material. Several consequences are possible.

(1) Portions of the material may be removed from the back surface – spallation (see Figure 6-5).

(2) Fragments of the material may separate from the front surface – blowoff.

(3) The material may separate between front and back surfaces – delamination.

(4) Agglomerates or layers of dissimilar materials bonded together will tend to separate at the interfaces – also called delamination.

(5) In brittle crystalline materials (e.g., Si or Ge), crystal fracture can occur.

Generally, effects of this nature are referred to as thermomechanical shock effects. Obviously, the consequences of these effects can be catastrophic. An example important to transistors and inte-

[redacted]

[redacted]

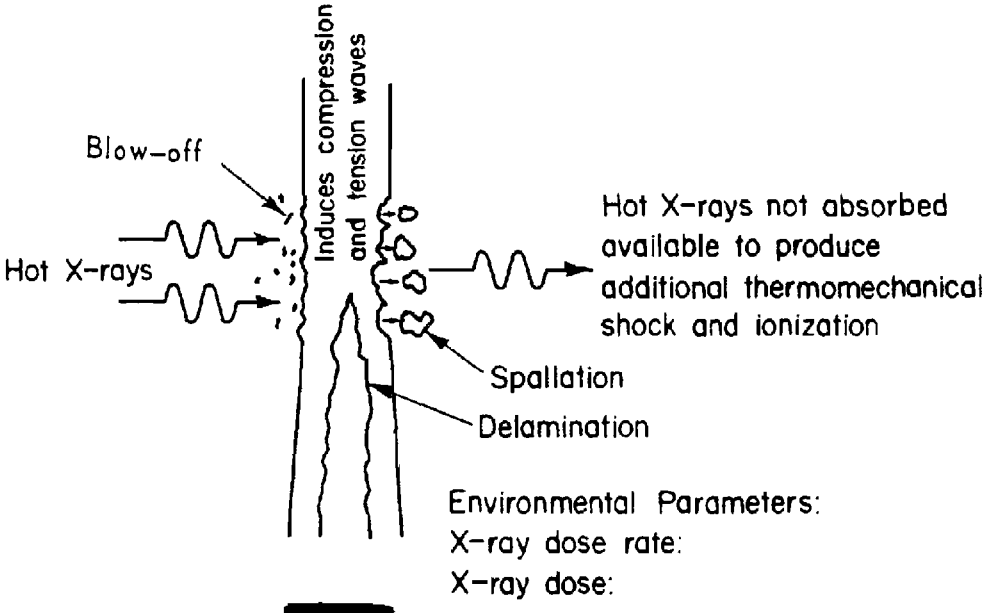

Figure 6-5. [redacted] Thermomechanical Shock Effects [redacted]

[redacted]

grated circuits is the delamination of the electrical contacts to the semiconductor chip, resulting in complete loss of the device function. The thermomechanical-effect damage threshold is difficult to determine. It depends not only on the energy deposition and energy spectrum but also on the thickness of the materials, the compressibility, the expansion coefficient, and the dynamic strength of the materials. Thermomechanical effects on materials are discussed in more detail in Section VII of Chapter 9.

[redacted]

[redacted]

BIBLIOGRAPHY

DASA EMP (Electromagnetic Pulse) Handbook, DASA 2114-1, DASIAC, Santa Barbara, California, September 1968, [redacted] (to be replaced by DNA 2114H-1 during calendar year 1972).

DASA EMP (Electromagnetic Pulse) Handbook, Classified Supplement [redacted] DASA 2114-2, DASIAC, Santa Barbara, California, September 1968, [redacted] (to be replaced by DNA 2114H-2, 2114H-3, and DNA 2114H-4 during calendar year 1972).

Gwyn, C. W., D. L. Scharfetter, and J. L. Wirth, *The Analysis of Radiation Effects in Semiconductor Junction Devices,* SC-R-67-1158, Sandia Corporation, Albuquerque, New Mexico, July 1967 [redacted]

Kalinowski, J. J., *A Management Guide to Transient-Radiation Effects on Electronics (TREE)* [redacted] DNA 2051H, Battelle Memorial Institute, Columbus, Ohio, February 1972 [redacted]

Larin, F., *Radiation Effects in Semiconductor Devices,* John Wiley and Sons, Inc., New York, 1968 [redacted]

TREE (Transient-Radiation Effects on Electronics) Handbook [redacted] Vol. 1 Edition No. 3, DNA 1420H-1, Battelle Memorial Institute, Columbus, Ohio, December 1971 [redacted]

TREE (Transient-Radiation Effects on Electronics) Handbook [redacted] *(Classified Supplement),* Edition 2, Revision 2, DASA 1420-1, Battelle Memorial Institute, Columbus, Ohio, September 1970, [redacted] (to be replaced by DNA 1420H-2 during calendar year 1972).

TREE Preferred Procedures (Selected Electronic Parts), DASA 2028, Defense Atomic Support Agency, Washington, D.C., May 1968, [redacted] (to be replaced by DNA 2028H during calendar year 1972).

Vook, F. L., Editor, *Radiation Effects in Semiconductors,* Proceedings of the Santa Fe Conference on Radiation Effects in Semiconductors, Plenum Press, New York, 1968 [redacted]

[redacted]

AD-A955 391

Chapter 7

ELECTROMAGNETIC PULSE (EMP) PHENOMENA

The nuclear electromagnetic pulse (EMP) is the time-varying electromagnetic radiation resulting from a nuclear burst. It has a very broad frequency spectrum, ranging from near dc to several hundred MHz.

The generation of EMP from a nuclear detonation was predicted even before the initial test, but the extent and potentially serious degree of EMP effects were not realized for many years. Attention slowly began to focus on EMP as a probable cause of malfunction of electronic equipment during the early 1950s. Induced currents and voltages caused unexpected equipment failures during nuclear tests, and subsequent analysis disclosed the role of EMP in such failures. Finally in 1960 the possible vulnerability of hardened weapon systems to EMP was officially recognized. Increased knowledge of the electric and magnetic fields became desirable for both weapons diagnostics and long-range detection of nuclear detonations. For all these reasons a more thorough investigation of EMP was undertaken.

Theoretical and experimental efforts were expanded to study and observe EMP phenomenology and to develop appropriate descriptive models. A limited amount of data had been gathered on the phenomenon and its threat to military systems when all aboveground testing was halted in 1962. From this time reliance has been placed on underground testing, analysis of existing atmospheric test data, and nonnuclear simulation for experimental knowledge. Extended efforts have been made to improve theoretical models and to develop associated computer codes for predictive studies. At the same time, efforts to develop simulators capable of producing threat-level pulses for system coupling and response studies have been expanded.

This chapter describes the EMP generation mechanism and the resulting environment for various burst regimes. The description is largely qualitative, since the complexity of the calculations requires that heavy reliance be placed on computer code calculations for specific problems. Some results of computer code calculations are presented, but generalization of these results is beyond the scope of this chapter. More complete treatments of the EMP phenomena may be found in the "DNA EMP (Electromagnetic Pulse) Handbook (U)" (see bibliography).

ENVIRONMENT – GENERAL DESCRIPTION

7-1 Weapon Gamma Radiation

The gamma radiation output from a nuclear burst initiates the processes that shape the development of an electromagnetic pulse. The gamma radiation components important in EMP generation are the prompt, air inelastic, and isomeric gammas (see Chapter 5). Briefly, the prompt gammas arise from the fission or fusion reactions taking place in the bomb and from the inelastic collisions of neutrons with the weapon materials. The fraction of the total weapon energy that may be contained in the prompt gammas will vary nominally from about 0.1% for high yield weapons to about 0.5% for low yield weapons, depending on weapon design and size. Special designs might increase the gamma fraction, whereas massive, inefficient designs would decrease it. This component is generated within

This document has been approved for public release and sale; its distribution is unlimited.

[redacted]

[redacted]

less than a microsecond of detonation time. High energy neutrons, which result from the fusion process, emerge from the bomb debris with energies on the order of four to fourteen MeV. For a surface or air burst, these neutrons lose their energies primarily through a large number of inelastic collisions with the surrounding air molecules over a time period of many microseconds. This gives rise to a source of gammas over the same time span. Isomeric gammas are given off by nuclei of certain fission products in decaying from excited states to the ground state. They are important at times after the peaks in prompt and air inelastic contributions (see Section 1, Chapter 5).

7-2 Compton Current [redacted]

[redacted] When gamma radiation from any of the sources mentioned in the preceding paragraph impinges upon air molecules, high energy electrons are created by the Compton effect. In this effect, illustrated in Figure 7-1, the incident gamma ray interacts with an electron in the shell of an atom, imparting to it a large amount of energy. Both the electron and a less energetic

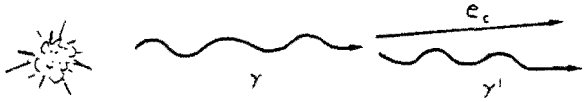

Figure 7-1. (U) The Compton Effect (U)

gamma ray scatter, primarily in the forward direction, and the scattered gamma rays frequently retain sufficient energy to repeat the process. In addition to the generation of Compton electrons, over ten percent of the gamma rays with energy above 5 MeV may generate electron-positron pairs (pair production). The positrons will cause ionization by inelastic collisions and eventually will be annihilated on collision with an electron, resulting in two 0.511 MeV gamma rays. The radial beams of scattered high energy electrons comprise a current termed the Compton current. If certain spatial and time conditions are met by a current, an electromagnetic field is generated. Since the prompt gamma ray pulse increases rapidly to a peak value and then decays (Section 1, Chapter 5), and since the Compton electrons lose energy as described in the following paragraph, the Compton current rises to a peak value rapidly and then decays as illustrated in Figure 7-2.

7-3 Ai. Conductivity [redacted]

[redacted] The high energy electrons in the Compton current lose some energy to the surrounding air molecules through inelastic collisions. The energy lost in these collisions goes into the freeing of additional electrons from the air molecules, i.e., further ionization. A drastic change in the conductivity of air takes place as it is ionized to become a plasma consisting of molecules, atoms, ions, electrons and accompanying electromagnetic radiation (see paragraph 4-2, Chapter 4). The conductivity will vary in space and time with the density and mobility of the ions and electrons, and the mobility depends on the electric field strength. Under certain conditions of air density and distance the x-rays from the bomb may contribute significantly to the air conductivity. Further complications are introduced by the recombination of ions and electrons. Initially the dominant process is the attachment of electrons to neutral oxygen molecules, reducing their mobility. Later the negative ions and electrons recombine with positive ions, reducing the charge density. Both processes, which are strongly dependent on air density, water content of the air, and the electric field, tend to reduce the conductivity of this partially ionized plasma. Figure 7-3 shows an example of air conductivity. The sudden rise at 8 microseconds

QUALITY INSPECTED 4

[redacted]

UNANNOUNCED

[redacted]

[redacted]

DNA
(4X1)

Figure 7-2 [redacted] Compton Current at 500 Meters from a 4200 TJ (1 Mt) Ground Burst [redacted]

[redacted]

Deleted

DNA
(6)(1)

[redacted]

Figure 7-3 [redacted] Conductivity at 500 Meters from a 4200 TJ (1 Mt) Low-Altitude Burst [redacted]

[redacted]

is due to the local arrival of the neutron flux that produces ionization by nuclear reactions other than inelastic collision, namely (n,p) and (n,γ) reactions; however, earlier times are of greatest interest for the generation of EMP.

7-4 Radical Electric Field [redacted]

[redacted] If a nuclear burst occurs in homogeneous (constant density) atmosphere, with no geomagnetic fields present, a charge-separation model may be used to describe the resulting electric fields. Positive and negative charges are separated as the Compton electrons sweep off in a radial direction from the explosion, while the heavier ions tend to remain behind. Thus, two shells of charge are created, an inner positive ion shell and an outer shell of electrons. This separation produces a large local electric field in the radial direction shown as E_r in Figure 7-4. The magnitude of the field is limited as the air conductivity rises to permit return currents. Conductivity is higher closer to the burst where the current are more dense, so this region is the first to saturate and to limit the radial field although the radial electric field is higher when saturation occurs. These effects are depicted schematically in Figure 7-5.

[redacted] It is to be noted, however, that the total current distribution and the resulting radial electric field are perfectly spherically symmetric in this hypothetical illustration. It is a fundamental property of such a current distribution that no magnetic field is generated and no electromagnetic field is radiated away. The various asymmetries that occur in practice, and the resulting fields that are generated in the source region or radiated away are discussed in the following paragraphs.

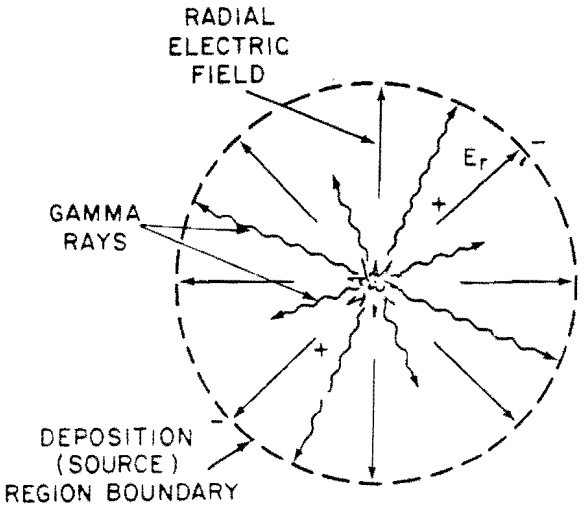

Figure 7-4. [redacted] Charge Separation Model [redacted]

[redacted] ELECTROMAGNETIC FIELD GENERATION [redacted]

7-5 Medium Altitude Air Burst [redacted]

[redacted] This category of nuclear explosions is defined to include weapon bursts under about 30 kilometers (19 miles) altitude, but sufficiently high that the deposition region containing the source currents does not touch the earth. In this case there are three principal factors tending to destroy the spherical symmetry of the current distribution discussed in the preceding paragraph: the atmospheric density gradient, the earth's magnetic field, and the configuration of the weapon itself. Since the earth's magnetic field is a much more important influence in less dense atmosphere, it will be discussed in succeeding paragraphs in connection with high-altitude bursts.

[redacted]

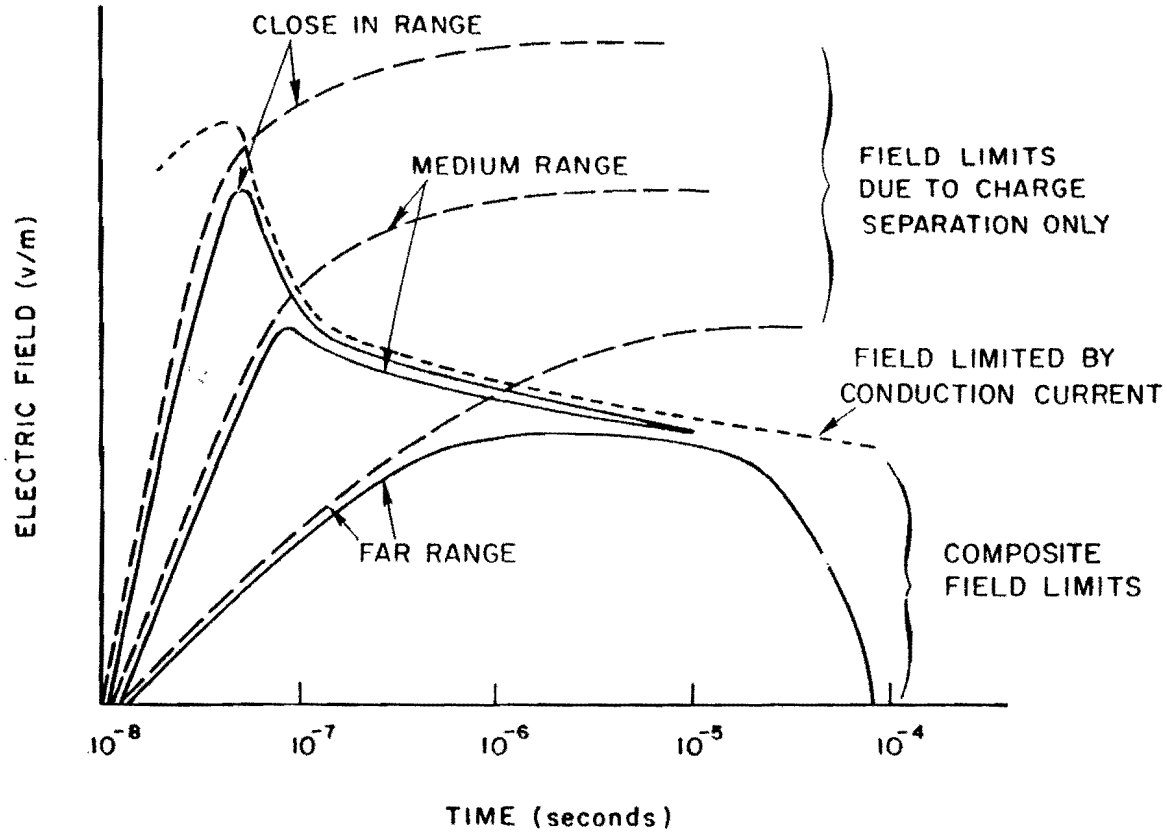

Figure 7-5. [redacted] Limits on Electric Field Waveforms [redacted]

[redacted]

The density gradient in the lower atmosphere leaves the current distribution in the deposition region symmetric in azimuth only, since the strength of all the deposition region interactions depends on the density of its constituents. Thus there is a net vertical current component, the strength of which is expresed in terms of a dipole moment. This quantity is responsible for the generation of a magnetic field in the deposition region and the radiation of an electromagnetic wave from this region. These effects are shown in Figure 7-6, assuming no weapon asymmetry. The radiation, which is in the form of a simple vertical electric dipole, is a high intensity brief pulse that includes a broad spectrum of frequencies up to many MHz. Figure 7-7 demonstrates the relationship of energy per unit frequency as a function of frequency. The electric field as a function of range, R, and azimuth, θ, follows the form

$$E(t) = \frac{R_o}{R} E_o(t) \sin\theta \quad .$$

where R_o is the radius of the deposition region and E_o is the time dependent electric field at R_o. The angular dependence of radiated electromagnetic radiation is such that maximum intensity is radiated horizontally from the burst and is minimum directly above or below the burst. Simplified general waveforms of the quantities discussed here are presented in Figure 7-8.

[redacted]

DNA (6)(1)

[redacted]

DNA (6)(1)

7-6 Surface Burst

The presence of the ground introduces a strong asymmetry in addition to the ones described above. The ground is a very good absorber of neutrons and gamma rays and a good conductor of electricity compared with air. Therefore, the deposition region consists approximately of a hemisphere, resulting in a very large dipole moment and consequently large radiated fields. Further, the conducting ground allows an effective return path for the electron shell near the surface with the result that current loops are formed. That is, electrons travel outward from the burst in the air, then return through the higher conductivity ground toward the burst point. These current loops form a toroidal shaped solenoid resulting in very large azimuthal magnetic fields in the deposition region, especially close to the ground. These effects are shown in Figure 7-9. Figure 7-10 shows a typical toroidal magnetic field waveform in the deposition region near the surface.

There can be extremely large electric and magnetic fields as well as the presence of a highly conducting plasma within the deposition region. As a result of the number of variables that can affect the magnitude and shape of the fields, it is not possible to provide a simple description of the fields.

The peak radiated electric fields are ten to a hundred times stronger than for a similar air burst. The range, R_o, at which the radiation region begins is a function of weapon yield as shown in Table 7-1.

The magnitude of the peak value of the radiated electric waveform for a surface burst is a weak function of yield, varying from about 1,300 volts per meter at R_o for a 4.2 TJ (1KT)

[redacted]

[redacted]

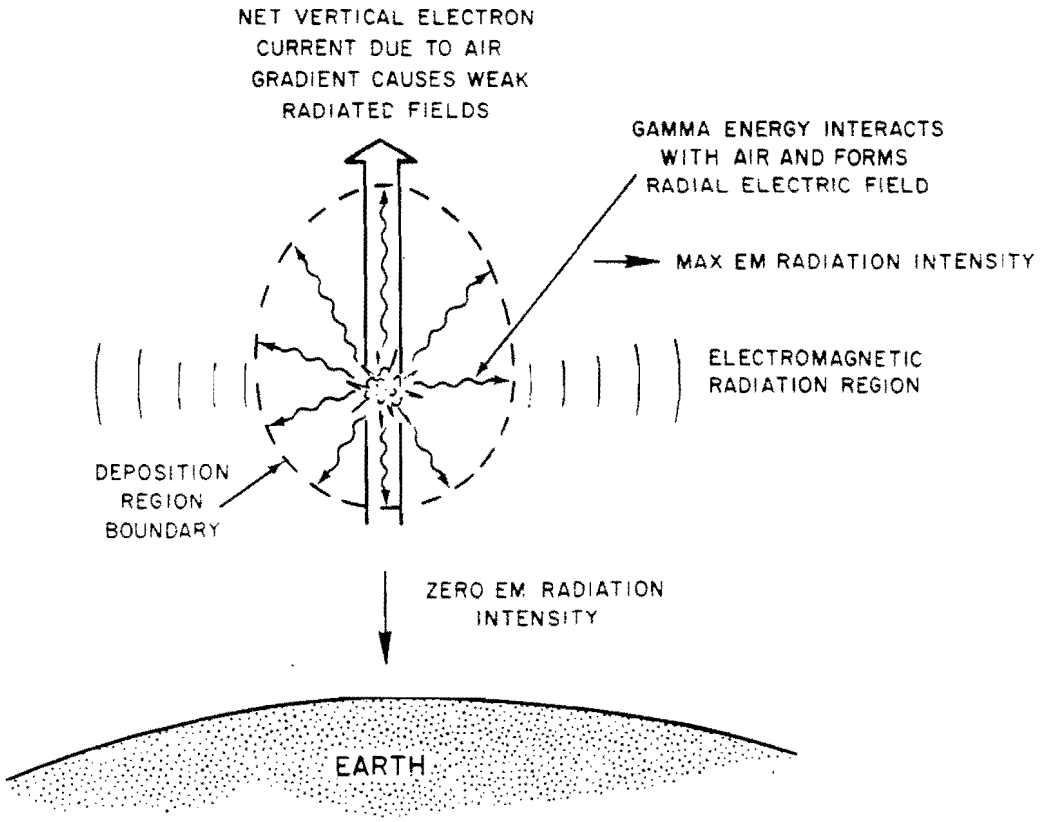
NET VERTICAL ELECTRON CURRENT DUE TO AIR GRADIENT CAUSES WEAK RADIATED FIELDS
GAMMA ENERGY INTERACTS WITH AIR AND FORMS RADIAL ELECTRIC FIELD
MAX EM RADIATION INTENSITY
ELECTROMAGNETIC RADIATION REGION
DEPOSITION REGION BOUNDARY
ZERO EM RADIATION INTENSITY
EARTH

Figure 7-6. [redacted] Simple Illustration of Air-Burst EMP [redacted]

[redacted]

[redacted]

Deleted

DNA
(6)(1)

Figure 7-7 [redacted] Normalized Frequency Spectrum of the Electric-Dipole Radiated EMP for Air Bursts [redacted]

[redacted]

[redacted]

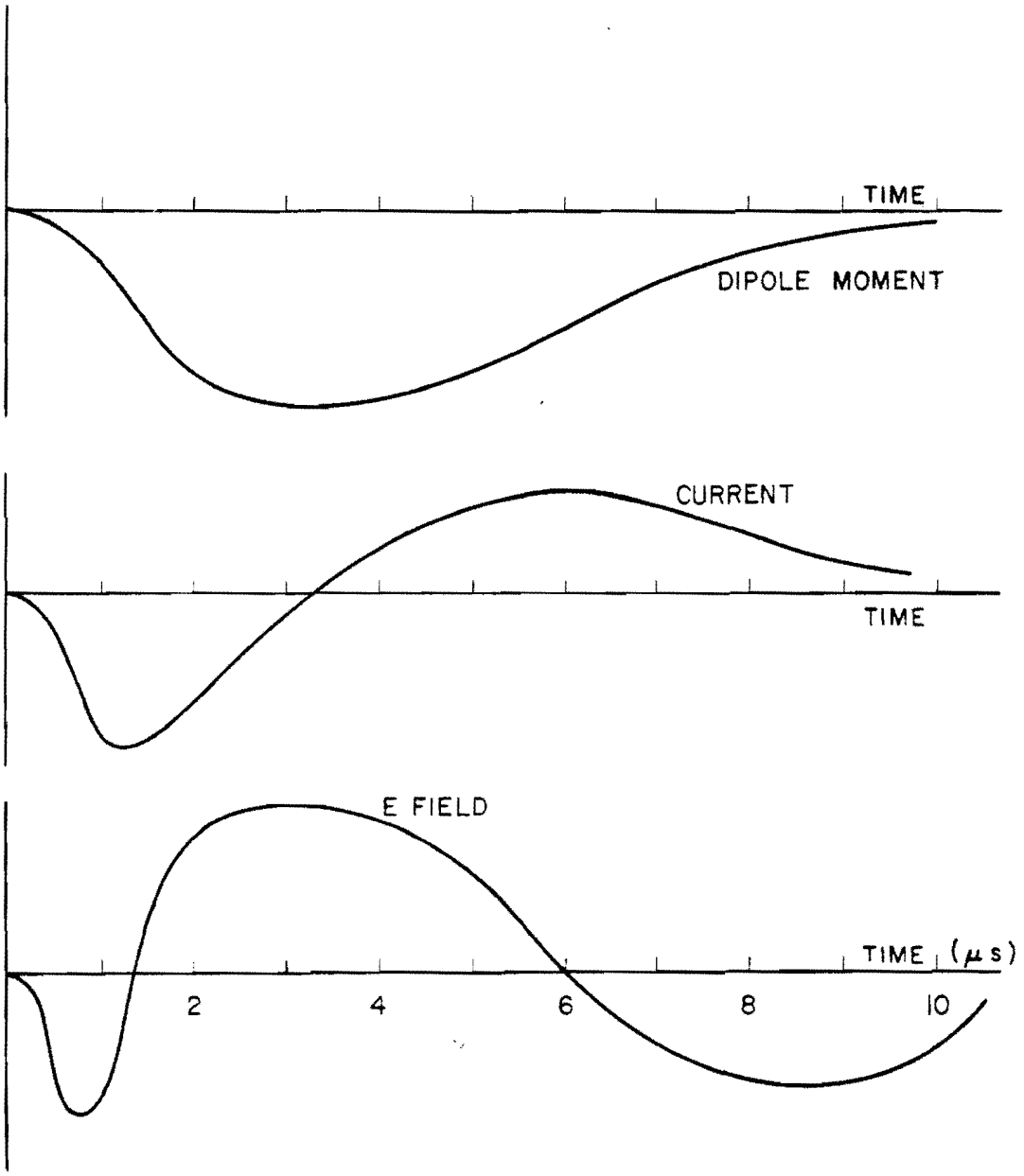

Figure 7-8 [redacted] Comparison of General Waveforms for the Dipole Moment, the Current, and the E-Field for and Air Burst [redacted]

[redacted]

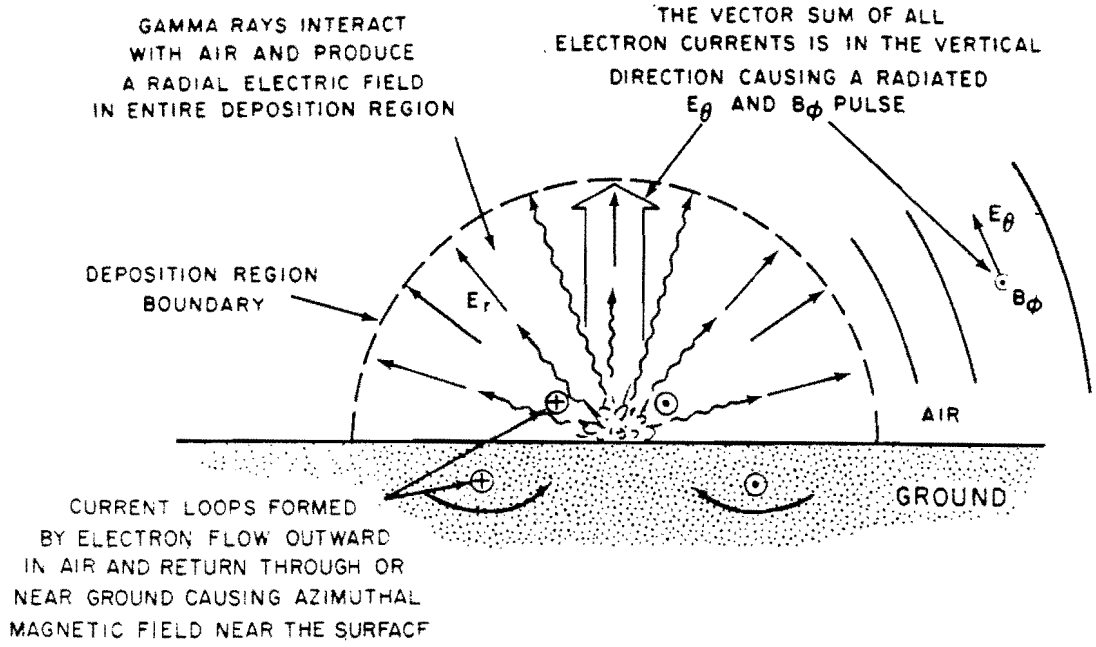

Figure 7-9 Simple Illustration of Surface Burst EMP

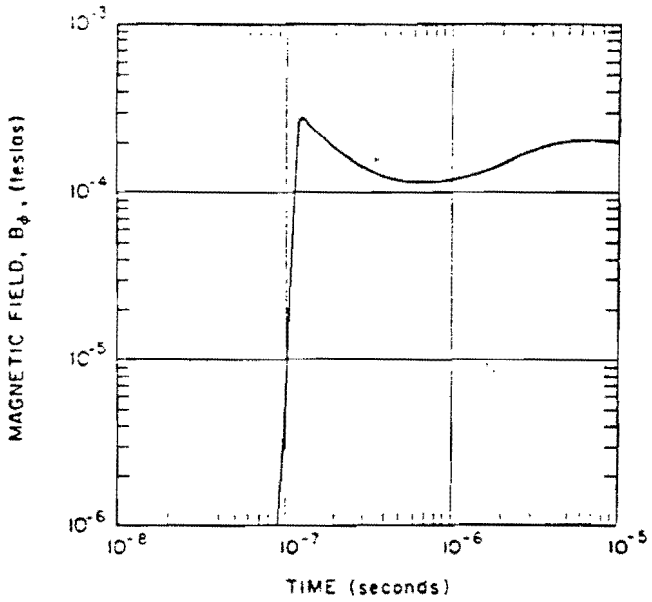

Figure 7-10 Shape of Magnetic Field for Toroid Model

explosion to about 1,670 volts per meter for a 4.2×10^4 TJ (10 MT) explosion. For most cases, a value of 1,650 volts per meter may be assumed. At ranges along the surface beyond R_o, the peak radiated electric field varies inversely with the distance from the burst. Thus, the magnitude of the peak radiated electric field along the surface may be estimated from the equation

$$E = \frac{R_o}{R} E_o ,$$

where R_o is the range to the beginning of the radiation region, R is the distance along the surface to the point of interest, E_o is the peak value of the radiated field at R_o (assumed to be about

[redacted]

Table 7-1. [redacted] Variation of Range, R_O' at which the Radiation Region Begins, with Yield [redacted]

[redacted]

DNA (H)(3)

1,650 volts per meter), and E is peak value of the radiated field at R. For example, the peak electric field 10 kilometers from a 4200 TJ (1 MT) surface burst would be

$$E = \left(\frac{7.2}{10}\right)(1{,}650) \approx 1{,}200 \text{ v/m}.$$

The peak electric field at the same distance from a 420 TJ (100 KT) surface burst would be

$$E = \left(\frac{5.8}{10}\right)(1{,}650) \approx 950 \text{ v/m}.$$

The spatial distribution of the radiated signal involves not only the inverse range attenuation discussed above, but also the polar angle. The magnitude of the $R \cdot E_\theta$ product follows a complicated function of the polar angle, θ. Figure 7-11 shows the computed variation of the radiated EMP signals as a function of θ. The variation in the waveform shape, as well as in the peak amplitude, as a function of angle should be noted. Because of the greater rise time of the waveforms as the vertical is approached, it is apparent that the high frequency content of the signals decreases. The frequency spectrum is an important parameter for coupling analysis. Figure 7-12 shows the normalized frequency spectrum of the horizontally radiated EMP from a surface burst. Comparing this spectrum with that shown in Figure 7-7 shows significantly greater high frequency content for the surface burst.

[redacted] The preceding discussion was intended to illustrate the general characteristics of the EMP fields generated by surface bursts and the variation of the peak radiated electric fields in space. In addition to the behavior of the electric and magnetic fields, the air conductivity is important for more accurate coupling analysis. A few selected examples of these quantities are presented in later sections of this chapter; however, it is beyond the scope of this manual to provide complete EMP environmental data upon which vulnerability analyses may be based.

7-7 High Altitude Burst [redacted]

[redacted] This burst regime is defined to include any nuclear burst at an altitude above about 30 kilometers (19 miles). In this regime the atmosphere is so sparse above the burst that relatively little Compton current is generated there. The deposition region, departing far from spherical symmetry, consists principally of a pancake shaped volume extending from about 20 to 50 kilometers (12 to 30 miles) in altitude and to the horizon as viewed from the burst. Thus, very high altitude bursts may cover vast geographical areas. A further asymmetry, the earth's magnetic field, is responsible for the form of the radiation. The Compton electrons, which result from collisions of the prompt gammas and x-rays with the air molecules in the deposition regions, are deflected by the earth's field to follow helical paths significantly long

[redacted]

[redacted]

Deleted

DNA
(6)(1)

Figure 7-11 [redacted] Variation of the Radiated EMP for a Surface Burst with Angle θ Measured from the Vertical in Radians [redacted]

[redacted]

[redacted]

DNA
(LXI)

Deleted

Figure 7-12 [redacted] Normalized Frequency Spectrum of the Horizontally Radiated EMP for a Surface Burst [redacted]

[redacted]

during the time between collisions in the rare-field medium. The accelerated electrons produce the characteristic synchrotron radiation with a large high-frequency content. The peak amplitude of the electric field near the surface may be quite large, a few tens of thousands of volts/meter for high bursts. Figure 7-13 illustrates the basic geometry of this burst.

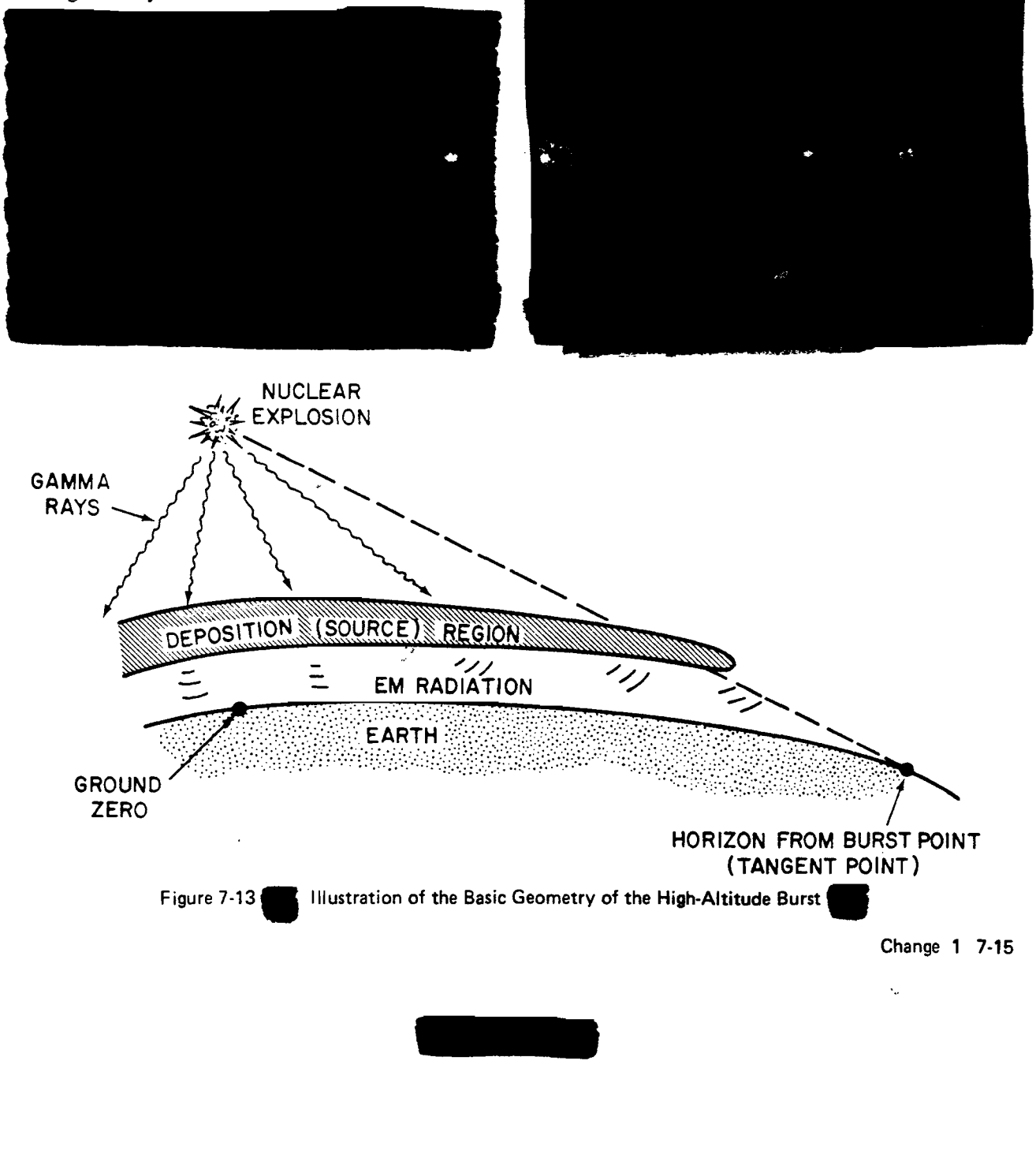

Figure 7-13 Illustration of the Basic Geometry of the High-Altitude Burst

[redacted]

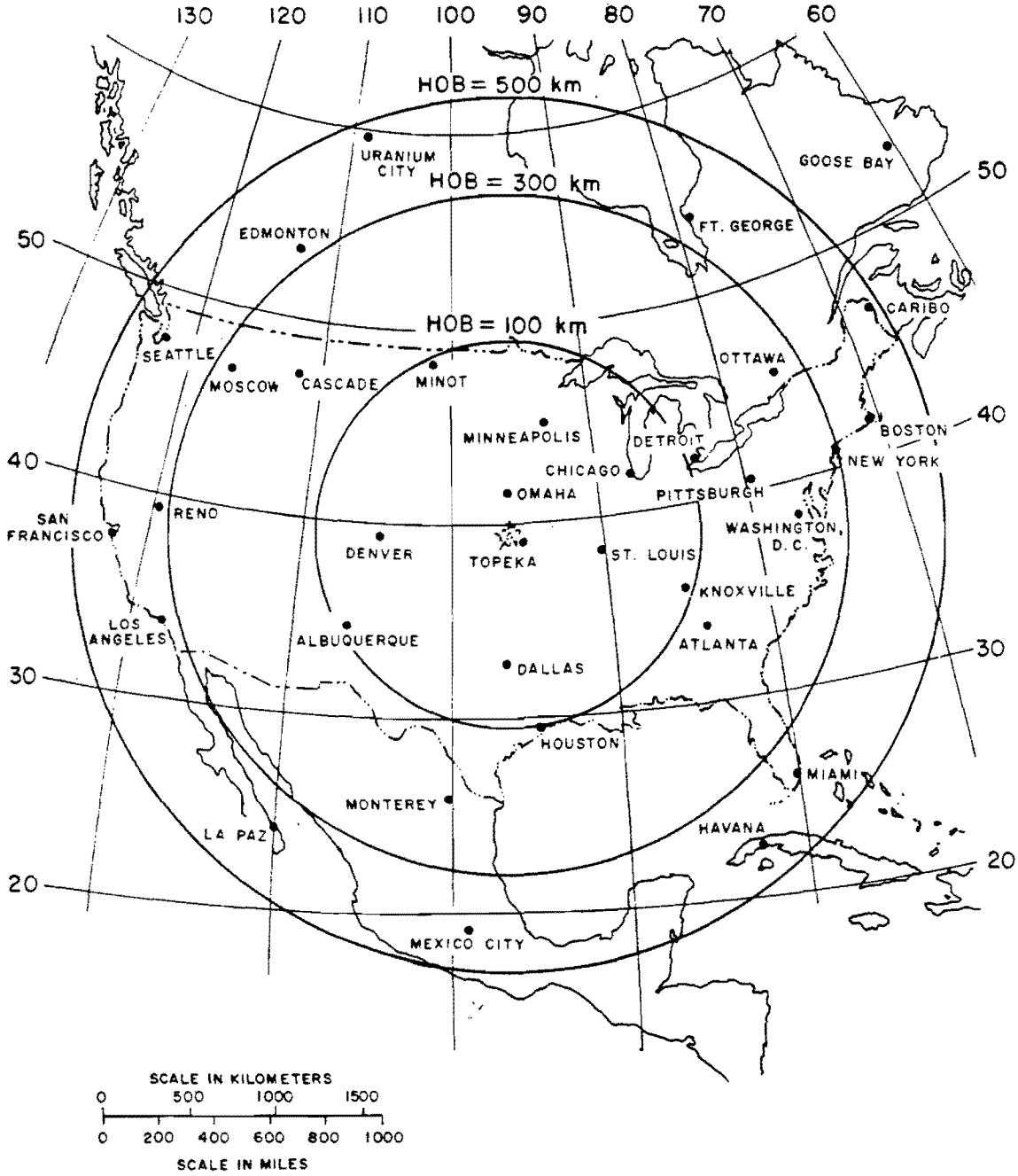

Figure 7-14 [redacted] Ground Coverage for Bursts of 100, 300, and 500 km (about 62, 186, and 310 miles) for a Large Yield Burst Above the Geographical Center of the (counterminous) United States [redacted]

[redacted]

[redacted]

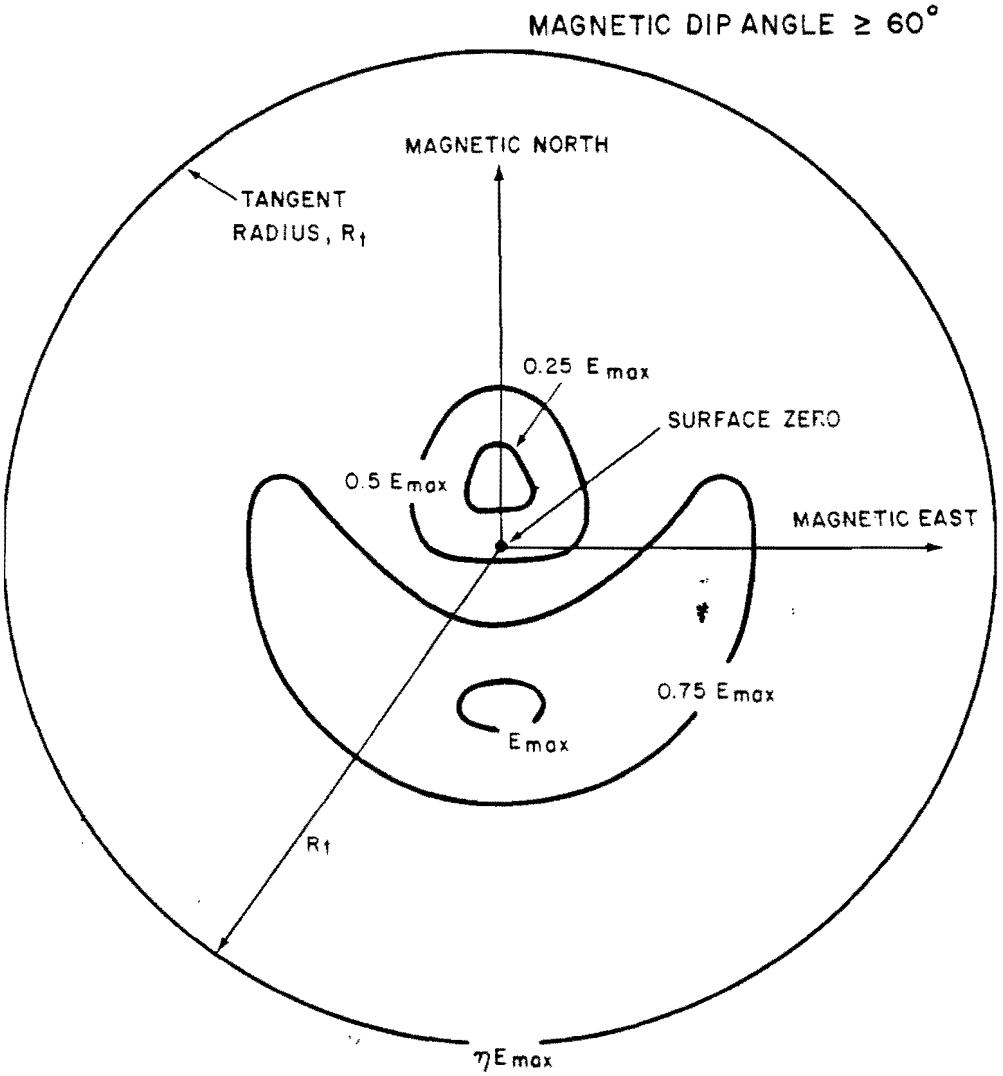

Figure 7-15 [redacted] Basic Variations in Incident Peak Electric Field for Locations on the Earth's Surface for HOB above 500 km [redacted]

[redacted]

[redacted]

DNA (G)(3)

DNA (G)(1)

DNA (G)(3)

Deleted

Figure 7-16 [redacted] Maximum Peak Electric Field as a Function of Gamma Ray Yield for Selected Burst Heights [redacted]

[redacted]

[redacted]

[redacted]

DNA (6)(1)

The radiated EMP from a high altitude burst rises to a peak value much more rapidly than that from a surface or low air burst. Figure 7-17 illustrates the time waveform of the radiated signal from a high altitude burst. The analytic expression

$$E(t) = 5.3 \times 10^4 \, (e^{-4t} - e^{-476t}) \text{ v/m} ,$$

where t is in microseconds, describes the waveform in Figure 7-17. The frequency spectrum of this pulse is illustrated in Figure 7-18. As the gamma yield of the weapon decreases, the pulse width tends to increase, decreasing the relative high frequency content of the signal. Similarly, increasing the angle between the line-of-sight and the vertical through the burst point increases the pulse width.

[redacted] The high altitude burst is the dominant threat to exoatmospheric systems. The most severe EMP environment for such a system comes from a line-of-sight path that passes

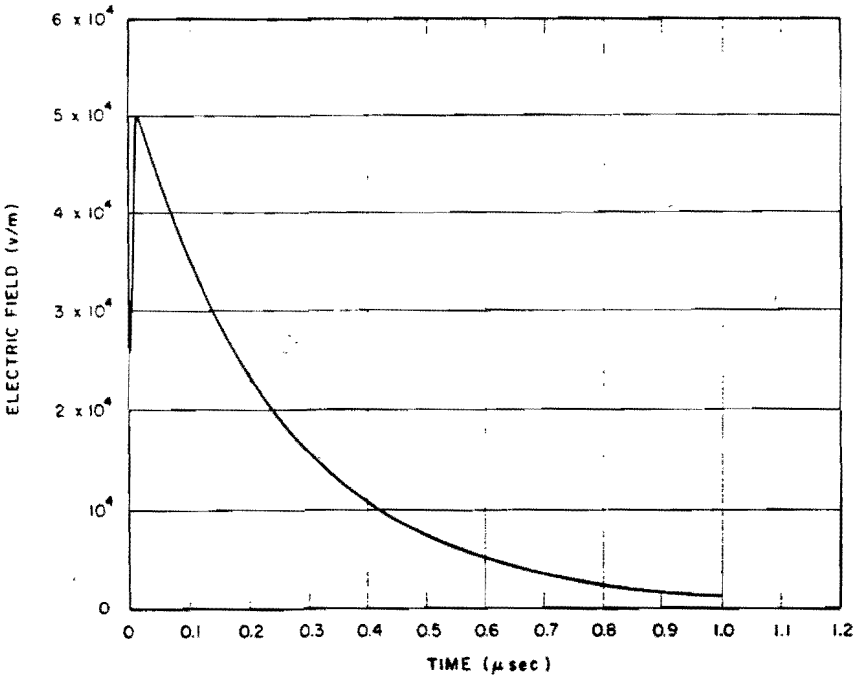

Figure 7-17 [redacted] Time Waveform of High-Altitude Radiated [redacted]

[redacted]

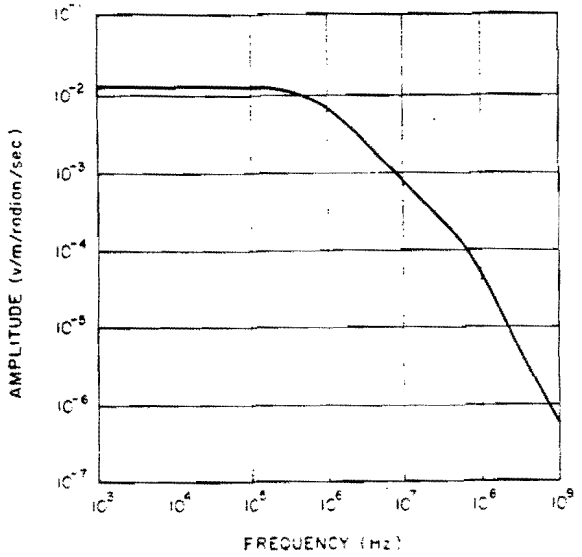

Figure 7-18 Amplitude of High-Altitude Radiated Signal

through the deposition region but misses the earth and is propagated through the ionosphere (see Figure 7-19). The ionosphere acts as a high pass filter, and only frequencies above a given cutoff are observed. The cutoff frequency depends on the altitude, time of day and sunspot activity, and, for example, varies between about 3 and 14 MHz at night, depending on the altitude of the observer. Daytime cutoff frequencies of 30 MHz may be encountered for a 1000 km high observer. In addition, the effective index of refraction, and therefore the group velocity of the EMP signal also varies, with the higher frequencies traveling fastest. Also, the transmission for frequencies near the cutoff is very large, rising to near unity for higher frequencies. Although the amplitude of the dispersed pulse will be much smaller than that of the undispersed pulse, the signal will be stretched out greatly in time. For frequencies above the cutoff there will be little energy loss. Figure 7-20 shows a predicted dispersed EMP (DEMP) signal from a high altitude burst as viewed by an observer at 100 km altitude. This is based on a nighttime ionosphere at sunspot minimum.

SYSTEM GENERATED EMP

7-8 General Description

The term System Generated Electromagnetic Pulse (SGEMP) refers to the fields and currents generated by the interaction of weapons-produced radiation (principally X-rays and gamma rays) with a system or portion of a system. The system generated electromagnetic pulse is produced inside or in the vicinity of a system when an incident photon pulse interacts with the material of the system. Photoelectric and Compton electrons are created, and the resulting emission current produces electric and magnetic fields. Internal EMP, or IEMP, which refers to the electromagnetic fields interior to systems and containers, and which is generally generated by gamma rays, or high energy X-rays, is included in the general category of SGEMP. SGEMP specifically excludes the internal effects associated with transient radiation effects on electronics (TREE).

The system-generated EMP is most important for electronic components in satellites and ballistic systems above the deposition region that would be exposed directly to the nuclear radiations from a high-altitude burst. The system-generated EMP can also be significant for surface and moderate-altitude bursts if the system is within the deposition region but is not subject to damage by other weapons effects. This could possibly occur for surface systems exposed to a burst of relatively low yield or for airborne (aircraft) systems and burst of higher yield.

[redacted]

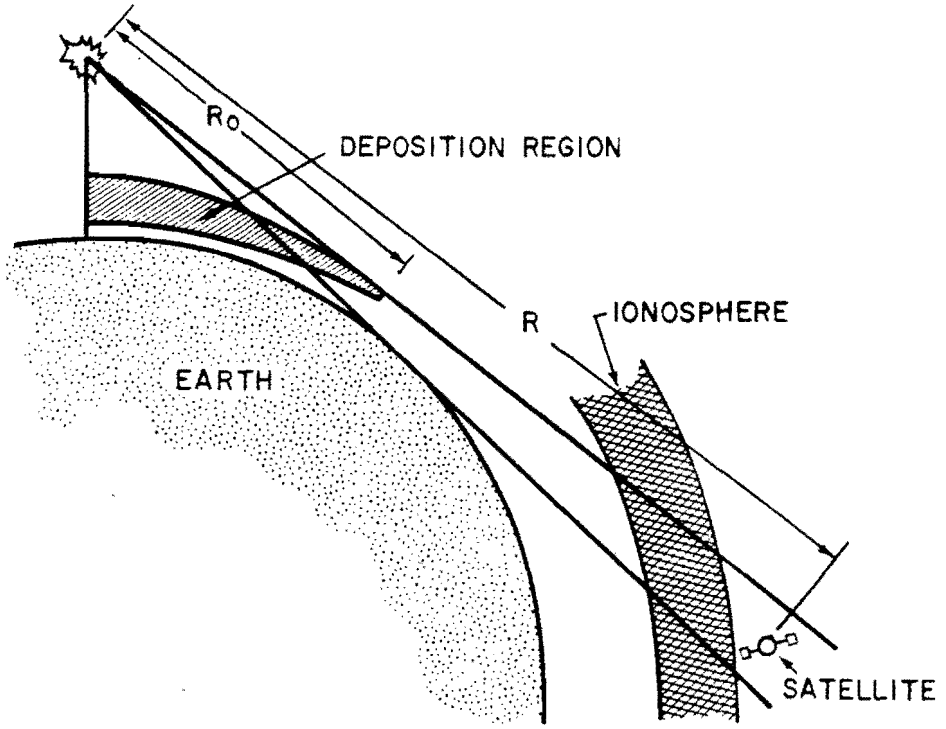

Figure 7-19 [redacted] The Geometry for Producing Dispersed EMP for Exoatmospheric Systems [redacted]

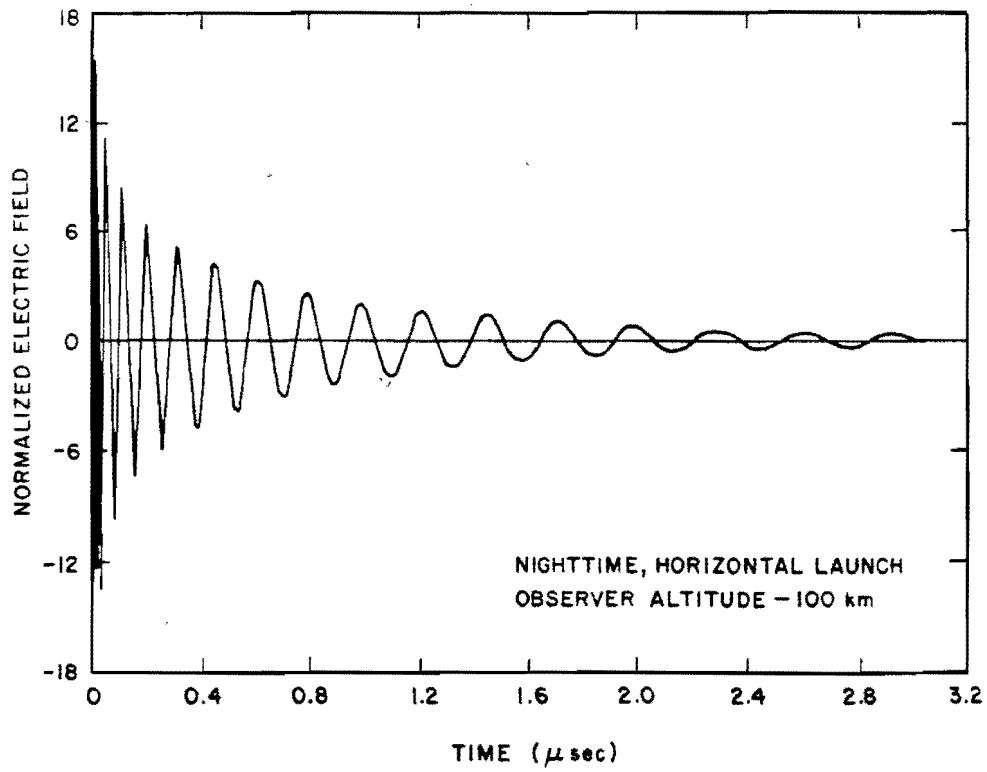

Figure 7-20 [redacted] Electric Field Time Waveform of High-Altitude EMP after Dispersion by Nighttime Ionosphere [redacted]

[redacted]

[redacted]

7-9 SGEMP Generation [redacted]

[redacted] The generation of SGEMP is a complex function of many physical phenomena. The complexity of the problem precludes quantifying SGEMP generation for any broad class of systems. This section, therefore, will attempt to describe some of the generation phenomena for one simple problem. The "DNA EMP (Electromagnetic Pulse) Handbook," DNA 2114H-3, Volume 3, should be consulted for an in-depth treatment of the subject (see bibliography).

[redacted] Figure 7-21 illustrates SGEMP generation in a cavity. The incident X-rays and gamma rays create photo- and Compton electrons, respectively, within the cavity walls. The generation is, of course, dependent on the energy flux of the incoming photons and the properties of the wall material. The photo- and Compton electrons subsequently interact with the atoms of the wall material to produce secondary electrons. Those electrons created near the surface (within an electron mean-free-path) with velocity vectors toward the surface generally will be emitted. The net electron currents, both within and without the cavity, gives rise to a magnetic field which will induce currents in circuit loops via magnetic coupling.

[redacted] For this discussion, it is assumed that the electron emission and subsequent field generation are separable problems. Further, the electron emission from the external wall surfaces will be ignored. The problem under consideration is thus one in which electrons are emitted from two internal surfaces of the cavity in the forward and reverse directions, the emission being described as a time and energy dependent electron flux.

[redacted] As the emitted electrons traverse the cavity, a net forward current will be observed within the cavity while a space charge is established concurrently. If the cavity is at vacuum or near-vacuum conditions (0.13 pascal - 10^{-3} Torr or less) and of appropriate size, space charge limitation will occur. This will result in the creation of high electric fields (10^5 - 10^6 volts/meter) near the walls.

[redacted] If the cavity pressure is above 0.13 pascal, another phenomenon will occur in sufficient intensity to alter the SGEMP. The emission electrons will interact with the gas molecules to produce additional secondary electrons (hereafter called gas electrons) and positive ions. The gas electrons will tend to "stream" to the cavity walls in comparison to the heavier and slower gas ions that are created concurrently. The gas ions will neutralize the space charge, thereby allowing more electrons to traverse the cavity. Thus the E-field intensity near the walls will decrease while the current in the cavity, and concurrently the magnetic field, will increase. It should be noted that quantitative analysis of the electron emission and subsequent SGEMP generation for even this simple problem requires the use of complex computer codes on large computers.

7-10 Problem Definition [redacted]

[redacted] It is emphasized that the above discussion dwells on only *one* small aspect of the SGEMP problem: the generation of an idealized SGEMP in a simplified geometry. A complete treatment of the SGEMP for a given system must start with the threat definition and the incoming photon flux. This must then be translated into electron emission from all surfaces, cables, components, etc., of the system. From the emission, fields and currents throughout and external to the system must be determined in a self-consistent manner. Next, coupling of the fields and currents to the system electronics must be established. Finally, the reaction of the electronics to the coupled energy must be determined and evaluated.

[redacted]

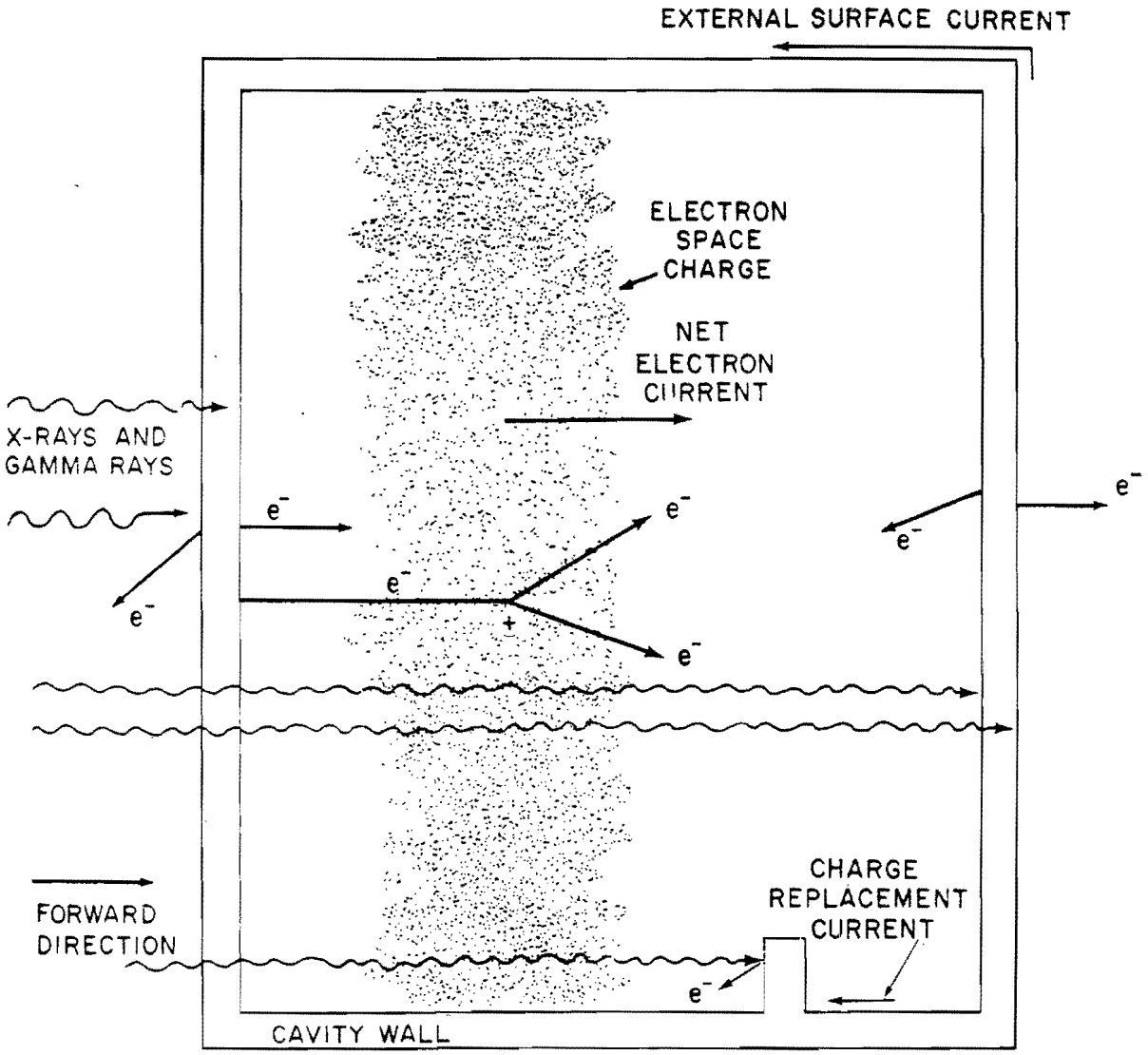

Figure 7-21 SGEMP Generation

[redacted]

It is possible that this evaluation procedure may be terminated after any given step. For example, consider an electronically very "hard" system for which the "threat" is specified as 4.2×10^4 joules/meter^2 (1 cal/cm^2) received uniformly over a period of a year. By inspection, SGEMP is not a problem. At the other extreme, consider a system that is easily upset by small (milliamp), short duration (30 nsec) electrical pulses. If the threat for this system is 4.2×10^5 joules/meter^2 (10 cal/cm^2) in a period of 100 nanoseconds, SGEMP *may* be a significant problem. An in-depth analytical/experimental program must be undertaken to make an evaluation of SGEMP effects.

Clearly, the above examples are extremes. They only serve to illustrate that an all encompassing definition of SGEMP problems is impossible because of the highly complex, system-specific nature of this phenomenon. Likewise, it is not possible to formulate a specific solution to the SGEMP threat for general application. Thus, the susceptibility and vulnerability of each system to SGEMP effects must be considered separately.

[redacted] COMPUTER CODE DESCRIPTIONS [redacted]

7-11 Code Utility [redacted]

From the physical descriptions provided in the preceding paragraphs, it is apparent from the large number of variables involved that even approximate solutions to practical problems of interest demand a large investment in electronic computation. The complete problem of the coupling of the EMP from a specific detonation into the components of a specific system is an extremely complex problem. There are no computer codes which even remotely approach a treatment of the complex problem. As a consequence, various aspects of the EMP problem are studied individually with the aid of existing codes, and good engineering judgment must be used to couple these various parts of the solution into a quantitative estimate of the effects of EMP upon a given system.

7-12 Code Classes [redacted]

There are three general classes of computer codes in use: environment codes, system generated EMP codes, and circuit-analysis codes. The codes that are currently in use are described in the "DNA EMP (Electromagnetic Pulse) Handbook," Volume 4 (see bibliography).

[redacted] SYSTEMS EFFECTS [redacted]

7-13 System Definitions [redacted]

Many systems that are physically different can be grouped together in terms of the EMP environments they will encounter. For this purpose it is useful to consider classification of systems in terms of operating altitude and nuclear hardness.

From the previous description of the EMP environment, the altitude categories suggested in Figure 7-22 are evident. It should be noted that certain systems may operate successively in more than one category.

For the purposes of this manual it is adequate to consider system hardness in only two categories. A hard system is one that has been designed to operate in some nuclear environment. A soft system is not so designed, and its hardness is due solely to its inherent design. For a ground system, the blast usually is considered to be the indicator of the nuclear hardness of the system. The dominant effect will change from blast to nuclear radiation, defined here in terms of the total dose in rad (Si), as the system altitude increases. A system is considered to be

[redacted]

[redacted]

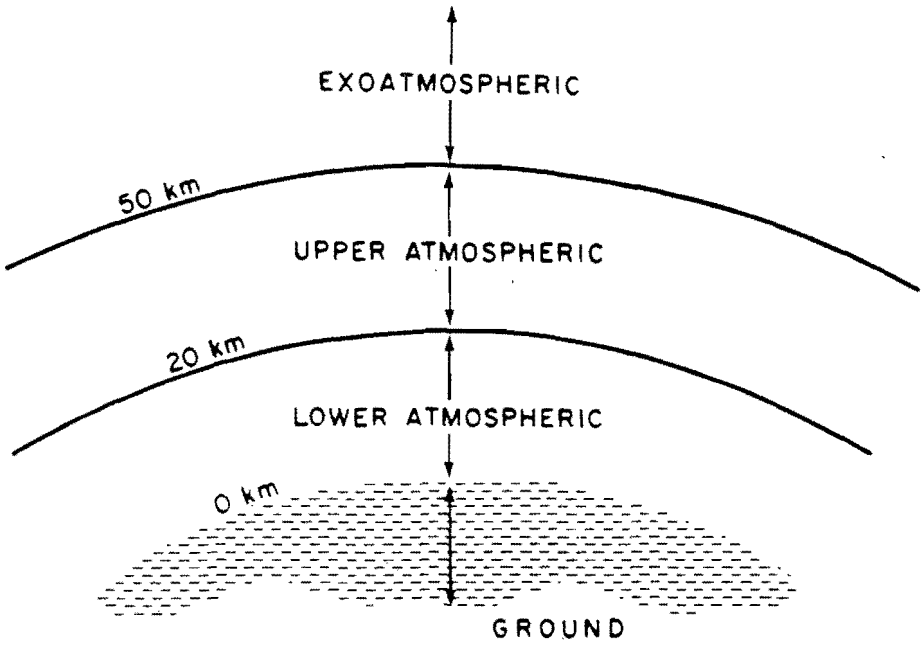

Figure 7-22 [redacted] Categories of System Operation Regions [redacted]

[redacted]

hard if it is built to withstand blast overpressures of about 70 kilopascals (10 psi) or more or a radiation dose of 1 rad (Si) or more. Corresponding figures for a soft system are 7 kilopascals (1 psi) or less and 0.1 rad (Si) or less. Systems marginal with respect to either criterion should be reviewed in both categories.

[redacted]

DNA (L)(1)

7-14 Threat Definition [redacted]

[redacted]

DNA (L)(1)

[redacted]

[redacted]

[redacted]

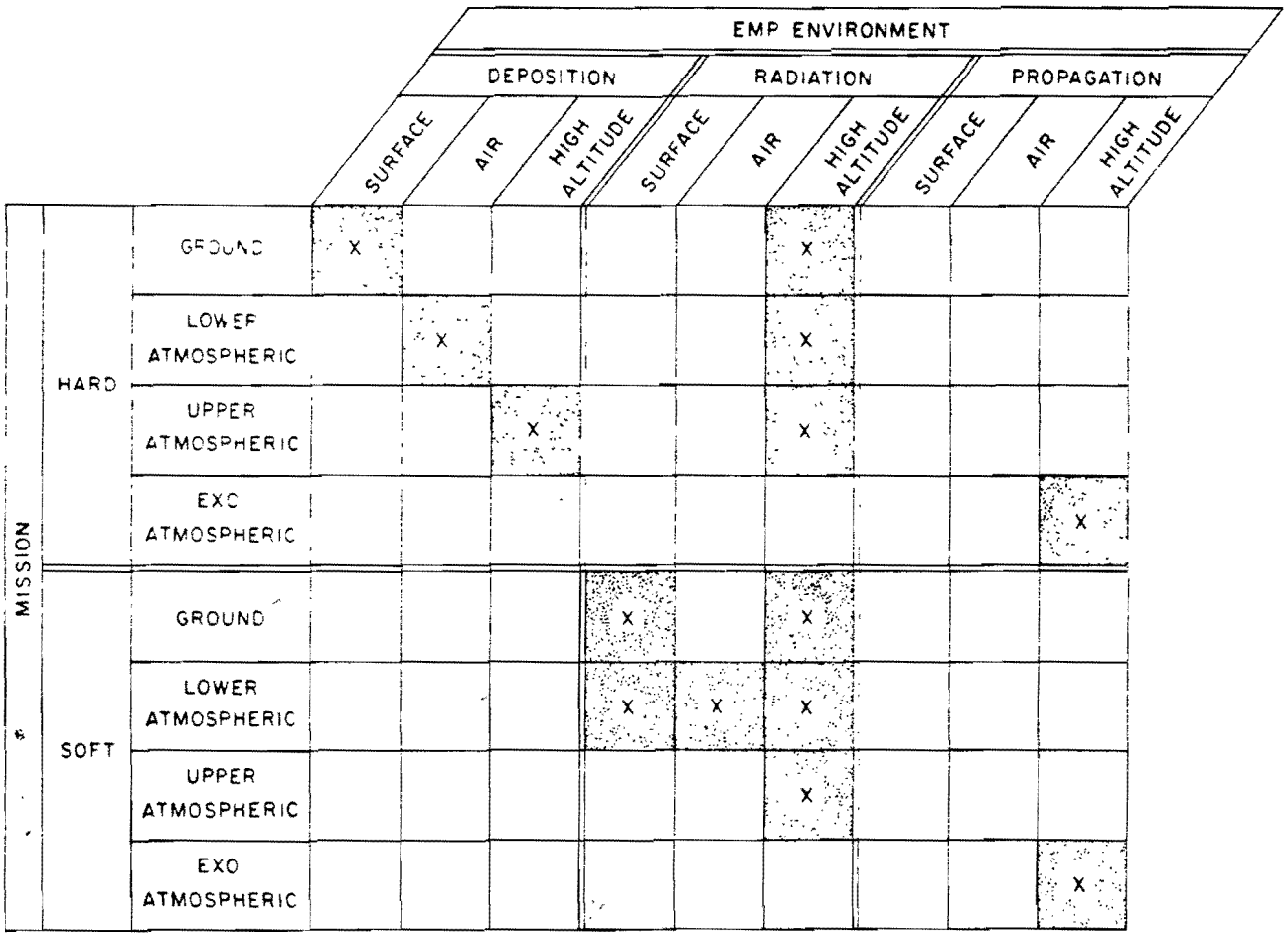

Figure 7-23 [redacted] Mission/Environment Matrix [redacted]

[redacted]

[redacted]

DNA 6)(1)

[redacted]

[redacted] Blocks are shaded in on the diagram on the basis of dominant environments for a given mission, not on the basis of whether EMP exists at all for that situation. Thus, based on the definitions given, Figure 7-23 may be used as a guide for which environments constitute a dominant threat for given situations of interest.

7-15 Effects Comparisons [redacted]

[redacted] It is well beyond the scope of this chapter to attempt meaningful effects comparisons for every system altitude, burst altitude, and environment combination for which EMP may be the dominant threat. However, it is instructive to consider one such combination in order to gain some impression of how the magnitude of the threat might be compared to other effects. Accordingly, the deposition region environment created by a surface burst will be examined with regard to the effects on hardened ground systems, a category in which the EMP threat may dominate according to Figure 7-23. As mentioned previously, the nuclear hardness of such a system is generally described in terms of its over-pressure level. Using this quantity as an indicator of hardness, the EMP field waveforms, peak values and frequency content for the principal field components $B\varphi$, E_r, and E_θ, as defined in Figure 7-24 and the associated air conductivity waveforms and peak values will be examined.

[redacted] The peak values as a function of overpressure are considered first. Figures 7-25, 7-26, and 7-27 show these values for the three field components for two yields and two values of ground conductivity (σ_g). It should be kept in mind that a large shift in frequencies present can occur between 70 and 7,000 kilopascals (10 and 100 psi). The coupling of systems to the fields in this intense region is complicated by the high air conductivity. Figure 7-28 shows how peak air conductivity varies with overpressure. It should be noted that the lower yield weapon produces higher conductivity for a given overpressure level.

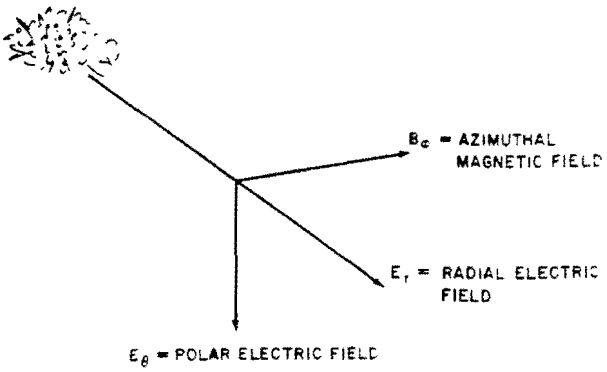

Figure 7-24 [redacted] Field Directions of Ground-Burst EMP [redacted]

[redacted] The variation of these same quantities in time for the 4,200 terajoules (1 MT) yield and a ground conductivity of 10^{-2} mho/m is illustrated next. The waveform for the $B\varphi$ component is shown for various overpressure levels in Figure 7-29, and the frequency spectrum is illustrated in Figure 7-30. Corresponding waveforms and spectra for E_r and E_θ components are shown in Figures 7-31, 7-32, 7-33, and 7-34. Finally, the corresponding air conductivity waveforms are presented in Figure 7-35.

[redacted] It is apparent from these figures that meaningful effects comparisons can be made and presented to the systems designer for a given set of physical conditions. However, it is also clear that the results vary drastically with changes in

[redacted]

[redacted]

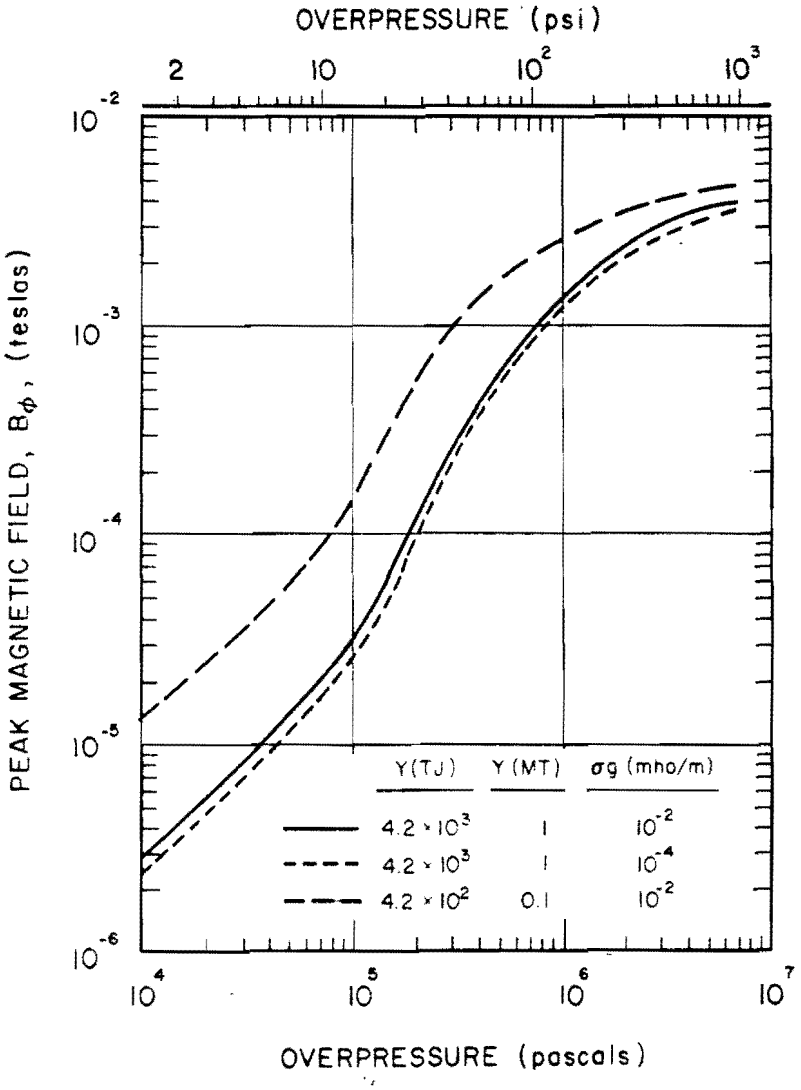

Figure 7-25 [redacted] Peak Magnetic Field B_ϕ Versus Overpressure for Varying Ground Conductivities and Yields [redacted]

[redacted]

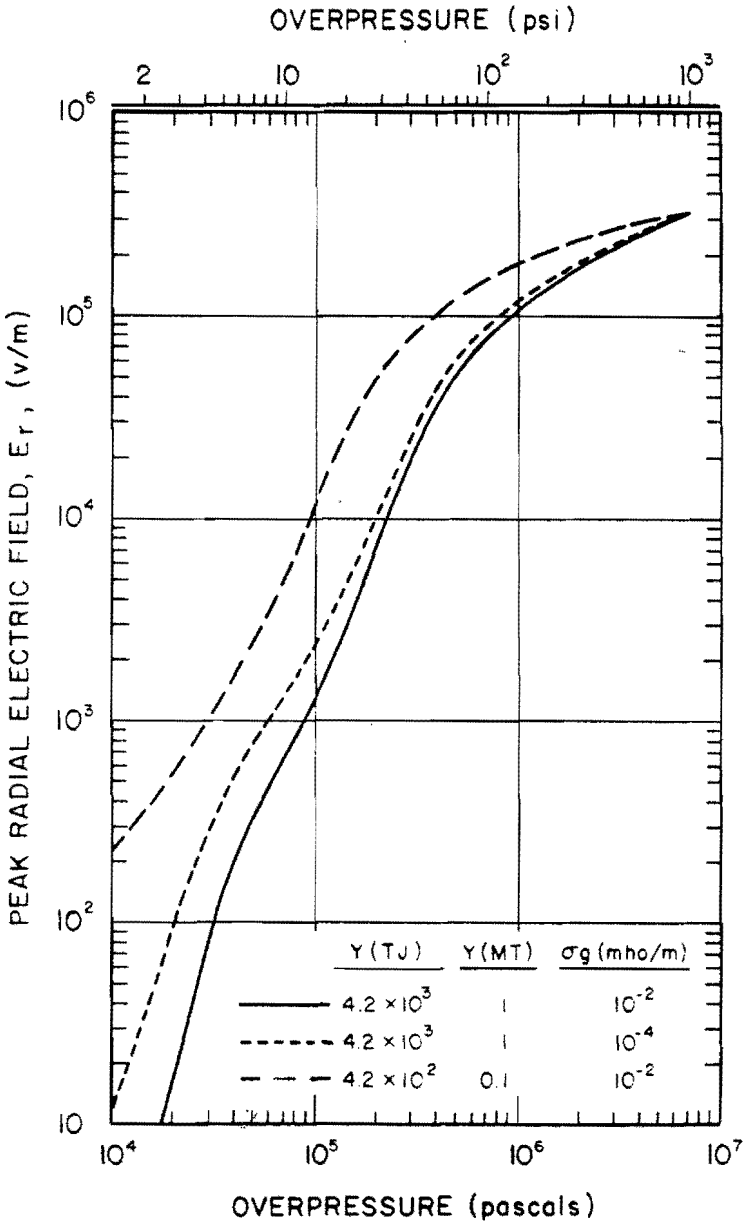

Figure 7-26 Peak Radial Electric Field E_r Versus Overpressure for Varying Ground Conductivities and Yields

[redacted]

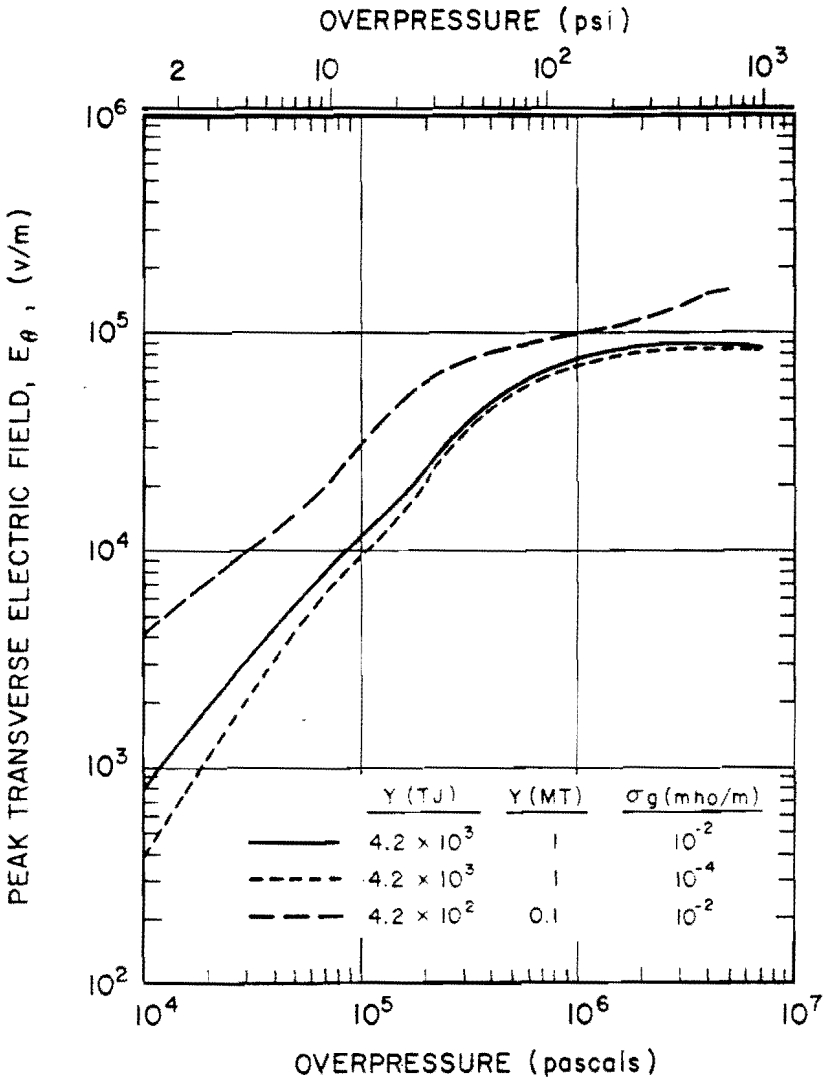

Figure 7-27[redacted] Peak Transverse Electric Field E_θ Versus Overpressure for Varying Ground Conductivities and Yields[redacted]

[redacted]

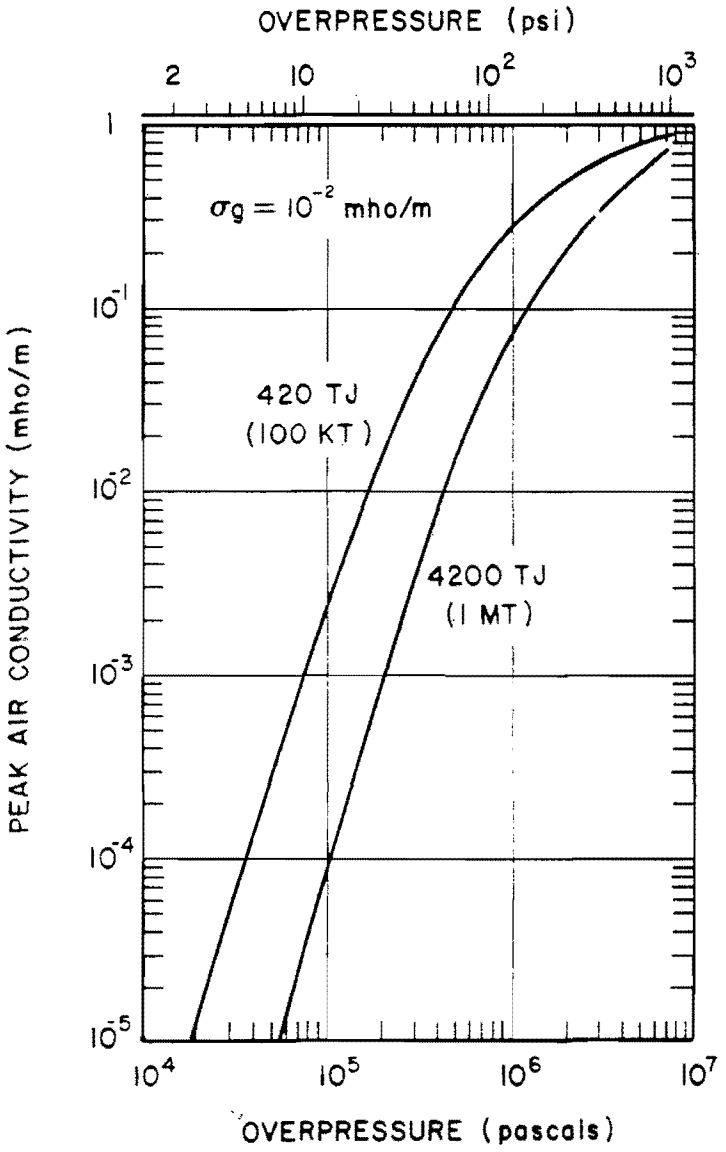

Figure 7-28 Peak Air Conductivity Versus Overpressure for Yields of 420 TJ (100 kt) and 4.2 x 10^3 TJ (1 Mt)

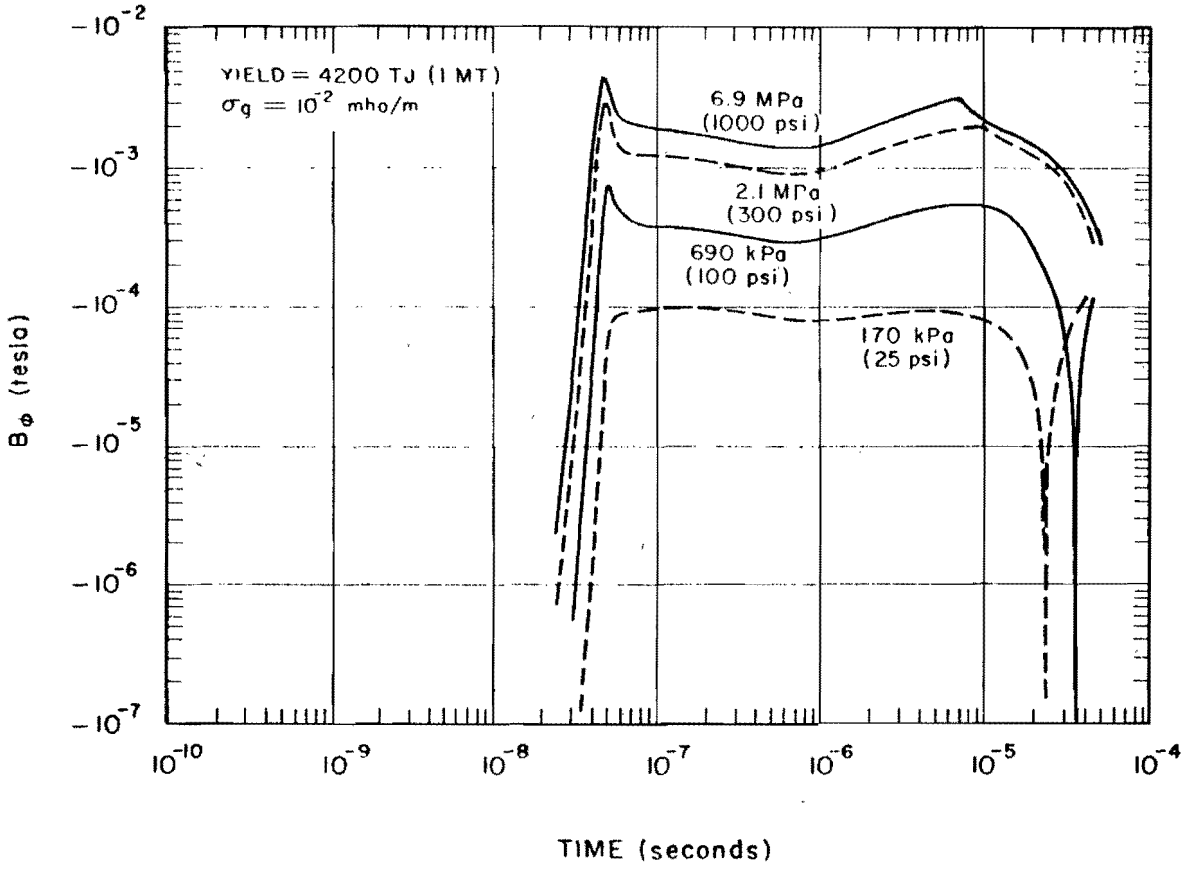

Figure 7-29 $B\varphi$ Time Waveform at the Air-Ground Interface for Several Pressure Levels

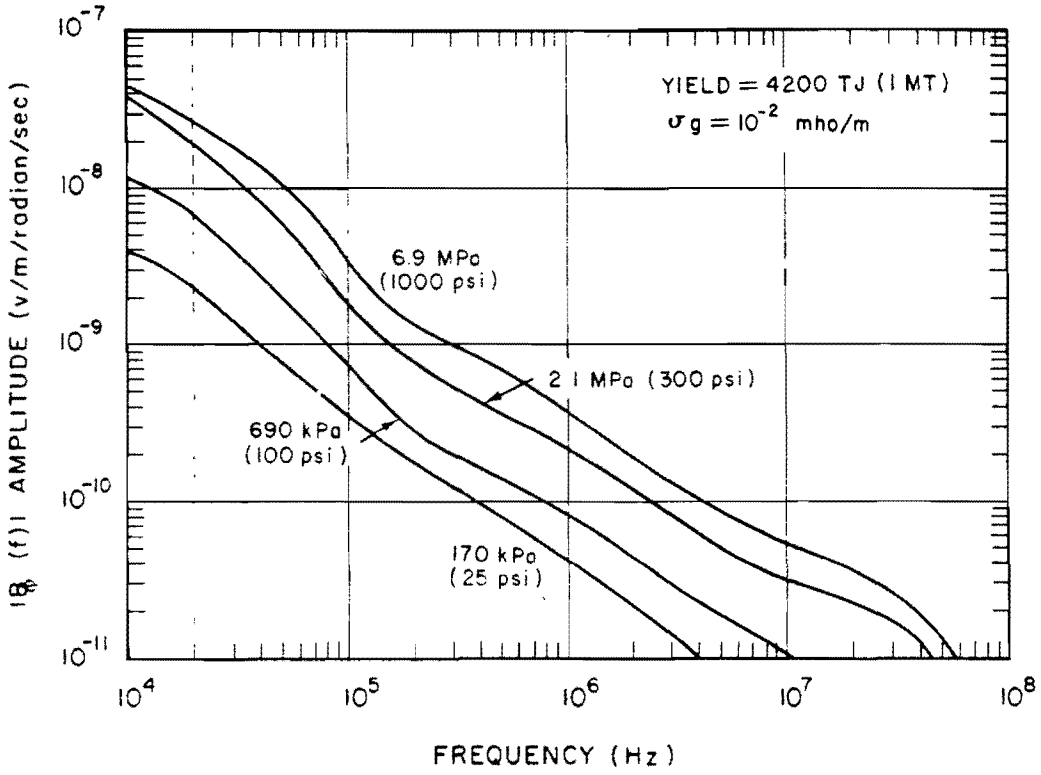

Figure 7-30 Fourier Amplitude of B_ϕ Waveform of Figure 7-29

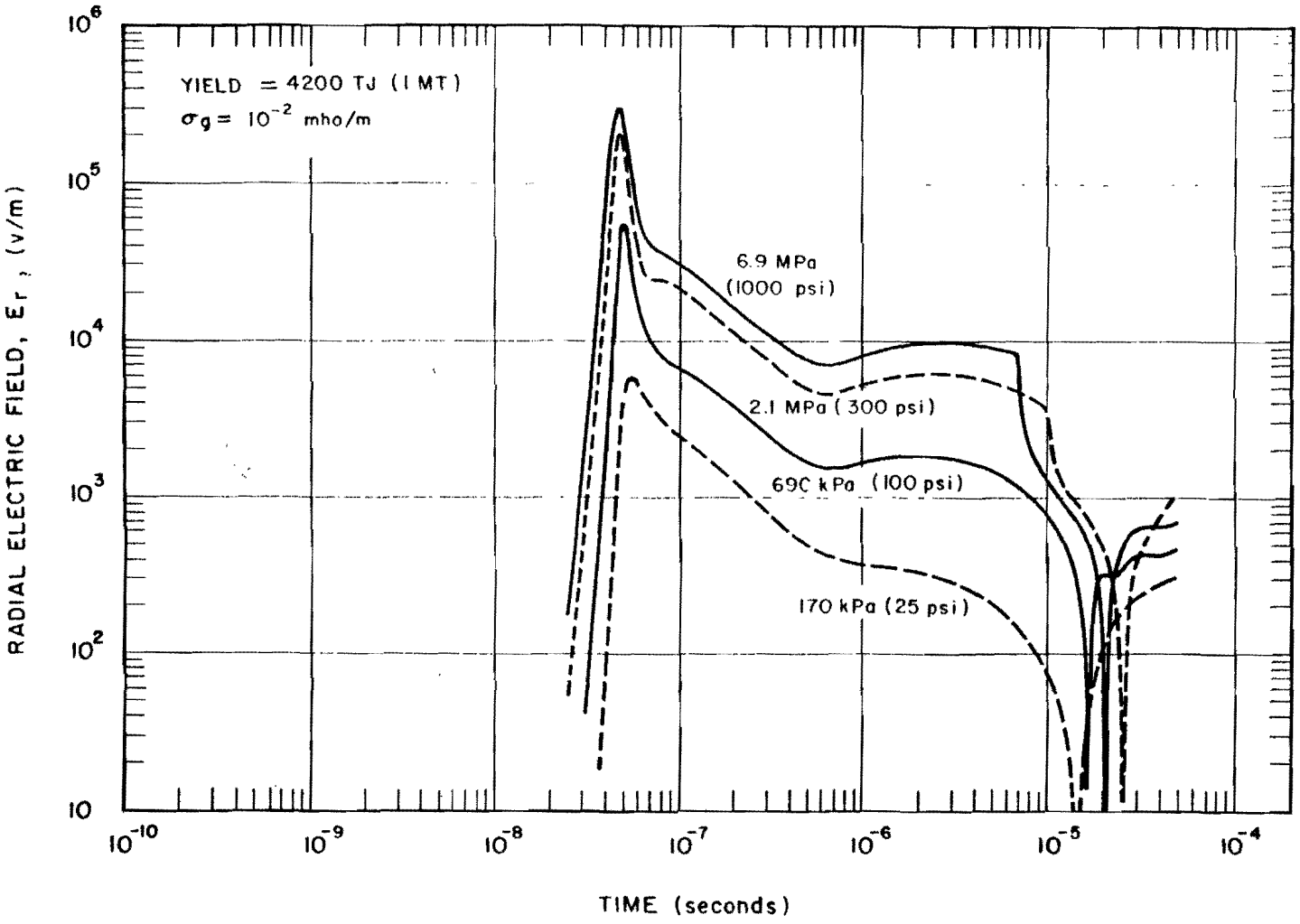

Figure 7-31 [redacted] E_r Time Waveform at the Air-Ground Interface for Several Pressure Levels, $\sigma_g = 10^{-2}$ mho/m [redacted]

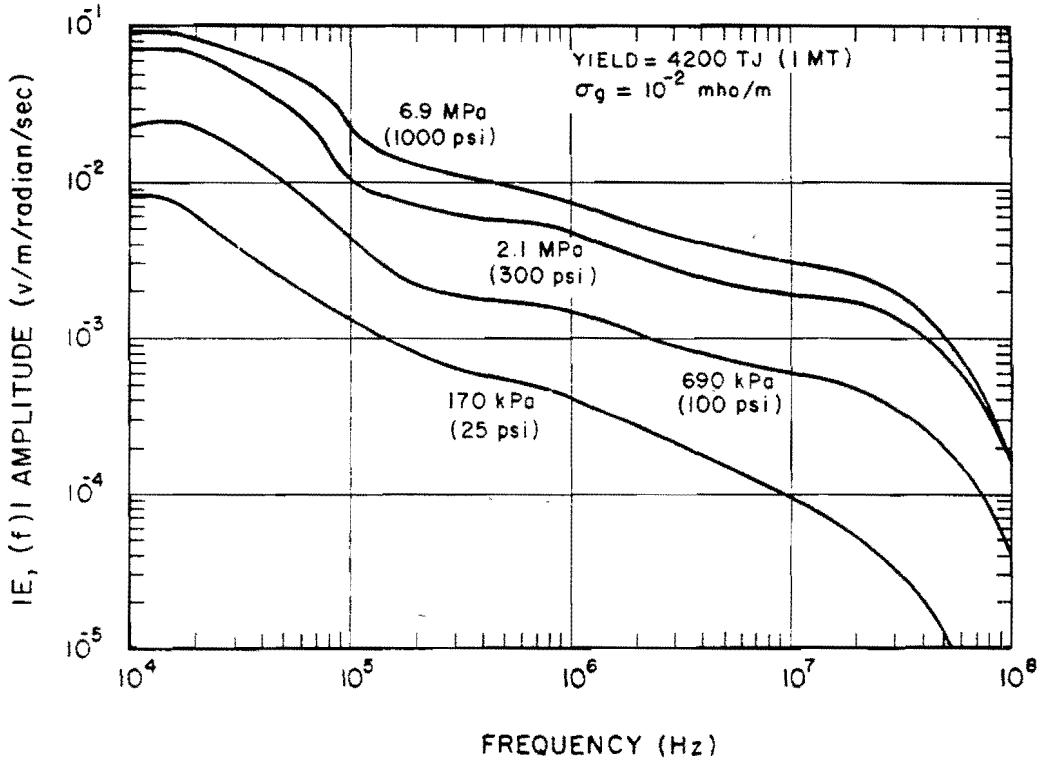

Figure 7-32 Fourier Amplitude of E_r Waveform of Figure 7-31

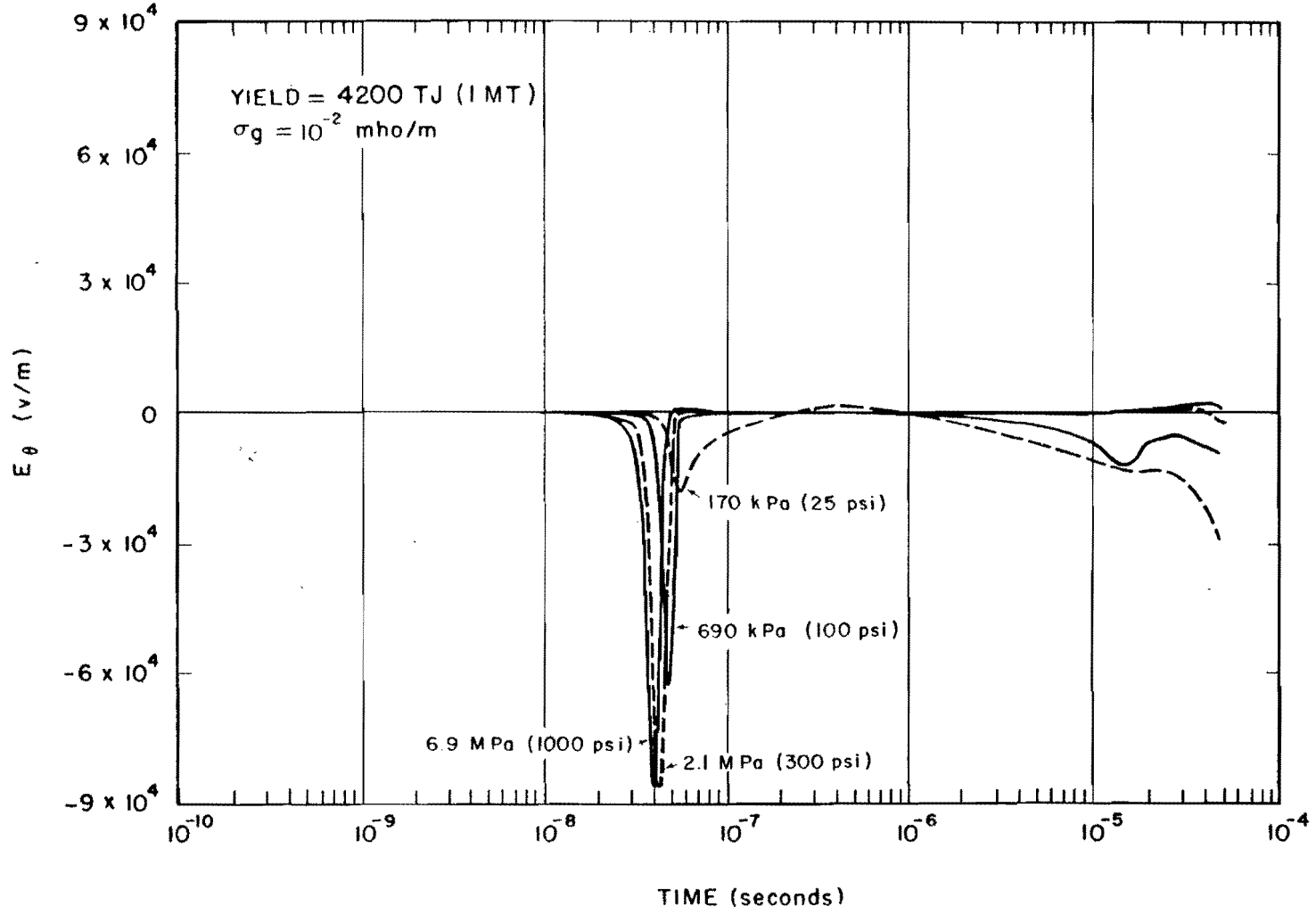

Figure 7-33 E_θ Time Waveform at the Air-Ground Interface for Several Pressure Levels, $\sigma_g = 10^{-2}$ mho/m

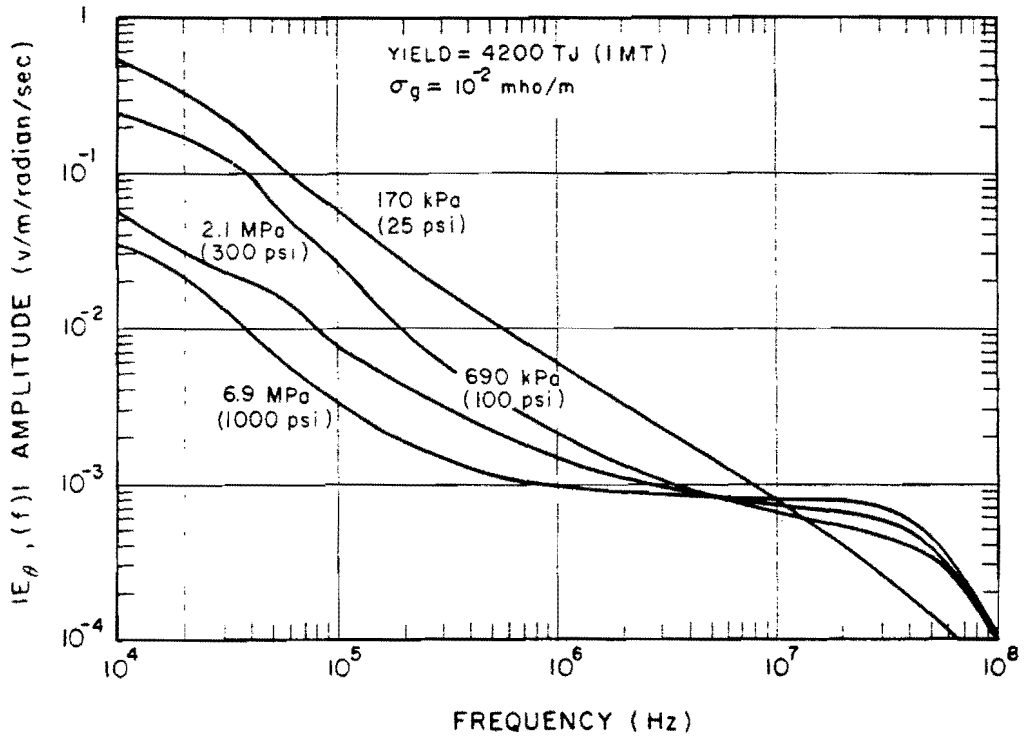

Figure 7-34 Fourier Amplitude of E_θ Waveform of Figure 7-33

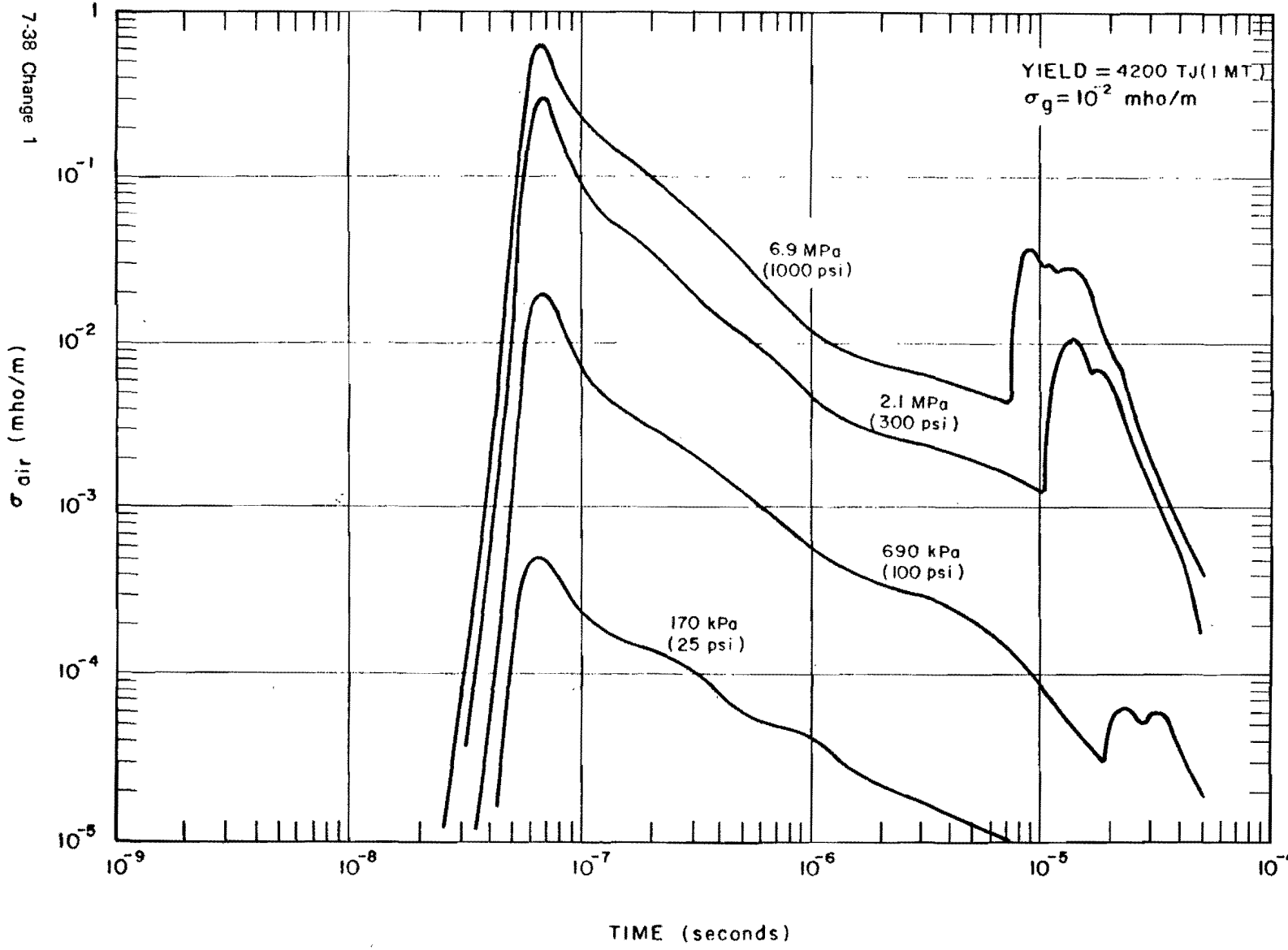

Figure 7-35 Air Conductivity Time Waveforms at the Air-Ground Interface for Several Pressure Levels, $\sigma_g = 10^{-2}$ mho/m

[redacted]

[redacted]

the conditions, and that the very many combinations possible in the conditions preclude concise generalizations to cover every situation. Strictly speaking, a system imbedded in the deposition region must be included as part of the environment itself in formulating the problem. This limitation should be kept in mind while examining the figures described.

[redacted]

[redacted]

[redacted] BIBLIOGRAPHY [redacted]

DNA EMP (Electromagnetic Pulse) Handbook [redacted] DNA 2114H-1, DNA 2114H-2, DNA 2114H-3, DNA 2114H-4, Defense Nuclear Agency, Washington, D.C., August 1976. (I, II, IV – [redacted] III – [redacted]

EMP Simulator Study [redacted] DASA 2049, DASIAC SR-92, DASIAC, Santa Barbara, California, May 1968 [redacted]

Glasstone, S. and P. J. Dolan, eds., *The Effects of Nuclear Weapons*, Third Edition, U.S. Department of Defense and U.S. Department of Energy, December 1977 [redacted]

Jordan, T. M., et al., *Prediction of Internal Electromagnetic Pulse* [redacted] DNA 2966D, Defense Nuclear Agency, Washington, D.C., August 1972 [redacted]

Longmire, C. L., *Ground Fields and Cable Currents Produced by Electromagnetic Pulse from a Surface Nuclear Burst* [redacted] DASA 1913, DASIAC SR-54, DASIAC, Santa Barbara, California, March 1968 [redacted]

Proceedings, DASA EMP Technical Conference – 1969 [redacted] DASA 2280, DASIAC SR-91, DASIAC, Santa Barbara, California, March 1969 [redacted]

Schlegel, G. K., M. A. Messier and W. A. Radasky, (edited by W. C. Hart), *Electromagnetic Pulse Environment Handbook* [redacted] AFWL EMP PHENOMENOLOGY 1-1, Air Force Weapons Laboratory, Albuquerque, N.M., January 1972 [redacted]

Tompkins, J. E., and J. A. Rosado, *Internal Electromagnetic Pulse: Electric and Magnetic Fields in Complex Enclosures* [redacted] HDL-TR-1500, Harry Diamond Laboratories, Washington, D.C., June 1970 [redacted]

[redacted]

DTIC FILE COPY

DTIC ELECTE 2 MAR 1989 S D E

Chapter 8

PHENOMENA AFFECTING ELECTROMAGNETIC PROPAGATION[1]

AD-A955 392

INTRODUCTION

The two principal phenomena caused by a nuclear detonation that affect electromagnetic propagation are electromagnetic emissions and ionization of the atmosphere. The short duration electromagnetic pulse described in Chapter 7 is in the first category. Also included in this first category are continuing thermal radiation and emissions from various chemical reactions within the atmosphere. These radiations and emissions produce noise throughout the radio and optical spectra. The second phenomenon, atmospheric ionization, involves alterations of the electrical properties of the atmosphere that can affect the propagation of electromagnetic waves. Both types of effects are caused by energy radiated from the nuclear explosion, from the subsequent fireball, and from the radioactive debris. The severity of the effects on the propagation of electromagnetic waves may vary from being completely negligible to intolerable degradation of system performance.

For the purpose of discussing the effects on propagation, the electromagnetic spectrum is divided into two frequency bands: the radio band, which includes radar applications, and the optical band, as shown in Figure 8-1. The most important effects in the radio band usually are those that affect the propagation of the desired electromagnetic signal (effects that change the amplitude, phase, direction, etc.). Electromagnetic radiations from the fireball and other regions can interfere with desired signals, and in some cases, interference from other sources (e.g., atmospheric noise) will be enhanced or diminished. The most important effect in the optical band is radiation from the fireball and other regions that interferes with desired signals. The source of this radiation is described in Chapter 3.

The current state of knowledge concerning the effects of nuclear detonations on electromagnetic wave propagation stems from full scale tests, laboratory experiments, theoretical studies, and simulation with certain atmospheric phenomena. Meaningful testing of high-altitude nuclear weapon effects requires a sophisticated space capability (e.g., instrumented rocket probes), and only a relatively few high-altitudes tests were performed prior to the test moratorium in 1962.

While those tests provided information to develop models to calculate the various phenomena, considerable uncertainty exists in scaling to burst or atmospheric conditions that are much different from those of the tests. All of the high-altitude tests have been single bursts. Significant differences are expected when two or more nuclear detonations occur near one another in time and space.

Detailed theoretical descriptions for most burst phenomena are highly complex and require specification of poorly known parameters for quantitative results. Laboratory measurements have been used to obtain estimates of some parameters, but usually the results have to be scaled to conditions much different than those

[1] Although the English system of units for measuring distance is given priority throughout most chapters of this manual, wavelengths and other dimensions dealing with electromagnetic wave propagation usually are given in the metric system. Therefore, in this chapter and in Chapter 17, the metric system is used for distance dimensions. Conversion factors from the metric system to the English system are provided in Appendix B.

This document has been approved for public release and sale; its distribution is unlimited.

'89 3 02 041

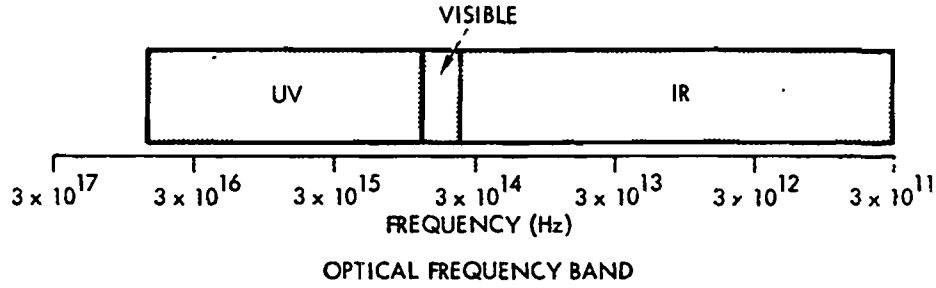

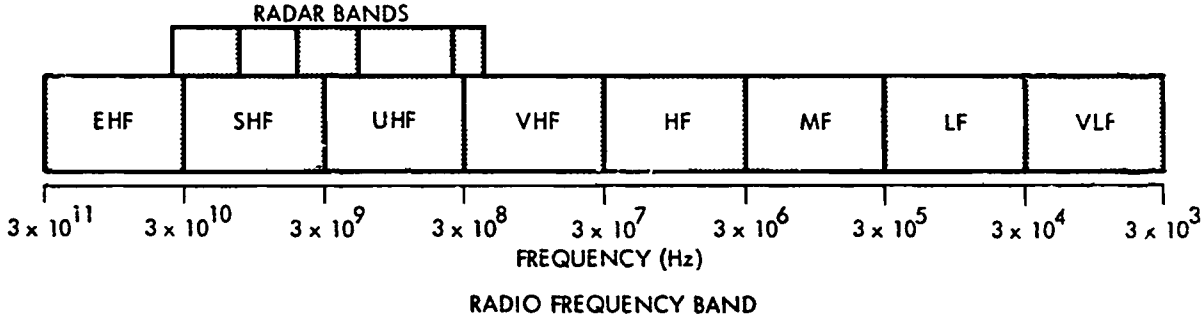

Figure 8-1. Optical and Radio Frequency Bands

used in the measurements. Some understanding of electromagnetic propagation in disturbed environments has been obtained from propagation measurements during eclipses, solar flares, and auroral disturbances. However, natural phenomena often involve the superposition of different phenomena than those brought about by nuclear bursts, and extrapolation to burst conditions can be misleading.

SECTION 1
PHENOMENA AFFECTING RADIO FREQUENCIES

The number of free electrons in the atmosphere is increased greatly by weapon radiations from high altitude bursts. These free electrons can absorb energy from electromagnetic waves and can change the phase velocity of the waves (changing the direction of propagation and signal characteristics). Electromagnetic radiations from heated regions and from trapped electrons are a source of noise.

IONIZATION AND DEIONIZATION

Most of the energy of a nuclear detonation is emitted in forms that can produce ionization.[2] Some of this energy is in particulate matter (neutrons, beta particles, and high-speed debris that originally constituted the warhead and adjacent structure), and some is in photons (thermal radiation from the weapon case and gamma rays). Between 90 and 95 percent of the energy is emitted promptly (within a microsecond); about 5 to 10 percent is delayed radiation from the radioactive decay of fission debris.

[2]The ionization process is described in paragraph 6-4, Chapter 6.

QUALITY INSPECTED 4
UNANNOUNCED
By
Distribution/
Availability Codes
Dist | Avail and/or Special

[redacted]

[redacted] If a nuclear explosion occurred in a vacuum with no magnetic field, the flux of radiated energy would decrease as the square of the distance traveled. In the atmosphere, collisions and scattering processes absorb energy and produce ionization and excitation. (See Chapters 3, 4, and 5 for discussion of atmospheric absorption of photons, neutrons, and beta particles.)

[redacted] Radiation entering the atmosphere from above is absorbed rapidly when it reaches the altitude, termed the stopping altitude, where the mean-free path equals one scale height (an altitude region over which the atmospheric density changes by a factor of e (approximately 2.7). Stopping altitudes for the principal radiations from a nuclear weapon are shown in Table 8-1.

Table 8-1 [redacted] Approximate Stopping Altitudes for Principal Weapon Outputs Causing Ionization [redacted]

Weapon Output	Stopping Altitude (km)
Prompt Radiation	
x-rays (1 kev radiator)	80
Neutrons	25
Gamma rays	25
Debris (kinetic energy)	115
Delayed Radiation	
Gamma rays	25
Beta particles (1 Mev)	60

[redacted] For detonations below the stopping altitude of a particular radiation, most of that radiation will be contained locally. When detonations occur above the stopping altitude of a particular radiation, that radiation can spread large distances before being deposited and causing ionization. About 3×10^4 ion pairs are produced for each 1 Mev of energy deposited in the atmosphere. Since about 3×10^{28} Mev are released per megaton of weapon yield, even a small fraction of the weapon output can cause large electron densities. The lifetime for many of the electrons produced is short, however, and it depends critically on the altitude at which they are produced.

[redacted] Electrons and ions produced by the ionization sources undergo various atmospheric reactions that change their number density. Four principal reactions must be considered:

1. Attachment. Electrons can attach to neutral air particles (primarily to oxygen molecules and/or atoms) to form negative ions.
2. Detachment. Once attached, electrons can be detached from negative ions by collisions, solar radiation, or radiation from the fireball.
3. Recombination. Electrons and positive ions can recombine to form neutral particles.
4. Mutual Neutralization. Positive ions can combine with negative ions formed by attachment, to produce neutral particles.

[redacted] The rate at which these reactions proceed is a strong function of altitude. Thus, the altitude distribution of electron density after a period of time generally will not coincide with the altitude distribution immediately after the deposition of weapon energy. Detailed solutions of the time history of electron density require consideration of a large number of atmospheric species. Many reaction-rate coefficients are not well known, even for the natural atmosphere. The uncertainties in these coefficients provide a significant source of uncertainty in the prediction of electron density time history. In the natural atmosphere above about 70 km, where neutral particle density is low, recombination accounts for the major electron loss. At lower altitudes, attachment becomes increasingly important in the removal of free electrons, particularly at night

[redacted]

[redacted]

when there is no photodetachment of electrons from negative ions by sunlight.

In heated or highly ionized regions, the air chemistry (interaction between species) is modified, and electron loss processes are changed. The expansion of heated regions also reduces the electron density.

In discussing electron density caused by nuclear weapons, it is convenient and useful to consider the electron density resulting from prompt radiation and delayed radiation separately. Also, since ionization and deionization processes are significantly different inside and outside the fireball, these regions will be discussed separately. Although electrons are the principal cause of effects on electromagnetic propagation, ions can affect propagation in the VLF and LF bands (frequencies below a few hundred kilohertz).

8-1 Electron Density Within the Fireball

Initially the incandescent region termed the fireball is highly ionized. For detonations below about 60 km, thermal ionization of air and debris from the weapon and carrier maintains high electron densities until the fireball cools below about 2500°K. For cooler fireballs, beta particles deposited within the fireball may be a significant ionization source. Predictions of electron density within the fireball require knowledge of the distribution of temperature and debris within the fireball, the shape of the fireball as a function of time, and the detailed chemistry of heated regions.

Detailed calculations, which have been performed for a few burst conditions, are imprecise, particularly with regard to inhomogeneities and gradients in fireball properties. However, for many cases, relatively simple fireball models in which the mass density and temperature are assumed uniform within the fireball can be used. Figures 8–2 and 8–3 show calculated values of average fireball electron density and temperature following 1-Mt detonations at altitudes of 25 and 50 km, respectively. The calculations contained the assumption that the fireball gas was in thermal equilibrium, as well as being homogeneous.

When detonations occur above about 60 km, losses of free electrons within the fireball are slower and the electron density does not decay rapidly enough to remain in equilibrium with the cooling fireball. Volume expansion controls the decline of electron density during the first few tens of seconds following detonation. Later, recombination of electrons with positive atomic ions predominates.

For detonations at altitudes above about 80 km, the geomagnetic field influences the fireball expansion and location. After a few tens of seconds, magnetic forces cause the expansion across the magnetic field to become slower, while expansion along the magnetic field continues. Thus, the fireball becomes elongated along the magnetic field in a roughly cylindrical or tube shape. Figures 8–4 and 8–5 show calculations of average fireball electron density and temperature following 1-Mt detonations at altitudes of 75 and 150 km, respectively.

Photographs of fireballs affected by the magnetic field show many field-aligned striations within the fireball (see Figure 1–4C). The optical striations also indicate large variations of electron density within the fireball. The size of the striations and the variation of electron density from the average value cannot be scaled accurately with burst parameters at present.

For detonations at altitudes above about 300 km, the mean-free path of both X-rays and debris particles is large, and localized fireballs may not form around the detonation point. However, debris particles initially directed downward may heat and ionize a region below the detonation point. This region, if sufficiently disturbed, is termed a fireball region. The formation of a fireball region depends on the detonation altitude, the weapon yield, and the atmospheric density

[redacted]

[redacted]

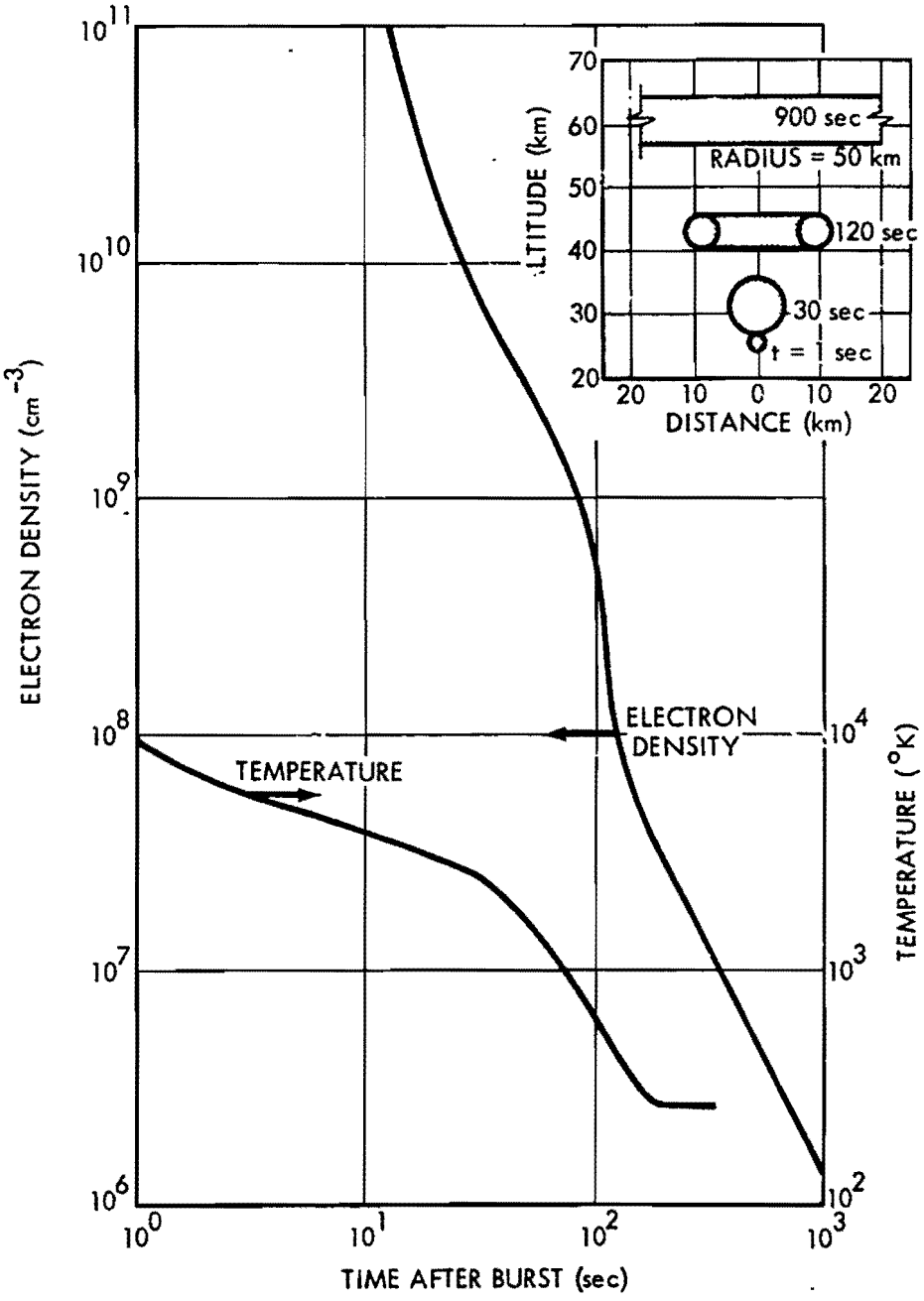

Figure 8-2. [redacted] Fireball Electron Density and Temperature, 1-Mt at 25 km [redacted]

[redacted]

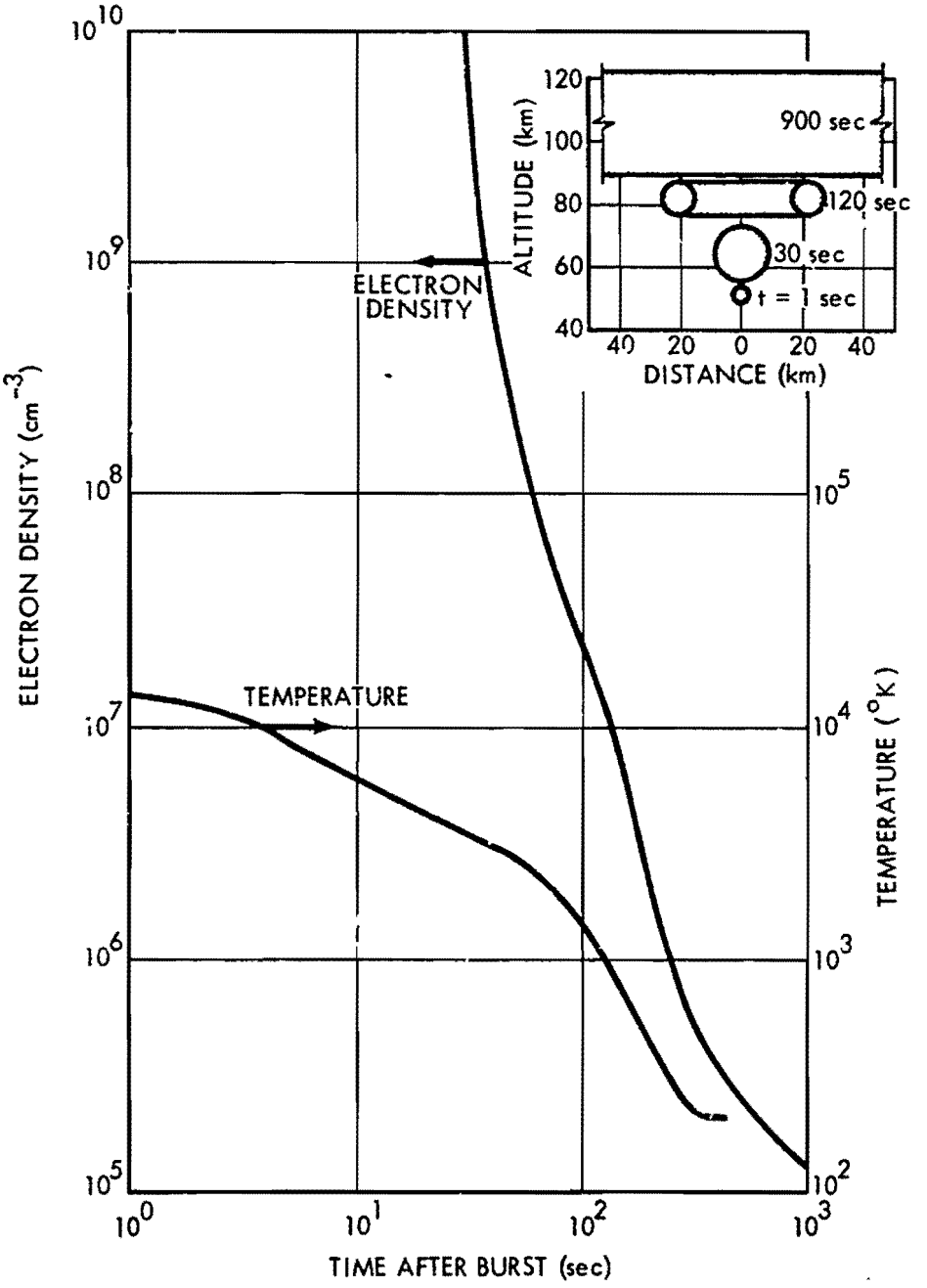

Figure 8-3. Fireball Electron Density and Temperature, 1-Mt at 50 km

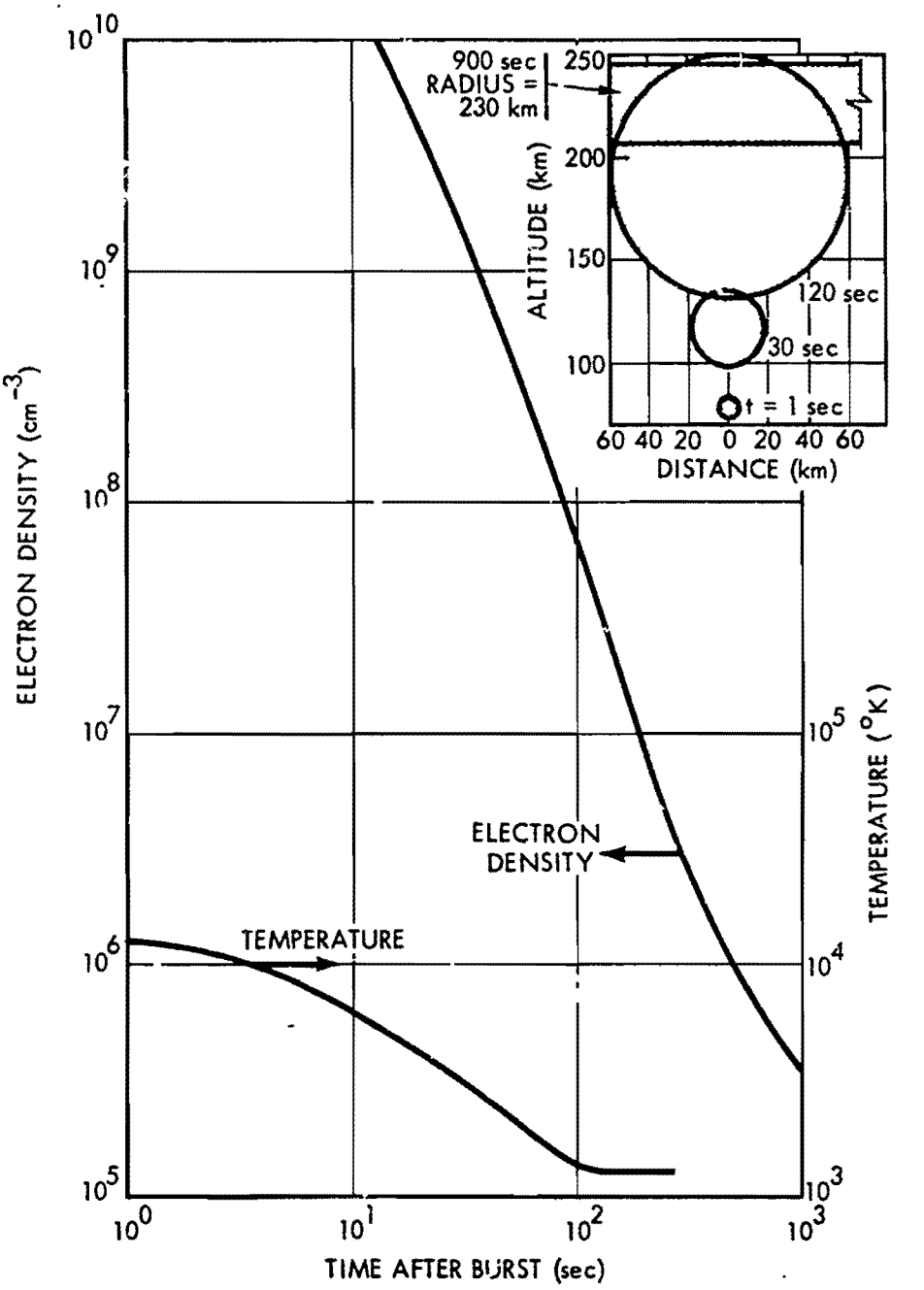

Figure 8-4. Fireball Electron Density and Temperature, 1-Mt at 75 km

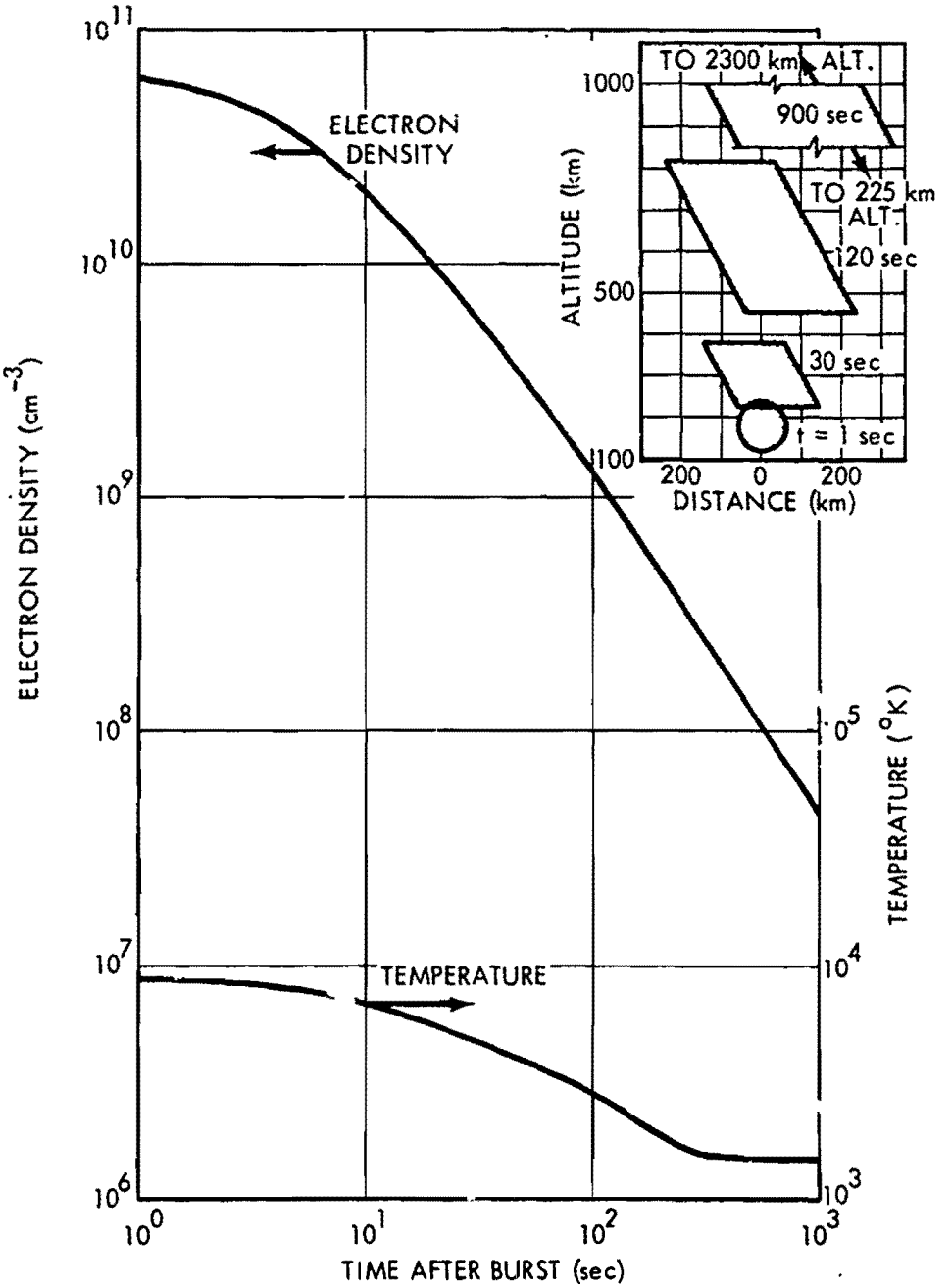

Figure 8-5. [redacted] Fireball Electron Density and Temperature, 1-Mt at 150 km [redacted]

at burst time. Figure 8–6 shows calculated values of electron density and temperature within the fireball following a 1-Mt detonation at an altitude of 400 km.

Only a few nuclear tests have been carried out by the U.S. at detonation altitudes above 80 km; therefore, theoretical calculations of fireball formation, size, location, and properties are dependent on parameters that are poorly known. Calculations of fireball properties for detonations at altitudes above 80 km should be considered illustrative of the general order of magnitude rather than as detailed quantitative results.

8-2 Electron Density Caused by Prompt Radiation Outside the Fireball

Ionization produced outside the fireball by prompt gamma rays can be neglected insofar as effects on radio propagation are concerned. For detonations at altitudes below about 25 km, both neutrons and X-rays are deposited within or close to the fireball, and the effects of prompt radiation outside the fireball are minimal. For detonation altitudes between 25 and about 80 km, X-rays are largely confined, but neutrons produce ionization over distances of several hundred kilometers. For higher altitude detonations, both X-rays and neutrons cause widespread ionization. Figure 8–7 shows the initial ionization caused by prompt radiation from a nominal megaton weapon detonated at 120 km. Because of earth's curvature, radiation reaching a given altitude at large horizontal distances from the source must pass through lower altitudes where it is strongly attenuated by the denser air.

The decay of electron and ion densities following the ionization impulse depends on electron and ion loss rates, which are functions of altitude and time of day. Below about 100 km, the electron and ion density after 1 second will be essentially independent of the initial ionization if the initial ion pair density is greater than 10^7 ion pairs cm^{-3}. This condition is termed saturation; larger initial ionization will not increase the electron or ion density remaining after 1 second. Figure 8–7 shows that the initial ion-pair density below 100 km exceeds 10^7 ion pairs cm^{-3} out to about 500 km from the burst.

Figure 8–8 shows the altitude dependence of the electron density for several times after a saturation impulse. At night the electron concentration decays rapidly, particularly at low altitudes where attachment of electrons to neutral particles is the predominant reaction. During the day, electron densities greater than normal can persist for tens of minutes. The insert in Figure 8–8 illustrates the horizontal extent of the region that can be saturated by prompt radiation as a function of detonation altitude. The decay of electron and ion densities above 100 km depends on processes that may be affected by atmospheric chemistry changes caused by the deposition of prompt radiation. Because of the additional complications introduced at those altitudes, a simple representation of the decay is not possible.

Many of the neutrons produced by the explosion will travel upward and will escape the atmosphere. Since neutrons are not affected by the geomagnetic field, they will spread isotropically over a large area. Each neutron eventually disintegrates spontaneously into a proton, a neutrino, and a beta particle (half-life for disintegration is about 12 minutes). Since the beta particle (a high-energy electron) is charged, it can move only in the direction of the geomagnetic field (motion normal to the magnetic field direction causes the beta particle to spiral around the magnetic field lines). The beta particles are guided by the geomagnetic field until reaching altitudes near the beta-particle stopping altitude (see paragraph 8-4 and Figure 8–10), where they deposit their energy to produce ionization. The amount of ionization caused by neutron-decay beta particles is small, but it has been noted at distances of many thousands of kilometers from the burst point.

[redacted]

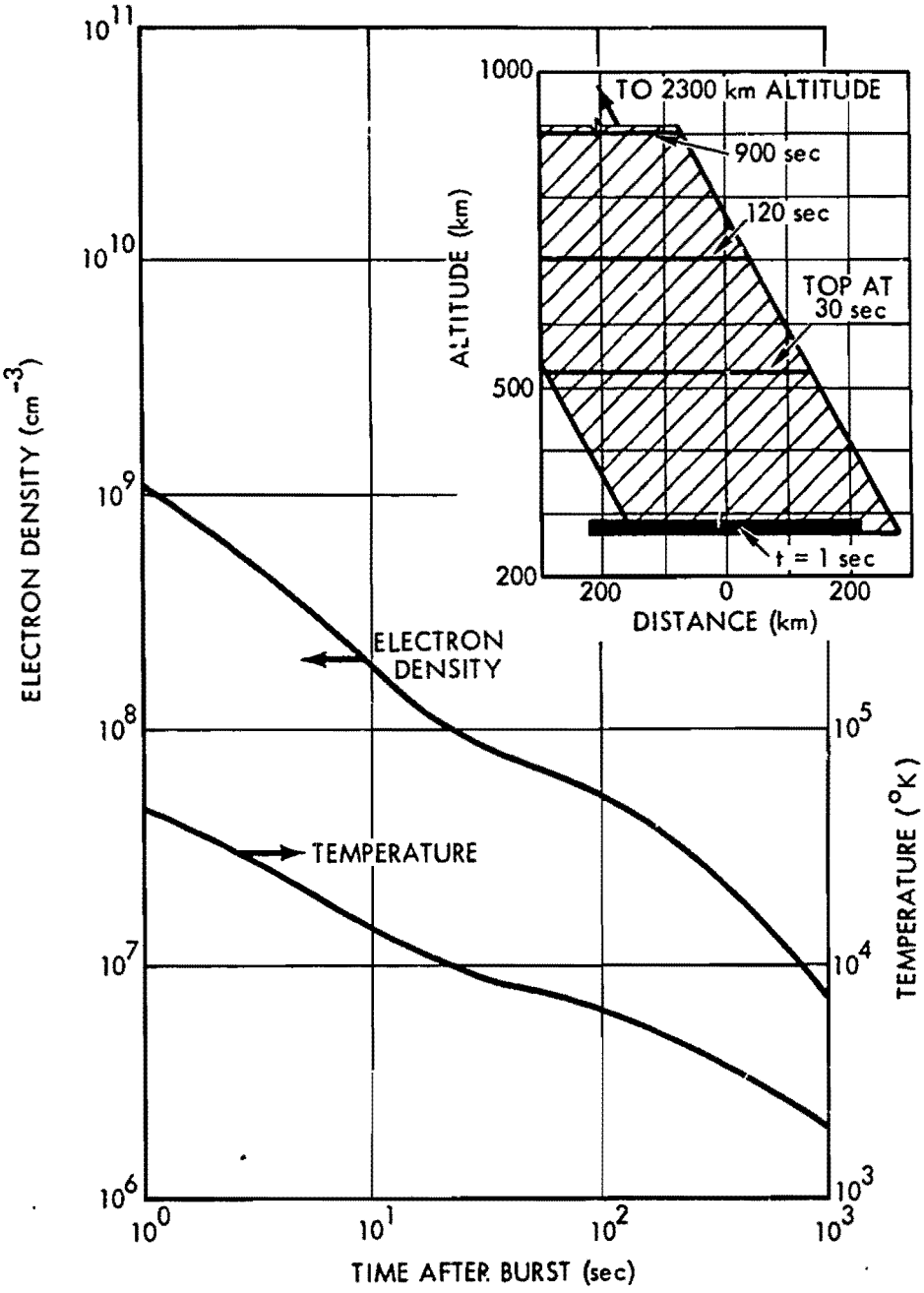

Figure 8-6. [redacted] Fireball Electron Density and Temperature, 1-Mt at 400 km [redacted]

[redacted]

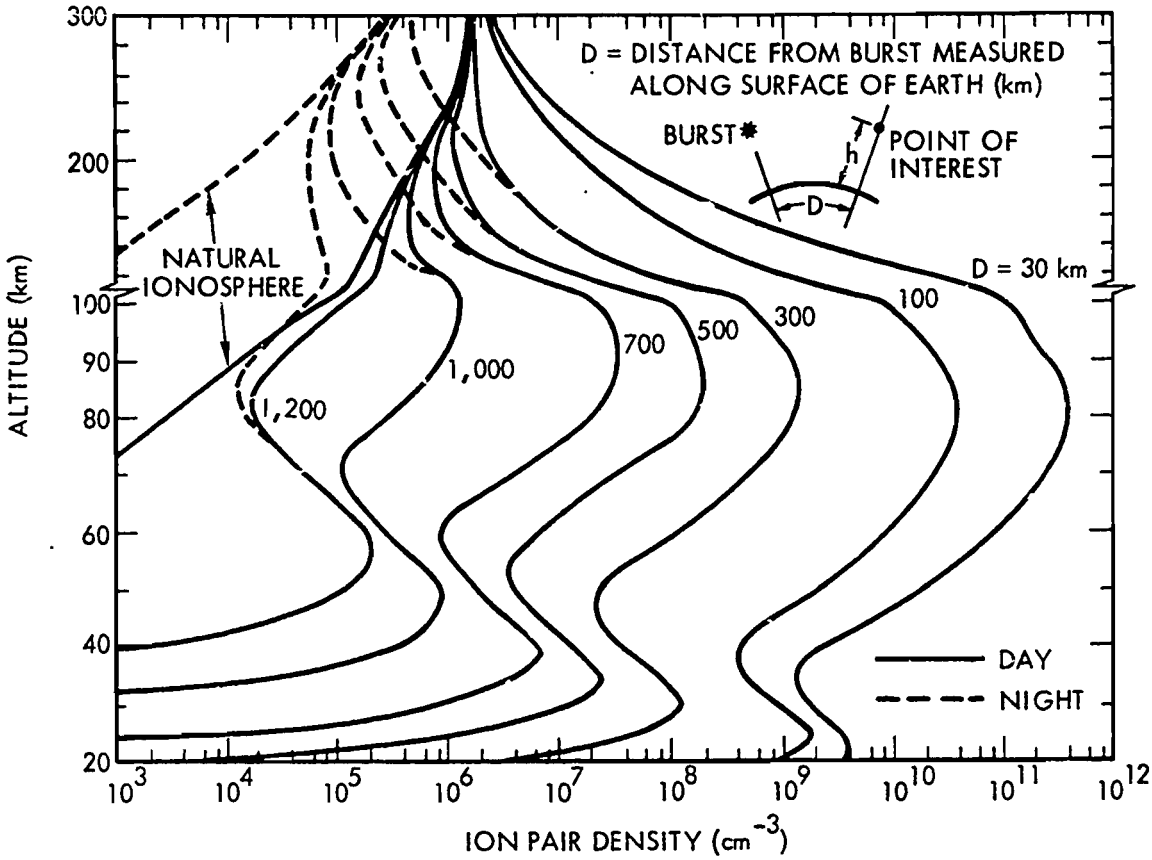

Figure 8-7. [redacted] Ion-Pair Density Due to Prompt Radiation from a 1-Mt Burst Detonated at 120 km, t = 0 [redacted]

8-3 Electron Density Caused by Delayed Gamma Radiation Outside the Fireball [redacted]

[redacted] In addition to prompt radiation, delayed gamma rays and beta particles (discussed in Section III, Chapter 5) are produced during the radioactive decay of the fission debris. This continuing radiation produces ionization characterized by a production rate of ion pairs per unit volume per unit time. For detonations below several hundred kilometers, the fission debris (assumed to be mixed with the total weapon debris) is initially within the fireball and is carried upward as the fireball rises and expands.

[redacted] When the debris is below the gamma-ray stopping altitude, gamma rays can only penetrate a short distance, and the ionized region that they produce around the fireball is small. If the debris rises above the gamma-ray stopping altitude, gamma rays produce ionization over larger distances. The resulting electron and ion densities are a function of both the ion-pair production rate and the electron and ion loss processes. Most of the gamma-ray energy is deposited near the stopping altitude, but the electrons produced below about 40 km are lost quickly by attachment. Maximum electron density usually occurs at higher altitudes where the electron lifetimes

[redacted]

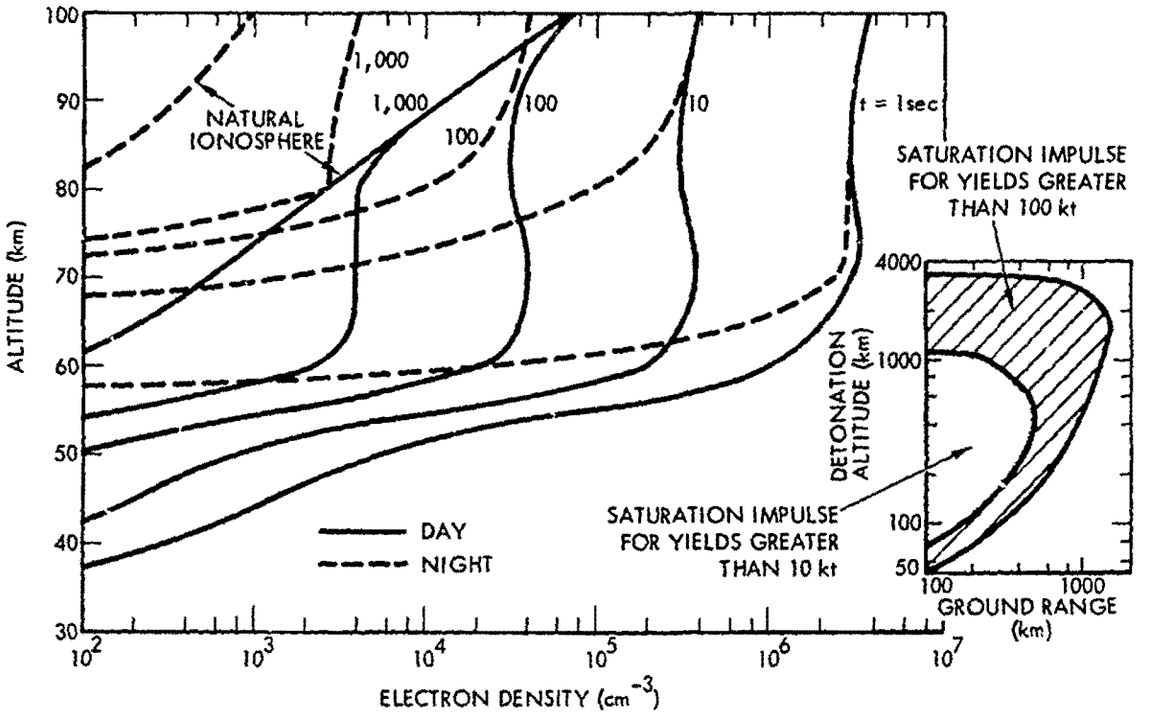

Figure 8-8. [redacted] D-Region Electron Density Caused by Prompt Radiation (Saturation) [redacted]

[redacted]

are longer. Near the debris region, where the gamma ray flux is large, substantial electron densities can be maintained even though the debris is at an altitude where free electrons are lost by attachment rapidly.

[redacted] When the fission debris and the point of interest are both well above the gamma-ray stopping altitude, the ion-pair production rate and electron and ion densities caused by gamma rays can be expressed conveniently in terms of a radiation intensity parameter, I_γ, defined by

$$I_\gamma = \frac{4 \times 10^{-7} W_F}{4\pi R^2 (1+t)^{1.2}} \text{ watts } m^{-2},$$

where

W_F = fission yield in megatons,

R = radial distance from debris center to point of interest in km,

t = time after detonation in seconds.

Figure 8-9 shows quasi-equilibrium electron densities for particular values of I_γ. The values are called quasi-equilibrium because they are the values that would be reached if the production rate remained constant and if sufficient time were allowed for equilibrium conditions to be reached. In an actual situation, the production rate changes with time because of the radioactive decay of the fission debris and the changing geometry as the debris moves. However, for most cases, the time to reach equilibrium is short, and the quasi-equilibrium values are close approximations to the electron densities. The insert in Figure 8-9 illustrates the horizontal extent as a function of

[redacted]

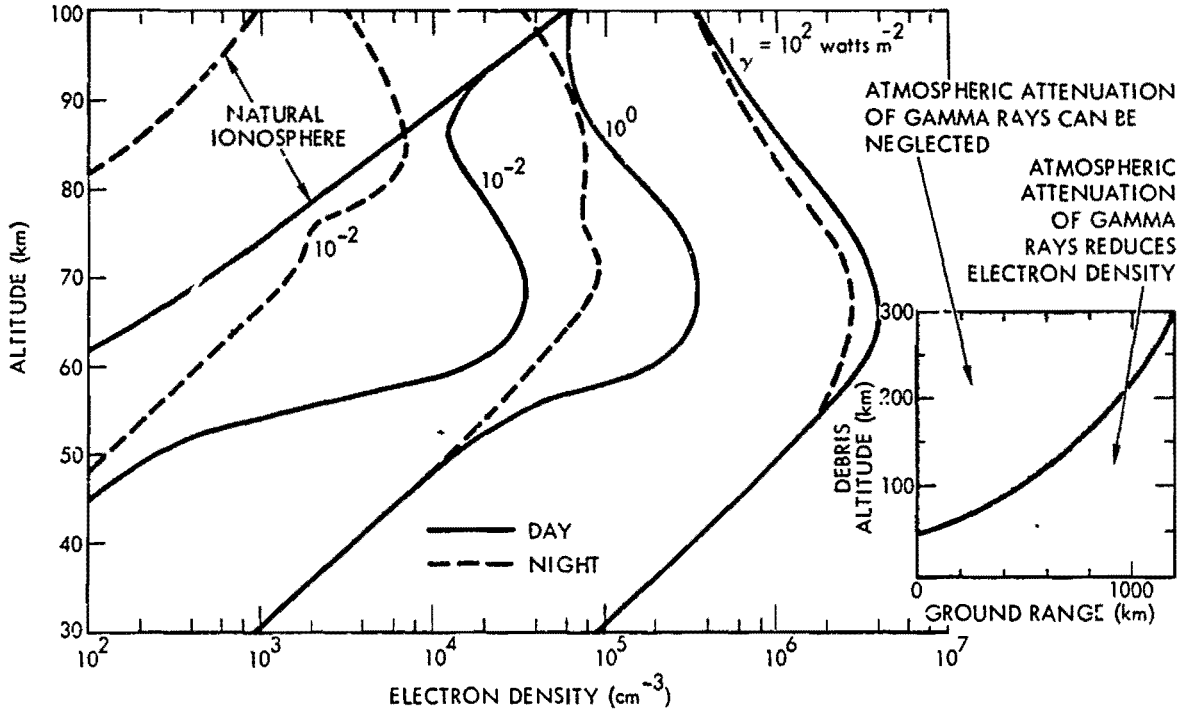

Figure 8-9. Quasi-Equilibrium Electron Density Due to Gamma Rays

debris altitude for which the electron densities are applicable.

Most delayed gamma rays deposit their energy in the atmosphere by first producing high-energy electrons (Compton electrons). Compton electrons travel very short distances in the lower atmosphere; however, some Compton electrons produced above about 60 km can escape to the conjugate region, as described for beta particles in paragraph 8-4. Ionization in the conjugate region caused by Compton electrons is of interest primarily for studies of propagation in and below the HF band (frequencies below 30 megahertz).

8-4 Electron Density Caused by Beta Particles Outside the Fireball

Since beta particles are electrically charged, their motion in the atmosphere is affected by the geomagnetic field. When the fission debris is above the beta-particle stopping altitude, about half of the betas will travel down the geomagnetic field lines, producing ionization (similar to auroral ionization at high latitudes) until they are deposited near the stopping altitude. The other half of the betas (those emitted upward) will follow the geomagnetic field lines across the geomagnetic equator and will produce ionization at the geomagnetic conjugate.[3]

Figure 8-10 illustrates the location of the beta-particle ionization regions. Because of the slope (dip angle) of the magnetic field lines, the beta-particle ionization region is offset from the debris. When the geomagnetic field is undisturbed by the detonation, the location of the

[3] As used herein, geomagnetic conjugate points are points at the north and south ends of a geomagnetic field line that are at corresponding altitudes.

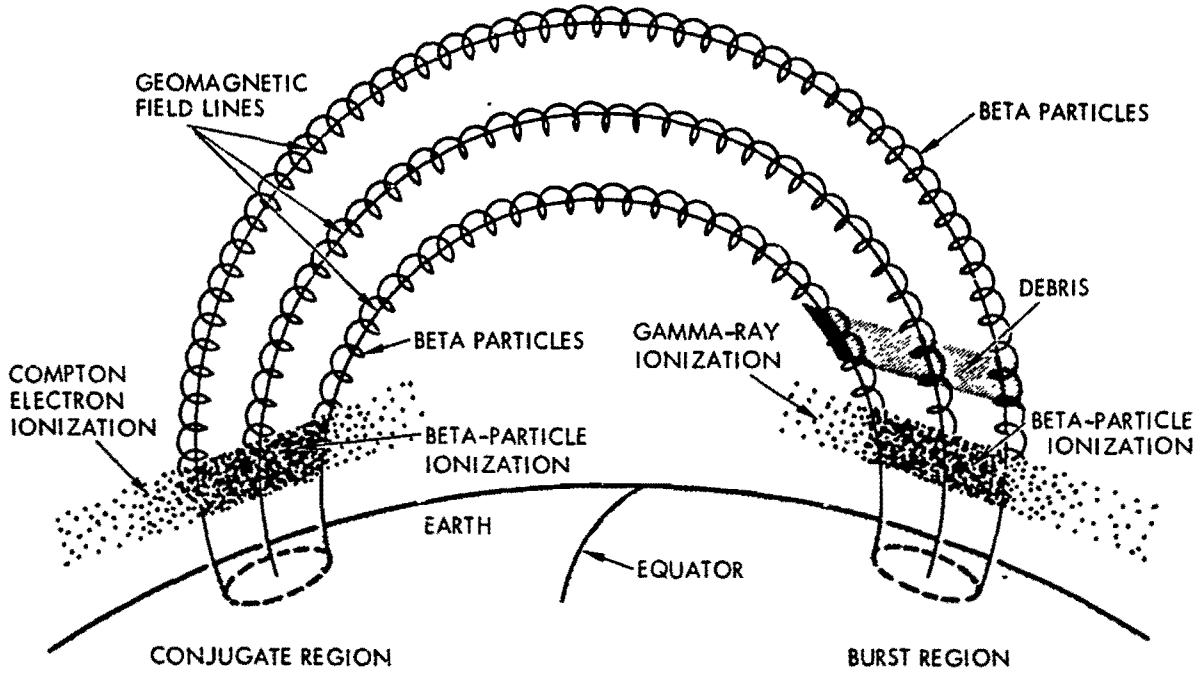

Figure 8-10. Location of Delayed Ionization Regions

beta-particle ionization region can be determined from a knowledge of the size and location of the debris region and the geomagnetic field lines. However, the geomagnetic field can be severely distorted for tens of seconds after a nuclear detonation. Determination of the magnetic dip angle and location of the conjugate point for undisturbed magnetic-field conditions are discussed in Problems 8-8 and 8-9.

The location of the gamma-ray ionization region and the region ionized by Compton electrons escaping to the conjugate region are also illustrated in Figure 8-10.

The ion-pair production rate and electron density caused by beta particles can be expressed conveniently in terms of a radiation intensity parameter, N_β, defined by:

$$N_\beta = \frac{8.8 \times 10^{15} W_F}{A(1+t)^{1.2}} \ betas \ cm^{-2} sec^{-1}, \quad (8.1)$$

where

A = area covered by fission debris in square kilometers.

Figure 8-11 shows the quasi-equilibrium electron density caused by beta particles for particular values of N_β. These curves apply if the fission debris is well above the beta stopping altitude and if the debris is uniformly distributed over the area A.

8-5 Electromagnetic Propagation in Ionized Regions

An electromagnetic wave propagating through an ionized region does work on charged particles in the region and transfers a portion of the wave energy to charged-particle kinetic energy. The electric field exerts a force on all charged particles; however ions, because of their larger mass, absorb less energy than electrons and can usually be neglected (an exception is wave

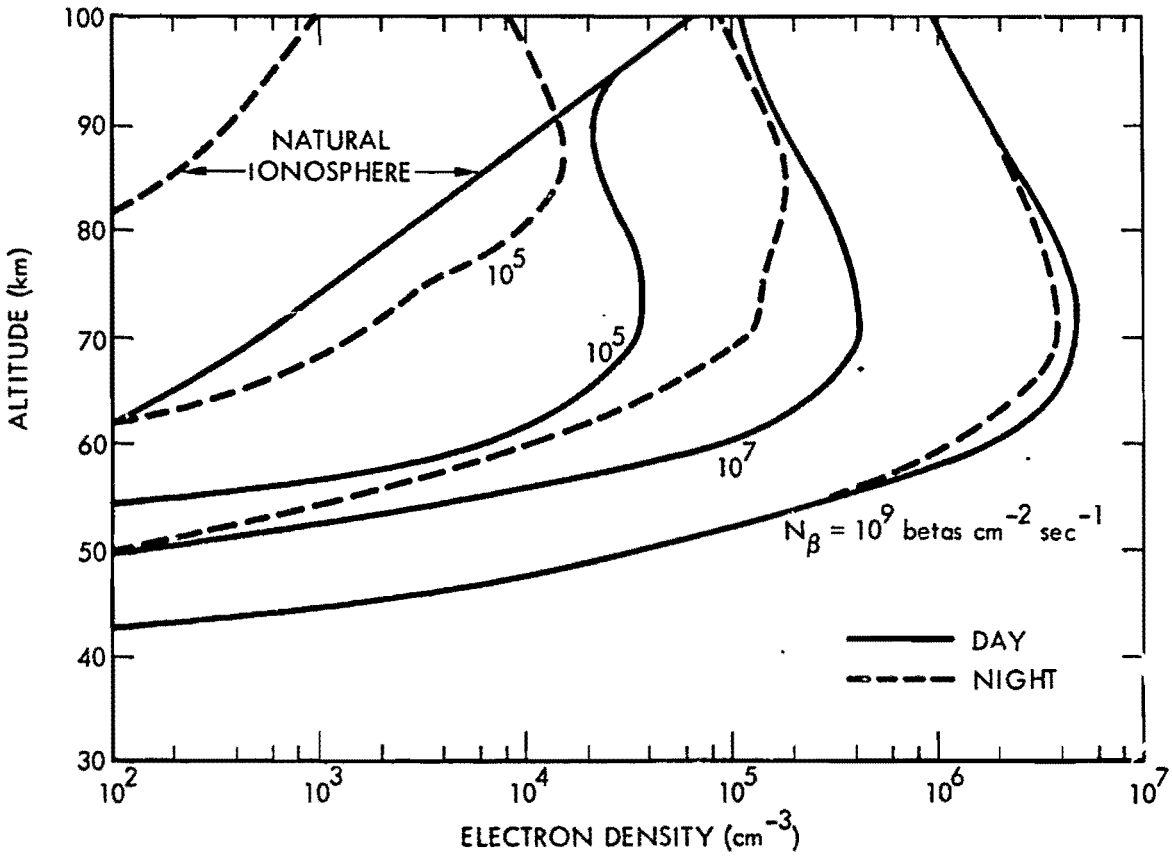

Figure 8-11. [redacted] Quasi-Equilibrium Electron Density Due to Beta Particles, Debris Altitude Greater than 60 km [redacted]

[redacted]

propagation at frequencies below a few hundred kilohertz). If the electrons do not collide with other particles, the energy is returned to the propagating wave without loss, but the phase of the wave is modified. Unless the geomagnetic field is parallel to the electric field of the propagating wave, some of the energy returned to the wave will have an electric field that is perpendicular to the incident electric field. The propagation wave then can be described as the sum of two plane waves termed the ordinary and the extraordinary waves—which have different phase velocities. One effect is to change the polarization of the propagation wave as it travels through the ionized medium. Electron collisions with other particles change the ordered motion of electrons into random motion (heat), and energy is absorbed from the wave. For many cases of interest, detonation-produced absorption is the overriding effect on electromagnetic propagation and it is the effect that is understood best.

[redacted] TRAVELING DISTURBANCES IN E AND F REGIONS OF IONOSPHERE [redacted]

[redacted] The preceding paragraphs discuss ionization sources from a nuclear explosion that add to the free electron content of the atmosphere. Following Teak and Orange (megaton

[redacted]

[redacted]

detonations at altitudes of 76 and 43 kilometers, respectively: 1958 test series) and again during Operation Fish Bowl (1962 test series), the normal E-region and F-region electron content appeared to be disturbed by hydrodynamic or hydromagnetic waves created by the detonation (the E-region includes the volume from 90 to 160 kilometers altitude, and the F-region begins at about 160 kilometers).

DNA (b)(3)

[redacted]

DNA (b)(5)

[redacted] ELECTROMAGNETIC RADIATIONS [redacted]

[redacted] A heated region emits thermal radiation according to its temperature and emissivity. The emissivity at a given frequency approaches unity as the absorption becomes large (10 decibels or more). The fireball may remain hotter than several thousand degrees Kelvin for about a hundred seconds. It may be sufficiently emissive for frequencies less than a few gigahertz that systems with antennas pointing at the fireball would register antenna temperatures equal to the fireball temperature if there were no intervening absorption outside the fireball. Generally, absorption caused by prompt and delayed radiation outside the fireball will reduce the escaping thermal radiation. The effective antenna noise temperature will depend on the size of the fireball relative to the antenna beam width, the location of the fireball relative to the antenna beam, and the absorption outside the fireball, as well as the temperature and emissivity of the fireball.

[redacted] A second source of electromagnetic radiation in the radio band is synchrotron radiation, which is caused by beta particles spiraling along geomagnetic field lines. A spiraling beta particle continually accelerates, and, therefore, it radiates electromagnetic energy. The radiation is maximum in the HF band, and it is approximately inversely proportional to frequency cubed for higher frequencies. The radiation is concentrated in the direction of the vector of electron motion. Because of its directivity, low intensity, and frequency dependence, synchrotron radiation does not appear to degrade present military systems seriously.

[redacted] ABSORPTION [redacted]

[redacted] Exact expressions for the absorption or energy loss involve components of the earth's magnetic field as well as electron density, collision frequency (number of collisions an electron makes per second), and wave frequency. For frequencies above about 10 megahertz and when bending of the wave is negligible, the incremental path absorption can be found from the following equation.

$$a = 4.6 \times 10^4 \frac{N_e \nu}{\omega^2 + \nu^2} \, dB/km, \qquad (8.2)$$

where

N_e = electron density (electrons/cm^3)

ν = collision frequency (collisions/sec)

ω = wave frequency (radians/sec).

[redacted]

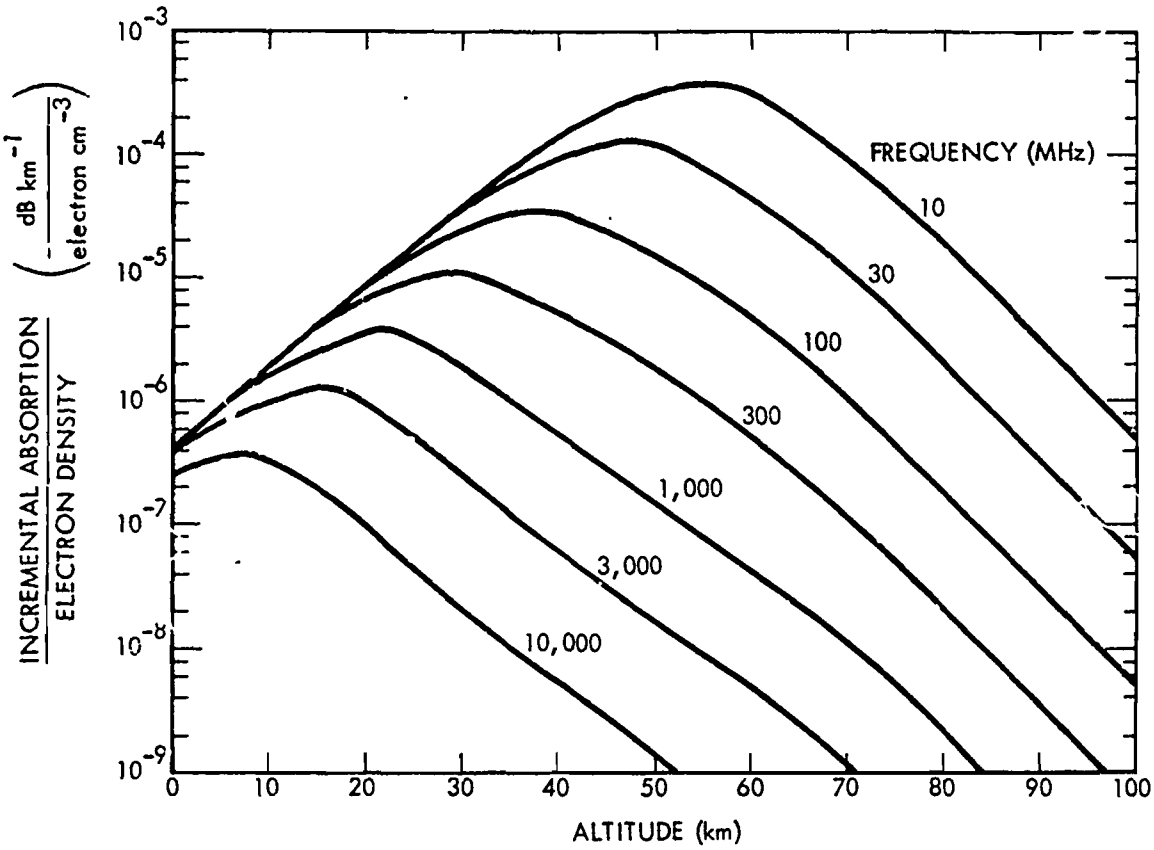

Figure 8-12. [redacted] Incremental Absorption Due to Electron-Neutral Collisions [redacted]

[redacted] Figure 8-12 shows incremental path absorption per electron per cubic centimeter as a function of altitude due to electron-neutral collisions. Above about 100 km, where the neutral particle density is low, absorption due to electron-neutral collisions is small; however, absorption due to electron-ion collisions may be important. Figure 8-13 shows incremental absorption due to electron-ion collisions for a temperature of 1000°K (approximate value of the atmospheric temperature above 200 km). The incremental absorption is proportional to $(1000/T)^{3/2}$ for other temperatures. The dotted portion of the curves indicates the volume where the electron density causes considerable bending of the wave, and a more detailed solution is required to obtain better values for the absorption. Figures 8-12 and 8-13 can be used with estimates of electron density (obtained from Figures 8-2 through 8-9 and 8-11) to determine incremental path absorption. The integral of the incremental path absorption along the propagation path gives the total path loss. Equation 8.1 and Figures 8-12 and 8-13 neglect ion-neutral collisions, which are important at low frequencies (VLF and LF bands). Problems 8-4 through 8-7 provide methods for estimating total one-way path absorption for various propagation paths.

[redacted] As was the case for electron density, it is convenient and useful to present absorption in-

[redacted]

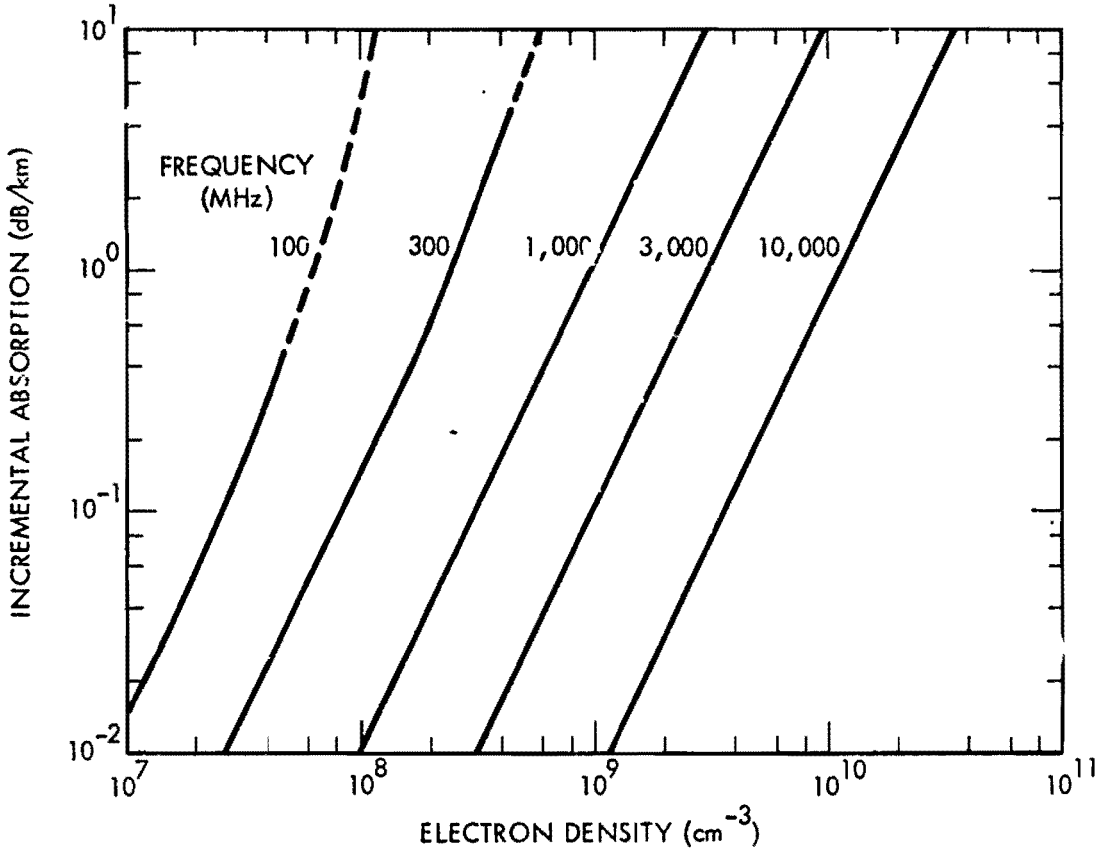

Figure 8-13. [redacted] Incremental Absorption Due to Electron-Ion Collisions, Electron Temperature = 1,000°K [redacted]

[redacted] side the fireball and absorption caused by prompt and delayed radiation outside the fireball separately. With the exception of propagation paths that pass close to the fireball, absorption outside the fireball is maximum in the D-region (40 to 90 km). Generally it is sufficiently accurate to consider the largest of the separate absorptions as the total absorption along a particular propagation path.

[redacted] Scaling relations for the attenuation of low frequencies (VLF and LF bands) are difficult to present, because the amount of absorption for a particular propagation path depends in detail on the penetration of the wave into the atmosphere. A description of low-frequency propagation in nuclear environments is given in Chapter 17. Scaling relations for absorption of propagation at frequencies greater than a few megahertz are given in succeeding paragraphs; however detailed solutions of absorption for propagation paths associated with communication and radar systems usually require numerous calculations that cannot be obtained readily from simple hand-computation procedures. Figure 8-14 shows the burst conditions (detonation altitudes and yield) for which prompt and delayed radiation can cause absorption outside the fireball. The figure can be used in conjunction with the discussion in para-

[redacted]

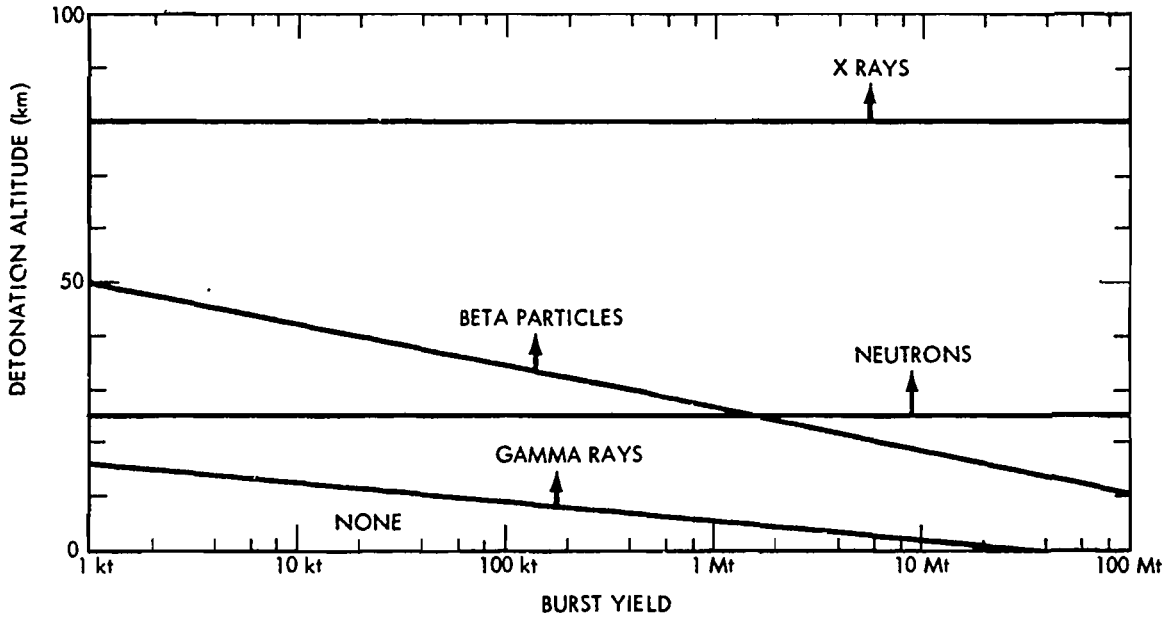

Figure 8-14. [redacted] Radiation Sources Causing Absorption Outside the Fireball [redacted]

[redacted] graphs 8-7 and 8-8 to determine whether absorption outside the fireball need be considered and which radiation sources are important.

8-6 Absorption Within the Fireball [redacted]

[redacted] Fireball ionization is localized and very intense: for most purposes, the fireball may be considered opaque at all radio frequencies for at least a few seconds. Calculations of the magnitude of absorption at a given time, or the duration of a given magnitude of absorption, are subject to considerable error because of uncertainties in predictions of the electron density within the fireball (see paragraph 8-1) and the fireball geometry. Methods for estimating fireball size and absorption through the fireball are given in Problems 8-1 through 8-4.

[redacted] For detonations below about 80 km and weapon yields greater than 100 kt, absorption through the fireball is expected to exceed 25 decibels for about 50 seconds at 10 gigahertz and for longer than 100 seconds at 1 gigahertz. Because the fireball rises a significant distance during these time periods, the duration of degradation due to absorption will generally be determined by the relative motion of fireball and propagation path.

[redacted]

[redacted]

[redacted]

[redacted]

DNA (b)(3)

8-7 Absorption Caused by Prompt Radiation Outside the Fireball [redacted]

[redacted] Absorption outside the fireball caused by prompt radiation may last from tens of seconds in the VHF band to tens of minutes in the HF band for daytime conditions. At night the absorption decreases more rapidly. For bursts below about 100 kilometers, the horizontal radius of the prompt absorption region only extends a few hundred kilometers from the burst point; for higher detonations the extent can be much longer.

8-8 Absorption Caused by Delayed Radiation Outside the Fireball [redacted]

[redacted] Absorption caused by delayed radiation (gamma rays and beta particles) is a function of the location and distribution of the fission debris. Estimates of debris rise and expansion for use in computing delayed-radiation effects are given in Problems 8-1 through 8-3.

[redacted] Delayed gamma rays can produce significant absorption when the debris is at altitudes above about 25 kilometers. Problem 8-6 describes methods that can be used to estimate one-way path absorption. The horizontal extent of the absorption region caused by gamma rays depends on weapon fission yield, debris altitude, time after burst, and wave frequency. The insert in Figure 8-9 shows the maximum possible extent of ionization and, thus the maximum extent of absorption; for most cases the region of significant absorption will be smaller.

[redacted] When the debris is above about 60 kilometers, beta particles produce D-region absorption at the burst locale and on the opposite side of the magnetic equator. Figures 8-49 through 8-51 can be used to obtain estimates of absorption caused by beta particles in terms of the beta-radiation intensity parameter that was defined in paragraph 8-4 for debris above the beta-particle stopping altitude (60 km). The location of the absorption region is offset from the debris region because of the effect of the geomagnetic field on the motion of beta particles, as illustrated in Figure 8-10. The horizontal radius of the absorption region is approximately equal to the debris radius. This radius can vary from a few kilometers to a few thousand kilometers depending on weapon yield, detonation altitude, and time after burst.

[redacted] PHASE CHANGES [redacted]

[redacted] Phase changes resulting from propagation through a region of uniform electron density affect propagation velocity and signal characteristics. Relative phase changes due to gradients in electron density change the direction of propagation and scatter energy from the propagating wave. Some phase effects become important only for electron densities that cause significant absorption. Evaluation of direction changes and scattering requires detailed information concerning the spatial distribution of electron density, which is difficult to predict theoretically and for which there is only limited experimental data.

8-9 Velocity of Propagation [redacted]

[redacted] Within an ionized region the phase velocity is increased over that in vacuum, but the group velocity, associated with the transmission of energy, is reduced. The increased time required to propagate energy through the region is proportional to the integral of electron density along the propagation path. Typical values of time delays associated with ionization caused by nuclear bursts range from a few nanoseconds to a few tens of microseconds. The larger time delays usually are accompanied by significant absorption when the ionized region occurs below 100 km.

[redacted] The phase velocity in an ionized region depends on the frequency. Therefore, the region

[redacted]

[redacted]

separates waves of different frequencies, i.e., the region is dispersive. The significance of dispersion depends critically on the type of signal being propagated and the type of signal processing being employed. For frequency-modulated signals, dispersion causes intermodulation and harmonic distortion. For digital systems, dispersion causes pulse-envelope distortion. Dispersion effects caused by electrons below 100 kilometers appear to be negligible when compared to absorption. At higher altitudes, electrons can only cause important dispersion effects for wide-band signals (bandwidths of the order of 1 percent or more of the carrier frequency), and these effects will probably only occur for propagation paths through fireball regions after the electron density has decreased sufficiently that absorption is not overriding.

8-10 Frequency of Propagation

A time-dependent phase change is equivalent to a frequency shift. The frequency shift is proportional to the time rate of change of the electron density integral along the propagation path. Frequency changes may be caused by changes in electron density with time along a fixed propagation path or by motion of the propagation path in a region of inhomogeneous electron density. For a fixed propagation path, frequency changes caused by nuclear-weapon-produced ionization are small (a few hertz for a 10 megahertz signal) by a few seconds after burst. Larger frequency changes may occur when the propagation path moves through regions of high electron density, such as the fireball; however, in those cases absorption generally will be overriding.

8-11 Direction of Propagation

Spatial gradients in electron-density can change the direction of propagation. When the electron density gradient is steep, part of the energy can be reflected. Reflection is important in the propagation of low frequencies (tens of kilohertz) over paths that are remote from the fireball. It also may be important in the propagation of much higher frequencies for paths that pass near the fireball, where high electron density gradients can exist.

Smaller electron-density gradients cause ray bending (refraction). Refraction in the ambient ionosphere (E- and F-region) is important for beyond-the-horizon propagation in the HF band. For radar systems, refraction in the D-region caused by nuclear-burst-produced ionization normally is accompanied by significant absorption. Possible exceptions may occur if the propagation path passes close to the fireball or close to regions ionized by beta particles (particularly when the propagation path is nearly parallel to the geomagnetic field lines). Changes in the E- and F-region electron density caused by the fireball or by traveling disturbances may modify HF and VHF propagation significantly. E- and F-region electron densities sufficient to change the direction of propagation at higher frequencies by a few degrees can occur without causing significant absorption.

8-12 Scatter and Scintillation

Inhomogeneities in the propagation medium (variations in the dielectric constant of the medium) cause a small amount of incident energy to be scattered away from the original propagation direction. The direction of scatter depends on the shape of the inhomogeneities and their orientation relative to that of the incident beam. Energy that is forward scattered as the wave traverses inhomogeneous regions can cause fluctuations in the amplitude and the phase of the wave, called scintillation. The phase fluctuations are equivalent to fluctuations in the direction of propagation that result in random variations in the angle of arrival of received signals. Small amounts of backscattered energy can produce interference to radar systems called clutter.

The analysis and quantitative description

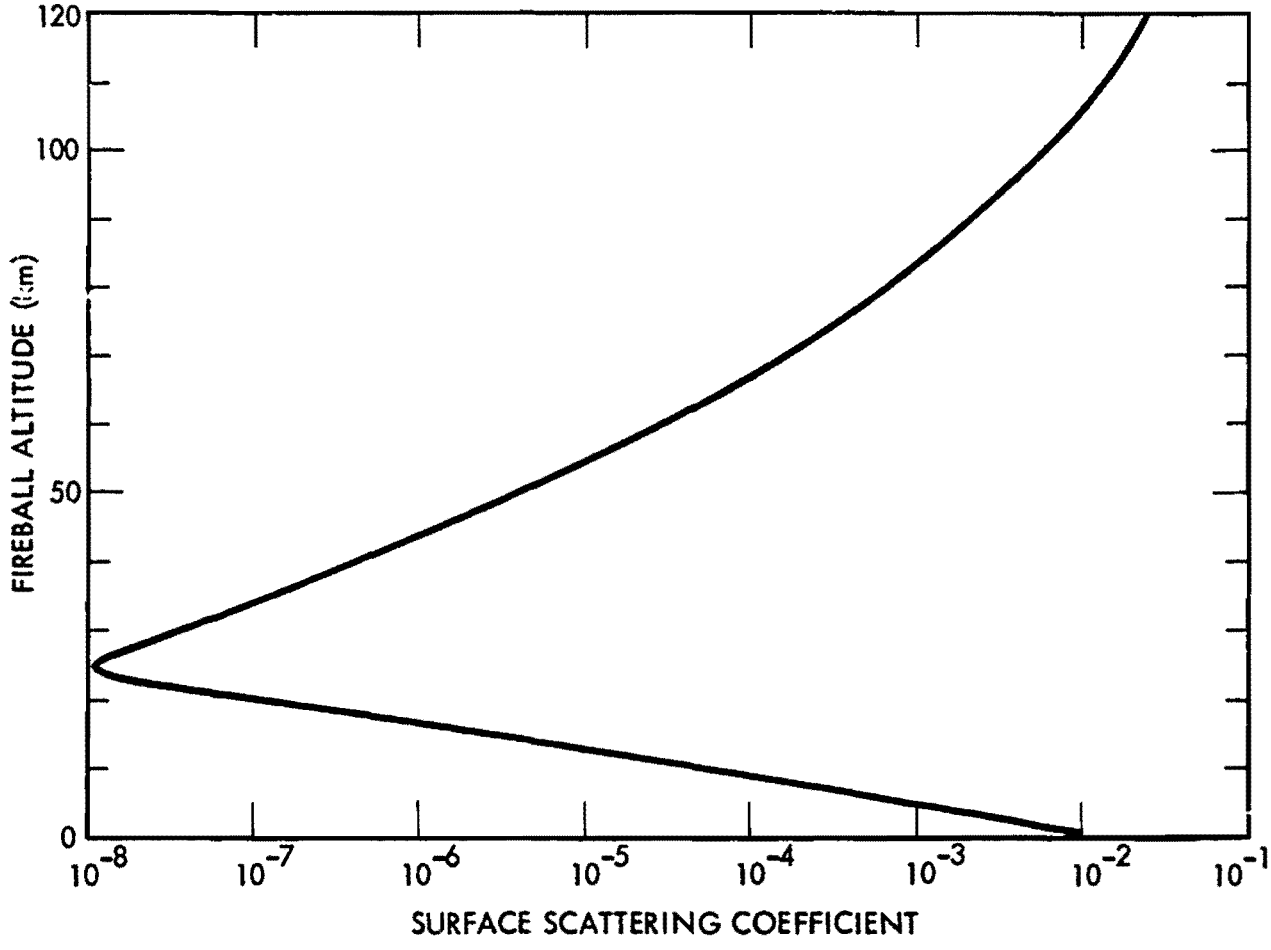

Figure 8-15. [redacted] Apparent Fireball Surface Scattering Coefficient at 400 MHz [redacted]

[redacted] of scatter requires a statistical model of the spatial distribution of inhomogeneities in the propagating medium. Sufficient information from which such models could be constructed for nuclear-weapon-produced ionization is not available. There are limited experimental data from nuclear weapon tests concerning backscatter; however, interpretation of these data is difficult, and sufficient information for the construction of a complete empirical model is not available.

[redacted] Significant backscatter has been observed from fireball regions from a few tens of seconds to a few minutes after burst. Figure 8-15 shows the general order of magnitude of the surface scattering coefficient (multiply by the area of the scattering surface to obtain radar cross section) derived from experimental data. Below about 20 km, scattering is apparently due to variations in air density across fireball boundaries and across shock waves. For surface bursts, dust, dirt, and water vapor appear to cause backscatter

[redacted]

[redacted]

from the stem of the rising cloud. Backscatter from fireballs above 20 km can be explained in terms of partial reflection, or scatter from inhomogeneities in electron density in the fireball or in the shock fronts. The cross section appears to decrease with increasing frequency. The minimum in the apparent cross section near 20 km is due to several mechanisms, the prime of which is the absorption sheath caused by beta particles escaping from the fireball. The scattering coefficients shown in Figure 8-15 are only illustrative; observed values vary over an order of magnitude, depending on the relative geometry of propagation path and fireball, the characteristics of radars used in obtaining the data, and the time after burst.

[redacted] Backscatter is also observed from regions of field-aligned ionization (ionized regions that are elongated along the geomagnetic field, often referred to as auroral ionization) which can be produced above about 80 km by beta particles. Field-aligned ionization can also occur within the fireball after a few tens of seconds for detonations above about 80 kilometers. The magnitude of backscatter is aspect sensitive; maximum backscatter occurs when the propagation path is normal to geomagnetic field lines. Backscatter from field-aligned ionization is thought to be a volume effect; volume scattering coefficients of about 10^{-13} m^2/m^3 at 400 MHz have been observed from beta-particle ionization regions. Significantly larger coefficients may occur from field-aligned ionization caused by the fireball. The cross section scales inversely as about the 4.5 power of frequency. Returns have been recorded for several hours after burst.

[redacted] SECTION II
METHODS FOR CALCULATING ABSORPTION OF RADIO FREQUENCIES [redacted]

[redacted] As discussed previously, absorption frequently is the most important phenomena affecting propagation of radio frequencies; however, detailed solutions of absorption for propagation paths associated with communication and radar systems usually require numerous computations that cannot be obtained readily by hand calculations. The procedure for calculating absorption that are described below offer a means for obtaining reasonable estimates of radio frequency absorption for many situations of interest, however, the user should maintain awareness of the limitations defined for each of the calculations.

[redacted] The calculation of the absorption of radio frequencies will be described separately for three conditions: absorption of propagation paths going through the fireball, absorption caused by prompt radiation outside of the fireball, and absorption caused by delayed radiation outside of the fireball (this last condition is divided further into absorption caused by delayed gamma rays and absorption caused by delayed beta particles).

[redacted] Prior to the determination of the absorption along any of the paths discussed above, the size and location of the fireball region and/or the debris region must be determined. The spatial and temporal characteristics of the fireball and the debris regions created by nuclear bursts are complex. Idealized geometric models have been adopted for the purpose of analysis. The dimensions of three scaling models, based largely on interpolations of data from high-altitude nuclear tests, are used to represent detonations in three burst altitude regimes; below 80 kilometers, between 85 and 120 kilometers, and above 120 kilometers. The characteristics of the fireball and the debris are discussed separately for these three burst altitude regimes in succeeding paragraphs. Figure 8-16 illustrates the idealized geometric models referred to in the discussions. Dimensions shown in Figure 8-16 are defined in the discussions or in the illustrative problems that follow.

[redacted]

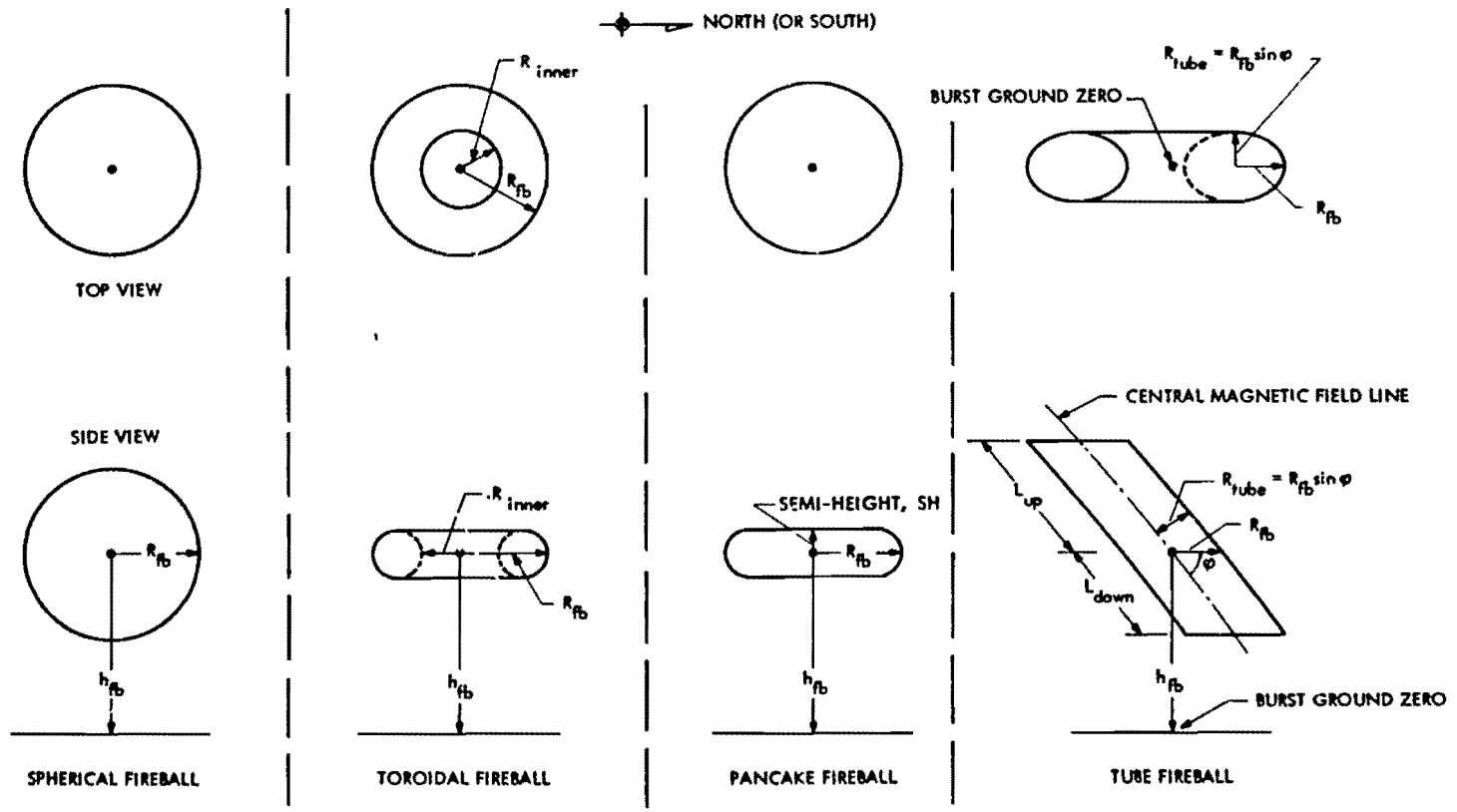

Figure 8-16. Examples of Fireball Geometry

[redacted]

8-13 Size and Location of Fireball and Debris Regions for Detonations Below 85 Kilometers [redacted]

[redacted] When a nuclear weapon is detonated at an altitude below about 85 kilometers, the fireball initially is a reasonably well defined and relatively small spherical region (see Chapter 1). After the fireball is formed, it expands and rises above the detonation point, carrying the fission debris with it. Depending on the weapon yield and the detonation altitude, the fireball may become toroidal in shape as it rises. After rising, the fireball will become stabilized in altitude and will diffuse into a pancake shape.

[redacted] If the fireball rises above 200 kilometers, it is assumed to fall back to 200 kilometers. If the peak altitude of the fireball is less than 200 kilometers, it is assumed to stabilize at its peak altitude.

[redacted] The initial fireball radius is the parameter used to determine whether the fireball will form a toroid. The toroid is assumed to transform into a pancake at 7 minutes after burst, with a vertical thickness equal to the vertical dimension of the toroid at 7 minutes. If the fireball does not form a toroid, the fireball is assumed to transform from a sphere to a pancake when the radius becomes 100 kilometers. The vertical thickness of the pancake is assumed to be 100 kilometers.

[redacted] The model provided for determining the location of the debris is intended for calculation of delayed-radiation (gamma rays and beta particles) effects. For times later than a few tens of minutes after burst, the size and location of the debris region will depend on atmospheric winds and diffusion, and the model may be considerably in error.

[redacted] Figures 8-19 through 8-25 are used to determine the spatial and temporal history of the fireball (and the debris), for bursts that occur below 85 kilometers.

8-14 Size and Location of Fireball and Debris Regions for Detonations Between 85 and 120 Kilometers [redacted]

[redacted] When a nuclear detonation occurs between 85 and 120 kilometers, the fireball transforms from a sphere to a cylinder or tube aligned along the geomagnetic field. The model used for the calculations described herein assumes that the fireball stabilizes at its maximum altitude above ground zero. The fireball radial dimension also is assumed to remain constant after 7 minutes. A fireball region is not defined for times longer than 2 hours after burst.

[redacted] Delayed radiation (gamma rays and beta particles) is assumed to be emitted from a single debris pancake, which is assumed to rise with the fireball and then to settle slowly along the geomagnetic field until it reaches 200 kilometers altitude at approximately 2 hours after burst. As the debris settles, the center is offset from ground zero toward the nearest magnetic pole, as illustrated in Figure 8-17. Figures 8-19 through 8-29 are used to determine the spatial and temporal history of the fireball (and the debris) for bursts that occur at altitudes between 85 and 120 kilometers.

8-15 Size and Location of Fireball and Debris Regions for Detonations Above 120 Kilometers [redacted]

[redacted] Theoretical and experimental data are incomplete for this altitude region; therefore, scaling relations are given only for a few parametric yields and detonation altitudes. Three shapes are used to model the fireball region: a sphere, a pancake, and a cylinder or tube aligned along the geomagnetic field. Figure 8-16 illustrates the fireball geometry.

[redacted] As the detonation altitude is increased above 120 kilometers, the debris is distributed over a larger region. Some debris can be transported across the magnetic equator. The single-pancake debris region used at lower altitudes to

[redacted]

[redacted]

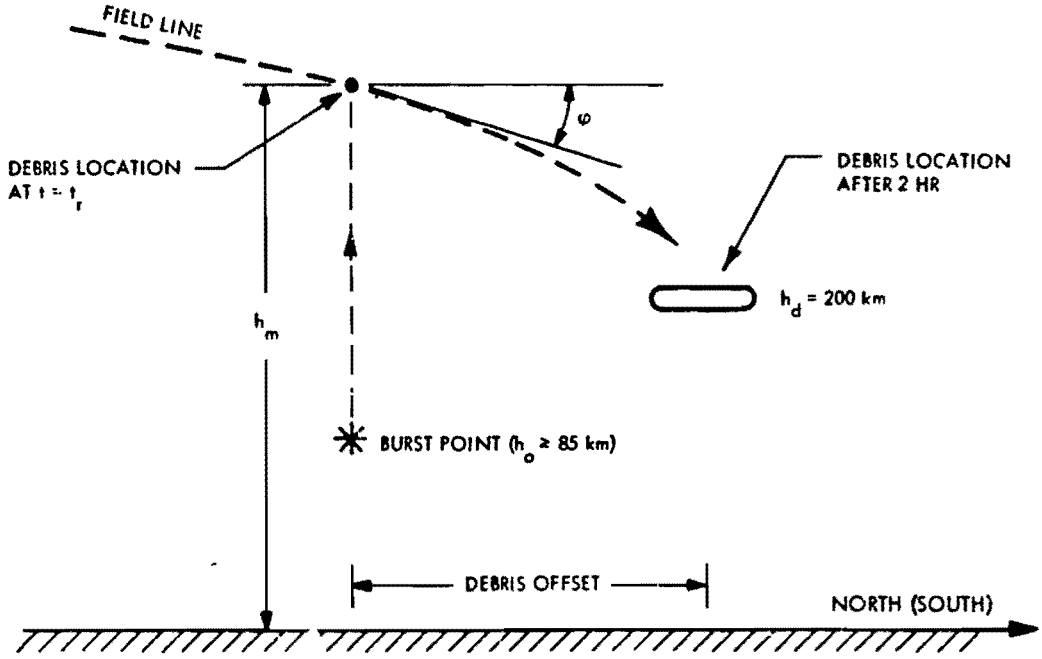

Figure 8-17. [redacted] Debris Behavior for Detonation Altitudes Greater Than 85 km [redacted]

[redacted]

model delayed radiation effects is not adequate, so multiple regions are used.

[redacted] Up to three debris regions are used to determine the delayed radiation resulting from detonations above 120 kilometers. Figure 8-18 illustrates the geometry. Two of these regions (Regions 1 and 2) model debris in the burst region, and the third (Region 3) models debris transported across the magnetic equator to the conjugate region. For convenience and because little is known about the debris location in the conjugate region, the beta-particle ionization in the burst and conjugate regions associated with Debris Region 3 is assumed to coincide with that associated with Debris Region 1. Debris Region 3 is used to compute gamma-ray ionization in the conjugate region. For weapons detonated above 250 kilometers, Region 2 is used to determine both gamma-ray and beta-particle ionization.

[redacted] in the model used herein, the fraction of debris transported across the magnetic equator is assumed to be independent of geomagnetic dip angle for detonations above 250 kilometers. A small amount of debris can reach the conjugate region for detonations below 250 kilometers and low dip angles. The time required for the debris to reach the conjugate region depends on detonation altitude and geomagnetic dip angle; however, for purposes of calculating delayed gamma radiation, the debris can be assumed to reach the conjugate region immediately after burst.

[redacted] About 20 percent of the debris for detonations above 120 kilometers is not accounted for in the model. This debris is assumed to escape to large distances; some may be carried into space and some may be spread world-wide. At least part of this debris will be trapped on the magnetic field lines above the burst. While this debris probably is not important for single bursts, it could cause significant delayed radiation after

[redacted]

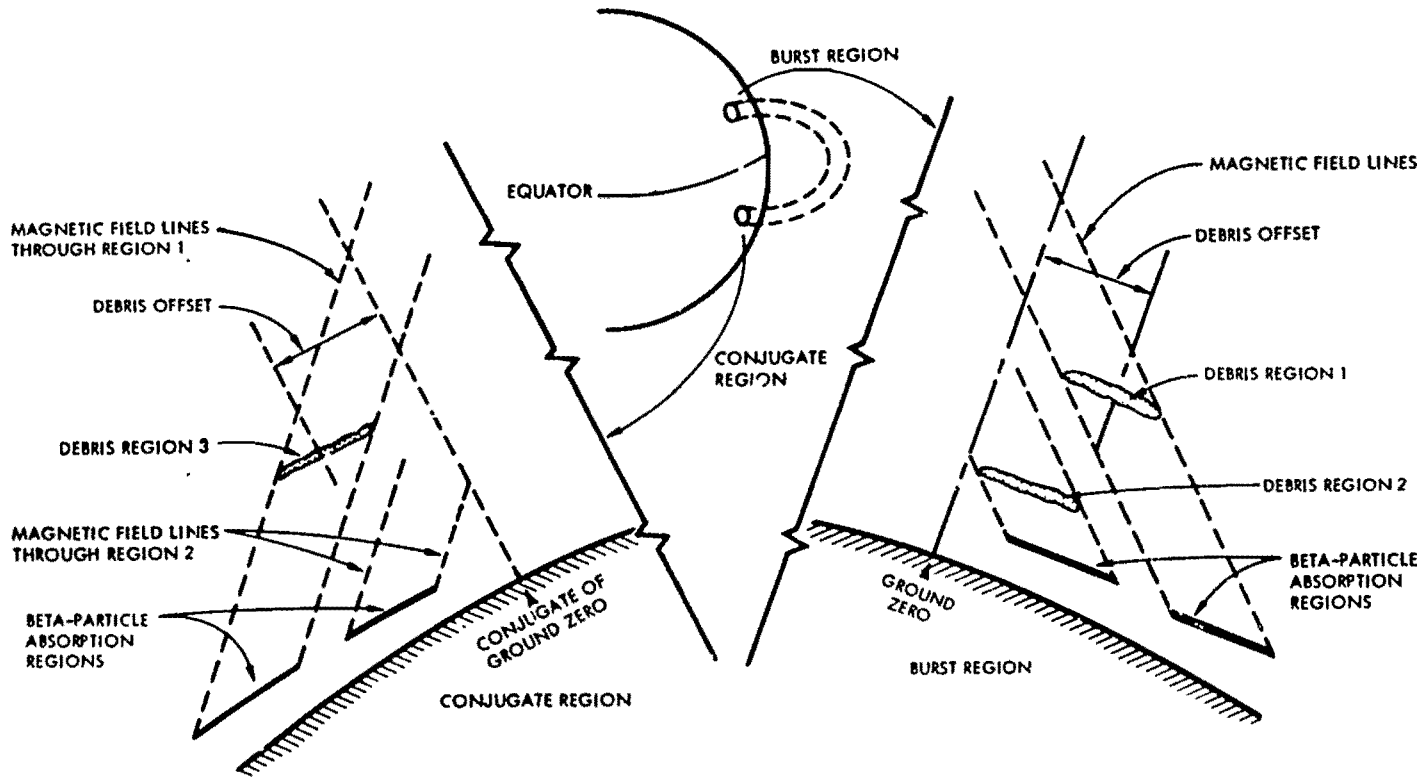

Figure 8-18. [redacted] Illustration of Debris and Beta-Particle Absorption Regions for Times Later Than 10 Minutes After Burst, H_0 Above 120 km [redacted]

[redacted]

[redacted]

multiple weapon detonations.

[redacted] After rising to peak altitude, the three debris regions are assumed to settle along the geomagnetic field lines until they reach 200 kilometers altitude at about 2 hours after burst. The debris regions are offset from ground zero or the conjugate of ground zero toward the magnetic pole.

[redacted]

Problem 8-1 Calculation of Fireball Size, Shape, and Location for a Burst Below 85 Kilometers

[redacted] Figures 8-19 through 8-25 contain families of curves with which the size, shape, and location of the fireball resulting from a nuclear detonation below 85 kilometers may be estimated. For bursts in this altitude regime, the debris altitude h_d is assumed to be the same as the fireball altitude h_{fb}. The debris is distributed non-uniformly within the fireball region. However, for simplified calculations of delayed radiation effects, the debris region can be assumed to be a thin pancake region with radius R_d equal to the fireball radius R_{fb}.

[redacted] The altitude of the fireball at a time t after burst is obtained from Figures 8-19 through 8-22 by a series of steps, as follows:

1. Enter Figure 8-19 with the weapon yield and detonation altitude h_o to obtain h_r, the distance the fireball will rise above the detonation point. The maximum fireball altitude, h_m, is

$$h_m = h_o + h_r \text{ km.}$$

Enter Figure 8-20 with h_r to obtain the time required to reach maximum altitude t_r. If $t \geq t_r$ and $h_m \leq 200$ km, go to 3; otherwise go to 2.

2. If $t < t_r$, enter Figure 8-21 with time after burst and h_r to obtain h_N, an altitude normalizing factor. If $h_m > 200$ km, enter Figure 8-22 with $\tau = t/t_r$ to obtain f_h, the fireball height factor.

3. Compute h_{fb}, the fireball altitude at time t:

$$h_{fb} = \begin{cases} (h_o + h_N h_r) \text{ km} \\ \quad \text{when } t < t_r \\ h_m \text{ km} \\ \quad \text{when } t \geq t_r,\ h_m < 200 \\ [200 + f_h\,(h_m - 200)] \text{ km} \\ \quad \text{when } t > t_r,\ h_m > 200 \end{cases}$$

[redacted] The radius and shape of the fireball at a time t after burst are obtained from Figures 8-23 through 8-25, as follows:

1. Enter Figure 8-23 with weapon yield and detonation altitude h_o to obtain the initial fireball radius R_o. If $R_o < 4$ km, go to 2; otherwise go to 3 when $t < 7$ minutes or go to 4 when ≥ 7 minutes.

2. Determine t_{toroid}, the time of toroid formation, from Figure 8-24 by selecting the fireball radius curve for the value of R_o determined above, by locating the intercept of this curve with the toroid formation time curve, and by reading t_{toroid} on the abscissa.

3. Enter Figure 8-24 with the time of interest t and the initial fireball radius R_o. Determine R_{fb}, the fireball radius at time t, then go to 5.

4. Enter Figure 8-24 with $t = 7$ minutes and the initial fireball radius R_o; obtain the fireball radius at 7 minutes after burst, $R_{fb}(7)$. Enter Figure 8-25 with t and h_m to obtain ΔR. Compute R_{fb}, as follows:

$$R_{fb} = R_{fb}(7) + \Delta R.$$

5. The fireball will be a

sphere if $R_o \leq 4$ km and $t < t_{toroid}$, or if

$$R_o > 4 \text{ km and } R_{fb} < 100 \text{ km;}$$

toroid if $R_o < 4$ km and $t_{toroid} \leq t < 7$ minutes;

pancake if $R_o \leq 4$ km and $t \geq 7$ minutes, or if

$$R_o > 4 \text{ km and } R_{fb} \leq 100 \text{ km.}$$

If the fireball shape is a toroid, compute the inner toroid radius:

$$R_{inner} = \frac{R_{fb}}{2}$$

[redacted]

If the fireball shape is a pancake, compute the pancake semithickness:

$$SH = \begin{cases} \frac{1}{4} R_{fb}(7) & R_o \leq 4 \text{ km} \\ 50 & R_o > 4 \text{ km.} \end{cases}$$

Example

Given: A 1 Mt weapon burst at an altitude of 50 km.

Find: The size, shape, and location of the fireball and debris region 2 minutes after the burst.

Solution:

a. From Figure 8-19 $h_r \approx 50$ km for a 1 Mt weapon burst at 50 km.

b. $h_m = h_o + h_r = 50 + 50 = 100$ km.

c. From Figure 8-20, $t_r = 10$ min for $h_r = 50$ km.

d. From Figure 8-21, $h_N = 0.6$ for $t = 2$ min and $h_r = 50$ km.

e. Since $t < t_r$.

$h_{fb} = h_o + h_N h_r = 50 + (0.6)(50) = 80$ km

f. From Figure 8-23, $R_o = 2$ km for a 1 Mt weapon detonation at 50 km.

g. From Figure 8-24, $t_{toroid} = 1.7$ min for $R_o = 2$ km.

h. From Figure 8-24, $R_{fb} = 30$ km 2 min after a burst with $R_o = 2$ km.

i. Since $t_{toroid} < t < 7$ minutes, the fireball shape is a toroid, and

$$R_{inner} = \frac{R_{fb}}{2} = \frac{30}{2} = 15 \text{ km.}$$

Answer: The fireball is a toroid centered at 80 kilometers altitude. The outer radius is 30 kilometers and the inner radius is 15 kilometers (see Figure 8-16). The altitude and radius of the debris pancake are 80 kilometers and 30 kilometers, respectively.

Reliability The size and location of the debris region depend on atmospheric winds and diffusion. Since these effects are neglected in the model described herein, the results predicted by the model may be considerably in error.

Related Material See paragraph 8-13.

[redacted]

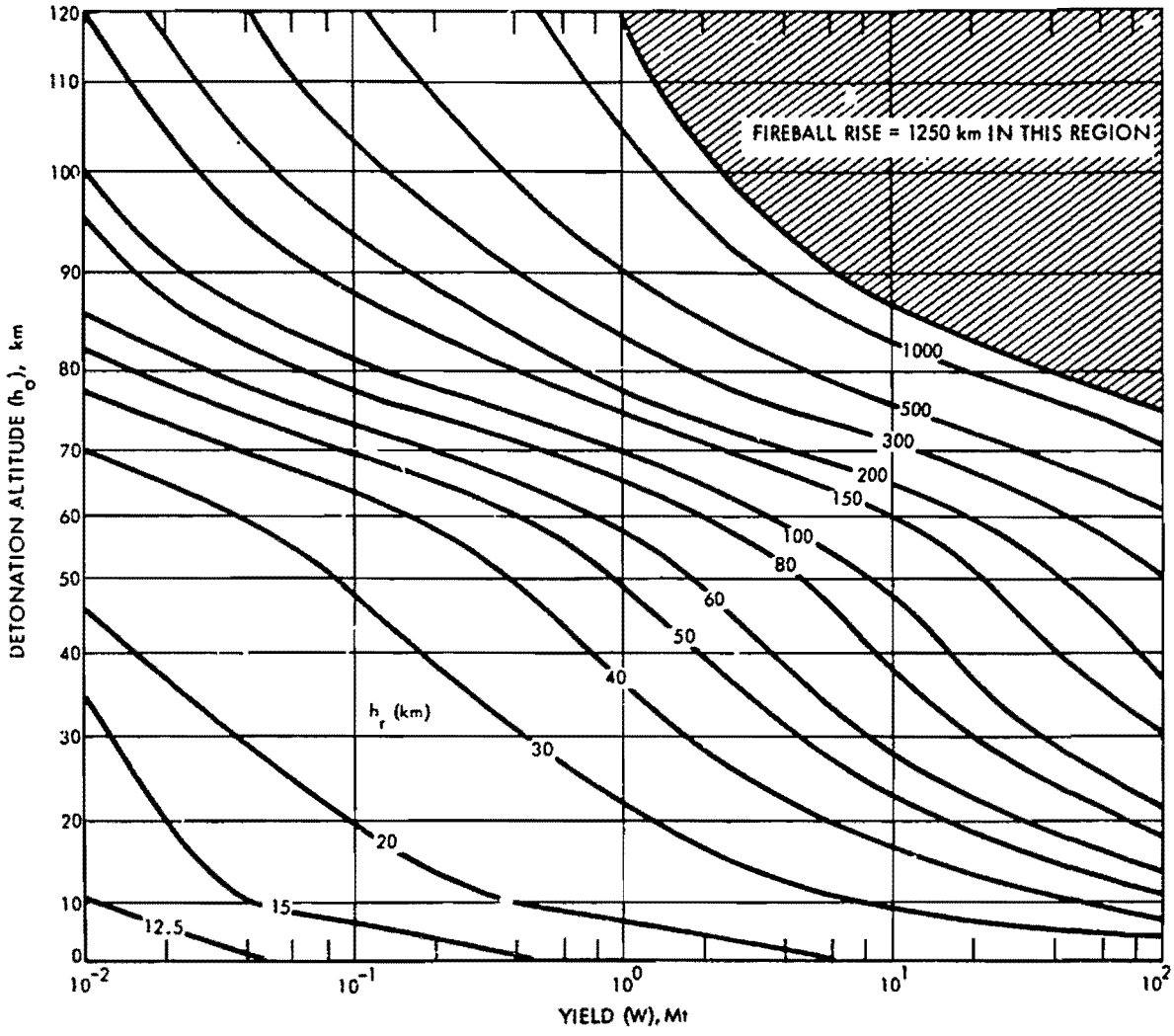

Figure 8-19. [redacted] Maximum Fireball Rise [redacted]

[redacted]

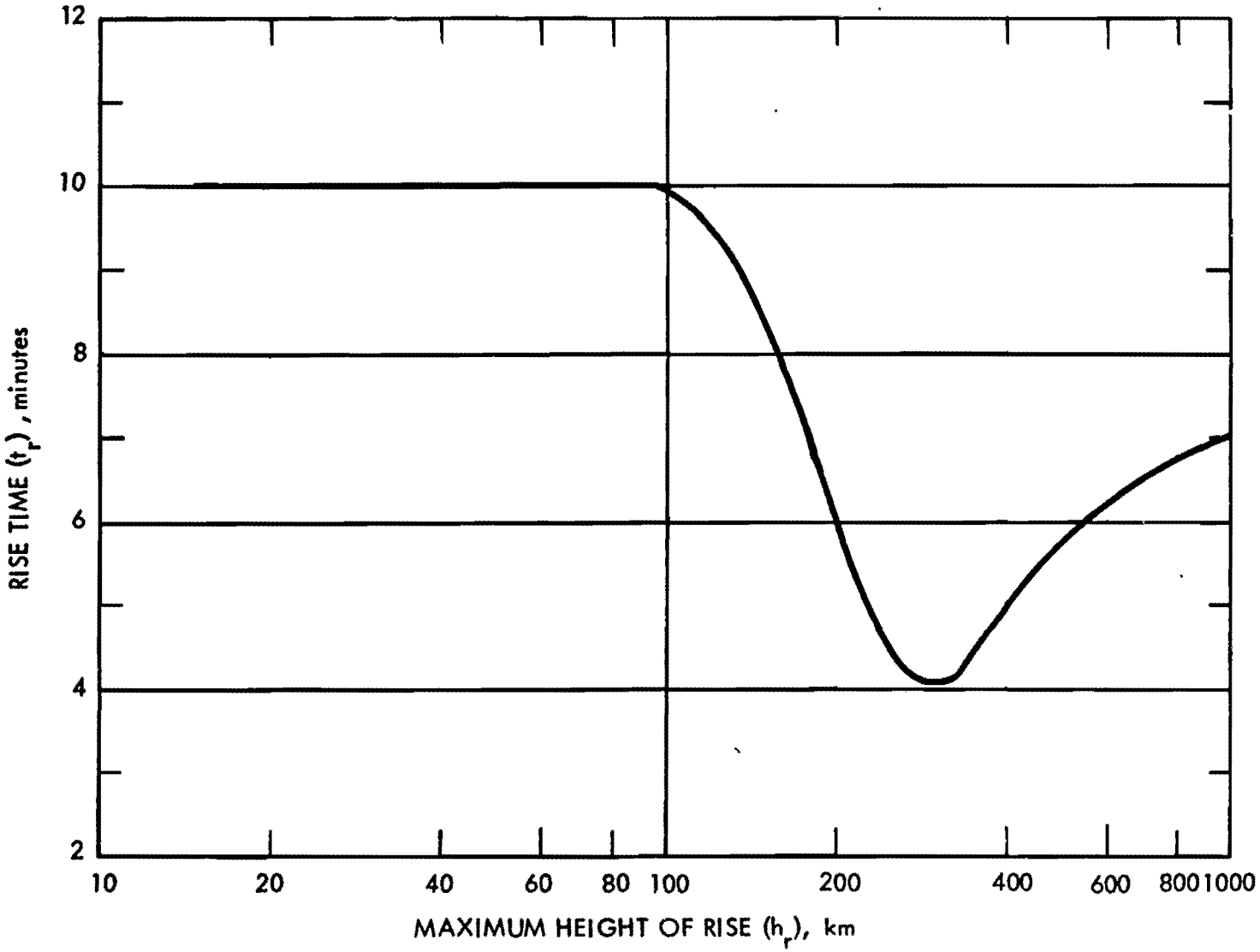

Figure 8-20. [redacted] Time for Fireball to Reach Its Maximum Altitude [redacted]

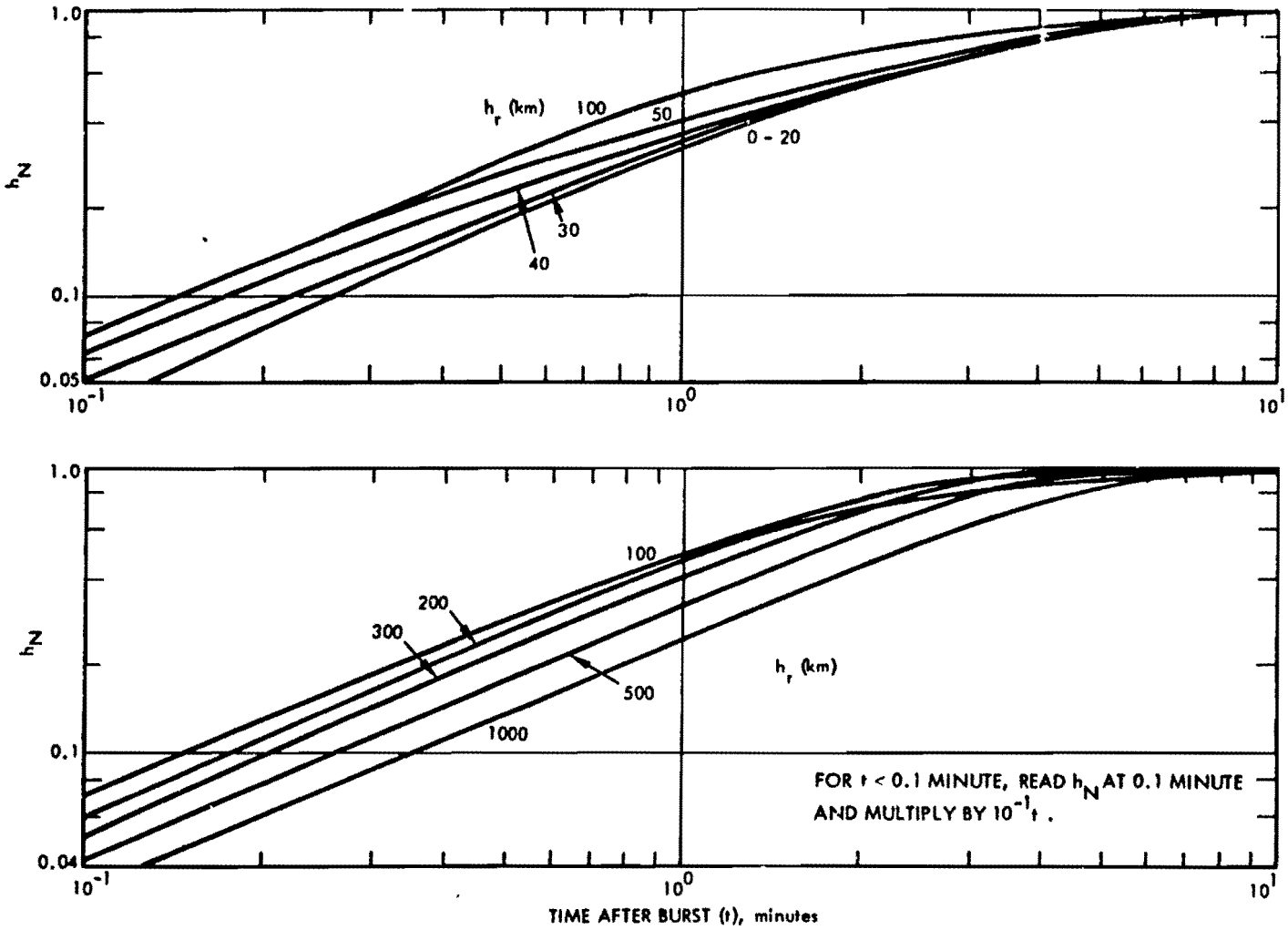

Figure 8-21. [redacted] Altitude Normalizing Factor h_N [redacted]

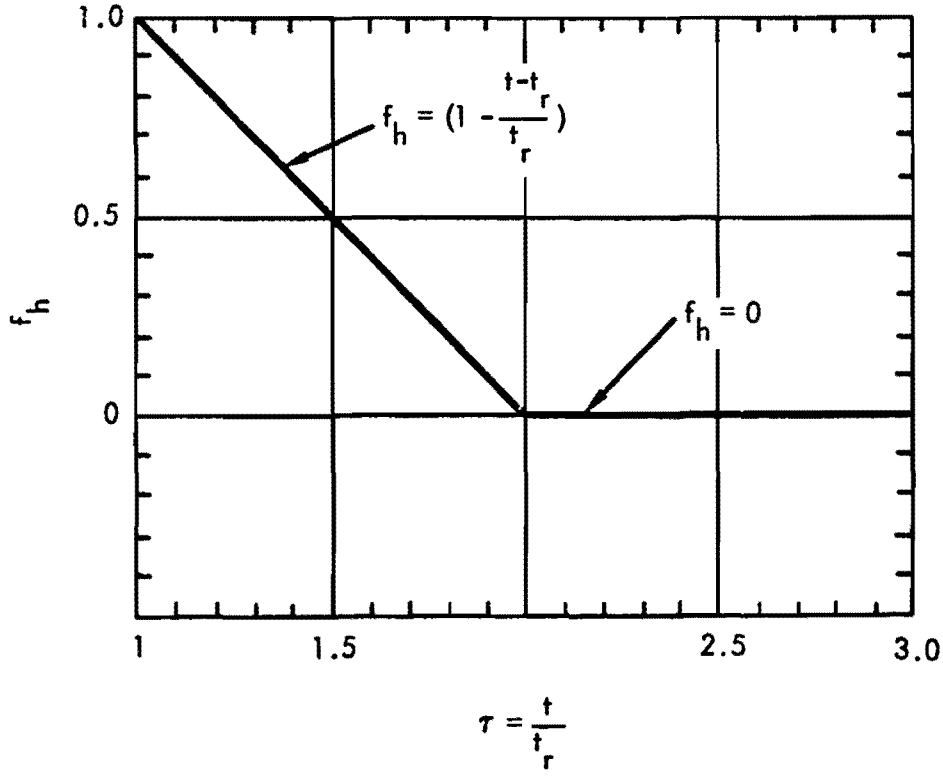

Figure 8-22. [redacted] Fireball Height Factor [redacted]

[redacted]

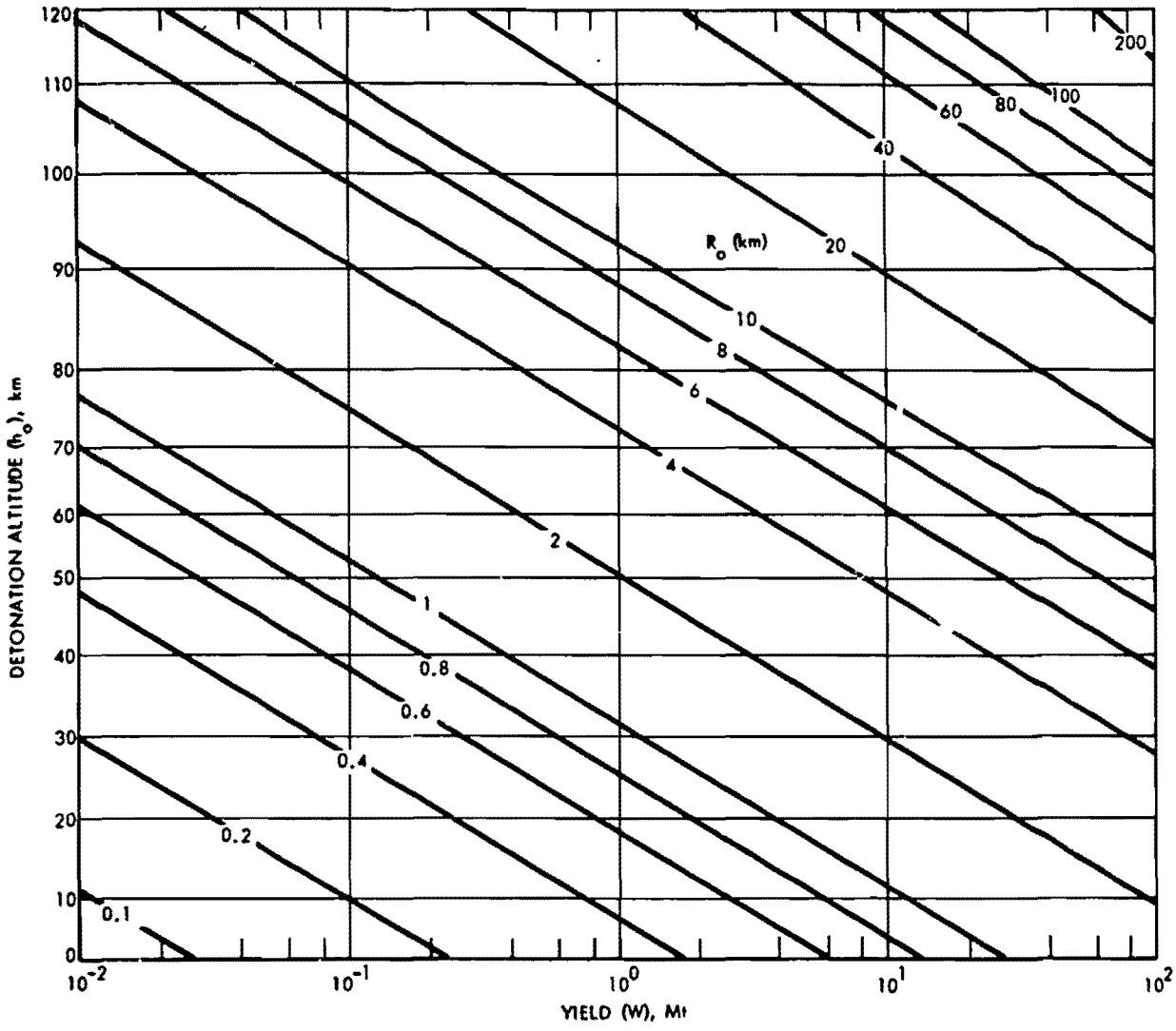

Figure 8-23. [redacted] Initial Fireball Radius [redacted]

[redacted]

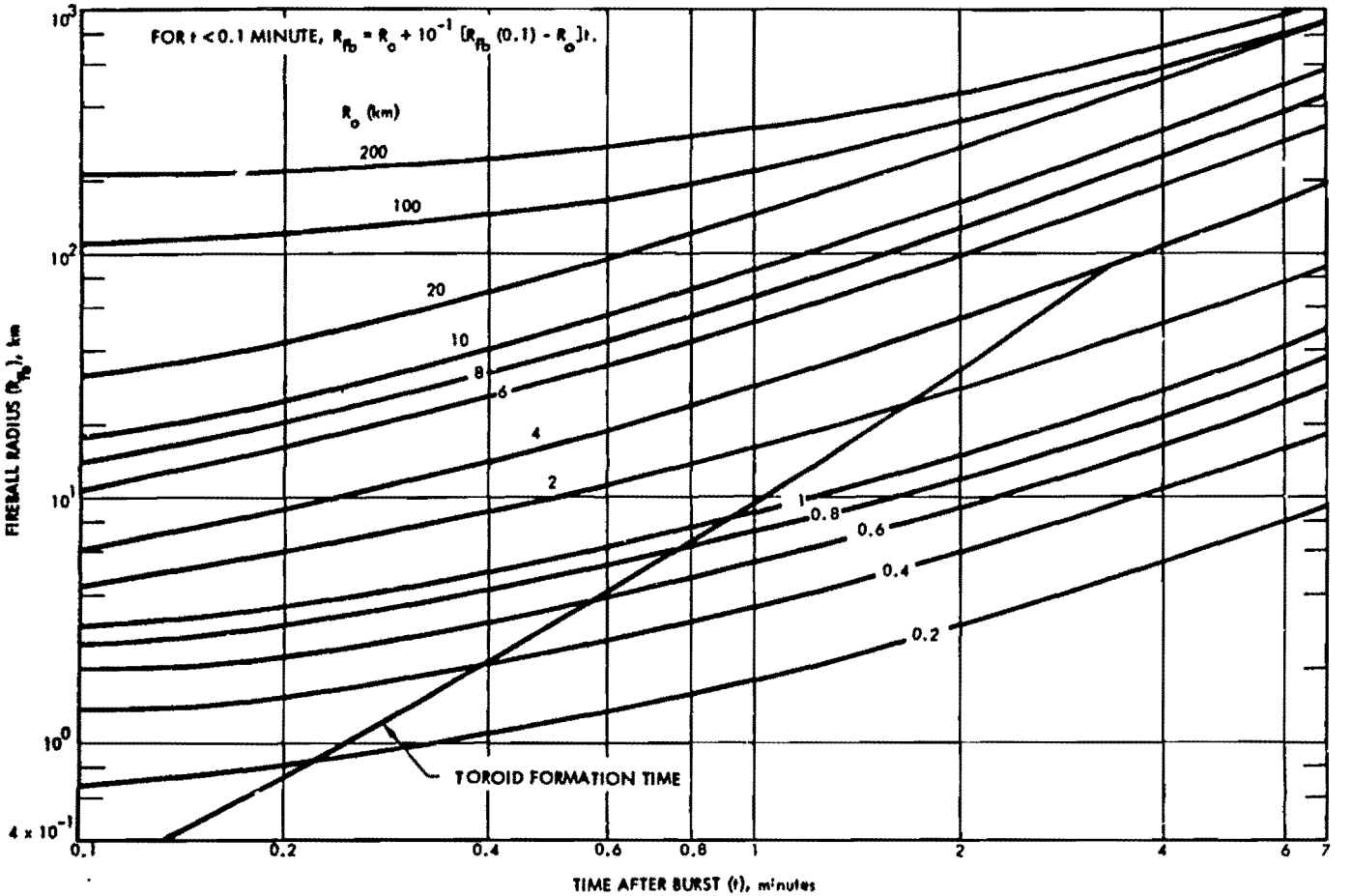

Figure 8-24. [redacted] Fireball Radius [redacted]

[redacted]

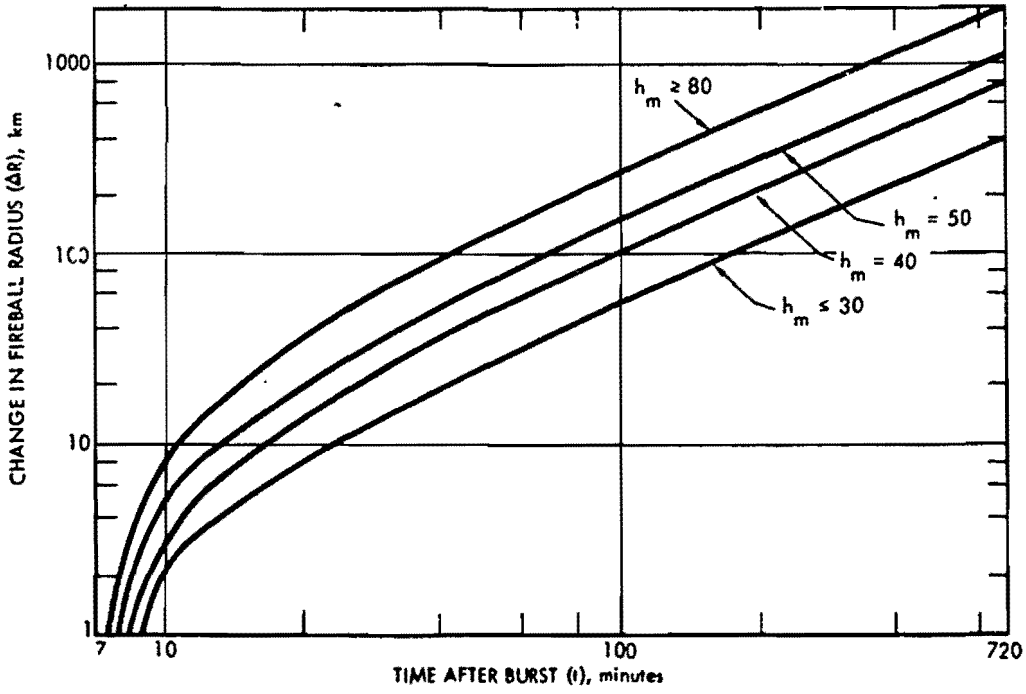

Figure 8-25. [redacted] Change in Fireball/Debris-Region Radius After Sever Minutes [redacted]

[redacted]

[redacted]

Problem 8-2 Calculation of Fireball Size, Shape, and Location for a Burst Between 85 and 120 kilometers

[redacted] Figures 8-19 through 8-29 contain families of curves with which the size, shape, and location of the fireball resulting from a nuclear detonation between 85 and 120 kilometers may be estimated. For bursts in this altitude regime, the fireball transforms from a sphere to a cylinder or tube aligned along the geomagnetic field line. A fireball region is not defined for times after burst greater than 2 hours.

[redacted] The altitude of the fireball at a time t after burst is obtained from Figures 8-19 through 8-21 by a series of steps, as follows:

1. Enter Figure 8-19 with weapon yield W and detonation altitude h_o to obtain h_r, the distance the fireball will rise above the detonation point. The maximum fireball altitude, h_m, is

$$h_m = h_r + h_o \quad km.$$

Enter Figure 8-20 with h_r to obtain the time to reach maximum altitude t_r. If $t \geq t_r$ go to 3; otherwise go to 2.

2. If $t < t_r$, enter Figure 8-21 with time after burst and h_r to obtain h_N, and altitude normalizing factor.

3. Compute h_{fb}, the fireball altitude at time t:

$$h_{fb} = \begin{cases} (h_o + h_N h_r) \quad km \\ \qquad t < t_r \text{ minutes} \\ h_m \quad km \\ \qquad t_r < t < 120 \text{ minutes} \end{cases}$$

[redacted] The radius and shape of the fireball at a time t after burst are obtained from Figures 8-23, 8-24, and 8-26, as follows:

1. Enter Figure 8-23 with weapon yield and detonation altitude h_o to obtain fireball radius R_o. Enter Figure 8-26 with weapon yield to obtain the magnetic equilibrium radius R_{eq}. Determine the time to reach R_{eq}, t', from Figure 8-24 by selecting the fireball radius curve for the value of R_o obtained from Figure 8-23 and by determining the time when the fireball radius (R_{fb}) is equal to R_{eq}. If $t > t'$, go to 3; otherwise go to 2.

2. Enter Figure 8-24 with t and R_o to obtain R_{fb}, the fireball radius at time t. Go to Step 4.

3. Compute R_{fb}:

$$R_{fb} = \begin{cases} (R_{eq} + (t - t')\, R_o \quad km \\ \qquad t < 7 \text{ minutes}, \\ (R_{eq} + (7 - t')\, R_o) \quad km \\ \qquad t \geq 7 \text{ minutes}. \end{cases}$$

4. The fireball shape will be a

sphere if $t < t'$

tube if $t \geq t'$.

[redacted] If the time of interest t is greater than t', the time to reach the magnetic equilibrium radius, the tube fireball dimensions are obtained as follows:

1. If $t' > t_r$ (obtained from Figure 8-20 above), go to 2; otherwise enter Figure 8-21 with $t = t'$ and h_r (from Figure 8-19) and obtain $h_N(t')$.

2. Compute $h_{fb}(t')$:

$$h_{fb}(t') = \begin{cases} (h_o + h_N(t')h_r) \quad km \\ \qquad t' \leq t_r \text{ minutes}, \\ h_m \quad km \\ \qquad t' > t_r \text{ minutes}. \end{cases}$$

Compute the altitude of the base of the

[redacted]

tube h_b (h_b is taken as the altitude of the base if $h_b > 200$ km):

$$h_b = h_{fb}(t') - R_{eq} \quad km.$$

Compute the length of the fireball up the tube in the direction of the magnetic field line, L_{up}:

$$L_{up} = 6\ (t - t')\ R_o + R_{fb} \quad km.$$

Compute the quantity L':

$$L' = \begin{cases} \dfrac{h_{fb} - h_b}{\sin \varphi} \ km & h_b \leqslant 200 \text{ km} \\ \dfrac{h_{fb} - 200}{\sin \varphi} \ km & h_b > 200 \text{ km}, \end{cases}$$

where φ is the magnetic dig angle at the burst location. If the magnetic dip angle is not known for the burst location, it can be determined from Figure 8-54. The length of the fireball down the tube will be the smaller of L_{up} and L'.

If the time of interest t is equal to or less than t_r, the time to reach maximum altitude, or if the maximum fireball altitude, h_m, is less than 200 kilometers, the debris altitude, h_d, is determined from the fireball altitude as described below. If the time of interest is equal to or greater than the time to reach maximum altitude ($t \geqslant t_r$), and the maximum fireball altitude is greater than 200 kilometers ($h_m > 200$), Figure 8-27 is entered with the quantity $(t - t_r)$ to obtain the debris height factor f_h. The debris altitude is then determined as follows:

$$h_d = \begin{cases} h_{fb} \ km \\ \quad t \leqslant t_r \text{ min} \\ h_m \ km \\ \quad t \geqslant t_r \text{ min}, \ h_m \leqslant 200 \text{ km} \\ [200 + f_h(h_m - 200)] \ km \\ \quad t \geqslant t_r \text{ min}, \ h_m \geqslant 200 \text{ km} \end{cases}$$

If the maximum fireball altitude, h_m, is equal to or less than 200 kilometers, the debris offset is zero (see Figure 8-17). If h_m is greater than 200 kilometers, enter Figure 8-28 with h_m and the magnetic dip angle, φ, to obtain the maximum debris offset D_d. Then enter Figure 8-29 with the quantity $(t - t_r)$ to obtain a value of the debris offset correction factor f_o. The debris offset, Δd, is:

$$\Delta d = f_o D_d \quad (h_m > 200 \text{ km}).$$

The radius of the debris is obtained from previously determined dimensions, as follows:

$$R_d = \begin{cases} R_{fb} \ km \\ \quad t \leqslant 120 \text{ minutes} \\ [R_{eq} + (7 - t')\ R_o \\ \quad + 3\ (t - 120)] \ km \\ \quad t > 120 \text{ minutes} \end{cases}$$

Example

Given: A 1 Mt weapon burst at an altitude of 100 km, at a location where the magnetic dip angle, φ, is 60°.

Find: The shape, size, and location of the fireball, and the altitude, radius, and offset of the debris region 20 minutes after the burst.

Solution:

a. From Figure 8-19, h_r = 800 km for a 1 Mt weapon burst at 100 km.

b. $h_m = h_r + h_o = 800 + 100 = 900$ km.

c. From Figure 8-20, t_r = 7 minutes for h_r = 800 km.

d. Since $t_r < t$,

$$h_{fb} = h_m = 900 \text{ km}$$

e. From Figure 8-23, R_o = 15 km for a 1 Mt burst at 100 km altitude.

f. From Figure 8-26, R_{eq} = 100 km for a 1 Mt weapon.

g. From Figure 8-24, t' = 0.9 min for R_o = 15 km and $R_{fb} = R_{eq}$ = 100 km.

h. Since $t > 7$ min, the fireball shape is a tube, and

$$R_{fb} = R_{eq} + (7 - t')\, R_o$$
$$= 100 + (6.1)(15) = 192 \text{ km}$$

i. From Figure 8-21, $h_N(t)$ = 0.25 for $t = t'$ = 0.9 min and h_r = 800 km.

j. Since $t' < t_r$,

$$h_{fb}(t') = h_o + h_N(t')\, h_r$$
$$= 100 + (0.25)(800) = 300 \text{ km.}$$

k. The height of the fireball base is

$$h_b = h_{fb}(t') - R_{eq} = 300 - 100 = 200 \text{ km}$$

l. The length up the fireball tube is

$$L_{up} = 6(t - t')\, R_o + R_{fb}$$
$$= (6)(19.1)(15) + 192 = 1911 \text{ km}$$

m. Since h_b = 200 km, the quantity L' is

$$L' = \frac{h_{fb} - h_b}{\sin \varphi} = \frac{900 - 200}{0.87} = 810 \text{ km}$$

n. Since $L' < L_{up}$

$$L_{down} = L' = 810 \text{ km.}$$

o. Since $t > t_r$ and $h_m > 200$ km, the quantity f_h must be determined from Figure 8-27. Entering Figure 8-27 with $t - t_r$ = 13, the quantity is determined to be

$$f_h = 0.9.$$

The altitude of the debris is, therefore,

$$h_d = 200 + f_h(h_m - 200)$$
$$= 200 + (0.9)(900 - 200) = 830 \text{ km.}$$

p. From Figure 8-28, the maximum debris offset D_d = 350 km for $\varphi = 60°$ and h_m = 900 km. From Figure 8-29, the debris offset correction factor is f_o = 0.1 for $(t - t_r)$ = 13 min. Therefore, the debris offset is

$$\Delta d = f_o D_d = (0.1)(350) = 35 \text{ km.}$$

q. Since $t < 120$ minutes,

$$R_d = R_{fb} = 192 \text{ km.}$$

Answer:

a. The fireball is a tube with dimensions as follows (refer to Figure 8-16):

$$h_{fb} = 900 \text{ km,}$$
$$R_{fb} = 192 \text{ km,}$$
$$L_{up} = 1911 \text{ km,}$$
$$L_{down} = 810 \text{ km.}$$

b. The debris region is a pancake with a radius of 192 km centered at an altitude of 830 km. It is offset 35 km towards the north pole from the burst point (refer to Figure 8-17).

Reliability The size and location of the fireball and debris, particularly late time debris expansion, are affected by atmospheric winds and diffusion. Since these effects are neglected in the model described herein, the results predicted by the model may be considerably in error.

Related Material See paragraph 8-14.

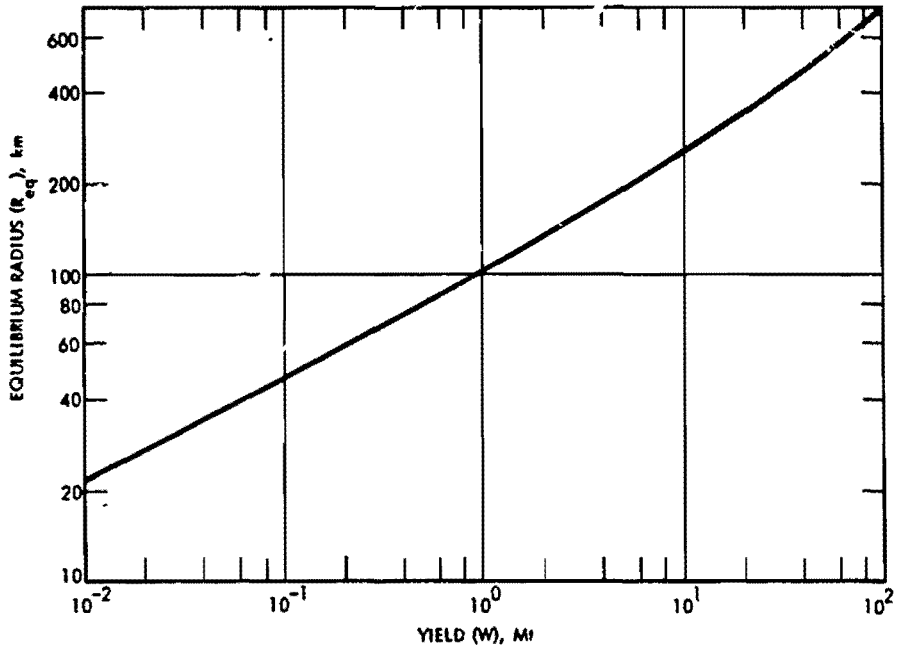

Figure 8-26. [redacted] Magnetic Equilibrium Radius [redacted]

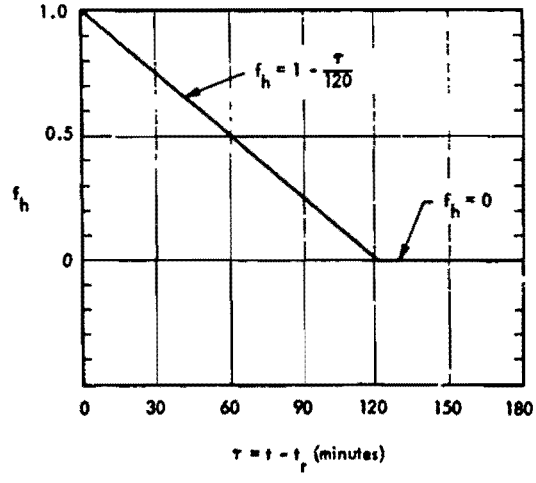

Figure 8-27. [redacted] Debris Height Factor [redacted]

[redacted]

[redacted]

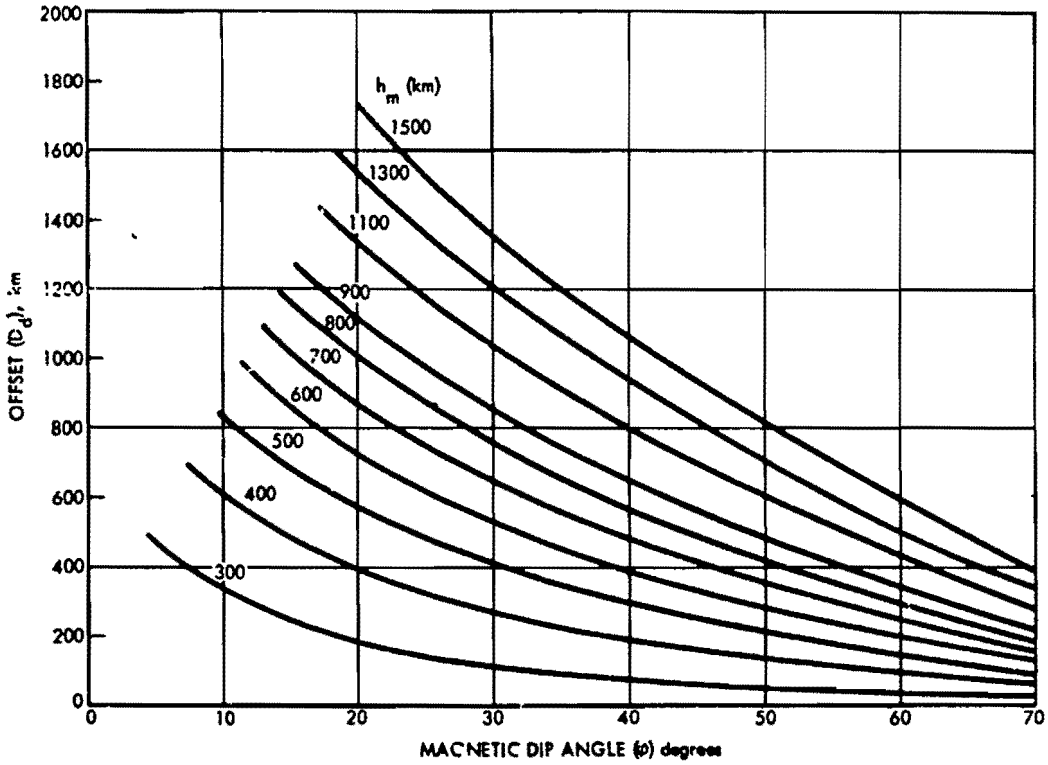

Figure 8-28. [redacted] Maximum Debris Offset [redacted]

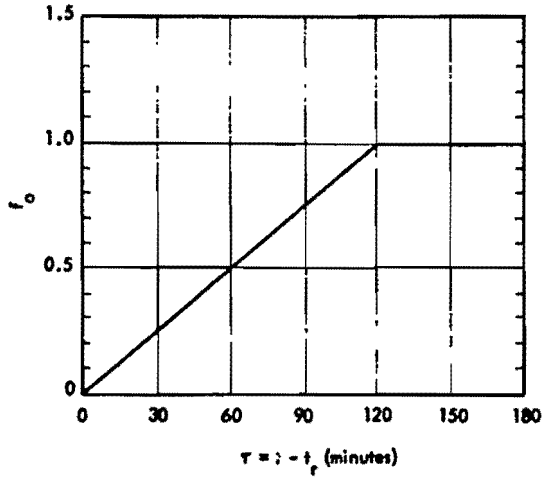

Figure 8-29. [redacted] Debris Offset Correction Factor [redacted]

[redacted]

[redacted]

Problem 8-3 Calculation of Size, Shape, and Location of Fireball and Debris Regions for a Burst Above 120 kilometers

[redacted] Table 8-2 and Figures 8-27 through 8-38 contain data with which estimates may be made of the size, shape, and location of the fireball and the debris regions for nuclear detonations above 120 kilometers. As discussed in paragraph 8-15 and shown in Figure 8-18, three separate debris regions are considered. Three shapes are used to model the fireball region: a sphere, a pancake, and a tube (cylinder) along the geomagnetic field. The shapes are illustrated in Figure 8-16.

[redacted] Table 8-2 is used to determine the fireball size, shape, and location (note that time after burst is given in *seconds* in Table 8-2). The table provides relations for a few parametric yields and detonation altitudes. In view of the uncertainties in both theoretical and experimental data in this burst altitude regime, interpolation between sections of Table 8-2 is not warranted. Data provided in the table for the yield and altitude combination nearest to those desired should be used. If either the desired yield or the desired detonation altitude is midway between values given in the table, values for the next higher yield and/or detonation altitude should be used. The phenomenology is very uncertain for yields greater than 10 Mt. If estimates are required for yields greater than 10 Mt, the dimensions and location given for a 10 Mt burst should be used. Table 8-2 indicates the shape of the fireball for the various yields and burst altitudes as a function of time (in seconds) after burst. The size and location of the fireball are determined as described below.

1. If the fireball is a sphere, the fireball altitude, h_{fb}, and fireball radius, R_{fb}, are read directly from Table 8-2 for the time of interest.

2. If the fireball is a pancake, the fireball altitude, h_{fb}, and the fireball radius, R_{fb}, are read directly from Table 8-2 for the time of interest. The semithickness of the pancake in kilometers (see Figure 8-16) is equal to the value shown in the column headed "x" in Table 8-2. Together, these values provide the size and location of the fireball at the desired time.

3. If the fireball is a tube, the fireball altitude, h_{fb}, and fireball radius, R_{fb}, are once again read directly from Table 8-2. The fireball lengths up and down the tube (see Figure 8-16) are determined from the values in the columns headed "x" and "y" in Table 8-2, as follows:

$$L_{down} = \frac{h_{fb} - 200}{|\sin \varphi|} \text{ km, or}$$

$$L_{down} = \frac{x}{2|\sin \varphi|} \text{ whichever is smaller,}$$

$$L_{up} = \frac{y}{2|\sin \varphi|} \text{ km,}$$

where φ is the magnetic dip angle at the burst point. If the magnetic dip angle is not known, it can be obtained from Figure 8-54. A negative value for y in Table 8-2 means that both x and y are dimensions down the geomagnetic field and the fireball is below h_{fb}.

[redacted] Figures 8-30 through 8-38 contain families of curves with which the size and location of the three debris regions may be estimated. Once again, the uncertainties in the data are such that interpolation between figures is not warranted. Data on the figure for the yield nearest to that desired should be used. If the desired yield is midway between values provided, data for the next higher value should be used.

[redacted] The fraction of the total weapon debris in each of the debris regions is obtained by use of Figure 8-30 and the calculations described below. Enter Figure 8-30 with the magnetic dip angle φ and the altitude of detonation h_o to obtain the fraction of debris going to debris region

[redacted]

[redacted]

3, X (see Figure 8-18). Compute the fraction of the debris in each of the three regions as follows:

$$FF1 = \begin{cases} 0.8 - X & h_o \leq 250 \text{ km}, \\ 0.6 - X & h_o > 250 \text{ km}, \end{cases}$$

$$FF2 = \begin{cases} 0 & h_o \leq 250 \text{ km}, \\ 0.2 & h_o > 250 \text{ km}, \end{cases}$$

$$FF3 = X,$$

where FF1, FF2, and FF3 are the fractions of total weapon debris in regions 1, 2, and 3, respectively. The sum of the three fractions is always less than 1.0, since some debris is assumed to escape to long distances (see paragraph 8-15).

[redacted] The altitude, h_d, for debris region 1 is obtained from Figures 8-31 through 8-34 by selecting the figure with the yield closest to that desired, and by determining h_{d1} for the time and burst altitude of interest. The maximum altitude to which the debris rises in region 1, h_{m1} should also be obtained for use in determining the debris offset as described later.

[redacted] The debris radius, R_{d1}, for debris region 1 is obtained from Figures 8-35 through 8-38 by selecting the figure with the yield closest to that desired, and by determining R_{d1} for the time and burst altitude of interest.

[redacted] If $t \leq 10$ minutes, the offset for debris region 1, Δd, is zero. If $t > 10$ minutes, the offset of debris region 1 is determined as follows.

1. Obtain the maximum debris offset D_d from Figure 8-28 for $h_m = h_{m1}$, as determined above, and the magnetic dip angle, φ, of interest.
2. Calculate τ:

$$\tau = t - 10 \text{ min}.$$

Enter Figure 8-29 with τ to obtain the debris offset correction factor f_o.

3. The offset of debris region 1 is

$$\Delta d_1 = f_o D_d \text{ km}.$$

[redacted] Debris region 2 is only defined for bursts above 250 km. The size and location are determined by a series of steps, as follows. If $t \leq 10$ minutes, go to 2; otherwise go to 1.

1. Enter Figure 8-27 with $\tau = t - 10$ min to obtain the debris height correction factor f_h.
2. Compute the maximum altitude, h_{m2}, for debris region 2:

$$h_{m2} = h_o + 500\ W^{1/3} \text{ km}$$

Compute the altitude for debris region 2 at time t:

$$h_{d2} = \begin{cases} h_{m2} \text{ km} \\ \quad t \leq 10 \text{ min}, \\ 200 + f_h(h_o + 500\ W^{1/3} - 200) \text{ km} \\ \quad t > 10 \text{ min}, \end{cases}$$

where W is the weapon yield in megatons.

3. Compute the radius for debris region 2, R_{d2}:

$$R_{d2} = \begin{cases} 500\ W^{1/3} \text{ km} \\ \quad t \leq 120 \text{ min}, \\ 500\ W^{1/3} + 3\ (t - 120) \text{ km} \\ \quad t > 120 \text{ min}, \end{cases}$$

4. If $t \leq 10$ minutes, the debris offset, Δd_2, equals zero. If $t > 10$ minutes, Δd_2 is determined from Figures 8-28 and 8-29. Enter Figure 8-28 with magnetic dip angle, φ, and $h_m = h_{m2}$ to obtain D_d. Calculate τ:

$$\tau = t - 10 \text{ min}.$$

Enter Figure 8-29 to obtain the debris offset

[redacted]

correction factor, f_o. Calculate Δd_2, the debris offset for region 2:

$$\Delta d_2 = D_d f_o.$$

The debris altitude, radius, and offset for debris region 3 are assumed to be the same as those determined for debris region 1, but they are located in the magnetic conjugate area (see Figure 8-18).

Example

Given: A 1 Mt weapon detonated at 250 km altitude at a location where the magnetic dip angle is 60°.

Find: The shape, size, and location of the fireball, and the altitude, radius, and offset of the debris regions 2 minutes after the burst.

Solution:

a. Since the altitude of interest is midway between the altitudes provided in Table 8-2, the larger (300 km) is used. From the data provided in Table 8-2 for 1 Mt at a burst altitude of 300 km, the following values are obtained for t = 120 sec:

Fireball shape is a tube.

$$h_{fb} = 290 \text{ km}$$

$$R_{fb} = 150 \text{ km}$$

$$x = 160$$

$$y = 300$$

b.

(1) $$\frac{h_{fb} - 200}{|\sin \varphi|} = \frac{290 - 200}{0.87} = 103 \text{ km.}$$

(2) $$\frac{x}{2|\sin \varphi|} = \frac{160}{(2)(0.87)} = 92 \text{ km.}$$

Since the result obtained in (2) is less than that obtained in (1),

$$L_{down} = 92 \text{ km.}$$

$$L_{up} = \frac{y}{2|\sin \varphi|} = \frac{300}{(2)(0.87)} = 172 \text{ km.}$$

c. From Figure 8-30, the fraction of debris transported to debris region 3, X, is 0.2 for a burst altitude of 250 km. Therefore,

$$FF1 = 0.6$$

$$FF2 = 0$$

$$FF3 = 0.2$$

d. From Figure 8-33,

$$h_{dl} = 625 \text{ km, and}$$

$$h_{ml} = 800 \text{ km.}$$

e. From Figure 8-37,

$$R_{dl} = 150 \text{ km.}$$

f. Since $t < 10$ min, $\Delta d_1 = 0$.

g. Since the burst altitude is not greater than 250 km, no debris region 2 is defined.

h. The size and altitude of debris region 3 are the same as those of debris region 1, but debris region 3 is centered over the magnetic conjugate of the burst point.

Answer:

a. The fireball is a tube with the following dimensions (see Figure 8-16 for illustration of the meaning of the dimensions):

$$h_{fb} = 290 \text{ km}$$

$$R_{fb} = 150 \text{ km}$$

$$L_{down} = 92 \text{ km}$$

$$L_{up} = 172 \text{ km}$$

b. There are two debris pancake regions for use in determining delayed radiation effects. Debris region 1 is a pancake centered over the burst point with an altitude and radius of 625 km and 150 km, respectively. Debris region 3 is a pancake directly over the conjugate of the burst

[redacted]

[redacted]

point, and it has the same altitude and radius as debris region 1. Sixty percent of the fission debris is in debris region 1, and twenty percent is in debris region 3. (Twenty percent is assumed to escape to large distances.)

[redacted] *Reliabilit*[redacted] Because of the theoretical and experimental uncertainties concerning bursts above 120 km, together with the uncertainties introduced by using fixed parametric yield/detonation altitude combinations, results predicted by the model described above may be considerably in error.

[redacted] *Related Materia*[redacted] See paragraph 8-15.

[redacted]

Table 8-2 [redacted] Fireball Location and Dimensions for Detonations Above 80 km [redacted]

Time is in seconds, distances are in kilometers. E refers to the power of 10, e.g., 1.5E4 = 1.5×10^4.

10 kt, 150 km

t	Shape	h_{fb}	R_{fb}	x	y
1	Sphere	1.5E2	1.2E1		
3	"	1.6E2	1.3E1		
10	"	1.6E2	1.7E1		
30	Tube	1.9E2	2.2E1	3.0E1	3.0E1
60	"	2.1E2	2.6E1	6.0E1	6.0E1
120	"	2.4E2	3.2E1	1.0E2	1.0E2
300	"	2.6E2	5.1E1	1.4E2	2.2E2
600	"	2.7E2	6.3E1	1.6E2	4.4E2
900	"	"	"		6.4E2
1800	"	"	"		1.4E3

10 kt, 200 km

t	Shape	h_{fb}	R_{fb}	x	y
1	Sphere	2.0E2	1.8E1		
3	"	2.1E2	1.9E1		
10	Tube	"	2.2E1	4.0E1	4.0E1
30	"	2.3E2	2.3E2	5.0E1	5.0E1
60	"	2.6E	2.6E1	6.0E1	6.0E1
120	"	2.8E2	3.2E1	1.0E2	1.0E2
300	"	3.0E2	4.9E1	1.4E2	2.0E2
600	"	"	6.1E1	"	4.2E2
900	"	"	"	"	6.0E2
1800	"	"	"	"	1.3E3

10 kt, 300 km

t	Shape	h_{fb}	R_{fb}	x	y
1	Tube	3.1E2	3.2E1	4.0E1	4.0E1
3	"	"	"	"	"
10	"	3.2E2	3.3E1	5.0E1	5.0E1
30	"	3.4E2	3.5E1	6.0E1	6.0E1
60	"	3.7E2	3.8E1	8.0E1	8.0E1
120	"	4.0E2	4.5E1	1.4E2	1.4E2
300	"	4.2E2	6.5E1	2.6E2	2.6E2
600	"	4.3E2	7.8E1	4.0E2	4.8E2
900	"	"	"	"	7.0E2
1800	"	"	"	"	1.5E3

10 kt, 400 km

t	Shape	h_{fb}	R_{fb}	x	y
1	Tube	4.1E2	4.7E1	6.0E1	6.0E1
3	"	"	4.8E1	"	"
10	"	4.2E2	4.9E1	8.0E1	8.0E1
30	"	4.[illegible]2	5.1E1	1.0E2	1.0E2
60	"	[illegible]2	5.5E1	1.2E2	1.2E2
120	"	5.2E2	6.3E1	1.6E2	1.6E2
300	"	5.4E2	8.4E1	3.0E2	3.0E2
600	"	5.5E2	1.0E2	5.6E2	5.6E2
900	"	"	"	"	8.0E2
1800	"	"	"	"	1.9E3

Table 8-2 [redacted] Fireball Location and Dimensions for Detonations Above 80 km (Continued) [redacted]

Time is in seconds, distances are in kilometers. E refers to the power of 10, e.g., 1.5E4 = 1.5×10^4.

10 kt, 500 km

t	Shape	h_{fb}	R_{fb}	x	y
1	Tube	5.1E2	6.5E1	8.0E1	8.0E1
3	"	5.2E2	6.5E1	"	"
10	"	"	6.6E1	1.0E2	1.0E2
30	"	5.6E2	6.9E1	1.2E2	1.2E2
60	"	5.9E2	7.3E1	1.4E2	1.4E2
120	"	6.4E2	8.2E1	2.0E2	2.0E2
300	"	6.6E2	1.0E2	3.4E2	3.4E2
600	"	6.7E2	1.2E2	6.2E2	6.2E2
900	"	"	"	8.8E2	8.6E2
1800	"	"	"	"	1.9E3

100 kt, 150 km

t	Shape	h_{fb}	R_{fb}	x	y
1	Sphere	1.6E2	2.7E1		
3	"	"	2.9E1		
10	"	1.8E2	3.6E1		
30	Tube	2.3E2	4.8E1	8.0E1	8.0E1
60	"	2.9E2	5.5E1	1.2E2	1.2E2
120	"	3.9E2	6.8E1	2.0E2	2.0E2
300	"	4.8E2	1.0E2	4.4E2	4.4E2
600	"	"	1.3E2	5.2E2	8.4E2
900	"	"	"	"	1.2E3
1800	"	"	"	"	2.6E3

100 kt, 200 km

t	Shape	h_{fb}	R_{fb}	x	y
1	Sphere	2.1E2	4.0E1		
3	"	2.2E2	4.2E1		
10	Tube	2.3E2	4.7E1	6.0E1	6.0E1
30	"	2.7E2	5.1E1	8.0E1	8.0E1
60	"	3.3E2	5.6E1	1.2E2	1.2E2
120	"	4.2E2	6.8E1	2.0E2	2.0E2
300	"	4.8E2	1.0E2	4.2E2	4.2E2
600	"	"	1.2E2	5.2E2	7.8E2
900	"	"	"	"	1.2E3
1800	"	"	"	"	2.4E3

100 kt, 300 km

t	Shape	h_{fb}	R_{fb}	x	y
1	Tube	3.2E2	7.0E1	1.0E2	1.0E2
3	"	3.3E2	7.1E1	8.0E1	8.0E1
10	"	3.4E2	7.2E1	1.2E2	1.2E2
30	"	3.9E2	7.6E1	1.4E2	1.4E2
60	"	4.6E2	8.3E1	1.8E2	1.8E2
120	"	5.7E2	9 6E1	2.6E2	2.6E2
300	"	6.7E2	1 3E2	5.2E2	5.2E2
600	"	"	1.6E2	9.0E2	8 6E2
900	"	"	"	"	1.3E3
1800	"	"	"	"	2.9E3

Table 8-2 [redacted] Fireball L ocation and Dimensions for Detonations Above 80 km (Continued) [redacted]

Time is in seconds, distances are in kilometers. E refers to the power of 10, e.g., 1.5E4 = 1.5 x 10^4.

100 kt, 400 km

t	Shape	h_{fb}	R_{fb}	x	y
1	Tube	4.3E2	1.1E2	1.4E2	1.4E2
3	"	4.4E2	"	"	"
10	"	4.6E2	"	1.6E2	1.6E2
30	"	5.1E2	"	1.8E2	1.8E2
60	"	5.8E2	1.2E2	2.2E2	2.2E2
120	"	7.1E2	1.3E2	3.4E2	3.4E2
300	"	8.5E2	1.7E2	7.0E2	7.0E2
600	"	"	2.0E2	1.1E3	1.1E3
900	"	"	"	1.3E3	1.5E3
1800	"	"	"	"	3.3E3

100 kt, 500 km

t	Shape	h_{fb}	R_{fb}	x	y
1	Tube	5.5E2	1.4E2	2.0E2	2.0E2
3	"	"	1.5E2	"	"
10	"	5.7E2	"	"	2.2E2
30	"	6.3E2	"	2.4E2	2.4E2
60	"	7.1E2	1.6E2	3.0E2	3.0E2
120	"	8.5E2	1.8E2	5.0E2	5.0E2
300	"	1.0E3	2.2E2	6.4E2	8.0E2
600	"	"	2.5E2	1.1E2	1.2E3
900	"	"	"	1.6E2	1.8E3
1800	"	"	"	"	3.6E3

1 Mt, 150 km

t	Shape	h_{fb}	R_{fb}	x	y
1	Sphere	1.8E2	6.1E1		
3	"	1.9E2	6.4E1		
10	"	2.2E2	7.7E1		
30	Tube	3.0E2	1.1E2	1.4E2	1.4E2
60	"	4.2E2	1.2E2	2.2E2	2.2E2
120	"	6.5E2	1.4E2	3.6E2	3.6E2
300	"	1.1E3	2.0E2	8.0E2	8.0E2
600	"	1.2E3	2.5E2	1.4E3	1.4E3
900	"	"	"	2.0E3	2.0E3
1800	"	"	"	"	4.8E3

1 Mt, 200 km

t	Shape	h_{fb}	R_{fb}	x	y
1	Sphere	2.4E2	9.1E1		
3	"	2.5E2	9.5E1		
10	Tube	2.8E2	1.1E2	1.4E2	1.4E2
30	"	3.5E2	1.1E2	2.0E2	2.0E2
60	"	4.6E2	1.2E2	2.4E2	2.4E2
120	"	6.7E2	1.4E2	4.0E2	4.0E2
300	"	1.0E3	2.0E2	8.0E2	8.0E2
600	"	1.1E3	2.4E2	1.4E3	1.4E3
900	"	"	"	1.8E3	2.0E3
1800	"	"	"	"	4.6E3

Table 8-2 [redacted] Fireball Location and Dimensions for Detonations Above 80 km (Continued) [redacted]

Time is in seconds, distances are in kilometers. E refers to the power of 10, e.g., 1.5E4 = 1.5×10^4.

1 Mt, 300 km

t	Shape	h_{fb}	R_{fb}	x	y
1	Pancake	2.2E2	1.5E2	9.1E0	
3	"	"	"	1.7E1	
10	"	2.5E2	"	4.6E1	
30	Tube	2.9E2	"	1.1E2	1.1E2
60	"	"	"	1.6E2	1.6E2
120	"	"	"	"	3.0E2
300	"	"	"	"	6.5E2
600	"	"	"	"	2.4E3
900	"	"	"	"	3.6E3
1800	"	"	"	"	8.0E3

Mt, 400 km

t	Shape	h_{fb}	R_{fb}	x	y
1	Pancake	2.8E2	2.2E2	1.1E1	
3	"	2.9E2	"	2.2E2	
10	"	3.3E2	"	6.2E2	
30	Tube	3.9E2	"	2. E2	2.8E2
60	"	"	"	"	4.0E2
120	"	"	"	"	6.6E2
300	"	"	"	"	1.4E3
600	"	"	"	"	2.6E3
900	"	"	"	"	3.8E3
1800	"	"	"	"	8.2E3

1 Mt, 500 km

t	Shape	h_{fb}	R_{fb}	x	y
1	Pancake	3.4E2	3.0E2	1.2E1	
3	"	3.5E2	"	2.7E1	
10	"	4.0E2	"	8.0E1	
30	Tube	4.8E2	"	3.2E2	3.4E2
60	"	"	"	"	4.6E2
120	"	"	"	"	7.2E2
300	"	"	"	"	1.4E3
600	"	"	"	"	2.6E3
900	"	"	"	"	3.8E2
1800	"	"	"	"	8.2E3

10 Mt, 150 km

t	Shape	h_{fb}	R_{fb}	x	y
1	Sphere	2.5E2	1.5E2		
3	"	2.6E2	1.5E2		
10	"	2.9E2	1.7E2		
30	"	3.9E2	2.1E2		
60	"	5.2E2	2.7E2		
120	Tube	7.9E2	3.0E2	5.2E2	5.2E2
300	"	1.3E3	3.7E2	1.0E3	1.0E3
600	"	1.5E3	4.1E2	1.8E3	1.8E3
900	"	"	"	2.6E3	2.6E3
1800	"	"	"	"	5.6E3

Table 8-2 [redacted] Fireball Location and Dimensions for Detonations Above 80 km (Concluded) [redacted]

Time is in seconds, distances are in kilometers. E refers to the power of 10, e.g., 1.5E4 = 1.5×10^4.

10 Mt, 200 km

t	Shape	h_{fb}	R_{fb}	x	y
1	Sphere	3.4E2	2.2E2		
3	"	3.5E2	2.3E2		
10	"	3.8E2	2.4E2		
30	Tube	4.8E2	2.7E2	3.8E2	3.8E2
60	"	6.1E2	2.8E2	4.4E2	4.4E2
120	"	8.8E2	3.0E2	5.2E2	6.2E2
300	"	1.4E3	3.7E2	7.0E3	1.0E3
600	"	1.6E3	4.2E2	2.0E3	2.0E3
900	"	"	"	2.8E3	2.8E3
1800	"	"	"	"	5.6E3

10 Mt, 300 km

t	Shape	h_{fb}	R_{fb}	x	y
1	Pancake	1.6E2	3.1E2	7.6E0	
3	"	1.7E2	"	1.3E1	
10	"	1.8E2	"	3.1E1	
30	Tube	2.1E2	"	1.2E2	1.6E2
60	"	"	"	"	2.8E2
120	"	"	"	"	5.4E2
300	"	"	"	"	1.2E3
600	"	"	"	"	2.4E3
900	"	"	"	"	3.6E3
1800	"	"	"	"	8.0E3

10 Mt, 400 km

t	Shape	h_{fb}	R_{fb}	x	y
1	Pancake	2.0E2	4.7E2	8.6E0	
3	"	2.1E2	"	1.6E1	
10	"	2.3E2	"	4.1E1	
30	Tube	2.7E2	"	1.6E2	2.0E2
60	"	"	"	"	3.2E2
120	"	"	"	"	5.8E2
300	"	"	"	"	1.3E3
600	"	"	"	"	2.5E3
900	"	"	"	"	3.7E3
1800	"	"	"	"	8.1E3

10 Mt, 500 km

t	Shape	h_{fb}	R_{fb}	x	y
1	Pancake	2.4E2	6.4E2	9.6E0	
3	"	2.5E2	"	1.9E1	
10	"	2.8E2	"	5.1E1	
30	Tube	3.2E2	"	1.0E2	2.4E2
60	"	"	"	"	3.6E2
120	"	"	"	"	6.2E2
300	"	"	"	"	1.3E3
600	"	"	"	"	2.6E3
900	"	"	"	"	3.8E3
1800	"	"	"	"	8.2E3

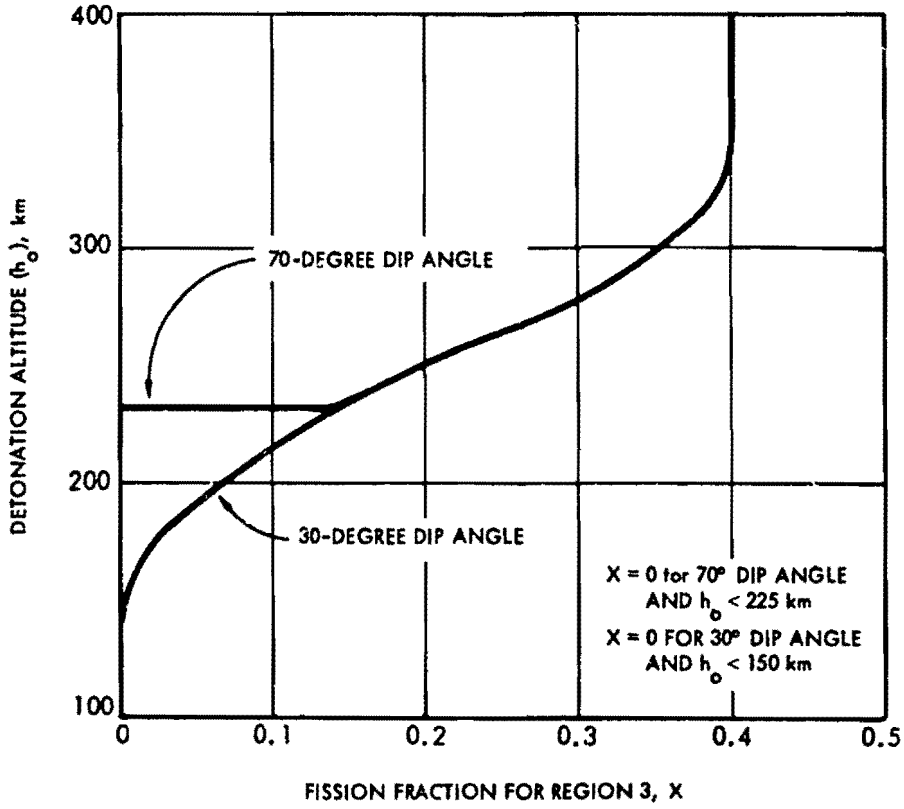

Figure 8-30. [redacted] Fraction of Total Debris Transported to Conjugate Region (Region 3) [redacted]

[redacted]

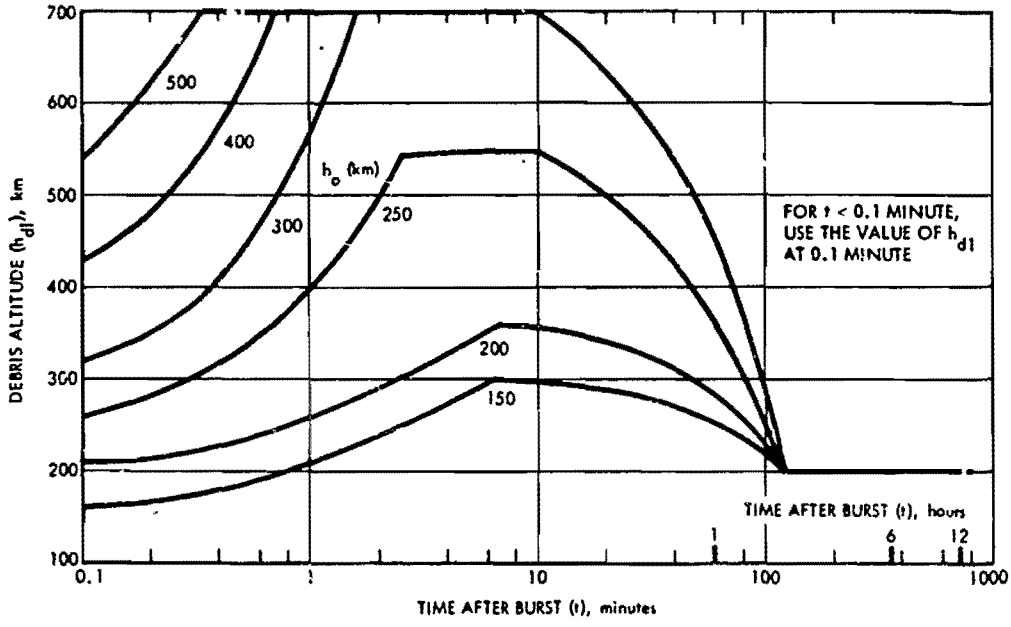

Figure 8-31. [redacted] Altitude of Debris Region 1, 10-kt Burst [redacted]

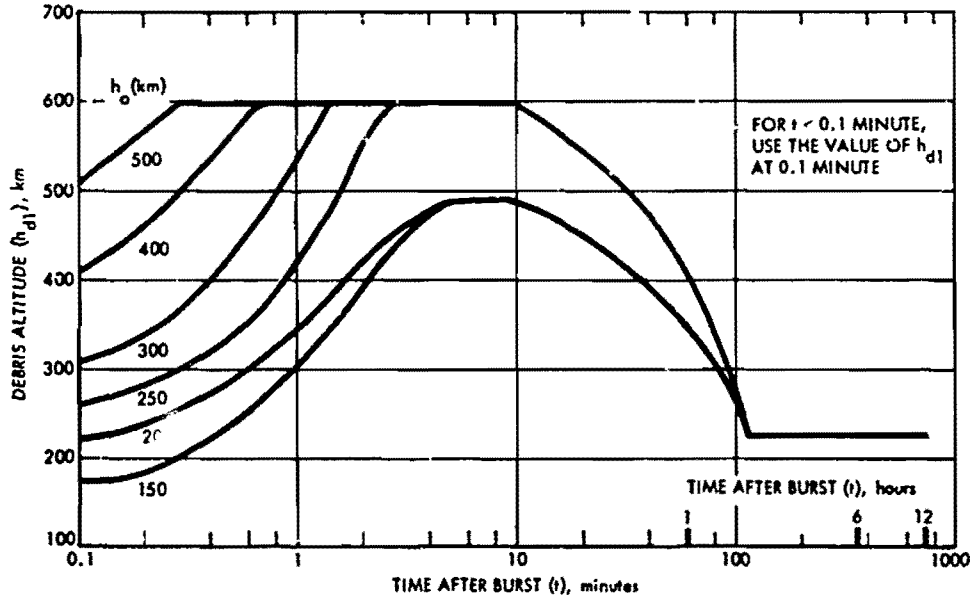

Figure 8-32. [redacted] Altitude of Debris Region 1, 100-kt Burst [redacted]

[redacted]

[redacted]

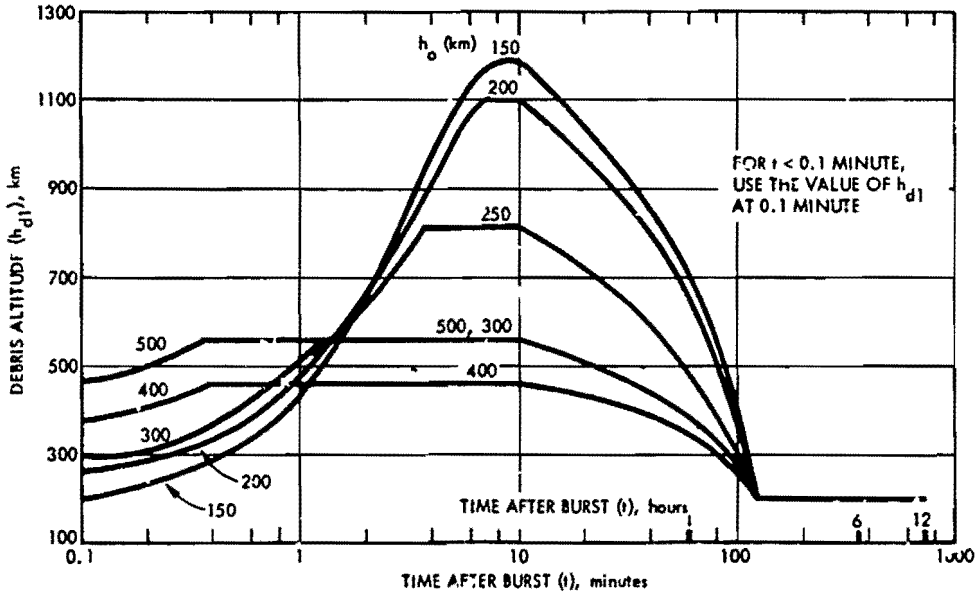

Figure 8-33. [redacted] Altitude of Debris Region 1, 1-Mt Burst [redacted]

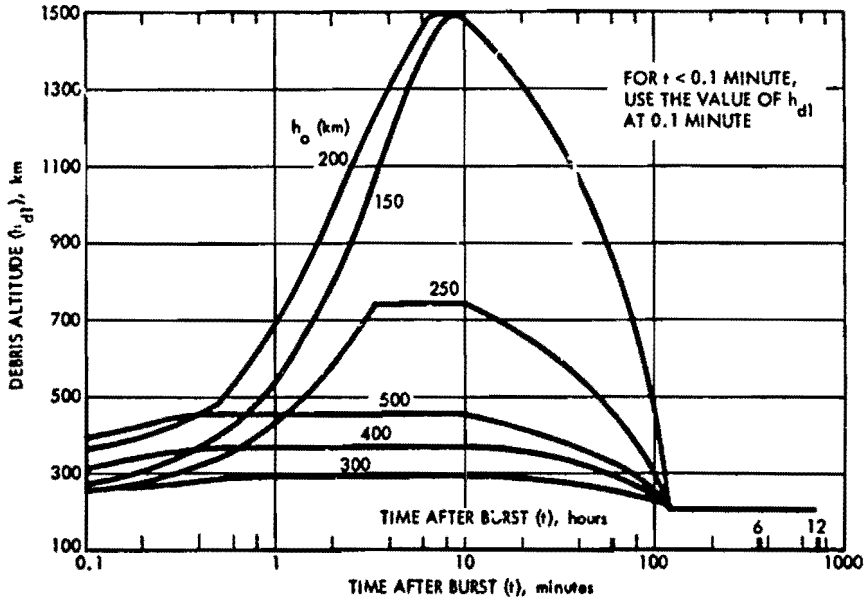

Figure 8-34. [redacted] Altitude of Debris Region 1, 10-Mt Burst [redacted]

[redacted]

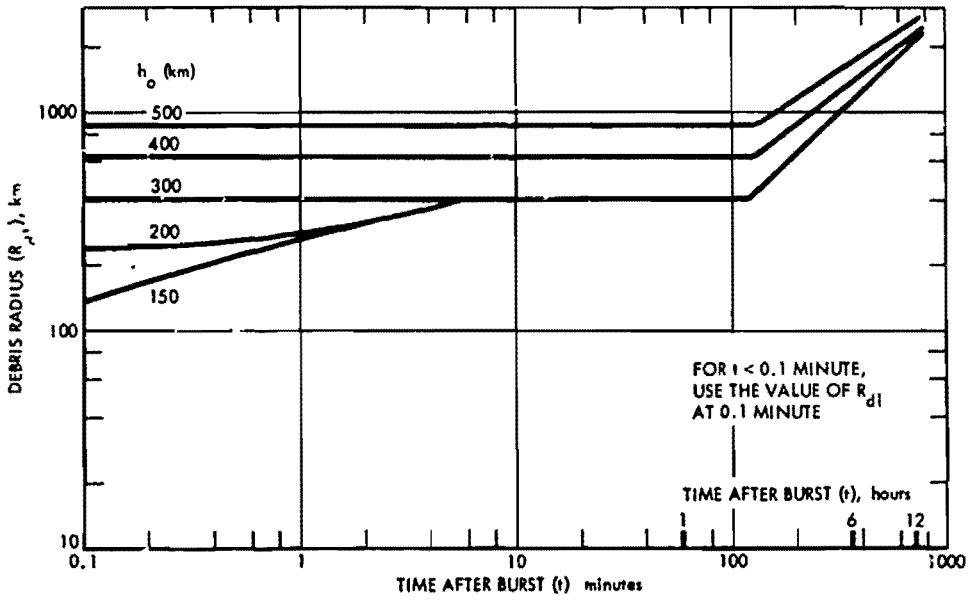

Figure 8-35. [redacted] Radius of Debris Region 1, 10-kt Burst [redacted]

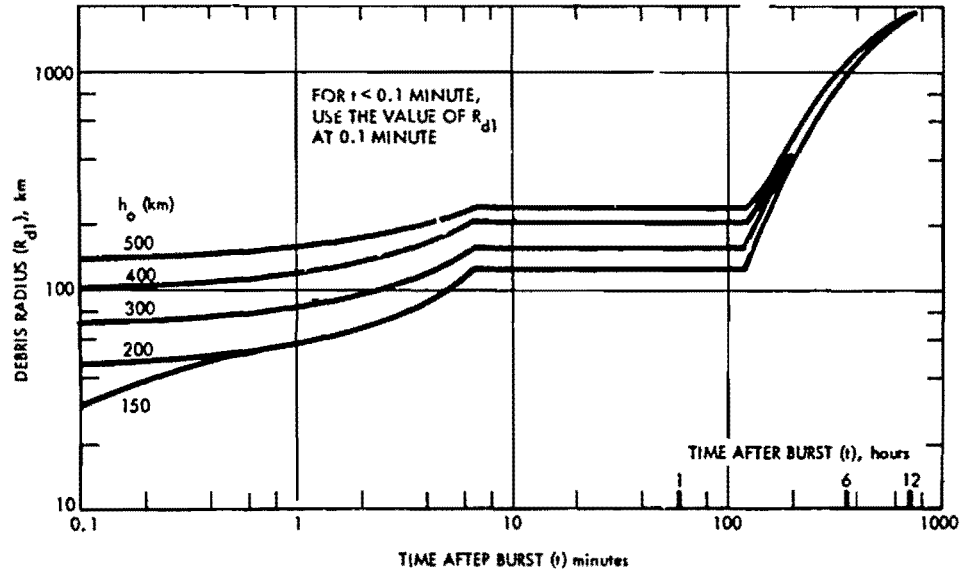

Figure 8-36. [redacted] Radius of Debris Region 1, 100-kt Burst [redacted]

[redacted]

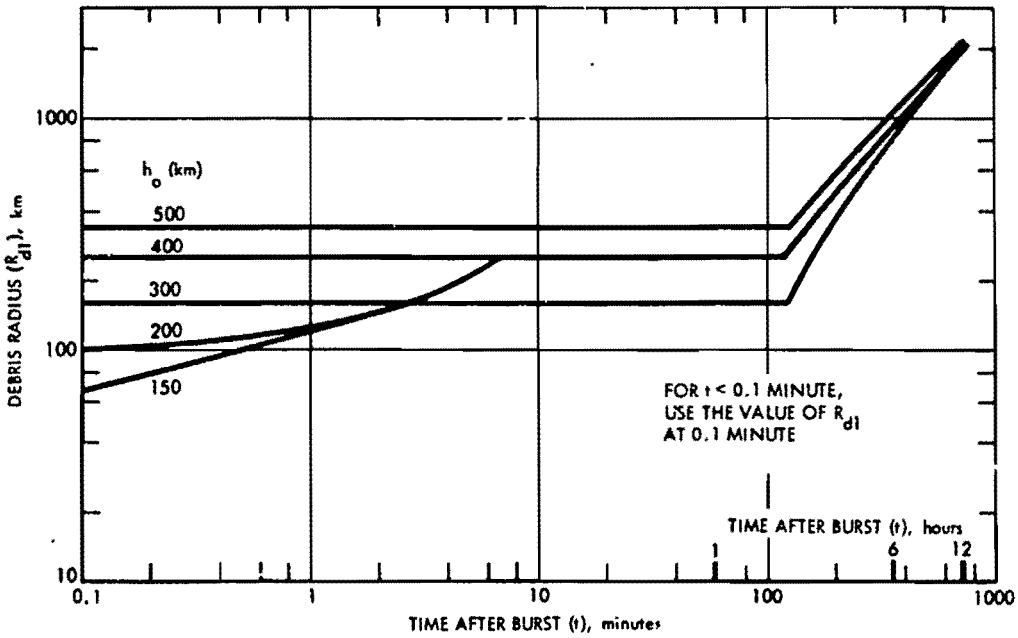

Figure 8-37. [redacted] Radius of Debris Region 1, 1-Mt Burst [redacted]

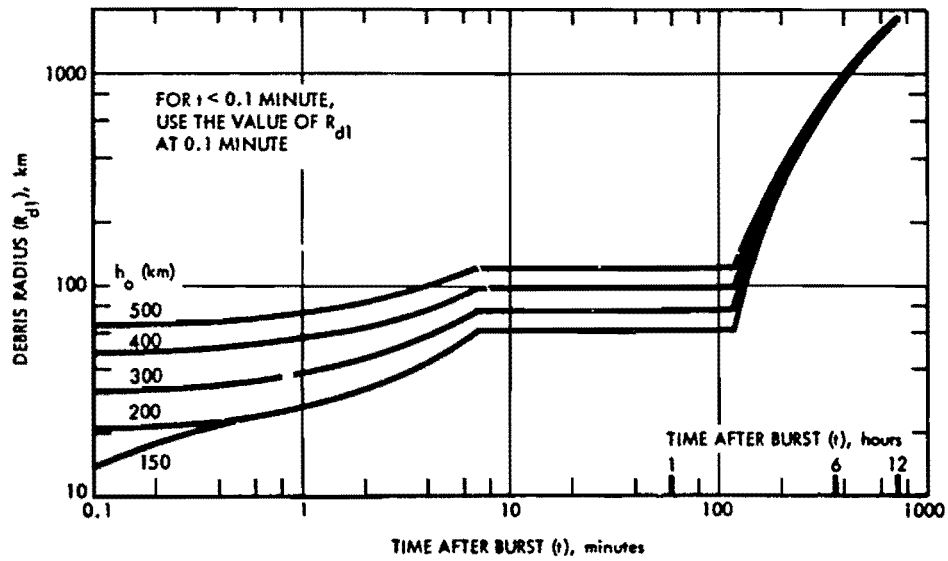

Figure 8-38. [redacted] Radius of Debris Region 1, 10-Mt Burst [redacted]

[redacted]

[redacted]

Problem 8-4 Absorption through the Fireball [redacted]

[redacted] Tables 8-3 through 8-7 and Figure 8-39 are used to obtain estimates of the absorption of signals propagating through the fireball for parametric burst yields and detonation altitudes. The temperature and electron density within the fireball are assumed to be uniformly distributed; thus, the absorption through the fireball is linearly dependent upon the distance the propagation path travels through the fireball. The fireball location and size can be determined from Table 8-2 and Figures 8-16 through 8-38, as described in Problems 8-1 through 8-3.

[redacted] The absorption data are given for a path length through the fireball equal to the fireball diameter if the fireball is a sphere, equal to the diameter of the toroid arm if the fireball is a toroid, equal to the vertical thickness of a pancake if the fireball is a pancake, or equal to the diameter of the tube if the fireball is a tube. For detonations that occur above about 50 km, the fireball absorption scales inversely with the square of the frequency.

[redacted] When the fireball is below an altitude of about 60 km, beta particles deposit their energy within the fireball, and they are the major source of ionization and absorption after the fireball has cooled to the atmospheric temperature. When the altitude of the fireball is greater than 60 km, absorption caused by beta-particle ionization should be determined by the methods described in Problem 8-7.

[redacted] Tables 8-3 through 8-6 provide data to determine absorption of signals propagating through the fireball of bursts that occur below 80 km at times after burst less than 300 seconds and fireball altitudes greater than 60 km (the fireball altitude at the time of interest may be obtained by the methods described in Problem 8-1). If the detonation altitude is below 50 km, the absorption A_{fb} is read directly from the table with the weapon yield closest to the desired yield at the closest detonation altitude, time after burst, and frequency given in the table. If the detonation altitude is 50 km or greater (but not greater than 80 km), the absorption for 1000 MHz, A'_{fb} is read from the appropriate table at the closest detonation altitude and time after burst. The absorption is then calculated as follows:

$$A_{fb} = A'_{fb} \frac{10^6}{f^2} ,$$

where f is the desired frequency in MHz.

[redacted] if the time after burst is greater than 300 seconds and the fireball altitude is less than 60 kilometers, the absorption of signals propagating through the fireball may be estimated from Figure 8-39. The quantity L'_a is obtained from Figure 8-39 for the appropriate fireball altitude and frequency. The absorption is then calculated as follows:

$$A_{fb} = L'_a \frac{N_\beta}{10^9} ,$$

where N_β is the beta particle radiation intensity parameter defined by equation 8.1 in paragraph 8-4.

[redacted] Table 8-7 provides data to determine absorption of signals propagating through the fireball of bursts that occur at altitudes above 80 km. The absorption of a 1000 MHz signal (A'_{fb}) is read from Table 8-7 for the weapon yield and altitude closest to those desired. The absorption at the desired frequency (A_{fb}) is then calculated as follows:

$$A_{fb} = A'_{fb} \frac{10^6}{f^2} ,$$

where f is the frequency in MHz.

[redacted]

[redacted]

Example 1

Given: A 1 Mt weapon burst at an altitude 50 km.

Find: The absorption of a 400 MHz signal propagating through the fireball 2 min after burst.

Solution: From Table 8-5, the absorption of a 1000 MHz signal 2 min after a burst at 50 km is

$$A'_{fb} = 0.2 \text{ dB};$$

therefore,

$$A_{fb} = (0.2)\frac{10^6}{(400)^2} = 1.25 \text{ dB}.$$

Answer: The absorption of a 400 MHz signal propagating through the fireball of a 1 Mt weapon 2 min after the weapon was detonated at an altitude of 50 km is 1.25 dB.

Example 2

Given: A 4 Mt weapon burst at an altitude of 150 km.

Find: The absorption of a 400 MHz signal propagating through the fireball 15 min after burst.

Solution: The yield and time nearest to those desired that are tabulated in Table 8-7 are 1 Mt and 10 min (600 sec). The absorption for a 1000 MHz signal 10 min after a 1 Mt burst at 150 km is

$$A'_{fb} = 3.2 \text{ dB};$$

therefore,

$$A_{fb} = (3.2)\frac{10^6}{(400)^2} = 20 \text{ dB}.$$

Answer: The absorption of a 400 MHz signal propagating through the fireball of a 4 Mt weapon 15 min after the weapon was detonated at an altitude of 150 km is approximately 20 dB.

Reliability The uncertainties in predicting fireball dimensions and electron density are such that estimates of the duration of a given level of absorption are uncertain by at least a factor of two. In general, the duration of absorption caused by the rising fireball will be determined by how long the fireball interdicts the propagation path, rather than the time period that the fireball remains absorbing at a given frequency.

Related Material See paragraph 8-6 and Problems 8-1 through 8-3.

[redacted]

[redacted]

Table 8-3 [redacted] Absorption (dB) Through Fireball for Detonations Below 80 km, W = 10 kt [redacted]

Time (sec)	Freq. (MHz)	Detonation Altitude (km)								
		0	10	20	30	40	50	60	70	80
10	100	8.5E3	2.0E4	2.7E5	9.1E6	1.7E7				
	400	8.5E3	1.9E4	2.4E5	2.5E6	1.4E6				
	1,000	8.5E3	1.9E4	1.4E5	5.0E5	2.2E5	1.4E5	1.1E3	3.8E2	1.7E2
	4,000	8.2E3	1.2E4	1.7E4	3.3E4	1.4E4				
	10,000	6.7E3	3.7E3	2.8E3	5.3E3	2.2E3				
20	100	3.1E3	1.2E4	2.9E4	5.2E4	3.0E5				
	400	3.2E3	1.2E4	2.4E4	1.2E4	2.2E4				
	1,000	3.1E3	1.2E4	1.3E4	2.3E3	3.6E3	1.3E4	3.7E2	1.0E2	2.7E1
	4,000	3.0E3	6.7E3	1.4E3	1.5E2	2.3E2				
	10,000	2.4E3	2.0E3	2.3E2	2.3E1	3.6E1				
30	100	7.4E2	8.5E3	2.2E4	3.8E4	1.5E4				
	400	7.4E2	8.4E3	1.8E4	7.5E3	1.1E3				
	1,000	7.3E2	8.0E3	8.7E3	1.4E3	1.7E2	7.5E1	2.7E2	4.2E2	8.8E0
	4,000	7.0E2	4.1E3	8.5E2	8.7E1	1.1E1				
	10,000	5.4E2	1.1E3	1.4E2	1.4E1	1.7E0				
40	100	7.3E1	3.2E3	1.7E4	2.9E4	9.9E3				
	400	7.3E1	3.1E3	1.4E4	5.0E3	6.9E2				
	1,000	7.3E1	3.0E3	6.0E3	8.9E2	1.0E2	1.7E1	1.8E1	2.0E1	3.8E0
	4,000	6.9E1	1.4E3	5.5E2	5.7E1	7.0E0				
	10,000	5.2E1	3.5E2	9.0E1	9.1E0	1.1E0				
50	100	4.6E0	4.7E2	1.2E4	2.3E4	7.0E3				
	400	4.6E0	4.7E2	8.6E3	3.5E3	4.8E2				
	1,000	4.6E0	4.3E2	3.5E3	6.1E2	7.6E1	1.1E1	1.1E1	2.2E0	1.9E0
	4,000	4.3E0	1.8E2	3.0E2	3.9E1	4.9E0				
	10,000	3.2E0	4.4E1	4.9E1	6.2E0	7.7E-1				
60	100	2.6E-1	3.9E1	3.8E3	1.8E4	5.1E3				
	400	2.6E-1	3.9E1	2.7E3	2.4E3	3.4E2				
	1,000	2.6E-1	3.5E1	1.0E3	4.1E2	5.5E1	8.0E0	6.6E0	1.3E0	1.1E0
	4,000	2.3E-1	1.4E1	8.3E1	2.6E1	3.4E0				
	10,000	1.7E-1	3.1E0	1.4E1	4.2E0	5.5E-1				
90	100	5.6E-3	4.8E-1	3.3E1	6.5E2	1.5E3				
	400	5.6E-3	4.6E-1	2.0E1	6.9E1	9.9E1				
	1,000	5.6E-3	4.0E-1	6.1E0	1.2E1	1.6E1	3.3E0	2.1E0	3.4E-1	7.7E-2
	4,000	5.0E-3	1.2E-1	4.5E-1	7.2E-1	9.9E-1				
	10,000	3.2E-3	2.4E-2	7.3E-2	1.2E-1	1.6E-1				
120	100		3.1E-1	1.7E1	2.2E-2					
	400		2.9E-1	8.4E0	1.9E-1					
	1,000		2.3E-1	2.2E0	3.2E0	1.7E0	9.0E-1	7.8E-1	1.1E-1	3.5E-2
	4,000		5.8E-2	1.7E-1	2.1E-1					
	10,000		1.0E-2	2.4E-2	3.2E-2					
150	100		2.7E-1	1.5E1	1.7E2					
	400		2.6E-1	6.4E0	1.4E1					
	1,000		2.0E-1	1.5E0	2.3E0	1.2E0	5.5E-1	4.3E-1	6.0E-2	2.3E-2
	4,000		3.8E-2	1.0E-1	1.4E-1					
	10,000		6.9E-3	1.7E-2	2.3E-2					
180	100		2.4E-1	1.3E1	1.3E2					
	400		2.2E-1	4.9E0	1.0E1					
	1,000		1.6E-1	1.1E0	1.7E0	8.8E-1	4.0E-1	2.6E-1	3.6E-2	1.6E-2
	4,000		2.6E-2	6.9E-2	1.0E-1					
	10,000		4.9E-3	1.2E-2	1.7E-2					
300	100		1.3E-1	5.7E0	5.0E1					
	400		1.2E-1	1.7E0	3.5E0					
	1,000		6.9E-2	3.2E-1	5.6E-1	3.4E-1	1.7E-1	4.4E-2	4.9E-3	1.2E-3
	4,000		8.2E-3	2.1E-2	3.5E-2					
	10,000		1.4E-3	3.3E-3	5.6E-3					

Notes: E refers to the power of 10, e.g., 1.5E4 = 1.5×10^4. If f^{-2} scaling applies, only 1,000 MHz values are given.

[redacted]

[redacted]

Table 8-4 [redacted] Absorption (dB) Through Fireball for Detonations Below 80 km, W = 100 kt [redacted]

Time (sec)	Freq. (MHz)	Detonation Altitude (km)								
		0	10	20	30	40	50	60	70	80
10	100	1.3E5	6.5E5	4.3E6	2.5E7	4.8E7				
	400	1.3E5	6.4E5	3.7E6	6.5E6	3.8E6				
	1,000	1.3E5	6.2E5	2.1E6	1.3E6	6.1E5	4.8E5	2.1E3	9.5E2	9.2E2
	4,000	1.2E5	3.7E5	2.3E5	8.2E4	3.8E4				
	10,000	1.0E5	1.1E5	3.9E4	1.3E4	6.1E3				
20	100	9.0E3	4.3E4	1.0E5	3.5E6	4.7E6				
	400	9.0E3	4.3E4	8.3E4	6.9E5	3.3E5				
	1,000	3.3E3	2.4E4	2.5E4	3.4E3	3.7E3	4.0E3	2.3E2	3.1E1	2.5E1
	4,000	8.6E3	2.2E4	3.9E3	8.0E3	3.4E3				
	10,000	6.8E3	6.0E3	6.5E2	1.2E3	5.4E2				
30	100	3.3E3	2.6E4	8.1E4	1.3E5	3.3E5				
	400	3.3E3	2.6E4	6.1E4	2.0E4	2.3E4				
	1,000	5.8E2	1.4E4	1.7E4	2.1E3	5.5E2	1.2E2	1.1E2	1.2E1	2.1E0
	4,000	3.1E3	1.1E4	2.2E3	2.2E2	2.3E2				
	10,000	2.3E3	2.8E3	3.7E2	3.5E1	3.7E1				
40	100	5.8E2	1.5E4	6.7E4	9.4E4	2.3E4				
	400	5.8E2	1.5E4	4.7E4	1.2E4	1.6E3				
	1,000	5.8E2	1.4E4	1.7E4	2.1E3	2.5E2	1.7E2	1.1E2	1.2E1	9.1E0
	4,000	5.4E2	5.5E3	1.4E3	1.3E2	1.6E1				
	10,000	4.0E2	1.3E3	2.3E2	2.1E1	2.5E0				
50	100	5.5E1	5.5E3	5.7E4	7.1E4					
	400	5.5E1	5.4E3	3.6E4	8.0E3					
	1,000	5.5E1	4.8E3	1.2E4	2.3E3	1.6E2	9.2E1	6.0E1	5.7E0	4.2E0
	4,000	5.0E1	1.7E3	8.8E2	8.5E1					
	10,000	3.5E1	3.6E2	1.4E2	1.4E1					
60	100	4.0E0	8.9E2	4.2E4	5.5E4					
	400	4.0E0	8.7E2	2.4E4	5.5E3					
	1,000	4.0E0	7.5E2	6.9E3	9.1E2	1.1E2	1.4E1	3.3E1	3.0E0	2.2E0
	4,000	3.6E0	2.2E2	5.0E2	5.7E1					
	10,000	2.4E0	4.5E1	8.1E1	9.1E0					
90	100	2.3E-2	3.6E0	7.0E2	1.5E4					
	400	2.3E-2	3.5E0	2.8E2	1.2E3					
	1,000	2.2E-2	2.7E0	6.3E1	2.0E2	3.9E1	4.5E0	1.7E0	1.3E-1	5.4E-1
	4,000	2.0E-2	5.4E-1	4.3E0	1.2E1					
	10,000	1.1E-2	1.0E-1	6.9E-1	2.0E0					
120	100	1.4E-2	2.2E0	1.7E2	1.1E3					
	400	1.4E-2	2.0E0	4.7E1	8.0E1					
	1,000	1.4E-2	1.5E0	9.2E0	1.3E1	7.7E0	1.6E0	4.6E-1	4.8E-2	3.5E-2
	4,000	1.2E-2	2.1E-1	6.7E-1	9.1E-1					
	10,000	5.4E-3	3.3E-2	9.6E-2	1.3E-1					
150	100	1.2E-2	2.2E0	1.6E2	8.2E2					
	400	1.2E-2	2.0E0	3.4E1	5.6E1					
	1,000	1.2E-2	1.1E0	6.2E0	9.1E0	3.6E0	7.8E-1	2.2E-1	2.9E-2	1.7E-2
	4,000	9.0E-3	1.4E-1	4.0E-1	5.7E-1					
	10,000	4.0E-3	2.4E-2	6.4E-2	9.1E-2					
180	100	1.0E-2	2.2E0	1.5E2	6.1E2					
	400	1.0E-2	1.8E0	2.6E1	4.1E1					
	1,000	1.0E-2	9.8E-1	4.7E0	6.6E0	2.5E0	4.5E-1	1.2E-1	1.9E-2	7.9E-3
	4,000	7.2E-3	1.0E-1	2.9E-1	3.9E-1					
	10,000	3.0E-2	1.7E-2	4.8E-2	6.6E-2					
300	100	6.1E-3	1.7E0	8.5E1						
	400	6.1E-3	1.2E0	9.3E0						
	1,000	5.8E-3	4.2E-1	1.6E0	2.2E0	9.3E-1	8.6E-2	1.5E-2	2.6E-3	5.7E-4
	4,000	3.4E-3	3.4E-2	9.8E-2						
	10,000	1.0E-3	5.5E-3	1.6E-2						

Notes: E refers to the power of 10, e.g., 1.5E4 = 10^4. If f^{-2} scaling applies, only 1,000 MHz values are given.

[redacted]

[redacted]

Table 8-5 [redacted] Absorption (dB) Through Fireball for Detonations Below 80 km, W = 1 Mt [redacted]

Time (sec)	Freq. (MHz)	Detonation Altitude (km)								
		0	10	20	30	40	50	60	70	80
10	100	3.4E5	1.8E6	1.4E7	9.7E7	1.8E8				
	400	3.4E5	1.8E6	1.2E7	1.9E7	1.3E7				
	1,000	3.4E5	1.8E6	3.4E7	2.2E6	7.5E6	7.5E6	1.6E4	1.4E4	3.2E3
	4,000	3.3E5	1.0E6	6.2E5	2.2E5	1.4E5				
	10,000	2.7E5	3.0E5	1.0E5	3.5E4	2.2E4				
20	100	5.2E4	2.4E5	1.5E6	1.1E7	9.2E6				
	400	5.2E4	2.3E5	1.1E6	1.4E6	6.0E5				
	1,000	5.2E4	2.2E5	4.5E5	2.4E5	9.7E4	6.8E4	1.2E3	9.2E2	2.3E2
	4,000	5.0E4	1.0E5	3.8E4	1.5E4	6.0E3				
	10,000	3.8E4	2.6E4	6.3E3	2.4E3	1.0E3				
30	100	1.4E4	8.8E4	9.0E5	1.4E6	9.5E5				
	400	1.4E4	8.6E4	5.7E5	1.5E5	6.1E4				
	1,000	1.4E4	7.8E4	1.9E5	2.4E4	9.7E3	4.2E3	2.4E2	1.7E2	4.7E1
	4,000	1.3E4	3.0E4	1.4E4	1.5E3	6.0E2				
	10,000	1.0E4	6.8E3	2.3E3	2.5E2	9.7E1				
40	100	5.8E3	6.3E4	2.7E5	1.0E6	1.1E5				
	400	5.8E3	6.1E4	1.4E5	8.4E4	6.7E3				
	1,000	5.7E3	5.4E4	4.0E4	1.4E4	1.1E3	4.0E2	7.0E1	4.6E1	1.6E1
	4,000	5.3E3	1.7E4	2.9E3	8.6E2	1.7E1				
	10,000	3.7E3	3.4E3	4.6E2	1.4E2	1.1E1				
50	100	1.3E3	4.5E4	2.4E5	6.5E5	6.2E4				
	400	1.3E3	4.3E4	1.0E5	5.1E4	3.9E3				
	1,000	1.3E3	3.6E3	2.5E4	8.3E3	6.2E2	4.0E1	2.6E1	1.7E1	6.8E0
	4,000	1.1E3	8.9E3	1.7E3	5.2E2					
	10,000	7.4E2	1.7E3	2.7E2	8.3E1					
60	100	1.6E2	2.5E4	2.2E5	1.0E5					
	400	1.6E2	2.4E4	7.4E4	7.4E3					
	1,000	1.6E3	1.9E4	1.6E4	1.2E3	3.8E2	2.2E1	1.1E1	7.4E0	3.5E0
	4,000	1.4E2	3.8E3	1.1E3	7.5E1					
	10,000	8.7E1	6.9E2	1.7E2	1.2E1					
90	100	2.4E-1	2.2E2	7.8E4	3.4E4					
	400	2.4E-1	1.9E2	1.5E4	2.3E3					
	1,000	2.4E-1	1.2E2	2.6E3	3.6E2	2.4E1	4.5E0	1.6E0	1.3E0	6.4E-1
	4,000	1.9E-1	1.5E1	1.7E2	2.3E1					
	10,000	9.4E-2	2.6E0	2.7E1	3.6E0					
120	100	7.0E-2	2.7E1	3.1E3	7.6E3					
	400	7.0E-2	2.1E1	3.6E2	4.8E2					
	1,000	6.9E-2	9.3E0	6.1E1	7.8E1	6.8E0	2.0E-1	3.5E-1	3.2E-1	1.3E-1
	4,000	5.2E-2	9.6E-1	4.9E0	6.6E0					
	10,000	1.9E-2	1.4E-1	6.2E-1	7.8E-1					
150	100	6.9E-2	2.8E1	2.1E3						
	400	6.8E-2	1.9E1	2.0E2						
	1,000	6.6E-2	7.1E0	3.3E1	2.5E1	3.1E0	7.5E-2	3.2E-2	1.6E-1	9.5E-3
	4,000	4.3E-2	5.8E-1	2.1E0						
	10,000	1.4E-2	9.4E-2	3.4E-1						
180	100	6.8E-2	3.2E1	1.8E3						
	400	6.7E-2	1.9E1	1.5E2						
	1,000	6.5E-2	6.0E0	2.5E1	1.6E1	1.5E0	3.2E-2	1.8E-2	7.4E-2	3.9E-3
	4,000	3.6E-2	4.3E-1	1.5E0						
	10,000	1.1E-2	7.3E-2	2.5E-1						
300	100	5.2E-2	3.6E1	8.5E2						
	400	5.1E-2	1.2E1	5.8E1						
	1,000	4.6E-2	2.5E0	9.3E0	4.7E0	4.7E0	2.4E-3	3.3E-3	1.0E-3	1.8E-4
	4,000	1.7E-2	1.7E-1	5.8E-1						
	10,000	3.8E-3	2.7E-2	9.3E-2						

Notes: E refers to the power of 10, e.g., 1.5E4 = 1.5×10^4. If f^{-2} scaling applies, only 1,000 MHz values are given.

[redacted]

[redacted]

Table 8-6 [redacted] Absorption (dB) Through Fireball for Detonations Below 80 km, W = 10 Mt [redacted]

Time (sec)	Freq. (MHz)	Detonation Altitude (km)								
		0	10	20	30	40	50	60	70	80
10	100	1.2E6	7.4E6	8.4E7	8.8E8	1.0E10				
	400	1.1E6	7.4E6	6.2E7	2.9E8	5.2E9				
	1,000	1.1E6	7.0E6	2.5E7	6.0E7	1.4E9	1.2E10	7.8E4	2.5E4	8.2E3
	4,000	1.1E6	3.7E6	2.1E6	4.0E6	1.0E8				
	10,000	8.8E5	1.0E6	3.4E5	6.4E5	1.6E7				
20	100	1.3E5	6.6E5	1.2E7	5.0E7	1.8E8				
	400	1.3E5	6.4E5	4.9E6	4.5E6	1.2E7				
	1,000	1.3E5	5.9E5	1.1E6	7.3E5	2.0E6	8.8E6	4.8E3	1.6E3	5.9E2
	4,000	1.2E5	2.3E5	7.8E4	4.6E4	1.2E5				
	10,000	9.1E4	5.3E4	1.3E4	7.4E3	2.0E4				
30	100	9.0E4	5.3E5	4.3E6	2.4E6					
	400	8.9E4	5.1E5	1.1E6	1.6E5					
	1,000	8.9E4	4.4E5	2.2E5	2.6E4	4.5E4	7.1E4	7.4E2	2.5E2	1.2E2
	4,000	8.2E4	1.3E5	1.4E4	1.6E3					
	10,000	5.7E4	2.5E4	2.3E3	2.6E2					
40	100	6.8E4	4.7E5	3.4E6						
	400	6.8E4	4.4E5	6.1E5						
	1,000	6.7E4	3.5E5	1.1E5	4.0E3	1.8E3	2.3E3	1.8E2	6.7E1	3.9E1
	4,000	6.1E4	7.4E4	6.9E3						
	10,000	3.9E4	1.4E4	1.1E3						
50	100	2.1E4	4.3E5	2.7E6						
	400	2.1E4	4.0E5	3.4E5						
	1,000	2.1E4	2.8E5	5.9E4	1.4E3	2.5E2	5.9E1	6.0E1	2.4E1	1.7E1
	4,000	1.8E4	4.5E4	3.7E3						
	10,000	1.1E4	7.9E3	5.9E2						
60	100	9.2E3	2.0E5	2.0E6						
	400	9.2E3	1.7E5	2.1E5						
	1,000	9.1E3	1.1E5	3.4E4	6.9E2	9.2E1	1.6E1	2.4E1	1.1E1	1.7E0
	4,000	7.6E3	1.3E4	2.2E3						
	10,000	4.0E3	2.3E3	3.4E2						
90	100	7.4E1	7.7E4	2.3E5						
	400	7.3E1	5.4E4	1.7E4						
	1,000	7.2E1	2.1E4	2.7E3	1.4E2	8.9E2	1.3E0	3.1E0	1.8E0	2.0E-1
	4,000	5.1E1	1.7E3	1.7E2						
	10,000	2.0E1	2.8E2	2.7E1						
120	100	6.6E-1	1.3E3	6.2E4						
	400	6.5E-1	6.3E2	4.1E3						
	1,000	6.2E-1	1.6E2	6.5E2	6.8E0	1.2E0	1.7E-1	6.4E-1	6.1E-2	3.1E-2
	4,000	4.3E-1	2.0E1	5.2E1						
	10,000	1.0E-1	1.8E0	6.5E0						
150	100	5.5E-1	7.6E2							
	400	5.4E-1	2.5E2							
	1,000	5.1E-1	5.3E1	1.8E2	2.5E0	9.1E-2	5.3E-2	2.2E-2	1.1E-2	1.4E-2
	4,000	2.3E-1	3.5E0							
	10,000	5.6E-2	5.6E-1							
180	100	5.9E-1	8.2E2							
	400	5.7E-1	2.0E2							
	1,000	5.2E-1	3.8E1	9.6E1	1.0E0	2.7E-2	2.0E-2	2.2E-2	8.9E-3	4.5E-3
	4,000	1.9E-1	2.3E0							
	10,000	4.3E-2	3.9E-1							
300	100	6.5E-1	9.3E2							
	400	6.1E-1	9.8E1							
	1,000	4.6E-1	1.6E1	2.1E1	5.3E-2	5.8E-4	9.8E-4	4.0E-4	2.0E-4	2.7E-4
	4,000	8.7E-2	1.0E0							
	10,000	1.6E-2	1.6E-1							

Notes: E refers to the power of 10, e.g., 1.5E4 = 1.5×10^4. If f^{-2} scaling applies, only 1,000 MHz values are given.

[redacted]

[redacted]

Table 8-7 [redacted] Absorption (dB) Through Fireball at 1000 MHz for Detonations Above 80 km [redacted]

Time (sec)	Yield (Mt)	Detonation Altitude (km)								
		100	150	200	250	300	350	400	450	500
10	0.01	5.2E2	7.9E2	1.7E2	1.4E1	6.1E0	2.1E0	6.1E-1	2.0E-1	7.3E-2
	0.1	1.1E3	2.0E3	3.8E2	3.1E1	1.4E1	4.8E0	1.4E0	4.5E-1	1.6E-1
	1	3.2E3	5.4E3	9.0E2	5.0E1	5.5E0	7.9E-1	1.5E-1	3.3E-2	8.7E-3
	10	1.4E4	2.0E4	3.3E3	2.6E3	3.5E2	6.9E1	1.7E1	4.9E0	1.6E0
20	0.01	7.2E1	2.1E2	1.2E2	1.2E1	5.4E0	1.9E0	5.5E-1	1.8E-1	6.8E-2
	0.1	1.4E2	5.8E2	2.8E2	2.6E1	1.2E1	4.3E0	1.3E0	4.2E-1	1.5E-1
	1	4.1E2	1.8E3	6.7E2	4.3E1	5.1E0	7.6E-1	1.4E-1	3.2E-2	8.4E-3
	10	2.2E3	8.0E3	1.9E3	1.4E3	2.7E2	5.9E1	1.5E1	4.5E0	1.5E0
30	0.01	2.2E1	1.3E2	9.6E1	1.0E1	4.8E0	1.7E1	5.1E-1	1.7E-1	6.4E-2
	0.1	3.8E1	3.0E2	2.2E1	2.3E1	1.1E1	4.0E0	1.2E0	3.9E-1	1.5E-1
	1	1.2E2	7.2E2	5.3E2	4.6E1	6.2E0	1.0E0	2.0E-1	4.8E-2	1.3E-2
	10	6.6E2	4.0E3	1.5E3	3.2E3	8.4E2	2.2E2	6.5E1	2.1E1	7.4E0
40	0.01	9.2E0	8.8E1	7.7E0	9.1E0	4.4E0	1.6E0	4.7E-1	1.6E-1	6.0E-2
	0.1	1.5E1	2.0E2	1.8E2	2.1E1	1.0E1	3.7E0	1.1E0	3.7E-1	1.4E-1
	1	4.6E1	4.9E2	4.3E2	3.6E1	5.3E0	9.1E-1	1.8E-1	4.4E-2	1.2E-2
	10	2.7E2	2.3E3	1.2E3	1.0E3	5.9E2	1.7E2	5.4E1	1.8E1	6.5E0
50	0.01	4.6E0	6.4E1	6.4E1	8.2E0	4.0E0	1.5E0	4.4E-1	1.5E-1	5.7E-0
	0.1	7.1E0	1.5E2	1.5E2	1.9E1	9.2E0	3.4E0	1.0E0	3.5E-1	1.3E-1
	1	2.2E1	3.6E2	3.5E2	3.0E1	4.6E0	8.2E-1	1.7E-1	4.1E-2	1.1E-2
	10	1.4E2	1.4E3	1.0E3	1.3E3	4.4E2	1.4E2	4.5E1	1.6E1	5.8E0
60	0.01	2.3E0	4.9E1	5.4E1	7.5E0	3.7E0	1.4E0	4.2E-1	1.4E-1	5.4E-2
	0.1	4.8E0	1.1E2	1.2E2	1.7E1	8.6E0	3.2E0	9.7E-1	3.3E-1	1.3E-1
	1	1.1E1	2.7E2	3.0E2	2.4E1	4.1E0	7.4E-1	1.6E-1	3.9E-2	1.1E-2
	10	7.3E1	9.3E2	8.7E2	9.3E2	3.4E2	1.1E2	3.9E1	1.4E1	5.2E0
90	0.01	9.9E-1	2.7E1	3.6E1	6.0E0	3.1E0	1.8E0	3.6E-1	1.2E-1	4.7E-2
	0.1	1.5E0	6.0E1	8.2E1	1.4E1	7.1E0	2.7E0	8.4E-1	2.9E-1	1.1E-1
	1	3.7E0	1.4E2	2.0E2	1.5E1	2.9E0	5.7E-1	1.3E-1	3.2E-2	9.2E-3
	10	2.0E1	4.1E2	5.8E2	4.2E2	1.8E2	6.8E1	2.5E1	9.9E0	3.9E0
125	0.01	4.7E-1	1.6E-1	2.5E1	5.0E1	2.6E0	1.0E0	3.1E-1	1.1E-1	4.2E-2
	0.1	5.5E-1	3.5E1	5.7E1	1.1E1	6.0E0	2.4E0	7.4E-1	2.6E-1	9.9E-2
	1	1.5E0	8.3E1	1.4E2	9.7E0	2.1E0	4.4E-1	1.0E-1	2.7E-2	7.8E-3
	10	6.8E0	2.3E2	3.9E2	1.8E2	1.0E2	4.2E1	1.8E1	7.1E0	3.0E0
180	0.01	2.8E1	9.9E0	1.8E1	4.0E0	2.1E0	8.6E-1	2.7E-1	9.4E-2	3.7E-2
	0.1	2.1E-1	2.1E1	3.8E1	9.2E0	5.0E0	2.0E0	6.4E1	2.2E1	8.7E0
	1	5.6E-1	4.8E1	9.0E1	5.9E0	1.4E0	3.3E-1	8.0E-2	2.1E-2	6.4E-3
	10	2.6E1	1.3E2	2.5E2	6.8E1	5.0E1	2.5E1	1.1E1	4.9E0	2.1E0
300	0.01	4.5E-2	4.6E0	1.0E1	2.8E0	1.6E0	6.5E-1	2.1E-1	7.5E-2	2.9E-2
	0.1	5.9E-2	7.7E0	2.0E1	6.4E0	3.6E0	1.5E0	4.9E-1	1.8E-1	6.9E-2
	1	1.3E-1	2.0E1	4.5E1	2.4E0	7.0E-1	1.8E-1	4.9E-2	1.4E-2	4.4E-3
	10	5.6E-1	4.9E1	1.2E2	1.4E1	1.2E1	9.1E0	5.0E0	2.4E0	1.2E0
600	0.01	7.3E-3	9.3E-1	3.3E0	1.3E0	7.1E-1	3.1E-1	1.2E-1	4.6E-2	1.8E-2
	0.1	1.1E-2	1.6E0	5.8E0	2.6E0	1.6E0	8.1E-1	3.0E-1	1.1E-1	4.4E-2
	1	1.7E-2	3.2E0	1.2E1	4.1E-1	2.4E-1	7.6E-2	2.3E-2	7.2E-3	2.4E-3
	10	7.0E-2	1.2E1	3.6E1	1.6E0	1.5E0	1.4E0	1.1E0	8.5E-1	4.5E-1
2000	0.01	2.2E-4	2.7E-2	1.2E-1	1.1E-1	8.5E-2	5.1E-2	2.2E-2	9.1E-3	4.0E-3
	0.1	2.8E-4	5.3E-2	2.5E-1	2.4E-1	2.1E-1	1.3E-1	5.9E-2	2.6E-2	1.2E-2
	1	5.7E-4	1.2E-1	5.7E-1	1.2E-2	10.0E-3	7.0E-3	4.1E-3	1.7E-3	6.4E-4
	10	2.2E-3	5.2E-1	2.3E0	3.5E-2	3.7E-2	3.9E-2	3.8E-2	3.5E-2	3.0E-2

Note: E refers to the power of 10, e.g., 1.5E4 = 1.5×10^4.

[redacted]

[redacted]

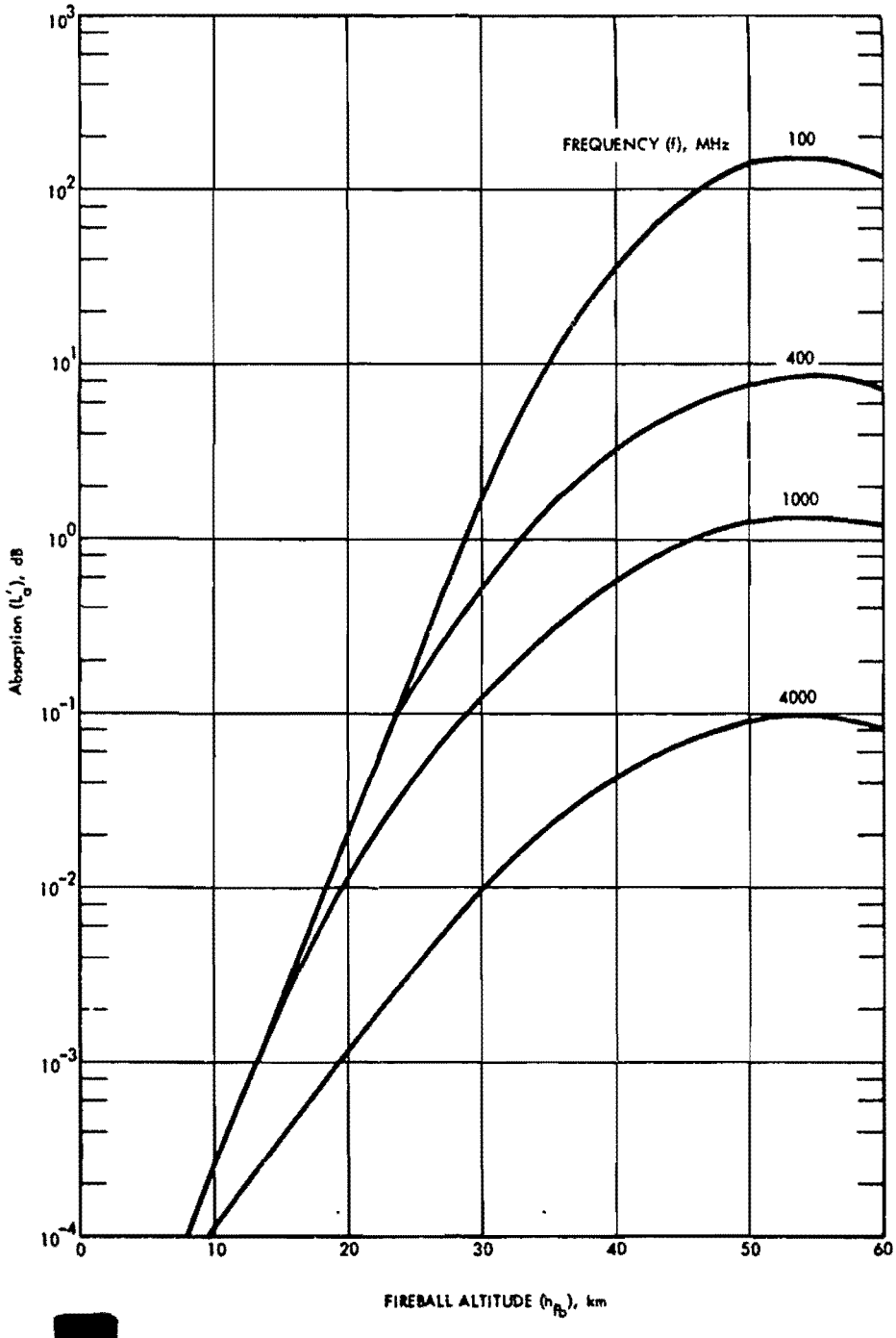

Figure 8-39. [redacted] One-Way Absorption Through Debris Region Due to Beta-Particle Ionization [redacted]

[redacted]

[redacted]

Problem 8-5 Absorption Due to Prompt Radiation Outside the Fireball [redacted]

[redacted] Figures 8-40 and 8-41 are used to obtain the one-way absorption along a propagation path caused by prompt radiation in terms of the one-way vertical absorption (the absorption for a single vertical traversal of the atmosphere) at a time t after burst. The absorption for the vertical path may be converted to that for an oblique path by using the secant of the angle of incidence at the altitude of peak absorption (approximately 65 km, see Problem 8-10).

[redacted] Using the detonation altitude and the ground range between the burst and the point where the propagation path intersects 65 km altitude, a reference yield W_r is obtained from Figure 8-40 (note that W_r differs for night and day). The location of the 65-km intersect point with respect to the propagation-path ground location can be determined from Figure 8-55 as described in Problem 8-10. If the actual weapon yield, W, is less than W_r, go to 2; otherwise go to 1.

1. Enter Figure 8-41 with time after burst in seconds and the radio frequency to obtain A_p', the one-way vertical absorption (note that the absorption differs for night and day). Go to 3.

2. Compute t_r:

$$t_r = \frac{W_r}{W} \text{ sec},$$

where W_r and W are both in Mt or kt. If $t > t_r$, go to 4; otherwise go to 3.

3. Enter Figure 8-41 with time after burst equal to t_r and the frequency to obtain $A_p'(t_r)$. Compute A_p':

$$A_p' = \frac{t_r A_p'(t_r)}{0.5t_r + 1.5t}.$$

Go to 5.

4. Enter Figure 8-41 with time after burst, t, and the frequency to obtain $A_p'(t)$. Compute A_p':

$$A_p' = \frac{tA_p'(t)}{t + t_r}.$$

5. Compute A_p, the one-way path absorption along the oblique path:

$$A_p = A_p' \sec \theta,$$

where $\sec \theta$ is the secant of the angle of incidence at 65 km determined from Figure 8-55.

[redacted] *Example 1* [redacted]

Given: A 1 Mt weapon detonated at an altitude of 300 km. The ground range between the burst and the propagation path is 800 km; the secant of the angle of incidence ($\sec \theta$) at 65 km is 3 for the propagation path.

Find: The one-way path absorption due to prompt radiation for a 100 MHz signal 10 seconds after the burst during the daytime.

Solution:

a. From Figure 8-40, W_r = 100 kt for a detonation altitude of 300 km and a ground range of 800 km.

b. Since $W_r < W$, A_p' is determined to be 12 dB from Figure 8-41.

c. $A_p = A_p' \sec \theta = (12)(3) = 36$ dB.

Answer: The one-way path absorption for a 100 MHz signal having a propagation path with an angle of incidence at 65 km whose secant is 3, resulting from prompt radiation from a 1 Mt weapon detonated at an altitude of 300 km, is 36 dB 10 seconds after burst at a ground range of 800 km from the burst point.

[redacted] *Example 2* [redacted]

Given: A 1 Mt weapon detonated at an

[redacted]

[redacted]

altitude of 200 km. The ground range between the burst and the propagation path is 1000 km; the secant of the angle of incidence (sec θ) at 65 km is 3 for the propagation path.

Find: The one-way path absorption due to prompt radiation for a 100 MHz signal 10 seconds after the burst during the daytime.

Solution:

a. From Figure 8-40, W_r = 5 Mt for a detonation altitude of 200 km and a ground range of 1000 km.

b. $t_r = \frac{W_r}{W} = 5.$

c. $t > t_r$; therefore, from Figure 8-41 $A_p'(t)$ = 12 dB, and

$$A_p' = \frac{tA_p'(t)}{t + t_r} = \frac{(10)(12)}{10 + 5} = 8 \text{ dB}.$$

d. $A_p = A_p' \sec \theta = (8)(3) = 24$ dB.

Answer: The one-way path absorption for a 100 MHz signal having a propagation path with an angle of incidence at 65 km whose secant is 3, resulting from prompt radiation from a 1 Mt weapon detonated at an altitude of 200 km, is 24 dB 10 seconds after burst at a ground range of 1000 km from the burst point.

[redacted] *Reliability* [redacted] The procedures given for computing absorption due to prompt radiation outside the fireball are based on simplified weapon design, atmospheric chemistry, and geometry models. More detailed models are required for specific communications and radar system problems.

[redacted] *Related Material* [redacted] See paragraph 8-2 and Problem 8-10.

[redacted]

[redacted]

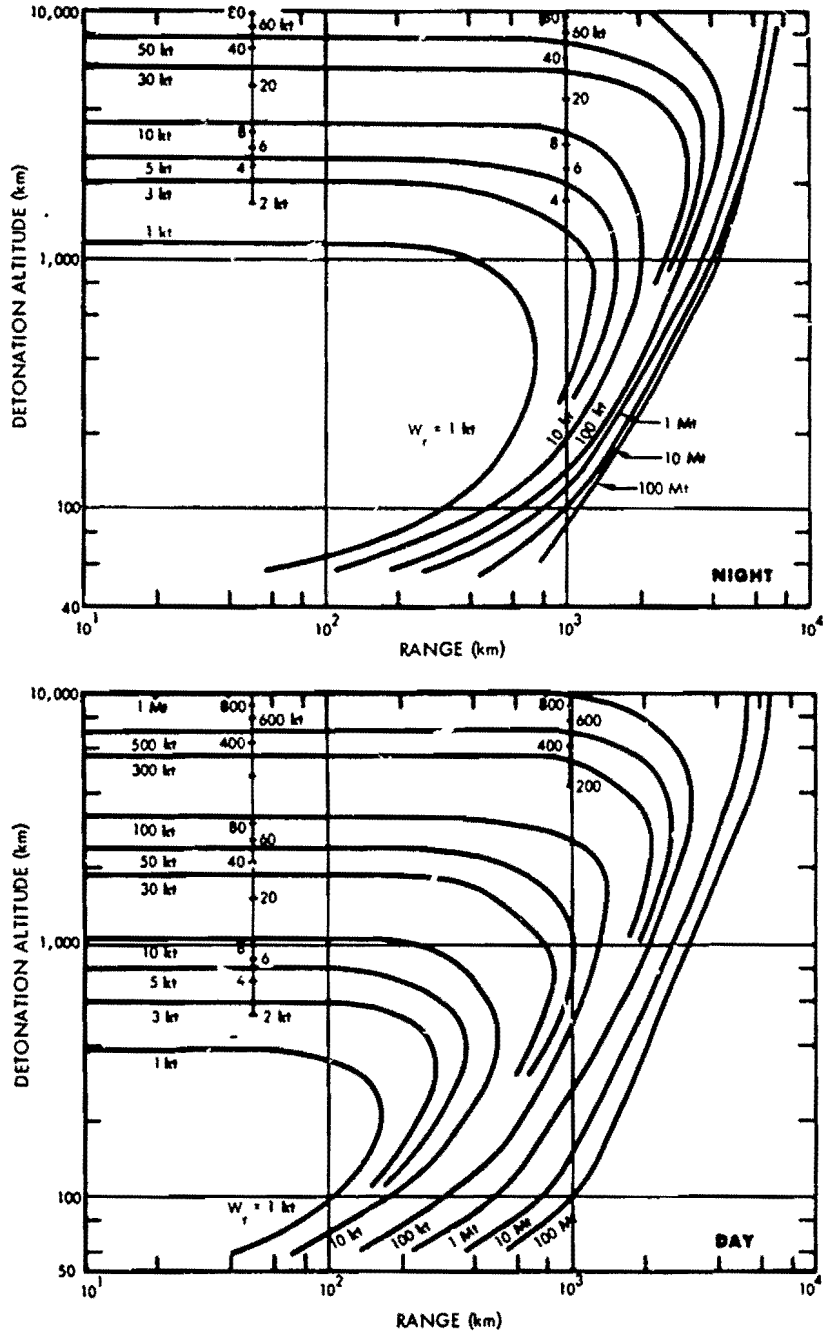

Figure 8-40. [redacted] Reference Weapon Yield W_r [redacted]

[redacted]

[redacted]

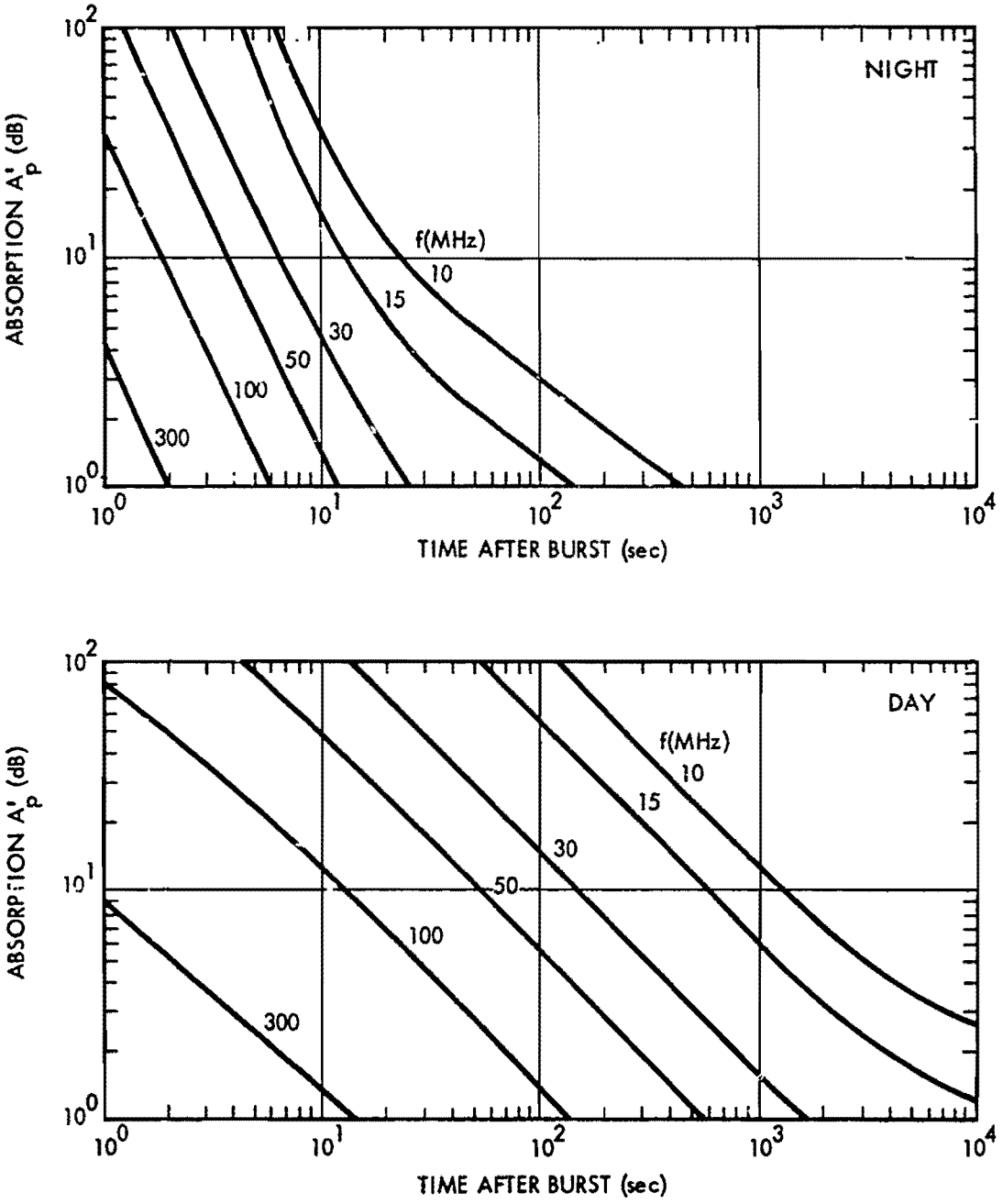

Figure 8-41. [redacted] One-Way Vertical Absorption Due to Prompt Radiation [redacted]

[redacted]

Problem 8-6 Absorption Outside the Fireball Due to Delayed Gamma Rays

Figures 8–42 through 8–48 are used to estimate the absorption caused by gamma rays emitted by the radioactive decay of fission debris. When the propagation path is within 100 km of the debris region and the debris region is below 120 km, the absorption depends on the orientation of the propagation path with respect to the debris region. Data are provided for three cases: a vertical path, a path passing above the debris region, and a path passing below the debris region. The geometry is illustrated in Figure 8–42.

If the debris is at an altitude greater than 120 km or if the propagation path passes farther than 100 km from the debris region, absorption caused by gamma rays is given in terms of the gamma ray intensity parameter, I_γ. In determining I_γ, the debris region is modeled as a thin pancake region. Methods to determine the altitude and radius of the pancake debris region as a function of the burst parameters are described in Problems 8–1 through 8–3. If the altitude of detonation is below 85 km, the debris region is centered over the burst point (see Problem 8–1). For higher detonation altitudes, the center of the debris region is offset horizontally from the burst point toward the nearest magnetic pole after reaching maximum altitude (see Problem 8–2 and Figure 8–17). If the detonation altitude is greater than 120 km, up to three debris regions are defined (see Problem 8–3 and Figure 8–18).

Figures 8–42 through 8–45 are used to obtain the one-way path absorption for bursts below 120 km and ground ranges from the debris less than 100 km. Choose the figure with the angle θ_d (see Figure 8–42) closest to the case of interest. Enter the figure with debris altitude, h_d, closest point of approach, X_d (see Figure 8–42), and time of day (day or night); obtain A_γ', the one-way path absorption for a 1000 MHz signal 10 seconds after a 1 Mt fission yield detonation. Compute A_γ, the one-way path absorption:

$$A_\gamma = A_\gamma' W_F \frac{18}{(1 + t)^{1.2}} \frac{10^6}{f^2}$$

where W_F is the fission yield in Mt, t is the time in sec, and f is the propagation frequency in MHz.

Figures 8–46 through 8–48 are used to obtain the one-way path absorption for bursts above 120 km or for cases where the ground range from the debris to the point where the propagation path intersects the altitude of 65 km is greater than 100 km. The following series of steps describe the procedure for obtaining the absorption.

1. Compute the quantity R', as follows:

$$R' = \begin{cases} \left[D^2 + (h_d - 60)^2\right]^{1/2} & D > R_d/2 \\ \left[\left(\frac{R_d}{2}\right)^2 + (h_d - 60)^2\right]^{1/2} & D \leq R_d/2 \end{cases}$$

where D is the ground range between the debris center and the point where the propagation path intersects 65 km altitude (see Figures 8–42 and 8–55 and Problem 8–10), and h_d and R_d are the debris altitude and radius, respectively (see Problems 8–1, 8–2, and 8–3).

2. Determine the debris-region fission yield W_F':

$$W_F' = W_F \qquad h_o \leq 120 \text{ km}$$

$$W_F' = FF\ W_F \qquad h_o > 120 \text{ km}$$

where FF is the fraction of the total weapon fission yield in the debris region (see Problem 8–3).

3. Enter Figure 8-46 with debris-region fission yield (W_F'), time after burst t, and R' to obtain I_γ'.

4. Enter Figure 8-47 with debris altitude h_d, debris radius R_d, and the ground range where the propagation path intersects 65 km altitude D, to obtain C_γ. Compute I_γ:

$$I_\gamma = C_\gamma I_\gamma'.$$

If there is more than one debris region (if the detonation is above 120 km or if there are multiple bursts), the radiation intensity parametric I_γ should be found for each debris region and the sum of the radiation intensity parameters used to obtain the absorption.

5. Enter Figure 8-48 with I_γ, time of day (day or night), and frequency to obtain A_γ', the one-way vertical absorption. Compute A_γ, the one-way path absorption:

$$A_\gamma = A_\gamma' \sec \theta$$

where sec θ is the secant of the angle of incidence at 65 km (see Problem 8-10).

[redacted] *Example 1* [redacted]

Given: A 1 Mt weapon, 50% fission (W_F = 0.5 Mt), detonated at an altitude of 30 km during the daytime.

Find: The one-way absorption resulting from gamma ray ionization for a 1000 MHz signal 2 min after burst if the ground range between debris center and the propagation path is less than 100 km, the closest point of approach of the propagation path to the debris center, X_d, is 20 km, and θ_d is 60° (see Figure 8-42).

Solution: By the methods described in Problem 8-1, the debris altitude is determined to be:

$$h_d = 49 \text{ km}.$$

From Figure 8-43, A_γ' = 14 dB for h_d = 49 km and X_d = 20 km. Therefore,

$$A_\gamma = A_\gamma' W_F \frac{18}{(1+t)^{1.2}} \frac{10^6}{f^2},$$

$$A_\gamma = (14)(0.5)\frac{18}{(121)^{1.2}}\frac{10^6}{10^6} = 0.4 \text{ dB}$$

Answer: The one-way path absorption for a 1000 MHz signal propagating on a path as described above 2 min after a daytime 1 Mt burst (W_F = 0.5 Mt) is 0.4 dB.

[redacted] *Example 2* [redacted]:

Given: A 1 Mt weapon, 50% fission, detonated at an altitude of 30 km during the nighttime.

Find: The one-way path absorption resulting from gamma ray ionization for a 100 MHz signal 2 min after burst if the ground range between the debris center and the point where the propagation path intersects 65 km is 200 km and sec θ = 3.

Solution:

a. By the methods described in Problem 8-1, the debris height, h_d, and radius, R_d, are determined to be:

$$h_d = 49 \text{ km},$$

$$R_d = 15 \text{ km}.$$

b. Since $D > R_d/2$,

$$R' = \left[D^2 + (h_d - 60)^2\right]^{1/2}$$

$$R' = \left[(200)^2 + (49 - 60)^2\right]^{1/2} \approx 200 \text{ km}$$

c. From Figure 8-46, I_γ' = 0.15 watts m^{-2}, for W_F = 0.5 Mt, $(1 + t)$ = 121 sec, and R' = 200 km.

d. From Figure 8-47, C_γ = 0.8 for $(D - R_d)$ = 185 km and h_d = 49 km. Therefore,

$$I_\gamma = C_\gamma' I_\gamma' = (0.8)(0.15) = 0.12 \text{ watts m}^{-2}$$

e. From Figure 8-48, $A_\gamma' = 1.0$ dB for $I_\gamma = 0.12$ watts m^{-2} and $f = 100$ Mc during the night. Therefore,

$$A_\gamma = A_\gamma' \sec\theta = 3.0 \text{ dB}.$$

Answer: The one-way path absorption for a 100 MHz signal propagating on a path as described above 2 min after a nighttime 1 Mt burst ($W_F = 0.5$ Mt) is 3.0 dB.

Example 3

Given: A 1 Mt weapon, 50% fission, detonated at an altitude of 300 km during the day at a location where the magnetic dip angle θ is 60°:

Find: The one-way path absorption resulting from gamma ray ionization for a 30 MHz signal 60 min after burst if the ground range between the point where the propagation path intersects 65 km is 1000 km due magnetic north of the burst point and sec $\theta = 3$.

Solution:

a. By the methods described in Problem 8-3, the height, h_d, radius, R_d, offset, Δd, and fraction of the debris, FF for the three debris regions (see Figure 8-18), are found to be:

Debris Region	h_d (km)	R_d (km)	Δ_d (km)	FF
1	390	170	75	0.25
2	550	500	125	0.2
3	390	170	75	0.35

Debris region 1 is centered 75 km magnetic north of the burst point. The ground range, D, between the debris center and the point where the propagation path intersects 65 km is 1000 – 75 = 925 km. The ground range between the center of debris region 2 and the propagation path is 875 km. Debris region 3 is offset 75 km south of the conjugate of the burst point and is too far from the propagation path to produce gamma ray ionization.

b. The quantity R' for debris region 1 is:

$$R_1' = \left[D^2 + (h_d - 60)^2\right]^{1/2}$$

$$= \left[(925)^2 + (330)^2\right]^{1/2} = 980 \text{ km}.$$

c. The debris region 1 fission yield is:

$$W_{F1}' = FF_1 \; W_F = 0.125 \text{ Mt}.$$

d. From Figure 8-46, $I_{\gamma 1}'$ is 2×10^{-5} watts m^{-2} for $W_{F1}' = 0.125$ Mt, $t = 3600$ sec, and $R_1' = 980$ km.

e. From Figure 8-47, $C_{\gamma 1}$ is 1 for $(D - R_d) = 775$ km and $h_d = 390$ km.

f. $I_{\gamma 1} = C_{\gamma 1} I_{\gamma 1}' = 2 \times 10^{-5}$ watts m^{-2}.

g. The quantity R' for debris region 2 is:

$$R_2' = \left[(875)^2 + (490)^2\right]^{1/2} = 1000 \text{ km}$$

h. The debris region 2 fission yield is:

$$W_{F2}' = FF_2 \; W_F = 0.1 \text{ Mt}$$

i. From Figure 8-46, $I_{\gamma 2}'$ is 1.5×10^{-5} watts m^{-2} for $W_{F2}' = 0.1$ Mt, $t = 3600$ sec, and $R_2' = 1000$ km.

j. From Figure 8-47, $C_{\gamma 2}$ is 1 for $(D - R_d) = 375$ km and $h_d = 550$ km.

k. $I_{\gamma 2} = C_{\gamma 2} I_{\gamma 2}' = 1.5 \times 10^{-5}$ watts m^{-2}.

l. $I_\gamma = I_{\gamma 1} + I_{\gamma 2} = 3.5 \times 10^{-5}$ watts m^{-2}.

m. From Figure 8-48, $A_\gamma' = 1$ dB for $I_\gamma = 3.5 \times 10^{-5}$ watts m^{-2} and $f = 30$ MHz.

n. $A_\gamma = A_\gamma' \sec\theta = 3$ dB.

Answer: The one-way path absorption for a 30 MHz signal propagating on a path as described above 60 min after a daytime burst ($W_F = 0.5$ Mt) is 3 dB. If the propagation path had been located near the conjugate of the burst point, gamma rays from debris regions 1 and 2 would not reach the path, and only debris region 3 would have been considered.

[redacted]

[redacted] *Reliability* [redacted] The procedures given for computing absorption due to gamma ray ionization are based on simplified-debris, atmospheric-chemistry, and geometry models. More detailed models are required for most radar and communication system problems.

[redacted] *Related Material* [redacted] See paragraphs 8-3, 8-8, 8-13, 8-14, and 8-15, and Problems 8-1, 3-2, and 8-3.

[redacted]

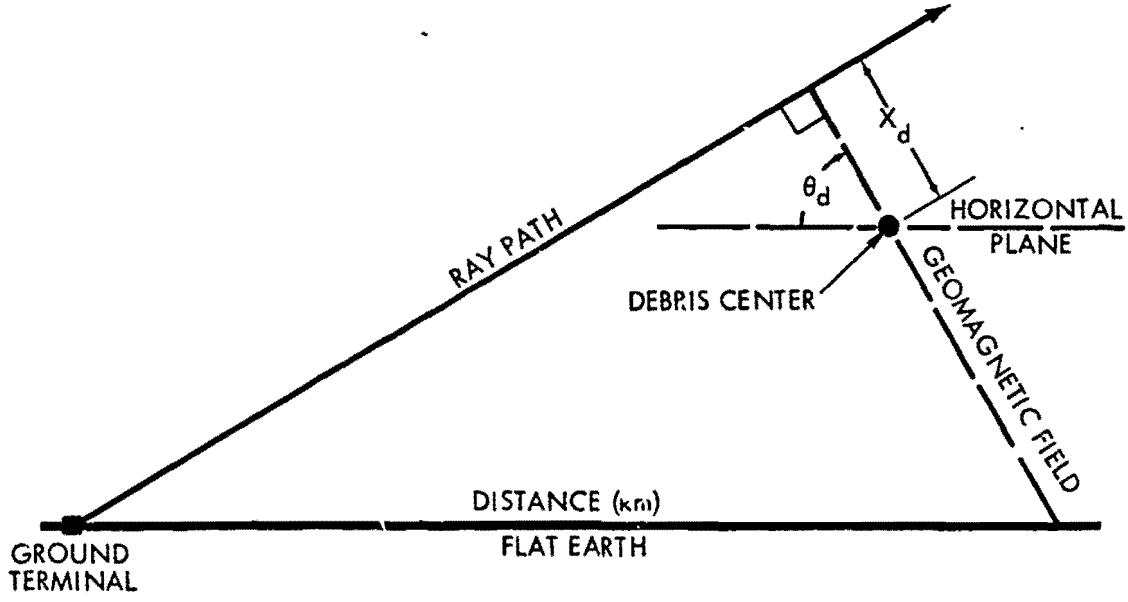

Figure 8-42. Geometry for Gamma Ray Absorption

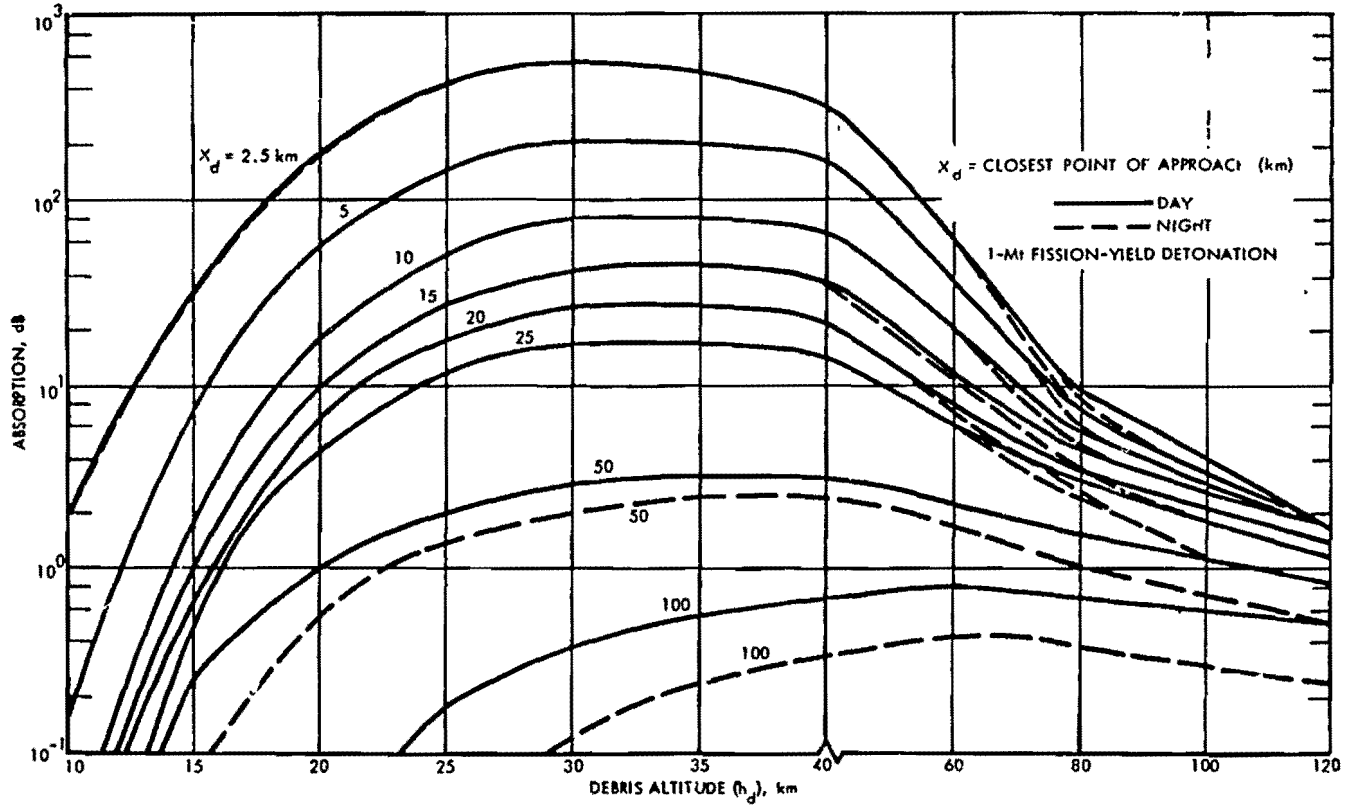

Figure 8-43. [redacted] One-Way Absorption Due to Gamma Rays, f = 1000 MHz, θ_d = +60 Degrees [redacted]

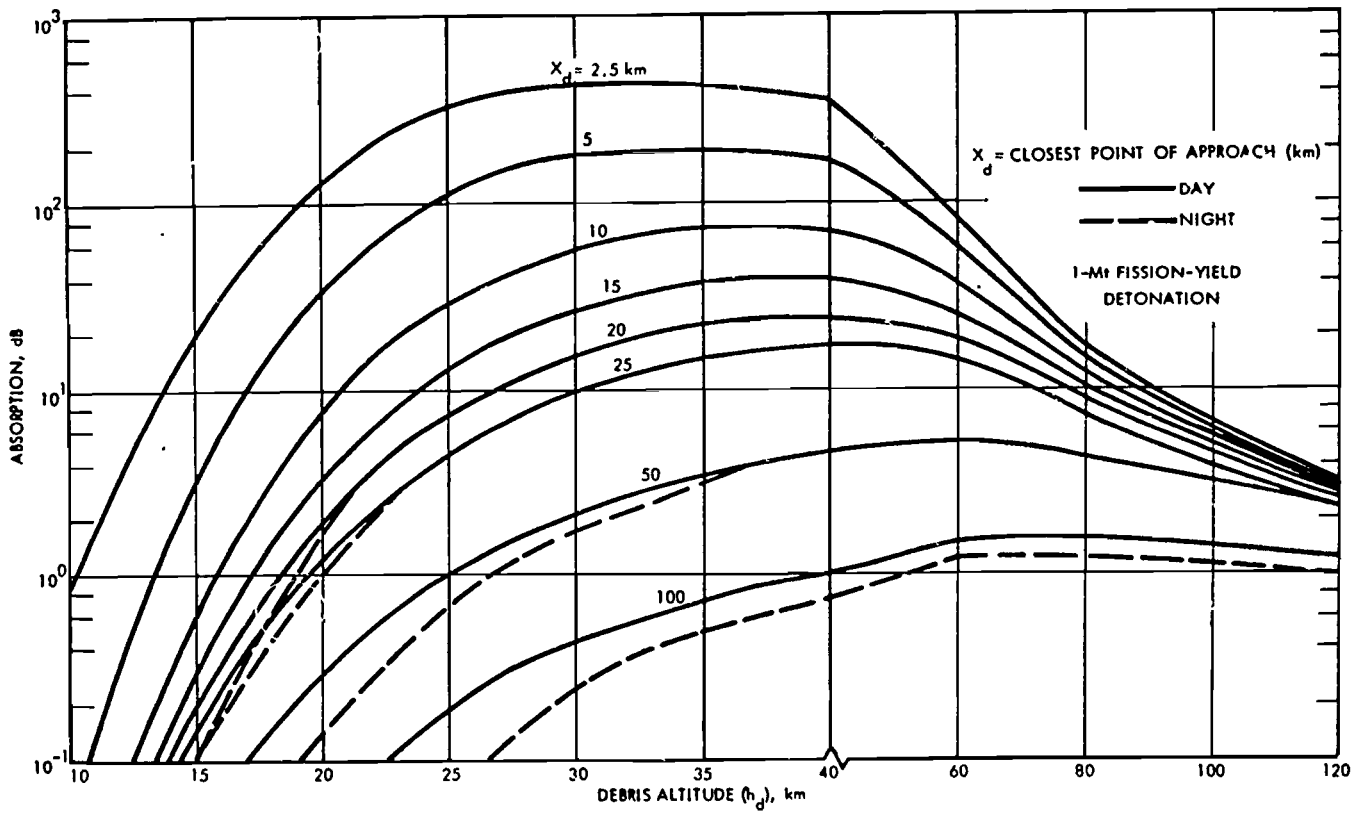

Figure 8-44. [redacted] One-Way Absorption Due to Gamma Rays, f = 1000 MHz, θ_d = 0 Degrees [redacted]

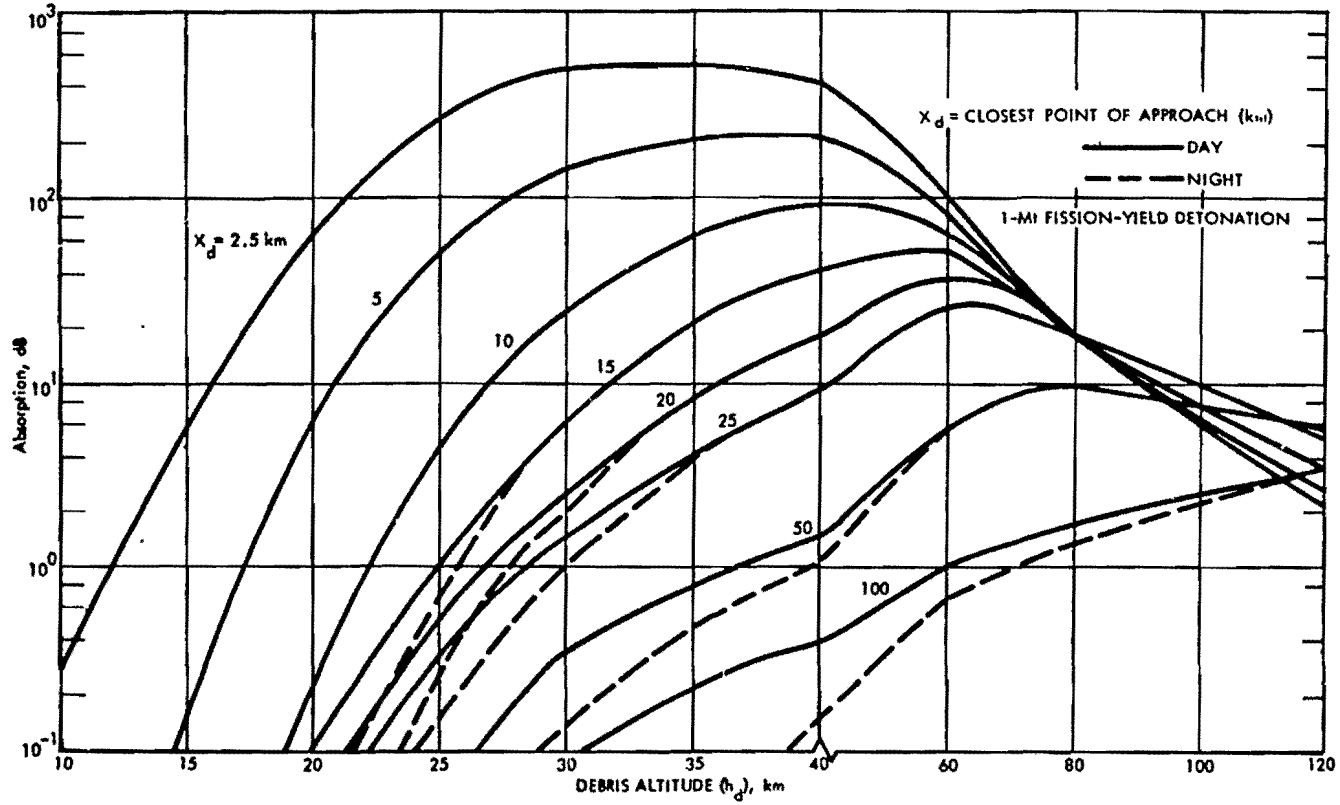

Figure 8-45. [redacted] One-Way Absorption Due to Gamma Rays, f = 1000 MHz, θ_d = -60 Degrees [redacted]

[redacted]

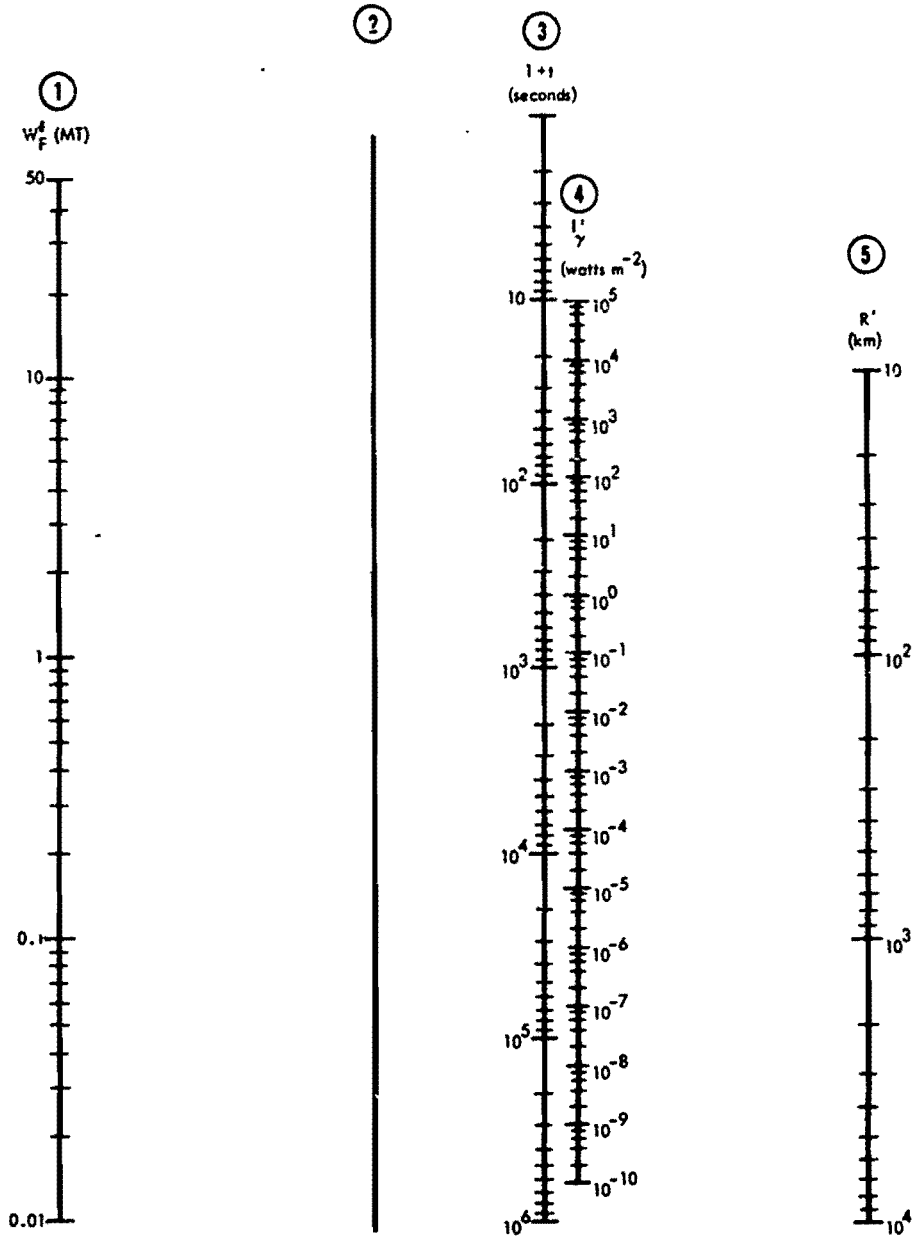

INSTRUCTIONS: To find I'_γ connect a straight line from fission yield (Scale 1) to time after detonation on Scale 3 (note this is a 1+t scale). Mark the intersection on Scale 2. Connect a straight line from the point determined on Scale 2 to the appropriate distance, R', on Scale 5. The intersection with Scale 4 is I'_γ.

Figure 8-46. [redacted] Gamma Radiation Intensity Nomogram [redacted]

[redacted]

[redacted]

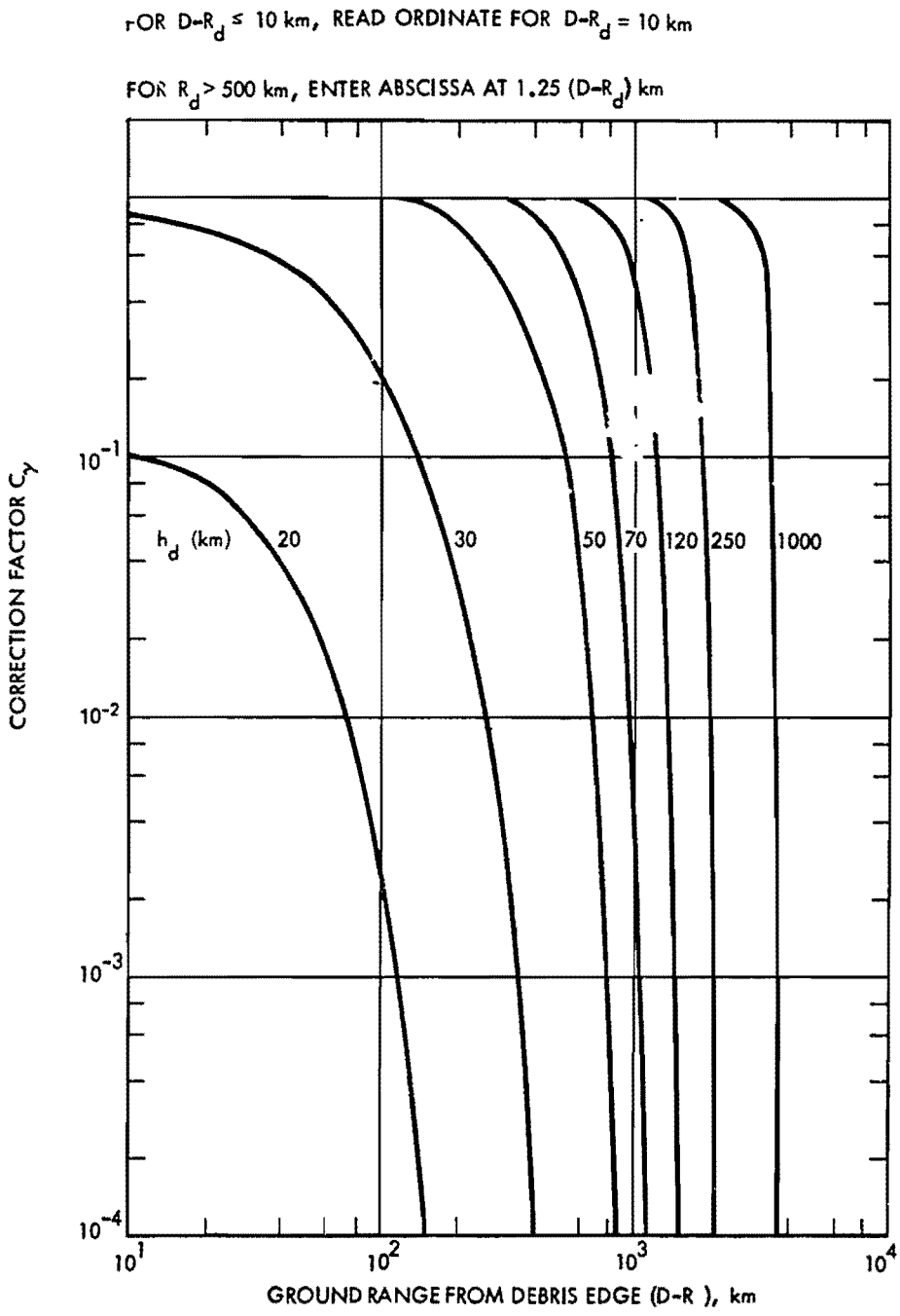

Figure 8-47. [redacted] Correction Factor for Gamma Ray Flux [redacted]

[redacted]

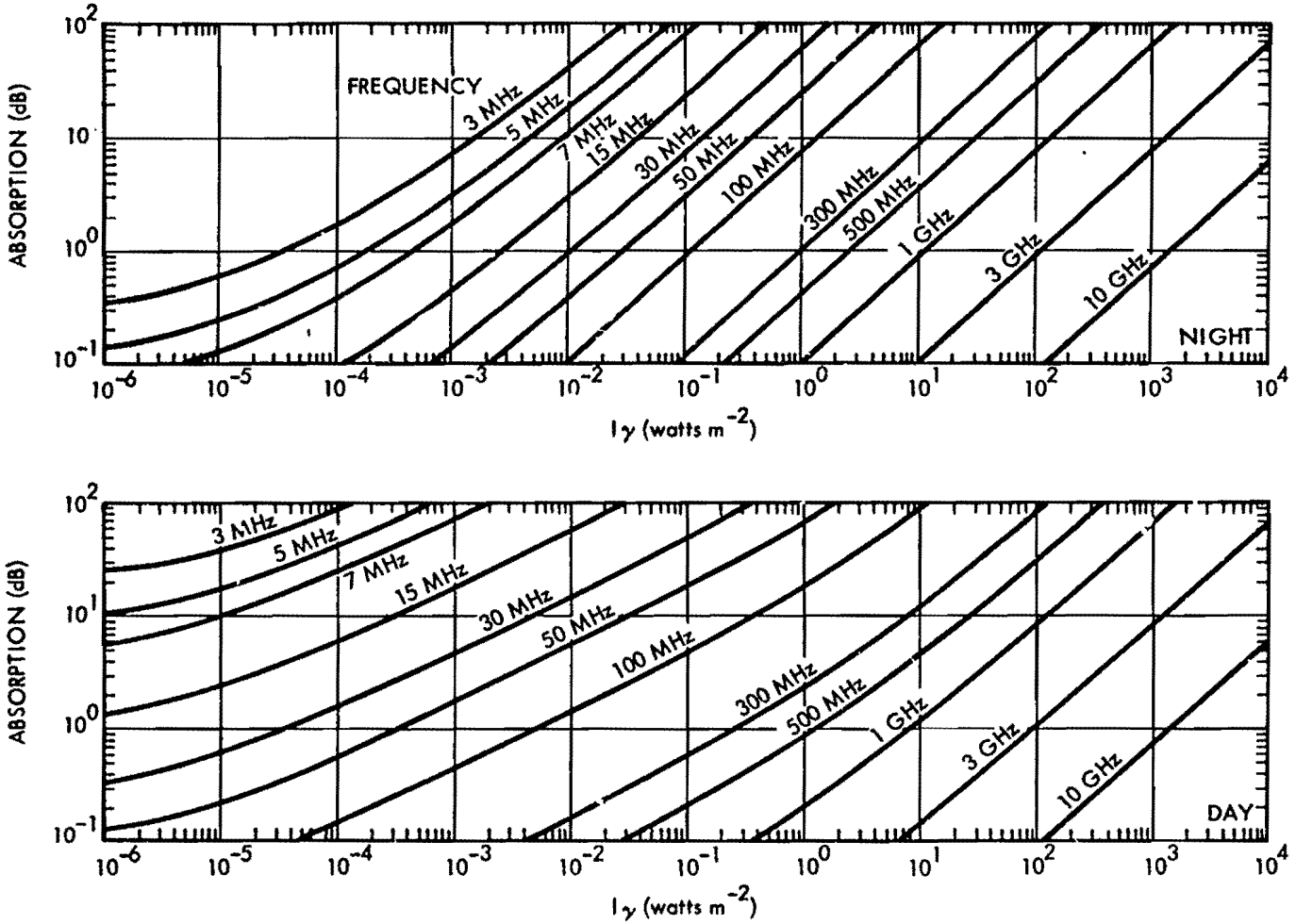

Figure 8-48. [redacted] One-Way Vertical Absorption Due to Gamma Rays [redacted]

[redacted]

Problem 8-7 Calculation of Absorption Outside the Fireball Due to Beta Particles [redacted]

[redacted] Figures 8-49 through 8-51 are used to estimate the absorption outside the fireball region caused by beta particle ionization when the fission debris is above 60 km. If the debris is below 60 km, the absorption caused by beta particle ionization can be computed by the methods described in Problem 8-4.

[redacted] When the fission debris is above 60 km, the location of the beta particle absorption region with respect to the debris region is determined by the geomagnetic field (see paragraph 8-4). Most of the absorption occurs between the altitudes of 60 and 80 km. The predictions of absorption apply to beta particle radiation from fission debris that is uniformly distributed in a thin pancake-shaped region.

[redacted] Obtain the debris altitude, h_d, and debris radius, R_d, by the methods described in Problems 8-1, 8-2, or 8-3. If the detonation altitude, h_o, is greater than 85 km and the time after burst is greater than 10 minutes, determine the maximum debris altitude, h_m (km). Compute h:

$$h = h_d \quad \begin{cases} h_o < 85 \text{ or if} \\ h_o \geq 85 \text{ and } t < 10 \text{ minutes.} \end{cases}$$

$$h = h_m \qquad h_o \geq 85 \text{ and } t > 10 \text{ minutes.}$$

Enter Figure 8-49 with h and φ, the magnetic dip angle at the burst point to obtain Δ_β, the offset of the beta particle absorption region. If the magnetic dip angle at the burst point is not known, it can be obtained from Figure 8-54 as described in Problem 8-9.

[redacted] There are two beta particle absorption regions for each debris region; one is in the burst region and is offset a distance Δ_β from ground zero toward the nearest magnetic pole (see Figure 8-49), and the other is in the conjugate region and is offset from the conjugate of ground zero toward the nearest magnetic pole. Location of the conjugate of ground zero can be estimated from Figure 8-53 as described in Problem 8-8. The horizontal extent of the beta particle absorption region is approximately the same as that of the debris region (this neglects convergence of the magnetic field).

[redacted] If the propagation path passes through a beta particle absorption region, the one-way absorption can be found by the following procedure:

1. Determine the debris region fission yield, W_F':

$$W_F' = W_F \qquad h_o \leq 120 \text{ km}$$

$$W_F' = FF\ W_F \qquad h_o > 120 \text{ km}$$

where FF is the fraction of the total weapon fission yield in the debris region (see Problem 8-3).

2. Enter Figure 8-50 with debris region fission yield, W_F', time after burst, t, and debris radius, R_d, to obtain N_β. If the propagation path passes through more than one beta particle absorption region, compute the value of N_β for each region and use the sum to compute the one-way vertical absorption.

3. Enter Figure 8-51 with N_β, the frequency, f, and the time of day (day or night) to obtain A_β', the one-way vertical absorption. Compute A_β, the one-way absorption:

$$A_\beta = A_\beta' \sec \theta,$$

where $\sec \theta$ is the secant of the angle of incidence of the propagation path at 65 km which may be determined by the methods described in Problem 8-10.

[redacted]

[redacted]

Example 1

Given: A 1 Mt weapon, 50% fission, detonated at an altitude of 80 km at a location where the magnetic dip angle is 60° during daytime.

Find: The one-way absorption resulting from beta particle ionization for a 400 MHz signal 5 min after burst if sec $\theta = 3$.

Solution:

a. By the methods described in Problem 8-1, the debris height and radius are determined to be:

$$h_d = 305 \text{ km},$$

$$R_d = 200 \text{ km}.$$

b. Since $h_o < 85$ km,

$$h = h_d = 305 \text{ km}.$$

c. From Figure 8-49, $\Delta_\beta = 150$ km for $h = 305$ km, and $\theta = 60°$.

d. Since $h_o < 120$ km,

$$W_F' = W_F = 0.5 \text{ Mt}.$$

e. From Figure 8-50, $N_\beta = 4 \times 10^7$ betas cm^{-2} sec^{-1} for $W_F' = 0.5$ Mt, $t = 300$ sec, and $R_d = 200$ km.

f. From Figure 8-51, $A_\beta' = 2$ dB; therefore,

$$A_\beta = A_\beta' \sec \theta = 6 \text{ dB}.$$

Answer: There are two absorption regions caused by beta particle ionization. One is in the burst locale and is centered 150 km towards the nearest magnetic pole. The other is on the opposite side of the magnetic equator and is centered 150 km towards the nearest magnetic pole from the conjugate of the burst point. The horizontal radius of each absorption region is 200 km. The one-way path absorption for a 400 MHz signal passing through either absorption region is 6 dB.

Example 2

Given: A 1 Mt weapon, 50% fission, detonated at an altitude of 300 km at a location where the magnetic dip angle is 60° during daytime.

Find: The one-way absorption resulting from beta particle ionization for a 40 MHz signal 60 min after burst if the ground terminal is at burst ground zero, the propagation path is at an elevation of 15° along a zero degree magnetic azimuth, and sec $\theta = 3.4$.

Solution:

a. By the methods described in Problem 8-3, the height, h_d, radius, R_d, maximum altitude of rise, and fraction of the debris, FF, for the three debris regions (see Figure 8-18) are found to be:

Debris Region	h_d (km)	R_d (km)	h_m (km)	FF
1	390	170	550	0.25
2	550	500	800	0.2
3	390	170	550	0.35

b. Since $h_o > 85$ km and $t > 10$ min:

$$h_1 = h_{m1} = 550 \text{ km},$$

$$h_2 = h_{m2} = 800 \text{ km},$$

$$h_3 = h_{m3} = 550 \text{ km}.$$

c. From Figure 8-49, the beta particle absorption region offsets are:

$$\Delta_{\beta 1} = 300 \text{ km},$$

$$\Delta_{\beta 2} = 450 \text{ km},$$

$$\Delta_{\beta 3} = 300 \text{ km}.$$

d. Since $W_F = 0.5$ Mt, the fission yields contained in the debris regions are:

$$W_{F1}' = 0.125 \text{ Mt},$$

$$W_{F2}' = 0.1 \text{ Mt},$$

$$W_{F3}' = 0.175 \text{ Mt}.$$

[redacted]

[redacted]

e. Entering Figure 8-50 with the debris radii from "a," the fission yields from "d," and a time t = 3600 sec, the following values of N_β are obtained:

$$N_{\beta 1} = 10^6 \text{ betas cm}^{-2} \text{ sec}^{-1},$$

$$N_{\beta 2} = 8 \times 10^4 \text{ betas cm}^{-2} \text{ sec}^{-1},$$

$$N_{\beta 3} = 1.75 \times 10^6 \text{ betas cm}^{-2} \text{ sec}^{-1},$$

f. A sketch of the location of the absorption regions in the burst locale caused by beta particle ionization is shown in Figure 8-52. The propagation path chosen for this example traverses the absorption regions caused by all three debris regions. Thus, the values of N_β for each debris region are added together before finding the absorption.

$$N_\beta = N_{\beta 1} + N_{\beta 2} + N_{\beta 3}$$
$$= 2.8 \times 10^6 \text{ betas cm}^{-2} \text{ sec}^{-1}$$

g. From Figure 8-51, the one-way vertical absorption for a 40 MHz signal is

$$A'_\beta = 40 \text{ dB}$$

and

$$A_\beta = A_\beta \sec \theta = 136 \text{ dB}.$$

Answer: The one-way path absorption for a 40 MHz signal propagating on the path as described above 60 min after a 1 Mt (W_F = 0.5 Mt) daytime burst at 300 km is the sum of the absorptions caused by all three debris regions and is 136 dB.

[redacted] *Reliability* [redacted]: The procedures given for computing absorption due to beta particle ionization are based on simplified debris, atmospheric chemistry, and geometry models. More detailed models are required for most radar and communication system problems.

[redacted] *Related Material* [redacted] See paragraphs 8-4, 8-5, 8-8, 8-13, 8-14, and 8-15, and Problems 8-1, 8-2, and 8-3.

[redacted]

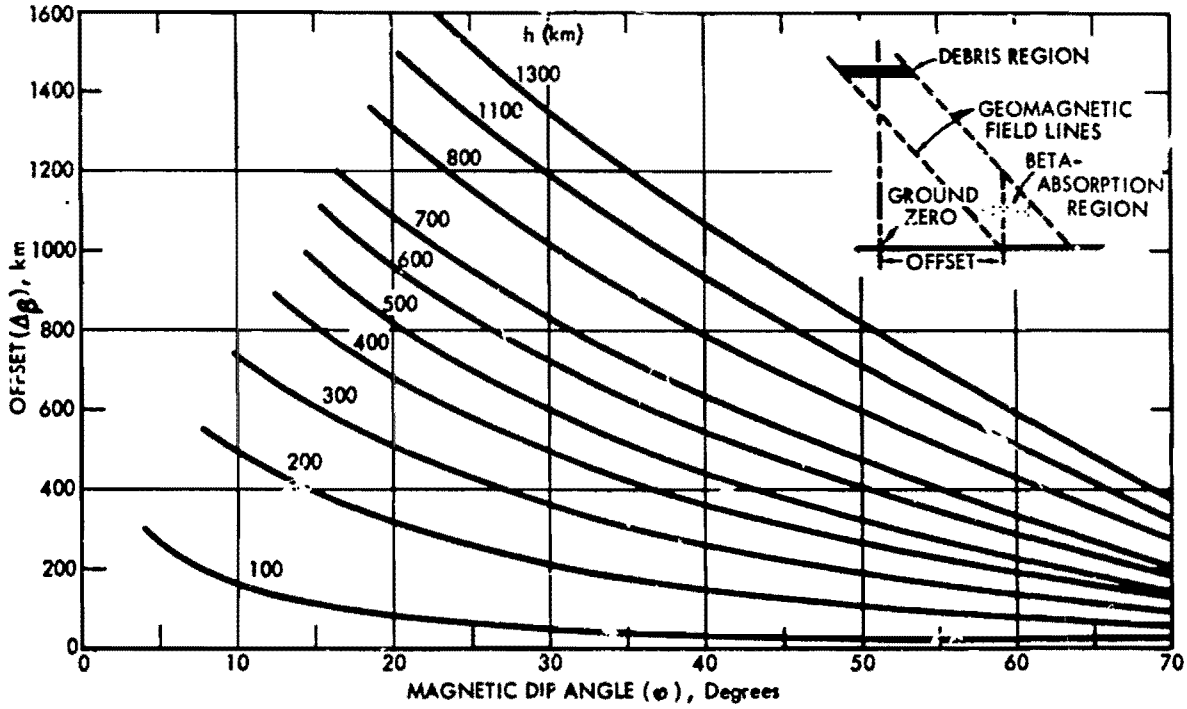

Figure 8-49. [redacted] Offset of Beta-Absorption Region [redacted]

[redacted]

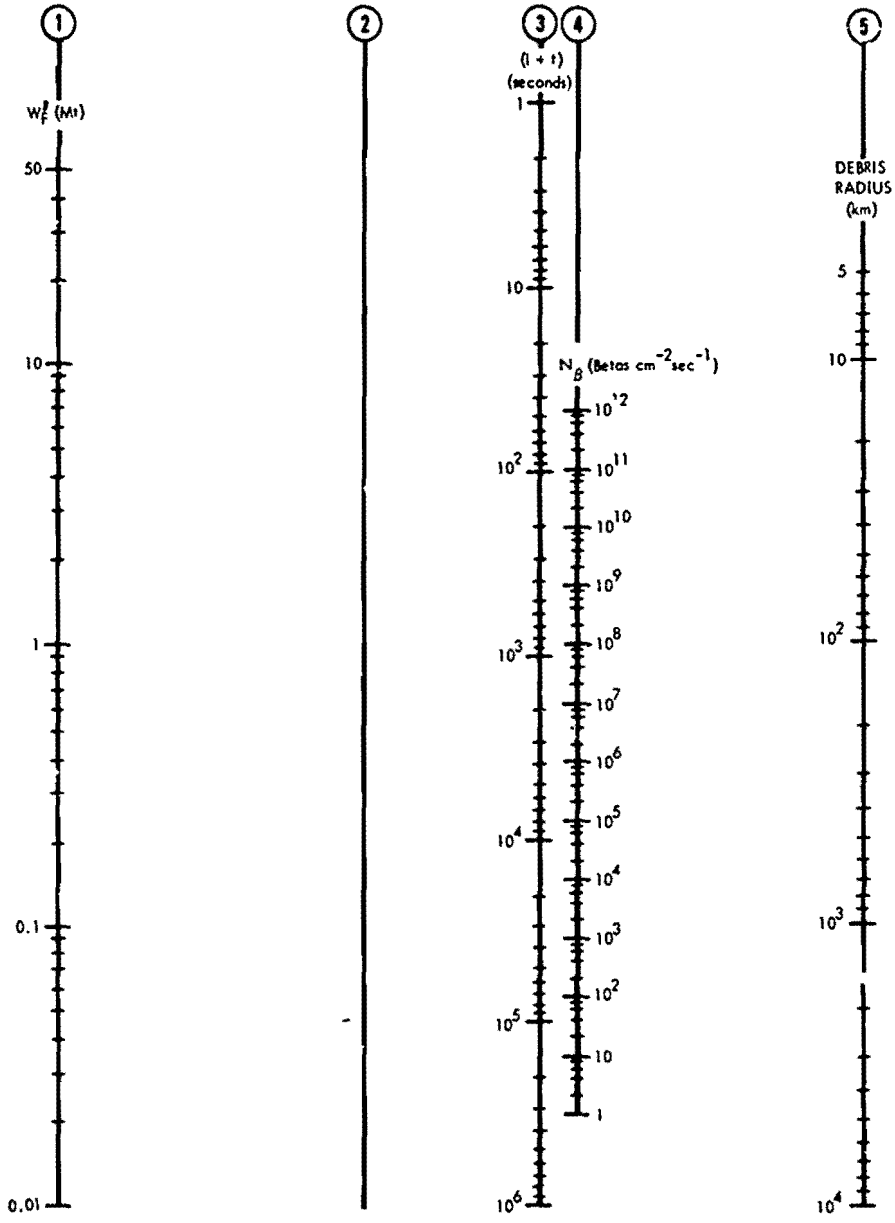

INSTRUCTIONS: To find N_β connect a straight line from fission yield (Scale 1) to time after detonation (Scale 3- this is a 1 + t scale). Mark the point of intersection of this line with Scale 2. Then draw a straight line from this point to the appropriate debris radius on Scale 5. The intersection of the latter line with Scale 4 is N_β.

Figure 8-50. [redacted] Beta Radiation Intensity Nomogram [redacted]

[redacted]

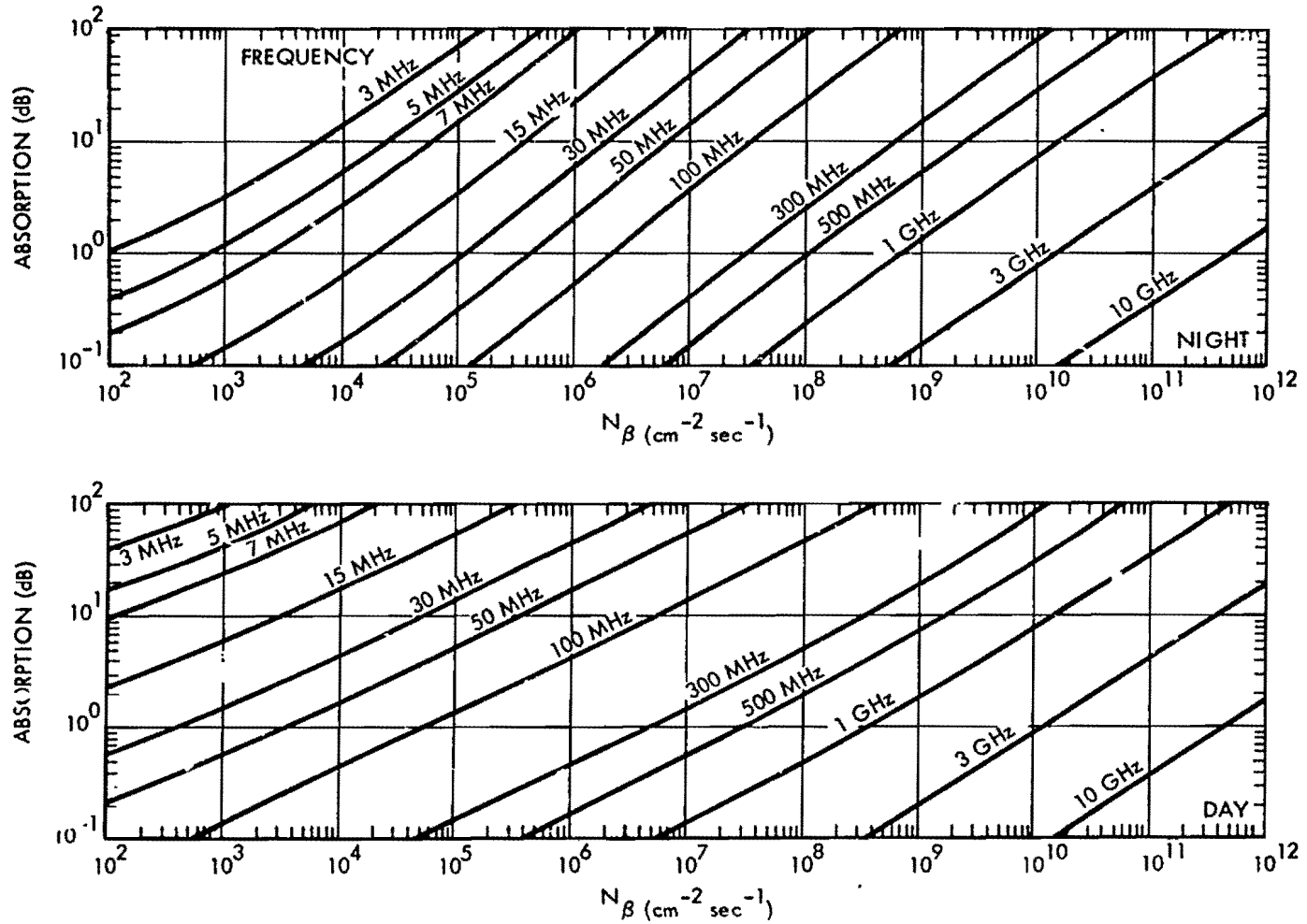

Figure 8-51. [redacted] One-Way Vertical Absorption Due to Beta Particles, Debris Altitude Above 60 km [redacted]

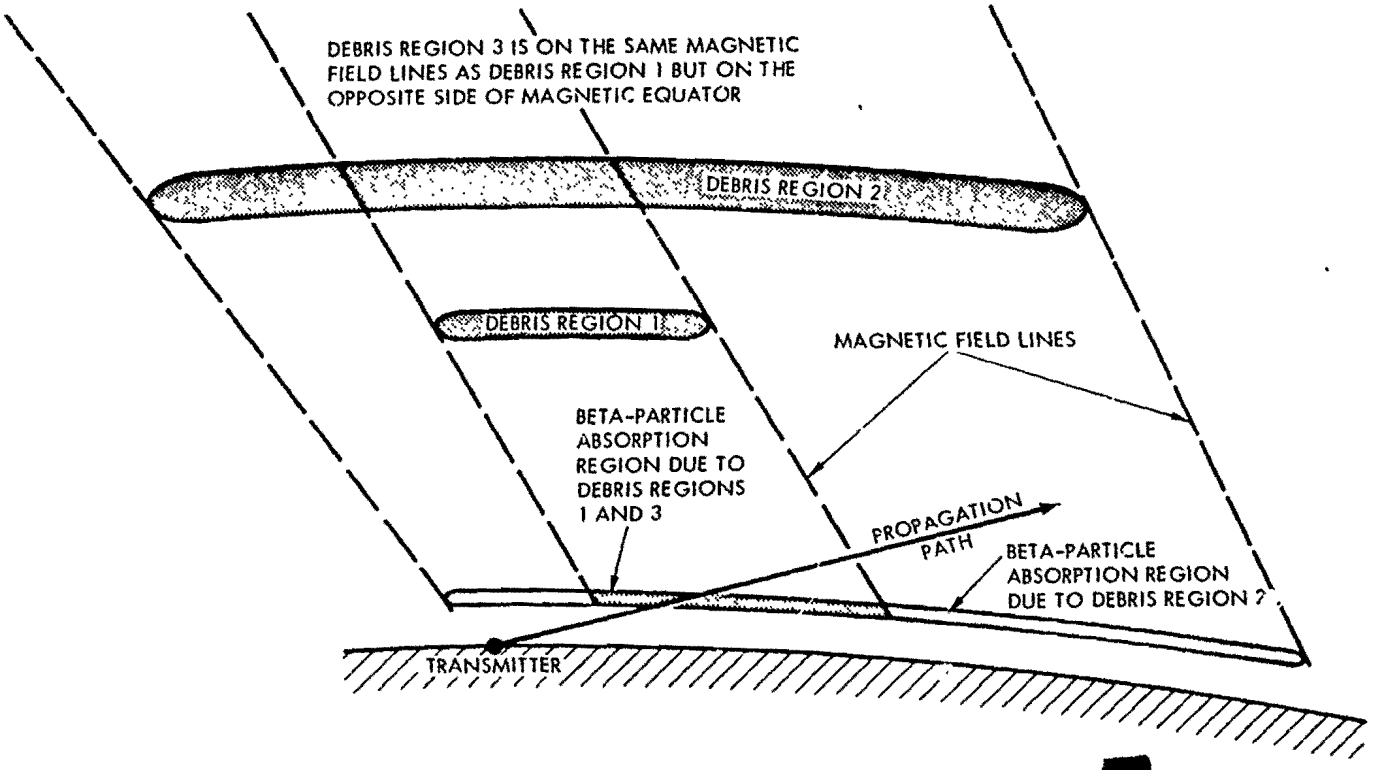
DEBRIS REGION 3 IS ON THE SAME MAGNETIC FIELD LINES AS DEBRIS REGION 1 BUT ON THE OPPOSITE SIDE OF MAGNETIC EQUATOR
DEBRIS REGION 2
DEBRIS REGION 1
MAGNETIC FIELD LINES
BETA-PARTICLE ABSORPTION REGION DUE TO DEBRIS REGIONS 1 AND 3
PROPAGATION PATH
BETA-PARTICLE ABSORPTION REGION DUE TO DEBRIS REGION 2
TRANSMITTER

Figure 8-52. Sketch of Absorption-Region Geometry for Example 2

[redacted]

Problem 8-8 Magnetic Conjugate Map [redacted]

[redacted] Figure 8-53 presents the location of geomagnetic conjugate points on the earth's surface. Using the geographic coordinates of a given point, enter Figure 8-53 on the straight-line rectangular grid, and read the geographic coordinates of the magnetic conjugate point on the heavy curved grid.

[redacted] In reading Figure 8-53, note that the east-west curved dashed lines indicate conjugate latitude, plus for degrees north latitude and minus for degrees south latitude. Similarly, the north-south curved solid lines indicate conjugate longitude, plus for degrees east longitude and minus for degrees west longitude:

[redacted] *Example* [redacted]

Given: Geographic coordinates 45°N, 77°W (point near Ottawa, Canada).

Find: The coordinate of the conjugate point.

Solution: The given coordinates occur at the intersection of the -71° and -93° heavy grid lines.

Answer: The approximate geographic coordinates of the conjugate point are 71°S and 93°W.

[redacted] *Reliability* [redacted] In addition to uncertainties in the geomagnetic field, distortions of the geomagnetic field caused by the burst may persist for tens of seconds. Thus, the locations of conjugate debris and beta particle ionization regions may be significantly different than predicted by Figure 8-53.

[redacted] *Related Material* [redacted] See paragraph 8-4.

[redacted]

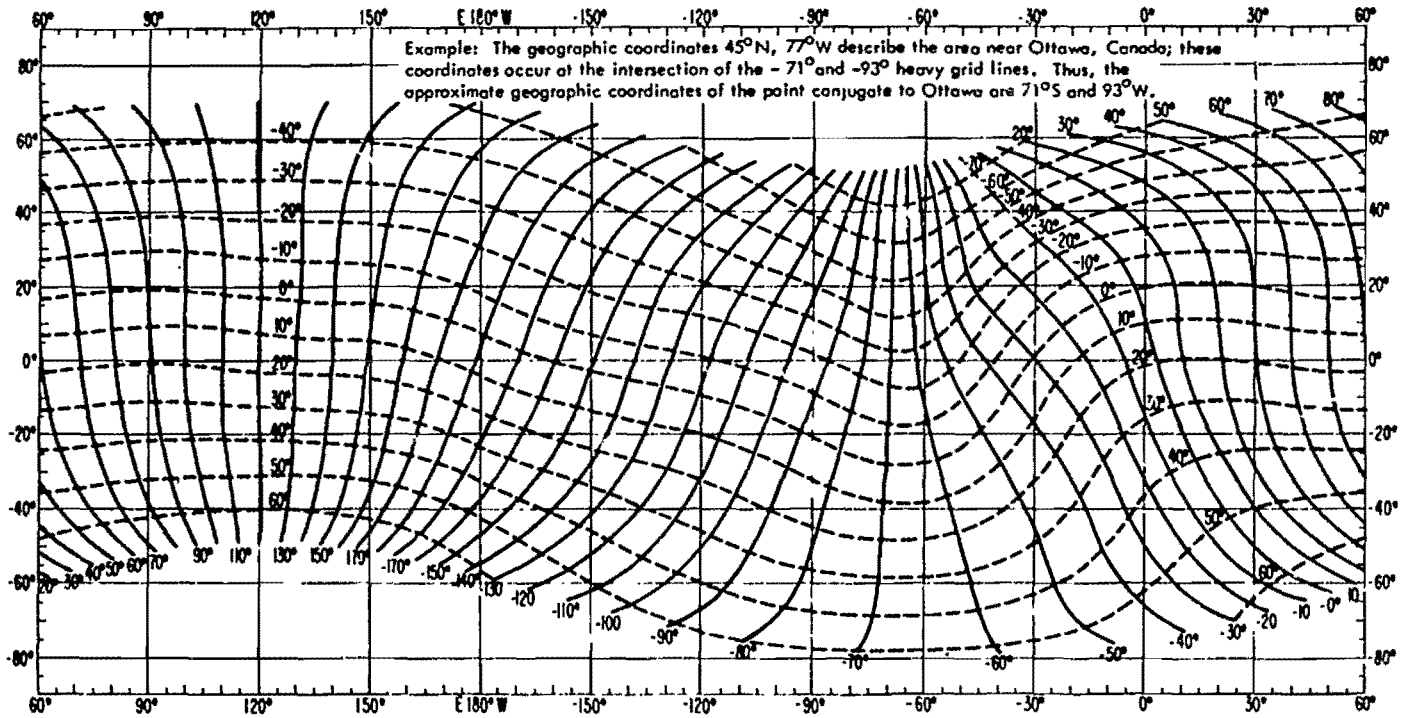
Example: The geographic coordinates 45°N, 77°W describe the area near Ottawa, Canada; these coordinates occur at the intersection of the -71° and -93° heavy grid lines. Thus, the approximate geographic coordinates of the point conjugate to Ottawa are 71°S and 93°W.

Figure 8-53. [redacted] Magnetic Conjugate Map [redacted]

[redacted]

Problem 8-9 Geomagnetic Dip Angle Map [redacted]

[redacted] Figure 8-54 presents the geomagnetic dip angle (declination) as a function of the geographic coordinates of a position on the earth's surface.

[redacted] *Example* [redacted]

Given: A point with geographic coordinates 40°N latitude, 100°W longitude.

Find: The geomagnetic dip angle.

Answer: From Figure 8-54 the magnetic dip angle is 70°.

[redacted] *Reliability* [redacted] Figure 8-54 shows the geomagnetic dip angle for undisturbed magnetic field conditions. The geomagnetic field may be distorted for tens of seconds after a nuclear detonation. Therefore, the locations of the debris and beta particle ionization regions may differ significantly from those predicted by Figure 8-54.

[redacted] *Related Material* [redacted] See paragraph 8-4.

[redacted]

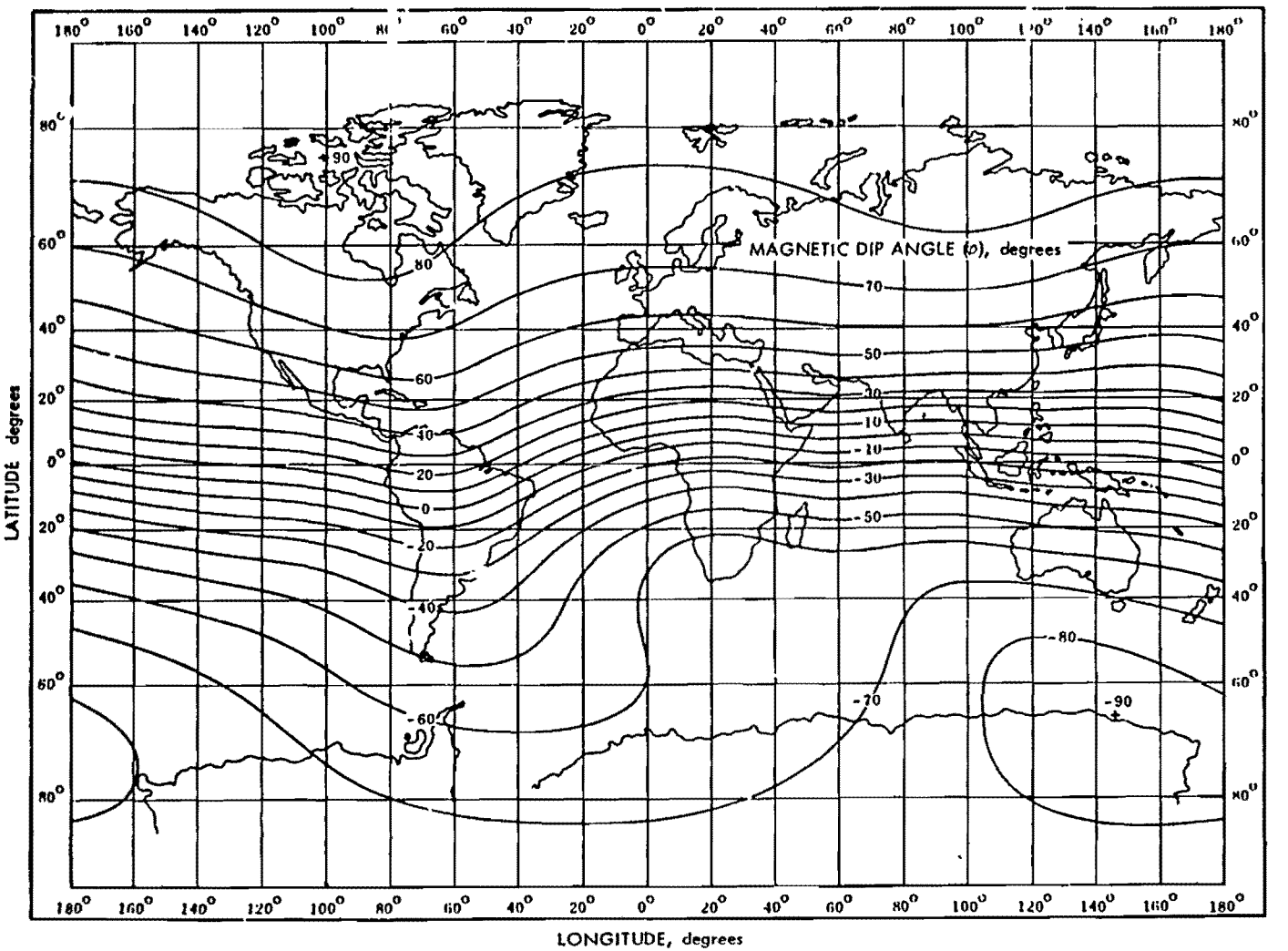

Figure 8-54. [redacted] World Map of Magnetic Dip [redacted]

[redacted]

Problem 8-10 Secant θ Chart [redacted]

[redacted] Figure 8-55 presents the secant of the angle of incidence of a ray path at 65 km altitude as a function of elevation angle or distance from the ground terminal to E- and F-region reflection points. The angle of incidence, θ, is illustrated in the sketch in Figure 8-55.

[redacted] *Example 1* [redacted]

Given: A propagation path with a 10-degree elevation angle (β).

Find: The horizontal distance from the ground terminal to the point where the propagation path intersects 65 km altitude, and the secant of the angle of incidence θ at the intersection.

Solution: Enter Figure 8-55 on the line sloping downward to the right labeled 10 degrees. Locate the intersection of this line with the line sloping upward to the right labeled h = 65 km. The abscissa of this intersection is the horizontal distance, and the ordinate is secant θ.

Answer: The horizontal distance from the ground terminal to the point where the propagation path intersects 65 km altitude is 320 km. The secant of the angle of incidence at the intersection is 4.6.

[redacted] *Example 2* [redacted]

Given: A HF propagation path that reflects from the F-region (300 km), 1500 km from the ground terminal.

Find: The horizontal distance from the ground terminal to the point where the propagation path intersects 65 km altitude, and secant θ at the intersection.

Solution: Enter the abscissa of Figure 8-55 at 1500 km. Proceed upward to the line labeled F-region Reflection Altitude (300 km). Note the elevation angle (β) corresponding to this point. Find the intersection of the elevation angle line with the line labeled D-region Absorption Altitude (65 km). The abscissa of this intersection is the desired horizontal distance, and the ordinate is secant θ.

Answer: The horizontal distance from the ground terminal to the point where the propagation path intersects 65 km altitude is 500 km. The secant of the angle of incidence at the intersection is 6.

[redacted] *Reliability* [redacted] The curves of Figure 8-55 are accurate for the simplified geometry assumed; however, the D, E, and F absorption and reflection altitudes are not single lines but occupy a volume of space which changes in ltitude with time of day and which may be affected by solar activity. Therefore, more detailed models are generally required for radar and communication system problems.

[redacted] *Related Material* [redacted] See paragraphs 8-1, 8-3, 8-4, 8-6, 8-7, 8-8, and Problems 8-1 through 8-6.

[redacted]

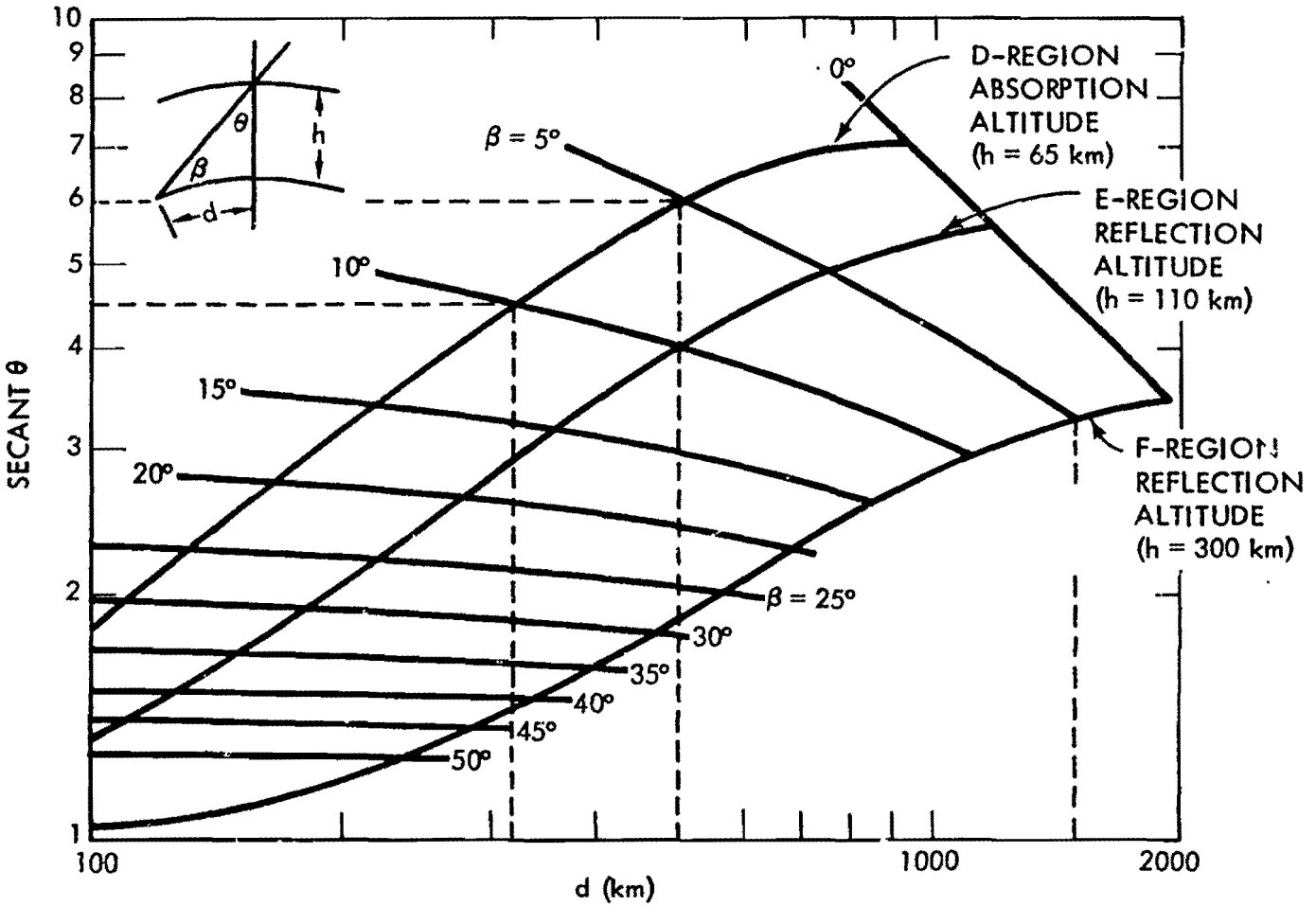

Figure 8-55. [redacted] Secant θ Chart [redacted]

[redacted]

[redacted] BIBLIOGRAPHY [redacted]

Atmospheric Ionization and Effects on Radar and Communications, A Bibliography, DASA 2069, Defense Atomic Support Agency, Washington, D.C., January 1968 [redacted]

Bibliography of Open and Unclassified Literature Pertaining to the Effects of High Altitude Nuclear Explosions, Parts I and II, Final Report, DASA 1795, Defense Atomic Support Agency, Washington, D.C., May 1966 [redacted]

DASA Reaction Rate Handbook, DASA 1948, Defense Atomic Support Agency, Washington, D.C., October 1967 [redacted] (will be revised as DNA 1948H during calendar year 1972).

Electromagnetic Blackout Handbook [redacted] Second Edition, Volume I: *Guide to Systems Effects* [redacted] DASA 1580, Defense Atomic Support Agency, Washington, D.C., December 1964 [redacted]

Electromagnetic Blackout Handbook [redacted] Second Edition, Volume II: *Nuclear Weapons Effects* [redacted] DASA 1580-1, Defense Atomic Support Agency, Washington, D.C., February 1965 [redacted]

High Altitude Tests Measurement Summary [redacted] DASA 1970, Defense Atomic Support Agency, Washington, D.C., September 1967 [redacted]

Knapp, W. S., and P. G. Fischer, *Aids for the Study of Electromagnetic Blackout*, DASA 2499, General Electric, TEMPO, Santa Barbara, Calif., July 1970 [redacted]

RANC IV, Computer Simulation of Radar Propagation in a Nuclear Environment, Volume I: *Computational Models*, DASA 2497-1, Defense Atomic Support Agency, Washington, D.C., July 1970 [redacted]

Weapon Effects Computer Code Directory, DASA 1727, Special Report 43, Defense Atomic Support Agency, Washington, D.C., April 1969 [redacted]

[redacted]

[redacted]

This page intentionally left blank

[redacted]

[redacted]

(This page intentionally left blank)

[redacted]